



HAL
open science

**Proceedings of the Second International Symposium on
Flutter and its Application, ISFA 2020, 12-14 May 2020,
Paris, France**

Xavier Amandolese, Pascal Hémon

► **To cite this version:**

Xavier Amandolese, Pascal Hémon. Proceedings of the Second International Symposium on Flutter and its Application, ISFA 2020, 12-14 May 2020, Paris, France. 2023. hal-04070879

HAL Id: hal-04070879

<https://cnam.hal.science/hal-04070879>

Submitted on 19 Apr 2023

HAL is a multi-disciplinary open access archive for the deposit and dissemination of scientific research documents, whether they are published or not. The documents may come from teaching and research institutions in France or abroad, or from public or private research centers.

L'archive ouverte pluridisciplinaire **HAL**, est destinée au dépôt et à la diffusion de documents scientifiques de niveau recherche, publiés ou non, émanant des établissements d'enseignement et de recherche français ou étrangers, des laboratoires publics ou privés.

Proceedings of the
Second
International Symposium on Flutter and its Application

Flutter



ISFA 2020
12-14 May 2020
PARIS, France

Edited by
X. Amandolese & P. Hémon

Preface

ISFA, the International Symposium on Flutter and its Application, is a cycle of conferences initiated by the Japan Research Association on Flutter (JRAF). After ISFA2016, organized in Tokyo in May 2016, the Second ISFA was supposed to be held in Paris on 12-14 May 2020. Unfortunately, due to the Covid19 sanitary crisis, ISFA2020 had to be cancelled.

However, to recognize the important work done by more than 160 authors from all over the world, we have decided to publish numerical proceedings of the symposium and to hold the PhD award. On behalf of the organizing committee of the Second International Symposium on Flutter and its Application (ISFA2020), we would like to warmly thank all authors for their scientific contribution to these proceedings.

To quote Dr. Jiro NAKAMICHI, Chair of ISFA2016, "the objectives of this symposium are to investigate the integration of traditional and fundamental technologies of flutter in a multidisciplinary research environment, involving aerospace engineering, mechanical engineering, civil engineering, architecture and biological engineering, and to establish new areas such as energy conversion, explorations of bio-flight mechanisms and propulsions through analytical and experimental concept of flutter phenomena."

As you will see in these proceedings, ISFA2020 would have been, after ISFA2016, a great opportunity for students, scholars, researchers and engineers from more than 21 countries to scrutinize and exchange on flutter and fluid-structure instability topics, encompassing a great and stimulating variety of disciplines and applications.

Sponsored by the Japan Research Association on Flutter, ISFA2020 was concurrently organized by the Hydrodynamics Laboratory (LadHyX/CNRS-Ecole Polytechnique), the Structural Mechanics and Coupled Systems Laboratory (LMSSC/Cnam) and the French aerospace agency (ONERA).

On behalf of the organizing committee, we would like to warmly thank the Japan Research Association on Flutter for their support, the international scientific committee for their work and all our partners and sponsors for their contributions.

Best regards and we hope you will enjoy reading these proceedings!

X. Amandolese and P. Hémon
Chairmen of ISFA2020

LOCAL ORGANIZING COMMITTEE

X. Amandolese (LMSSC/Cnam)

A. Geeraert (DAAA/ONERA)

P. Hémon (LadHyX/CNRS-Ecole Polytechnique)

C. Liauzun (DAAA/ONERA)

O. Marquet (DAAA/ONERA)

STEERING COMMITTEE

X. Amandolese (LMSSC/Cnam)

H. Arizono (Japan Aerospace Exploration Agency)

O. Flamand (CSTB)

P. Hémon (LadHyX/CNRS-Ecole Polytechnique)

E. de Langre (LadHyX/Ecole Polytechnique)

J. Nakamichi (Japan Aerospace Exploration Agency)

K. Saitoh (Japan Aerospace Exploration Agency)

INTERNATIONAL SCIENTIFIC COMMITTEE

T. Andrianne, U. Liège, Belgium
H. Arizono, JAXA, Japan
P. Bot, Ecole Navale, France
E. Caetano, U. Porto, Portugal
S. Cao, Tongji U., China
L. Carassale, U. Genova, Italy
C. Cesnik, U. Michigan, USA
J.-C. Chassaing, Sorbonne U., France
J. Cooper, U. Bristol, UK
G. Dimitriadis, U. Liège, Belgium
E. Dowell, Duke U., USA
O. Flamand, CSTB, France
F. Gosselin, Ecole Polytechnique Montréal, Canada
R. Govardhan, Indian Inst. of Sci., India
F. Huera Huarte, Univ. Rovira i Virgili, Spain
K. Hourigan, Monash U., Australia
K. Isogai, Kyushu U., Japan
E. de Langre, Ecole Polytechnique, France
A. Larsen, COWI, Denmark
Y.Z. Liu, Shanghai Jiao Tong U., China
H. Liu, Chiba U., Japan
J. Macdonald, U. Bristol, UK
A. Md. Mahbub, U. Town, China
C. Mannini, U. Florence, Italy
M. Matsumoto, U. Kyoto, Japan
G. Michon, ISAE-Supaéro, France
T. Mizota, Fukuoka Inst. of Tech., Japan
Y. Modarres-Sadeghi, U. Massachusetts, USA
J. Nakamichi, JAXA, Japan
O. Øiseth, NTNU, Norway
P. Oshkai, U. Victoria, Canada
D. Poirel, Royal Military College, Canada
S. Pospisil, ITAM, Czech Republic
D. Raveh, Fac. Aero. Eng., Technion, Israel
P. Reis, EPFL, Switzerland
S. Ricci, Politecnico di Milano, Italy
K. Saitoh, JAXA, Japan
G. Schewe, DLR, Germany
I. Taylor, U. Glasgow, UK
I. Yamamoto, U. Nagasaki, Japan

Contents

KEYNOTES	1
Aerodynamics and Flutter Problems of Sports Ball Flight. T. Mizota	2
Nonlinear flutter in practice. G. Dimitriadis	48
FLUTTER AND BUFFETING (AIRCRAFT, WING, SECTION-MODEL)	67
Nonlinear flutter analysis for very flexible wing. L. Yi, C. Xiaolong, Hehaibo . . .	68
Effects of turbulence models on the unsteady transonic aerodynamics of an oscillating airfoil. K. Isogai	78
Aeroelastic risks of interflap seals. R. Dubois, T. Andrianne, B. Bernay and G. Dimitriadis	79
Research on Elastic Wing Flutter Considering Propeller Slipstream. Z. Zhitao, X. Changchuan, Y. Lan and Y. Chao	80
Preliminary Combat Aircraft CFD Wind Tunnel Testing on Vortex Induced Loads. J.C.I. Zastrow	81
Aeroelastic stability assessment of a V-tail with integrated propulsion units. C. Koch and J. Arnold	82
Effect of a bluff-body wake on the flutter characteristics of a pitch-plunge aeroelastic system. C. Bose and G. Dimitriadis	92
Modal Analysis of Aerodynamic Damping of Light Dynamic Stall on a Pitching Airfoil. W. Mallik and D.E. Raveh	93
Unsteady Aerodynamic Response of a Swept Wing in the Presence of Shock Buffet. L. Poplinger and D.E. Raveh	106
Investigations into the dynamics of a pitch-plunge airfoil with non-smooth structural and aerodynamic nonlinearities. S.V. Gali, R.V. Bethi and J. Venkatramani	118
Nonlinear Aeroelastic Simulation of Thin Airfoil Model. H. Arizono, H.R. Kheirandish	129
Influence of laminarity on the aeroelastic behaviour of the NLR7301 aerofoil. H. Mai, M. Braune and A. Hebler	134
Static aeroelastic analysis of spanwise variable camber morphing wings with corrugated structures. K. Soneda, T. Yokozeki, T. Imamura and N. Tsushima	135
Experimental and theoretical investigation of stall flutter in an elastic wing. T. M. Currier, X. Amandolese and Y. Modarres-Sadeghi	145

Development of a CFD-based industrial procedure for supporting the aircraft certification with application to A400M T-tail flutter. E. Santos, J. Barrera, Á. Martínez, P. Martínez, V.R. de la Cruz, F. Arévalo, M. Karpel and H. Climent	146
Aeroelastic stability of a flexible high aspect-ratio wing with an imperfect end-support. M. Riazat, M. Kheiri	156
Nonlinear flutter instability with laminar flow model. J. Moulin and O. Marquet	166
Numerical and wind tunnel studies of highly flexible composite plates for HALE wing aeroelastic tailoring applications. O. Montagnier, B. Kirsch, and T.M. Faure	167
FLUTTER (BLADE, WIND TURBINE, PROPELLER)	177
Study on influence of tip vortex on aerodynamic noise of half ducted propeller fan for air conditioner. T. Iwase, T. Kishitani	178
The investigation of the design parameters influence on blade flutter boundaries. F. Abdukhakimov, M. Kolotnikov, P. Makarov and V. Vedeneev	187
Experimental Evidence of Coupled-Mode Flutter in Relatively Large-Scale Wind Turbine Blades. P. Boersma, B. Benner, T. Currier, Y. Modarres-Sadeghi	188
Numerical investigation of flutter in low-speed transonic fan. Q. Rendu and M. Vahdati	189
Diagnostics of the aeroelastic vibrations of aircraft gas turbine engine blades at bench tests. S. Danilkin, V. Shkurov, T. Mazikina, D. Redkin and V. Teleshev	190
Coupling DNS-1DOF for the Simulation of Transition Induced Vibration over Marine Propeller Sections. S. George, A. Ducoin and J.A. Astolfi	191
Aerodynamic characteristics of wind turbines with various cross-sectional tower shapes. Y.C. Kim and Y. Tamura	193
FLUTTER IN AXIAL FLOW (PANEL, PIPE, FLAG)	195
Nonlinear Theoretical/Computational Model of a Plate in Hypersonic Flow with Arbitrary In-Plane Stiffness at the Boundaries. M. Freydin and E.H. Dowell	196
Nonlinear flutter analysis of a rectangular sheet in uniform flow. K. Hiroaki and M. Watanabe	206
Snap-through oscillation induced by uniform flow. H. Kim, J. Kim and D. Kim .	216
Why inverted flags flap: An experimental study. M. Tavallaeinejad, M.P. Paidoussis, M.F. Salinas, M. Legrand, M. Kheiri and R.M. Botez	217
The fluttering flag: Reynolds number, mass ratio, and mode shape. R.C. Mysa, K. Venkatraman	227

Flutter and drag of a highly deformable beam under flow. T. Leclercq, N. Peake and E. de Langre	241
Experimental and Theoretical Investigation into the Dynamics of A Pipe Simultaneously Subjected to Internal and External Flows. A.R. Abdelbaki, A.K. Misra and M.P. Païdoussis	242
Flapping dynamics and heat transfer of turbulent channel flow with dual inverted flags. Y. Chen and Y. Liu	243
Investigation of a panel flutter under different initial disturbances. A.S. Shishaeva, V.V. Vedeneev, G.B. Sushko, A.A. Aksenov	244
Experiments on the Aeroelastic Stability of Plates in High Subsonic and Low Supersonic Flow. J. Lübker	245

FLAPPING WING, PITCHING FOIL **247**

Quasi-nonlinear Aeroelastic Analysis of a Membrane-type Flapping Wing Utilizing Structural Nonlinearity. H. Nagai, K. Nakamura, M. Murozono, K. Fujita, H. Arizono, S. Nagasaki and S. Yashiro	248
Transitionary flight of a flapping wing flyer: A two dimensional perspective. R. Sundar, D. Majumdar and S. Sarkar	258
Hydrodynamics of forced pitching hydrofoil. Z. Muhammad and Md. Mahbub Alam	259
Nonlinear aeroelastic behavior of a flapping wing with low-order chord-wise flexibility. D. Majumdar, C. Bose, and S. Sarkar	260
Hydrodynamic interaction of self-propelled flapping wings in an infinite array. L. Benetti Ramos, G. Raynaud, O. Marquet, M. Bergmann and A. Iollo	261
Survival of the fastest: evolving wing shapes for flapping locomotion. S. Ramanarivo, T. Mitchel and L. Ristroph	262

FLUTTER IN BIOMECHANICS AND BIO-INSPIRED SYSTEMS **263**

Elastic oscillating fin technology and its application to robotic fish. I. Yamamoto	264
Fluid-structure interaction dynamics of a flexible filament in the wake of an elliptical bluff body. R. Chatterjee, C. Bose, S. Gupta and S. Sarkar	270
Bifurcation behavior in vocal folds and its impact on physiological conditions. J. Emilian, V.S. Kanduri, C. Bose, J. Venkatramani and J. Horacek	271
Symmetry-breaking of a flexible splitter plate: experiment and quasi-static model. M. Couliou, R. Allandrieu, J-L. Pfister and O. Marquet	272
Stability and resolvent analyses of boundary-layer flows interacting with finite-length visco-elastic coatings. J-L. Pfister and O. Marquet	273
Fluid-structure interaction in plant- and coral-inspired biomechanics problems. F.P. Gosselin	274

FLUTTER IN SPORTS ENGINEERING **275**

- Experiment and Numerical Simulation of a Rotating Pipe in Flight.** G. Kato, Y. Naito, H. Tanigawa, J. Ishimoto, M. Nakano, T. Noguchi, K. Hirata 276
- Roughness in sports aerodynamics: the cricket ‘reverse’ swing.** L. Tadrist, S. Naresh, A. Intesaaf and T. Andrianne 277

FLUTTER OF BRIDGES **279**

- On the roles of small-scaled vortices in bridge wind engineering.** D. Gao, W. Chen and H. Li 280
- The influence of angle of attack on twin-box bridge deck flutter.** A. Larsen and M. Rønne 281
- Re-evaluation of aerodynamic stability of suspension bridges in Seto-Ohashi Bridges.** N. Toyama, M. Takeguchi and T. Hanai 291
- Study on direct identification of rational function approximation coefficients of self-excited forces.** H. Katsuchi, H. Yamada and H. Irpanni 301
- Flutter stabilization of super long span suspension bridges with aerodynamic countermeasures.** Y. Ge, Y. Yang, L. Zhao and F. Cao 311

VIV AND GALLOPING **321**

- Effects of the existence of small protruding lips of flanges of a diagonal member in a steel truss bridge on aerodynamic vibration.** K. Matsuda, K. Kato, N. Cao and K. Shigetomi 322
- Wake features of a rectangular cylinder undergoing unsteady galloping oscillations in smooth and turbulent flow.** C. Mannini, T. Massai 332
- Assessing maximum amplitude and corresponding frequency for vortex-induced vibrations.** Ø. M. Ellingsen, X. Amandolese, P. Hémon 333
- Flow-Induced Vibrations of a periodically rotating circular cylinder.** F. Huera-Huarte 342
- Stochastic analysis of vortex-induced vibrations by means of a randomized wake-oscillator model.** V. Denoël 343
- Dependence of cross-sectional aspect ratio and attack angle on forces and wake of elliptical cylinder.** X. Shi, Md. Mahbub Alam and H. Bai 344
- Observation of galloping on four-bundled conductors transmission line.** H. Matsumiya, T. Yukino, T. Nishihara, M. Shimizu and S. Taruishi 353
- Flow-Induced Vibrations of Tandem Cylinders in the Transcritical flow regime.** R. Dubois, G. Dimitriadis and T. Andrianne 354
- Vortex Induced Vibration Analysis of a Cantilevered Hydrofoil by Laser Vibrometry and TR-PIV.** J.A. Astolfi, P. Bot and L. Leroy 355
- Vortex induced vibration of two tandem cylinders in subcritical regime.** F. Rigo, V. Denoël and T. Andrianne 365

ENERGY HARVESTING

367

- Energy harvesting from FIV of different diameter cylinders. Md. Mahbub Alam, C. Zhenlin, Q. Bin and Y. Zhou 368
- Influence of the sweep angle on power extraction performance of a fully-passive oscillating-plate hydrokinetic turbine prototype. W. Lee, G. Dumas and P. Oshkai 376
- Reliability Study of a Fully-Passive Oscillating-Foil Turbine Concept. D. Iversen, W. Lee, G. Dumas, P. Oshkai 377
- A parametric study of vertical axis hydrokinetic turbines with chordwise-flexible blades. P-O. Descoteaux and M. Olivier 387
- Investigating the energy harvesting potential of intermittent oscillations in a pitch-plunge aeroelastic system. A.R. Paramasivam, A. Roy and J. Venkatramani 388
- Flow-induced vibration of a cylinder between two walls for energy harvesting. J. Kim and D. Kim 399
- Blockage effects on the fully-passive flapping-foil turbine. K. Gunther and G. Dumas 400
- Leaf Flutter Mechanism and its Application in the Wind Energy Harvesting. K. Wang, W. Xia, H. Feng and S. Shen 401
- Axial transducer for energy harvesting from galloping. M. Hage Hassan, V. Bernard, X. Amandolese and P. Hémon 402
- Numerical study on energy harvesting from VIV and galloping by a square cylinder. P. Han, G. Pan and B. Zhang 412
- Piezoelectric energy harvesting from panel flutter oscillation of laminated plates. M. Kameyama, K. Ikegami and N. Kasahara 413
- Numerical analysis of a flapping flat plate for power generation. C. Usoh, J. Young and J.C.S. Lai 421
- Aero-elastic oscillations of circle cylinder with power takeoff. P.R. Andronov, S.V. Guvernyuk, G.Y. Dynnikova 431
- Performance of Wind Vibrational Power Generator by Flow-Induced Vibration of a Prism and Magnetostrictive Material. R. Nagase, T. Kiwata, T. Kono and T. Ueno 432
- Parameterised reduced order modelling of flutter-induced piezoelectric energy harvesters. C. Hoareau, L. Shang and A. Zilian 433

CONTROL AND MITIGATION

435

- Control of vortex-induced vibration of a single bridge girder by using active wake slit jets. G-B. Chen, W-L. Chen and D-L. Gao 436
- Investigating Amplitude Death as a Possible Flutter Suppression Mechanism in a Pitch-Plunge Aeroelastic System. A.R. Paramasivam, S. Mondal and J. Venkatramani 437

Some computational aspects of active flutter suppression for co-design. E. Faisse, R. Vernay, F. Vetrano, D. Alazard and J. Morlier	438
Mitigating the galloping of a square prism with a purely non-linear energy sink. M.M. Selwanis, S.W. Rishmawi, G. Rosa Franzini, C. Béguin and F.P. Gosselin	439
Flutter Suppression Test of Two-dimensional Supercritical Wing in Transonic Region. K. Saitoh and N. Yoshimoto	440
Optimal wall deformation for mitigating the boundary layer instability. T. Leclercq and O. Marquet	450
Passive flutter control of aeroelastic wing with a flap-NES. C. Fernandez-Escudero, S. Prothin, G. Michon, E. Laurendeau and A. Ross	451
Mitigation of aeroelastic instability for rectangular tapered shape structure. O. Flamand	452
Vortex-induced vibration control research on Long-span Bridge by passive jets. Y. Wenhan, C. Wenli and L. Hui	462
Flutter suppression using magnetorheological dampers and a LMI-based controller. P.H. Foster Stangarlin, F.A. Ribeiro, R.M. Botez and D.D. Bueno	463
Passive alleviation of static and dynamic loads via aeroelastic tailoring of a composite wing. N. Fabbiane, F-X. Irisarri and A. Lepage	472
Mitigation of trailing edge flow-induced vibrations of hydrofoil with piezoelectric resonant shunt. L. Pernod, B. Lossouarn, J.A. Astolfi, J-F. Deü and X. Amandolese	483
Topology Optimization of Control Surface with Aeroelastic Effect. L. Jinan, G. Li, W. Xinjiang	484
 FLUTTER (FUNDAMENTALS)	 487
A new divergence mechanism. V. Vedenev	487
A Note on Mechanism of Two-Degree-of- Freedom Flutter. M. Tamayama and J. Nakamichi	498
 FLUTTER ANALYSIS (METHODS AND MODELS)	 509
A Deep Learning Approach to Model Nonlinear Aerodynamic Forces. H. Mei, H. Liao and J.H.G. Macdonald	510
Aeroelastic optimisation of aeronautical composite structures considering uncertainties. M. Sharifi, A. Vicenti and J-C. Chassaing	511
Flutter Analysis of Large Flexible Aircraft based on Structural ROM Method and Nonlinear Substructure Method. A. Chao, X. Changchuan and Y. Chao	512
Parameter identification of fluid-rigid body interactions using data assimilation. J-C. Chassaing, V. Mons	521

Flutter analysis based on state-space model of unsteady vortex- lattice method. L. Yang, C. Xie and C. Yang	522
Investigating Stochastic Resonance in a Classical Flutter System using Recurrence Networks. H.S. Varun, M.S. Aswathy and S. Sarkar	530
A Long Short-Term Memory neural network-based self-excited force model of nonlinear post-critical flutter. W. Li, S. Laima and H. Li	531
Model-Free Nonlinear Flutter Forecasting in Fluid-Structural Systems with Multiple Varying Parameters. C. Riso, C.E.S. Cesnik and B.I. Epureanu . .	532
Response-Based Stability Analysis and Test Applications Using Parametric Flutter Margins. M. Karpel	543
Improvement of the Unsteady Two-color PSP Applicable to Wind- Tunnel Experiments Using Dynamically-vibrated Airfoil Models. A. Wakayama and D. Numata	544
Flutter Analysis of Wing Model with Metal Additive Manufacturing for Wind Tunnel Test. N. Tsushima, K. Saitoh, H. Arizono, and K. Nakakita	554
A Novel Feature-Based Recombined Deep Learning Method for Aeroelasticity. Y. Wang, R. Han and G. Chen	562
Structural and Aerodynamic Models for Aeroelastic Analysis of Corrugated Morphing Wings. N. Tsushima, H. Arizono, K. Soneda, T. Yokozeki, T. Imamura, and W. Su	572
Time domain and time spectral reduced order models for aeroelasticity. F. Di Donfrancesco, A. Placzek and J.-C. Chassaing	573
Assessment of flutter methods by numerical correlations with wind tunnel test data on U-tail configuration. S. Dequand, A. Geeraert and G-D. Mortchelewicz	583
Development of Bi-Luminophore Anodized-Aluminum Pressure-Sensitive Paint for Flutter Wind-Tunnel Experiment. D. Numata, and A. Wakayama	584
Self-excited force models of nonlinear coupled flutter and model parameter identification via free vibration sectional model test. L-D. Zhu, G-Z. Gao .	592

Keynotes

Aerodynamics and Flutter Problems of Sports Ball Flight

Taketo MIZOTA¹

¹Professor Emeritus of Fukuoka Institute of Technology, Fukuoka, Japan, mizota@fit.ac.jp

Keyword: sports ball aerodynamics, flutter, 3-D trajectory, golfball, baseball, soccer ball

Summary

The strange behavior of three kinds of sport balls flying in the air are studied.

First, the three-dimensional flight trajectory theory for golf ball has been described. The bank concept of a ball rotation axis was introduced instead of side spin one, which has been described for over 100 years. Drag and lift around the body axis of a golf ball in flight are converted into drag, lift, and lateral forces in ground coordinates by vector analysis. These results were verified by field experiments in still air and atmospheric boundary layer flow.

Next, the mechanism of strange orbit change of baseball ball has been studied. The research of pitching, yawing, and rolling knuckle balls focuses on the changes in surface seam position with slight rotation. The transition from laminar to turbulence boundary layer flow result in large shift of separation line. We are studying the SFF called front door ball or back door ball as a mechanism of the trajectory change of 2-seam ball and 4-seam ball. It also describes how to measure the aerodynamic three-component force and aerodynamic friction torque on the golfball and baseball ball by wind tunnel experiments.

Finally, the aerodynamic mechanism of the unstable behavior of a slowly rotating soccer ball was investigated. This phenomenon was clarified by the relationship between the unsteady force and the wake behaviour. Before in this study, in the supercritical Reynolds number region of the smooth sphere, the irregular change of Ω -shaped and two longitudinal vortices position had been discovered. This is topologically similar with the bound vortex and wing tip vortex of an aircraft in stable. This finding could be applied to the strange behavior of a soccer ball flying with supercritical flow due to the seam effect.

We will also report some topics and products that have been commercialized or are under development as the application examples of this work.

1 Introduction

Mehta¹ discusses cricket, baseball, and golf balls as a comprehensive report of

aerodynamic research on sports balls. Azuma² reports on the flight of various sports balls, including flight-related quantities from an aerodynamic point of view. He covered the physical factors related to flying sports not only for baseball, volleyball, shot put, soccer, table tennis, golf, tennis, but also for frisbees, boomerangs, spears and arrows.

(1) Golfball flight aerodynamics.

The golf balls are hit by various golf clubs such as wood, irons, and wedges. Professional golfers can fire balls at a maximum speed of 288 km / h (80 m / s) with a driver and a rotational speed of 10,000 rpm (183 rps) with a wedge. The maximum flight distance is more than 300m. This is a flight distance of more than 7,000 times the ball diameter, in which are biggest in the ball sports. Players are fighting with the technology of landing accuracy of pinpoint less than 1% of the total distances. Predicting the flight trajectory of a golf ball requires very accurate experiments in the aerodynamics.

The aerodynamic description of how a golf ball hooks and slices was described by J. J. Thomson³ in the concept of side spin. Golf instructors have explained this concept to golfers since then, to more than 100 years. Davies⁴ conducted an experiment in which a golf ball was given 8000 rpm (130 rps) of rotation and dropped in a wind tunnel airflow to identify aerodynamic force from its trajectory. The precise measurement of the aerodynamic force of a rotating golf ball has been performed by Bearman and Harvey⁵ using a 2.5 times larger ball. The two-dimensional results of numerical calculations have been good agreement with the experiment of two-dimensional flight trajectory.

Tavares et al.⁶ measured the decreasing rotational speed of a golf ball during flight by using a radar technique. As a result, the aerodynamic damping coefficient has been successfully measured. This was confirmed in our wind tunnel experiments.

The flight trajectory and the rotation speed of a golf ball in flying are easily detected nowadays with the advent of precise electronic measuring instruments using echoes of reflected radio waves.

The fact that the rotation axis is tilted from the Cartesian coordinate system can be explained by the construction of the rotation vector around each axis. However, it is physically difficult to understand that a golf ball with rigid rotation has two axes, such as back spin and side spin. Therefore, we explain the results of constructing a three-dimensional flight trajectory equation under the physical condition that one rotation axis has a bank angle to the X axis of the initial shooting plane.

By the way, Ohnishi⁷ and Jorgensen⁸ pointed out that the physical mechanism that changes the trajectory of a golf ball in three dimensions is not a side spin but a bank of spin axes. However, it was not formulated.

In this equation^{9,10}, the aerodynamic force, which is an external force, must be

determined by a wind tunnel experiment, so it can be called a semi-experimental method.

Four new technologies were developed in this golf ball research. (1) A technology for rotating a commercially available golf ball without a resonance speed of up to 200 rps in the wind tunnel flow. (2) Wind tunnel experimental technology that continuously measures aerodynamic and friction torque with high accuracy. (3) Measuring method of the flight distance in still air^{9, 10} or in the atmospheric boundary layer¹¹ have been developed. (4) New smoke wire method effective at flow speed up to at least 40 m / s ,10 times or more of conventional SW method.

As a product based on this theory, a hitting ball analyzer has been commercialized. The ball movement immediately after firing is shot with a camera while slightly changing the shooting time. From this image analysis, the initial conditions of the ball motion are detected. The subsequent ball flight trajectory is determined by this built-in equation of motion.

(2) Baseball ball flight aerodynamics.

According to Ichiro Tani¹², there is a report¹³ that this is an illusion that baseball curves appear to be curved despite the observation with a high-speed camera. In smooth ball rotation experiments by Maccoll¹⁴negative Magnus forces appear in a practical range. It was pointed out that the trajectory of the smooth ball does not change quantitatively unless the rotation speed increases significantly. However, in the next issue of Life, experienced catchers testify that the ball will curve. The magazine, Look¹⁵, provides evidence that not only curved balls, but also so-called straight balls, are curved. Early researchers may have been obsessed with the negative Magnus effect of the smooth spheres, ignoring the importance of baseball seam effects.

However, Tani¹⁶ performed a wind tunnel experiment on a rotating baseball ball and stated that a negative Magnus effect did not appear in a baseball ball and that the value of the lateral force generated by the seam effect caused a curved ball. Tani¹⁶ had also interested in the study of knuckle balls by Watts & Sawyer¹⁷. Ichiro made many achievements in the US Major League, but Japanese fluid mechanic scholar Ichiro pioneered baseball science, also.

One result of wind tunnel study state that the drag of the ball has Re dependence¹⁸, and another paper argues¹⁹ against to this issue. Although the effects of seams have been discussed, they are not fully understood. The knuckleball equation of motion was constructed by Watts & Sawyer¹⁷. Weaver²⁰, a student at the University of Calgary at the time, pointed out the effects of aerodynamic friction torque in an interesting question. An answer to this question is obtained in the current study. In recent years, new orbit changing balls have been recognized one after another. Recent performance

improvement and technical research of baseball pitchers themselves have made remarkable progress with the times. We will call them the scientists on the mound.

Modern pitchers throw balls at speeds ranging from 70 km / h (19 m / s) to 170 km / h (47 m / s). Rotational speeds range from 0 rpm (0rps) to 3000 rpm (50rps). Strangely changing balls, collectively known as knuckle balls and SFF, are created by the relationship between the direction of the axis of rotation and the seams. There are many types of changing balls, called straight balls, curves, shoots, sliders, and folk balls. In the baseball world, if the pitcher himself declares my ball to be such a changing ball, it tends to be recognized as it is. From the standpoint of conducting research, another definition is needed. Here, we describe the research results focusing on the initial state at the moment when the pitcher releases his hand.

The initial conditions refer to the initial speed U of the ball, the rotation speed N , the relationship between the ball seam and the rotation axis, the direction of the rotation axis, and the direction of travel of the ball. Only gravity and aerodynamic forces act on the flying ball. In this research, we deal with a changing ball called a magic ball. Motivated by this research, Mizuno Co. developed a sensor ball called MA-Q, will appeared in 5-2 (1).

(3) Slowly spinning soccer ball aerodynamics.

The last topics is a study on the magical change of a soccer ball flying with a slowly rotation. Phenomena such as balloons on going to the high sky exhibiting strange fluctuation behavior had been observed for a long time. Taneda²¹ explained this by observing bound vortices and random wake motion in the supercritical Re number region of a smooth surface sphere. Mizota²² described this phenomenon by adapting it to the erratic behavior of a weakly rotating soccer ball in flight. The soccer ball's flight speed ranges from 5m / s to 30m / s. In the smooth sphere, the flow is almost in the subcritical Re number range. The rotation speed is ranging 0 to 10 rps.

The surface of the soccer ball is made up of pentagonal and hexagonal panels. The 8-shaped panels have been also used since 2014. Between the panels there is a groove of about 1-2 mm deep seam. This makes the surface of the soccer ball rough, which has the effect of lowering the critical Re number. Due to this roughness, the boundary layer on the soccer ball surface becomes turbulent. It has the effect of lowering the resistance by flying in the supercritical region. At the same time, the random position change of the bound vortex and the wake is important for this phenomenon. The reaction force by the random movement of the vortex flow, quantitatively generates a random movement of the soccer ball. Research on recent differences in panel shape is also being conducted²³.

When a sports ball flies in the still air, it develops a three-dimensional motion under the

influence of aerodynamic force and gravity g . The aerodynamic factors related to the motion in the still air, when limited to the three types of balls discussed in this paper, are as follows.

- ① Geometric factors: ball diameter d , surface roughness (golf ball: dimple²⁴, baseball ball: seam, soccer ball: groove between surface panels),
- ② Kinematic factors: Initial velocity U , number of rotations N , relationship between ball advancing direction and rotation axis (or relation with seam),
- ③ Physical properties of air: air density ρ , static (dynamic) viscosity coefficient μ (ν) of air.

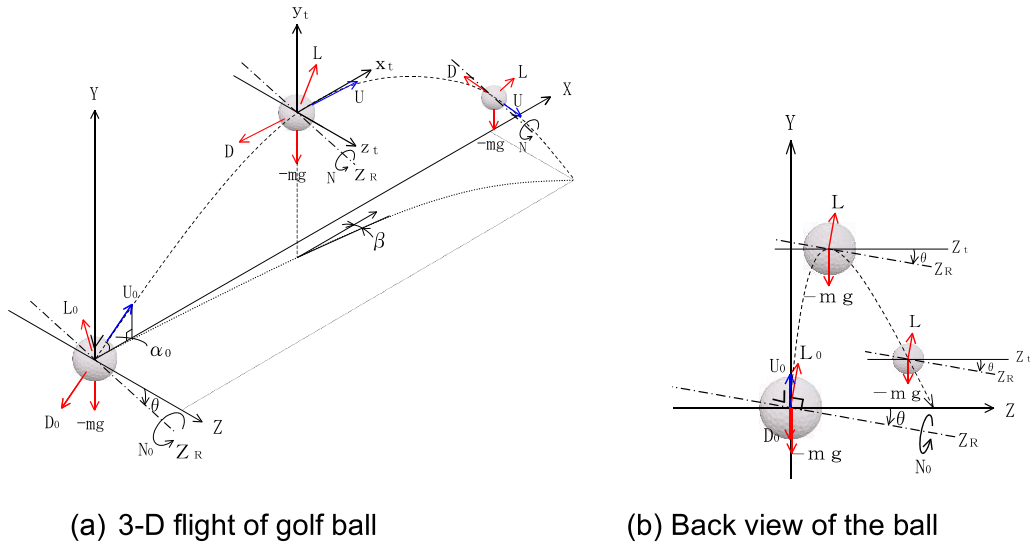
According to the results of the dimensional analysis, the aerodynamic force F (F_x , F_y , F_z and aerodynamic torque T) $= (D, L, S, M)$ on the ball is represented by the Reynolds number $Re = Ud / \nu$ and the spin parameter $Sp = \pi Nd / U$ (Tangential velocity of the ball surface with spin/ Ball speed). $D = C_D 0.5 \rho U^2 A$, $L = C_L 0.5 \rho U^2 A$, $S = C_S 0.5 \rho U^2 A$, $M = C_M 0.5 \rho U^2 A d$, $(C_D, C_L, C_S, C_M) = f(Re, Sp)$, D : Drag, L : Lift, S : Side force, M : Aerodynamic torque, (C_D, C_L, C_S, C_M) : Aerodynamic (drag, Lift, Side force, torque) coefficient.

2. Golf Ball 3D Flight Equation and Wind Tunnel Experiment^{9,10}

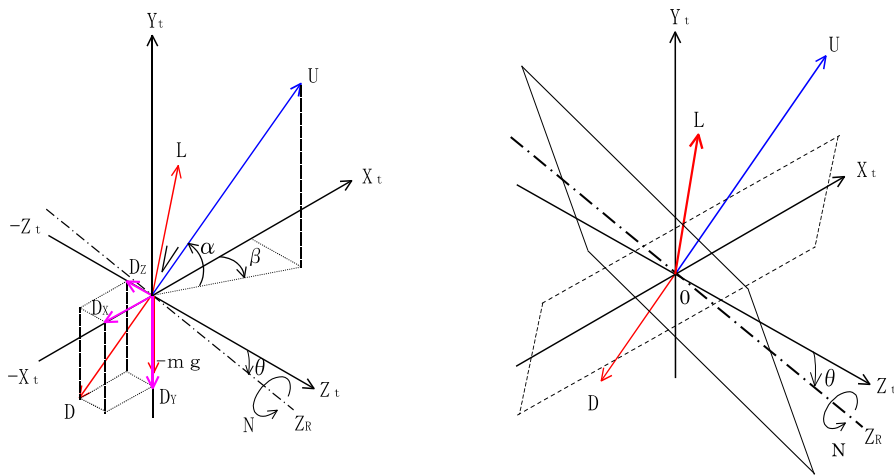
2-1 Three-dimensional flight theory of golf ball

The coordinate system of the equation of motion for a three-dimensional flight of a golf ball in the absence of wind are shown in Fig. 2-1 (a) and (b). The initial launch direction of the ball is in the XY plane. Each symbol is listed at the end of this section. The initial conditions for ball movement are determined at the time of recovery from impact deformation on the club surface. The equation of motion is built under the following assumptions:

- 1) The bank of the axis of rotation is determined by the ball's initial conditions, and this bank angle does not change until the ball lands on the ground.
- 2) When the axis of rotation is banked, the lift based on the body axis tilts, so a horizontal lateral force is generated.
- 3) In the initial state of the ball, the rotation axis of the ball has no yaw angle with respect to the initial firing direction. Even if a small yaw angle occurs, the lift does not change, and no lateral force is generated.



(a) 3-D flight of golf ball (b) Back view of the ball
 Figure 2-1(a), (b) Drag and lift on golf ball flight with banked spinning axes



(a) The drag D is opposite to the traveling direction U of the ball, (b) The lift L acts in a direction orthogonal to U and the rotation axis Z_R .

Figure. 2-2 Relationship between velocity U , drag D and lift L during ball flight.

The origin of the coordinate axes (X_t, Y_t, Z_t) is the center of the ball during flight.

(1) Drag D and lift L in bank angle θ

The drag vector D is in the opposite direction to the ball velocity vector U . Lift vector L is orthogonal to velocity vector U and rotation axis Z_R . Since the rotation axis direction is $Z_R (0, -\sin\theta, \cos\theta)$, the drag vector D and the lift vector L are as follows.

$$D = |D| (-\cos\alpha\cos\beta, -\sin\alpha, -\cos\alpha\sin\beta) \quad (1)$$

$$L = |L| (\sin\theta\cos\alpha\sin\beta + \cos\theta\sin\alpha, \cos\theta\cos\alpha\cos\beta, \sin\theta\cos\alpha\cos\beta) \quad (2)$$

(2) Aerodynamic force F_x, F_y, F_z in ground coordinate axis direction

Thus, the aerodynamic forces in the direction of the ground coordinate axes are as follows.

$$F_x = -1/2(C_D \cos \alpha \cos \beta + C_L (\sin \theta \cos \alpha \sin \beta + \cos \theta \sin \alpha)) \rho A V_B^2 \quad (3)$$

$$F_y = -1/2(C_D \sin \alpha - C_L \cos \theta \cos \alpha \cos \beta) \rho A V_B^2 - mg \quad (4)$$

$$F_z = 1/2(C_D \cos \alpha \sin \beta + C_L \sin \theta \cos \alpha \cos \beta) \rho A V_B^2 \quad (5)$$

Here, $|\mathbf{U}| = V_B = (V_x^2 + V_y^2 + V_z^2)^{1/2}$. (6)

(3) Orbital equation of motion and fluid friction torque

The flight trajectory was obtained by numerically calculating the following equation of motion by the integral progression method (Euler method).

$$\mathbf{F} = m d\mathbf{U}/dt \quad (7)$$

The initial rotational speed given by the club during the flight is reduced momentarily by the fluid friction torque as follows.

$$N(t+\Delta t) = -\rho A d C_m(t) V_B(t) 2\Delta t / (4\pi I) + N(t) \quad (8)$$

(4) Initial condition and measurement method of ball motion

The initial conditions of the flight speed and the rotation speed of the ball are given by the following equations.

$$V_x(0) = V_B(0) \cos \alpha_0 \quad (9)$$

$$V_y(0) = V_B(0) \sin \alpha_0 \quad (10)$$

$$V_z(0) = 0 \quad (11)$$

$$N(0) = N_0 \quad (12)$$

These initial conditions are obtained by photographing the ball motion immediately after launch with two flash and CCD camera sets at optimal time intervals. We select the light emission interval etc. so that two ball images are shot within the shooting screen. These initial motion conditions were obtained by the DLT method from two or more marks attached to the ball.

In an outdoor experiment described later, an initial lateral shift angle β_0 always exists. β_0 is also measured, and the coordinates are converted during calculation.

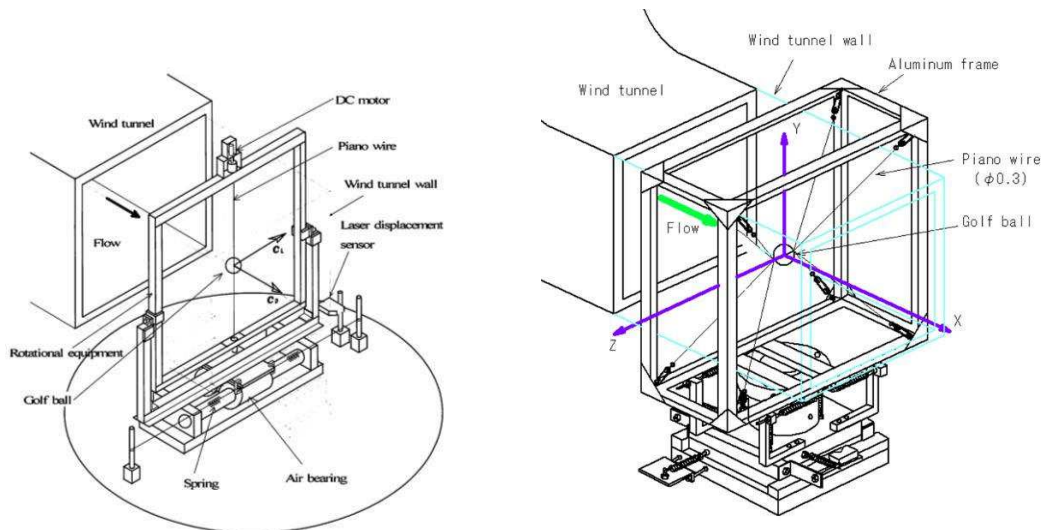
The main symbols used here are as follows.

d: golf ball diameter 0.0427 [m], m: mass 0.0456 [kg], g: gravitational acceleration [m/s²], A: cross-sectional area by ball diameter [m²], ρ : air density [kg/m³], ν : Kinematic viscosity coefficient of air [m²/s], I: Moment of inertia of ball $I = 8.10 \times 10^{-6}$ [kg · m²], U: Ball flight speed or wind tunnel airflow speed [m/s], N: Golf ball rotation speed [rps], α : elevation angle [deg.], β : sideways angle [deg.], θ : bank angle of ball rotation axis [deg.], **D**: Drag vector or drag [N], **L**: Lift vector or lift [N],

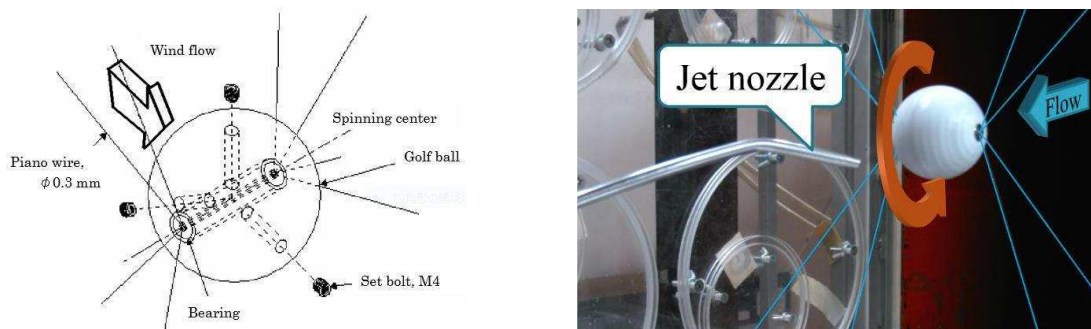
T: fluid friction torque [N · m] , C_D : drag coefficient $C_D = D / (0.5\rho U^2 A)$, C_L : lift coefficient $C_L = L / (0.5\rho U^2 A)$, C_m : fluid friction torque coefficient $C_m = T / (0.5\rho U^2 A d)$, S_p , Sp : spin parameter $S_p = \pi d N / U$, (peripheral speed due to ball rotation) / (ball speed or ball flight speed), Re : Reynolds number $Re = Ud/\nu$.

2-2 Wind tunnel experiment of aerodynamic force and fluid friction torque measurements

In this experiment, aerodynamic three-component force and fluid friction torque are obtained by a wind tunnel experiment with a commercially available golf ball. Fig. 3(a) shows the setup of the wind tunnel test equipment in the early days. The subsequent improvement results are shown in (b), (c), and (d).



(a) Measurement set-up of wind tunnel, early stage (b) Set-up configuration, now.



(c) Balancing technique of ball spinning (d) Jet nozzle flow for ball spinning

Figure 2-3(a) At the beginning of this study, the ball was suspended by a single vertical piano wire ($\phi 0.3\text{mm}$) and rotated by a motor. (b) The ball is now supported by four piano wires through the central axis. (c) A mechanism that tunes three set bolts to balance the rotation, and (d) The rotation of the golf ball is given by a jet stream.

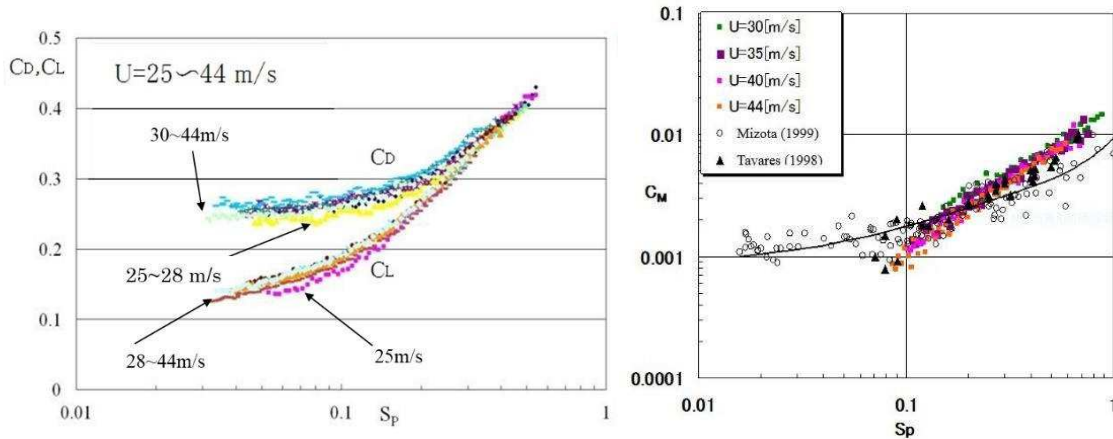
In the early stage of the development of the aerodynamic three-component force measurement method, as shown in Fig.2-3(a), a golf ball is suspended by a 0.3mm diameter piano wire penetrating the wind tunnel wall without contact. The motor for rotating the ball is attached to the upper part of the frame, and the other end of the piano wire is attached to the lower part of the frame via a bearing. This frame is on the load cell. When the fluid friction torque acts on the ball, the piano wire is twisted, so that the time delay between the ball and the end of the piano wire can be measured to determine the twist angle. A ball with good rotation balance is selected by dipping in a liquid such as high-concentration saline. The probability was one or two per dozen.

In the updated apparatus, golf ball is suspended by four piano wires as shown in Fig.2-3 (b). The rotating shaft is embedded in the ball, and miniature bearings attached to the both ends. Four piano wires are fixed to the outer frame after passed through the bearing and wind tunnel wall. The frame is on the 3-components load cell or air suspended load cell. On the equator of the ball, three set bolt holes are arranged every 120° , adjust the depth of the set bolts to keep the static balance. As a result, all the practical golf balls did not show a resonance rotation speed from a maximum of 200 rps to 0 rps, and smoothly rotated. In the wind tunnel experiment, the rotation easily reached 200 rps by the jet stream from the jet nozzle as shown in Fig. 2-3(d). The rotation speed slowly decreased to about 20 rps during 180 seconds in still air. In the wind tunnel flow, the fluid friction damping torque increased, so the rotation speed dropped to 20 rps for 60 seconds. The damping torque coefficients of the fluid friction was determined from the decrease rate of the rotation speed. Aerodynamic data could be measured by continuous measurement because the degree of rotation decay was slow.

The ratio of drag on the piano wire supporting the golf ball was about 50 % of the total drag. In the baseball case, in the next chapter, this value was 25%.

2-3 Measurement results of aerodynamic three-component and friction damping torque coefficients

Fig.2-4(a) shows the drag coefficient C_D and lift coefficient C_L change with the spin parameter Sp . The result of the fluid friction damping torque coefficient C_M is shown in Fig.2-4(b). The spin parameter when the ball hit by a professional golfer flies in an actual game varies depending on the club and during the flight. In the case of 1W or 3W, it is around $Sp = 0.1$ to 0.25 , and for the 5I it is around $Sp = 0.2$ to 0.7 . In the results of this wind tunnel experiment shown in Fig.2-4(a), the Re number dependence appears at a ball speed in 25 m / s , but the it does not appear so much at more than the practical speeds of 30 m / s . However, owing to the dimple shape, Re number dependence



(a) Drag and lift coefficients of golf ball

(b) Fluid friction torque coefficient

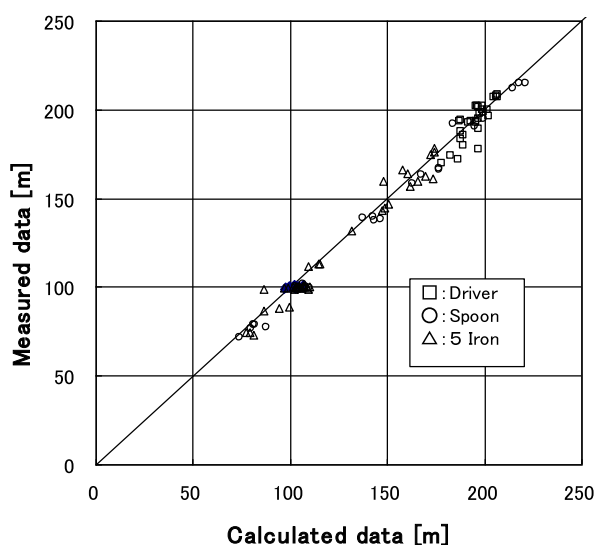
Figure 2-4(a) Drag and lift coefficients of golf ball by wind tunnel experiment. (b) Fluid friction torque coefficient. ○: Motor driven method, ▲: Tavares⁶ by radar method, Other symbols by free rotation method. Free rotation results are well coincident with radar method.

happened to appear in a higher flow velocity region, and such a ball confuses the player. Each manufacturer pays close attention to the development of the ball. According to Fig.2-4(b), which shows the measurement results of the fluid friction torque coefficient, the result of the free-rotation method by Mizota⁹ is closer to the result of the radar method by Tavares⁶.

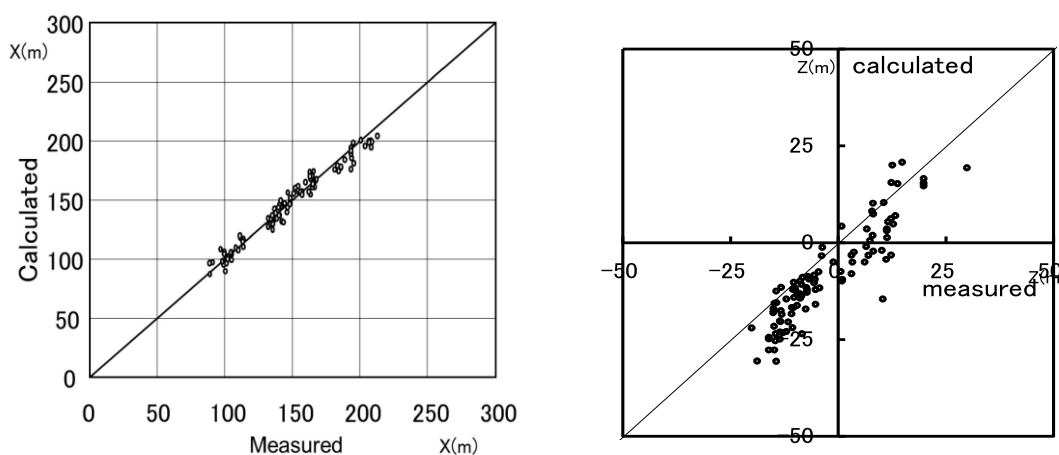
In the early stage of the research, the measurement results of the aerodynamic coefficients sometimes showed a large dependence on the Re number, and sometimes varied. This was caused by the rotational vibration of the ball. The double amplitude of the vibration of the ball or piano wire was taken with a camera. If it is over 90 μm , the aerodynamic coefficient does not appear stably. The data became stable below 50 μm .

2-4 Verification of measured aerodynamic force by flight experiment in still air

Fig.2-5(a) shows the flight distance X at a bank angle $\theta = 0$ without natural wind. The measured and calculated results were on a 45-degree line, confirming the validity of this calculation method and the correctness of the aerodynamic data from wind tunnel experiments. The measured and calculated results of flight distance X with a bank angle $\theta \neq 0$ of a robot shooting with no side slip angle $\beta_0 = 0$ are shown in Fig.2-5(b). Fig.2-5(c) shows the lateral distance Z in this case. These results are reasonably good but may need some more detailed experiment in still air.



(a) Robot hit distance X , bank angle $\theta = 0$, initial side slip angle $\beta_0 = 0$.



(b) Left: Calculated and measured X in 3D hit by Robot. Bank angle $\theta \neq 0$, initial side slip angle $\beta_0 = 0$. Caution to the change of axes with Fig.(a).

(c) Right: Lateral distance Z . The calculated value (vertical axis) and the measured value (horizontal axis).

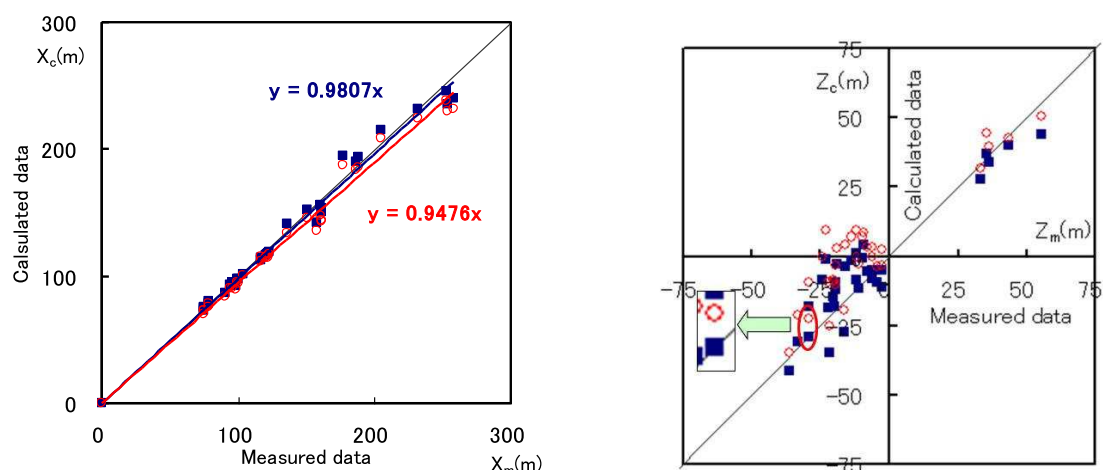
Figure2-5 Measured and calculated distance X or Z in still air experiment.

2-5 Flight experiment in natural wind¹¹

Golf balls trajectory in the air are greatly affected by natural wind. An outdoor experiment was performed to investigate whether the three-dimensional trajectory equation was valid under the wind influence of the atmospheric boundary layer. This was conducted on a terrain where the natural wind blows stably for a long time. The experiment was performed on a sandy beach where the sea breeze blows from the north about 5.5 to 7.0 m / s speed. Two types of experiments were performed in which the wind

was blown from the right 107° (wind from the right side) and 157° (wind from the right rear) with respect to the hitting direction X.

The 5m height natural wind speed was measured at 5 points under the ball trajectory. The natural wind speed against the ball flight was extrapolated from the atmospheric boundary layer theory. The ball was shot by a professional golfer and the ball initial conditions were measured using Pythagoras²⁵.



- (a) Comparison of flight distance X. Horizontal axis: measured value X. Vertical axis: calculated one X. ○: Only with initial conditions of the ball motion, ■: Including the effect of natural wind speed. The slope of the graph was improved from 0.9476 to 0.981, closer to the 45° line.
- (b) Lateral distance Z. Horizontal axis: Measured Z. Vertical axis: calculated Z. ○: Without considering natural wind. ■: Calculated value incorporating the effect of natural wind. The results of wind effects incorporation approach the 45° line.

Figure 2-6 Measured and calculated distance X or Z direction in atmospheric boundary layer by professional golfer's hit.

A flight experiment of a golf ball under the influence of natural wind was shown in Fig.2-6(a) and (b). (a) The experimental range of flight distance is 80-270 m. By incorporating atmospheric boundary layer wind speed data, the slope of the graph was closer to 45° , with an improvement of about 4%. The correction for the lateral displacement distance (b) is also effective, and it is closer to the 45° line. Further confirmation experiments are needed, but the validity of this calculation method is demonstrated.

Finally, three assumptions in constructing this three-dimensional trajectory theory are described. Regarding section 2-1 1), we have experimentally observed that "the bank angle of the ball's rotation axis remains unchanged until it touches the ground." In addition, a wind tunnel experiment was conducted with respect to the point of I that "the

Yaw angle does not occur at the moment of hitting the club, or the new aerodynamic lateral force is small even if the Yaw angle occurs". Wind tunnel experiments were performed by changing the Yaw angle of the rotation axis from 0 to 30 °, but no new lateral force was generated in this range.

When I presented this study in Port Douglas (2002, BBVIV3)²⁶, P.W. Bearman said, "Take to, this 3D theory is fine, but I want you to develop it in the next step. When curved to the right or left, can you develop a ball that returns correctly?" I responded seriously, "it would find the R & A to be a complete violation." But the correct answer at that time was "OK, my next research topics is your order."

3. Various changing ball of baseball^{27~35}

3-1 A hopping straight ball

The straight ball is backspinned and thrown by the 4-seam ball as shown in Fig.3-1. Magnus force lifts the ball weight. If the ball's speed and rotation speed are fast, it will rise up with same height of the ball diameter between 18.44 m (distance of mound plate and home base). A ball speed of 160 km / h (44.4 m / s) and a rotation speed of 40 rps

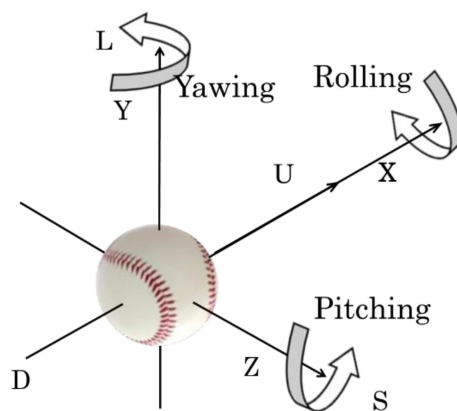


Figure 3-1 A coordinate system of the traveling direction X of the baseball and the seams.

2-seam ball: \pm Rolling rotation around the X axis or \pm Yawing (Side spinning) rotation ball around the Y axis with the ball seam arrangement in this figure.

4-seam ball: A ball that rotates \pm Pitching (Back or Top spinning) around the Z axis.

are the boundaries where the upward Magnus force balances the ball weight. If the latest fastest ball is 170 km / h (47.2 m / s) at the same rotation speed of 40 rps, hop larger than one ball diameter. In the past, it was said that hopping balls could not be physically possible, but in recent years aerodynamics have certainly been realized due to improved

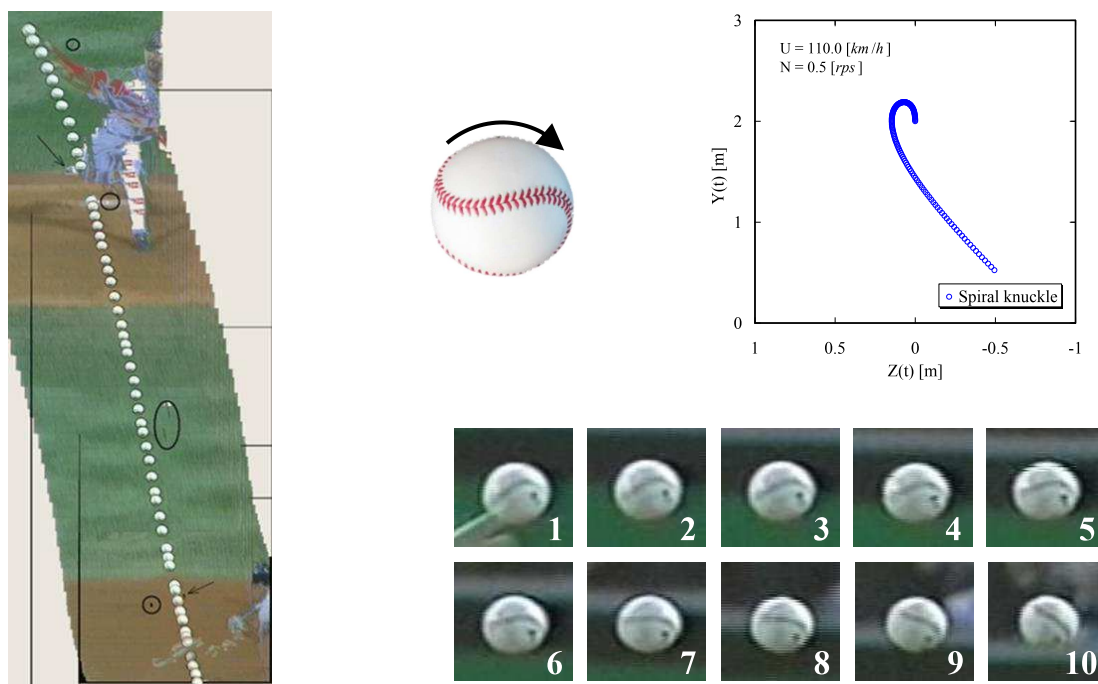
performance of players. It is the largest changing ball that can be lifted by aerodynamic lift at a distance of 0.74m falling by gravity.

Instead of a straight high-speed ball, there is a magic ball with a bank rotation axis of 10° or more to the left or right. This is the same principle of hooks and slices on golf balls. The horizontal component of maximum Magnus force, lift, in which acts in the perpendicular direction of spinning axis, generated by tilting the axis of rotation causes the ball to shift left or right between 18.44m. If this shift could be skillfully changed at a ball speed of 150km / h from 7cm to 20cm, it would be very difficult for the batter to respond. Often missed or become a grounder. NYY's M. Rivera was succeed in this magic ball called "Rivera's cut ball".

3-2. Quasi-stationary theory of knuckle ball and effect of seam²⁷⁻³²

(1) Observation of magical trajectory of knuckle ball

A strobe image of the flight trajectory was obtained from a TV image of a knuckle ball thrown by pitcher T. Wakefield (Boston Redsox). Fig. 3-2 (a), (b), (c) and (d), including



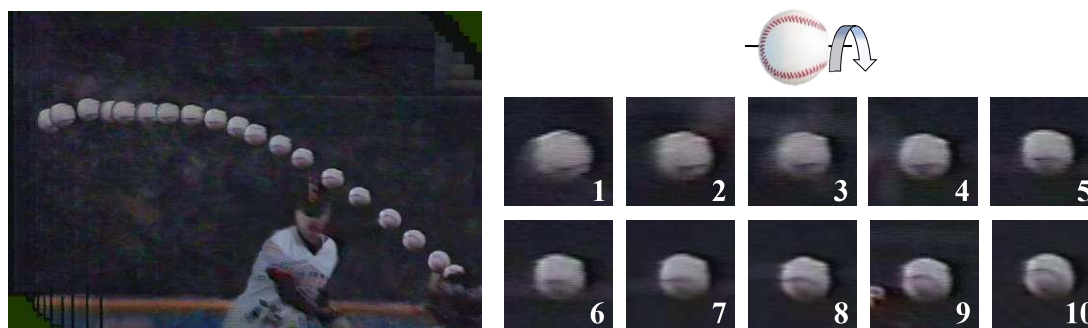
(a) Left: Trajectory of rolling knuckleball (b) Center: Rolling ball from Pitcher's view.
 (c) Right upper, Catcher's view: Calculated trajectory of one seam Rolling knuckleball. $U=110(30.55\text{m/s})$ Km/h, $N=0.5\text{rps}$, (d) Spinning of this rolling knuckleball, every $5/240$ sec., Pitcher's view.

Figure 3-2 1-seam (Rolling) knuckleball by Tim Wakefield

the results of knowing the seam position during flight, are shown. Let's call it one seam rolling knuckle ball^{30, 31)} or Rollin knuckleball. Fig.3-2 (a) shows the strobe image trajectory of the ball flight. (b) clockwise rotation from the pitcher side. (c) Calculated trajectory using later data, in which measured with wind tunnel experiment. (d) show the strobe image of spinning every 5/240 second.

Fig.3-3 shows the (a) strobe trajectory and (b) the rotation of the ball observed from the catcher side by the same pitcher's 4-seam back spin (pitching rotation)^{27, 28)}. The lateral displacement of the side (Yawing) spin knuckle ball³⁰⁾ is shown in Fig.3-4, in which was thrown by the same pitcher. This is a flutter that oscillates in the horizontal direction for about 1.5 cycles during flight with a twice amplitude of about 10 mm during flight.

Two kinds of knuckle ball launcher (named Fairy 1: Rubber powered catapult system, Fairy 2: Pneumatic system) were handmade. Fig. 3-5 (a) to (d) show the results of shooting a ball with the same setting conditions, photographed with a video camera, and processed to strobe image. The flight trajectory of the ball corresponding to the images of these four cases is shown as Fig. 3-5 (e) Observation from the third base side, and (f) Observation from above. It draws various orbits so that it returns to the original orbit or not to return while flying to the home base (18.44m) but does not follow the same orbit



(a) Trajectory of back spin knuckle ball (b) Back spin knuckle ball, 1/4 revolution.

Figure 3-3 Back spin knuckleball by Tim Wakefield (Catcher's view).

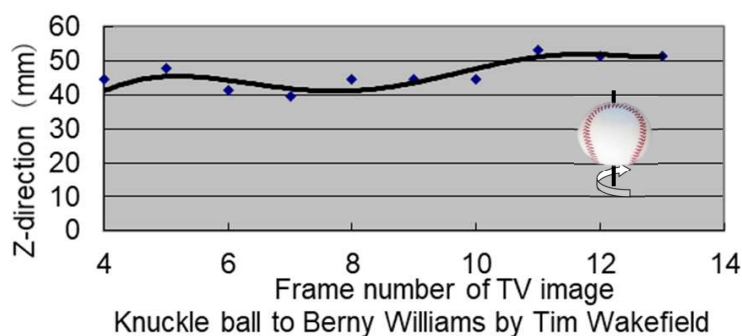
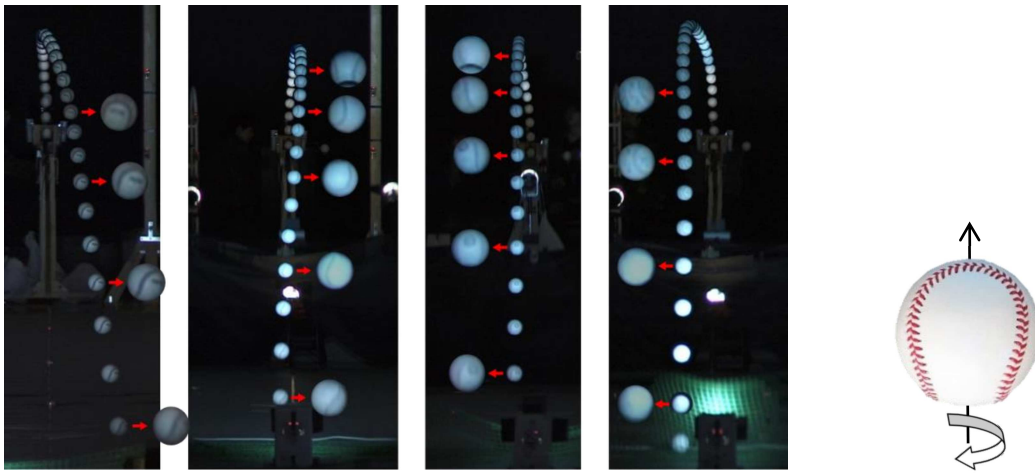
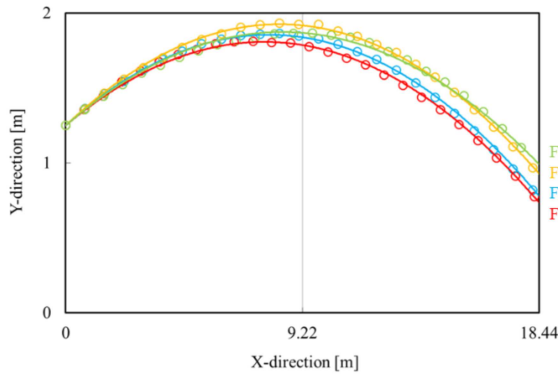


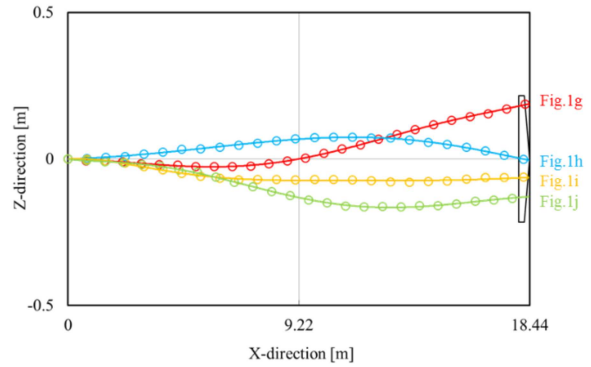
Figure 3-4 Double amplitude of side (Yawing) spin Knuckleball²⁷⁾



(a) Yawing spin Knuckle ball with pitching machine, Catcher's view. (b)
 (Left to right, Fig.1g, 1h, 1i, 1j)



(c) Side view from third base



(d) Top View

Figure 3-5 Yawing or side spin knuckleball by shooting machine, named Fairly1. Local numbering of Fig.1g, 1h, 1i, 1j in Figure 3-5(c) and (d) are correspond with Figure 3-5(a).

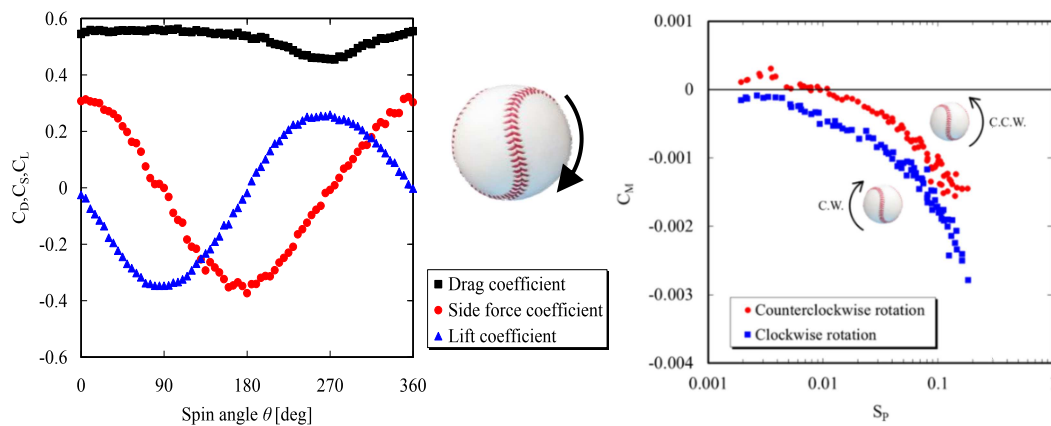
as one. Oscillatory changes in the vertical direction are difficult to discern.

(2) Aerodynamic force and friction torque of knuckleball³⁰

Fig. 3-6 (a) shows the measurement results of the aerodynamic three-component force coefficient of a rolling 1-seam knuckle ball. In the case of the seam arrangement $\theta = 35^\circ$ shown on the right side of the fig, the lateral force of the body axis is maximum as described later, and the lift is zero. This lateral force acts obliquely by the rolling rotation with the ball and is decomposed into a lateral force and a lift. The value of C_D should stay constant during 360° but drops off at around 270° . This is because the wake was inclined and at about 270° , the support rod resulted in the wake and the base pressure changed. The aerodynamic friction torque coefficient C_M is shown in (b). It is interesting

that this change follows a different history depending on the initial rotation direction. The aerodynamic friction coefficient of CCW changes to a higher value over the entire region of S_p compared to CW. The coefficient value in the case of CCW changes from 0 to the positive (driven) value at a low rotation speed. Currently, rotation stops once and then starts reverse direction to CW. When the wind tunnel velocity was around 40 m / s, the steady rotation speed was 36.4 rpm (0.606 rps). This may be the riblet effect due to the seam, but the details are unknown.

Rolling Knuckle ball is thrown at the ball speed of about $U = 108$ km / h (30 m / s). If the initial spin speed is 0, the ball will rotate only 5.8° during 18.44 m flight. The effect of aerodynamic friction torque is not significant.



(a) Aerodynamic 3-component coefficients with rolling rotation. (b) Aerodynamic friction coefficients in rolling with CCW or CW.

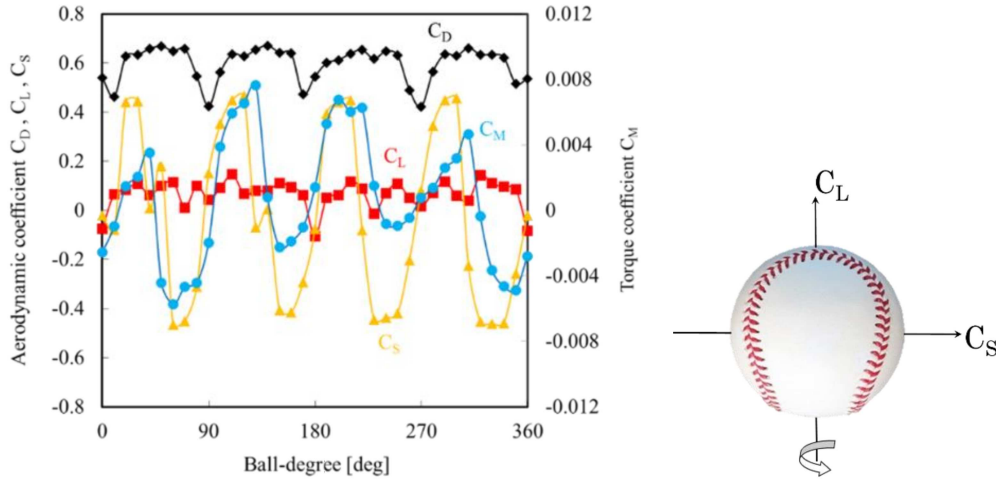
Figure 3-6 Aerodynamic coefficient and friction torque coefficient with 1-seam rolling.

Next, Fig. 3-7 (a) and (b) show the aerodynamic three-component coefficient and the aerodynamic friction torque coefficient during a 360° side spin with a 4-seam ball. This measurement was performed at each fixed angle. Aerodynamic side forces vary with the same trend as Watts & Sawyer¹⁷. Aerodynamic friction torque was measured by the following two methods. Angle correction load torque method: The rotation angle of the ball is set to a predetermined angle every 10° , and the angle change caused by the action of aerodynamic friction torque is returned to the predetermined angle by the correction torque. Strain gauge method: Obtained from the signal displayed on the leaf spring strain gauge by aerodynamic friction torque.

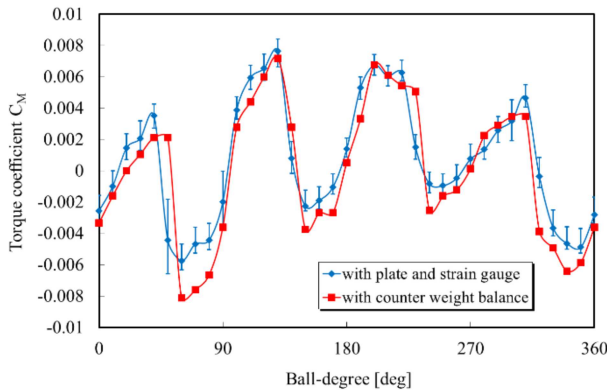
The side force coefficients show the characteristic peak values in the degree of 35° , 125° , 215° and 305° .

Similarly, the aerodynamic friction torque coefficient changes by four periods per

rotation with an amplitude C_M of about 0.006 due to the yawing rotation of the ball. As



(a) Aerodynamic force coefficient.



(b) Aerodynamic friction torque coefficient. Strain gauge and added torque method.

Figure 3-7 Aerodynamic force coefficient and friction torque of side (Yawing) spin knuckleball.

described later, the 4-seam knuckle ball is displaced up to 1.17 m, in one direction when the initial rotation speed approaches 0 with the peak side force angle. In the case of the maximum aerodynamic driven torque acts, the ball angle changes by about 8.8° . It is unlikely that this angular change will significantly affect the trajectory.

It should be noted that even in the 4-seam yawing rotation, automatic rotation of 5 rps at 10 m / s and nearly 20 rps at 40 m / s was observed in the wind tunnel experiments. In the still air, the ball supported with less friction continues about 5 minutes rotation at an initial rotation speed of 60 rps.

(3) Knuckle ball flutter equation and verification by wind tunnel experiment^{27, 28, 35}

For a knuckle ball, the value of (ball speed) / (ball peripheral speed) is $1 / Sp = 133.5$ to

1780. A quasi-stationary approximation can be applied to the aerodynamic forces acting on a knuckle ball in flight. If this lateral force is used as a periodic function, a flutter equation representing the lateral displacement can be obtained.

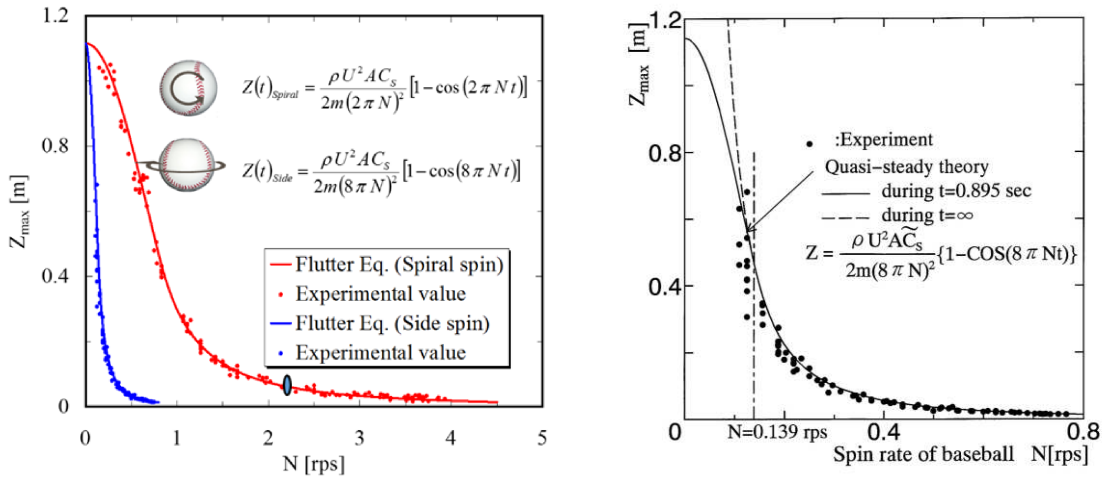
Lateral displacement $Z(t)_{spiral}$ of Rolling type knuckle ball is

$$Z(t)_{spiral} = (\rho U^2 A C_s / (2m(2\pi N)^2)) \cdot [1 - \cos(2\pi N t)] \quad (13)$$

The lateral amplitude $Z(t)_{side}$ of the Yawing (side spin) knuckle ball is

$$Z(t)_{side} = (\rho U^2 A C_s / (2m(8\pi N)^2)) \cdot [1 - \cos(8\pi N t)] \quad (14)$$

A flutter experiment was conducted with two types of knuckle balls. The ball is set with a support rod in the center of the wind tunnel test section and placed on a trolley below the wind tunnel. The ball and bogie reciprocate on the rails due to the aerodynamic lateral



(a) Rolling knuckleball ($U=30.5$ m/s), ball oscillation $N > 0.813$ rps. (b) Side (Yawing) spin knuckleball ($U=21.5$ m/s), ball oscillation $N > 0.139$ rps.

Figure 3-8 Double amplitude of flutter experiment and quasi-steady theory.

vibration force exerted by the rotation of the ball. Vibration amplitude is measured with a laser displacement meter. The added mass and mechanical friction are modified in the equations.

Fig. 3-8 (a) shows the experimental results of the full (double) amplitude value and the results of the flutter Eq. 13. Fig. 3-8 (a) also shows the experimental results of the side spin knuckle for comparison. Fig. 3-8 (b) shows a more detailed experimental result of the side spin knuckle and the flutter Eq. 14. Distance Z_{max} means the maximum amplitude converted during a flight of 18.44m. These vibration amplitude results are in good agreement with the calculations. The knuckle ball indicates that it is a flutter that

can be formulated by a quasi-stationary approximation.

The amplitude terms in Eq. 13 and Eq. 14 are for the rolling knuckle ($\rho U^2 A C_s / (2m (2\pi N)^2)$) and for the side spin knuckle ($\rho U^2 A C_s / (2m (8\pi N)^2)$).

At the same speed U and rotation speed N , the vibration amplitude of the rolling knuckle ball is 16 times larger than that of the side spin knuckle. Rolling knuckles are actually thrown at 1.5 times speed, so they have 36 times the amplitude. According to Knuckler's opinion, as described below, it is actually more complex and very serious.

There is an interesting testimony about the trajectory of the knuckle ball shown in Fig. 3-8 (a) and (b). In connection with that testimony, (a) in a rolling knuckle ball, the trajectory of the ball repeats at least one cycle between 18.44 m with $N > 0.813$ rps, and (b) in a side spin knuckle ball, the trajectory of the ball is note that it oscillates in the range of $N > 0.139$ rps.

On the other hand, the impression expressions of the batters are as follows.

- 1) It's like a spacewalk.
- 2) I can't hit without a tennis racket.
- 3) It's like a butterfly.
- 4) Shake and fail a couple of times, I've seen it but never hit it.
- 5) It's like catching flying flies with chopsticks.

The knuckler himself are not outdone.

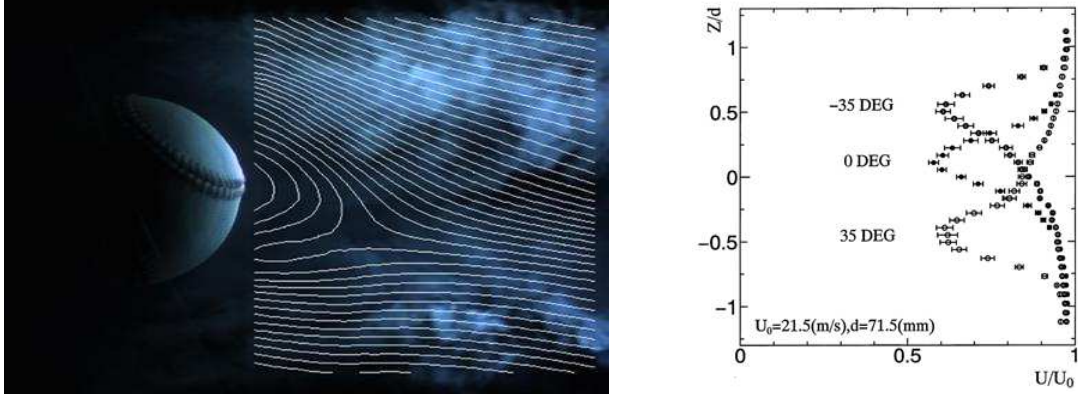
- 1) I don't even know the ball where to go.
- 2) Please ask the ball its destination.
- 3) Even though I told him I would throw it now, so he stood with his back to home base after giving up.

These fuzzy expressions show large swinging or oscillating trajectories. It is in good agreement with the flutter experiment of Fig.3-8.

If the ball seam is arranged so that the maximum lift acts in the + Y direction, and the ball speed is 30 (20) m / s, this ball will have 0.38 (0.73) g in the downward direction. I had the opportunity to hit such a knuckle ball thrown by knuckler Shigeru Mizuno. I could hit 100% if it was a ball other than a knuckle, but the ball passed 30 cm above my bat swing.

Fig.3-9 (a) shows the side view of the streamline pattern at the ball with pitching angle $\theta = 0$ and $\pm 35^\circ$ (40m / s) at which the maximum lift force occurs²⁷. The wake is significantly shifted by the action of the seam, consistent with the generation of a large lift force. Fig.3-9 (b) shows the velocity defect distribution behind the ball (measured by the one diameter behind with hot-wire). The peak position of the velocity defect is shifted downward as same degree of the ball radius. The streamlines in Fig. 3-9 (a) were based

on the PIV method. The original flow pattern was effective at 40 m / s by the modified smoke-wire method³⁴.

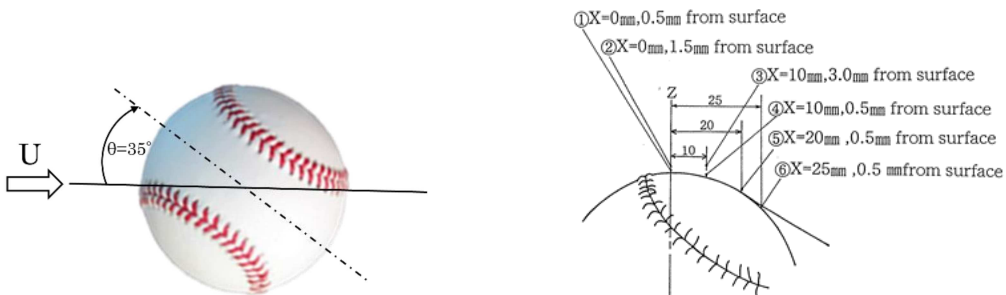


(a) Streamline pattern by PIV behind the ball at $\theta = 35^\circ$, acting on the maximum side force (with top view) or lift force (with side view). Visualization by smoke wire method. $U = 30 \text{ m / s}$. 2114 frames average, 15,000 fps. (b) Large shift of wake velocity profile with ball angle ($\theta = 0^\circ, \pm 35^\circ$), model at rest, hot-wire measurement, ($\theta = \pm 35^\circ, X/d = 1.5$ from ball center).

Figure 3-9 Streamline³⁵ and Velocity distribution of the wake,

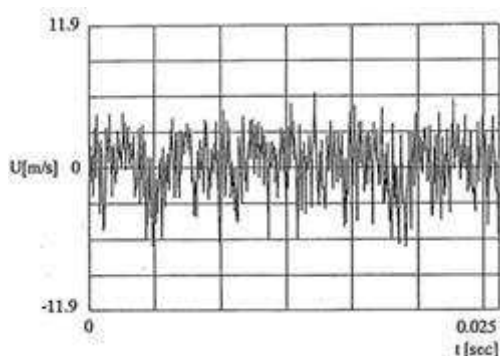
The cause of this large lateral force is related to the wake shift by a single-sided tripping wire effect on seam turbulence. Unsteady flow velocity was measured by inserting a hot-wire into the position shown in Fig. 3-10 (b) at the yawing angle of 35° in Fig. 3-10 (a). Output signals are shown in Fig.3-10 (c), (d), (e), (f).

- (c) Point ① $X = 0 \text{ mm}$, 0.5 mm above the surface: Turbulence signal.
- (d) Point ② $X = 0 \text{ mm}$, 1.5 mm above the surface: Laminar flow signal.
- (e) Point ③ $X = 10 \text{ mm}$, 3.0 mm above surface: Laminar flow signal.
- (f) Point ④ $X = 10 \text{ mm}$, 0.5 mm above surface: Turbulence signal.

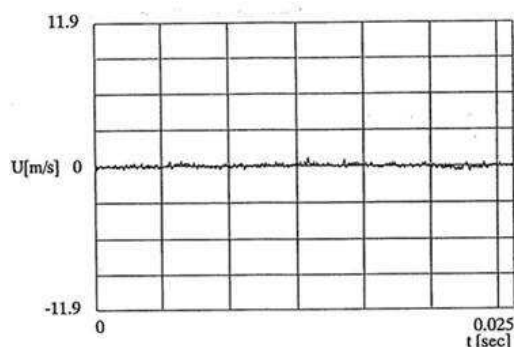


(a) Baseball ball in $\theta = 35^\circ$.

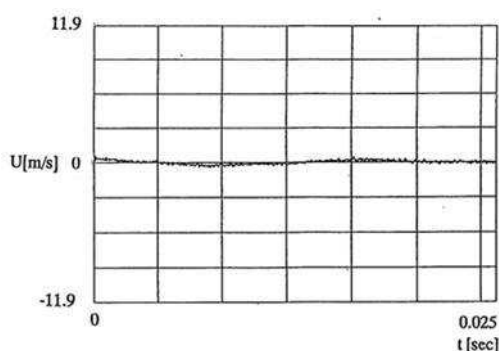
(b) Measured position near the surface.



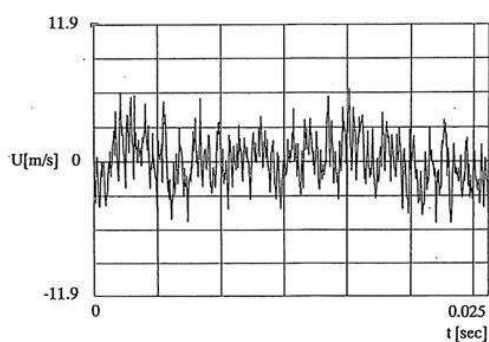
(c) Point ① $X = 0$ mm, 0.5 mm above the surface: Turbulence signal.



(d) Point ② $X = 0$ mm, 1.5 mm above the surface: Laminar flow signal.



(e) Point ③ $X = 10$ mm, 3.0 mm above surface: Laminar flow signal.



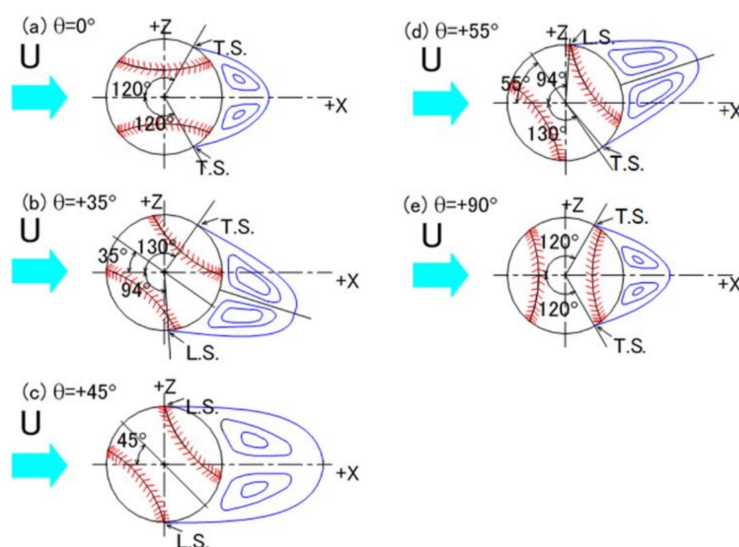
(f) Point ④ $X = 10$ mm, 0.5 mm above surface: Turbulence signal.

Figure 3-10 Flow velocity signal near the ball surface, $\theta = 35^\circ$, $U = 21.5$ m / s

On the upper surface of the ball, the boundary layer becomes turbulent due to the tripping wire effect. The position of the separation line recedes around 130° from the front surface of the ball. On the other side of the ball, the seam does not trigger turbulence due to the low flow velocity outside the seam. The position of the separation remains at 90° . A large non-symmetric flow occurred in the wake³⁶, and results in a large lateral force^{37, 38}.

The results of the knuckleball study are summarized as follows.

- (1) The wake of a 4-seam side(top)-spin knuckle ball repeats its wake oscillation every 90° cycles as shown in Fig. 3-11.
- (2) The one-seam rolling knuckle ball corresponds to (b) $\theta = 35^\circ$ with rotation around X axis creating the fluctuating lateral force and lift one as shown in Fig. 3-6 (a).



- (a) $\theta = 0^\circ$: Small wake area with minimum drag, (b) $\theta = 35^\circ$: Wake area inclined maximum, + Z side force maximum, (c) $\theta = 45^\circ$: Expanded wake area, (d) $\theta = 55^\circ$: Reverse lateral force of (b) $\theta = 35^\circ$, (e) $\theta = 90^\circ$: Same flow as (a).

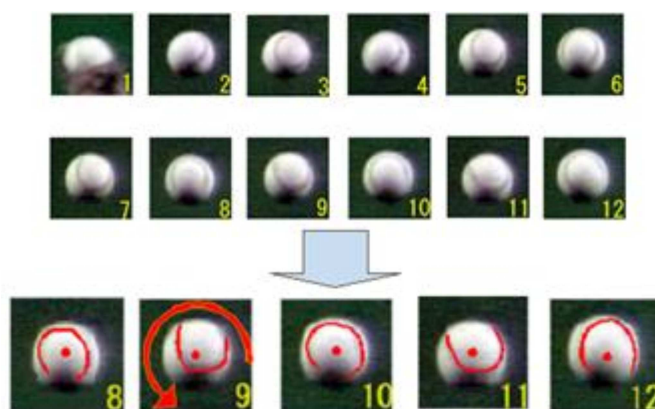
Figure 3-11 The characteristic wake flow of Knuckle ball wake. Wake flow during CW quarter period. As a top view, this is Side (Yawing) spin knuckle ball. As a side view, this is Back spin knuckle ball.

3-3 Split finger first ball (SFF) with rotation axis in the X direction

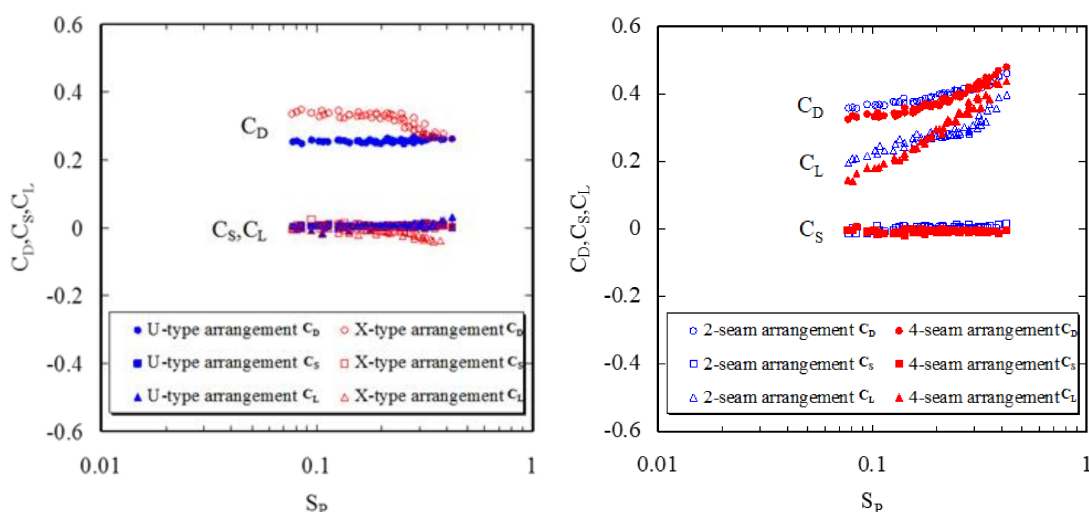
The SFF ball is thrown with a slight gap between the index and middle fingers. It is thrown by devising how to put and hold a finger on the ball, or the action at the moment of release. There is no reliable way to throw this magic ball, and pitching methods vary widely depending on the pitcher. Unlike typical straight balls and curves whose ball rotation axis is in the YZ plane of Fig. 1, many balls can be thrown at various angles (0° to 30° to 60° , etc.) from the X axis. As a result, a lateral or a downward aerodynamic force acts, and the ball slides while flying or slides while sinking, producing various magical ball-like changes.

Fig.3-12 (a) shows an image of a ball thrown by pitcher Daisuke Matsuzaka (Seibu Lions (NPB 11 years), BOS (MLB 8 years)), which is called a vertical slider³³. The ball rotation axis faces correctly toward the catcher. It is thrown with around $Sp = 0.259$ ($U=140\text{km/h}$, $N=45$ rps). According to the wind tunnel experiment, the aerodynamic three-component force characteristics of this ball are as shown in Fig. 3-12 (b). The drag coefficient of $C_D = 0.26$ is smaller than that of the 4-seam straight ball of $C_D = 0.40$ as shown in Fig. 3-12 (c). Compared to a 4-seam ball, there is no lift and drag is low, so under the same speed, during 18.44m length, vertical slider ball reaches about 35 cm

faster. This ball, which falls sharply by the gravity force, is a troublesome magic ball for a batter.



(a) SFF ball called Daisuke Matsuzaka's vertical slider³³. 90fps shooting. $N = 45\text{rps}$, 140km/h (39m/s).



(b) Aerodynamic three-component force coefficient of gyro (vertical slider) rotating ball.

(c) Aerodynamic three-component force coefficient of 2 and 4-seam back spin ball. $S_p = 0.259$, $C_D = 0.40$.

Figure 3-12 SFF ball image, it's aerodynamic force coefficient of gyro-rotating ball and 2 or 4seam spinning ball.

This is a 2-seam ball with $S_p = 0.259$ and the axis of rotation pointing correctly toward the catcher. The ball falls sharply due to gravity. At the same time, it is a troublesome sphere that approaches the batter's hand quickly due to the low drag coefficient $C_D=0.26$.

This ball was called a gyro-ball and was accidentally spread out as a magic ball where the ball lifts. If the axis of rotation is oriented in the direction of travel, no lift act on and it

falls by gravity. Since the drag is small, the deceleration is small and it reaches the batter quickly, and it is a troublesome ball. It is currently called a gyro-rotating ball.

3-4 Magic ball SFF with yaw angle change of rotation axis^{34, 35}

At the end of the magic ball topics, we will discuss the so-called “front door ball” or “back door ball” aerodynamic issues. The pitcher throws this ball along the ball course. The batter cannot predict the ball to become a strike, finally. The ball coming from the 3-base side of the home base is the “front door ball” for the right-handed batter’s box and the “back door ball” coming from the opposite side (1-base side). The opposite is true for left-handed batter.

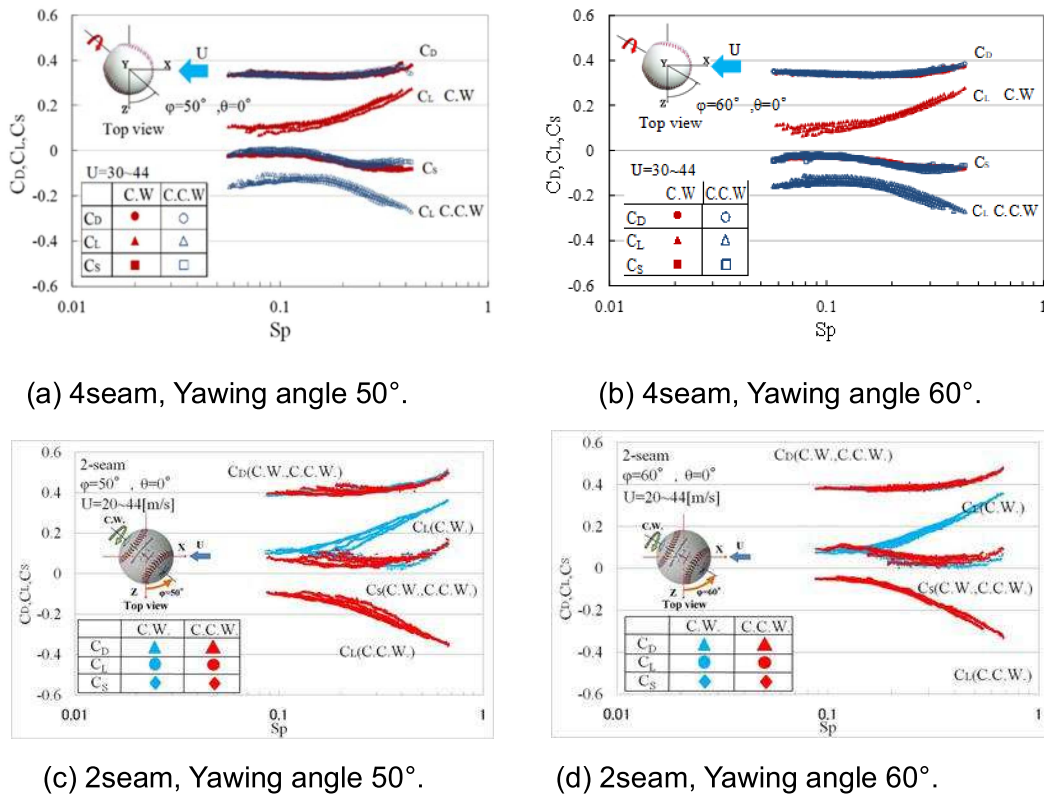


Figure.3-13 Aerodynamic characteristics of (a), (b) 4-seam ball and (c), (d) 2-seam ball. Compare with both sign of Side force C_s in Yawing angle 50° and 60°.

The aerodynamic three-component force coefficients are shown in Fig.3-13 as (a) Yaw angle 50°, (b) 60° of 4-seam rotation and (c) 50°, (d) 60° of 2-seam one. The experimental results of both top spin (CCW) and back spin (CW) are shown. In each figure, the drag coefficient C_D and the lateral force coefficient C_S do not change depending on the rotation direction, but the lift coefficient C_L acts in the opposite direction by the reverse rotation. The lateral force C_S showed a difference in the opposite direction

depending on the seam arrangement not by the different direction of rotation. In the case of 4-seam rotation, both (a) 50 ° and (b) 60 ° have a negative value (-) in the C_S over the entire range of Sp , but in the case of 2-seam rotation, (c) C_S changes to a positive value (+) for both 50 ° and (d) 60 °

Considering the repeatability of the seam shape on the entire ball surface, Fig. 3-14 shows the aerodynamic three-component coefficients near $Sp = 0.2$ in the range of Yaw angle $\theta = 0^\circ$ to 90° . Both lateral force coefficients C_S tend to take a negative value, but in the case of a 2-seam ball, the value changes to a positive value in a narrow range of $\theta = 40^\circ$ to 70° . Focusing around 60° , this lateral force shifts the 2-seam ball to the right and the 4 seam ball shifts to the left. The pitcher can throw a back-door ball with a 2 (4) seam ball and a front-door ball with a 4 (2) seam ball to the right (left)-handed batter.

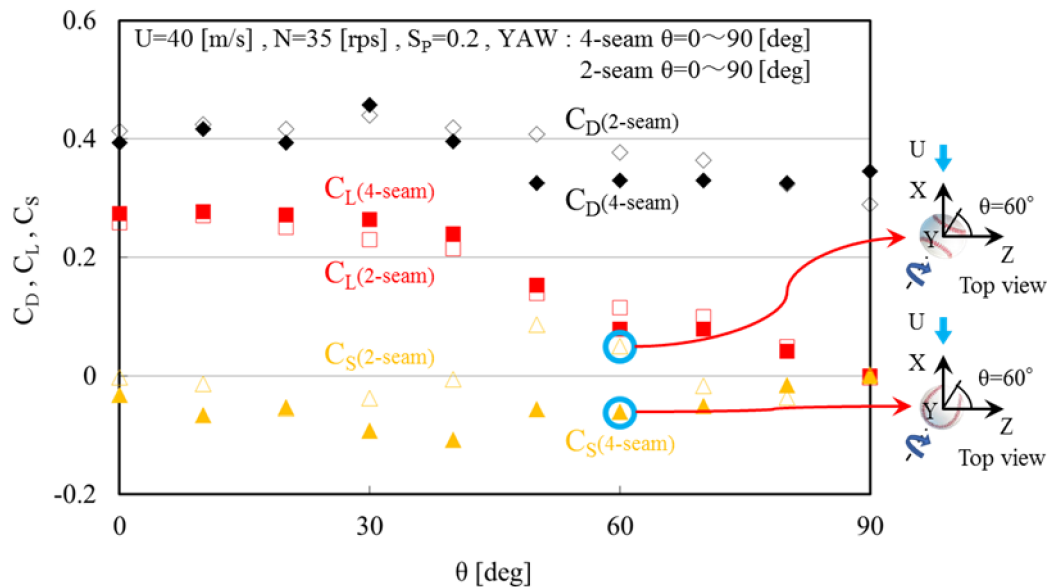


Figure 3-14 Aerodynamic 3-component force coefficient between 0° and 90° of Yawing angle. Note that the direction of the lateral force in $\theta=60^\circ$ is opposite for 2-seam ball and 4-seam ball.

Fig. 3-15 (a) and (b) show the flutter experiment conducted by giving a ball with same $\theta=60^\circ$ yawing angle on a platform moving left and right. (a) 4-seam ball moves to the leftward as a front-door ball for a right-handed batter. (b) 2-seam moves to the rightward as a back-door ball for a right-handed batter. These reflect the result of the aerodynamic lateral force. In wind tunnel experiments, the effect of the ball surface on the ball support rod and the edge of the spinning axis is not zero. To eliminate these effects as much as possible, it is effective to throw the actual ball itself and check the results of the wind tunnel experiment. Therefore, the pitcher of the college baseball team threw 2-seam ball

and 4-seam ball. Fig.3-16 shows a strobe image of a high-speed camera. Image (a) is a 4-seam ball with $\theta = 60^\circ$ shifted to the left. Image (b) is a 4-seam ball at $\theta = 46^\circ$ and moves to the right without inconsistency with previous flutter experiment. The ball attitude was not exactly the same as the wind tunnel experiment, but the results showed the same direction of change as the aerodynamic and flutter experiments. Flight trajectory simulation calculations are also being performed.

It is difficult for the same pitcher to subtly change the direction of the rotation axis in actual games and practice. However, it is relatively easy to throw while changing the

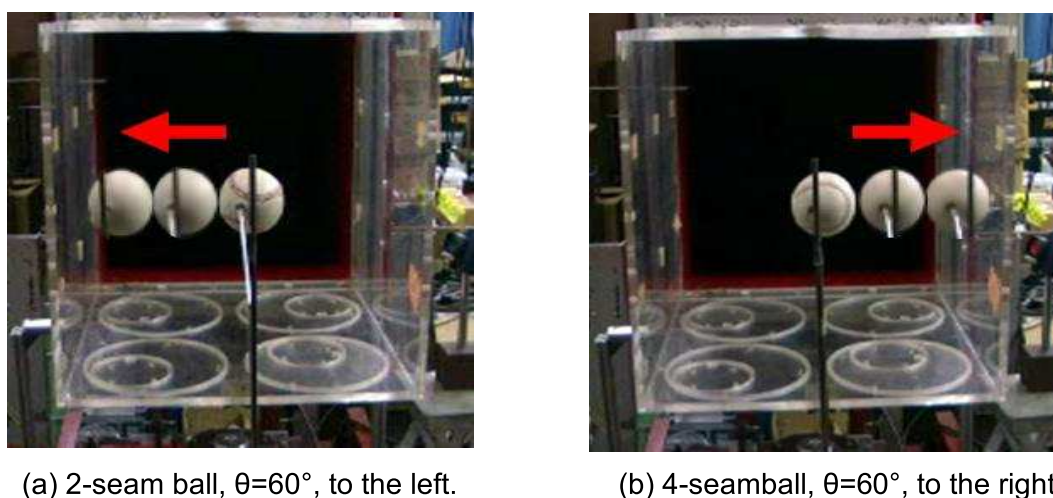
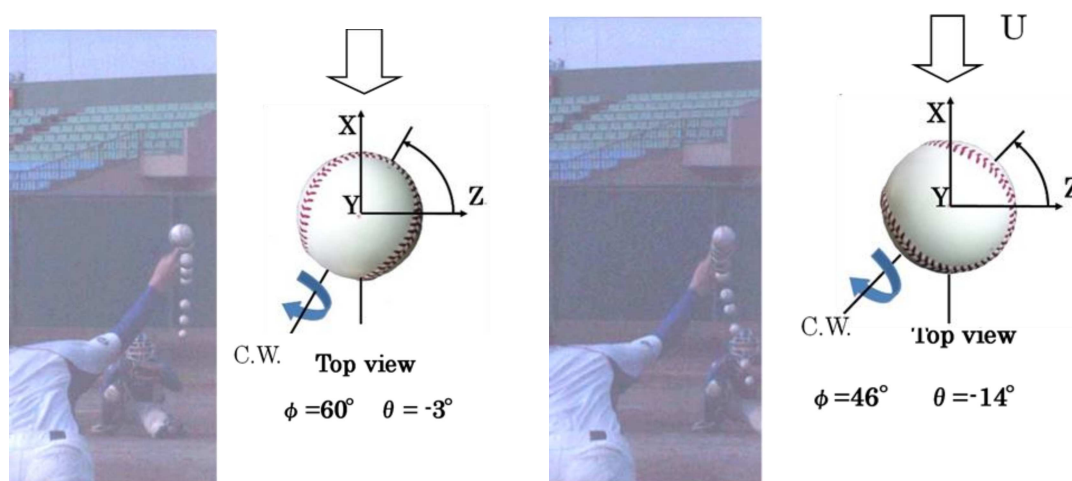


Figure 3-15 Flutter experiments of 2 and 4-seam ball with $\theta=60^\circ$ yawing angle rotation. Balls in the wind tunnel center are at rest, other's are spinning in wind tunnel flow, $U=35$ m/s.



(a) Yaw angle 60° , 4-seam pitching. Shifted to left direction. (b) Yaw angle 46° , 2-seam pitching. Shifted to right direction.

Figure.3-16 Strobe video image of high-speed camera. SFF ball pitched by Yano (FIT).

relationship between the seam and the rotation axis. Nevertheless, it is surprising that the pitcher finds that the two-seam ball moves sideways within 20° of the yaw angle and uses it separately as a 4-seam.

On the other hand, there is a magic ball called a ghost fork (by Koudai Senga, Soft Bank Hawks, 2017 WBC). The ball is thrown with about 30 degrees downward direction of rotation axis from the X axis. This ghost fork ball falls more vigorously than the vertical slider ball in Fig.3-12. The total downward force is 1.3 g because the air force is added to the gravity forces.

Also, there is a magic ball utilizing aerodynamic characteristics near $\theta = 0^\circ$ to 30° in Fig.3-14. In this angle range, the values of C_D and C_L hardly change. Although θ around 30° , the lateral force of a 4-seam ball acts at $C_S = -0.1$, and the ball slides about 30 cm to the left between 18.44 m. The vertical trajectory is the same as a speed ball thrown at $\theta = 0^\circ$. When the ball is thrown towards a right-handed batter, he tries to escape to avoid it, but the ball moves to the left and strikes mercilessly. This magic ball has been thrown for a long time and it is difficult to respond without predicting the change.

3-5 Discussion on the wonder of baseball trajectory

(1) Report of knuckler Ryo Sanogawa³⁹ and observation by Philip Nieklo

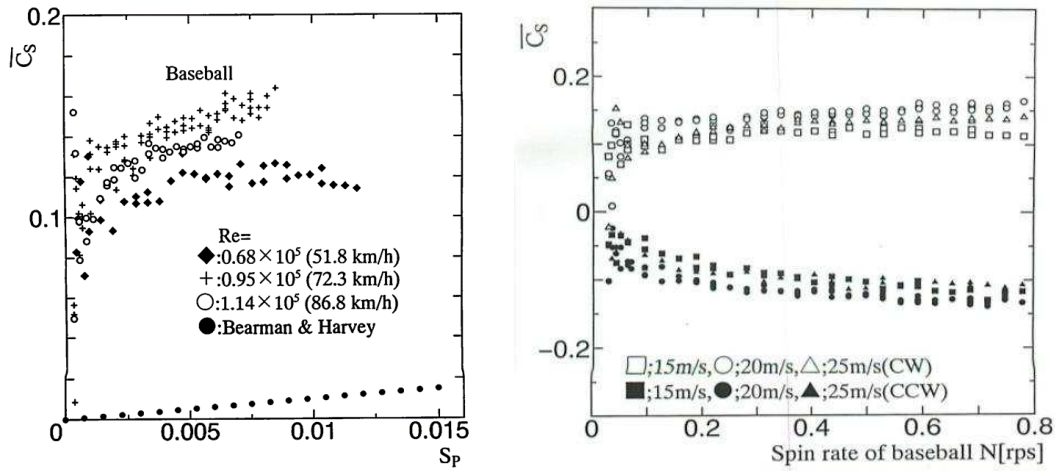
Knuckle pitcher Ryo Sanogawa had also played in the French Baseball League (2017, MVP in the All-Star Game). He had a valuable opportunity to talk with Philip Nieklo (knuckle pitcher, MLN, ATL, NYY, et al., between 26 and 48 years old, 318 major league wins).

"Nieklo liked my knuckle ball. And I met Chris Nowlin, a knuckler who has been throwing in the minor league for 10 years and gained a lot of knowledge. The topics was the rotation of the ball.

(a) Wakefield (BOS, etc.) and Charlie Hough (TEX, etc.) seemed to throw a 1/4 turn with top spin knuckle ball.

(b) Spiral (Rolling) knuckle ball looks good, but it is dangerous to keep throwing it, because of easy to prediction the trajectory, so only one step away from missing. The back-spin knuckle is a complete failed ball. Although the side spin fluctuates, it seems that the change is easy to predict because it only shifts to one way of direction of rotation. "

The wind tunnel results of the side spin knuckle ball related to the observations by Nieklo is shown in Fig.3-17(a) and (b).



(a) Side force in $Sp=0.0005\sim 0.015$. $Sp=0.005$ means $N=0.53$ rps ($U=24.1$ m/s). \bullet : Side force of Golfball. (b) Side force in $Sp=0.015\sim 0.8$. $Sp=0.015$ means $N=1.61$ rps ($U=24.1$ m/s).

Figure 3-17 Side force on slowly and side spinning 4-seam ball

Side spin balls produce steady lateral forces in the same direction as Magnus forces with $C_s = 0.15$ to 0.1 , even at low rotation speeds, such as $Sp = 0.01$ to 0.001 (1.1 ~ 11 second period). This phenomenon of fluid memory or hysteresis may not occur in golf ball⁵⁾ with a uniform surface roughness. This may occur with seam effect turbulence. The Niekro's observation on the mound as the ball shift toward its rotation direction was confirmed by wind tunnel experiments.

(2) Mystery of 2 & 4-seam ball

The correct reason concerning the Fig.3-14 and Fig.3-15, why a leftward lateral force acts when a 4-seam ball is thrown at a yaw angle of 0 to 90° , and a right lateral force acts on a 2-seam ball only in the range of 40° to 70° is unknown in this stage. In the case where the whole area covered with roughness such as dimples of a golf ball, the lateral force was almost 0 in the range of the Yaw angle of 0 to 30° . There is a curved seam on the baseball ball surface, and the position changes with the ball rotation. Depending on the speed of the outer flow of the seam on the front side, it may be a trigger to the turbulence of the boundary layer, which greatly affects the separation area. The separation phenomenon seems to have hysteresis and is complicated, and the experimental facts have been clarified, but the details of the mechanism are still unknown.

(3) Ball speed U and sharp lateral change Z .

Simplify that the average speed is U , between 18.44 m, and let Z be the distance that changes by the action of the lateral force F_s . $Z = 0.5 (F_s / m) t^2$, flight time is $t = 18.44 /$

U, lateral force is $F_s = 0.5\rho U^2 A C_s$, and $Z = (\rho A 18.44^2 / 4m) C_s$. If $C_s = 0.1$, $Z = 2.84 C_s = 0.281$ [m], which is independent of the ball speed². If the ball is fast, the flight time is short, and the ball will change by the same distance in a short time, so that the batter will feel a sharp change, and difficult to deal with. The natural fall due to vertical gravity is about 1[m] at $U = 140 \sim 150$ km / h, but if it is applied with aerodynamic force, it will fall about 1.284m.

4. The strange flight behaviour of slowly spinning soccer balls²²

There is no reasonable qualitative aerodynamic explanation for the mechanism of the erratic flight trajectory of soccer balls. In the subcritical Reynolds number region, vortex shedding from the spheres with smooth surface was previously investigated⁴⁰. For higher Re numbers, some observations of steady fluid forces on the sphere with smooth surface were reported⁴¹, including the effect of surface roughness⁴² on the drag crisis phenomenon^{37,38}. The mechanism of unsteady forces acting on smooth spheres with supercritical Re numbers was explained by Taneda²¹ through observations of bound and wake vortices; that is, the longitudinal twin - vortices irregularly move on the surface of a sphere and in a wake. A model calculation of ring vortex shedding was performed to explain the generations of unsteady lift and drag forces on spheres⁴³. Some research also indicated^{44, 45} that the cause of the erratic behaviour of low-spinning soccer balls is strongly related to the findings of Taneda. The steady aerodynamic forces were calculated by CFD methods, and the flight trajectory estimation was conducted under the quasi-steady approximation with the ball slow rotation⁴⁶. The aerodynamic forces of strange flight trajectory of soccer ball depend on the Re number and spin parameter (Sp), in which Sp is a non-dimensional parameter of (ball surface speed due to spin)/ (ball speed).

4-1 Flight test image and Reynolds number

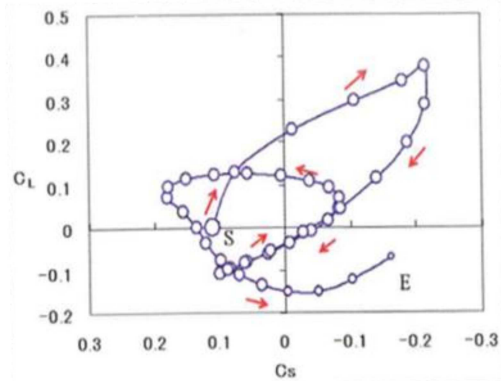
The initial speed of a low-spinning ball that was kicked by Keisuke Honda^{47, 48} was 104 km/h (28.9 m/s), and a goalkeeper hardly moves to stop the soccer ball because of the erratic behaviour. A stroboscopic image from a free-fall experiment under natural low-wind conditions is shown in Fig.4-1(a). A strange displacement of the soccer ball was observed during free-fall. The maximum amplitude within the horizontal plane (Y-Z plane) was approximately 0.75m during a 4.3s period, the ball shift frequency was approximately $f=1.2$ Hz, and, the maximum speed was approximately 22.5 m/s in Fig.4-1(a), and the ball speed continued to be still accelerated. According the measured value of drag coefficient, the final speed of the ball could be estimated to be about 30m/s under

higher free-fall drop test. The relationships between the lift and side forces are indicated in Fig.4-1(b). In this free-fall experiment, the lift and side force direction were defined toward upward and right directions, respectively, in Fig. 4-1(a). The abrupt change in aerodynamic coefficients (C_L , C_S) is a characteristic feature of the final falling stage, because of faster ball speeds.

The flight trajectory results obtained using a shooting machine showed strange erratic behaviour as shown in Fig. 4-2(a), (b) and (c), ($U=82$ km/h, 22.8 m/s) and Fig. 4-2(d), (e) and (f), (105 km/h, 29.2 m/s), including the Y-Z plane trajectory (Fig.4-1(b) and (e)) and time trace of the side force coefficients C_S (Fig.4-1(c) and (hf)). We observed erratic trajectories along dissimilar flight with probabilities greater than 80%. Ball shift magnitudes in the Y-Z plane perpendicular to the beam of the camera image were calculated. The results did not indicate a smooth shift of aerodynamic forces in the Y and Z directions. In Fig.4-1(e), the initial direction of the ball is +Z, the side forces are acting toward -Z (as in Fig.4-1(f)), and the maximum displacement is approximately 0.9 m. As a result, the amplitude of the side force coefficient C_S and period are within the approximate range of 0.1-0.15 and 1.3 s, respectively, as shown in Fig.4-2(c)and (f). The Sp values were 0.002 in the free-fall experiment and about 0.03 in the machine shooting experiments, respectively. Such the low spinning rates did not affect the strange behaviour of soccer ball. As a result, the aerodynamic force in flight is available in the quasi-steady condition.



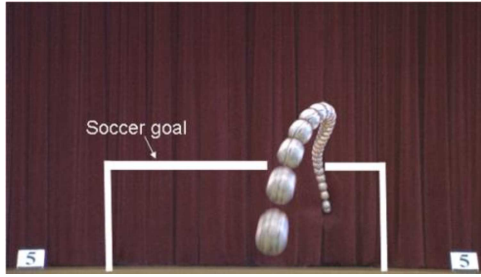
(a) 65 m free fall strobe image



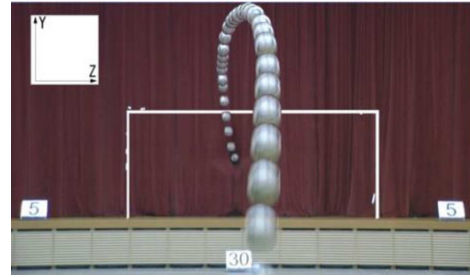
(b) aerodynamic coefficients (C_L and C_S)

Figure 4-1 Strobe image of a 65m free-fall soccer ball and changes in aerodynamic side force coefficients in flight.

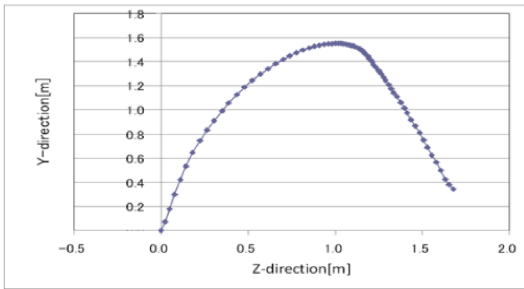
(C_L and C_S) were obtained from the two-step time derivative of position change. The red arrow indicates the lapse of time from start S to landing E. $N = 1 / 16$ rps, high-speed camera shooting at 250fps, $Sp = \pi Nd / U = 0.002$.



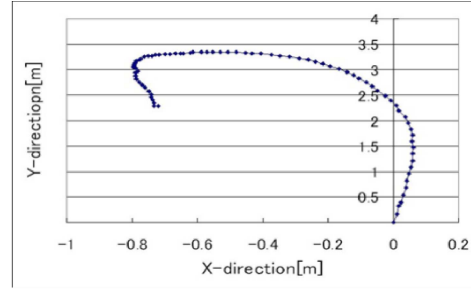
(a) Machine launched flight pass



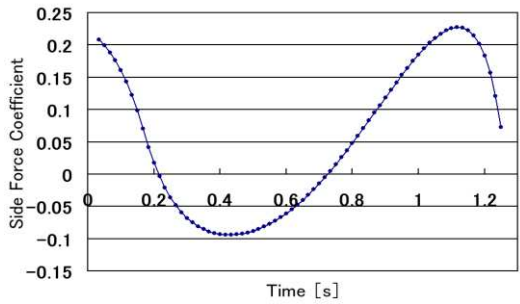
(d) Other example of machine launched



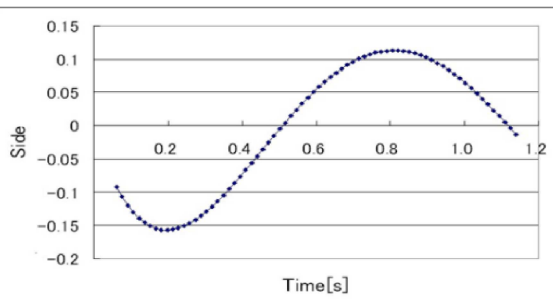
(b) Displacement of Y-Z plain of



(e) Displacement of Y-Z plain of (f)



(c) Time traces of side force coefficient (Cs) of (a) and (b).



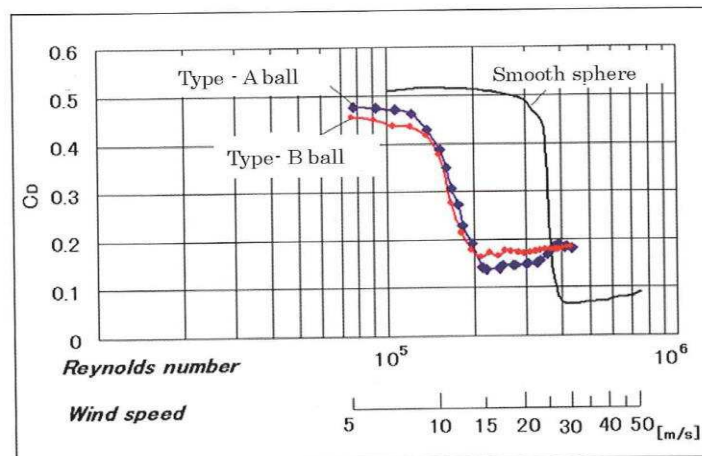
(f) Time traces of side force coefficient (Cs) of (d) and (e).

Figure 4-2 Free-flight ball trajectories and aerodynamic forces of soccer balls launched by shooting machine.

(a - c) and (d - f) are two examples of three-dimensional flight by a shooting machine. (a) and (c) display stroboscopic images of balls shot by the machine. The initial speeds in (a) and (d) were $U_0=82$ km/s (22.8 m/s) and 105km/h (29.2 m/s), respectively. The spin rates were about 1rps, and Sp was =0.03. (b) and (e) present displacements in the Y-Z plane based on the stroboscopic image in (a) and (d). (c), (f), Time traces of the side force coefficient (Cs). The Cs amplitude and period were 0.10-0.15 and 1.3 s, respectively, in both cases. The accuracy of the measured ball position may be within +5.0~ - 5.0 cm, due to the digitised pixel number.

4-2 Time-averaged drag on soccer balls and spheres with smooth surfaces

The time-averaged drag C_D on soccer balls was measured in a wind tunnel with uniform flow and indicated in Fig.4-3(a) with smooth-surfaced spheres⁴⁹. For a sphere with a smooth surface, the phenomenon of drag crisis appears at $Re=3.5 \times 10^5$, under low-turbulence flow. This result is due to the natural transition from the laminar boundary layer to the turbulent boundary layer. However, many patches exist on surface of a soccer ball that are surrounded by regions with approximate depths of 1.50-1.60mm, which artificially promotes the transition of the boundary layer flow from laminar flow to turbulent flow, and results in a drag crisis in the lower Re number region. These surface roughness effects of soccer balls correspond well with spheres⁴¹ and soccer balls⁵⁰. The supercritical Re number flow around soccer balls is similar to the flow around smooth spheres ($Re=3.8 \times 10^5$ ($U=26.0$ m/s, in soccer ball diameter)), which is higher than $Re=2.0 \times 10^5$ ($U=13.2$ m/s) as shown in Fig.4-3(b) and (c) for Type A-ball and Type B-ball,



(a) Time-averaging drag coefficients of a sphere with smooth surface and soccer balls.



(b) Type A-ball, +Teamgeist, Molten. (c) Type B-ball, truncated icosahedron, Mizuno
Figure 4-3 Time-averaged drag coefficients of a sphere with smooth surface and soccer balls at various Re numbers. Type A-ball, Type B-ball.

respectively. All the experiments of the unsteady force measurements and flow visualizations are conducted using Type A-ball in this study.

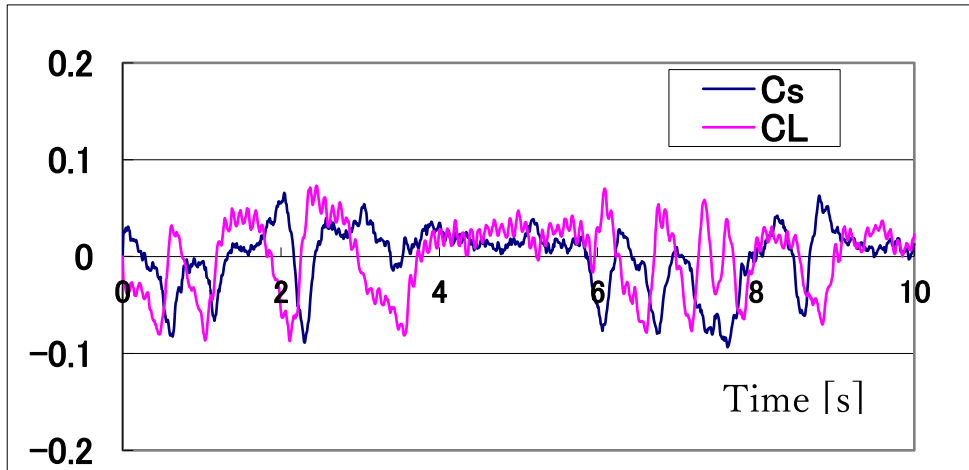
Fig.4-3(a) shows drag coefficients C_D of soccer balls and sphere with smooth surfaces.

The drag coefficients depend on Re , d is the ball diameter, (0.225 m) and ν is the dynamic viscosity of the air. The drag crisis appeared at approximately $U=25$ m/s for smooth sphere and 10 m/s for soccer balls. (b) Type A-ball, +Teamgeist, Molten: the groove depth is 1.51 mm (average value of 10 locations on a random sample), and the standard deviation is 0.042 mm. (c) Type B-ball, truncated icosahedron, Mizuno: the groove depth is 1.69 mm (average value of 10 locations on a random sample), and the standard deviation is 0.058 mm. The representation of these ball photographs (b) and (c) are under the permissions of Adidas Co. and MIZUNO Co.

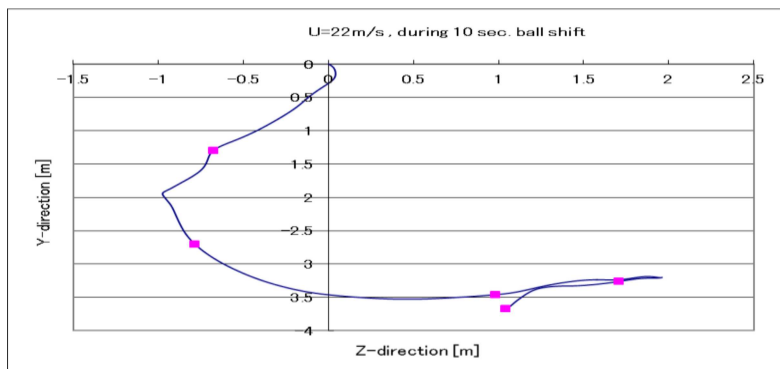
4-3 Unsteady aerodynamic forces and flight trajectory⁵¹

Unsteady aerodynamic forces on Type A-ball (Fig.4-3(b)) were measured with a soccer ball at rest in a wind tunnel flow. The coefficients of unsteady lift C_L and side force C_S for $U=22$ m/s are shown in Fig.4-4(a). These measured results exhibit purely random characteristics, even when assessed by spectrum analysis. In this example, the results were simultaneously constant for a few seconds as they centered for approximately 5 s. The ball shift magnitudes were obtained by a two-step time integration as shown in Fig.4-4(b) (10 s) and Fig.4-4(c) (2 s during a period of approximately 6.0-8.0 sec.). In these calculations, the ball speeds are constant at 22.0 m/s and the gravity force is neglected to emphasise the effect of aerodynamic forces. For 1.2 s during an approximately 6.8-8.0 s period, the ball shifts 0.3 m right and rapidly returns to the reverse direction by 0.3 m.

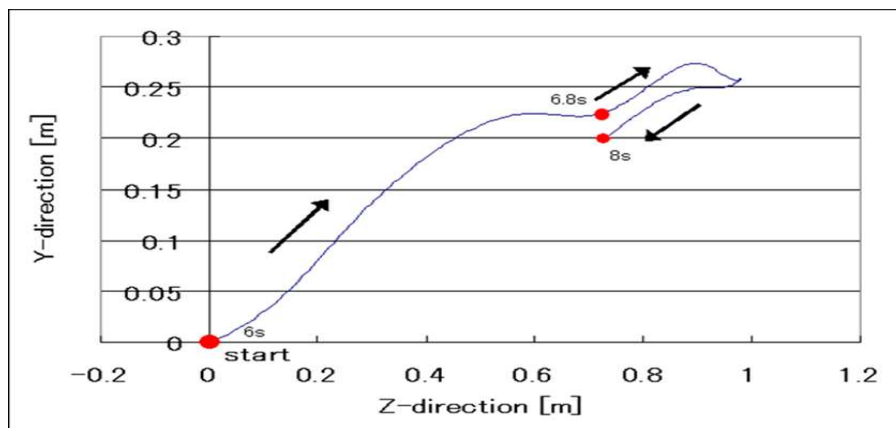
These unsteady aerodynamic forces are induced by unsteady flow in the wake of the ball. High-speed camera images of condensed smoke in the longitudinal vortex flows, which will be mentioned later in the discussion, are shown in Fig.4-4(d) ① - ⑥ and Fig.4-4(e) - (g). The frame rate of high - speed camera was 250 fps, with images taken every 0.004 s period, and the images in these figures represent every 0.128 s. During these sampling times, the dominant positions of the vortex fall in the lower-right position. Through precise observations within this sequence of 0.640 s, we were able to recognise that the phases of these vortices change in every 0.128 s frames. The pattern of vortex phase undergoes various changes from a pair of adjacent twin vortex to a pair of clearly separated twin vortex (Fig.4-4(d)④0.384 s→Fig.4-4(d)⑤0.512 s or ⑥0.640 s) and from a pair of clearly separated twin vortex to a pair of adjacent twin vortex (Fig.4-4(e)→Fig.4-4(f) and (g)) within a short time period. Other examples show a pair of clearly separated twin vortex during a 0.34 s period or no phase change for more than 1 s.



(a) Unsteady forces on soccer, Unsteady aerodynamic forces C_L (red line) and C_s (blue line) on the type A-ball during a 10 s period ($Re=3.3 \times 10^5$, $U=22.0$ m/s, 50 Hz sampling frequency).

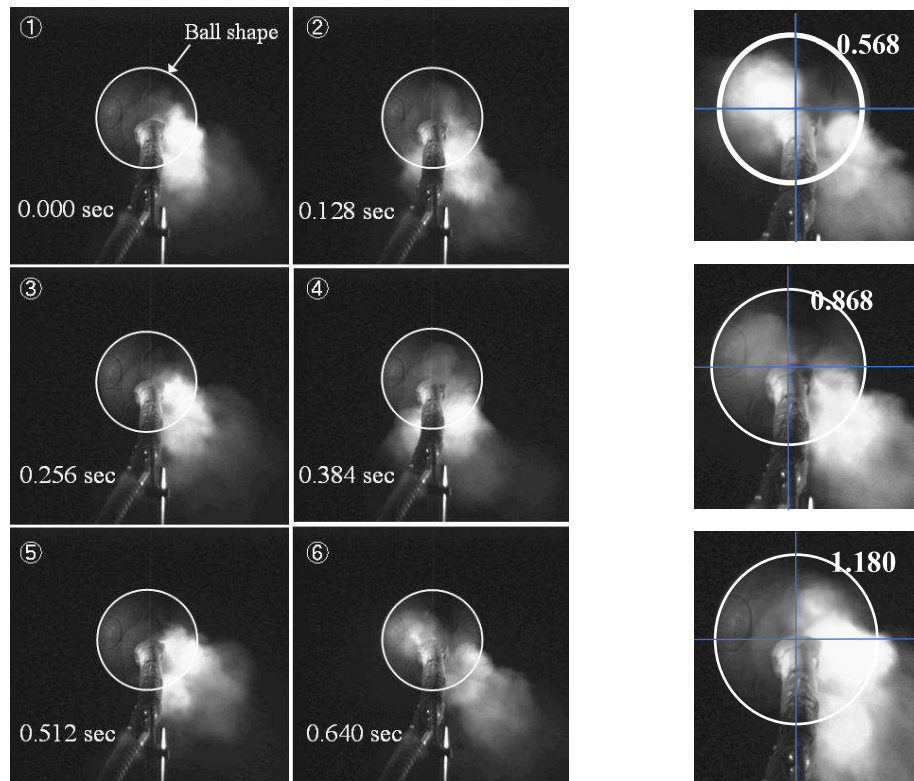


(b) Unsteady ball shift magnitudes. Ten seconds ball shift in the Y-Z plane during the unsteady aerodynamic force of (a) ($U=22.0$ m/s).



(c) Unsteady ball shift magnitudes. Magnification of the Y-Z plane ball shifts between 6 and 8 s of (a) and (b), ($U=22.0$ m/s).

Figure 4-4 Unsteady aerodynamic forces and ball shift magnitude during 10 seconds and 6-8 seconds.



(a) Left : Images for each 0.128 s time step, ①~⑥.

(b)Right: Mode change in the twin vortex.

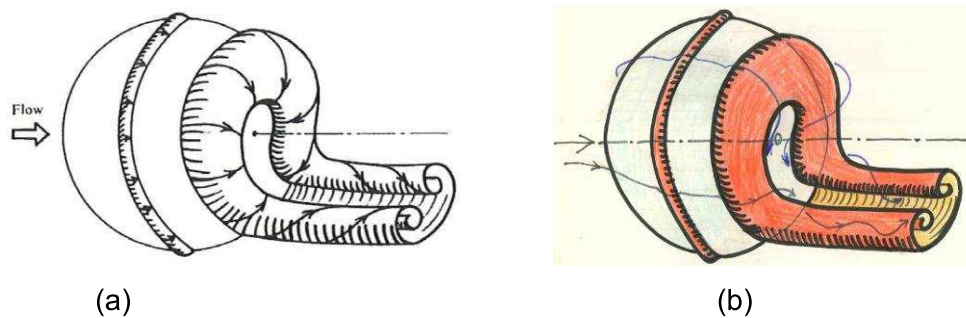
Figure4-5 Unsteady flow patterns visualized by the smoke method. (a)Various image of vortices. (b) Mode change in twin vortex.

Fig.4-5, ①~⑥ show various mode of vortices. During these periods of Fig.4-5(a), the vortices primarily exist in the lower-right position with small variations. Two longitudinal vortices are in close proximity. Between $t=0.512$ and 0.640 s, one vortex suddenly separates as it passes two vortices. Fig. 4-5(b) show the mode change in the twin vortex images 0.568 sec. to one vortex 0.868 sec., followed by the two vortices or the twin vortex pattern, 1.180 sec.

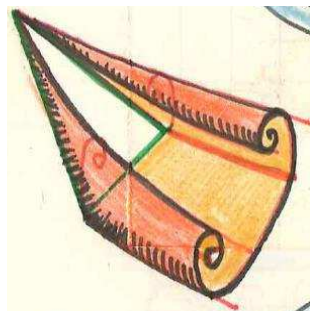
4-4 Discussion of strange trajectory of slowly spinning soccer ball

Instantaneous flow images of smooth spheres²¹ in the supercritical Re flow region are illustrated in Fig.4-6(a), where the 3-D boundary layer flow on the surface is integrated into a Ω -shaped vortex that transforms into twin longitudinal vortices. Fig.4-6(b) displays the flow image in the same region, which had appeared in the article by Taneda²¹⁾ the colour image was directly copied from his research notebook provided by his bereaved family. This conceptual sketch, which appears very similar to the bound and tip vortices

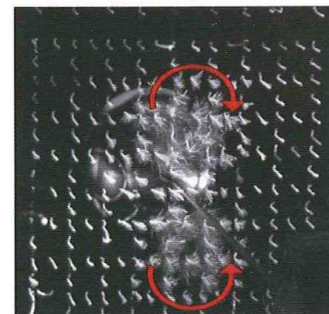
produced by airplane wings, as well as to the general flow around 3-D bodies, is a reasonable shape from a topological stand-point, as is his sketch of the flow around a delta wing in Fig.4-6(c). However, the asymmetric vortices of the sphere have the freedom to rotate or oscillate around a central axis in the main flow direction behind a sphere. The reaction force to a momentum change by the unsteady vortex flow is the main cause of the unsteady aerodynamic force on a sphere.



(a)Image obtained by Taneda²¹ of flow around a smooth sphere at the supercritical Re number, $Re=3.8 \times 10^5$. This flow is an integrated streak line of the surface boundary layer into a Ω -shaped or U-type vortex and two-line flows of the longitudinal vortices. (b)The colour version was reproduced from the research notebook of Dr. Taneda with permission from his bereaved family. This figure was dated at March 9, 1976.



(c)



(d)

(c)Flow around delta wing in his sketch. This figure was dated at February 24, 1976. (d)Typical twin longitudinal vortices as shown in a. $U=26.0$ m/s with 25 integrated frames during a 0.1 s period.

Fig. 4-6 Ω -shaped and two longitudinal vortices of a smooth sphere by Taneda²¹

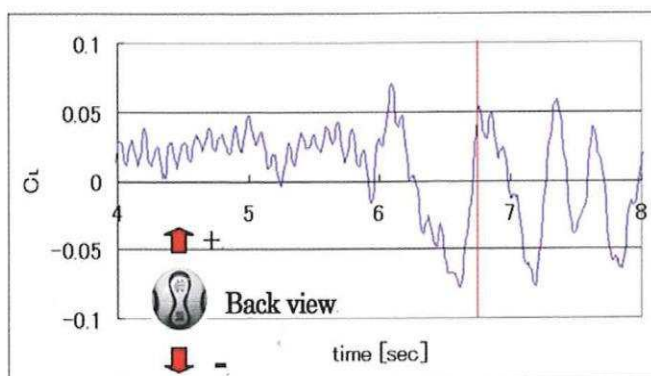
The other observation of flow behind the soccer ball, which is shown in Fig.4-6(d), yields $U=26.0$ m/s, 250 fps and an integration of 25 frames during a 0.1 s period. The integrated tuft images indicate clear twin vortices and show the longitudinal twin vortex

flow.

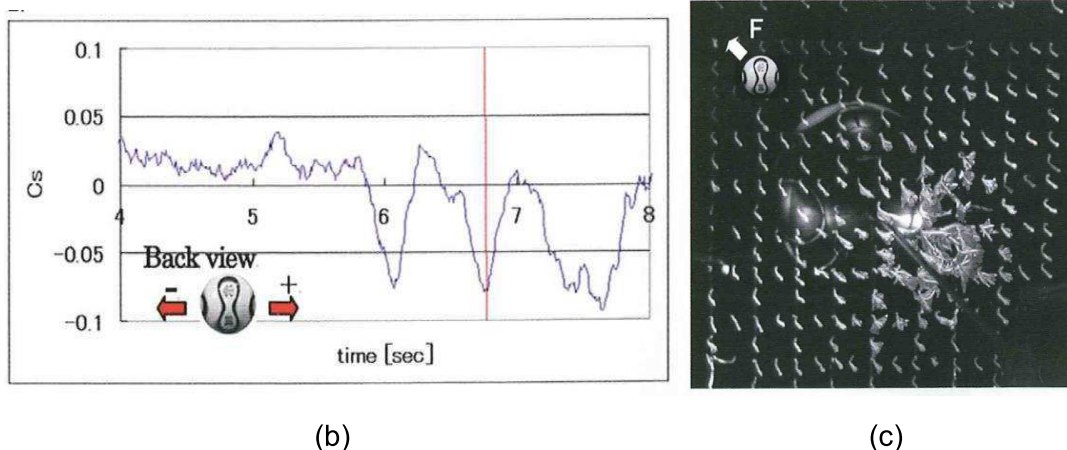
Simultaneous observations of flow visualisation and unsteady force measurements are shown in Fig.4-7(a) and (b), (the same series as that shown in Fig.4-4(a)). In the first 2 s, both amplitudes were small; then, they suddenly began to oscillate. The amplitudes of unsteady lift force C_L and the side force C_s were approximately 0.05, and the frequency was not constant, ranging from 0.7 - 2.5 Hz. In both figures, the vertical red lines indicate at $t=6.80$ s. Flow visualisation by the tuft method, with an integration of 25 frames during a 6.75 - 6.85 s, is shown in Fig.4-7(c). The resultant force vector \mathbf{F} of the unsteady lift and side forces is oriented toward the upper and left direction as Fig.4-7(c). In this instance, the longitudinal vortex is observed to be toward the right and downward direction, which is just opposite to the direction of \mathbf{F} .

In this relationship between the unsteady flow momentum and the aerodynamic forces, a quasi-steady flow condition must be ensured as a precondition. The Strouhal number is an index of this condition, being the order 0.01 ($St=f \cdot d/U$, where: $f=1.0$ Hz, $U=20$ m/s and d (ball diameter)=0.225 m). This small value indicates that the flow-phenomenon may be treated as quasi-steady conditions.

The strange change in the flight trajectory of low-spinning soccer ball occurs for masses in the range of 0.410 - 0.450 kg . The values of mass ratio $m/(\rho V) = 64$, for an example, were suitable for these strange trajectory flight caused by the unsteady aerodynamic forces. In this example value of 64, m is mass of the soccer ball (0.425 kg), ρ is the air density (1.205 kg/m^3) under 1 atm and 20 degree, and V equals to the volume of the soccer ball.



(a)



(a -b), Unsteady aerodynamic force coefficients (C_L and C_s) at 4-8 s, in Fig. 4-4(a).

(b) The averaging flow pattern during 0.1 sec. (6.76-6.85 second) around the red line in Figure 4-7 (a) and (b).

Figure 4-7 The relations between unsteady forces and flow direction around a soccer ball.

In the case of spinning balls, the unsteady resultant lift and side forces may disappear and an increase in the rotational speed of the ball generates the steady Magnus force, which should result in a curved ball. The values N of the ball rotational speeds under the conditions ranging from purely random conditions to nearly steady conditions, was determined experimentally to be approximately 2 - 3 rotations per second⁵¹. The other hand, we observed that the free-fall experiments (in Fig.4-1(a)) showed only less than 1/8 rotation of the ball during 65m fall process, in which the Sp value equals 0.002. In the machine shooting experiments (in Fig.4-2 (a) and (d)), we observed that the ball rotates less than one round during 30 m flight, in which the value of Sp equals about 0.03.

Our results indicate that the random behaviour of the flight of low-spinning soccer balls is mainly caused by the unstable movements of the Ω vortex and the twin longitudinal vortices behind the ball. Grooves on the surfaces of soccer balls promote the transition of boundary layer from laminar flow to turbulent flow and yield a supercritical Re number flow around soccer balls. Incidentally, we recognised that strangely behaving volleyballs that undergo floater serve exhibits the same type of moving behaviour and aerodynamic mechanism of the soccer balls. Scientific viewpoints regarding similar types of sports ball phenomena have generally been ignored in literature, but this finding may evoke scientific interests in sports science.

Fig. 4-7(c) shows the flow pattern observed in multiple images in 25 frames during the

0.1 s period of 6.75-6.85 s centered around the red lines of (a) and (b). A longitudinal vortex exists in the lower-right directions. The resultant aerodynamic force \mathbf{F} , which is indicated by the arrow in (c), was oriented the opposite direction of the vortex position at the symmetrical position of the ball center axes.

5. Applied products by aerodynamic study of sports balls

5-1 By the golfball flight research

(1) Inspection of golf ball characteristics by aerodynamic experiment

The current method of qualifying the aerodynamic properties of golf balls is flight testing. We suggest that public committees such as R & A and the USGA consider this wind tunnel testing.

(2) Development of the hit ball analyzer Pythagoras²⁵

An analysis device called Pythagoras, which measures these initial conditions and calculates the flight trajectory, has been developed²⁵. This device has been delivered to 400 golf shops in Japan. It is used to assess the suitability of a club when a player purchases it. Consistent results are reputed compared to existing devices because the equations of motion are correctly incorporated.

(3) A learning device "Spin-Axis" is approved by the Japan Professional Golf Association⁵².

Inspired the bank concept, Masafumi Wakao, a professional golfer, invented learning equipment. This link device called the Spin-Axis is an excellent learning tool that can visualize how the rotation axis of the ball banks when set the swing trajectory of the golf club head and the normal direction of the club surface. The Spin-Axis has been certified as an official teaching material of the Japan Professional Golf Association.

(3) NHK is trying to improve the accuracy of robots' camera work by predicting the orbit with this theory.

5-2 By the baseball research

(1) Development of MA-Q⁵³

Mizuno has embedded various acceleration sensors in a model baseball ball. A sensor ball has been developed that can detect the pitching speed U , rotation speed N , and three-dimensional direction of the rotation axis. Among them, the three-dimensional direction of the rotation axis is obtained by detecting the earth's magnetism with a high-sensitivity magnetic sensor. Although MA-Q is this product name, it has the same pronunciation as "MAKYU: Magic Ball" in Japanese.

(2) Advanced Topgun: Pneumatic launcher⁵⁴ equipped with changing ball generation function

A study of the magic ball of a baseball has revealed the initial conditions (initial speed, rotation speed N , direction of the rotation axis, the direction of ball advance, and the seam) immediately after the pitcher's hand is released. We are conducting R & D to make it possible with launchers. A gyro-rotating ball launching device has already been patented⁵⁵.

5-3 By the soccer ball erratic flight research

The only way to create this magic ball is to kick the soccer ball with a slight spin. Shoes for that were developed⁵⁶. Wearing these shoes (Wave Ignitus by MIZUNO Co.), Keisuke Honda had shot a historic ball⁵⁷ at the 2010 FIFA World Cup (Japan 2-1 Denmark), in South Africa.

6. Conclusions

Aerodynamic studies of a sports ball flying will have three main implications.

- 1) Creates even more mysterious excitement for audiences and TV watchers.
- 2) Improving the performance and early recovering from damages.
- 3) Related goods developments.

The main conclusions of this study are as follows.

1) 3D trajectory formulation of golf ball flight

Instead of the concept of side spin for over 100 years, we introduced the concept of a bank of rotating axes. A three-dimensional trajectory equation has been constructed. The technology to measure aerodynamic three-component force and aerodynamic torque in a wind tunnel experiment has been completed. These results have been verified by outdoor experiments under the influence of still air and natural wind. A device called Pythagoras that can analyze the trajectory of a ball and a learning machine for players have been developed.

2) Research of baseball erratic flight

The aerodynamic mechanism of the strange changing ball of a baseball thrown by a pitcher has been studied in relation to ball speed, rotation speed, direction of rotation axis, and seams. A technique has been developed to accurately measure the aerodynamic three-component force and aerodynamic torque applied to a baseball ball rotating in a wind tunnel airflow.

The mechanism of the rolling knuckle ball and yawing knuckle ball is flutter expressed by quasi-stationary theory. Knuckler, however, has chosen a ball that moves more

irregularly. The effect of friction torque is not so great. SFF balls, called front door balls or back door balls, could be described experimentally in relation to the axis of rotation and seams. Until now, it had been said that no hopping ball, but recent pitcher skills have made it possible to hop higher than one ball height.

3) The erratic behaviour of slowly spinning soccer ball

The strange flight of a slowly spinning soccer ball is caused by a change in the position of the bound vortex and the subsequent vertical vortex. This is a purely random flutter, similar to the supercritical Re number smooth sphere studied by Taneda²¹. The simultaneous measurement of the unsteady force and the unsteady flow pattern around the soccer ball revealed these mechanisms.

Acknowledgments

Thanks to the Scientific Committee for taking up the research on the irregularly flight sports balls in their keynote speech at ISFA 2020.

In the sports of Judo, Japanese has maxims as “Mind, Skill, and Body”. I believe that there are endless themes that must be pursued in a scientific way for each of “Mind, Skill, and Body”. We hope that this research will increase the interest in developing the aerodynamic properties of sports balls and in pursuing the scientific knowledge of sports.

On December 11, 2010, we visited Prof. Taneda with familiar researchers. Using a PowerPoint, I explained that the mysterious trajectory of a soccer ball could be explained by Taneda's study of a smooth sphere²¹). I asked him that this vortex behind the sphere is, after all, similar to a pair of bound vortex and wing tip vortex of an aircraft. His paper does not mention the flow around the delta wing (Fig.4-4 (c)). Instead of direct answer to this question, he only laughed out loud. I think it was an empathetic laugh with me. June 10, 2011, after a half year of his laugh, Dr. Taneda had passed away at the age of 86.

Thanks to Professor Emeritus, Kanazawa University, Atsushi Okajima, Professor Emeritus of Kyushu University, Yuji Ohya and Dr. Takeshi Naruo Mizuno Co. for their endless discussions.

We thank Kanji Tanaka, President of Topgun and Kazuo Yoshida, an engineering designer who is currently developing some products together. We would like to thank Dr. Daiichiro Kato of NHK, who is constructing a flight image analysis system for golf balls, for providing various information.

We thank many students who graduated from the Department of Intelligent Mechanical Engineering at Fukuoka Institute of Technology for their long-standing research.

It will be appeared the articles of interviews with Tim Wakefield, high speed camera

observation of free fall of sports balls from Aso-Choyo-ohhashi and other related topics
. (<https://www.fit.ac.jp/~mizota/profile.html>).

References

1. R. D. Mehta, R. D., (1985). Aerodynamics of Sports ball. (1985): Ann. Rev. of Fluid Dynamics, Vol.17, pp.151-189.
2. Azuma, A. (1992). Aerodynamics in Sports. Jour. JSME, Vol.95, No.888, p.979-983,1992.
3. Thomson, J. J. (1910). The dynamics of a golf ball. Nature, no. 2147, Vol. 85, 251-257.
4. Davies, J. M.: The Aerodynamics of Golf Balls. (1949). J. Apply. Phys. 20, 821-828.
5. Bearman, P. W. & Harvey, L. K. (1976). Golfball aerodynamics. Aeronaut. Q. 27, pp.112-122.
6. Tavares, G., K. & Melvin, T. (1998). Golf ball and spin decay model based on radar Measurements. Science and Golf III (E. & F. N. Spon, London) 464-472
7. Ohnishi, H. (1986). Golf ball, the secret of its flight. (1986). Popular Science Book, Nikkan-Kogyo-Shinbun, p.74.
8. Jorgensen, T. P. (1994). The Physics of Golf. American Institute of Physics, New York.
9. Mizota, T. Naruo, T., et. al. (2002). 3-Dimensional Trajectory Analysis of Golf Balls. Science and Golf IV (E. & F. N. Spon, London) 349-358.
10. Naruo, T., & Mizota, T., (2004). Aerodynamic force measurement of a golf ball and 3D trajectory analysis. Nagare, Vol.23, pp.203-211.
11. Mizota, T., Park, S., et. al. (2004). 3-D flight formulation of golf ball under atmospheric boundary layer and experiment. Proceedings of Wind Engineering Symposium, Vo.18, pp.281-286.
12. Ichiro Tani, (1950). Curved ball in baseball.: Kagaku, Iwanami, Vol.20, No.9, pp.21-25.
13. Baseball's curved balls may be optical illusion. (1941). Life, Vol.11, No.11, p.83.
14. Maccoll, J. H. (1928). Aerodynamics of a spinning sphere. J. Roy. Aero. Soc., Vol.32. No.777.
15. Visual proof that a baseball curves. (1949). Look, Vol.13, No.15, p.74.
16. Ichiro Tani, (1979). Again, Curved ball in baseball. Kagaku, Iwanami, Vol.49, No.1, pp.51-59.
17. Watts, R. G. & Sawyer, E., (1975). Aerodynamics of a knuckleball. Am. J. Phys. Vol.43, pp.960-963.
18. Briggs, L. J., (1959). Effect of spin and speed on the lateral deflection (curve) of a

- baseball: and the Magnus Effect for smooth spheres.: Am. J. Phys. Vol.27, pp.589-596.
19. Watts, R. G. & Ferrer, R., (1987). The lateral force on a spinning sphere. Aerodynamics of curveball. Am. J. Phys. Vol.55, pp.40-44.
 20. Weaver, R. (1976). Comment on "Aerodynamics of a knuckleball". Am. J. Phys. 44, 1215.
 21. Taneda, S. (1978). Visual observations of the flow past a sphere at Reynolds numbers between 10^4 and 10^6 . J. Fluid Mech., Vol.85, pp.187-192.
 22. Mizota, T., Kurogi, et. al. (2013). The strange flight behaviour of slowly spinning soccer balls. Scientific Reports, Vol.3, Article number 1871.
 23. Hong, S. & A., (2014). Effect of panel shape of soccer ball on its flight characteristics., Scientific Reports, Vol.4, Article number: 5068.
 24. Beratlis, N., Balaras, E., et. al. (2019). On the origin of the drag force on dimpled spheres. Journal of Fluid Mechanics, 879, 147-167. doi:10.1017/jfm, 647.
 25. Naruo, T. (2002). Measurement of Golf Impact and Trajectory Simulation. J. of IEICE, Vol.85, No.1, pp.2-5.
 26. Mizota, T., Naruo, T., et. al. (2002). 3-D Trajectory Analysis of Golf Ball Flight by Inclined Back Spin Axis.: Proceedings of Conference on Bluff Body Wakes and Vortex-Induced Vibrations (BBVIV3), pp.207-210, Port Douglas, Australia, 17-20 December.
 27. Mizota, T., Kuba, H., et. al. (1995). Erratic behavior of knuckleball (1) Quasi-steady flutter analysis and experiment. J. of Wind Eng., Vol.62, pp.3-13.
 28. Mizota, T., Kuba, H., et. al. (1995). Erratic behavior of knuckleball (2) Wake field and aerodynamic forces. J. of Wind Eng., Vol.62, pp.15-21.
 29. Mizota, T., & Kawamura, Y. (2007). 3-D trajectory analysis of side-spin knuckle ball and quasi-steady side-force in flight.: JSME(B), Vol.73, pp.1987-1992.
 30. Nishikiori, D., & Mizota, T. (2004). Research on spiral-spin knuckle ball. JSME, Fluid Engineering Conference, 222.
 31. Nishikiori, D., Mizota, T., et. al. (2004). Erratic behavior of knuckle ball (The 3rd Report). Wind Engineers, No.99, 105-106.
 32. Mizota, T., Kuba, H., et. al. (1997). Erratic behavior of forkball (Aerodynamic mechanism of sinking forkball). J. of Wind Engineering, No. 70, pp.27~38.
 33. Mizota, T., Nishikiori, D., et. al. (2007). Aerodynamics and trajectory of vertical slider of baseball ball. JSME, Ser. B, 73, 1987-1992.
 34. Hasegawa, J., Sakamoto, S., et. al. (2011). Aerodynamic force on spinning baseball ball with change of rotation axis direction by wind tunnel Test. JSME, No.11-17, A4,

- pp.31-34, Sports and Human Dynamics in Kyoto Oct.31-Nov. 3.
35. Mizota, T. (2015). Strange behavior of sports ball flight and its aerodynamics. Research Institute for Mathematical Sciences, Kyoto University, RIMS Kokyuroku 1940, pp.40-58.
 36. Mizota, T., Takita, K., et. al. (2014). Progress of new smoke wire method up to 40 m/s wind tunnel flow and PIV observations of rotating sports ball wake. Research Report of Electronics Research Center, Fukuoka Institute of Technology, Vol.31, pp.25-29,2014.
<https://www.fit.ac.jp/~mizota/profile.html>
 37. Prandtl, R. (1914). Nachr. Ges. Wiss. Göttingen, Math. -Phys. Klasse, 177.
 38. Batchelor, G. K. (1967). An Introduction to Fluid Dynamics. p.342, Cambridge University Press, Cambridge.
 39. Sanogawa, R. KnuckleBall Institute Japan: <http://Knuckleballinstitute.wordpress.com/>
 40. Sakamoto, H., & Haniu, H. (1990). A study on vortex shedding from sphere in a uniform flow. (1990). Trans. of the ASME Vol. 112, pp.386-392.
 41. Achenbach, E. (1972). Experiments on the flow past spheres at very high Reynolds numbers. J. Fluid Mech., Vol.54, pp.565- 575.
 42. Achenbach, E. (1974). The effects of surface roughness and tunnel blockage on the flow past spheres. J. Fluid Mech., Vol.65, pp.113-125.
 43. Home, M. S., et. al. (2001). Aerodynamic lift and drag fluctuations of a sphere, J. Fluid Mech., Vol.436, pp.41- 57.
 44. Mizota, T. (2007). The measurement of unsteady aerodynamic force acting on a low turn soccer ball by a wind tunnel experiment. Proc. JSME, Fluid Engineering Conference, No.07-16, 1202, pp.208-211.
 45. Mizota, T., Kurogi, K., et. al. (2008). Strange 3-D trajectory mechanism of less rotation soccer ball flight, Proceedings of 8th UK Conference on wind Engineering, University of Surry, July 14-16, Guildford England.
 46. Barber, S., et. al. (2009). Sports ball aerodynamics: a numerical study of the erratic motion of soccer balls, Computational Fluid Dynamics, Vol.38, pp.1091-1100.
 47. <http://www.youtube.com/watch?v=MdrXnsUkzDw>
 48. Honda, K. (2007). May 16, Hong Kong, U-22 Hong Kong vs. U-22 Japan, Beijing Olympic Asia-2nd preliminary match.
 49. Schlichting, H. (1979). Boundary-Layer Theory, p.17.
 50. Asai, T., Seo, K. et. al. (2005). Basic research of soccer ball aerodynamic, JSME, Fluid dynamics division, Oct. 29-30, Kanazawa, p.236.
 51. Zhao Lingbo, Mizota, T., et. al. (2012). Non-spinning and spinning soccer ball

aerodynamics with wind tunnel and shooting experiments: 9th Conference of the International Sports Engineering Association (ISEA), July 7-13, Lowell Mas., <http://continuinged.uml.edu/isea2012/schedule.htm>

52. Wakou, M. <http://www.spin-axis.com/en/index.html>
53. Naruo, T. <https://www.mizuno.jp/baseball/products/MAQ/>
54. Tanaka, K. <http://www.pmx-topgun.co.jp/>
55. Tanaka, K., Tanaka, S., & Mizota, T. (2017). Pat. No.: JP 6178691 B2 9/8/2017.
56. Naruo, T. (2011). Research and development of a soccer spike for a moving ball, J. of Japanese Society of Science and Football, Vol.6, No.1, pp.4~10, 2011.
57. Keisuke Honda: <https://www.youtube.com/watch?v=XIY8q9Zuljo> .

Nonlinear flutter in practice

Grigorios Dimitriadis¹

¹ *Aerospace and Mechanical Engineering Department, University of Liège, Liège, Belgium, gdimitriadis@uliege.be*

Abstract

Classical descriptions of nonlinear flutter phenomena are based on bifurcation theory, as described in the nonlinear dynamic literature. These descriptions generally involve the occurrence of a subcritical or supercritical Hopf bifurcation, followed by one or more fold bifurcations of limit cycles. The behaviour of simple aeroelastic models with basic nonlinearities conforms perfectly with this description of nonlinear flutter. However, real aeroelastic systems generally display more complex and, sometimes, surprising behaviour. This work presents four wind tunnel experiments on nonlinear aeroelastic systems, featuring aerodynamic and/or structural nonlinearity. It is shown that one of the systems conforms indeed to the classical description of nonlinear flutter. The other three feature more complex behaviour, such as the abrupt appearance of nonlinear oscillations in the absence of a linear aeroelastic instability, or a two-parameter bifurcation that can change the nature of the flutter from subcritical to supercritical.

Keywords: Nonlinear Aeroelasticity, Flutter, Limit Cycle Oscillations, Bifurcation, Wind Tunnel Experiments

1 Introduction

Over the last 40 years, nonlinear aeroelasticity has become an increasingly important area of research. Nonlinear aeroelastic systems exhibit much more complex behaviour than their linear counterparts, including the existence of multiple solutions at the same parameter values, as well as the phenomenon of Limit Cycle Oscillations (LCO). Hence, nonlinear flutter is not understood or described as well as linear flutter. Typical theoretical descriptions of nonlinear flutter (Lee *et al.*, 1999; Dowell, 2004; Dimitriadis, 2017) are inspired from the nonlinear dynamic literature (e.g. Kuznetsov (1998); Guckenheimer & Holmes (1983)) and analyse the phenomenon using bifurcation theory. Nonlinear flutter is therefore presented as the result of a Hopf bifurcation, which can be subcritical or supercritical and can lead to high amplitude LCOs at subcritical conditions or low amplitude LCOs at supercritical conditions, respectively. Dowell has categorised these phenomena using the terms 'bad LCO' for the subcritical case and 'good LCO' for the supercritical case. Furthermore, simple nonlinear aeroelastic models (typically 2D airfoils with pitch and plunge degrees of freedom and with cubic stiffness) conform to this description of nonlinear flutter, although they can sometimes also display richer and more complex behaviour.

Experimental investigations of nonlinear aeroelastic systems can also conform to the classical description of nonlinear flutter. However, in many cases the phenomena observed in practice are more complex and more difficult to categorise. The purpose of the present paper is to present

four examples of wind tunnel experiments on nonlinear aeroelastic systems and to discuss how the behaviours observed differ from the typical Hopf analysis. The nonlinearities featured in these experiments can be due to structural stiffness effects, structural damping effects or aerodynamic effects. Furthermore, some of these nonlinearities, particularly the structural damping are not designed for, they are just natural byproducts of the mechanics of the system (e.g. friction in bearings). The paper starts with a discussion of classical nonlinear flutter theory and then presents the experimental test cases.

2 Classical nonlinear dynamics for fluid-structure interaction

A general form of the flow equations can be written as

$$\frac{\partial}{\partial t} \begin{pmatrix} \rho \\ \rho \mathbf{u} \\ \rho E \end{pmatrix} + \nabla \cdot \begin{pmatrix} \rho \mathbf{u} \\ \rho \mathbf{u} \otimes \mathbf{u} + p \mathbf{I} - \boldsymbol{\tau} \\ \rho \mathbf{u} E + \rho \mathbf{u} \cdot \boldsymbol{\tau} - \boldsymbol{\tau} \cdot \mathbf{u} - \kappa \nabla T \end{pmatrix} = \mathbf{Q} \quad (1)$$

where t is the time, ρ is the flow density, $\mathbf{u} = [u \ v \ w]^T$ is the flow velocity vector, E is the total energy, p is the pressure, $\boldsymbol{\tau}$ is the viscous stress tensor, κ is the thermal conductivity, T is the temperature and \mathbf{Q} is a generic source term. Furthermore, ∇ is the gradient operator, $\nabla \cdot$ is the divergence operator and \otimes is the vector outer product. For a Newtonian fluid, the viscous stress tensor is written as

$$\boldsymbol{\tau} = \mu (\nabla \mathbf{u} + \nabla \mathbf{u}^T) \quad (2)$$

and, for gas flows, closure can be achieved by use of the gas state equation.

The flow equations can be simplified by assuming incompressible and/or inviscid flow. They can also be written in the Random Averaged Navier-Stokes (RANS) form by averaging them in time in order to remove the effect of small turbulent fluctuations. Whichever form of the equations is used, it is solved numerically by discretising the flow domain into $i = 1, 2, \dots, n_f$ nodes. Writing the flow state vector at the i th node as

$$\mathbf{x}_i = \begin{pmatrix} \rho_i \\ \rho_i \mathbf{u}_i \\ \rho_i E_i \end{pmatrix}$$

we can assemble the complete flow state vector

$$\mathbf{X}_f = \begin{pmatrix} \mathbf{x}_1 \\ \mathbf{x}_2 \\ \vdots \\ \mathbf{x}_{n_f} \end{pmatrix}$$

and reformulate the semi-discretized flow equations as

$$\dot{\mathbf{X}}_f = \mathbf{f}_f(\mathbf{X}_f) \quad (3)$$

where \mathbf{f}_f is a vector of nonlinear functions. In expression 3 the source term has been set to zero, the gas state equation has been implemented and viscosity has been assumed constant.

The reason for discretising equations 1 in space but not in time is to show that the flow equations can be written in the form of a first order nonlinear dynamical system. The flow can be specified in more detail by defining the free stream flow velocity \mathbf{U}_∞ , density ρ_∞ and pressure p_∞ . Equations 3 then can feature these parameters

$$\dot{\mathbf{X}}_f = \mathbf{f}_f(\mathbf{X}_f, \mathbf{U}_\infty, \rho_\infty, p_\infty) \quad (4)$$

The structural deformation equations can be semi-discretised in the same way, using finite element modelling for example, leading to equations of motion of the form

$$\dot{\mathbf{X}}_s = \mathbf{f}_s(\mathbf{X}_s) \quad (5)$$

where \mathbf{X}_s is the vector of structural states at the n_s structural nodes and \mathbf{f}_s is a vector of nonlinear functions.

In typical fluid-structure interaction problems the flow applies loads to the structure and the structure deforms, such that that the flow boundary changes and so do the fluid loads. A general form of a fluid structure interaction equation is then

$$\dot{\mathbf{X}} = \mathbf{f}(\mathbf{X}, \mathbf{U}_\infty, \rho_\infty, p_\infty) \quad (6)$$

where the combined state vector is

$$\mathbf{x} = \begin{pmatrix} \mathbf{X}_f \\ \mathbf{X}_s \end{pmatrix}$$

and \mathbf{f} is another set of nonlinear functions that reflect flow physics, structural physics and fluid-structure coupling physics. Equations 6 can be studied using standard nonlinear dynamic analysis (Dimitriadis, 2017). Consider the fixed point \mathbf{X}_E , for which

$$\mathbf{f}(\mathbf{X}_E, \mathbf{U}_\infty, \rho_\infty, p_\infty) = \mathbf{0}$$

The nonlinear function can be linearised around this fixed point by applying a Taylor expansion, such that

$$\mathbf{f}(\mathbf{X}_E + \mathbf{x}, \mathbf{U}_\infty, \rho_\infty, p_\infty) \approx \mathbf{f}(\mathbf{X}_E, \mathbf{U}_\infty, \rho_\infty, p_\infty) + \left. \frac{\partial \mathbf{f}}{\partial \mathbf{X}} \right|_{\mathbf{X}_E} \mathbf{x}$$

where $|\mathbf{x}| \ll |\mathbf{X}_E|$. Substituting back into equation 6 we obtain

$$\dot{\mathbf{x}} = \mathbf{A}(\mathbf{U}_\infty, \rho_\infty, p_\infty) \mathbf{x} \quad (7)$$

where

$$\mathbf{A}(\mathbf{U}_\infty, \rho_\infty, p_\infty) = \left. \frac{\partial \mathbf{f}}{\partial \mathbf{X}} \right|_{\mathbf{X}_E}$$

is the system's Jacobian around fixed point \mathbf{X}_E . The parameters $\mathbf{U}_\infty, \rho_\infty, p_\infty$ are bifurcation parameters that govern the stability of the system. Equation 7 is a linear Ordinary Differential Equation with solution

$$\mathbf{x}(t) = \sum_{i=1}^m \mathbf{v}_i e^{\lambda_i t} c_i \quad (8)$$

where m is the total number of states, \mathbf{v}_i and λ_i are the eigenvectors and eigenvalues of \mathbf{A} respectively and c_i is the i th element of vector $\mathbf{c} = \mathbf{V}^{-1}\mathbf{x}(0)$, $\mathbf{V} = [\mathbf{v}_1 \dots \mathbf{v}_m]$ being the eigenvector matrix of \mathbf{A} and $\mathbf{x}(0)$ being initial conditions.

Flutter is usually defined on linear systems of the form of equation 7. The critical flutter condition is the combination of parameters \mathbf{U}_∞ , ρ_∞ , p_∞ for which one pair of complex conjugate eigenvalues of \mathbf{A} becomes purely imaginary. At this condition, the steady state response of equation 8 is purely harmonic, with frequency $|\lambda_{crit}|$, the magnitude of the pair of imaginary eigenvalues. The critical flutter condition splits the possible values of the system's flow parameters into two sets:

- At subcritical conditions the fixed point attracts response trajectories and the system is said to be stable as it undergoes damped oscillations whose amplitude decays towards the fixed point. This situation is displayed in the phase-plane plot of figure 1(a), which plots the velocity response of a system, $x_1(t) = \dot{x}_2(t)$, against its displacement, $x_2(t)$. The response trajectory starts at the initial condition $x_1(0) = 0$, $x_2(0) = 0.1$ and spirals inwards around the phase plane, all the while approaching the fixed point lying on $x_1 = x_2 = 0$.
- At supercritical conditions the fixed point repels response trajectories and the system is unstable, undergoing oscillations whose amplitude increases exponentially with time. This situations is exemplified in the phase-plane plot of figure 1(b). The initial condition is the same as in figure 1(a) but this time the response trajectory spirals outwards, moving faster and faster away from the fixed point.

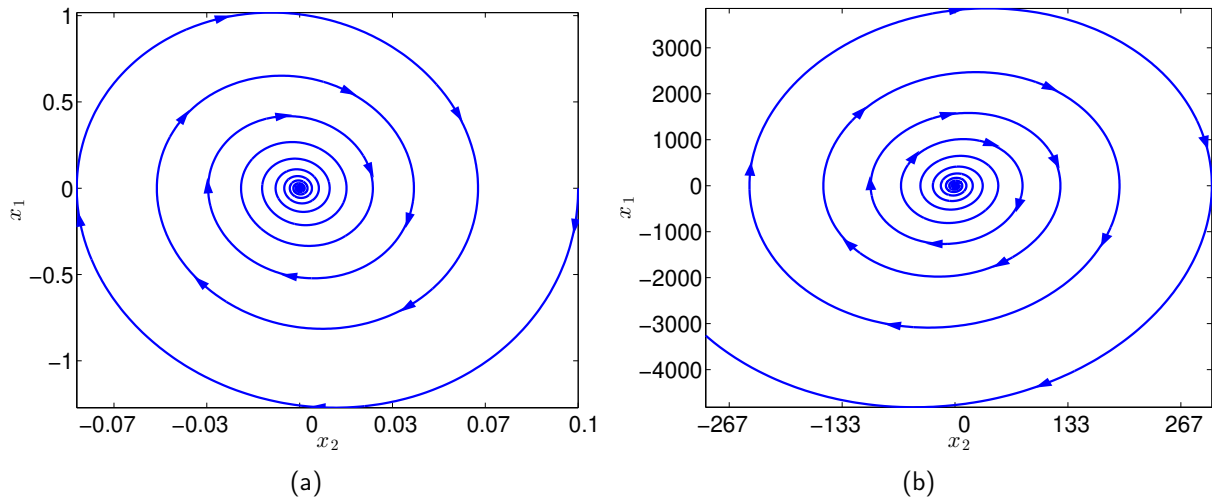


Figure 1: Stable and unstable oscillatory responses of a linear system.

Nonlinear systems behave in a similar manner very close to the fixed point but display more complex behaviour further away from this point. The term nonlinear flutter is usually applied to the Hopf bifurcation, whose critical condition is identical to the linear flutter condition. Nonlinear systems are characterised by the fact that they can have more than one solutions at the same parameter values, hence their steady state response depends on the initial conditions. As the parameters are varied, these solutions also vary and form solution branches. A bifurcation

is the intersection of two or more such solution branches. A Hopf bifurcation is the intersection of a branch of static solutions (the fixed point) with a branch of oscillatory solutions, known as a limit cycle branch. Limit cycles can attract or repel response trajectories in the same way that fixed points do. Responses that decay onto a limit cycle are oscillations with limited amplitude, known as Limit Cycle Oscillations (LCO). This type of response is displayed in the phase plane plot of figure 2(a), where response trajectories starting either outside or inside the limit cycle spiral towards the latter. An unstable limit cycle causes the exact opposite behaviour, as shown in figure 2; response trajectories starting either inside or outside the limit cycle spiral away from the latter.

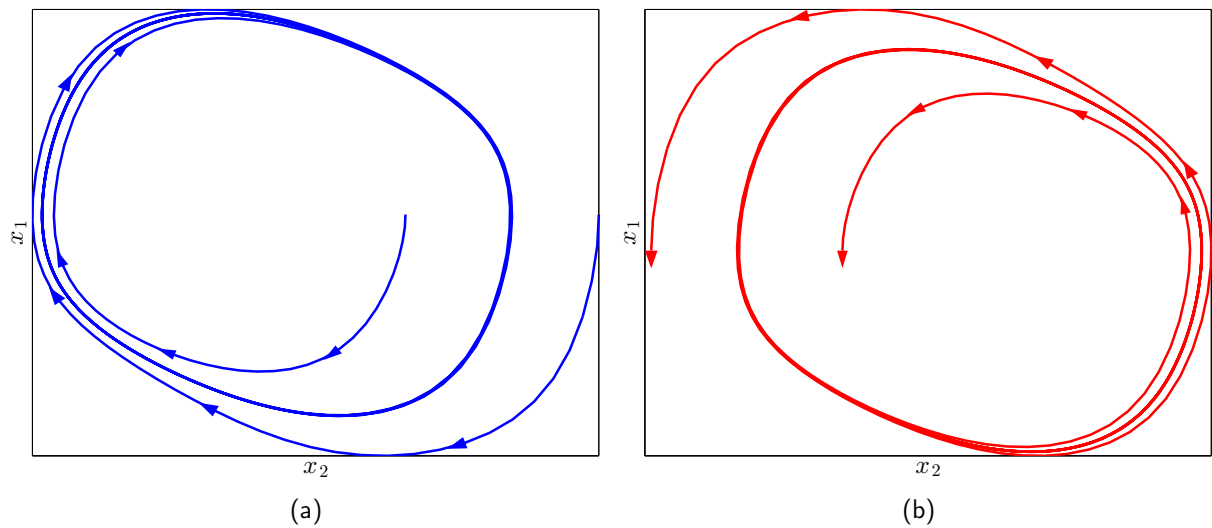


Figure 2: Stable and unstable limit cycle oscillations.

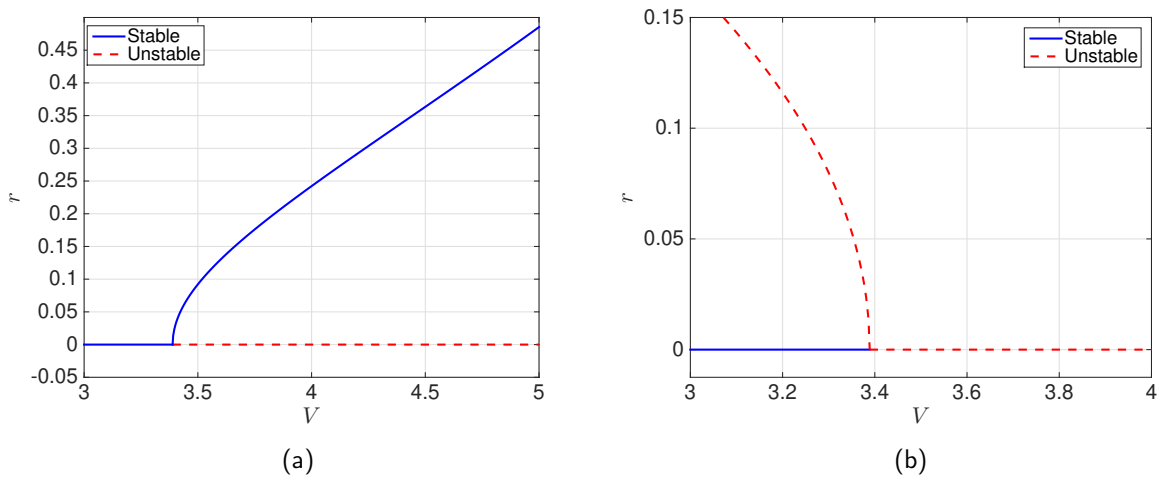


Figure 3: Supercritical (left) and subcritical (right) Hopf bifurcations.

At the Hopf bifurcation point, the fixed point still exists but its stability changes. Furthermore, a limit cycle starts to grow around it. Two major cases of Hopf bifurcation exist:

- Supercritical Hopf bifurcation: The fixed point is stable at parameter values lower than the Hopf condition and unstable at higher parameter values. A stable limit cycle branch emanates from the Hopf point in the direction of increasing parameter value. This phenomenon is demonstrated in figure 3(a), where the limit cycle amplitude r is plotted against the bifurcation parameter V . As the Hopf condition and the linear flutter condition are identical, it follows that a linear flutter analysis can predict the parameter value at which LCOs will begin.
- Subcritical Hopf bifurcation: The fixed point is again stable at parameter values lower than the Hopf condition and unstable at higher parameter values. An unstable limit cycle branch emanates from the Hopf point in the direction of decreasing parameter value. This phenomenon is demonstrated in figure 3(b). A linear flutter analysis can still predict the Hopf point but the usefulness of such a prediction is limited, as the system can be unstable at airspeeds below the flutter condition, if the initial condition lies outside the unstable limit cycle.

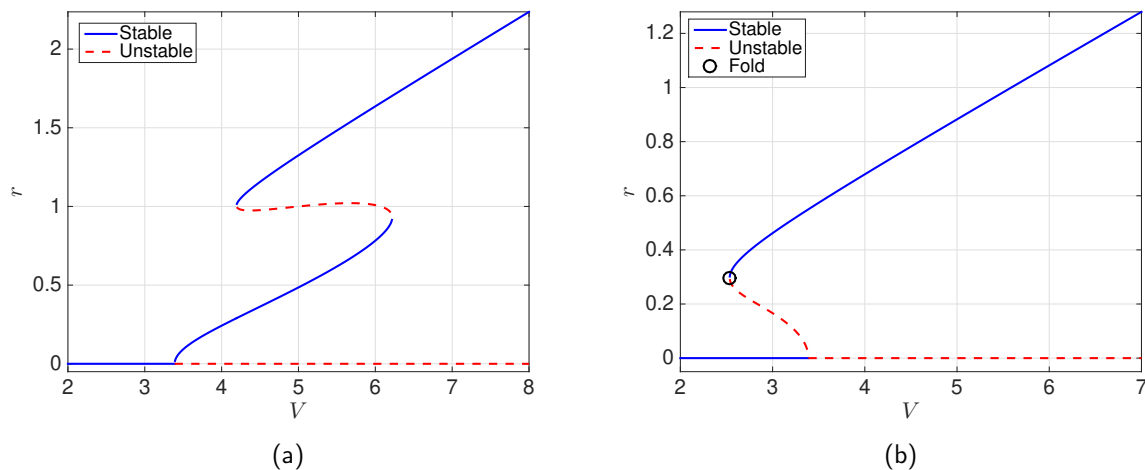


Figure 4: Folds after supercritical (left) and subcritical (right) Hopf bifurcations.

Hopf bifurcations can sometimes be followed by fold bifurcations of limit cycles. These phenomena cause the limit cycle branch to change its stability and to reverse its direction. Figure 4 demonstrates two examples of such folds:

- In figure 4(a) a supercritical Hopf bifurcation is followed by two fold bifurcations. The limit cycle branch is initially stable and propagates towards the right. After the first fold the branch becomes unstable and propagates towards the left. After the second fold, the branch becomes stable again and propagates towards the right. In the parameter range between $V = 4.2$ and 6.2 the system's response trajectories can undergo either a low-amplitude or a high-amplitude LCO, depending on the initial conditions.
- In figure 4(b) a subcritical Hopf bifurcation is followed by a single fold bifurcation. The limit cycle branch is initially unstable and propagates towards the left. After the fold

the branch becomes stable and propagates towards the right. This means that high-amplitude LCOs are possible at parameter values significantly lower than Hopf condition. Linear analysis cannot predict the occurrence of such LCOs.

LCOs can occur as a result of other types of bifurcation, such as the grazing bifurcation occurring in systems featuring non-smooth nonlinear functions. Furthermore, LCOs can have very small amplitude or can even be suppressed in the presence of high damping. Hence, the occurrence of a Hopf bifurcation is not necessarily catastrophic in the linear flutter sense. Nonlinear flutter is much more complex than linear flutter and it is not easy to split the possible values of the flow parameters into safe and unsafe categories. The following experimental examples will demonstrate that real nonlinear aeroelastic systems can conform to the Hopf/fold bifurcation model describe above but they can also display surprising and more complex behaviour.

3 Cantilever flat plate wing

The first example concerns a cantilever flat plate wing installed vertically in the wind tunnel (De Oro Fernández *et al.* , 2020). It is a flat plate made from aluminium with a thickness of 1 mm. The Aspect Ratio is 2.11, the span $b = 0.96$ m and the taper ratio $\lambda = 0.82$. Figure 5 shows a photograph of the wing installed in the aeronautical working section of the wind tunnel for the University of Liège. The wing was placed on a flat steel base lifted 0.3 m off the floor of the working section by means of a steel support rod in order to ensure that the wind tunnel's boundary layer will not affect the flow. The wing was secured to the steel base using two right angle sections, one on each side. Two SICK laser sensors (OD2-P250W15OU0) were used to measure the vibrations of the wing's surface with a sampling frequency of 1 kHz.

Eternal excitation was administered by tugging on a string attached to the wingtip's trailing edge. The response signals were assumed to be impulse responses and were analysed using an in-house version of the Least-Squares Complex Frequency-Domain (LSCF) modal parameter estimator, commercially known as PolyMAX (Peeters *et al.* , 2004). As this type of excitation cannot provide enough energy to the higher modes of vibration, only 2-3 modes could be identified, depending on the airspeed. The modal parameters of the first three wind-off modes of vibration are tabulated in table 1.

Table 1: Wind off modal parameters

	Mode 1	Mode 2	Mode 3
Frequency (Hz)	3.29	9.91	16.69
Damping (%)	2.6	2.2	2.1

The wing was tested at a range of airspeeds, from $U_\infty = 0$ to 24.4 m/s. Figure 6 plots the time responses of the laser sensors at four of the airspeeds. It can be seen that the damping is increased significantly by the effect of the aerodynamics, up to an airspeed of 22.9 m/s when the wing starts to undergo limit cycle oscillations with a small amplitude of around 0.03 cm. LCOs also occur at all higher airspeeds. The decays of the signals at subcritical airspeeds are



Figure 5: Cantilevered flat plate wing in wind tunnel

exponential, as predicted by equation 8 for systems whose eigenvalues have all negative real parts.

Figures 7(a) and 7(b) plot the variations of the natural frequency and damping ratios of the first two modes of the wing for all the tested airspeeds. Both experimental data and predictions obtained from an aeroelastic model based on the Vortex Lattice Method (Dimitriadis *et al.*, 2018) are plotted. The natural frequencies of the first and second modes (corresponding to the first bending and first torsion modes) approach each other as the airspeed increases. Furthermore, the damping ratio of the bending mode becomes very big, while that of the torsion mode drops to zero. This is a classical binary flutter mechanism involving the first bending and first torsion modes. Figure 7(c) plots the variation of the LCO amplitude with airspeed. The first limit cycles appear at 22.9 m/s and their amplitude is small; the amplitude increases steadily over the next three airspeeds. This behaviour is typical of a supercritical Hopf bifurcation.

The nonlinearity present in the system is thought to be mostly dependent on geometric stiffening effects due to high displacements. Some amount of dynamic stall may also be occurring, particularly since the leading edge is rectangular and not rounded off. The results obtained from the cantilevered flat plate wing conform to the classical theory of nonlinear flutter:

- The subcritical behaviour of the system around its fixed point is equivalent to that of the underlying linear aeroelastic system. A typical bending-torsion flutter mechanism brings

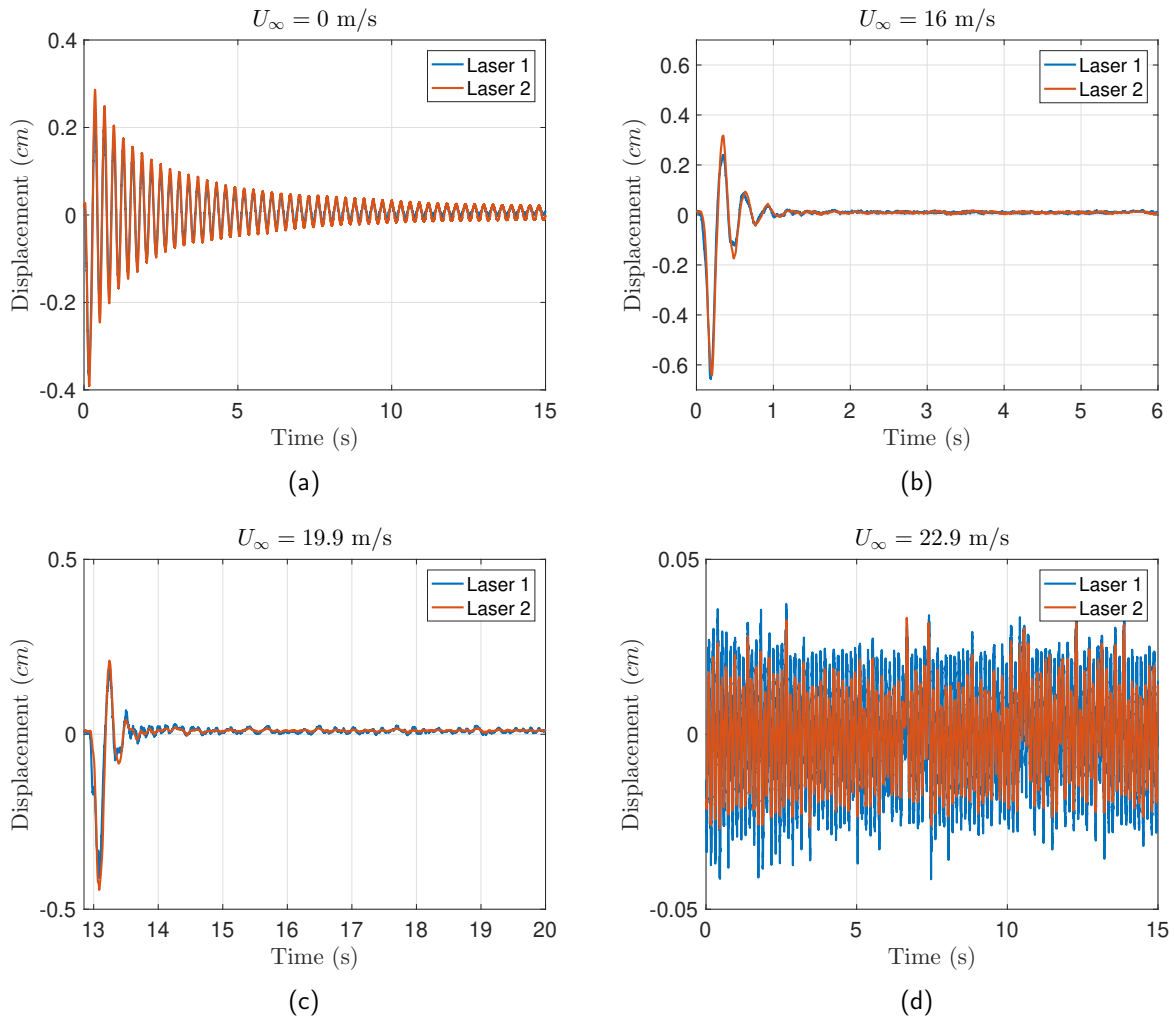


Figure 6: Time response of cantilevered flat plate wing at different airspeeds.

about the loss of stability.

- At supercritical airspeeds, small amplitude oscillations appear but their amplitude increases with airspeed.

It should be noted that many other flat plate wings of the same thickness but with different geometries were tested in the wind tunnel. The bifurcation behaviour was qualitatively the same, even though the LCO critical speeds, frequencies and amplitudes were different.

4 Pitch-plunge wing

This example concerns a finite wing with pitch and plunge degrees of freedom tested in the wind tunnel of the University of Liège. The wing was installed vertically on a support structure that consisted of a base plate (lifting the wing outside the wind tunnel's boundary layer) and a spring assembly that provided restoring loads in the pitch and plunge degrees of freedom. The

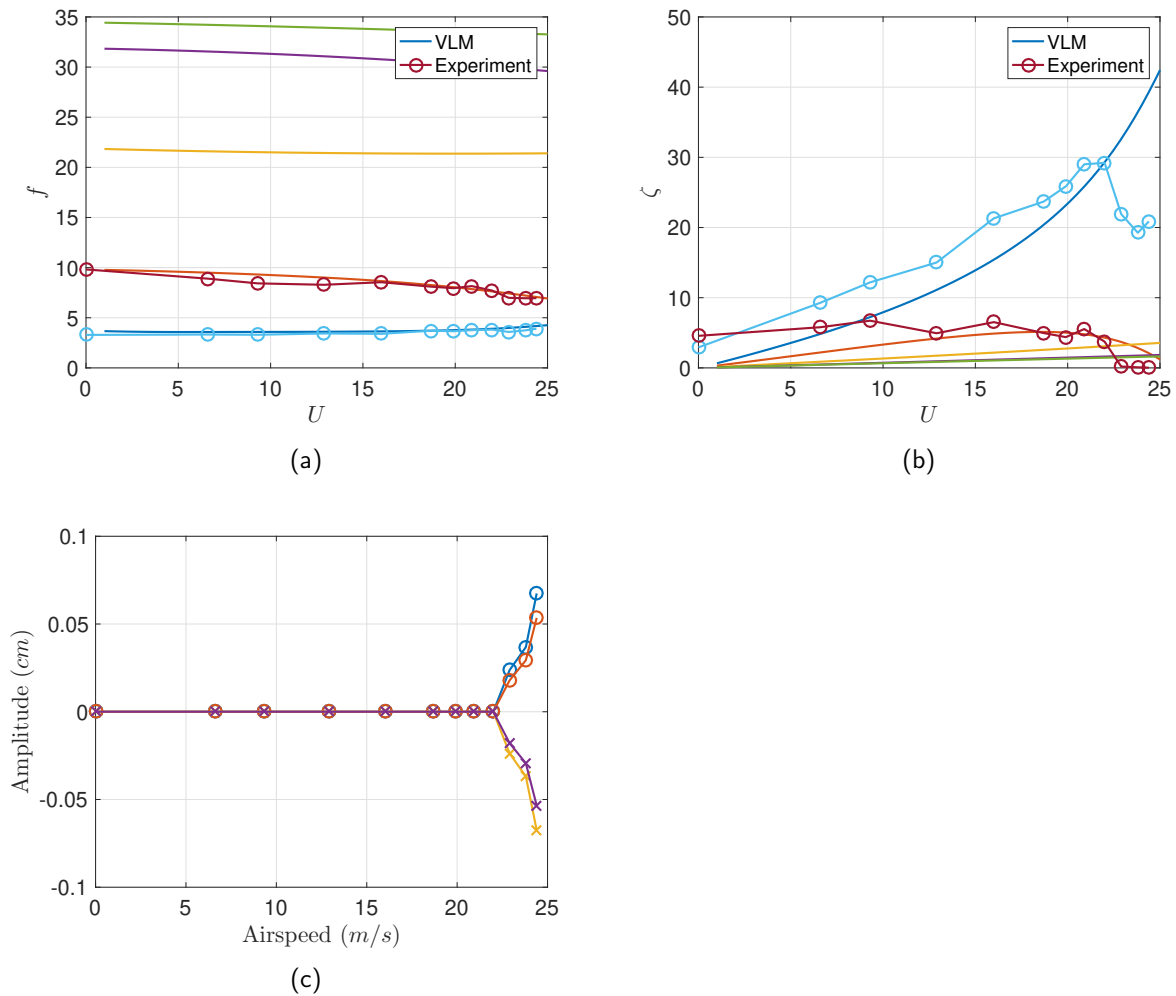


Figure 7: Frequency, damping and amplitude variation with airspeed.

wing had a mass $m = 3.3$ kg, a NACA 0012 section, a chord $c = 0.146$ m and a span $b = 0.47$ m, leading to an aspect ratio of 3.2. The mean angle of attack was set to zero. Figure 8 shows a photo of the wing and its support structure installed in the wind tunnel.

The pitch axis lay at $0.3c$ and the spring supports were designed such that the plunge and pitch degrees of freedom had wind off frequencies of 4 Hz and 8 Hz respectively. Three accelerometers were placed on the wing's surface to measure its motion, two near the wingtip's leading and trailing edges and one on the pitch axis near the root. The accelerometer signals were acquired with a sampling frequency of 1 kHz using a National Instruments Data Acquisition system managed by the Labview software package. The wing was excited by pulling a string attached to the pitch axis under the root. The response signals were assumed to be impulse responses and were again analysed using the LSCF modal parameter estimator. The modal parameters of the first four wind off modes are tabulated in Table 2. The first two modes are the plunge and pitch degrees of freedom; the next two modes could be harmonics of the plunge or they could be additional modes due to undesigned flexibility.



Figure 8: Pitch-plunge wing in wind tunnel

Table 2: Wind off modal parameters

	Mode 1	Mode 2	Mode 3	Mode 4
Frequency (Hz)	3.96	7.81	11.64	16.26
Damping (%)	6.8	8.0	3.3	4.4

The wing was tested at airspeeds ranging from $U_\infty = 0$ to 10.4 m/s; figure 9 plots the time responses of the three accelerometers at three different airspeeds. The responses damp out in figures 9(a) to 9(c) for $U_\infty = 0$, 7.1 and 7.5 m/s respectively. Note that, unlike the flat plate wing case, the decays are not exponential, the decay envelopes are in fact nearly triangular, particularly at the lowest airspeeds. These decays cannot be predicted by equation 8; this phenomenon is probably due to friction in the bearings. At $U_\infty = 7.5$ m/s the response could decay, as shown in figure 9(c), but could also undergo LCOs, as shown in figure 9(d). This was also the case for $U_\infty = 7.8$ m/s. At all higher airspeeds only LCOs were encountered.

All the responses were analysed using the LSCF method, noting that at least four excitations were applied at each airspeed. Figure 10 plots the variation of the natural frequencies and damping ratios of the first four modes of the system, as well as the variation of the LCO amplitude recorded by the three accelerometers, with airspeed. Several aspects of these graphs are interesting:

- The natural frequencies vary very little with airspeed (see figure 10(a)). As mentioned previously, the usual binary flutter mechanism dictates that two of the frequencies must approach each other in order to cause flutter. This is clearly not the case here.
- The damping ratios all decrease with airspeed and jump abruptly to zero when the LCOs start (figure 10(b)). Again, this phenomenon is incompatible with the classical binary flutter mechanism, whereby one of the damping ratios goes to zero while the other

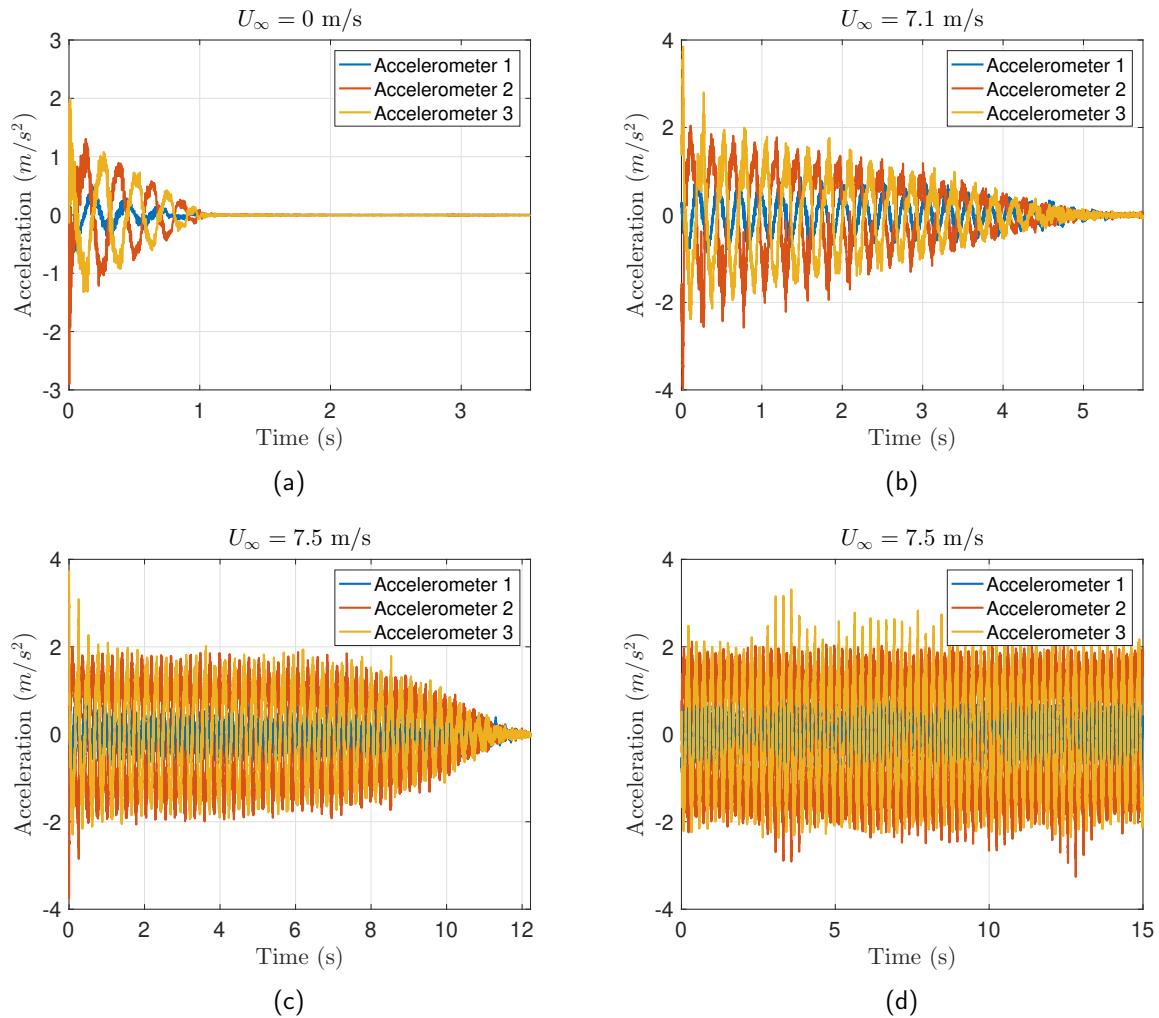


Figure 9: Time response of pitch-plunge wing at different airspeeds.

becomes very high. Note that the damping ratios are very high at wind-off conditions, which is compatible with the previous observation that there may be significant friction in the bearings.

- The first limit cycles encountered at $U_\infty = 7.5$ have a finite, non-negligible amplitude (figure 10(c)). Furthermore, at two airspeeds both stable and LCO responses are encountered. It can be concluded that the LCOs are a result of a subcritical Hopf bifurcation.

The nonlinearity causing the LCOs is not known. Clearly, high amplitude oscillations can lead to dynamic stall and, hence, stall flutter. This could be the case here, as there is no discernible flutter mechanism at subcritical airspeeds. However, significant friction is also present and further undesigned structural nonlinearity cannot be excluded. In any case, the aeroelastic instability observed in figure 10 appears to bypass the classical Hopf mechanism. This could mean that stall flutter (if that is truly the phenomenon occurring here) does not require a classical flutter mechanism to occur; dynamic stall can cause LCOs on an otherwise stable

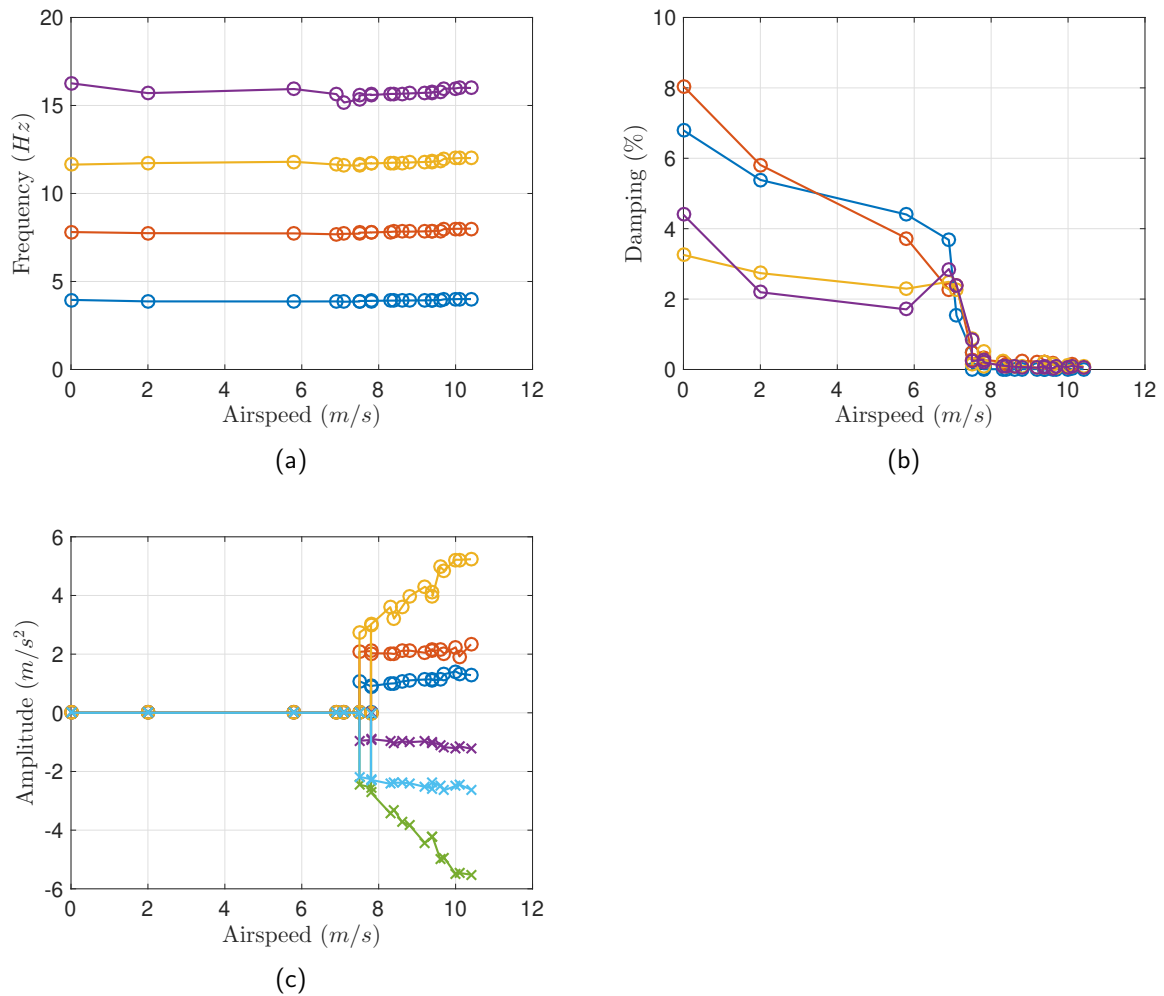


Figure 10: Frequency, damping and amplitude variation with airspeed.

aeroelastic system far from its flutter speed. Nevertheless, at airspeeds $U_\infty \geq 8.3$ m/s, stable responses are no longer possible; only LCOs can occur. This could mean that the Hopf point lies at this airspeed but that the frequency coalescence phenomenon is hidden by the fact that the wing already undergoes LCOs at airspeeds above $U_\infty = 7.8$ m/s. Nevertheless, it is also possible that the non-standard subcritical behaviour seen in figure 10 is due mostly to the high amounts of friction present in the system.

5 4:1 rectangular cylinder undergoing torsional oscillations

This experiment investigated the LCO behaviour of a rectangular cylinder with aspect ratio 4:1 and a pitch degree of freedom (Andrianne & Dimitriadis, 2013). The rectangle had a chord $c = 0.08$ m, height $d = 0.02$ m and span $b = 1$ m. The pitch axis passed through the centre of the rectangle and the pitching motion was measured by means of two accelerometers installed on an adaptor arm. Figure 11 shows a photo of the rectangular cylinder installed horizontally

in the wind tunnel. The root of the cylinder was adjacent to an end-plate while the tip was adjacent to the wind tunnel's wall, ensuring quasi-2D flow. The spring assembly providing a restoring moment in the pitch direction was chosen such that the wind-off natural frequency of the system was 8.15 Hz while the wind-off damping ratio was 2.6%. The critical airspeed for vortex-induced vibrations was much lower than the airspeeds at which LCOs occurred. The nonlinearity in this system is mostly due to dynamic separated flow and, in particular, associated with the shedding of a Motion Induced Vortex. Some structural nonlinearity occurs at angles higher than the highest LCO amplitude recorded during the experiments but this does not preclude other types of undesigned structural nonlinearity, including friction in the bearing.



Figure 11: 4:1 rectangular cylinder in wind tunnel

The cylinder was tested at airspeeds between $U_\infty = 0$ and 14.6 m/s. Initial condition excitation was imposed; the rectangle was held at initial pitch angles between 1° and 10° and then released. Figure 12 plots the variation of the LCO amplitude and frequency with airspeed. LCOs first occurred at $U_\infty = 6.7$ m/s. However, the system needed an initial pitch angle of at least 3° in order to start undergoing LCOs at this airspeed; lower initial pitch angles led to decaying responses. At 6.9 m/s an initial pitch angle of 2° was sufficient to cause LCOs while at higher airspeeds up to 13.9 m/s the LCOs were started using an initial pitch angle of 1° . Nevertheless, at all these airspeeds the system remained stable if the initial pitch angle was 0° . The only airspeed at which LCOs were obtained even with a 0° initial condition is the highest airspeed that was tested, $U_\infty = 14.6$ m/s. Figure 12(a) plots the initial conditions necessary for LCO responses as black circles. It can also be seen that the LCO amplitude variation with airspeed is discontinuous at 9.4 m/s, where the amplitude jumps up by about 5° . The variation of the LCO frequency (in Hz) with airspeed is plotted in figure 12(b). Unlike the amplitude, there is no discontinuity in the frequency. Furthermore, plotting period against amplitude in figure 12(c) we can see that all the points lie on a straight line and that the period increases with amplitude or, equivalently, that the frequency is inversely proportional to the amplitude. This means that the nonlinearity in this system is softening; such systems are usually associated with subcritical bifurcations that lead to static instability. This is clearly not the case here.

The behaviour of figure 12 could be explained in terms of classical nonlinear dynamics, if it is assumed that a subcritical Hopf bifurcation takes place at $U_\infty = 14.6$ m/s. The unstable limit cycle branch would then propagate down to 6.7 m/s before folding, becoming stable and

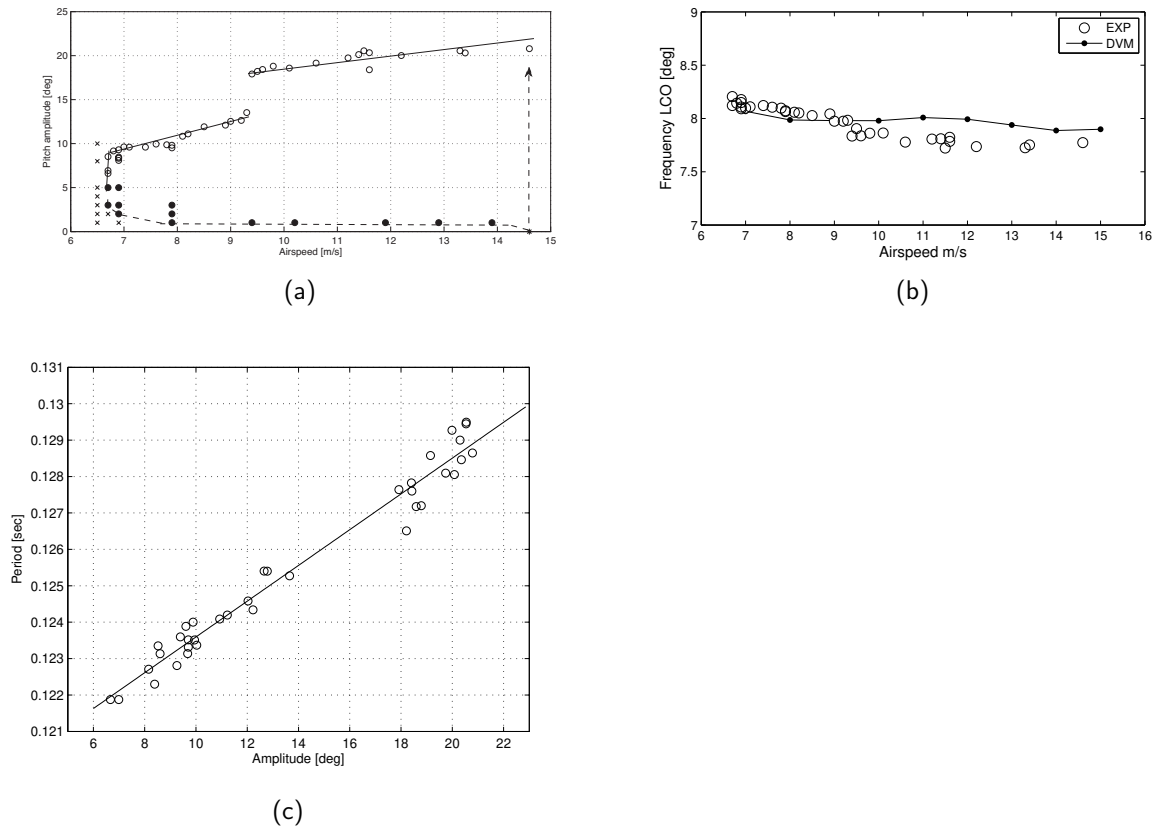


Figure 12: LCO amplitude and frequency variation with airspeed.

reversing direction. The amplitude jump at 9.4 m/s could be the result of a second fold. However, the behaviour could also be explained as the effect of friction in the bearing. It could be that a supercritical Hopf bifurcation occurs at $U_\infty = 6.7$ m/s but, if the initial condition is too low, the friction is sufficient to dissipate the energy absorbed from the flow and the response will decay. Then, at $U_\infty = 14.6$ m/s excitations due to the wind tunnel's natural turbulence and due to vortex shedding from the rectangle would become sufficient to overcome the dissipative effect of the friction and to start the LCOs.

6 Fully suspended finite wing

The previous examples included one case without bearings (the cantilevered flat plate wing) and two cases with at least one bearing. The case without bearings exhibited a classical nonlinear flutter behaviour while the cases with bearings had more complicated bifurcations. However, the present example will demonstrate that this is not a general case; it concerns a rectangular wing with a NACA 0018 section suspended horizontally from 8 extension springs, as shown in figure 13 Abdul Razak *et al.* (2013). The pitch axis lay at 37% of the chord. The wing's chord was 0.36 m and its span 1 m, resulting in an aspect ratio of 2.78. The wing was hollow and contained 16 pressure tapings in its mid-span position, connected to 16 piezoresistive pressure transducers. The wing's motion was measured by means of four accelerometers attached to the

spring adaptor arms and sampled at 1 kHz. A time-resolved Particle Image Velocimetry (PIV) system was used to visualise sections of the flow on the upper surface. The equilibrium angle of attack of the wing, α_{eq} was set to different angles, from 11° to 16° and the wing was tested at airspeeds between 0 m/s and 26 m/s.

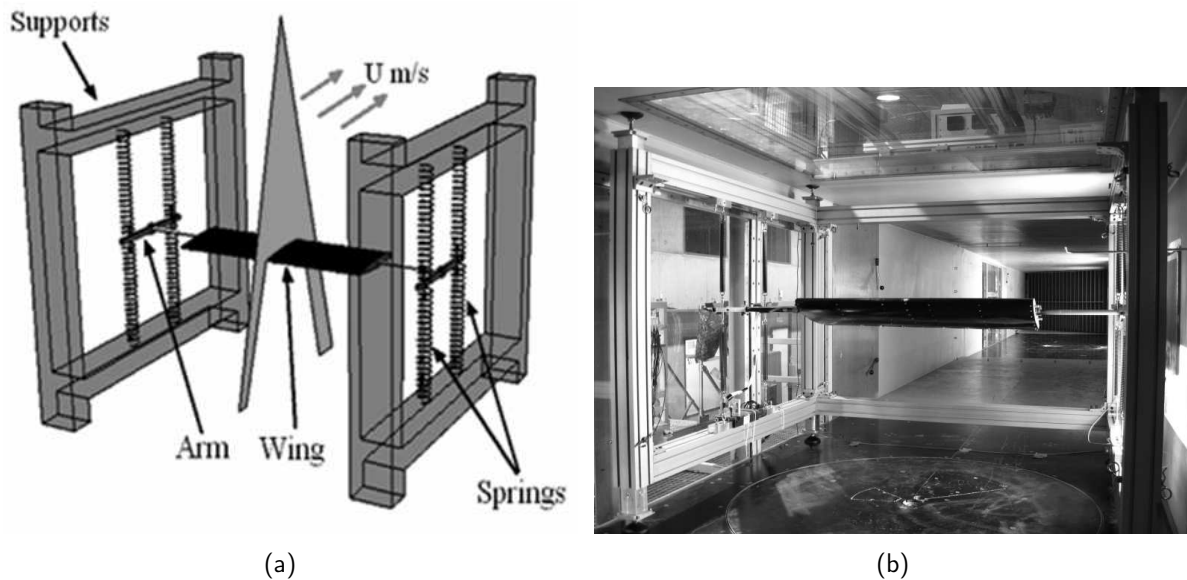


Figure 13: Fully suspended finite wing in the wind tunnel.

As the wing was fully suspended, it had 6 degrees of freedom but its motion was nearly exclusively in the pitch direction, around the pitch axis. The nonlinearity was purely aerodynamic, as the spring assembly behaved in a linear manner throughout the tested extension range and there were no bearings. The interesting aspect of this experiment was that the bifurcation behaviour of the system changed both quantitatively and qualitatively as the equilibrium angle of attack was varied. The complete bifurcation diagram can be seen in figure 14. Its most important characteristics are the following:

- At $\alpha_{eq} = 11^\circ$ the wing underwent a very abrupt bifurcation at 25.2 m/s, which changed the nature of the response from stable to very high amplitude LCOs. The amplitude increased even more at 25.5 m/s, at which speed the test was terminated to preserve the structural integrity of the system. The highest amplitude measured was 15° .
- At $\alpha_{eq} = 12^\circ$ small amplitude LCOs appeared at 20.8 m/s but the amplitude increased abruptly at 21.2 m/s. It increased further with airspeed before the test was terminated. Clearly, two regions of LCO were encountered, a short low-amplitude region and a longer high-amplitude region.
- At $\alpha_{eq} = 13^\circ$ the behaviour was qualitatively similar to the 12° case but all the LCOs appeared at lower airspeed and the low-amplitude region was longer with respect to the high-amplitude region. Furthermore, there was an airspeed range in which both low- and high-amplitude LCOs were possible.

- At $\alpha_{eq} = 14^\circ$ the bifurcation behaviour was changed again, as the jump in amplitude observed in the two previous cases disappeared. Now the LCO amplitude changed smoothly from zero to the highest value of around 10° , although there were three inflection points at around 15, 16 and 18 m/s.
- Finally, at $\alpha_{eq} = 16^\circ$, the number of inflection points in the LCO amplitude-airspeed graph was reduced to one. The critical airspeed was the lowest encountered throughout the tests.

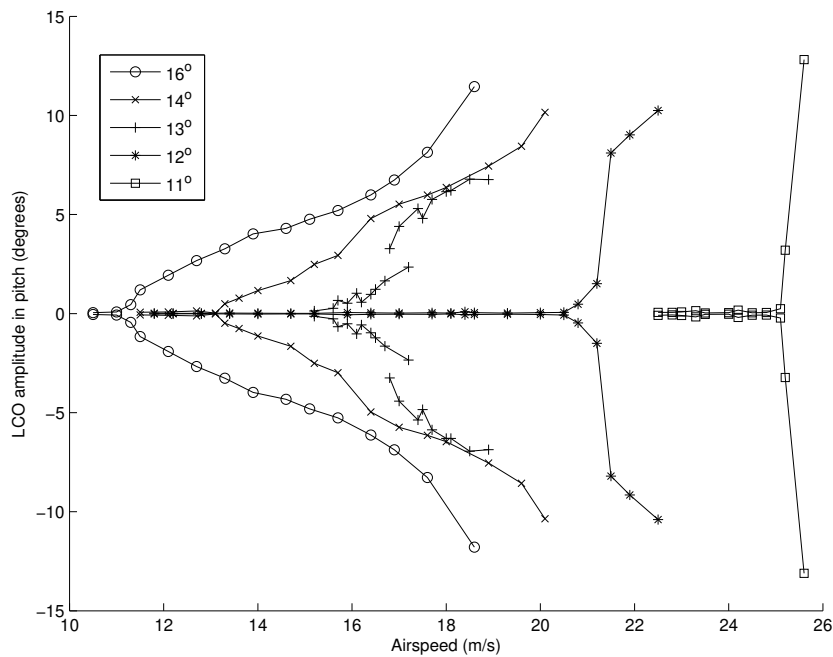


Figure 14: Complete bifurcation diagram for the fully suspended rectangular wing

Interestingly, the fundamental LCO frequency remained nearly constant at all airspeeds and angles of attack, between 5.5 Hz and 6 Hz. The two-parameter bifurcation observed in figure 14 can be described in terms of the Generalised Hopf bifurcation presented in the nonlinear dynamics literature. As the equilibrium angle of attack is increased, the nature of the bifurcation changed from subcritical to sub-critical. At $\alpha_{eq} = 11^\circ$ the bifurcation results in nearly linear flutter; it can be idealised as a subcritical Hopf undergoing a fold at high amplitudes. At $\alpha_{eq} = 12^\circ$ and $\alpha_{eq} = 13^\circ$ the bifurcation is supercritical but the limit cycle branch undergoes a fold, resulting in high amplitude LCOs. At higher equilibrium pitch angles the fold disappears.

In this test case, the bifurcation behaviour is governed completely by dynamic stall. PIV measurements demonstrated that a Leading Edge Vortex is generated near the leading edge and shed over the surface of the wing during the LCOs, at least for $\alpha_{eq} = 13^\circ$. Nevertheless, it is not clear exactly which aspect of the dynamic stall phenomenon causes the bifurcation between low- and high-amplitude LCOs and how the equilibrium angle of attack changes the bifurcation from subcritical to supercritical.

7 Conclusions

This work has presented four wind tunnel tests on nonlinear aeroelastic systems. The nonlinearities were either aerodynamic (dynamic stall) or structural (geometric stiffening or friction). The cantilever flat plate wing conformed to the classical description of nonlinear flutter, which involves a supercritical or subcritical Hopf bifurcation, sometimes followed by one or more fold bifurcations of limit cycles. For the cantilever wing, mostly linear subcritical behaviour turned into LCOs of increasing amplitude at supercritical conditions. However, the pitch-plunge wing system displayed marked differences with classical theory. The subcritical behaviour did not betray the existence of a flutter mechanism, the damping ratios all decreased abruptly to zero and non-zero amplitude limit cycle oscillations appeared abruptly. In classical subcritical Hopf cases, the underlying linear system still features a flutter mechanism; here, there was no evidence of such a mechanism. The bifurcation behaviour of the 4:1 rectangular cylinder could be described as a subcritical Hopf followed by three folds. However, the unstable part of the limit cycle branch would then have a constant and very low amplitude, which is incompatible with the classical quadratic variation of limit cycle amplitude close to a Hopf point. Finally, the fully suspended finite wing demonstrates a two-parameter bifurcation behaviour, whereby the nature of the Hopf and the existence of folds depend on the chosen value of the equilibrium angle of attack.

Acknowledgements

The author would like to acknowledge all his co-workers who contributed to the experiments presented here: Thomas Andrianne, Norizham Abdul Razak and Elena De Oro Fernández.

References

- Abdul Razak, N., Andrianne, T., & Dimitriadis, G. 2013. Flutter and Stall Flutter of a Rectangular Wing in a Wind Tunnel. *AIAA Journal*, **49**(10), 2258–2271.
- Andrianne, T., & Dimitriadis, G. 2013. Experimental and numerical investigations of the torsional flutter oscillations of a 4:1 rectangular cylinder. *Journal of Fluids and Structures*, **41**, 64–88.
- De Oro Fernández, E., Andrianne, T., & Dimitriadis, G. 2020 (Jan.). A database of flutter characteristics for simple low and medium aspect ratio wings at low speeds. *In: Proceedings of AIAA SciTech Forum*.
- Dimitriadis, G. 2017. *Introduction to nonlinear aeroelasticity*. Chichester, West Sussex, UK: John Wiley & Sons, Inc.
- Dimitriadis, Grigorios, Giannelis, NF, & Vio, GA. 2018. A modal frequency-domain generalised force matrix for the unsteady Vortex Lattice method. *Journal of Fluids and Structures*, **76**, 216–228.
- Dowell, E. H. (ed). 2004. *A Modern Course in Aeroelasticity*. 4th edn. Kluwer Academic Publishers.

- Guckenheimer, J., & Holmes, P. 1983. *Nonlinear oscillations, dynamical systems, and bifurcations of vector fields*. Springer.
- Kuznetsov, Y. A. 1998. *Elements of Applied Bifurcation Theory*. 2nd edn. New York Berlin Heidelberg: Springer.
- Lee, B. H. K., Price, S. J., & Wong, Y. S. 1999. Nonlinear aeroelastic analysis of airfoils: bifurcation and chaos. *Progress in Aerospace Sciences*, **35**(3), 205–334.
- Peeters, B., Van Der Auweraer, H., Guillaume, P., & Leuridan, J. 2004. The PolyMAX frequency-domain method: a new standard for modal parameter estimation? *Shock and Vibration*, **11**(3-4), 395–409.

Flutter and buffeting (aircraft, wing, section-model)

Nonlinear flutter analysis for very flexible wing

Liu Yi¹, Cao Xiaolong¹, Hehaibo¹

¹ *Beijing Electro-Mechanical Engineering Institute, Beijing, China,
liuyibuaa@126.com*

Abstract

Because of the extraordinary light weight and flexible structure, the large aspect ratio wing may induce large elastic deformations when undergoing aerodynamic loads and present notable geometric nonlinearity. Thus, the structural stiffness and dynamic characteristics may vary under different aerodynamic loads and deformations, and then the flutter characteristics may change and also present nonlinearity. In this paper, nonlinear flutter will be analyzed under large structural deformation for flexible wings. The analysis results indicate that the flutter speed obtained by nonlinear analysis is much lower than the linear case and even the flutter coupling modes changed. The horizontal bend mode obviously contains twist component and contribute to the unsteady aerodynamics and causes the decline of flutter speed according to the investigation of nonlinear flutter. So the nonlinear flutter analysis can clearly reflect the structural dynamics under large deformation and becomes inevitable.

Keyword: flexible wing, geometric nonlinearity, nonlinear flutter

1 Introduction

The chase for extraordinary flight performance and the wide application of composite materials in aircraft design make the structure flexible and then the flexible aircrafts continue to come forth, such as large-aspect-ratio UAVs, solar-powered UAVs and flying wing UAVs. The flexible aircrafts often utilize large aspect-ratio wing to obtain the good lift-drag ratio and flight performance but the wing may induce large deformations under aerodynamic loads and present notable geometric nonlinearity. The traditional linear aeroelastic analysis based on small deformation hypotheses is no longer suitable and the nonlinear aeroelastic stability and response analysis for flexible aircraft considering the geometric nonlinearity is urgently demanded.

The geometric nonlinear aeroelasticity means the structural large elastic deformations and loads conditions make the structure present notable geometric nonlinearity and change the aircraft configuration. Thus the aircraft stiffness and dynamic characteristics may vary under different deformation and change the flutter characteristics. So for flexible wings the nonlinear flutter speed often lower than the linear flutter speed and make the nonlinear flutter analysis necessary and essential.

Due to the discussions above, the geometrically nonlinear flutter analysis methods are established in this paper. The structural quasi-modes, obtained under nonlinear equilibrium state are combined with unsteady aerodynamic based on deformed configuration to form the flutter equations in frequency domain and solve the critical flutter speed and coupling style. This nonlinear flutter analysis methods can well consider the effect of deformation and loads condition on structural geometric stiffness and stress stiffness and obtain the geometrically nonlinear flutter characteristics. This flutter analysis is much closer to the real

physical scene and get more accurate flutter results.

2 Theory

2.1 Structural geometric nonlinearity

Because of the light weight and weak stiffness, the flexible wing may induce large bend and twist deformations and make the linear small deflection hypotheses vanished. The structural geometric nonlinearity roots form the nonlinear geometric equation, which includes the quadric term of the displacement differential, and requires the nonlinear force equilibrium equation established on the deformed state of the structure. Meanwhile, the linear stress-strain constitutive relationship is still applicable. Structural geometrically nonlinear problems are often solved by the nonlinear incremental finite element methods. In this paper the Updated Lagrange Formula is adopted in this study, and the primary equations are presented briefly below.

The relationship between the nonlinear Lagrange/Green strain and displacement is

$${}^t\varepsilon_{ij} = \frac{1}{2}({}^t u_{i,j} + {}^t u_{j,i} + {}^t u_{k,i} {}^t u_{k,j}) \quad (1)$$

Despite large elastic deformations, the material remains within the elastic limitation for a small strain. So the final element-governing equation can be expressed as:

$$\left({}^t\mathbf{K}_N + {}^t\mathbf{K}_{NL}\right)\mathbf{u} = {}^{t+\Delta t}\bar{\mathbf{Q}} + {}^t\mathbf{F} \quad (2)$$

The stiffness matrix in Eq.(2) can be decomposed into a linear part and nonlinear part. The linear part is only related to the structure itself, whereas the nonlinear part is related to the deformed configuration, load condition and strain quality, each of which should be updated in each computation step.

For aeroelastic stability problems, an assumption of small-amplitude vibration around the nonlinear static equilibrium state is suitable for many dynamic problems, including dynamic stability flexible aircraft:

$$\mathbf{u} = \bar{\mathbf{u}} + \mathbf{x} \quad (3)$$

the vibration equation of the system and the linearized structural quasi-mode can be obtained by generalized diagonalization,

$$\mathbf{M}_T \ddot{\mathbf{x}} + \mathbf{K}_T \mathbf{x} = 0 \quad (4)$$

Despite the hidden nonlinear relations, the form the equations is consistent with the linear free vibration equations, thus the classical solving methods can be adopted. The mode shapes and frequencies under different equilibrium states can be deduced from Eq.(4). The modes get through the linearized dynamic equation is called “quasi-modes”, and that can be utilized in nonlinear flutter analysis.

2.2 Non-planar Doublet Lattice Method(NDLM)

To meet the demand of non-planar aerodynamic computations, mesh dividing should be determined on the deformed surface and updated along with the structure deflection, as shown in Figure 1. In addition to the spatial lattices, local coordinates should be established to reflect the exact non-planar configuration of the wing. The non-planar effect not only is reflected geometrically but also should be contained in the kernel uncton \square . In this section, the DLM code is extended into non-planar cases to account for the 3D unsteady loads of large-aspect-ratio wings with large deflections and can be successively applied in engineering practice.

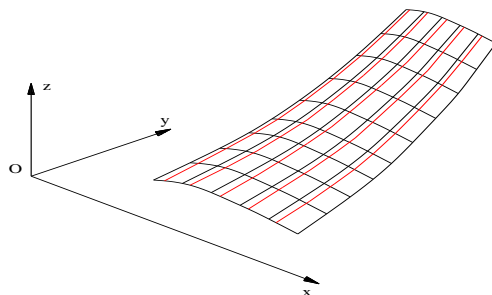


Figure 1: Captions should be centered below figures and above tables.

Figure1 Typical non-planar lattice on a curved lifting surface

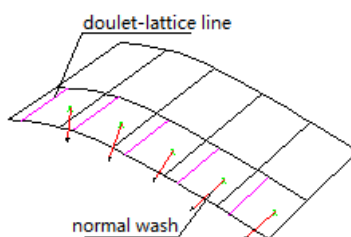


Figure2 Non-planar lattice and the normal wash direction

The kernel function can be expressed as

$$K = \lim_{n_i \rightarrow 0} \frac{\partial}{\partial n_i} \left\{ e^{-i\omega \bar{x}/U_\infty} \int_{-\infty}^{\bar{x}} \frac{\partial}{\partial n_j} \left[\frac{1}{R'} \cdot e^{i\omega(\lambda_1 - M_\infty R')/M_\infty} \right] d\lambda_1 \right\} \quad (5)$$

The critical problem of NDLM is the implementation of exact geometric boundary conditions. The local normal wash velocity can be is computed spatial distributed doublet lattice via kernel function and the boundary condition should be determined by geometrically nonlinear curve lifting surface. Unlike traditional doublet-lattice methods, the local normal wash should be concerned and the linearized model shape obtained around nonlinear equilibrium state should be introduced in unsteady aerodynamic computation in frequency domain. Since the linearized modals may be vary under different equilibrium states, so the unsteady aerodynamics may also be vary and present different characteristics.

Due to the large deformation, the wing can not be treated as vibrating around xy plane, the actual curved boundary condition should be taken into account. \mathbf{n} is the normal vector of lifting surface $S(x,y,z)=0$, $(\mathbf{n},x), (\mathbf{n},y), (\mathbf{n},z)$ are the angles between normal vector and coordinate axis, the motion of lifting surface can be written as $S = S e^{i\omega t}$, so the normal motion velocity can be expressed as

$$(U_n)_S = \left(\frac{\partial x}{\partial t} \right)_S \cos(\mathbf{n},x) + \left(\frac{\partial y}{\partial t} \right)_S \cos(\mathbf{n},y) + \left(\frac{\partial z}{\partial t} \right)_S \cos(\mathbf{n},z) \quad (6)$$

All these geometrically nonlinear managements make it quite different from traditional DLM. Also, the NDLM aerodynamics can be expressed as follows:

$$\mathbf{w} = \mathbf{D}\Delta\mathbf{c}_p \quad (7)$$

\mathbf{D} is the spatial doublet-lattice influence coefficient matrix. Solve the equations above the unsteady pressure can be obtained.

PK method, which is also utilized for flutter analysis, combined with NDLM can be used to implement the nonlinear flutter analysis for very flexible wings to obtain the nonlinear flutter boundary considering the large structural effects.

2.3 Nonlinear flutter analysis

Small disturbance hypotheses are adopted around the nonlinear equilibrium state and “quasi-modes” are introduced in the dynamic equations, then we got:

$$\mathbf{M}\ddot{\mathbf{q}} + \mathbf{K}\mathbf{q} = \mathbf{Q} \quad (8)$$

Using p-k method to solve the equations, it can be rewritten as

$$\left[\left(p^2 \mathbf{M} - p \frac{b}{2k} \rho V \mathbf{Q}^I + \left(\mathbf{K} - \frac{1}{2} \rho V^2 \mathbf{Q}^R \right) \right) \mathbf{q} = 0 \right. \quad (9)$$

$$\left. k = \frac{b}{V} |\text{Im}(p)| \right.$$

The geometrically nonlinear flutter analysis flow chart is shown below, in can be concluded as:

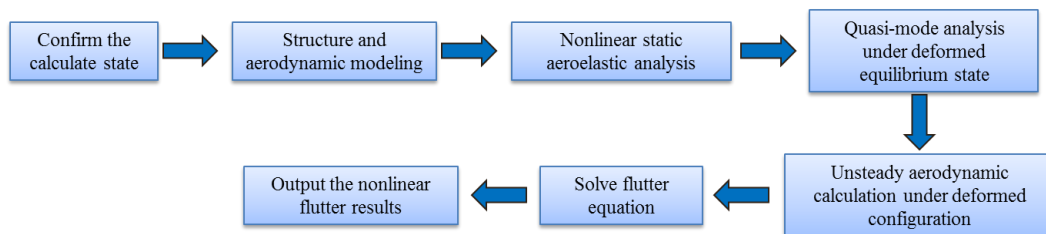


Figure 3 Nonlinear flutter analysis flow chart

- 1) First, conduct the geometrically nonlinear static aeroelastic analysis to get the structural deformation, aerodynamic loads under deformed configuration and the linearized dynamic mass and stiffness matrix.
- 2) Linearized dynamic vibration analysis around nonlinear equilibrium state to get the “quasi-mode”.
- 3) Unsteady aerodynamic calculation under deformed configuration with “quasi-mode”.
- 4) Establish the aeroelastic flutter equations and solve it with *p-k* methods in frequency domain.
- 5) Obtain the nonlinear flutter speed and flutter characteristics for very flexible wings.

3 Example

The calculated example wing is constructed with 3 main beams located at front, middle and back, 17 ribs, 4 stringers and skin. While in the FEM model, they are modeled with beam elements and shell elements shown in Figure 4. The detailed calculation conditions are listed in Table 1.

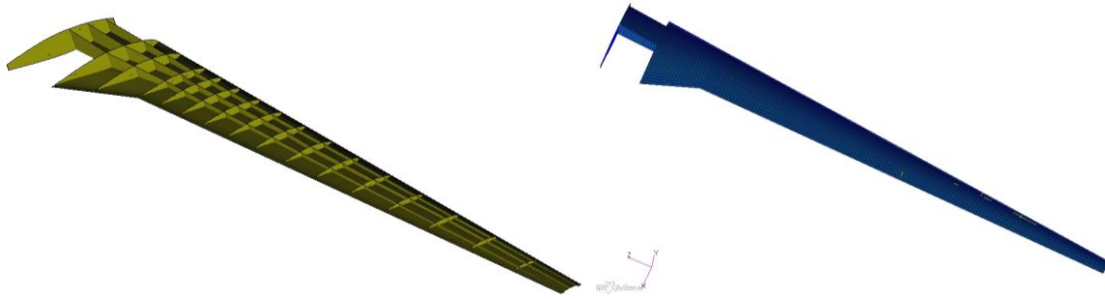


Figure 4 Wing model
Table 1 Calculate conditions

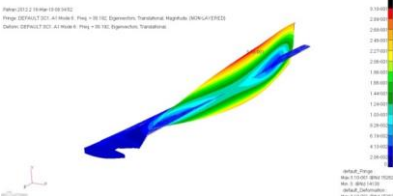

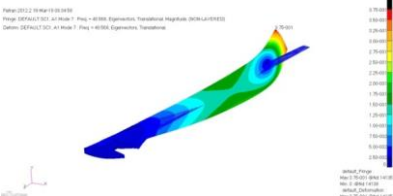
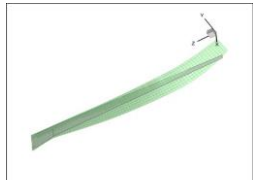
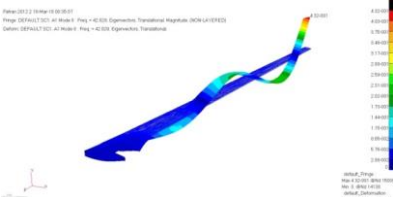

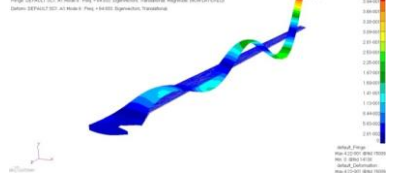

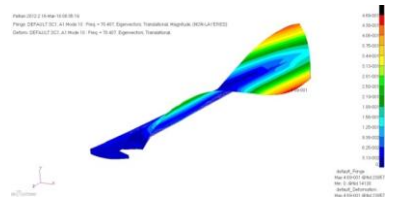

Altitude	Mach	Angle of attack
5000m	0.5	1°

3.1 Linear flutter analysis

The linear flutter analysis is only related with linear structural modes and unsteady aerodynamics but nothing on deformations and load conditions. The linear structural modes and interpolated unsteady aerodynamic modes are shown in Table 2.

Table 2 Linear structural modes

No.	Frequency /Hz	description	Mode shape	Aerofdynamic modes
1	3.46	1 st verticla bend		
2	10.78	2 nd verticla bend		
3	12.39	1 st horizontal bend		
5	24.24	3 rd vertical bend		

6	38.19	1 st twist		
7	40.56	2 nd horizontal bend		
8	42.82	4 th vertical bend		
9	64.83	5 th vertical bend		
10	70.40	2 nd twist		

Solving the flutter equations with p-k method can get the varying tendency of mode frequency and damping with the increase of speed. When the mode damping turns to positive from negative, that indicate the flutter occurs and the critical flutter speed corresponding to the zero damping. Here are the linear flutter analysis results.

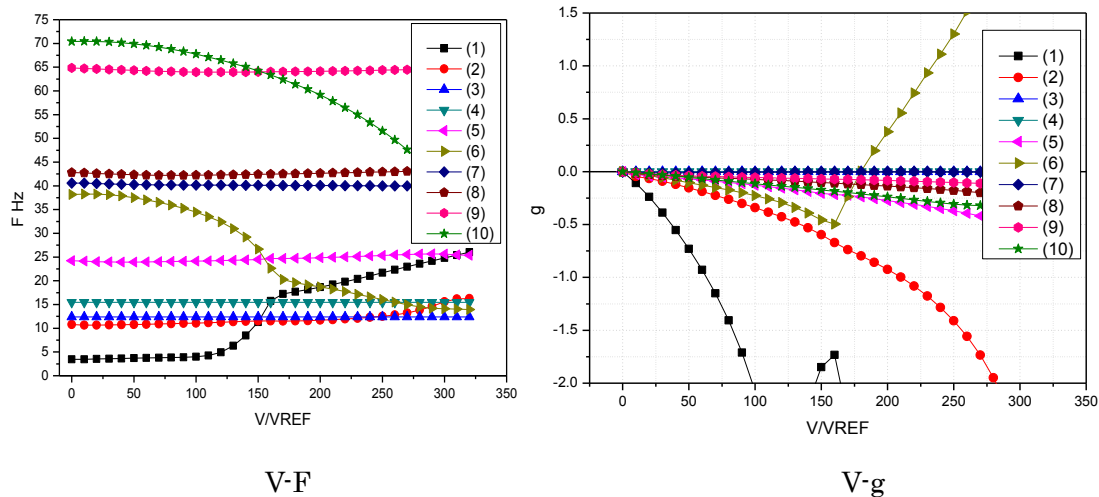


Figure 5 Linear flutter V-g and V-F curve

The analysis results in Figure 5 indicate that the wing presents a typical bend/twist coupling flutter(1st vertical bend coupled with 1st twist) in linear analysis. With the increase of speed, the 1st twist mode tends to unstable under the speed of 179m/s, with the frequency at 19.6Hz.

3.1 Nonlinear flutter analysis

Before the nonlinear flutter analysis, the geometrically nonlinear static aeroelastic analysis should be conducted first. Apply the aerodynamic load on the flexible wing and use the updated Lagrange formula to get the nonlinear structural deformation, which is shown below.

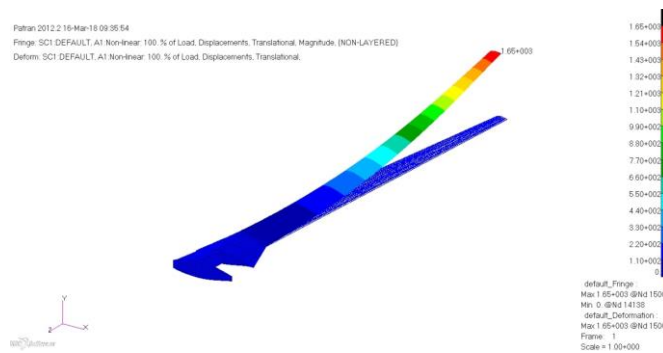


Figure 6 Nonlinear static deformation

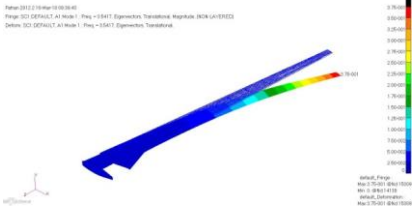

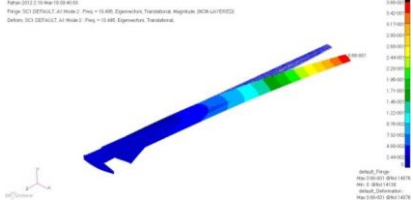

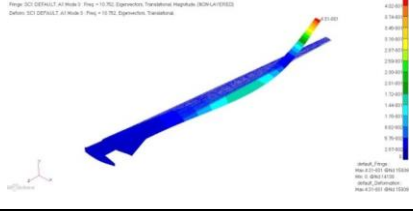
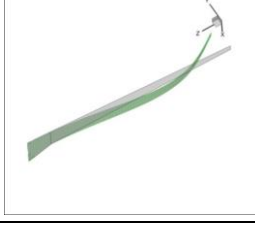
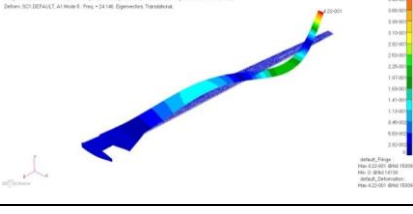
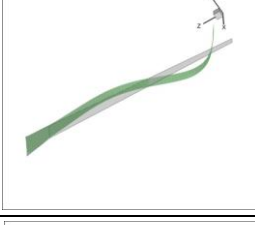
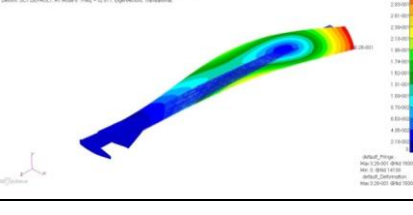

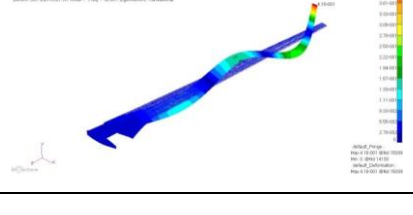
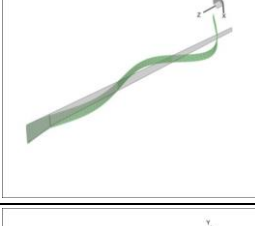
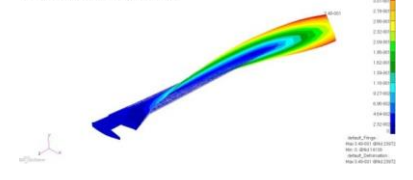
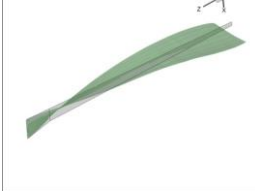
Table 3 Wingtip deflections

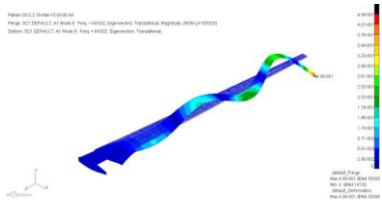
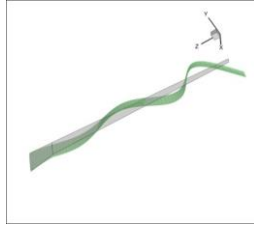
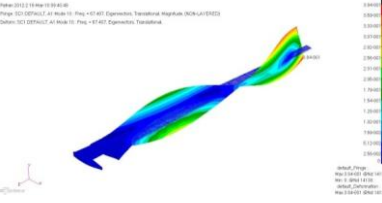

Wingtip deflections	x-axis	y-axis	z-axis	Relative vertical deflection Compared with semispan
	49.81mm	1638.83mm	187.51mm	14.89%

The nonlinear static analysis indicate that the vertical deflection of wingtip is 1638mm(almost 15% of the semispan), and the chordwise(x-axis) and spanwise(z-axis) deflections are also significant, which can not be reflected and often ignored in linear analysis. However, it is quite important in nonlinear analysis and has a big influence on structural dynamic characteristics.

After the nonlinear static analysis, the linearized dynamic characteristics are analyzed and the obtained “quasi-mode” are shown below.

Table 4 The linearized “quasi-mode”

No.	Frequency /Hz	description	Mode shape	Aerodynamic modes
1	3.542	1 st vertical bend		
2	10.495	1 st horizontal bend		
3	10.752	2 nd vertical bend		
5	24.146	3 rd vertical bend		
6	32.817	2 nd horizontal bend+twist		
7	42.681	4 th vertical bend		
8	54.825	1 st twist		

9	64.632	5 th vertical bend		
10	67.407	2 nd twist		

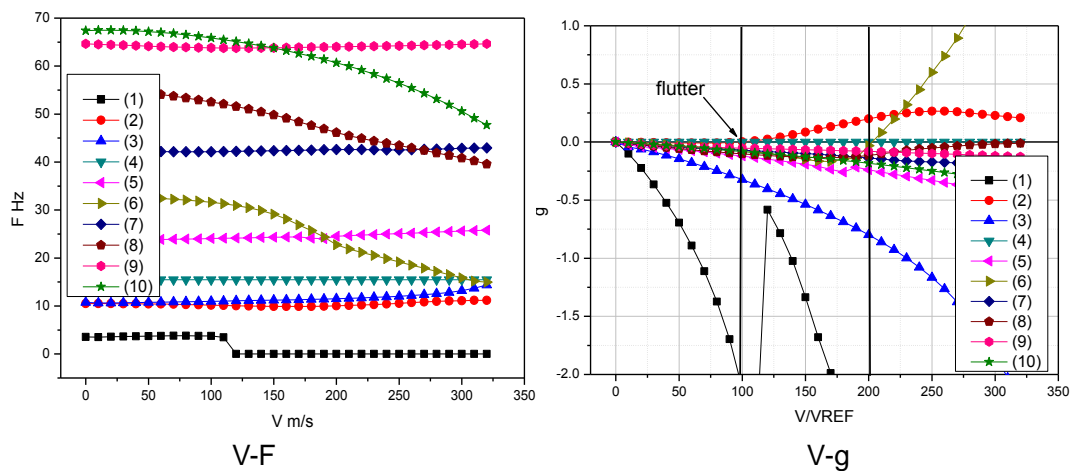


Figure 7 Nonlinear flutter V-g and V-F curve

In nonlinear flutter analysis, there are two modes across the critical damping line and become unstable, which is quite different from the linear analysis results. The lowest flutter speed is 97m/s, at the frequency of 10.2Hz, which is coupled with 1st vertical bend and 1st horizontal bend. The second flutter speed is 203m/s at the frequency of 22.5Hz. It can be concluded that because of the geometric nonlinearity not only the flutter speed is decreased but the flutter coupled modes are also changed. The traditional bend/twist coupling form are not typical and instead the horizontal bend mode participate and become the key mode in flutter, changing the flutter coupling style and decreasing the flutter speed.

Conclusion

Nonlinear flutter analysis method in frequency domain considering the geometric nonlinearity caused by large deformation for very flexible wing is established in this paper and an example flexible wing are analyzed to validate the method and demonstrate the nonlinear flutter characteristics. The analysis results indicate that the large structural deformation may change the stiffness and dynamic characteristics, and as a consequence, the flutter characteristics are changed. Because of the structural large deformation and geometric nonlinearity, the linearized horizontal bend modes frequencies declined and the modes shape contain twisting components, thus the flutter speed and flutter coupling form are both changed. The coupling form is changed from typical bend/twist coupling form, which is usually presented in linear flutter, to vertical bend modes coupled with horizontal

bend modes. Additionally, the nonlinear flutter speed decreases dramatically. Therefore, the nonlinear flutter analysis considering about the structural large deformations and geometric nonlinearity is inevitable and it can prevent the flight performance decline and the defect of flight envelope.

References

- E. Dowell, J. Edwards, and T. Strganac, "Nonlinear aeroelasticity," *Journal of Aircraft*, vol. 40, no. 5, pp. 857-874, 2003.
- M. J. Patil and D. H. Hodges, "On the importance of aerodynamic and structural geometrical nonlinearities in aeroelastic behavior of high-aspect-ratio wings," in *Proceedings of the 41st AIAA/ASME/ASCE/AHS/ASC Structures, Structural Dynamics, and Materials Conference*, pp. 799-809, Atlanta, Ga, USA, April 2000, AIAA-2000-1448.
- M. Y. Harmin and J. E. Cooper, "Aeroelastic behaviour of a wing including geometric nonlinearities," *The Aeronautical Journal*, vol. 115, no. 1174, pp. 767-777, 2011.
- E. Albano and W. P. Rodden, "A doublet-lattice method for calculating lift distributions on oscillating surfaces in subsonic flows," *AIAA Journal*, vol. 7, no. 2, pp. 279-285, 1969.
- MSC, *Nastran 2001 Books-Aeroelastic Analysis*.
- Changchuan Xie, Yi Liu, Chao Yang, J.E. Cooper. Geometrically Nonlinear Aeroelastic Stability Analysis and Wind Tunnel Test Validation of a Very Flexible Wing. *Shock and Vibration*, vol.2016, Article ID 5090719, 17 pages, 2016. Doi:10.1155/2016/5090719.
- C. C. Xie and C. Yang, "Linearization method of nonlinear aeroelastic stability for complete aircraft with high-aspect-ratio wings," *Science China Technological Sciences*, vol. 54, no. 2, pp.403-411, 2011.
- Yi L, Changchuan X, Chao Y. Aeroelastic Trim Analysis of Flexible Aircraft Based on 3-D Lifting-line Theory, 54th AIAA/ASME/ASCE/AHS/ASC Structures, Structural Dynamics, and Materials Conference April 8-11, 2013, Boston, Massachusetts
- S. Tianxia, *Nonlinear Structure Finite Element Computation*, HuaZhong University of Science & Technology Press, Wuhan, China, 1996 (Chinese).
- Yi Liu, Changchuan Xie, Chao Yang, Jialin Cheng. Gust response analysis and wind tunnel test for a high-aspect ratio wing[J]. *Chinese Journal of Aeronautics*, 2015. DOI:10.1016/j.cja.2015.12.013

Effects of turbulence models on the unsteady transonic aerodynamics of an oscillating airfoil

Koji Isogai

Professor Emeritus, Kyushu University, Fukuoka, Japan, koji.isogai@nifty.com

Keyword: turbulence model, unsteady transonic flow, CFD, RANS code

The unsteady transonic aerodynamics is very important in the sense that the swept back wing experiences the sharp drop of the flutter speed in transonic region. In this paper, the accuracy and reliability of the turbulence models, that are indispensable for the prediction of the unsteady transonic aerodynamic forces at high Reynolds numbers using the RANS (Reynolds Averaged Navier-Stokes) code, are extensively examined. The turbulence models examined are the Baldwin and Lomax algebraic model and the SST $k - \omega$ model. The detailed comparisons of the unsteady pressure distributions and the aerodynamic forces with the experimental data obtained for the NACA64A010 at Reynolds number 1.2×10^7 are conducted. Both the models give satisfactory agreement with those of the experiment as far as the boundary layer is attached. However, the B & L model shows poor agreement with the experimental data obtained at $Re = 1.2 \times 10^7$ in the case where the shock induced flow separation occurs, while the SST $k - \omega$ model shows a fair agreement with those of the experiment. In Fig. 1, the typical flow patterns (iso-density contours) around the NACA64A010 airfoil oscillating in pitch around the quarter chord point at Mach=0.80 and the mean angle of attack of 4 degree, that are computed using the B & L model and the SST $k - \omega$ model, are shown as an example of the computations. As seen in the figures, both the models predict the shock induced flow separation. However the B & L model predicts too strong and too aft-positioned shock wave compared with that of the SST $k - \omega$ model which gives better agreement of the shock pattern with that of the experiment.

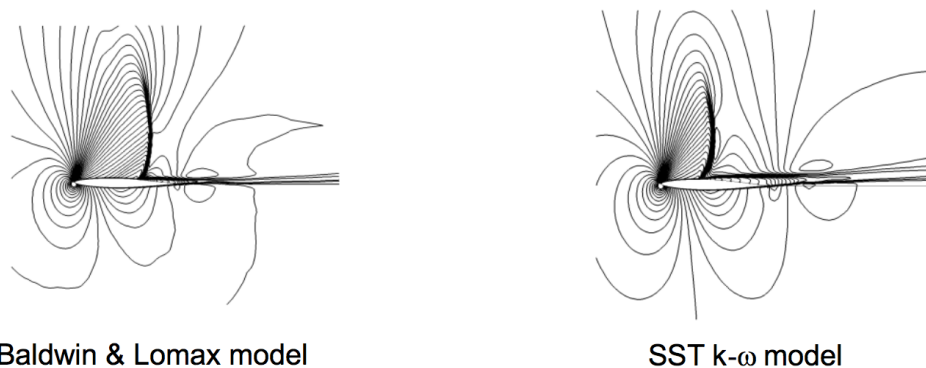


Figure 1: Flow pattern (iso-density contour) around oscillating NACA64A010 airfoil. ($M_\infty = 0.80$, $\alpha = 4^\circ + 1^\circ \sin(kt)$, $k = 0.204$, $Re = 1.2 \times 10^7$).

Aeroelastic risks of interflap seals

Raphaël Dubois¹, Thomas Andrianne¹, Bruno Bernay² and Grigorios Dimitriadis¹

¹ *Department of Aerospace and Mechanical Engineering, University of Liège, Allée de la Découverte 9, 4000 Liège, Belgium, raphael.dubois@student.uliege.be*

² *Systems team, SONACA, Route Nationale 5 1/Z, 6041 Charleroi, Belgium*

Keyword: Aeroelastic risks, CFD, modal analysis, interflap seals, vortex shedding

The work aimed to initiate the investigation of aeroelastic risks of interflap seals. The latter - located between the inboard and outboard flaps - suffered from aeroelastic phenomena during the first test flights performed by the aircraft manufacturer. A methodological study was therefore carried out to identify the features which can be at the origin of the vibrations the seals suffered from.

To do so, a two-dimensional CFD analysis at low-subsonic conditions was first performed by means of unsteady RANS simulations. The analysis revealed the shedding of vortices at the trailing-edge of the flap. This is illustrated in Fig. 1. The vortex shedding causes periodic aerodynamic load oscillations on the flap which may induce the seals to vibrate.

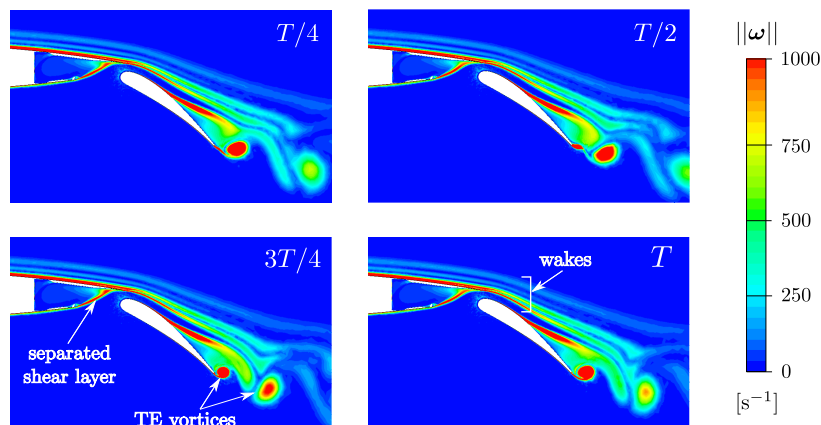


Figure 1: Vorticity contours at different time instances in a period of oscillation.

Once modal analyses of the structure were computed, a qualitative comparison between the results from the CFD analysis and the modal properties was made to briefly introduce and discuss the potential aeroelastic risks the structure may encounter in the nominal flight conditions. The evolution of the aerodynamic forces on the flap reported non-negligible amplitudes of oscillation with respect to the time-averaged values, especially considering flexible bodies such as the investigated seals. The excitation frequency (shedding frequency) was found particularly close to the resonance frequencies of two modes of a particular stacking version. The excitation mechanism finally confirmed the possibility for those modes to be excited.

Note that an experimental set-up will be developed to reproduce the aeroelastic behaviour of the seals in a wind tunnel. The experimental measurements will therefore serve as validation data for further numerical simulations.

Research on Elastic Wing Flutter Considering Propeller Slipstream

Zhang Zhitao¹, Xie Changchuan¹, Yang Lan¹ and Yang Chao¹

¹School of Aeronautic Science and Engineering, Beihang University, Beijing, China,

zhangzhit1605@buaa.edu.cn

Keywords: propeller slipstream, elastic wing, flutter, unsteady vortex lattice

Abstract

Due to its excellent performance, the propeller aircraft plays an important role in the military filed. As a matter of fact, high-speed rotation of the propeller produces slipstream. The slipstream has complex mutual aerodynamic interference with other parts of the aircraft, such as wing and tail. Flutter is a dynamic aeroelastic instability, which is an undesirable phenomenon in aircraft. The propeller slipstream effect on elastic wing aerodynamics and flutter is one of the most important issues in the research of aerodynamic layout design of propeller aircraft^{[1][2]}.

The aerodynamic load is calculated by unsteady vortex lattice method(UVLM). As shown Fig.1, we get the aerodynamic model of propeller and slipstream. Now, we are developing a rapid computational method to predict the propeller slipstream-elastic wing aerodynamic interaction. All calculations in this paper will be based on this aerodynamic global coordinate system.

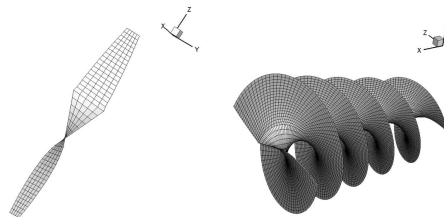


Figure 1 propeller aerodynamic model

As shown in Fig.2, we use the “elastic wing / propeller” model to develop the flutter characteristics.

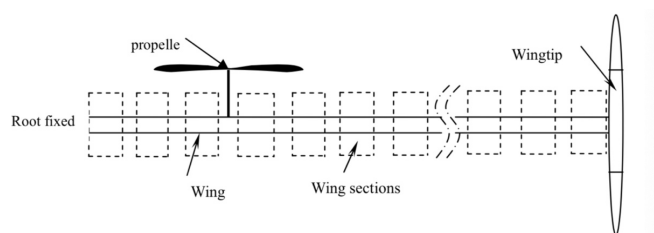


Figure 2 Structure of the “Elastic Wing / Propeller” system

The work presented here uses UVLM for aerodynamic modeling and FEM for elastic wing/propeller system modeling. A method to predict elastic wing flutter in the time domain based on unsteady vortex lattice is in processing. In final paper, completed flutter analysis will be illustrated.

[1] Agostinelli C,Liu C H,Allen C B,et al. Propeller-flexible wing interaction using rapid computational methods, AIAA-2013-2418[R].San Diego:AIAA,2013.

[2] Ognev V , Rosen A . Influence of Using Various Unsteady Aerodynamic Models on Propeller Flutter Prediction[J]. Journal of Aircraft, 2011, 48(5):1708-1721.

Preliminary Combat Aircraft CFD Wind Tunnel Testing on Vortex Induced Loads

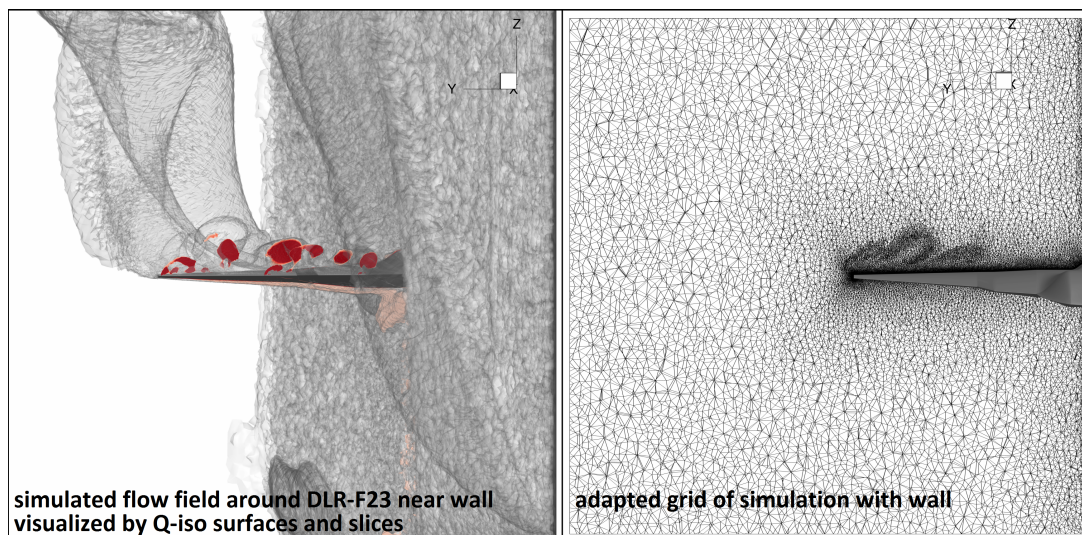
J. C. I. Zastrow¹

¹ DLR-AE, Goettingen ,Germany, jonas.zastrow@dlr.de

Keywords: vortex breakdown, leading edge separation, grid adaptation, delta wing, buffeting

Even though the progress in CFD-development is very rapid, unsteady and aperiodic phenomena in fluid mechanics are still mostly the domain of experiments, since the numerical results are either not precise enough, the calculations demand too many resources or both applies. Consequently important effects on fighter aircraft such as buffeting, control reversal and force-motion hysteresis ask for thoroughly planned wind tunnel experiments, which binds a lot of personnel and financial resources. Accompanying the planning of the investigated flight regime and the wind tunnel model's sensor instrumentation by numerical calculations is a mandatory task. Preliminary investigations decrease the resulting risks for the experiment dramatically, while they increase its effectiveness through adapted parameter settings.

An upcoming wind tunnel test campaign with a next generation fighter jet planform DLR-F23, which runs in scope of the DLR-project "Diabolo", shall be investigated on beforehand numerically with the usage of a grid adaptation technique. The implementation of this technique leads to skipping the laborious process of grid design almost completely¹.



¹ Zastrow, J. (2019). Characterizing a Multi Delta Wing for Aeroelastic Wind Tunnel Experiments. International Forum on Aeroelasticity and Structural Dynamics 2019.

Aeroelastic stability assessment of a V-Tail with integrated propulsion units

Christopher Koch¹, Jürgen Arnold¹

¹ *DLR Institute of Aeroelasticity, Göttingen, Germany, Christopher.Koch@dlr.de*

Abstract

This paper deals with the aeroelastic stability assessment of the empennage section of the hybrid-electric motor glider FVA 30. Because of its integrated propulsion units at the tips it is prone to a special kind of aeroelastic instability called whirl flutter. This instability of the V-tail involves the whirl modes of the propellers. Parameter studies regarding the most important structural parameters are carried out to evaluate the design space and identify critical flutter modes. The models are also checked for empennage flutter and ground resonance. Due to the early design phase this is done by numerical studies with simplified models using the in-house flutter process, PySTAB, and strip theory propeller aerodynamics. The investigations show the possibility of a V-tail flutter due to insufficient mass balance of the combined elevator/rudder control surface. In contrast, the empennage structure shows large margins regarding whirl flutter of the tailplane structure itself. The pylon and engine mount are assumed to be rigid though due to lacking design data. Ground resonance of the elastic propeller blades is prohibited by the dynamic couplings due to blade twist.

Keyword: aeroelastic stability, motor glider, V-tail, whirl flutter

1 Introduction

The FVA 30 is a hybrid-electric motor glider which is currently being designed by the FVA, a student association based in Aachen, Germany. The aircraft will be a two-seated touring motor glider (TMG) in side-by-side configuration and powered by two electric motors at the two tips of a V-tail (shown in Fig. 1). To speed up the design, the front part of the fuselage as well

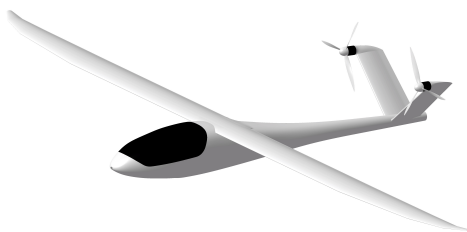


Figure 1: Design of the hybrid electric motor glider FVA 30

as the wings are adopted from the eGenius, an aircraft built by the university of Stuttgart (Schumann 2018). The project is now moving towards the critical design review (CDR) and the configuration shall be evaluated for its aeroelastic stability beforehand. Due to the large propellers mounted at remote locations this evaluation especially involves instability phenomena caused by these propellers, namely whirl flutter and ground resonance. This is done before the CDR to account for any necessary changes in the design.

2 Methods

Before moving on to the model of the FVA 30 empennage and the stability results, an introduction into the theory and used methods is given. This includes the basic whirl flutter theory as well as its integration into the in-house flutter process, PySTAB. As the theory and stability analysis for ground resonance differ from this, it will be summarised separately. For a more detailed discussion of the methods refer to Koch et al. (2019).

2.1 Theory of (whirl-) flutter analysis

A rotating propeller in a flexible engine bed is subjected to gyroscopic whirl modes. Due to the aerodynamic forces these whirl modes can become unstable (Čečrdle 2015). This phenomenon is called whirl flutter. A simple model to describe this behaviour is shown in Fig. 2. This system consists of a rigid propeller on a shaft with a yaw and pitch degree of freedom (cf. top of Fig. 3). The yaw and pitch modes merge to a forward and backward whirl mode due to gyroscopic coupling under rotation. Considering the aerodynamic forces caused by this whirling motion the backward whirl mode eventually becomes unstable (Čečrdle 2015).

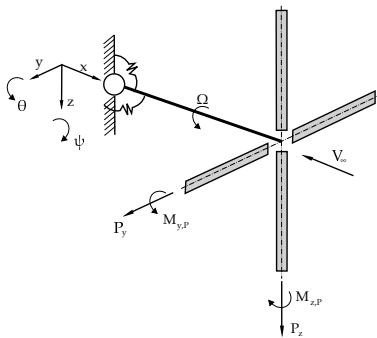


Figure 2: Rigid propeller with two tilting-DOF

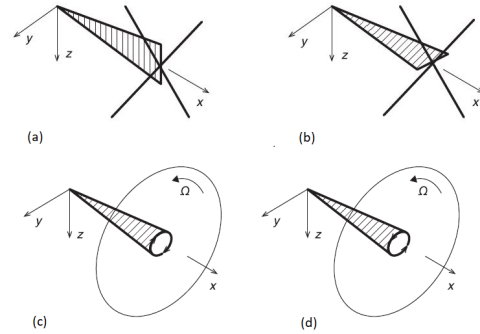


Figure 3: Basic behaviour of a propeller in a flexible engine bed

Considering a linear strip theory one can describe the propeller aerodynamics by stiffness and damping terms for the propeller hub point (Houbolt and Reed III 1962). In Eq. 1 these terms are expressed as non-dimensional derivatives. $C_{m\psi}$ for example is the non-dimensional pitching moment m due to a yaw angle ψ . In general these depend on the forward and rotational speed.

$$\frac{F_P}{2q_\infty \pi R^3} = \begin{bmatrix} 0 & 0 & \frac{C_{y\theta}}{2R} & \frac{C_{y\psi}}{2R} \\ 0 & 0 & \frac{C_{z\theta}}{2R} & \frac{C_{z\psi}}{2R} \\ 0 & 0 & C_{m\theta} & C_{m\psi} \\ 0 & 0 & C_{n\theta} & C_{n\psi} \end{bmatrix} \begin{pmatrix} y \\ z \\ \theta \\ \psi \end{pmatrix} + \begin{bmatrix} -\frac{C_{y\psi}}{2RV} & \frac{C_{y\theta}}{2RV} & \frac{C_{yq}}{2V} & \frac{C_{yr}}{2V} \\ -\frac{C_{z\psi}}{2RV} & \frac{C_{z\theta}}{2RV} & \frac{C_{zq}}{2V} & \frac{C_{zr}}{2V} \\ -\frac{C_{m\psi}}{V} & \frac{C_{m\theta}}{V} & \frac{C_{mq}R}{V} & \frac{C_{mr}R}{V} \\ -\frac{C_{n\psi}}{V} & \frac{C_{n\theta}}{V} & \frac{C_{nq}R}{V} & \frac{C_{nr}R}{V} \end{bmatrix} \begin{pmatrix} \dot{y} \\ \dot{z} \\ \dot{\theta} \\ \dot{\psi} \end{pmatrix} \quad (1)$$

To analyse more complex systems than the one in Fig. 2, the propeller aerodynamics has to be coupled with a structural model (e.g. the empennage structure of the FVA 30). This is done by adding the stiffness and damping terms of the propeller to the structural model in physical coordinates (Rodden and Rose 1989). To reduce the number of degrees of freedom for

the stability analysis, the complete model is transformed into modal coordinates. This results in Eq. 2:

$$M_{gen}\ddot{q} + K_{gen}q = \phi^T K_P \phi q + \phi^T D_P \phi \dot{q} + \frac{1}{2} \rho_\infty V_\infty^2 Q_{hh}(k) \quad (2)$$

M_{gen} and K_{gen} represent the modal mass and stiffness matrix of the base structure, ϕ is the modal matrix transforming physical into modal coordinates q . K_P and D_P represent the propeller terms from Eq. 1 including the gyroscopic terms. The last part of Eq. 2 allows for the inclusion of frequency-domain aerodynamics for the remaining part of the aircraft. $Q_{hh}(k)$ represents the generalized aerodynamic forces, that depend on the reduced frequency k . In this case, the aerodynamics for the tailplane and the control surface are calculated by an unsteady acceleration potential method, ZONA6 (Chen et al. 1993). If these are included in the stability analysis, the problem changes from a set of explicit eigenvalue problems (first terms in Eq. 2 are only velocity-dependant) to an implicit flutter problem. These can be solved e.g. using the g-method for flutter solutions (Chen 2000). The solution of Eq. 2 in different varieties is a very common problem for aircraft flutter application and is therefore automated in the in-house tool PySTAB.

2.2 Linear Frequency Domain Flutter Process : PySTAB

To analyse aircraft configurations w.r.t their flutter stability in the linear frequency domain, a python environment is used to automate the flutter analysis process. This environment uses the commercial software ZAERO as a core and allows for the consideration of different aspects like engine gyroscopic loads, in-plane aerodynamic forces, propeller forces or even more sophisticated generalized aerodynamic forces (GAF) from the CFD Solver TAU-LFD (cf. Fig. 4). By switching to state-space formulation, aeroservoelastic calculations can be carried out. Depending on the needs of the configuration to be analysed, the user can decide which effects to be included. In the case of the FVA 30 empennage section, propeller gyroscopic and aerodynamic loads are considered, while the aerodynamics for the tailplane are the standard ZONA6 aerodynamics, as flight speeds and Mach numbers are moderate.

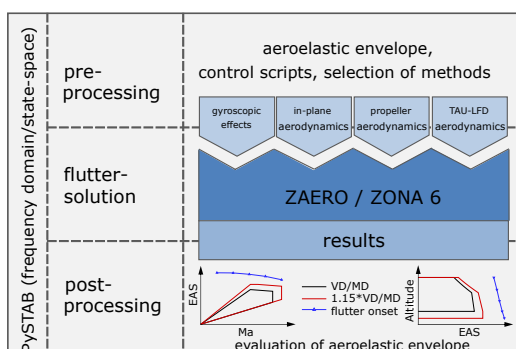


Figure 4: PySTAB: linear frequency domain stability process

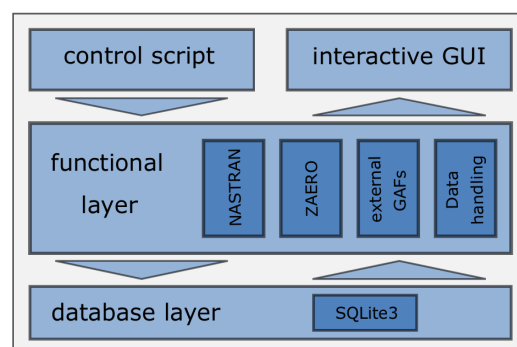


Figure 5: PySTAB software architecture

As the flutter assessment of an aircraft usually needs a lot of parameter studies (Mach number, density, mass cases, control system, structural parameters,...), PySTAB uses a three-layer architecture (cf. Fig. 5). A underlying database stores all data for the different configurations and analysis steps, while a functional layer manages all the tasks during the analysis. Finally, control scripts and a GUI provide easy access and control over the simulations and results.

2.3 Ground Resonance

If flexibility of the rotor blades is considered, there is the possibility of another instability phenomenon called ground resonance, which is of completely different nature. While (whirl-)flutter involves aerodynamic forces, ground resonance is a pure mechanical instability (Bielawa 1992). It is well known in the field of helicopter dynamics, but can also become relevant in case of very flexible propeller blades.

The mechanism causing this instability is an energy transfer from the drive system through a rotating blade mode into the support (Cardinale et al. 1969). The rotor mode involved is the so called regressive cyclic mode. The blades oscillate with a 120 deg phase shift in this mode. For a lead-lag-degree of freedom, this is shown in Fig. 6. This phase shift leads to a whirling motion of the rotor center of gravity around the hub. In the regressive cyclic mode, this whirling motion is inverse to the direction of rotation, which also affects the frequency characteristics with increasing rotational velocity. Looking at the eigenfrequencies of a simple rotor on an elastic support, one can observe the regressive rotor mode dropping in frequency (branch labelled $|\omega_\zeta - \Omega|$ in Fig. 7) till it reaches a point of zero frequency. From this rotational speed on the rotation of the whirling motion changes to forward. This low frequency forward cyclic mode (also called supercritical cyclic mode) can now couple with the underlying support, leading to the described instability called ground resonance (coupling regions are marked with dashed circles in Fig 7).

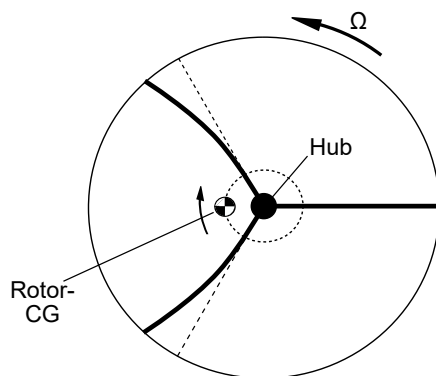


Figure 6: Regressive cyclic lead-lag mode shape with shifted rotor-CG

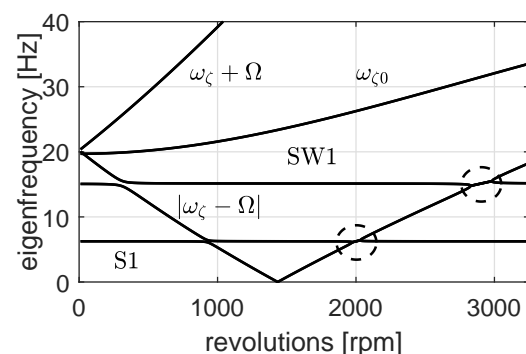


Figure 7: Example for a Campbell-diagram with two regions of ground resonance

To assess a system for ground resonance, a coupled dynamic description of the rotor blades and the support structure is needed. Johnson (1974) developed a dynamic description of a flexible rotor at the tip of a wing structure. The model includes two degrees of freedom per blade, one lead-lag and one flap mode, as well as the first three eigenmodes of the wing structure (in- and out-of-plane-bending as well as torsion).

If more degrees of freedoms shall be incorporated or a more sophisticated dynamic description of the model is necessary, numerical multi-body-simulations (MBS) can be used to capture more effects (cf. Arnold and Waitz (2018)). In this case, the MBS-software SIMPACK is used to couple a modal description of the propeller blades with the flexible tailplane structure. The MBS-model is linearised at different rotational speeds and the resulting state space model is subjected to an eigenvalue analysis. Beforehand the rotating blade degrees of freedom have to be transformed into rotor degrees of freedom in the non-rotating frame. This is done using multi-blade coordinate transformation (Bir 2008).

3 Models

After summing up the theory and methods used to analyse the empennage structure, a brief introduction into the modelling of that structure will be given before moving on to the results. The basic structural layout of one side of the V-tail consists of a box beam stiffened by four stringers and five ribs (cf. Fig. 8 left). A control surface takes up the trailing 35 % of the lifting surface. The rotational degree of freedom around the hinge axis has no stiffness and the control surface can therefore rotate freely. The main structure will be manufactured from carbon composite and is modelled as a finite-element shell-model in MSC.NASTRAN.

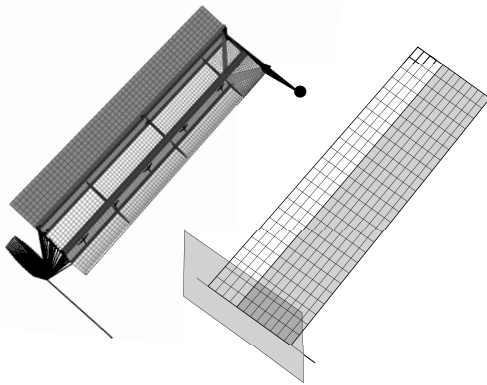


Figure 8: Structural and aerodynamic model of one empennage half

Table 1: Frequency ranges for the first three eigenmodes of one V-tail half. For the definition of the base configuration see Koch et al. (2019)

	f_{min} [Hz]	f_{base} [Hz]	f_{max} [Hz]
out-of plane	5.9	6.7	10.6
in-plane	12.7	16.2	30.6
torsion	44.0	66.3	75.0

The electric propulsion unit is mounted in front of the leading edge at the tip of the V-tail (marked with a black marker in Fig. 8 left). It is structurally modelled as a point mass that is rigidly attached to the base structure. Both sides of the V-tail are attached to a beam representing the fuselage degrees of freedom. The unsteady aerodynamics of the lifting surfaces are calculated by an acceleration potential method, ZONA6 (Chen et al. 1993). One side is therefore discretized into 24 x 12 panels (cf. Fig. 8 right) and connected to the structure by an infinite plate spline to interpolate deformations and forces between the different grids. A node at the propeller hub serves as interface for the propeller forces in Eq. 1. Due to the early design phase, most of the structural parameters are not clearly defined. To include these uncertainties into the stability assessment, parameter studies for the driving uncertainties are carried out to evaluate their effect on the stability. These include the mass balance of the control surface, the motor mass and its distance from the leading edge as well as the number of composite layers in the main structure. By combining several values a large set

of parameter combinations is formed around the nominal design. Using the automation capabilities in PySTAB this parameter space can easily be covered. The variation of structural parameters mainly affects the eigenfrequencies. The ranges for the first three eigenmodes are shown in Tab. 1, together with the corresponding mode shapes in Fig. 9 - 11.

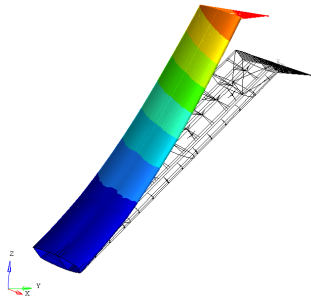


Figure 9: First out-of-plane bending mode

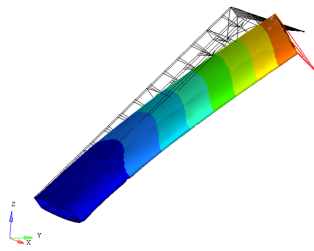


Figure 10: First in-plane bending mode

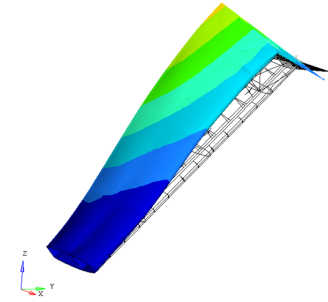


Figure 11: First torsional mode

4 Results

Moving on to the results of the stability assessment, this section will start off with presenting the results focussing on tail flutter. Afterwards the stability with rotating propeller is investigated and results for whirl flutter and ground resonance are shown.

4.1 Tail Flutter

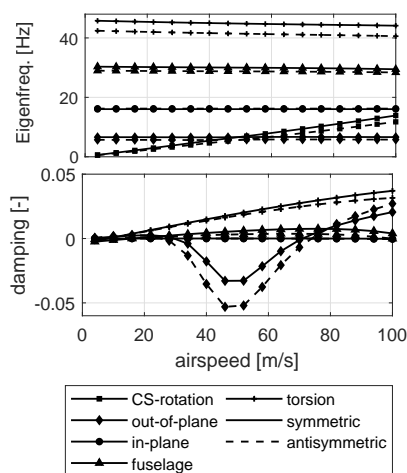


Figure 12: Frequency and damping trends for the base configuration

Using the full model of the FVA 30 empennage including both sides, the control surface and the fuselage beam, flutter calculations are carried out for the whole design space to check for flutter stability. Frequency and damping for the first ten eigenmodes of the base configuration are plotted in Fig. 12 for increasing velocities up to the certification speed of 1.2 times the dive speed V_D equal to 100 m/s. Two instabilities indicated by negative damping arise between 30 - 70 m/s. One is a symmetric control surface flutter, the second one is its antisymmetric counterpart. Both instabilities are caused by a coupling of the control surface mode with the first tailplane bending mode as the control surface mode increases in frequency with airspeed due to aerodynamic stiffness terms. In case of approaching frequencies the control surface movement extracts energy from the flow and feeds it into the bending mode. Due to the phase lag between both motions the bending mode becomes unstable (Försching 1974). The phase lag is a result of insufficient mass balance of the control surface. The center of gravity (CG) of the control surface usually lies aft the hinge axis.

This leads to a mass coupling between heave motion and control surface rotation. A mass balance reduces this coupling by shifting the control surface CG forward, eventually eliminating the instability. The effect of increasing mass balance on the damping of the first tailplane bending mode is shown in Fig. 14. A full mass balance (100%) is equivalent to a control surface CG lying on the hinge axis (and therefore completely removing the coupling). It can be seen that above a certain value of mass balance the model stays stable over the whole range of velocities. The mass balance needed to stabilise the control surface flutter varies over the design space. Fig. 13 shows the percentage of unstable configurations in the design space depending on the value of the mass balance. Below a mass balance of 70% almost all configurations show control surface flutter, while above 87% the whole design space is stable. This also implies, that no other flutter mechanism besides control surface flutter occurs.

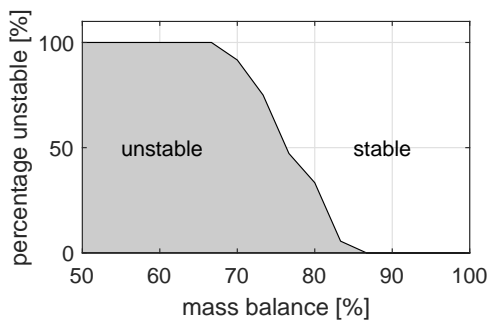


Figure 13: Share of unstable configurations depending on the mass balance

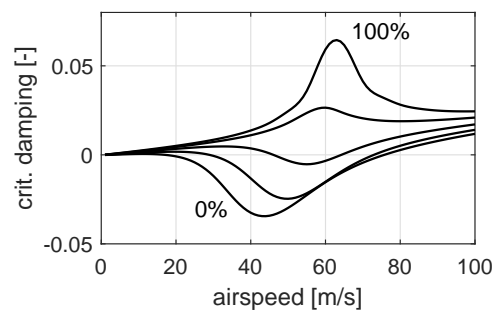


Figure 14: Effect of mass balance on the damping trends

4.2 Whirl Flutter

Taking the gyroscopic and aerodynamic terms for the propeller into account, the possibility of whirl flutter arises. First the system is checked for whirl flutter without taking the tailplane aerodynamics into account (neglecting the last term in Eq. 2). The design space is evaluated for its whirl stability and margins for the driving parameters, e.g. first eigenfrequencies are identified. The effect of the combined consideration of propeller and tailplane aerodynamics is shown exemplarily for the base configuration (c.f. Tab. 1).

The stability of a whirl system is heavily dependant on the first eigenfrequencies of the support structure showing a significant tilting of the propeller plane. Therefore these (in form of the entries of the generalized stiffness matrix K_{gen} in Eq. 2) are scaled, until the system becomes unstable. Fig. 15 plots a parameter space for the first two eigenfrequencies with a tilting of the propeller plane (cf. Fig. 10 and 11). The black line marks the limit of stability. Higher frequencies (upper right corner) are stable, lower frequencies result in whirl flutter. The dark grey area surrounding the stability limit marks the area of uncertainty gained from repeating this process throughout the design space. It should be noticed, that this stability limit marks the frequencies, at which the system would theoretically become unstable due to whirl flutter. The actual frequencies of the in-plane and torsion modes are marked as a point and a light grey area for the uncertainty. It can be seen clearly in Fig. 15 that the area of the actual frequencies lies far beyond the stability limit in the stable range, leaving a minimal margin factor of 4.5.

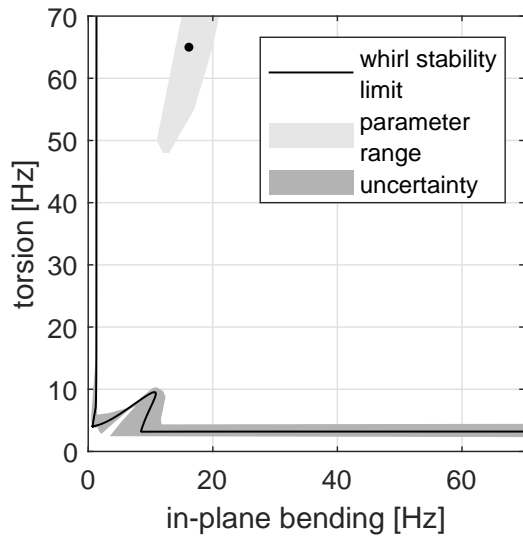


Figure 15: Whirl flutter stability limit with uncertainty ranges

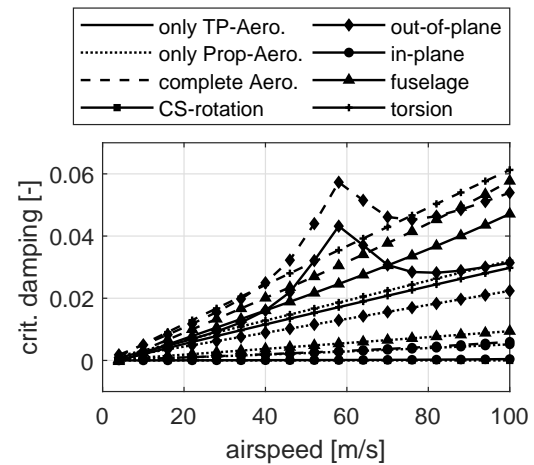


Figure 16: Damping trends for symmetric empennage modes with different aerodynamics considered

The safety margins increase even further when taking the tailplane aerodynamics into account. Fig. 16 shows the damping trends for the first five symmetric empennage eigenmodes for the base configuration including 100 % mass balance to suppress the control surface flutter. Trends only considering the tailplane aerodynamics are drawn continuously, the ones considering only the propeller aerodynamics in dotted lines and the ones combining both aerodynamics and solving Eq. 2 including all terms are depicted as dashed lines. As expected for a linear system, damping effects add up and the complete system shows higher damping ratios. In this case a separate evaluation of empennage and whirl flutter stability is therefore a conservative approach.

4.3 Ground Resonance

By considering flexibility of the propeller blades the model is also checked for ground resonance. Because ground resonance requires a supercritical cyclic mode, one has to look for the behaviour of the regressive cyclic modes with increasing rotational velocity. The Campbell diagram showing the structural eigenfrequencies of the base configuration is shown in Fig. 17. Continuous lines are calculated using the analytical model developed by Johnson (1974) whereas the dashed lines result from numerical analysis using MBS SIMPACK. Two blade degrees of freedom are considered, called flap and lead-lag. In case of a three-bladed rotor these form three rotor modes, which are marked with diamond and square markers respectively. The regressive modes drop in eigenfrequency, but none reaches a supercritical state. The model is therefore free of ground resonance.

To ensure stability even for more flexible blade designs this is captured by a parameter study, gradually decreasing the first blade eigenfrequencies. The effect is shown in Fig. 18 for the first blade mode. It can be seen, that instead of reaching a supercritical state, all trends approach a linear asymptote. This is due to centrifugal stiffening caused by the out-of-plane motion. Despite the categorisation into flap and lead-lag mode, both modes show in- and out-of-plane movement originating in the large blade twist and the resulting coupled flap and lead-lag dynamics. It can therefore be stated, that due to the highly twisted blades the regressive modes cannot turn supercritical, preventing ground resonance from occurring.

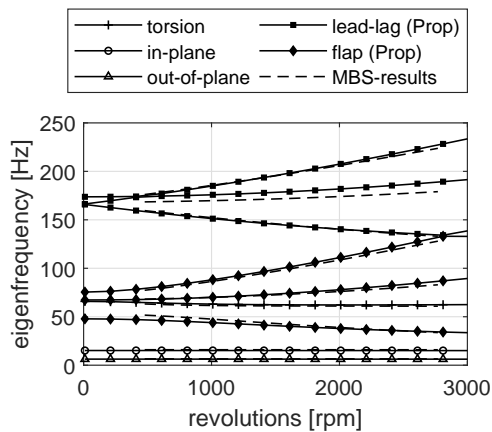


Figure 17: Campbell diagram for one V-tail half and two flexible blade modes considered

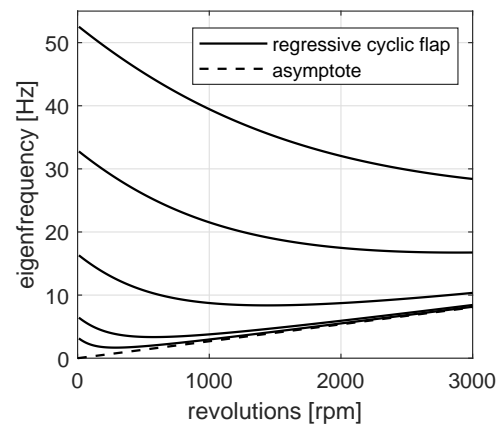


Figure 18: Frequency trends for the regressive cyclic flap mode with decreasing non-rotating frequency

5 Conclusions

The aeroelastic stability of the empennage of a hybrid-electric motor glider including a V-tail with tip-mounted electric motors and propellers was analysed. The in-house tool PySTAB was used to assess the model for empennage and whirl flutter. Supplementing analyses to find a possible ground resonance were conducted with an analytical model and MBS simulations. The only instability found was a control surface flutter resulting from a coupling of the control surface rotation with the first tailplane bending mode. A sufficient amount of mass balance prevents this coupling and removes any instability.

The margins against whirl flutter of the whole tailplane structure were found to be quite large even without considering the tailplane aerodynamics, which further increase the system's stability. Whirl flutter of the pylon structure was not investigated due to the lack of adequate design data and has to be evaluated at a later stage.

Ground resonance due to coupling of elastic blade modes with the supporting tailplane structure is prohibited by the highly twisted blades. These result in a coupling between lead-lag and flapping motion, ultimately preventing the occurrence of supercritical modes.

References

- Arnold, Jürgen and Stefan Waitz (2018). "Using Multibody Dynamics for the Stability Assessment of a New Double-Swept Rotor Blade Setup". In: *ERF 2018 Proceedings*. Vol. 44.
- Bielawa, Richard L. (1992). *Rotary wing structural dynamics and aeroelasticity*. AIAA education series. Washington, DC: American Institute of Aeronautics and Astronautics. ISBN: 1-56347-031-4.
- Bir, Gunjit (2008). "Multi-Blade Coordinate Transformation and its Application to Wind Turbine Analysis". In: *46th AIAA Aerospace Sciences Meeting and Exhibit*. Reston, Virginia: American Institute of Aeronautics and Astronautics, p. 8. ISBN: 978-1-62410-128-1. DOI: 10.2514/6.2008-1300.
- Cardinale, S., R. Donham, and I. Sachs (1969). "Ground and air resonance characteristics of a soft in-plane rigid-rotor system". In: *VTOL Research, Design, and Operations Meeting*. Reston, Virginia: American Institute of Aeronautics and Astronautics. DOI: 10.2514/6.1969-205.
- Čečrdle, Jiří (2015). *Whirl flutter of turboprop aircraft structures*. Woodhead Publishing in mechanical engineering. Sawston, Cambridge, UK: Woodhead Publishing is an imprint of Elsevier. ISBN: 978-1-782421-86-3.
- Chen, P. C. (2000). "Damping Perturbation Method for Flutter Solution: The g-Method". In: *AIAA Journal* 38.9, pp. 1519–1524. ISSN: 0001-1452. DOI: 10.2514/2.1171.
- Chen, P. C., H. W. Lee, and D. D. Liu (1993). "Unsteady subsonic aerodynamics for bodies and wings with external stores including wake effect". In: *Journal of Aircraft* 30.5, pp. 618–628. ISSN: 0021-8669. DOI: 10.2514/3.46390.
- Försching, Hans Wilhelm (1974). *Grundlagen der Aeroelastik*. Berlin, Heidelberg: Springer Berlin Heidelberg. ISBN: 978-3-642-48286-1. DOI: 10.1007/978-3-642-48285-4.
- Houbolt, John C. and Wilmer H. Reed III (1962). "Propeller-Nacelle Whirl Flutter". In: *Journal of the Aerospace Sciences* 29.3, pp. 333–346.
- Johnson, Wayne (1974). *Dynamics of tilting proprotor aircraft in cruise flight*. Vol. D-7677. NASA TN. Washington, DC.
- Koch, C., J. Arnold, and H. Schmidt (2019). *Aeroelastische Untersuchung eines V-Leitwerks mit integrierten Antriebseinheiten*. Ed. by Deutsche Gesellschaft für Luft- und Raumfahrt - Lilienthal-Oberth e.V. Bonn. DOI: 10.25967/490238.
- Rodden, W. P. and T. L. Rose (1989). "Propeller/nacelle whirl flutter addition to MSC/nastran". In: *Proceedings of the 1989 MSC World Users Conference*. Vol. 1, pp. 12–24.
- Schumann, Len (2018). *Reduktion des Energiebedarfs mittels eines batterieelektrischen Antriebs am Beispiel eines Kleinflugzeugs: Dissertation*. Stuttgart: Universität Stuttgart. DOI: 10.18419/opus-9750.

Effect of a bluff-body wake on the flutter characteristics of a pitch-plunge aeroelastic system

Chandan Bose¹, Grigorios Dimitriadis²

¹*Dept. of Applied Mechanics, IIT Madras, Chennai, India. - cb.ju.1991@gmail.com*

²*Dept. of Aerospace and Mechanical Engineering, University of Liege, Liege, Belgium. - gdimitriadis@ulg.ac.be*

Keyword: Limit-cycle oscillation, Wake-induced vibration, Aeroelasticity, Bifurcation analysis

Studying the unsteady interactions of a wing and incident vortex structures coming from an upstream bluff-body or another wing is currently a topic of considerable interest due to its numerous applications in biologically-inspired propulsion systems and energy harvesting among others. Several studies have been carried out to understand how an actively flapping system utilizes the energy of the incident vortex structures to augment its aerodynamic performance¹; few such studies² have taken aeroelasticity into account. The oscillation amplitude of an aeroelastic system, situated in the primary wake formation region of an upstream bluff-body, can attain a considerably high value if the coupled system frequency locks in with the shedding frequency of the bluff-body; thus having a significant energy extraction potential. This paper investigates the flutter characteristics of a pitch-plunge aeroelastic system in the wake of an upstream bluff-body through high-fidelity numerical simulations. The present FSI framework is developed by coupling a Navier-Stokes solver with the nonlinear structural model using a partitioned approach. The focus of this work is on characterizing the wake-induced limit-cycle oscillation (LCO) behavior of the elastically mounted wing in the presence of both structural and aerodynamic nonlinearities in the low Reynolds number regime. The aeroelastic system is seen to undergo successive Hopf bifurcations leading to an interesting bifurcation scenario at low values of mass-ratios in the uniform flow condition (when the bluff-body is absent)³. This is considered as the base case to assess the effect of the bluff-body wake on the nonlinear aeroelastic response dynamics. The present study also aims to investigate the effect of different bluff-body shapes and spatial locations relative to the wing in order to tune the oncoming vortex shedding frequency in comparison to the natural frequencies of pitch and plunge. In this way, it will be possible to study how the strength of the wake vortices and the shedding frequency influence the flutter boundary and the post-flutter characteristics of the wing as compared to the case without a bluff-body. Moreover, it will be interesting to study how the variation in the structural properties such as pitch and plunge stiffness changes the sensitivity of the aeroelastic response to the oncoming vertical disturbances by altering the vortex energy transfer from the wake to the wing.

1. Lau, Y. L., So, R. M. C., & Leung R.C.K. (2004). Flow induced vibration of elastic slender structures in a cylinder wake. *Journal of Fluids and Structures*, 19(8), 1061-1083.
2. Kirschmeier, B., & Bryant, M. (2018). Experimental investigations of wake-induced aeroelastic limit cycle oscillations in tandem wings. *Journal of Fluids and Structures*, 81, 309-324.
3. Bose, C., Gupta, S., & Sarkar, S. (2019). Transition to chaos in the flow-induced vibration of a pitching-plunging airfoil at low Reynolds numbers. *International Journal on Non-Linear Mechanics*, 109, 189-203.

Modal Analysis of Aerodynamic Damping of Light Dynamic Stall on a Pitching Airfoil

Wrik Mallik¹ and Daniella E. Raveh¹

¹ *Technion-IIT, 3200003 Haifa, Israel, emails: wrik.mallik@technion.ac.il (Wrik Mallik), daniella@technion.ac.il (Daniella E. Raveh)*

Abstract

This study presents a modal analysis of the aerodynamic damping associated with delayed detached eddy simulations (DDES) of light dynamic stall on a pitching NACA 0012 airfoil using Dynamic Modal Decomposition (DMD) and Proper Orthogonal Decomposition (POD) techniques. The DDES results indicated negative aerodynamic damping for this light dynamic stall case. It was observed that the DMD technique, which results in single-frequency modes, provided a single DMD mode representing the complete aerodynamic damping of the system. Also, this DMD mode had a constant intra-cycle aerodynamic damping owing to its single frequency. On the other hand, the total aerodynamic damping was distributed among several POD modes. Also, all POD modes were comprised of multiple frequencies, leading to the variation of intra-cycle aerodynamic damping with the phase of the pitching motion. Such variation of intra-cycle damping renders POD modes intractable for aerodynamic damping distribution analysis, which may have potential application for devising flow control strategies. Also, the aerodynamic damping distribution of DMD mode 2 indicates that during light dynamic stall at high, turbulent Reynolds numbers, the leading and trailing edge regions of the chord are the major contributors to the negative aerodynamic damping.

Keyword: Dynamic stall, DMD, POD, Aerodynamic Damping

1 Introduction

Dynamic stall is a complex fluid dynamics phenomenon that manifests itself during rapid, transient motion in which the angle of incidence surpasses the static stall limit. It has been an active area of research for helicopters, wind turbine blades, unmanned aerial vehicle (UAV) and micro aerial vehicle (MAV) applications, as well as low-Reynolds number insect and flapping-wing bird flight. Dynamic stall can be separated into a light stall and a deep stall regime. In light dynamic stall regime, the excursion of the peak dynamic angle of attack from the static stall angle is smaller than in the deep dynamic stall regime, leading to a less abrupt drop in the lift and moment coefficients [12]. The nature of the pitching moment response during light dynamic stall, under certain conditions, can lead to positive aerodynamic work. In an aeroelastic system (an elastic wing or a spring-suspended airfoil), light dynamic stall might lead to instability, such as stall flutter. Thus, the aerodynamic damping of light dynamic stall needs to be investigated carefully, especially for wind-turbine blades and UAVs subjected to strong gust excitations, which often experience light dynamic stall. Although the computation of aerodynamic work or aerodynamic damping is important for light dynamic stall, it has not been discussed comprehensively in recent studies apart from Ref. [4]. This is the main focus of the current study.

The inherent complexity and flow separation during dynamic stall require high-fidelity computational fluid dynamic (CFD) simulations for accurate analysis. The choice of governing equations to be solved numerically is important. Reynolds Averaged Navier Stokes (RANS) equations, often used in the past to study dynamic stall, [7, 1, 19], may be susceptible to inaccuracies in the presence of significant flow separation. An alternative is to use Large Eddy Simulations (LES) in which, the smaller turbulent length scales are modeled and the larger ones are resolved [18]. However, owing to the large computational cost associated with LES, hybrid RANS/LES methods capable of representing a RANS-type behavior in the vicinity of the solid boundary and an LES-type behavior far away from the wall boundary, have also been used extensively [5].

Modal analysis of complex dynamic phenomena often leads to key insight into the physics of the problem. This has led to the application of techniques like proper orthogonal decomposition (POD) [2] and dynamic mode decomposition (DMD) [15] for studying various flow phenomena associated with separation and complex flow structures. Both POD and DMD are data-based techniques that extract dominant dynamic features from time-resolved measurements of the flow-field, but while POD modes are ranked according to energy, DMD modes are ranked according to the dynamic behavior. Both these techniques will be employed to study the aerodynamic damping of the system experiencing light dynamic stall phenomenon.

Here, we explore the light dynamic stall regime at high, turbulent Reynolds number, where many UAVs and wind turbine blades operate. In the present study, DMD and POD are used to analyze computational, time-resolved snapshots of pressure obtained via a RANS-LES hybrid, delayed detached eddy simulations (DDES), with a $k - \omega$ SST turbulence model. Although either the velocity magnitude snapshots or velocity component snapshots were used in previous studies [13], the pressure flowfield is selected here as it can be used for computation of the pitching moment response, and subsequently the aerodynamic work due to individual DMD or POD modes.

2 Test Case

The light dynamic stall case studied is that of a NACA 0012 airfoil with pitching oscillations about the quarter-chord point. The flow has a Mach number $M_\infty = 0.3$ and Reynolds number $Re_\infty = 4 \times 10^6$. The pitching motion has a reduced frequency of $k = 0.1$ and an amplitude of $\alpha_1 = 5^\circ$. The mean angle of attack is $\alpha_0 = 11^\circ$. The unsteady pitching angle of the airfoil can be written as,

$$\alpha(t) = \alpha_0 + \alpha_1 \sin(\omega t) \quad (1)$$

Equation 1 can be written in terms of nondimensional parameters as,

$$\alpha(t_{nd}) = \alpha_0 + \alpha_1 \sin(2kM_\infty t_{nd}) \quad (2)$$

The experimental results were presented in [11], which considers a mean angle of attack of 10° . However, more recent experiments of NACA 0012 airfoil at a similar Reynolds number and Mach number [14] show that the angle of attack for maximum steady c/l lies somewhere between 15° and 16° . Thus dynamic stall cannot be observed at $\alpha = 15^\circ$, which was also corroborated by the DDES results. It is reasonable to suspect that wall effects or some potential measurement error may have led to experimental dynamic stall at the slightly lower angle of attack. The

mean angle of attack in the DDES simulations was increased accordingly to 11° to obtain an $\alpha_{max} = 16^\circ$.

3 Computational Setup

DDES [17, 16] is performed here using the $k - \omega$ SST turbulence model in EZNSS [8], an in-house code developed by the Israeli CFD center. The unified hybrid RANS/LES DDES in EZNSS is formulated according to Ref. [16]. The mesh used here is an O-type mesh with periodic boundary conditions and consisting of 6.7 million grid points. The mesh dimension is $651 \times 251 \times 41$ with 0.25 chord along the spanwise or Y direction. The first dimension (651) represents the number of grid points along the airfoil surface. Grid points are concentrated near the airfoil in order to capture the DSV formation and initial convection. An illustration of the mesh with various levels of magnification is provided in Fig. 1.

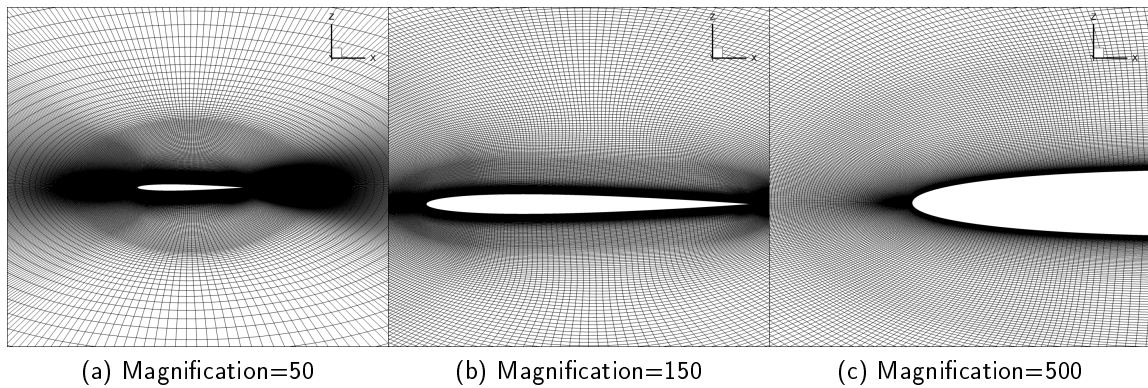


Figure 1 – Mesh used for $k - \omega$ SST DDES

A reduced computational domain (shown in ref. [10]) consisting of a slice around the suction surface of the airfoil including the leading and trailing edges, was used for taking the DMD and POD snapshots. The 3D high-fidelity snapshots generated from the DDES were averaged in the spanwise direction, along the Y direction. The snapshots were sampled in intervals of 17 time steps, where each nondimensional time step for the DDES is 2.053×10^{-2} . Thus, the nondimensional sampling time interval, Δt_{nd} , for obtaining the DMD snapshots is 0.3491, resulting in 300 snapshots in a single pitch cycle. As explained in Ref. [13], such a sampling rate will not be able to capture the small-scale highly fluctuating structures in the shear-layer but will capture the primary structures of interest. The DDES pitching simulations were carried out with the second-order accurate, dual-time stepping scheme available in EZNSS. The criterion for convergence of the dual-time step solution at each time step is the reduction of the residual by two orders of magnitude (OOM), for both the mean-flow equations and the turbulence model. The criterion for OOM reduction of the residual and the dual-time step procedure in EZNSS has been explained further in Ref. [9].

4 Mathematical Model

Both the DMD and POD algorithms used in this article require snapshots of the flow past the airfoil. The sampling frequency of the snapshots and the pre-processing of the DDES results are discussed in the next section. The mathematical details of the POD and DMD techniques used for this study can be obtained from Ref. [10].

5 Aerodynamic damping and stall flutter

Aerodynamic damping is used as a measure of the effect that aerodynamic forces may have on the stability of an aeroelastic system (for example, if the airfoil was suspended in springs). Positive damping indicates a stabilizing aerodynamic force whereas negative damping might lead to aeroelastic instabilities. The cycle-averaged aerodynamic damping coefficient, Ξ , indicates the potential of the dynamic stall phenomenon to lead to aeroelastic instabilities like stall flutter. For pure pitching motion, Ξ can be derived as,

$$\Xi = -\frac{1}{\pi\alpha_1^2} \oint cm d\alpha \quad (3)$$

where $c\bar{m}$ and α_1 are the amplitudes of the pitching moment coefficient and angle of attack, respectively. For dynamic stall, the pitching moment response becomes non-linear. Thus, for pitching moment measured at the quarter chord, the cycle aerodynamic damping is computed from the area enclosed in the cycle variation of the pitching moment coefficient as:

$$\Xi = \frac{1}{\pi\alpha_1^2} \int_{\alpha_{min}}^{\alpha_{max}} (cm_{y,x/c=0.25}^D - cm_{y,x/c=0.25}^U) d\alpha \quad (4)$$

For simple harmonic input and output, we can write $\alpha = \alpha_1 e^{i\omega t}$ and $cm = c\bar{m} e^{i(\omega t + \psi)}$, where ψ is the phase difference between the pitching moment response and the excitation. These can be substituted in equation 3 to obtain the aerodynamic damping coefficient. A lagging pitching moment response ($-\pi < \psi < 0$) indicates negative work done or stable airloads. On the other hand, a phase lead ($0 < \psi < \pi$) indicates positive work done, or unstable airloads. A complete derivation of the aerodynamic damping coefficient is provided in ref. [10].

6 Results

6.1 DDES results

Four cycles of DDES of the pitching airfoil were simulated in EZNSS. The phase-averaged lift coefficient, and the pitching moment coefficient at the quarter-chord obtained from four cycles of the DDES are compared against available experimental results in Fig. 2. Overall, the phase-averaged DDES results show a close correlation to the experimental results with some differences during the pitch-down phase. The largest differences are observed just after the moment and lift stall as the flow slowly recovers from the stall. Similar behavior has been observed and explained in other dynamic stall studies [6]. A negative cycle-averaged aerodynamic damping value of $\Xi_{cycle} = -0.23$ was obtained from the DDES pitching moment response compared to

$\Xi_{cycle} = -0.05$ in the experiment. Mesh convergence of the DDES results are provided in Ref. [10].

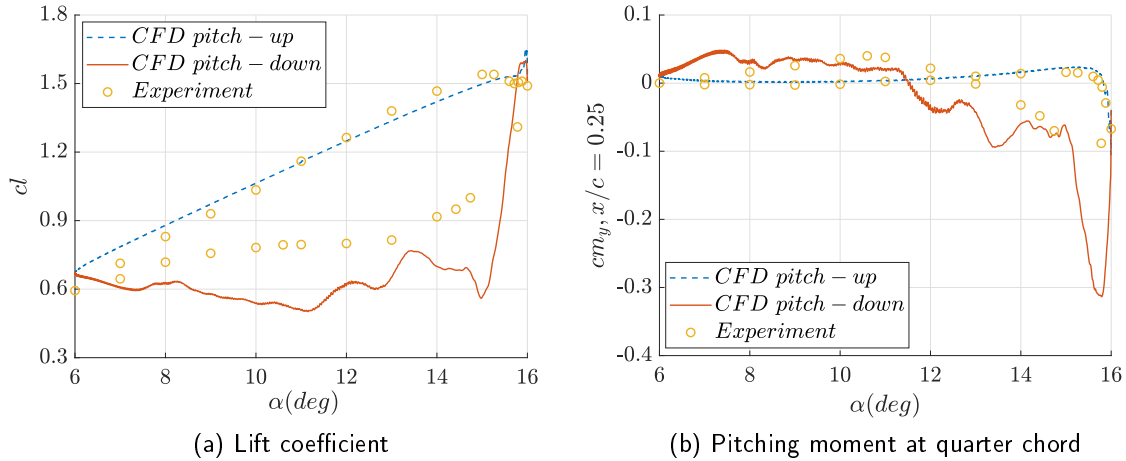


Figure 2 – Comparison of $k - \omega$ SST DDES results with experiments

The dynamic stall phenomenon is further investigated by looking at the suction coefficient, $-cp$, on the upper surface of the airfoil at different phases of the pitching motion and comparing it to the cl and $cm_{y,x/c=0.25}$ variations with the phase in Fig. 3. Here, we define the phase as $\Phi = \omega t$. Fig. 3 (a) shows a large suction at the leading edge of the airfoil till $\Phi = 80^\circ$ ($\alpha = 14.2^\circ$). This is denoted as the leading edge suction (LE suction) phase of the dynamic stall. At $\Phi = 80^\circ$ ($\alpha = 14.2^\circ$), a locally formed high suction region is observed at about 35% of the chord, indicating the formation of the dynamic stall vortex (DSV). As expected for the light dynamic stall regime at high Reynolds number, the DSV is formed at the location of maximum airfoil thickness. Such behavior was reported earlier and explained in Refs. [12, 11]. We can also observe that the DSV formed at $\Phi = 80^\circ$ ($\alpha = 14.2^\circ$), eventually moves along the airfoil and leaves the trailing edge at $\Phi = 125^\circ$ ($\alpha = 15.44^\circ$). Another locally formed high suction region at the trailing edge at $\Phi = 125^\circ$ ($\alpha = 15.44^\circ$) is considered the trailing edge vortex (TEV). The moment stall is observed around $\Phi = 85^\circ$ ($\alpha = 14.38^\circ$), shortly after the formation of the DSV. The pitching moment coefficient at the quarter-chord decreases as the DSV travels towards the trailing edge of the airfoil. The lift stall is observed around $\Phi = 105^\circ$ ($\alpha = 14.97^\circ$) as the DSV reaches the trailing edge. While the airfoil recovers from the moment stall, the cl reduces further as the DSV leaves the trailing edge completely. Eventually, the flow reattaches and the airfoil recovers from both the lift and moment stall.

6.2 Modal Analysis of Aerodynamic Damping

The DMD and POD analyses were used to investigate the contribution of the various modes to the cycle-averaged aerodynamic damping. As we have already seen from the experimental and DDES pitching moment response, the present case has a negative cycle aerodynamic damping indicating a potential for stall flutter when attached to an aeroelastic system. Thus, if we can

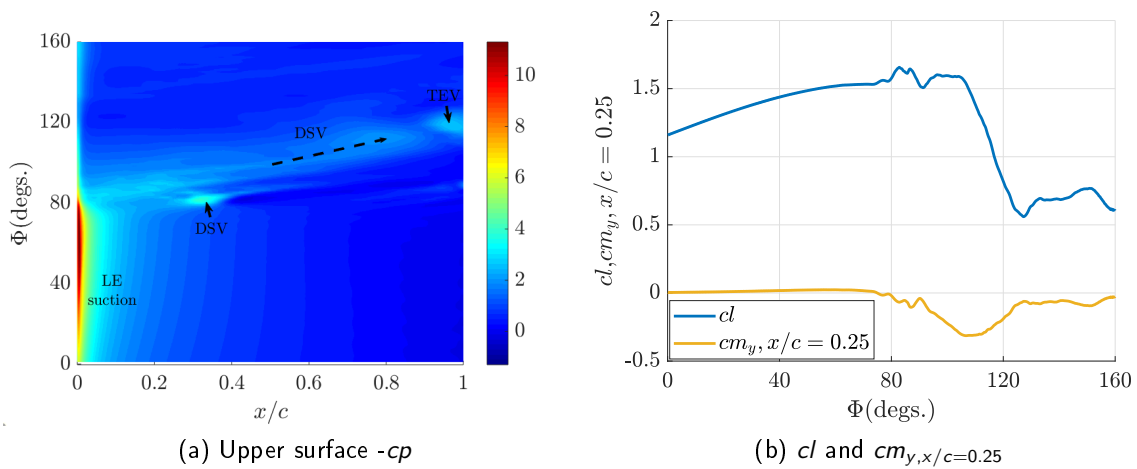


Figure 3 – Variation of aerodynamic forces with change in the phase of the pitching motion

find specific DMD or POD modes having a major contribution to the negative aerodynamic damping of the system, such modes can be further investigated to understand possible causes for such damping and also devise possible control strategies of any potential instabilities.

First, the DMD analysis was performed on the phase-averaged snapshots of the pressure coefficient cp . The DMD modes obtained from the analysis have complex conjugate pairs of eigenvalues except for the first mode, which has a real eigenvalue. All the DMD modes, except the first mode, have frequencies that are multiples of the pitching motion frequency. They are ranked in ascending order of their reduced frequency. The first seven DMD modes are presented in Table 1 along with their eigenvalues and reduced frequencies. The first mode, having a zero eigenvalue, is a stationary mode. This mode represents the mean flow it was demonstrated that it shows excellent correlation to the cp obtained by time-averaging the phase-averaged pressure snapshots [10]. This indicates the convergence of the DMD analysis. DMD mode 2 has the same reduced frequency of the prescribed pitching motion ($k = 0.1$). The next higher modes can be considered the higher harmonics of the pitching motion. Each of the complex conjugate pairs associated with each of the modes 2-7, were multiplied with their corresponding complex conjugate modal amplitudes to obtain real-valued cp values. The process is elaborated in Ref. [10]. The cp values thus obtained for each DMD mode was integrated to compute the pitching moment and subsequently the aerodynamic damping associated with them via Eq. 4).

The POD analysis was also performed on the phase-averaged snapshots of the pressure coefficient cp . All the POD modes have real eigenvalues, eigenvectors and modal amplitudes. The first mode represents the time-averaged solution of the DDES snapshots. Thus, the first POD mode shape is identical with the first DMD mode shape. However, the first POD mode is not a stationary mode unlike DMD mode 1. This can be attributed to the fact that the DMD modes are orthogonal in time whereas the POD modes are orthogonal in space [15]. Physically this means that each DMD mode is represented by a single frequency but each POD mode consists of several frequencies. The modal amplitude of the first six POD modes are shown in figure 4 showing that each POD mode consists of several frequencies. Since the POD modes

Table 1 – Eigenvalues and reduced frequency of DMD modes

Mode	Eigenvalue (μ_k)	Reduced frequency (\bar{f})
1	1.0	–
2	$0.9997 \pm 0.0209i$	0.1000
3	$0.9992 \pm 0.0420i$	0.2007
4	$0.9983 \pm 0.0626i$	0.2990
5	$0.9961 \pm 0.0832i$	0.3977
6	$0.9936 \pm 0.1049i$	0.5022
7	$0.9921 \pm 0.1265i$	0.6056

are ranked according to energy, the modal amplitude of the POD modes decreases with an increase in the mode number.

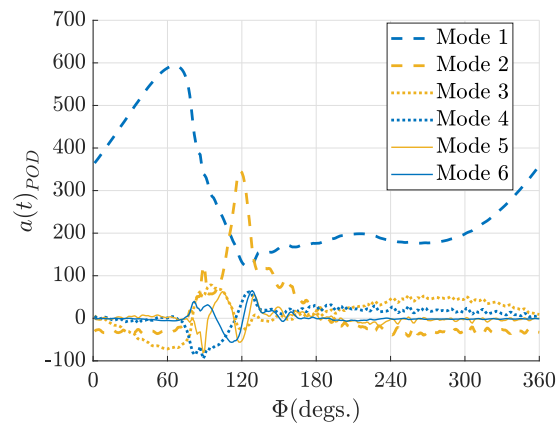


Figure 4 – POD modal amplitude

Since the DMD and POD analyses were performed on a reduced computational domain consisting mainly of the upper surface of the airfoil, the $cm_{y,x/c=0.25}$ was computed with only the airfoil surface grid points of the reduced computational domain. The aerodynamic damping for the POD and DMD modes, as well for the DDES snapshots on the reduced domain were computed using equation 4. The absolute value of the aerodynamic damping coefficients of the first eight DMD modes, Ξ_{DMD} , normalized by the DDES reduced-domain aerodynamic damping, Ξ_{DDES} , are presented in Table 2 (a). These values indicate the contribution of various modes for the aerodynamic damping of the system. The sign of the aerodynamic damping of the various modes is also provided to indicate if they contribute positively or negatively to the stability of the system. It can be observed that since DMD mode 1 is a stationary mode, it does not have any aerodynamic damping. DMD mode 2 has a negative aerodynamic damping coefficient. Also, a relative damping coefficient of 0.9958 indicates that it is responsible for almost all of the negative aerodynamic damping of the system. The contribution of modes 3-8 to the aerodynamic damping is negligible. Thus, the aerodynamic damping of the whole

dynamic stall phenomenon can be represented by a single DMD mode, DMD mode 2.

A similar analysis performed for the POD modes is presented in Table 2 (b). For the POD modes, we see that mode 2 contributes to 95% of the damping of the system. Similar to DMD mode 2, POD mode also provides negative aerodynamic damping. However, POD mode 1 and POD modes 3-6 also generate a non-negligible amount of aerodynamic damping.

Mode	$sign(\Xi_{DMD})$	$ \Xi_{DMD}/\Xi_{DDES} $	Mode	$sign(\Xi_{POD})$	$ \Xi_{POD}/\Xi_{DDES} $
1	...	0	1	+	0.0870
2	-	0.9958	2	-	0.9544
3	-	3.1e-04	3	-	0.1106
4	-	0.0061	4	+	0.0103
5	+	0.0053	5	-	0.0479
6	+	0.0013	6	+	0.0322
7	-	0.0052	7	-	0.0025
8	-	0.0078	8	-	0.0035

(a) Normalized cycle aerodynamic damping of first eight DMD modes

(b) Normalized cycle aerodynamic damping of first eight POD modes

Table 2 – Normalized modal aerodynamic damping

The $cm_{y,x/c=0.25}$ computed for the DDES snapshots are shown in Fig. 5 (a). It can be observed that the $cm_{y,x/c=0.25}$ computed for the reduced computational domain shows reasonable correlation with its counterpart computed for the full domain, presented in Fig. 2 (b). The $cm_{y,x/c=0.25}$ computed for DMD mode 2 and POD mode 2 are compared to the DDES reduced-domain $cm_{y,x/c=0.25}$ in Figs. 5 (b) and (c), respectively. It is seen that going from pitch-up to pitch-down, all the three pitching moment responses have an overall clockwise nature. This indicates that they are contributing to positive aerodynamic work or negative aerodynamic damping [6]. However, only the DMD mode 2 has a constant phase as it is a single-frequency response.

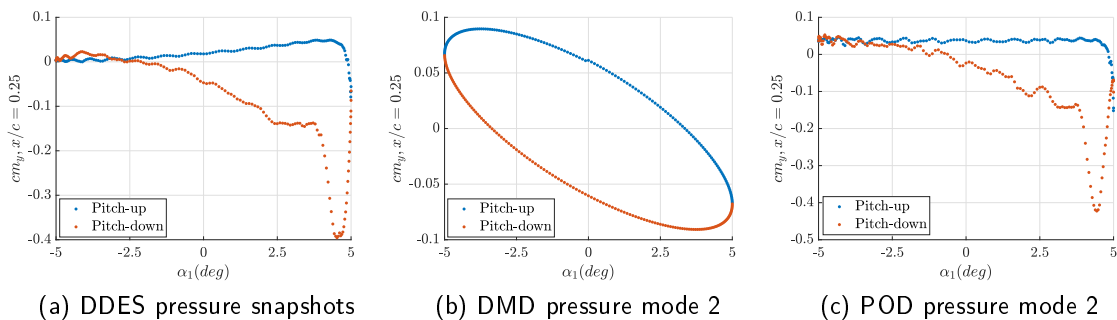


Figure 5 – Comparison of $cm_{y,x/c=0.25}$ obtained for the reduced computational domain

The DMD mode 2 $cm_{y,x/c=0.25}$ is compared to the pitching moment response computed via Theodorsen's function for the same pitching oscillation frequency but considering a smaller mean angle of attack, for a case when the flow would be fully attached. The expression for the pitching moment response predicted by Theodorsen's function is calculated from Ref. [3] as,

$$cm_{y,x/c=0.25,us} = \frac{\pi k}{4} \alpha_1 \sqrt{1 + \frac{9}{64} k^2} \sin \left[\omega t - \arctan \left(\frac{8}{3k} \right) \right]$$

where the subscript *us* indicates that it was only calculated for the upper surface to keep it consistent with DMD calculations. These two pitching moment responses are compared in figure 6. One can see that for an attached flow condition, using Theodorsen's functions, the pitching moment response always lags behind the pitching oscillation. In this case, the phase lag is 88° . This indicates negative aerodynamic work over a cycle, or positive aerodynamic damping. On the other hand, DMD mode 2 has a phase lead of 137.5° .

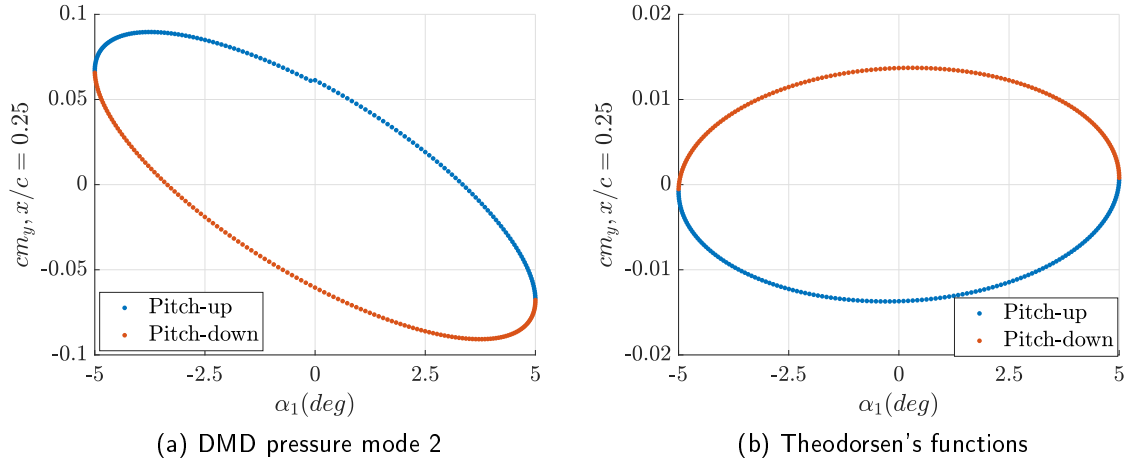


Figure 6 – Comparison of $cm_{y,x/c=0.25}$ for separated flow during dynamic stall to attached flow

A constant phase difference between the pitching moment response and the pitching motion leads to a constant intra-cycle aerodynamic damping coefficient, Ξ_ϕ , as expressed in figure 7, where the intra-cycle damping for the attached flow case, DMD mode 2 and POD mode 2 are compared. For a constant phase difference between the pitching moment response and the pitching motion, the intra-cycle aerodynamic damping can be directly computed from equation 3, the same equations used for computing cycle-averaged aerodynamic damping. For variable-frequency case, however, intra-cycle aerodynamic damping is computed via a Hilbert transform of the pitching moment time response, as demonstrated in Ref. [4]. In the present study, the Hilbert transform technique was employed to compute the intra-cycle damping for POD mode 2.

For a constant phase difference between the pitching angle and the pitching moment coefficient, one can relate the cycle aerodynamic damping to the aerodynamic damping distribution

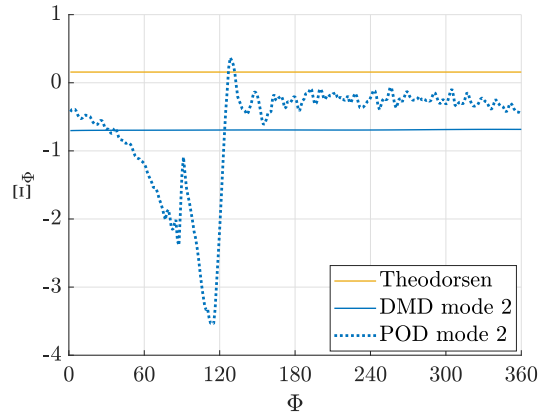


Figure 7 – Comparison of intra-cycle aerodynamic damping

over the airfoil surface at any phase of the motion as,

$$\bar{\Xi} = \int_0^1 \Xi_{x/c} d\frac{x}{c} = \int_0^1 cp_{x/c} \left(\frac{x}{c} - \frac{c}{4} \right) d\frac{x}{c} \quad (5)$$

where $cp_{x/c}$ is the coefficient of pressure at various locations along the airfoil. The aerodynamic damping distribution along the chord for DMD mode 2 and Theodorsen's functions, normalized by the absolute value of the total cycle-average aerodynamic damping, is computed using equation 5, and compared in figure 8. One can see that for an attached flow case, analyzed via Theodorsen's function, the section of the airfoil ahead of the quarter-chord, leads to negative damping, whereas, the section behind the quarter-chord leads to a much larger positive damping. For DMD mode 2 (representing the dynamic stall case), the leading edge and trailing region generate negative damping. On the other hand, the region around the quarter-chord contributes to a much smaller positive damping. The distinctly different pitching moment and aerodynamic damping distribution observed here for DMD 2 compared to an attached flow case, is caused by the phenomenon of light dynamic stall. Such knowledge of the aerodynamic damping distribution will be useful for someone interested in flow control, especially for control or mitigation of stall flutter for the present case. Similar results cannot be obtained for a variable intra-cycle aerodynamic damping scenario, like POD mode 2, where the aerodynamic damping distribution will also vary with the phase of the pitching motion. This also makes it difficult to associate positive or negative damping with any particular dynamic stall flow features or to target a specific region of the airfoil for flow control.

7 Conclusions

In this study, modal analysis of the dynamic stall phenomena of a pitching NACA 0012 airfoil, occurring at high, turbulent Reynolds numbers and in the light stall regime, was performed with the DMD and POD techniques. The DMD and POD techniques were applied to snapshots of the pressure distribution obtained via delayed detached eddy simulations (DDES). The DMD technique resulted in a stationary mode and subsequent modes that were represented by the

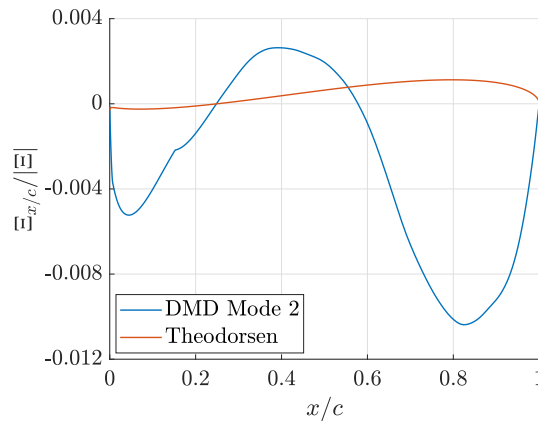


Figure 8 – Aerodynamic damping distribution

frequency of the pitching motion and its higher harmonics. The POD technique ranks modes based on the energy content of the flow. So, unlike the DMD modes, each POD mode consisted of a combination of frequencies and there was no stationary mode.

It was observed that DMD mode 2 had negative aerodynamic damping and contributed to 99.58% damping of the system. All the other DMD modes had negligible aerodynamic damping. The DDES pitching moment response for the full domain as well as experimental results also predicted negative aerodynamic damping. This indicated that a single DMD mode, with the frequency of the prescribed motion, is sufficient to represent the complete aerodynamic damping associated with the light dynamic stall phenomena. POD mode 2 consisted of 95.44% of the aerodynamic damping of the system and had a negative sign. However, there were other POD modes having non-negligible aerodynamic damping values of differing signs.

Since DMD mode 2 consists of a single frequency, it has a constant phase difference with respect to the pitching oscillation. This is a very favorable attribute as the moment associated with this mode could be directly compared to the moment response obtained via Theodorsen's function, for attached flow conditions (for the same oscillation frequency and amplitude). DMD mode 2 can also be used to easily compute the aerodynamic damping associated with the pitching motion at light dynamic stall. The same cannot be achieved for the DDES results or POD mode 2, which consist of multiple frequencies and have a variable phase difference between the pitching moment response and the motion of the pitching oscillation.

Analysis of the aerodynamic damping of DMD mode 2 showed that in light dynamic stall the regions around the leading and trailing edges generate a large amount of negative aerodynamic damping while the region around the quarter-chord contributes to a much smaller amount of positive aerodynamic damping. The overall effect is negative aerodynamic damping. This can be used to target flow control efforts that aim at stabilizing the aeroelastic response due to light dynamic stall.

Acknowledgments

During this research, the first author was supported in part at the Technion by a fellowship of the Israel Council for Higher Education. The authors also thank Yair Mor Yossef at the Israeli CFD Center for his help in the mesh development and useful insights regarding the DDES.

References

- [1] Barakos, G. and Drikakis, D. (2003). Computational study of unsteady turbulent flows around oscillating and ramping aerofoils. *International journal for numerical methods in fluids*, 42(2):163–186.
- [2] Berkooz, G., Holmes, P., and Lumley, J. L. (1993). The proper orthogonal decomposition in the analysis of turbulent flows. *Annual review of fluid mechanics*, 25(1):539–575.
- [3] Bisplinghoff, R. L., Ashley, H., and Halfman, R. L. (2013). *Aeroelasticity*. Dover Publications.
- [4] Bowles, P. O., Corke, T. C., Coleman, D. G., Thomas, F. O., and Wasikowski, M. (2014). Improved understanding of aerodynamic damping through the Hilbert transform. *AIAA Journal*, 52(11):2384–2394.
- [5] Chaouat, B. (2017). The state of the art of hybrid RANS/LES modeling for the simulation of turbulent flows. *Flow, Turbulence and Combustion*, 99(2):279–327.
- [6] Corke, T. C. and Thomas, F. O. (2015). Dynamic stall in pitching airfoils: aerodynamic damping and compressibility effects. *Annual Review of Fluid Mechanics*, 47:479–505.
- [7] Ekaterinaris, J. A. and Platzer, M. F. (1998). Computational prediction of airfoil dynamic stall. *Progress in aerospace sciences*, 33(11-12):759–846.
- [8] Levy, Y. and Raveh, D. (2015). THE EZNSS CFD CODE THEORETICAL AND USER'S MANUAL.
- [9] Mallik, W. and Raveh, D. (2019). Gust responses at high angles of attack. *AIAA Journal*, 57(8):3250–3260.
- [10] Mallik, W. and Raveh, D. E. Modal analysis of light dynamic stall on a pitching airfoil. *under review*, https://www.researchgate.net/publication/337474664_Modal_Analysis_of_Light_Dynamic_Stall_on_a_Pitching_Airfoil.
- [11] McCroskey, W. and Puccif, S. (1982). Viscous-inviscid interaction on oscillating airfoils in subsonic flow. *AIAA Journal*, 20(2):167–174.
- [12] McCroskey, W. J., McAlister, K., Carr, L., Pucci, S., Lambert, O., and Indergrand, R. (1981). Dynamic stall on advanced airfoil sections. *Journal of the American Helicopter Society*, 26(3):40–50.

- [13] Mohan, A. T., Gaitonde, D. V., and Visbal, M. R. (2016). Model reduction and analysis of deep dynamic stall on a plunging airfoil. *Computers & Fluids*, 129:1–19.
- [14] Raveh, D. E. (2011). Aerodynamic gust response in high angles of attack. In *54th AIAA/ASME/ASCE/AHS/ASC Structures, Structural Dynamics, and Materials Conference*. AIAA-2013-1638.
- [15] Schmid, P. J. (2010). Dynamic mode decomposition of numerical and experimental data. *Journal of fluid mechanics*, 656:5–28.
- [16] Shur, M. L., Spalart, P. R., Strelets, M. K., and Travin, A. K. (2008). A hybrid RANS-LES approach with delayed-DES and wall-modelled LES capabilities. *International Journal of Heat and Fluid Flow*, 29(6):1638–1649.
- [17] Spalart, P. R., Deck, S., Shur, M. L., Squires, K. D., Strelets, M. K., and Travin, A. (2006). A new version of detached-eddy simulation, resistant to ambiguous grid densities. *Theoretical and computational fluid dynamics*, 20(3):181.
- [18] Visbal, M. R. and Garmann, D. J. (2017). Analysis of dynamic stall on a pitching airfoil using high-fidelity large-eddy simulations. *AIAA Journal*, pages 46–63.
- [19] Wang, S., Ingham, D. B., Ma, L., Pourkashanian, M., and Tao, Z. (2010). Numerical investigations on dynamic stall of low Reynolds number flow around oscillating airfoils. *Computers & Fluids*, 39(9):1529–1541.

Unsteady Aerodynamic Response of a Swept Wing in the Presence of Shock Buffet

Lior Poplinger¹ and Daniella E. Raveh²

¹ Faculty of Aerospace Engineering, Technion-IIT, 3200003 Haifa, Israel, lior.pop@campus.technion.ac.il

² Faculty of Aerospace Engineering, Technion-IIT, 3200003 Haifa, Israel, daniella@technion.ac.il

Abstract

The current study presents numerical investigation of the fundamental properties of 3D shock buffet on a swept wing, studied experimentally in the AVERT project, using fluid modal analysis. Specifically, the Dynamic Mode Decomposition (DMD) method used in this study enables the extraction of coherent structures of the flow and the associated dynamic properties. Preliminary results of the unsteady aerodynamic response of the swept wing to prescribed pitching motion at shock buffet conditions are presented. The interaction between the prescribed motion and the developed buffet flow for some excitation parameters results in lock-in of the buffet flow with the prescribed motion excitation frequency. Other excitation parameters result in an unsteady response in both the buffet and excitation frequencies.

Keywords: Unsteady Aerodynamics, Shock Buffet, CFD, DMD

1 Introduction

Shock buffet is an aerodynamic instability phenomenon that occurs at transonic flow over both airfoils and wing configurations. It was extensively investigated, both experimentally and numerically, for 2D airfoil configurations [3]. However, the literature is much more limited for the 3D wing shock buffet. Moreover, the study of the interaction between structural motion, either prescribed or aeroelastic response, and shock buffet is very lacking in the published literature. Thus, further investigations are required in order to establish the relation between the buffet mechanism and unsteady aerodynamic response and the aeroelastic response of flexible structures.

Several experimental studies investigated the 3D shock buffet phenomenon, mostly on swept wings that are typical of transonic aircraft [2]. The main difference with respect to 2D buffet is the change in the frequency content of the pressure fluctuations on the wing. The 3D buffet involves oscillations in a broadband frequency range, which is about one order-of-magnitude higher than the 2D buffet ($St \approx 0.2 - 0.3$).

Numerical studies [1, 4] were performed to investigate the 3D buffet. The presence of a substantial 3D flow phenomenon, that is the propagation of "buffet cells" [4] along the span, was identified. This flow feature is distinctive of 3D buffet and was also observed and quantified in experimental studies [2, 7]. Further numerical studies [14, 15] used Unsteady Reynolds-Averaged Navier-Stokes (URANS) simulations and high-fidelity Delayed Detached-Eddy Simulations (DDES) to investigate the phenomenon for different Angles-of-Attack (AoAs) and Mach

numbers. The broadband frequency nature of the 3D buffet was simulated in these studies and the suitability of URANS simulations for buffet prediction and analysis was established.

Recently, several studies focused on fluid modal decomposition methods to investigate the 3D buffet. Ohmichi et al. [11] used incremental POD and DMD to study the shock buffet over NASA's Common Research Model (CRM). A dominant mode at the buffet frequency ($St \approx 0.4$) exhibiting periodic structures resembling the well-known buffet cells propagating towards the wing tip was identified. Another, low-frequency ($St \approx 0.05$), mode was also found in which pressure propagates towards both wing tip and root. Other modes were attributed to the broadband nature of the buffet. The low-frequency mode may be a reminiscent of a low-frequency disturbance found experimentally [2]. In a recent study by Masini et al. [9] POD and DMD were used in an extensive analysis of experimental Dynamic Pressure-Sensitive-Paint (DPSP) data at buffet onset on the RBC12 wind-tunnel model [8]. Focusing on the DMD results, both high- and low-frequency dominant modes were found, similarly to the numerical results in [11].

Only few studies investigated the behavior of a 3D wing at buffet conditions with prescribed motion. Timme and co-authors [17, 18] investigated the response of a half wing-body configuration to prescribed motion resembling torsional deformation of the wing using CFD simulations. The prescribed motion was in a broad range of frequencies. As the AoA reached buffet onset, a distinct peak at $St \approx 0.11$, similar to the 2D unsteady response to prescribed motion [10], appeared in the wing frequency response, alongside secondary peaks at $St \approx 0.3 - 0.7$ that correspond to the broadband 3D buffet. Kataras and Timme [5] extended the previous work with the same torsional excitation and investigated the effect of excitation amplitude and frequency near buffet onset. It was found that at pre-buffet conditions, as the excitation amplitude increases the lift coefficient response follows the structural excitation completely. Close to buffet onset, the excitation frequency trace in the lift coefficient response is growing in magnitude as the excitation amplitude increases; however, lock-in of the buffet flow field to the excitation frequency, as observed for 2D airfoils [13], was not observed for the investigated 3D wing.

The current study focuses on the analysis of the shock buffet flow field on a typical swept wing. The baseline, static wing, buffet is studied using both conventional and modal techniques. Then, preliminary results of the flow field unsteady response at developed buffet conditions for an oscillating wing are presented and analyzed using conventional methods with the goal to characterize fluid-structure interactions at buffet conditions.

2 Test Case

The swept wing studied experimentally in the AVERT project [2] was used in this study. The experimental campaign was performed at ONERA S2MA wind tunnel and included a half body-wing configuration. The wing cross section is based on the OAT15A airfoil. The model has a semi span of $b = 1.225 [m]$ and mean-aerodynamic-chord (MAC) of $c = 0.3375[m]$ with taper ratio of $c_t/c_r = 0.5$. The wing is swept by 30° and twisted from root to tip.

Model instrumentation included steady and unsteady pressure measurements and accelerometers. The model was tested at several Mach numbers (0.78-0.86) and several AoAs. The current study focuses on a single Mach number of $M_\infty = 0.82$ with test conditions $P_\infty = 60kPa$ and $T_\infty = 300K$, resulting in Reynold number (based on MAC) of $3.6M$.

Brunet and Deck [1] studied the same configuration using a Z-DES approach, showing good comparisons with the experimental results and noting the advantage of DES-type computations

over URANS in capturing the separated region.

In the current study, only the wing was simulated using a symmetry boundary condition. Fig. 1 shows the computational grids generated for this configuration applying the overset approach. The main wing (blue mesh in Fig. 1) is meshed using an O-type topology with 311, 65 and 101 grid points in the chordwise, spanwise and perpendicular directions. A cap mesh (red mesh in Fig. 1) is used for the wing tip and a rectangular world mesh (black mesh in Fig. 1) confines the two wing grids. This computational setup includes a total of 3.6M flow cells.

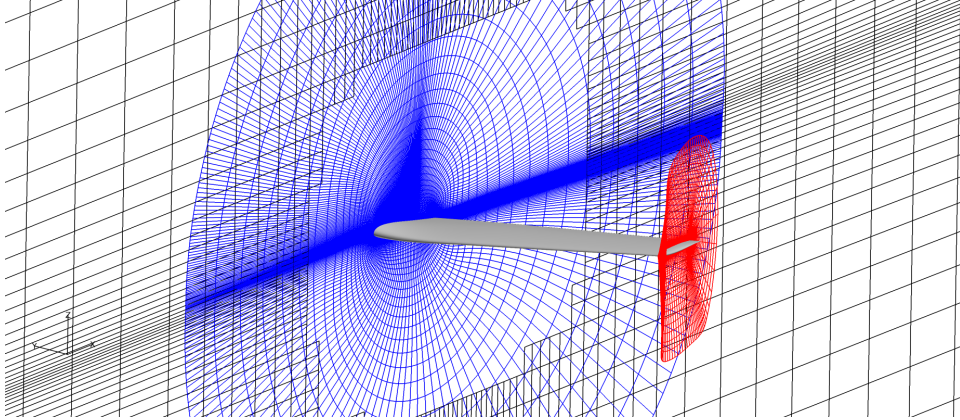


Figure 1: Computational meshes of the wing configuration used in this study

3 Computational Setup

In this study, URANS simulations were conducted using the EZAir solver [6]. EZAir is a finite-volume, structured, multizone, multiblock Euler/Navier-Stokes solver developed by the Israeli CFD Center. The solver includes an automatic chimera procedure that was used to assemble the computational domain (Fig. 1). For the convective flux approximation, the second order in space Harten, Lax, and van-Leer approximated Riemann solver scheme with contact discontinuity treatment (HLLC) was used. The time-accurate nature of the flow was simulated using the second order in time dual time stepping (DTS) method. The turbulence model for all simulations was the SA model with Edwards and Chandra's modification and compressibility correction.

The numerical methodology for the static buffet simulations is formed from a steady-state simulation at a given set of AoA and Mach number, followed by a time-accurate simulation using a physical time-step of $\Delta t = 1 \cdot 10^{-5}[s]$.

For the prescribed motion simulations, a sinusoidal pitching angle is prescribed to the wing grids (within the static world grid) and the numerical computation is continued from the static buffet simulation until several cycles are obtained (based on the lift coefficient time evolution). The same time step of $\Delta t = 1 \cdot 10^{-5}[s]$ is used.

Modal analysis using the Dynamic Mode Decomposition method [16] was performed using the Python library available online ¹. All modal analyses were performed using pressure snapshots at equally spaced time steps obtained from the surface flow solution. Dominant modes

¹<https://github.com/cwrowley/dmdtools> [retrieved 4 January 2020]

were extracted using Greedy method as outlined by Ohmichi et al. [11]. Pressure snapshots are used because the flow modes can be analyzed from a pressure propagation point of view, thus enabling analysis of the buffet mechanism.

4 Results

4.1 Shock Buffet over Static Swept Wing

In order to characterize the shock buffet phenomenon on realistic swept wing configuration, two approaches are considered. First, conventional analysis of the lift coefficient and the pressure distribution of the wing is presented. Then, modal analysis using the Dynamic Mode Decomposition (DMD) method is performed in order to shed further light on the inherent dynamics of the phenomenon.

Time accurate flow simulations were performed for several AoA values at $M = 0.82$. Fig. 2 shows the lift coefficient time history for the simulated AoAs. Buffet onset is between 3.5 deg (in which no lift oscillations were observed) and 4.0 deg AoA. The experimental buffet onset [2] was measured at about 3.1 deg AoA. This may indicate that an AoA correction of $\Delta\alpha \approx 0.5$ deg is required.

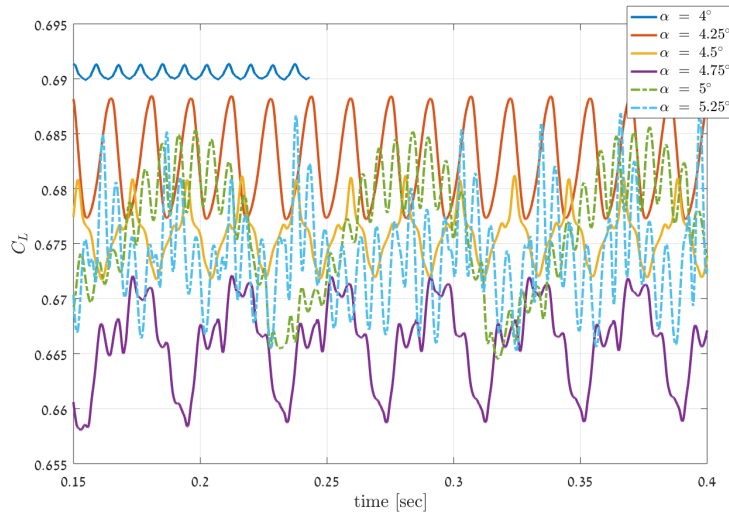


Figure 2: Lift coefficient time-history, $M = 0.82$

As the AoA increases, the lift time history becomes irregular and its fluctuation amplitude increases. This corresponds to the pressure coefficient Root-Mean-Square (RMS) distribution (Fig. 3) that indicates that the pressure fluctuations increase in magnitude and extent over the wing and advance towards the Leading-Edge (LE) of the wing. Comparing these results to Brunet and Deck [1], it is noted that the use of high-fidelity simulation resolves higher pressure fluctuations in the wake region, compared to the URANS simulation. Thus, broadband frequency content of pressure fluctuations is not expected to be reproduced by URANS simulations.

At $\alpha = 5.25$ deg, the pressure fluctuations region shrinks and becomes more curved. Future work will examine the entire flow field at this AoA and higher AoAs to explain this change of

trend. Finally, it is noted that some anomalies in the RMS distribution can be observed for $\alpha = 5.25$ deg. These appear to be mesh-induced discrepancies due to insufficient resolution in the spanwise direction. This will be investigated in future work.

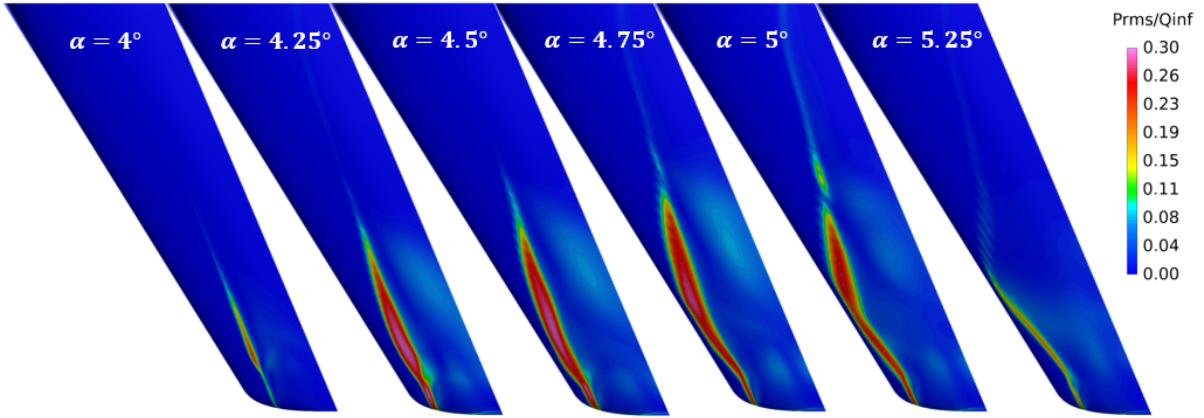


Figure 3: Pressure RMS for various AoAs, $M = 0.82$

Fig. 4 shows pressure coefficient RMS values for several AoAs compared to experimental results at spanwise station of $y/b = 75\%$. It can be seen that the RMS values are slightly over-predicted by the CFD approach at the shock wave location. Nevertheless, the trends are captured well by the computation - as the AoA is increased, the shock wave moves towards the leading-edge (LE) of the wing. It is noted that the experimental data does not have pressure measurements at $x/c < 0.3$.

For all AoAs, the pressure fluctuations on the wing surface are characterized by buffet cells in the high-RMS region of the pressure fluctuations that are convected towards the wing tip. Fig. 5 depicts a snapshot of the pressure fluctuations for the examined AoAs. The buffet cells are convected towards the wing tip and synchronize with low-high pressure fluctuations, indicating alternating separation pattern behind the shock wave ripples. Again, as for the lift coefficient time history, an evolution of the periodic structures with increasing AoA can be noticed - as the AoA increases, the periodic structures become less regular and organized. Based on the pressure fluctuations on the wing, it is observed that for the studied configuration, there is a strong interaction between the buffet cells and the wing tip flow field. An examination of the entire flow field is required to shed further light on this interaction.

Concerning the lift coefficient frequency content, Fig. 6 shows the Fourier-Transform (FT) of the lift coefficient time history for $M = 0.82$ in terms of Strouhal number defined as $St = f \cdot MAC/U_\infty$, where U_∞ is the freestream speed. It can be seen that the frequency content for the low AoA (close to buffet onset) is periodic with a dominant frequency and higher harmonics. As the AoA increases, the frequency content is more irregular and broadband at the typical shock buffet frequency ($St \approx 0.2$).

Compared to the experimental results (which study the frequency content of the pressure measurements), the frequency content herein is more narrow-band. The frequency content for the near-onset AoAs is lower than what was reported in other 3D buffet studies. It is closer to 2D buffet characteristic frequencies. In his experimental study, Dandois [2] noted that at buffet onset AoA ($\alpha = 3$ deg) the pressure Power Spectral Density is centered at lower St numbers

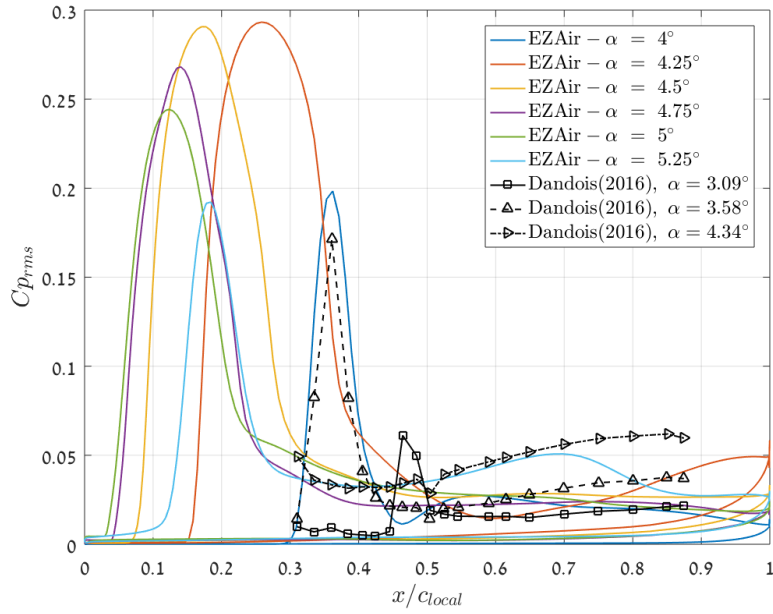


Figure 4: Pressure coefficient RMS distribution at $y/b = 75\%$, $M = 0.82$

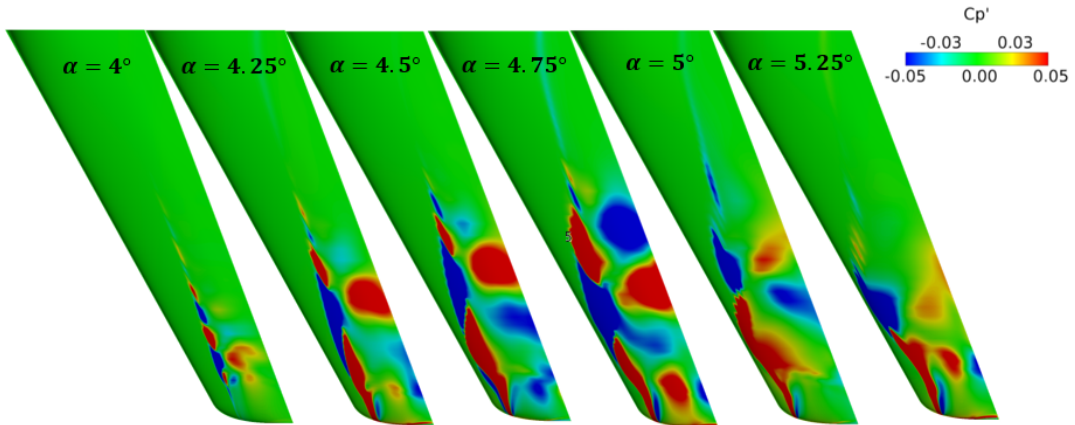


Figure 5: Snapshot of pressure coefficient fluctuations (Cp'), $M = 0.82$

between 0.02 and 0.2 (compared to the St number of 0.26 that was computed for the buffet AoA of 3.5 deg). This range compares well with the frequency content in the present study for $\alpha = 4 - 4.75$ deg. It may indicate that a wind-tunnel correction is required. No experimental results are available for other AoAs.

It is noted that other numerical studies, which investigated other swept wing geometries, did not report this low frequency content close to buffet onset. It may be attributed to different wing geometries, different spectral analysis approaches or the fact that in the current study a larger range of AoA was investigated.

DMD analysis based on pressure snapshots was performed for several AoAs. Only the first

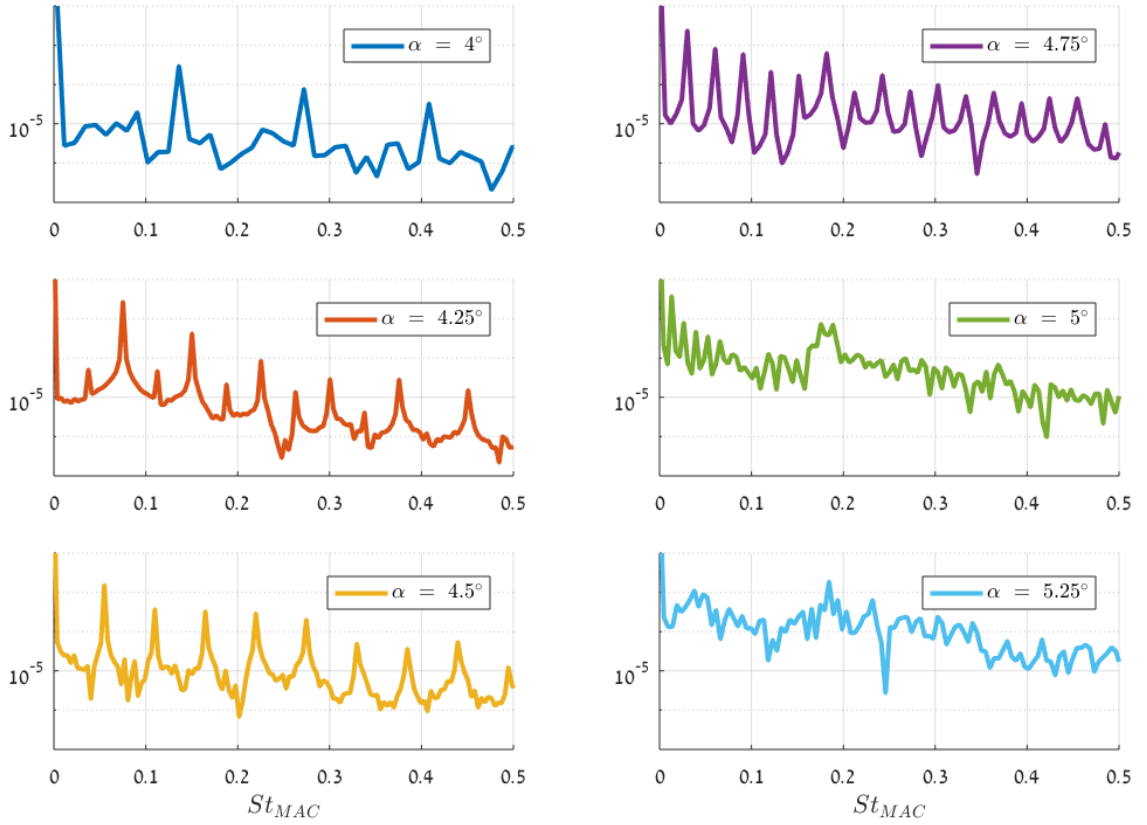


Figure 6: Lift coefficient frequency content (St based on MAC), $M = 0.82$

30 dominant modes (based on the Greedy method) are analyzed. The dominant DMD modes have the same frequencies as the lift coefficient. These dominant modal eigen-values lie on the unit circle and have close-to-zero damping, typical of the linear representation of a neutrally stable system.

Using 1500 pressure snapshots, equally spaced in time with $\Delta t_{snap} = 10\Delta t$, Fig. 7 depicts the main properties of the dominant DMD modes for $\alpha = 4.25$ deg. The frequencies of the dominant modes depict two branches that grow linearly with the mode order. Based on the modal amplitude, it appears that the modes at the lower branch (corresponding to sub-harmonic frequencies) are less important for the flow field reconstruction. Examining the modal amplitude, it can be seen that the Greedy method retrieves the dominant modes that correspond to highest modal amplitude. Finally, the reconstruction error is below 5% using the first 15 modes. The trends of the dominant modes' properties resemble those observed in modal analysis performed by the authors on 2D airfoil [12]. It is noted, however, that for higher AoA, as $\alpha = 5.25$ deg, this behavior is altered and becomes less organized. DMD results at higher AoAs resemble the results obtained by Ohmichi et al. [11] and require further investigation.

Fig. 8 shows the time-space modal history for the first three dominant oscillatory DMD modes (i.e. excluding the static mode) for $\alpha = 4.25$ deg. It can be seen that the first oscillatory mode (at $St \approx 0.07$) depicts two pressure propagation paths - one towards the wing root which resembles a straight shock front and another towards the wing tip which depicts large buffet

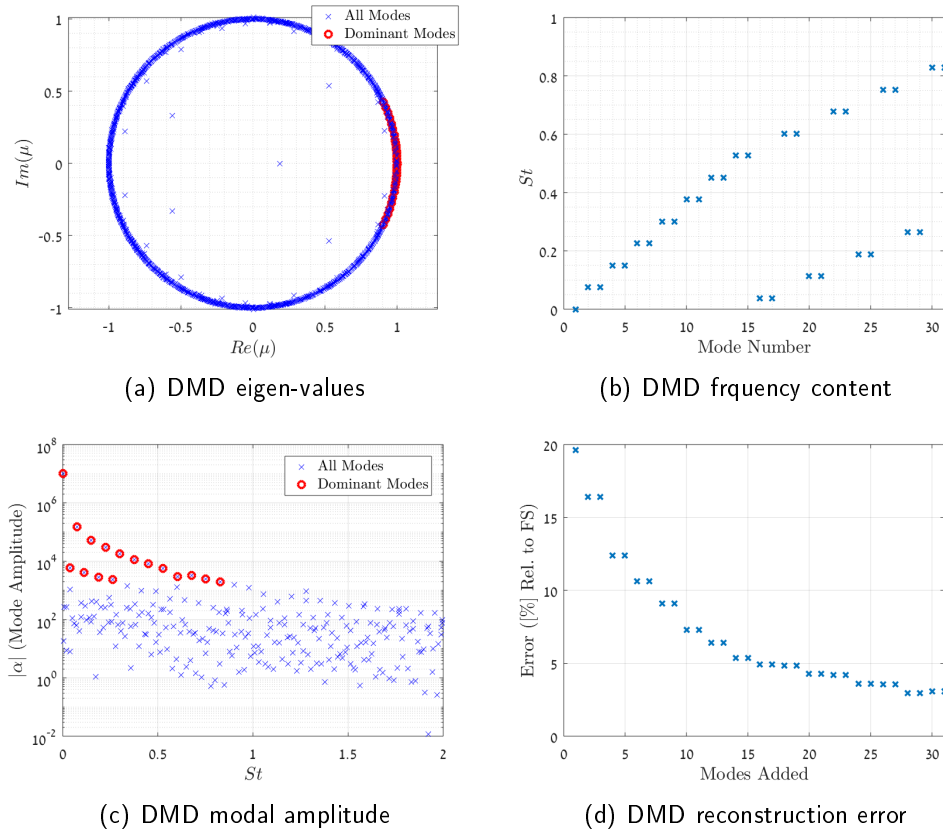
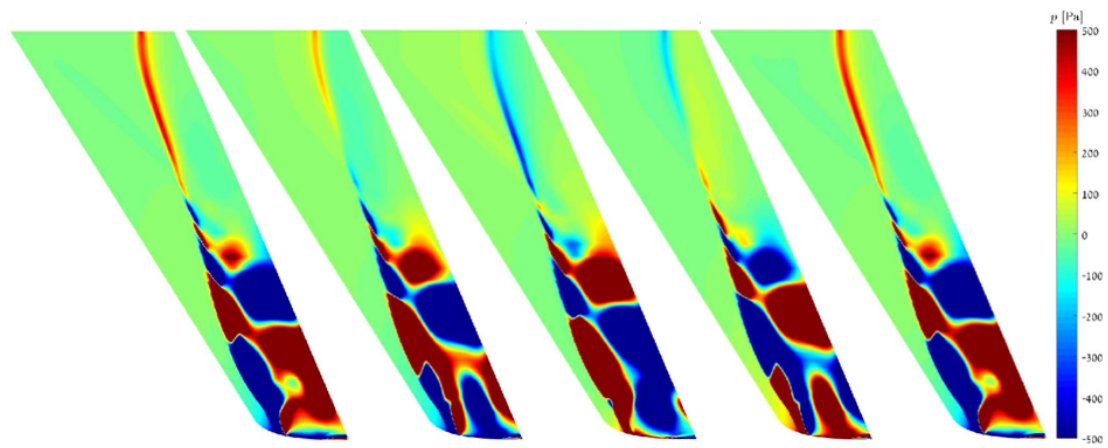


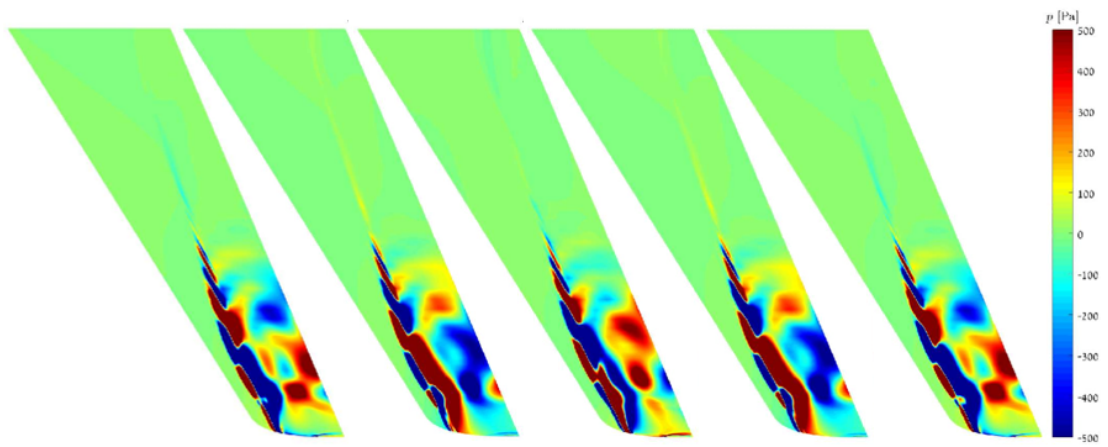
Figure 7: DMD Properties, $\alpha = 4.25$ deg, $M = 0.82$

cells. The other two modes depict smaller coherent structures within the large buffet cells, also convected towards the wing tip. Both propagation paths originate from the λ -shock triple point as observed by Iovnovich and Raveh [4].

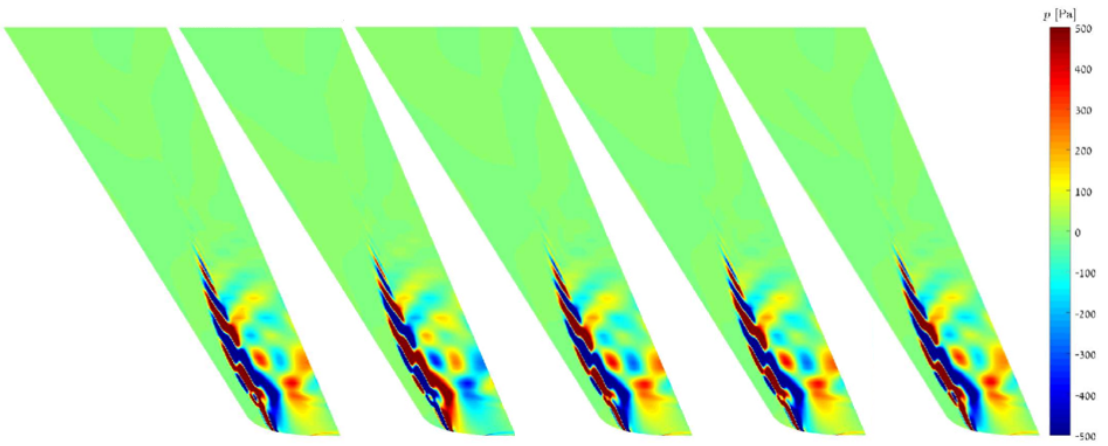
Comparing to previous numerical and experimental modal analyses, some results require further investigation. Ohmichi et al. [11] and Masini et al. [9] observed two dominant DMD modes. A low-frequency mode that depicts pressure propagation both inboard and outboard having a straight shock front pattern and higher frequency modes characteristic of 3D buffet that depict buffet cells propagation towards wing tip. However, they did not observe buffet cells pattern in the low-frequency DMD mode.



(a) $St_{MAC} = 0.075$



(b) $St_{MAC} = 0.15$



(c) $St_{MAC} = 0.226$

Figure 8: Time-space modal history of dominant DMD modes, $\alpha = 4.25$ deg, $M = 0.82$

4.2 Pitching Swept Wing at Shock Buffet Conditions

In this section, preliminary results of the lift coefficient behavior of a wing undergoing prescribed pitching motion at buffet conditions are presented. Recently, Kataras and Timme [5] presented an analysis of a swept wing that is excited with a torsional mode near buffet conditions. In the present study, the excitation is performed about developed buffet conditions at 5 deg AoA. Also, in the present study, a rigid-body pitching motion is prescribed to the entire wing, rather than simulating a structural-like torsional motion.

We prescribed pitching motion at a frequency which is twice the buffet frequency and at several amplitudes ($\alpha_p = 0.001, 0.01, \text{ and } 1.5 \text{ deg}$) about developed buffet flow at $\alpha = 5 \text{ deg}$. Fig. 9 shows the lift coefficient time history for several prescribed motion cases. The corresponding frequency content is depicted in Fig. 10.

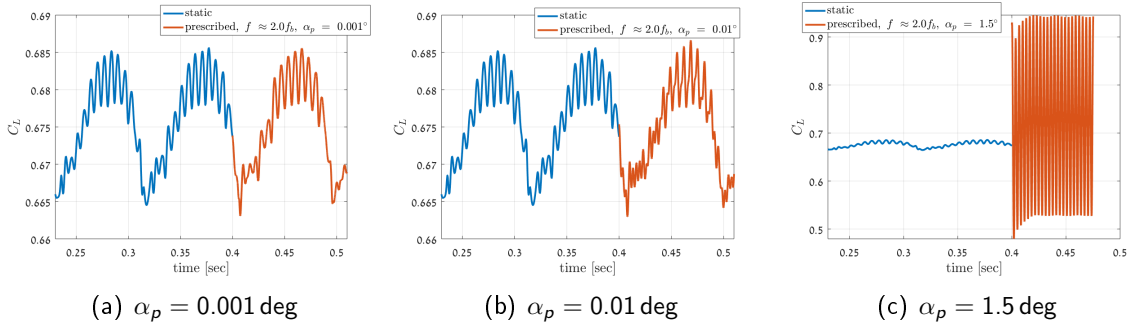


Figure 9: Lift coefficient time history at different excitation amplitudes and excitation frequency of $2.0f_{buffet}$, $\alpha_0 = 5.0 \text{ deg}$, $M = 0.82$

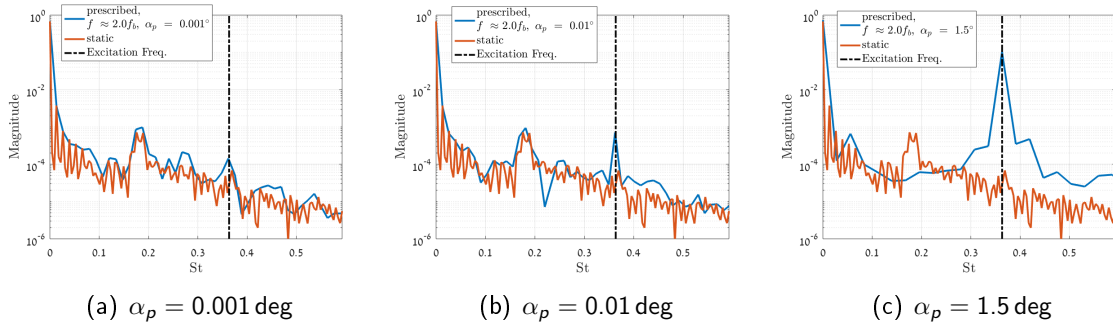


Figure 10: Lift coefficient FFT at different excitation amplitudes and excitation frequency of $2.0f_{buffet}$, $\alpha_0 = 5.0 \text{ deg}$, $M = 0.82$

For the small pitching amplitude of 0.001° , the frequency content of the lift response resembles that of buffet, with a dominant response at $St \approx 0.18$. For $\alpha_p = 0.1^\circ$ both the buffet frequency ($St \approx 0.18$) and the pitching motion frequency ($St \approx 0.36$) are seen in the lift response. This is similar to the observation in [5].

For pitching amplitude of 1.5° , the prescribed motion frequency dominates the lift coefficient response. This is practically a lock-in mechanism for 3D swept wing configuration at developed buffet conditions, similar to the lock-in mechanism observed in 2D airfoils. The lock-in can be

attributed to the fact that the lift amplitudes due to buffet (Fig. 2) are small in comparison to those due to the excitation so that the buffet flow field is suppressed and the flow field is dominated by shock wave oscillations induced by the prescribed oscillating AoA.

Future investigation is required to explore a larger envelope of prescribed-motion frequencies and amplitudes. This will be combined with a modal analysis of the excited flow field in order to assess the effect of prescribed motion on the dominant flow structures as observed for the static wing.

5 Summary and Future Work

An analysis of the shock buffet flow field on a typical swept wing was presented. The baseline, static wing, buffet flow was studied using both conventional and modal technique (DMD). Dominant modes depict the buffet cell structures convected towards the wing tip. Some observed phenomena differ from those reported in other studies in the literature and require further investigation.

Preliminary results of the unsteady response at developed buffet conditions of an oscillating wing were presented and analyzed. The interaction between the prescribed motion excitation and the buffet flow is dependent on the prescribed-motion amplitude. A lock-in mechanism (similar to the one in 2D airfoils) was observed for large excitation amplitudes and excitation frequency which was set to twice the buffet frequency. Smaller prescribed-motion amplitudes result in an unsteady response in both the buffet and the excitation frequency. Future studies will explore an extended excitation amplitude-frequency envelope applying the DMD method to assess the effect of prescribed motion on the dominant flow structures as observed for the static wing.

References

- [1] V. Brunet and S. Deck. Zonal-Detached Eddy Simulation of transonic buffet on a civil aircraft type configuration. In *38th Fluid Dynamics Conference and Exhibit*, number 4152, pages 1–12, Seattle, Washington, 2008.
- [2] Julien Dandois. Experimental study of transonic buffet phenomenon on a 3D swept wing. *Physics of Fluids*, 28(1), 2016.
- [3] Nicholas F Giannelis, Gareth A Vio, and Oleg Levinski. A review of recent developments in the understanding of transonic shock buffet. *Progress in Aerospace Sciences*, pages 1–46, 2017.
- [4] Michael Iovnovich and Daniella E. Raveh. Numerical Study of Shock Buffet on Three-Dimensional Wings. *AIAA Journal*, 53(2):1–15, 2014.
- [5] Panagiotis Belesiotis Kataras and Sebastian Timme. Harmonic Forcing Amplitude Effect in Globally Unstable Transonic Wing Flow. In *AIAA Scitech 2020 Forum*, number January, pages 1–12, 2020.
- [6] Yae'er Kidron, Yuval Levy, and Mark Wasserman. The EZAir CFD Solvers Suite: EZAir Theoretical and User's Manual - Version 3.54. Technical Report August, ISCFDC, 2016.

- [7] Shunsuke Koike, Makoto Ueno, Kazuyuki Nakakita, and Atsushi Hashimoto. Unsteady Pressure Measurement of Transonic Buffet on NASA Common Research Model. *34th AIAA Applied Aerodynamics Conference*, (June):1–25, 2016.
- [8] Simon Lawson, Doug Greenwell, and Mark K. Quinn. Characterisation of Buffet on a Civil Aircraft Wing. *54th AIAA Aerospace Sciences Meeting*, (January):1–19, 2016.
- [9] L. Masini, S. Timme, and A. J. Peace. Analysis of a civil aircraft wing transonic shock buffet experiment. *Journal of Fluid Mechanics*, 884(A1):1–42, 2020.
- [10] Jens Nitzsche. A Numerical Study on Aerodynamic Resonance in Transonic Separated Flow. In *International Forum on Aeroelasticity and Structural Dynamics*, pages 1–15, 2009.
- [11] Yuya Ohmichi, Takashi Ishida, and Atsushi Hashimoto. Modal Decomposition Analysis of Three-Dimensional Transonic Buffet Phenomenon on a Swept Wing. *AIAA Journal*, 56(10):1–13, 2018.
- [12] Lior Poppingher, Daniella E. Raveh, and Earl H. Dowell. Modal Analysis of Transonic Shock Buffet on 2D Airfoil. *AIAA Journal*, pages 1–16, 2019.
- [13] Daniella E. Raveh. Numerical Study of an Oscillating Airfoil in Transonic Buffeting Flows. *AIAA Journal*, 47(3):505–515, 2009.
- [14] F Sartor and S Timme. Reynolds-Averaged Navier-Stokes Simulation of Shock Buffet on Half Wing – Body Configuration. In *53rd AIAA Aerospace Sciences Meeting*, number January, pages 1–14, 2015.
- [15] Fulvio Sartor and Sebastian Timme. Delayed Detached–Eddy Simulation of Shock Buffet on Half Wing–Body Configuration. *AIAA Journal*, 55(4):1230–1240, 2017.
- [16] Peter J. Schmid. Dynamic mode decomposition of numerical and experimental data. *Journal of Fluid Mechanics*, 656:5–28, 2010.
- [17] Sebastian Timme and Kataras Panagiotis Belesiotis. Numerical Study of Incipient Transonic Shock Buffet on Large Civil Aircraft Wings. In *2018 Applied Aerodynamics Conference*, number July, pages 1–12, 2018.
- [18] Sebastian Timme and Reik Thormann. Towards Three-Dimensional Global Stability Analysis of Transonic Shock Buffet. In *AIAA Aviation*, pages 1–13, 2016.

Investigations into the dynamics of pitch-plunge airfoil with non-smooth structural and aerodynamic nonlinearity

Sai Vishal Reddy Gali¹, Rajagopal Vinod Bethi¹ and J Venkatramani¹

¹ *Department of Mechanical Engineering, Shiv Nadar University, Greater Noida, India, sg882@snu.edu.in*

Abstract

Aeroelastic systems with non-smooth nonlinearities can exhibit a variety of rich dynamics that are not commonly observed otherwise. Typical sources of non-smooth nonlinearities in aeroelastic systems arise from either the structure possessing a freeplay or from the flow undergoing separation and typically giving rise to dynamic stall or a combination of both. Hitherto literature has made a number of interesting observations in aeroelastic systems possessing non-smooth nonlinearities, ranging from abrupt jump to a new attractor, period doubling and/or chaos even below the linear flutter boundary, grazing-sliding genre of bifurcations, and even intermittent time responses. Owing to the richness of the dynamics and its underlying physics, and its hand-in-hand impact on the structural safety, investigating such nonlinear aeroelastic systems has gained considerable interest amongst the aeroelastic community. However, one observes that the treatment of aeroelastic systems have largely focused on a single source of nonlinearity (either arising from freeplay or from dynamic stall), though coupled non-smooth nonlinearities can give rise to richer dynamical signatures with perhaps deeper impact on the structural safety. The present study is devoted to address this specific concern. To that effect, a pitch-plunge aeroelastic system possessing a freeplay in pitch degree of freedom is considered. The dynamic stall arising due to large angles is captured using a nonlinear aerodynamic formulation described through the semi-empirical Leishman Beddoes (LB) model. A systematic response analysis is carried out to discern the bifurcation characteristics as the flow speed changes. The role of structural parameters, freeplay gap size, and the extent of pitch angle on the bifurcation characteristics is systematically investigated. Finally, insights into the structural safety are presented in light of the bifurcation analysis undertaken in this study.

Keyword: Dynamics Stall, Freeplay, Leishman Beddoes Model, Bifurcations

1 Introduction

Flexible aeroelastic structures when exposed to on-coming fluid loads results often in a highly nonlinear flow-structure coupling (Fung, 2008). Such fluid-structure interactions, owing to the presence of nonlinearities, have the potential to display phenomenologically rich dynamical signatures - for example, sustained limit cycle oscillations (LCOs), chaotic oscillations, abrupt jump to a new attractor, grazing bifurcations etc to name a few. A key aspect of this fluid-structure interaction induced dynamical responses is its impact on the safety of the underlying aeroelastic system. Indeed, sustained oscillations that arise due to the fluid-elastic coupling can lead to structural failure due to accumulation of fatigue damage or due to overloading. Consequently,

typical aeroelastic studies resorts to a systematic bifurcation analysis of the aeroelastic system as a first step towards design of the same (Lee et al., 1999; Q. Ding and D.-L Wang, 2006; D. Poirel and S.J. Price, 2007).

However, carrying out a bifurcation analysis of aeroelastic systems is not a trivial exercise. The ubiquitous presence of a variety of nonlinearities pose challenge in identifying and modeling the same (Lee et al., 1999). Indeed, aeroelastic systems can possess nonlinearities that arise either from the flow (Fragiskatos, 2000; S.S. Bhat and R.N. Govardhan, 2013; H Devathi and S. Sarkar, 2016) or from the structure (Haunstein et al., 1992; B. Lee and L. Jiang, 1999) or a combination of both (D. Tang and E. Dowell, 1992). Further, the nature of nonlinearity can be either continuous or discontinuous or a combination of both. Examples of the above scenarios that has demanded attention from the aeroelastic community are as follows. Large deformations can result in a cubic form (or a similar polynomial approximation) of the structural stiffness - in turn giving rise to supercritical or subcritical type of Hopf bifurcation (Lee et al., 1999). The presence of loose hinges or ageing parts in the structure can, however, give rise to discontinuous forms of nonlinearities such as, freeplay (H Alighanbari, 1996). The presence of freeplay in the structure can dramatically change the aeroelastic dynamics by shifting the flutter limit (H Alighanbari, 1996), giving rise to chaotic responses in the pre-flutter responses (Liu et al., 2002), chaotic transients in the response dynamics (Dai et al., 2014) and even give rise to discontinuity induced bifurcations (DIB) (U Galvanetto et al., 2008).

Exceeding of the pitch angle over a critical limit (static stall angle), on the other hand, introduces aerodynamic genre of nonlinearities. Marked by a complex series of events spanning from flow separation to re-attachment, the airfoil undergoes a nonlinear aerodynamic phenomenon called dynamic stall (McCroskey et al, 1976). Here as well, at a critical flow speed, the airfoil loses stability and undergoes sustained LCOs marking the onset of stall flutter. Interestingly, dynamic stall is characterized by a set of events that is discontinuously nonlinear, and therefore capable of giving rise to DIB. Recent studies (Rajagopal et al., 2019) in the literature have shown a variety of DIBs possible in an aeroelastic system undergoing dynamic stall.

A distinct feature of DIBs is the abrupt jump in the dynamics to a new attractor. Such sharp changes often pose considerable impact on the structural safety of aeroelastic systems. This problem becomes exacerbated when multiple sources of discontinuous nonlinearities are present. Indeed, the presence of coupled nonlinearities can give rise to radically different dynamics (Lee et al, 2006) that are not observed otherwise. A practical example for such coupled nonlinearities is the presence of freeplay in the stiffness of an airfoil, subjected to dynamic stall. Here, both the structure and aerodynamics possess discontinuous nonlinearities. Such coupled discontinuously nonlinear aeroelastic systems have received minimal attention in the hitherto literature (Kalmar-Nagy et al., 2016). The present study is devoted towards addressing this concern.

This study focuses on investigating the bifurcations in a pitch-plunge airfoil possessing freeplay nonlinearity in pitch degree of freedom and subjected to dynamic stall. The nonlinearity in the aerodynamics is captured by using a Leishman Beddoes (LB) formulation. For various values of freeplay gap, and for different ranges of airfoil angle, response analysis is systematically carried out with respect to flow speed as a control parameter. The obtained responses and bifurcation characteristics are corroborated in light of structural safety.

The rest of the paper is organized as follows. Section 2 presents the mathematical model of the aeroelastic system and its associated aerodynamic forces. The salient findings obtained

are presented in Section 3 along with relevant discussions. The key findings from this study are summarized in Section 4.

2 Mathematical Modelling

2.1 Structural Model

A typical pitch-plunge airfoil is used in the present study; see Fig. 1. The airfoil is allowed to move in vertical direction (plunge ξ) and rotate about its elastic axis (pitch α). The chord length of the airfoil is denoted by c and the semi-chord $b = c/2$. The elastic axis is located at

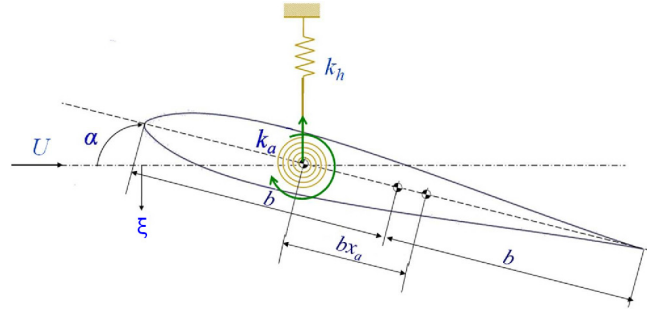


Figure 1: Schematic of a pitch-plunge airfoil.

$a_h b$ from semi-chord and the center of gravity is located at $x_\alpha b$ from elastic axis. The bending and torsional springs (k_ξ and k_α) are attached to the elastic axis along with dampers (c_ξ and c_α). The equations of motion in non-dimensional form can be written as (Fung 2008).

$$\xi'' + x_\alpha \alpha'' + 2\zeta_\xi \frac{\bar{\omega}}{U} \xi' + \left(\frac{\bar{\omega}}{U} \right)^2 G(\xi) = -\frac{1}{\pi\mu} C_L(\tau), \quad (1)$$

$$\frac{x_\alpha}{r_\alpha^2} \xi'' + \alpha'' + 2\zeta_\alpha \frac{1}{U} \alpha' + \left(\frac{1}{U} \right)^2 M(\alpha) = \frac{(0.5 + a_h)}{\mu\pi r_\alpha^2} [C_L(\tau) \cos \alpha + C_D(\tau) \sin \alpha] + \frac{2}{\pi\mu r_\alpha^2} C_M(\tau). \quad (2)$$

Here, ϖ is the ratio of pitch and plunge natural frequencies, ζ_ξ and ζ_α are the viscous damping ratios of plunge and pitch respectively, U is the flow speed, μ represents the reduced mass and r_α is the radius of gyration computed about the elastic axis. $G(\xi)$ and $M(\alpha)$ account for the non dimensional stiffness in plunge and pitch and are functions of ξ and α respectively. The function used to represent the non-smooth freeplay effects is given as

$$M(\alpha) = \begin{cases} \alpha + \delta & \text{if } \alpha < -\delta \\ 0 & \text{if } -\delta \leq \alpha \leq \delta \\ \alpha - \delta & \text{if } \alpha > \delta \end{cases} \quad (3)$$

2.2 Leishman-Beddoes model (LB model)

The aerodynamical forces are modeled using the LB formulation. A brief description of the same is provided. Interested readers are referred to (Rajagopal et al., 2019) for further details on the modules of LB model. The LB model in its state space form is described in (Leishman J.G and Beddoes T.S, 1989). The LB dynamic stall model is defined by a set of first order ODEs,

$$\dot{x} = f(x, \hat{\alpha}, q). \quad (4)$$

Where the $\hat{\alpha}$ is the effective pitch angle, q is the non-dimensional pitch rate and $x = [x_1, x_2, \dots, x_{12}]$ are the twelve aerodynamic states. The aerodynamic co-efficients are given by,

$$C_i = g_i(x, \hat{\alpha}, q) \quad i = C, N, M, \quad (5)$$

where, C, N, M are the chord, normal and moment respectively experienced by the airfoil.

The LB model uses a modified version of the Wagner's function by taking into account the free stream Mach number (M_∞) and compressibility of the flow. The Wagner function has two aerodynamic states but the LB model has 8 aerodynamic states under the attached flow components due to contributions from the added mass effect and the compressibility of flow (see Eq. 6).

$$\begin{bmatrix} \dot{x}_1 \\ \dot{x}_2 \\ \dot{x}_3 \\ \dot{x}_4 \\ \dot{x}_5 \\ \dot{x}_6 \\ \dot{x}_7 \\ \dot{x}_8 \end{bmatrix} = \text{diag} \begin{bmatrix} -\frac{2V}{c} b_1 \beta^2 \\ -\frac{2V}{c} b_2 \beta^2 \\ -\frac{1}{K_\alpha T_I} \\ -\frac{1}{K_q T_I} \\ -\frac{1}{b_3 K_{qM} T_I} \\ -\frac{b_4 K_{\alpha M} T_I}{1} \\ -\frac{2V}{c} b_5 \beta^2 \\ -\frac{1}{K_{qM} T_I} \end{bmatrix} \begin{bmatrix} x_1 \\ x_2 \\ x_3 \\ x_4 \\ x_5 \\ x_6 \\ x_7 \\ x_8 \end{bmatrix} + \begin{bmatrix} 1 & \frac{1}{2} \\ 1 & \frac{1}{2} \\ 1 & 0 \\ 0 & 1 \\ 1 & 0 \\ 1 & 0 \\ 0 & 1 \\ 0 & 1 \end{bmatrix} \begin{bmatrix} \hat{\alpha} \\ q \end{bmatrix} \quad (6)$$

The Wagner function ($\phi(t)$) was modified to account for the compressibility by defining $\phi^C(t) = 1 - A_1 e^{-\frac{b_1 \beta^2 U t}{b}} - A_2 e^{-\frac{b_2 \beta^2 U t}{b}}$. Here, β is the compressibility factor and is given by $\beta = \sqrt{1 - M^2}$ (Dimitriadis, 2017). However, due to dependency of stall flutter onset on flow separation, computing the trailing edge separation component becomes pertinent. The LB model captures the same and is explained next.

The LB model accounts for the flow separation at trailing edge and the subsequent drop in the lift force as well as the moment. The three state space variables x_9 (delayed normal force), x_{12} (dynamic trailing edge separation point) and x_{10} (delayed version of x_{12}) are given by

$$\dot{x}_9 = \frac{(C_N)^C + C_N' - x_9}{T_P} \quad (7)$$

$$\dot{x}_{10} = \frac{f\left(\frac{x_9}{C_{N\alpha}}, \alpha\right) - x_{10}}{T_f} \quad (8)$$

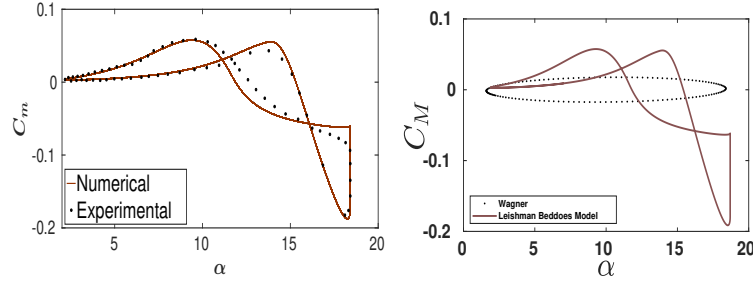


Figure 2: C_M Variation of LB Model compared against experimental data provided in McCroskey et al. (1976) (left image) and the aerodynamic load computed using the Wagner Model (right image).

$$x_{12}' = \frac{f(\hat{\alpha}, \alpha) - x_{12}}{0.63 T_{f0}} \quad (9)$$

The aerodynamic forces associated with trailing edge separation component are given by

The Vortex shedding component describes the missing aerodynamic state x_{11} as the lift produced by the leading edge vortices.

$$x_{11}' = \begin{cases} c_v' - \frac{x_{11}}{T_v}, & \text{if } \alpha c_v' \geq 0 \text{ and } 0 < \tau_v < 2T_{vI} \\ -\frac{x_{11}}{T_v}, & \text{otherwise} \end{cases} \quad (10)$$

The coefficient of moment calculated from the LB model is validated against experimental data found in McCroskey et al. (1976); see Fig. 2(a) and also compared with that obtained using the Wagner model; see Fig. 2(b). Evidently, as the angle α increases, the LB model captures the hysteresis rigorously and matches well with the experimental observations.

3 Results and Discussions

The governing equations of motions are solved using an adaptive Runge Kutta method in MATLAB. The system parameters based on Liu et al. (2002) and are $\varpi = 0.2$, $r_\alpha = 0.5$, $\mu = 100$, $x_\alpha = 0.25$, and $a_h = -0.5$. The representative value of freeplay gap considered in this study, $\delta = 0.1$. Throughout the findings are presented for either of these two freeplay gaps, and with the airfoil undergoing dynamic stall. The initial conditions used throughout are $\alpha(0) = 20^\circ$, $\alpha'(0) = 0^\circ$, $\xi(0) = 0^\circ$ and $\xi'(0) = 0^\circ$. The Mach number based parameters used in this study correspond to a Mach number $M = 0.3$ and further details can be found in (Rajagopal et al, 2019).

The initial pitch amplitude is deliberately taken as a high value so as to force the airfoil into dynamic stall region. As the flow speed U is gently increased, one observes the response exhibiting a decaying signature as shown in Fig. 3. Further increase in U results in interesting dynamics as shown in Fig. 4. The aeroelastic response exhibits low amplitude LCOs as presented in Fig. 4(a). It is worthwhile to note that the birth of LCO is perhaps not due to the effect of dynamic stall. In other words, the LCOs perhaps do not represent a stall flutter onset. Rather, the small amplitude LCOs can be attributed to the freeplay in the pitch stiffness. A visual inspection of the phase space of the response trajectory substantiates this argument; see Fig.

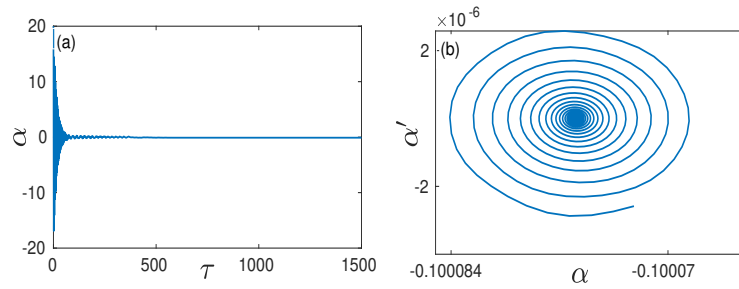


Figure 3: (a) Time response (b) Phase portrait of the system at $U = 0.75$.

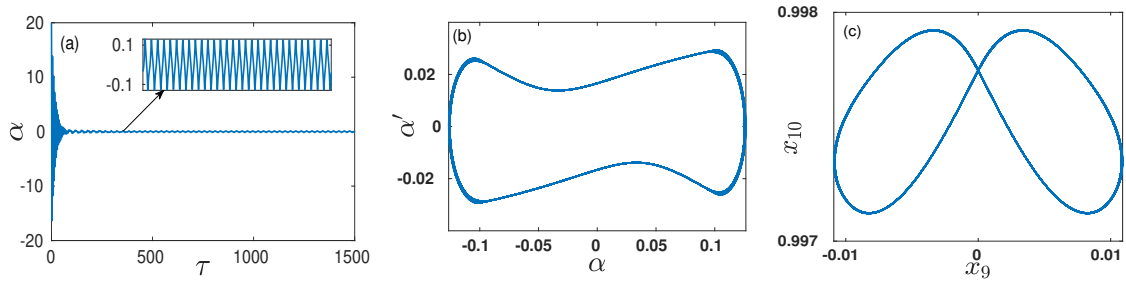


Figure 4: (a) Time response (b) Phase portrait (c) x_9 v x_{10} plot at $U = 0.8$.

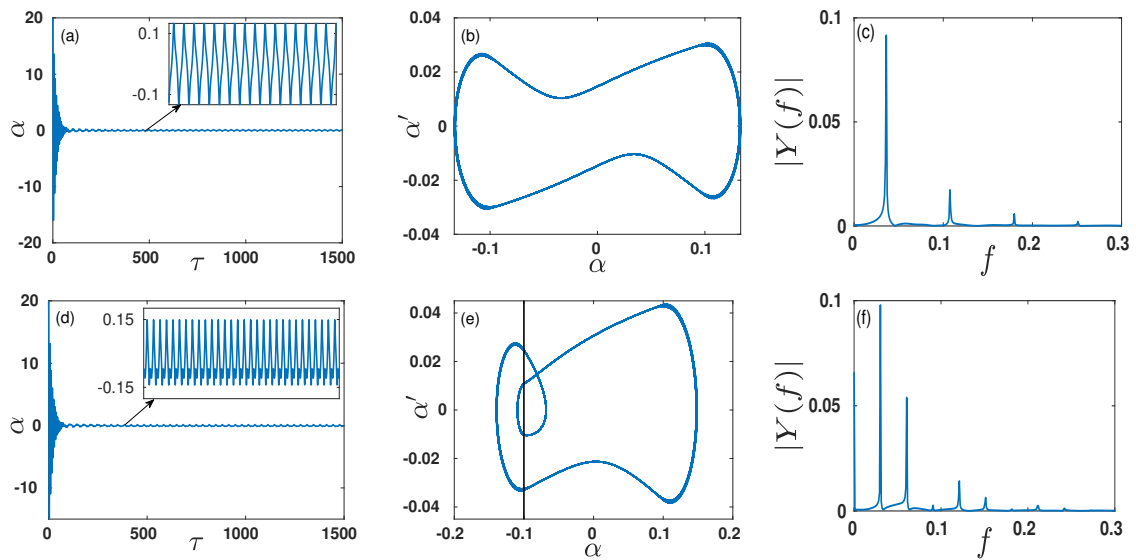
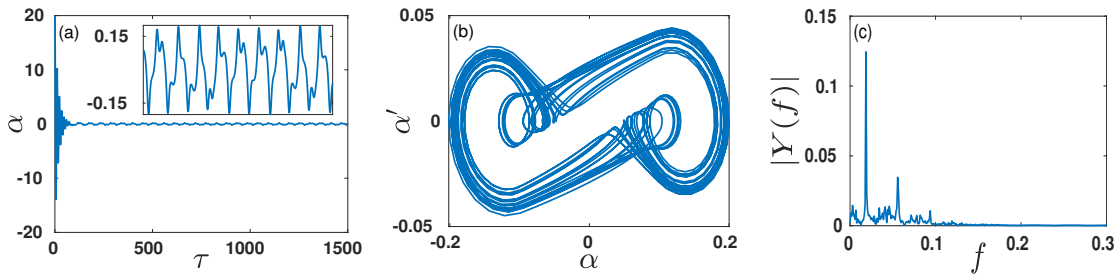
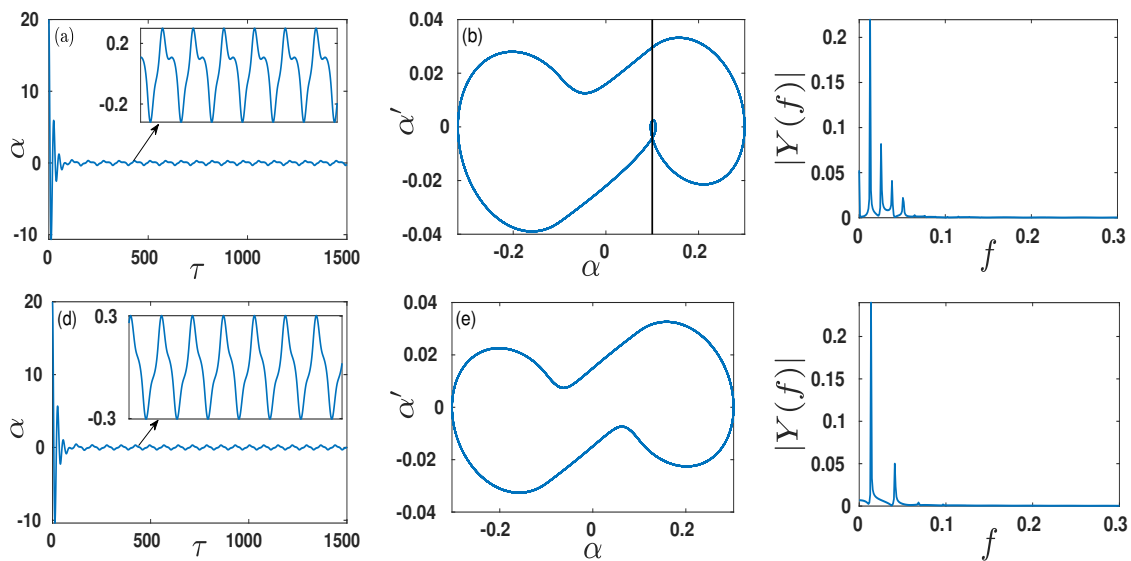


Figure 5: (a) Time response (b) Phase portrait (c) FFT at $U = 1.1$ (before the transition) (d) Time response (e) Phase portrait (f) FFT at $U = 1.15$.


 Figure 6: (a) Time response (b) Phase portrait (c) FFT at $U = 2$.

 Figure 7: (a) Time response (b) Phase portrait (c) FFT at $U = 3.7$ (d) Time response (e) Phase portrait (f) FFT at $U = 3.9$.

4(b). The amplitudes of the response are bound around -0.1 to 0.1 , and in turn coinciding with the gap size of the freeplay. Further, tracking the flow separation variables, namely x_9 and x_{10} , as shown in Fig. 4(c), we observe that the flow is considerably attached to the airfoil structure. It is to be remembered that x_{10} approaches unity for completely attached flows.

When U is increased further ($U = 1.1$), one observes the low amplitude LCOs to still persist; see Figs. 5(a)-(c). As U approaches 1.15, the dynamical signature transitions into a period doubling behavior; see Figs. 5(d)-(f). Note that the phase plot shows that the period addition is formed along one of the freeplay boundary (here $\alpha \approx -0.1$). The trajectories associated with the additional period appear to form a tangent to the discontinuous boundary and in turn indicating a possible grazing type bifurcation occurring in the aeroelastic system (Vasconcellos et al, 2014).

Next, as the flow speed is systematically increased, the response transitions from period doubling behavior to chaotic behavior as shown in Fig. 6. Here as well, the bifurcations are largely attributed to the presence of freeplay nonlinearity, than the aerodynamic nonlinearity. A visual inspection of the flow behaviors via x_9 and x_{10} plots reveals the same. The notion

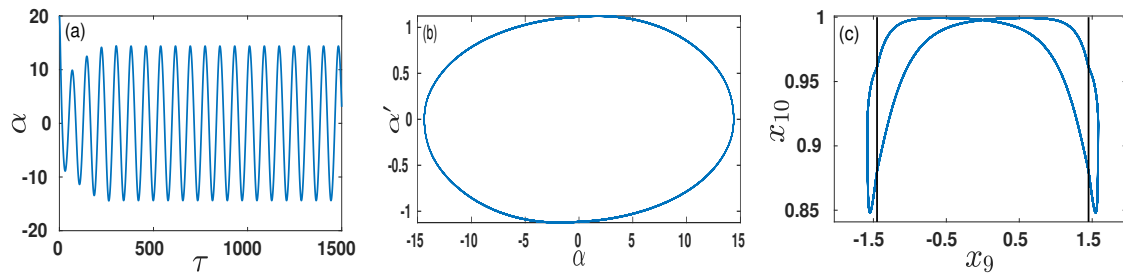


Figure 8: (a) Time response (b) Phase portrait (c) FFT at $U = 5.9$ where flow transitions back into LCO response.

of period doubling route to chaos is typical in aeroelastic systems with freeplay nonlinearity (Liu et al., 2002) and in the absence of flow separation, it is conjectured that the structural nonlinearity dictates the present (low flow speed) bifurcation characteristics.

The next considerable change in the dynamics occurs at $U = 3.75$; see Fig. 7. The response dynamics now transforms itself into a period doubling signature again. However, the phase plot (Fig. 7(b)) shows the presence of the additional loop in tangent to the discontinuity boundary and implying a possible grazing bifurcation in the system. Evidently, the flow is remaining attached here as well (as observed from the x_9 and x_{10} variations). At $U = 3.9$, the tangency signature disappears and the response dynamics transforms itself into a single period oscillation; see Fig. 7(d)-(f). The loss of tangency at the discontinuity boundary itself is an indicator of grazing bifurcations in the underlying dynamical system (Vasconcellos et al., 2014).

It is worthwhile to note that it is presently unclear on whether the DIBs observed have no contribution from the aerodynamic nonlinearity. Studies by (G. Dimitriadis and J. Li, 2009) have shown that while aerodynamically dynamic stall is possible at lower flow speeds, stall flutter occurs at higher flow speeds. However, in the present study, it would be premature to comment on the same without rigorous analytical studies or experimental observations.

Once the flow speed reaches sufficiently high values, say, $U = 5.9$, sustained LCOs are encountered again. However, the amplitudes of LCOs are considerably higher in comparison to the ones observed at lower values of flow speed; see Fig. 8. An inspection of the x_9 and x_{10} reveals a flow separation along with vortex shedding occurring and suggestive a stall induced dynamics. Increasing U led to the development of high amplitude period doubling oscillations as shown in Fig. 9.

Increasing U to 12.5 resulted in the dynamics resembling a period-3 signature; see Fig. 10. Such period addition signatures are typical of systems possessing strong forms of discontinuous nonlinearities - namely, freeplay in the structure and dynamic stall behavior via the flow (Rajagopal et al., 2019). It would be interesting to track the dynamics for higher ranges of flow speeds and is, however, beyond the scope of the present study. It appears that as the flow speed increases, the aerodynamic nonlinearity (via dynamic stall) dictates the response dynamics in comparison to the structural freeplay. However, without an ensemble of time responses or analytical/experimental corroboration, attributing the dynamics to specific nonlinearities would be premature.

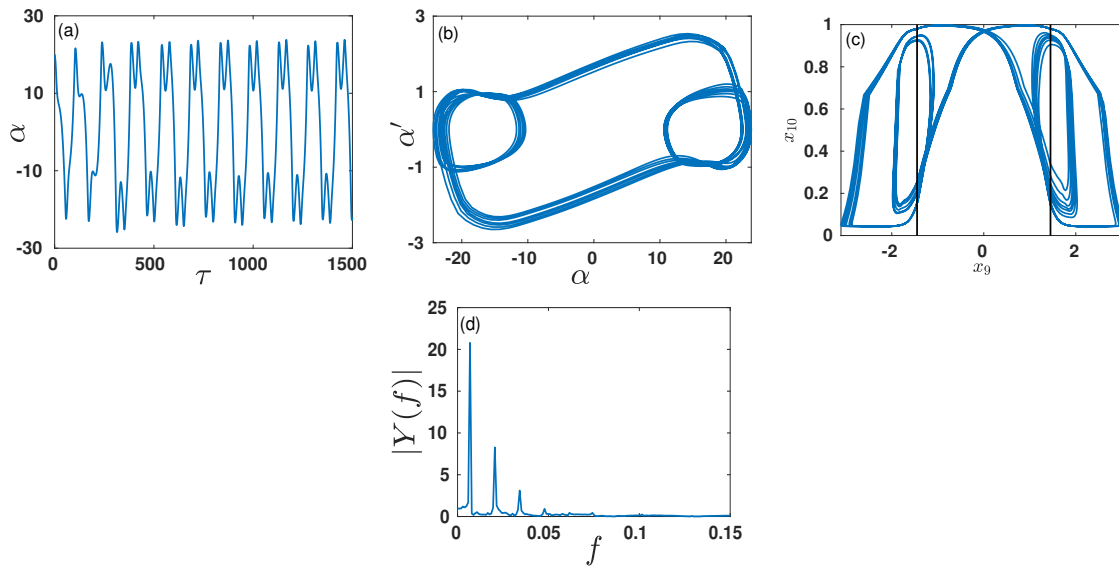


Figure 9: (a) Time response (b) Phase portrait (c) variation of x_9 and x_{10} at $U = 8.5$. Flow transitions into a high amplitude Period-3 oscillations.

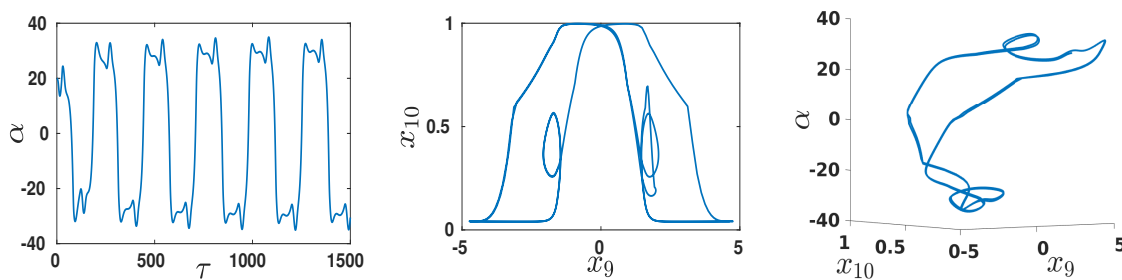


Figure 10: (a) Time response (b) Phase portrait (c) variation of x_9 and x_{10} at $U = 12.5$. Flow transitions from Period -3 into a Period-3 with harmonics.

4 Conclusions

The present study focused on investigating the response dynamics of a pitch-plunge airfoil possessing discontinuous nonlinearities in both structural and aerodynamic fronts. Accordingly, the airfoil was considered under dynamic stall conditions and the pitch stiffness was assumed to possess a freeplay nonlinearity. It was observed that at a low flow speed, a Hopf bifurcation exists, followed by a period doubling cascade that ultimately led to chaotic oscillations. Such signatures are typical of systems possessing freeplay nonlinearities. The effect of aerodynamic nonlinearities, tracked using the flow specific state variables, seemed to have insignificant contributions at lower flow speeds. Consequently, the amplitudes of oscillations at low flow speeds were also observed to be small. As the flow speed increased, the effect of aerodynamic nonlinearity, marked by dynamic stall, becomes pronounced. Nevertheless, rigorous investigations into the physics of the problem is necessary to obtain deeper insights into the dynamics. The authors are presently investigating the same.

Acknowledgements

The authors gratefully acknowledge the funding received from DST-SERB start up research grant (grant no SRG/2019/000077) towards the present research work.

References

- Alighanbari, H., 1996. Flutter analysis and chaotic response of an airfoil accounting for structural nonlinearities (Ph.D. thesis). McGill University.
- Bethi, R.V., Gali, S.V. and Venkatramani, J., 2020. Response analysis of a pitch-plunge airfoil with structural and aerodynamic nonlinearities subjected to randomly fluctuating flows. *Journal of Fluids and Structures*, 92, p.102820.
- Bhat, S.S. and Govardhan, R.N., 2013. Stall flutter of NACA 0012 airfoil at low Reynolds numbers. *Journal of Fluids and Structures*, 41, pp.166-174.
- Dai, H., Yue, X., Xie, D. and Atluri, S.N., 2014. Chaos and chaotic transients in an aeroelastic system. *Journal of Sound and Vibration*, 333(26), pp.7267-7285.
- Devathi, H. and Sarkar, S., 2016. Study of a stall induced dynamical system under gust using the probability density evolution technique. *Computers Structures*, 162, pp.38-47.
- Dimitriadis, G. and Li, J., 2009. Bifurcation behavior of airfoil undergoing stall flutter oscillations in low-speed wind tunnel. *AIAA journal*, 47(11), pp.2577-2596.
- Dimitriadis, G., 2017. *Introduction to Nonlinear Aeroelasticity*. John Wiley Sons.
- Ding, Q., Wang, D.-L., 2006. The flutter of an airfoil with cubic structural and aerodynamic nonlinearities. *Aerosp. Sci. Technol.* 10 (5), 427-434.
- Fragiskatos, G., 2000. *Non-linear Response and Instabilities of a Two-Degree-of-Freedom Airfoil Oscillating in Dynamic Stall*.
- Fung, Y.C., 2008. *An Introduction to the Theory of Aeroelasticity*. Courier Dover Publications.
- Galvanetto, U., Peiro, J., Chantharasenawong, C., 2008. An assessment of some effects of the nonsmoothness of the Leishman-Beddoes dynamic stall model on the nonlinear dynamics of a typical aerofoil section. *J. Fluids Struct.* 24 (1), 151-163.
- Hauenstein, A., Zara, J., Eversman, W., Qumei, I., 1992. Chaotic and nonlinear dynamic response of aerosurfaces with structural nonlinearities. *AIAA J.* 92, 2367-2376.
- Kalmar-Nagy, T., Csikja, R. and Elgohary, T.A., 2016. Nonlinear analysis of a 2-DOF piecewise linear aeroelastic system. *Nonlinear Dynamics*, 85(2), pp.739-750.
- Lee, B., Jiang, L., 1999. Flutter of an airfoil with cubic restoring force. *J. Fluids Struct.* 13, 75-101.
- Lee, B., Price, S., Wong, Y., 1999. Nonlinear aeroelastic analysis of airfoils: bifurcation and chaos. *Progr. Aerosp. Sci.* 35 (3), 205-334.
- Lee, B.H., Liu, L., 2006. Bifurcation analysis of airfoil in subsonic flow with coupled cubic restoring forces. *J. Aircraft* 43 (3), 652-659.
- Leishman, J.G. and Beddoes, T.S., 1989. A Semi-Empirical model for dynamic stall. *Journal of the American Helicopter society*, 34(3), pp.3-17.
- Liu, L., Wong, Y., Lee, B., 2002. Non-linear aeroelastic analysis using the point transformation method, part 1: Freeplay model. *J. Sound Vib.* 253 (2), 447-469.
- McCroskey, W.J., Carr, L.W., McAlister, K.W., 1976. Dynamic stall experiments on oscillating airfoils. *AIAA J.* 14 (1), 57-63.
- Poirel, D., Price, S.J., 2007. Bifurcation characteristics of a two-dimensional structurally non-linear airfoil in turbulent flow. *Nonlinear Dyn.* 48 (4), 423-435.

Tang, D., Dowell, E., 1992. Flutter and stall response of a helicopter blade with structural nonlinearity. *J. Aircr.* 29 (5), 953-960.

Vasconcellos, R., Abdelkefi, A., Hajj, M.R. and Marques, F.D., 2014. Grazing bifurcation in aeroelastic systems with freeplay nonlinearity. *Communications in Nonlinear Science and Numerical Simulation*, 19(5), pp.1611-1625.

Nonlinear Aeroelastic Simulation of Thin Airfoil Model

Hitoshi Arizono¹ and Hamid Reza Kheirandish²

¹ *Japan Aerospace Exploration Agency, Tokyo, Japan, arizono.hitoshi@jaxa.jp*

² *Advanced Science & Intelligence Research Institute, Tokyo, Japan*

Abstract

This paper describes that a new aeroelastic simulation code based on the unstructured CFD solver is developed. Computations are performed for AGARD 445.6 wing model. The flutter boundary predicted by the developed code are presented and compared with the experimental data.

Keyword: Aeroelastic simulation, CFD

1 Introduction

Air traffic in worldwide is predicted to increase considerably over the next decades. By 2034, both air passenger traffic and air freight traffic are expected to more than double, compared to 2016. Passenger traffic is expected to reach over 14 trillion PRKs with a growth of 4.5 percent per annum, and freight will expand by 4.2 percent annually over the same time period, to 466 billion FTKs (ICAO 2016). It is essential to establish technology to realize efficient and speedy development of Aircraft. JAXA has been promoting a research program to build a multidisciplinary integrated simulation platform from 2018. This program is aimed at enabling sophisticated look ahead designs that can be used with full flight envelopes as well as cruise conditions currently used in aircraft design. In this program, the development of simulation technology and the acquisition of validation data on the following themes; (1) high/low speed buffet prediction, (2) flutter prediction, (3) outside aircraft and cabin noise prediction, (4) water spray prediction, (5) control effectiveness and dynamic stability prediction and (6) Reynolds number effects prediction.

JAXA has been developing a fast unstructured flow solver FaSTAR (Hashimoto 2012). FaSTAR solves the full Navier-Stokes equations using a cell-center finite volume method. The Harten-Lax-van Leer-Einfeldt-Wada (HLLEW) method (Burg 2005) used for numerical flux computations. The special accuracy is second order with the Unstructured Monotonic Upstream-centered Scheme for Conservation Laws (U-MUSCL) method (Obayashi 1995). The gradients are computed with GLSQ method (a hybrid method of Green-Gauss and Least-Square) (Shima 2013) and Hishida's limiter (a Venkatakrishnan-like limiter that is complementary with difference of neighboring cell size) (Hishida 2011). The viscous terms are evaluated by edge-normal scheme. For time integration, the Lower/Upper Symmetric Gauss-Seidel (LU-SGS) implicit method (Men'shov 1995) with a preconditioning method is used in order to avoid the stiffness problem associated with solving low Mach number flows using compressible flow solvers. As for the turbulence mode, Spalart-Allmaras model (SA) (Spalart 1992) and Menter's shear stress transport k-omega model (SST) (Menter 2003) can be used.

In recent years, in order to meet the needs for fluid analysis around moving/deforming body problems, FaSTAR-Move which is an overset unstructured CFD code has been developing based on FaSTAR. The objectives of developing FaSTAR-Move are to enhanced the current CFD capability for moving/deforming body problems and to establish basic technologies for aircraft development. FaSTAR-Move uses the unstructured overset grids to compute a fluid flow and an equation of motion around complex geometries. Due to the implementation fo Alternating Digital Tree (ADT) algorithm (Roget 2010) and the parallelization of the hole-cut process, the computational time for the hole-cut process which was a critical problem in the overset process could be shorten. FaSTAR-Move has been successfully applied to a store separation problem and showd reasonable results. This paper presents the modification of FaSTAR-Move for the aeroelastic simulations and the results of validation.

2 Modification for Aeroelastic Simulation

The aeroelastic equations are needed to solve the dynamic aeroelastic problems. The following subroutines are added to FaSTAR-Move; (1) read the vibration characteristics, (2) calculate pressures on the surfaces, (3) solve the aeroelastic equations, (4) move surface grids, (5) move spatial grids. The subroutine (2) to (5) are used in each time step. The governing aeroelastic equations of motion are solved using modal approach. These equations of motion are derived by assuming that the deformation of the body under consideration can be described by a separation of variables involving the summation of free vibration modes weighted by generalized displacements. The time integration of the governing equations is employed the Wilson's theta method.

The non-dimensional form of aeroelastic equations for modal method is as follows:

$$\ddot{q}_i + 2\xi_i k_i \dot{q}_i + k_i^2 q_i = \frac{l_0^3 Q_\infty}{m_i a_\infty^2} \iint_S (\Delta C_p + C_f) n \Phi_i dS \quad (1)$$

which q_i is generalized coordinates, ξ_i is structural damping, k is reduced frequencies, l_0 is reference length, Q_∞ is dynamic pressure, m_i is generalized mass, a_∞ is sound of speed, n is unit vector, Φ_i is eigenvectors, i is mode number.

When the above equations are solved, new body surface grid points are determined.

$$\vec{X}_S^{\text{new}} = \vec{X}_S^0 + \sum_{i=1}^{\text{mode}} q_i \Phi_i \quad (2)$$

The spacial grid points are determined by inverse distance weighted interpolation.

$$\vec{X}^{\text{new}} = \vec{X}^0 + w \Delta \vec{X}_S \quad (3)$$

which \vec{X} , $\Delta \vec{X}_S$ and w are non deformed grid points, moving distance of nearest grid points on body surface and weighted function determined according to the distance from the body surface, respectively.

3 Results

3.1 AGARD 445.6

AGARD 445.6 wing model (Yates 1989) is used for the validation of modified FaSTAR-Move. This wing model is widely applied to validate the flutter prediction. This wing is a semispan model made of the NACA65A004 airfoil that has a quarter-chord sweep angle of 45 degree, a panel aspect ratio of 1.65, and a taper ratio of 0.66. It was tested in the Transonic Dynamic Tunnel at NASA Langley Research Center. Figure 1 shows the surface grid which is generated using HexaGrid (Hashimoto 2010). The number of grid points of around wing grid and background grid are 1.2 million and 3.4 million.

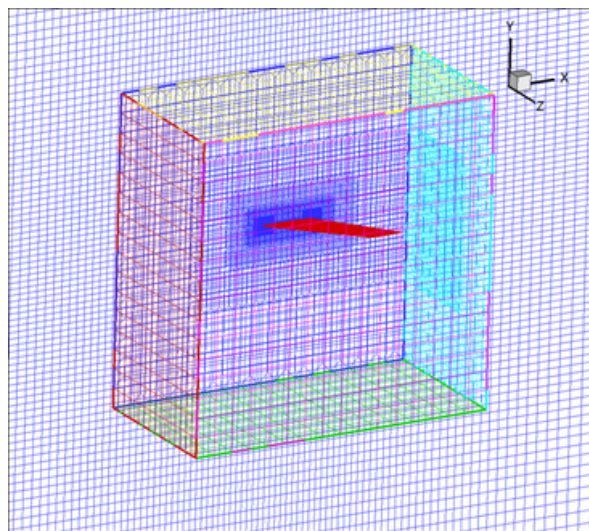


Figure 1: Computational grid around AGARD 445.6 wing model

The mode shapes are interpolated to the surface grid using Thin Plate Spline method (Smith 2013) from FEM model. The interpolated surface grids are shown in Figure 2. Up to 10th mode were used for aeroelastic simulations. Figure 3 shows the results of flutter simulation at Mach number 0.678. The damping ratio is calculated from these results and the flutter boundary is determined. Figure 4 shows the comparison of simulated and experimental flutter boundary. The results of the predicted flutter boundary agree well with the wind tunnel experimental results.

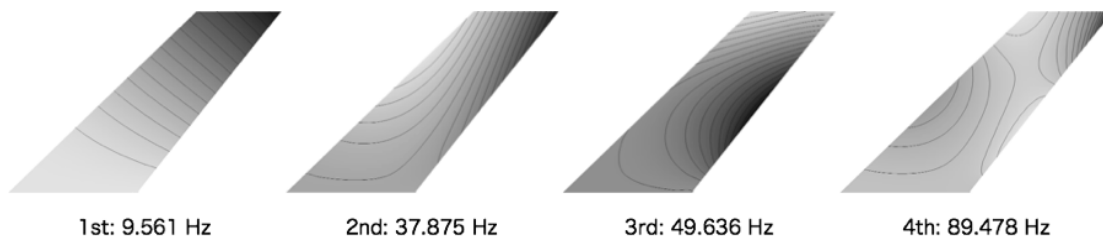


Figure 2: Vibration characteristics of AGARD 445.6 wing model

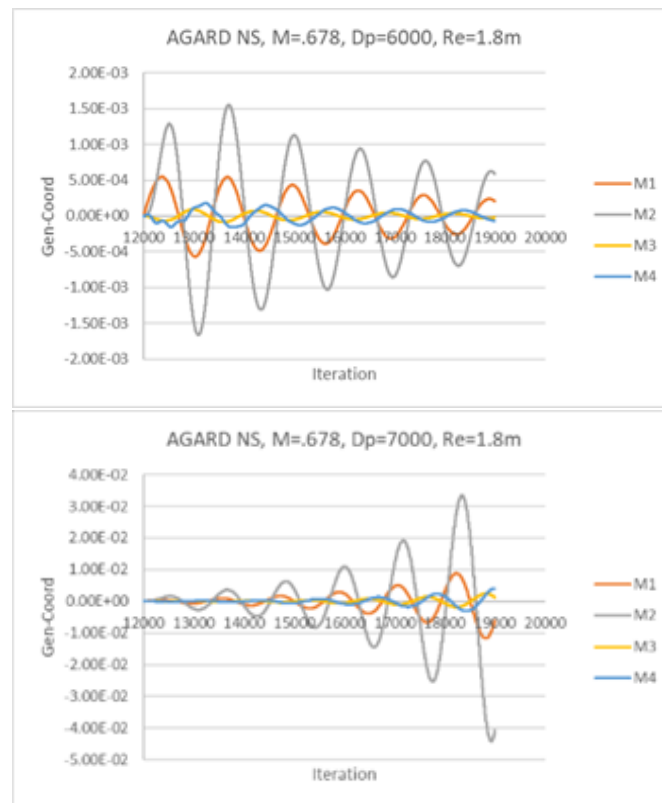


Figure 3: Time history of generalized modal displacement

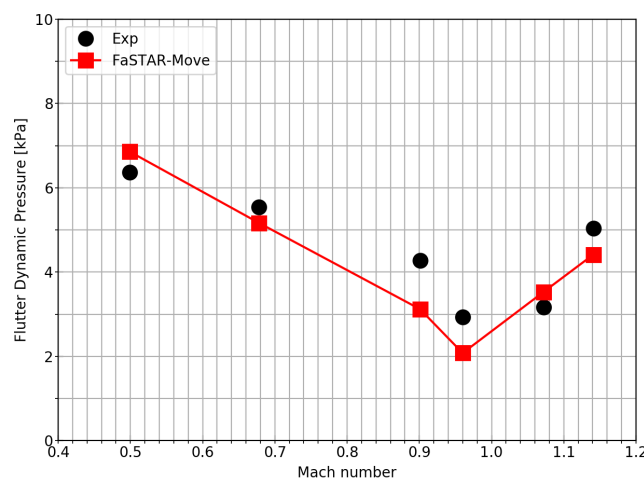


Figure 4: Flutter boundary of AGARD 445.6 wing model

4 Concluding Remarks

A new aeroelastic simulation code based on FaSTAR-Move is developed and validated using AGARD 445.6 wing model. The results of the predicted flutter boundary of AGARD 445.6

agree well with the wind tunnel experimental results. For future, the unsteady aerodynamics will be validated using the results of Aeroelastic Prediction Workshop and other experimental results.

References

- Burg, C. O., 2005. Higher Order Variable Extrapolation for Unstructured Finite Volume RANS Flow Solvers, AIAA Paper 2005-4999.
- Hashimoto, A., Murakami, K., Aoyama, T., et al., 2010. Drag Prediction on NASA CRM Using Automatic Hexahedra Grid Generation, AIAA Paper 2010-1417.
- Hashimoto, A., Murakami, K., Aoyama, T., et al., 2012. Toward the Fastest Unstructured CFD Code "FaSTAR". 50th AIAA Aerospace Sciences Meeting, AIAA Paper 2012-1075.
- Hishida, M., Hashimoto, A., Murakami, K., et al., 2011. A New Slope Limiter for Fast Unstructured CFD Solver FaSTAR, JAXA-SP-10-012.
- ICAO, 2016. ICAO Long Term Traffic Forecast.
- Men'shov, I. and Nakamura, Y., 1995. Implementation of the LU-SGS Method for an Arbitrary Finite Volume Discretization, 9th Japanese Symposium on CFD.
- Menter, F. R., Kuntz, M. and Langtry, R., 2003. Ten Years of Industrial Experience with the SST Turbulence Model, Turbulence, Heat and Mass Transfer IV.
- Obayashi, S. and Guruswamy, G. P., 1995. Convergence Acceleration of a Navier-Stokes Solver for Efficient Static Aeroelastic Computations, AIAA Journal, Vol.35, No.6, 1134-1141.
- Roget, B. and Sitaraman, J., 2010. Robustness and Accuracy of Donor Search Algorithms on Partitioned Unstructured Grids, 10th Symposium on Overset Composite Grids and Solution Technology.
- Shima, E., Kitamura, K. and Haga, T., 2013. Green-Gauss/Weighted-Least-Squares Hybrid Gradient Reconstruction for Arbitrary Polyhedra Unstructured Grids, AIAA Journal Vol.51, No.11, 2740-2747.
- Smith, M. J., Hodges, D. H. and Cesnik, C. E. S., 2000. Evaluation of Computational Algorithms Suitable for Fluid-Structure Interaction, Journal of Aircraft, Vol.37, No.2, 282-294
- Spalart, P. R. and Allmaras, S. R., 1992. A One-Equation Turbulence Model for Aerodynamic Flows, 30th Aerospace Sciences Meeting and Exhibit, AIAA Paper 92-0439.
- Yates, Jr., E. C., 1989. AGARD Standard Aeroelastic Configurations for Dynamic Response, NASA TM-19246, NASA.

Influence of laminarity on the aeroelastic behaviour of the NLR7301 aerofoil

Holger Mai¹, Marc Braune² and Anne Hebler³

German Aerospace Center (DLR), Institute of Aeroelasticity, Goettingen, Germany,
¹ holger.mai@dlr.de, ² marc.braune@dlr.de, ³ anne.hebler@dlr.de

Keyword: Flutter, Aeroelastic Stability, NLR7301, Transition, Nonlinearities

In the past it has been shown that the laminar aerofoil CAST 10-2 exhibits a strong nonlinear behaviour in its steady and unsteady aerodynamics in the transonic flow regime, which can be associated with the motion of the laminar to turbulent boundary-layer transition¹. Free transition leads to a decrease of the aeroelastic stability limit compared to the same case with a fully turbulent boundary layer flow². In addition, manifestations of various flutter phenomena could be observed. Among other things, the aeroelastic behaviour of the CAST 10-2 aerofoil is composed of single degree of freedom flutter cases, limit cycle oscillations, subcritical bifurcations and hystereses³. Those phenomena can be attributed to a complex unsteady shock-boundary layer interaction⁴, as it is shown in Fig. 1.

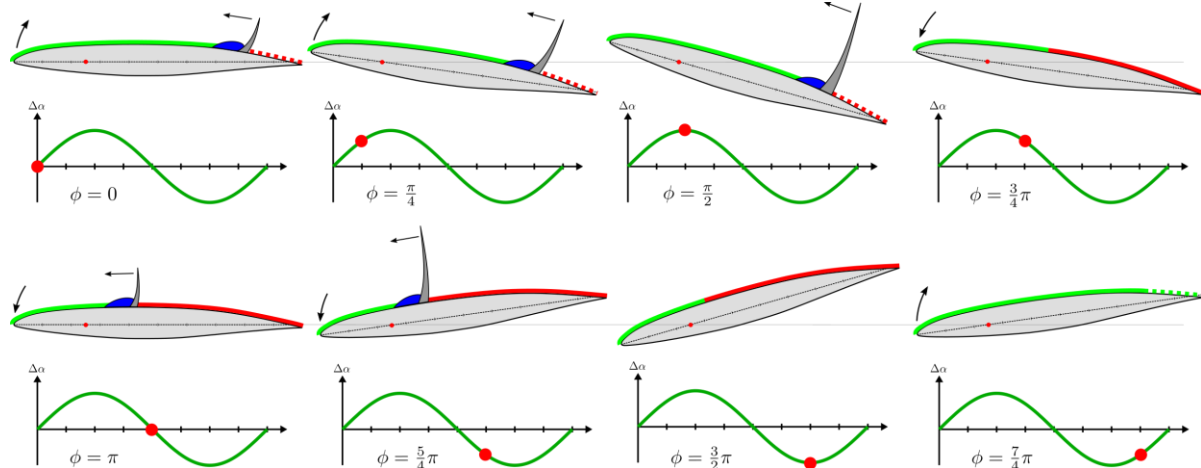


Figure 1: Shock-boundary interaction on the CAST 10-2 aerofoil during limit cycle oscillation⁴.

Previous extensive investigations on the NLR7301 aerofoil showed comparable nonlinear effects⁵. In a recent transonic wind-tunnel flutter test with the NLR7301 aerofoil model, the aeroelastic behaviour was investigated with a focus on the influence of the laminar to turbulent boundary-layer transition. Recent results of the flutter test will be presented and discussed.

- [1] Hebler, A., Schojda, L., Mai, H. (2013). Experimental investigation of the aeroelastic behaviour of a laminar wing in transonic flow. IFASD 2013
- [2] Hebler, A. (2017). Experimental assessment of the flutter stability of a laminar airfoil. IFASD 2017
- [3] Braune, M., Hebler, A. (2018). Experimental investigation of transonic flow effects on a laminar airfoil leading to limit cycle oscillations. AIAA Aviation Forum 2018
- [4] Braune, M., Koch, S. (2019). Application of Hot-film Anemometry to resolve the Unsteady Boundary Layer Transition of a Laminar Airfoil experiencing Limit Cycle Oscillations. FLUCOME 2019
- [5] Schewe, G., Mai, H., Dietz, G. (2003). Nonlinear effects in transonic flutter with emphasis on manifestations of limit cycle oscillations. *Journal of Fluids and Structures*, 18, 3-22.

Static aeroelastic analysis of spanwise variable camber morphing wings with corrugated structures

Kensuke Soneda¹, Tomohiro Yokozeki², Taro Imamura² and Natsuki Tsushima³

¹*The University of Tokyo, Hongo Bunkyo-ku Tokyo, Japan,
soneda@aastr.t.u-tokyo.ac.jp*

²*The University of Tokyo, Hongo Bunkyo-ku Tokyo, Japan*

³*Japan Aerospace Exploration Agency, Mitaka Tokyo, Japan*

Abstract

This paper studies the designs of the corrugated morphing wings with spanwise continuous camber change. A three-dimensional static aeroelastic analysis method with drag estimation is developed using vortex lattice method, two dimensional CFD and finite element method. Aeroelastic analyses with this method are conducted with various design parameters such as corrugation angles, the number of actuation mechanisms and their location. While the corrugation angle is not effective to drag reduction, the number of actuation systems is proved to have a great influence on the deformation or drag characteristics of the wing. It is also revealed that to change the actuation location enables further drag reduction. Considering the drag performance and necessary actuation force, the suitable design of the corrugated morphing wing is suggested.

Keyword: morphing wing, static aeroelasticity, corrugated structures

1 Introduction

Wing morphing technologies have been attracting much attention from researchers as the technologies to be implemented in the next-generation aircrafts. Modern aircrafts use stiff structures made of metals or composites and have high lift devices or control surfaces on their wings (Weisshaar, 2013). However, there are edges or gaps on the surfaces of the wings when they are actuated, which leads to the increase of drags or noises. Seamless and adaptive change of wing shapes not only improves the aerodynamic properties, but also reduce the weight and noises (Barbarino et al., 2013). Morphing technologies are expected to contribute to environmentally friendly flights.

The structures of morphing wings are required to be flexible to easily deform and to be stiff enough to carry the loads. As candidate materials to meet these requirements, corrugated structures were proposed (Yokozeki et al., 2006). Prototypes were manufactured using carbon fiber reinforced plastics and tested in the wind tunnel. The experiments proved that the morphing could be achieved even under air flow, and that the morphing concept is feasible (Yokozeki et al., 2014; Takahashi et al., 2016).

Previous researches confirmed the feasibility of corrugated morphing wings as camber morphing wings, but they assumed that the cross sections are constant along the span. Morphing in spanwise direction could also improve the aerodynamic performances in terms of induced drags or bending root moments. Variable Camber Continuous Trailing Edge Flap (VCCTEF) system is one of the concepts for spanwise wing morphing (Nguyen et al., 2015). In VCCTEF system, multiple flaps are implemented along the span and the gaps between flaps are filled by flexible materials. Bend-twist coupling structures were also

suggested to fill the gaps between morphing flaps, which showed higher aerodynamic performances than those without the transition structures (Woods et al., 2016).

The design tools are also very important in the development of the morphing wings. Because many concepts of morphing wings use flexible structures or materials, structural dynamics and aerodynamics should be considered at the same time. In addition to this, studies related to morphing wings are still in the early stage and need to conduct lots of analyses. The computational cost is also one of the important elements for the design tools. A two dimensional aero-structural design tool was developed, where a two-dimensional flexible beam model and a panel method (XFOIL) were combined (Sato et al., 2017). Regarding three dimensional aeroelastic framework, Tsushima et al. (2019) developed a framework combining corotational shell finite element methods and unsteady vortex lattice method. However, a light three dimensional aeroelastic analysis tool which can estimate drag performance remains to be developed.

This paper focuses on morphing wings with corrugated structures and analyses their performance as morphing wings with continuous trailing edge deformations. A static aeroelastic model using vortex lattice method for aerodynamic simulations and finite element methods for structural simulations is constructed. A two-dimensional CFD code UTCart is used to create a database for the estimation of parasite drag. Changing the design parameters such as the corrugation angle (described in Section 2.3), the number actuation mechanisms and their location, the suitable designs of corrugated morphing wings are investigated.

2 Aeroelastic model

2.1 Aerodynamic model

Different fidelity of aerodynamic analysis tools can be used to calculate the 3D aerodynamic performances: CFD, vortex lattice method (VLM), panel method and others. Users should choose an appropriate fidelity of solvers with the consideration of computational costs. In this paper, many cases of aerodynamic analyses will be performed, and therefore an aerodynamic solver based on VLM is chosen.

An open aerodynamic analysis solver Athena Vortex Lattice (AVL) developed by Drela and Youngren is implemented in the aerodynamic model. In this solver, multiple chordwise and spanwise flat panels are created and the strength of the vortex on each panel is calculated. The model for AVL is shown in Fig. 1. Regarding the modelling, the entire half wing is modelled, and the other half wing is considered in the mirrored shape.

Because this paper deals with the deformation of corrugated morphing wings, the deformed camber data from the structural analysis are needed to be input. Airfoil coordinate data at each station are prepared after the structural analysis and the airfoil data are read when the aerodynamic analysis starts.

VLM can only calculate the induced drag and it cannot estimate the parasite drag. In order to calculate this drag, a two-dimensional CFD code UTCart (Imamura et al., 2017; Tamaki et al., 2017) is utilized. The parasite drag is estimated in the following way. Before aeroelastic analyses, a database to calculate the parasite drag is prepared. Two dimensional aerodynamic analyses are performed for the airfoils whose deflection angles are -1 to 10 deg (every 1 deg) with several angles of attacks, and the results are interpolated using a radial basis function interpolation using the quintic function. After each aeroelastic analysis, the parasite drag components for the airfoils at each station are calculated using the database, and the parasite drag coefficient is obtained by integrating

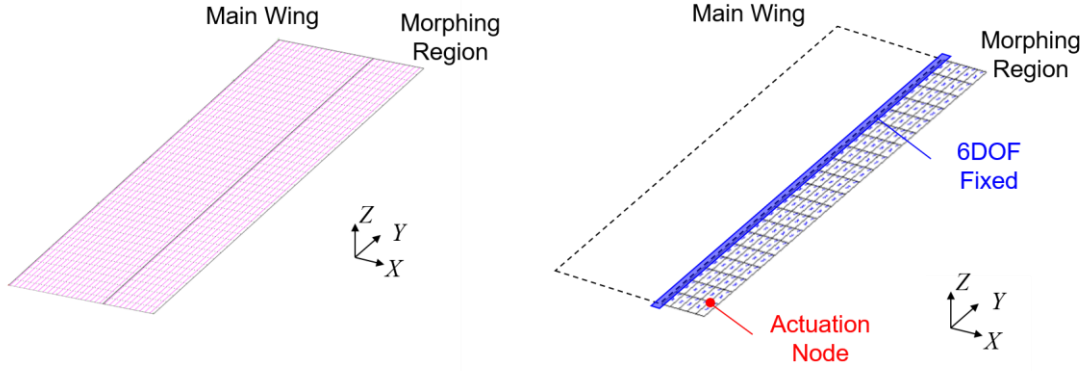


Figure 1: The models in the aerodynamic and structural analysis

them along the span.

2.2 Structural model

This paper uses a commercial nonlinear finite element analysis software MSC. Marc 2017.1.0 in the structural analyses. Full models of corrugated structures with shell elements need much computational time, and therefore this paper treat corrugated structures as plates with equivalent stiffness. 8-node shell elements are used to model the homogenized plates.

In the structural model, only the morphing region is modelled, and the main wing region is treated as rigid. Regarding the displacement boundary conditions, the nodes in the leading-edge side are all fixed. This simulates the attachment of the morphing region to the main wing region. In terms of the load boundary conditions, two conditions are applied. One is to simulate the actuation loads with wires. Details are explained in Section 2.4. The other is to simulate the aerodynamic forces. The pressures calculated by AVL are applied to each element.

2.3 Corrugated Structure

A homogenization method for corrugations proposed by previous researches are used (Xia et al, 2012; Mohammadi et al, 2015). By neglecting the extension-bending coupling stiffness terms, the constitutive equations are written as

$$\begin{Bmatrix} \bar{N}_x \\ \bar{N}_y \\ \bar{N}_{xy} \\ \bar{M}_x \\ \bar{M}_y \\ \bar{M}_{xy} \end{Bmatrix} = \begin{bmatrix} \bar{A}_{11} & \bar{A}_{12} & 0 & 0 & 0 & 0 \\ \bar{A}_{12} & \bar{A}_{22} & 0 & 0 & 0 & 0 \\ 0 & 0 & \bar{A}_{66} & 0 & 0 & 0 \\ 0 & 0 & 0 & \bar{D}_{11} & \bar{D}_{12} & 0 \\ 0 & 0 & 0 & \bar{D}_{12} & \bar{D}_{22} & 0 \\ 0 & 0 & 0 & 0 & 0 & \bar{D}_{66} \end{bmatrix} \begin{Bmatrix} \bar{\varepsilon}_x \\ \bar{\varepsilon}_y \\ \bar{\gamma}_{xy} \\ \bar{\kappa}_x \\ \bar{\kappa}_y \\ \bar{\kappa}_{xy} \end{Bmatrix} \quad (1)$$

$$\begin{Bmatrix} \bar{Q}_{yz} \\ \bar{Q}_{zx} \end{Bmatrix} = \begin{bmatrix} \bar{A}_{s,11} & 0 \\ 0 & \bar{A}_{s,22} \end{bmatrix} \begin{Bmatrix} \bar{\gamma}_{yz} \\ \bar{\gamma}_{zx} \end{Bmatrix} \quad (2)$$

where N , M , Q are the resultant stress, resultant moment, shear force respectively, and ε , γ , κ are the in-plane strain, transverse shear strain, curvature respectively. The overlines

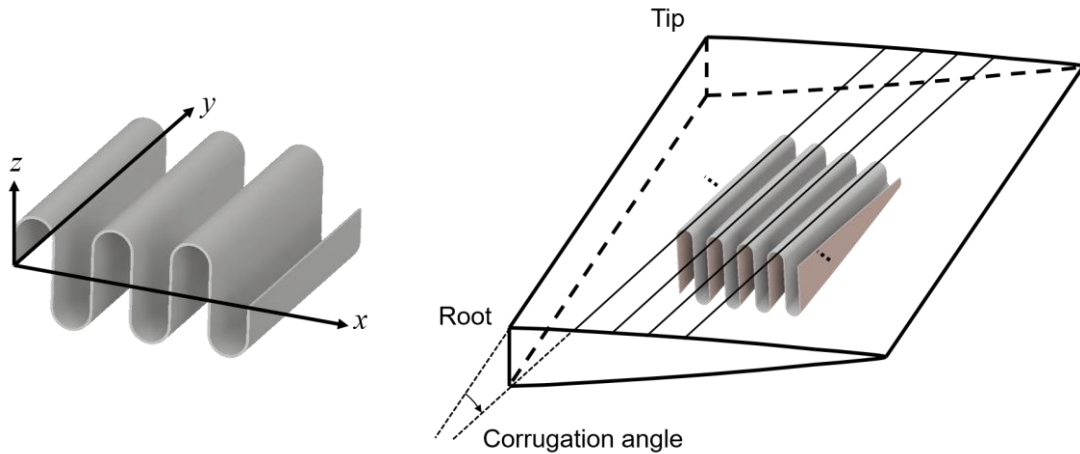


Figure 2: Corrugated structures: the coordinate for corrugations (left) and the definition of corrugation angle (right)

mean that the values are homogenized ones. Each element in the stiffness matrices can be calculated from the material properties and geometric parameters of corrugation.

The variations of the stiffness can have influences on the deformations of the wings. In this paper, the corrugation angle is considered as a design parameter; this angle is defined as the angle between the spanwise direction of the wing and the stiff direction of the corrugation (see Fig. 2). This angle produces an apparent bend-twist coupling effect, which changes the deformation of the wing or the necessary actuation energy. In the structural analysis, the effect of the corrugation angle is considered by rotating the stiffness matrices by the corrugation angle.

2.4 Actuation Mechanism

The actuation mechanism is one of the important elements in the design of morphing wings. In this paper, a plain actuation system with wires and servomotors are employed. As mentioned above, this type of actuation mechanism is verified to be feasible in the previous researches (Yokozeki et al., 2014; Takahashi et al., 2016). One end of the wire is attached to the corrugation with an offset from the center line. The actuation can be modelled with three forces: the x and z component of the wire tension force and the moment around the y axis because of the offset. The magnitude of the applied force is controlled in the structural analysis to realize the target deflection angle at the target node, which are defined at the

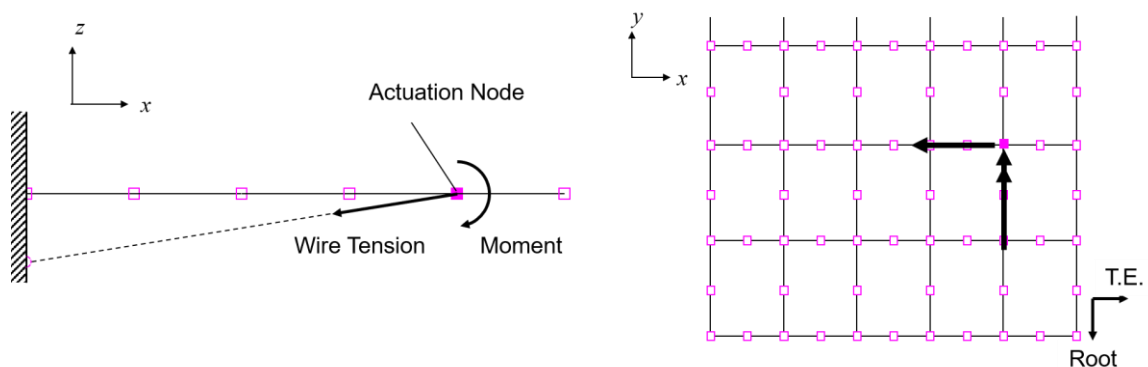


Figure 3: Actuation system with wires

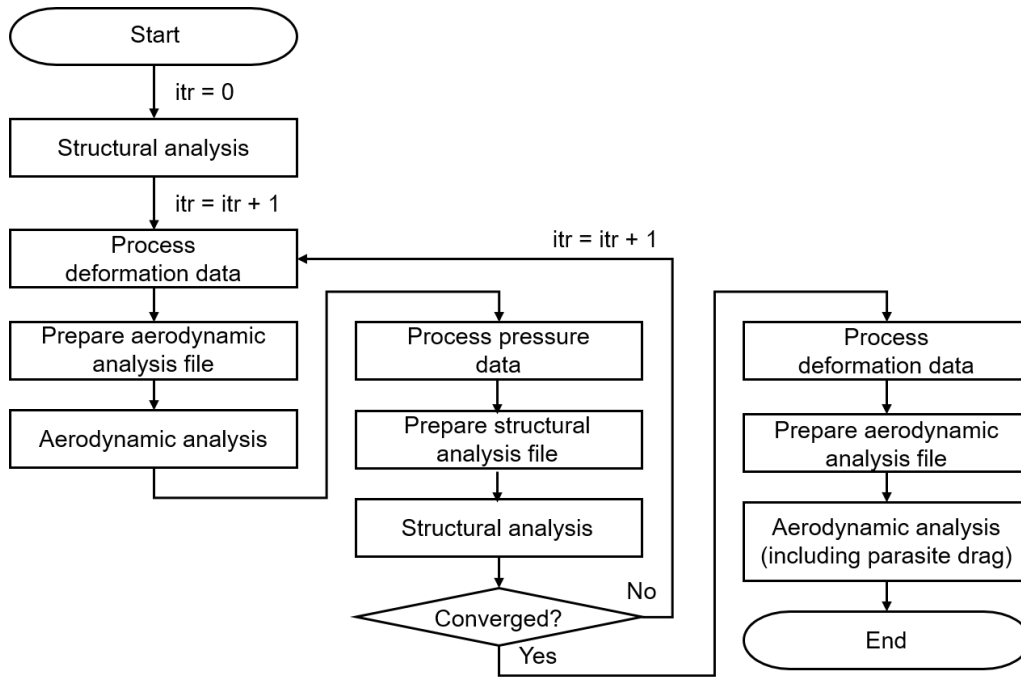


Figure 4: Coupling procedure for static aeroelastic analysis

beginning of the analysis by the user. This actuation model is summarized in Fig. 3.

2.5 Coupling Procedure for Static Aeroelastic Analysis

The aerodynamic and structural models are described above. The aeroelastic analysis in this research is conducted by carrying out aerodynamic and structural analyses alternately. The coupling procedure is as following: First carry out a structural analysis without aerodynamic forces. Next, carry out an aerodynamic analysis and a structural analysis with aerodynamic forces again. Check the convergence of the deformation of the wing and repeat each analysis alternately until it is obtained. Finally carry out an aerodynamic analysis again to calculate aerodynamic properties of the converged wing configuration. At this step, the parasite drag component is also calculated from the database obtained by two-dimensional UTCart. The procedure is summarized in Fig. 4.

3 Drag Reduction

3.1 Target Aircraft

This paper deals with an aircraft whose specifications are listed in Tab. 1. The morphing region is after 65% chord length. Near the trailing edge, the thickness of the airfoil is very thin, and it is difficult to manufacture corrugations with such small heights. Therefore, the region where corrugations are inserted ends at 93% chord length, and after that, only the stiffness of skins are considered. To note, in the region where corrugations are inserted, the stiffness of skins are neglected. The Young's modulus and Poisson's ratio of the material are 74.0 GPa and 0.34, respectively. The radius of corrugations is 3.5 mm and the thickness of the material is 0.5 mm.

Table 1: Specifications of the target aircraft

Base Airfoil	Span [mm]	Chord [mm]	Morphing Region	Flight Velocity [m/s]	Lift Coefficient
NACA0012	2400	300	65% c_{\sim}	20	0.3

Table 2: Computational conditions for UTCart

Governing equation	RANS equation
Minimum cell size	0.0002
Convection scheme	SLAU scheme
Time integration	LU-SGS
Spatial discretization	Cell-centered finite volume method
Turbulence model	SA-noft2 + SA based wall function

3.2 Solver Setting

The static aeroelastic analysis tool describe in Section 2 is utilized. For VLM simulations, aerodynamic models are meshed into 20 and 40 panels in the chordwise and spanwise direction in the non-morphing region, and 10 and 40 respectively in the morphing region. In the analyses by UTCart to obtain the database for parasite drag, the setting listed in Tab. 2 is used. The fluid cell number is about 110,000 for each case. For FEM simulation, a structural model is meshed into 5 and 20 elements.

3.3 Single Actuation near the Root

Here, the node which is located 60 mm (corresponds to the spanwise length of one element, or 5% of the semi-span length) inside from the root and 21 mm (corresponds to the chordwise length of one element) forward from the trailing edge is selected as the actuation node, and the deflection angle at the root is controlled by the actuation method described in Section 2.4.

The corrugation angles and deflection angles are selected as parameters, and the ranges for the two parameters are 0 to 10 deg and 1 to 10 deg, respectively. The both parameters are changed by 1 degree and 110 analysis cases are created in total. For each parameter setting, the static aeroelastic analysis is conducted and the deformation shapes and aerodynamic performances are calculated. The analysis results obtained are interpolated using the radial basis function interpolation. The function used is

$$\phi(r) = \sqrt{(r/\epsilon)^2 + 1} \quad (3)$$

where ϵ is a tuning parameter and the value is determined by error evaluation processes using the analysis results with random 20 parameter settings.

The response surfaces are shown in Fig. 5. The direct analysis results at 110 analysis sets are also plotted in the same figures. It can be observed that the response surfaces capture the trends of the responses to the parameter changes precisely. Using these response surfaces, the optimum parameter set for drag reduction is investigated. The optimization is performed to minimize the induced drag coefficient or the drag coefficient.

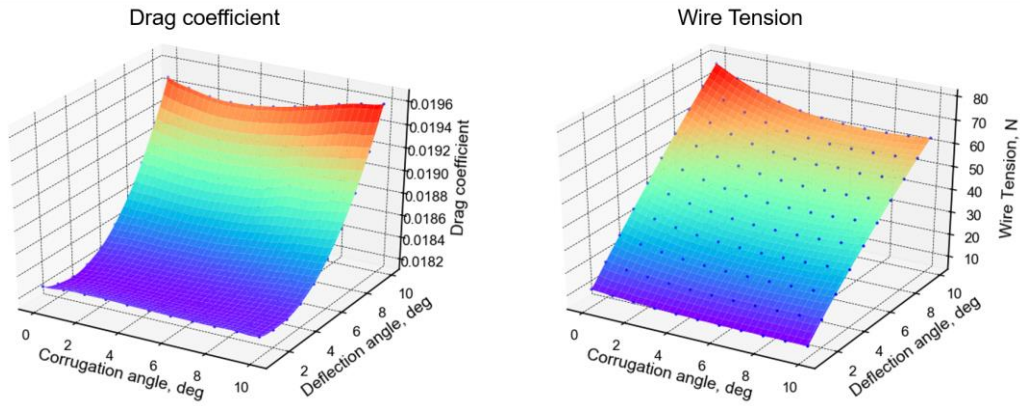


Figure 5: Response surface: drag coefficient (left) and wire tension (right)

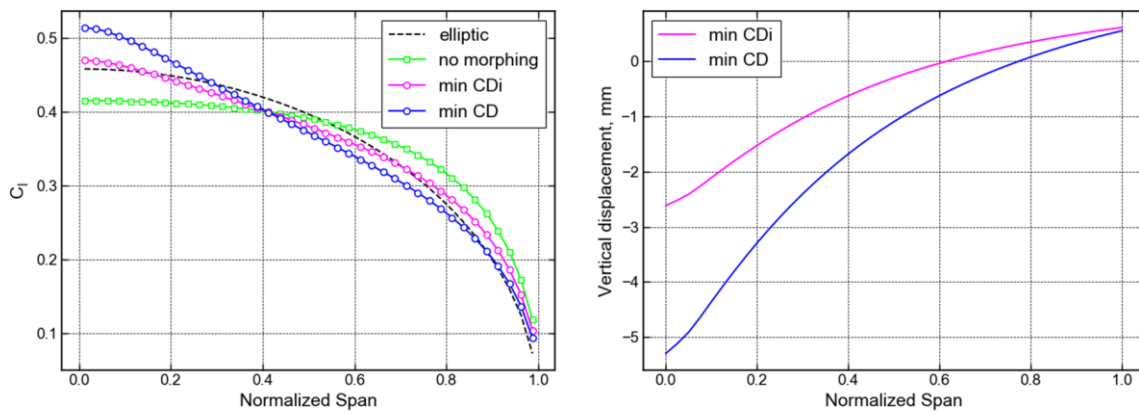


Figure 6: Lift distributions and vertical displacement distributions of the optimum cases

The solver used is GlobalSearch from MATLAB. The optimization shows the following parameter sets are best to reduce the induced drag or the total drag.

$$\begin{cases} \beta = 0.28^\circ, & \theta_{root} = 1.44^\circ & \text{for minimum } C_{Di} \\ \beta = 0.14^\circ, & \theta_{root} = 2.92^\circ & \text{for minimum } C_D \end{cases}$$

From these results, it can be said that the corrugation angle contributes to the reduction of the actuation forces, while it does not so much to the reduction of the drag. The lift distributions and vertical displacement distributions are shown in Fig. 6. In the case of the minimization of the total drag, the lift distribution is not so close to the elliptic lift distribution, which is theoretically optimum to reduce the induced drag, as in the case of the minimization of the induced drag alone. Regarding the deformation, the deflection at the root is larger when the total drag is minimized than when the induced drag alone is minimized. This result suggests that to reduce the total drag, the lift should be kept by the larger deflection angles and a smaller angle of attack than those necessary to minimize the induced drag alone. In the case of the minimization of the drag coefficient, 0.8% drag reduction is obtained by this morphing compared to the no-morphing case.

Table 3: Analysis cases with double actuations

θ_{ip}	1 ~ 5 deg (every 1 deg)
$\Delta\theta$	0 ~ 5 deg (every 1 deg)

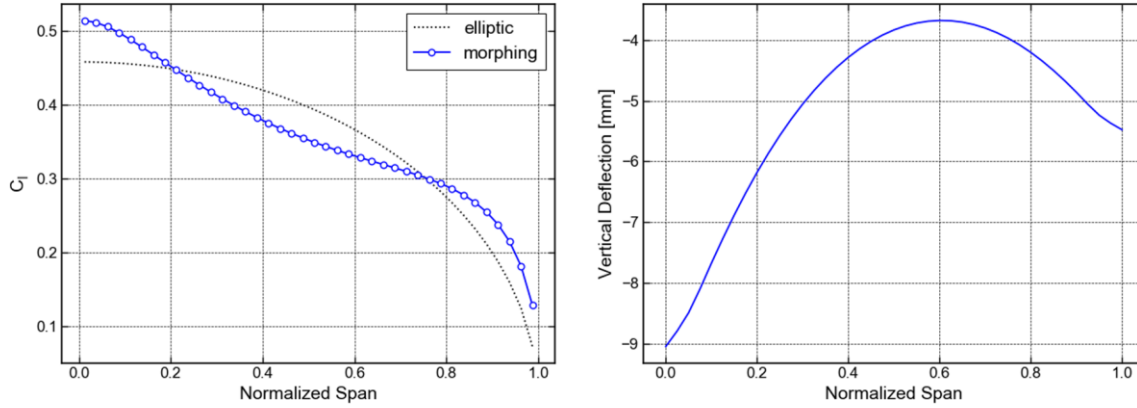


Figure 7: Lift distribution and vertical displacement distribution of the optimum case with double actuation systems

3.4 Double Actuations

In this subsection, the number of the actuation systems is increased from one to two. Considering the results in Section 3.3, the corrugation angle is set 0 degrees. The two actuation systems are located at 5% semi-span length (near root) and 95% semi-span length, and the magnitudes of the actuation forces are calculated referring to the deflection angles at the root θ_{root} and those at the tip θ_{ip} , respectively.

Here, a constraint that θ_{root} is always equal to or larger than θ_{ip} is applied. The difference between the two angles is denoted by $\Delta\theta$. The analysis cases summarized in Tab. 3 are performed. Among the cases, the best actuation method in terms of drag is

$$\theta_{root} = 5^\circ, \quad \theta_{ip} = 3^\circ, \quad (\Delta\theta = 2^\circ)$$

In this case, the drag coefficient is 0.017969 and 2.1% of drag reduction is achieved. It is revealed that the increase of actuation systems enables further drag reduction compared to the cases with single actuation system. On the other hand, the lift distribution and vertical displacement distribution of the case are shown in Fig. 7. It can be seen that the middle region does not deform so much as the root or tip, where the actuation mechanisms are installed. This phenomenon implies that the locations of actuation systems have great influences on the entire deformation of the morphing wing and further control of deformation shapes could be achieved by changing the actuation locations.

Next, the influences of actuation locations on the total deformation are investigated. Here, the actuation location near the root (5% semi-span length) is fixed, and the actuation location near the tip (95% semi-span length) is changed from 60% semi-span length to 95% semi-span length by 5% semi-span length. Here the analysis case is named after the actuation locations. For example, the case in Fig. 7 is named as “R05T95”.

The deformation shapes are shown in Fig. 8. This shows that the deformation shapes of the entire wings can be controlled by changing the actuation locations. The drag

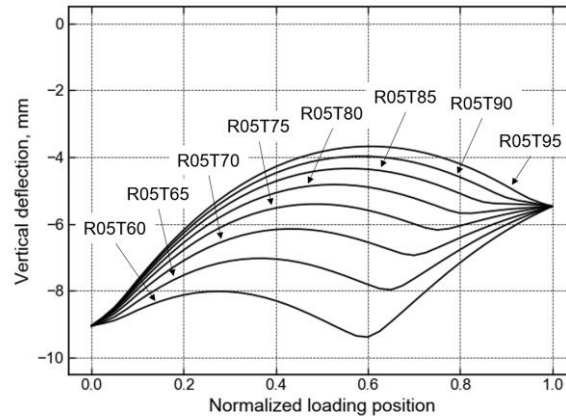


Figure 8: Deformation shapes of the trailing edge for various actuation locations

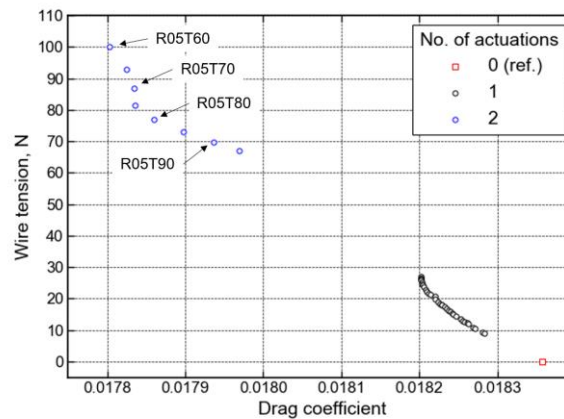


Figure 9: Drag coefficients and wire tensions

coefficients and wire tensions for each case are shown in Fig. 9. Note that the red square corresponds to the no-morphing configuration, and black circles are obtained using the response surfaces in Section 3.3. The drag is reduced as the tip-side actuation location is moved towards the root. In the case R05T60, the drag coefficient is 3.0% reduced compared to the no-morphing case. On the other hand, as the entire deformation becomes larger, the necessary actuation forces increase. In terms of the effectiveness of actuation forces against drag reduction, the case R05T80 is the most effective design point with this actuation method.

4 Conclusion

This paper focused on the design of corrugated morphing wings for continuous trailing-edge deflections. Three dimensional static aeroelastic analysis tool where VLM and FEM are combined was developed. a two-dimensional CFD solver UTCart was also utilized to obtain the database to estimate parasite drag. Parametric studies were conducted with varying corrugation angles and root deflection angles with single actuation mechanism near the root. The results showed that the corrugation angle has influences on reducing the necessary actuation forces, while the parameter is not effective on the reduction of the drag. The analyses with double actuation systems are also performed and it is shown that morphing with two actuation systems can further improve the drag performance of the wing.

The actuation location is also proved to be an important design parameter and the best design point considering the drag performance and the necessary actuation force is suggested.

Acknowledgements

The authors acknowledge JSPS for the financial support of this project (Grant-in-Aid for Scientific Research, 18K18909).

References

- Barbarino, S., Bilgen, O., Ajaj, R.M., Friswell, M.I., Inman, D.J., 2011. A Review of Morphing Aircraft. *Journal of Intelligent Material Systems and Structures*, 22(9), 823-877.
- Drela, M., Youngren, H., 2017. AVL 3.36 User Primer.
Retrieved from http://web.mit.edu/drela/Public/web/avl/avl_doc.txt
- Imamura, T., Tamaki, Y., Harada, M., 2017. Parallelization of a compressible flow solver (UTCart) on cell-based refinement Cartesian grid with immersed boundary method. *Parallel CFD' 2017, 29th International Conference on Parallel Computational Fluid Dynamics*, Glasgow, Scotland, UK.
- Mohammadi, H., Ziaei-Rad, S., Dayyani, I., 2015. An equivalent model for trapezoidal corrugated cores based on homogenization method. *Composite Structures*, 131, 160-170.
- Takahashi, H., Yokozeki, T., Hirano, Y., 2016. Development of variable camber wing with morphing leading and trailing sections using corrugated structures. *Journal of Intelligent Material Systems and Structures*, 27(20), 2827-2836.
- Tamaki, Y., Harada, M., Imamura, T., 2017. Near-wall modification of Spalart-Allmaras turbulence model for immersed boundary method. *AIAA Journal*, 55(9), 3027-3039.
- Nguyen N., Kaul, U., Lebofsky, S., Ting, E., Chaparro, D., Urnes, J., 2015. Development of variable camber continuous trailing edge flap for performance adaptive aeroelastic wing," *SAE 2015 AeroTech Congress and Exhibition*. SAE Technical Paper 2015-01-2565, Seattle, WA.
- Sato, K., Yokozeki, T., 2017. Aero-structural evaluation of morphing control surface using corrugated panels. *Transactions of the Japan Society for Aeronautical and Space Sciences, Aerospace Technology Japan*, 15(API SAT-2016), a7-a15.
- Tsushima, N., Yokozeki, T., Su, W., Arizono, H., 2019. Geometrically nonlinear static aeroelastic analysis of composite morphing wing with corrugated structures. *Aerospace Science and Technology*, 88, 244-257.
- Xia, Y., Friswell, M. I., Flores, E. I. S., 2012. Equivalent models of corrugated panels. *International Journal of Solids and Structures*, 49(13), 1453-1462.
- Yokozeki, T., Takeda, S., Ogasawara, T., Ishikawa, T., 2006. Mechanical properties of corrugated composites for candidate materials of flexible wing structures. *Composite Part A: Applied Science and Manufacturing*, 37(10), 1578–1586.
- Yokozeki, T., Sugiura, A., Hirano, Y., 2014. Development of Variable Camber Morphing Airfoil Using Corrugated Structure. *Journal of Aircraft*, 51(3), 1023-1029.
- Weisshaar, T. A., 2013. Morphing Aircraft Systems: Historical Perspectives and Future Challenges. *Journal of Aircraft*, 50(2), 337–353.
- Woods, B. K. S., Parsons, L., Coles, A. B., Fincham, J. H. S., Friswell, M. I., 2016. Morphing elastically lofted transition for active camber control surfaces. *Aerospace Science and Technology*, Vol.55, 439-448.

Experimental and theoretical investigation of stall flutter in an elastic wing

Todd M. Currier¹, Xavier Amandolese^{2,3} and Yahya Modarres-Sadeghi¹

¹ *University of Massachusetts, Amherst, United States, tcurrier@umass.edu*

² *LMSSC, Conservatoire National des Arts et Métiers, Paris, France*

³ *LadHyX, Ecole Polytechnique, Palaiseau, France*

Keyword: stall flutter, elastic wing, wind tunnel, continuous model

A highly flexible continuous wing model has been built to study either coupled-mode flutter or stall flutter in a wind tunnel. This model utilizes a composite cantilever beam arrangement that provides the bending and torsional stiffness, cladding segments representing a NACA0012 geometry and an added slender body allowing for the control of the ratio of the torsional and flapwise natural frequencies (Fig. 1a). In the present paper we will focus on a series of stall flutter experiments, tracking the motion of the tip of the wing to capture post-critical oscillation modes (Fig. 1b). A bifurcation diagram showing the evolution of the tip LCO amplitude in torsion versus the wind velocity is shown in (Fig. 1c). Following the work of Tang Dowel¹, the associated nonlinear post-critical behavior, due to both dynamic stall and static deflection, will also be studied using a continuous model including the ONERA dynamic stall formulation² for the unsteady aerodynamics.

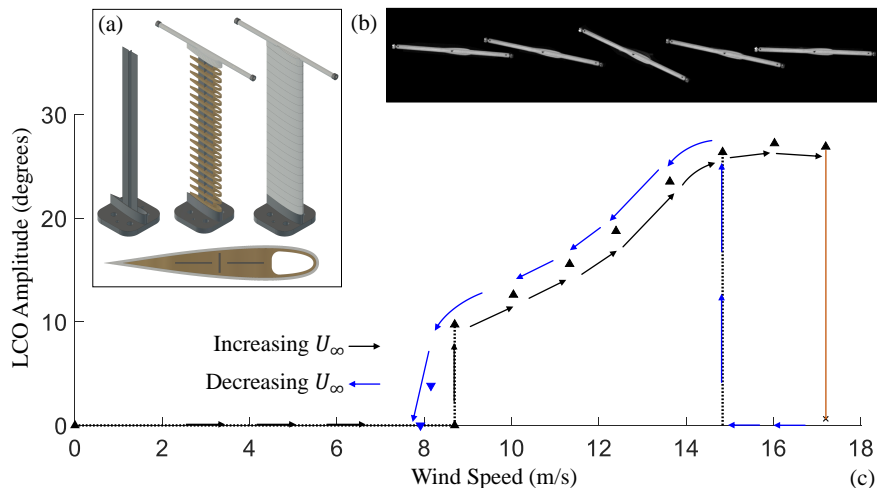


Figure 1: The flexible continuous wing model (a); an example of the trajectory of the tip of the wing (b); tip LCO amplitude in pitch versus wind velocity (c).

¹ Tang, D., & Dowell, E. (2001). Experimental and theoretical study on aeroelastic response of high aspect-ratio wings. *AIAA Journal*, 39, 1430-1441.

² Tran, C. T., Petot, D. (1981). Semi-Empirical Model for the Dynamic Stall of Airfoils in View to the Application to the Calculation of Responses of a Helicopter Blade in Forward Flight. *Vertica*, 5(1), 35-53.

Development of a CFD-based industrial procedure for supporting the aircraft certification with application to A400M T-Tail flutter

Emilio Santos, Jesús Barrera, Álvaro Martínez, Pablo Martínez,
Víctor Rafael de la Cruz, Félix Arévalo, Moti Karpel and Héctor Climent

AIRBUS Defence and Space, Getafe, Spain, emilio-santos@airbus.com

Abstract

This paper describes the AIRBUS Defence and Space (AIRBUS-DS) methods for predicting flutter with high-fidelity unsteady Computational Fluid Dynamics (CFD), using a partitioned approach with MSC.Nastran as Computational Structural Mechanics (CSM) code, ANSYS-Fluent as CFD code, and AIRBUS-DS in-house DYNRESP software as dynamic solver. The methodology is applied to aircraft empennages with T-tail configuration, where the standard Doublet-Lattice Method (DLM) exhibits certain inherent limitations because of non-included effects. These limitations have been successfully overcome in the past by using the so-called augmented DLM, a procedure that AIRBUS-DS developed to support Heavy Military Transport aircraft certification. This paper is focused on using a T-tail configuration with experimental flutter-related data as test case for assessing the capability of the CFD-based codes on predicting such complex unsteady aerodynamic effects.

Keyword: Flutter, Aircraft Certification, T-Tail, CFD

1 Introduction to CFD-based unsteady aerodynamics to solve T-tail flutter

The classical aerodynamic methods used in aeroelastic applications are based on linearized potential theories. One of these methods, the Doublet-Lattice Method (Albano and Rodden, 1969) is still a reference in aeroelastic analyses at an industrial environment, both for flutter clearance and gust response. The benefits of the method justify this long-time success: it is fast and robust, easy to implement and permits to perform a wide range of parametric sensitivity analyses. In addition, it has to be maintained to support legacy products and is widely accepted by the Airworthiness Authorities.

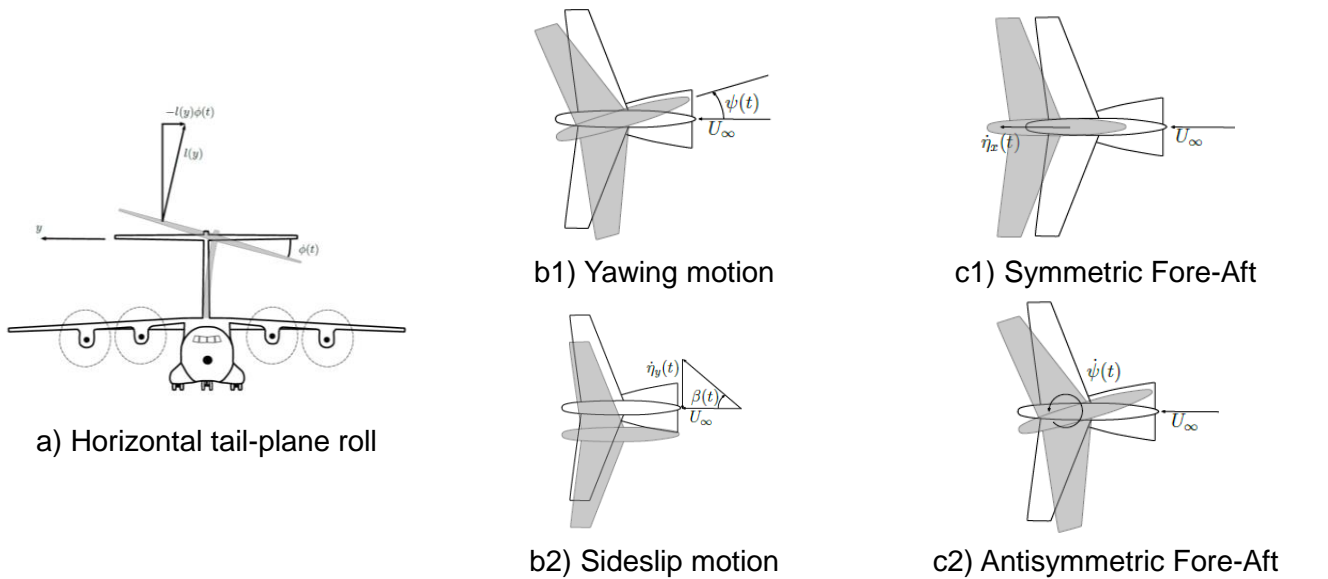
Classical aerodynamic methods, however, have some limitations. The limit imposed by transonic flow for linear potential theories is especially relevant. When transonic effects appear, the aerodynamic behavior becomes inherently nonlinear. The presence of mixed subsonic and supersonic flow regions, with physically complex phenomena such as shock waves moving and interacting with the boundary layer, plays a fundamental role in transonic aeroelastic phenomena (Bendiksen, 2011).

Another limitation of the standard Doublet-Lattice Method concerns T-tail type aircraft empennages. Among the list of particularities of T-tail flutter (Murua et al., 2014), the steady loading and in-plane dynamics of the horizontal tail-plane are of special relevance. The dynamics caused by the interaction of these effects, not included in the standard DLM method, can be described according to Jennings and Berry (1977):

- The motion in roll of the horizontal tail-plane (HTP) rotates the line of action of the vertical steady force distribution $l(y)$ an angle $\phi(t)$ and, therefore, produces a

side component of the force, Δf_y (see Fig. 1(a)).

- The in-plane motion of the horizontal tail-plane has a double effect on incremental aerodynamic forces: first, the motion in yaw $\psi(t)$, caused by fin torsion, and lateral η_y , caused by fin bending, produces an additional distribution of lift due to the variation of steady lift with sideslip angle $\partial l(y)/\partial \beta$ (see Fig. 1(b1) and Fig. 1(b2)); second, symmetric and antisymmetric chordwise motion modifies the relative airspeed and thus the dynamic pressure (see Fig. 1(c1) and Fig. 1(c2)).



$$\Delta f_y(y, t) = -l(y)\phi(t) \quad \Delta f_z(y, t) = \frac{\partial l(y)}{\partial \beta} \left(\psi(t) + \frac{\dot{\eta}_y}{V_\infty}(t) \right) \quad \Delta f_z(y, t) = -2l(y) \frac{\dot{\eta}_x(t) - y\dot{\psi}(t)}{V_\infty}$$

Figure 1: In-plane dynamic effects of the horizontal tail-plane in T-tail configurations

Different methodologies based on potential-flow have been developed to overcome these natural limitations of the standard Doublet-Lattice Method. Murua et al. (2014) describe in detail some of these methods. In particular, the addition of supplementary T-tail effects as additional terms to the Doublet-Lattice Method aerodynamics was successfully applied to the case of Heavy Military Transport aircraft (Fig. 2), where T-Tail effects were measured in flight using tests from a wake-vortex encounter campaign.

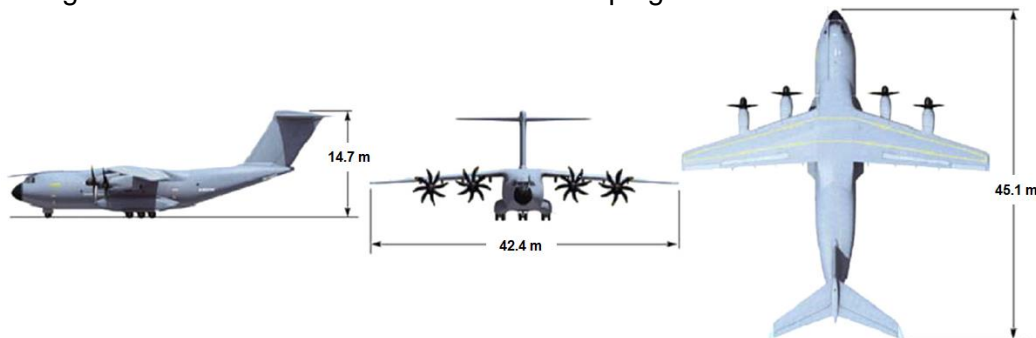


Figure 2: Heavy Military Transport aircraft views and dimensions

These previous considerations reveal the T-tail as an appropriate test case to explore the advantages of novel advanced-aerodynamics computational codes. In fact, the objective of this paper is to demonstrate that flutter calculations based on high-fidelity Computational Fluid Dynamics (CFD) can capture accurately T-tail effects by default without the need of any special treatment. To this end, Section 2 describes the methodologies and tools developed by AIRBUS-DS to integrate CFD in aeroelastic calculations. Section 3 includes a description of the aeroelastic T-tail model presented in van Zyl and Mathews (2011), and compares the experimental flutter speed with the results obtained using the augmented Doublet-Lattice Method and unsteady CFD aerodynamics.

2 AIRBUS-DS flutter procedures based on unsteady CFD aerodynamics

2.1 Introduction to the two procedures: Uncoupled and Coupled analyses.

The aeroelastic framework developed by AIRBUS-DS to integrate unsteady CFD aerodynamics is based on the partitioned approach to solve Fluid Structure Interaction (FSI) problems. In partitioned analyses, each discipline, structure and aerodynamics, is computed individually using specific methods widely tested and validated:

- The structure is modelled using the Finite Element Method (FEM) technique as Computational Structural Mechanics (CSM) code implemented in MSC.Nastran to obtain the normal modes of the aircraft.
- The unsteady aerodynamic flow is solved by the Euler and Navier-Stokes Computational Fluid Dynamic (CFD) code ANSYS-FLUENT.
- The CSM and the CFD codes are coupled in the frequency- or time-domain with DYNRESP software (Karpel, 2019a).

Since structural and aerodynamic meshes are usually dissimilar, the transference of information between these disciplines is a key aspect in partitioned FSI methods. The displacements are interpolated from Finite Element grids to the aerodynamic surface grids by the equation:

$$\{x_k\} = [G_{kg}]\{x_g\}, \quad (1)$$

where $\{x_k\}$ is the vector with displacements in the aerodynamic vertices; $\{x_g\}$, the displacements at the structural Degrees-Of-Freedom and $[G_{kg}]$, the interpolation matrix. The interpolation options need to be selective by aircraft component (fuselage, wing, empennage, engines, etc.) and a special treatment to maintain the continuity and smoothness of the mesh in the interface of different component surfaces is required.

Aeroservoelastic response and stability analyses can be solved using uncoupled and coupled schemes. In the case of uncoupled analyses, the linear unsteady aerodynamic forces are obtained by a CFD simulation forcing a prescribed structural motion according to a mode shape. The unsteady forces are then post-processed to obtain generalized aerodynamic forces (GAFs) in the frequency domain, which are the input to linear flutter methods. These analyses are also called one-way because the information is exclusively transferred from the structural side to the aerodynamic solver (see the solution flowchart in Fig. 3). On the contrary, in coupled analyses the structural and aerodynamic solvers interchange information in every time step to compute the time response of the aircraft to an initial excitation (see Fig. 4). Since the aerodynamic forces computed are not linearized, these simulations can retain aerodynamic non-linearities. The initial excitation is applied as a one-minus-cosine generalized force to excite a specific range of frequencies.

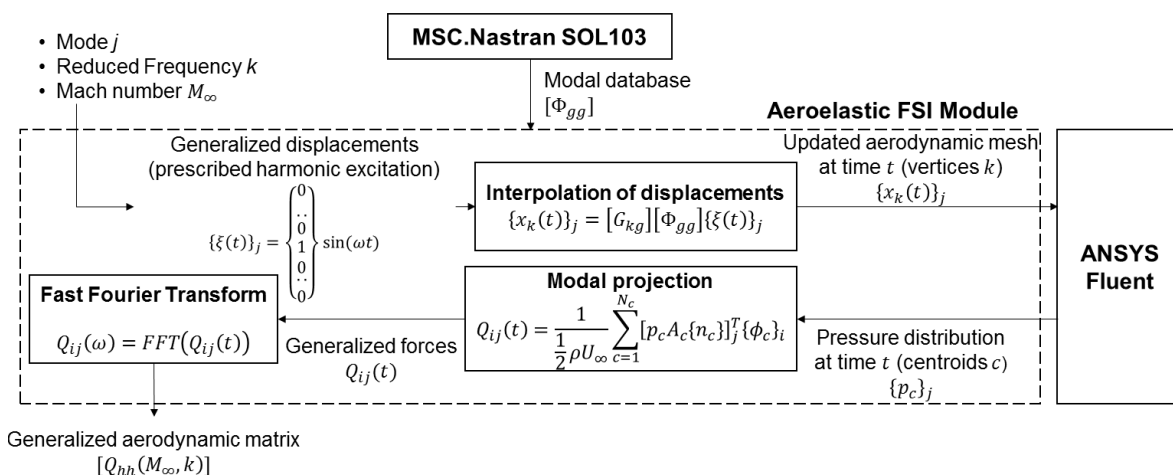


Figure 3. Uncoupled Fluid-Structure Interaction scheme flowchart

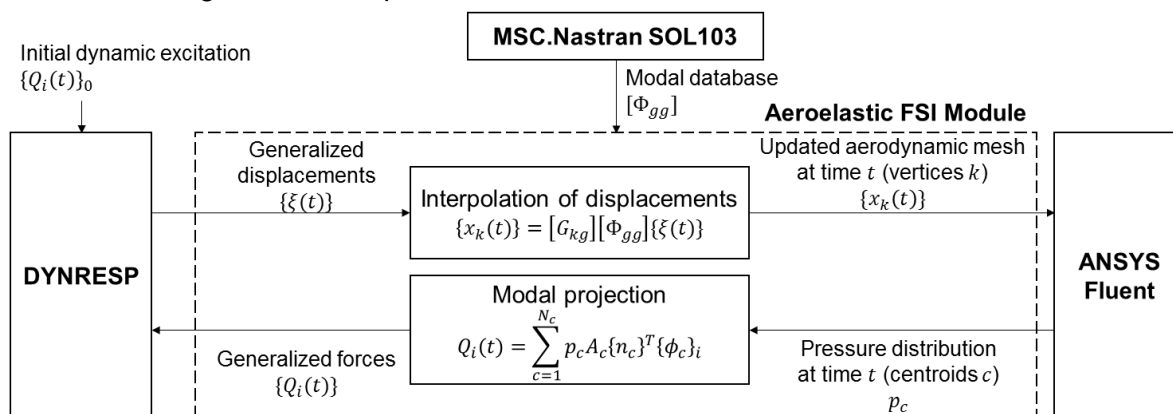


Figure 4. Coupled Fluid-Structure Interaction scheme flowchart

The following sections present each solution method in detail.

2.2 Uncoupled analysis: Generalized aerodynamic matrices

The procedure for calculating the generalized aerodynamic matrices (also known as $[Q_{hh}]$) using unsteady aerodynamics based on CFD is (see Fig. 3):

1. The flutter equation is solved using the classical aeroelastic model with Doublet-Lattice aerodynamics. The flutter mechanism to be studied is isolated to select the relevant normal modes and range of reduced frequencies, $k = \omega L / 2U_\infty$, where ω is the natural frequency in [rad/s], L is a reference length (typically the mean aerodynamic chord), and U_∞ is the flight speed.
2. For each normal mode j and reduced frequencies k selected in the previous step, a prescribed harmonic motion is imposed to the structure:

$$\{\xi(t)\}_j = [0 \dots 0 \ 1 \ 0 \dots 0]^T \sin(\omega t), \quad (2)$$

where ξ is the vector with the generalized coordinates. The structure is deformed thru the relation $\{x_g\}_j = [\Phi_{gg}]\{\xi\}_j$, where $\{x_g\}_j$ is a vector with the Finite Element structural grids displacements and $[\Phi_{gg}]$ is a matrix with the normal modes as columns. The natural frequency is given by the relation $\omega = \frac{2kU_\infty}{L}$.

3. The structural displacements are interpolated into the aerodynamic surface mesh:

$$\{x_k(t)\}_j = [G_{kg}][\Phi_{gg}]\{\xi(t)\}_j. \quad (3)$$

4. The aerodynamic solver updates the fluid volume and calculates the unsteady pressure distribution at the wet surface at each time step. Typically, the simulation converges after a total of three periods.
5. When the simulation is completed, the forces are projected onto all the normal modes (sub-index i) to compute the time-histories of the generalized aerodynamic forces (GAFs):

$$Q_{ij}(t) = \frac{1}{\frac{1}{2}\rho U_\infty} \sum_{c=1}^{N_c} [p_c A_c \{n_c\}]_j^T \{\phi_c\}_i, \quad (4)$$

where p_c is the pressure, A_c , the area, $\{n_c\}$, the unitary normal vector of the aerodynamic face (moving according to normal mode j) and $\{\phi_c\}_i$, the modal displacements in normal mode i . The sub-index c indicates the centroid of the face.

6. The Fast Fourier Transform is performed to the last period of the time-domain GAFs to calculate the frequency-domain GAFs:

$$Q_{ij}(\omega) = \text{FFT} \left(Q_{ij}(t) \right). \quad (5)$$

7. When all modes and reduced frequencies are calculated, the generalized aerodynamic matrix $[Q_{hh}]$ is assembled with the columns computed:

$$Q_{hh}(k, M_\infty) = \begin{bmatrix} \dots & \dots & Q_{1j} & \dots & \dots \\ \dots & \dots & Q_{2j} & \dots & \dots \\ \dots & \dots & \vdots & \dots & \dots \\ \dots & \dots & Q_{nj} & \dots & \dots \end{bmatrix}. \quad (6)$$

8. The flutter equation is solved using the aerodynamic matrix $[Q_{hh}]$ obtained with unsteady CFD aerodynamics.

While the linear generalized aerodynamic forces $[Q_{hh}]$ depend exclusively on the Mach number M_∞ and the reduced frequency k , the CFD simulations are based on physical variables: flight speed U_∞ , frequency f , temperature T and density ρ . This translation of variables is done by selecting a flight level, H (ft), which leads to the airspeed as $U_\infty = a_\infty M_\infty$, where a_∞ is the speed of sound, which only depends on the flight level H . The excitation frequency is obtained by the relation $f = kU_\infty/\pi L$.

2.3 Coupled analysis: Time-marching simulation

The uncoupled frequency-domain analyses described in previous section 2.2 are valid as long as the linear approach (aero-forces proportional to the generalized coordinates) for solving the flutter equation remains valid.

Nevertheless, for those flight conditions which can require considering non-linear aerodynamics, the structural and aerodynamic disciplines need to interact using a time-marching coupling scheme where the information is interchanged at each time-step. This section describes the procedure developed by AIRBUS-DS to couple the CSM and CFD codes thru an interface software, in this case the aero-servo-elastic solver implemented in DYNRESP software, developed by Karpel Dynamic Consulting Ltd. (Karpel, 2019a).

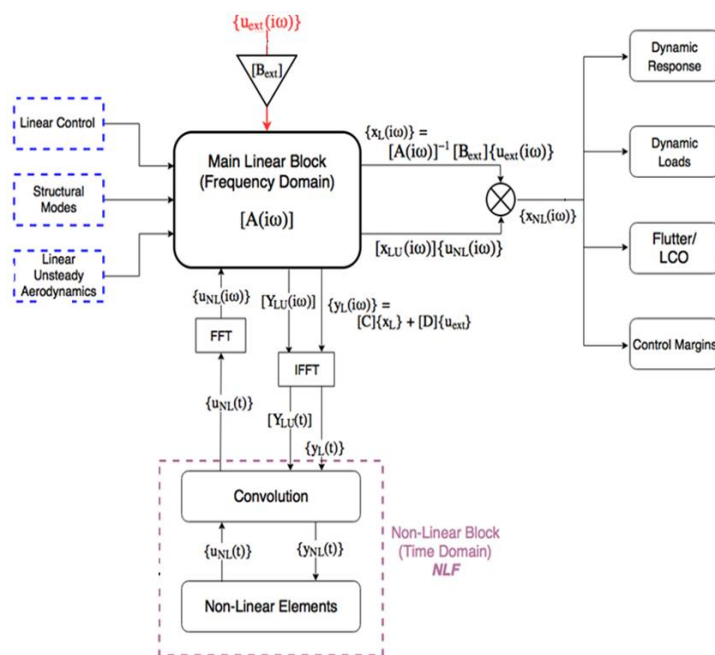


Figure 5: Increased Order Modelling (IOM) block diagram (from Karpel et al. 2020).

DYNRESP is based on the Increased Order Modelling method (Karpel, 2019b), which is schematically depicted in Fig. 5, and it has been used in numerous dynamic applications such as morphing configurations (Karpel et al., 2015) or wake encounter simulation (Claverías et al., 2014). This method is based on a main linear block that is stable when disconnected from the nonlinear elements, and a nonlinear block that expresses all the nonlinearities as feedback loops. The response calculations are performed in 3 stages: (a) Frequency-Domain response of the linear block with the nonlinear block disconnected; (b) addition of nonlinear effects using Time-Domain nonlinear elements and convolution integrals; and (c) complementary Frequency-Domain response of the linear block to inputs from the nonlinear block to generate the final output.

In the case of the integration of DYNRESP with unsteady CFD aerodynamics, the process is performed following the list of sequential steps:

1. The simulation starts by applying a predefined excitation to the aircraft, for example, a one-minus-cosine generalized force is applied on one normal mode.
2. The linear block is solved in the frequency-domain to obtain the generalized displacements at the time step i , $\{\xi_L(t_i)\}$, where the sub index L indicates output from the linear block. The linear model can include linear aerodynamics to improve the approximation to the final non-linear displacements.
3. The generalized displacements obtained in the linear block, $\{\xi_L(t_i)\}$ are interpolated to obtain the displacements in the aerodynamic mesh:

$$\{x_k(t_i)\} = [G_{kg}][\Phi_{gg}]\{\xi(t_i)\}, \quad (7)$$

4. The aerodynamic solver updates the fluid flow mesh and calculates the unsteady pressure distribution at the current time step i .
5. The pressure distribution is integrated and projected onto all the normal modes (sub-index i) to compute the generalized aerodynamic forces (GAFs):

$$Q_i(t) = \sum_{c=1}^{N_c} p_c A_c \{n_c\}^T \{\phi_c\}_i. \quad (8)$$

6. The non-linear generalized forces $\{Q_i(t)\}$ are introduced as feed-back forces to obtain, by convolution integrals, the final non-linear displacements at time i , $\{\xi_{NL}(t_i)\}$, where the sub index NL indicates the output from non-linear analysis.
7. The time step advances to $i + 1$ and back to step 2 until the end of the simulation.

Both CFD-based frequency- and time-domain procedures have been successfully applied to test wing models (Karpel et al., 2020) and to AIRBUS-DS aircraft components, such as the radome of an AWACS configuration (Arévalo et al. 2017). Next section applies this methodology on the T-tail configuration, which has been proven in the introduction as an excellent reference to test the goodness and limitations of CFD-based methods and tools.

3 Application to the flutter instability prediction of a T-tail model

This section presents the application to the T-tail empennage presented in van Zyl and Mathews (2011), where the flutter onset airspeed was measured experimentally for different incidence angles (or trimmed angles) of the horizontal tail-plane.

3.1 T-tail experimental model

The wind-tunnel T-tail model was constructed from steel and aluminium and covered with balsa wood and plastic film. The vertical tail-plane is a swept-back untapered surface, with a height of 0.497 m, a chord of 0.425 m and a swept back angle of 33.1 degrees. Mounted on top, there is a unswept fairing with a height of 0.098 m and a constant-on-span chord of 0.528 m.

The horizontal tail-plane, attached at the mid-height of the fairing, has no dihedral, a root chord of 0.363 m, a semispan of 0.625 m, a taper ratio of 0.276 and a leading-edge sweep angle of 36.5 degrees, with a NACA 23015 airfoil section. The pitch axis (rotation center to change the incidence angle) is parallel to the y-axis and passes through the 74.1% of the HTP root chord and the 60.6% of the fin tip fairing chord.

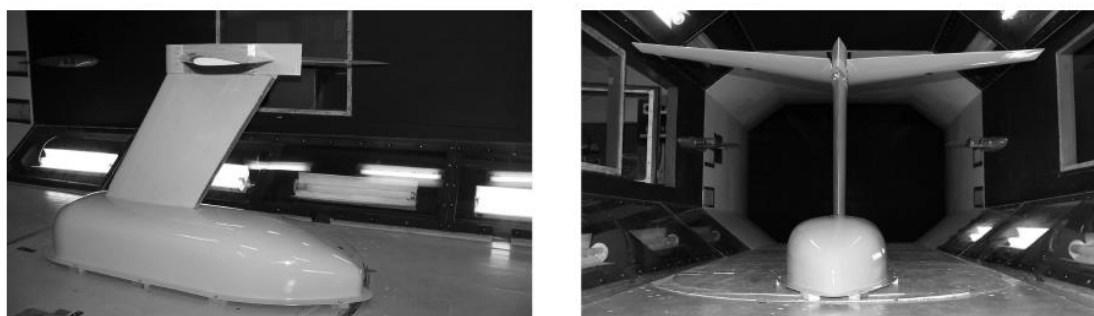


Figure 6: Setup of wind-tunnel T-tail model. From van Zyl and Mathews (2011)

The high-stiffness construction of the horizontal tail-plane was designed to remove the uncertainty of the stabilizer dihedral induced by static load. Therefore, the flexibility of the model was limited to the vertical tail-plane and the roll degree-of-freedom in the mounting. The measured first fin bending mode has a frequency of 2.62 Hz and a damping ratio of 0.6% and the fin torsion mode, a frequency of 4.64 Hz and a damping ratio of 2.1%.

3.2 T-tail aeroelastic mathematical model

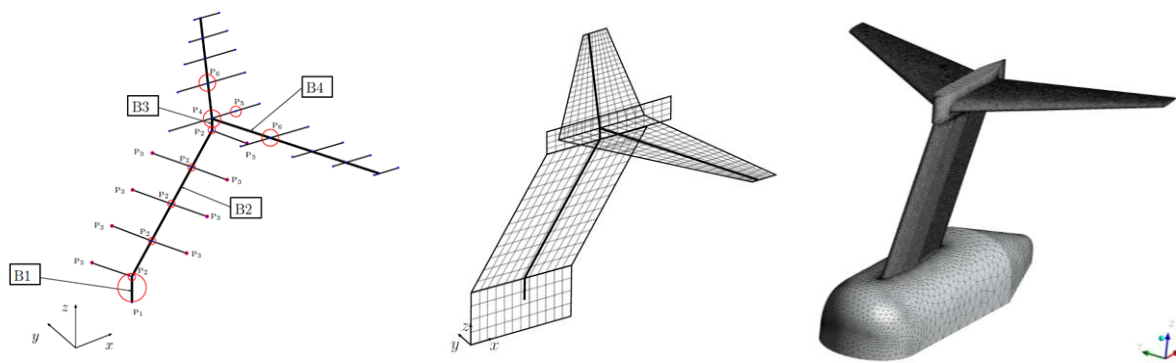
The structural model is built by beams to represent the stiffness, and lumped masses in MSC.Nastran, as depicted in Fig. 7(a). The geometry and properties can be consulted in Murua et al. (2014). The three first normal mode frequencies of the structure computed with Lanczos method are shown in Tab. 1:

Table 1: Normal modes analysis using MSC.Nastran SOL103 (Lanczos method)

Mode	1 st VTP bending	1 st VTP torsion	2 nd VTP bending
Frequency (Hz)	2.62	4.64	13.68

The aerodynamic Doublet-Lattice model is the simplified one employed in Murua et al. (2014), with a homogenous spatial discretization of 12x12 in the vertical tail-plane, 20x10 in horizontal tail-plane and 14x4 in tip fairing (see Fig. 7(b)). The convergence studies presented by van Zyl and Mathews (2011) show a relatively low sensitivity to the panel size.

The unsteady CFD aerodynamic mesh (wet surface shown in Fig. 7(c)), suitable for inviscid Euler solver, is composed of 3.6 million tetrahedral elements with a fluid domain extended 10 chords upwards and 30 chords downwards. The structural displacements are transferred to the aerodynamic surface by radial-basis interpolation functions of the type Thin-Plate Spline (TPS), described in Rendall and Allen (2008). Dedicated efforts have been made to guarantee the continuity of the mesh in the interface between VTP, HTP and tip fairing surfaces. The smoothing diffusion method, implemented in the CFD code, adjusts the aerodynamic cells to the mesh deformation in order to guarantee the level of quality in the fluid domain during the entire simulation.



(a) Finite Element model (b) Doublet-Lattice model (c) CFD-Euler wet surface

Figure 7: Numerical aeroelastic model

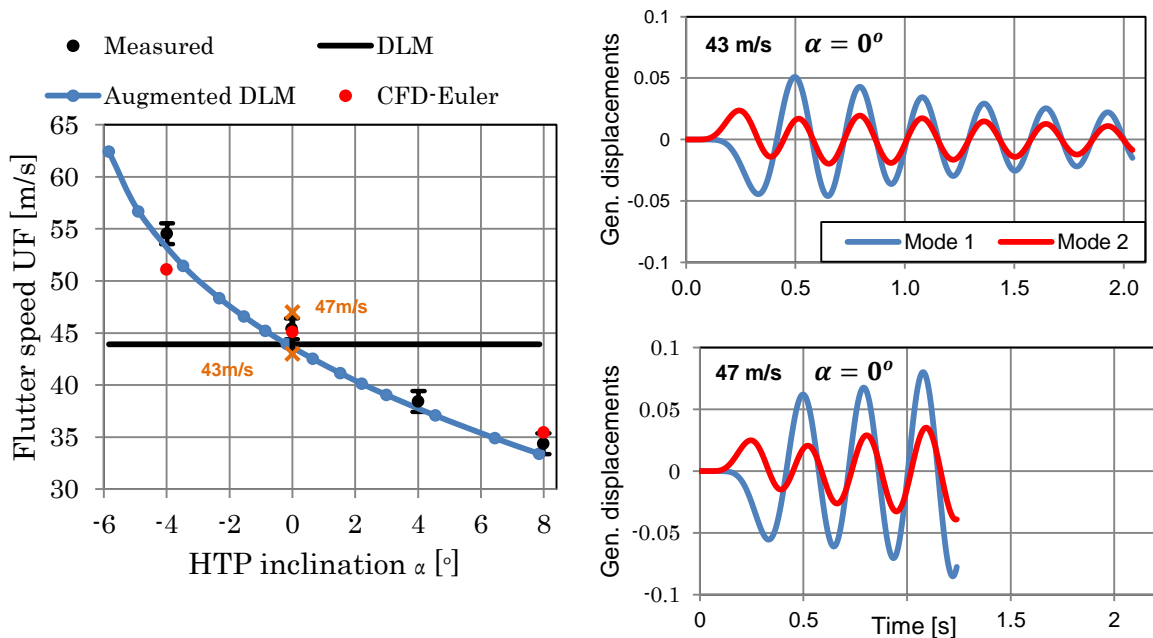
3.3 T-Tail Flutter results

Flutter airspeed results are shown in Fig. 9 comparing the experimental, augmented Doublet-Lattice Method and CFD-Euler-based (frequency-domain with Q_{hh} approach) results as a function of the angle of incidence of the horizontal tail-plane. The uncertainty range of the experimental measurements is below 2 m/s in all cases, which is around the 4% of the nominal flutter airspeed at zero incidence.

The flutter onset in all cases is caused by a classical VTP bending-torsion mechanism at low frequency (3.6 Hz). Since the flutter airspeed can be reproduced exactly with only the two first modes, the analyses only retain these modes. The zero-speed structural damping ratio corresponds to the value measured experimentally.

Experimental results show that positive aerodynamic loading on a swept-back horizontal tailplane deteriorates the T-tail flutter behavior, leading to a lower flutter onset speed when compared with the zero incidence (zero aerodynamic loading) case. The non-corrected standard Doublet-Lattice method (black line) predicts constant flutter airspeed because the method does not account for unsteady aerodynamic effects derived from the horizontal tailplane load. However, both augmented DLM and CFD predictions are aligned with the experimental results.

In particular, the augmented Doublet-Lattice Method, which constitutes the current practice method at AIRBUS-DS, reproduces closely the experimental results with a constant conservative biasing, and therefore proving evidence of its accuracy and robustness. For its part, the results based on CFD-Euler unsteady aerodynamics computed in frequency-domain accurately predict the nominal flutter airspeed at zero incidence, giving a value inside the range of uncertainty of the experimental measurements. In addition, the method proves to be capable of capturing naturally the tendency of flutter speed with the incidence angle, even though there is a slight under-prediction of the effects of steady loads on the flutter speed at positive values of the incidence angle (less critical case).



(a) CFD-based flutter airspeed (b) Evolution of gen. disp. in coupled simulation.
 Figure 10: T-tail model flutter airspeed and coupled analyses results.

These results have been complemented with fully coupled simulations in time-domain performed at two airspeeds for the nominal zero-incidence case. The dynamic evolution of the structure as a consequence of the initial excitation one-minus-cosine generalized force (0.3 s duration) acting on the first fin torsion mode is computed. Fig. 10 shows the evolution of generalized displacements, where the normalization is to unitary mass matrix. In the first case (airspeed 43 m/s, below flutter onset) the dynamic system shows a damped behavior, while in the second (airspeed 47 m/s, above flutter onset) the oscillation amplitude increases in time until the deformation exceeds the limits imposed by the aerodynamic mesh.

4 Conclusions

This paper presents the latest developments of Airbus Defence and Space (AIRBUS-DS) in Fluid-Structure Interaction (FSI) for aeroelastic applications. In particular, two different methodologies to integrate unsteady Computational Fluid Dynamics (CFD) aerodynamics in aeroelastic calculations have been described: first, the uncoupled approach, where the linear generalized aerodynamic forces in the frequency domain are obtained to be the input to traditional linear flutter solvers; second, the coupled approach with DYNRESP software, where the structural and aerodynamic solvers interchange data in a time-marching manner.

The flutter airspeed of a T-tail model in low subsonic regime is computed and compared to experimental results. Since the phenomenon of flutter in T-tail structures is highly dependent on the steady loads on the horizontal tail-plane, the applicability of the standard Doublet-Lattice Method is limited. The current practice in AIRBUS-DS, the augmented Doublet Lattice, adds those particular forces in T-Tail as complementary effects to the generalized forces computed by the Doublet-Lattice Method, giving results closely matched to the experimental measurements. In the case of unsteady aerodynamics based on CFD computations, the nominal flutter at zero incidence is accurately predicted, and the tendency of flutter speed with the incidence angle is naturally captured. There is, however, a slight under-prediction of the effect of the steady loading on flutter speed for positive incidence angles, suggesting that further work is needed to determine the source of this difference: improve the structure-aerodynamic interpolation, adding turbulence modelling (RANS equations) and including quadratic modes (as described in Murua et. al., 2014).

References

- Arévalo, F., Climent, H., Reyes, M., Martínez, P., Pérez, J.L., and Barrera, J. 2017. Airbus Defence and Space AWACS Prototypes: AWACS-Dome Aeroelastic and Dynamic Loads Challenges, In: Proceedings of the International Forum on Aeroelasticity and Structural Dynamics, Como, Italy.
- Bendiksen, O., 2011. Review of unsteady transonic aerodynamics: Theory and Applications, Progress in Aerospace Sciences, 47, 135-167.
- Claverías, S., Cerezo, J., Torralba, M.A., Reyes, M., Climent, H. and Karpel, M., 2014. Dynamic Loads in Response to Wake Encounter," Proceedings of the 54th IACAS Conference, Tel Aviv, Israel.
- Jennings W.P., Berry M.A., 1977. Effect of stabilizer dihedral and static lift on t-tail flutter, Journal of Aircraft, 14(4), 364-367
- Murua, J., Martínez, P., Climent, H., van Zyl, L., Palacios, R., 2014. T-tail flutter: Potential-flow modelling, experimental validation and flight tests, Progress in Aerospace Sciences, 71, 54-84.
- Karpel, M., Romm, A., Reyes, M., and Climent, H., 2015. Aircraft Dynamic Loads with Varying Geometry and Flight Mechanics Effects, In: Proceedings of the International Forum on Aeroelasticity and Structural Dynamics, Paper No. 2015-183, Saint Petersburg, Russia.
- Karpel, M., 2019a. DYNRESP-12.3 User's Manual. Karpel Dynamic Consulting Ltd. Tel Aviv, Israel.
- Karpel, M., 2019b. Unified Framework for Aeroservoelastic Response and Stability Analysis, Design and Testing, In: Proceedings of the International Forum on Aeroelasticity and Structural Dynamics, Paper No. 2019-118, Savannah, GA, USA.
- Karpel, M., Weiss, M., Barrera, J., Santos, E., Arévalo, F., Climent, H., 2020. Aeroservoelastic response and Stability Framework with Computational Aerodynamics, AIAA SciTech 2020 Forum.
- Rendall, T.C.S., Allen, C.B., 2008. Unified fluid-structure interpolation and mesh motion using radial basis functions, International Journal for Numerical Methods in Engineering, 74, 1519-1559.
- Albano, E. and Rodden, W.P., 1969. A Doublet-Lattice Method for Calculating Lift Distributions on Oscillating Surfaces in Subsonic Flows, AIAA Journal, 7(2), 279-285.
- van Zyl, L. H. and Mathews, E. H., 2011. Aeroelastic Analysis of T-Tails Using an Enhanced Doublet Lattice Method, Journal of Aircraft, 48(3), 823-831.

Aeroelastic stability of a flexible high aspect-ratio wing with an imperfect end-support

Mahdi Riazat¹ and Mojtaba Kheiri²

¹ *Fluid-Structure Interactions & Aeroelasticity Laboratory, Concordia University, Montréal, Canada, m_riazat@encs.concordia.ca*

² *Fluid-Structure Interactions & Aeroelasticity Laboratory, Concordia University, Montréal, Canada, mojtaba.kheiri@concordia.ca*

Abstract

This paper examines the aeroelastic stability of a flexible high aspect-ratio wing-like structure imperfectly-supported at one end and free at the other. The equations of motion are obtained within the extended Hamilton's principle framework. The bending and torsional dynamics of the wing are approximated using the Euler-Bernoulli beam theory. The aerodynamic lift and pitching moment are modelled using the unsteady aerodynamics for arbitrary motion of a two-dimensional airfoil section extended by the strip flow theory. The imperfect support is modelled as a linear torsional spring the effect of which is included directly in the equation of motion. The Galerkin method is used for the spatial discretization. The numerical results show that both divergence and flutter speeds are sensitive to the support imperfection. The sensitivity may be great or insignificant depending on the end-spring stiffness. Some unusual dynamical behaviour have also been observed, which are discussed in detail.

Keyword: imperfect end-support, aeroelastic stability, flexible wing, unsteady aerodynamics

1 Introduction

Structures with airfoil cross-section are found in many engineering systems; fixed- and rotary-wing aircraft, wind turbines, compressors and gas turbines, just to name a few. Aeroelastic stability analysis is an essential step in the design process of such systems. In an aircraft, all the lifting surfaces, such as the wing, tails, high-lift devices and control surfaces have to be flutter-free. Analytical models may be used to predict flutter speed of a wing-like structure, where the wing is commonly considered to be clamped (or fixed) at one end and free at the other. There are ample examples of such studies; for example, see [Patil et al. \(2001\)](#); [Qin and Librescu \(2003\)](#).

However, in reality no structure or attachment is perfect. Imperfections may be created, for example, during manufacturing, because of structural fatigue (tear and wear), and/or during installation, and they may be in various forms (e.g. geometric, and material) and locations (e.g. end-supports). Studies have indicated the importance of monitoring imperfections and defects to ensure the good health of wing-like structures. For instance, blades "root attachment problems" are a common cause of vibration and failures in axial compressors ([Meher-Homji et al., 1998](#)). In a civil aircraft airframe, fatigue may cause cracks to quickly spread in susceptible structural elements, such as the over-wing fuselage attachment (see [Munns and Kent, 2000](#) for more details). This seems particularly crucial as composite materials are becoming increasingly widespread in aerospace and wind energy applications. Although some research has been conducted in the past to examine the effects of structural damage, such as surface cracks, on the

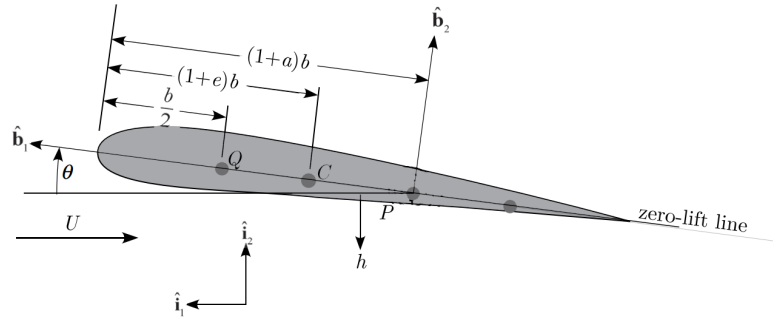


Figure 1 – Cross-sectional view of the wing, where h and θ represent bending and torsional dynamics, respectively. Points Q, C, and P represent, respectively, the aerodynamic centre, the centre of gravity, and the elastic axis; also, $b = 2c$ is the semi-chord, and e and a are dimensionless variables (Hodges and Pierce, 2011).

aeroelastic behaviour of wings, the effects of imperfect end-supports on the aeroelastic stability are still unknown. The objective of the present paper is to explore such effects by modelling the support imperfection by linear translational and torsional springs.

2 Theoretical model

The high-aspect ratio flexible wing is structurally-modelled as an Euler-Bernoulli beam with spanwise bending and torsion dynamics; see Fig. 1. The equation of motion is obtained within the extended Hamilton's principle framework in a similar fashion set in Hodges and Pierce (2011). The imperfect end-support is modelled as a linear torsional spring. Following the approach introduced by Kheiri et al. (2014), the effects of the end-spring are considered in the equation of motion rather than the boundary conditions.

Furthermore, the indicial aerodynamic theory based on the Wagner function is used to represent the unsteady aerodynamic force and moment in the time domain for small arbitrary motion of the wing. The two-dimensional formulation given in Lee et al. (1999) is extended to the three-dimensional using the strip flow theory, and the virtual work due to aerodynamic forces and moments are added to the Lagrangian of the system. It is noted that since the wing is assumed to be of high aspect-ratio, the three-dimensionality of the flow and tip vortices effects are neglected.

The equation of motion may be written as

$$\int_0^L \left(-m \left(\frac{U}{b} \right)^2 h'' + mbx_\theta \left(\frac{U}{b} \right)^2 \theta'' - EI \frac{\partial^4 h}{\partial y^4} + \mathcal{L} \right) \delta h \, dy = 0, \quad (1)$$

$$\int_0^L \left(-I_p \left(\frac{U}{b} \right)^2 \theta'' + mbx_\theta \left(\frac{U}{b} \right)^2 h'' + GJ \frac{\partial^2 \theta}{\partial y^2} + \mathcal{M} + K\theta\bar{\delta}(y) \right) \delta \theta \, dy = 0,$$

where m is the mass per unit length of the wing, y is the spanwise coordinate, L is the length of the wing, and b is the semi-chord (i.e. $c = 2b$, where c being the chord length); $x_\theta = e - a$; EI and GJ are the bending and torsional rigidities, respectively; I_p is the mass moment of inertia, U is the flow velocity, h and θ are the bending and torsional displacements, respectively, and

δh and $\delta \theta$ are their corresponding virtual displacements; also, K is the torsional spring stiffness (to model the imperfect support), and $()' = \partial/\partial \tau$, where $\tau = t/Ub$ is the non-dimensional time; \mathcal{L} and \mathcal{M} represent the lift and pitching moment, respectively; $\bar{\delta}(y)$ denotes the Dirac delta function.

According to Wagner's problem of the step change in angle of attack, lift may be written as (refer to [Fung, 2002](#); [Bisplinghoff et al., 1996](#))

$$\mathcal{L} = \mathcal{L}_1 + \mathcal{L}_2 + \mathcal{L}_3, \quad (2)$$

in which

$$\begin{aligned} \mathcal{L}_1 &= 2\pi\rho bU \left(w_{3/4}(0)\phi(\tau) + \int_0^\tau \frac{dw_{3/4}(\sigma)}{d\sigma} \phi(\tau - \sigma) d\sigma \right), \\ \mathcal{L}_2 &= \pi\rho U^2 (h'' - ab\alpha''), \\ \mathcal{L}_3 &= \pi\rho bU^2 \alpha'; \end{aligned} \quad (3)$$

pitching moment may also be written as

$$\mathcal{M} = \left(\frac{1}{2} + a \right) b\mathcal{L}_1 + ab\mathcal{L}_2 - \left(\frac{1}{2} - a \right) b\mathcal{L}_3 + \mathcal{M}_a, \quad (4)$$

where

$$\mathcal{M}_a = -\frac{1}{8}\pi\rho b^2 U^2 \alpha''. \quad (5)$$

The well-known approximation for the Wagner function, $\phi(\tau)$, may be written as:

$$\phi(\tau) = 1 - \gamma_1 e^{-\varepsilon_1 \tau} - \gamma_2 e^{-\varepsilon_2 \tau}, \quad (6)$$

where $\gamma_1 = 0.165$, $\gamma_2 = 0.335$, $\varepsilon_1 = 0.0455$, and $\varepsilon_2 = 0.3$.

By substituting Eq. 6 into the expression for \mathcal{L}_1 (see Eq. 3), we obtain:

$$\begin{aligned} \mathcal{L}_1 &= 2\pi\rho bU^2 \left\{ \left[\phi(0) + \phi'(0)\left(\frac{1}{2} - a\right) \right] \alpha + \phi(0)\left(\frac{1}{2} - a\right) \alpha' + \phi'\left(\frac{h}{b}\right) + \phi(0)\left(\frac{h'}{b}\right) \right. \\ &\quad \left. + \sum_{j=1}^2 \left[\gamma_j \varepsilon_j \left(1 - \left(\frac{1}{2} - a\right) \varepsilon_j\right) A_j - \gamma_j \varepsilon_j^2 \frac{H_j}{b} \right] - \phi'(0) \left[\frac{h(0)}{b} + \left(\frac{1}{2} - a\right) \alpha(0) \right] \right\}, \quad (7) \end{aligned}$$

where A_j and H_j ($j = 1, 2$) are:

$$A_j = \int_0^\tau e^{-\varepsilon_j(\tau-\sigma)} \alpha(\sigma) d\sigma, \quad H_j = \int_0^\tau e^{-\varepsilon_j(\tau-\sigma)} h(\sigma) d\sigma. \quad (8)$$

Galerkin's method is utilized to discretize the equation of motion in space by letting $h = \sum_{i=1}^N \Phi_i(y) \eta_i(t)$ and $\theta = \sum_{k=1}^N \Theta_k(y) \zeta_k(t)$, where $\Phi_i(y)$ and $\Theta_k(y)$ are, respectively, the bending and torsional mode shapes, and $\eta_i(t)$ and $\zeta_k(t)$ are their corresponding generalized coordinates; also, N is the number of modes, which is assumed to be the same for bending and torsion. In this study, clamped-free mode shapes for bending and free-free mode shapes for torsion are used. Thus, the final form of the equation of motion becomes:

$$\mathbf{M}\mathbf{X}'' + \mathbf{C}\mathbf{X}' + \mathbf{K}\mathbf{X} = \mathbf{0}, \quad (9)$$

where $\mathbf{X} = [h_1, \dots, h_N, \theta_1, \dots, \theta_N, A_{1_1}, \dots, A_{1_N}, A_{2_1}, \dots, A_{2_N}, H_{1_1}, \dots, H_{1_N}, H_{2_1}, \dots, H_{2_N}]^T$; also, \mathbf{M} , \mathbf{C} , and \mathbf{K} are, respectively, the mass, damping and stiffness matrices.

Next, Eq. 9 is transformed to the state-space form to be used for eigenvalue solutions.

Table 1 – Parameters of a high aspect ratio wing adopted from Patil et al. (2001).

Parameter	Value
Half span, L	16 m
Chord, $c = 2b$	1 m
Mass per unit length, m	0.75 kg/m
Moment of inertia (50% chord), $I_{1/2}$	0.1 kg.m
Spanwise elastic axis, $(1 + a)b$	50% chord
Center of gravity, $(1 + e)b$	50% chord
Bending rigidity, EI	2×10^4 N.m ²
Torsional rigidity, GJ	1×10^4 N.m ²
Density of air, ρ	0.0889 kg/m ³

Table 2 – Comparison between present study results and those from Patil et al. (2001).

Parameter	Present study	Patil et al. (2001)	Difference
Flutter Speed, U_{cf} (m/s)	33.36	32.21	3.5%
Flutter Frequency, Ω_f (rad/s)	22.02	22.61	2.6%
Divergence Speed, U_{cd} (m/s)	37.15	37.29	0.4%

 Table 3 – Numerical solution convergence study using different number of mode shapes. Parameters are the same as those in Tab. 1 with $\kappa = 0.6487$ for the end-support stiffness.

Parameter	$N = 5$	$N = 10$	$N = 15$	$N = 20$
Flutter Speed, U_{cf} (m/s)	25.26 (0.1%)	25.23 (0.2%)	25.18 (0.0%)	25.18
Flutter Frequency, Ω_f (rad/s)	13.25 (3.2%)	12.83 (0.8%)	12.73 (0.5%)	12.66
Divergence Speed, U_{cd} (m/s)	24.41 (1.2%)	24.11 (0.4%)	24.02 (0.1%)	23.99

3 Results and discussion

3.1 Validation and convergence of numerical solutions

Prior to proceeding with the investigation of the effects of imperfect end-support on the dynamics and stability of the system, we present some numerical results to serve as a verification of the present aeroelastic model. The parameters listed in Tab. 1 are adopted from Patil et al. (2001) for a clamped-free wing (i.e. perfectly-supported wing or when $K \rightarrow \infty$). As seen from Tab. 2, the values of critical flow velocities for flutter (U_{cf}) and divergence (U_{cd}) as well as the flutter frequency (Ω_f) predicted by the present aeroelastic model are in very good agreement with those reported by Patil et al. (2001).

Moreover, in order to find the minimum number of mode shapes required for obtaining accurate numerical results, we obtained the values of U_{cf} , U_{cd} and Ω_f for different number of mode shapes used in the Galerkin approximation for an imperfectly-supported wing. The design parameters of the wing are the same as those in Tab. 1, with $\kappa = 0.6487$, where $\kappa = 4KL/\pi^2GJ$

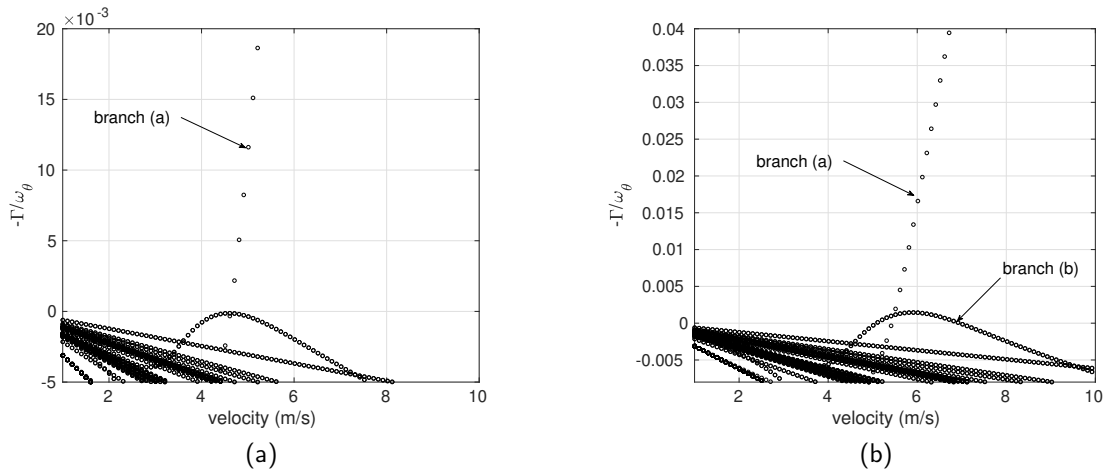


Figure 2 – Variation of the negative, dimensionless modal damping as a function of the flow velocity: (a) divergence occurs at $U_{cd} = 4.71$ m/s when $\kappa = 0.01293$, and (b) flutter occurs at $U_{cf} = 5.11$ m/s when $\kappa = 0.01744$ — the type of instability changes from divergence to flutter.

is the dimensionless counterpart of K . As seen from Tab. 3, with 15 modes for bending and torsional dynamics, the results are within an acceptable range ($< 0.5\%$) with respect to those with 20 modes; thus, $N = 15$ is used for the rest of numerical solutions in this paper.

3.2 Stability Analysis

Numerical studies show that the dynamics of a flexible wing-like structure with an imperfect end-support is very complex. Depending on the design parameters of the structure, such as the bending-to-torsional rigidity ratio (EI/GJ), mass ratio ($\mu = m/\pi\rho b^2$), and the dimensionless radius of gyration ($r^2 = I_p/mb^2$) and as the dimensionless stiffness of the torsional end-spring (κ) is varied, flutter or divergence may occur. Four different types of dynamical behaviour (by considering only the first instability), which we call type-1, type-2 and so on, were identified in the course of a large numerical investigation campaign. In type-1, divergence is the only form of instability, regardless of the value of κ . In type-2, divergence occurs at low values of κ , but it switches to a flutter instability from moderate values of κ . In type-3, flutter is prevalent for low values of κ ; however, divergence occurs at moderate values of κ , which switches back at slightly higher values of κ to flutter that remains operative up to large values of κ . Finally, in type-4, switching between divergence and flutter occurs frequently as κ is varied from low to high values: divergence at low values of κ ; flutter at moderate values of κ ; then, divergence for slightly higher values of the torsional stiffness, and eventually flutter for high values of κ .

As an example of the type-4 dynamical behaviour, Fig. 2 shows the change from divergence (Fig. 2a) to flutter (Fig. 2b) as κ is varied from 0.01293 to 0.01744. In the figures, the variation of the negative, dimensionless modal damping, $(-\Gamma/\omega_\theta)$, is shown as a function of the dimensional flow velocity. A branch of solution crossing the half-plane from negative values of $(-\Gamma/\omega_\theta)$ to positive values indicate an instability. In the figures, 'branch (a)' and 'branch (b)' refer to the divergence and flutter solution branches, respectively. On the other hand, Fig. 3 shows the change in the type of instability from flutter to divergence, again, for a system with the type-4 dynamics. Flutter occurs as the first instability at $U_{cf} = 6.81$ m/s for $\kappa = 0.0293$,

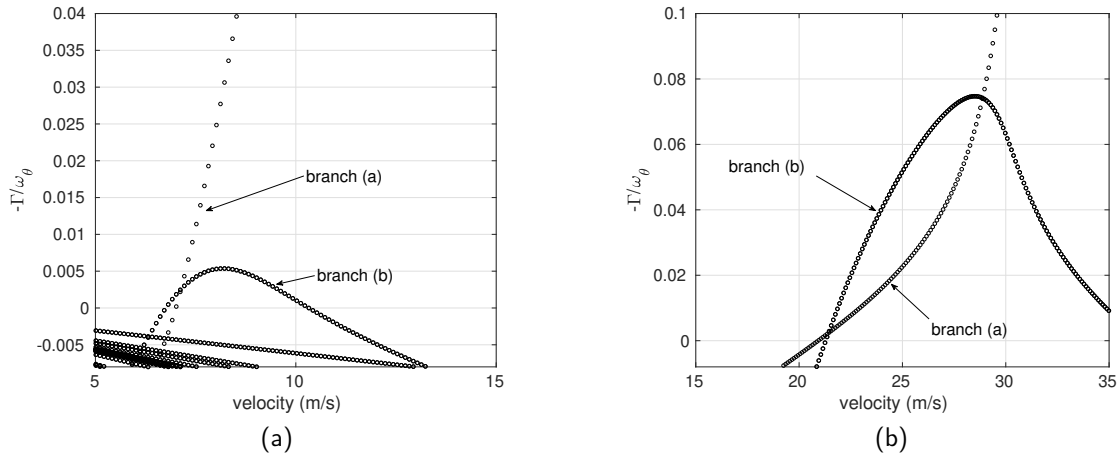


Figure 3 – Variation of the negative, dimensionless modal damping as a function of the flow velocity: (a) flutter occurs at $U_{cf} = 6.81$ m/s when $\kappa = 0.02931$, and (b) $U_{cd} = 20.45$ m/s when $\kappa = 0.3237$ — the type of instability changes from flutter to divergence.

while the same wing with $\kappa = 0.3236$ undergoes divergence first at $U_{cd} = 20.45$ m/s.

3.3 Divergence

One way to find the divergence speed is to solve the static version of the equation of motion by ignoring all terms with a time derivative. In other words, Eq. 9 reduces to $\mathbf{K}\mathbf{X} = \mathbf{0}$. By letting the determinant of the stiffness matrix to zero, a polynomial is obtained as a function of the flow velocity, where the non-negative real roots correspond to divergence speeds. Using only two modes for bending and two modes for torsion, the following closed form equation is obtained for the dimensionless critical flow velocity for divergence, u_{cd} :

$$u_{cd} = \mathcal{F}(\kappa) \sqrt{\frac{r^2 \mu}{1 + 2a}}, \quad (10)$$

where $\mathcal{F}(\kappa) = 0.31831 \left(19.7392 + 14.8044\kappa - \sqrt{219.17\kappa^2 + 194.8182\kappa + 389.6363} \right)^{1/2}$.

Fig. 4 shows the variation of u_{cd} as a function of κ obtained from Eq. 10 (circle markers) as well as the solution using $N = 15$ (star markers). As seen, as κ is decreased — the end-support becomes more imperfect — u_{cd} decreases, meaning that the system becomes more unstable. The reduction in u_{cd} is gradual for large values of κ ; however, it becomes dramatic for moderate to low values of κ . It is also worth mentioning that for $\kappa < 0.5$ Eq. 10 predicts u_{cd} with a fairly good agreement with the value obtained using $N = 15$ modes; however, as κ is increased to higher values, it is advisable to use more and more number of modes for the solution.

Eq. 10 indicates that u_{cd} is linearly dependent on the dimensionless radius of gyration, while it is increasing with the square root of the mass ratio. In addition, moving the elastic axis more towards the trailing edge – increasing a – makes the system statically more unstable. It is also very interesting to see that the expression given in Eq. 10 is very similar to the equation derived for divergence speed of a typical airfoil section with pitching and plunging degrees-of-freedom, i.e. $u_{cd} = \sqrt{r^2 \mu / (1 + 2a)}$; see Hodges and Pierce (2011) for more details. It is also

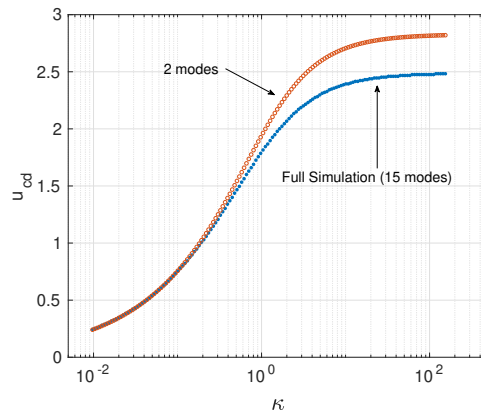


Figure 4 – Variation of the dimensionless critical flow velocity for divergence, u_{cd} , as a function of the dimensionless end-spring stiffness, κ . The circle markers (orange, online) show the numerical values obtained from Eq. 10, while the star markers (blue, online) show the solution obtained via $N = 15$.

interesting to draw the reader's attention to the similarity between the divergence problem of a wing (i.e. cross-flow problem) and that of a pipe conveying fluid or a cylinder in axial flow. In both of these situations, the dimensional divergence speed, U_{cd} , is inversely proportional to the square-root of the fluid mass per unit length.

3.4 Flutter

Figs. 5a,b show the variation of the dimensionless critical flow velocity for flutter, u_{cf} , and the dimensionless flutter frequency, ω_f , as a function of the dimensionless end-spring stiffness, κ , respectively, for four different values of the mass ratio: $\mu = 5, 10, 15,$ and 20 . The rest of parameters are: $EI/GJ = 3$ and $r^2 = 0.3$. Generally speaking, both u_{cf} and ω_f decrease as κ is decreased, that is when the end-support becomes less perfect. More precisely, three different regions may be observed in a $u_{cf} - \kappa$ curve as we move from a perfectly-supported case (i.e. high κ) towards to an imperfectly-supported one (i.e. low κ).

For moderate to large values of κ , the curve plateaus, and u_{cf} changes only slightly as the end-support becomes less perfect — region I. As κ is decreased further, u_{cf} also decreases; however, within a small range of moderate to low values of κ which marks region II ($0.5 \lesssim \kappa \lesssim 1.5$), surprisingly, u_{cf} increases as κ is decreased, meaning that the system becomes more stable as the stiffness of the end-spring is reduced. Such an unusual behaviour has also been observed for other systems involving fluid-structure interactions, such as imperfectly-supported pipes conveying fluid; e.g., refer to [Kheiri et al. \(2014\)](#). Finally, for relatively loosely-supported wings (i.e. $\kappa < 0.5$), the change of u_{cf} with κ is very dramatic, and u_{cf} decreases sharply as κ is decreased — region III. On the other hand, ω_f is decreasing, with a lower rate in region I and a higher rate in region III, as κ is decreased. Except for an abrupt transition between region I and region III at higher values of μ , no unusual behaviour is observed in region II of κ -values in the frequency plot.

As also seen from Fig. 5a, u_{cf} is increased as the mass ratio is increased. This is expected as a high mass ratio may be interpreted as a lower density fluid flow and thus weaker fluid-

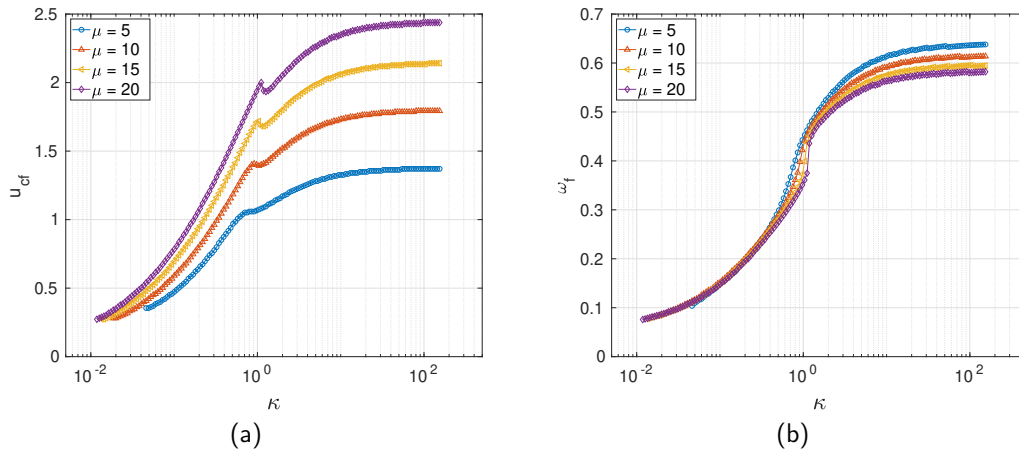


Figure 5 – Variation of (a) the dimensionless critical flow velocity for flutter, u_{cf} , and (b) the dimensionless flutter frequency, ω_f , as a function of the dimensionless end-spring stiffness, κ , for different values of the mass ratio: $\mu = 5, 10, 15$, and 20 ; also, $EI/GJ = 3$ and $r^2 = 0.3$.

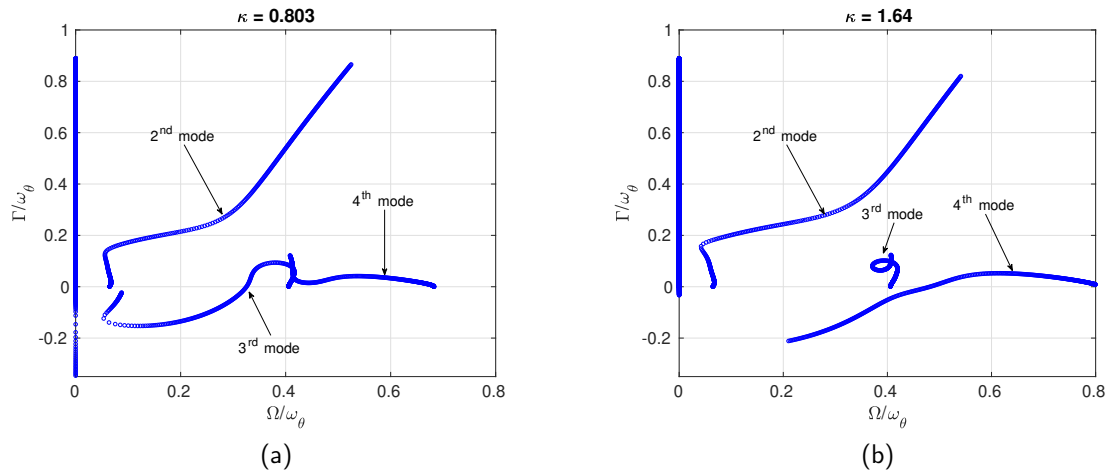


Figure 6 – Argand diagrams showing the evolution of first four eigenfrequencies of the system as a function of dimensionless flow velocity: (a) $\kappa = 0.803$, and (b) $\kappa = 1.64$. The rest of system parameters are: $\mu = 20$, $EI/GJ = 3$, and $r^2 = 0.3$.

dynamic forces which needs to be compensated by a higher flow velocity at the onset of flutter. In addition, region II becomes more pronounced at higher values of μ . Moreover, the difference between u_{cf} values for different μ values becomes wider at larger values of κ . On the other hand, as seen from Fig. 5b, ω_f is weakly dependent on the mass ratio, and it slightly decreases in region I as μ is increased.

The unusual behaviour observed in the $0.5 \lesssim \mu \lesssim 1.5$ range in Fig. 5a may be explained further by examining the evolution of solution modes (or branches) in Argand diagrams. In the Argand diagrams shown in Figs. 6a,b, the evolution of first four complex eigenfrequencies of the system has been shown as a function of u for $\kappa \approx 0.8$ (region II) and $\kappa \approx 1.6$ (region I), respectively. The x- and y-axes in the Argand diagrams show the real part (i.e. dimensionless frequency) and imaginary part (i.e. negative dimensionless damping) of eigenfrequencies,

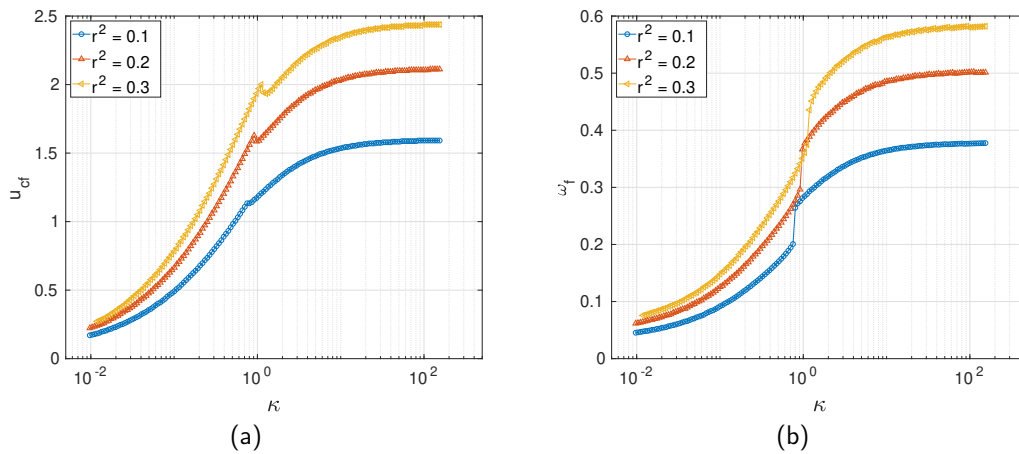


Figure 7 – Variation of (a) the dimensionless critical flow velocity for flutter, u_{cf} , and (b) the dimensionless flutter frequency, ω_f , as a function of the dimensionless end-spring stiffness, κ , for different values of the dimensionless radius of gyration: $r^2 = 0.1, 0.2$, and 0.3 ; also, $\mu = 20$ and $EI/GJ = 3$.

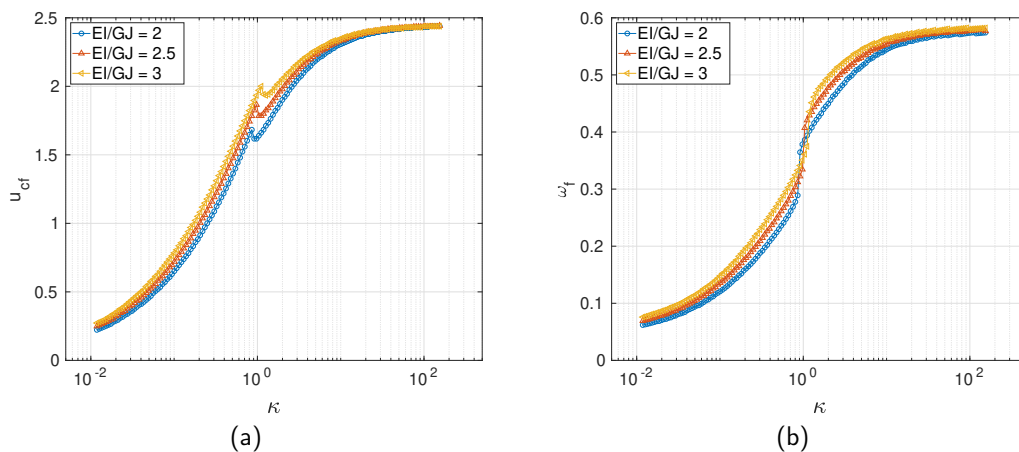


Figure 8 – Variation of (a) the dimensionless critical flow velocity for flutter, u_{cf} , and (b) the dimensionless flutter frequency, ω_f , as a function of the dimensionless end-spring stiffness, κ , for different values of the bending-to-torsional rigidity ratio: $EI/GJ = 2, 2.5$, and 3 ; also, $\mu = 20$ and $r^2 = 0.3$.

respectively. As seen from Fig. 6a, for $\kappa \approx 0.8$, flutter occurs in the third mode which also crosses the 4th mode locus. At $\kappa \approx 1.6$, however, the third mode remains stable, and flutter occurs in the 4th mode. This appears as an example of the so-called ‘role reversal’ or ‘mode exchange,’ which often results into an unexpected dynamical behaviour, and that is also a well-known feature of the dynamics of flexible pipes conveying fluid (for more details, please refer to Païdoussis, 2014).

Figs. 7a,b show, respectively, the variation of u_{cf} and ω_f as a function of κ for three different values of the dimensionless radius of gyration: $r^2 = 0.1, 0.2$, and 0.3 . The rest of system parameters are: $EI/GJ = 3$ and $\mu = 20$. Similar trends and regions as those observed in Fig. 5 are also seen from the plots in Fig. 7 with the exception that ω_f is strongly dependent on r^2 .

One interesting aspect of the frequency curve, which is more noticeable in Fig. 7b than Fig. 5b, is the sharp fall in the ω_f value in region II.

Figs. 8a,b show, respectively, the variation of u_{cf} and ω_f as a function of the dimensionless end-spring stiffness (used for modelling the imperfect support) for $EI/GJ = 2, 2.5,$ and 3 ; the rest of system parameters are: $\mu = 20$ and $r^2 = 0.3$. A similar trend for the variation of u_{cf} and ω_f to that seen in Figs. 5 and 7 is also observed here. It is interesting to see that the EI/GJ magnitude is affecting u_{cf} and ω_f , mostly in regions II and III (moderately- to loosely-supported systems), and it is minimally changing them in region I (strongly-supported systems).

4 Concluding remarks

The numerical results presented in this paper show that the end-support imperfection for a flexible wing-like structure may considerably reduce the critical flow velocities for divergence and flutter. The sensitivity of the aeroelastic stability to the imperfection was found to be different depending to the degree of imperfection (i.e. end-support stiffness). An unusual dynamical behaviour was observed in a finite range of the end-support stiffness, where by increasing the stiffness, the dimensionless flutter speed decreased.

Acknowledgements

The authors appreciate the support by the Natural Sciences and Engineering Research Council of Canada for a Discovery Grant and the Gina Cody School of Engineering and Computer Science of Concordia University for the Faculty Research Support.

References

- M. J. Patil, D. H. Hodges, C. E. S. Cesnik, Nonlinear aeroelasticity and flight dynamics of high-altitude long-endurance aircraft, *Journal of Aircraft* 38 (2001) 88–94.
- Z. Qin, L. Librescu, Dynamic aeroelastic response of aircraft wings modeled as anisotropic thin-walled beams, *Journal of Aircraft* 40 (2003) 532–543.
- C. B. Meher-Homji, G. Gabriles, et al., Gas turbine blade failures-causes, avoidance, and troubleshooting., in: *Proceedings of the 27th turbomachinery symposium*, Texas A&M University. Turbomachinery Laboratories, 1998.
- T. E. Munns, R. M. Kent, Structural health monitoring: Degradation mechanisms and system requirements, in: *19th DASC. 19th Digital Avionics Systems Conference. Proceedings (Cat. No. 00CH37126)*, volume 2, IEEE, 2000, pp. 6C2–1.
- D. H. Hodges, G. A. Pierce, *Introduction to Structural Dynamics and Aeroelasticity*, volume 15, Cambridge University Press, 2011.
- M. Kheiri, M. Païdoussis, G. C. Del Pozo, M. Amabili, Dynamics of a pipe conveying fluid flexibly restrained at the ends, *Journal of Fluids and Structures* 49 (2014) 360–385.
- B. Lee, S. Price, Y. Wong, Nonlinear aeroelastic analysis of airfoils: bifurcation and chaos, *Progress in aerospace sciences* 35 (1999) 205–334.
- Y. Fung, *An Introduction to the Theory of Aeroelasticity*, Dover Phoenix Edition: Engineering, Dover Publications, 2002.
- R. L. Bisplinghoff, H. Ashley, R. L. Halfman, *Principles of Aeroelasticity*, New York: Dover Publications, Inc., 1996.
- M. P. Païdoussis, *Fluid-Structure Interactions: Slender Structures and Axial Flow*, volume 1, 2nd ed., Academic Press, 2014.

Nonlinear flutter instability with laminar flow model

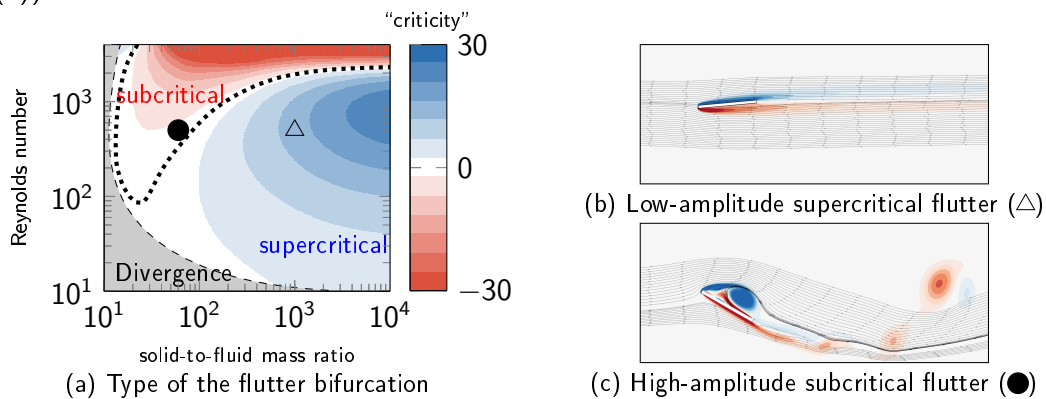
Johann Moulin¹, Olivier Marquet¹

¹ ONERA-DAAA/MAPE, Meudon, France, johann.moulin@onera.fr

Keyword: fluid nonlinearity, Hopf bifurcation, weakly nonlinear analysis, Harmonic Balance.

The evaluation of the flutter risk often consists in determining the critical flutter velocity, that is, the wind velocity above which the steady-state with the fixed wing becomes *linearly unstable*, due to fluid-structure coupling. It has been pointed out by many researchers¹ that, depending on the nonlinearities of the system, flutter may occur below the critical velocity, thus making the latter an irrelevant stability criteria. A large part of the research focused on the effect of nonlinearities coming from the structure¹. More recently, fluid nonlinearities like shocks in transonic flows² or transitional effects³ have been considered. In this talk, we numerically investigate the role of the fluid nonlinearities at play in laminar ($10^2 < Re < 10^4$) incompressible flows.

We consider a two-dimensional setup, similar to the one experimentally studied by Amandolèse et al⁴, which consists in a thin rigid plate, mounted on fully linear heaving and pitching springs. The fluid is modeled by the incompressible 2D Navier–Stokes equations. As a first step, the linear stability of the coupled system is assessed in order to retrieve the linear flutter thresholds in the (mass ratio, Reynolds number) parameter space. Then, a weakly nonlinear analysis is performed, allowing us to derive the normal form associated to the flutter Hopf bifurcation (Fig (a)). From there, two scenarios are encountered : (i) a *supercritical* Hopf bifurcation leading to smoothly increasing, low-amplitude, LCO solutions, above the critical velocity (Fig (b)) or (ii) a *subcritical* Hopf bifurcation allowing high-amplitude LCO's, even below the critical velocity (Fig (c)).



¹ Lee B., Price S. & Wong Y. (1999). Nonlinear aeroelastic analysis of airfoils: bifurcation and chaos. *Progress in Aerospace Sciences*, 35, 205-334.

² Thomas J., Dowell E. & Hall K. (2004). Modeling viscous transonic limit-cycle oscillation behavior using a harmonic balance approach. *Journal of Aircraft*, 41, 1266-1274.

³ Poirel D. & Mendes F. (2014). Experimental Small-Amplitude Self-Sustained Pitch-Heave Oscillations at Transitional Reynolds Numbers. *AIAA Journal*, 52, 1581-1590.

⁴ Amandolèse X., Michelin S. & Choquel M. (2013). Low speed flutter and limit cycle oscillations of a two-degree-of-freedom flat plate in a wind tunnel. *Journal of Fluids and Structures*, 43, 244-255.

Numerical and wind tunnel studies of highly flexible composite plates for HALE wing aeroelastic tailoring applications

1st Olivier Montagnier¹, 2nd Bertrand Kirsch¹ and 3rd Thierry M. Faure¹

¹ *Centre de Recherche de l'École de l'air, BA 701, F-13661 Salon air, France, olivier.montagnier@ecole-air.fr*

Abstract

This paper is dedicated to aeroelastic tailoring of very flexible aircraft (VFA) both from the numerical and the experimental point of view. The first objective of this work is to present an open source simulation tool called GEBTAero devoted to this kind of application and based on low order models. Because of the limited availability of experimental data about very flexible wing, the second objective is to propose a wind tunnel test campaign to identify the aeroelastic critical speed of highly flexible isotropic and anisotropic plates in order to validate the simulation tool. Aside from the good agreement between numerical and experimental critical speed and frequency, this campaign highlights the typical hysteresis phenomenon and limit cycle oscillations related to high aspect ratio flexible wing.

Keyword: aeroelastic tailoring, HALE UAV, wind tunnel, low order method.

1 Introduction

Recent progress made in the field of solar cells, energy storage and composite materials pave the way for a new aircraft concept, namely High Altitude Long Endurance (HALE) Unmanned Aerial Vehicle (UAV) whose goal is to reach an endurance almost infinite. To achieve this far-reaching goal, aerodynamic and structural performances are stretched to their limits. As a consequence, HALE wings are extremely vulnerable to aerostatic static divergence and flutter (e.g. NASA's Helios mishap). A way to improve composite wing performance versus these instabilities is the aeroelastic tailoring concept. It consists in using laminate layup without mirror symmetry and/or unbalanced layup. The emerging structural coupling induced on the aerodynamic side a coupling between the bending, due to lift forces, and the twisting of the wing which determines the local Angle of Attack (AoA) and consequently an impact on aeroelastic behavior.

The computational cost of high fidelity aeroelastic simulation on Very Flexible Aircraft (VFA) is still prohibitive, prompting the need for suitable reduced order model. Many reduced order model tools have been developed during the last decades as for example, NATASHA [Patil and Hodges, 2006], SHARP [Murua et al., 2012], UM/NAST [Shearer and Cesnik, 2007] or Aeroflex [Ribeiro et al., 2012]. Recently, an open source simulation tool called GEBTAero has been developed by the authors, well fitted for the computationally intensive task of aeroelastic tailoring optimization [Kirsch et al., 2020].

On the experimental side, there is only little data available in the literature concerning flexible wings. We could mention the wind tunnel test conducted in [Tang and Dowell, 2016] on a flexible wing made of a steel flat plate with a balsa wing skin. Although this experiment gives

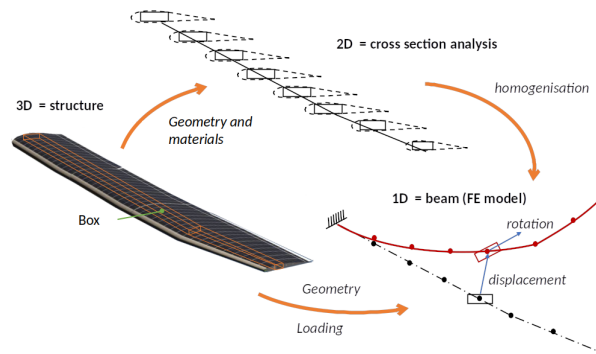


Figure 1: Structural definition in GEBTAero

interesting results, notably in terms of Limit Cycle Oscillation (LCO) studies, the aeroelastic tailoring effect is not taken into account on this isotropic wing.

This paper concerns a wind tunnel test campaign conducted on flexible flat plates, both metallic and composites in order to obtain validation data for aeroelastic tailoring purpose. First, GEBTAero used for simulation is presented. Then, after a short presentation of the experimental setup, the flutter speed and frequency of an aluminum flat plate are evaluated depending on the half-span. Finally, experimental results on different laminates producing bending-twisting coupling are provided.

2 Aeroelastic reduced order model

The main objective of GEBTAero is to define a fast implementation of a proper reduced order aeroelastic model well fitted for the computationally intensive task of aeroelastic tailoring optimization. The high-aspect-ratio wing assumption gives us the opportunity to neglect three-dimensional effects and thus to use a strip theory which can be easily linked to a beam formulation. A tight coupling is chosen, done by integrating aerodynamic loads directly into the weak formulation of the beam theory. It permits the determination of the aeroelastic modes of the wing about a geometrically non linear steady state, namely frequencies, modal shapes and damping factors.

On the structural side (Fig 1), to ensure a proper modeling of the laminate anisotropy and geometrical non linearity, the choice fell on an open source tool named GEBT (Geometrically Exact Beam Theory) developed by Yu and Blair [Yu and Blair, 2012] designed for composite slender structures under large deflections and rotations, assuming the strains to be small. This tool coded in Fortran 90/95 implements a mixed variational formulation based on exact intrinsic equations for dynamics of moving beams developed by Hodges [Hodges, 1990]. The cross section parameters of the anisotropic beam are determined using an homogenization tool following a method developed by Cartraud and Messenger [Cartraud and Messenger, 2006]. It consists in a three-dimensional finite element calculation realized with the open source solver CalculiX on a Representative Volume Element (RVE) of the beam using periodic boundary conditions along beam axis direction [Kirsch et al., 2018]. The RVE is a 3D mesh written in Abaqus input format.

On the aerodynamic side, the unsteady two-dimensional finite state approximation model devel-

Table 1: Patil wing flutter speed and frequency [Kirsch et al., 2020].

program	Undeformed wing		Deformed wing	
	speed	frequency	speed	frequency
	<i>m/s</i>	<i>rad/s</i>	<i>m/s</i>	<i>rad/s</i>
present ($N = 10$; $N_S = 6$)	32.2	22.6	23.3	11.9
NATASHA [Patil, 1999]	32.2	22.6	-	-
UM/NAST [Shearer and Cesnik, 2007]	32.2	22.6	23.2	10.3
Aeroflex [Ribeiro et al., 2012]	32.6	22.3	23.4	12.2

oped by Peters et al. [Peters et al., 1995] is used and directly introduced in the weak formulation in order to obtain a tightly coupled aeroelastic model.

The resulting formulation permits different applications both in time domain and frequency domain. The capabilities of the resulting program are summarized in figure 2. A particular aspect of this computation code is its capability to quickly compute critical speeds, thanks notably to a modal resolution strategy based on the computation of only a few modes of interest using Arpack modal solver, and the use of sparse matrix .

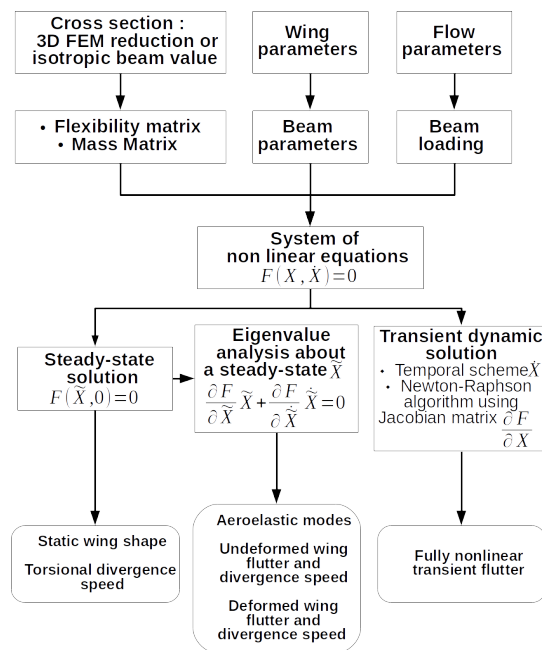


Figure 2: GEBTAero computation features [Kirsch et al., 2020].

The validation of the code has been carried out on two cases. The first one is the Goland wing, which is widely used in the literature but which is not representative of VFA. The Patil wing [Patil, 1999] proposes a more suitable test case to assess the impact of geometrical non linearities on VFA behavior, but still with an isotropic wing. GEBTAero gives successful results for both cases as it can be seen for the Patil wing in the Tab. 1 in comparison with other simulation tools. Fig. 3 shows an illustration of a temporal simulation.

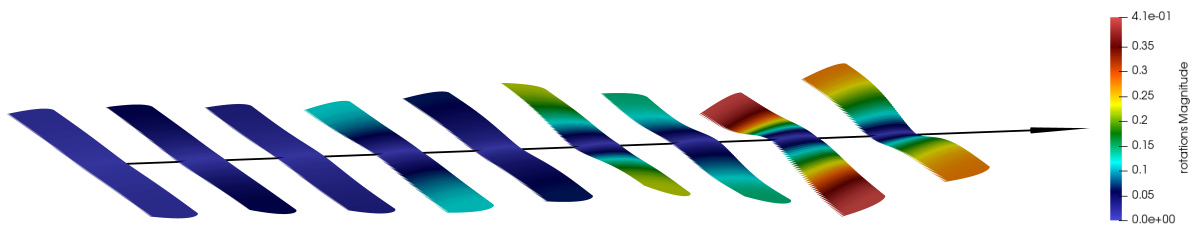


Figure 3: Real time flutter instability of the Patil wing; altitude = 20 km; velocity = 38 m/s [Kirsch et al., 2020].

3 Wind tunnel tests and comparison with simulation

3.1 Experimental setup

The experimental campaign is conducted in a wind tunnel with a test section of $450 \times 450 \times 700$ mm and a speed range from 5 to 45 m/s. The flat plate is mounted using a 3D printed device linked to the side wall of the wind tunnel. The AoA is adjustable using a rotating disk mounted on an axis (Fig. 4). Thereafter, all the tests are done with an AoA set to zero. The mean flow speed is measured using a differential pressure sensor between the inlet and the outlet of the nozzle placed upstream of the test section. In order to evaluate the accuracy of flutter speeds computed by GEBTAero, this experiment focuses on the flutter boundary without the need of studying LCO. In this regard, flat plates could be a good choice. Indeed, provided that the relative thickness is small enough to avoid the need for a milled leading edge and trailing edge, flat plates are good candidates for test cases because of their simplicity. The elastic, inertial and geometrical parameters are easy to determine and the shape is adapted to aerodynamic model as long as the angle of attack remains small.

Concerning measurements, the large displacement and rotation of the plate, the flexibility and the small weight of such a plate make it difficult to choose a proper type of sensors to assess flutter speed and frequency. To tackle those constraints, two micro-accelerometers are used. They are little intrusive and allow to retrieve speed and displacement data through signal integration. They are positioned side by side at 300 mm from the wing tip in order to obtain the vertical acceleration (mean values of the two signals) and the angular acceleration (difference between the two signals scaled by the lever arm). The global setup is shown in Fig. 4.

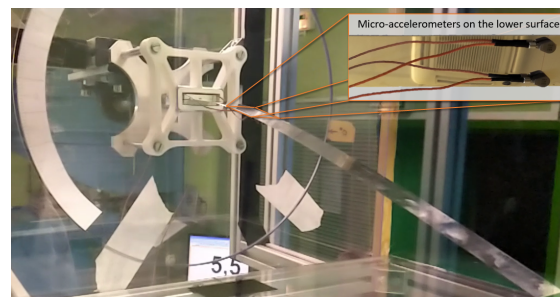


Figure 4: Aluminum plate experimental setup with micro-accelerometers on the lower surface.

3.2 Flexible aluminum plates

In [Kirsch et al., 2019], a study is proposed to find the ideal metallic plate to be representative of VFA aeroelasticity considering wind tunnel capabilities. The choice falls on the aluminum plate, with a chord of 30 mm, a thickness of 0.5 mm, and a length of 450 mm ensuring a compromise between the Reynolds number and aspect ratio.

First of all, for a half-span of 450 mm, we could mention a large flow speed hysteresis: instability starts between 11 and 11.5 m/s and stops below 7 m/s. Then, the order of magnitude difference between stable and unstable domain is large, allowing us to easily set the frontier. We can also see two harmonics typical of a non linear instability [Kirsch et al., 2019]. To assess the flutter speed and frequency correlation with numerical simulation in a more general manner, the same experiment is done for various half-span ranging from 380 mm to 450 mm. Flutter instability for half-span smaller than 380 mm is too violent and damages the plate. One measurement is made for the fundamental frequency and is compared to the second and third mode simulated by GEBTAero (figure 5a). According to the simulation, the unstable mode is the third one (in green) which corresponds, without flow, to the first twisting mode. However, the correlation with the second mode (in orange) which correspond, without flow, to the second bending mode, seems to be better.

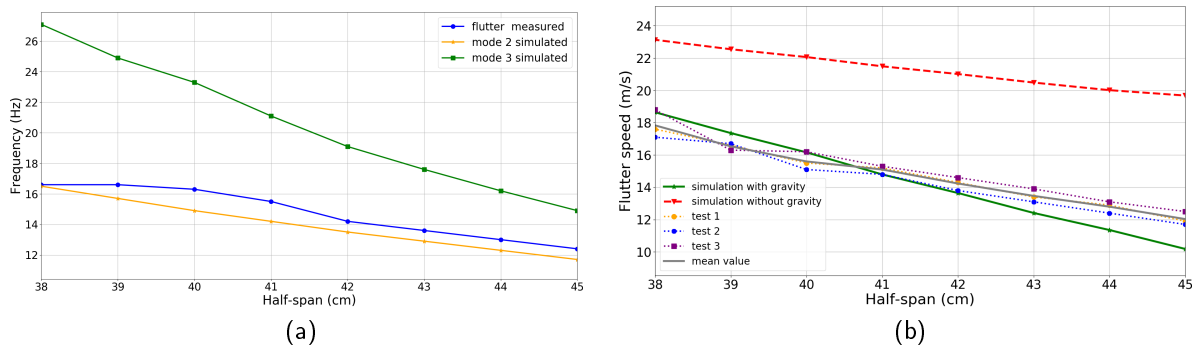


Figure 5: Comparison between experimental and numerical frequencies (a) and flutter speed (b) for a flexible aluminium plate with a section of 0.5 mm \times 30 mm and a variable length.

Concerning the flutter speed, the measurements are made on three different plates with the same dimension to assess repeatability (figure 5b). As we can see, the flutter speed is slightly underestimated for the largest values of half-span. It could be an effect of the pressure losses due to the side effect of the wind tunnel. Overall, the agreement between simulation and experiment is quite good. The repeatability is correct, however, especially for largest speeds, a very slow bending mode tends to modify the static deflection of the plate, which is a key parameter of the flutter speed.

3.3 Flexible composite plates

In order to evaluate the anisotropic capability of GEBTAero, the same type of experiment is conducted on flexible laminate plates with bending/twisting coupling. The UniDirectional (UD) prepreg used is a UD150/CHS/M10R, its characteristics are given in [Kirsch et al., 2019].

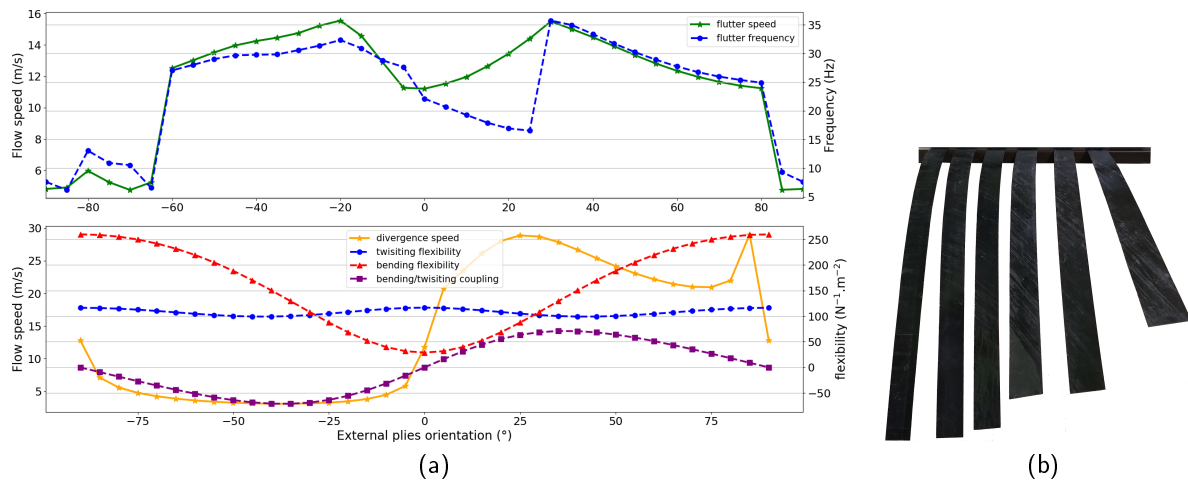


Figure 6: a) Flutter speed, frequency, divergence speed and flexibility of a 420 mm half-span composite plate with a central ply oriented at 0° and two external plies with various orientation ; b) Laminate static deflection, from left to right : $[90, 0, 90]$, $[60, 0, 60]$, $[45, 0, 45]$, $[30, -30, 30]$, $[30, 0, 30]$ and $[15, 0, 15]$.

In the same way as for metallic plates, simple solutions are seeking to produce relevant test cases. A laminate layup is defined by the orientation of its plies $[\theta_1, \dots, \theta_n]$. According to the Classical Laminate Theory (CLT), a laminate without mirror symmetry, i.e. without symmetrical plies to the middle plan with the same orientation, has a traction/twisting coupling. This coupling could be exploited in a wing box configuration, providing that the bending of the wing produces a traction or a compression of the upper side and lower side. Thin plates exploit another type of coupling, generated by unbalanced layup, i.e. without a balance between positive and negative orientation. For example, for a balanced layup, every 45° oriented ply is compensated by a -45° ply.

The simplest unbalanced layup consists in a laminate with a single orientation. Although it permits to produce a bending/twisting coupling, such a flexible plate is too fragile and may break between two fibers. The next configuration in terms of complexity is a two-ply laminate with two different fiber orientations. In that case, because mirror symmetry is not respected, the large difference between longitudinal and transverse coefficient of thermal expansion produces an undesired twisting of the plate during the cool down. Then, the simplest usable layup consists in a three-ply laminate with external plies oriented in the same direction. To obtain the proper static deflection and for sturdiness purposes, the central ply is oriented at 0° . The divergence and flutter speed, the flutter frequency and the flexibility matrix coefficients simulated by GEBTAero for different external plies orientations are plotted in figure 6a. The half-span is set to 420 mm in order to alleviate wind tunnel test section side effect.

According to the simulation, five layups are produced : $[15, 0, 15]$, $[30, 0, 30]$, $[45, 0, 45]$, $[60, 0, 60]$ and $[90, 0, 90]$, allowing to simulate various aeroelastic behaviors. A sixth one is produced to evaluate another central ply orientation, namely $[30, -30, 30]$. Theoretically, it gives us five more layup by returning the plate ($[15, 0, 15]$ becomes $[-15, 0, -15]$). In fact, negative external plies orientation implies a very low divergence speed with massive stall and is therefore unusable. To illustrate the structural coupling of this laminates, static deflection

of plates are shown in figure 6b. Beyond the obvious discrepancy in term of bending flexibility, it shows us the structural coupling between the bending due to weight and the twisting of the cross section (except from the uncoupled $[90, 0, 90]$ laminate). To produce a spectrogram, the flow speed is slowly increased until flutter instability and then decreased. The mean flow speed is plotted in the spectrogram. The results for the layups $[30, 0, 30]$ and $[30, -30, 30]$ are plotted in figure 7 and 8, compared to the aeroelastic modes plotted by GEBTAero. However, because the vacuum was not perfectly controlled during the cure process, a discrepancy exist in the laminate thickness (measured from 0.48 mm to 0.55 mm instead of the nominal 0.48 mm), while it is a key parameter in terms of aeroelastic behavior sensitivity, according to CLT, a thickness correction has been applied on the results.

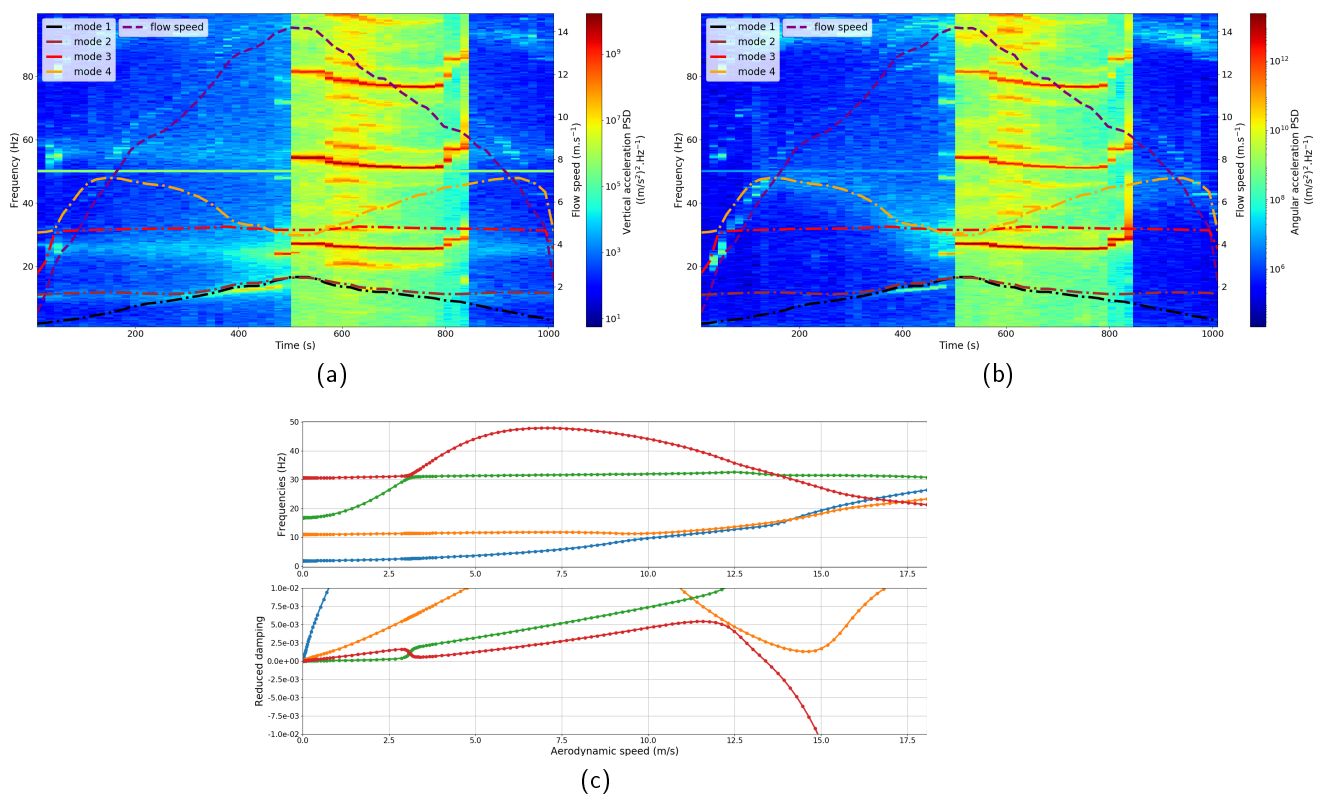


Figure 7: 420 mm half-span $[30, 0, 30]$ laminate test result: a) vertical acceleration spectrogram, b) angular acceleration spectrogram, c) GEBTAero aeroelastic modes plot.

First of all, it can be noticed that flow speed appeared in the spectrogram and can be directly linked to the rotational frequency of the fan. Secondly, the blue band area corresponding to the stable domain. A good correlation is obtain between the simulated frequencies and the experimental ones. It depends mainly on the type of mode: bending mode, torsional mode or coupled mode (e.g. mode 1 and 2 in Fig. 7 a)-b) and mode 4 only in b) ; idem in Fig. 8). Note that energy is relatively low in these modes because the excitation is only due to the motor vibrations and the airflow turbulence. Thirdly, the green/red band area corresponds to the flutter domain. This part exhibit a much more complex aeroelastic behavior. For example, Fig. 7 shows a LCO with several harmonics while Fig. 8 shows a chaotic motion. We also

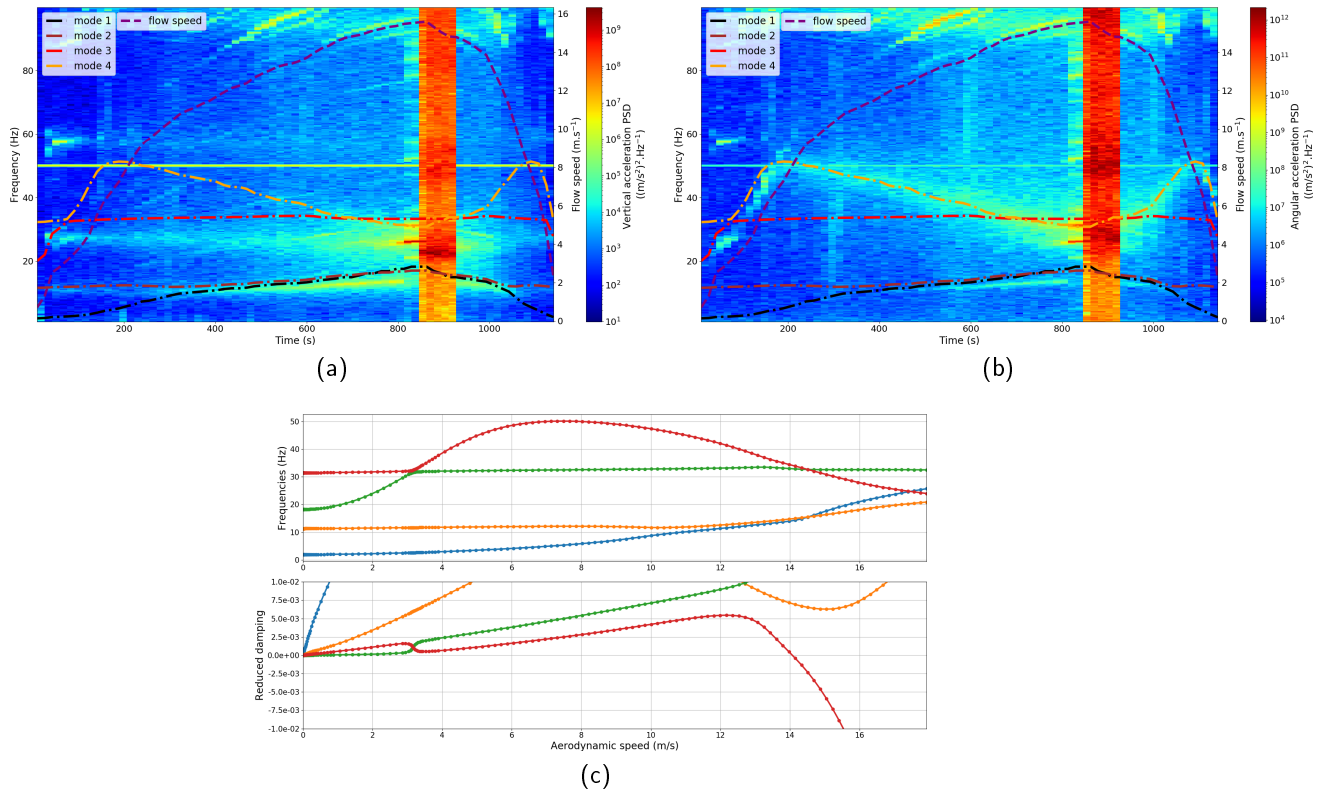


Figure 8: 420 mm half-span $[30, -30, 30]$ laminate test result: a) vertical acceleration spectrogram, b) angular acceleration spectrogram, c) GEBTAero aeroelastic modes plot.

could mention a large flutter speed hysteresis. For the $[30, 0, 30]$ plate (Fig. 7), instability starts around 14 m/s and stops around 9 m/s. To illustrate that complexity of high amplitude motion, phase portrait of the vertical degree of freedom (dof) is proposed for various laminates and speeds (Fig. 9).

Finally, flutter speeds (figure 10) are compared to the values simulated by GEBTAero for the five layups with a central ply oriented at 0° . Regarding frequencies, the first four modes are also plotted. On the one hand, for the flutter speed, the simulation tends to overestimate the value. The other remarkable point is that the bending/twisting coupling tends to compensate the effect of the large deflection due to gravity in terms of flutter speed. $[90, 0, 90]$ laminate is the only one impacted by this static deflection.

4 Conclusion

Design challenges induced by HAPS in terms of aeroelastic performances show the need for an accurate reduced order model able to simulate non linear behavior of an anisotropic high-aspect-ratio wing. The present work presents a solution based of the geometrically exact beam theory coupled with a two-dimensional unsteady finite state aerodynamic model implemented into an open source solver. In addition, to emphasize geometrical non linearities and anisotropic capabilities, a wind tunnel campaign is conducted. For the sake of simplicity, flexible metallic and

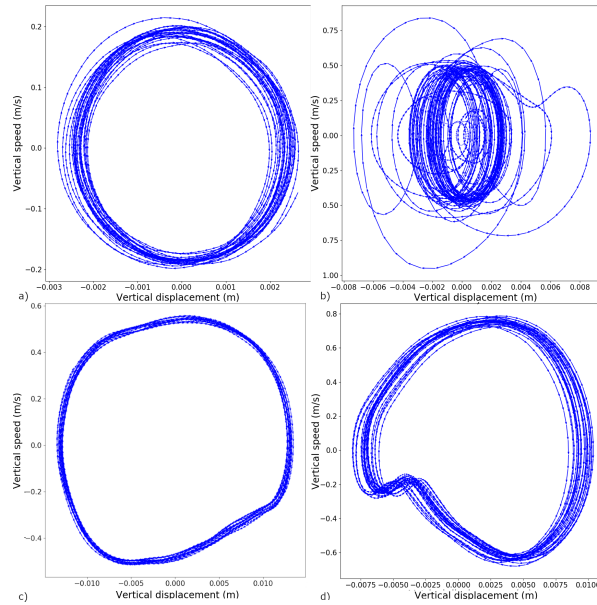


Figure 9: LCO of 420 mm half-span composite plate for various laminates and speeds: a) [15, 0, 15] at 9.9 m/s 550s; b) [15, 0, 15] at 12 m/s ; c) [90, 0, 90] at 5.3 m/s ; d) [60, 0, 60] at 6 m/s.

composite flat plates are tested, the latter with the simplest layup exhibiting bending/twisting coupling, namely a three-ply laminate with external plies oriented in the same direction. Experimental results show a good agreement, especially for metallic plates. Furthermore, composite plate experiments highlight the complex behavior of such anisotropic flexible wings, with highly coupled aeroelastic modes leading to various kind of LCO and large flutter speed hysteresis.

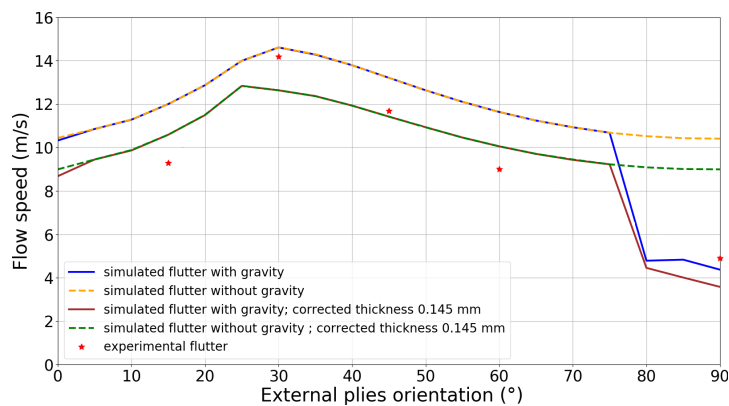


Figure 10: Flutter speed of a 420 mm half-span $[\theta, 0, \theta]$ carbon epoxy laminate: computation versus experimental wind tunnel tests

References

- [Cartraud and Messenger, 2006] Cartraud, P. and Messenger, T. (2006). Computational homogenization of periodic beam-like structures. *International Journal of Solids and Structures*, 43(3-4):686–696.
- [Hodges, 1990] Hodges, D. H. (1990). A mixed variational formulation based on exact intrinsic equations for dynamics of moving beams. *International journal of solids and structures*, 26(11):1253–1273.
- [Kirsch et al., 2018] Kirsch, B., Montagnier, O., Bénard, E., and Faure, T. (2018). Assessment of aeroelastic tailoring effect on high-aspect-ratio composite wing flutter speed using an open source reduced order model solver. In *18 th European Conference on Composite Materials*, pages 24 – 28, Athens, Greece.
- [Kirsch et al., 2020] Kirsch, B., Montagnier, O., Bénard, E., and Faure, T. M. (2020). Tightly coupled aeroelastic model implementation dedicated to fast aeroelastic tailoring optimisation of high aspect ratio composite wing. *Journal of Fluids and Structures*, in press.
- [Kirsch et al., 2019] Kirsch, B., Montagnier, O., Faure, T. M., and Bénard, E. (2019). Numerical and experimental study of aeroelastic tailoring effect using flexible composite laminates for haps application. In *Proceedings of International Forum on Aeroelasticity and Structural Dynamics*, Savannah, Georgia.
- [Murua et al., 2012] Murua, J., Palacios, R., and Graham, J. M. R. (2012). Assessment of wake-tail interference effects on the dynamics of flexible aircraft. *AIAA Journal*, 50(7):1575–1585.
- [Patil, 1999] Patil, M. J. (1999). *Nonlinear aeroelastic analysis, flight dynamics, and control of a complete aircraft*. PhD thesis, Citeseer.
- [Patil and Hodges, 2006] Patil, M. J. and Hodges, D. H. (2006). Flight dynamics of highly flexible flying wings. *Journal of Aircraft*, 43(6):1790–1799.
- [Peters et al., 1995] Peters, D. A., Karunamoorthy, S., and Cao, W.-M. (1995). Finite state induced flow models. I-Two-dimensional thin airfoil. *Journal of Aircraft*, 32(2):313–322.
- [Ribeiro et al., 2012] Ribeiro, F. L. C., Paglione, P., da Silva, R. G. A., and de Sousa, M. S. (2012). Aeroflex: a toolbox for studying the flight dynamics of highly flexible airplanes. In *VII Congresso Nacional de Engenharia Mecânica*, São Luís - Maranhão, Brasil.
- [Shearer and Cesnik, 2007] Shearer, C. M. and Cesnik, C. E. (2007). Nonlinear flight dynamics of very flexible aircraft. *Journal of Aircraft*, 44(5):1528–1545.
- [Tang and Dowell, 2016] Tang, D. and Dowell, E. (2016). Experimental aeroelastic models design and wind tunnel testing for correlation with new theory. *Aerospace*, 3(2):12.
- [Yu and Blair, 2012] Yu, W. and Blair, M. (2012). GEBT: A general-purpose nonlinear analysis tool for composite beams. *Composite Structures*, 94:2677–2689.

Flutter (blade, wind turbine, propeller)

Study on influence of tip vortex on aerodynamic noise of half ducted propeller fan for air conditioner

Taku Iwase¹, Tetsushi Kishitani²

¹*Research & Development Group, Hitachi, Ltd., 832-2, Horiguchi, Hitachinaka, Ibaraki, Japan, taku.iwase.mf@hitachi.com*

²*Global Product Department, Hitachi-Johnson Controls Air Conditioning, Inc., 390, Muramatsu, Shimizu-ku, Shizuoka, Japan*

Abstract

Flow fields in 2-blade and 4-blade half-ducted propeller fans for the outdoor units of air conditioners were calculated with finite element method-based large eddy simulation with the aim of investigating what influence of tip vortex had on aerodynamic noise in this study. Increase of aerodynamic noise is an indication of blade vibration. Prediction and understanding mechanism of aerodynamic noise are therefore useful knowledge for suppression of vibration induced by tip vortex. The aerodynamic noise of 2-blade propeller fan was smaller than that of the 4-blade. We already confirmed that the tip vortex (TV) had a great influence on half-ducted propeller fans in the previous paper. In this study, we confirmed that the minimum distance between the TV and the adjacent blade or the bell mouth, and the vorticity at the point were dominant parameters in the aerodynamic noise.

Keyword: propeller fan, tip vortex, aerodynamic noise, large eddy simulation

1 Introduction

Development of silent air conditioners is one of the most important problems in recent changes of life-styles. Aerodynamic noise from fans contributes to a large percentage of the overall noise from air conditioners. Therefore, the development of silent fans would contribute to reducing the noise levels of air conditioners. Moreover, increase of aerodynamic noise is an indication of blade vibration. Prediction and understanding mechanism of aerodynamic noise are therefore useful knowledge for suppression of vibration induced by tip vortex. Under this demand, we have developed the silent fan by decreasing the blade number from 4-blade to 2-blade (Funabashi et al., 2004). The noise level of the 2-blade propeller fan was smaller than that of the 4-blade propeller fan experimentally at an operating flow rate.

The fans in many air conditioners with outdoor units have a casing that only covers the near region of the propeller tips. As a result, part of the blade tip near its leading edge is open to the upstream. These propeller fans are called half-ducted propeller fans. They have a very complicated flow field near the propeller tips.

Half-ducted propeller fans have been mainly developed by using experimental methods. Predictions of aerodynamic noise were based on estimates from static flow field characteristics and experimental coefficients (Hakamaya et al., 1999). However, it is difficult to develop radically silent fans by using traditional methods. We therefore need new methods of predicting aerodynamic noise for understanding the mechanism and developing

silent fans. Computational Fluid Dynamics (CFD) is a powerful tool for solving these needs. Many researchers have studied flow fields by using Large Eddy Simulation (LES) (Kato et al., 2003; Yamade et al., 2006; Reese et al., 2007; Jang et al., 2001).

Many researchers have also studied the development of silent fans. Beiler et al.(1999) analyzed blade-to-blade flow fields by using CFD and hot wire, and they developed a silent fan with skewed blades. Okamoto et al.(2009) proposed an optimized blade shape for a propeller fan by using an inverse design method and CFD. Sugio(2003) optimized blade number of propeller fan. Ito et al.(2009) investigated influences of blade tip clearance, treatment of outlet roundness, and spoke skew for small axial fan. However, there were few studies about detail investigation on the relationship between tip vortex and aerodynamic noise.

The final goal of our study was aimed at designing silent fans. Authors (Iwase et al., 2017) already investigated the influence of blade number on aerodynamic noise of half ducted propeller fan. In this study, further investigations were therefore implemented to analyze the influence of tip vortex on aerodynamic noise.

2 Methods of numerical simulations

2.1 Test fan

This study was carried out on the half-ducted propeller fans used in the outdoor units of air conditioners. 2-blade and 4-blade propeller fans were intended as same as the previous paper (Iwase et al., 2017). Figure 1 shows configuration of the propeller fan and the bell mouth. The propeller tip diameter was 644 mm. The tip clearance was 10 mm. The noise level of the 2-blade propeller fan was smaller than that of the 4-blade propeller fan experimentally at an operating flow rate.

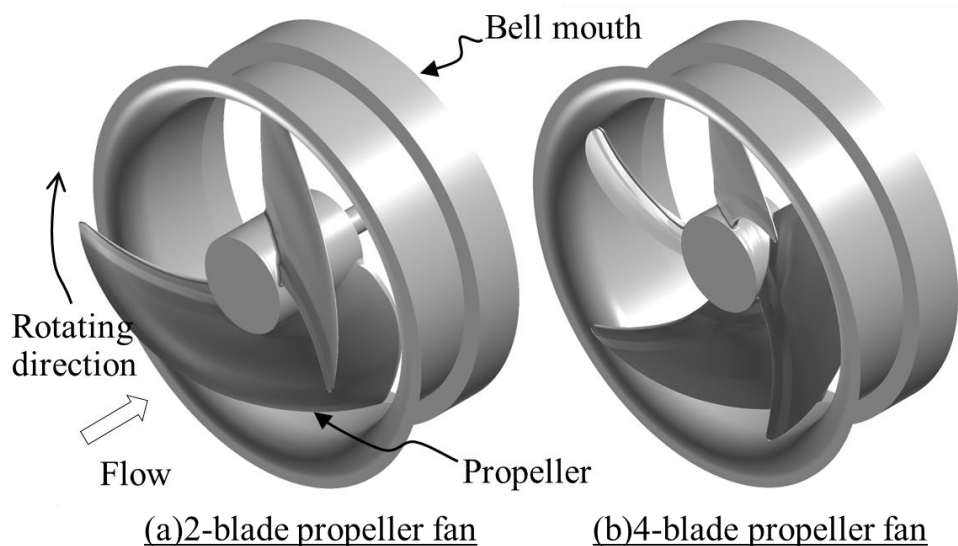


Figure 1: Configuration of propeller fan and bell mouth.

2.2 Large eddy simulation and computational conditions

The numerical simulation code we employed throughout the LES was FrontFlow/blue (FFB) as same as the previous paper (Iwase, et al., 2017). The FFB was developed by Kato et al.(2003, 2005). The FFB has been successfully used for simulating several axial flow fans (Iwase, et al., 2017; Yamade et al., 2006; Reese et al., 2007). The governing equations are the spatially filtered continuity equation and the Navier Stokes equation for the flow of an incompressible fluid. The effects of eddies that are not resolved by the grid (sub-grid scale eddies) are modeled by the dynamic Smagorinsky model (Germano et al., 1991; Lilly, 1992).

Figure 3 shows computational models. The computational model was the same as the previous paper. The number of grid elements was 10,619,900 in the 2-blade propeller fan. The number of grid elements was 10,888,908 in the 4-blade propeller fan. Each computational model consists of three parts, i.e., the inlet, propeller, and outlet parts. The propeller part is in the rotating frame of reference. The inlet and the outlet parts are in the stationary frames. The grid is composed of hexahedral elements. The calculated flow rate was 100 m³/min, which was operating flow rate. The rotational speed was 550 rpm. The time steps per a single revolution of propeller was 4,096.

The previous paper described the specification in detail.

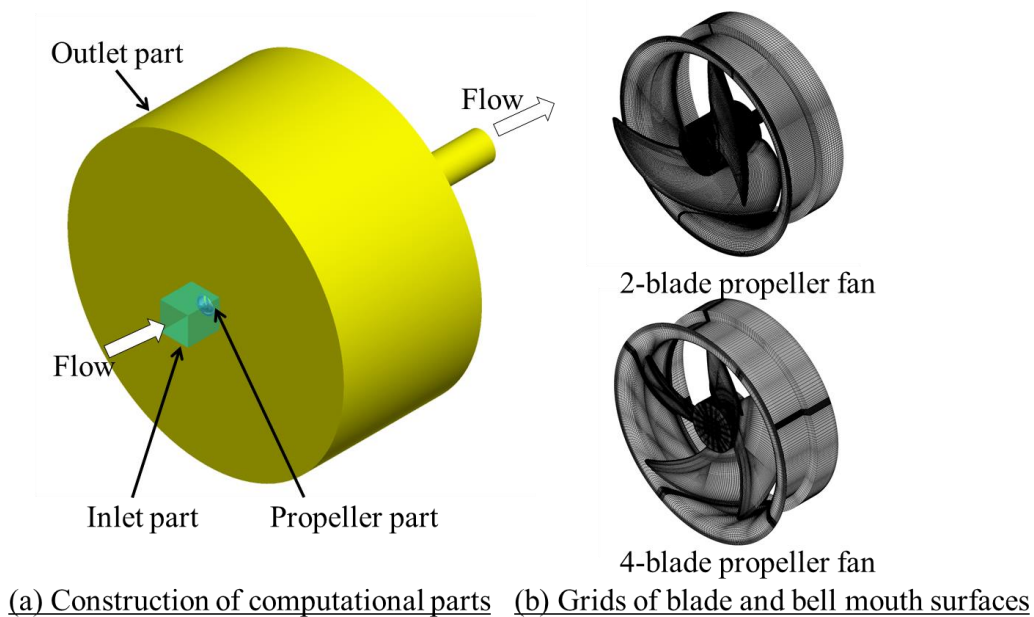


Figure 2: Computational models.

3 Results and discussions

3.1 Relationship between tip vortex and adjacent blade

In the previous paper (Iwase, et al., 2017), we already confirmed that the calculated static pressure rise and the shaft power reasonably agreed with the experimental results, and the tendency of the aerodynamic noise could be calculated qualitatively. We also confirmed that tip vortex (TV) had a great influence on flow structure in the half ducted propeller fans. The influence on aerodynamic noise on the tip vortex was therefore investigated by analyzing further the calculated results.

Figure 3 shows vortex cores colored with normalized helicity and streamline around TV colored with vorticity. The trajectory of the vortex center was identified with a semi-analytic method, which was based on critical-point theory, to enable the complicated flow field in the propeller fans to be better understood. It was possible to visualize the vortex core according to this method. Normalized helicity H_n was evaluated along the vortex cores to quantitatively analyze the nature of the vortex. The normalized helicity corresponds to the cosine of the angle between absolute vorticity and relative velocity. If $H_n = \pm 1$, this indicates there is a vortex core for the longitudinal vortex in the region. These visualizations of the vortex core and normalized helicity are useful tools for investigating the flow field of turbomachinery. Jang et al.(2001) and Kusano et al.(2011) give detail information of the visualization methods. The vorticity was normalized by the tip speed and density.

The tip vortex (TV) rolled up from the tip near the leading edge. Streamlines are displayed by showing around one of the TVs. The normalized helicity along the TV maintained almost $H_n = +1.0$, and the TV passed through the blade-to-blade passage. These TV flow structures are typical flow fields in the half ducted propeller fan. The length of the TV trajectory and the blade pitch for the 2-blade propeller fan were longer than those for the 4-blade propeller fan. The vorticity strength of the TV near the adjacent blade for the 2-blade propeller fan was weaker than that for the 4-blade propeller fan. Because the vorticity strength of the TV for the 2-blade propeller fan decayed greatly as the flow went downstream.

Figure 4 shows a comparison of static pressure fluctuations on the pressure surface. The pressure fluctuations are normalized by the tip speed and the density. The pressure fluctuation near the tip of the trailing edge of the 2-blade propeller fan was weaker than that of the 4-blade propeller fan. Because the weaker TV vorticity strength and the longer distance were suppressed the interaction between the TV and the adjacent blade in the 2-blade propeller fan. Aerodynamic noise was related to unsteady force according to Curle's equation defined by equation (1) (Howe, 2003).

$$p_d \approx \frac{x_i}{4\pi c_0 |x|^2} \frac{dF_i}{dt} \left(t - \frac{|x|}{c_0} \right) \quad (1)$$

Here, p_d is the dipole sound pressure, c_0 is the sound speed, x_i is the observation point, t is the time, and F_i is the unsteady force exerted on the fluid by the body. In this study, the body was the impeller. The aerodynamic noise was calculated at the same point as the measured one, 1 m away from the impeller on the rotating axis. The unsteady force was caused by the pressure fluctuations. Weaker pressure fluctuations made the 2-blade propeller fan more silent than the 4-blade propeller fan.

Figure 5 shows a comparison of distance between the TV and the adjacent blade. La indicates the distance shown in Figure 3. Horizontal axis indicates a tangential coordinate, the product of radius R and angle θ . The distance has a minimum value in each propeller fan. The minimum value in the 2-blade propeller fan was four times longer than that in the 4-blade propeller fan.

Figure 6 shows a relationship between the minimum distance of the TV and the adjacent blade, the vorticity at the minimum distance point, and the aerodynamic noise. The aerodynamic noise showed the experimental results. The distance was so far that the aerodynamic noise was small. Moreover, the vorticity was so small that the aerodynamic noise was also small. As a result, the minimum distance between the TV and the adjacent blade, and the vorticity at the point were dominant parameters in the aerodynamic noise.

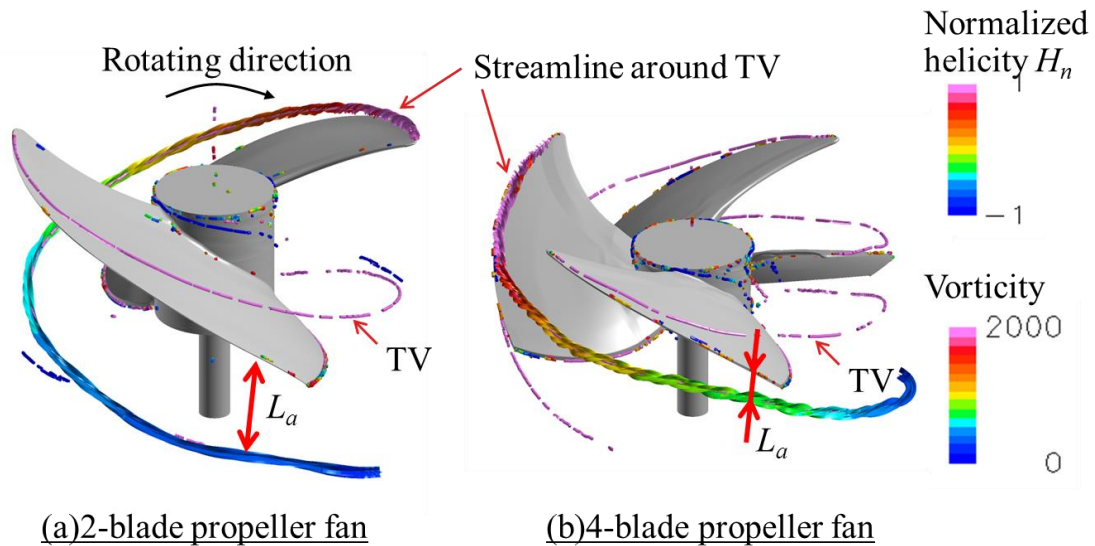


Figure 3: Vortex cores colored with normalized helicity and streamline around TV colored with vorticity.

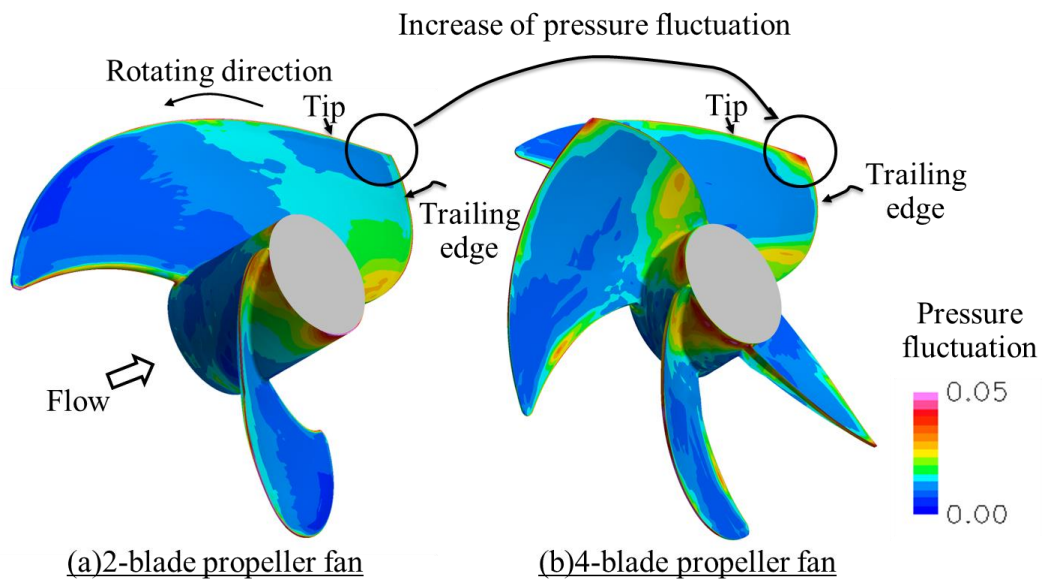


Figure 4: Comparison of static pressure fluctuations on pressure surface.

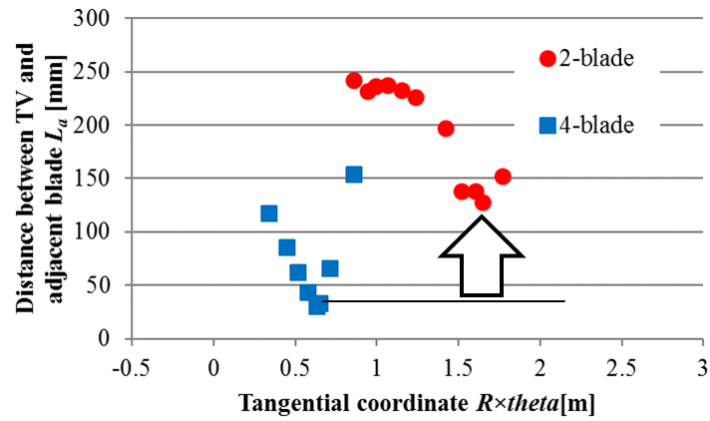


Figure 5: Comparison of distance between TV and adjacent blade.

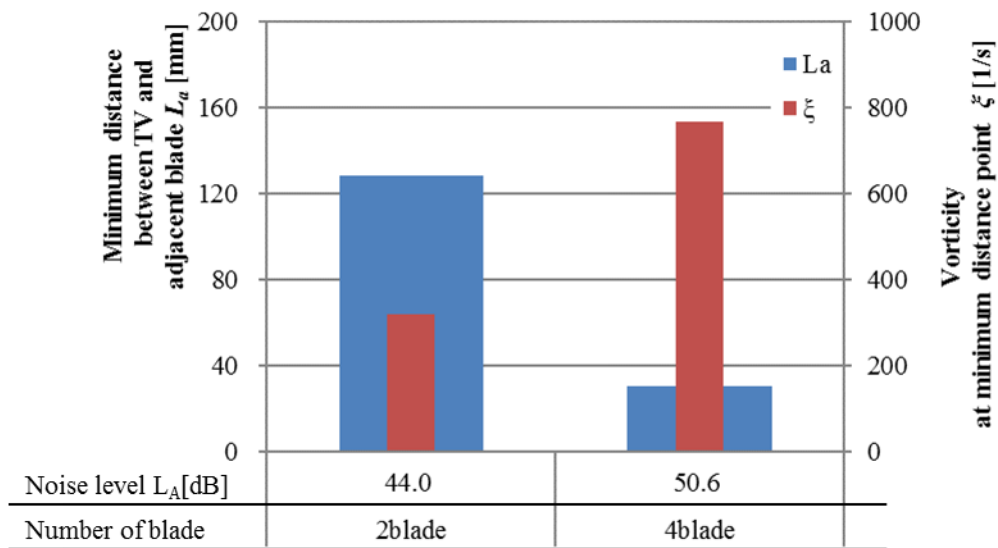


Figure 6: Relationship between minimum distance of TV and adjacent blade, vorticity at the minimum distance point, and aerodynamic noise.

3.2 Relationship between tip vortex and bell mouth

Figure 7 shows relationship between TV colored with vorticity and bell mouth. A blade length of the 2-blade propeller fan was longer than that of the 4-blade propeller fan. The point at which TV rolled up was therefore far from the inlet of the bell mouth in the 2-blade propeller fan. The vorticity strength of the TV near the inlet of the bell mouth of the 2-blade propeller fan was weaker than that of the 4-blade propeller fan. Because the vorticity strength of the TV decayed greatly as the flow went downstream. Circle A was the region in the minimum distance between the TV and the bell mouth.

Figure 8 shows a relationship between the minimum distance of the TV and the bell mouth, the vorticity at the minimum distance point, and the aerodynamic noise. L_b indicates the distance shown in Figure 7. As with the relationship between the TV and the adjacent blade, the distance was so far that the aerodynamic noise was small. Moreover, the vorticity was so small that the aerodynamic noise was also small. As a result, the minimum distance between the TV and the bell mouth, and the vorticity at the point were dominant parameters in the aerodynamic noise.

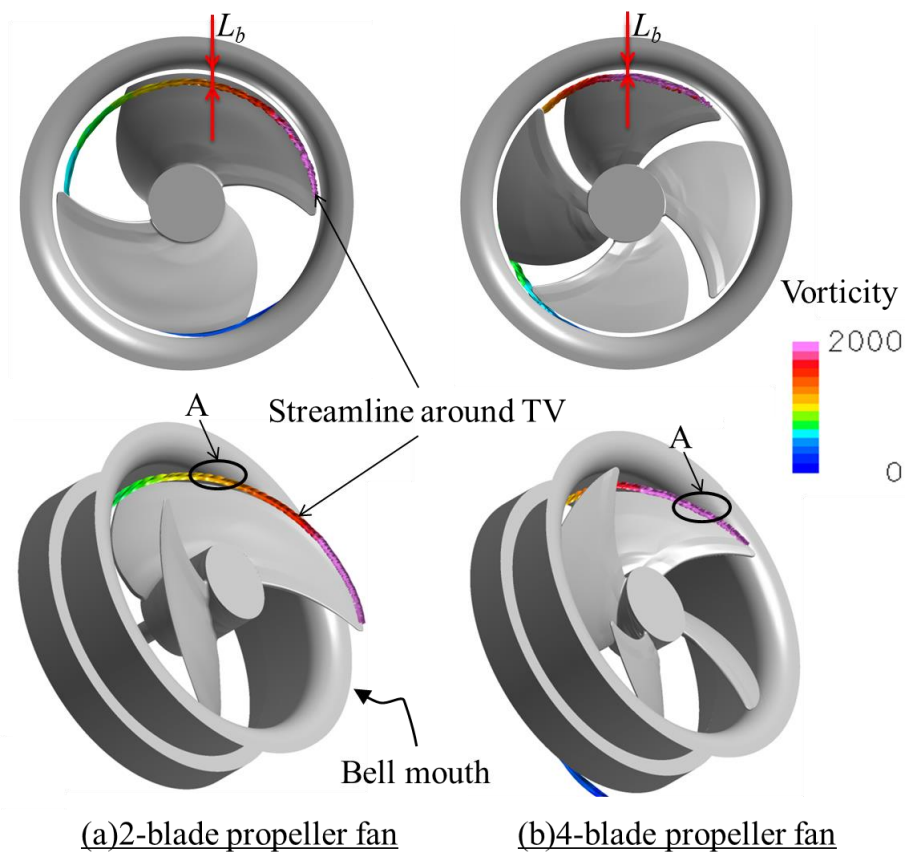


Figure 7: Relationship between TV colored with vorticity and bell mouth.

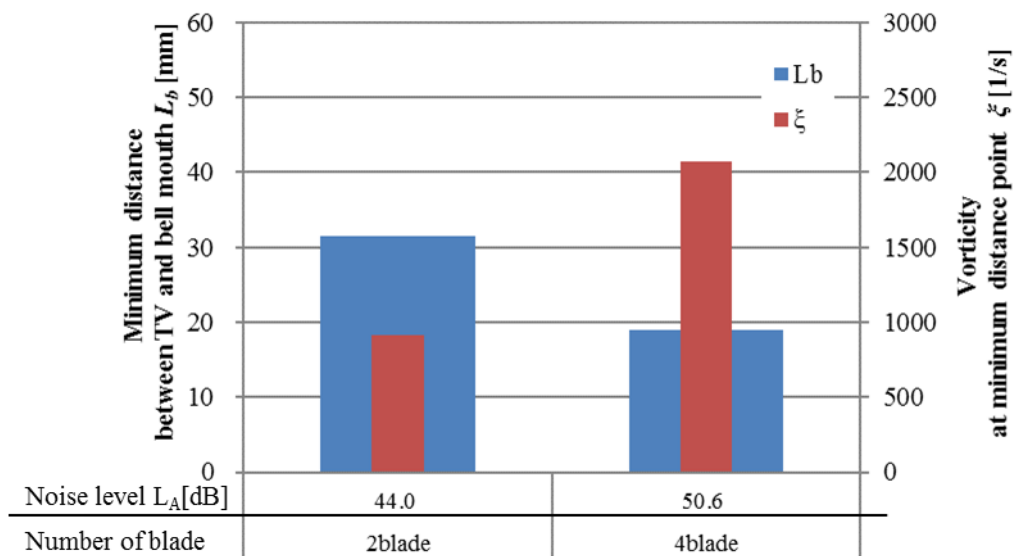


Figure 8: Relationship between minimum distance of TV and bell mouth, vorticity at the minimum distance point, and aerodynamic noise.

4 Conclusions

Flow fields in the half-ducted propeller fans for the outdoor units of air conditioners were calculated with Large Eddy Simulation based on finite element method with the aim of investigating the influence of tip vortex on aerodynamic noise in this study. Flow structure and aerodynamic noise of 2-blade and 4-blade propeller fans were studied. The three main results can be summarized as follows:

- (1) The minimum distance between the tip vortex and the adjacent blade, and the vorticity at the point were dominant parameters in the aerodynamic noise.
- (2) The minimum distance between the tip vortex and the bell mouth, and the vorticity at the point were also dominant parameters in the aerodynamic noise.

References

- Beiler, M. G., Carolus, T., 1999, Computation and Measurement of the Flow in Axial Flow Fans with Skewed Blades, ASME Journal of Turbomachinery, Vol.121, 59-66.
- Funabashi, S., Iwase, T., Sato, R., Kishitani, T., Nagai, M., 2004, Two-blade Propeller Fan for Packaged Air Conditioners, Proceedings of The International Symposium on New Refrigerants and Environmental Technology.
- Germano, M., Piomelli, U., Moin, P., Cabot, W. H., 1991, A Dynamic Subgrid-Scale Eddy-Viscosity Model, Physics of Fluids A, Vol. 3, No. 7, 1760-1765.
- Hakamaya, N., Funabashi, S., Takada, Y., 1999, A Model for Predicting Noise of Propeller Fans in Air Conditioners, Transactions of the Japan Society of Mechanical Engineers, Series B, Vol.65, No.640, 4015-4020.
- Howe, M. S., 2003, Theory of Vortex Sound, Cambridge Texts in Applied Mathematics, Cambridge University Press.
- Ito, T., Minorikawa, G., Fan, Q., 2009, Experimental Research for Performance and Noise of Small Axial Fan, International Journal of Fluid Machinery and Systems, Vol.2, No.2, 136-146.
- Iwase, T., Kishitani, T., Furukawa, M., 2017, Study on Influence of Blade Number on Aerodynamic

- Noise of Half-ducted Propeller Fan for Packaged Air-conditioners, *International Journal of Fluid Machinery and Systems*, Vol.10, No.4, 318-327.
- Jang, C. M., Furukawa, M., Inoue, M., 2001, Analysis of Vortical Flow Field in a Propeller Fan by LDV Measurements and LES Part 1: Three-Dimensional Vortical Flow Structures, *Transactions of the ASME, Journal of Fluids Engineering*, Vol.123, No.4, 748-754.
- Kato, C., Kaiho, M., Manabe, A., 2003, An Overset Finite Element Large Eddy Simulation Method with Application to Turbomachinery and Aeroacoustics, *J. Appl. Mech.*, Vol. 70, 32-43.
- Kato, C., Yamade, Y., Wang, H., Guo, Y., Miyazawa, M., Takaishi, T., Takano, Y., 2005, Numerical Prediction of Sound Generated from Flows with a Low Mach Number, *Computers & Fluids*, Vol. 36, No. 1, 53–68.
- Kusano, K., Jeong, J. H., Yamada, K., Furukawa, M., 2011, DETACHED EDDY SIMULATION OF UNSTEAD FLOW FIELD AND PREDICTION OF AERODYNAMIC SOUND IN A HALF-DUCTED PROPELLER FAN, AJK2011-22048, *Proceedings of the ASME-JSME-KSME Joint Fluids Engineering Conference*.
- Lilly, D. K., 1992, A proposed modification of the Germano subgrid-scale closure model, *Physics of Fluids A*, Vol.4, No.3, 633-635.
- Okamoto, H., Goto, A., Furukawa, M., 2009, DESIGN OF A PROPELLER FAN USING 3-D INVERSE DESIGN METHOD AND CFD FOR HIGH EFFICIENCY AND LOW AERODYNAMIC NOISE, FEDSM2009-78454, *Proceedings of the ASME 2009 Fluids Engineering Division Summer Meeting*.
- Reese, H., Carolus, T., Kato, C., 2007, Large Eddy Simulation of Acoustical Sources in a Low Pressure Axial-Flow Fan Encountering Highly Turbulent Inflow, *Transactions of the ASME, Journal of Fluids Engineering*, Vol.129, 263-272.
- Sugio, T., 2003, 2 Wings Mixed Flow Fan for the Outdoor Unit of a Room Air Conditioner, *Turbomachinery, Turbomachinery Society of Japan*, Vol.31, No.9, 520-524.
- Yamade, Y., Kato, C., Shimizu, H., Nishioka, T., 2006, Large Eddy Simulation and Acoustical Analysis for Prediction of Aeroacoustics Noise Radiated from an Axial-flow Fan, FEDSM2006-98303, *Proceedings of the ASME 2006 Fluids Engineering Division Summer Meeting*.

The investigation of the design parameters influence on blade flutter boundaries

Farrukh Abdukhakimov¹, Mikhail Kolotnikov², Pavel Makarov³ and Vasily Vedeneev¹

¹*Lomonosov Moscow State University, 1 Michurinskii prospect, Moscow 119192, Russia, farruh.abduhakimov7@gmail.com*

²*REP Holding, 51 AF, Obukhovskoy Oborony Pr., Sainkt-Petersburg 192029, Russia*

³*“Salut” Gas Turbine Engineering Research and Production Center, 16 Budionny Ave, Moscow 105118, Russia*

Keyword: blade flutter, energy method, compressor, gas-turbine engine.

Blade flutter is one of the main issues that designers of modern gas-turbine engines and steam turbines encounter. As a rule, blade flutter is analysed using simplified empirical criteria obtained based on the experience of design and testing of engines.

In this paper we study the effect of several design parameters on prediction of blade flutter in compressors of gas-turbine engines: the radial gap between the blade and the casing, the axial gap between the guide vane and the blade, the guide vane angle, the inlet pressure non-uniformity, and the mounting tension force in the blade shroud. Simplified empirical and probabilistic criteria are not applicable to evaluation of these parameters, which is why a numerical algorithm for flutter prediction based on the energy method is used.

The numerical algorithm is as follows [1]. We assume that the influence of the airflow on the blade natural modes is insignificant and leads only to aerodynamic damping, positive or negative; a condition that is almost always met for compressor blades. Therefore we can compute natural mode shapes and frequencies using standard methods and then simulate unsteady flow at given oscillations of the blade. As a result, the work done by unsteady pressure over one oscillation cycle is calculated (Eq. 1):

$$W = \int_{t_0}^{t_0+T} \int_S p(x, y, z, t) \mathbf{n}(x, y, z, t) \mathbf{v}(x, y, z, t) ds dt, \quad (1)$$

where T is the oscillation period of the blade, S is the blade surface, p is the pressure, \mathbf{n} is the normal to the blade surface, and \mathbf{v} is the velocity of the blade points. We neglect the viscous stresses in the air, because they usually do not affect the flutter boundaries. With this approach the flutter criterion is the sign of the work W .

The airflow model consists of three successive blade passages of one wheel. To calculate the transient airflow, the initial and boundary conditions are set from the steady flow calculated for the whole compressor and verified by full-scale engine tests. Mesh displacement in the form of travelling wave corresponding to the wheel natural mode with a specified number of nodal diameters is applied to each blade surface.

It is shown that the inter-blade tension has a significant influence on the flutter boundaries, while the effect of other design parameters under investigation is minor. The results can be used for efficient flutter suppression in compressor and turbine blades.

The work is supported by RFBR grants 18-01-00404 and 18-31-20057.

1. Vasily V. Vedeneev, Mikhail Kolotnikov, Pavel Makarov. Experimental validation of numerical blade flutter prediction// Journal of propulsion and power. 2015. Vol. 31. No. 5. P. 1281-1291.

Experimental Evidence of Coupled-Mode Flutter in Relatively Large-Scale Wind Turbine Blades

Pieter Boersma¹, Bridget Benner¹, Todd Currier¹, Yahya Modarres-Sadeghi¹

¹*University of Massachusetts Amherst, Amherst, USA, modarres@engin.umass.edu*

Keyword: coupled-mode flutter, wind turbine blade

Coupled-mode flutter in wind turbine blades has been investigated theoretically, with evidence suggesting that it can occur in wind turbine blades when the third flapwise and the first torsional modes are coupled.¹ Despite this prediction, coupled-mode flutter has not been observed experimentally in full-scale or small-scale wind turbine blades. Here, we present experimental evidence of coupled-mode flutter in a parked wind turbine blade, which is a scaled down version of the NREL 5 MW wind turbine blade. The original NREL 5 MW design has a length of ~61 meters, and the scaled down version that we have built for the present tests had a length of ~2 meters. The length of the blade was dictated by the size of the test section in the wind tunnel where we conducted the tests. While the two-meter blade is much smaller than the original NREL 5 MW blade, it is still considered rather large-scale for typical small-scale experiments. We designed and built the model blade such that the ratios of its flapwise natural frequencies to the first torsional natural frequency remained the same as those of the original blade. The blade was placed in the test section of the Wall of Wind's wind tunnel (located at the Florida International University) with a test section of 4.3 m x 6 m and a maximum wind speed of 60 m/s. The blade was clamped at its root and could not rotate, resembling a wind turbine blade that is parked in anticipation of severe weather.

The response of the blade was measured through two bending and one torsion strain gauges along the length of the blade and two accelerometers at the tip of the blade measuring accelerations in the flapwise and edgewise directions. Argand diagrams were produced from the strain gauge data for wind speeds before the onset of instability and it was observed that the third bending and the first torsional frequencies moved toward each other as the wind speed was increased and merged at a critical wind speed, giving rise to coupled mode flutter. Amplitude plots showed increasing displacement amplitudes for increasing wind speeds for wind speeds larger than the critical one. Oscillations were observed through the length of the blade, where a combination of flapwise and torsional motions was visible in the response. For very large wind speeds, oscillations purely in the torsional direction were observed, suggesting the possibility of stall flutter at these wind speeds.

1. Pourazarm, P., Modarres-Sadeghi, Y., & Lackner, M. (2016). A parametric study of coupled-mode flutter for MW-size. *Wind Energy*, 19, 497–514.

Numerical investigation of flutter in low-speed transonic fan

Quentin Rendu¹ and Mehdi Vahdati²

¹ *Mechanical Engineering, Imperial College, London, UK, q.rendu@imperial.ac.uk*

² *Mechanical Engineering, Imperial College, London, UK*

Keyword: fan flutter, linear aeroelasticity, turbomachinery

Due to large diameter and 3D design, modern jet engines fan blades are more prone to flutter. Two contributions drive stall flutter events: (i) the variation of incidence due to reflected acoustic waves upstream of the fan, which can be modelled by 1D acoustic model and (ii) the competition of shock-waves, pressure waves and boundary layer separation due to the blade's vibration. This work contributes to the understanding of this second contribution.

An Unsteady Reynolds-Averaged Navier-Stokes (URANS) compressible solver with moving grid is used to compute the unsteady flow around a vibrating fan blade over a large range of rotational speeds. Harmonic displacement of the blade is imposed in first flap mode with two nodal diameters.

Aerodynamic damping coefficient is plotted along mass-flow in Fig. 1 for different rotational speeds. All the rotational speeds exhibit positive aerodynamic damping close to design speed, which denotes aeroelastic stability, and negative damping close to stall, in the flutter bite region. Insights on the onset of flutter are obtained by analysing the local work distribution and by decomposing the modeshape in the radial direction. At high-speed ($M_{tip} = 1.13$), the destabilising shock-wave contribution decreases with mass-flow, reaches a minimum and increases. The source of this non-monotonic behaviour is the phase variation of the pressure waves generated at the trailing edge (two-dimensional mechanism). At part-speed ($M_{tip} = 0.91$), pressure wave generated below the shock-wave migrate radially toward the tip, where they trigger an unstable oscillation of the shock-wave (three-dimensional mechanism). Our work suggest that unstable events encountered in the same flutter bite can have different onsets.

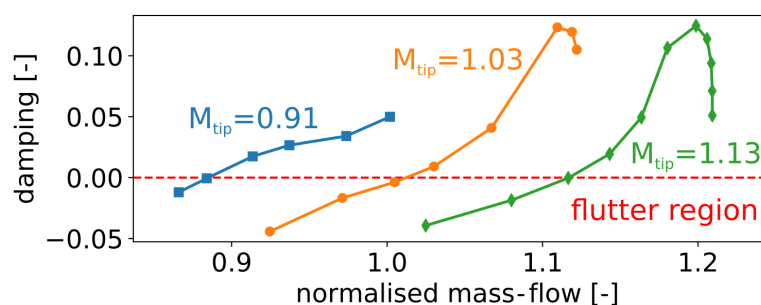


Figure 1: Aerodynamic damping along mass-flow for different rotational speed.

Diagnosics of the aeroelastic vibrations of aircraft gas turbine engine blades at bench tests

Sergey Danilkin, Vladimir Shkurov, Tatiana Mazikina, Dmitriy Redkin and
Victor Teleshev

*Central Institute of Aviation Motors named after P.I. Baranov (CIAM), Moscow, Russia,
d.s.y@inbox.ru*

Keyword: blade flutter, aircraft gas turbine engine, diagnostic of the aeroelastic processes, bench tests

The continuous trend to reduce the weight characteristics of aircraft engines leads to an increase in their vibration loading on the blades and contributes to the emergence of dangerous aero-elastic processes (flutter, rotating stall, resonant oscillations of the blades, surge). The pressure increasing in the stage and using blisks is characteristic for aircraft engines of the 5th and subsequent generations of engines, but this increases the aerodynamic load and reduces the vibration damping of the structure.

The aeroelastic processes in gas turbine engines are characterized by a complex interaction of gas flow and oscillating blades. The modern methods of designing gas turbine engines do not completely eliminate the emergence of dangerous aeroelastic oscillations in them due to the difficulty of predicting unsteady aerodynamic strength acting on the blades. The dangerous oscillations of the blades can occur depending on the action of unsteady aerodynamic strength and a combination of input and dissipated energy. Aeroelastic vibrations can occur under any mode of operation of an aircraft engine under certain conditions. Therefore, reliable early diagnosis of their occurrence and diagnosis of the type of oscillations in experimental research are an urgent problem.

The experts of department "Dynamics and Strength" (CIAM) have extensive experience in experimental studies of aeroelastic processes in gas turbine engines on CIAM stands and industrial plants using new technologies for processing and analyzing dynamic signals. In particular, methods for diagnosing blades flutter and other types of blade oscillations as part of an axial turbomachine were developed and patented, which are currently being successfully used in experimental studies of the dynamic strength of engine blades for various applications on CIAM stands and industrial plants.

The development of measurement and computational technologies over the past decade has given impetus to the development of new technologies for processing, analyzing and three-dimensional representation of the aeroelastic processes research results in gas turbine engines using algorithms based on fast Fourier transform, wavelet transforms and probabilistic-statistical methods.

At present, the computational capabilities of modern measuring equipment make it possible to carry out a spectral-correlation analysis of blades oscillations with a 3D display of relative spectral-phase and correlation characteristics in the research of the aircraft GTE parts dynamic strength.

The applying of modern technologies for processing and analyzing dynamic signals to study dangerous aeroelastic processes in gas turbine engines makes it possible to more effectively identify diagnostic evidence of flutter, rotating stall, surge and resonant oscillations of blades at an early stage, and, consequently, increase the reliability of gas turbine engines.

Coupling DNS-1DOF for the Simulation of Transition Induced Vibration over Marine Propeller Sections

Sijo GEORGE¹, Antoine Ducoin² and Jacques Andre ASTOLFI³
sijo.george@ec-nantes.fr

^{1,2} LHEEA laboratory (CNRS UMR 6598), Ecole Centrale de Nantes, France

³ Institut de Recherche de l'Ecole Navale (IRENav), Ecole Navale, 29240 Brest, France

Keyword: Transition, Laminar Separation Bubble, Direct Numerical Simulation, Degree of Freedom, Fluid-Structure Interaction

The laminar to turbulent transition occurring on marine propeller blades is known to be critical for the body performance and its structural integrity. Previous experimental laboratory researches have shown that under relatively high Reynolds numbers ($Re = 300,000$ to $800,000$), highly transitional flows are observed on laminar propeller section, which induces important structural vibrations with low damping, that can in some case get close to the resonance[1]. However, these experiments are mainly based on wall pressure and vibration measurements, and hence the interaction process has not been clearly identified and understood, and requires numerical and/or experimental observation of the boundary layer flow. The objective of this paper is to numerically investigate the behaviour of Laminar Separation Bubble(LSB) induced vibration on a NACA66 hydrofoil section. For this, a massively parallelized open source DNS code NEK5000[2] is used to solve the boundary layer flow. As shown by figure 1, the DNS domain is reduced to the near wall region, and velocity profiles are taken from the URANS calculation, implemented at the boundaries to reproduce the adverse pressure gradient inducing laminar separation. To study the transition induced vibration, a one degree of freedom system (1DOF) is considered at the elastic axis of the hydrofoil in order to reproduce the motion of a section, induced by the natural torsional mode. As a consequence, an equation of motion which consists of Inertia, stiffness and damper and the hydrodynamic loads(torque) computed by DNS is implemented inside Nek5000 . Hence, this numerical setup will allow to investigate the interaction between highly transitional flow and the pitching vibrating mode of a hydrofoil.

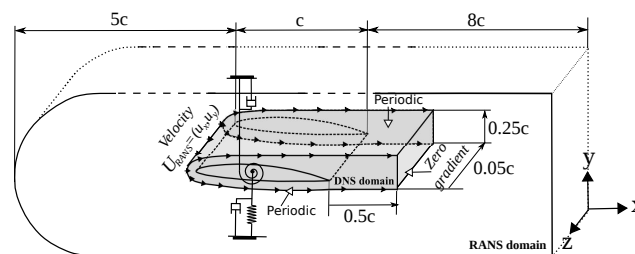
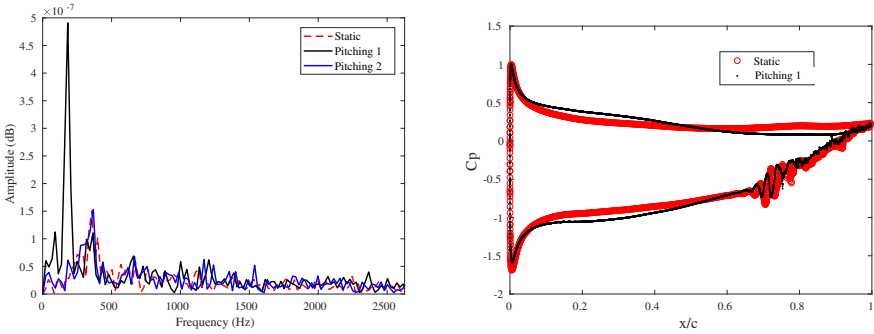


Figure 1: The simulation domain with classic support of the hydrofoil on translational and rotational spring-damper system.

Prior to the FSI case, two forced pitching cases are studied on NACA66 hydrofoil at $Re=450,000$. The hydrofoil is forced according to experimentally observed frequency and amplitude of vibration to study the effect of vibrations on wall pressure fluctuations and transition mechanism .



(a) Comparison of wall pressure spectra (b) Comparison of coefficient of pressure between the pitching and static cases between flexible and static foils at an instant. $x/c=0.8$

Figure 2: Simulation results of NACA66 at $Re=45,000$.

¹ A. Ducoin, J.A. Astolfi, M.L Gobert (2012). An experimental study of boundary -layer transition induced vibrations on a hydrofoil, *Journal of Fluids and Structures*, 32 , 37-51.
² P. Fishcer, M. Schmitt, and A. Tomboulides (2017). Recent developments in spectral element simulations of moving-domain problems, 213-244.

Aerodynamic characteristics of wind turbines with various cross-sectional tower shapes

Y.C. Kim¹ and Y. Tamura²

¹*Tokyo Polytechnic University, Atsugi, Japan, kimyc@arch.t-kougei.ac.jp*

²*Chongqing University, Chongqing, China, yukio@arch.t-kougei.ac.jp*

Keyword: wind tunnel test, wind turbine, wind pressure, modular tower

Since the late 1990's, introduction of wind turbines became active in Japan and their application has become more popular because of the environment-friendly characteristics in producing electricity. Traditionally, wind turbines with circular cross-section tower have been used¹, but weaknesses of circular cross-section tower have been pointed out recently as upsizing of wind turbines. The main weaknesses of circular cross-section tower include the problems related with manufacturing, decrease in strength and problems related with land transportations.

For the problems mentioned above, the concept of modular towers which will be assembled in the site was proposed. For most modular towers, the cross-sectional shapes are polygon such as octagon and/or tetradecagon, not simply circle, but their wind-resistant performance have not been clearly investigated.

In the present paper, the effect of cross-section of tower was investigated using wind tunnel test for 5MW wind turbine as shown in Fig. 1 and seven polygonal cross-sections were used and shown in Fig. 2, including square helical shape (not shown in Fig. 2). During the tests, pitch angle, wind direction and azimuth angle were considered as test parameters as well as cross-sectional shapes. Specifications of wind turbine were summarized in Tab. 1.

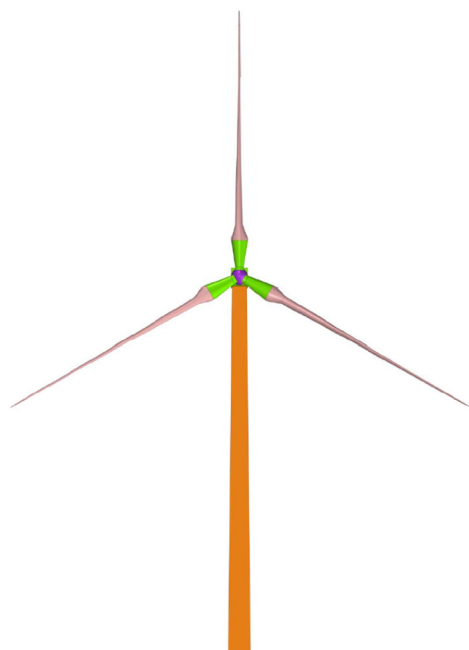


Figure 1: Wind turbine model.

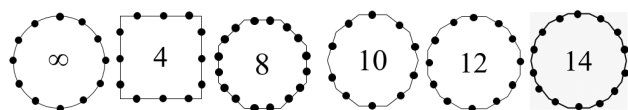


Figure 2: Cross-sectional shape (● is pressure tap).

Table 1. Specification of wind turbine.

Rated power	5MW
Rotor orientation	Upwind
Configuration	3 blades
Control	Pitch
Hub height	90m
Rotor / blade	124m / 60m
Overhang	5m
Shaft tilt	5°

1. Totsuka, Y., Imamura H., & Yde, A. (2016). Dynamic behaviour of parked wind turbine at extreme wind speed. First International Symposium on Flutter and its Application, Tokyo, Japan, 575-584.

Flutter in axial flow (panel, pipe, flag)

Nonlinear Theoretical/Computational Model of a Plate in Hypersonic Flow with Arbitrary In-Plane Stiffness at the Boundaries

Maxim Freydin¹ and Earl H. Dowell²

¹ *Duke University, Durham ,NC, maxim.freydin@duke.edu*

² *Duke University, Durham ,NC*

Abstract

It is well known that the nonlinear response of a (beam or) plate is sensitive to the assumptions made about the in-plane boundary constraints. This is true for any static or dynamic loading and especially for aerodynamic loadings that may lead to a dynamic instability (flutter) and limit cycle oscillations. In the prior literature the two limiting cases of complete constraints (zero displacement) and no constraint (zero stresses) at the boundary have been considered. In this work, a mathematical and computational model for the more general case has been created to allow for the full range of in-plane boundary constraints to be considered. This is of fundamental interest, but also of considerable practical interest in that physical structures usually fall somewhere between the two limiting cases. Comparisons between the present and prior models provide new insights into these issues.

Keyword: structural dynamics, fluid-structure interaction, panel flutter, hypersonic, piston theory.

1 Introduction

Nonlinear fluid-structure interaction of plates in hypersonic and supersonic flows has been an active field of research in the past 60 years [Mei et al., 1999, McNamara and Friedmann, 2011]. The coupling of fluid and structure in this flow regime challenges the existing structural models with complicated pressure and thermal loads, while the interaction of shock-wave, boundary-layer and structure complicates the problem even further [Clemens and Narayanaswamy, 2014]. Experimental, theoretical and computational studies have been conducted to better understand panel flutter in hypersonic flow and make it possible to accurately predict the onset of flutter and properties of limit cycle oscillations at post-flutter conditions utilizing linear and nonlinear models [Bismarck-Nasr, 1996, Mei et al., 1999]. Flutter onset condition and LCO properties were found to be sensitive to several effects studied extensively in prior literature. Among those are panel curvature [Dowell, 1969], orthotropicity [Eslami and Ibrahim, 1986, Nydick et al., 1995], in-plane loads [Yuen and Lau, 1991, Hess, 1970], transverse boundary conditions, temperature differential (and its distribution) [Nydick et al., 1995], static pressure differential [Ventres and Dowell, 1970, Kappus et al., 1971], and the plate's interaction with a cavity [Dowell, 1963]. In this work, we focus on the in-plane boundary constraints and its role in the nonlinear statics and dynamics by deriving a general model for an arbitrary distribution of elastic in-plane stiffness constraint at the edges of a flat, rectangular plate.

[Bolotin, 1963] was one of the earliest to propose a theoretical model that considered the effect of different in-plane boundary constraints in the context of nonlinear supersonic fluid-structure stability (flutter and buckling). Bolotin coupled the Von Karman plate equations with a linearized aerodynamic model to analyze the stability of plates and shells in supersonic flow. The structural model was formulated in terms of transverse displacement and the Airy stress function eliminating the need for two tangent displacement components, but at the same time making it challenging (or impossible) to impose constraints on the in-plane motion. The model was solved by the Galerkin method and with an appropriate choice of modal basis function for the Airy stress, the boundary condition for zero in-plane stress was satisfied exactly. The more physically accurate case of elastic edge constraint was introduced by averaging the normal component of the tensile force on each pair of opposite edges and equating it to the mean average displacement of the respective tangent component multiplied by the effective edge stiffness. The importance of in-plane constraints modeling was clearly noted in Bolotin's work, but the formulation of the structural equations in terms of Airy stress instead of tangent displacement components required simplifications and approximations to impose edge constraints which naturally reduced the accuracy of the model.

Dowell utilized and expanded Bolotin's model in theoretical and experimental studies. The effect of a cavity on one side of the plate was modeled by coupling the unsteady compressible potential flow equation with the plate dynamics [Dowell, 1963]. Flutter onset boundaries and natural modes of vibration (with and without cavity) were correlated with experiments in a wide range of supersonic Mach numbers [Dowell and Voss, 1965]. [Dowell, 1969] quantified the effect of curvature on two and three-dimensional plate's nonlinear dynamics in post flutter conditions (and on flutter onset). [Ventres and Dowell, 1970] utilized the nonlinear model in the Airy stress form to include static transverse and in-plane loads in flutter, limit cycle oscillation and natural modes of vibration analyses. They demonstrated by theory and experiment the sensitivity of the natural frequencies to a uniform static pressure differential across the plate for two limiting cases of in-plane boundary restraints: zero stress and zero displacement (as approximated by Bolotin). A comprehensive theory and experiment monograph on the topic is given by [Dowell, 1974]. Theoretical and experimental results obtained in [Dowell and Voss, 1965, Ventres and Dowell, 1970] are used for comparison in this work.

Recent experimental studies focused on shock-wave boundary-layer and structure interaction demonstrated the importance of nonlinear structural dynamics of flat plates in hypersonic flow. [Whalen et al., 2019] measured the deformed shape of an all-clamped plate installed on a compression ramp in a free stream flow of Mach number 5.8 at varying ramp angles. Variation of natural frequencies of the plate with ramp angle was measured and attributed to the combined effects of aerodynamic heating, static pressure differential and fluid-structure coupling [Freydin et al., 2019b]. [Spottswood et al., 2019] measured the plate's response to turbulent, heated flow with a static pressure differential load. Time series of the plate's deformation captured flutter onset, reaching high amplitude limit cycle oscillation and buckling due to aerodynamic heating in the transient process of wind tunnel start. Shock wave impinging on elastic plates in supersonic flow was considered by [Willems, S. et al., 2013] and [Bebernis et al., 2017]. Measurements obtained in these experimental studies demonstrate how the complicated aerodynamic loads, both static and dynamic, lead to a highly nonlinear structural response, prior and after flutter onset.

In this work, a theoretical computational model is derived which more accurately captures the

nature of the problem than was previously possible. In the following sections, model derivation is outlined and calculations made with the model are analyzed and compared with results from prior literature.

2 Theoretical Model

The structural model derivation consists of formulating the elastic and kinetic energies of a flat plate with general in-plane stiffness distribution at the edges in terms of three displacement components (in contrast to prior literature where the Airy stress function and a single transverse displacement are employed). Eq. 1 describes the stretching and bending elastic energies, and Eq. 2 is the elastic energy of in-plane stiffness distributed along the plate's edges (which may generally vary in space and time). Eq. 3 is the transverse kinetic energy.

$$\begin{aligned}
 U_E = & \frac{Eh}{2(1-\nu^2)} \iint \left\{ w_x^2 \left[u_x + \nu v_y + \frac{1}{4} w_x^2 - (1+\nu)\alpha T \right] + w_y^2 \left[v_y + \nu u_x + \frac{1}{4} w_y^2 - (1+\nu)\alpha T \right] \dots \right. \\
 & + w_x w_y \left[\frac{1}{2} w_x w_y + (1-\nu)(u_y + v_x) \right] \dots \\
 & \left. + \left[u_x^2 + 2\nu u_x v_y + v_y^2 + \frac{(1-\nu)}{2} (u_y^2 + v_x^2 + 2v_x u_y) - 2(1+\nu)\alpha T (u_x + v_y) \right] \right\} dx dy \dots \\
 & + \frac{D}{2} \iint \left[w_{xx}^2 + w_{yy}^2 + 2\nu w_{xx} w_{yy} + 2(1-\nu) w_{xy}^2 \right] dx dy
 \end{aligned} \tag{1}$$

$$\begin{aligned}
 U_K = & \frac{1}{2} \int \left[Ku(x=0, y, t)^2 + Ku(x=a, y, t)^2 \right] dy \dots \\
 & + \frac{1}{2} \int \left[Kv(x, y=0, t)^2 + Kv(x, y=b, t)^2 \right] dx
 \end{aligned} \tag{2}$$

$$T = \frac{1}{2} \iint m \left(\frac{\partial w}{\partial t} \right)^2 dx dy \tag{3}$$

Next, the problem is transformed to modal structural coordinates in all three components. The elastic and kinetic energies (where the in-plane inertia was neglected but is addressed in [Freydin and Dowell, 2019]) in Eq. 1, 2 and 3 are transformed and the Lagrangian is formulated in modal coordinates. Finally, Lagrange's Equations are used to obtain the equations of motion (with aerodynamic and static pressure differential loads added as non-conservative work).

Neglecting the in-plane inertia leads to algebraic equations for the u and v displacement components which allows the reduction of the system of equations to a form shown in Eq. 4. The effect of in-plane edge constraint is expressed through the linear structural stiffness matrix $G_{nk}^{(2)}$ and the nonlinear structural stiffness tensor $D_{nkrs}^{(2)}$. Fig. 1 and 2 show schematic views of the problem.

$$\underbrace{M_{nk} \ddot{w}_k + A_{\dot{w}_{nk}} \dot{w}_k + A_{w_{nk}} w_k}_{\text{PT aerodynamics}} + \underbrace{G_{nk}^{(2)} w_k + D_{nkrs}^{(2)} w_k w_r w_s}_{\text{NL structural stiffness}} + \underbrace{Q_n^s}_{\text{static pressure differential}} = 0 \tag{4}$$

Eq. 4 describes the fluid-structure system of equations of motion in modal coordinates with important terms underlined. The system is either solved as an eigenvalue problem following a

dynamic linearization about a nonlinear statically deformed plate or by direct time integration of the full dynamically nonlinear model. Each approach has advantages and provides different information about the fluid-structure system. Fast computation times make the eigenvalue approach suitable for design while direct time integration provides insight into nonlinear behavior of the system in post flutter conditions and LCO.

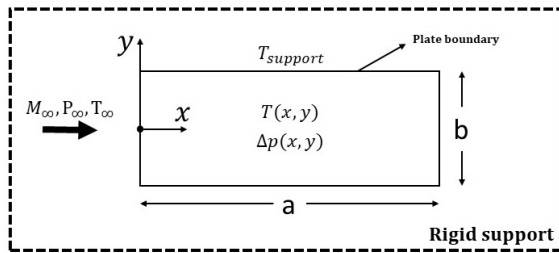


Figure 1 – Top view of a clamped panel in a free stream flow with static pressure and temperature differentials.

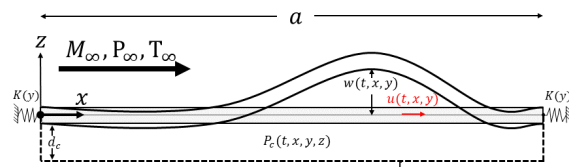


Figure 2 – Side view of a clamped panel with in-plane stiffness at the edges in a free stream flow and a cavity with stationary fluid. Cross section at $-b/2 < y < +b/2$.

The full derivation is provided by [Freydin and Dowell, 2019] (see Acknowledgement), including first order Piston Theory (PT) aerodynamics and a simplified cavity model which only includes the added stiffness effect and neglects added mass. Previous work considered the simplified models for zero-stress boundary conditions [Freydin et al., 2019b] and the one-dimensional problem with arbitrary in-plane stiffness at the edges [Freydin et al., 2019a] for experiment data analysis and experiment design, respectively.

3 Results Including Comparison With Previous Literature

3.1 Buckling Due to Uniform Temperature Differential

When compressive stresses due to temperature differential become large enough, the panel buckles. Physically, it is reasonable that for larger in-plane edge stiffness values, the panel should buckle for smaller temperature differentials because in that case a larger portion of the compressive stress will be counteracted by the panel, and not the springs at the edges. Fig. 3 shows how the uniformly distributed temperature differential ΔT_B for buckling varies with in-plane stiffness. For non-dimensional values of in-plane stress larger than 100, the temperature for buckling approaches a value of $\Delta T_B = 34.48K$ predicted by the zero in-plane displacement model. As $\frac{Ka}{Eh}$ approaches closer to zero, ΔT_B grows rapidly. According to results in Fig. 3, a clamped panel which is free to slide in-plane is not likely to buckle. These results agree with the physical intuition and quantify the influence of in-plane stiffness.

3.2 Comparison with Bolotin Model for Zero Displacement Boundary Condition using Spatially Averaged Boundary Conditions

The proposed theoretical model for an arbitrary in-plane stiffness is compared with the numerical and experimental works of [Ventres and Dowell, 1970] and [Dowell and Voss, 1965].

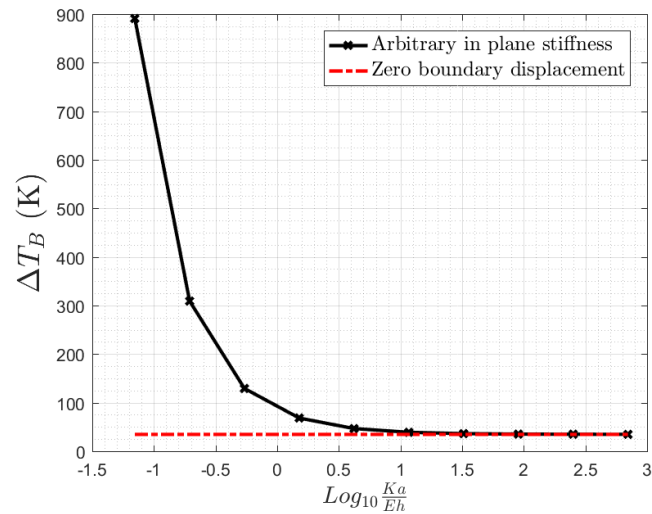


Figure 3 – Uniformly distributed temperature differential for buckling vs normalized in-plane stiffness, $a = 88.3\text{mm}$, $b = 88.9\text{mm}$, $h = 0.977\text{mm}$, AISI 4140 steel plate

Theoretical models used in these works are the [Bolotin, 1963] model for exact zero in-plane stress and spatially averaged zero in-plane displacement. The former represents the ideal case of $K \rightarrow 0$, i.e. completely free to move in-plane, and the later serves as an approximated model for $K \rightarrow \infty$. Several different comparisons are made to investigate the nonlinear effects of in-plane boundary conditions on limit cycle amplitude past flutter onset condition, natural frequencies increase due to static pressure differential and flutter onset condition change due to static pressure differential.

In Fig. 4 and 5 is shown the limit cycle amplitude variation with normalized free stream dynamic pressure for plates with edge length to width ratios of $a/b = 1$ and $a/b = 2$. The figures were created by time marching the system in Eq. 4 with a very small initial condition in the first modal displacement until a constant amplitude response was reached. The effect of a cavity was not included in this calculation. The agreement in flutter onset dynamic pressure is good in both cases of length to width ratios. This result is consistent with the fact that in-plane boundary conditions do not affect the linear stability of the fluid-structure system. Slightly after flutter onset dynamic pressure, the new model with extreme values of K agrees well with the idealized and approximated models of zero stress and zero displacement. But, as dynamic pressure increases, the difference between the models grows. Note that the spatially averaged zero displacement model predicts larger amplitudes at high λ values than the $Ka/Eh = 100$ case. This is physically consistent because the later model is more restricted in in-plane motion than the former. Smaller and larger values for Ka/Eh in the considered range of λ did not show significantly different amplitudes of limit cycle.

Fig. 6, 7 and 8 show natural frequency variation with static pressure differential of three modes. The calculations were conducted by linearizing Eq. 4 about a static nonlinear deformation of the plate and solving the eigenvalue problem with zero thermal stress, no fluid interaction and no cavity effect. A ratio of $a/b = 2$ was used in the calculations. Good agreement is shown in Fig. 6 and 8 between the theoretical models and experiment. As was noted

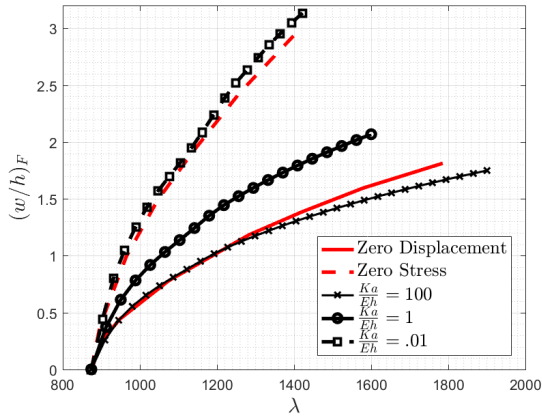


Figure 4 – Flutter amplitude at $x/a = 0.75$ vs dynamic pressure for $a/b = 1, \mu/M = 0.1$

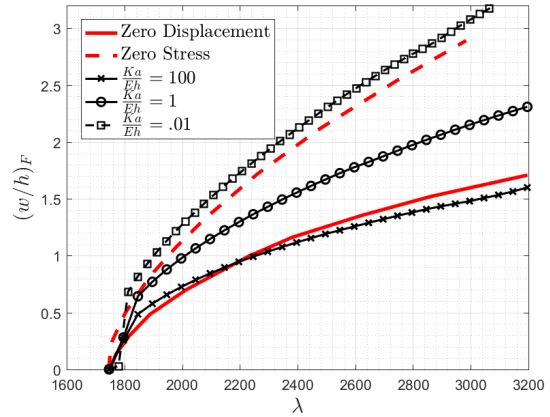


Figure 5 – Flutter amplitude at $x/a = 0.75$ vs dynamic pressure for $a/b = 2, \mu/M = 0.05$

by [Ventres and Dowell, 1970], the experimental results lie closer to the zero stress case, i.e. small Ka/Eh values. A value of $Ka/Eh = 0.05$ shows very good agreement between theory and experiment in Fig. 6. The large and small values of Ka/Eh agree well with the idealized and approximate models. Fig. 7 shows larger differences between the models and theory, but still within a 10% difference margin.

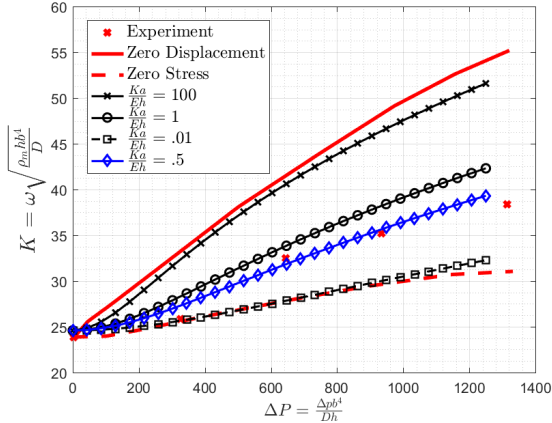


Figure 6 – Mode (1,1) natural frequency vs static pressure differential, $a/b = 2$

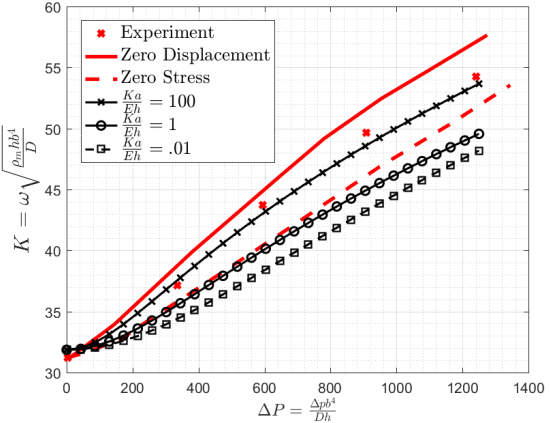


Figure 7 – Mode (2,1) natural frequency vs static pressure differential, $a/b = 2$

Fig. 9 and 10 show flutter onset vs static pressure differential for two plate length ratios. Plate naming convention follows definitions in [Dowell and Voss, 1965]. For example, the 20 – 10 – 25 plate has length of 20", width of 10" and thickness of 0.025". Due to panel installation, the effective structural dimensions of both plates were 18.5" x 8.5", making the considered ratios $a/b = 0.46$ and $a/b = 2.18$. Fig. 9 and 10 were obtained using the eigenvalue analysis previously described but with the addition of Piston Theory aerodynamics, a simplified cavity model (added stiffness), and zero thermal stress. The cavity static pressure was calculated based on external flow static pressure and the static pressure differential. Additionally, the

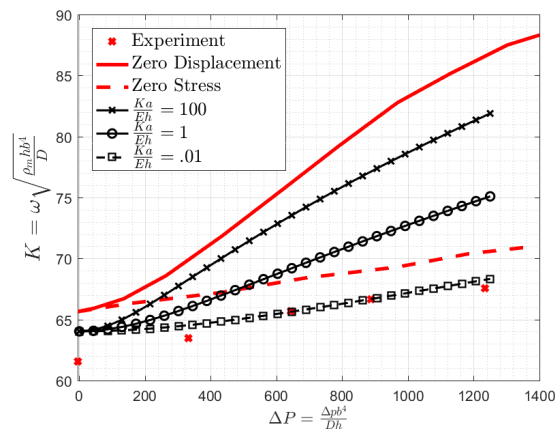


Figure 8 – Mode (1,2) natural frequency vs static pressure differential, $a/b = 2$

structural linear stiffness matrix of the nominal plate was calibrated based on experimental data in Tab. 1. Good agreement is shown in Fig. 9 between the new model with a small Ka/Eh value and the experiment results. On the other hand, Fig. 10 shows that theory overestimates the flutter onset dynamic pressure while the different models agree well in the general trends. An interesting behavior is predicted, as was noted by [Ventres and Dowell, 1970], that for completely restrained edges the panel might flutter at a smaller dynamic pressure with the increase of static pressure differential. This unexpected result disappears in this case when the effect of the cavity is removed from calculations.

Lastly, Table 1 shows the natural frequencies of the two plates considered in Fig. 9 and 10 as measured in experiments and predictions obtained using the current model with and without considering the effect of a cavity. The cavity effect was added in two different levels of accuracy. The first method utilized a simplified model which only considers the volume change in the cavity due to panel deformation. It was used to match the approach applied in the studies used for comparison [Ventres and Dowell, 1970, Dowell and Voss, 1965]. The second method is described in [Dowell, 1974] and provides a more accurate cavity model by considering the wave equation for the cavity pressure field and imposing boundary condition at the moving wall using Green's Theorem. For both "with cavity" columns, the nominal structural stiffness matrix was calibrated to match the values in the "Exp. No Cavity" column. In the simplified cavity model, natural frequencies of symmetric modes have increased while the antisymmetric remained without change. This is because, as noted in [Dowell et al., 1977], the simplified cavity model neglects the effect of added mass but does include added stiffness or compliance of the fluid in the cavity. On the other hand, the full cavity model predicts changes in all modes accounting for both effects which produces better agreement with experiment.

4 Conclusion

In this work, a theoretical and computational nonlinear structural (and linear aerodynamic) model was derived in terms of single transverse and two in-plane components of displacement. Physical effects typical to hypersonic fluid-structure interaction problems were modeled among

Table 1 – Plate Natural Frequencies, theory and experiments [Dowell and Voss, 1965, Ventres and Dowell, 1970]

Plate (L-w-h)	Mode Shape Order in (x,y)	Frequencies (Hz)				
		Exp. No Cavity	Exp. With Cavity	Theory No Cavity	Theory With Cavity Simplified	Theory With Cavity Acoustic Eqn.
10-20-20	1,1	60		66	165	
	1,2	89	84	82	89	70
	1,3	116	98	111	107	101
	1,4	158		152	158	148
	2,1	161	140	173	161	150
20-10-25	1,1	75		82	118	115
	2,1	94	83	102	94	77
	3,1	130	113	138		
	4,1	181		190		
	1,2	201		216		

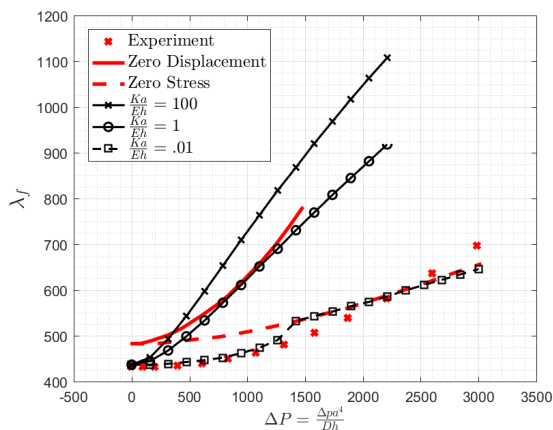


Figure 9 – Flutter dynamic pressure vs static pressure differential for the 10-20-20 plate, $a/b = 0.46$

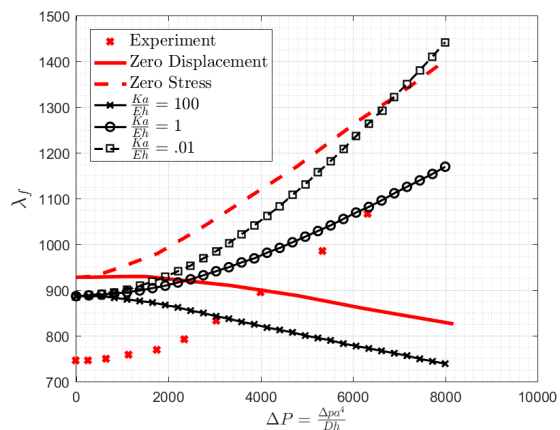


Figure 10 – Flutter dynamic pressure vs static pressure differential for the 20-10-25 plate, $a/b = 2.18$

which are the static pressure and temperature differentials. Linear eigenvalue and nonlinear time integration analyses were conducted. The linear eigenvalue method for stability and modal analysis was emphasized and developed to include the effect of added stiffness due to large initial deformation which can originate from thermal and static loads.

Results obtained with the new model were compared to those found in prior literature, which was based on approximated formulations of in-plane boundary conditions. Comparison between the new model with small and large values of in-plane stiffness produced good agreement with the limiting cases found in the literature.

The new model provides a more accurate tool for design and theoretical-experimental correlation and data analysis. Where previous works relied on approximations and limiting cases for

the in-plane edge constraints, future researchers may calibrate the in-plane boundary stiffness of their model by correlation of measured and computed natural frequencies with the plate under a static pressure load. The accuracy of in-plane edge stiffness modeling is important whenever nonlinear response, static or dynamic, is of interest. As shown throughout this work, accounting for in-plane boundary conditions is an integral part of fluid-structure interaction in hypersonic and supersonic flow.

Acknowledgement

A more extensive form of this paper has been submitted for publication in the Journal of Fluids and Structures [Freydin and Dowell, 2019].

References

- [Beberriss et al., 2017] Bebernis, T. J., Spottswood, S. M., Ehrhardt, D. A., and Perez, R. (2017). Dynamic response of a thin panel subjected to a shockwave impingement and thermal buckling. In *33rd AIAA Aerodynamic Measurement Technology and Ground Testing Conference*, page 3555.
- [Bismarck-Nasr, 1996] Bismarck-Nasr, M. N. (1996). Finite elements in aeroelasticity of plates and shells. *Applied Mechanics Reviews*, 49(10S):S17–S24.
- [Bolotin, 1963] Bolotin, V. V. (1963). *Nonconservative problems of the theory of elastic stability*. Macmillan.
- [Clemens and Narayanaswamy, 2014] Clemens, N. T. and Narayanaswamy, V. (2014). Low-frequency unsteadiness of shock wave/turbulent boundary layer interactions. *Annual Review of Fluid Mechanics*, 46:469–492.
- [Dowell, 1963] Dowell, E. H. (1963). The effect of a cavity on panel vibration. *AIAA Journal*.
- [Dowell, 1969] Dowell, E. H. (1969). Nonlinear flutter of curved plates. *AIAA Journal*, 7(3):424–431.
- [Dowell, 1974] Dowell, E. H. (1974). *Aeroelasticity of plates and shells*. Noordhoff International Publishing (now Springer).
- [Dowell et al., 1977] Dowell, E. H., Gorman, G., and Smith, D. (1977). Acoustoelasticity: General theory, acoustic natural modes and forced response to sinusoidal excitation, including comparisons with experiment. *Journal of Sound and Vibration*, 52(4):519 – 542.
- [Dowell and Voss, 1965] Dowell, E. H. and Voss, H. M. (1965). Theoretical and experimental panel flutter studies in the mach number range 1.0 to 5.0. *AIAA Journal*, 3(12):2292–2304.
- [Eslami and Ibrahim, 1986] Eslami, H. and Ibrahim, S. R. (1986). Nonlinear flutter analysis of specially orthotropic panels. In *27th Structures, Structural Dynamics and Materials Conference*, page 900.

- [Freydin and Dowell, 2019] Freydin, M. and Dowell, E. H. (2019). Nonlinear theoretical and computational aeroelastic model of a plate: From free to fixed in-plane boundary constraints. *Journal of Fluids and Structures*, *Under review*.
- [Freydin et al., 2019a] Freydin, M., Dowell, E. H., Currao, M., and Neely, A. J. (2019a). Computational study for the design of a hypersonic panel flutter experiment. In *The International Forum on Aeroelasticity and Structural Dynamics 2019*, Savannah, Georgia, USA.
- [Freydin et al., 2019b] Freydin, M., Dowell, E. H., Whalen, T., and Laurence, S. (2019b). Computational model of a plate in hypersonic flow. *Journal of Fluids and Structures*, *Under review*.
- [Hess, 1970] Hess, R. W. (1970). Experimental and analytical investigation of the flutter of flat built-up panels under streamwise inplane load. *NASA TR R-330*, Langley Research Center.
- [Kappus et al., 1971] Kappus, H., Lemley, C., and Zimmerman, N. (1971). An experimental investigation of high amplitude panel flutter. *NASA CR-1837*.
- [McNamara and Friedmann, 2011] McNamara, J. J. and Friedmann, P. P. (2011). Aeroelastic and aerothermoelastic analysis in hypersonic flow: Past, present, and future. *AIAA Journal*, 49(6):1089–1122.
- [Mei et al., 1999] Mei, C., Abdel-Motagaly, K., and Chen, R. (1999). Review of nonlinear panel flutter at supersonic and hypersonic speeds. *Applied Mechanics Reviews*, 52(10):321–332.
- [Nydick et al., 1995] Nydick, I., Friedmann, P., and Zhong, X. (1995). Hypersonic panel flutter studies on curved panels. In *36th Structures, Structural Dynamics and Materials Conference*, New Orleans, LA, USA.
- [Spottswood et al., 2019] Spottswood, S. M., Beberniss, T. J., Eason, T. G., Perez, R. A., Donbar, J. M., Ehrhardt, D. A., and Riley, Z. B. (2019). Exploring the response of a thin, flexible panel to shock-turbulent boundary-layer interactions. *Journal of Sound and Vibration*, 443:74 – 89.
- [Ventres and Dowell, 1970] Ventres, C. S. and Dowell, E. H. (1970). Comparison of theory and experiment for nonlinear flutter of loaded plates. *AIAA Journal*, 8(11).
- [Whalen et al., 2019] Whalen, T., Laurence, S., Sullivan, B., Bodony, D., Freydin, M., Dowell, E. H., and Buck, G. (2019). Hypersonic fluid-structure interactions in compression corner shock-wave boundary-layer interaction. *AIAA J.*, *Under review*.
- [Willems, S. et al., 2013] Willems, S., Gülhan, A., and Esser, B. (2013). Shock induced fluid-structure interaction on a flexible wall in supersonic turbulent flow. *Progress in Flight Physics*, 5:285–308.
- [Yuen and Lau, 1991] Yuen, S. W. and Lau, S. L. (1991). Effects of in-plane load on nonlinear panel flutter by incremental harmonic balance method. *AIAA journal*, 29(9):1472–1479.

Nonlinear flutter analysis of a rectangular sheet in uniform flow

Keiichi Hiroaki¹ and Masahiro Watanabe¹

¹*Aoyama Gakuin University, Kanagawa, Japan, hiroaki@me.aoyama.ac.jp*

Abstract

Flexible sheets are used in many industrial applications. During the manufacturing processes of the sheets, flutter occurs due to the coupling of the sheet motion and airflow. The flutter causes severe quality defects, such as scratches and scattering of coated liquid. To avoid these serious defects, a detailed understanding of the fluttering mechanisms and characteristics is essential. In this paper, a nonlinear flutter analysis of a cantilevered rectangular sheet in uniform flow is performed. Post-critical behavior was examined by numerical simulation, and experiments were conducted to validate the model.

Keyword: sheet flutter, self-excited vibration, nonlinear analysis, Doublet-point Method

1 Introduction

Flexible sheets (thin elastic plates) are used in many industrial applications such as polarizing films for liquid crystal displays (LCD). These sheets are made through many engineering processes, such as coating and drying. Under the processes, it is reported that flutter occurs to the sheet due to the interaction between the motion of the sheet and fluid flow, when the flow velocity of drying air flow becomes high. The flutter can cause severe damage to the sheet surface, including the scattering of coating liquids and scratches on the sheet surface. To avoid these serious defects, a detailed understanding of the fluttering mechanisms and characteristics is essential.

Up to the present time, many theoretical studies analyzing the linear stability of the rectangular sheet in uniform flow are reported. These studies are divided into two categories: two-dimensional and three-dimensional analysis. For analysis of stability of the sheet which has large aspect ratio, many two-dimensional models assuming infinite span are developed (Huang, 1995), (Yamaguchi et al., 2000), (Watanabe et al., 2002). In addition, several three-dimensional studies targeted finite-span sheet have been reported (Eloy et al., 2007), (Gibbs et al., 2012), (Hiroaki et al., 2015).

On the other hand, several nonlinear studies are reported. Tang and Paidoussis (Tang and Paidoussis, 2007) and Chen et al. (Chen et al., 2014) performed nonlinear analysis utilizing a two-dimensional discrete vortex method. Tang et al. (Tang et al., 2003) have carried out analysis of a LCO (Limit Cycle Oscillation) response utilizing a three-dimensional linear vortex lattice method and nonlinear structural model. Moreover, Sawada and Hisada (Sawada and Hisada, 2007) developed a two-dimensional numerical model (Navier-Stokes solver) utilizing ALE finite element method. In the study, flow field around the fluttering sheet is analyzed in detail through the CFD simulation. Nevertheless, detailed characteristics of post-critical behavior and mechanism of the LCO are not sufficiently clarified.

To a deeper understanding of these phenomena, this paper focuses on the development of a nonlinear fluid-structure interaction model that includes nonlinear fluid frictional and damping forces. Flutter amplitude and frequency, and the work done by the fluid force

acting on the sheet surface were examined through the nonlinear analysis to understand the sustaining mechanism of the LCO. The validation of the developed model was performed by comparison with experimental results.

2 Nonlinear flutter modeling and numerical methodology

2.1 Analytical model of the sheet

Fig.1 shows a schematic of a sheet in axial fluid flow. The upstream edge of the sheet is clamped and the others are free. The sheet is modeled as a cantilevered beam assuming a two-dimensional deformation (lateral deformation) of the sheet. The sheet has chord L , span b , thickness h and density ρ_s . The sheet is divided by quadrangular elements into $N (= N_x \times N_y)$ in order to calculate fluid force acting on the sheet surface, where N_x is division number of x -direction and N_y is division number of y -direction. The fluid around the sheet is incompressible with density ρ_f and flowing in the x -direction with constant velocity U . Moreover, c denotes curvature coordinate along the sheet.

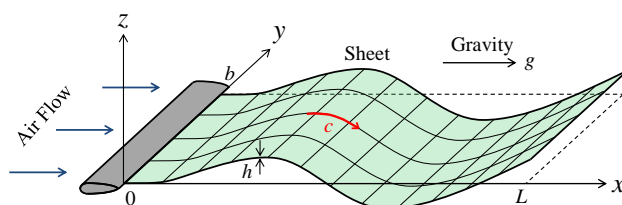


Figure 1: Schematic of the analytical model of a sheet in uniform flow.

2.2 Equation of motion of the sheet

To take into account large deformation of the sheet, an appropriate nonlinear equation of motion of the sheet is developed shown in Eq.(1) using the Von Karman nonlinear beam theory based on the Hamilton's principle (Tang and Paidoussis, 2007). The left hand side of the eq. (1) is nonlinear equation of motion of the sheet, where α is coefficient of material damping (assuming Kelvin-Voigt type damping model) and D is bending stiffness $D = Eh^3/[12(1 - \nu^2)]$, where E and ν are Young's modulus and the Poisson ratio, respectively. The right hand side represents the fluid force acting on the sheet surface. Note that the structural model is based on the inextensibility condition of axial direction. Unsteady fluid force acting on the sheet surface Δp is calculated by the Doublet-point Method (DPM) (Ueda and Dowell, 1982), (Ueda, 1987) based on three dimensional potential flow. Moreover, nonlinear fluid frictional force p_f and nonlinear fluid damping force p_d are introduced to include the effect of the fluid viscosity (fluid friction due to boundary layer on the sheet surface/flow separation).

$$\begin{aligned}
 & \rho_s h \ddot{w} + D \left(1 + \alpha \frac{\partial}{\partial t} \right) \left\{ \frac{\partial^4 w}{\partial c^4} \left(1 + \left(\frac{\partial w}{\partial c} \right)^2 \right) + 4 \frac{\partial w}{\partial c} \frac{\partial^2 w}{\partial c^2} \frac{\partial^3 w}{\partial c^3} + \left(\frac{\partial^2 w}{\partial c^2} \right)^3 \right\} - \frac{\partial^2 w}{\partial c^2} \left\{ \frac{3}{2} \left(\frac{\partial w}{\partial c} \right)^2 \rho_s h g + \rho_s h g \right\} (L - c) \\
 & + \rho_s h g \frac{\partial w}{\partial c} + \frac{\partial w}{\partial c} \int_0^c \rho_s h \left\{ \left(\frac{\partial \dot{w}}{\partial c} \right)^2 + \frac{\partial w}{\partial c} \frac{\partial \ddot{w}}{\partial c} \right\} ds - \frac{\partial^2 w}{\partial c^2} \int_c^L \int_0^c \rho_s h \left\{ \left(\frac{\partial \dot{w}}{\partial c} \right)^2 + \frac{\partial w}{\partial c} \frac{\partial \ddot{w}}{\partial c} \right\} dc dc \\
 & = \underbrace{\Delta p + \frac{\partial^2 w}{\partial c^2} \left\{ \frac{3}{2} \left(\frac{\partial w}{\partial c} \right)^2 (\rho_f U^2 C_f) \right\}}_{p_f} (L - c) - \underbrace{\frac{1}{2} \rho_f C_d \dot{w} |\dot{w}|}_{p_d}
 \end{aligned} \tag{1}$$

2.3 Calculation of fluid force acting on the sheet surface

The unsteady fluid force acting on the sheet surface is derived from unsteady lifting theory and discretized utilizing DPM. The complex amplitude of pressure jump distributions on the oscillating sheet surface $\Delta\bar{p}'$ and complex amplitude of up-wash velocity \bar{u}' are related by the following Küssner's singular integral equation, which is based on three-dimensional potential flow (Küssner, 1941).

$$\bar{u}'(x', y') = \frac{1}{8\pi} \iint_{S'} \Delta\bar{p}'(\xi', \eta') \cdot K(x'_0, y'_0) d\xi' d\eta' \quad (2)$$

S' denotes the region of the sheet surface and the kernel function $K(x'_0, y'_0)$ is given by

$$K(x'_0, y'_0) = e^{-s x'_0} B(s, r, X), \quad B(s, r, X) = \int_{-\infty}^X \frac{e^{sv}}{\{v^2 + r^2\}^{3/2}} dv \quad (3)$$

$$X = x'_0 = x' - \xi', \quad r = |y'_0| = |y' - \eta'| \quad (4)$$

where s is the Laplace variable. Trailing vortex affects the up-wash distribution. Thus the up-wash induced between the two trailing lines of the horseshoe vortex is hidden in the r^2 singularity of the kernel function $K(x'_0, y'_0)$. Therefore, the effect of wake is taken into account in the kernel function $K(x'_0, y'_0)$. The prime symbols in Eqs. (3) and (4) denote dimensionless variables, are defined as follows by using velocity U and span length b .

$$x' = x/b, \quad y' = y/b, \quad z' = z/b, \quad \xi' = \xi/b, \quad \eta' = \eta/b, \quad \zeta' = \zeta/b, \quad \bar{u}' = \bar{u}/U, \quad \Delta\bar{p}' = \Delta\bar{p}/(\rho_f U^2/2) \quad (5)$$

For the calculation of the unsteady fluid forces using DPM, doublet and up-wash points are located at the coordinates (ξ'_i, η'_i) and (x'_i, y'_i) of the divided elements respectively, and according to the 1/4~3/4 chord rule, as shown Fig. 2. With respect to Kutta condition at the trailing edge, as well as in the vortex lattice method, the 1/4~3/4 chord rule allows to not imposing directly the Kutta condition on the pressure distribution. Fluid force distribution on the divided elements is concentrated at the doublet point (ξ'_i, η'_i) . This means doublet sources of the strength $\Delta\bar{p}'(\xi'_i, \eta'_i)$ are set at the doublet points, in which the elements have the area Δ'_j . The kernel function K corresponds to an up-wash velocity field that is produced by a point doublet of the acceleration potential located at (ξ'_i, η'_i) , and the point (x'_i, y'_i) is taken as representative for the whole up-wash distribution on an element surface. These assumptions make it possible to discretize the integral Eq. (2) into linear algebraic equations. The discretized fluid force is given by the following Eq. (6).

$$\Delta\bar{\mathbf{p}}' = \mathbf{C}(s)\bar{\mathbf{u}}' \quad (i, j = 1 \cdots N) \quad (6)$$

$$\bar{\mathbf{u}}' = \{\bar{u}'(x'_i, y'_i)\}, \quad \Delta\bar{\mathbf{p}}' = \{\Delta\bar{p}'(\xi'_j, \eta'_j)\}, \quad \mathbf{D}(s) = [d_{ij}] = \left[\frac{\Delta'_j}{4\pi K} \cdot (x'_i - \xi'_j, y'_i - \eta'_j) \right], \quad \mathbf{C}(s) = \mathbf{D}(s)^{-1} \quad (7)$$

Here, the up-wash velocity \bar{w}' is calculated from a given oscillatory mode shape of the sheet $w(x', y', t)$. \bar{w}' is the complex amplitude of oscillatory normal displacement of the sheet obtained by Galerkin decomposition.

$$\bar{u}'(x', y') = \frac{\partial}{\partial x'} \bar{w}'(x', y') + \frac{sb}{U} \bar{w}'(x', y') \quad (8)$$

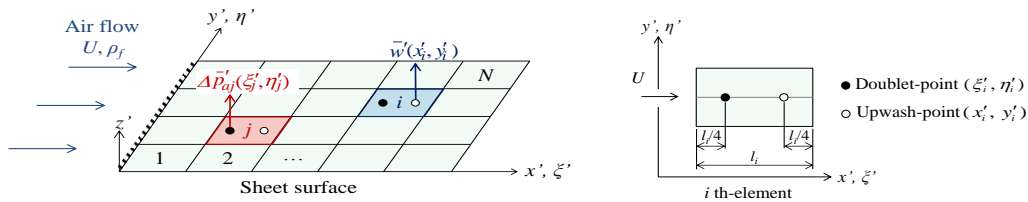


Figure 2: Location of doublet and upwash point for calculation of fluid force.

2.4 Modal approximation

Galerkin decomposition is applied to the Eq.(1). The lateral deflection of the sheet w can be written as

$$w(c,t) = \sum_{m=1}^{N_m} \phi_m(c) q_m(t) \quad (9)$$

where ϕ_m denotes the mode function of the cantilever beam *in vacuo*, q_m is generalized coordinate and N_m is number of Galerkin decomposition. Substituting Eq.(9) into Eq.(1) and multiplying by ϕ_l and integrating from $c = 0$ to L (chord direction) and from $y = 0$ to b (span direction), gives following nonlinear equation on the generalized coordinate q . In the equation, structural terms M_L , K_L , M_{NL} and K_{NL} are shown in previous paper (Tang et al., 2003).

$$\begin{aligned} & M_L b \ddot{q}_l + K_L b q_l + \sum_{m=1}^{N_m} G_{L1} b q_l - \sum_{n=1}^{N_m} \sum_{o=1}^{N_m} \sum_{p=1}^{N_m} G_{NL} b q_n q_o q_p - \sum_{m=1}^{N_m} G_{L2} b q_l + \sum_{n=1}^{N_m} \sum_{o=1}^{N_m} \sum_{p=1}^{N_m} M_{NL} b (q_n q_o \ddot{q}_p + q_n \dot{q}_o \dot{q}_p) \\ & + \sum_{n=1}^{N_m} \sum_{o=1}^{N_m} \sum_{p=1}^{N_m} (K_{NL} b q_n q_o q_p) + \sum_{n=1}^{N_m} \sum_{o=1}^{N_m} \sum_{p=1}^{N_m} \alpha K_{NL} b (\dot{q}_n q_o q_p + q_n \dot{q}_o q_p + q_n q_o \dot{q}_p) \end{aligned} \quad (10)$$

$$\begin{aligned} & = \frac{1}{2} \rho_f U^2 Q + \sum_{n=1}^{N_m} \sum_{o=1}^{N_m} \sum_{p=1}^{N_m} F_f b q_n q_o q_p - \frac{1}{2} \rho_f C_d b \int_0^L \sum_{a=1}^{N_m} \phi_a \dot{q}_a \left| \sum_{b=1}^{N_m} \phi_b \dot{q}_b \right| ds \\ & G_{L1} = \rho_s h g \sum_{m=1}^{N_m} \int_0^L \phi_l(c) \frac{\partial \phi_m(c)}{\partial c} dc, \quad G_{L2} = \rho_s h g \sum_{m=1}^{N_m} \int_0^L (L-c) \phi_l(c) \frac{\partial^2 \phi_m(c)}{\partial c^2} dc, \end{aligned} \quad (11)$$

$$\begin{aligned} & G_{NL} = \frac{3}{2} \rho_s h g \sum_{n=1}^{N_m} \sum_{o=1}^{N_m} \sum_{p=1}^{N_m} \int_0^L (L-c) \phi_l(c) \frac{\partial \phi_n(c)}{\partial c} \frac{\partial \phi_o(c)}{\partial c} \frac{\partial^2 \phi_p(c)}{\partial c^2} dc \\ & F_f = \frac{3}{2} \rho_f U^2 C_f \sum_{n=1}^{N_m} \sum_{o=1}^{N_m} \sum_{p=1}^{N_m} \int_0^L (L-c) \phi_l(c) \frac{\partial \phi_n(c)}{\partial c} \frac{\partial \phi_o(c)}{\partial c} \frac{\partial^2 \phi_p(c)}{\partial c^2} dc \end{aligned}$$

$$Q = \int_0^b \int_0^L \phi_l(c, y) \cdot \Delta p \, dc dy \equiv \underbrace{\sum_{r=1}^{N_m} \sum_{i=1}^N \sum_{j=1}^N c_{ij}(s) \cdot \phi_l(\xi_i, \eta_j) \cdot s_i \cdot \left(\frac{s}{U} \phi_r(x_j, y_j) + \frac{\partial}{\partial c} \phi_r \Big|_{x=x_j, y=y_j} \right)}_{Q_r} q_r \quad (12)$$

Fluid force matrix \mathbf{Q} and generalized coordinate vector \mathbf{q} are defined as follows:

$$\mathbf{Q}(s) = [Q_r] \quad (13)$$

$$\mathbf{q} = [q_1 \quad q_2 \quad \cdots \quad q_r \quad \cdots \quad q_{N_m}]^T \quad (14)$$

Then, fluid force matrix \mathbf{Q} shown in Eq.(13) belongs to the Laplace domain. Therefore, it is need to switch to the time domain in order to carry out time history response analysis. The fluid force matrix is approximated to a quadratic polynomial on Laplace parameter s shown in Eq.(15) by least-squares method.

$$\mathbf{Q}(s) \mathbf{q} \approx (\mathbf{Q}_{s0} + \mathbf{Q}_{s1} s + \mathbf{Q}_{s2} s^2) \mathbf{q} \quad (15)$$

$$\mathbf{Q}_{s0} = [Q_{s0lr}], \quad \mathbf{Q}_{s1} = [Q_{s1lr}], \quad \mathbf{Q}_{s2} = [Q_{s2lr}] \quad (16)$$

Finally, the fluid force matrix shown in Eq.(13) is switched to the time domain as Eq.(17) by inverse Laplace transformation.

$$\mathbf{Q} \mathbf{q} = \mathbf{Q}_{s0} \mathbf{q} + \mathbf{Q}_{s1} \dot{\mathbf{q}} + \mathbf{Q}_{s2} \ddot{\mathbf{q}} \quad (17)$$

2.5 Numerical method (time integration scheme)

To carry out time integration, the Houbolt method (Semler et al., 1996) is adopted because the governing equation Eq.(1) contains nonlinear inertia term. Adopting finite difference

approximation by the Houbolt method, time derivative of generalized coordinate $\dot{q}_i^{(k+1)}$ and $\ddot{q}_i^{(k+1)}$ are expressed by Eq.(18). Note that the Houbolt method is fourth order backward scheme and concluded that the method is efficient time integration scheme for dynamic analysis of flexible structures such as plastic films (Semler et al., 1996). Moreover, coefficients $\lambda_{1i}^{(k+1)}$ and $\lambda_{2i}^{(k+1)}$ are determined using the solutions of the previous time step $q_i^{(k-2)}$, $q_i^{(k-1)}$ and $q_i^{(k)}$.

$$\dot{q}_i^{(k+1)} = \frac{1}{\Delta t} \underbrace{\left(-\frac{1}{3}q_i^{(k-2)} + \frac{3}{2}q_i^{(k-1)} - 3q_i^{(k)} + \frac{11}{6}q_i^{(k+1)}\right)}_{\lambda_{1i}^{(k+1)}}, \ddot{q}_i^{(k+1)} = \frac{1}{(\Delta t)^2} \underbrace{\left(-q_i^{(k-2)} + 4q_i^{(k-1)} - 5q_i^{(k)} + 2q_i^{(k+1)}\right)}_{\lambda_{2i}^{(k+1)}} \quad (18)$$

Substituting Eq.(18) into Eq.(10) a set of nonlinear equations for $q_i^{(k+1)}$, which are the unknown generalized coordinate at time step $k + 1$ are derived. Then, the nonlinear simultaneous equations ($l = 1 - N_m$) are solved by iterative calculation using the Newton-Raphson method.

$$\begin{aligned} & \left(M_L b q_l^{(k+1)} + M_L \lambda_{2l}^{(k+1)}\right) + K_L b q_l^{(k+1)} + \sum_{m=1}^{N_m} G_{L1} b q_l^{(k+1)} - \sum_{n=1}^{N_m} \sum_{o=1}^{N_m} \sum_{p=1}^{N_m} G_{NL} b q_n^{(k+1)} q_o^{(k+1)} q_p^{(k+1)} - \sum_{m=1}^{N_m} G_{L2} b q_l^{(k+1)} \\ & + \sum_{n=1}^{N_m} \sum_{o=1}^{N_m} \sum_{p=1}^{N_m} (K_{NL} b q_n^{(k+1)} q_o^{(k+1)} q_p^{(k+1)}) \\ & + \alpha \sum_{n=1}^{N_m} \sum_{o=1}^{N_m} \sum_{p=1}^{N_m} K_{NL} b \left(\frac{11}{2\Delta t} q_n^{(k+1)} q_o^{(k+1)} q_p^{(k+1)} + \lambda_n^{(k+1)} q_o^{(k+1)} q_p^{(k+1)} + q_n^{(k+1)} \lambda_o^{(k+1)} q_p^{(k+1)} + q_n^{(k+1)} q_o^{(k+1)} \lambda_p^{(k+1)}\right) \\ & + \sum_{n=1}^{N_m} \sum_{o=1}^{N_m} \sum_{p=1}^{N_m} M_{NL} b \left(\frac{2}{(\Delta t)^2} q_n^{(k+1)} q_o^{(k+1)} q_p^{(k+1)} + q_n^{(k+1)} q_o^{(k+1)} \lambda_{2p}^{(k+1)}\right) \\ & + \sum_{n=1}^{N_m} \sum_{o=1}^{N_m} \sum_{p=1}^{N_m} M_{NL} b \left(q_n^{(k+1)} \lambda_o^{(k+1)} \lambda_p^{(k+1)} + \frac{11}{6\Delta t} q_n^{(k+1)} \lambda_o^{(k+1)} q_p^{(k+1)} + \frac{11}{6\Delta t} q_n^{(k+1)} q_o^{(k+1)} \lambda_p^{(k+1)} + \frac{121}{36(\Delta t)^2} q_n^{(k+1)} q_o^{(k+1)} q_p^{(k+1)}\right) \\ & = \frac{1}{2} \rho_f U^2 s_i \sum_{r=1}^{N_m} Q_{s0lr} q_r^{(k+1)} + \frac{1}{2} \rho_f U^2 s_i \sum_{r=1}^{N_m} Q_{s1lr} \frac{11}{6\Delta t} q_r^{(k+1)} + \frac{1}{2} \rho_f U^2 s_i \sum_{r=1}^{N_m} Q_{s1lr} \lambda_{1r}^{(k+1)} \\ & + \frac{1}{2} \rho_f U^2 s_i \sum_{r=1}^{N_m} Q_{s2lr} \frac{2}{(\Delta t)^2} q_r^{(k+1)} + \frac{1}{2} \rho_f U^2 s_i \sum_{r=1}^{N_m} Q_{s2lr} \lambda_{2r}^{(k+1)} + \sum_{n=1}^{N_m} \sum_{o=1}^{N_m} \sum_{p=1}^{N_m} F_f b q_n^{(k+1)} q_o^{(k+1)} q_p^{(k+1)} \\ & - \frac{1}{2} \rho_f C_d b \int_0^L \phi_l \left\{ \sum_{a=1}^{N_m} \phi_a (\lambda_{1a}^{(k+1)} + \frac{11}{6\Delta t} q_a^{(k+1)}) \right\} \left| \sum_{b=1}^{N_m} \phi_b (\lambda_{1b}^{(k+1)} + \frac{11}{6\Delta t} q_b^{(k+1)}) \right| dc \end{aligned} \quad (19)$$

2.6 Work done by fluid force acting on the sheet surface

To investigate the sustaining mechanism of the LCO, the local work done by fluid force acting on the sheet surface is determined by following equation. In the equation, P_{dp} , P_f and P_d denote work done by fluid force determined by the DPM, work done by fluid friction and work done by fluid drag, respectively.

$$E_i = \int_0^\tau \dot{w}_i \cdot f_i dt = \int_0^\tau \underbrace{(\dot{w}_i \cdot \Delta p_i)}_{P_{dp}} + \underbrace{\dot{w}_i \cdot p_f}_{P_f} + \underbrace{\dot{w}_i \cdot p_d}_{P_d} dt \quad (20)$$

3 Experimental setup

Fig.3 shows a photograph and a schematic of the experimental setup. Experiments were carried out in a vertical wind-tunnel to validate the results of the numerical simulation. A rectangular test sheet whose material is polyethylene is set in upstream side of the wind tunnel. The upstream edge of the sheet is clamped by two rigid support plates. The support

plates used in the clamped section are made of SUS304. The clamped section is processed into thin aerofoil to suppress flow turbulence.

The vibration displacement of the sheet was measured by using a laser displacement sensor installed at the test section. During the experiment, the vibration displacement of the sheet was measured while gradually increasing the flow velocity of air. Then flow velocity U was measured using hot-wire probe. The flow velocity at which the flutter occurs is determined as a flutter velocity U_f and then dominant frequency f_f is defined as a flutter frequency. Moreover, vibration modes of the fluttering sheet were visualized with a high-speed digital camera and a strobe light.

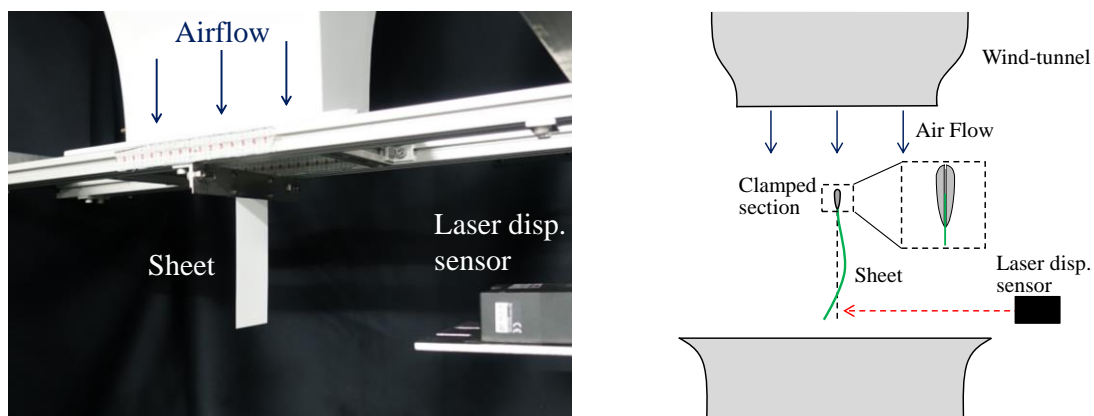


Figure 3: Photograph and schematic of the experimental setup.

4 Calculation parameters

Table 1 lists the parameters used in calculation. The division number of x and y directions were set to 15 and 13, respectively and number of Galerkin decomposition N_m was set in 4. These values are sufficiently convergent number. Additionally, three different values of C_f and C_d were used. Note that a $C_d = 1.8$ corresponds to a measurement value of a statically deformed sheet in air flow (Buchak, 2010).

Table 1: Parameters used in calculation

L [mm]	120	C_f	0.025, 0.05, 0.1
b [mm]	60	C_d	1.5, 1.8, 2.5
h [mm]	0.2	g [m ² /s]	9.81
E_s [GPa]	3.2	Δt [s]	1.0×10^{-4}
ν_s	0.4	N_x	15
ρ_s [kg/m ³]	1380	N_y	13
α	1.0×10^{-3}	N_m	4
ρ_f [kg/m ³]	1.2		

5 Experimental results

Fig.4 shows RMS displacement w_{RMS} and flutter frequency f_f of the sheet with changing flow velocity. In the figures, two results are shown: the first is the result which is gradually increasing flow velocity from 6.0m/s to 9.0m/s (shown in open circle) and the second is the

results which is decreasing flow velocity from 9.0m/s to 6.0m/s (shown in open triangle). Displacement was measured at a position which is 25mm from the trailing edge of the sheet. From the Fig.4(a), The amplitude of the sheet suddenly increased when flow velocity reached 7.5 m/s and continued increasing with increasing flow velocity. Then, there is no remarkable change of amplitude in the case of decreasing flow velocity. Therefore, the hysteretic behavior reported in previous study (Tang et al., 2003) is not observed in the present experiment. Moreover, flutter frequency increases monotonically with increasing flow velocity.

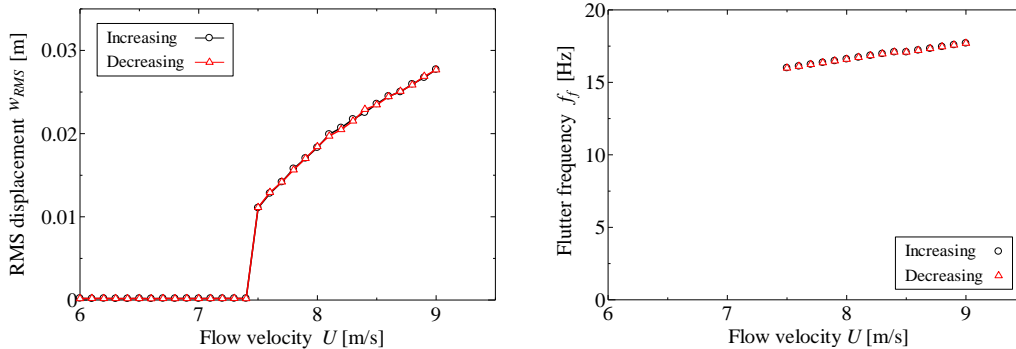


Figure 4 : RMS displacement(a) and flutter frequency(b) with changing flow velocity.

6 Analytical results and discussion

6.1 Time history and spectrum of vibration displacement

Time histories(a), spectrum(b) and modal amplitude(c) are shown in Fig.5 at flow velocities is 10.0m/s (30% higher than critical velocity). From time histories (Fig.5(a)), amplitude gradually increases and finally reaches limit cycle. Then, it is seen that single frequency is dominant from spectrum (see Fig.5(b)). In addition, a higher harmonic wave is weakly observed. Moreover, from Fig.5(c), the first two modal numbers significantly contribute to flutter amplitude, while the higher modes show little contribution.

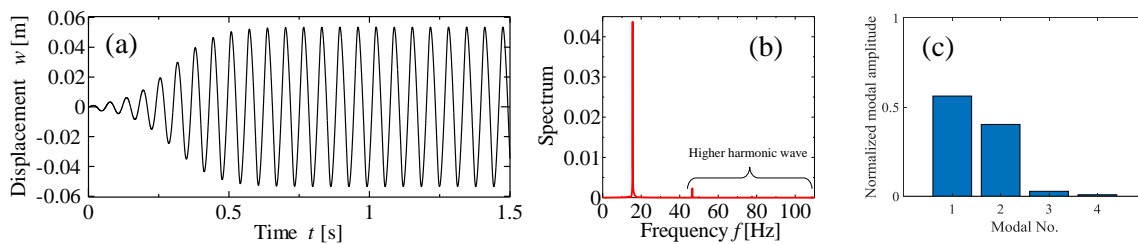


Figure 5 : Time histories(a), spectrum(b) and modal amplitude(c).

6.2 Influence of coefficient of fluid drag C_d and friction C_f

Fig.6 shows RMS flutter amplitude and frequency with changing flow velocity for various C_d and C_f . In the previous study, it is reported that C_d and C_f depend on upwash velocity(normal flow velocity) induced on the sheet surface (Ehrenstein et al., 2014). Therefore, influence of C_d and C_f on flutter characteristics was investigated. From these figures, increasing of C_d and C_f decreases flutter amplitude. Then, critical velocity and flutter amplitude are in good agreement with experimental results shown in Fig.4. On the other hand, the order of flutter frequency is almost same value, but change tendency of frequency toward flow velocity has difference between analysis and experiment. The reason may be because the nonlinearity of the fluid force is not sufficiently considered in the present

analytical model : in the present model, the nonlinearity of fluid force is simply summarized in nonlinear fluid drag and frictional terms.

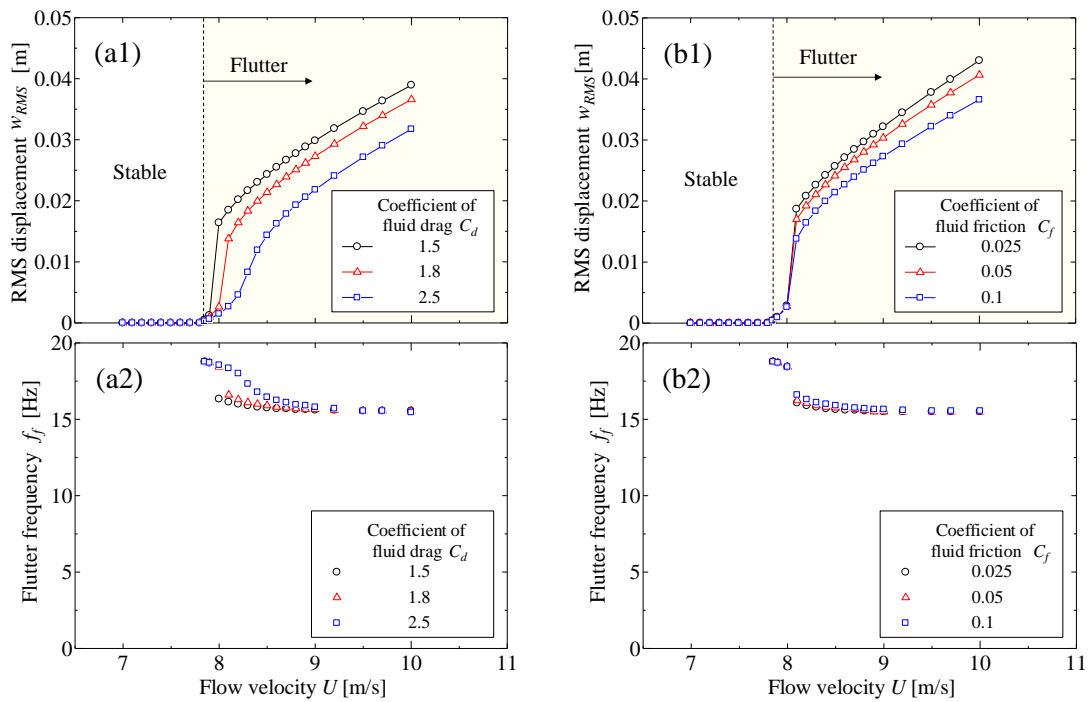


Figure 6 : Influence of C_d (a1), (a2) and C_f (b1), (b2) on flutter amplitude and frequency.

6.3 Flutter modes

Fig.7 shows photographs of observed flutter motion in experiment and calculation results. These visualizations of flutter modes were carried out at critical velocity and higher flow velocity (30% higher than critical velocity). From these results, experiment and theoretical predictions are in good agreement. Traveling-wave type modes are observed from both of experiment and analysis.

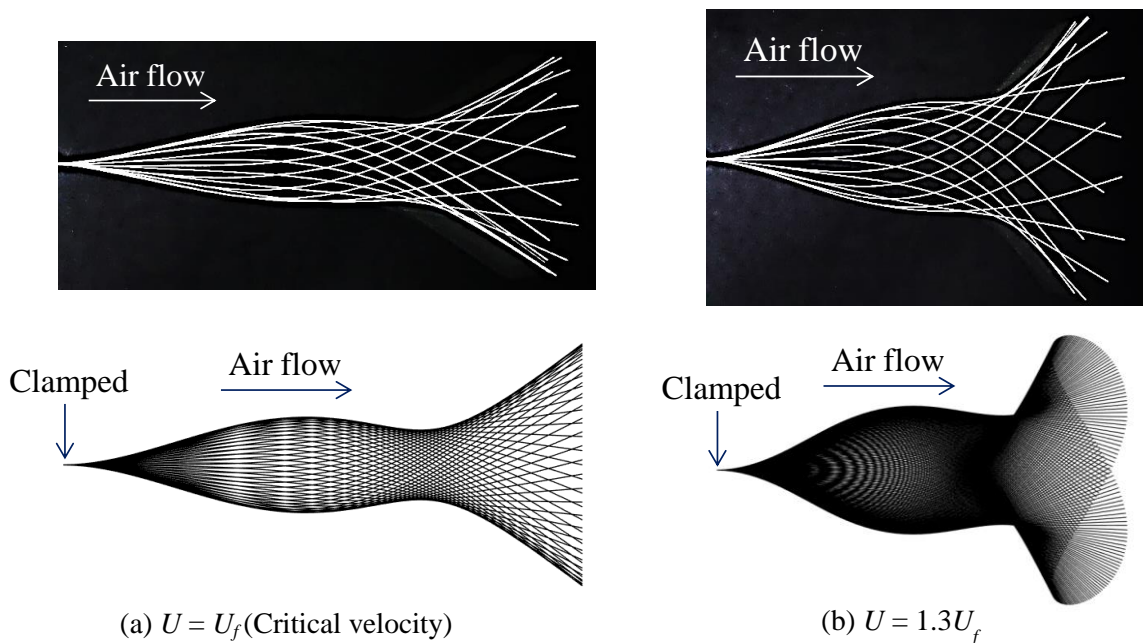


Figure 7 : Flutter modes visualized in experiment and predicted by analysis.

6.4 Local work done by fluid force acting on the sheet surface

Fig.8 shows the local work done by the fluid force at each position ((a): $x = 0.028\text{m}$, (b): $x=0.062\text{m}$, (c): $x = 0.114\text{m}$) on the sheet surface derived by the theoretical calculation in the case of $U = 10.0\text{m/s}$ (27% higher than critical velocity). From the Fig.8(b1), the local work done is positive around the midstream region on the sheet. On the other hands, around the trailing edge of the sheet, the local work is negative (Fig.8(c1)). Moreover, the amount of work around the leading edge (Fig.8(a1)) is small compared to other positions. Thus, LCO is sustained by balancing of positive work around the midstream region and negative work around the trailing edge of the sheet. In regard to work done by fluid drag, negative work is dominant around the trailing edge (Fig.8(c4)) and largely contribute to sustaining of LCO. In addition, negative work by fluid friction is dominant at the middle of the sheet (Fig.8(b3)) which has high curvature.

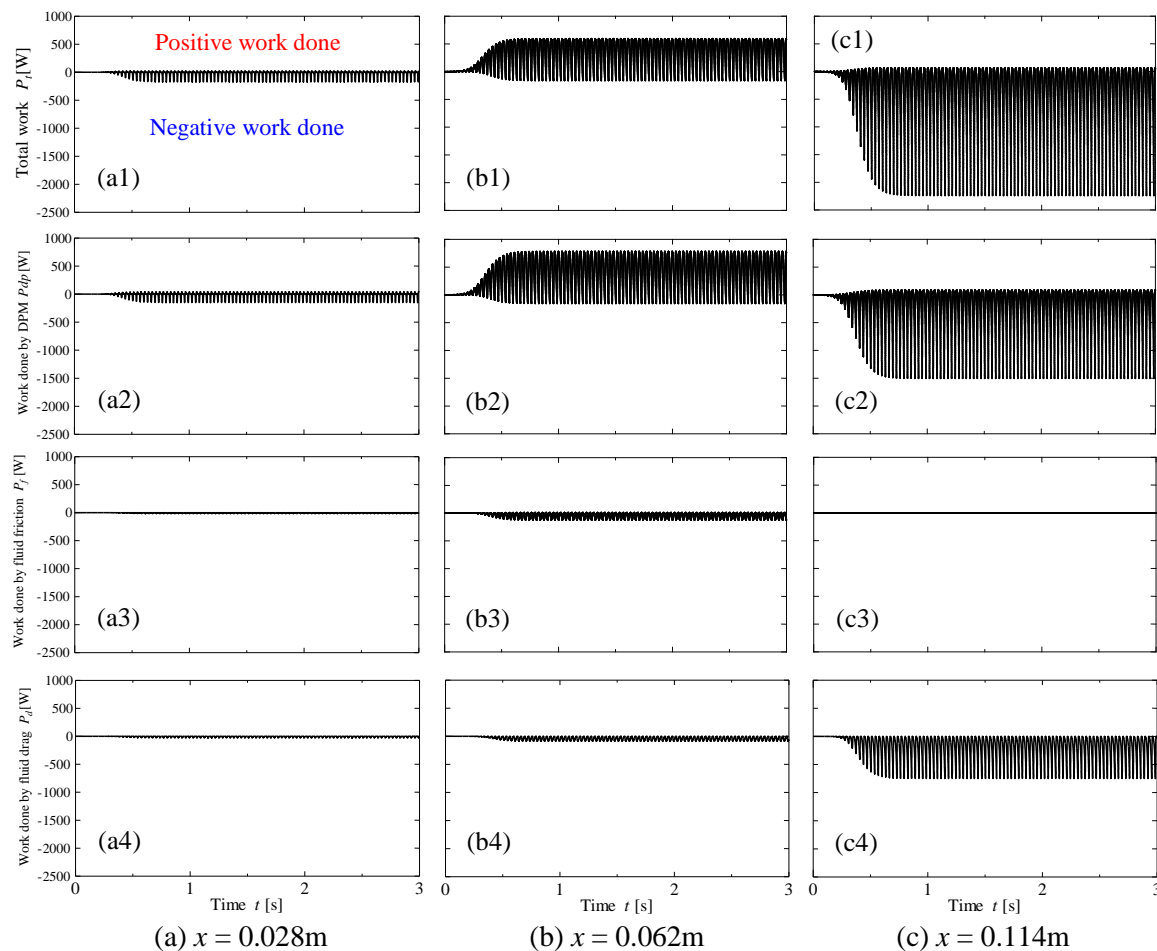


Figure 8 : Work done by fluid force acting on the sheet surface at different positions (x).

7 Conclusions

In the present paper, we performed a nonlinear flutter analysis of a cantilevered sheet in uniform fluid flow. The analytical and experimental results are in good agreements for the flutter amplitude and mode. Moreover, the local work done by the fluid force acting on the sheet surface was determined. The results obtained in present study are summarized as follows:

- (1) The first two modal numbers significantly contribute to increasing flutter amplitude, while

- the higher modes show little contribution.
- (2) Increasing of coefficient of fluid drag C_d and coefficient of fluid friction C_f decrease flutter amplitude.
 - (3) LCO is sustained by balancing of positive work around the midstream region and negative work around the trailing edge of the sheet.

Acknowledgements

The authors gratefully acknowledge the experimental assistance by Prof. Satoru Yoneyama (Aoyama Gakuin University).

References

- Buchak, P., Eloy, C. and Reis, P. M., 2010. The clapping book : wind-driven oscillations in a stack of elastic sheets. *Physical review letters*, 105, 194301.
- Chen, M., Jia, L., Wu, Y., Yin, X. and Ma, Y., 2014. Bifurcation and chaos of a flag in an inviscid flow. *Journal of Fluids and Structures*, 45, 124-137.
- Ehrenstein, U., Marquillie, M., and Eloy, C., 2014. Skin friction on a flapping plate in uniform flow, *Philosophical Transactions of the Royal Society A*, 372, 20130345.
- Eloy, C., Souilliez, C. and Schouveiler, L., 2007. Flutter of a rectangular plate. *Journal of Fluids and Structures*, 23, 904-919.
- Gibbs, C. S., Wang, I. and Dowell, E. H., 2012. Interaction between a cantilevered-free flexible plate and ideal flow. *Journal of Fluids and Structures*, 34, 68-83.
- Hiroaki, K., Watanabe, M. and Morita, R., 2015. Flutter analysis and experiments of a rectangular sheet supported by a wire. *Proceedings of ASME PVP2015*, No.PVP2015-45061.
- Huang, L., 1995. Flutter of cantilevered plates in axial flow. *Journal of Fluids and Structures*, 9, 127-147.
- Küssner, H.G., 1941. General airfoil theory. NACA TM 979.
- Sawada, T. and Hisada, T., 2007. Fluid-structure interaction analysis of the two-dimensional flag-in-wind problem by an interface-tracking ALE finite element method. *Computers & Fluids*, 36, 136-146.
- Semler, C., Gentleman, W. C. and Paidoussis M. P., 1996. Numerical solutions of second order implicit non-linear ordinary differential equations. *Journal of sound and vibration*, 195, 553-574.
- Tang, D. M., Yamamoto, H. and Dowell, E.H., 2003. Flutter and limit cycle oscillation of two-dimensional panels in three-dimensional axial flow. *Journal of Fluids and Structures*, 17, 225-242.
- Tang, L. and Paidoussis, M. P., 2007. On the instability and the post-critical behavior of two-dimensional cantilevered flexible plates in axial flow. *Journal of Sound and Vibration*, 305, 97-115.
- Ueda, T. and Dowell, E.H., 1982. A new solution method for lifting surface in subsonic flow. *AIAA Journal*, 20, 348-355.
- Ueda, T., 1987. Lifting surface calculations in the Laplace domain with application to root loci. *AIAA Journal*, 25, 698-704.
- Watanabe, Y., Isogai, K., Suzuki, S. and Sugihara, M., 2002. A theoretical study of paper flutter. *Journal of Fluids and Structures*, 16, 543-560.
- Yamaguchi, N., Yokota, K. and Tsujimoto, Y., 2000. Fluttering limits and behaviors of a flexible thin sheet in high-speed flow – I: analytical method for prediction of the sheet behavior. *ASME Journal of Fluids Engineering*, 122, 65-73.

Snap-through oscillation induced by uniform flow

Hyeonseong Kim¹, Junsoo Kim² and Daegyoun Kim²

¹*Department of Mechanical Engineering, KAIST, Daejeon, Republic of Korea, hskim213@kaist.ac.kr*

²*Department of Mechanical Engineering, KAIST, Daejeon, Republic of Korea*

Keyword: Periodic snap-through, Buckled elastic sheet, Critical velocity

When both ends of an elastic sheet are clamped with shorter distance between the ends than its length, the sheet has a buckled shape. By using various external energy inputs such as point load¹, capillary force² and viscous flow force in a channel³, rapid transition from the one buckled shape to the other buckled shape can be induced, which is called as “snap-through” motion.

Here, we investigate the dynamics of the snap-through motion using an elastic sheet and a uniform flow. Periodic snap-through is observed beyond a specific critical free-stream velocity. The critical velocity can be obtained theoretically using the quasi-steady aerodynamic force model and the elastic beam model. Unlike the typical flag configuration which has one clamped end and one free end, in this configuration, compressive force should be considered additionally to maintain a balance between bending force and aerodynamic force.

From scaling analysis, we found that dimensionless critical free-stream velocity derived from the equation of the motion was inversely proportional to length ratio to the power of a specific value, where the length ratio is a ratio of distance between two clamped points to sheet length. Additionally, we confirmed that the effect of mass ratio, relative magnitude of sheet mass against fluid mass, on the critical velocity was negligible, which indicates that snap-through instability is divergence instability.

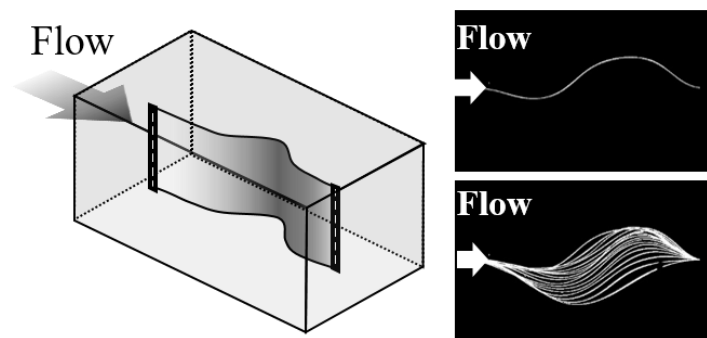


Figure 1: Flow-induced snap-through motion

1. Pandey, A., Moulton, D. E., Vella, D. and Holmes, D. P. (2014), Dynamics of snapping beams and jumping poppers. *Europhysics Letters*, 105(2), 24001.
2. Fargette, A., Neukirch, S. and Antkowiak, A. (2014) Elastocapillary snapping : Capillarity induced snap-through instabilities in small elastic beams. *Physical Review Letters*, 112(13), 137802
3. Gomez, M., Moulton, D. E. and Vella, D. (2017) Passive control of viscous flow via elastic snap-through. *Physical Review Letters*, 119, 144502.

Why inverted flags flap: An experimental study

Mohammad Tavallaeinejad¹, Michael P. Païdoussis¹, Manuel Flores Salinas²,
Mathias Legrand¹, Mojtaba Kheiri³, and Ruxandra Mihaela Botez²

¹ *Department of Mechanical Engineering, McGill University, Montréal, Québec, Canada*

² *Ecole de Technologie Supérieure, Montréal, Québec, Canada*

³ *FSI & Aeroelasticity Laboratory, Concordia University, Montréal, Québec, Canada*

Corresponding author: mohammad.tavallaeinejad@mail.mcgill.ca

Abstract

The experiments described in this paper aim to examine the global dynamics of inverted flags and to explore the impact of periodic vortex shedding from the leading and trailing edges thereon. The effect of vortex shedding from both leading and trailing edges was investigated. It is shown that suppression of the leading and trailing edge vortices, and also inhibition of the interaction between the two counter-rotating vortices (if they exist), resulted in relatively small quantitative changes in the critical flow velocity, amplitude and frequency; but, the overall dynamics of the system remain intact. More importantly, the large-amplitude flapping persisted for all flags tested in the experiments.

Force measurements provide some insights into the relationship between vortex shedding and large-amplitude flapping; a difference between the dominant frequency of the lift and that of flapping was observed for some cases. Moreover, for heavier inverted flags, additional peaks appear in the frequency spectrum of the lift signal, with amplitudes comparable to that matching the dominant frequency of flapping.

The experimental results suggest that *fluidelastic instability* is the underlying mechanism for the flapping motion of heavy inverted flags. The near-identical qualitative behaviour of normal inverted flags and serrated ones with a splitter plate at the trailing edge suggests that the global (or qualitative) dynamics of heavy inverted flags is independent of unsteady vortex shedding from the leading and trailing edges; i.e., periodic vortex shedding is not the cause but an effect of large-amplitude flapping.

Keyword: fluid-structure interactions, inverted flags, large-amplitude flapping, fluidelastic instability, flutter

1 Introduction

This paper focuses the fluid-structure interaction (FSI) of a flexible thin plate in axial flow: a cantilevered thin plate (or flag) of length L and height H subjected to a fluid flowing axially with velocity U and directed from the free end towards the clamped one, otherwise known as an 'inverted flag;' see figure 1.

Inverted flags are known to exhibit large-amplitude periodic flapping around the undeflected equilibrium. A number of studies on the dynamics of inverted flags suggest that the physical

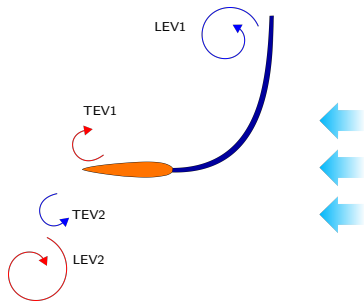


Figure 1 – Inverted flag in large-amplitude regime, shedding leading-edge vortices (LEV) and trailing-edge vortices (TEV) in the wake.

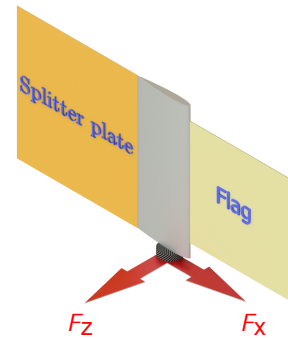


Figure 2 – Experimental set-up for a serrated inverted flag with the rigid splitter plate, showing the measured forces at the flagpole, utilizing a force balance.

mechanism underlying large-amplitude flapping may be *Vortex-Induced Vibration* (VIV) (e.g., Sader et al. 2016). In these studies, the flapping phenomenon is attributed to the periodic formation and synchronized shedding of trailing-edge vortices (TEV) and leading-edge vortices (LEV), which is a characteristic of VIV (see figure 1).

Although several aspects of the dynamics may be explained through the VIV mechanism, there are some circumstances where vortex shedding, which plays a central role in VIV, may not occur for a flapping inverted flag, hence posing a challenge to the credence of the VIV mechanism. For instance, in an experimental study, Pazhani and Acharya (2019) investigated the effect of leading-edge serrations. They found that the serrated flag *does* display large-amplitude flapping, even though vortex formation and shedding from the leading edge was not observed. Moreover, via a scaling analysis, Sader et al. (2016) predicted that VIV cannot occur for heavy flags or small mass ratios¹, yet large-amplitude flapping does. Goza et al. (2018) explored computationally the physical mechanisms for large-amplitude flapping of inverted flags, concluding that for a specific set of system parameters, large-amplitude flapping cannot be attributed to classical VIV, and also for small-amplitude flapping. Finally, Gurugubelli and Jaiman (2019) performed simulations in which a rigid splitter plate was attached to the flag trailing edge, thus suppressing trailing-edge vortex shedding; they found that inverted flags undergo large-amplitude flapping even though the interactions between vortices detached from the leading-edge at the cycle extremities were eliminated – a prediction not yet verified experimentally, which is one of the objectives of the present experiments.

The primary purpose of experiments described in this paper is to explore the correlation between vortex shedding and the flapping mechanism; specifically, the qualitative and quantitative effects of suppression of both LEV and TEV on the onset, frequency, and amplitude of flapping.

The paper is organized as follows. First, experiments with a rigid splitter plate attached to the trailing-edge of the inverted flag are described (see Figure 2), aiming to evaluate the importance of the existence of TEV and to examine the effects of forced disconnection between counter-rotating LEV on large-amplitude flapping. Second, experiments with inverted flags with

¹The fluid-to-plate mass ratio is defined as $\mu = \rho_f L / \rho_p h$; ρ_f and ρ_p being the mass density of the fluid and plate, respectively, and h is the thickness of the plate. Small μ is associated with “heavy flags”.

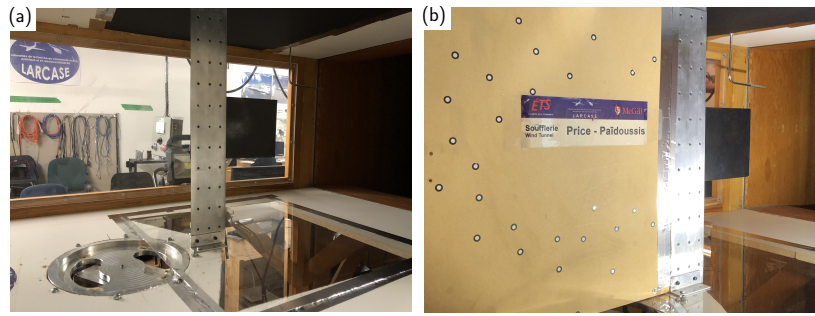


Figure 3 – Experimental set-up for the inverted flag (a) without and (b) with the rigid splitter plate.

a serrated leading-edge, similar to those used by [Pazhani and Acharya \(2019\)](#), are described. These experiments explore the effects of simultaneous suppression of LEV and TEV. Finally, the synchronization of lift and displacement and phase dynamics are studied.

2 Rigid splitter plate

The experiments were conducted in a subsonic wind tunnel with a fairly large test-section. The flow velocity in the test-section was incremented in small steps, and the flag motion was recorded via a high-speed camera at each step. An image processing technique was then utilized to extract the time history of oscillations. Brass plates, i.e. ‘flags’ ($H = 101$ mm, $L = 198$ mm, and thickness $h = 0.38$ mm), as well as polycarbonate flags with different dimensions (see [Table 1](#)) were used in the experiments. Experiments have been conducted with and without a rigid splitter plate. The splitter plate was made from a plywood sheet of thickness $h_s = 10$ mm, height $H_s = 610$ mm, and length $L_s = 1800$ mm, and was secured firmly to the walls of the test-section (see [figure 3](#)); no significant motion of the splitter plate was observed during the experiment, even at very high wind speeds.

[Figure 4\(a\)](#) shows bifurcation diagrams for the tip rotation of 160×160 mm polycarbonate flags C (circles) and flag D (diamonds), with the rigid splitter plate (filled symbols) and without it (empty symbols). A slight reduction is seen for the flapping amplitude of the flag with a splitter plate. This may be explained using observations made by [Gurugubelli and Jaiman \(2019\)](#). In their computational study, the inverted flag with the splitter plate exhibits only two counter-rotating vortices shed from the leading edge over the flapping cycle. The absence of the trailing edge vortices, and the inhibition of vortex-vortex interaction leads to a larger pressure distribution at the trailing edge and to a slightly smaller drag at the leading edge. This results in a smaller bending moment, which in turn leads to a reduction in the curvature along the flag.

The frequency of oscillation is also reduced slightly when the splitter plate is introduced, see [Figure 4\(b\)](#). For instance, the maximum reduction in flapping frequency for the $h = 1.02$ mm flag is at $U \simeq 20$ m/s, where the frequency is reduced by almost 8%. This may also be associated with loss of the trailing edge vortices, caused by the rigid splitter plate. More specifically, the trailing edge vortex formation and shedding accelerates the drop in the pressure distribution over the flag, which consequently leads to a faster transition from maximum deflection from one side to the other, hence to a higher frequency (see [Gurugubelli and Jaiman \(2019\)](#)).

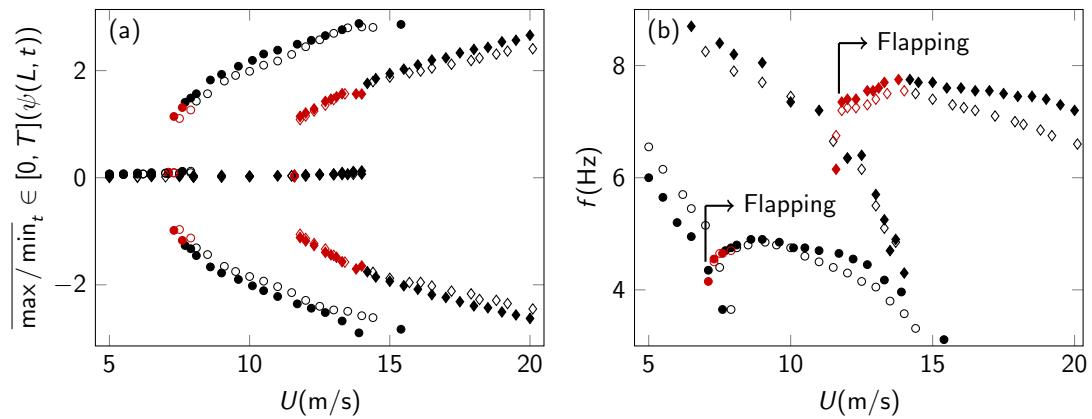


Figure 4 – Experimental results for inverted flags with $L = H = 160$ mm and [●] $h = 0.76$ mm, [◆] $h = 1.02$ mm; (a) bifurcation diagram (b) variation of the dominant frequency in PSD with the flow speed. The empty and filled markers correspond to the flags with and without the splitter plate, respectively; the black and red symbols correspond to the wind speed sweep up and down, respectively.

Figure 5 shows that the onset of large-amplitude flapping for all flags tested (except for flag B) is delayed when the splitter plate is added. This may be linked to the pressure reduction close to the leading edge of the inverted flag due to the splitter plate: the presence of the splitter plate introduces a small additional damping to the dynamical system; consequently, the critical flow velocity for large-amplitude flapping increases, and the flapping amplitude and frequency become smaller at the onset of large-amplitude flapping.

However, all these differences are very minimal. The main and most significant conclusion is that introducing a splitter plate has a minimal influence on the critical flow velocity for large-amplitude flapping, its amplitude and frequency.

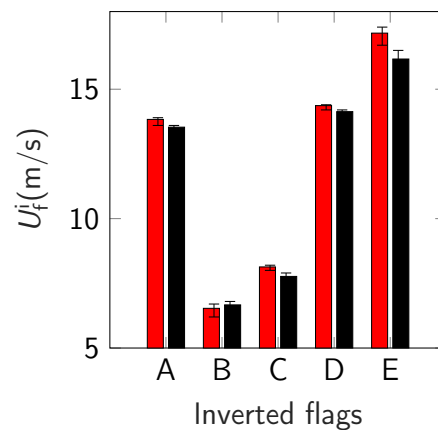


Figure 5 – Critical flow speed for the onset of large-amplitude flapping of different inverted flags with sweeping up the wind speed; [■] with and [■] without the rigid splitter plate.

Flag	Material	$L \times H$ (mm)	h (mm)
A	Polycarbonate	150×225	1.02
B	Polycarbonate	150×600	0.76
C	Polycarbonate	160×160	0.76
D	Polycarbonate	160×160	1.02
E	Brass	198×101	0.38

Table 1 – Labels and dimensions of pairs of inverted flags tested in experiments with and without the rigid splitter plate.

3 Serrated inverted flags

In order to further understand the effect of vortex shedding on the global dynamics of inverted flags, a serrated leading-edge geometry (chevron) with height $H_s = 10$ mm and width $W_s = 10$ mm was introduced to polycarbonate flags of different aspect ratios, see Figure 6(a).

Using flow visualization techniques, Pazhani and Acharya (2019) have shown that this serrated geometry produces small counter-rotating pairs of vortices, which suppresses the formation and periodic shedding of vortices from the leading edge.

The Pazhani and Acharya (2019) experiments with serrated flags have been repeated in the present study, with wider flags – to minimize three-dimensionality of the flow caused by the side edges – also introducing a rigid splitter plate at the trailing edge of the flag to interrupt the communication of the separated shear layers. Mainly, qualitative experiments were conducted. Insofar as the onset and amplitude of large-amplitude flapping is concerned, the responses are similar to those of normal inverted flags. For instance, the experimental results for flags of $\mathcal{R} = 3.0$ in figure 6(b) show no notable differences in the critical values of flow velocity and the amplitude of oscillation, with and without the splitter plate and serrations.

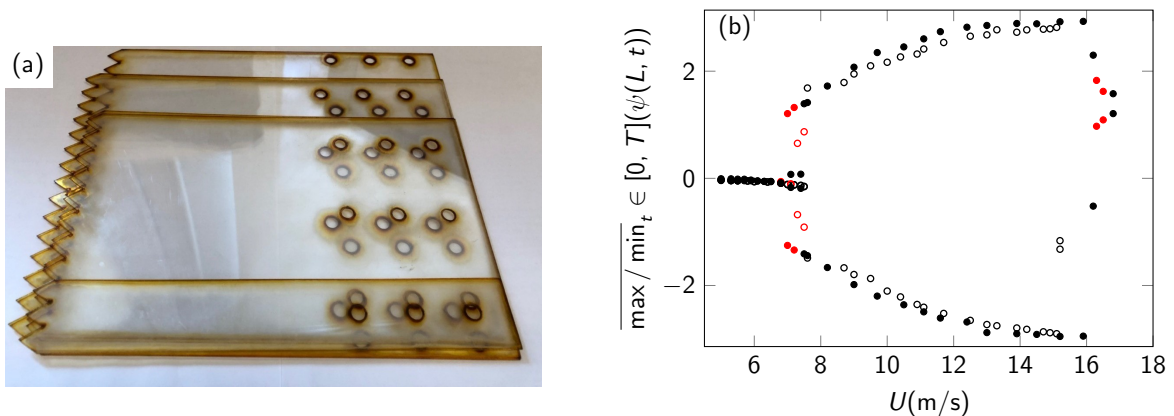


Figure 6 – Experiments with serrated inverted flags: (a) specimens used in the experiments with a similar serration geometry but different flag dimensions, (b) bifurcation diagram for an inverted flag with flat leading edge and no splitter plate (filled circles) and a serrated flag with the splitter plate at the trailing edge (empty circles); both flags are of $\mathcal{R} = 3.0$. The black and red symbols correspond to the wind speed sweep up and down, respectively.

The observed behaviour shows that, for the range of parameters investigated in these experiments, the dynamical characteristics of inverted flags are not very sensitive to (i) the formation and periodic shedding of vortices from the leading and trailing edges, and (ii) vortex-vortex interaction (if any exists). Hence, another mechanism must be the cause of large-amplitude flapping; namely, it may be a fluidelastic *self-excited flutter*.

4 Synchronization of lift and displacement and phase dynamics

Several experiments were conducted to measure simultaneously the forces acting on the flag (i.e. lift and drag) and its motion. The phase difference between the time traces of the fluid

Table 2 – Stainless-steel inverted flags with $H = 75$ mm, $h = 0.08$ mm, and varying length utilized in experiments.

Flag	L (mm)	μ	\mathcal{R}
A	100	0.21	0.75
B	70	0.15	1.07
C	50	0.10	1.50
D	35	0.07	2.14

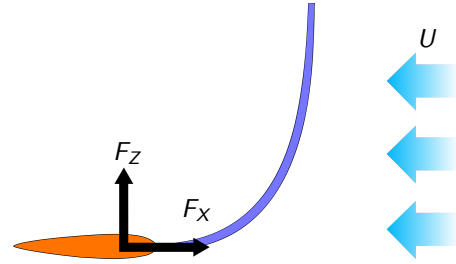


Figure 7 – Measured forces at the flagpole, utilizing a force balance.

forces and flag displacements were examined. Moreover, the dominant frequencies of the fluid forces were obtained.

These experiments were motivated by the observation made by [Goza et al. \(2018\)](#) for large-amplitude flapping of heavy inverted flags. They reported that, compared to light flags, several additional vortices are shed per cycle for heavy (low μ) ones, resulting in additional peaks in the frequency spectrum of the lift signal. Moreover, the frequency associated with the largest peak in the lift spectrum was different from that of the displacement spectrum. This led [Goza \(2019\)](#) to refer to the large-amplitude flapping of massive flags as “not-classical VIV”.

In order to investigate experimentally the existence of synchronization between the lift force and displacement for heavy inverted flags, stainless steel flags of varying length (hence, varying mass ratio) were tested (see Table 2). The transverse (lift) and streamwise (drag) components of the fluid flow force were simultaneously measured at the flagpole, utilizing an in-house built aerodynamic balance (A Mini45-E Array Technology Incorporated Inc). Time traces of the lift, $F_z(0, t)$, and the drag, $F_x(0, t)$, components (see Figure 7) were collected at 1000 Hz; the sampling rate for the tip transverse displacement, $w(L, t)$, was 160 – 280 Hz.

4.1 Frequency characteristics

Figure 8 shows the time traces and PSDs of $w(L, t)$ and the lift signals for a stainless-steel inverted flag with $L = 100$ mm. In the PSD plots for the lift signal, the peaks are labeled sequentially as f_{L1} , f_{L2} etc. from lower to higher frequencies. As seen from figures 8(b,d), higher harmonics of nearly the same magnitude as the main frequency, f_1 , appear in the PSD of the lift, while the motion is periodic, supporting the [Goza et al.](#) observations discussed above. By increasing the flow velocity, motion becomes chaotic-like at $U = 8.3$ m/s; the loss of synchronization with departure from a periodic behaviour can be seen in figures 8(e,f).

The spectrograms of the displacement and lift signals are presented in figures 8 (g) and (h), respectively, showing an increase in dynamic activity and the presence of additional frequency peaks in the lift dynamics with increasing U . The increase in number and the strength of higher harmonics in the lift frequency spectrum suggests that the conjectured VIV-associated oscillation is gradually replaced by another mechanism.

Figure 9 shows the time traces and PSDs for flags with (a,b) $L = 70$ mm, (c,d) $L = 50$ mm, and (e,f) $L = 35$ mm, respectively. Strikingly, the PSDs of lift and displacement show the same frequency peaks (i.e., $f_{L1} = f_1$), with the lift showing harmonics nearly equal or larger than the dominant frequency of the motion. For example, the frequency associated with the dominant

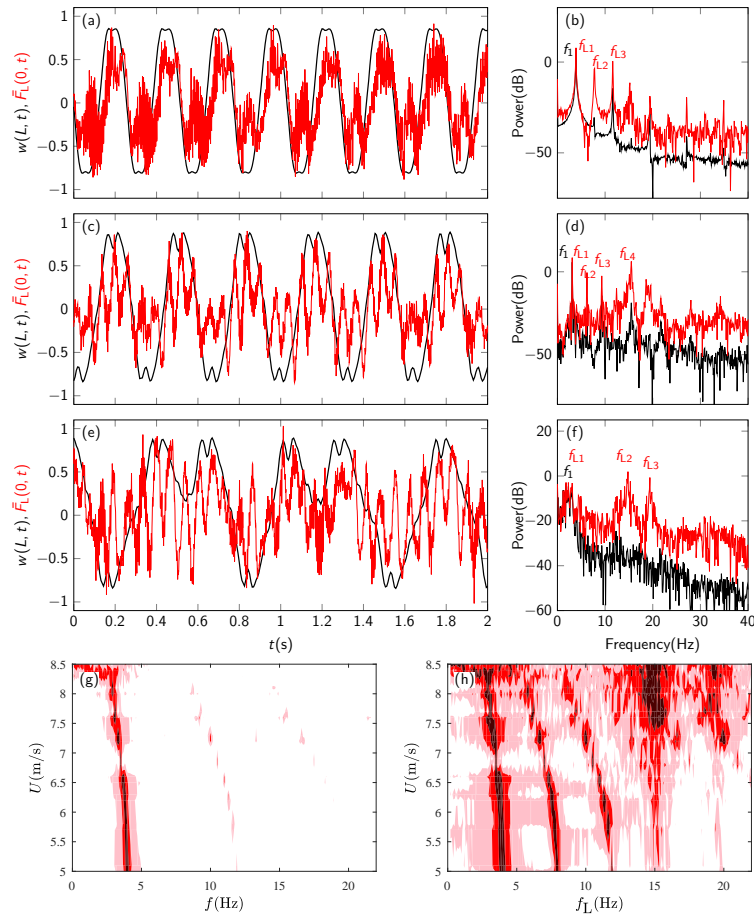


Figure 8 – (a,c,e) tip transverse displacement [—] and the normalized lift [—] at $U = 5.7$ m/s, $U = 7.7$ m/s, and $U = 8.3$ m/s; (b,d,f) associated PSDs for a stainless-steel inverted flag with $L = 100$ mm; (g-h) experimental spectrograms for the flag motion and lift, respectively – the magnitude of the power spectrum is measured in dB.

peak in the displacement PSD plot shown in figure 9(d) for $L = 50$ mm flag at $U = 14.4$ m/s is $f_1 = 18$ Hz, while the dominant peak in the lift PSD plot occurs at $f_{L2} = 2f_1 = 36$ Hz, and subdominant peaks occur at $f_{L1} = f_1 = 18$ Hz, $f_{L3} = 3f_1 = 54$ Hz, and $f_{L4} = 5f_1 = 90$ Hz, whereas the contribution of these harmonics in the flag oscillation is very weak. This indicates that vortex shedding may be synchronized to a higher displacement frequency; in the present case, the vortex shedding frequency is twice the flapping frequency, giving rise to a 1:2 synchronization.

4.2 Phase dynamics

It is known that in the case of VIV-driven motion of a circular cylinder in cross-flow, sharp changes occur in the phase angle between the fluid forces and cylinder motion at resonance, as the flow velocity is varied. In particular, the phase between the cross-flow force and the transverse displacement of the cylinder jumps from near 0 to near π (refer to Khalak and

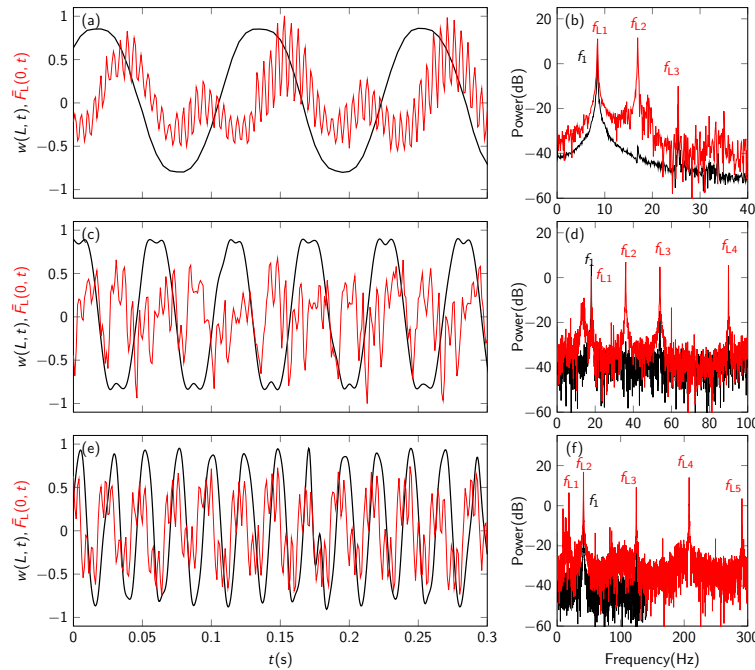


Figure 9 – (Left) tip transverse displacement [—] and the normalized lift [—] for stainless-steel inverted flags with (a) $L = 70$ mm at $U = 7.4$ m/s, with (c) $L = 50$ mm at $U = 14.4$ m/s, and with (e) $L = 35$ mm at $U = 19.0$ m/s; (right) their associated PSDs.

Williamson 1999, Zhao et al. 2014, Seyed-Aghazadeh et al. 2017).

Here, the instantaneous phase difference between the time series obtained for the transverse displacement of the flag and the lift are calculated using the Hilbert transform (Khalak and Williamson 1999, Konstantinidis et al. 2019). The instantaneous phase is defined as $\phi_w(t) = \text{atan}[w(L, t)/\hat{w}(L, t)]$ and $\phi_F(t) = \text{atan}[F_L(0, t)/\hat{F}_L(0, t)]$, where $\hat{w}(L, t)$ and $\hat{F}_L(0, t)$ are the Hilbert transforms of $w(L, t)$ and $F_L(0, t)$, respectively. Next, the instantaneous phase lag, $\phi_d(t)$, between the lift and the displacement is calculated as $\phi_d(t) = \phi_F(t) - \phi_w(t)$.

Figure 10 shows the variation of the time-averaged phase lag, denoted by ϕ_d , as a function of the dimensionless flow velocity for flags A-D (table 2). In all cases, the time-averaged phase difference never crosses 90° and remains bounded in the $[0 \ 50]$ range over the large-amplitude flapping regime. The different values of the phase difference may well be due to the effect of different values of structural damping for the different flags. Similar observations have been made by Seyed-Aghazadeh et al. (2017) for triangular prisms in cross-flow, reporting that the jump from ~ 0 to $\sim 180^\circ$ in phase difference between flow forces and the body motion did not occur, and hence the oscillation was concluded to be of the galloping type.

The above observations suggest that flag motion and vortex shedding influence each other reciprocally; however, vortex shedding does not appear to be the cause for flapping. The large-amplitude flapping of short inverted flags accompanied by high-frequency vortex shedding suggests that a *fluidelastic excitation* mechanism may be involved, and hence time-averaged aerodynamic forces govern the motion. A similar conclusion has been reached for slender prismatic bodies with bluff cross-section and sufficiently long afterbody by Nemes et al. (2012), Zhao et al. (2014) and Seyed-Aghazadeh et al. (2017), among others.

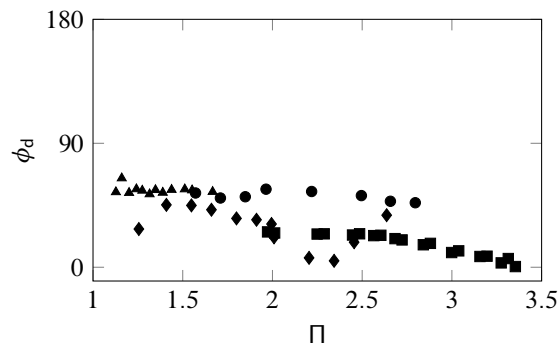


Figure 10 – Phase difference between transverse force (lift) and transverse displacement for stainless steel inverted flags with [■] $L = 100$ mm, [●] $L = 70$ mm, [◆] $L = 50$ mm, and [▲] $L = 35$ mm over the periodic large-amplitude flapping regime.

Additionally, these observations agree well with computational predictions of [Goza et al. \(2018\)](#), reporting that the dominant frequency of lift (largest peak in the PSD plot) is higher than that of the tip displacement, suggesting that the motion is not “classical VIV”.

5 Conclusions

Some experiments were described in this paper, aiming at examining the global dynamics of inverted flags and, in particular, at probing the impact of periodic vortex shedding from the leading and trailing edges thereon.

The effect of vortex shedding from both leading and trailing edges was investigated. It was shown that suppression of the leading and trailing edge vortices, and also inhibition of the interaction between the two counter-rotating vortices (if any exists), results in only minor changes in the critical velocity, amplitude and frequency. The overall dynamics and features of the system remained intact, and the large-amplitude flapping persisted for all flags tested in the experiments, with TEV and LEV present or suppressed.

Force measurements provided some insights into the relationship between vortex shedding and large-amplitude flapping; a difference between the dominant (peak) frequencies of the lift and flapping was found in some cases. Moreover, it was shown that for heavier inverted flags, additional frequency peaks appear in the lift frequency spectrum, with power as great as or larger than that matching the motion dominant frequency. In addition, the lift and tip displacements were found to be desynchronised in the chaotic-like flow regime for lighter flags.

The experimental results presented in Sections 2-4 suggest that a *fluidelastic instability* may be the underlying mechanism for the flapping motion of heavy inverted flags. The near-identical qualitative behaviour of normal inverted flags and those with a serrated leading edge and a splitter plate at the trailing edge suggests that the global (qualitative) dynamical characteristics of heavy inverted flags are not governed by the unsteady vortex shedding from the leading and trailing edges. In other words, periodic vortex shedding is not the cause, but an effect of large-amplitude flapping.

It is stressed that flow visualization was not carried out in the experiments with serrated flags and the splitter plate. The wake behind the flag may display three-dimensional characteristics;

yet, as reported by Pazhani and Acharya (2019), the dominant vortical features in the near wake is broken down and the coherent formation and shedding of vortices is disrupted.

There are definitely potential connections, yet to be discovered in the future, between the phase dynamics and the underlying mechanism for large-amplitude flapping. Further investigations would be desirable to better clarify the distinction between VIV and the underlying mechanism for large-amplitude flapping of heavy flags.

Acknowledgements

The financial support by the Natural Sciences and Engineering Research Council of Canada, the Solution Mining Research Institute (SMRI) and Pipeline Research Council International (PRCI) is gratefully acknowledged.

References

- A. Goza. Private communication (November). 2019.
- A. Goza, T. Colonius, and J. E. Sader. Global modes and nonlinear analysis of inverted-flag flapping. *Journal of Fluid Mechanics*, 857:312–344, 2018.
- P. S. Gurugubelli and R. K. Jaiman. Large amplitude flapping of an inverted elastic foil in uniform flow with spanwise periodicity. *Journal of Fluids and Structures*, 90:139–163, 2019.
- A. Khalak and C. H. Williamson. Motions, forces and mode transitions in vortex-induced vibrations at low mass-damping. *Journal of Fluids and Structures*, 13(7-8):813–851, 1999.
- E. Konstantinidis, J. Zhao, D. L. Jacono, J. Leontini, and J. Sheridan. Phase dynamics of effective drag and lift in vortex-induced vibration at low mass-damping. *Preprint*, 2019. [arXiv:1906.07375](https://arxiv.org/abs/1906.07375).
- A. Nemes, J. Zhao, D. L. Jacono, and J. Sheridan. The interaction between flow-induced vibration mechanisms of a square cylinder with varying angles of attack. *Journal of Fluid Mechanics*, 710:102–130, 2012.
- K. M. Pazhani and S. Acharya. An experimental investigation of the dynamics of an inverted serrated flag. In *AIAA Scitech 2019 Forum*, page 1891, 2019.
- J. E. Sader, J. Cossé, D. Kim, B. Fan, and M. Gharib. Large-amplitude flapping of an inverted flag in a uniform steady flow – a vortex-induced vibration. *Journal of Fluid Mechanics*, 793:524–555, 2016.
- B. Seyed-Aghazadeh, D. W. Carlson, and Y. Modarres-Sadeghi. Vortex-induced vibration and galloping of prisms with triangular cross-sections. *Journal of Fluid Mechanics*, 817:590–618, 2017.
- J. Zhao, J. Leontini, D. Lo Jacono, and J. Sheridan. Fluid–structure interaction of a square cylinder at different angles of attack. *Journal of Fluid Mechanics*, 747:688–721, 2014.

The fluttering flag: Reynolds number, mass ratio, and mode shape

Ravi Chaithanya Mysa^{1,2}, Kartik Venkatraman²

¹ *Singapore University of Technology and Design, Singapore, ravichaithanya.mysa@gmail.com*

² *Indian Institute of Science, Bengaluru, India*

Abstract

Numerical simulations were carried out for determining the flutter instabilities of a flag. The flag is modeled as a Euler-Bernoulli beam and is coupled with the flow physics. The detailed governing equations and the validation results are discussed in detail elsewhere¹. The dependence of flutter instability on the Reynolds number is studied in detail with respect to flutter mode shape, flutter boundary, phase relations between foil shape and differential pressure. With decrease in Reynolds number, the region in which flutter occurs decreases. There exists a critical Reynolds number for a given mass ratio where the flag is immune to flutter. As the mass ratio increases, the flutter mode changes. Near the region of flutter mode shift, the flutter velocity, frequency, and amplitude change drastically. The effect of mass ratio and Reynolds number on the envelope, mode shape, and vorticity flow contours is analyzed in detail to understand the instability behavior.

Keyword: flutter, incompressible flow, DNS.

1 Introduction

The fluttering flag serves as a fundamental model for studying fluid-elastic interactions. Applications range from oro-nasal snoring, flutter of grasses and leaves, energy harvesting, to high speed printing on paper. Typically, the fluid flow is low speed and therefore assumed incompressible. The Reynolds number too is low and therefore laminar. The flag itself is either assumed infinite span and fluid flow two-dimensional, or finite span and fluid flow three-dimensional.

One of the earliest experimental investigations on flag flutter was reported by Taneda (1968). Flags were made from different material with different chord and span length. Some of the key findings include: flutter frequency increases almost linearly with flow speed; the Strouhal number of the fluttering flag oscillation frequency decreases as $-1/2^{th}$ power of the Reynolds number; and that the critical Reynolds number at which the flag flutters is independent of the mass ratio.

Potential flow analysis has been used to address flutter mechanism and flutter boundary in literature (Alben and Shelley, 2008; Argentina and Mahadevan, 2005; Huang, 1995; Michelin, Smith, and Glover, 2008; Watanabe et al., 2002a). The experimental studies on fluttering flag are reported by Huang, 1995; Shelley, Vandenberghe, and Zhang, 2005; Watanabe et al., 2002b; Zhang et al., 2000. Huang (1995) analyzed the flexible flat plate in relation to oro-nasal snoring. The fluid loads were evaluated using Theodorsen's classical solution and is coupled to linear beam theory for analysis of flutter. The numerical results obtained using potential flow

model matched well with experiments. Zhang et al. (2000) examined the stability of a filament in a flow using a soap film experiment. They observed hysteresis effect from stationary state to the flapping state by varying the length of the filament. They observed a von Kármán vortex sheet for the stationary state and also that there exists a critical length where the filament flaps in a sinusoidal motion giving rise to wake resembling Kelvin-Helmholtz instability. The Reynolds number is of order 10^4 . Watanabe et al. (2002a,b) studied the flutter of paper both experimentally and numerically respectively. They too observed hysteresis.

Argentina and Mahadevan (2005) used incompressible potential flow for the fluid model and linear bending theory for the flat plate to predict flutter boundaries of a flag. In this model they introduced the tension of the plate, boundary layer effect, and three dimensional effects, which were found to increase the stability of the system. Shelley, Vandenberghe, and Zhang (2005) experimentally investigated the fluttering of flags. They too report hysteresis effect in flutter. Alben and Shelley (2008) computationally investigated the flutter of a flag within an inviscid fluid model. They captured hysteresis in the onset of flutter as reported in experiments (Shelley, Vandenberghe, and Zhang, 2005; Zhang et al., 2000). The necking of the flutter boundary is reported by Eloy et al. (2008) and Michelin, Smith, and Glover (2008). Eloy et al. (2008) conducted experiments and Michelin, Smith, and Glover (2008) carried potential flow based numerical experiments on a fluttering foil. Maître, Scanlan, and Knio (2003) used an incompressible Navier-Stokes equations for flutter analysis of spring mounted NACA0012 airfoil. They focused on the effect of Reynolds number and airfoil thickness on the flutter derivatives. They observed that Reynolds number has insignificant effect on flutter boundary.

In this study, we consider a one dimensional flag in a two dimensional viscous incompressible flow, and investigate the variation in flow velocity at which flutter occurs in as a function of mass ratio. We have done this simulations at three different Reynolds numbers. Below a Reynolds number of 200 the occurrence of flutter is rather rare. Moreover, as the Reynolds number is lowered, the wave length of the shear layers shed from the oscillating flexible foil changes; and there is considerably lower roll-up of the shear layers. The nature of the vorticity contours are a function of the flutter velocity, frequency, amplitude, and Reynolds number.

2 Fluid-elastic model

The fluid model is a two-dimensional incompressible flow and the solid is a Bernoulli-Euler one-dimensional model of flexure. The numerical implementation of the fluid dynamics is using a sharp-interface immersed boundary technique and the Bernoulli-Euler solid model is discretized using finite elements. Their dynamics are coupled using a predictor-corrector algorithm.

The equation of motion of the flexible foil is the Bernoulli-Euler model of a one-dimensional elastic solid in flexure (Clough and Penzein, 1993)

$$m \frac{\partial^2 h(x, t)}{\partial t^2} + c \frac{\partial^5 h(x, t)}{\partial t \partial x^4} + E I_{yy} \frac{\partial^4 h(x, t)}{\partial x^4} = \Delta p(x, t) \hat{\mathbf{n}} \cdot \hat{\mathbf{k}}; \quad 0 < x < L. \quad (1)$$

The boundary conditions for the cantilever beam are the no-displacement and no-slope condition at the fixed end and no-shear force and no-bending moment at the free end. Each term in Equation (1) has the dimensions of pressure since we are considering a section of the elastic foil to comply with the assumption of two-dimension fluid dynamics. $h(x, t)$ is the elastic transverse deflection of the beam in flexure. The amplitude, slope, curvature, and frequency

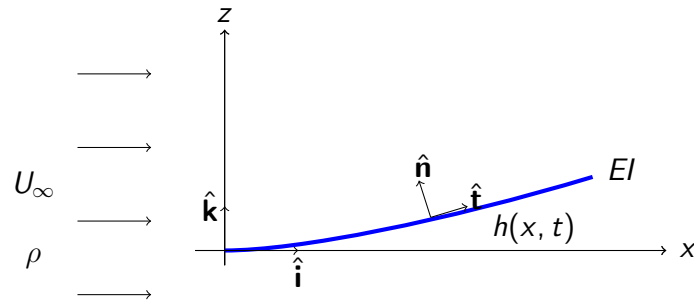


Figure 1: Fluttering foil in a fluid flow

of the foil in oscillation are restricted by the assumptions inherent in the Bernoulli-Euler beam theory. The parameters that define the flexural motion of the foil are: m is the mass per unit length per unit span of the foil. EI_{yy} is the flexural rigidity per unit span of the foil with E denoting Young's modulus of the material of the foil and I_{yy} is its sectional second moment of area per unit span about the y axis of the coordinate system attached to the beam. c is the damping coefficient per unit span of the material of the beam based on a model wherein the damping force induced in the material of the beam due to vibration is proportional to the strain rate. $\Delta p(x, t)$ is the pressure differential across the top and bottom surface of the foil due to the unsteady fluid flow on the beam. $\hat{\mathbf{n}}$ is the vector denoting the normal to the neutral axis of the foil.

The pressure $\Delta p(x, t)$ over the foil is computed using an incompressible Navier-Stokes solver using a sharp interface immersed boundary technique (Mittal et al., 2008). The coupled elastodynamic Equation (1) is solved using standard Euler-Bernoulli flexure finite elements. The pressure calculated from the viscous flow solver is used in the finite element based structural solver. At a given instant of time, the Lagrangian center point of the finite element of the foil is surrounded by Eulerian grid points in the fluid. At every time step, after the flow solver computes the pressure at the Eulerian nodes, the pressure at the Lagrangian center point of the finite element is interpolated from the values of the pressure at the surrounding nodes of the Eulerian grid. This value of pressure calculated at the center of the finite element is assumed to be constant along the finite element. The details of the finite element and immersed boundary method with validation examples, together with numerical implementation is given in (Mysa and Venkatraman, 2016). The Reynolds number is defined with reference to the length of the foil L ; simulations were carried out at three different Reynolds numbers—1000, 400, and 200.

3 Results and discussion

We have arranged the results broadly as flutter onset characteristics, envelope shapes, and vorticity contours. These simulations were conducted at three Reynolds numbers, namely, 1000, 400, and 200. The non-dimensional parameters used are the mass ratio $\mu = m/\rho L$; the oscillation frequency ratio $\bar{\omega} = \omega/\omega_c$ where ω_c is the characteristic frequency or dynamic stiffness; the fluid velocity $\bar{U} = U/L\omega_c$; the reduced frequency of oscillation of the flag $k = fL/U$; and the amplitude ratio $\bar{A} = A/L$. Note that the Strouhal number can be expressed in

terms of the reduced frequency of oscillation and the amplitude ratio $Sr = \bar{A}k$.

3.1 Flutter characteristics

Figure 2(a) shows the free stream velocity UL/ω_c at which flutter onset occurs at a given mass ratio. At a given value of mass ratio, for fluid free stream velocities below the curve, the fluid-elastic system is stable or the response to an initial condition is decaying, and above the curve the fluid-elastic system is unstable. Note that for $Re = 1000$, $Re = 400$, and 200 the stability boundaries are almost the same with peaks occurring at almost the same mass ratio and the flutter onset velocity displaced lower as the Reynolds number increases. However at $Re = 200$ note that the flutter velocity shows a rather abrupt increase as we change the mass ratio μ from 1 to 1.5, whereas at the other two Reynolds numbers, this abrupt increase occurs as one goes from a mass ratio of 1.5 to 2. As we see later, these abrupt changes occur with transitions in flutter modes of displacement.

The non-dimensional amplitude A/L at flutter onset as function of mass ratio is shown in Figure 2(d). These curves too follow the same trend as in the case of the flutter velocity except that for a Reynolds number of 200 the amplitude peaks slightly earlier at a mass ratio of 1.5 rather than around 2 as in the case of $Re = 1000$ and $Re = 400$.

Figure 2(b) shows the frequency ratio at flutter onset f/ω_c . For $Re = 1000$ the flutter frequency peaks first at $\mu = 2.5$; for $Re = 400$ the first peak occurs at $\mu = 4.3$; and for $Re = 200$ the first peak in the flutter frequency occurs much later between $\mu = 2$ and $\mu = 3$. So, the observation here is that local maxima in flutter frequency do not coincide with the local maxima for flutter velocity or flutter amplitude. Further note that as the Reynolds number changes from 1000 to 400 there is no change in the frequency ratio curve. However, as we move to a lower Reynolds number of 200 there is a definite change in the frequency at which flutter occurs.

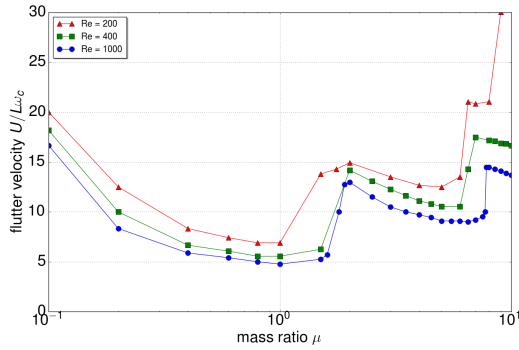
We discuss the reduced frequency at flutter onset fL/U first, as shown in Figure 2(c). The reduced goes through a minima at those mass ratios where the flutter velocity has a maxima.

The Strouhal number fA/U is the product of the reduced frequency fL/U and the amplitude ratio A/L . In fact we have placed this Figure 2(e) just below that for the amplitude Figure 2(d) to show that the Strouhal number maxima coincide very closely with those of the amplitude ratio.

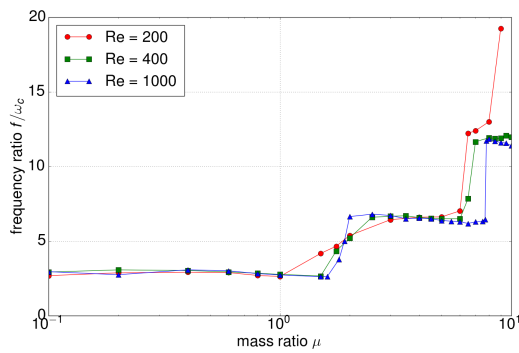
We also carried out simulations at Reynolds number of 100. We did not observe flutter at the mass ratios that we simulated which corresponds to those we simulated for the Reynolds numbers presented above. The inference that one draws from this is that the dissipation at low Reynolds number prevents instability from setting in.

3.2 Displacement profiles

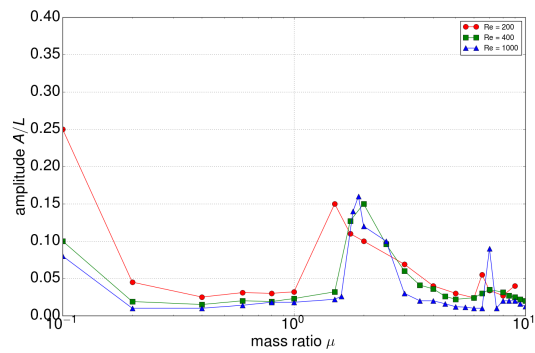
We view the displacement profiles during flutter in the vicinity of those mass ratios where one observes an abrupt change in velocity or amplitude. We do this for all the three Reynolds numbers.



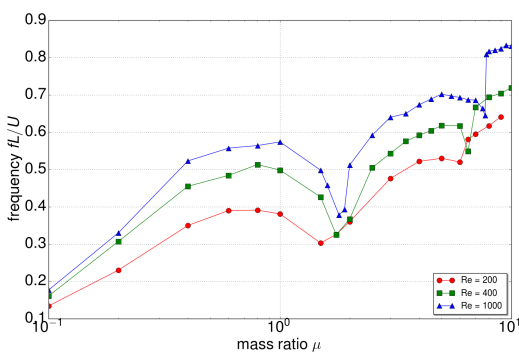
(a) Free stream velocity at flutter onset $U/(L\omega_c)$ as a function of mass ratio μ .



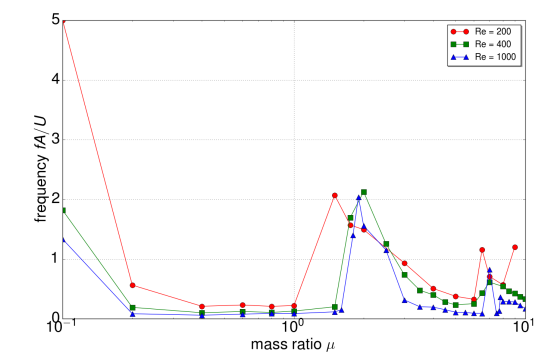
(b) Frequency ratio at flutter onset f/ω_c as a function of mass ratio μ .



(d) Amplitude at flutter onset A/L as a function of mass ratio μ .



(c) Reduced frequency at flutter onset fL/U as a function of mass ratio μ .



(e) Strouhal number at flutter onset fA/U as a function of mass ratio μ .

Figure 2: Flutter characteristics as a function of mass ratio for three different Reynolds numbers

3.2.1 $Re = 1000$

We look at transitions in flutter velocity or the around $\mu = 2$ and $\mu = 8$ as shown in Figure 3. As one can observe, there is definite change in the displacement profile as we move from $\mu = 1$ to $\mu = 2$. At $\mu = 2$ one observes the appearance of a node-like behavior close to $x/L = 0.4$. In fact, not shown here, at $\mu = 1.9$ the displacement profile is closer to that at $\mu = 2$ with node-like appearance less prominent. Similarly at $\mu = 8$ where the flutter velocity goes through a sharp increase one notices the appearance of a node-like formation near $\mu = 3$. In terms of *in-vacuo* vibration natural modes, if one were allowed such an analogy, there is a transition from mode 2 to mode 3 at $\mu = 2$ and a transition from mode 3 to 4 at $\mu = 8$.

3.2.2 $Re = 400$

Shown here are the displacement profiles for the first peak in the flutter velocity versus mass ratio curve for $Re = 400$ shown in Figure 2(a). The abrupt change in flutter velocity occurs close to $\mu = 2$. We have shown the displacement profiles over one cycle of oscillation at $\mu = 1.5$, $\mu = 2$, and $\mu = 2.5$. Note the change in the displacement profile at flutter as the flutter velocity changes abruptly. One goes from a mode 2 behavior to a mode 3 behavior as one transits from $\mu = 1.5$ to $\mu = 2$, and remains in the same mode as we increase the mass ratio from $\mu = 2$ to $\mu = 2.5$. At the next abrupt change in flutter velocity that occurs at a mass ratio below $\mu = 8$ the displacement profile shifts from mode 3 to mode 4 as one transits through $\mu = 8$.

3.2.3 $Re = 200$

At $Re = 200$ one observes a similar pattern in the qualitative change in the displacement profile as one goes from $\mu = 1$ through $\mu = 1.5$ and again as it passes through an abrupt increase in flutter velocity at a mass ratio close to $\mu = 7$. We have shown here the displacement profile for the mass ratio 2. The displacement profile is based on mode 2 natural vibration mode.

3.3 *Vorticity contours*

The vorticity contours should necessarily change as the mass ratio increases as these not only change the flutter velocity and displacement profile of oscillation, but also change the frequency and amplitude of oscillation. Note that vortex shedding over a moving boundary is strongly influenced by the slope and curvature of that boundary.

3.3.1 $Re = 1000$

We show the vorticity contours here at two mass ratios $\mu = 1$, in Figure 6, and $\mu = 2$ in Figure 7. Note the change in vorticity pattern shed from the upper and lower surface. For the lower mass ratio case, the shear layer does not separate and there is no roll-up as the frequency and amplitude are low, as well as the changes in slope are more gradual. At the higher mass ratio of 2, there is an abrupt change in the amplitude and frequency of oscillation, and the changes in slope are also many, resulting in the roll-up of shear layers.

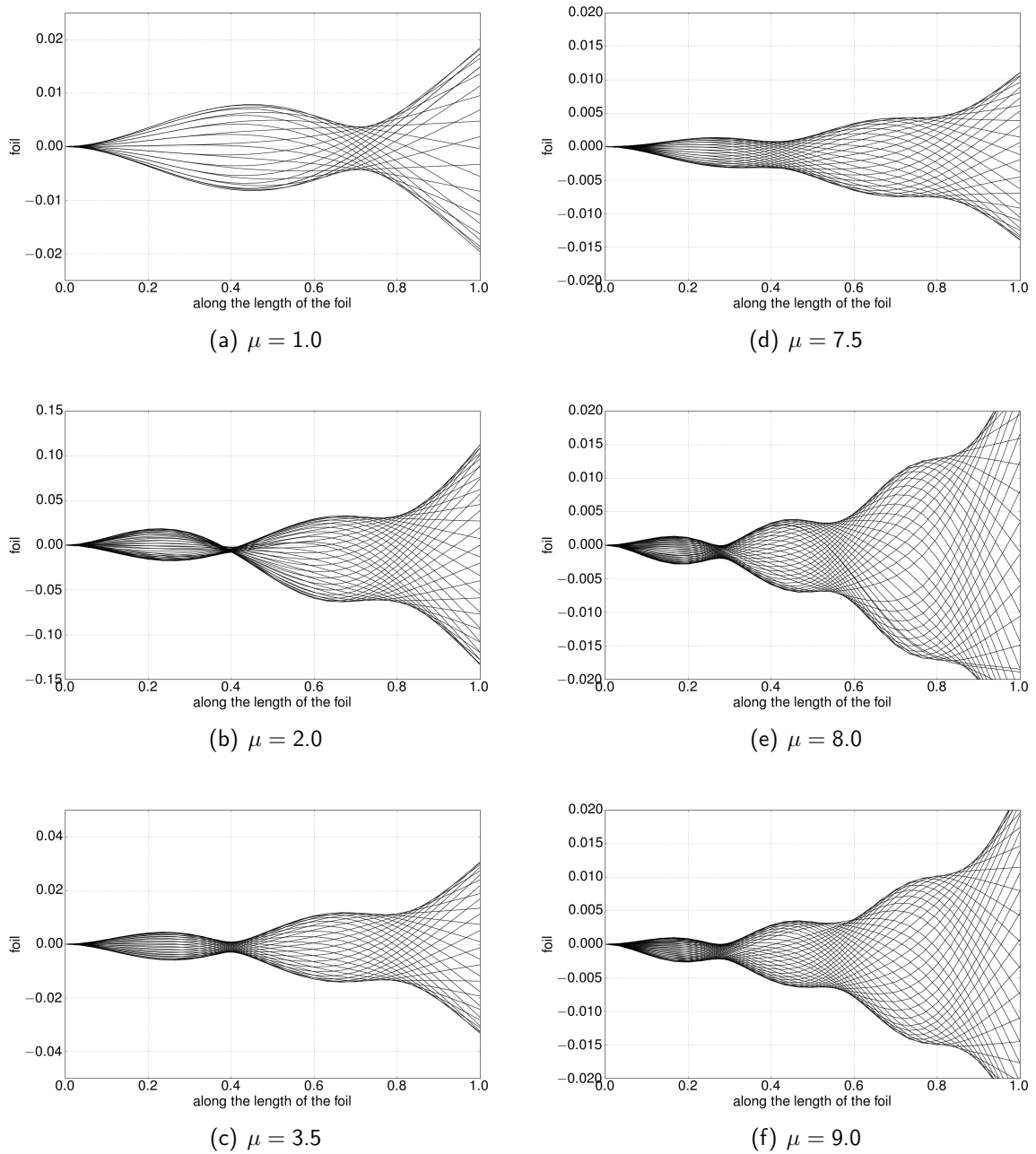
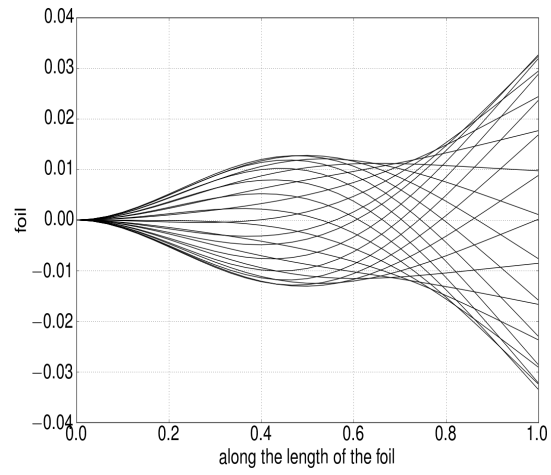
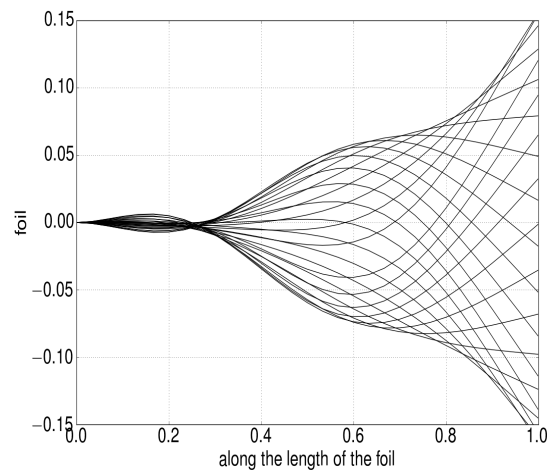


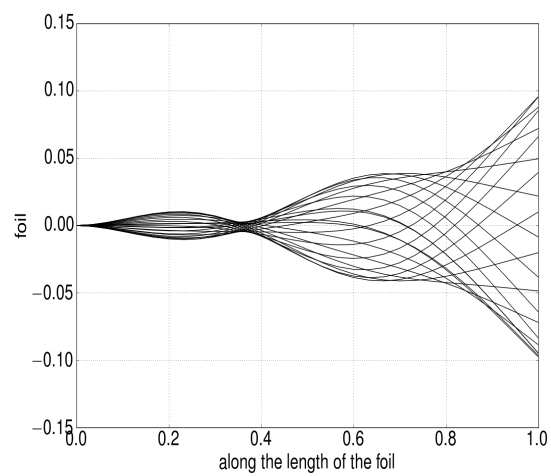
Figure 3: Displacement envelopes at flutter at $Re = 1000$ for different mass ratios



(a) $\mu = 1.5$



(b) $\mu = 2.0$



(c) $\mu = 2.5$

Figure 4: Displacement envelopes at flutter at $Re = 400$ for different mass ratios

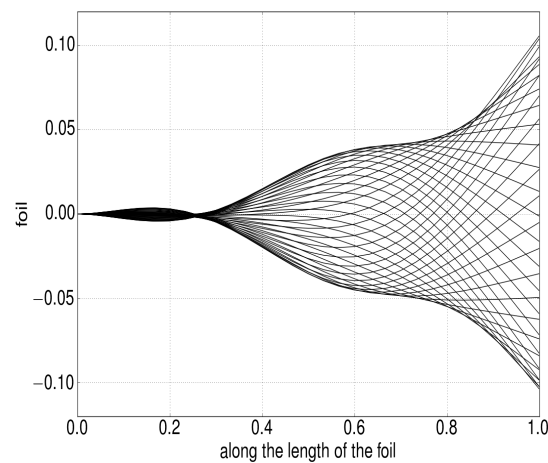


Figure 5: Displacement envelope at flutter at $Re = 200$ for mass ratio $\mu = 2$

3.3.2 $Re = 400$

The vorticity contour for mass ratio $\mu = 2$ is shown in Figure 8. If we compare this vorticity profile with that at Reynolds number 1000, one notices that the wavelength of the undulating alternate shear layer changes as we decrease the Reynolds number. Also at the lower Reynolds number of 400 there is lesser roll-up of the shear layers.

3.3.3 $Re = 200$

As we go further down the Reynolds number range to $Re = 200$ —Figure 9—the shear layers shed from the oscillating foil are thicker, there is almost no roll-up of these layers, and the wavelength further reduces.

4 Conclusions

Numerical simulations of a one dimensional flag in a two dimensional incompressible viscous flow show changes in flutter velocity, flutter frequency, and flutter amplitude as the mass ratio of the density of the elastic solid to the fluid density increases. The displacement envelopes at the flutter values also show substantial changes. And consequently the vorticity contours also change. Across Reynolds numbers as, as we go towards lower Reynolds numbers, there is a definite thickening of the shed shear layer from the upper and lower surface of the flexible foil, the wavelength of the vorticity decreases, and there is considerably less vortex roll-up.

References

- Alben, Silas and Michael J. Shelley (2008). “Flapping states of a flag in an inviscid fluid: Bistability and the transition to chaos”. In: *Physical Review Letters* 100.7, 074301(1–4).
- Argentina, M. and L. Mahadevan (2005). “Fluid-flow-induced flutter of a flag”. In: *Proceedings of the National Academy of Sciences* 102.6, pp. 1829–1834.

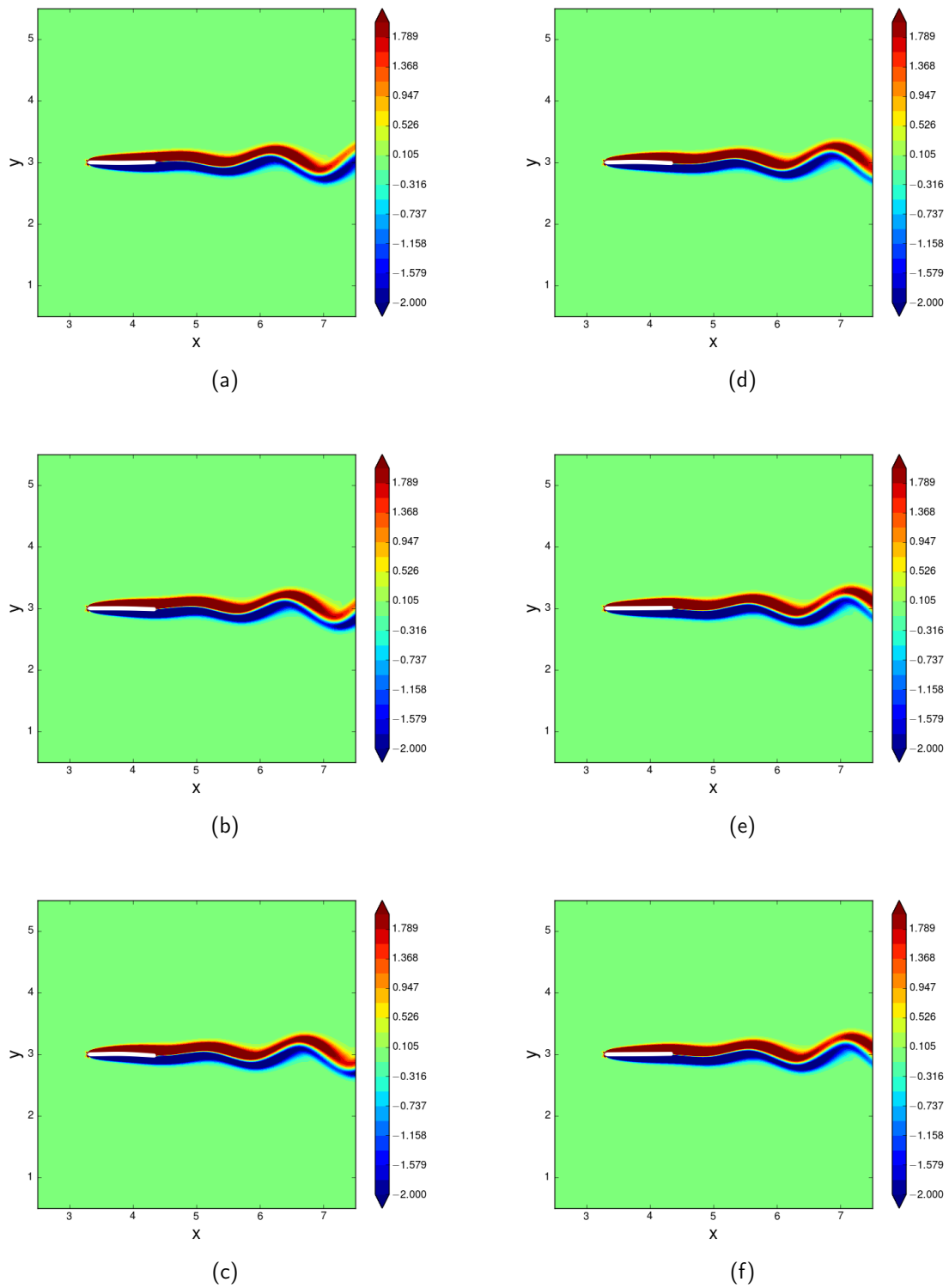


Figure 6: Snapshots of vorticity contours at flutter at $Re = 1000$ and mass ratio $\mu = 1$

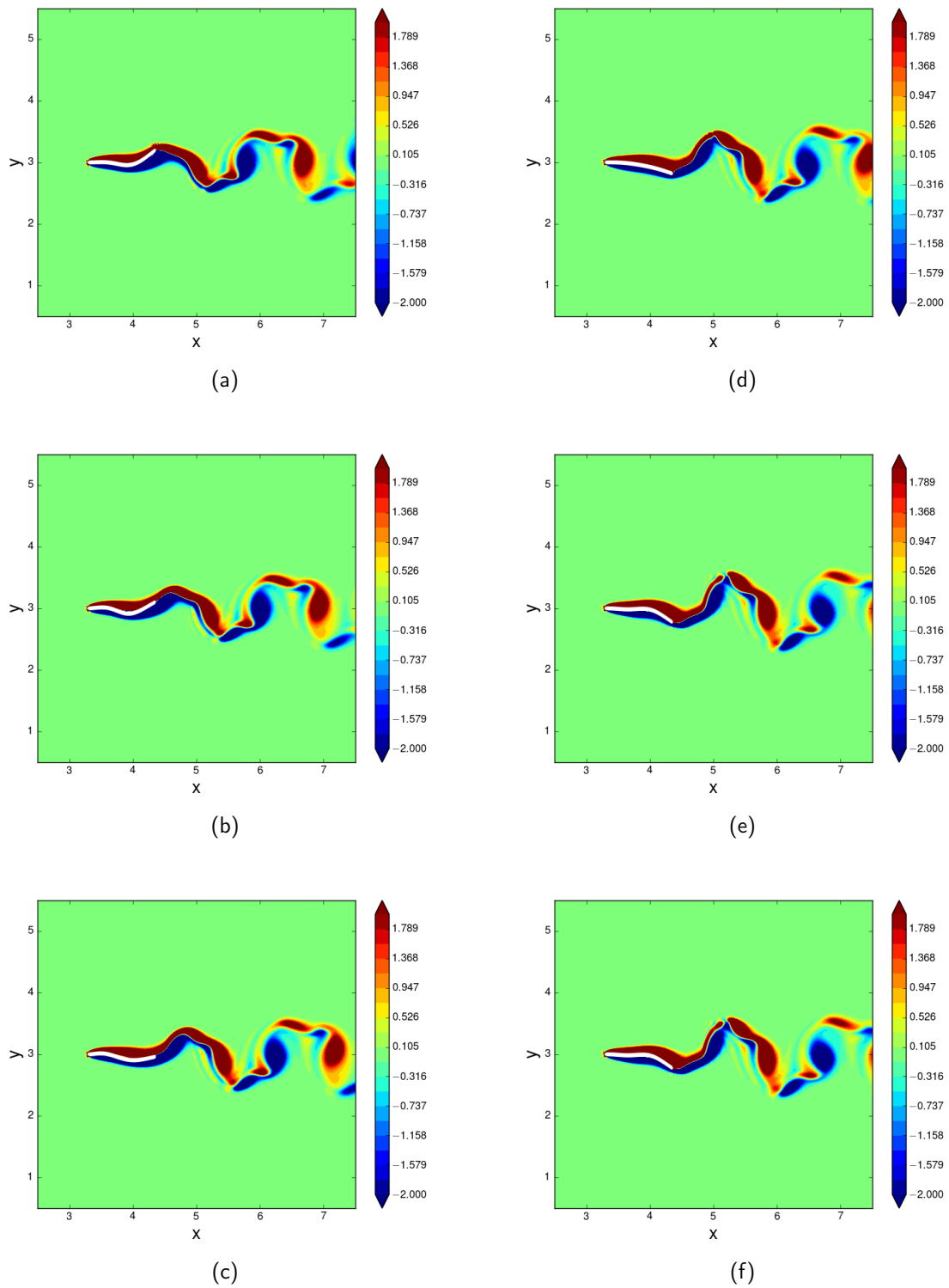


Figure 7: Snapshots of vorticity contours at flutter at $Re = 1000$ and mass ratio $\mu = 2$

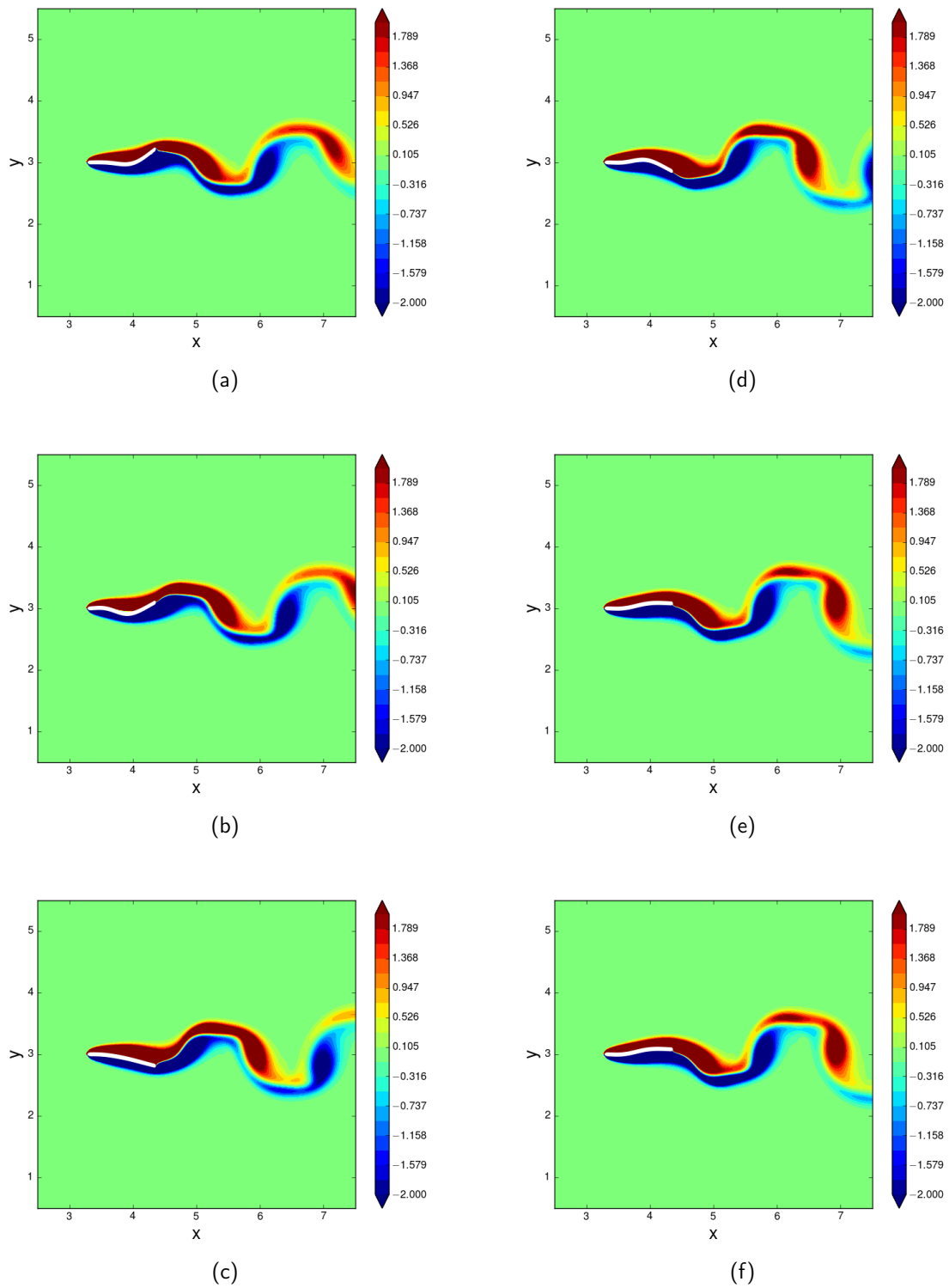


Figure 8: Snapshots of vorticity contours at flutter at $Re = 400$ and mass ratio $\mu = 2$

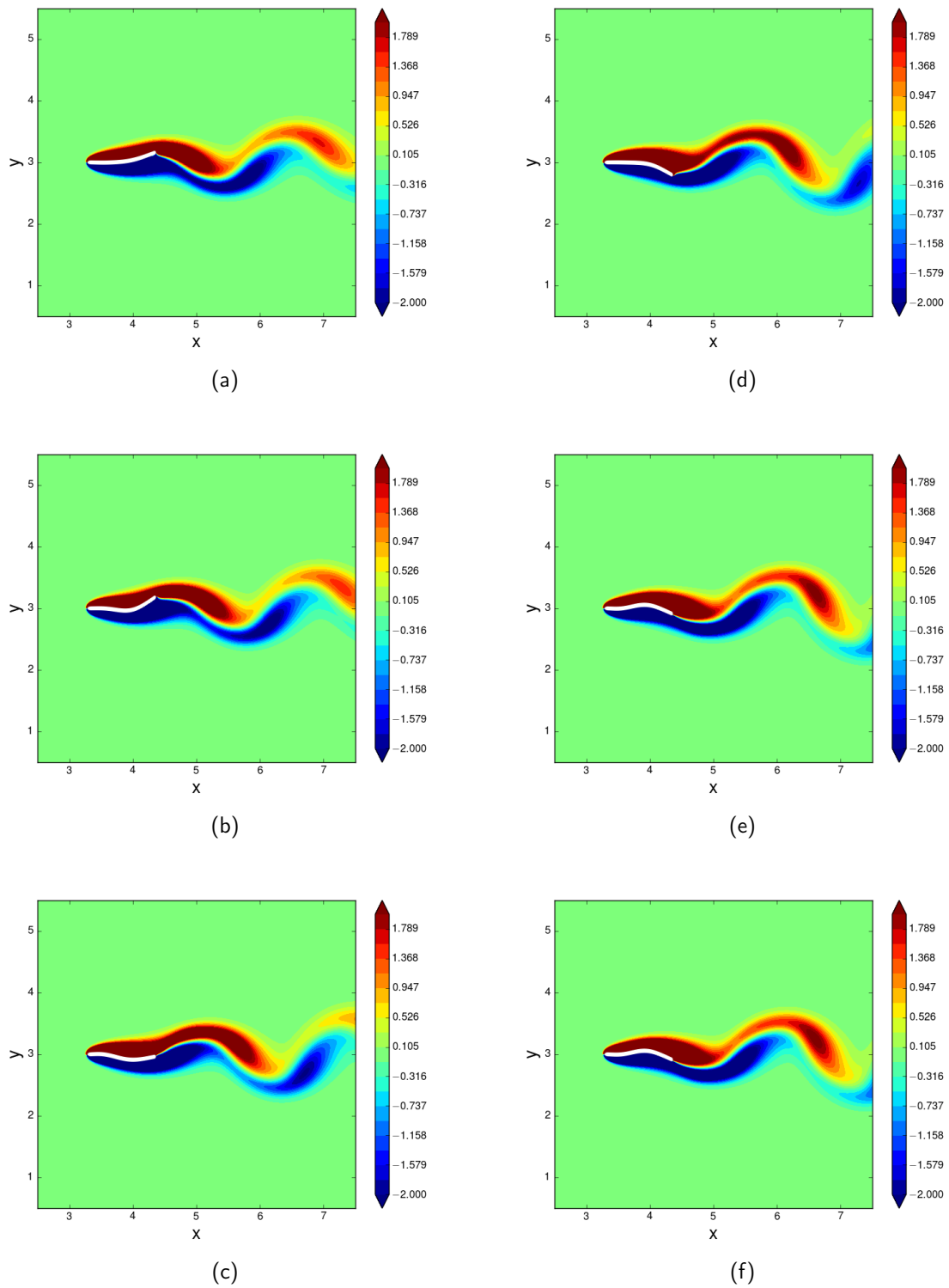


Figure 9: Snapshots of vorticity contours at flutter at $Re = 200$ and mass ratio $\mu = 2$

- Clough, R. W. and J. Penzein (1993). *Dynamics of structures*. McGraw-Hill, Inc.
- Eloy, C. et al. (2008). "Aeroelastic instability of cantilevered flexible plates in uniform flow". In: *Journal of Fluid Mechanics* 611, pp. 97–106.
- Huang, L. (1995). "Flutter of cantilevered plates in axial flow". In: *Journal of Fluids and Structures* 9, pp. 127–147.
- Maître, O. P. le, R. H. Scanlan, and O. M. Knio (2003). "Estimation of the flutter derivatives of an NACA airfoil by means of Navier-Stokes simulation". In: *Journal of Fluids and Structures* 17.1, pp. 1–28.
- Michelin, S., S. G. Llewellyn Smith, and B. J. Glover (2008). "Vortex shedding model of a flapping flag". In: *Journal of Fluid Mechanics* 617, pp. 1–10.
- Mittal, R. et al. (2008). "A versatile sharp interface immersed boundary method for incompressible flows with complex boundaries". In: *Journal of Computational Physics* 227.
- Mysa, Ravi C. and Kartik Venkatraman (2016). "Intertwined vorticity and elastodynamics in flapping wing propulsion". In: *Journal of Fluid Mechanics* 787, pp. 175–223.
- Shelley, M., N. Vandenberghe, and J. Zhang (2005). "Heavy flags undergo spontaneous oscillations in flowing water". In: *Physical Review Letters* 94.9, 094302(1–4).
- Taneda, S. (1968). "Waving motion of flags". In: *Journal of the Physical Society of Japan* 24.2, pp. 392–401.
- Watanabe, Y. et al. (2002a). "A theoretical study of paper flutter". In: *Journal of Fluids and Structures* 16.4, pp. 543–560.
- Watanabe, Y. et al. (2002b). "An experimental study of paper flutter". In: *Journal of Fluids and Structures* 16.4, pp. 529–542.
- Zhang, J. et al. (2000). "Flexible filaments in a flowing soap film as a model for one-dimensional flags in a two-dimensional wind". In: *Nature* 408, pp. 835–839.

Flutter and drag of a highly deformable beam under flow

T. Leclercq¹, N. Peake² and E. de Langre³

¹*Ecole polytechnique, Palaiseau, France, tristan.leclercq@polytechnique.edu*

²*DAMTP, University of Cambridge, United Kingdom, n.peake@damtp.cam.ac.uk,*

³*Ecole polytechnique, Palaiseau, France, delangre@ladhyx.polytechnique.fr*

Keywords: Flutter, reconfiguration, drag reduction

We consider the idealized case of a cantilevered beam in large bending deformation as a consequence of a uniform cross flow. This is numerically simulated using reduced order modelling of the flow (reactive and resistive force models) and of the beam (elastic model). Both static and dynamic deformations are considered. As the flow magnitude is increased, the bending of the beam results in a reduction of drag in comparison with that of a rigid beam: this is classically known as drag reduction by reconfiguration. But the large deformation of the beam also results in an alignment with the flow of the extremity, and a possibility of flag-type flutter. This is observed numerically above a critical threshold in terms of flow velocity. The flow induced flutter then results either in periodic limit cycle oscillation (see fig. 1, left) or in chaotic motion (fig. 1, right). As a consequence of flutter, drag is found to re-increase, but never over the drag of the rigid beam, except for some rare snapping events. A detailed parameter analysis shows that drag reduction by flexibility is robust to flutter¹. The effect of the parameters on this dynamics will be discussed, as well as the localization of the maximum of stress.

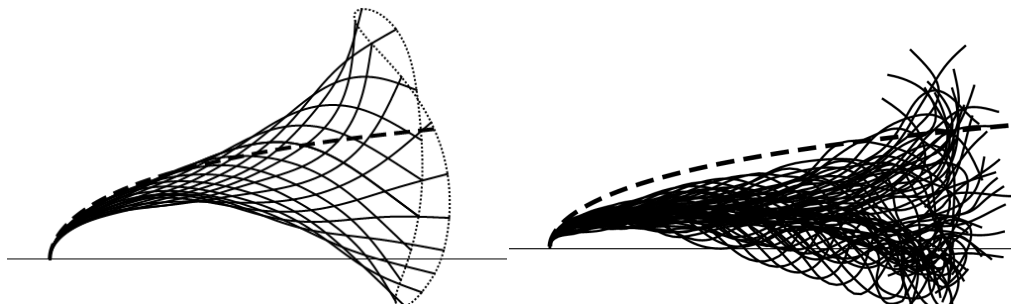


Figure 1: Limit cycle of flutter motion of highly deformed beam under flow.
Flow is from left to right

1. Leclercq, T., Peake, N., & de Langre, E. (2018). Does flutter prevent drag reduction by reconfiguration?. *Proceedings of the Royal Society A: Mathematical, Physical and Engineering Sciences*, 474(2209), 20170678.

Experimental and Theoretical Investigation into the Dynamics of A Pipe Simultaneously Subjected to Internal and External Flows

Ahmed R. Abdelbaki¹, Arun K. Misra and Michael P. Païdoussis

Department of Mechanical Engineering, McGill University, Montreal, Québec, Canada

¹Corresponding author, e-mail address: ahmed.abdelbaki@mail.mcgill.ca

Keyword: Dynamics, instability, flutter, pipe conveying fluid, axial flow

In this paper, a flexible cantilevered pipe discharging fluid into a fluid-filled tank is considered. The fluid exits the tank through a rigid tube shorter than the pipe, as shown in Fig. 1(a), forming an annular region surrounding the pipe over its upper portion. This flow configuration models one of the *modi operandi* for salt-mined caverns used for storage and subsequent retrieval of hydrocarbons. The flow velocity is required to be sufficiently high to ensure quick retrieval, but without any instability of the pipe. In the present study, the dynamics of the pipe is examined with increasing flow velocity. The influence of varying the ratio of external to internal flow velocities $r = U_o/U_i$ on stability is also investigated.

Experiments were conducted using a silicone-rubber pipe (length $L = 431$ mm, $D_o = 16$ mm, and $D_i = 6.35$ mm). For the annulus, $L' = 206.5$ mm and $D_{ch} = 31.5$ mm; hence, the external flow is confined over $\approx 50\%$ of the length of the pipe. Two pumps were utilized to control r . Five values of $r = 0.055, 0.2, 0.4, 0.6, 0.8$ were tested. For each r , the flow velocity was increased stepwise and the rms amplitude of oscillation of the free end of the pipe was determined, as shown in Fig. 1(b). It was found that the pipe generally undergoes flutter at U_{cr} ; increasing r has a severe destabilizing effect on the system. Theoretical analysis was also undertaken, and theoretical predictions were found to be in fair qualitative and quantitative agreement with experimental observations, as shown in Table 1.

Table 1: Critical flow velocities, U_{cr} , in m/s, for different r .

r	0.055	0.2	0.4	0.6	0.8
Experiments	5.61	1.76	0.99	0.63	0.35
Theory	7.17	5.84	1.16	0.59	0.39

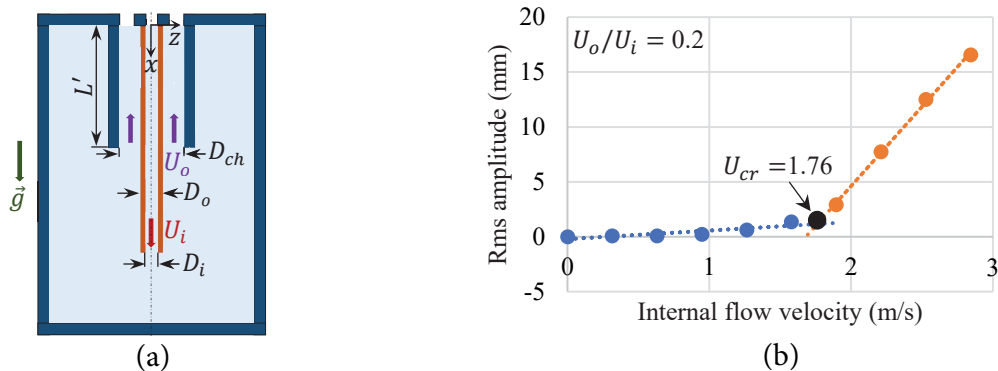


Figure 1: (a) Diagram of the system under study; (b) rms amplitude of oscillation versus U_i .

Flapping dynamics and heat transfer of turbulent channel flow with dual inverted flags

Yujia Chen¹, Yingzheng Liu¹

¹ Key Lab of Education Ministry for Power Machinery and Engineering, School of Mechanical Engineering, Shanghai Jiao Tong University, Shanghai, China, chenyujia@sjtu.edu.cn.

Keyword: inverted flags, heat transfer, flapping dynamics, TSP

As power consumption of electrical devices grows continuously along with their reduced size and compact package, thermal management has always called for innovative cooling technologies to avoid the potential thermal damage. The placement of inverted flags [1] (free at the leading edge, but clamped at the trailing edge) in the channel flow, which are successfully excited into flapping motions at a low Reynolds number, can enable extreme gains in wall heat removal. This study experimentally determined flapping dynamics of dual tandem self-oscillating inverted flags and the resultant enhancement of wall heat removal. The highly unsteady flapping motion of the inverted flag was captured using a high-speed camera (Fig. 1) and identified by the structure boundary detection algorithm. The resultant temperature fields were determined by temperature sensitive paint measurement. The results show that the self-oscillating inverted flag in flapping mode exhibited the most energetic motion, with a maximum amplitude of 1.75 times of the flag length and a Strouhal number 0.17. This significantly promoted heat removal from the heated wall, with a considerable local Nusselt number ratio exceeding 1.5. Tandem flags flapped synchronously with the same frequency at a low Reynolds number and a close distance G^* between two inverted flags, and the phase difference depended linearly on separation distance. Increases in separation distance and Reynolds number led to decoupling behavior.

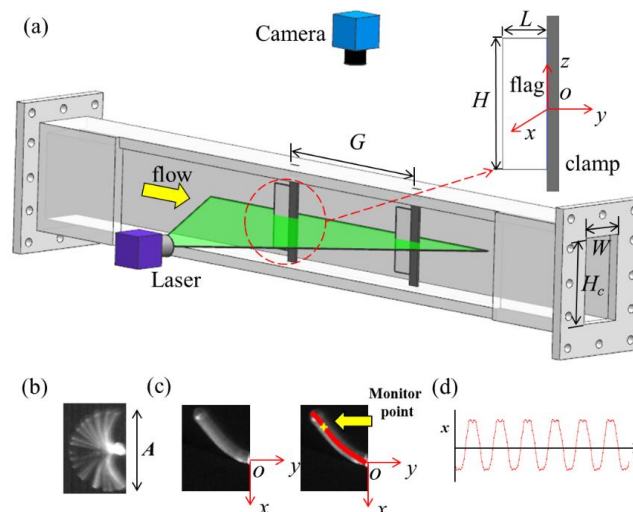


Fig. 1 Flag flapping dynamics: (a) schematic diagram of experimental setup; (b) superimposed trajectory of the inverted flag; (c) profile of the inverted flag; (d) transverse displacement of monitor point.

1. Chen, Y., et al., Heat transfer enhancement of turbulent channel flow using tandem self-oscillating inverted flags. *Physics of Fluids*, 2018. 30(7): p. 075108.

Investigation of a panel flutter under different initial disturbances

A.S. Shishaeva^{1,2}, V.V. Vedeneev¹, G.B.Sushko², A.A. Aksenov²

¹*Lomonosov Moscow State University, Moscow, Russia*
anastasiashishaeva@rambler.ru

²*Tesis LTD, Moscow, Russia*

Keyword: aeroelasticity, panel flutter, single-mode flutter, initial disturbance.

Aeroelastic instability of skin panels in supersonic gas flow, known as panel flutter, is divided into two main types: single mode and coupled mode.

The coupled-mode panel flutter occurs at high supersonic gas speed, while at low supersonic speed the single-mode flutter is dominating. A single-mode flutter regime is more energy-intensive and, thus, more dangerous. Our recent study [1] has shown that there are different types of single-mode flutter at small supersonic gas speeds. Some of these types include two, three or more natural modes and an internal resonance between them. Furthermore, different limit cycle oscillations can coexist at the same flow conditions because of linear growth mechanism and nonlinear interaction between growing eigenmodes. In that case one limit cycle can be transformed to the other by applying a small disturbance to the plate. In the work we study an effect of a disturbance applied to the plate.

In this work we consider an interaction of an elastic plate with an external sub- and supersonic gas flow. The elastic plate is mounted to rigid plates parallel to the gas flow. The gas flow is varied while other parameters of plate and flow stay constant. The subsequent plate-flow interaction is calculated using two coupled software programs: Abaqus for simulating the plate deformation and FlowVision for simulating the gas flow. The interaction between the programs is organized through the direct coupling mechanism along the surface of the deformed plate.

We investigate an effect of initial disturbance on the plate behavior. We investigate the effect of a small disturbance with combined modes and large disturbances with different single modes. We consider deviation, frequencies and energy of vibration of the plate depending on the Mach number of the flow and initial disturbance of the plate.

This work is supported by the grant of Russian Foundation for Basic Research (project 18-01-00404).

1. Shishaeva, A.S., Vedeneev, V.V., Aksenov A.A. (2015). Nonlinear single-mode and multi-mode panel flutter oscillations at low supersonic speeds. *Journal of fluids and structures*, 56, 205-223.

Experiments on the Aeroelastic Stability of Plates in High Subsonic and Low Supersonic Flow

Jannis Lübker¹

¹*DLR, Göttingen, Germany, Jannis.Luebker@DLR.de.*

Keyword: Panel Flutter, Aeroelastic Stability, Flat and Rectangular Plates, Wind Tunnel Experiments, Forced Motion, Aerodynamic Response

In the years preceding the first manned moon landing within the Apollo 11 mission, extensive engineering was carried out on the Saturn V rocket that included, among others, thorough studies on an aeroelastic instability known as panel flutter. Under certain flow conditions, the damping of the aeroelastic system of a flow exposed plate or shell structure disappears and self-excited oscillations arise. As a result of the structure's nonlinear characteristics, those oscillations are usually of a limit cycle type and can lead to structural failure.

Theoretical models developed in the 1960s and 70s provide satisfactory results for subsonic and high supersonic flows, but are inaccurate in predicting the aeroelastic behavior of those structures exposed to transonic flows. In the recent years, new fluid-structure interaction (FSI) methods by means of coupled computational fluid dynamics (CFD) and finite element method (FEM) computations have shown an increased accuracy in this Mach number range. Experimental data is required though to gain a deeper understanding of the underlying fluidic mechanisms and to allow for the validation of numerical approaches.

The work at hand presents experimental data on the aeroelastic stability of plate and shell structures exposed to high subsonic and low supersonic flows. The performed tests comprise the measurement of structural deformation and the associated aerodynamic response by means of unsteady pressure data. The described tests are performed in the Transonic Wind Tunnel Göttingen (DNW-TWG) within a Mach number range of $0.7 < M_\infty < 1.2$ and Reynolds numbers at $2.5 \cdot 10^6 < Re < 7.5 \cdot 10^6$. The main aim of the activity is the determination of the aerodynamic response evoked by the structural deformation of the used rectangular and flat plate model. The experiments are based on a forced motion conception, which focuses on the first two streamwise bending eigenmode shapes of the structure. The deformations of the plate, which are caused by actuators, are measured by a stereo pattern recognition system, over a wide range of amplitudes and frequencies. The induced aerodynamic response is measured by highly sensitive and unsteady miniature pressure transducers that are arranged in both streamwise and spanwise sections. The measured data is validated with theoretical approaches based on potential flow theory.

Based on the measured data, the influence of the Mach number and the structural parameters is identified and the generalized aerodynamic forces are calculated to obtain information on the system's stability. The generalized aerodynamic forces indicate an aerodynamic damping, which increases with increasing excitation frequency of the structural deformation, in both the high subsonic and the low supersonic domain. This damping decreases for the latter with further increasing Mach number, whereas for the subsonic domain a decrease is obtained with decreasing Mach number.

Flapping wing, pitching foil

Quasi-nonlinear Aeroelastic Analysis of a Membrane-type Flapping Wing Utilizing Structural Nonlinearity

Hiroto Nagai^{1,2}, Kazutaka Nakamura³, Masahiko Murozono⁴, Koki Fujita⁴, Hitoshi Arizono⁵, Shuji Nagasaki⁶, and Shigeki Yashiro⁶

¹*Kyushu University, Fukuoka, Japan, nagai@aero.kyushu-u.ac.jp.*

²*Nagasaki University, Nagasaki, Japan*

³*Murata Manufacturing Co., Ltd., Yasu, Japan*

⁴*Nippon Bunri University, Oita, Japan*

⁵*Japan Aerospace Exploration Agency, Chofu, Japan*

⁶*Kyushu University, Fukuoka, Japan*

Abstract

A quasi-nonlinear aeroelastic analysis is proposed to simulate the unsteady response for the membrane-type flapping wing. The flapping wings have been employed for almost all the successful flapping-wing type micro air vehicle and provide a preferable passive feathering motion utilizing the structural nonlinearity, such as large deformation, stress-stiffening of the membrane, and snap-through buckling. In the proposed method, the nonlinear equation of motion in modal space is modeled using the post-buckling analysis and the perturbed modal analysis with finite element method, prior to the aeroelastic analysis. Then, the 3D Navier-Stokes equation with finite difference method is solved, coupled with the nonlinear equation of motion. The numerical result shows a good qualitative agreement with the experimental one.

Keyword: Flapping Wing, Aeroelasticity, Structural Nonlinearity, MAV, Snap-through.

1 Introduction

Flapping-wing type micro air vehicles (FMAVs) are characterized by a light-weight body and flexible flapping wings with complex wing motions. These characteristics contribute to high flight maneuverability, high collision safety for objects, and low noise, compared to the conventional rotary-wing type drones. Therefore, a FMAV is expected as a human/nature-friendly drone in various applications close to humans, animals, and plants. Recently, a few FMAV have succeeded in autonomous hovering flight with the size less than 20 cm. The "Nano hummingbird" developed by Aerovironment, Inc. is one of the most successful FMAV, which is 16 cm size and 19 g weight (Kennon et al. 2012). The Nano hummingbird has been followed by the several other successful FMAVs (Roshanbin et al. 2017; Phan et al. 2019) Coibri, KUbeetle). Murata Manufacturing Co., Ltd. and our research group have also developed a FMAV, which is a tailless two-winged autonomous flying robot with the full span of 18 cm and the body weight of 20.5 g. The developed flying robot is characterized as follows. (1) The elastic wing structure is made of light-weight membrane reinforced by an anisotropic CFRP vein pattern. (2) The flapping wings are actuated by the novel flapping mechanism, which consists of crank-slider linkage with double connecting rods has an energy recovery system by using a mechanical elasticity. (3) A feedback control for the pitch and roll angles of the body attitude was made by moving the center of gravity. We have

succeeded in an autonomous hovering flight and vertical take-off/on in a wireless feedback control as shown in Fig. 1 (Nakamura and Nagai, 2019).

These successful FMAVs have employed the similar membrane-type flapping wings, which provide preferable passive torsion, or feathering rotation, utilizing the structural nonlinearity, such as snap-through buckling, stress stiffening of the membrane, and large deformation, as shown in Fig. 2. The elastic response of the flapping wing with the structural nonlinearity is a very complex phenomenon, and a reliable numerical analysis has not been provided because of the complexity and high computation costs. Therefore, the design and development of the flapping wings still depends on trial and errors (Kennon et al, 2012).

In this study, we propose a quasi-nonlinear aeroelastic analysis for the membrane-type flapping wing, considering the structural nonlinearity: large deformation, stress-stiffening, and snap-through buckling. The numerical result is compared to the experimental one to validate the numerical method.

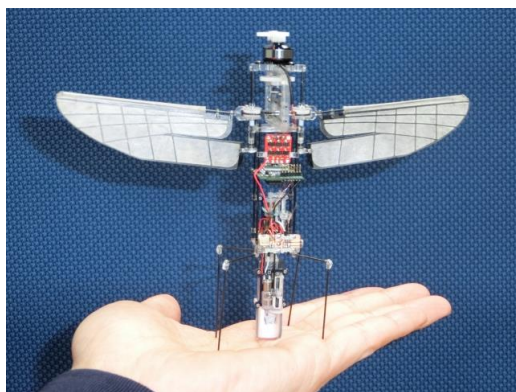


Figure 1: The developed tailless two-winged FMAV and the wireless autonomous flight.

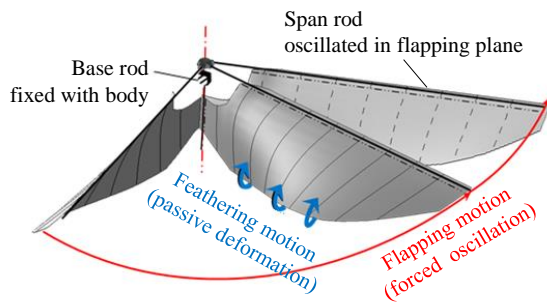


Figure 2: Passive feathering rotation.

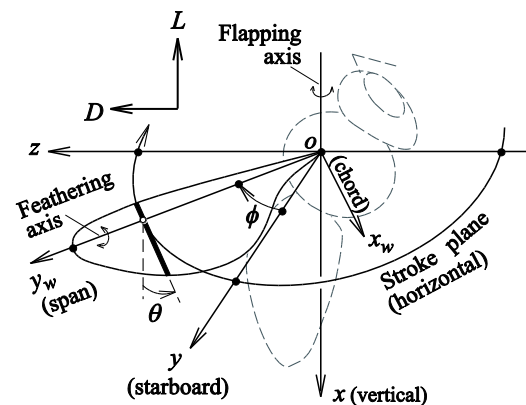


Figure 3: Coordinate systems of a flapping wing.

2 Flapping Wing Model

Figure 3 shows the three-dimensional coordinate systems of a flapping wing. The $oxyz$ is fixed at the body, and the $ox_wy_wz_w$ is fixed at the starboard wing. The flapping stroke plane of the wing is on a horizontal plane because only the hovering condition is considered in this study. The x -axis is in the vertical direction and coincides with the flapping axis of the wing. Hence, the y - z plane denotes the stroke plane of the flapping wing. The y_w -axis is in the spanwise direction, the x_w -axis is in the chordwise direction, and the z_w -axis is in the out-of-plane direction of the wing surface. The flapping angle ϕ is a rotating angle around the

flapping axis (x -axis), defined as the angle between the y - and y_w -axes. The feathering angle θ is a rotating angle around the feathering axis, defined as the angle between the x - and x_w -axes. The wing is forced-oscillated in the flapping direction at the wing base by a flapping mechanical system with a DC motor, and the feathering motion is passively provided due to the aeroelastic deformation.

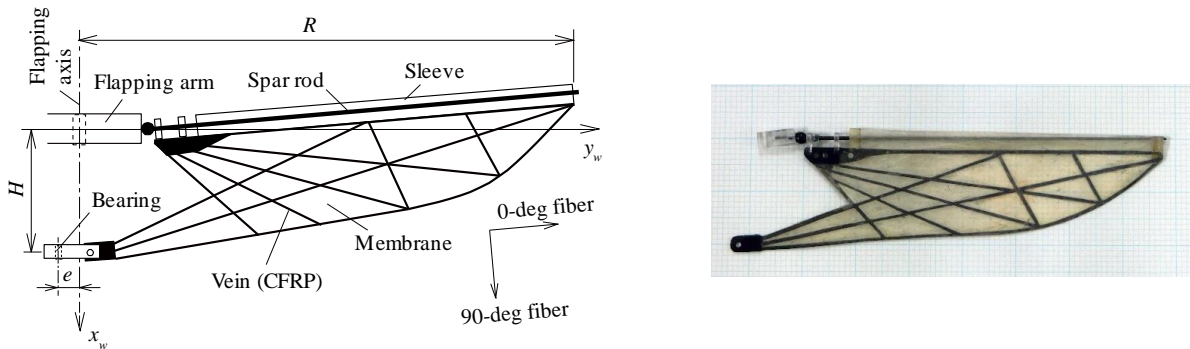


Figure 4: Wing model for experiment and numerical simulation.

The wing model used in this study are shown in Fig 4. The span length R was 80.7 mm, and the width H at the wing base was 20.3 mm. The wing consisted of a spar rod and a vein-reinforced membrane. The spar rod was made of a unidirectional CFRP (carbon fiber reinforced plastic) with a diameter of 0.8 mm. The membrane with a thickness of 13.5 μm was made of a nonwoven fabric sheet with PET (polyethylene terephthalate) impregnated. In addition, the membrane was reinforced by a CFRP vein pattern. The vein pattern was cut out with a line width of 0.75 mm from a CFRP laminate $[90^\circ/0^\circ/90^\circ]$ with a thickness of 78 μm . The membrane was simply supported at the leading-edge and the wing base. There was a sleeve along the leading-edge of the membrane with an internal diameter of 1 mm to pass the spar rod, which allowed the membrane to rotate around the spar rod. However, the membrane was not able to slide along the spar rod due to the stopper at the wing base. In addition, the membrane was connected to a bearing at the wing base, which was also allowed to rotate around the flapping axis. When an out-of-plane force acts on the simply supported membrane, in-plane tensile stress is produced in the membrane, which reinforces the bending stiffness of the membrane due to the so-called stress stiffening effect. The bearing at the wing base was fixed after pushing a little by $e = 2.3$ mm into the tip side from the natural length of the wing. Consequently, an out-of-plane buckling occurs on the membrane because the leading-edge of the membrane was not allowed to slide in the spanwise direction. When the base of the spar rod is forcedly oscillated in the flapping direction, a large aeroelastic deformation occurs in addition to the out-of-plane buckling, which passively provides a preferable large torsion angle (or feathering angle) during a flapping stroke. When the wing stroke is reversed in the opposite direction, a snap-through buckling occurs, which provides a faster feathering rotation at the stroke reversal.

In numerical analysis, a finite element model for the wing was constructed using the commercial FEM (finite element method) software (ANSYS 19.1). Four-nodes shell elements were employed for the membrane, sleeve, and the reinforced plates at the wing base. Beam elements were used for the leading-edge spar and the veins. The anisotropy of veins was considered on the basis of the classic composite laminate theory. Joint elements were used at the base of the leading-edge and the wing base bearing. The contact between the sleeve and the spar were also considered.

In the measurement of lift and wing response, the wing was mounted on the flapping

apparatus so that the leading-edge of the wing was directed vertically downward. The mean lift generated downward by the flapping wing was measured with the electric balance (GX-2000, A&D). At the same time, the wing response was recorded by three high-speed video cameras (FASTCAM 1024PCI, Photron) with the frame rate of 3000 fps. The ten points on the wing (at the leading- and trailing-edges and the chord center in the 25%, 50%, and 75% span station in addition to the wing tip) were traced during a flapping cycle and analyzed with the 3D motion analysis software (Dipp-Motion PRO V2.24a, Ditect).

3 Aeroelastic analysis considering structural nonlinearity

We calculated an unsteady aeroelastic response of the membrane type flapping wing with structural nonlinearity, coupling CFD (computational fluid dynamics) and FEM. The 3D Navier-Stokes equations based on the finite difference method were solved with implicit time-integration (Isogai et al. 2004; Nagai et al. 2009), coupled with the equation of motion in modal space (Nagai et al. 2016). However, the conventional modal analysis based on the linear elastic theory cannot be employed for the nonlinear structural model. Instead, we employed a quasi-nonlinear modal method to solve the nonlinear equation of motion in modal space. The structural nonlinear model including snap-through buckling, membrane stress stiffness, and large deformation was constructed with nonlinear FEM analysis, prior to the aeroelastic analysis.

3.1 Quasi-nonlinear modal analysis

The equation of motion for the elastic flapping wing with structural nonlinearity is represented as:

$$[M]\{\mathbf{w}\} + \{N(\mathbf{w})\} = \{\mathbf{f}\} \quad (1)$$

where $\{\mathbf{w}\}$ is the displacement vector, $[M]$ is the mass matrix, $\{\mathbf{f}\}$ is the external force vector, and $\{N\}$ is the internal force vector in the structure. In this study, the external force consists of the aerodynamic force and the inertial force caused by the forced flapping oscillation, given by,

$$\{\mathbf{f}\} = \{\mathbf{p}_{aero}\} - [M]\{\mathbf{a}(\phi)\} \quad (2)$$

where $\{\mathbf{p}_{aero}\}$ is the aerodynamic pressure distribution on the wing surface, and $\{\mathbf{a}\}$ is the acceleration distribution caused by the forced flapping oscillation. Let us consider the displacement $\{\mathbf{w}\}$ can be divided into a primary displacement $\{\mathbf{w}_0\}$ and a perturbed displacement $\{\delta\mathbf{w}\}$, as follows,

$$\{\mathbf{w}\} = \{\mathbf{w}_0\} + \{\delta\mathbf{w}\} \quad (3)$$

Accordingly, the internal force can be approximated as a linear function, as follows,

$$\{N \mathbf{w}\} = \{N \mathbf{w}_0\} + [K_t \mathbf{w}_0]\{\delta\mathbf{w}\} \quad (4)$$

where $[K_t]$ is the tangential stiffness matrix. Substituting Eqs. (3) and (4) into Eq. (1), we obtain the following equation with respect to $\{\mathbf{w}_0\}$:

$$[M]\{\mathbf{w}_0\} + \{N \mathbf{w}_0\} = \{\mathbf{f}\} - \{\delta\mathbf{f}\} \quad (5)$$

where $\{\delta\mathbf{f}\}$ is the perturbed force and given by,

$$[M]\{\delta w\} + [K_t w_0]\{\delta w\} = \{\delta f\} \quad (6)$$

The displacement of the membrane wing is mainly attributed to the out-of-plane buckling. Thus, the primary displacement $\{w_0\}$ is approximately represented by only the buckling displacement shape $\{\Phi_0\}$, as follows:

$$\{w_0\} \cong \{\Phi_0\}\xi_0(t) \quad (7)$$

where ξ_0 is the modal coordinate of the buckling displacement. In this study, the buckling displacement mode is named as 0th mode. How to choose $\{\Phi_0\}$ is explained in Set. 3.2. In Eq. (5), the contribution of the perturbed force $\{\delta f\}$ is considered to be negligible compared to the other terms. By the coordinate transformation from $\{w_0\}$ to ξ_0 , the following 1DOF equation of motion is obtained for the primary vibration:

$$M_0 \ddot{\xi}_0 + N_0 \dot{\xi}_0 = Q_0 \quad (8)$$

where,

$$\text{Generalized mass in 0th mode:} \quad M_0 = \{\Phi_0\}^T [M] \{\Phi_0\} \quad (9)$$

$$\text{Generalized internal force in 0th mode:} \quad N_0 \dot{\xi}_0 = \{\Phi_0\}^T \{N(\xi_0)\} \quad (10)$$

$$\text{Generalized external force in 0th mode:} \quad Q_0 = \{\Phi_0\}^T \{f\} \quad (11)$$

Equation (6) denotes a linear perturbed equation of motion, which has perturbed natural frequencies ω_k and perturbed normal modes $\{\Phi_k\}$ dependent on the primary displacement $\{w_0\}$. Thus, the perturbed displacement $\{\delta w\}$ can be represented as a superposition of the normal modes, as follows:

$$\{\delta w\} = \sum_{k=1}^n \{\Phi_k(\xi_0)\} \xi_k(t) \quad (12)$$

where ξ_k is the modal coordinate in the k -th perturbed mode. In this study, the perturbed modes are named as 1st, 2nd, ... modes. On the basis of the modal orthogonality, Eq. (6) is represented in the perturbed modal space, as follows:

$$M_k \ddot{\xi}_k + M_k \{\omega_k \xi_0\}^2 \cdot \xi_k = \delta Q_k \xi_0 \quad (13)$$

where,

$$\text{Generalized mass in } k\text{-th mode:} \quad M_k = \{\Phi_k\}^T [M] \{\Phi_k\} \quad (14)$$

$$\text{Generalized stiffness in } k\text{-th mode:} \quad M_k \{\omega_k \xi_0\}^2 = \{\Phi_k\}^T [K_t(\xi_0)] \{\Phi_k\} \quad (15)$$

$$\text{Generalized force in } k\text{-th mode:} \quad \delta Q_k(\xi_0) = \{\Phi_k\}^T \{\delta f \xi_0\} \quad (16)$$

From Eq. (5), the perturbed force is approximately represented as follows:

$$\{\delta f\} = \{f\} - \{N \xi_0\} - [M] \{\Phi_0\} \xi_0 \quad (17)$$

Accordingly, the corresponding generalized perturbed force in k -th mode is given by,

$$\delta Q_k \xi_0 = Q_k \xi_0 - N_k \xi_0 - M_k^{cp} \xi_0 \cdot \xi_0 \quad (18)$$

where,

$$\text{Generalized external force in } k\text{-th mode:} \quad Q_k(\xi_0) = \{\Phi_k\}^T \{f\} \quad (19)$$

$$\text{Generalized internal force in } k\text{-th mode:} \quad N_k \xi_0 = \{\Phi_k\}^T \{N(\xi_0)\} \quad (20)$$

$$\text{Coupling mass between 0th and } k\text{-th modes:} \quad M_k^{cp} \xi_0 = \{\Phi_k\}^T [M] \{\Phi_0\} \quad (21)$$

The coupling mass between the buckling mode (0th) and the k -th perturbed mode appears because there is no orthogonality each other.

Once the nonlinear relations of $\{N(\xi_0)\}$, $\{\Phi_k(\xi_0)\}$, and $\omega_k(\xi_0)$ are obtained, the modal coordinates ξ_0 and ξ_k are calculated at each time step by the time-integration of Eqs. (8) and (13), and the aeroelastic deformation of the flapping wing is determined. These nonlinear functions can be obtained by solving the post buckling analysis and the perturbed modal analysis described in Set. 3.2, prior to the aeroelastic analysis. However, storing and reading the data of the vector function $\{N(\xi_0)\}$ and $\{\Phi_k(\xi_0)\}$ at each ξ_0 take an extra numerical cost. In this study, $\{\Phi_k\}$ is fixed to that at the representative primary deformation; therefore, it is independent of ξ_0 . Furthermore, $\{N(\xi_0)\}$ is approximated by using $N_0(\xi_0)$ and $\{\Phi_0\}$ as follows:

$$\{N \xi_0\} \approx \frac{\{\Phi_0\}^T \{N \xi_0\}}{\|\Phi_0\|^2} \{\Phi_0\} = \frac{N_0(\xi_0)}{\|\Phi_0\|^2} \{\Phi_0\} \quad (22)$$

Accordingly, the corresponding generalized internal force in k -th mode is given by,

$$N_k \xi_0 = \{\Phi_k\}^T \{N \xi_0\} = \frac{\{\Phi_k\}^T \{\Phi_0\}}{\|\Phi_0\|^2} N_0 \xi_0 = R_k^{cp} N_0 \xi_0 \quad (23)$$

where R_k^{cp} is the coupling of the mode shapes between the 0th and k -th modes. Since $\{\Phi_k\}$ is independent of ξ_0 , only the scalar nonlinear functions of $N_0(\xi_0)$ and $\omega_k(\xi_0)$ are necessary, prior to the aeroelastic analysis. In addition, M_k^{cp} and R_k^{cp} are constant values independent of ξ_0 . In the next section, how to obtain the representative mode shapes and the nonlinear scalar functions.

3.2 Non-linear structural modeling

To obtain the nonlinear characteristics of the wing model, we conducted the post-buckling analysis with FEM model. First, the wing deformation was calculated in the initial attachment condition with no external load. In this case, an out-of-plane buckling occurs as shown in Fig. 5b, because the wing base is pushed in the $+y_w$ -direction to attach the base bearing to the flapping axis as shown in Fig. 4; consequently, a constant torsional angle appears in span direction. Then, a static pressure distribution with a spanwise gradient, which models the aerodynamic pressure due to the flapping motion, was applied on the wing surface. With changing the magnitude of the pressure load, the torsion angle slightly increases in the wing tip area (Figs. 5b–5d). However, the torsion angle does not increase any more with increasing external load (Fig. 5d) because of the stress stiffening effect of the membrane. On the other hand, the torsional angle decreases with increasing the negative pressure. Then, any converged solution was not obtained at a negative pressure (after the result shown in Fig. 5a), which implies that the snap-through buckling occurs at the negative load. In this study, the deformation just after the snap-through shown in Fig. 5c was employed as the representative buckling deformation $\{\Phi_0\}$. The modal coordinate ξ_0 was also determined on the basis of $\{\Phi_0\}$ normalized to the modal mass. Transforming the relation of the pressure load and the deformation in the modal space of $\{\Phi_0\}$, we obtained the nonlinear function $N_0(\xi_0)$, or the generalized internal force in 0th mode, as shown in Fig. 6.

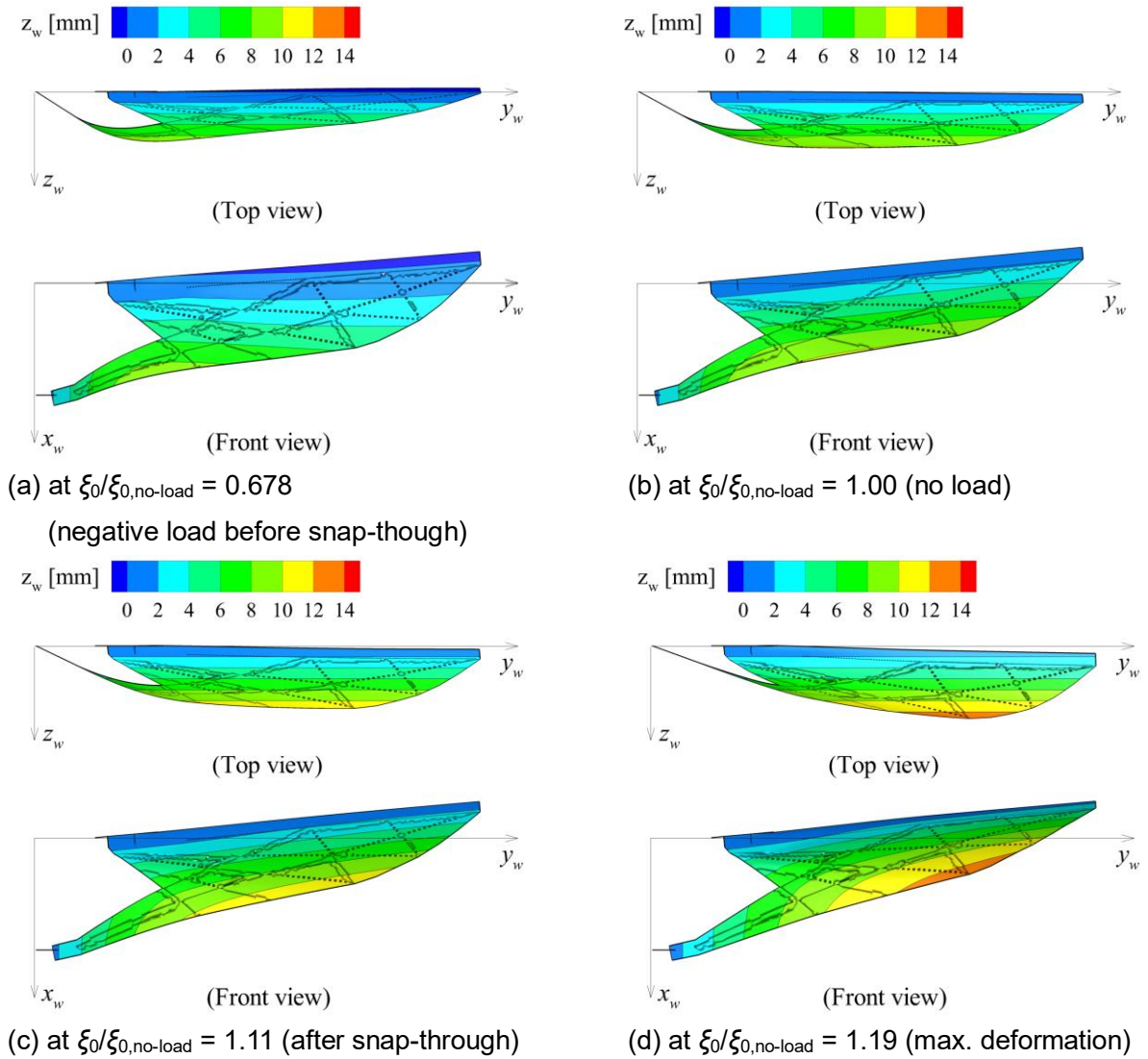


Figure 5: Wing deformation with the static pressure in the post-buckling analysis.

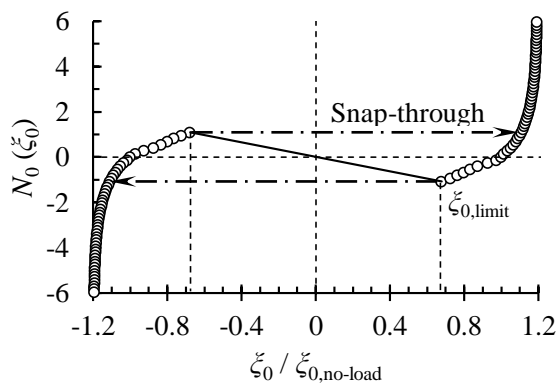


Figure 6: Post-buckling analysis.

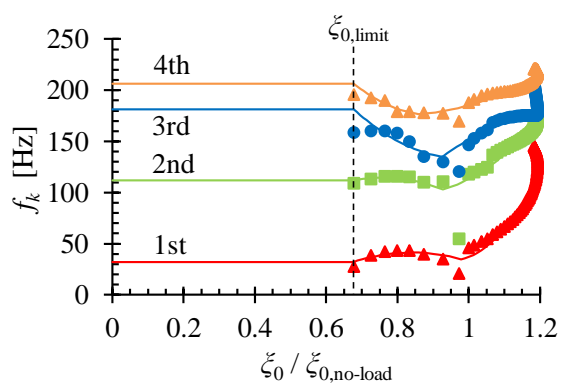


Figure 7: Perturbed modal analysis.

Next, we conducted the perturbed modal analysis under the post-buckling deformation with each pressure load. The perturbed natural frequencies f_k under each post-buckling deformation are shown in Fig. 7. Each perturbed natural frequency is enhanced due to the stress stiffening effect of the membrane. Using the discretized results at each load, we

obtained curve fitting functions based on two quadratic functions in $\xi_{0,\text{limit}} < \xi_0 < \xi_{0,\text{no-load}}$ and $\xi_0 > \xi_{0,\text{no-load}}$. During the snap-through ($\xi_0 < \xi_{0,\text{limit}}$), the perturbed natural frequencies were fixed at constant values. The obtained functions were employed as $\omega_k(\xi_0)$ in Eq. (13). The perturbed mode shapes under the representative buckling deformation just after the snap-through were employed as the representative perturbed mode shapes $\{\Phi_k\}$. Figure 8 shows the representative perturbed mode shapes, where the mode shapes are normalized to unity for illustration. The first perturbed mode provides a camber to the wing cross-section.

The conventional mode superposition based on the linear elastic deformation cannot represent a large deformation and rotation. For the wing model in this study, the chordwise deformation includes large rotation, whereas the spanwise deformation is small. Hence, the spanwise deformation was represented as the conventional mode superposition, whereas the chordwise deformation was represented by the integration of the chordwise gradient under the condition that the chordwise arc length does not change after deformation.

$$\begin{aligned}
 x_w s &= \int_{s_{spar}}^s \cos \eta ds + x_{spar}, & z_w s &= \int_{s_{spar}}^s \sin \eta ds + z_{spar} \\
 \eta s &= \sum_{i=0}^n \frac{\partial \Phi_i}{\partial s} \xi_i, & z_{spar} &= \sum_{i=0}^n \Phi_i(s_{rod}) \xi_i
 \end{aligned} \tag{22}$$

where s is the curvilinear coordinate along the chordwise wing surface, η is the chordwise gradient, and x_{spar} and z_{spar} is the position of the spar.

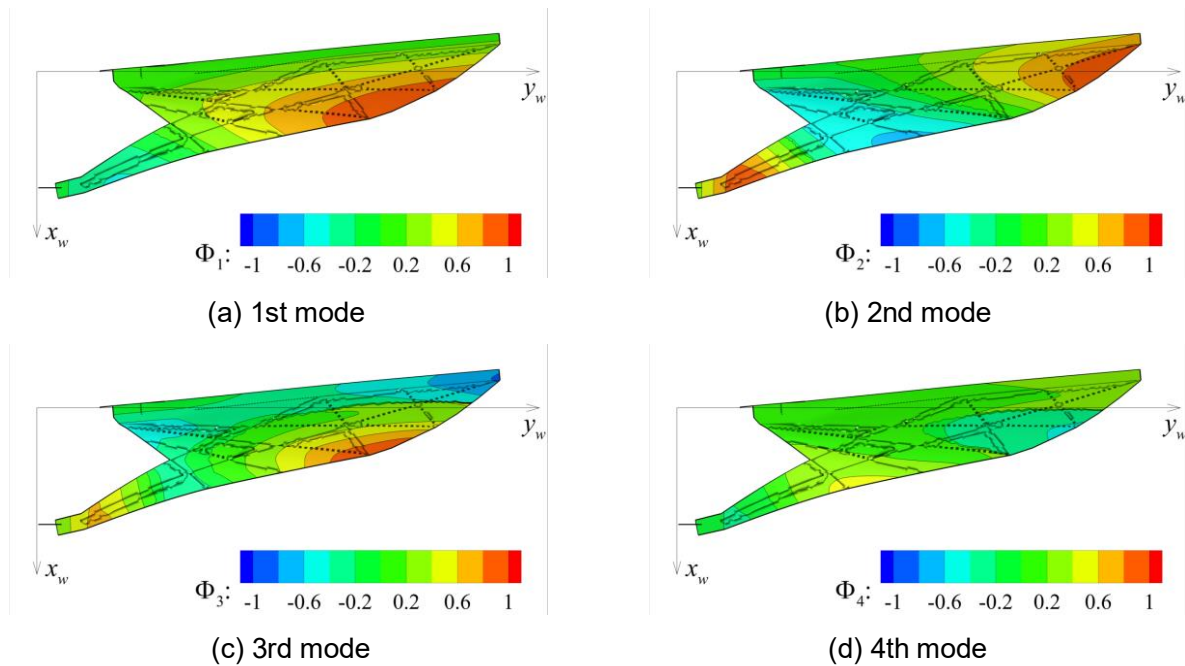


Figure 8: Representative perturbed mode shapes at $\xi_0/\xi_{0,\text{no-load}} = 1.11$ (after snap-through).

4 Results and Discussion

The quasi-nonlinear aeroelastic analysis based on the nonlinear structural model was conducted for the wing model forced-oscillated in the flapping direction. The flapping motion at the wing base measured with the high-speed video camera was input to the numerical model. Figure 9 shows the wing responses during the up- and downstrokes at the input

frequency of 30 Hz, comparing the experimental and numerical results. The numerical response shows a good agreement in the tendency with the experimental one. Figure 10a and 10b show the time history of the wing angles and the camber ratio, respectively, at 25%, 50%, and 75% span stations at 30 Hz. In Fig. 10a, the passive feathering angle for the numerical result agrees well in the amplitude, and rotational (or snap-through) time and timing with that for the experimental result. However, the numerical result includes a high-frequency oscillation with a larger amplitude after the end of the snap-through (in the first half of each stroke). On the other hand, the time history of camber ratio shows large differences between the experimental and numerical results due to the high-frequency oscillation. Figure 11 shows the time history of the modal coordinates during a flapping cycle at 30 Hz. From Fig. 11, the wing response is mainly attributed to the 0th mode (buckling) in accordance with our assumption. The time history of the perturbed first mode, which provides a camber to the wing cross-section, agrees well with the time history of the camber ratio shown in Fig. 10b. Figure 12 shows the mean lift at four input flapping frequencies. Although there is a quantitative discrepancy, the qualitative tendency of lift with input flapping frequency shows a good agreement between the experimental and numerical results.

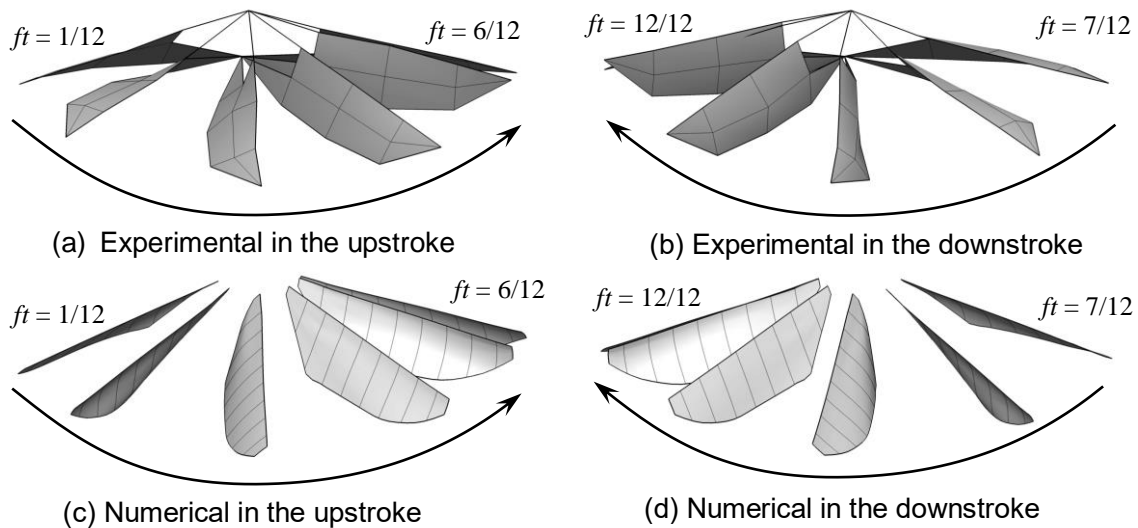


Figure 9: Wing response sequences during a cycle at the input frequency of 30 Hz.

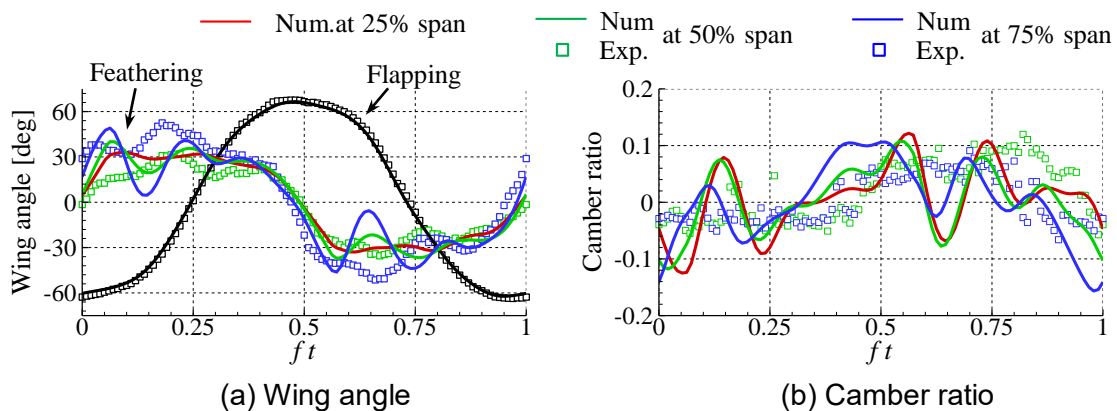


Figure 10: Time history of aeroelastic response during a flapping cycle at 30 Hz.

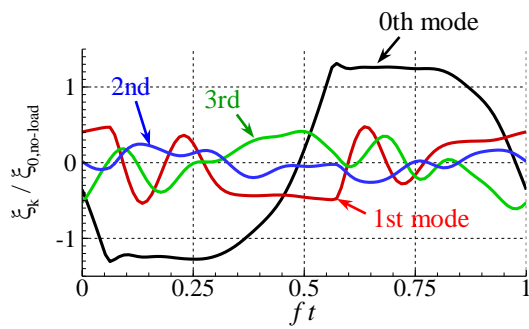


Figure 11: Time history of modal coordinates during a cycle at 30 Hz.

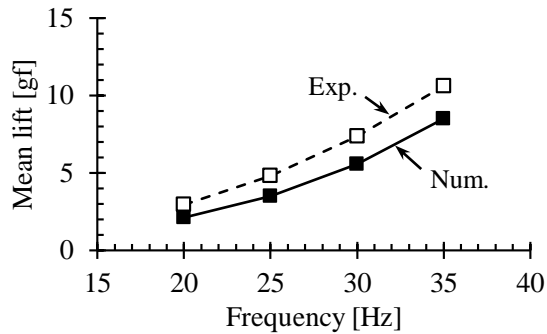


Figure 12: Mean lift vs input frequency.

5 Conclusions

The quasi-nonlinear aeroelastic analysis considering the snap-through, stress stiffening, and large rotation were proposed for the membrane type flapping wing. The proposed method is based on the non-linear equation of motion in modal space approximately modeled by the post-buckling analysis and the perturbed modal analysis, prior to the aeroelastic analysis. The numerical result shows a good qualitative agreement with the experimental results. Although there are some quantitative disagreement, the proposed numerical method provides a useful tool to design and analyze the flapping wings of FMAVs.

Acknowledgements

This work was supported by Murata Manufacturing Co., Ltd. and Japan Society for the Promotion of Science KAKENHI (Grant Numbers JP19K04838). The authors thank Issei Tanaka and Shota Yonemoto for their support in the experiment.

References

- Keennon, M., Klingebiel, K., Won, H., and Andriukov, A., 2012. Development of the Nano Hummingbird: A Tailless Flapping Wing Micro Air Vehicle, Proc. 50th AIAA Aerospace Sciences Meeting including the New Horizons Forum and Aerospace Exposition, AIAA-2012-0588, , 24pp.
- Roshanbin, A., Altartouri, H., Karásek, M., and Preumont, A., 2017. COLIBRI: A hovering flapping twin-wing robot, International Journal of Micro Air Vehicles, Vol, 9, No. 4, pp. 270-282.
- Phan, H.V., Aurecianus, S., Kang, T., and Park, H.C., 2018. Attitude Control Mechanism in an Insect-like Tailless Two-winged Flying Robot by Simultaneous Modulation of Stroke Plane and Wing Twist, Proc. 10th International Micro-Air Vehicle Conference, 6pp.
- Nakamura, K., Nagai, H., 2019. Development of Autonomous Flying Type 18 cm-class Flapping Robot, Proc. the 57th Aircraft symposium, JSASS-2019-5021, 6pp. (in Japanese).
- Isogai, K., Fujishiro, S., Saitoh, T., Yamasaki, M., and Matsubara, M., 2004. Unsteady Three-Dimensional Viscous Flow Simulation of Dragonfly Hovering, AIAA J, Vol. 42, No. 10, pp. 2053–2058.
- Nagai, H., Isogai, K., Fujimoto, T., and Hayase, T., 2009. Experimental and Numerical Study of Forward Flight Aerodynamics of Insect Flapping Wing, AIAA Journal, Vol. 47, No. 3, pp. 730–742.
- Nagai, H. Nakamura, S., Murozono, M., Ono, K., and Uda, N., 2016. Structural Design of Aeroelastic Flapping Wing, Porc. 1st International Symposium on Flutter and its Application, ISFA-3R07, 10pp.

Transitional flight of a flapping wing flyer: A two dimensional perspective

Rahul Sundar¹, Dipanjan Majumdar² and Sunetra Sarkar²

¹ Department of Aerospace Engineering, IIT Madras, Chennai, India, rahul.sundar95@gmail.com

² Department of Aerospace Engineering, IIT Madras, Chennai, India

Keyword: Transitional flight, flapping wing, temporal change of frequency, plunging airfoil.

Avians and insects have always intrigued human kind for they enjoy the boon of flight. Their flights typically involve multiple stages¹ and transitions of different time scales within those stages^{1,2}. The transitions in flight stages manifest through transient change in the body/wing kinematics. Significant work has been done to numerically study the flow and load generation characteristics in different flight regimes independently. The current challenges however lie in understanding the unsteady aerodynamics of transitional flights, maneuvers and gust effects³ to enable optimal design and control of mechanical flapping wing flyers.

Flapping wing kinematics in reality is three dimensional, involving a whole range of physical parameters. However, it is helpful to develop a fundamental understanding by studying the effects of each parameter independently in two dimensions and later to extend to three dimensions. In that pursuit, Makoto *et.al*⁴ have recently reported that active lift inversion occurs when there is a temporal reduction in the frequency of a pure heaving flat plate. Through the present study we extend the efforts of Makoto *et.al*⁴ by developing a kinematic model that mimics our understanding of transition from forward to ascending flights or forward to descending flights. The kinematic model is realised by temporally varying the plunging amplitude and frequency. We look at the effects of individual and combined temporal changes of these two parameters on the associated load generation, power consumption and vortex dynamics for an elliptical airfoil section. The numerical studies are carried out using an in-house Immersed Boundary Method based unsteady Navier Stokes solver.

¹ Chin, D. D., & Lentink, D. (2016). Flapping wing aerodynamics: from insects to vertebrates. *Journal of Experimental Biology*, 219(7), 920-932.

² Tobalske, B. W. (2001). Morphology, velocity, and intermittent flight in birds. *American Zoologist*, 41(2), 177-187.

³ Shyy, W., Aono, H., Chimakurthi, S. K., Trizila, P., Kang, C. K., Cesnik, C. E., & Liu, H. (2010). Recent progress in flapping wing aerodynamics and aeroelasticity. *Progress in Aerospace Sciences*, 46(7), 284-327.

⁴ Ima, M., Yokoyama, N., & Senda, K. (2019). Active lift inversion process of heaving wing in uniform flow by temporal change of wing kinematics. *Physical Review E*, 99(4), 043110.

Hydrodynamics of forced pitching hydrofoil

Zaka Muhammad and Md. Mahbub Alam

*Institute for Turbulence-Noise-Vibration Interaction and Control, Harbin Institute of Technology (Shenzhen), Shenzhen 518055, China
Email: alam@hit.edu.cn; alamm28@yahoo.com*

Keyword: forced pitching, hydrofoil, thrust, power.

This paper presents a parametric study on a forced pitching hydrofoil, where diameter based Strouhal number (St_d) and amplitude ratio (A^*) of the hydrofoil are varied as $0.21 < St_d < 0.33$ and $0.55 < A^* < 0.8$, respectively. The numerical solution of the problem is obtained using Large Eddy Simulation (LES). Coefficients of thrust, power, and efficiency of the hydrofoil are calculated and presented on $St_d - A^*$ plane. The evolution of the flow structure around the oscillating hydrofoil is clarified for the conditions corresponding to both drag and thrust generations (Fig. 1). A flow model is hypothesized. An outstanding mathematical analysis of the flow model, involving Euler, Coriolis and centrifugal accelerations in non-inertial frame, is developed to assimilate the physical insight into the thrust generation and power input. The analysis provides theoretical relationships of thrust, power, and efficiency as functions of St_d and/or A^* . The data from the numerical simulation tangibly support the relationships.

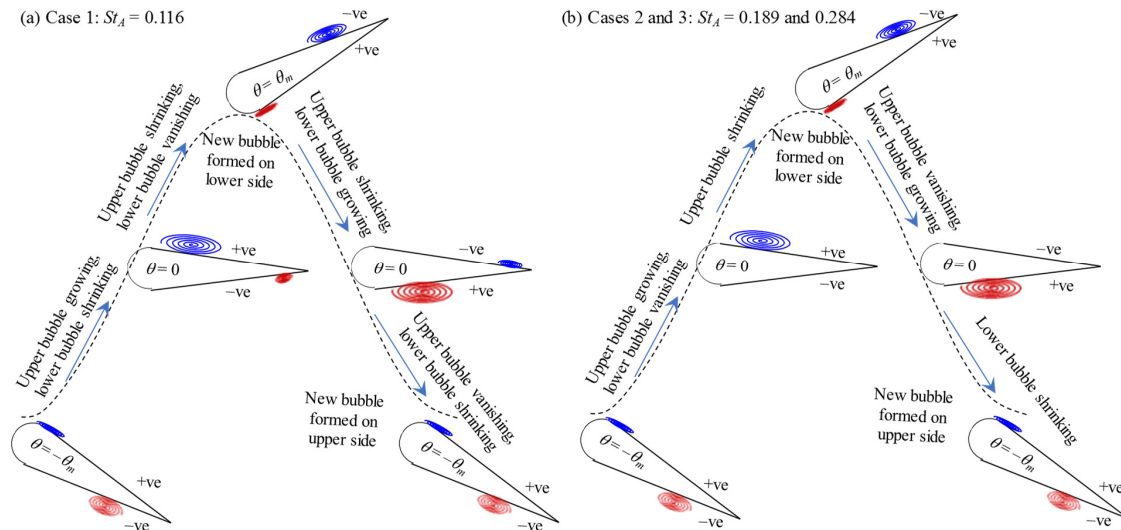


Figure 1: Sketch showing the evolution of recirculation bubble and pressure pattern. ‘+ve’ and ‘-ve’ indicate positive and negative pressure, respectively.

Nonlinear aeroelastic behavior of a flapping wing with low-order chord-wise flexibility

Dipanjan Majumdar¹, Chandan Bose² and Sunetra Sarkar¹

¹ Department of Aerospace Engineering, Indian Institute of Technology Madras, Chennai, India, dipanjanmajumdar100@gmail.com

² Department of Applied Mechanics, Indian Institute of Technology Madras, Chennai, India

Keyword: Fluid-structure interaction, Lower-order flexibility, Bifurcation analysis

Chord-wise flexibility of wings of natural flyers can play a pivotal role in achieving high propulsive efficiency. However, high-fidelity simulations of the fluid-elastic behavior of chord-wise flexible wings involve prohibitive computational cost. Hence, the present study attempts to capture the essential dynamics of the fluid-structure interaction (FSI) system using a limited-mode chord-wise flexible structural model¹ coupled with a high-fidelity Navier-Stokes (N-S) solver. The wing is modelled as two elliptic rigid links connected by a non-linear torsional spring as schematically shown in Fig. 1(a). The torsional spring incorporates the chord-wise bending stiffness of the flapping foil. While the front link is subjected to an active pitching-plunging motion, the rear link undergoes flow-induced passive oscillations. The aerodynamic loads on the foil are computed using an Immersed Boundary Method² (IBM) based in-house N-S solver which is coupled with the structural solver to simulate the FSI response. A bifurcation study has been performed considering the free-stream velocity as the control parameter in the presence of both structural and aerodynamic nonlinearities in a low Reynolds number flight regime. The flow-field around the body corresponding to the different dynamical states of the system and the associated vortex interactions are examined in detail and will be discussed in the full length paper. A typical representative flow-field of the wing depicting a downward deflected wake pattern is shown in Fig. 1(b).

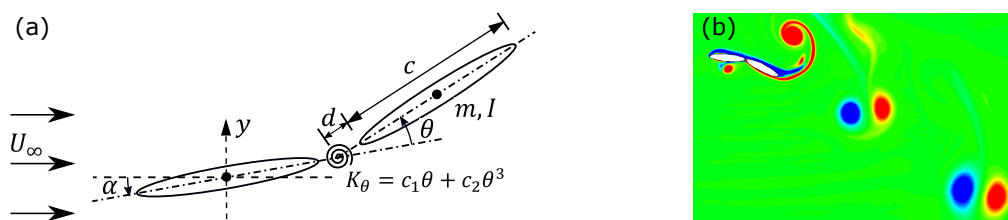


Figure 1: (a) Schematic of the aeroelastic model, (b) Representative flow-field.

¹ Eldredge, J. D., Toomey, J., & Medina, A. (2010). On the roles of chord-wise flexibility in a flapping wing with hovering kinematics. *Journal of Fluids Mechanics*, 659, 94-115.

² Kim, J., Kim, D., & Choi, H. (2001). An immersed-boundary finite-volume method for simulations of flow in complex geometries. *Journal of Computational Physics*, 171, 132-150.

Hydrodynamic interaction of self-propelled flapping wings in an infinite array

L. Benetti Ramos¹, G. Raynaud¹, O. Marquet¹, M. Bergmann^{2,3} and A. Iollo^{2,3}

¹ ONERA - The French Aerospace Lab, Meudon, France, ibenetti@onera.fr

² Institut de Mathématiques de Bordeaux, Univ. Bordeaux, 33400 Talence, France

³ INRIA Bordeaux Sud-Ouest, 33405 Talence, France

Keyword: Flapping propulsion, Flow-structure interaction.

Bird flocks and fish schools are natural examples of collective dynamics that might result in improved energetic efficiency or group speed. Although those animals dispose of specific mechanisms¹ to sense the surrounding flow thus adapting their trajectory to benefit from these unsteady mechanisms, recent studies^{2,3} reveal that passive hydrodynamic wake-body interaction appears to play a key role on the emergence of stable formations of agglomerated bodies.

Following previous numerical and experimental studies², we investigate the collective motion of equally-spaced infinite arrays of flapping wings by solving the incompressible Navier-Stokes equations coupled to the solid free horizontal motion in a periodic computational domain. Under imposed vertical motion, we vary the gap between flapping wings (corresponding to the size of the computational domain) to analyse the influence of the wake-body interaction on the time-averaged group speed. Decreasing progressively the gap between wings, we generally observe that the wake-body interaction tends to smoothly decrease the averaged speed, except for critical distances where higher-speed solutions are captured. The existence of several periodic solutions will be further discussed and analyzed.

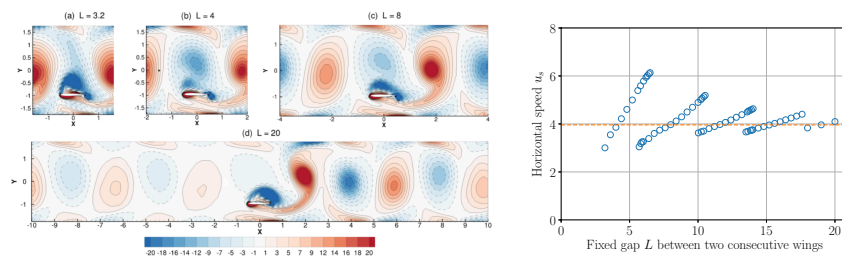


Figure 1: Vorticity contours (left) and horizontal speeds obtained for different gaps(right).

¹ Liao JC. (2006). The role of the lateral line and vision on body kinematics and hydrodynamic preference of rainbow trout in turbulent flow. *J Exp Biol* 209:4077-90.

² Becker, A., Masoud, H., Newbolt, J., Shelley, M., Ristroph, L., (2015). Hydrodynamic schooling of flapping swimmers, *Nature Communications* 6, 1-8.

³ Ramanarivo, S., Fang, F., Oza, A., Zhang, J., Ristroph, L., (2016). Flow interactions lead to orderly formations of flapping wings in forward flight, *Physical Review Fluids* 1 (7), 071201.

Survival of the fastest: evolving wing shapes for flapping locomotion

Sophie Ramananarivo¹, Thomas Mitchel² and Leif Ristroph²

¹*LadHyX, Ecole Polytechnique, Palaiseau, France.*

sophie.ramananarivo@ladhyx.polytechnique.fr

²*Applied Math Lab, Courant Institute, New York University, New York, USA*

Keyword: flapping flight, optimal locomotion, evolutionary algorithm

How would we shape the wings of a bird-inspired flyer to improve its propulsive performance? While conventional aeronautics has accumulated a wealth of knowledge on the steady flight characteristics of different airfoils, less explored is how shape affects the unsteady aerodynamics at work in flapping-wing flight.

Here we use an evolutionary or genetic algorithm to modify shape and improve the forward speed of 3D-printed wings that heave up-and down and propel within water. In this scheme, genes are mathematical parameters that define shape, breeding is the combination (and mutation) of genes from parent wings to form a child, and a wings measured swimming speed is its fitness that dictates likelihood of breeding. This “survival of the fastest” process leads to marked improvement in relatively few generations, and discovers a fastest teardrop-like wing whose shape most effectively controls the generation and interaction of vortex flows (Fig.1). An analysis of the larger population of faster swimmers identifies shared features that are most critical for propulsion, implicating slenderness, location of maximum thickness and fore-aft asymmetries in edge sharpness or bluntness.

These results demonstrate artificial evolution in laboratory experiments as a successful strategy for tailoring shape to improve propulsive performance. Optimal solutions might also be efficiently determined for related unsteady flow-structure problems such as flexible-wing propulsion or energy harvesting from flows.

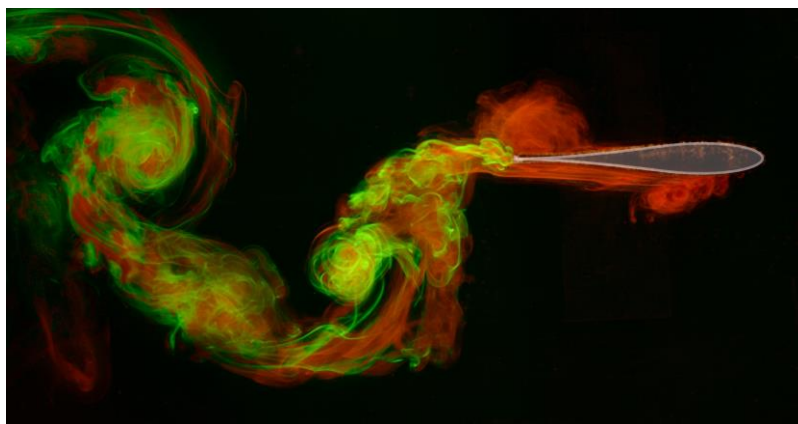


Figure 1: Color-coded flows separating off the edges of the fastest evolved wing. Wing shape affects the formation and shedding of vortices and their subsequent dynamics and interaction with one another and the foil surface.

Flutter in biomechanics and bio-inspired systems

Elastic oscillating fin technology and its application to robotic fish

Ikuo Yamamoto¹

¹ *Nagasaki University, Nagasaki, Japan, iyamamoto@nagasaki-u.ac.jp*

Abstract

Elastic oscillating fin technology is very important in order to create a new kind of propulsion for such as marine vehicles. The author developed the elastic oscillating fish fin during the 1980's and applied it to ship propulsion (Ikuo Yamamoto et al., 1993 ; Ikuo Yamamoto et al., 1995).

From 1993 to 1995 the first life-like swimming robotic fish were developed. The first was an untethered battery operated seabream type robotic fish which was highly recognized worldwide by its life-like swimming (Ikuo Yamamoto, 2001).

Keyword: Elastic oscillating fin, ship, robotic fish, medical instrument

1 Introduction

The author and his colleagues have developed 20 kinds of robotic fish based on elastic oscillating fin technology, such as a coelacanth, carp, whale, manta, tuna, shark ray, and dolphin shown in Fig.1 (Ikuo Yamamoto, 2016). Now, a robotic mermaid, which has an oscillating fin and working hands, is under development. Also, this robotic fish technology has helped to create new medical devices, such as forceps. These devices are being used by medical surgeons and have led a significant reduction in operating time (exceeding 50 percent) compared with conventional forceps. Oscillating fin and robotic fish technologies may continue to provide inspiration to develop new vehicle mechatronic technologies.



FIGURE 1 : Robotic Dolphin

2 Bio-based underwater robots

Robots that have been researched and developed based on the movements and mechanisms of underwater organisms such as fish and aquatic mammals are called bio-based underwater robots.

2.1 Development history

The development of the bio-based underwater robot originated in Japan in the 1980s with a study on an elastic vibrating wing propulsion system, a study on a biomimetic type vibration system in Germany, and a hydrodynamic study on a tethered tail fin in the United States (Ikko Yamamoto, 2001). In the 1990s, the world's first fish robot using an elastic vibrating wing propulsion system to swim exactly like a tethered fin was realized (Ikko Yamamoto, 2016). In recent years, various researchers have developed a variety of biologically-based underwater robots.

2.2 Robot configuration

In 1995, an untethered fish robot that looked like a real fish was developed. As shown in Fig. 2, the fish robot oscillated or vibrated like a fish fin to generate propulsion using an elastic vibrating wing, powered by a motor, and controlled by computer control logic to control the fish robot movement, within the environment provided. A sensory system detects the environment and position using sonar, a camera is provided for image acquisition, a pump and ballast system to control buoyancy, a battery for power and a wireless communication system for remoted operation. The movement of the tail fin's vibrating wing is adjusted to the Strouhal number of the fish. As a result, it is possible to swim exactly like the one shown in Fig. 3. With this technology, in 1997, a coelacanth robotic fish (Fig. 4) controlled by an automatic swimming system (Fig. 5), a carp robotic fish (Fig. 6), a robotic golden Kinschachi (Fig. 7), and a tuna robotic fish (Fig. 8) were developed. After the coelacanth robot, not only the tail fin but also such as the pectoral fin are actuated, enabling more freedom of movement.

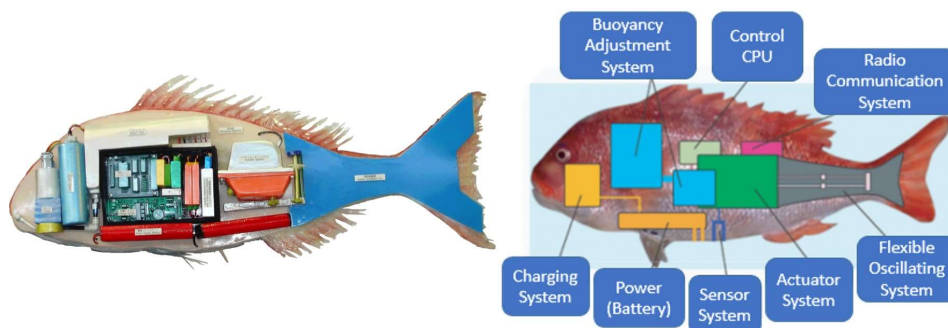


FIGURE 2 : Internal structure of sea bream robotic fish



FIGURE 3 : Sea bream robotic fish



FIGURE 4: Coelacanth robotic fish

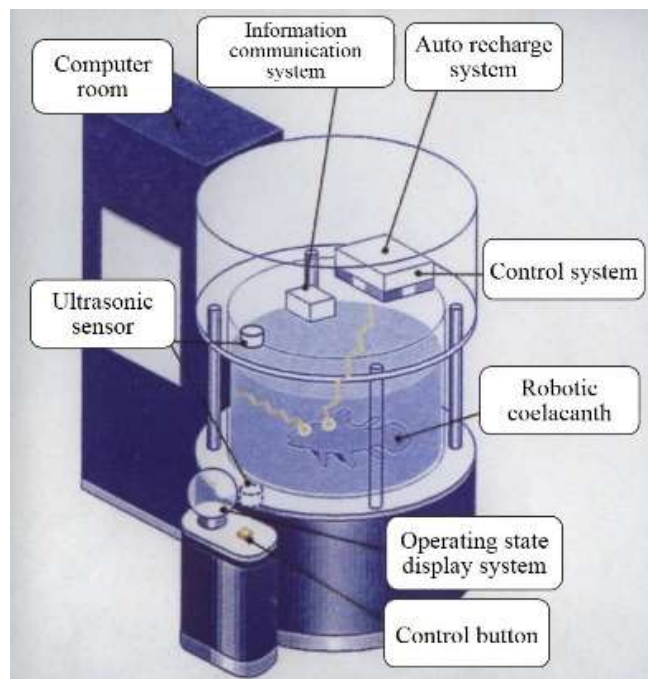


FIGURE 5: Robotic fish automatic swimming system

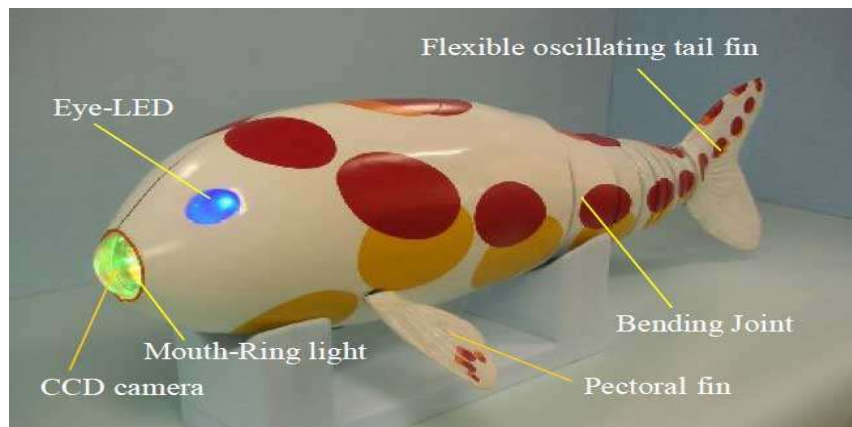


FIGURE 6 : Carp robotic fish



FIGURE 7 : Golden robotic Kinschachi for Nagoya EXPO JAPAN in 2006



FIGURE 8 : Tuna robotic fish

In addition, the developed fish-type underwater robot propelled by oscillation is well suited to the marine environment (Fig. 9) in that if it becomes entangled in a fish net, it can untangle itself by the reversing the operation of the vibrating wing. The manta robot, developed in 2004, uses dual elastic vibrating wings to enable a smooth direction change by somersaulting while swimming underwater (Fig. 10). A shark ray robotic fish (Fig. 11) was developed in 2009. The robot is driven by flapping wings and a long tail fin, and has the ability to turn around on the spot without slowing down. A dolphin robot (Fig. 1) was developed in 2013 as an underwater robot that simulates the movement of aquatic mammals. Here the elastic vibrating wing is used horizontally for the tail fin, this motor driven dolphin robot is 1m long. Since 2015, a mermaid robot (Fig. 12) that moves with a tail fin with a double-armed robot arm for underwater work has been under development.

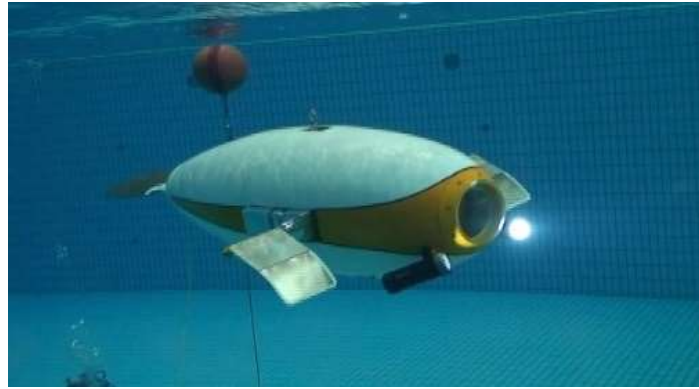


FIGURE 9 : Fish type underwater robot

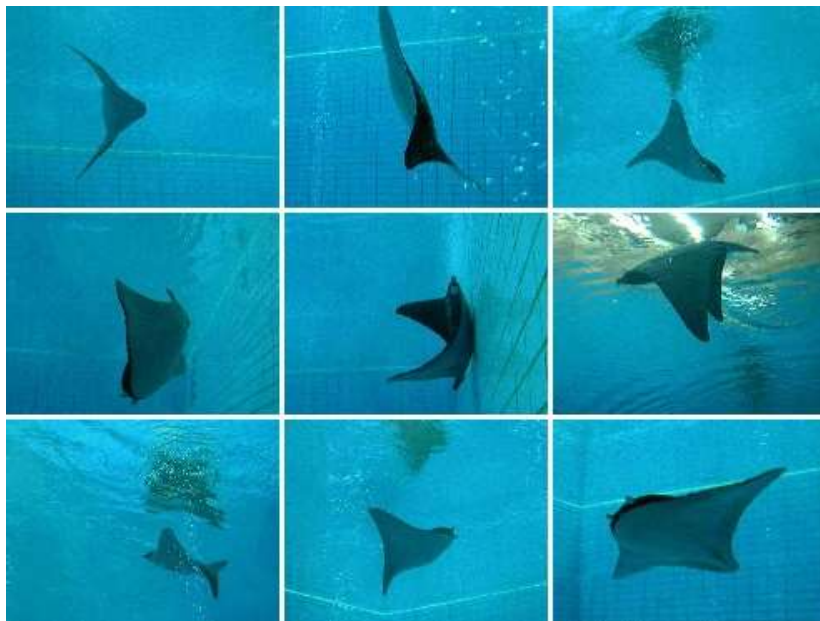


FIGURE 10 : Flapping flat fish



FIGURE 11 : Shark ray robotic fish



FIGURE 12 : Mermaid robot

3 Conclusion

The author has created elastic oscillating fin technology and successfully developed robotic fish to use this fin propulsion system.

Acknowledgements

The author expresses his sincere gratitude to Mitsubishi Heavy Industries, Ltd., JAMSTEC, the university of Kitakyushu, and Nagasaki University for their cooperation in the development of this robotic fish technology.

References

- Ikuo Yamamoto, Yuuzi Terada, Tetsuo Nagamatsu, Yoshiteru Imaizumi, Research on Propulsion Control System of Oscillating Fin, Proc. IEEE OCEANS, Vol.3, pp.259-263, 1993.
- Ikuo Yamamoto, Yuuzi Terada, Tetsuo Nagamatsu, Yoshiteru Imaizumi, Propulsion system with flexible/rigid oscillating fin, IEEE Journal of Oceanic Engineering, Vol.20, No.1, pp.23-30, 1995.
- Ikuo Yamamoto, Robust and non-linear control of marine system, International Journal of Robust and Nonlinear Control, John Wiley & Sons Ltd., IFAC-AFFILIATED JOURNAL, vol.11, No.13, pp.1285-1341, 2001.
- Ikuo Yamamoto, Practical Robotics and Mechatronics: Marine, Space and Medical Applications, IET (The Institution of Engineering and Technology), UK, pp.1-192, 2016.

Fluid-structure interaction dynamics of a flexible filament in the wake of an elliptical bluff body

Rajanya Chatterjee^{1*}, Chandan Bose¹, Sayan Gupta¹ and Sunetra Sarkar¹

¹IIT Madras, Chennai 600036, India, *rajanya02@gmail.com (corr. author)

Keyword: Fluid-Structure Interaction; Wake-Induced Vibration; Flexible Filament.

Flow-induced vibrations of flexible filament-like structures have sparked significant research interest due to their potential application in many engineering systems such as micro flow-energy harvesters or self-propelled flapping devices. Utilization of fluid-body interaction phenomena by living organisms in their locomotion has promoted the idea of designing self propelled flexible robots. The bio-propulsion systems are often greatly affected by oncoming disturbances or vortex streets, generated by bluff-body shaped obstructions situated upstream. Presence of such flow disturbances or upstream wakes can dictate the dynamic response characteristics of the flexible filament and its load generation capabilities. Flow-induced oscillations of such flexible filaments, fitted with piezo-electric patches can also be successfully exploited for their energy harvesting potential. The present paper aims to investigate the wake-induced vibrations (WIV) of a flexible filament subjected to the wake of an upstream elliptical bluff-body (minor axis kept along the stream-wise direction). An incompressible Navier-Stokes solver is strongly coupled with a chord-wise flexible structure using partitioned approach for the present study. The fluid-structure interaction (FSI) dynamics is seen to be strongly influenced by the variation of a number of system parameters, e.g., the bluff body shape, its distance from the filament, the offset location and the filament length. As can be seen from Fig.1, an aperiodic behaviour of the coupled FSI system (shown in terms of filament oscillations as well as the flow-field) can become periodic by tuning the offset length from 0 to 0.25D. Here, 'D' refers to the length of the major axis of the ellipse. The transition is clearly seen from the response time histories (Figs. 1(a), 1(b) and 1(c)) as well as vorticity contours at time $t = 10s$ (Figs. 1(d), 1(e) and 1(f)). The change in the dominant mode-shapes of the flapper and the flow-field dynamics around it are studied in details in terms of the location of the impingement of shed vortices and the associated Strouhal frequencies. Effect of the variation of other relevant system parameters also show similar interesting dynamical transitions and will be shown in the full length paper.

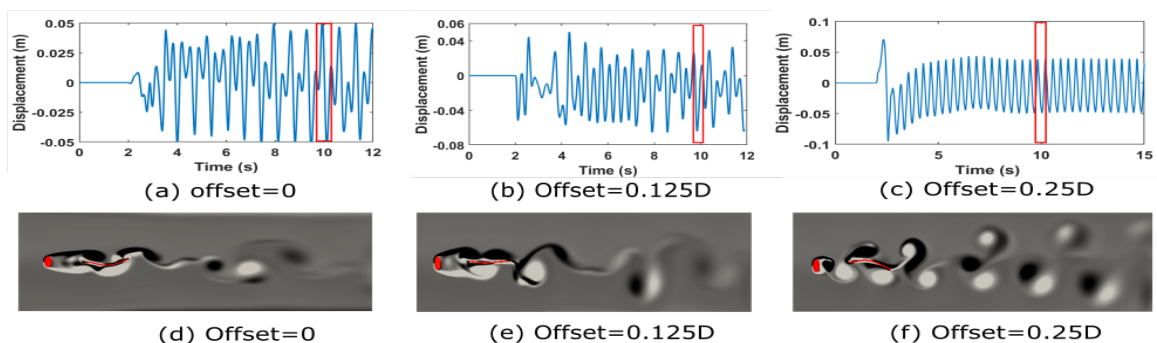


Figure 1: (a),(b) and (c) are time histories of tip of the filament; (d),(e) and (f) are vorticity contours at $t=10s$

Bifurcation behavior in vocal folds and its impact on physiological conditions

James Emilian¹, Veda Samhitha Kanduri¹, Chandan Bose², J. Venkatramani^{1*}
and Jaromir Horacek³

¹ *Department of Mechanical Engineering, Shiv Nadar University, Greater Noida, India, j.venkatramani@snu.edu.in**,

² *Department of Applied Mechanics, IIT-Madras, Chennai, India,*

³ *Institute of Thermomechanics, Academy of Sciences of the Czech Republic, Czechia.*

Keyword: Vocal fold dynamics, Bifurcation analysis, Chaos, Physiological conditions.

The dynamics of voice production have recently spawned significant research interest due to the presence of phenomenological bifurcations and instabilities observed in both healthy and unhealthy patterns of phonation. Human voice is created by self-sustained limit-cycle oscillations (LCOs) of the vocal folds situated in the larynx. Several factors, like subglottal pressure, tension in the vocal folds and their prephonatory position (adducted position) influence the onset of LCOs and the post-flutter characteristics. Though investigating the mechanism of phonation in humans has received considerable attention, establishing an appropriate link between the dynamics of the vocal folds and pathological conditions requires further investigation. The present study attempts to fill this gap by carrying out an extensive bifurcation study with system parameters like glottal airflow rate, subglottal pressure, etc. as bifurcation parameters. To that end, the vocal fold is modelled using a 3-mass representation, which, unlike typically used 2-mass models, captures large amplitude oscillations of the vocal fold. This study primarily focuses on capturing the plethora of dynamics that underlie various pathological conditions, such as aphonia, dysphonia etc., within the purview of the considered low order model. This study also aims to subsequently incorporate higher order flow and structure models to investigate the underlying flow-physics and, in turn, its impact on the bifurcation and physiological scenarios. A preliminary result showing variation of glottal areas (a_1 , a_2 and a_3) during the flow-induced oscillations is presented in Fig. 1.

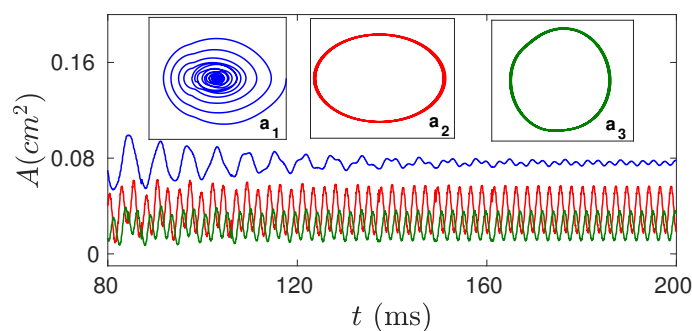


Figure 1: Time histories of glottal areas during the flow-induced oscillations along with the corresponding phase portraits.

Symmetry-breaking of a flexible splitter plate: experiment and quasi-static model

Marie Couliou¹, Remi Allandrieu¹, Jean-Lou Pfister¹ and Olivier Marquet¹

¹ DAAA, ONERA, 8 rue des Vertugadins, 92190 Meudon, France, marie.couliou@onera.fr

Keyword: splitter plate, quasi-static model, fluid-structure interaction

The symmetry-breaking of a flexible splitter plate clamped to the rear of a rigid cylinder is investigated in a vertical flowing soap film. A time-averaged bending of the splitter plate has been previously observed ¹ for short splitter plates, i.e. $L/D < 3.5$ where L is the splitter plate's length and D the cylinder's diameter. In the present study, we have first reproduced this experiments for the Reynolds number $Re_D \sim 350$ and various non-dimensional lengths of the splitter plate in the range $0 < L/D < 9$. Similarly to results of the original experiments, long splitter plates ($L/D > 3.6$) flap symmetrically around the flow direction, while a time-averaged bending occurs for short splitter plates. We have carefully characterized the deviation for short splitter plates and found that the symmetry-breaking vanishes for very short splitter plates $L/D < 0.65$ (Figure 1).

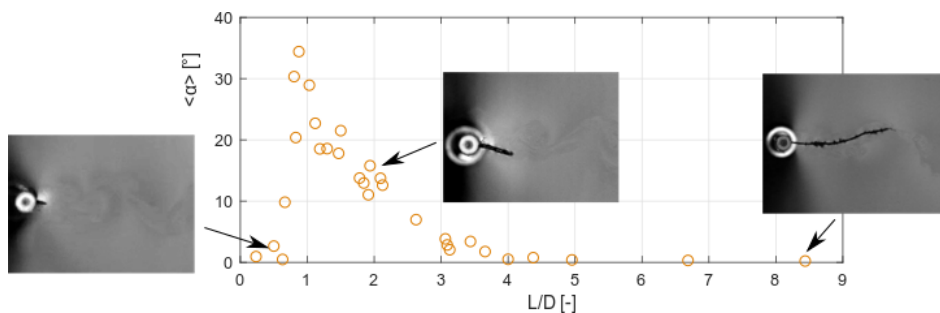


Figure 1: Time-averaged deviation angle as a function of the adimensional splitter plate length

In a second step, two-dimensional numerical simulations have been performed to confirm these experimental results and to further explore the physical mechanism responsible for the deviation. In addition to unsteady fluid-structure simulations, we derive a quasi-static model that governs the amplitude of (one or two) bending modes of the splitter plate. Using solely an hydrodynamic solver, we will explain how to compute the coefficients of the fluid added-stiffness matrix, that accounts for the (time-averaged) interaction of the free-vibration modes with the flow. Thus, we will show that the time-averaged bending of the splitter plate in the range $0.65 < L/D < 3.6$ results from a divergence instability, occurring when the added-stiffness generated through the interaction with the time-averaged flow exceeds the restoring elastic force of the splitter plate. The one bending-mode model well predicts the divergence instability at $L/D = 3.6$ but cannot explain the restabilization at $L/D = 0.65$, that we capture with the two bending-modes model.

¹ Lācis, U., Brosse, N., Ingreneau, F., Mazzino, A., Lundell, F., Kellay, H., & Bagheri, S. (2014). Passive appendages generate drift through symmetry breaking. *Nature communications*, 5, 5310.

² Pfister, J. L. & Marquet. (2019) Temporal simulations and stability analyses of elastic splitter plates interacting with cylinder wake flow. Submitted to *Journal of Fluid Mechanics*.

Stability and resolvent analyses of boundary-layer flows interacting with finite-length visco-elastic coatings

Jean-Lou Pfister¹ and Olivier Marquet¹

¹ DAAA, ONERA, Université Paris Saclay, 8 rue des Vertugadins, 92190 Meudon, France, olivier.marquet@onera.fr

Keyword: compliant wall, boundary-layer, global stability, resolvent analysis

The use of compliant walls to delay the laminar/turbulent transition in boundary layers was inspired by the properties of soft skin animal. It is now well established that three types of instabilities occur in laminar boundary-layer flows developing over *infinite-length* compliant walls: Tollmien-Schlingthing (TS) waves, Travelling Waves Flutter (TWF) and Static Divergence instability. Here, we investigate the development of such instabilities for *finite-length* coating in the streamwise and cross-stream directions, made of materials with visco-elastic properties. The stability of such fluid-structure configuration is investigated numerically using an exact linearization of the Arbitrary-Lagrangian-Eulerian equations that describes the temporal evolution of the (Lagrangian) fluid-structure perturbation ¹. First, a modal analysis of the fluid-solid Jacobian operator allows to determine the long-term temporal stability ². The coupling of a purely elastic coating with the flow induces here the destabilization of high-frequency eigenmodes corresponding to Traveling Waves Flutter instabilities, that are stabilized when considering visco-elastic coatings. Secondly, a resolvent analysis of the fluid-solid Jacobian operator allows to investigate the attenuation of low-frequency Tollmien-Schlichting Waves thanks to elastic and visco-elastic coatings. A decomposition of the fluid-structure resolvent mode will be introduced to show that elastic coatings, excited by the incoming TS waves, generate fluid-structure waves that are out of phase with the incoming TS waves, thus leading to their attenuation.

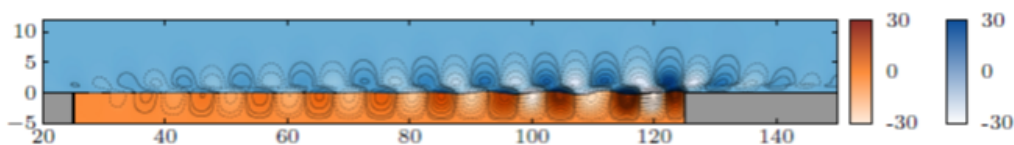


Figure 1: Travelling Wave Flutter instability: cross-stream velocities of the fluid (blue) and solid (orange) perturbations.

¹ Pfister, J. L., Marquet, O., & Carini, M. (2019). Linear stability analysis of strongly coupled fluid-structure problems with the Arbitrary-Lagrangian-Eulerian method. *Computer Methods in Applied Mechanics and Engineering*, 355, 663-689.

² Tsigklifis, K., & Lucey, A. D. (2017). The interaction of Blasius boundary-layer flow with a compliant panel: global, local and transient analyses. *Journal of Fluid Mechanics*, 827, 155-193.

Fluid-structure interaction in plant- and coral-inspired biomechanics problems

Frédéric P. Gosselin

*Laboratory for Multiscale Mechanics, Polytechnique Montréal, Montréal, Canada
frederick.gosselin@polymtl.ca*

Keyword: Biomechanics, Plants, Corals, Flutter, Reconfiguration, Vortex-Induced Vibrations

Plants and other sessile organisms like soft coral colonies deform with large amplitude when subjected to fluid flow. This large flexibility gives rise to fluid-structure interaction (FSI) phenomena not found in traditional engineering applications. Here I present an overview of specialised developments in biomechanics FSI from my research group at Polytechnique Montreal.

Firstly, we consider the trade-off brought by flexibility to plants: drag reduction by large amplitude reconfiguration versus flow-induced flutter and the dynamic loads that come with it. We consider the problem of a flexible beam reconfiguring in the flow until it starts fluttering (Fig. 1 left). We couple a finite volume flow solver with a finite difference beam solver to find the ideal flexibility allowing maximal drag reduction by reconfiguration without leading to flutter. We find that for heavier fluids, the beam can reconfigure more before losing stability.

Secondly, we simulate numerically the rate at which a spring-mounted circle intercepts advected particles (Fig. 1 right). This system represents a 2D idealisation of a branch cross-section of soft coral *Antillogorgia bipinnata*. This species is a filter feeder which captures food particles brought by the ocean currents. Our simulations show that in the lock-in range of vortex-induced vibrations, the vibrating cylinder is up to 50% more effective at intercepting particles than a fixed one. This could represent a significant evolutionary advantage.

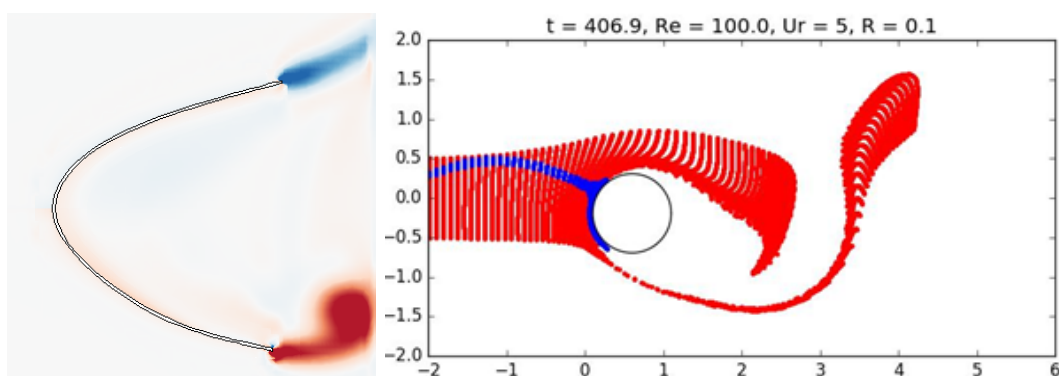


Figure 1: Left: An initially straight beam clamped at its centre is subjected to a normal flow which bends it downstream and causes it to undergo a flutter instability. The red and blue colours indicate the vorticity computed in the flow. Right: A spring-mounted circle with two degrees of freedom undergoes vortex-induced vibrations. These vibrations increase the rate at which the circle intercepts advected particles. Blue particles get captured and red ones escape.

Flutter in sports engineering

Experiment and Numerical Simulation of a Rotating Pipe in Flight

Go Kato¹, Yusuke Naito¹, Hirochika Tanigawa², Jun Ishimoto³, Masami Nakano⁴,
Takashi Noguchi¹, Katsuya Hirata¹

¹Department of Mechanical Engineering, Doshisha University, Kyoto 610-0321, Japan

²Department of Mechanical Engineering, Maizuru National College of Technology, Maizuru
625-8511, Japan

³Institute of Fluid Science, Tohoku University, Sendai, 980-8577 Japan

⁴New Industry Creation Hatchery Center, Tohoku University, Sendai, 980-8577, Japan

Keyword: Video analysis, Numerical simulation, Pipe, Rotation

To investigate the aerodynamics of the flying hollow cylinder, or the flying pipe, in rotation, field observations of the flight of commercial model and its simplified model was conducted. The models' motion (trajectory and attitude) was analyzed three-dimensionally, using a pair of high-speed video cameras. The numerical simulations of the flow around the rotating pipe revealed details of the flow around the pipe. Figure 1 shows the time sequence of the model's attitude during its flight at various x_E , where x_E is the horizontal flight distance from take off. The fluctuation of the posture decreases as x_E . The video motion analysis showed that the rotation has rather small effect on the aerodynamics.

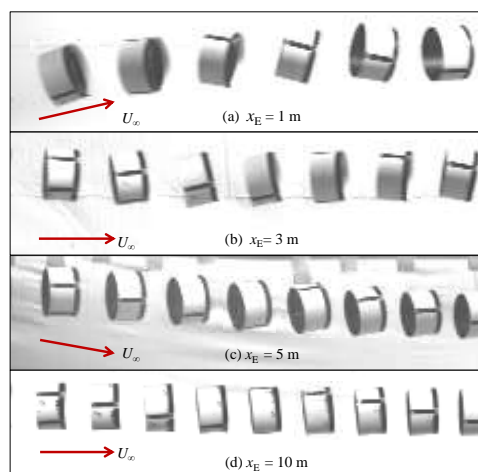


Figure 1: Time sequence of model's flight attitude. Arrows indicate the flight direction.

Roughness in sports aerodynamics: the cricket ‘reverse’ swing

Tadrist Loïc¹, Sampara Naresh², Ashraf Intesaaf¹ and Thomas Andrianne¹

¹ University of Liège, Liège, Belgium, loic.tadrist@uliege.be

² University of Nottingham, Nottingham, United Kingdom

Keywords: Sports aerodynamics, Cricket, Roughness.

Curved trajectories are widely used in sports played with balls. Most of the balls are launched with some spin and rely on the Magnus effect to bend the trajectory. However some other less common physical effects may also be used to deviate a ball. Here we investigate the effect of the differential roughness on the aerodynamics of a cricket ball. The differential roughness that appears between the two hemispheres of the cricket ball during a game may be used by the bowler to create ‘reverse’ or ‘contrast’ swing. This technique is specific to cricket because of the ball manufacture in two distinct hemispheres.

The differential wear of the cricket ball creates a large aerodynamic side force (*i.e.* large side aerodynamic coefficient C_s), see Figure 1a. This force deviates the ball from the straight trajectory making the launch unpredictable for the batsman.

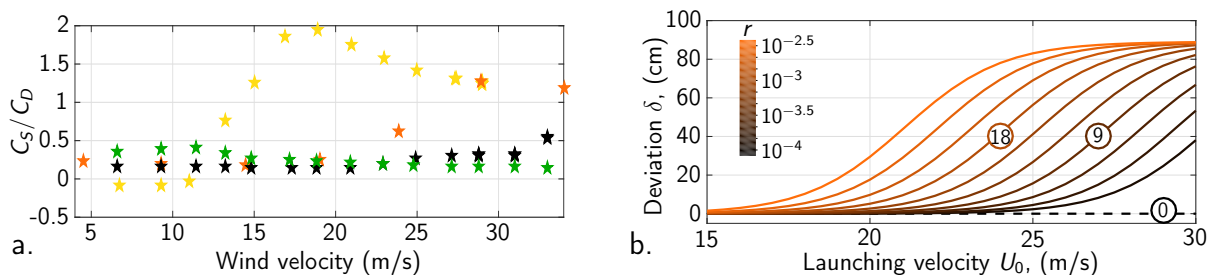


Figure 1: a. C_s/C_D for different surface’s roughness as a function of the wind speed. (\star) Smooth field hockey ball, (\star) unworn cricket ball, (\star) one-sided rough cricket ball with normal roughness and (\star) one-sided rough cricket ball with large roughness. b. Lateral deviation of a one-sided rough cricket ball as a function of the launching velocity U_0 . Colour indicates the roughness r of the rough ball varying logarithmically between 10^{-4} and $10^{-2.5}$. The corresponding number of launches to achieve a given ball roughness are indicated within circles.

We quantify this force through wind tunnel experiments varying the roughness on one hemisphere of the ball. We also measure the side-to-side differential wear generated on a cricket ball as a function of the number of launches. Finally we model the minimum velocity required to achieve contrast swing and the expected deviation as a function of launch number and game conditions, see Figure 1b. We also discuss the game conditions (dry pitch and cold weather) that favours ‘reverse’ swing.

¹ Tadrist, L., Sampara, N., Ashraf, I., & Andrianne T. (2019). When can you expect contrast swing in a cricket game? And how to obtain it. *submitted to the Journal of Sports Engineering*.

Flutter of bridges

On the roles of small-scaled vortices in bridge wind engineering

Donglai Gao¹, Wenli Chen² and Hui Li³

¹ Harbin Institute of Technology, Harbin, P. R. China, donglai.gao@outlook.com

² Harbin Institute of Technology, Harbin, P. R. China

³ Harbin Institute of Technology, Harbin, P. R. China

Keyword: small-scaled vortices, multi-modal VIV, multi-modal RWIV, bridge aerodynamics

The important roles that multiple vortices play in fluid-structure interactions and bridge wind engineering have been recently recognized in the past decades. We present some progress in our group on some typical aspects of multiple vortices in bridge wind engineering, i.e., multi-modal vortex induced vibrations (VIVs) and rain-wind induced vibrations (RWIVs), wind induced vibrations of bridge decks and mitigation counter-measures with flow control methods.

A typical case is the excitation mechanism of rain-wind induced cable vibrations. It was observed that the first, second and third-mode dominated RWIVs take place successively with the increase of wind speed. Besides, two or three adjacent modes have a chance to overlap (mode switch) for a particular wind speed. These observations are similar to the coupled-wake flutter (CWF) mechanism¹ usually observed in multi-modal VIVs. By using direct numerical simulations, the physical process of real rain droplets falling onto the cable surface was uncovered². A long bubble (detachment flow) and a short bubble (reattachment flow) behind the water rivulet are identified. In addition, the alternating structures of von Kármán vortex are alleviated by the small-scaled vortices which are generated by the dynamic bubble burst. Also, the wake flow structures of RWIV cable become more disordered and small-scaled and the vortex strength is increased, due to the existence and oscillation of the upper rivulet. As RWIV develops, the von Kármán vortex shedding is alleviated and the small-scaled vortical structures become more present. A new excitation scenario of RWIVs is proposed as follows³. The vibration of the cable drives the movement of separation point and the upper rivulet. The movement of upper rivulet result in a bubble burst and a stall phenomenon due to the Kelvin–Helmholtz instability in the boundary layer. As a consequence, the von Kármán vortex shedding is alleviated and the vortex shedding frequency substantially decreased. As the decreased vortex shedding synchronize with the cable's structure frequency, large-amplitude RWIVs develop.

¹De Langre, E., (2006). Frequency lock-in is caused by coupled-mode flutter. *Journal of Fluids and Structures*, 22, 783-791.

² Cheng, P., Li, H., Fuster, D., Chen, W., Zaleski, S., (2015). Multi-scale simulation of rainwater morphology evolution on a cylinder subjected to wind. *Computers and Fluids*, 123, 112-121.

³ Gao, D., Chen, W., Eloy, C. & Li, H. (2018). Multi-mode responses, rivulet dynamics, flow structures and mechanism of rain-wind induced vibrations of a flexible cable. *Journal of Fluids and Structures*, 82, 154-172.

The influence of angle of attack on twin-box bridge deck flutter

Allan Larsen¹ and Maja Rønne^{1,2}

¹*COWI, Lyngby, Denmark, aln@cowi.dk*

²*Danish Technical University, Lyngby, Denmark*

Abstract

Wind tunnel tests of twin-box or tri-box suspension bridge deck sections carrying wind screens reveal that the critical wind speed for onset of flutter is higher when set at a nose-up angle of attack than at horizontal. The present paper reviews and analyses experimental aerodynamic derivatives available to the authors with a view to gain physical insight into the "nose-up" effect and to assemble a predictive model for onset of flutter.

Keyword: Flutter prediction, aerodynamic derivatives, nose-up effect, twin-box girders.

1 Introduction

Suspension bridges having main spans less than 1200 m - 1500 m can, as a rule of thumb, be designed with streamlined trapezoidal mono-box deck sections to fulfil common code of practice requirements to flutter wind speeds. Also, it is well known that streamlined mono-box bridge deck commonly achieves the highest flutter wind speeds at 0° angle of attack (deck chord aligned with the mean wind) and that placement of wind screens along the girder edges will lead to degradation of the flutter wind speed compared to the deck without wind screens (Larsen, 1993).

To achieve flutter stability for suspended spans longer than approximately 1500 m it often becomes necessary to split the deck into two box structures separated by a central air gap and interconnected by cross beams at regular intervals – the so-called twin-box bridge deck. Aerodynamic design efforts related to the twin-box bridge deck often focuses on optimizing the deck shape and appendages with a view to maintain a requested minimum critical wind speed for onset of flutter and to ensure a desirable traffic wind climate. Wind tunnel tests of elastically sprung section models carried out for a design study of a chain of suspension bridges for crossing of the Strait of Gibraltar revealed that twin-box decks carrying large 50% open area ratio wind screens at the deck edges achieved higher critical wind speeds than the similar deck without the wind screens (Larsen and Astiz, 1998). A result at odds with the well-known behaviour for the mono-box deck and not fully understood at the time.

More recent tests made for the design of the tri-box deck for the Messina Bridge and the twin-box deck for the 1915 Çanakkale Bridge revealed similar trends for the flutter speed to increase as a function of a "nose-up" or positive rotation angle of the deck relative to horizontal. The aerodynamic derivatives obtained for the Messina and the 1915 Çanakkale bridges are reviewed to assemble a model that provides some physical insight into the "nose-up" effect and allow the effect to be included in flutter predictions taking into account the mode shapes and wind induced static twist angle of the complete bridge span.

2 1915 Çanakkale suspension bridge

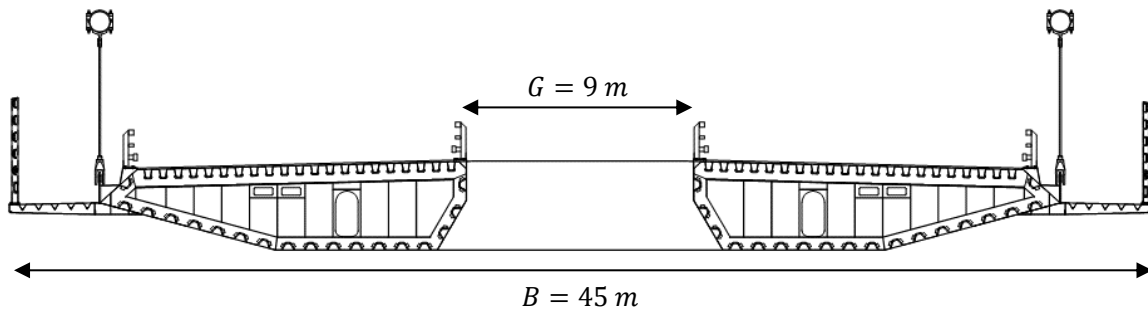


Figure 1: Twin-box deck cross section, 1915 Çanakkale Bridge.

The 1915 Çanakkale Bridge currently under construction spans a total length $L = 3563$ m and a main span of 2023 m. The bridge features a 45 m wide twin-box deck with a central 9 m wide air gap. The bridge deck includes 4 m tall 50% open area ratio wind screens located along the outer edges of the cantilevered inspection walkways, Fig. 1.

Static wind tunnel tests of the twin-box section revealed a positive moment coefficient at 0° angle of attack as well as a positive moment slope ensuring that the elastically supported deck model would meet the wind at ever increasing angles of attack (nose-up) for increasing wind speeds, Fig. 2, left. Flutter tests of the elastically sprung model starting at a rotation angle of 0° (no wind) did not identify a critical wind speed for onset of flutter. The free movements of the model were limited by physical restrictions in the wind tunnel when the model encountered a rotation angle of about 8.7° reached at a full-scale wind speed of 97 m/s, Fig. 2, right. By changing the initial (no wind) rotation angle setting to -1° (nose down) flutter was encountered at a full-scale wind speed $U_{cr} = 68$ m/s at a rotation angle of 0.5° . Critical wind speeds and corresponding rotation angles obtained for other initial angle of attack settings support the observation that the critical wind speed of the twin-box section increases with increasing positive angles of rotation.

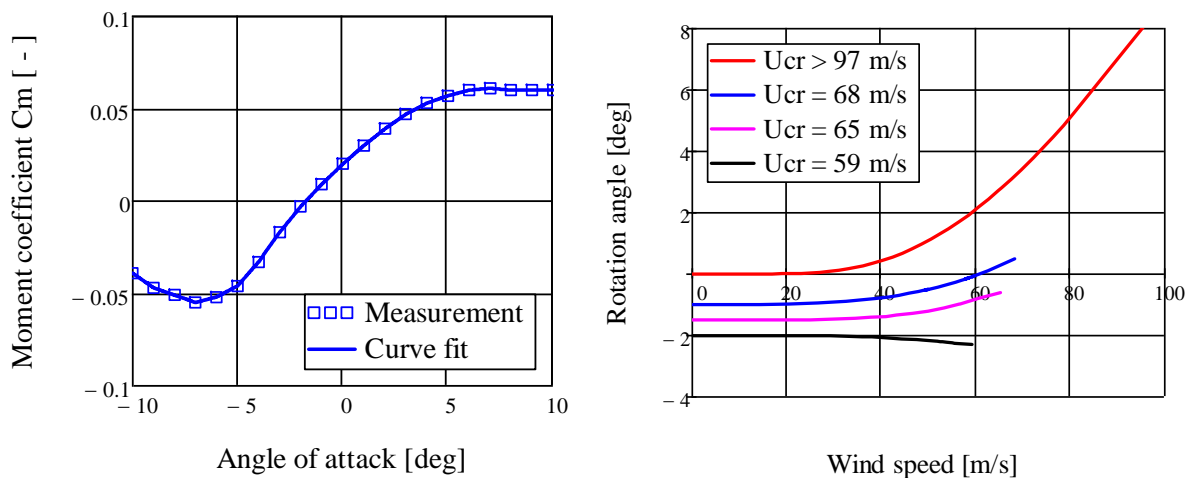


Figure 2: Left: Moment coefficient C_M . Right: Rotation angle as function of full-scale wind speed measured for the elastically sprung Çanakkale bridge deck section model.

3 Çanakkale aerodynamic derivatives

Aerodynamic derivatives (flutter coefficients) were measured for the Çanakkale twin-box section by means of the free oscillation technique. This test method involves fitting of a two-degree-of-freedom oscillator model to traces of torsion and bending oscillations measured in the wind tunnel. The free oscillation technique works well at low wind speeds where the torsion and vertical bending modes are well separated and forced initial displacements decay over several cycles of oscillation. At the flutter point and beyond, the torsion and vertical bending frequencies coincides, and the measured decay or growth traces become very short yielding numerical difficulties when fitting the model equations of motion to the measurements. As a result, the estimated flutter coefficients may be inaccurate at non-dimensional wind speeds approaching the flutter speed. An advantage of the free oscillation technique is that the model is free to assume the correct equilibrium position under the influence of elastic and aerodynamic forces.

The measured aerodynamic derivatives $H_{1..4}^*$, $A_{1..4}^*$ as function of the non-dimensional wind speed $U^* = U/fB$ obtained for an initial rotation angle setting of -1° are shown in Appendix A. It is noted that the measured values of the H_2^* , H_3^* , A_2^* , A_3^* coefficients for $U^* > 9$ and the H_1^* , H_4^* , A_1^* , A_4^* coefficients for $U^* > 20$ (red x) display a lot of scatter suggesting different trends than at lower U^* (blue \square). The approach to derive suitable input to flutter calculations was to fit second order polynomials to the lower U^* measurements and to adjust A_1^* , A_2^* , A_3^* slightly to make the flutter prediction coincide with $U_{cr} = 68$ m/s at which wind speed the cross section is at 0.5° nose-up as noted from Fig. 2. The polynomial representations are discussed further in section 4. The polynomial fitting process and calibration was not possible for the test starting at initial rotations angle of 0° as flutter was prohibited physically by model impact with the wind tunnel wall.

4 Messina tri-box aerodynamic derivatives and allowances for deck rotation angle

Flutter tests of an elastically sprung section model of the Messina tri-box deck, Fig. 3, displayed similar flutter behaviour as the Çanakkale twin-box i.e. the critical wind speed for onset of flutter increased with increasing nose-up angles of rotation. The two bridge decks are similar in that they both have open air gaps in between the solid semi-streamlined box girders and carry large wind screens along the outer edges of the cantilevered maintenance walkways. A design feature believed to create the nose-up aerodynamic moment at 0° angle of attack. The ratio of the total gap width to the over-all deck width G/B is 0.27 for Messina deck section and 0.2 for Çanakkale deck section.

Contrary to Çanakkale the aerodynamic derivatives for the Messina tri-box deck were measured by means of the forced oscillation technique (Larsen 2016). Forced motion tests does not allow the section angle to change continuously as function of the wind speed. Thus, the aerodynamic derivatives were measured for three nose-up angles of attack of 0° , 2° and 4° to allow flutter calculations for different portions of the bridge girder when exposed to high winds. The aerodynamic derivatives measured at fixed rotation angles of 0° (red markers), 2° (blue markers) and 4° (black markers) are shown in Appendix B. It is noted that all eight aerodynamic derivatives are influenced by the rotation angle but to various degree.

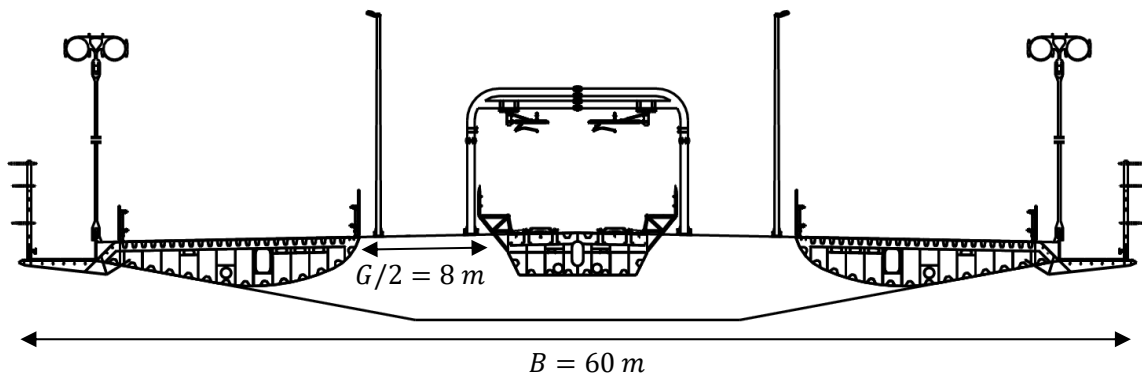


Figure 3: Tri-box deck cross section, Messina Bridge.

The result of a flutter prediction for 0° , 2° and 4° rotation angle is shown in Fig. 4 along with the proper section properties for Messina. The critical wind speeds are obtained as the intersection of the aerodynamic damping curves with the horizontal line (dashed) at the structural damping level $g = 2\zeta$ (Larsen 2016), here marked by vertical arrows.

Torsion freq f_α	0.081 Hz
Bending freq f_h	0.068 Hz
Mass m	58100 kg/m
Mass moment of inertia I	$28.93 \cdot 10^6$ kgm ² /m
Damp $g = 2\zeta$	0.013

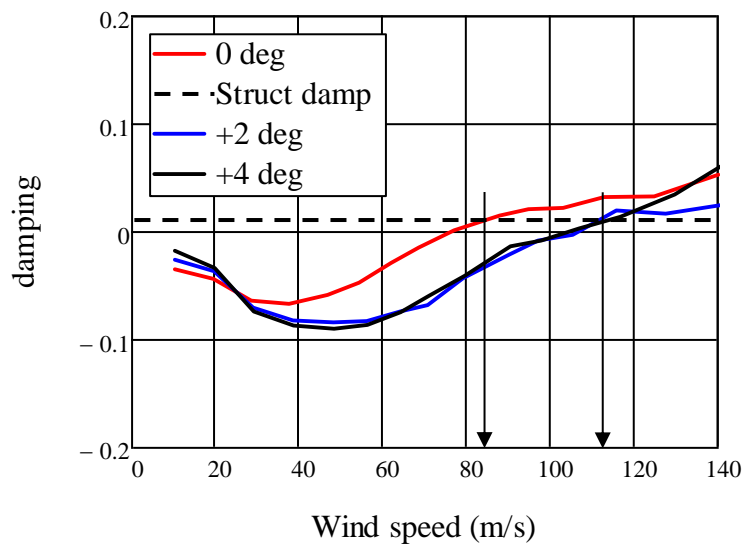


Figure 4: Flutter calculation for the Messina Bridge tri-box deck section

It is noted that the critical wind speed obtained for 0° angle of attack is $U_{cr} = 86$ m/s where as $U_{cr} = 112$ m/s is obtained for 2° and $U_{cr} = 115$ m/s for 4° emphasizing the sizable influence of the rotation angle on the critical wind speed for onset of flutter.

From Appendix B, it is noted that the section rotation angle influences the aerodynamic derivatives and shift the 2° and 4° cases along the amplitude axis relative to the 0° case. For a given non-dimensional wind speed the amplitudes appear to increase or decrease depending on the rotation angle. Fig. 5 shows the ratio of the individual aerodynamic derivatives, say A_1^* at 0° to the same derivative at 2° , $A_1^*(0)/A_1^*(2)$, and 4° , $A_1^*(0)/A_1^*(4)$, respectively indicated by solid markers. Also Fig. 5 displays linear functions $\varphi(\theta)$ of the rotation angle fitted for each derivative. The linear fits in rotation angle θ are not perfect but appear to be an acceptable approximation to the trend displayed by the measurements.

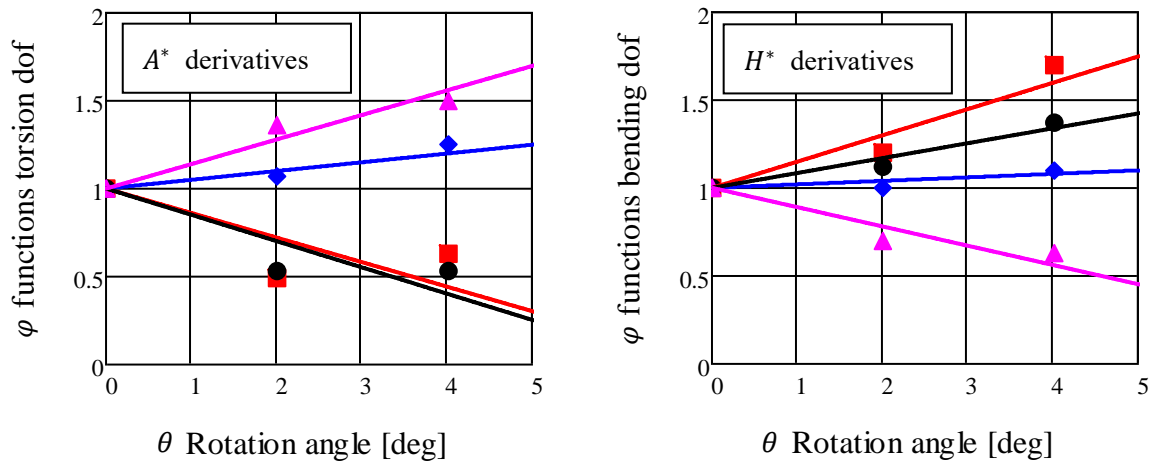


Figure 5: Ratios of Messina aerodynamic derivatives at 0° and 2° , 0° and 4° and fitted linear functions. Markers: \blacksquare : A_1^*, H_1^* . \blacklozenge : A_2^*, H_2^* . \bullet : A_3^*, H_3^* . \blacktriangle : A_4^*, H_4^* .

The underlying idea is to be able to express a given aerodynamic derivative as function of non-dimensional wind speed U^* and rotation angle θ (in degrees) analytically. As an example: $A_1^*(U^*, \theta) = \varphi_{A1}(\theta) \cdot A_1^*(U^*, \theta)$, with $\varphi_{A1}(\theta) = (1 - 0.14\theta)$.

The above method only strictly applies to the Messina aerodynamic derivatives and within the angles of rotation of $0^\circ - 4^\circ$. However, having demonstrated that the onset of flutter of the Messina deck section is influenced by section rotation angle much the same way as the Çanakkale deck section, it will be assumed that the φ -functions derived in Fig. 5 also apply to this deck. Table 1 presents the Çanakkale aerodynamic derivatives displayed as the red curves in Appendix A (polynomials in U^* in square brackets) multiplied by the linear approximations of the angle of attack effect (in rounded brackets) shown in Fig. 5. Table 1 constitutes the aerodynamic data needed for estimation of the angle of rotation effect on the flutter speed for the Çanakkale deck cross section.

Table 1: Çanakkale aerodynamic derivatives including allowances for section rotation angle

Torsion derivatives	Vertical bending derivatives
$A_1^* = -(1 - 0.14\theta)[3.5 \cdot 10^{-3}U^{*2} + 0.09U^*]$	$H_1^* = -(1 + 0.15\theta)[0.013U^{*2} + 0.259U^*]$
$A_2^* = -(1 + 0.05\theta)[2.0 \cdot 10^{-3}U^{*2} + 0.04U^*]$	$H_2^* = (1 + 0.022\theta)[-0.02U^{*2} + 0.167U^*]$
$A_3^* = (1 - 0.15\theta)[0.012U^{*2} - 0.021U^*]$	$H_3^* = (1 + 0.085\theta)[0.024U^{*2} + 0.122U^*]$
$A_4^* = -(1 + 0.14\theta)[1.386 \cdot 10^{-3}U^{*2} + 0.024U^*]$	$H_4^* = (1 - 0.11\theta)[-0.012U^{*2} + 0.061U^*]$

5 Estimation of critical wind speeds for the Çanakkale deck section

Estimates of the flutter wind speeds for the Çabakkale Bridge deck at the angles of rotation at which the elastically sprung model encountered flutter are carried out. The results are shown in Fig. 6 along with the structural section properties for Çanakkale Bridge section. For a rotation angle $\theta = 8.7^\circ$ flutter is not predicted to occur (no intersection for $U < 100$ m/s) which fits the observation that the elastically sprung model did not encounter flutter for wind speeds below 97 m/s. It is noted however, that $\theta = 8.7^\circ$ exceeds 4° and thus is well

Torsion freq f_α	0.147 Hz
Bending freq f_h	0.072 Hz
Mass moment of inertia I	$6.215 \cdot 10^6$ kgm ² /m
Mass m	28524 kg/m
Damp $g = 2\zeta$	0.013

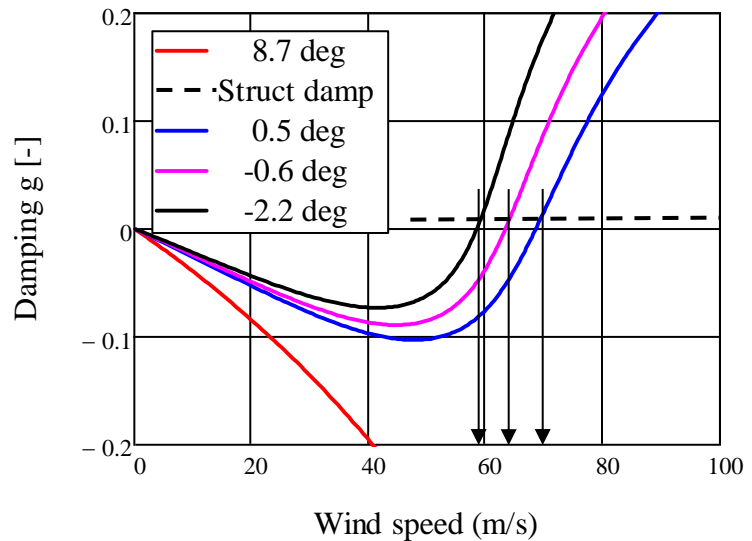


Figure 6: Flutter calculation for the Çanakkale bridge twin-box deck section including allowances for section rotation angles

beyond the expected range of application. For $\theta = 0.5^\circ$ the flutter prediction yields $U_{cr} = 69$ m/s compared to $U_{cr} = 68$ m/s obtained in Fig. 2. For $\theta = -0.6^\circ$ the prediction yields $U_{cr} = 64$ m/s compared to $U_{cr} = 65$ m/s and for $\theta = -2.2^\circ$ $U_{cr} = 59$ m/s compared to $U_{cr} = 59$ m/s. A rather satisfactory result remembering that the allowances are derived from the Messina data.

6 Flutter prediction for the complete Çanakkale Bridge

A full bridge is dynamically different to the section model in that the section rotation angles due the static (mean) wind loading varies continuously along the span. Further torsion and vertical flutter responses are expected to occur in a combination of the lowest torsion and bending eigenmodes of the bridge, Fig. 7.

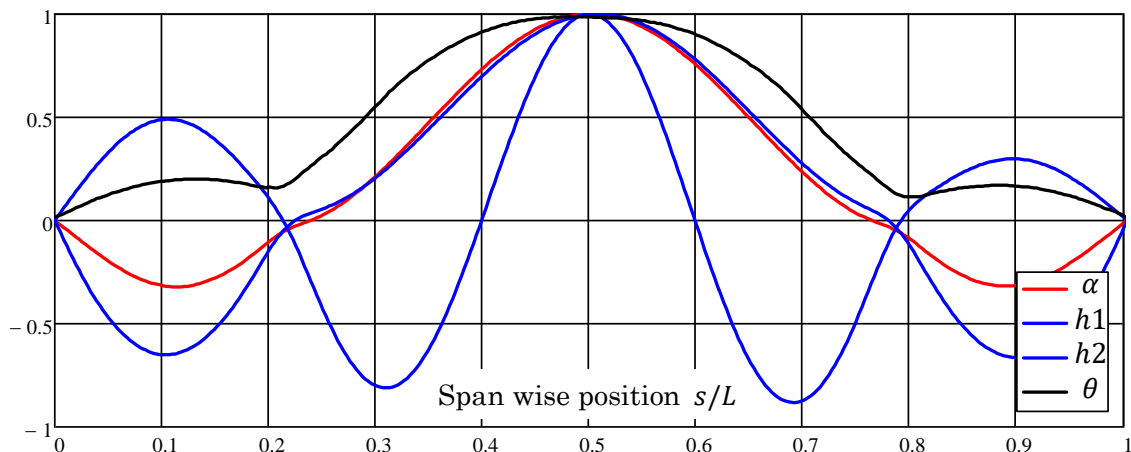


Figure 7: Lowest normalized symmetrical torsion (red), vertical bending (blue) modes and mean rotation angle (black) due to mean wind loading of the Çanakkale bridge.

The mean section rotation angle $\theta(s)$ as function of span wise position s , the lowest torsion mode shape $\alpha(s)$ and the lowest two vertical bending mode shapes $h1(s)$, $h2(s)$, Fig. 7, were obtained from a finite element model of the bridge. The maximum rotation angle at mid span is found to be $\theta(L/2) = 2.8^\circ$ at a mean wind speed of 95 m/s.

Assembly of the flutter determinant proceeds as outlined in (Larsen, 2016). The influence coefficients that couple the aerodynamic derivatives and the mode shapes now involve the allowances for section angle of rotation as follows as an example for the real (R) and imaginary (I) parts of the $C_{\alpha\alpha}$, $C_{\alpha h1}$, $C_{h1\alpha}$ and C_{h1h1} coefficients:

$$\begin{aligned}
 C_{\alpha\alpha R} &= \frac{1}{L} \int_0^L \varphi_{A3}(\theta(s)) \alpha(s)^2 ds, & C_{\alpha\alpha I} &= \frac{1}{L} \int_0^L \varphi_{A2}(\theta(s)) \alpha(s)^2 ds \\
 C_{\alpha h1 R} &= \frac{1}{L} \int_0^L \varphi_{A4}(\theta(s)) \alpha(s) h1(s) ds, & C_{\alpha h1 I} &= \frac{1}{L} \int_0^L \varphi_{A1}(\theta(s)) \alpha(s) h1(s) ds \\
 C_{h1\alpha R} &= \frac{1}{L} \int_0^L \varphi_{H3}(\theta(s)) \alpha(s) h1(s) ds, & C_{h1\alpha I} &= \frac{1}{L} \int_0^L \varphi_{H2}(\theta(s)) \alpha(s) h1(s) ds \\
 C_{h1h1 R} &= \frac{1}{L} \int_0^L \varphi_{H4}(\theta(s)) h1(s)^2 ds, & C_{h1h1 I} &= \frac{1}{L} \int_0^L \varphi_{H1}(\theta(s)) h1(s)^2 ds
 \end{aligned} \tag{1}$$

The advantage of the above formulation is that effects relating to the angle of rotation of the individual deck sections along the span are lumped with the mode shape integrals and thus are not functions of the non-dimensional wind speed as are the aerodynamic derivatives.

Having combined the rotation angle effect and the mode shapes it is possible to make a flutter prediction for the complete span representative of the Çanakkale bridge. The prediction involves the first symmetrical torsion mode $\alpha(s)$ and the symmetrical vertical bending modes $h1(s)$, $h2(s)$ having lower eigenfrequencies than the torsion, Fig. 7. The result of the flutter prediction, Fig. 9, yields a critical wind speed $U_{cr} = 92$ m/s when the span wise variation in rotation angle $\theta(s)$ is included (red curve). Results of a 1:190 full bridge model test of the bridge, Fig. 8, indicates flutter to occur at wind speeds just above 93 m/s. Neglecting the variation in rotation angle, taking $\theta(s) = 0.5^\circ$ along the entire span yields $U_{cr} = 75$ m/s (blue curve). This is higher than $U_{cr} = 68$ m/s obtained for the section model at $\theta = 0.5^\circ$ illustrating that mode shape allowances enhance aerodynamic stability.

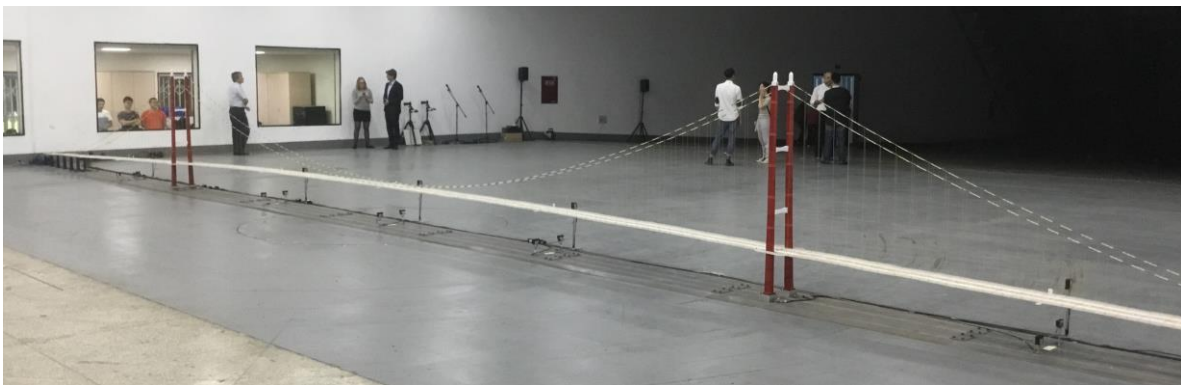


Figure 8. 1:190 scale aeroelastic model of the Çanakkale Bridge at RCWE wind tunnel.

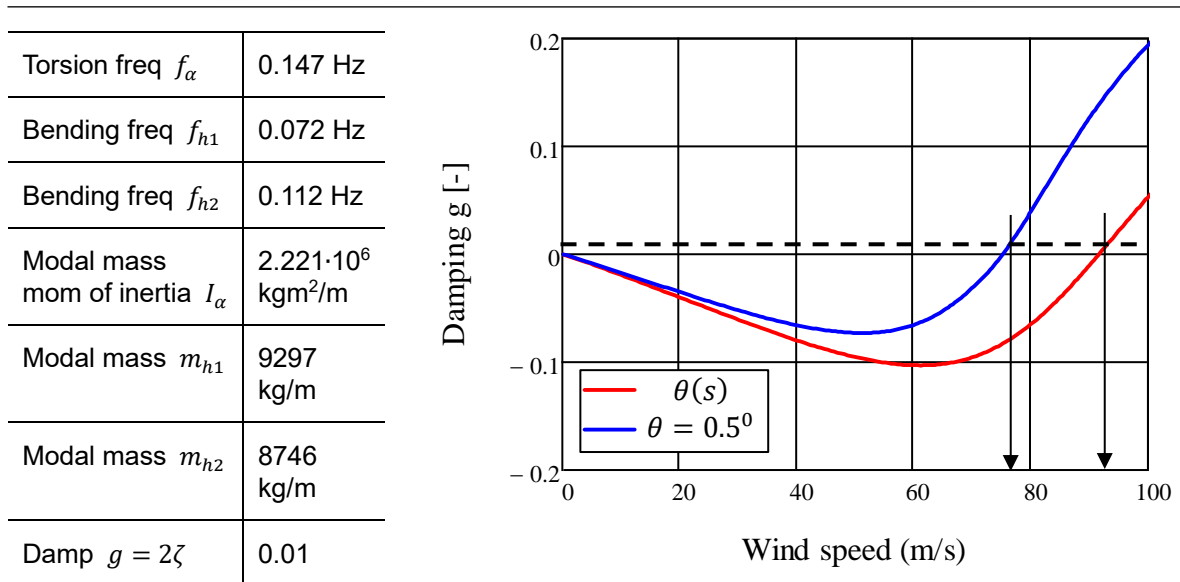


Figure 9: Flutter calculation representative of the full span of the Çanakkale Bridge. Red curve: including section angles of rotation due to mean wind. Blue curve: section rotation angles not included.

7 Conclusions

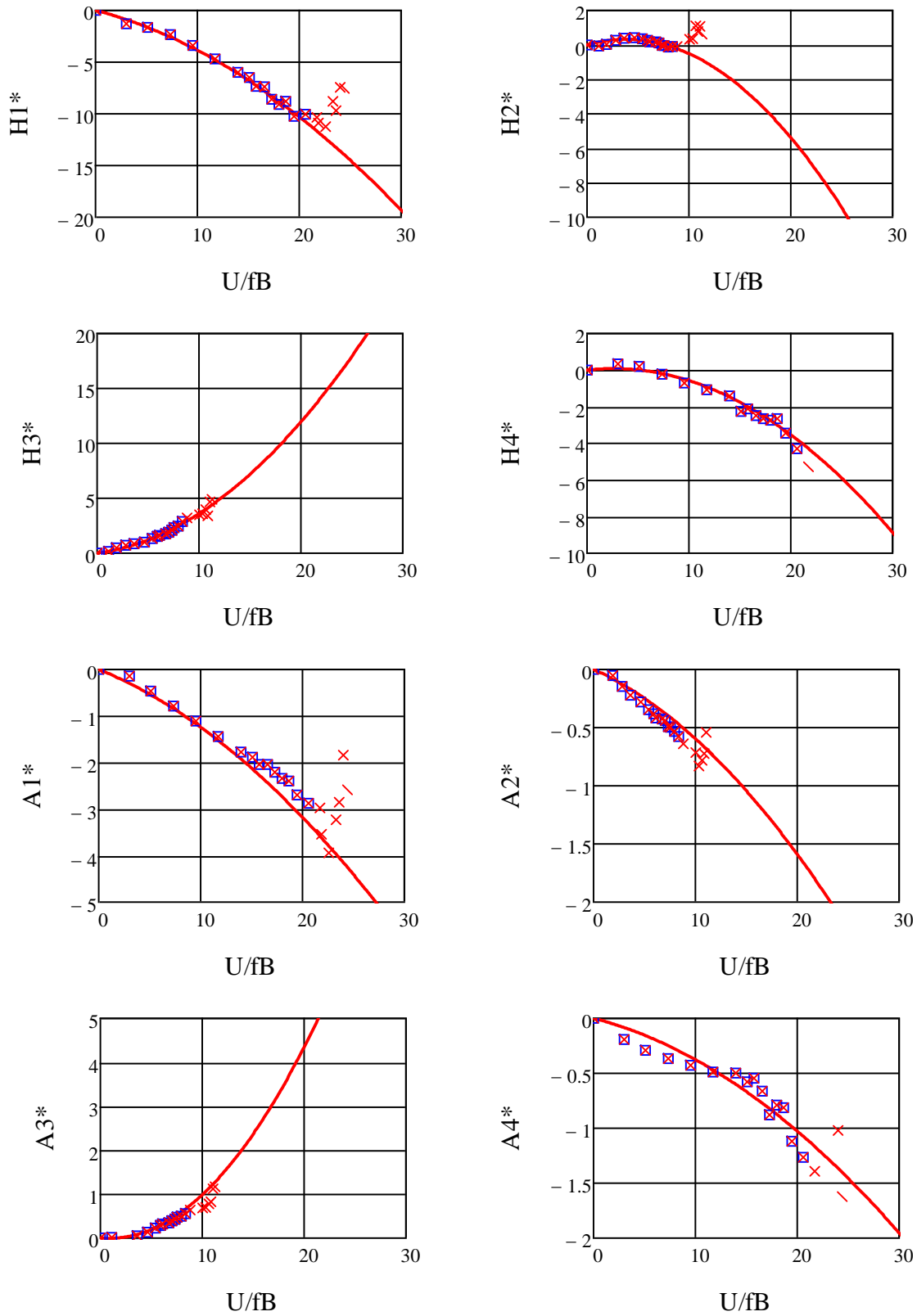
Experimental aerodynamic derivatives obtained for a twin-box and a tri-box suspension bridge deck section has been reviewed with a view to provide physical insight into the observation that this type of decks is found to possess higher aerodynamic stability when equipped with large wind screens than without the wind screens. It is found that the deck sections equipped with the wind screens display a "nose-up" aerodynamic moment and corresponding deck twist at increasing mean wind speeds. A flutter model is developed which allows prediction of the increase of the critical wind speed for onset of flutter as function of deck section rotation angle. Predicted critical wind speeds are in fair agreement with flutter speeds obtained from direct observations of an elastically sprung section model and a full aeroelastic bridge wind tunnel model.

An important conclusion following from the above considerations is that bridges featuring twin-box or tri-box deck sections may be designed to achieve longer spans without encountering flutter than indicated by the state-of-the-art knowledge if the "nose-up" effect is duly accounted for and exploited. This is the topic of the PhD project of the junior author of the present paper.

References

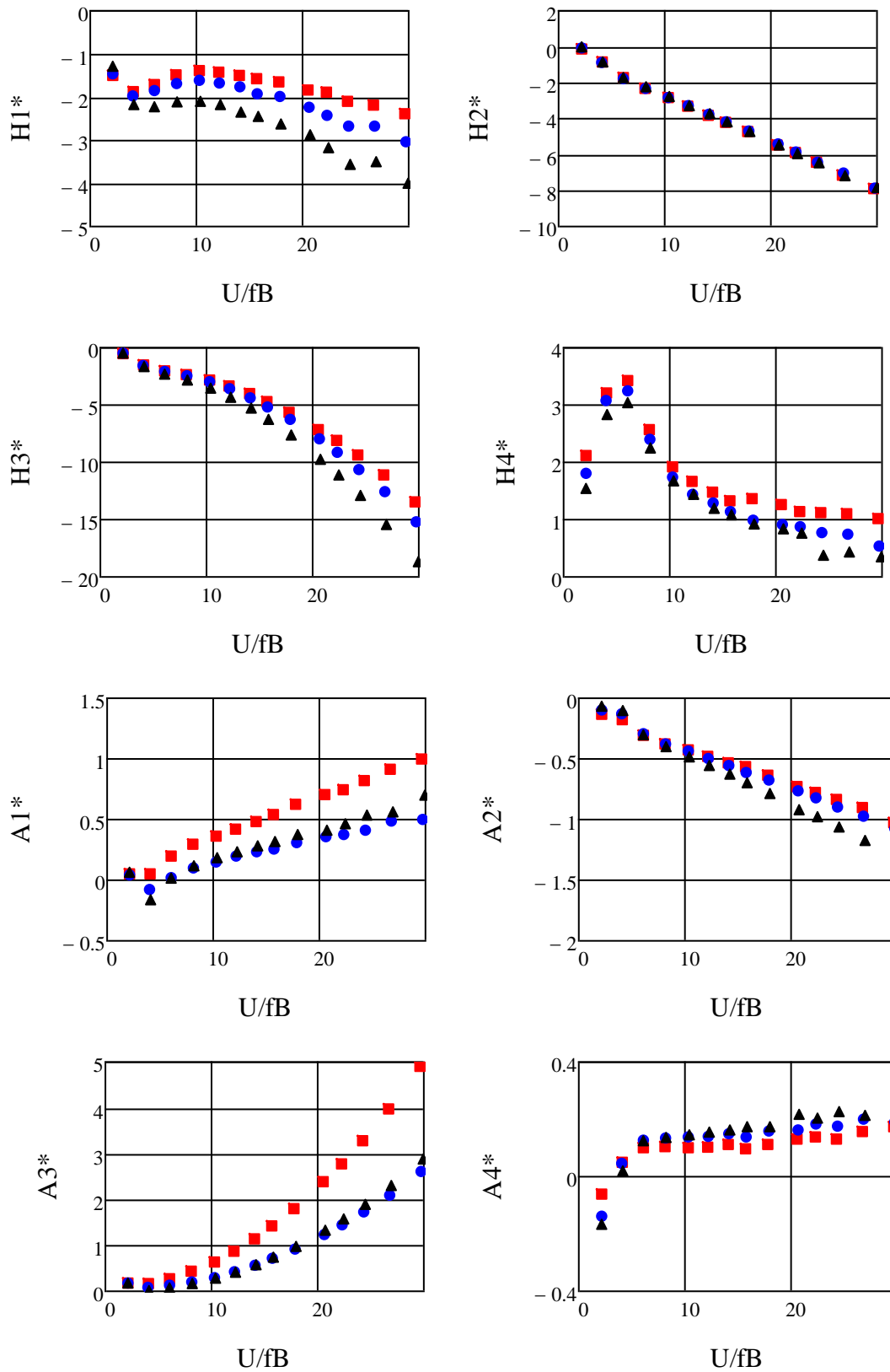
- Larsen, A. 1993. Aerodynamic aspects of the final design of the 1624 m suspension bridge across the Great Belt. *Journal of Wind Engineering and Industrial Aerodynamics* (48).
- Larsen, A. and Astiz, M. A. 1998. Aeroelastic considerations for the Gibraltar Bridge feasibility study. *Bridge Aerodynamics*, Larsen & Esdahl (eds), Balkema, 165-173.
- Larsen, A. 2016. The role of horizontal aerodynamic derivatives in bridge flutter calculations. *First international symposium on flutter and it's application*, Tokyo.

Appendix A: Aerodynamic derivatives, Çanakkale Bridge twin-box section. Free oscillation tests.



Aerodynamic derivatives for initial rotation angle of -1.0° . Markers (x and \square): Experimental points. Curves: Polynomial fits for experimental points \square .

Appendix B: Aerodynamic derivatives, Messina Bridge tri-box section. Forced oscillation tests.



The aerodynamic derivatives measured at fixed rotation angles of 0° (■), 2° (●) and 4° (▲).

Re-evaluation of aerodynamic stability of suspension bridges in Seto-Ohashi Bridges

Naoki TOYAMA¹, Masahiro TAKEGUCHI² and Taku HANAI³

¹ *Manager, Long-span Bridge Engineering Center, Honshu-Shikoku Bridge Expressway Co., Ltd., Kobe, Japan, naoki-toyama@jb-honshi.co.jp*

² *Director, Long-span Bridge Engineering Center, Honshu-Shikoku Bridge Expressway Co., Ltd., Kobe, Japan*

³ *Manager, Shimanami-Imabari Operation Center, Honshu-Shikoku Bridge Expressway Co., Ltd., Imabari, Japan*

Abstract

Suspension bridges in Seto-Ohashi Bridges which connect Honshu and Shikoku Islands in Japan are highway-railway combined bridges, and have two levels in girder to accommodate highway and railway traffics in the upper and lower levels respectively. In order to secure the aerodynamic stability of the bridges, open gratings are installed at the center and both sides of road deck. However, it is disadvantageous to have such openings on the road deck because small objects may drop through the openings, and that may endanger railway operation in lower level. Therefore, the possibility of closing the gratings are examined. As the result of three-dimensional flutter analysis, we found that it is possible to close all the gratings by installing center barrier as aerodynamic countermeasure.

Keyword: suspension bridge, wind, flutter, analysis, maintenance

1 Introduction

The Honshu-Shikoku Bridges are group of 17 long span bridges, which connects Honshu and Shikoku Islands in Japan by 3 routes. Since these bridges are located over the sea, the bridges designed considering strong winds due to typhoon and seasonal winds. The center route called Seto-Ohashi Bridges completed in 1988, and consists of three suspension bridges, two cable stayed bridges and one truss bridge and the length of them is 9.4 km.

The three suspension bridges are highway-railway combined suspension bridges and Minami Bisan-Seto Bridge is the second longest highway-railway combined bridge in the world. The cross sections of stiffening truss girders in these three bridges are identical and have two levels for transportation. Upper level is used for highway and lower level is used for railway (Figure 1). Kita Bisan-Seto Bridge is next to Minami Bisan-Seto Bridge and they share anchorage. Figure 2 shows the elevations of the three suspension bridges of the Seto-Ohashi Bridges.

In order to satisfy aerodynamic stability of the suspension bridges of the Seto-Ohashi Bridges, open gratings have been installed at the center and both sides of road deck since the completion. However, since small objects may drop through open grating at the center of road deck in upper level and endanger railway operation in lower level, it is disadvantageous to use open grating at the center of road deck in terms of maintenance. Therefore, narrowing the range of the span requiring open grating at the center of road deck

was considered.

At the design stage of the Seto-Ohashi Bridges, the aerodynamic stability was examined through two-dimensional wind tunnel test assuming that the cross-section of bridge girder was identical throughout the bridge axis, and the three dimensional effects of the long-span bridge was not fully considered.

For the design of the Akashi-Kaikyo Bridge, about 10 years after the completion of the Seto-Ohashi Bridges, a new evaluation method employing the three dimensional flutter analysis was established. Currently, the evaluation method is widely applied to the aerodynamic design of other long-span bridges in and out of Japan. Utilizing the evaluation method, the aerodynamic stability of the above three suspension bridges in the Seto-Ohashi Bridges were re-evaluated and the possibility of closing the open gratings were examined.

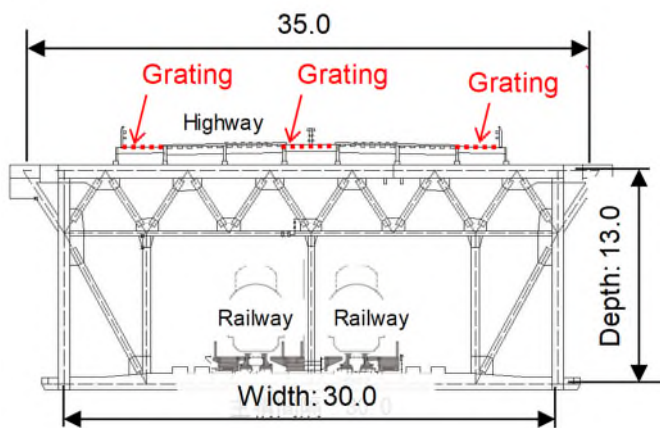


Photo 1: Grating on the bridge deck

Figure 1: Cross section of truss girder (unit:m)

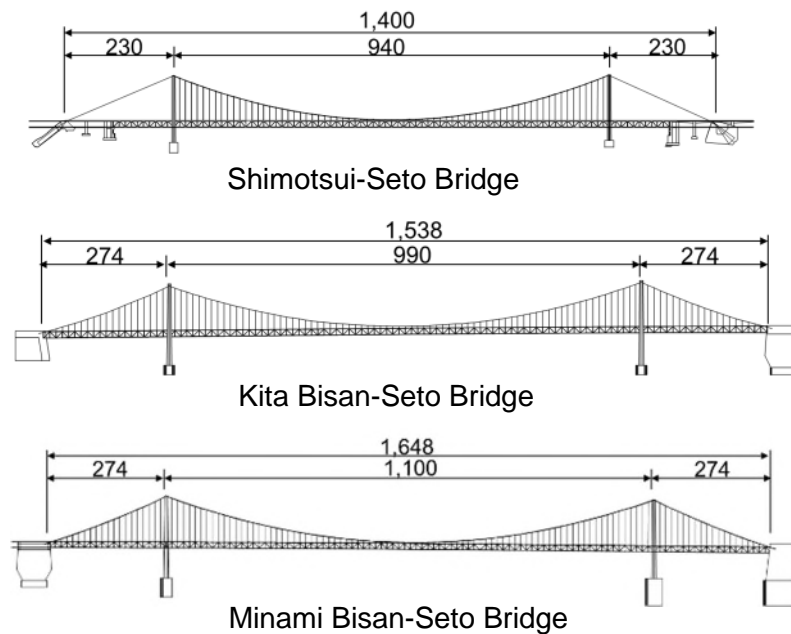


Figure 2: Seto-Ohashi suspension bridges (unit:m)

2 Procedures in the re-evaluation of aerodynamic stability

As mentioned in the previous section, the three dimensional effects in the aerodynamic design was not fully considered at the design stage of the Seto-Ohashi suspension bridges. However, the three dimensional effects such as the deformation in transversal direction, and the difference in aerodynamic forces at different location in longitudinal direction are essential in proper assessment of the aerodynamic stability of long-span suspension bridges. There are two ways to consider the above effects.

- i) Wind-tunnel test with whole bridge model
- ii) Three dimensional flutter analysis

If the test shown i) is conducted, the aerodynamic stability can be evaluated. However, since the model become large, the testing facility is limited because the full scale model is large. In addition, this test is too expensive because of modelling and operation of huge wind tunnel facility. On the other hand, a spring supported wind-tunnel test using two dimensional model is not so expensive as the three dimensional test, and can simulate well the wind effect of structural detail on its stability. If the coefficient of three-component forces and unsteady aerodynamic forces are obtained through the spring supported wind-tunnel test, the obtained coefficients are used as the inputs for the three dimensional flutter analysis (ii). In this study, this re-evaluation was conducted by three dimensional flutter analysis. The wind-tunnel test was conducted based on Manual of Wind Tunnel Test for Honshu Shikoku Bridges (Honshu Shikoku Bridge Authority, 2001).

2.1 Wind tunnel test

1) Spring supported wind-tunnel test

Before measuring the coefficients of three-component forces and unsteady aerodynamic forces for flutter analysis, the spring supported wind-tunnel test (Photo 2) was conducted on conditions shown in Table 1. Wind-tunnel facility was closed-circuit type wind tunnel owned by Yokohama National University. The scale of model for the test was 1/80 and its length was 1.25 m. Since the cross-section of the girders of suspension bridges were not symmetry from west and east, and the east wind is critical to the bridges according to the results of wind tunnel tests conducted during the construction period, the stability of the bridges were evaluated in east wind.

2) Coefficients of three component forces

During consideration of the aerodynamic stability of the Akashi-Kaikyo Bridge, which completed in 1998, it was found that three-dimensional deformation was not negligible. In this study, the coefficients of three component forces, drag and lift forces and moment, were measured to evaluate the three dimensional deformation properly. The measurement of the three component forces was conducted for each cross section at the attack angle between -10 deg. and +10 deg., and wind velocity of 8 and 12 m/s. The measured wind forces were normalized using the following equations.

$$C_D = \frac{P_D}{0.5 \rho U^2 DL} \quad (1)$$

$$C_L = \frac{P_L}{0.5 \rho U^2 B L} \quad (2)$$

$$C_M = \frac{P_M}{0.5 \rho U^2 B^2 L} \quad (3)$$

where C_D , C_L and C_M are mean coefficients of drag and lift forces and moment. ρ is air density. B , D and L are width, depth and length of truss girder, respectively.

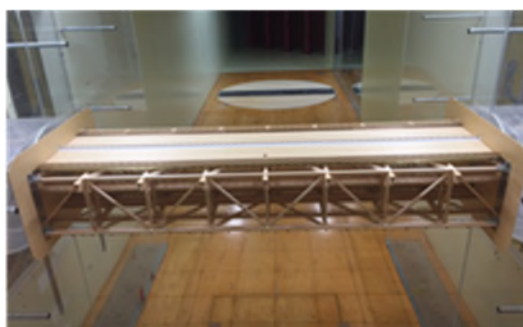


Photo 2: Two dimensional wind tunnel test model (scale: 1/80)

Table 1: Condition of spring supported test

	Bridge	Model		Error (Allowable*)
		Required	Measured	
Girder Width B (m)	30.0	0.375	0.375	0%
Girder Depth D (m)	13.0	0.1625	0.1625	0%
Mass m (kg/m)	40.63×10^3	6.348 [7.936]	[8.095]	+2% ($\leq 2\%$)
Polar Moment of Inertia (kgm^2/m)	7.630×10^3	0.1863 [0.2328]	[0.2281]	-2% ($\leq 2\%$)
Natural Frequency (Hz)	Vertical (a)	0.166	-	1.869
	Torsional (b)	0.329	-	3.296
	(b)/(a)	1.98	1.98	1.76
Logalythmic Decrement	Vertical	0.03	0.03	0.0322 (+0.0022 (± 0.005))
	Torsional	0.03	0.03	0.0263 (-0.0037 (± 0.005))

* Allowable range according to Manual of Wind Tunnel Test

** Does not meet requirement because consistency in polar moment of inertia was the highest priority.

[] Values per model length 1.25m.

3) Coefficients of unsteady aerodynamic forces

Since bridges are not streamlined shape, it is unable to calculate unsteady aerodynamic forces by theoretical way because of complex configuration of bridge girder. Therefore, they were measured by spring supported wind tunnel tests. The measurements of the aerodynamic forces were conducted from -5 to +5 degree of angles of attack, and the coefficients of unsteady aerodynamic forces were derived by modal decomposition and re-assembly method (Yamada and Miyata, 1996). The following is the equation of motion for

the coupled vibration in vertical and torsional directions.

$$[[M]]\{\ddot{u}\} + [[C]]\{\dot{u}\} + [[K]]\{u\} = [[F]]\{\ddot{u}\} \tag{4}$$

where:

$$[[M]] = \begin{bmatrix} m & 0 \\ 0 & I \end{bmatrix}, \quad [[C]] = \begin{bmatrix} 2mh_z\omega_z & 0 \\ 0 & 2Ih_\theta\omega_\theta \end{bmatrix}, \quad [[K]] = \begin{bmatrix} m\omega_z^2 & 0 \\ 0 & I\omega_\theta^2 \end{bmatrix}, \quad [[F]] = \begin{bmatrix} L_z & L_\theta \\ M_z & M_\theta \end{bmatrix},$$

$$L_z = -\pi\rho B^2(L_{zR} + iL_{zI}), \quad L_\theta = -\pi\rho B^2(L_{\theta R} + iL_{\theta I}),$$

$$M_z = -\pi\rho B^4(M_{zR} + iM_{zI}), \quad M_\theta = -\pi\rho B^4(M_{\theta R} + iM_{\theta I})$$

then, m is mass per unit length, I is polar moment of inertia per unit length, ω_z and ω_θ are natural frequencies of vertical and torsional vibrations, L_{jR} and L_{jI} are real and imaginary parts of unsteady aerodynamic lift forces due to vibration in j-direction, M_{jR} and M_{jI} are real and imaginary parts of unsteady aerodynamic moment due to vibration in j-direction, j is direction of vibration, z is vertical and θ is torsional directions, respectively.

2.2 Flutter analysis

Fish-bone models of the suspension bridges composed of cable, suspender rope and truss girder are prepared (Figure 3). To verify the numerical models of the suspension bridges, eigenvalues of the models were calculated and compared with results which were calculated during construction (Table 2). Since these errors are small, and we found that these models could reproduce the behavior of the actual bridges.

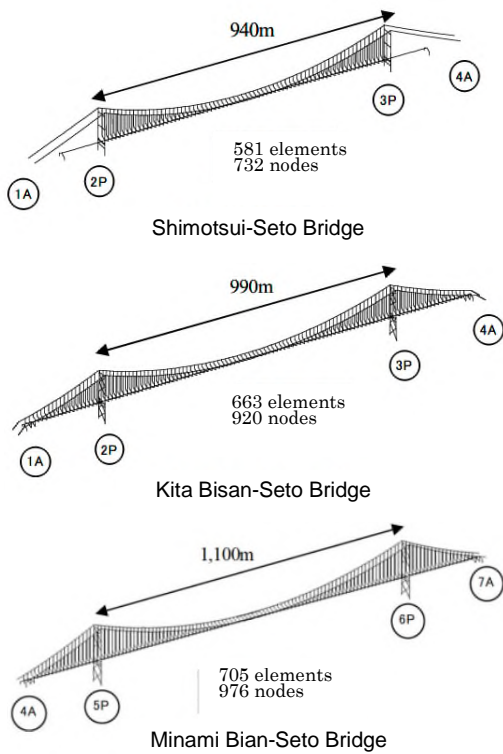


Figure 3: Flutter analysis models

Table 2: Eigen value analysis result

Natural frequency (Hz)		Shimotsui-Seto	Kita Bisan-Seto	Minami Bisan-Seto
Horizontal mode	Symmetry	0.106 (0.107)	0.087 (0.088)	0.076 (0.076)
	Asymmetry	0.259 (0.257)	0.210 (0.212)	0.176 (0.176)
Vertical mode	Symmetry	0.202 (0.202)	0.171 (0.173)	0.167 (0.166)
	Asymmetry	0.152 (0.160)	0.158 (0.147)	0.135 (0.133)
Torsional mode	Symmetry	0.375 (0.374)	0.347 (0.355)	0.327 (0.329)
	Asymmetry	0.535 (0.521)	0.47 (0.482)	0.451 (0.453)

Top: Result of this study

(Bottom): Result of the study during construction period

3 Evaluation of aerodynamic stability with open gratings closed

3.1 Aerodynamic characteristics of typical cross sections

1) Spring supported wind-tunnel test

Four types of girder cross sections were tested as shown in Figure 4. Cross section 1 represents the current typical cross section of the girder with openings at the center and both side shoulders. Cross section 2 and 3 represent the cross sections whose open gratings are closed to see the possibility of closing the openings. Also, cross section 3 and 4 applied to some portions to reduce noise that disturbs neighboring residents, and for the cross section 4, noise barriers are installed in the side and bottom of railway tracks. And the application of cross section 3 and 4 is limited to side spans and vicinity of towers where the girders' aerodynamics does not contribute to the stability of the whole bridge very much.

The test results are shown in Figure 5. Flutter onset velocity in actual wind speed with respect to the attack angle of approach wind are plotted. Flutter onset velocity of the cross section 1 is much higher than the reference wind speed, 79.1m/s. On the other hand, the aerodynamic stability degrades in the wind of positive attack angle (blowing up wind) when the opening at the center is closed (cross section 2). In particular, flutter occurs below the reference wind speed at +3 degree, and the contribution of the openings at the center to the aerodynamic stability is confirmed. Cross section 3 shows the same trend as the cross section 2. Cross section 4 with noise barriers does not satisfy reference wind speed between - 3 and + 3 degrees.

2) Coefficients of three component force

Coefficients of three component force of cross section 1 and 2 measured in wind tunnel tests are shown in Figure 6. The gradient and absolute value of the lift force coefficient, C_L , of cross section 2 is larger than those of cross section 1. Other coefficients, C_D and C_M , are almost the same.

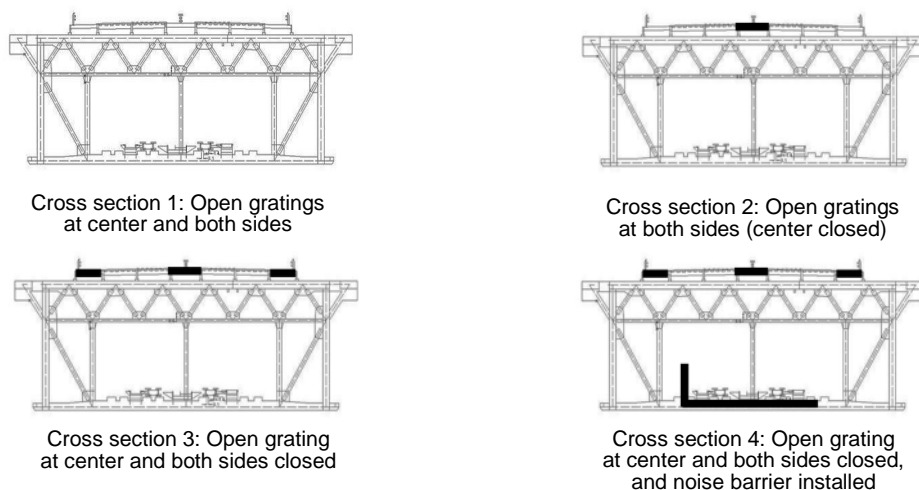


Figure 4: Studied cross sections

3) Coefficients of unsteady aerodynamic force

Coefficients of unsteady aerodynamic forces of cross section 1 and 2 at +3 degree are shown in Figure 7. It was found that the measurement result could be almost regressed into quadratic polynomial equation.

Two dimensional flutter analysis was carried out to validate the coefficients of unsteady

aerodynamic forces obtained through wind tunnel tests. The result of the flutter analysis and wind tunnel tests are compared in Figure 8, and the both results agree well.

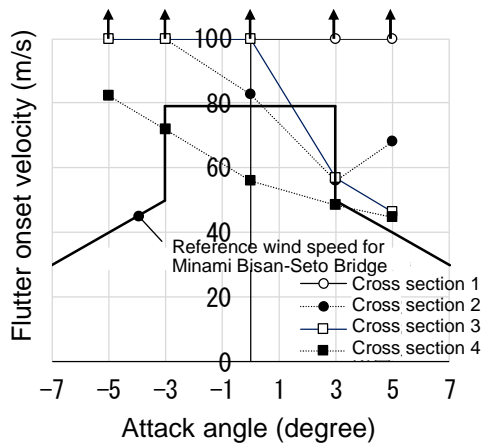


Figure 5: Spring supported test result

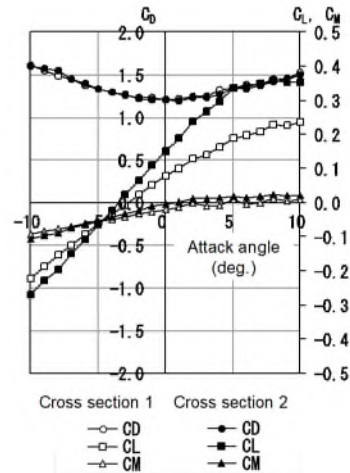
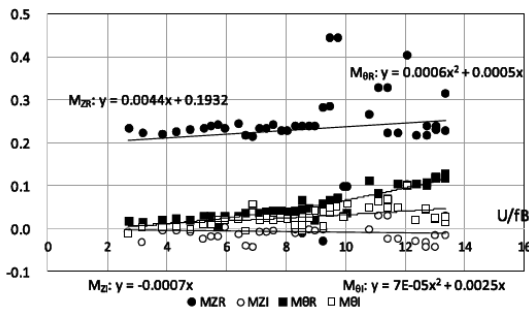
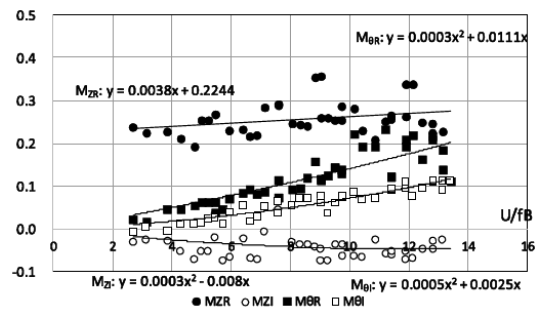


Figure 6: Coefficients of three component forces



Cross section 1: attack angle of +3 deg.



Cross section 2: attack angle of +3 deg.

Figure 7: Coefficients of unsteady aerodynamic forces

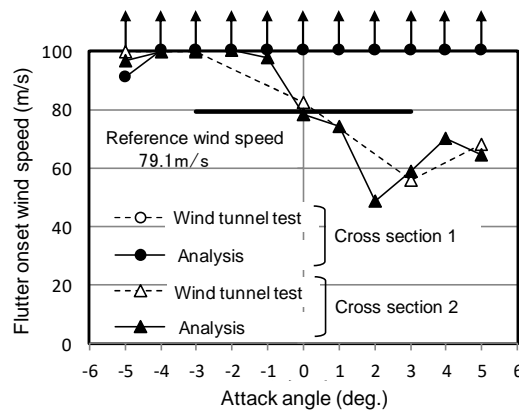


Figure 8: Comparison of flutter wind speed

3.2 Closable range of open gratings

To optimize the range of the grating at the three suspension bridges, three dimensional flutter analysis was conducted closing the open gratings at the center of bridge deck toward the center of the bridge span gradually. Because the wind resistant stability was degraded at the attack angle of +3 degree as mentioned in 3.1, the flutter analysis was conducted for +3

degree. The results of the flutter analysis for the Shimotsui-Seto Bridge is shown in Figure 9, and the arrangement of cross sections and the flutter onset wind speed derived from the analysis are tabulated. The Open Rate (OR) is defined in the following formula.

$$(OR \%) = (\text{The range of cross section 1}) / (\text{Total girder length}) \times 100 \quad (5)$$

As the result of the flutter analysis, we found that the reference wind speed is satisfied even though all the gratings at the center of the bridge deck is closed (OR: 0%). In the same manner as the Shimotsui-Seto Bridge, flutter analysis were conducted for the other two bridges, Kita and Minami Bisan-Seto Bridges, and the analysis yielded the same results as shown in Table 3.

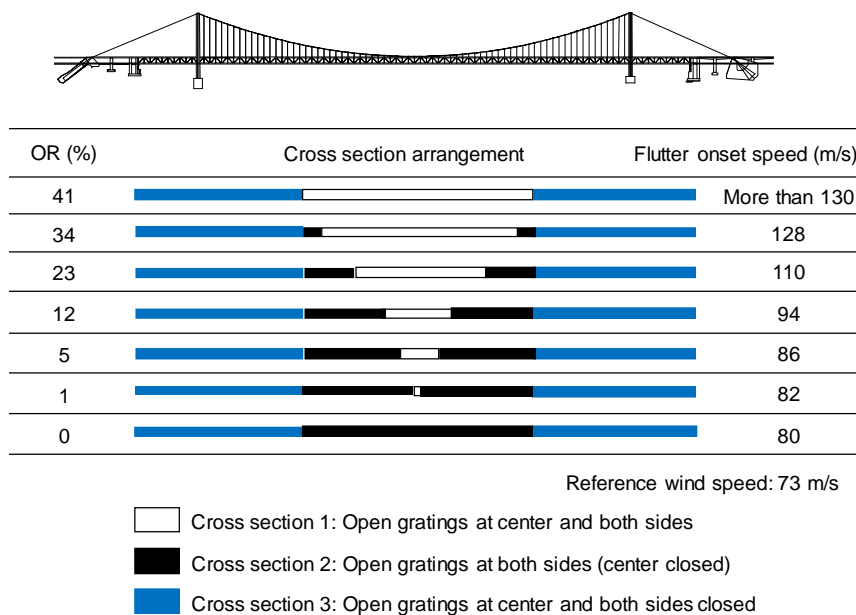


Figure 9: Result of three dimensional flutter analysis (Shimotsui-Seto Bridge)

Table 3: Minimum Open Rate (OR) of center grating to secure aerodynamic stability

	Shimotsui Seto	Kita Bisan-Seto	Minami Bisan-Seto
Open Rate (OR)(%)	0	0	0

4 Improvement of aerodynamic stability by center barrier

As mentioned in the previous section, we found that all the open gratings at the center of the bridge deck can be closed. In order to examine the possibility of closing all the gratings at center and both sides of the bridge deck, the installation of center barrier, a kind of solid wall as the aerodynamic countermeasure is considered (Figure 10; Cross section 5). The center barrier is installed on the existing medial divider, and the height of the barrier is 1.2m. Such kind of solid barrier was found to be effective in the past study (Yasuda and Hirahara, 1989). Figure 11 shows the result of spring supported wind tunnel test for the cross section 5 comparing with the result for the cross section 3, and the wind resistant stability is improved at around positive angles of attack, +3 and +5 degrees.

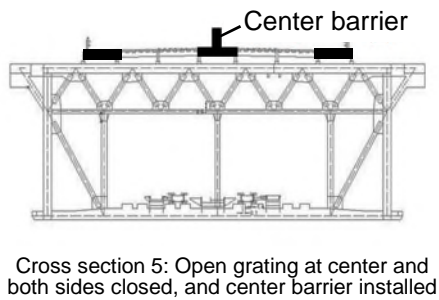


Figure 10: Studied cross section

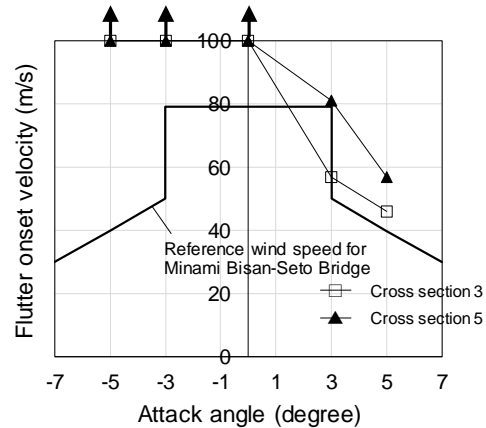


Figure 11: Spring supported test result (cross section 5)

And again, the three dimensional flutter analysis was conducted replacing the cross section 1 with the cross section 5 (center barrier installed), and decreasing the number of center barrier replacing the cross section 5 with the cross section 3 little by little. The “Center Barrier Rate (CBR)” is defined in the following formula.

$$(CBR (\%)) = (\text{The range of cross section 5}) / (\text{Total girder length}) \times 100 \quad (6)$$

The result of flutter analysis for the Shimotsui-Seto Bridge is shown in Figure 12, and all the gratings can be closed securing the aerodynamic stability when the CBR is more than 23%. In the same manner as the Shimotsui-Seto Bridge, flutter analysis were conducted for the other two bridges, Kita and Minami Bisan-Seto Bridges. As shown in Table 4, all the gratings of the Kita and Minami Bisan-Seto Bridges can be closed when the CBRs are more than 22% and 15% respectively.

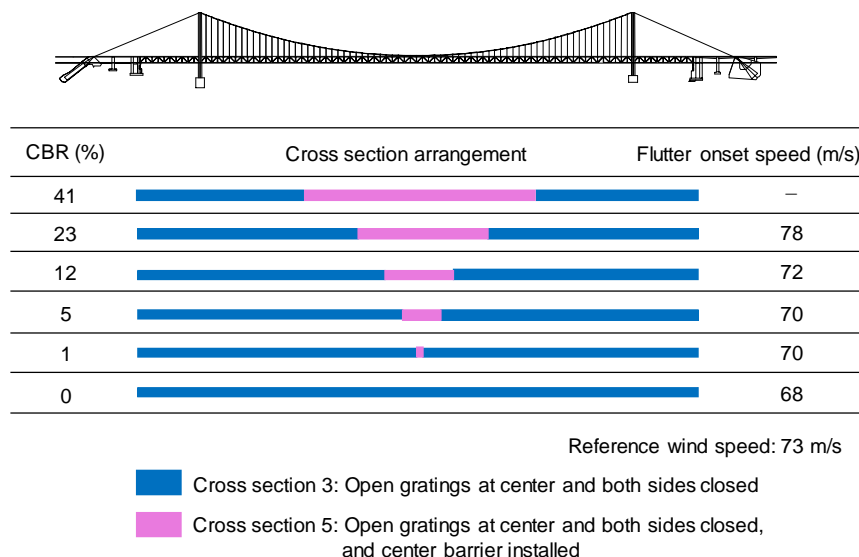


Figure 12: Result of three dimensional flutter analysis (Shimotsui-Seto Bridge; all gratings closed and center barrier installed)

Table 4: Minimum Center Barrier Rate (CBR) to secure aerodynamic stability

	Shimotsui Seto	Kita Bisan-Seto	Minami Bisan-Seto
Center Barrier Rate (CBR)(%)	23	22	15

5 Conclusions

In order to improve the maintainability of the suspension bridges of the Seto-Hashi Bridges, three dimensional flutter analysis was conducted, and the possibility of closing the open gratings was examined. As the result of the analysis, we found that it is possible to close all of the gratings at the center of road deck. Also, we found that it is possible to close all the gratings by installing center barrier as aerodynamic countermeasure.

However, the selection of the closing portion have to be conducted carefully taking into account of the damping characteristics of the actual bridges because the structural damping of torsional modes of truss girder tends to be smaller than that of vertical modes according to the previous study.

Also, the detail of the closing structure have to be carefully studied considering the load bearing capacity, serviceability and workability of the installation work.

Acknowledgements

This study is supported by professor Katsuchi, Yokohama National University, through the collaborative research on effective range of aerodynamic countermeasure of long span bridges (2015 - 2016) .

References

- Honshu Shikoku Bridge Authority, 1976. Wind Resistant Design Code.
- Honshu Shikoku Bridge Authority, 2001. Wind Resistant Design Code for Honshu Shikoku Bridges.
- Yamada, H., Miyata T., 1996. Three Dimensional Unsteady Aerodynamic Force Measurement by the Modal Decomposition and Reassemblage Method. Journal of Japan Society of Civil Engineers, No.543/I-36, 209-216.
- Yasuda, M., Hirahara N., 1989. Wind Resistant Characteristics in Akashi Kaikyo Bridge. Honshi Technical Report, Vol.13, No.52, 17-28.

Study on direct identification of rational function approximation coefficients of self-excited forces

Hiroshi Katsuchi¹, Hitoshi Yamada² and Herry Irpani³

¹*Yokohama National University, Yokohama, Japan, katsuci@ynu.ac.jp*

²*Yokohama National University, Yokohama, Japan*

³*Yokohama National University, Yokohama, Japan*

Abstract

A rational function approximation method is used to express self-excited forces with flutter derivatives in the time domain. Recently, a direct identification method of the rational function approximation coefficients by wind-tunnel experiment was developed. However, detailed conditions of the wind speed level and applicability of other complicated sections are still unknown. This study verifies the applicability of this direct approximation method by a numerical simulation for a flat plate, rectangular section and truss section. Result showed that two wind speed steps gave an accurate identification. Besides, high accuracy for the flat plate and rectangular section was confirmed while relatively lower accuracy for the truss section was confirmed.

Keyword: flutter derivative, rational function approximation, direct identification, time domain

1 Introduction

Self-excited forces of a bridge deck are normally formulated by using non-dimensional flutter derivatives which are obtained experimentally and functions of the reduced frequency. Applying the self-excited forces to equations of motion of a bridge structure and performing a complex eigenvalue analysis, flutter parameters such as aeroelastically influenced frequencies and damping are calculated. Then a flutter critical wind speed can be obtained. When one wants to analyze a time-history response of a bridge deck near the flutter critical wind speed, a formulation of self-excited forces in the time domain is necessary. So far, a rational function approximation of measured self-excited forces has been often used to analyze the time-history response.

Recently, a direct identification method of the rational function approximation coefficients by wind-tunnel experiment was developed by Cao et. al. (2012). They experimented a flat plate and a 1:5 rectangular cross section, and concluded that the measurement at two wind speed steps could give a satisfactory result. However, detailed conditions of the wind speed level and applicability of other complicated sections are still unknown.

This study verifies the applicability of this direct approximation method by a numerical simulation. In addition, effects of wind speed level and wind-speed steps on the approximation result are examined. Finally, a time-history response analysis demonstrates flutter evolution before/after the flutter onset.

2 Rational function approximation from time history response (MS-RFA method)

Formulation of self-excited force (lift and pitching moment) used in this study is shown in Eq. (1). This is the Minimum State Rational Function Approximation in the Laplace domain formulated by Karpel (1982) (hereinafter, MS-RFA method) where p ($= iK$, i is the imaginary unit, $K = B\omega/U$: reduced frequency) is the Laplace variable and $\hat{\ast}$ is the Laplace transform.

$$\begin{bmatrix} \hat{L}_{se} \\ \hat{M}_{se} \end{bmatrix} = V_f Q \hat{q} \\ = \begin{bmatrix} \frac{1}{2}\rho U^2 B & 0 \\ 0 & \frac{1}{2}\rho U^2 B \end{bmatrix} \begin{bmatrix} (\underline{A}_0)_{11} + (\underline{A}_1)_{11}p + \frac{(\underline{F})_{11}p}{p+\lambda} & (\underline{A}_0)_{12} + (\underline{A}_1)_{12}p + \frac{(\underline{F})_{12}p}{p+\lambda} \\ (\underline{A}_0)_{21} + (\underline{A}_1)_{21}p + \frac{(\underline{F})_{21}p}{p+\lambda} & (\underline{A}_0)_{22} + (\underline{A}_1)_{22}p + \frac{(\underline{F})_{22}p}{p+\lambda} \end{bmatrix} \begin{bmatrix} \hat{h}/B \\ \hat{\alpha} \end{bmatrix} \quad (1)$$

where ρ : air density, U : wind speed, B : deck width, h : vertical displacement, α : torsional displacement, and $\underline{A}_0, \underline{A}_1, \underline{F}, \lambda$ are rational function approximation coefficients which are corresponding to the flutter derivative.

Cao et al. (2012) developed a technique for directly identifying the rational function approximation coefficients from a time-history response on Eq. (1). Now, by performing the inverse Laplace transform by multiplying both sides of the Eq. (1) by $p+1$, the expression in the time domain is obtained as shown in Eq. (2).

$$\dot{L}_{se} + \lambda_L \frac{U}{B} L_{se} = \frac{1}{2}\rho U^2 B \left(\left(\frac{U}{B} \right) \underline{\psi}_1 q + \underline{\psi}_2 \dot{q} + \left(\frac{B}{U} \right) \underline{\psi}_3 \ddot{q} \right) \quad (2a)$$

$$\dot{M}_{se} + \lambda_M \frac{U}{B} M_{se} = \frac{1}{2}\rho U^2 B^2 \left(\left(\frac{U}{B} \right) \underline{\psi}_4 q + \underline{\psi}_5 \dot{q} + \left(\frac{B}{U} \right) \underline{\psi}_6 \ddot{q} \right) \quad (2b)$$

where (\bullet) represents the time derivative. And, $\underline{\psi}_1 \sim \underline{\psi}_6$ are a vector containing rational function approximation coefficients and are expressed as follows.

$$\underline{\psi}_1 = [\lambda_L (\underline{A}_0)_{11} \quad \lambda_L (\underline{A}_0)_{12}] \quad (3a)$$

$$\underline{\psi}_2 = [(\underline{A}_0)_{11} + \lambda_L (\underline{A}_1)_{11} + (\underline{F})_{11} \quad (\underline{A}_0)_{12} + \lambda_L (\underline{A}_1)_{12} + (\underline{F})_{12}] \quad (3b)$$

$$\underline{\psi}_3 = [(\underline{A}_1)_{11} \quad (\underline{A}_1)_{12}] \quad (3c)$$

$$\underline{\psi}_4 = [\lambda_M (\underline{A}_0)_{21} \quad \lambda_M (\underline{A}_0)_{21}] \quad (3d)$$

$$\underline{\psi}_5 = [(\underline{A}_0)_{21} + \lambda_M (\underline{A}_1)_{21} + (\underline{F})_{21} \quad (\underline{A}_0)_{22} + \lambda_M (\underline{A}_1)_{22} + (\underline{F})_{22}] \quad (3e)$$

$$\underline{\psi}_6 = [(\underline{A}_1)_{22} \quad (\underline{A}_1)_{22}] \quad (3f)$$

Rewriting Eqs. (2a) and (2b) to Eqs. (4a) and (4b), respectively, and expressing the first terms in the left-hand side as $\underline{A}_L, \underline{A}_M$, the second terms in the left-hand side as $\underline{X}_L, \underline{X}_M$ and the right-hand side as $\underline{b}_L, \underline{b}_M$, Eqs. (4a) and (4b) are rewritten by Eqs. (5a) and (5b).

$$\begin{bmatrix} \underline{\psi}_1 & \underline{\psi}_2 & \underline{\psi}_3 & -\lambda_L \end{bmatrix} \begin{bmatrix} \frac{1}{2}\rho U^2 B \left(\frac{U}{B} \right) q \\ \frac{1}{2}\rho U^2 B \dot{q} \\ \frac{1}{2}\rho U^2 B \left(\frac{B}{U} \right) \ddot{q} \\ \left(\frac{U}{B} \right) L_{se} \end{bmatrix} = \dot{L}_{se} \quad (4a)$$

$$\begin{bmatrix} \underline{\psi}_4 & \underline{\psi}_5 & \underline{\psi}_6 & -\lambda_M \end{bmatrix} \begin{bmatrix} \frac{1}{2} \rho U^2 B^2 \left(\frac{U}{B}\right) \underline{q} \\ \frac{1}{2} \rho U^2 B^2 \underline{\dot{q}} \\ \frac{1}{2} \rho U^2 B^2 \left(\frac{B}{U}\right) \underline{\dot{q}} \\ \left(\frac{U}{B}\right) M_{se} \end{bmatrix} = \dot{M}_{se} \quad (4b)$$

$$\underline{A}_L \underline{X}_L = \underline{b}_L, \quad \underline{A}_M \underline{X}_M = \underline{b}_M \quad (5a, b)$$

Finally, vectors \underline{A}_L and \underline{A}_M containing the rational function approximation coefficients are obtained using the least square method as follows.

$$\underline{A}_L = (\underline{b}_L \underline{X}_L^T) (\underline{X}_L \underline{X}_L^T)^{-1}, \quad \underline{A}_M = (\underline{b}_M \underline{X}_M^T) (\underline{X}_M \underline{X}_M^T)^{-1} \quad (6a, b)$$

Well-known flutter derivatives (Simiu and Scanlan, 1996) by Scanlan (H_i^* , A_i^* ($i = 1 - 4$) in Eqs. (7a) and (7b)) are related to the rational function approximation coefficients in this study as shown in Eqs. (8a - h) where Q_{**} expresses each component in the matrix of the second term in the right-hand side of Eq. (1).

$$L_{se} = \frac{1}{2} \rho U^2 B \left(KH_1^* \frac{\dot{h}}{U} + KH_2^* \frac{B \dot{\alpha}}{U} + K^2 H_3^* \alpha + K^2 H_4^* \frac{h}{B} \right) \quad (7a)$$

$$M_{se} = \frac{1}{2} \rho U^2 B^2 \left(KA_1^* \frac{\dot{h}}{U} + KA_2^* \frac{B \dot{\alpha}}{U} + K^2 A_3^* \alpha + K^2 A_4^* \frac{h}{B} \right) \quad (7b)$$

$$H_1 = \text{Im}(\underline{Q}_{11})/K^2, H_2 = \text{Im}(\underline{Q}_{12})/K^2, H_3 = \text{Re}(\underline{Q}_{12})/K^2, H_4 = \text{Re}(\underline{Q}_{11})/K^2 \quad (8a - d)$$

$$A_1 = \text{Im}(\underline{Q}_{21})/K^2, A_2 = \text{Im}(\underline{Q}_{22})/K^2, A_3 = \text{Re}(\underline{Q}_{22})/K^2, A_4 = \text{Re}(\underline{Q}_{21})/K^2 \quad (8e - h)$$

3 Validation of MS-RFA method for flat plate and rectangular cross section

In this section, using the rational function approximation coefficients of the flat plate ($B/D = 15$) and the rectangular cross section ($B/D = 5$) by Cao et al. (2012), the calculation algorithm described in Section 2 is verified.

Firstly, self-excited force time histories were generated with Eq. (9) (inverse Laplace transform of Eq. (1)) by known rational function approximation coefficients of the flat plate and rectangular cross section, and conditions in Table 1. Then, the rational function approximation coefficients were calculated according to the algorithm in Section 2. Finally, by performing the comparison with the first assumed coefficients, the MS-RFA technique was verified. Here, a white noise of 0.5% of the maximum displacement was added to the displacement time-history. Width (B) of the flat plate and rectangular cross section is 0.3 m and 0.16 m, respectively. Height (D) of those is 0.02 m and 0.032 m, respectively. Further, the time history was generated at wind speeds of 2.8 m/s and 14.4 m/s.

Table 2 shows a comparison of the rational function approximation coefficients between initially set ones and calculation results by the MS-RFA method. For the cross section of the flat plate, the rational function approximation coefficient by the MS-RFA method was able to reproduce with very high accuracy what was initially set, indicating that the identification method was properly reproduced. Here, a self-excited force time history is created from the

Table 1: Simulation conditions

Air density ρ	1.23 kg/m ³
Sampling frequency	625 Hz
Data length	10 s
Vertical displacement h	0.02×sin(2π×2.5t) m
Torsional displacement α	0.03×sin(2π×2.5t) rad

Table 2: Verification of MS-RFA method (Comparison of RFA coefficients)

	Flat plate				Rectangular cross section			
	Original		MS-RFA result		Original		MS-RFA result	
A_0	-0.3273	-6.2384	-0.3052	-6.2851	-0.0618	-7.9085	0.9917	-7.8894
	-0.097	1.3818	-0.1067	1.4012	-0.0387	-0.6258	0.0312	-0.7499
A_1	-3.7549	-1.4947	-3.7549	-1.4947	-0.782	7.3997	-0.7466	7.5402
	0.851	-0.3819	0.8510	-0.3819	-1.7649	-1.0621	-1.7644	-1.0610
F	-0.9484	1.3397	-0.9569	1.3661	-10.461	-5.7309	-9.7240	-5.0258
	0.2689	-0.1682	0.2739	-0.1839	-1.5021	2.9637	-1.4240	2.7457
λ_L	0.1843		0.1839		1.2048		1.1072	
λ_M	0.2239		0.2232		0.7091		0.6877	

known rational function approximation coefficients, and the rational function approximation coefficients are calculated again using the time history. Therefore, it is obvious that the same value as the original coefficient is obtained. However, it can be said that the stability of the present method is shown under the influence of noise simulating actual measurement. On the other hand, generally good reproduction results were obtained even with the rectangular cross section, but in the terms of $(A_0)_{11}$ and $(A_0)_{21}$, the sign was reversed although the absolute value was small, and there was some discrepancy. Figure 1 shows the comparison of flutter derivatives of the rectangular cross section between the original ones and calculation result by the MS-RFA method. $(A_0)_{11}$ and $(A_0)_{21}$ correspond to H_4^* and A_4^* , respectively and both are displacement proportional terms. It was found that an error occurred when calculating the self-excited force time history in Eqs. (9a, b). However, it could not be further improved by adjusting the analytical conditions. Since H_4^* and A_4^* are minor for bridge flutter, it proceeds to the next step using the present algorithm.

$$L_{se} = \frac{1}{2} \rho U^2 B \left\{ \left((A_0)_{11} + (F)_{11} \right) \frac{h}{B} + (A_1)_{11} \frac{\dot{h}}{U} - (F)_{11} \frac{\lambda_L U}{B^2} \int_0^t e^{-\frac{U}{B} \lambda_L (t-\tau)} h(\tau) d\tau \right. \\ \left. + \left((A_0)_{12} + (F)_{12} \right) \alpha + (A_1)_{12} \frac{B}{U} \dot{\alpha} - (F)_{12} \frac{\lambda_L U}{B^2} \int_0^t e^{-\frac{U}{B} \lambda_L (t-\tau)} \alpha(\tau) d\tau \right\} \quad (9a)$$

$$M_{se} = \frac{1}{2} \rho U^2 B^2 \left\{ \left((A_0)_{21} + (F)_{21} \right) \frac{h}{B} + (A_1)_{21} \frac{\dot{h}}{U} - (F)_{21} \frac{\lambda_L U}{B^2} \int_0^t e^{-\frac{U}{B} \lambda_M (t-\tau)} h(\tau) d\tau \right. \\ \left. + \left((A_0)_{22} + (F)_{22} \right) \alpha + (A_1)_{22} \frac{B}{U} \dot{\alpha} - (F)_{22} \frac{\lambda_M U}{B^2} \int_0^t e^{-\frac{U}{B} \lambda_M (t-\tau)} \alpha(\tau) d\tau \right\} \quad (9b)$$

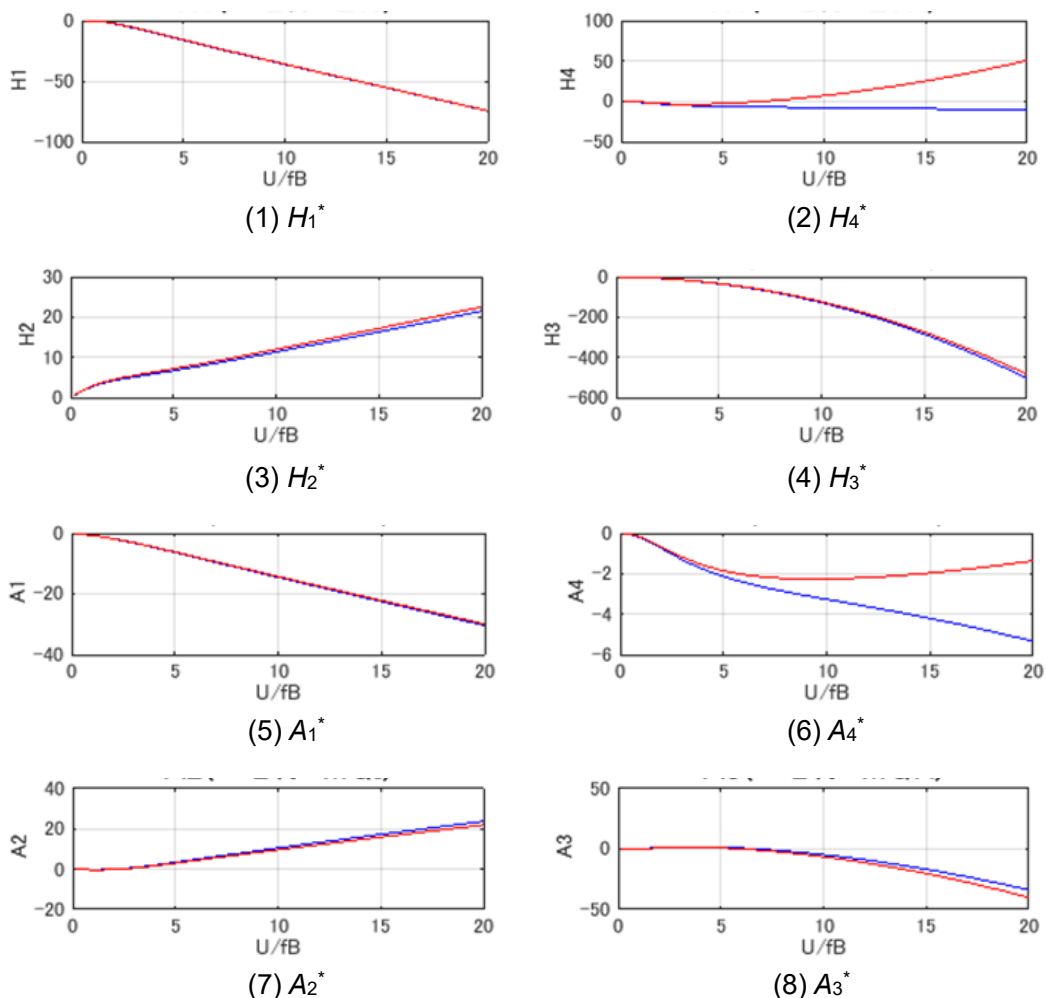


Figure 1: Comparison of flutter derivatives before and after applying the MS-RFA method (rectangular cross section) (Blue line: original, red line: MS-RFA method)

4 Verification with truss cross section and influence of wind speed step

In this section, using the truss section (see Fig. 2) for which the flutter derivative was identified by a free vibration method (Yamada et al., 1996) in the past study (Kusuhara et al., 2016), the applicability of the MS-RFA method is examined in the same manner as in the previous section. In addition, the influence of the wind speed level (magnitude of wind speed) and the step number of wind speed at which the MS-RFA method is applied are examined.

First, a free vibration displacement time history measured when the flutter derivative was identified was used for the input displacement signal. Incidentally, the measured free vibration signal was sampled at the frequency of 100Hz. Using the 2nd-order spline curve interpolation, the signal was adjusted with the sampling frequency of 625Hz, which is the same as one in Section 3. Next, using the flutter derivatives identified by the free vibration

method, a self-excited force time history was created by Eqs. (7a, b). Further, the wind speed of the time-history signal used was 3.65 m/s ($U/fB = 3.0$) and 9.63 m/s ($U/fB = 7.8$) where two wind speed steps were used, same as that in Cao et al. (2012). Rational function approximation coefficient and flutter derivative were calculated by the MS-RFA method.

Figure 3 shows the comparison of flutter derivatives identified by the free vibration method and MS-RFA method. As described later, Figure 3 shows the result by the wind speed level and step such that an error between the original flutter derivative and calculated one by the MS-RFA method is smallest. Although A_2^* shows a very good match, the difference is larger in H_2^* , H_3^* and A_4^* .

Next, the influence of the number of wind speed steps and the wind speed level of the time history data in the MS-RFA method on the calculated flutter derivative was examined. In this method, the rational function approximation coefficient (flutter derivative) is determined by the least square method as shown in Eq. (1). However, when viewed in the frequency domain, it is expected that the results will differ depending on the wind speed level and wind speed step number used in the calculation although Cao et al. (2012) concluded that two wind speed steps are sufficient. Figure 4 shows the result of the torsional damping related term and two coupling terms (H_1^* , A_2^* and A_3^*) for (1) one wind speed ($U/fB = 4.8$), (2) two wind speeds ($U/fB = 3.0$ and 4.8) and (3) three wind speeds ($U/fB = 3.0, 4.8$ and 7.8). From this, it can be seen that the influence on A_2^* and A_3^* is large, and the degree of reproduction is lower when the wind speed step number is three rather than two. The effects of the number of wind speed steps and wind speed level need to be further studied in the future.

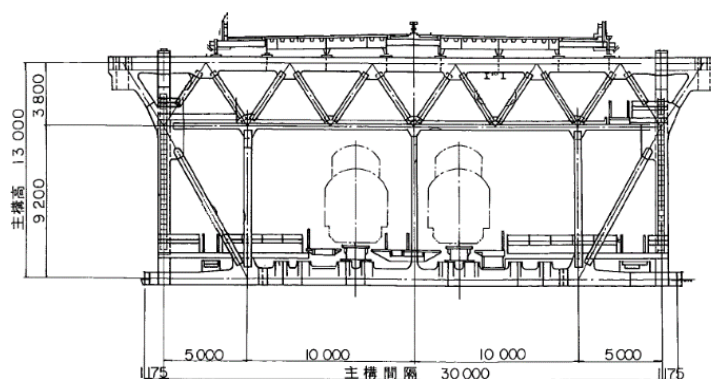


Figure 2: Truss cross section used

Table 2: Calculation parameters

Air density ρ	1.23 kg/m ³
Width B	0.375 m
Height D	0.1625 m
Sampling frequency f	625 Hz
Data length	10 s
Wind speed	3.65 m/s and 9.63 m/s
Vertical frequency	1.87 Hz
Torsional frequency	3.30 Hz

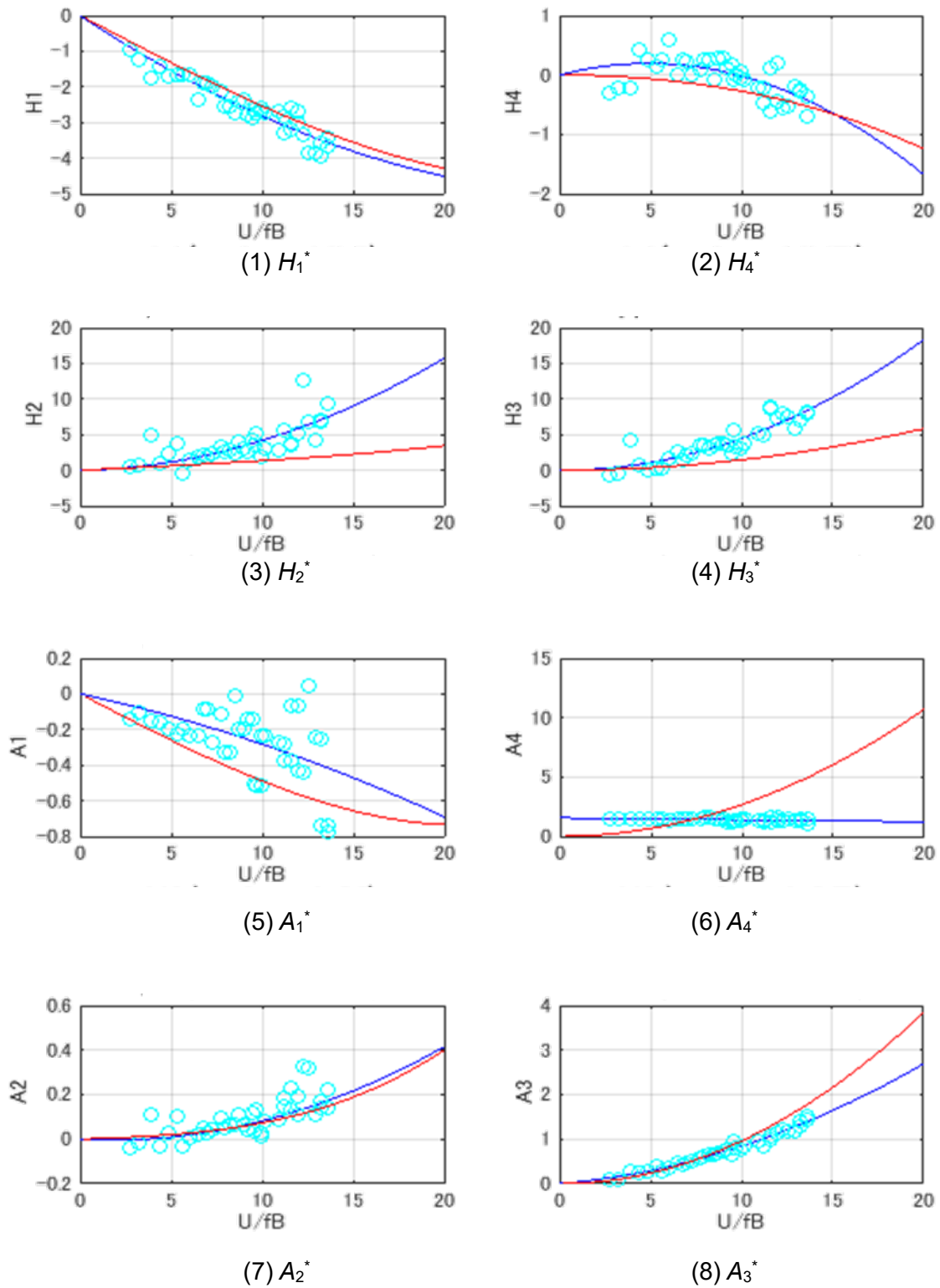


Figure 3: Reproduction of flutter derivatives by MS-RFA method (truss section)
 (○: free vibration method, blue line: regression curve of ○, red line: MS-RFA method)

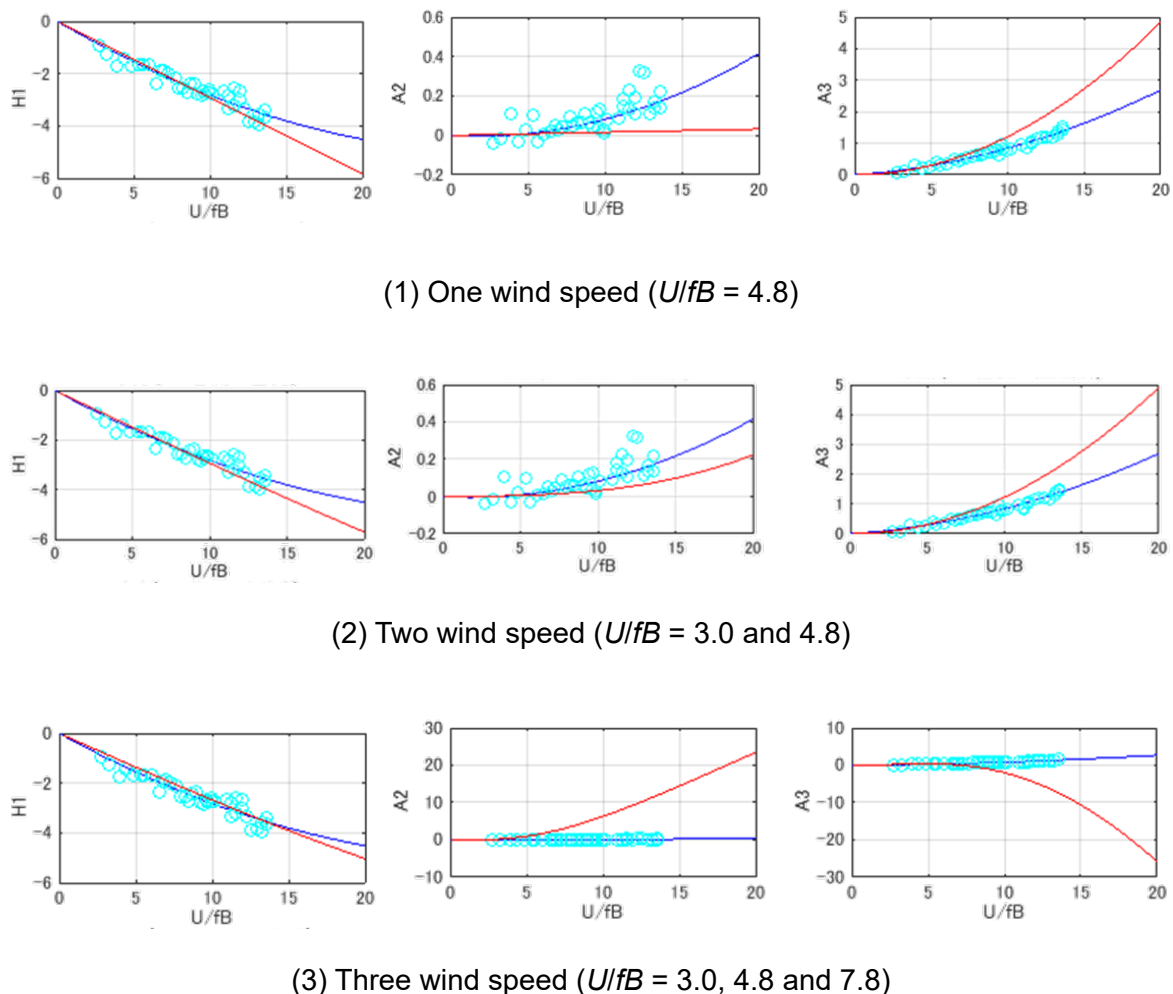


Figure 4: Reproduction of flutter derivatives by MS-RFA method (influence of wind speed step) (○: flutter derivatives identified by free vibration method, blue line: regression curve of ○, red line: flutter derivatives by MS-RFA method)

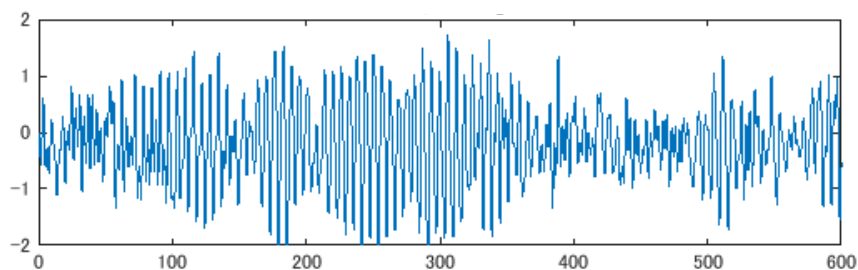
5 Time-history analysis with rational function approximation

In order to investigate the efficiency of the rational function approximation in the time-history analysis, a time-history analysis using the rational function approximation coefficients obtained in the last section was demonstrated. The time-history analysis was performed for the truss section in Figure 2 with the rational function approximation coefficients corresponding to the result in Figure 3 (two wind speed steps) and with parameters shown in Table 3. Not only self-excited force but also quasi-steady buffeting force were considered in the analysis.

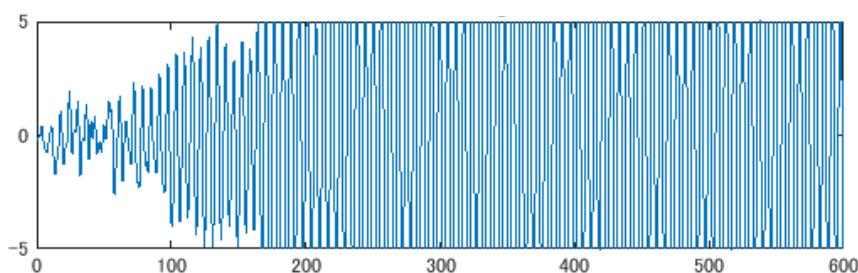
Figure 5 shows torsional response at wind speeds of 100 m/s and 120 m/s. The case at 100 m/s did not show any apparent divergent trend while the case at 120 m/s showed rapid divergent trend. Wind-tunnel test of this bridge at the design stage confirmed that flutter did not occur up to 100 m/s. In this regard, this time-history analysis gave a reasonable result and usefulness of the rational function approximation method.

Table 3 Analytical conditions in time-history analysis

Deck width	B	30.0 m
Deck height	D	13.0 m
Air density	ρ	1.23 kg/m ³
Time step	Δt	0.2 s
1st vertical frequency	f_h	0.166 Hz
1st torsional frequency	f_α	0.329 Hz
Vertical damping ratio	ξ_h	0.03/2 π
Torsional damping ratio	ξ_α	0.03/2 π
Mass per unit length	m	40.63×10 ³ kg/m
Polar moment of inertia per unit length	I	7,630×10 ³ kgm ² /m



(1) Wind speed of 100 m/s



(2) Wind speed of 120 m/s

Figure 5: Torsional response before (left) and after (right) flutter onset

6 Conclusions

This study reproduces the technique for directly identifying the flutter derivative in the time domain (MS-RFA method) proposed in the previous study by numerical simulation and verifies its applicability. In addition, its applicability for a truss cross section and the influence of calculation parameters were examined. As a result, the applicability for the flat plate section ($B/D = 15$) and the rectangular cross-section ($B/D = 5$) was confirmed as with previous studies. For the truss cross section, a very good match for A_2^* was confirmed while difference in H_2^* , H_3^* and A_4^* increased. Also, the wind speed steps used in the analysis

influenced the result for A_2^* and A_3^* and three wind speed steps lowered the reproducibility compared with two wind speed steps. The influence of the number of wind speed steps and the wind speed level is considered to depend on the cross-sectional shape, so further study is necessary in the future.

References

- Bochao, Cao and Partha, P. Sarkar, Identification of rational functions using two-degree-of-freedom model by forced vibration method, *Engineering Structures*, 43, pp.21-30, 2012.
- Karpel, M., Design for active flutter suppression and gust alleviation using state-space aeroelastic modeling, *J. Aircraft*, 19(3), pp.221-227, 1982.
- Simiu, E. and Scanlan, R., *Wind effects on structures*, Third edition, Wiley, 1996.
- Hitoshi Yamada, Toshio Miyata, Three dimensional unsteady aerodynamic force measurement by the modal decomposition and reassemblage method, *J. of Structural Engineering/Earthquake Engineering, JSCE*, No. 543/I-36, pp. 209-216, 1996.
- Shigeki Kusahara, Hiroshi Katsuchi, Masashi Naito, Akira Yamane, Yo Machida, Aerodynamic stability of Seto Ohashi Bridge at maintenance stage, *Proceedings of the 24th Symposium on Wind Engineering, Japan Society of Wind Engineering*, pp.181-186, 2016.

Flutter stabilization of super long span suspension bridges with aerodynamic countermeasures

Yaojun Ge¹, Yongxin Yang², Lin Zhao² and Fengchan Cao²

¹SLDRCE, Tongji University, Shanghai, China, yaojunge@tongji.edu.cn

²SLDRCE, Tongji University, Shanghai, China

Abstract

Long span suspension bridges have experienced aerodynamic flutter stabilization with adopting vertical stabilizer, slotted or twin box girder and their combination. With the happening and potential increase of span length, suspension bridges with super long span have been facing more challenging in aerodynamic flutter. The challenging stabilization for super long span suspension bridges has been introduced with some new attempts, including horizontal stabilizers, combination of horizontal and vertical stabilizers, optimization of twin box girder and widely slotted box girder or narrowly slotted box girder with stabilizers. The horizontal stabilizers on both sides of box girder can improve the flutter critical speed about 39%, and the further improvement of 8% can be realized with the combination of the horizontal and vertical stabilizers. There is still a room to optimize slot width and shape and girder depth for 2,000m spanned suspension bridges, and the widely slotted girder may provide 5,000m suspension bridge with high enough flutter critical speed after further study.

Keyword: Flutter stabilization, suspension bridge, super long span, aerodynamic countermeasure, horizontal stabilizer, twin box

1 Introduction

Modern suspension bridges originated from rattan chain and later iron chain supported bridges in China in ancient time have experienced a considerable development since Brooklyn Bridge with a span length of 486m in 1883. It took about 48 years for the span length of suspension bridges to jump to 1,067m of George Washington Bridge in 1931, as the first bridge with a span length over 1,000m. Although the further increase in the next 50 years was not so large in Humber Bridge of 1,410m in 1981, the new stiffening girder, orthotropic steel box girder, replaced the traditional steel truss girder. The latest span length record has been hold by 1,991m Akashi Kaikyo Bridge with truss girder built in 1998 and 1,650m Xihoumen Bridge with box girder in 2009 (Ge, 2016).

Ten longest-span suspension bridges completed in the world are listed in Table 1, including five in China and one in Japan, Denmark, Turkey, Korea and UK, respectively. Among these ten suspension bridges, seven of them have encountered aerodynamic problems including five in flutter and two in vortex induced vibration (VIV). Both Great Belt Bridge and the 4th Nanjing Bridge have simply used guide vanes to improve VIV, and the other five bridges suffered in flutter have adopted three kinds of control measures, including vertical stabilizer (Runyang Bridge), slotted or twin box girder (Xihoumen Bridge, Yi Sun-sen Bridge and Tsing Ma Bridge) and their combination (Akashi Kaikyo Bridge) (Ge, 2019).

Table 1: Ten longest-span suspension bridges

No.	Bridge Name	Span (m)	Girder	Problem	Control	Country	Year
1	Akashi Kaikyo	1991	Truss	flutter	slot/stabilizer	Japan	1998
2	Xihoumen Bridge	1650	box	flutter	slot	China	2009
3	Great Belt Bridge	1624	Box	vortex	guide vane	Denmark	1998
4	Osman Gazi Bridge	1550	Box	none	no	Turkey	2016
5	Yi Sun-sen Bridge	1545	Box	flutter	slot	Korea	2012
6	Runyang Bridge	1490	Box	flutter	stabilizer	China	2005
7	4th Nanjing Bridge	1418	Box	vortex	guide vane	China	2012
8	Humber Bridge	1410	Box	none	no	UK	1981
9	Jiangyin Bridge	1385	Box	none	no	China	1999
10	Tsing Ma Bridge	1377	Box	flutter	slot	China	1999

With the ever-growing span length, suspension bridges are becoming lighter, more flexible, and lower damping, which result in more sensitive to wind actions, in particular, aerodynamic flutter instability. After three successful aerodynamic stabilizations for long-span suspension bridges are reviewed, this paper presents the current flutter stabilization studies on five box-girder suspension bridges with a super long span from 1,666m to 2,016m even further to 5,000m listed in Table 2 (Ge, 2017b).

Table 2: Five suspension bridges with super long span

Order	Bridge Name	Span (m)	Girder	Problem	Country	Plane
1	Lingding Bridge	1666m	Box	Flutter	China	Construction
2	2nd Humen Bridge	1688m	Box	Flutter	China	Completed
3	Shuangyumen Bridge	1708m	Box	Flutter	China	Design
4	Sunda Strait Bridge	2016m	Box	Flutter	Indonesia	Feasibility
5	Taiwan Strait Bridge	5000m	Box	Flutter	China	Proposal

2 Horizontal stabilizers and their combination with vertical stabilizers

Recently, China has launched two long-span suspension bridges with wide box girder for eight traffic lanes, including the 2nd Humen Bridge with the main span of 1,688 m under the required flutter speed of 63.3 m/s and the 1,666 m spanned Lingding Channel Bridge with the required flutter speed of 83.7 m/s. The original box girder is 44.7 m wide and 4 m deep shown in Figure 1, and the wind tunnel tests have confirmed the minimum critical flutter speed of 55.7 m/s, which is much smaller than the requirements (Ge, 2017a).

2.1 Horizontal stabilizers

In order to improve flutter stability of the 2nd Humen Bridge, two kinds of horizontal

stabilizers (HS), 1.5m and 2.5m wide, have been studied through wind tunnel tests. The experimental results of critical flutter speeds through the sectional model (SM) and the full model (FM) testing are summarized for these three cross section girders, including 0m, 1.5m and 2.5m wide horizontal stabilizers, in Table 3. Although the critical flutter speeds of the full model testing are smaller than those of the sectional model testing, the horizontal stabilizers with 2.5m width can meet with the required flutter checking speed of 63.3m/s. The single box girder with 2.5m wide horizontal stabilizers has been finally selected as the proposed scheme (Ge et al., 2015).

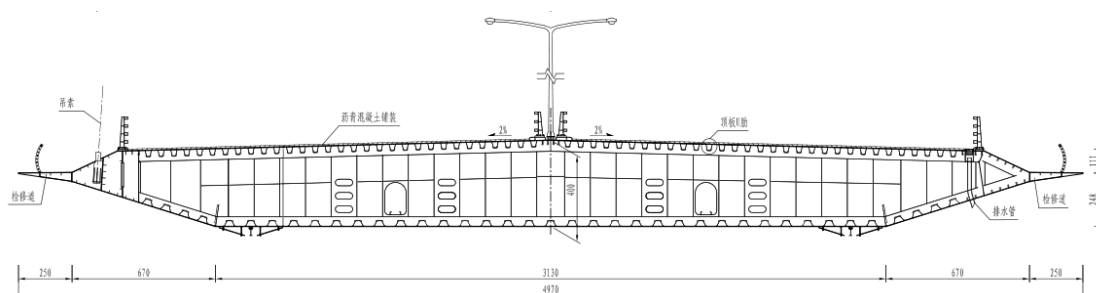


Figure 1: Single box girder with horizontal stabilizers (unit: cm)

Table 3: Critical flutter speeds of the 2nd Humen Bridge

HS Width	Testing	Critical flutter speed (m/s)			Min	Required (m/s)
		-3°	0°	+3°		
0.0 m	SM	83.5	56.7	55.7	55.7	63.3
1.5 m	SM	83.5	76.0	58.6	58.6	63.3
2.5 m	SM	77.7	77.9	82.5	77.7	63.3
2.5 m	FM	76.2	71.7	70.7	70.7	63.3

2.2 Horizontal and vertical stabilizers combination

For further improvement in Lingding Channel Bridge, three more kinds of vertical stabilizers, including up, down and the combination vertical stabilizers, have been tried with different heights. The critical flutter speeds due to the sectional model tests are summarized for three combinations of horizontal and vertical stabilizers, including 1.2m up, 0.8m down and 1.2m up plus 0.8m down vertical stabilizers, in Table 4. Although the minimum critical flutter speed of the last combination scheme is 84.0m/s, which is greater than the requirement of 83.7m/s, the safety margin is not large enough to overcome the difference between sectional model testing and full model testing. The depth of the single box girder has been proposed to increase from 4m to 5m, and the minimum critical flutter speed has been raised up to 87m/s. It is necessary to confirm this result by full aeroelastic model testing in the next step (Ge et al., 2018a).

Table 4: Critical flutter speeds of Lingding Channel Bridge

Vertical stabilizer		Critical flutter speed (m/s)			Required	
Up	Down	-3°	0°	+3°	Min	(m/s)
No	No	77.7	77.9	82.5	77.7	83.7
1.2 m	No	83.0	90.0	83.5	83.5	83.7
No	0.8 m	80.5	82.9	81.7	81.7	83.7
1.2 m	0.8 m	87.5	92.5	84.0	84.0	83.7

3 Optimization of slotted or twin box girders

With the increase of span length and required flutter checking speed of suspension bridges, vertical stabilizer, horizontal stabilizers and their combinations mounted on single box girder may not be enough to guarantee aerodynamic flutter stability, and slotted or twin box girder could be a better choice. In order to further optimize the twin box girders used in Xihoumen Bridge and Yi Sun-sen Bridge, two proposed super-long span suspension bridges, Shuangyumen Bridge in China and Sunda Strait Bridge in Indonesia, are discussed with the emphasis on twin box girder optimization.

3.1 Optimization of slot width and shape

Located in the Zhoushan Archipelago in China, Shuangyumen Bridge was preliminarily designed as a suspension bridge with a single span of 1,708m and a deck width for only 4 traffic lanes. Due to the adverse wind environment at the bridge site, the required flutter checking speed is 80m/s, and two possible girder schemes were proposed, single box girder with the combination of vertical and horizontal stabilizers and twin box girder, shown in Figure 2.

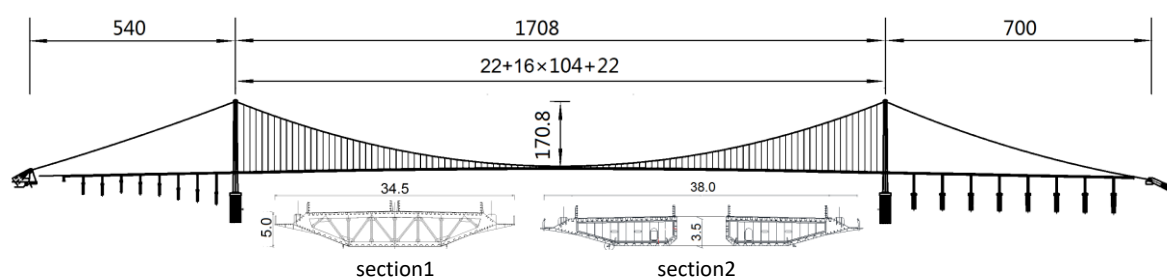


Figure 2: General layout and alternative box girders of Shuangyumen Bridge

As far as flutter performance is concerned, twin box girder is a better solution compared with single box girder even with the combination of vertical and horizontal stabilizers. In this investigation, the slot width ratio, b/B , and the chamfering size, hxd , of the inner corner were selected as two optimization parameters shown in Figure 3, the results from sectional model wind tunnel tests are listed in Table 5. The flutter performance is improved by the increasing of slot width ratio as the chamfering size of inner corner is fixed to $hxd = 0.9 \times 0.9\text{m}$, while the enlarging of inner corner chamfering will also increase the flutter critical wind speed. All five cases have critical wind speed higher than 89.6m/s, which suggests that central slot has

certain superiority in flutter control domain (Ge et al., 2016b).

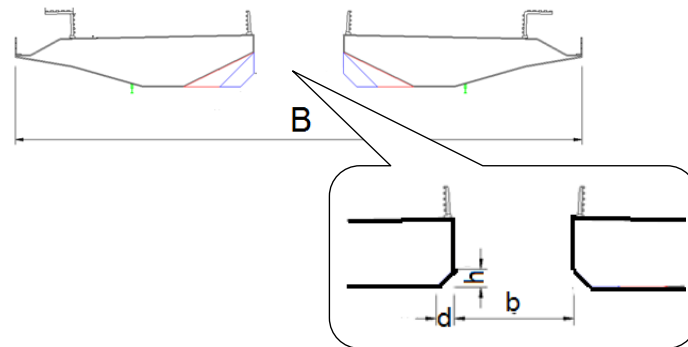


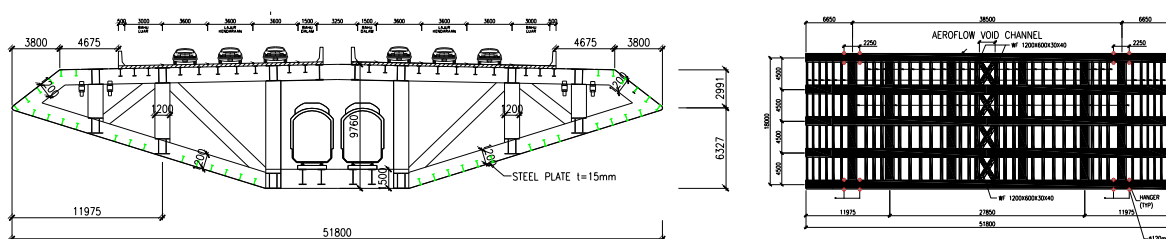
Figure 3: Twin box girder with slot width of b and slot shape of hxd

Table 5: Critical flutter speeds of Shuangyumen Bridge

b / B	$h \times d$	Critical flutter speed (m/s)			Required	
		-3°	0°	$+3^\circ$	Min	(m/s)
5 / 37	0.9×0.9	89.6	>100	>100	89.6	89.6
5.5 / 37.5	0.9×0.9	91.8	>100	>100	91.8	89.6
6 / 38	0.9×0.9	92.4	>100	>100	92.4	89.6
6 / 38	2.3×2.3	94.1	>100	>100	94.1	89.6
6 / 38	4.7×2.3	95.2	>100	>100	95.2	89.6

3.2 Optimization of girder depth and slot width

As a main part of the Trans Asian & Asean Highway and Railway in Indonesia, Sunda Strait Bridge linking Sumatra Island and Java Island is planned as a super-long span suspension bridge with the span arrangement of 792+2016+792m and the cable sag to span ratio of 1/10. In the conceptual design stage, there are two stiffening girder design schemes provided by the designers, that is, the deep twin box girder and the shallow twin box girder in Figure 4. The deep twin box girder is 51.8m wide and 9.76m deep with a central slot of 2.25m, and the shallow one is 60.35m wide and 5.8m deep with a slot of 10.8m. The ventilation ratios of these two girders can be calculated by dividing net slot area by total slot area, and have the values of 31% in the deep scheme and 53% in the shallow scheme, respectively, which are very important to aerodynamic flutter stability.



a) Deep twin box girder

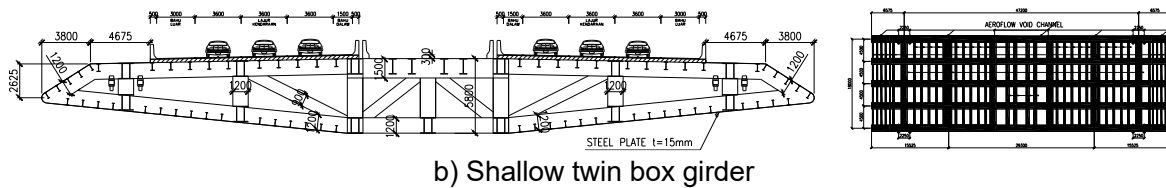


Figure 4: Stiffening girder of Sunda Strait Bridge (Unit: mm)

The experimental results of the flutter critical speeds under different angles of attack are listed and compared in Table 6. The minimum flutter critical speed is 82m/s for the deep twin box girder scheme and 93m/s for the shallow twin box girder scheme, respectively. Since the flutter checking speed of Sunda Strait Bridge is set to 93m/s, the aerodynamic flutter stability performance of both design schemes may need to be further improved in the next design stage. It is suggested that the further improvement can be realized by either increasing the width or ventilation ratio of central slot or adopting additional central stabilizer like the combination of stabilizer and slot in Akashi Kaikyo Bridge (Zhou et al., 2018).

Table 6: Critical flutter speeds of Sunda Strait Bridge

Stiffening girder	Critical flutter speed (m/s)			Required	
	-3°	0°	+3°	Min	(m/s)
Deep twin box girder	84	87	82	82	93
Shallow twin box girder	93	108	113	93	93

4 Widely slotted twin box girder

As a long-time dream and an engineering challenge, the technology of bridging larger obstacles has entered into a new era of crossing wider sea straits. One of the most interesting challenges has been identified as bridge span length limitation, in particular the span limits of suspension bridges as a bridge type with potential longest span. The dominant concerns of super long-span bridges to bridge designers are basically technological feasibility and aerodynamic considerations. With the emphasis on aerodynamic stabilization for longer span length, a typical three-span suspension bridge with a 5,000m central span and two 1,600m side spans as well as a cable sag of f or $n = f/L$ is considered as the limitation of span length for Taiwan Strait as shown in Figure 5 (Ge, 2011).

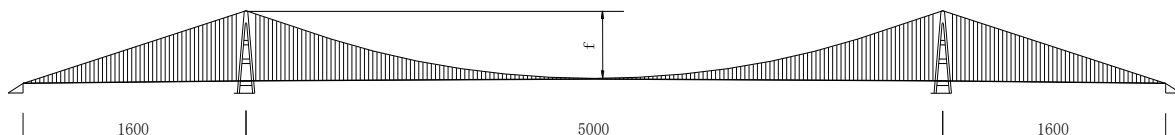


Figure 5: Span arrangement of Taiwan Strait Bridge (Unit: m)

4.1 Sectional model wind tunnel testing

With considering aerodynamic stabilization for super-long span, two kinds of generic twin box girders, namely widely slotted girder (WSG) without any stabilizers (Figure 6a) and narrowly slotted girder (NSG) with vertical and horizontal stabilizers (Figure 6b), were proposed and investigated through sectional model wind tunnel testing. The WSG cross section has a total deck width of 80m including a wide slot of 40m and four main cables for a 5,000m-span suspension bridge while the NSG provides a narrower deck solution of 50m including a narrow slot of 14m and two main cables (Ge, 2011).

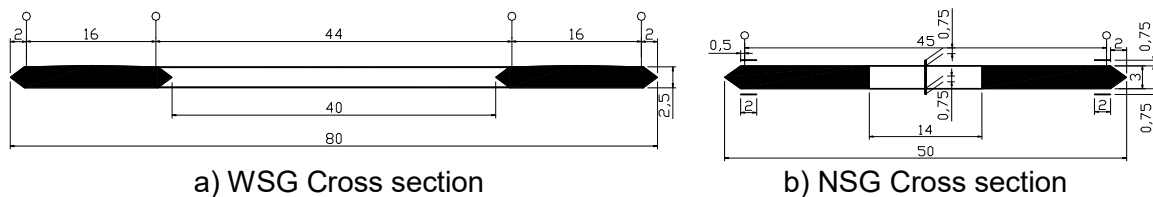


Figure 6: Stiffening girders of Taiwan Strait Bridge (Unit: m)

The results of critical flutter speeds at the attack angle of 0 degree are summarized in Table 7. For both twin box girders the critical flutter speed increases with the decrease of the cable sag ratio n , although the frequency ratio of torsion to vertical bending slightly decreases. The most important reason is the considerable increase of the generalized properties in the aerodynamic stability analysis. The minimum critical wind speeds for the WSG and NSG sections are 82.9 m/s and 74.7 m/s, respectively (Ge, 2011).

Table 7: Critical flutter speeds based on sectional model testing

Ratio $n = f/L$	Bending (Hz)		Torsion (Hz)		Critical speed (m/s)	
	WSG	NSG	WSG	NSG	WSG	NSG
1/8	0.0596	0.0594	0.0709	0.0907	82.9	74.7
1/9	0.0613	0.0612	0.0721	0.0893	88.8	77.4
1/10	0.0622	0.0620	0.0727	0.0865	90.9	78.9
1/11	0.0624	0.0622	0.0727	0.0840	98.9	82.7

4.2 Full aeroelastic model wind tunnel testing

In order to verify the sectional model testing results, a full-bridge aeroelastic model of a feasible suspension bridge with the span arrangement of 2,000m+5,000m+2,000m was designed and manufactured with the geometrical scale of 1:620, and the wind tunnel testing was carried out under smooth flow and the turbulent flow with different angles of attack in the TJ-3 Boundary Layer Wind Tunnel, which is 15m wide, 2m high and 14m long, shown in Figure 7 (Ge et al., 2018b).



Figure 7: Full aeroelastic model of Taiwan Strait Bridge

Table 8 shows the critical flutter speeds under different attack angles and flow conditions. It was found that there is a big difference in critical flutter speed between the proposed slotted twin box girder and the corresponding slot sealed girder, which verifies the necessity of adopting a widely slotted twin box girder in this super-long suspension bridge. Among three different angles of attack under smooth flow, the critical flutter speed has the maximum value of 80.9 m/s at the -3 degree angle of attack and the minimum value of 51.4m/s at 3 degree. Although the buffeting response in turbulent flow is quite small, on-coming turbulence does influence the critical flutter speed in unfavorable ways (Ge et al., 2018b).

Table 8: Critical flutter speeds based on full aeroelastic model testing

Stiffening Girder	Testing Flow	Critical flutter speed (m/s)			
		-3°	0°	+3°	Min
Slot sealed	Smooth		31.9		
WSG	Smooth	>80.9	69.2	51.5	51.5
WSG	10% Turbulence	>74.7	69.7	46.1	46.1

5 Conclusions

Long span suspension bridges have experienced aerodynamic flutter since the Tacoma Narrows Bridge failure, and most successful aerodynamic countermeasures are among vertical stabilizer, slotted or twin box girder and their combination to successfully overcome flutter instability in 1990s and 2000s. With the happening and potential increase of span length in 2010s, suspension bridges with super long span have been and are facing more challenging in aerodynamic flutter stabilization. The challenging flutter stabilization for super long span suspension bridges has been introduced with some new attempts, including horizontal stabilizers, combination of horizontal and vertical stabilizers, optimization of twin box girder and widely slotted box girder or narrowly slotted box girder with stabilizers, which have been used or tested in five suspension bridges or design schemes. The horizontal stabilizers on both sides of box girder can improve the flutter critical speed from 55.7m/s to 77.7m/s in the 2nd Humen Bridge, and the further improvement up to 84.0m/s can be realized with the combination of the horizontal and vertical stabilizers in Lingding Channel Bridge. There is still a room to optimize the slot width and shape for flutter stabilization in

Shuangyumen Bridge with a main span of 1,708m and the girder depth for flutter stabilization in Sunda Strait Bridge with a 2,016m span, and the widely slotted girder may provide a 5,000m span length as the aerodynamic limit to a suspension bridge with high enough flutter critical speed after further study.

Acknowledgements

The authors gratefully acknowledge the support for the research work jointly provided by the National Natural Science Foundation of China under the Grants 51778495 and 51978527 and by the Ministry of Science and Technology of China under the Grant SLDRCE19-A-04.

References

- Ge, Y.J., 2011. *Wind Resistance of Long Span Suspension Bridges*. People's Communications Press, Beijing, China.
- Ge, Y.J., Yang, Y.X., Cao, F.C. and Zhao, L., 2015. Study of Aerodynamic Performance of the 2nd Humen Bridge, *Technical Report WT201407*, State Key Laboratory of Disaster Reduction in Civil Engineering at Tongji University (in Chinese).
- Ge, Y.J., 2016a. Aerodynamic challenge and limitation in long-span cable-supported bridges. Proceedings of the 2016 World Congress on Advances in Civil, Environmental, and Materials Research (ACEM16), Jeju Island, Korea.
- Ge, Y.J., Yang, Y.X., Cao, F.C and Zhao, L., 2016b. Study of Aerodynamic Performance of Shuangyumen Bridge, *Technical Report WT201601*, State Key Laboratory of Disaster Reduction in Civil Engineering at Tongji University (in Chinese).
- Ge Y.J., 2017a. Challenge and innovation of long span bridges in China and over the world. Proceedings of the 39th IABSE Symposium – Engineering the Future. Vancouver, Canada.
- Ge, Y.J., 2017b. Aerodynamic stabilization and robustness evaluation of cable-supported bridges. Proceedings of the 9th Asia-Pacific Conference on Wind Engineering (APCWE 9), Auckland, New Zealand.
- Ge, Y.J., Zhao, L., Cao, F.C and Yang, Y.X., 2018a. Study of Aerodynamic Performance of Lingding Channel Bridge, *Technical Report WT201505*, State Key Laboratory of Disaster Reduction in Civil Engineering at Tongji University (in Chinese).
- Ge, Y.J., Xia, J.L., Zhao, L., and Zhao, S.Y., 2018b. Full aeroelastic model testing for examining wind-induced vibration of a 5,000 m spanned suspension bridge. *Frontiers in Built Environment* 4:20.
- Ge, Y.J., 2019. Dynamic and aerodynamic challenges of long span steel bridges. Proceedings of the 12th Pacific Structural Steel Conference (PSSC 2019), Tokyo, Japan.
- Zhou, Z.Y., Song, J.Z., Hu, X.H. and Ge, Y.J., 2018. Sectional Model Testing of Stiffening Girder of Sunda Strait Bridge, *Technical Report WT201506*, State Key Laboratory of Disaster Reduction in Civil Engineering at Tongji University (in Chinese).

VIV and galloping

Effects of small protruding lips of flanges of a diagonal member in a steel truss bridge on aerodynamic vibration

Kazutoshi Matsuda¹, Kusuo Kato², Nade Cao² and Kenta Shigetomi²

¹ *Kyushu Institute of Technology, Kitakyushu, Japan, matsuda@civil.kyutech.ac.jp*

² *Kyushu Institute of Technology, Kitakyushu, Japan*

Abstract

Wind tunnel model configurations were focused in this paper. Small protruding lips of flanges in steel structures have not usually been taken into account when manufacturing wind tunnel test models. Wind tunnel tests were carried out to clarify the effects of small protruding lips of flanges on motion-induced vortex vibration, Kármán vortex-induced vibration and galloping. Spring-supported tests, smoke flow visualizations and measurements of Strouhal number were performed with or without small protruding lips of flanges changing angle of attack. Models were forced-oscillating in smoke flow visualizations. All wind tunnel tests were conducted in a smooth flow. As a result, it was found that it could be very important to model small protruding lips of flanges in steel structures for wind tunnel tests, especially bracing members of long-spanned truss bridges.

Keyword: small protruding lips of flanges, motion-induced vortex vibration, Kármán vortex vibration, wind tunnel tests

1 Introduction

The vortices separated from rectangular cross sections are broadly classified into Kármán vortices and motion-induced vortices (vortices separated from the leading edge) (Komatsu and Kobayashi,1980; Shiraishi and Matsumoto,1983). The former are those that are accompanied by the interferences of two separated shear layers at both the top and bottom surfaces of the structures. The latter are the ones that are shedding separately from the leading edges of the top and bottom surfaces caused by the separated shear layers at the top and bottom surfaces excited alternately due to the vibration of the rectangular cross section. The vibration caused by the latter vortices was found in past wind tunnel tests (Novak,1971; Otsuki et al.,1971). The vibration is known as either motion-induced vortex vibration (Komatsu and Kobayashi,1980; Shiraishi and Matsumoto,1983) or impinging-shear-layer instability (Rockwell and Naudascher,1978; Nakamura et al.,1991; Ohya et al.,1992; Naudascher and Wang, 1993;). The onset wind speed of this vibration depends on the side ratio of the rectangular cross section and this relationship is schematically clarified (Shiraishi and Matsumoto, 1983; Naudasher and Wang, 1993). The mechanisms of the motion-induced vortex vibration of the rectangular section and H-shaped section cylinders are also revealed (Matsumoto et al.,1993; Kubo et al.,1992; Mills et al., 1995; Mills et al.,2003). This research is involved mainly in the motion-induced vortex vibration generated in a bracing member of a real truss bridge in Japan.

In 2009, Ikitsuki Bridge, a truss bridge in Nagasaki Prefecture with a center span length of 400 m, was discovered to have a crack in the diagonal member of the bridge (Nakamura et

al., 2014). The side ratio of the section was $B/D=1.18$ (B : along-wind length, 590mm, D : cross-wind length, 500mm). As a result of a field oscillation measurement, the primary cause of the crack was identified as Kármán vortex vibration. However, another aerodynamic vibration was also observed in the wind speed range lower than the resonance wind speed of the Kármán vortex vibration. Since the Scruton number of the bracing members was estimated to be approximately 2-3, the aerodynamic vibration was initially thought to be motion-induced vortex vibration. The Scruton number is defined as $Sc=2m\delta/(\rho D^2)$, in which m = mass of the structure per length; δ =structural damping (logarithmic decrement) measured in still air; ρ =air density. The generation of motion-induced vortex vibration is considered to be caused by the unification of separated vortices from the leading edge and secondary vortices at the trailing edge (Shiraishi and Matsumoto, 1983). Though motion-induced vortex vibration has been confirmed on rectangular cross sections with side ratios of $B/D=2-8$ according to the results of past wind tunnel tests, there is a little past research on motion-induced vortex vibration on a rectangular cross section of B/D of less than 2. For that reason, wind tunnel tests for $B/D=1.18$ was conducted to simulate the phenomenon in a closed circuit wind tunnel at Kyushu Institute of Technology. A new finding was that the vibration in the bracing member with a rectangular cross section ($B/D=1.18$) of Ikitsuki Bridge generated in the wind speed range of lower than Kármán vortex-induced vibration was suggested to possibly be motion-induced vortex vibration by the experimental results of the spring-supported test, the unsteady aerodynamic lift measurement and the flow visualization (Matsuda et al., 2013, 2015, 2016, 2017).

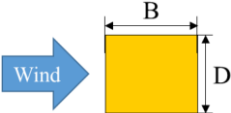
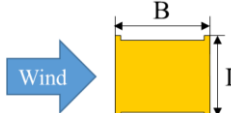
In this paper, the authors focused on the wind tunnel model configuration. Small protruding lips of flanges in steel structures have not been usually taken into consideration when manufacturing wind tunnel test models. Wind tunnel tests were carried out in order to clarify the effects of small protruding lips of flanges in steel structures on motion-induced vortex vibration. Spring-supported tests, smoke flow visualizations and Strouhal number measurement were performed with or without small protruding lips of flanges changing angle of attack. Models were forced-oscillating in smoke flow visualizations. All wind tunnel tests were conducted in a smooth flow.

2 Experimental setup

2.1 Section models

Table 1 shows the dimensional data of the section models, $B/D=1.18$, used in each test. Two cross-sections of a rectangular cross-section and a cross-section with flanges, a reproduction of the cross-section of the cracked bracing member of Ikitsuki Bridge, were used. "Flanges" here means the small protruding lips of the flanges.

Table 1: Section models($B/D=1.18$)

Wind Tunnel Tests	Without Flanges		With Flanges	
				
	B (mm)	D (mm)	B (mm)	D (mm)
Spring-supported Tests	107	90.0	107	90.0
Flow Visualization Tests	47.2	40.0	47.2	40.0

2.2 Spring-supported tests

The spring-supported test was conducted in a closed circuit wind tunnel (cross-section:1.8m high×0.9m wide) at Kyushu Institute of Technology. Table 2 shows the conditions for the spring-supported test. The primary experimental conditions for the model were: mass per unit length=3.32, 3.01 kg/m, natural frequency of heaving vibration=7.30, 7.69 Hz, logarithmic decrement of structural damping=0.0033, 0.0036 and Scruton number=2.23-2.29. Figure 1 shows a photo of the section model installed in the wind tunnel.

Table 2: Spring-supported test conditions

	Without Flanges	With Flanges
Angle of attack, α	3,4,5 deg.	
Mass per unit length, m	3.32 kg/m	3.01 kg/m
Natural frequency, f	7.30 Hz	7.69Hz
Structural damping (in logarithmic decrement), δ	0.0033	0.0036
air density: ρ	1.18-1.20 kg/m ³	1.19-1.20 kg/m ³
Scruton number, $Sc=2m\delta/\rho D^2$	2.25-2.29	2.23-2.25

D : Model height =0.090m, L : Model length=0.768m



Figure 1: Section model for spring-supported tests mounted in Kyushu Institute Technology wind tunnel

2.3 Flow visualization tests

Figure 2 shows the experimental system of the flow visualization tests. Flow visualizations around the model during oscillating times were conducted using a small-sized wind tunnel (0.4m high×0.4m wide) at Kyushu Institute of Technology. It was considered that the wind speeds in the wind tunnel of $V=0.6-1.0$ m/s are good for visualization, so $V=0.6$ m/s was selected. Accordingly, the experimental Reynolds number was $Re=VD/\nu=1.6\times 10^3$. The forced-oscillating non-dimensional amplitudes $2\eta/D$ were selected in accordance with the spring-supported test results. Figures 3 and 4 show the forced oscillation system and the installation status of the model, respectively. Table 3 shows the conditions for the flow field visualization tests.

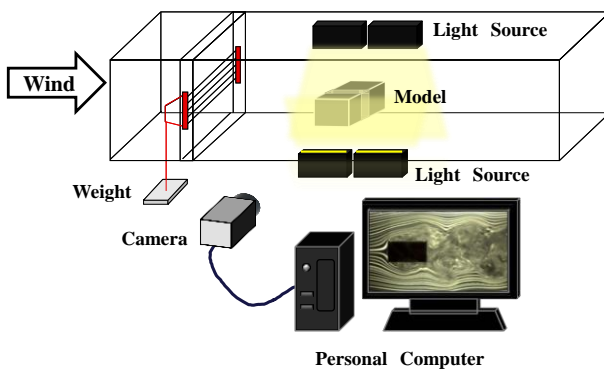


Figure 2: Flow visualization test system

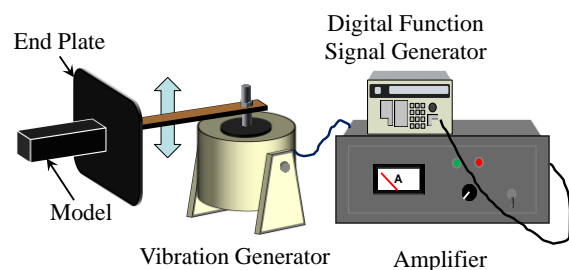


Figure 3: Forced oscillation system for flow visualization tests

Table 3: Flow visualization test conditions

	Wind speed region		
	Motion-induced vortex vibration	Kármán vortex-induced vibration	Galloping
Angle of attack, α	0,3,4,5,10 deg.	0,5,10 deg.	
Wind speed, V	0.6 m/s		
Frequency of forced oscillation method, f	5.0 Hz	1.95, 1.79 Hz	1.07 Hz
Reduced wind speed, $Vr=V/fD$	3.0	7.70, 8.40	14.0
Forced-oscillating non-dimensional amplitudes, $2\eta/D$	0.10	0.10	0.15

D : Model height =0.040m, L : Model length=0.150m

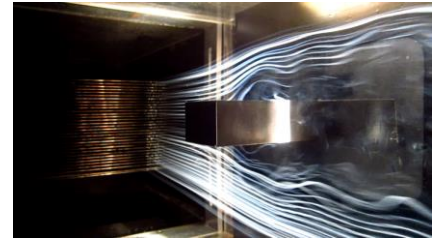


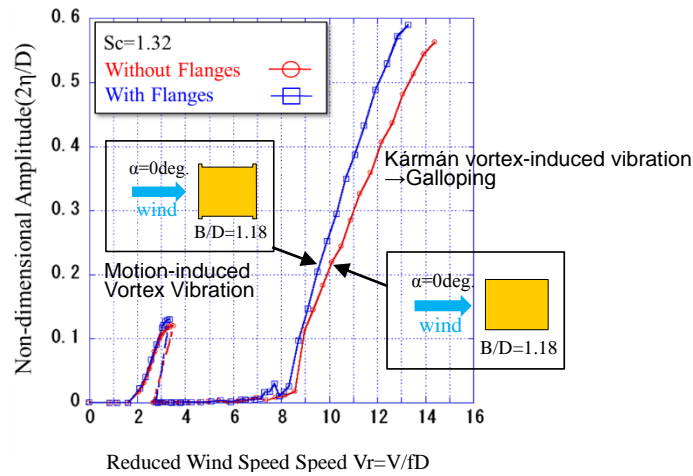
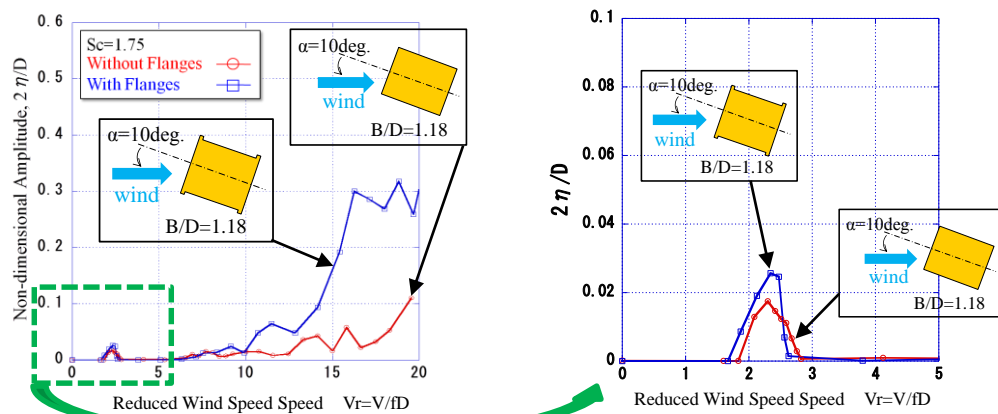
Figure 4: Section model for flow field visualization test

3 Experimental results and discussion

3.1 Spring-supported tests

Figure 5 shows the result of the spring-supported test for an angle of attack of 0 degrees (Matsuda et al., 2013, 2015). Vibrations were confirmed from the neighborhoods of reduced wind speed $Vr=2$ and 8. Because the reduced wind speed at motion-induced vortex vibration is calculated as $Vr=1.67 \times B/D=1.67 \times 1.18=2.0$ (Shiraishi and Matsumoto, 1983), vibrations around $Vr=2$ were considered to be motion-induced vortex vibration. The effects of the existence or non-existence of flanges on the maximum response amplitude of motion-induced vortex vibration are extremely small. However, Figure 6 shows the result of an experiment separately conducted with an angle of attack of 10 degrees that the maximum response amplitude of motion-induced vortex vibration in the case with flanges was approximately 1.5 times larger than that in the case with no flange. Moreover, the responses over the reduced wind speed of $Vr=10$ were quite different. The response of the model with flanges was much larger than without flanges. In other words, it turns out that as the angle of attack becomes larger, the existence or non-existence of flanges tends to exercise an effect on the patterns of the flows around the cross-section.

The Strouhal number measured on the cross-section with flanges was $St=0.124$ (Matsuda et al., 2013). Its inverse number is the critical reduced wind speed of beginning Kármán vortex-induced vibration, $Vr=1/St=8.1$. In other words, a vibration beginning in the neighborhood of a reduced wind speed of 8 can be judged as Kármán vortex-induced vibration. However, from the fact that the Scruton number in this experiment's case was small at $Sc=1.32$, it was found that Kármán vortex-induced vibration was changed to a galloping along with the increase in wind speed. Based on the above experimental results (Matsuda et al., 2013, 2015), additional wind tunnel tests were carried out in order to clarify the effects of rectangular column flanges in this study.


 Figure 5: Spring-supported test result ($\alpha=0$ deg.) (Matsuda et al., 2013, 2015)

 Figure 6: Spring-supported test result ($\alpha=10$ deg.) (Matsuda et al., 2013, 2015)

Figures 7, 8 and 9 show the results of the spring-supported test for angles of attack of 3, 4 and 5 degrees, respectively. The ratios of the response amplitude of motion-induced vortex vibration with flanges compared to without flanges at angles of attack of 3, 4 and 5 degrees were approximately 1.0, 1.2 and 1.6, respectively. The effects of flanges became large when angle of attack became greater than 3-4 degrees. In other words, as the angle of attack becomes larger, the existence or non-existence of flanges tends to have an effect on the patterns of flows around the cross section. On the other hand, the effect of the flange on Kármán vortex-induced vibration and galloping was hardly seen. As will be described later, discussion will be given to these causes based on the flow visualization test results. It was found that it could be very important to model small protruding lips of flanges in steel structures for wind tunnel tests, especially bracing members of long-spanned truss bridges from a wind engineering point of view.

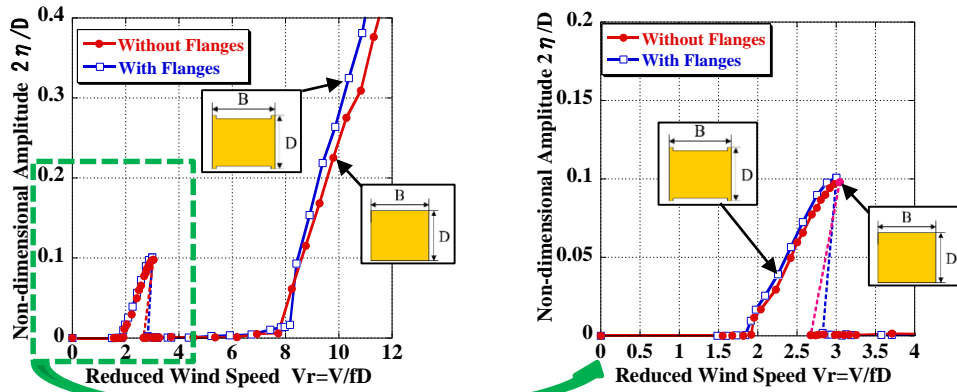


Figure 7: Spring-supported test result ($\alpha=3$ deg.)

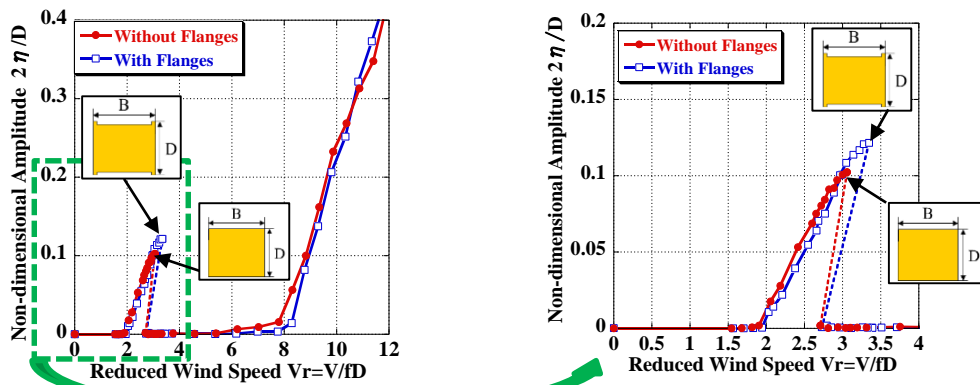


Figure 8: Spring-supported test result ($\alpha=4$ deg.)

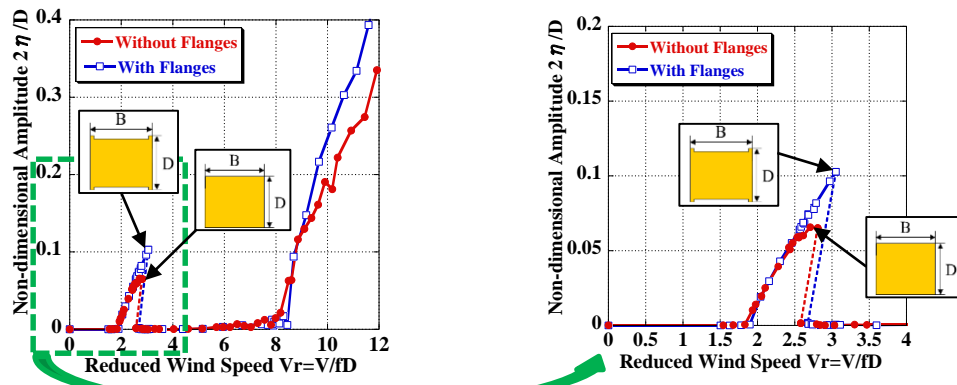


Figure 9: Spring-supported test result ($\alpha=5$ deg.)

3.2 Flow visualization tests

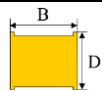
Figure 10 shows the results of flow visualization tests around forced-oscillating rectangular section models of $B/D=1.18$ at the top displacement at the maximum response wind speed of motion-induced vortex vibration. It was confirmed that as the angle of attack becomes larger, the formation of separated vortex from the leading edge on the lower surface of the model with flanges is larger than that without flanges. Generally, it is clear that the pressure tends to decrease in the vicinity of the center of the vortex as compared with the surroundings. Therefore, the larger the separated vortex from the leading edge becomes,

the larger the negative pressure on the lower surface becomes. It is supposed that the exciting force acting on the lower surface becomes larger. The separated vortex from the leading edge gradually separated from the upper surface of the cross sections and flowed downward as the angle of attack became larger.

Results of flow visualization tests around forced-oscillating rectangular section models of $B/D=1.18$ at the top displacement in the wind speed region of Kármán vortex-induced vibration is shown in the upper half of Figure 11. Even if the angle of attack becomes larger, the effects of the existence or non-existence of flanges on the flow pattern around the section model were hardly seen. Table 4 shows measured Strouhal number changing angle of attack. The effects were also not seen in the predominant vortex shedding frequency.

Results of the flow visualization tests around the forced-oscillating rectangular section models of $B/D=1.18$ at the top displacement in the wind speed region of galloping is shown in the lower half of Figure 11. Though the difference of flow patterns under the lower surface of the model between with and without flanges was not recognized at an angle of attack of 0 degrees, a larger flow separation occurs from the leading edge of the lower surface with flanges than that without flanges at an angle of attack of 10 degrees.

Table 4: Measured Strouhal Number $St=fD/V$

Cross Sections	Angle of Attack α (deg.)				
	0	3	4	5	10
	0.120	0.120	0.120	0.120	0.132
	0.121	0.121	0.122	0.122	0.131

4 Conclusions

The findings obtained from this research are as follows:

- (1) Though motion-induced vortex vibration has been confirmed on rectangular cross sections with side ratios of $B/D=2-8$ according to the results of past wind tunnel tests, it was found that the motion-induced vortex vibration were confirmed with a rectangular cross section even with a side ratio of $B/D=1.18$ by experimental results of a spring-supported test and a flow visualization test.
- (2) The effects of small protruding lips of flanges became large when angle of attack became greater than 3-4 degrees. According to smoke flow visualization test results, flow patterns around a model with small protruding lips of flanges were different from those around a model without small protruding lips of flanges.
- (3) It could be very important to model small protruding lips of flanges of rectangular columns in steel structures for wind tunnel tests, especially diagonal members of long-spanned truss bridges from a wind engineering point of view.

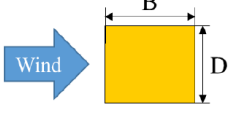
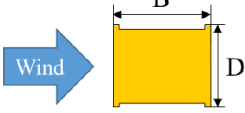
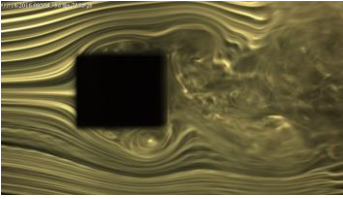
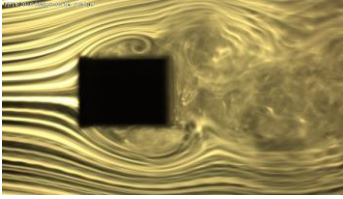
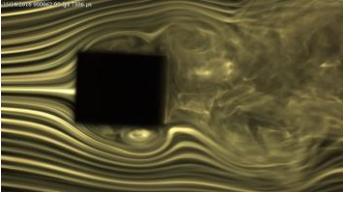
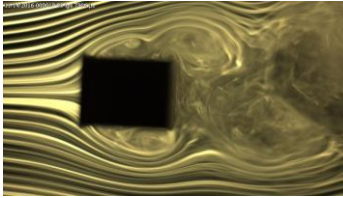
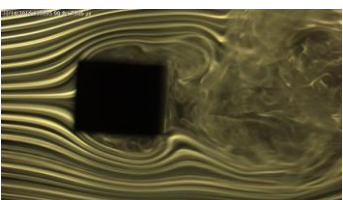
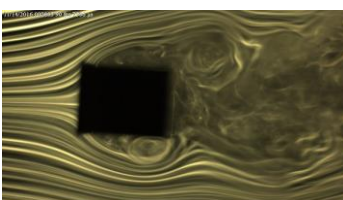
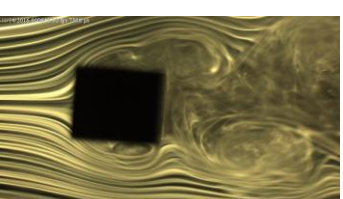
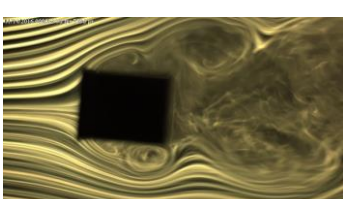
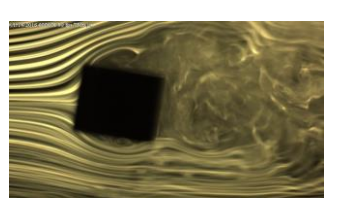
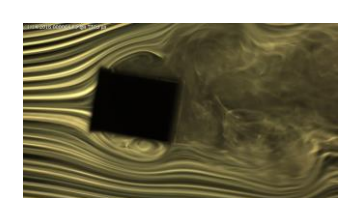
Reduced Wind Speed $V_r = V/fD$	Non-dimensional Forced-Oscillating Amplitude $2\eta/D$	Angle of Attack (deg.)	Without Flanges	With Flanges
				
3.0	0.10	0		
		3		
		4		
		5		
		10		

Figure 10: Results of flow visualization tests around forced-oscillating rectangular section models of $B/D=1.18$ at the top displacement at the maximum response wind speed of motion-induced vortex vibration

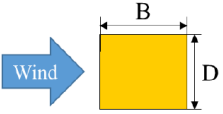
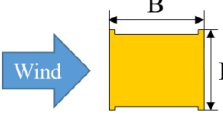
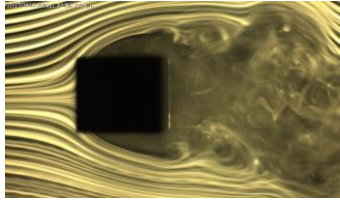
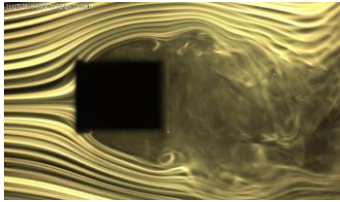
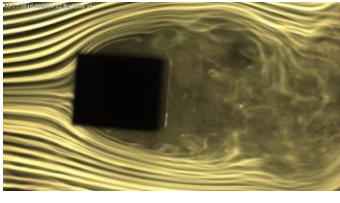
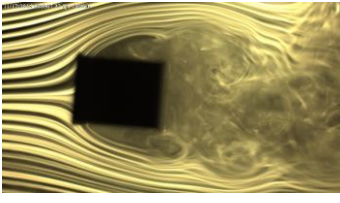
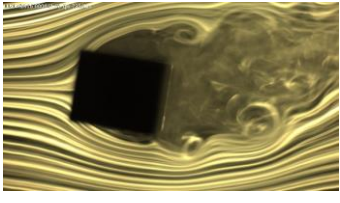
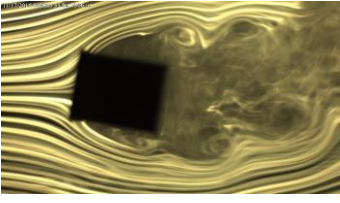
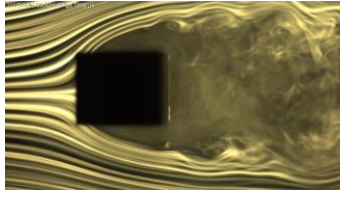
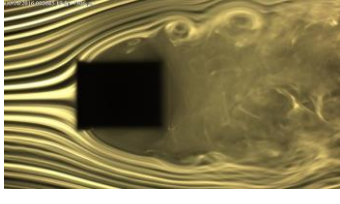
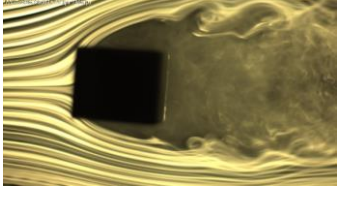
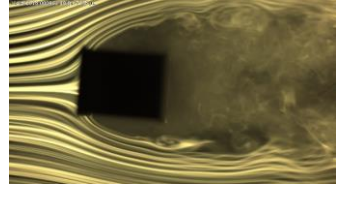
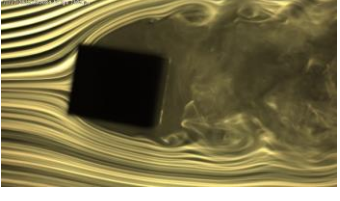
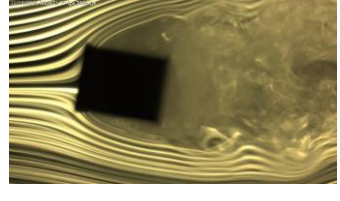
Reduced Wind Speed $V_r = V/fD$	Non-dimensional Forced-Oscillating Amplitude $2\eta/D$	Angle of Attack α (deg.)	Without Flanges	With Flanges
				
$V_r = 8.40$ ($\alpha = 0,5$ deg.) $V_r = 7.70$ ($\alpha = 10$ deg.) Wind speed region of Kármán vortex-induced vibration	0.10	0		
		5		
		10		
$V_r = 14.0$ Wind speed region of Galloping	0.15	0		
		5		
		10		

Figure 11: Results of flow visualization tests around forced-oscillating rectangular section models of $B/D=1.18$ at the top displacement in the wind speed regions of Kármán vortex-induced vibration and galloping

References

- Komatsu, S. and Kobayashi, H. 1980. Vortex-induced oscillation of bluff cylinders, *Journal of Wind Engineering and Industrial Aerodynamics*, Vol.6, 335-362.
- Kubo, Y., Hirata, K. and Mikawa, K., 1992. Mechanism of aerodynamic vibrations of shallow bridge girder sections, *Journal of Wind Engineering and Industrial Aerodynamics*, Vol.41-44, 1297-1308.
- Matsuda, K., Kato, K., Hisadomi, K. and Harada, K., 2013. Low speed instability of two-dimensional rectangular prisms, *Proceedings of the ASME 2013 Pressure Vessels and Piping Conference (PVP2013)*, 97353.
- Matsuda, K., Kato, K., Tamai, Y., Misawa, K. and Ikeda, I., 2015. Experimental Study on Aerodynamic Vibrations of a Bracing Member with a Rectangular Cross Section of The Long-Spanned Truss Bridge, *Proceedings of 14th International Conference on Wind Engineering*.
- Matsuda, K., Kato, K., Tamai, Y. and Suda, K., 2016. Experimental study on aerodynamic vibration of rectangular cross sections having low side ratios, *Proceedings of 8th International Colloquium on Bluff Body Aerodynamics and Applications*.
- Matsuda, K., Kato, K., Arise, K. and Ishii, H., 2017. Study on the Relation between Side Ratios of Rectangular Cross Sections and Secondary Vortices at Trailing Edge in Motion-induced Vortex Vibration, *Proceedings of the ASME 2017 Pressure Vessels & Piping Division Conference (PVP2017)*, 65565.
- Matsumoto, M., Shiraishi, N., Shirato, H., Stoyanoff, S. and Yagi, T., 1993. Mechanism of, and turbulence effect on vortex-induced oscillations for bridge box girders, *Journal of Wind Engineering and Industrial Aerodynamics*, Vol. 49, Issues 1-3, 467-476.
- Mills, R., Sheridan, J., Hourigan, K. and Welsh, M. C., 1995. The mechanism controlling vortex shedding from rectangular bluff bodies, *Proceedings of the twelfth Australasian Fluid Mechanics Conference*, Sydney, 227-230.
- Mills, R., Sheridan, J. and Hourigan, K., 2003. Particle image velocimetry and visualization of natural and forced flow around rectangular cylinders, *Journal of Fluid Mechanics*, Vol. 478, 299-323.
- Nakamura, S., Okumatsu, T., Nishikawa, T. and Okabayashi, T. 2014. A Fatigue Damage of a Diagonal Member in a Steel Truss Bridge Due to Wind-Induced Vibration, *Developments in International Bridge Engineering -Selected Papers from Istanbul Bridge Conference*, 211-220.
- Nakamura, Y., Ohya, Y. and Tsuruta, H., 1991. Experiments on vortex shedding from flat plates with square leading and trailing edge, *Journal of Fluid Mechanics*, Vol. 222, 437-447.
- Naudascher, E. and Wang, Y., 1993. Flow-induced vibrations of prismatic bodies and grids of prisms, *Journal of Fluids and Structures*, Vol.7, 341-373.
- Novak, M., 1971. Galloping and vortex induced oscillations of structures, *Proceedings of the Third International Conference on Wind Effects on Buildings and Structures*, Tokyo, Japan, 799-809.
- Ohya, Y., Nakamura, Y., Ozono, S., Tsuruta, H. and Nakayama, R., 1992. A numerical study of vortex shedding from flat plates with square leading and trailing edges, *Journal of Fluid Mechanics*, Vol. 236, 445-460.
- Otsuki, Y., Washizu, K., Tomizawa, H., Ohya, A. and Fujii, K., 1971. Experiments on the aeroelastic instability of prismatic bars with rectangular sections, *Proceedings of the Third International Conference on Wind Effects on Buildings and Structures*, Tokyo, Japan, 891-898.
- Rockwell, D. and Naudascher, E., 1978. Review- Self-sustaining oscillations of flow past cavities, *Transactions of the ASME, Journal of Fluids Engineering*, Vol.100, 152-165.
- Shiraishi, N. and Matsumoto, M., 1983. On classification of vortex-induced oscillation and its application for bridge structures, *Journal of Wind Engineering and Industrial Aerodynamics*, Vol.14, Nos.1-3, 419-430.

Wake features of a rectangular cylinder undergoing unsteady galloping oscillations in smooth and turbulent flow

Claudio Mannini¹, Tommaso Massai¹

¹ CRIACIV/Department of Civil and Environmental Engineering, University of Florence, Florence, Italy, claudio.mannini@unifi.it

Keyword: galloping, vortex shedding, rectangular cylinder, wake dynamics, flow measurements

For low to medium values of the mass-damping parameter (Scruton number), the transverse galloping instability presents unsteady features that cannot be captured by the classical quasi-steady theory. A prominent unsteady effect is the action of vortex shedding¹. In smooth flow, the main aspects of unsteady galloping are fairly clear. In contrast, the behavior in turbulent flow is more complicated, and several features have not been understood yet². In particular, the delay of the instability onset beyond the vortex-resonance wind speed (U_r) in case of small-scale incoming turbulence (Fig. 1) is a puzzling effect that still requires a sensible explanation.

Furthermore, in a previous paper³ the adaptation of a wake-oscillator model to the unsteady-galloping problem has suggested that the strong nonlinearity of the wake dynamics is essential to reproduce the strong interference between vortex shedding and galloping observed in the experiments. Such an effect may also be responsible for the previously mentioned delay of the galloping onset in turbulent flow. This conjecture is tested in the present work through detailed measurements in the wake of a rectangular cylinder with a side ratio of 1.5 (elastically suspended in the wind tunnel with the short side facing the flow).

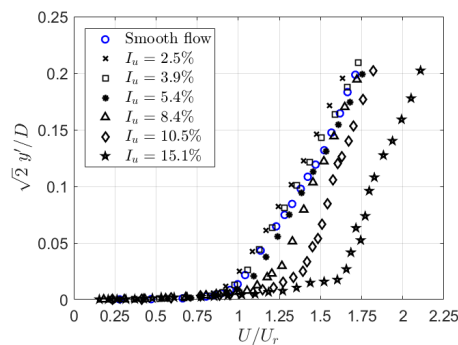


Figure 1: Amplitude-velocity curves recorded in the wind tunnel in small-scale turbulent flow of various intensities (I_u), for a medium value of the mass-damping parameter².

¹ Mannini, C., Marra, A. M., & Bartoli, G. (2014). VIV-galloping instability of rectangular cylinders: Review and new experiments. *Journal of Wind Engineering and Industrial Aerodynamics*, 132, 109-124.

² Mannini, C., Massai, T., & Marra, A. M. (2018). Unsteady galloping of a rectangular cylinder in turbulent flow. *Journal of Wind Engineering and Industrial Aerodynamics*, 173, 210-226.

³ Mannini, C., Massai, T., & Marra, A. M. (2018). Modeling the interference of vortex-induced vibration and galloping for a slender rectangular prism. *Journal of Sound and Vibration*, 419, 493-509.

Assessing maximum amplitude and corresponding frequency for vortex-induced vibrations

Øyvind Mortveit Ellingsen^{1,2}, Xavier Amandolese^{2,3}, Pascal Hémon²

¹ CAPE, CSTB, Nantes, France, oyvind@ladhyx.polytechnique.fr

² LadHyX, CNRS-École Polytechnique, Palaiseau, France

³ LMSSC, CNAM, Paris, France

Abstract

Vortex-induced vibrations can damage structures exposed to cross-flows. The current design estimates of structural amplitude are based on structural nonlinearity but we will here derive a different estimate based on a coupled system with nonlinear fluid forcing. Two estimates of maximum structural amplitude is investigated based on approximations the coupled system and fluid speed at maximum amplitude. Our result shows that both estimates are close to the maximum amplitude found using numerical integration but that the predicted fluid speed differs. With further refinement, the result presented may prove useful in designing structures to withstand vortex-induced vibrations.

Keyword: Vortex-induced vibrations, nonlinear approximation, design estimates, prediction error

1 Introduction

Structures in cross-flow will experience unsteady periodic, loading due to shedding of vortices (Blevins, 2001) that can lead to severe vortex-induced vibrations (VIV). For a designer, there are two useful pieces of information: when vibrations occurs and how severe vibration amplitudes are. These information pieces enables us to find the lifetime of a structure and to design a good tuned-mass damper.

When designing structures to withstand these aerodynamic loads, simple estimates of loading and response reduces the time spent iterating designs. In the Eurocode (2010) and CICIND (2010) building codes, structural excitation due to VIV is modeled using random vibration theory and a simplified structural nonlinearity (Vickery and Basu, 1983). This simplified model is made for the design offices of the early 1980s and often only the maximum response is found.

Another approach in modeling VIV is to couple a structural equation with a nonlinear equation describing or mimicking the vortex forcing. This approach was used Facchinetti et al. (2004) and several other researchers before them (Païdoussis et. al, 2010). A benefit of Facchinetti's model is that it has a simple but powerful coupling between wake and structure. The problem is that it's a set of nonlinear differential equations. This is numerically solvable but work is needed to make it as simple and useful as the current design model.

Why should a designer consider using something other than the existing design model? According to Lupi et al. (2018), it is overly conservative and can be unrealistic for many

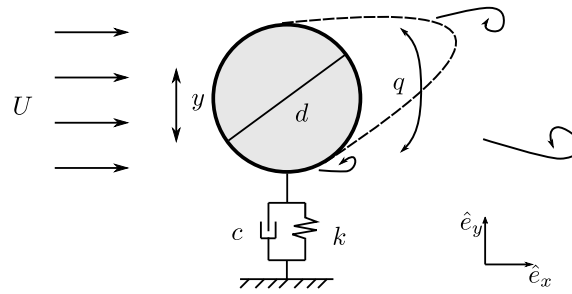


Figure 1 – Sketch of the vortex-induced vibration system

designs. This is partly due to the formulation of the method and the parameters used; their effect is especially prevalent at low Scruton numbers.

We will take steps to address the above concerns by creating a new predictive model that perform better at low Scruton number ($Sc < 10$). Based on an approximation of structural and forcing amplitudes, we will define two approximations of the fluid speed at maximum response. The speed estimates is then plugged back into the amplitude approximates. Amplitude and speed results from both estimates will then be compared with numerical simulations.

2 Vortex-induced vibrations model and approximation

2.1 Model definition

Fig 1 shows a simple system experiencing vortex-induced vibrations. The structure is left free to vibrate in the \hat{e}_y direction and the wake oscillates on it. This has been modeled using a combination of a linear structural oscillator and a nonlinear wake oscillator shown respectively in Eqs. 1 and 2 below

$$\ddot{y} + D\dot{y} + y = \omega_q^2 Mq, \quad (1)$$

$$\ddot{q} + \epsilon(q^2 - 1)\dot{q} + \omega_q^2 q = A\ddot{y}. \quad (2)$$

where the variables y and q are dimensionless. Here, A and ϵ are experimentally determined constants and M is the unsteady lift force, F , scaled by the mass-ratio μ ($M = F/\mu$). The parameters D , F and μ as defined as

$$\mu = \frac{m + 0.25\pi\rho d^2 C_m}{\rho d^2}, \quad (3)$$

$$D = 2\zeta + \frac{C_D}{4\pi\mu St}, \quad (4)$$

$$F = \frac{C_{Lo}}{16\pi^2 St^2}, \quad (5)$$

m is structural mass per unit length, ρ fluid density, d diameter, ζ critical damping ratio and St Strouhal number. C_m , C_D and C_{Lo} are the added mass, mean drag and unsteady lift amplitude coefficients respectively.

One variable is undefined and it's one of the most important: the fluid speed variable ω_q . It's defined as the product of the reduced velocity based on the structure's natural frequency and the Strouhal number ($\omega_q = U_R St$). It is therefore a reduced fluid frequency equivalent to the ratio of shedding frequency to the natural structural frequency.

If we assume that the equations are weakly nonlinear, then they can be approximated. This system can be shown to have the approximate steady-state solutions below when using the method of averaging:

$$r_y(\omega_q, \theta) = 2 \frac{\omega_q^2 M}{D} \left[1 + \frac{\omega_q AM \sin(\theta)}{\epsilon D} (\sin(\theta) - D \cos(\theta)) \right]^{0.5} \sin(\theta), \quad (6)$$

$$0 = \omega_q^2 (1 - AM) - 1 + \omega_q^2 AM \sin^2(\theta) + \left(\frac{D}{\sin(\theta)} + \frac{\omega_q^2 AM}{D} \sin(\theta) \right) \cos(\theta). \quad (7)$$

where r_y is the structural amplitude and θ is the phase difference between q and y , i.e. phase difference between force and motion. Notice that there is no equation for the wake amplitude. As the structural equation and coupling is linear, the equations for wake amplitude can be expressed as a function of phase difference only. This then enables us to write the structural amplitude as a function of phase difference only.

2.2 Amplitude scaling

If we ignore the square root term and the last $\sin \theta$ term in Eq. Eq. 6, we get an equation that depend linearly on the ratio of M to D . If we expand this ratio, we get the scaling relationship

$$r_y \propto \frac{2\pi F}{Sc + 2\pi^2 \zeta + \frac{C_D}{2St}}. \quad (8)$$

where Sc is the Scruton number defined as

$$Sc = \frac{4\pi \zeta m}{\rho d^2}. \quad (9)$$

In words, predicted amplitude is dependent on four parameters: geometry, mass, structural damping and aerodynamics. This differs from some previous notions on maximum amplitude scaling. However, it corroborates the opinion that combining mass and damping into a parameter is arbitrary (Sarpkaya 2004).

2.3 Model validation

To find the amplitude at a given speed, the first step is to find the phase difference using Eq. 7. This may look daunting, but it can be rewritten to a cubic equation. One of the closed form solutions corresponds to the high amplitude VIV response, another to low amplitude and the last to an unstable solution. Only the phase differences between 0 and 180° are used.

A "postcritical Reynolds" experiment with dampers by Belloli et al. (2015) is used for validation and for comparison with the maximum amplitude of the CICIND model (2010). See Tab. 1 for parameters. Fig. 2 shows the comparison and the design code over predict by more than a factor of 2. Our model does well at $\omega_q < 1$ and less well above. The maximum amplitude between experiment and model is similar as is the range of high amplitude vibrations.

Table 1 – Parameters used to compare the approximations and the numerical results.

Case	ϵ	A	γ	F	ζ	d	ρ
Exp.	0.3 [-]	12 [-]	0.479 [-]	0.0401 [-]	0.01200 [-]	0.72 [m]	1.225 [kg/m ³]
Low dam	0.3 [-]	12 [-]	0.442 [-]	0.0401 [-]	0.00191 [-]	2.00 [m]	1.225 [kg/m ³]
High damp	0.3 [-]	12 [-]	0.442 [-]	0.0401 [-]	0.00955 [-]	2.00 [m]	1.225 [kg/m ³]

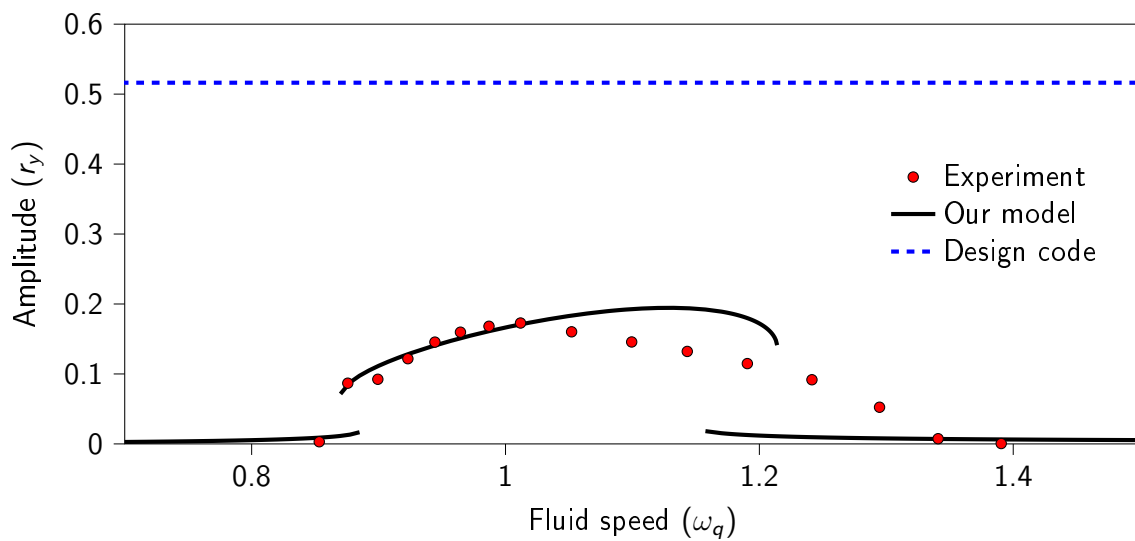


Figure 2 – Comparison of models and experiment of Belloli et al. (2015)

3 Estimates of maximum

3.1 The approximations

Two different approximates of the frequency at maximum amplitude are tested:

$$\omega_{q1} = \frac{1}{1 - \sqrt{AM}}, \quad (10)$$

$$\omega_{q2} = \sqrt{\frac{D(\sin(\theta) - D \cos(\theta))}{AMD \sin(\theta)^3 + AM \cos(\theta) \sin(\theta)^2 + D(1 - AM) \sin(\theta)}}. \quad (11)$$

The first approximate (Eq. 10), dubbed "method 1", is based on the work of de Langre (2006). Our guess is that maximum amplitude corresponds to the upper limit of the linear synchronization definition. In terms of Fig. 2, this corresponds to the start of our rightmost low amplitude solutions. Method 1 is independent of the structural damping parameter D and depends only on the coupling terms associated with forcing.

The second approximate, "method 2", is based on assuming that maximum response coincide with a specific phase difference. The form of method 2 is shown in Eq. 11 and includes structural damping and the forcing terms. An added benefit of this approach, is that it reduces the calculation process to one longer equation; we are assuming we know θ , so there is no need to calculate the value. By inspection, the phase difference at maximum response is $\approx 0.65\pi$.

The estimates of maximum amplitude and dimensionless fluid speed are compared to results from numerical simulations at several Sc using two damping cases. One corresponds to a low damping case and the other to a high damping. The values of μ are inferred from Sc using the constants given in Tab. 1 and Eqs. 3 and 9. For comparison, both absolute values and the relative difference in percentage are used in the next two subsections.

3.2 Approximation of fluid speed at maximum response

The evolution of dimensionless fluid speed as a function of Sc when structural damping is low is shown in Fig. 3. When comparing the results using method 1 and numerical, it is easy to spot differences. Predicted speed changes differently with Scruton number and the values are inconsistent for method 1 and numerical. The approximate speed using method 2 is consistently higher than the numerical result but does drop similarly with increasing Sc .

To further evaluate the approximations, a second damping case is studied. The evolution of fluid speed at maximum response when damping is five times greater is shown in Fig. 4. With the higher damping, predicted speed drops similarly for method 1 and numerical although the predicted speed is consistently much higher. Increasing damping barely changed the differences between numerical results and method 2. The main difference would be a slightly increased difference in predicted value.

3.3 Maximum response

Maximum response is predicted to decrease similarly to how the fluid speed at maximum response drops, i.e. like Sc^{-1} . This gives a rapid drop in predicted vibration amplitude as seen in Figs. 5 and 6 showing the progression for the lightly and higher damped cases respectively.

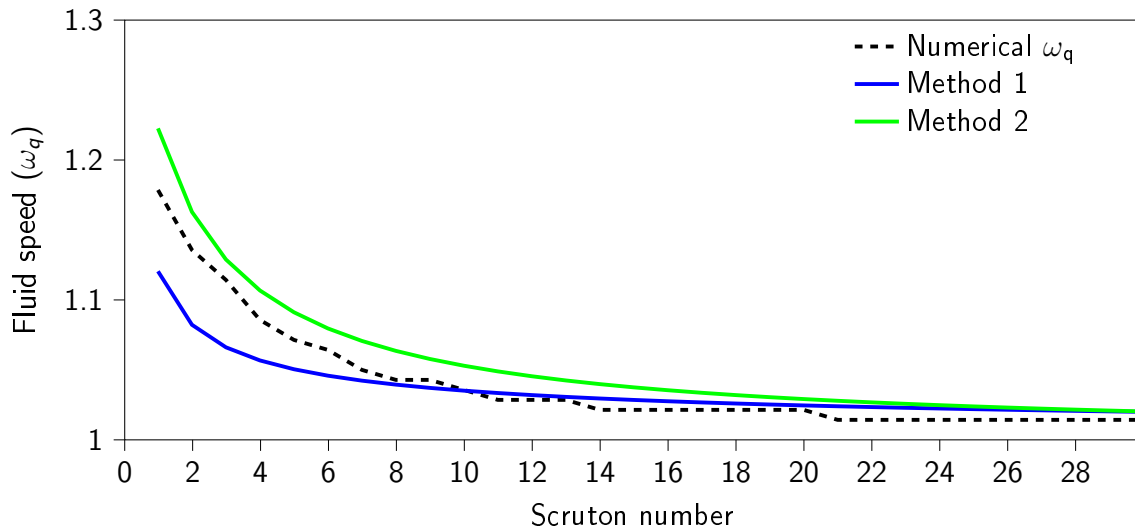


Figure 3 – ω_q corresponding to maximum r_y for low damping case

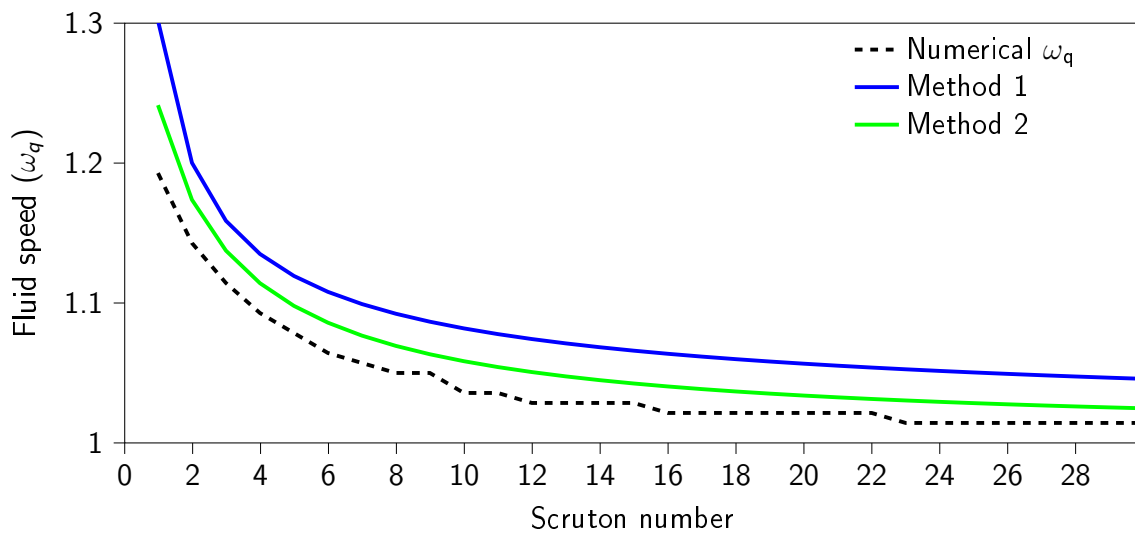


Figure 4 – ω_q corresponding to maximum r_y for high damping case

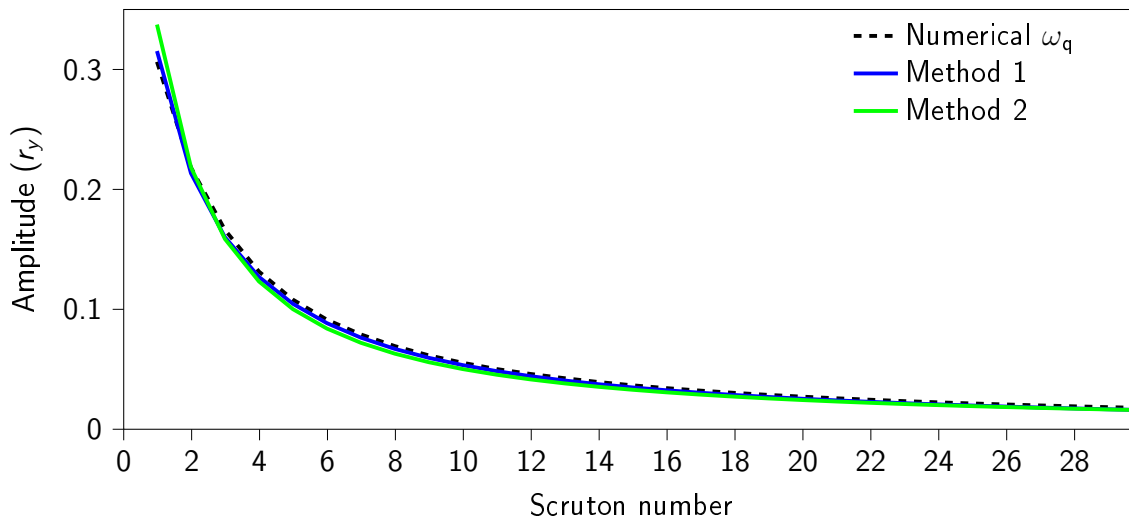


Figure 5 – Comparison of maximum response amplitude using approximates and numerical integration at low structural damping

Even with the difference in predicted speed, method 1 predicts similar amplitudes as the numerical results for most tested Scruton numbers in the lightly damped case. This could be an indication of low sensitivity in fluid speed when it comes to estimating maximum amplitude. For the higher damped case, this is not true. At Scruton numbers below 2, the amplitude becomes noticeably over predicted and then under predicts for all Scruton numbers. The more egregious error, is that the predicted speed corresponds to the low amplitude solution for Scruton numbers higher than nine.

Method 2 performs similarly to method 1 for the lightly damped case but with a difference, the predicted amplitude is noticeably higher at $Sc = 1$. The real point of improvement is in the higher damped case. While it has the same over predicting behavior at Scruton numbers below 2, the predicted amplitude is close to the numerical results for all other tested Scruton numbers. In other words, the maximum speed predicted is within the VIV region and close to the amplitude peak.

At the shown damping levels, method 1 performed passably for Scruton numbers less than 10. If we increase the damping, method 1 eventually under predicts for all Scruton numbers. The best estimate of maximum amplitude and fluid speed at maximum is method 2 which is based on assuming we know the phase difference that give maximum amplitude. The results are promising and in the next section we will further explore the usefulness of our estimate.

4 Applicability of our estimate of maximum amplitude

We have so far compared the absolute differences between our approximates and the numerical results for two different damping levels. This section is focused on the applicability of our predictions and a comparison with other predictive models, more specifically the model of Vickery and Basu used in building codes (CICIND, 2010; Eurocode, 2010).

As seen in section 2.3 and Fig. 2, there is room for improvement in the models used in the

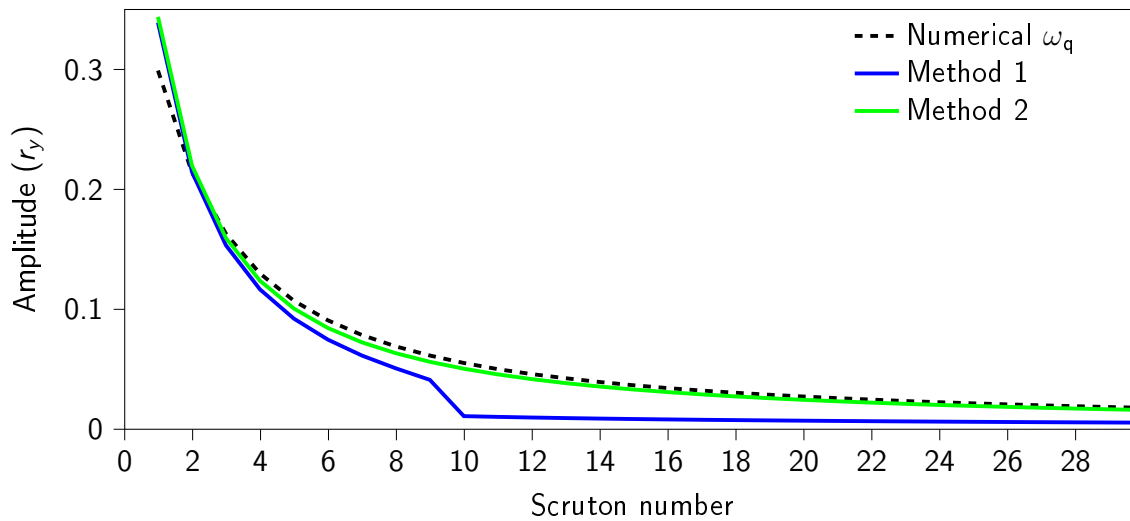


Figure 6 – Comparison of maximum response amplitude using approximates and numerical integration at high structural damping

mentioned building code. We will focus on two connected, negative properties. The first of them, is that they tend to be overly conservative in estimating amplitudes. Lupi et al. (2017) studied the difference between predicted and actual VIV amplitude and found that the predicted amplitude tended to be much larger than the actual vibration amplitude.

The second property has to do with predictive amplitude as a function of Scruton number (Lupi et al., 2017). The formulation used in the building codes can have abrupt jumps in predicted amplitude when slightly changing structural damping or aerodynamics. This is associated with a critical Scruton number that marks the transition from positive linear structural damping to negative. High amplitude prediction can also be connected with the imposed negative aerodynamic damping effect.

Our estimates of maximum amplitude follows a different trend and there is a smooth increase in predicted amplitude as Scruton number decreases without abrupt jumps. Our predicted maximum amplitude can have large changes with Scruton number at $Sc < 2$, but this is not as pronounced as the behavior of the design models..

How applicable is our two dimensional model in predicting the dynamic response of a three dimensional structure? Due to three dimensional effects, lengthwise force correlation and structural mode shapes, it is not unthinkable that our predictions will be wrong. But it may be possible to simplify and include the mentioned effects into our model. If we follow the same reasoning as Vickery and Basu (1983), we can modify our lift force by assuming a constant average speed over the top part of the cylinder. The lift force is then weighted and integrated over the cylinder length with a weighting factor proportional to the structural mode shape.

Another aerodynamic effect not accounted for in our model, but is in the design models, is the effect of turbulence and noise on the prediction. We can theoretically get the response amplitude using unsteady aerodynamic coefficients measured in turbulent conditions, but predicting the correct wind speed is harder; amplitude might be correct but the speed not. Getting the correct coefficients at super-critical (or "postcritical") Reynolds numbers is another story

and requires extensive work.

5 Conclusions

Two estimates of maximum structural amplitude due to vortex-induced vibrations has been tested and shown to accurately estimate maximum response. The best of the two is to assume that maximum amplitude occurs at a predefined phase difference between forcing and motion. Using a phase difference of $\theta = 0.65\pi$ gives an approximate fluid speed at maximum response slight higher than numerical results but similar evolution with Scruton number. The difference in fluid speed has a small effect on the difference in predicted maximum amplitude and the numerical result and estimate are similar.

References

- Belloli, M., Giappino, S., Morganti, S., Muggiasca, S., Zasso, A., 2015. Vortex induced vibrations at high Reynolds numbers on circular cylinders. *Ocean Eng*, 94, 140–154.
- Blevins, R. D., 2001. *Flow-Induced Vibration* (2nd ed.). Krieger Pub Co., Malabar, FL.
- CICIND, 2010. *CICIND Model Code for Steel Chimneys: September 2010 Revision 2*. CICIND.
- de Langre, E., 2006. Frequency lock-in is caused by coupled-mode flutter. *J Fluids Struct*, 22(6–7), 783–791.
- Eurocode., 2010. 1: *Actions on structures, Part 1–4: General Actions (EN–1991)*. Eurocode.
- Facchinetti, M.L., de Langre, E., Biolley, F., 2004. Coupling of structure and wake oscillators in vortex-induced vibrations. *J Fluids Struct*, 19(2), 123–140.
- Païdoussis, M. P., Price, S. J., de Langre, E., 2010. *Fluid-Structure Interactions Cross-Flow-Induced Instabilities*. Cambridge University Press., Cambridge, NY.
- Sarpkaya, T., 2004. A critical review of the intrinsic nature of vortex-induced vibrations. *J Fluids Struct*, 19(4), 389–447.
- Vickery, B.J., Basu, R., 1983. Simplified approaches to the evaluation of the across-wind response of chimneys. *J Wind Eng Ind Aerod*, 14(1), 153–166.

Flow-Induced Vibrations of a periodically rotating circular cylinder

Francisco Huera-Huarte¹

¹ Dept. of Mechanical Engineering, Universitat Rovira i Virgili (URV), Tarragona, Spain.
francisco.huera@urv.cat

Keyword: Vortex-induced vibration (VIV), Circular cylinder, wakes.

I will describe the cross-flow vortex-induced vibrations (VIV) of a rigid cylinder forced to oscillate periodically around its axis. The model hangs from an air bearing beam as seen in figure 1, so the one degree-of-freedom dynamic response and fluid loading acting on the system can be measured in detail when subject to different uniform currents imposed in a recirculating water tunnel. The experimental rig was especially designed for VIV studies¹ and has been modified in order to allow the forced rotations of the cylinder around its axis whilst undergoing VIV. The rotations can be applied to the cylinder in a controlled manner by means of a servo motor.

In this work I will show the effects on the VIV, of periodic rotations with varying frequency and amplitude. A very wide parameter space has been covered, including cases in which the forced frequency is controlled in closed loop using the frequency of VIV oscillations. The flow dynamics around the system have been measured using planar Particle Image Velocimetry for specific cases.

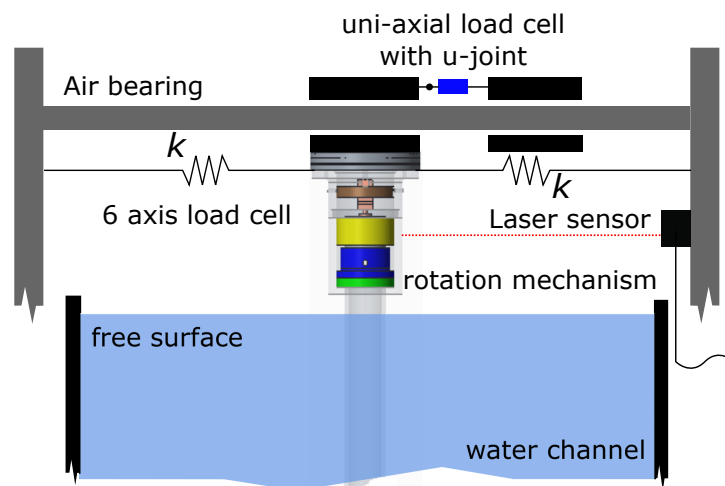


Figure 1: Experimental set-up and rotating cylinder model in the free surface water channel.

¹ Huera-Huarte, F.J. (2019). Dynamics and excitation in a low mass-damping cylinder in cross-flow with side-by-side interference. *Journal of Fluid Mechanics*, 850, 370-400.

Stochastic analysis of vortex-induced vibrations by means of a randomized wake-oscillator model

Vincent Denoël¹

¹ *University of Liège, Liège, Belgium, v.denoel@uliege.be*

Keyword: Vortex induced vibrations (VIV), Facchinetti-De Langre-Biolley model, random synchronization, stochastic Van der Pol oscillator, lock-in range, turbulence

There are three families of mathematical models to describe vortex-induced vibrations¹. By combining two governing equations for both the structure and the fluid, the so-called *wake-oscillator models* consist in the most advanced ones. Thanks to a nonlinear restoring force featuring a stable limit cycle in the wake equation, these models are able to capture the synchronisation of vortex detachment with imposed body motion. In this paper a randomized version of a well-known 2-D and constant U_∞ wake-oscillator model² is proposed in order to take into account the slow and small intensity fluctuation of the oncoming wind speed that is typical of the atmospheric boundary layer.

The analysis reported in the paper exploits the smallness of several parameters of the model: (i) the magnitude of the coupling forces (parameter A and ratio $M := \frac{1}{4}\rho U_\infty^2 DC_{Lo}/m_s\omega_s^2$, with same notations as in [2]), (ii) the total damping ratio ξ of the structure, (iii) the parameter ε of the deterministic model, as well as (iv) the smallness of the turbulence intensity and (v) the timescale separation of turbulence and structural/fluid oscillations. All these small numbers contribute to providing an accurate model of the problem by means of a single stochastic differential equation. Its solution provides simple expressions of the important responses of the problem (lock-in range, structural vibration amplitudes, etc.). In particular, the stochastic model is able to capture the well-known decrease of the VIV phenomenon with increasing turbulence intensity (under some conditions, which are also well-known by experimentalists³). It also explains that the timescale of the turbulence plays a major role in this reduction and finally reveals that the sensitivity to turbulence is governed by the dimensionless number

$$\mathcal{D} = \frac{\xi}{\varepsilon} + \frac{AM}{4\xi\varepsilon} \quad (1)$$

The proposed stochastic model for VIV is an innovative way of considering the influence of turbulence on VIV. Although the paper will mostly cover the mathematical derivation of the solutions, some comparisons with existing experiments in turbulent flow will be used for illustrations.

¹ Païdoussis, M. P., Price, S. J., De Langre, E. (2010). Fluid-structure interactions: cross-flow-induced instabilities. Cambridge University Press.

² Facchinetti, M. L., De Langre, E., and Biolley, F., "Coupling of structure and wake oscillators in vortex-induced vibrations", *Journal of Fluids and structures* 19, 2 (2004), pp. 123–140.

³ Goswami I., Scanlan R. H., and Jones N. P. Vortex-induced vibration of circular cylinders. i: experimental data. *Journal of Engineering Mechanics*, 119(11):2270–2287, 1993.

Dependence of cross-sectional aspect ratio and attack angle on forces and wake of elliptical cylinder

Xiaoyu Shi¹, Md. Mahbub Alam^{1,*}, and Honglei Bai²

¹*Institute for Turbulence-Noise-Vibration Interaction and Control, Harbin Institute of Technology (Shenzhen), Shenzhen 518055, China*

²*School of Aeronautics and Astronautics, Sun Yat-sen University (Shenzhen), China*

Email: alam@hit.edu.cn; alamm28@yahoo.com

Abstract

The dependences of cross-sectional aspect ratio $AR = (0.25 - 1.0)$ and attack angle $\alpha (= 0^\circ - 90^\circ)$ on forces and wake of elliptical cylinder are investigated at the Reynolds number $Re_D = 100$ and 150 , where Re_D is based on the freestream velocity and cylinder cross-section height normal to the freestream flow, AR is the ratio of the minor axis to the major axis of the elliptical cylinder, and α is the angle between the cylinder major axis and the incoming flow. With the changes in AR and α , two distinct wake patterns (patterns I, II) are observed at $Re_D = 100$, while three wake patterns (patterns I, II, III) are detected at $Re_D = 150$. 'Steady wake' (pattern I) is characterised by two steady bubbles forming behind the cylinder. Time-mean drag and fluctuating lift coefficients are small. Pattern II refers to 'Karman wake followed by steady wake' with the Karman street transmuting to two steady shear layers downstream. Inflection angle $\alpha_i = 32^\circ, 37.5^\circ$ and 45° are identified for $AR = 0.25, 0.5$ and 0.75 , respectively, where the wake asymmetry is the greatest. The α_i effectively distinguishes the dependence on α and AR of force and vortex shedding frequency at either Re_D . Pattern III is the 'Karman wake followed by secondary wake', where the Karman street forming behind the cylinder is modified to a secondary vortex street with a low frequency. At a given AR and α , $Re_D = 150$ renders higher fluctuating lift than $Re_D = 100$.

Keyword: elliptical cylinder, wake, secondary vortex shedding.

1 Introduction

The flow past a bluff body (e.g. circular or square cylinder) attracts much attention due to its significance in engineering applications (Alam 2016; Bai and Alam 2018; Rajesh and Alam 2018; Alam *et al.* 2016; Wang *et al.* 2017). Because of complexity in the geometry of an elliptical cylinder, less attention has been paid to the flow past an elliptical cylinder whose cross-sectional aspect ratio $AR (= \text{ratio of minor axis } b \text{ to major axis } a)$ changing from 0 to 1.0 leads to the modification of the cylinder shape from a flat plate to a circular cylinder. The structure with the elliptical section is also typical both in nature and in engineering applications. Recently, there has been a surge of interest in investigating the elliptical cylinder wake, given that a sea lion whisker (whose cross-section is elliptic) does not experience vortex-induced vibration and can easily detect preys (Hans *et al.* 2014; Beem and Triantafyllou 2015).

Jin *et al.* (1989) conducted a two-dimensional numerical study on an elliptical cylinder of $AR = 0.15$, with the attack angle α varying from $0^\circ - 90^\circ$. The Reynolds number Re_a , based on a , was $25 - 600$. They observed five flow regimes, including two steady wakes and three unsteady wakes. Johnson *et al.* (2001) further carried out two-dimensional numerical

simulations of the flow around a cylinder of $AR = 0.01 - 1.00$ at $Re_a = 30 - 200$ for a fixed $\alpha = 90^\circ$. A secondary vortex shedding on the wake was identified in their results. Afterwards, the formation mechanism of the secondary wake has been an interesting topic. By analyzing temporal wake evolution, Johnson *et al.* (2004), Paul *et al.* (2016), and Pulletikurthi *et al.* (2018) found three flow regions in the wake, namely linear, transition and saturation regions. For $Re_a = 75 - 175$, $\alpha = 90^\circ$ and $AR = 0.01 - 1.00$, Johnson *et al.* (2004) explored that increasing Re_a or decreasing AR led to the emergence of a secondary or tertiary frequency in the power spectra of the streamwise velocity at the wake centerline. The secondary or tertiary frequency (low-frequency unsteadiness) stems from the interaction between the two-dimensional instability of the far wake and vortex shedding from the cylinder. Paul *et al.* (2016) illuminated the low-frequency unsteadiness by means of a signal decomposition method on the velocity signal. They performed the two-dimensional simulation on elliptical cylinder varying from a flat plate ($AR = 0.1$) to a circle cylinder ($AR = 1.0$) with $\alpha = 90^\circ$ and $Re_a < 190$. They believed that the secondary frequency in the far wake comes from the transition region, and the saturation region is responsible only for the primary shedding frequency. Recently, Pulletikurthi *et al.* (2018) performed fast Fourier transform (FFT) of velocity fields (i.e. streamwise velocity, cross-stream velocity, and velocity magnitude) and scalar fields (i.e. pressure, temperature). Only one case ($AR = 0.4$, $\alpha = 90^\circ$ and $Re_a = 130$) was considered in their study. They accounted that the spectral source and physical source of the low-frequency unsteadiness are the signal in the transition region and the chaotic behavior of the flow structure aiding in the transmutation of their wavelength, respectively.

The review suggests that the near wake of an elliptical cylinder is strongly dependent on α , AR and Re_a . In the literature, with Re_a keeping constant, AR and/or α were varied. In such a case, the effective Reynolds number Re_D (based on the projected dimension D normal to the flow, Fig. 1a) is not constant, but varied. The effective Reynolds number (i.e. Re_D) thus changes as α increases from 0° to 90° , especially for small AR . In such a case, the results encompass not only the effect of α but also the effect of Reynolds number. To extract the effect of α only, the Reynolds should be kept constant. Since the flow around a bluff body is highly sensitive to Reynolds number particularly at low Re_D ($< 10^3$) (e.g. Bai and Alam 2018), it essentially needs to consider the effective Reynolds number, i.e. Re_D .

This work aims to conduct a systematic numerical study on the forces, Strouhal number and wake of an elliptical cylinder, involving a relatively wide range of α ($0^\circ - 90^\circ$) and AR ($= 0.25 - 1.0$). The effective Reynolds number $Re_D = 100$ and 150 is considered. The focus is given on the flow classification and connections between the flow structures and fluid force on the cylinder for the AR and α ranges.

2 Problem definitions

The elliptical cylinder is located at the origin of the coordinate system with x - and y -axis along the streamwise and cross-stream directions, respectively (Fig. 1b). The aspect ratio (AR) is defined as $AR = b/a$, where a and b are the lengths of the major and minor axes, respectively. The angle of attack (α) is the angle between the major axis and the freestream flow direction. The α is varied from 0° and 90° . The projection length (perpendicular to the freestream flow) of the cylinder cross-section is defined as D . The Re_D is the effect Reynolds number based on D and freestream velocity U_∞ . The flow is given from left to right, parallel to the x -axis. The AR varies as 0.25 , 0.50 , 0.75 and 1.0 . Given that the flow may be more sensitive at small α , a finer resolution of 5° in α was adopted for $\alpha < 30^\circ$ and a coarse resolution of 15° was muller for $\alpha > 30^\circ$. To determine the wake pattern boundary precisely, an additional α ($= 37.5^\circ$) is added. Two Re_D values of 100 and 150 are considered.

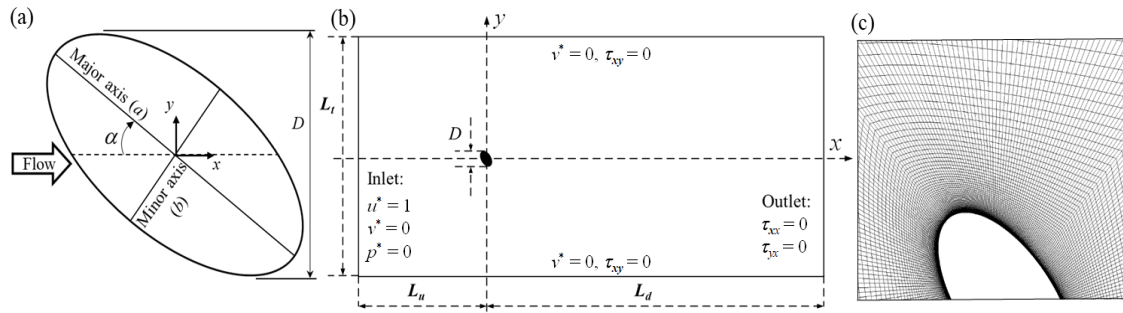


Fig. 1 (a) Cylinder model and definitions of symbols. (b) Computational domain (not to scale). (c) Mesh details around the cylinder.

2.1 Governing equations and numerical method

Two-dimensional simulations of the unsteady laminar flow around the elliptical cylinder are carried out. The incompressible continuity and Navier-Stokes (N-S) equations are solved on structural quadrilateral grids using the finite-volume method (FVM) in ANSYS Fluent. The governing equations in the dimensionless form are given below.

$$\frac{\partial \mathbf{u}^*}{\partial t^*} + (\mathbf{u}^* \cdot \nabla) \mathbf{u}^* = -\nabla p^* + \frac{1}{Re_D} \nabla^2 \mathbf{u}^* \quad \text{and} \quad (1)$$

$$\nabla \cdot \mathbf{u}^* = 0, \quad (2)$$

where t^* , \mathbf{u}^* and p^* are the dimensionless time, velocity vectors (u , v), and static pressure, respectively. The superscript "*" denotes normalization based on U_∞ and/or D unless otherwise stated.

The second-order implicit and second-order upwind differencing schemes are used for the spatial discretization of pressure and momentum, respectively. Additionally, the second-order implicit differencing scheme is applied for temporal discretization. Semi-Implicit Method for Pressure-Linked Equation (SIMPLE) is selected for the pressure-velocity coupling in the governing equation (Patankar and Spalding 1978). The non-dimensional computational time step is $\Delta t^* = \Delta t U_\infty / D = 0.0365$ ($Re_D = 100$), resulting in Courant-Friedrichs-Lewy (CFL) numbers < 1 . Statistical calculations (e.g., time-mean and root-mean-square values of the force) are made for more than 50 vortex-shedding periods after the simulation becomes statistically convergent.

2.2 Computational domain, mesh system, and boundary conditions

A rectangular computational domain (Fig. 1b) is considered, having the size of $(L_u + L_d) \times L_t = (50D + 100D) \times 100D$, where L_u is the upstream distance between the cylinder center and the inlet of the computational domain, L_d is the downstream distance between the cylinder center and the outlet of the domain, and L_t is the transverse distance between the lateral sides of the domain. The cylinder is located at the symmetric line of the computational domain. The size of the computational domain is large enough to ignore the influence the boundaries on the results.

The whole computational domain is given the structural grids. To decrease the node number and improve the computational efficiency, finer grids (Fig. 1c) are generated in the area of $10D \times 10D$ around the elliptical cylinder. A uniform grids spacing ($0.05D$) is applied

along the cylinder surface. The number of nodes on the surface strongly depends on the AR and α . For example, for $AR = 1.0$, the number of nodes on the cylinder surface is 63, while for $AR = 0.25$, $\alpha = 0^\circ$, it is 300. The first grid is $0.05D$ away from the cylinder surface, and the grids are stretched with an expansion ratio of 1.003 along the radial direction. The total grids in the entire domain are 72K to 76K, depending on AR and α .

A constant and uniform incoming velocity (U_∞) is imposed at the inlet of the computational domain while the outflow boundary conditions ($\frac{\partial u^*}{\partial x^*} = 0, \frac{\partial v^*}{\partial x^*} = 0$) are used at the outlet of the domain. The symmetry boundary condition ($v^* = 0, \frac{\partial u^*}{\partial y^*} = 0$) is applied for the lateral sides. The no-slip boundary condition ($u^* = v^* = 0$) is set on the cylinder surface.

3 Results

3.1 Dependence of flow on AR and α at $Re_D = 100$

At $Re_D = 100$, two distinct wake patterns are identified based on the flow structure and force distributions when AR is varied from 0.25 to 1.0 and α from 0° to 90° . They are named 'steady wake' (pattern I) and 'Karman wake followed by a steady wake' (pattern II). The dependence of the flow patterns on AR and α are summarized in Fig. 2. As indicated by the dashed lines, the boundary between the flow patterns is determined as the mid of the concerned points. Pattern I appears at $AR < 0.375$ and $\alpha < 12.5^\circ$ while pattern II covers the rest of AR and α domain.

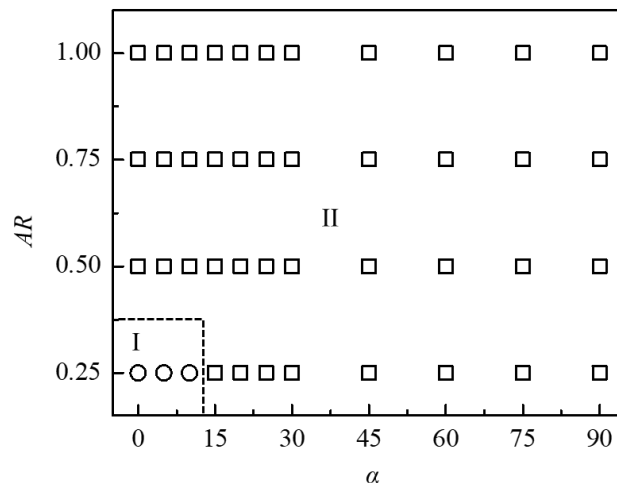


Fig. 2 Dependence of flow patterns on AR and α . \circ , pattern I: steady wake; \square , pattern II: Karman wake followed by steady wake. The dashed lines represent the boundaries between different patterns. ($Re_D = 100$)

Figure 3(a, b) shows instantaneous vorticity contours for pattern I ($AR = 0.25, \alpha = 0^\circ$) and pattern II ($AR = 0.25, \alpha = 90^\circ$), respectively. The streamwise velocities (u^*) at $(x^*, y^*) = (10, 0)$ and $(80, 0)$ for the two flow patterns are presented to show whether the wake is steady (Fig. 3c, d). For pattern I (steady wake), two steady shear layers form downstream (Fig. 3a). The corresponding u^* at each of the two locations is constant, indicating a steady wake. While for pattern II (Karman wake followed by a steady wake) the Karman vortex appears immediately

downstream of the cylinder and then transits to two steady shear layers (Fig. 3b). The u^* signal at $(x^*, y^*) = (10, 0)$ displays periodic fluctuations, while it is invariant at $(x^*, y^*) = (80, 0)$, suggesting the wake back to a steady state.

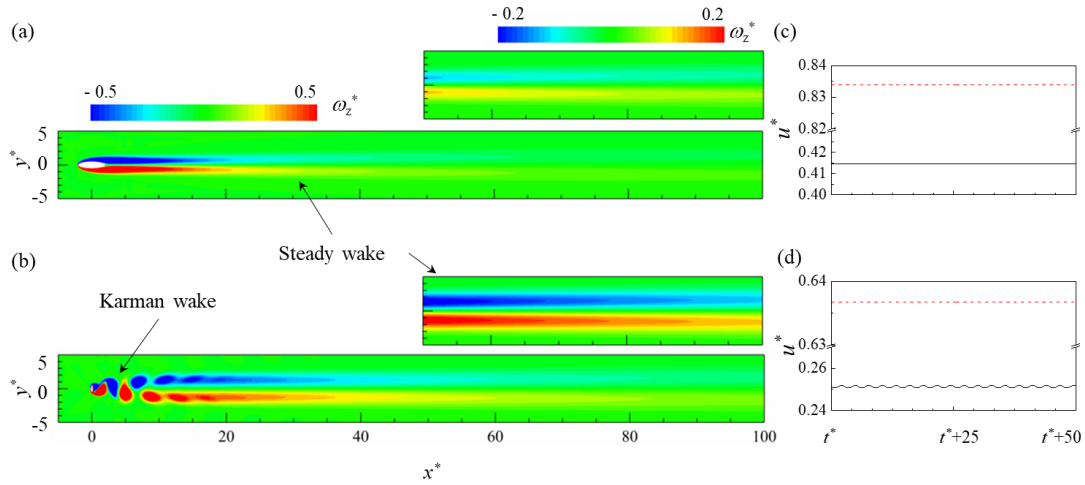


Fig. 3 Instantaneous vorticity contours at an instant corresponding to the maximum C_L . (a) Pattern I: steady wake ($AR = 0.25$, $\alpha = 0^\circ$). (b) Pattern II: Karman wake followed by the steady wake ($AR = 0.25$, $\alpha = 90^\circ$). Insets are the zoom-in views of the vorticity contours (color code rescaled) for $x^* = 50 - 100$. (c) and (d) are the streamwise velocity (u^*) signals at $(x^*, y^*) = (10, 0)$ (solid black line) and $(80, 0)$ (dashed red line) corresponding to the cases.

Variations in fluid forces ($\bar{C}_D, \bar{C}_L, C'_L$) with α for each AR are presented in Fig. 4. The horizontal dashed lines indicate the values for $AR = 1.0$ (circular cylinder). At $AR = 0.25$ and $\alpha < 12.5^\circ$ (pattern I), \bar{C}_D is the smallest, more or less constant, about 25% smaller than \bar{C}_{D0} (circular cylinder, $AR = 1.00$). For the same AR with $\alpha > 12.5^\circ$ (pattern II), \bar{C}_D grows with α , reaching a maximum of 2.1 at $\alpha = 90^\circ$. The same happens for the other AR (pattern II), \bar{C}_D increasing with α . The angle corresponding to $\bar{C}_D = \bar{C}_{D0}$ is distinct for different AR . We define this angle as the inflection (zero curvature) angle $\alpha_i = 32^\circ, 37.5^\circ$ and 45° for $AR = 0.25, 0.5$ and 0.75 , respectively. Interestingly, the rate of \bar{C}_D increase (i.e. $\partial^2 \bar{C}_D / \partial^2 \alpha$, curvature) is positive at $\alpha < \alpha_i$ and negative at $\alpha > \alpha_i$. At a small $\alpha (< 25^\circ)$, \bar{C}_D enhances with increasing AR , while the opposite relationship persists at a large $\alpha (> 37.5^\circ)$, \bar{C}_D waning with AR .

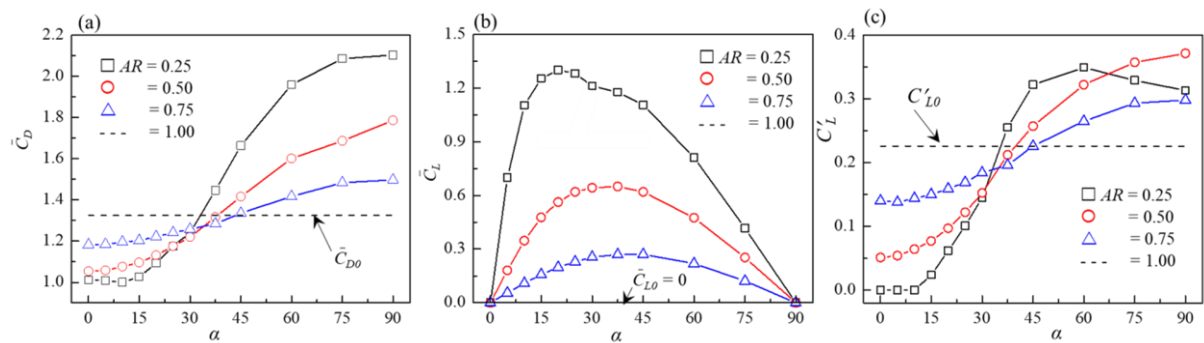


Fig. 4 (a) – (c) Variations in time-mean drag coefficient \bar{C}_D , time-mean lift coefficient \bar{C}_L and fluctuating lift coefficient (C'_L) with α for different AR . ($Re_D = 100$)

The dependence of \bar{C}_L on α is different from that of \bar{C}_D . The \bar{C}_L for a given AR initially increases with α , reaching a maximum, followed by a declination with further increase in α . The α_i links to the maximum \bar{C}_L (i.e. $\bar{C}_{L,max}$) for $AR = 0.5$ and 0.75 , while close to $\bar{C}_{L,max}$

for $AR = 0.25$. The value of \bar{C}_L signifies a degree of asymmetry in the wake. That is, the asymmetry of the wake is the largest at $\alpha = \alpha_i$. The C'_L for pattern I is zero due to the steady wake. Naturally, $\bar{C}_L = 0 = \bar{C}_{L0}$, for $AR = 1.00$, irrespective of α . A decrease in AR from 1.00 leads to an increase in \bar{C}_L for $0^\circ < \alpha < 90^\circ$. While C'_L increases with increasing α from 0° to 90° for $AR = 0.5$ and 0.75 , it decreases with increasing α at $\alpha > 60^\circ$ for $AR = 0.25$. The α_i again corresponds to a zero curvature in C'_L distributions, with $C'_L = C'_{L0}$ at α_i .

3.2 Reynolds number effects

The Reynolds number, particularly when low, dramatically affects the flow around a bluff body (Bai and Alam 2018). Here, the flow map for $Re_D = 150$ is presented in Fig. 5 that can be compared to Fig. 2 to assimilate the Reynolds number effect on the wake of the cylinder. One intriguing effect of Re_D is that at $Re_D = 150$ an additional flow pattern III (Karman wake followed by a secondary wake) appears at high α ($> 52^\circ - 82^\circ$) and small AR ($\leq 0.37 - 0.67$) (Fig. 5), where the Karman wake produced immediately downstream of the cylinder transmutes into a secondary wake with a low frequency, through generation of two elongated shear layers between the Karman and secondary wakes (Fig. 5b). Another Re_D effect is that the region of pattern I shrinks in the α domain ($\alpha < 2.5^\circ$) at $Re_D = 150$, compared to that ($\alpha < 12.5^\circ$) at $Re_D = 100$.

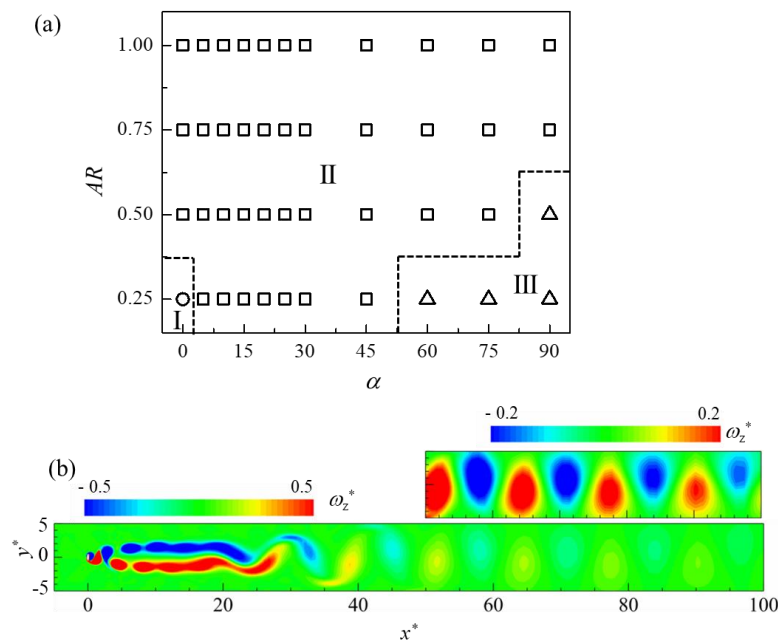


Fig. 5 (a) Dependence of flow patterns on AR and α . \circ , pattern I: steady wake; \square , pattern II: Karman wake followed by steady wake; \triangle , pattern III: Karman wake followed by secondary wake. The dashed lines represent the boundaries between different patterns ($Re_D = 150$). (b) Instantaneous vorticity contours for pattern III ($AR = 0.25$, $\alpha = 90^\circ$ and $Re_D = 150$)

A comparison of the forces (\bar{C}_D , \bar{C}_L and C'_L) between $Re_D = 100$ (upper row) and 150 (lower row) is shown in Fig. 6, with the flow maps superimposed on $AR - \alpha$ plane. The dashed lines mark the boundaries between flow patterns while the dotted-dash line represents $\alpha = \alpha_i$. The minimum and maximum values in color bars are the corresponding minimum and maximum values at $Re_D = 150$. The symbol ' \star ' in color bar indicates the value for $AR = 1.0$ (circular cylinder).

The dependences of \bar{C}_D on AR and α at the two Reynolds numbers are qualitatively similar to each other. Compared to those at $Re_D = 100$, the maximum and minimum magnitudes at $Re_D = 150$ are however large and small, respectively, perceived from the intensity of color. Although pattern III does not emerge at $Re_D = 100$, the maximum \bar{C}_D regime still locates at a similar region for both Reynolds numbers. The \bar{C}_D is highly sensitive to both AR and α , particularly at $AR < 0.75$, while Re_D largely affects the maximum and minimum magnitudes of \bar{C}_D . At a given α , the \bar{C}_D upturns with increasing AR . The influence of α on \bar{C}_D is nevertheless not straight forward, \bar{C}_D diminishing and growing with AR for $\alpha < \alpha_i$ and $\alpha > \alpha_i$, respectively.

The $\bar{C}_L = 0$ on the lines $\alpha = 0^\circ$ and 90° and $AR = 1.00$ (i.e. left, right and upper boundaries) at either Re_D . At given α , the maximum \bar{C}_L roughly corresponds to $\alpha = \alpha_i$. The magnitude of \bar{C}_L does not change much between the two Reynolds numbers (Fig. 6b, e) whilst that of C'_L significantly increases from $Re_D = 100$ to 150 (Fig. 6c, f). As expected, C'_L is zero for pattern I (steady wake), and it strengthens with the increasing AR and α . The maximum C'_L materializes at $AR = 0.50$, $\alpha = 75^\circ - 90^\circ$ for both Reynolds numbers.

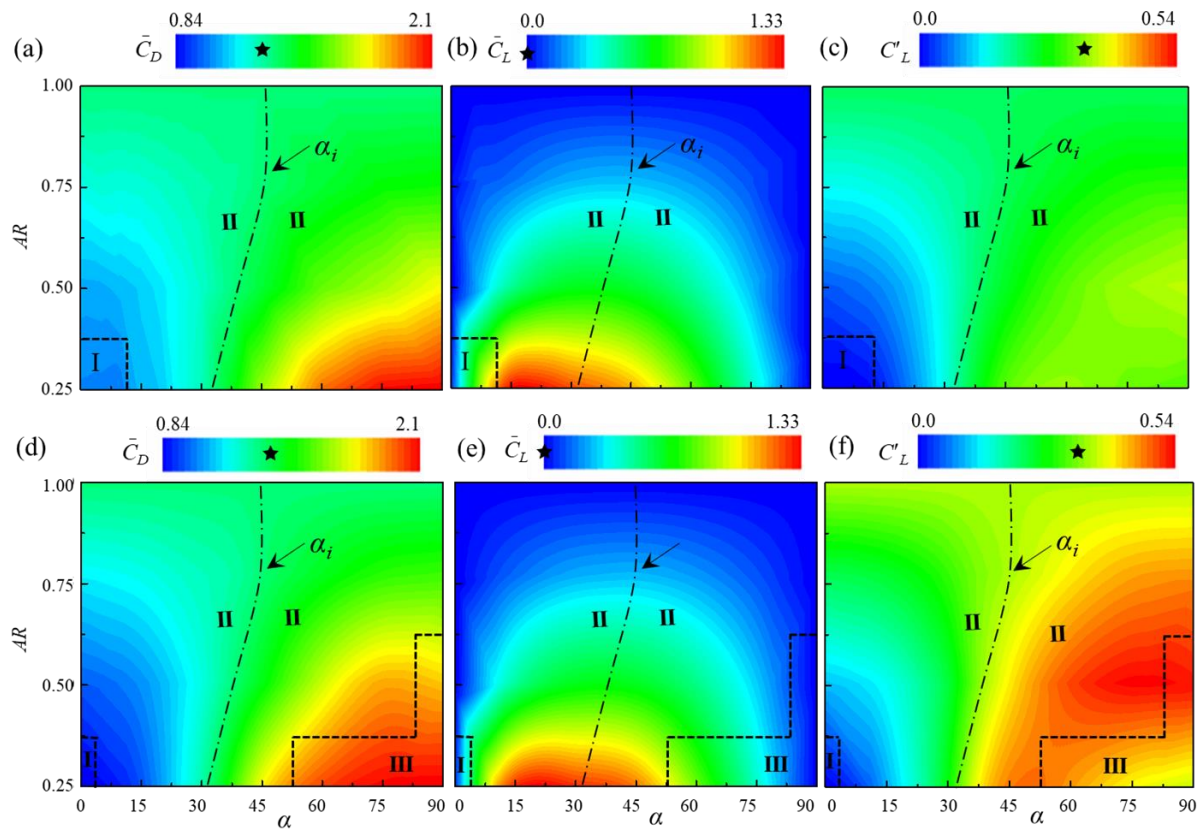


Fig. 6. Comparison of forces between $Re = 100$ and 150. (a – c) \bar{C}_D , \bar{C}_L and C'_L at $Re_D = 100$. (d – f) \bar{C}_D , \bar{C}_L and C'_L at $Re_D = 150$. Dashed lines mark the flow patterns while the dotted-dash line represent $\alpha = \alpha_i$. In the color code bars, the minimum and maximum values corresponding to the minimum and maximum values at $Re_D = 150$. The symbol '★' indicates the value for $AR = 1.0$ (circular cylinder).

Conclusions

A numerical investigation is conducted on the effects of AR ($= 0.25 - 1.0$), α ($= 0^\circ - 90^\circ$), and Re_D ($= 100$ and 150) on the cylinder wake, flow classification, forces. Base on the flow structure evolution in the wake, two flow patterns are identified at $Re_D = 100$, namely 'steady

wake (pattern I)' and 'Karman wake followed by a steady wake (pattern II)'. As Re_D is increased to 150, pattern III (Karman wake followed by a secondary wake) emerges for large α and small AR . While pattern I is characterized by a steady wake, pattern II features the Karman wake immediately behind the cylinder, with the Karman wake transmuting to a steady wake downstream. For pattern III, a secondary unsteady wake is generated downstream of the Karman wake. An inflection angle α_i is marked for each AR , where $\bar{C}_D = \bar{C}_{D0}$, $\bar{C}_L \approx \bar{C}_{L,max}$, and $C'_L = C'_{L0}$, with $\alpha_i = 32^\circ, 37.5^\circ$ and 45° for $AR = 0.25, 0.5$ and 0.75 , respectively.

Though a qualitatively similar dependence of \bar{C}_D , \bar{C}_L , and C'_L on AR and α is observed at both Reynolds numbers, the maximum and minimum magnitudes are however bigger and smaller, respectively, at $Re_D = 150$ than at $Re_D = 100$. The \bar{C}_D , \bar{C}_L , and C'_L all are highly dependent on both AR (< 0.75) and α ($= 0^\circ - 90^\circ$). The \bar{C}_D and C'_L both increases with increasing AR , while waning with increasing AR for $\alpha < \alpha_i$ and boosting for $\alpha > \alpha_i$. The maximum \bar{C}_L roughly corresponds to $\alpha = \alpha_i$. The magnitude of C'_L significantly enhances from $Re_D = 100$ to 150. The C'_L becomes maximum at $AR = 0.50$, $\alpha = 75^\circ - 90^\circ$ for both Reynolds numbers. The $St < St_0$ and $St > St_0$ at $\alpha < 45^\circ$ and $\alpha > 45^\circ$, respectively. For a given AR and α , the St is higher at $Re_D = 150$ than at $Re_D = 100$.

Acknowledgements

The authors wish to acknowledge the support given by the National Natural Science Foundation of China through Grants 11672096 and 91752112 and by Research Grant Council of Shenzhen Government through grant JCYJ20180306171921088.

References

- Alam, M. M., 2016. Lift forces induced by phase lag between the vortex sheddings from two tandem bluff bodies. *Journal of Fluids and Structures*, 65, 217-237.
- Alam, M. M., Bai, H. L., and Zhou, Y., 2016. The wake of two staggered square cylinders. *Journal of Fluid Mechanics*, 801, 475-507.
- Bai, H. L. and Alam, M. M., 2018. Dependence of square cylinder wake on Reynolds number. *Physics of Fluids*, 30(1), 015102.
- Beem, H. R. and Triantafyllou, M. S., 2015. Wake-induced 'slaloming' response explains exquisite sensitivity of seal whisker-like sensors. *Journal of Fluid Mechanics*, 783, 306-322.
- Hans, H., Miao, J. M., and Triantafyllou, M. S., 2014. Mechanical characteristics of harbor seal (*Phoca vitulina*) vibrissae under different circumstances and their implications on its sensing methodology. *Bioinspir Biomim*, 9(3), 036013.
- Jin, K. P., Seung, O. P., and Hyun, J. M., 1989. Flow Regimes of Unsteady Laminar Flow Past a Slender Elliptic Cylinder at Incidence. *International Journal of Heat and Fluid Flow*.
- Johnson, S. A., Thompson, M. C., and Hourigan, K., 2001. Flow Past Elliptical Cylinders at Low Reynolds Numbers. In: *Proc. 14th Australasian Fluid Mechanics Conference*, Adelaide University, South Australia, Dec (pp. 9-14).
- Johnson, S. A., Thompson, M. C., and Hourigan, K., 2004. Predicted low frequency structures in the wake of elliptical cylinders. *European Journal of Mechanics - B/Fluids*, 23(1), 229-239.
- Patankar, S. V., and Spalding, D. B., 1978. Computer analysis of the three-dimensional flow and heat transfer in a steam generator. *Forschung Im Ingenieurwesen*, 44(2), 47-52.
- Paul, I., Prakash, K. A., Vengadesan, S. and Pulletikurthi, V., 2016. Analysis and characterisation of momentum and thermal wakes of elliptic cylinders. *Journal of Fluid*

- Mechanics, 807, 303-323.
- Pulletikurthi, V., Paul, I., Prakash, K. A., and Prasad, B. V. S. S. S., 2018. Spectral analysis of flow and scalar primitive variables in near and far laminar wake of an elliptic cylinder.
- Rajesh, B. and Alam, M. M., 2018. Vibrations of a square cylinder submerged in a wake. *Journal of Fluid Mechanics*, 853, 301-332.
- Wang, L., Alam, M. M. and Zhou, Y., 2017. Two tandem cylinders of different diameters in cross-flow: effect of an upstream cylinder on wake dynamics, *Journal of Fluid Mechanics*, 836, 5-42.

Observation of galloping on four-bundled conductors transmission line

*Hisato Matsumiya¹, Teruhiro Yukino², Takashi Nishihara¹,
Mikio Shimizu¹ and Saki Taruishi¹

¹ Central Research Institute of Electric Power Industry, Chiba, Japan,
hisato-m@criepi.denken.or.jp

² NEWJEC Inc., Osaka, Japan

Keyword: Galloping, Overhead transmission lines, Field observation, ice accretion

This paper presents the field observation results of galloping on a four-bundled conductors transmission line. A field observation was conducted in a full-scale test line constructed at a site where ice accretion was found to occur frequently. The oscillation amplitude and tension variation of the line were measured. A total of 40 ice accretion events were observed in four winter seasons, and galloping data was obtained. In the time when the displacement data can be obtained by analysing the camera image, galloping occurs when the wind speed is over 9 m/s and the maximum total amplitude of vertical displacement is 6.6 m. However, the visibility of camera images often decreases because of the severe weather when galloping occurs, and the displacement data is not able to obtain in most of the events.

In almost all events, the conductors vibrated mainly in the two-loop/span mode (1st asymmetric mode). So, galloping occurrence condition can be clarified by considering the tension variation caused by the vibration in two-loop/span mode. Figure shows the relationship between wind speed, amount of ice accretion, and galloping occurrence condition. Vertical axis is mean tension which approximately corresponds to the amount of ice accretion. Size of circles means variation in tension through band-pass filter which is extracted the oscillation component in two-loop/span mode. The observation results suggest that the galloping oscillation becomes large under conditions where a certain relationship between wind speed and the amount of ice accretion is satisfied.

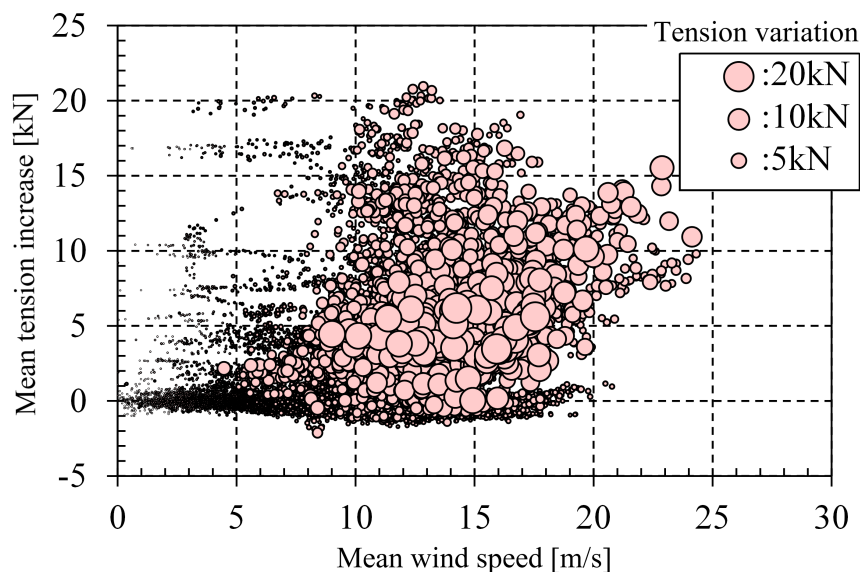


Figure: Galloping occurrence condition depending on wind speed and amount of ice accretion

Flow-Induced Vibrations of Tandem Cylinders in the Transcritical flow regime

Raphaël Dubois¹, Grigorios Dimitriadis¹ and Thomas Andrianne¹

¹ *Department of Aerospace and Mechanical Engineering, University of Liège, Allée de la Découverte 9, 4000 Liège, Belgium, raphael.dubois@uliege.be*

Keyword: Tandem cylinders, transcritical flow regime, aeroelasticity

A plethora of tandem configurations lying in a flowfield are found in engineering applications. This particular flow case was subjected to many studies^{1,2} throughout the years but most studies have been limited to the subcritical flow regime (i.e. $Re < 10^5$). Because of the continuous increase of the dimensions of engineering structures, it is now necessary to extend the understanding of the flow around tandem cylinders in the transcritical flow regime (i.e. $Re > 5 \cdot 10^6$) where the boundary layers, the separated shear layers and the vortices are turbulent.

An extensive experimental campaign will be performed in the low-subsonic wind tunnel of the University of Liège. A methodological study based on the surface roughness of the cylinder(s) is planned to trigger the transcritical flow regime. This method was successfully applied by *Okajima*³ for static tandem cylinders.

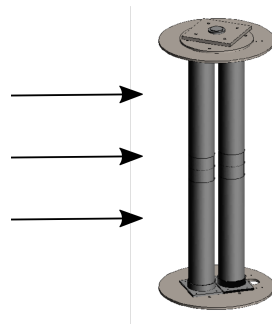


Figure 1: Experimental set-up of the tandem cylinders.

Once transcritical flow conditions will be reached, a parametric analysis are conducted to assess the effects of the geometric parameters (spacing between the cylinders and angle of attack) and the freestream parameters (turbulence intensity and integral length scale) on the behaviour of the flow around the static cylinders. To this end, a dedicated experimental set-up instrumented by pressure taps is being developed (see Fig.1). The experimental set-up will be further extended to analyse the aeroelastic behaviour of flexible tandem cylinders (by means of suspension springs and dampers). The instrumentation will consist in accelerometers to measure the streamwise and transverse responses of the two cylinders.

The outputs of this work consist in a novel characterization of (i) the different flow patterns around static cylinders and (ii) the aeroelastic behaviour of flexible tandem cylinders in the transcritical flow regime.

¹ Zdravkovich M.M. (1985), Flow induced oscillations of two interfering circular cylinders, *Journal of Sound and Vibrations*, 101 (4), 511-52

² Sumner D. (2010), Two circular cylinder in cross-flow: A review, *Journal of Fluids and Structures*, 26, 849-899

³ Okajima A. (1979), Flows around two tandem circular cylinders, *JSME*, 22 (166), 504-511

Vortex Induced Vibration Analysis of a Cantilevered Hydrofoil by Laser Vibrometry and TR-PIV

1st Astolfi J. A. ¹, 2nd Bot P.² and 3rd Leroy L.³

¹ *Naval Academy, Brest ,France, jacques-andre.astolfi@ecole-navale.fr*

² *Naval Academy, Brest ,France*

³ *Naval Academy, Brest ,France*

Abstract

The structural response of a steel cantilevered hydrofoil is analyzed through an experiment carried out in a hydrodynamic tunnel for Reynolds numbers ranging from 2×10^5 to 8.25×10^5 . The hydrofoil is set at a 17° angle to the flow direction, in order to maximize the hydrodynamic forcing issued from the vortex shedding, thus enhancing fluid structure interactions. The structural response is measured through the vibration velocity using a laser Doppler vibrometer. The flow dynamics are analyzed through Time Resolved-Particle Image Velocimetry (TR-PIV) and Proper Orthogonal Decomposition. An interaction between the vortex shedding phenomenon and the modal response of the structure is observed. A decrease of the modal frequencies occurs for Reynolds numbers above 4×10^5 . The modal frequencies are found to decrease towards the vortex shedding frequency as the velocity increases resulting in resonance flow velocities much lower than the ones predicted in a non coupling hypothesis. The experimental results presented in this paper will help to develop fluid-structure interaction models and simulations in naval applications.

Keyword: Vortex Induced Vibration, Hydrodynamics, vibrometry, hydrofoil

1 Introduction

Due to the large density of water and very small Mach numbers compared to air, Fluid Structure Interactions are much different for naval applications than for aerodynamic ones. The knowledge of the vibratory response of lifting bodies to hydrodynamic excitation is fundamental for the designing and sizing of naval systems such as marine propellers (Young, 2008), active control surfaces like rudders (Turnock and Wright,2000) or innovative tidal turbine blades (Nicholls-Lee et al.2009). Moreover flow induced vibrations are a major issue for naval ship discretion or passenger comfort. Indeed, marine propellers for instance are mainly designed considering the hydrodynamic aspect and less attention is paid to the deformations and vibrations of the structure interacting with the flow. In some extreme cases, the flow excitation can tune in with the structural response and cause major noise or dramatic deteriorations of the structure. Research have already enlightened interactions between viscous flow and the modal response of a hydrofoil in various flow conditions at the Naval Academy (Ducoin et al. 2012, Lelong et al. 2018).

One topic of great interest for naval applications is the coupling between vortex shedding and structural response (Blevins,1984) and the understanding of Fluid Structure Interaction on

elastic structures immersed in a high density fluid still requires experimental studies. The present paper deals with the study of a cantilevered rectangular NACA0015 hydrofoil modal response through an original experiment carried out in the French Naval Academy hydrodynamic tunnel for Reynolds number ranging progressively from 2×10^5 to 8.25×10^5 . The hydrofoil is set at a 17° angle to the flow direction, in order to maximize the hydrodynamic loading issued from the vortex shedding phenomenon, thus enhancing fluid structure interactions. The experimental set-up is presented in Section 2 where the vibration velocity measurement and time-resolved Particle Image Velocimetry are presented. Results are presented and discussed in Section 3 and concluding remarks are given in Section 4.

2 Experimental set-up

2.1 Hydrodynamic Tunnel

The experiments were carried out at the hydrodynamic tunnel of the Research Institute of the French Naval Academy. The test section is $0.192 \times 0.192 \text{ m}^2$ and 1 m long, as shown in figure 1. At the entrance of the test section, the upstream velocity and pressure are regulated with an accuracy of $\pm 2\%$ and $\pm 2.5\%$ respectively. In the test section, the upstream flow velocity ranges from 0.5 m.s^{-1} to 15 m.s^{-1} and the pressure ranges from 300 mbar to 3 bar to control cavitation inception and development.

For the present study, the upstream flow velocity U ranges from 2 m.s^{-1} to 8.25 m.s^{-1} by steps of 0.5 m.s^{-1} and a last step of 0.25 m.s^{-1} . The pressure in the test section is set to avoid the development of cavitation on the surface of the hydrofoil. The free stream turbulence intensity in the middle of the test section is 2%.

A stainless steel hydrofoil is mounted with an angle of incidence of $\alpha = 17^\circ$ at mid height of the test section (figure 2). The hydrofoil is clamped at the end of the rotation axis. The hydrofoil has a span-symmetrical NACA0015 section with a relative thickness of 15%, the chord is $c = 0.1 \text{ m}$ and the span is 0.191 m .

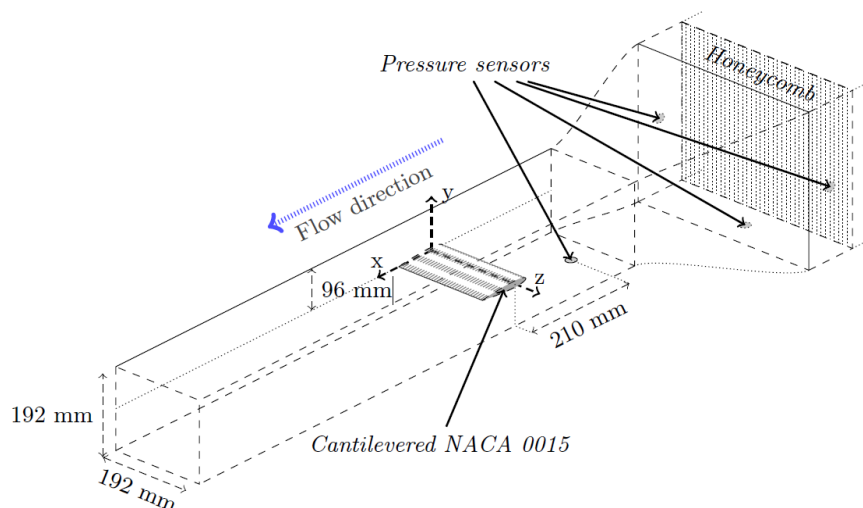


Figure 1: Test section of the hydrodynamic tunnel at the french naval academy

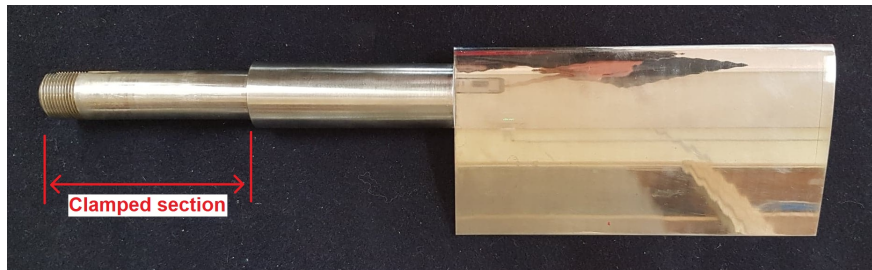


Figure 2: Cantilevered NACA0015 hydrofoil

2.2 Vibration measurements

The vibration measurements and modal analyses were performed with a Polytec® PSV-400 scanning laser vibrometer. The vibrometer measured the vibration of a single reference point situated near the trailing edge at the free tip of the structure. The laser vibrometer can detect vibration velocities from $0.01 \text{ m}\cdot\text{s}^{-1}$ to $10 \text{ m}\cdot\text{s}^{-1}$ using a HeNe laser ($\lambda = 633 \text{ nm}$) based on the Doppler effect. It is equipped with two analog velocity decoders VD-04 and VD-06. Time evolution of the vibration velocity is measured and is then post processed using a Fast Fourier Transform Algorithm to obtain the spectrum of the signal with a frequency resolution of 0.3125 Hz . Each spectrum used in this study comes from the mean of 64 individual measurements. The spectra amplitude can be presented in two ways: $\text{m}\cdot\text{s}^{-1}$ or dB. Conversion from $S=\text{m}\cdot\text{s}^{-1}$ to $\text{dB}=20\log(S/S_{\text{ref}})$, with $S_{\text{ref}} = 1 \text{ m}\cdot\text{s}^{-1}$. This allows us to detect the modal structure frequencies as well as hydrodynamic frequencies as the vortex shedding in the present study.

2.3 TR-PIV measurements

2D Time Resolved -Particle Image Velocimetry (PIV) technology was also used for the experimental characterization of the flow. The PIV measurement plane is located at mid-span. The PIV device consists of two pulsed YAG laser used to lighten the flow. A high precision CCD camera with a high resolution and a sampling frequency of 1KHz has been used. The Proper Orthogonal Decomposition was applied on the PIV measurements in order to analyze flow dynamics. Figure 3 shows the two first modes showing clearly the vortex shedding structure and dynamics. The analysis of the time series of the mode coefficients allows us to extract the frequency contents and particularly the vortex shedding frequency f_0 . This allows to clearly identify this frequency in the structural vibration spectra

3 Results and discussion

3.1 Modal response of the structure

Figure 4 shows the individual measured spectrum of the vibration for various stream velocities. Figure 5 shows the same results in a plane view representing the amplitude of vibration versus the frequency and the Reynolds number. Several peaks can be observed corresponding to the natural modes of the structure. Only the first 3 modes will be studied, due to their greater

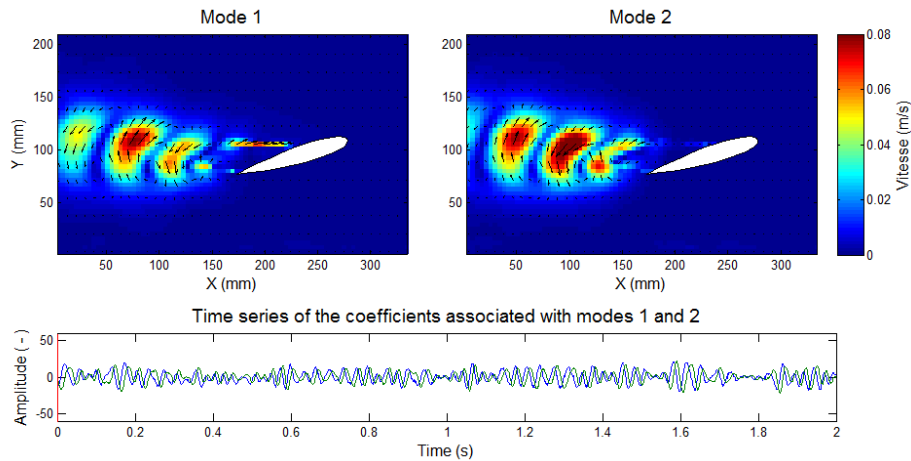


Figure 3: POD analysis, Inco hydrofoil, $\alpha = 17^\circ$, $U = 4m.s^{-1}$

amplitude compared to the others. The main peak frequency ranges from 105 up to 116 Hz, depending on the stream velocity and corresponds to the first mode (f_1). Then, a second peak from 194 Hz to 204 Hz corresponds to the second mode (f_2). Finally, a third peak ranges from 509 Hz to 552 Hz and corresponds to the third mode (f_3). According to the works of Lelong et al.(2018) on the same geometry, the nature of the first, second and third modes are respectively the first bending mode, the first twisting mode and the second bending mode.

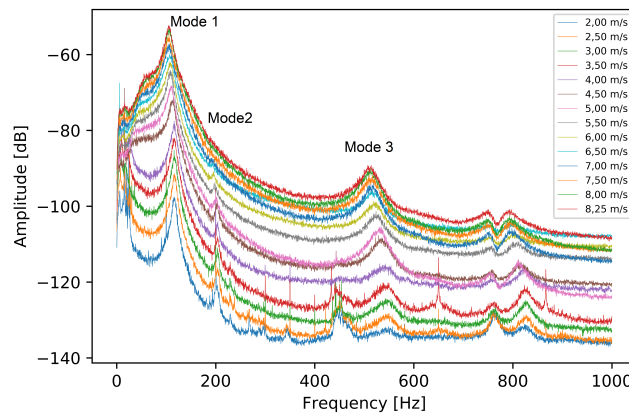


Figure 4: Vibration velocity spectra for various free stream velocities.

In order to correctly detect the local maxima corresponding to the 3 modes the spectra are smoothed using the moving average over 3Hz, avoiding small parasitic fluctuations. Then, the frequency of the 3 modes are extracted from each vibration spectrum by selecting the corresponding local maximum. They are reported on Figure 6 as a function of the flow velocity. For a clearer view on the same plot the evolution of these frequencies, f_1 has been multiplied by a factor of 4 and f_2 by a 2.5 factor.

Two distinct behaviors can be distinguished in figure 6. First, for flow velocities lower than 4 $m.s^{-1}$ the modal frequencies remain constant. Then, for higher flow velocities the modal frequencies tend to decrease with the stream velocity. This enlightens an interaction between

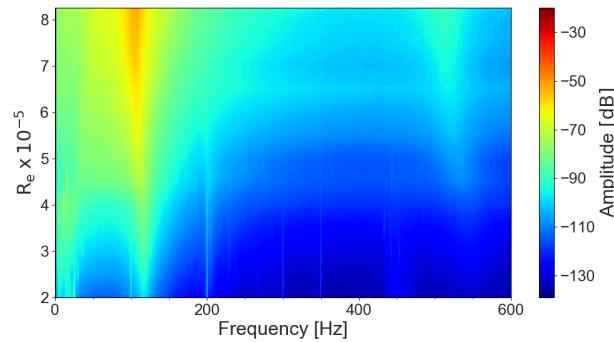


Figure 5: Power spectral density of the structure response versus frequency and Reynolds number.

the flow and the vibration of the hydrofoil. In taking a closer look around the first mode peak on figure 4, the start of the modal frequency decreasing is accompanied by a net increase of the vibration amplitude for flow velocities larger than $4 \text{ m}\cdot\text{s}^{-1}$. The matching of this increase with the vortex shedding phenomenon will be addressed in the next section.

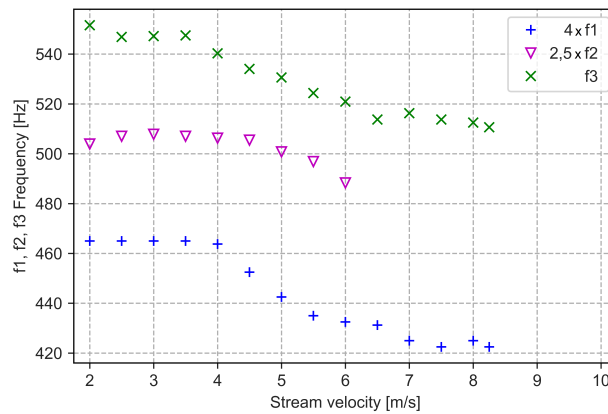


Figure 6: Modal frequencies versus free stream velocity.

3.2 Vortex shedding

A focused view on the low frequencies of the spectra can be seen in figure 7. The two different behaviors discussed in the previous section can thus be depicted further. The vibration spectra for flow velocities lower than $4 \text{ m}\cdot\text{s}^{-1}$ show a more or less well defined frequency peak. Increasing the flow velocity beyond $4 \text{ m}\cdot\text{s}^{-1}$ shows that the peak turns clearly into a change of slope inducing an inflexion zone into the vibration spectra with a global increase of the vibration level up to the bending mode.

In order to determine whether the peak or the inflexion point stands for the vortex shedding frequency (f_0), a Strouhal number is defined by :

$$St = \frac{f_0 \times c \times \sin(\alpha)}{U}$$

By setting $St=0.2$ it is clearly shown in figure 7, that the so calculated f_0 frequency corresponds to the noisy peak at low flow velocities and to the inflexion point for larger velocities. The present phenomenon can be described as the shedding of vortices inducing fluctuations of the pressure distribution along the surface of the hydrofoil, thus leading to a periodic variation of the lift force (Williamson and Govardhan, 2004). The structure vibrates under such a load so that the vortex shedding frequency is printed on the vibration spectra.

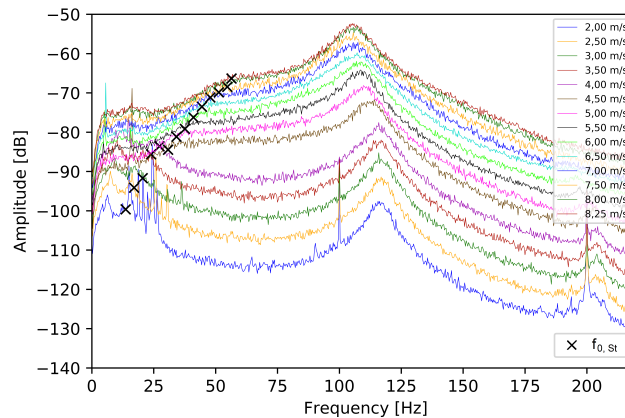


Figure 7: Vortex shedding frequency given by $St=0.2$, plotted (black symbols) on the vibration velocity spectra.

The experimental f_0 values can now be extracted from the vibration spectra on figure 8. The local maximum corresponding to the noisy peak is selected for spectra under $4\text{m}\cdot\text{s}^{-1}$. An interpolation on the interval $[25\text{Hz}, 75\text{Hz}]$, using the least square method, with a two piecewise line function is used for each spectrum above $4\text{m}\cdot\text{s}^{-1}$, the f_0 value corresponding to the intersection point. These experimental values are reported in figure 9 showing a fairly linear evolution. It can be pointed that the f_0 frequency extracted from the vibration spectra was found to be in very good agreement with the one issued from the POD analysis of the flow field. Finally the experimental Strouhal numbers extracted from the vibration spectra are plotted versus the stream velocity (figure 10), confirming that $St=0.2$ is fairly good especially at velocities larger than $4\text{m}\cdot\text{s}^{-1}$.

The extreme case of shedding frequency excitation occurs when the shedding frequency aligns with a natural frequency of the structure. This lock-in condition increases strongly the vibration magnitudes until other loss mechanisms dissipate the energy or catastrophic failure occurs. In the present case, for a stream velocity lower than $4\text{m}\cdot\text{s}^{-1}$ the vortex shedding excites the structure around one particular frequency f_0 . Then above $4\text{m}\cdot\text{s}^{-1}$ the vortex shedding phenomenon excites the structure evenly on a range of frequencies, from f_0 to f_1 .

In order to bring to light the start of a lock-in effect during this experiment, the RMS value of the vibration signals is calculated from the integration of the vibration spectra.

It is plotted versus the flow velocity on Figure 11. As shown, a net rise of the vibration intensity is clearly noticeable from $4\text{m}\cdot\text{s}^{-1}$ velocity. A power law interpolation shows that the RMS value evolves as the flow velocity to the power 2.7.

Therefore, when the range of frequencies from f_0 to f_1 are excited, the vortex shedding

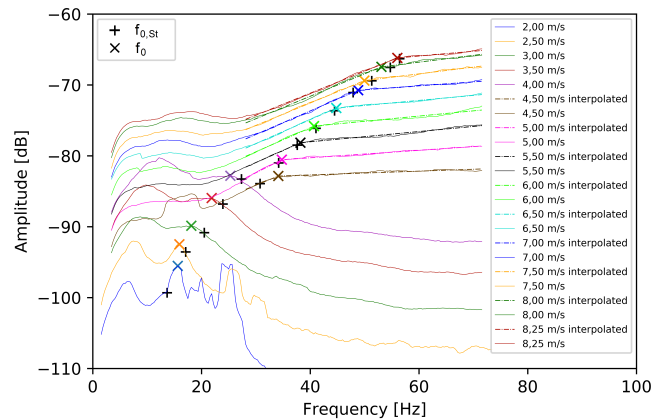


Figure 8: Vortex shedding frequency f_0 extraction on the vibration velocity spectra based on the inflexion point determination. Comparison with f_0 deduced from $St=0.2$ (black symbols)

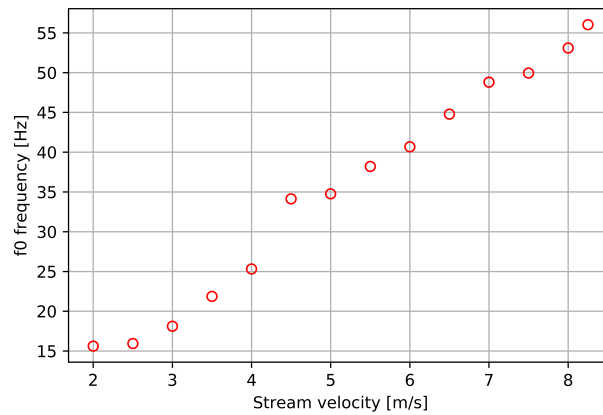


Figure 9: Experimental vortex shedding deduced from vibration spectra versus the flow velocity.

starts to tune in with the first mode of vibration. That lock-in seems to be the cause for the modal frequencies to decrease. This phenomenon is all the more interesting as it influences not only the first mode, but at least the first three modes.

Furthermore, the flow velocities for which the natural modes of the structure coincide to the vortex shedding phenomenon can be extrapolated from figure 12 considering a linear decreasing of the modal frequencies from a $4\text{m}\cdot\text{s}^{-1}$ along with the linear extrapolation of the vortex shedding frequency f_0 .

As shown in table 1 the resonance velocities are found to be much lower when considering the linear decreasing of modal frequencies versus the flow velocity due to flow structure coupling.

4 Conclusions

The experimental vibration response of a cantilevered NACA0015 hydrofoil has been analyzed using a laser Doppler vibrometer at 17° angle of incidence. The first three modes frequencies as well as the vortex shedding frequency could be extracted from the vibration spectra of the

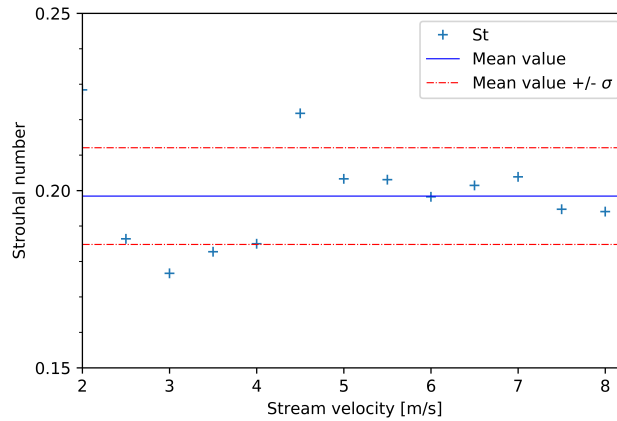


Figure 10: Experimental Strouhal number versus the flow velocity.

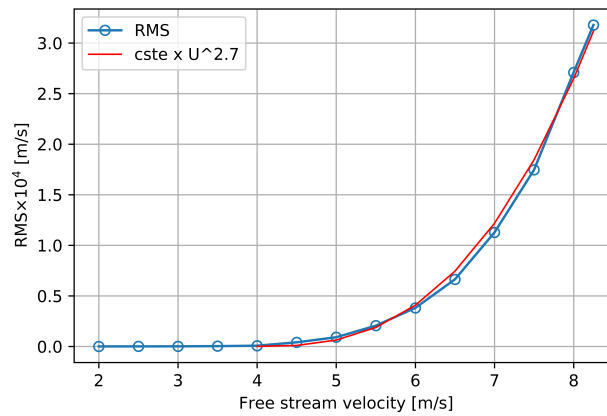


Figure 11: Vibration rms value versus flow velocity.

 Table 1: Extrapolated resonance velocities with constant modal frequencies or linear decreasing (unit $\text{m}\cdot\text{s}^{-1}$)

Extrapolation	Mode 1	Mode 2	Mode 3
constant	17,1	29,7	80,4
linear	13,3	21,9	35,1

hydrofoil.

Two behaviors have been identified. The first one at stream velocity lower than $4\text{m}\cdot\text{s}^{-1}$, the vortex shedding phenomenon excites the structure solely at the vortex shedding frequency. In that case the modal frequencies of the foil remain unaffected. The second one at higher stream velocity, the vortex shedding phenomenon excites the structure evenly on a range of frequencies from the vortex shedding frequency to the first mode frequency. In that case the modal frequencies are observed to decrease linearly with the stream velocity.

Furthermore, this decreasing of the modal frequencies causes the resonance phenomenon, be-

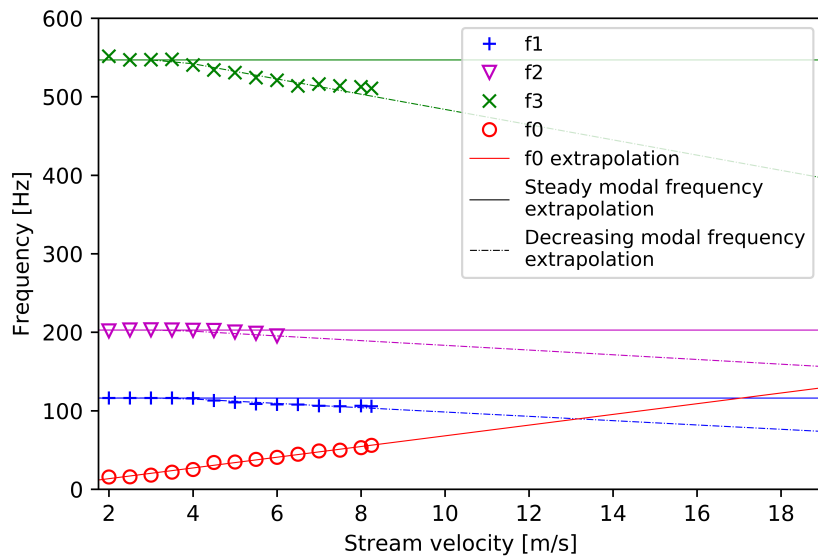


Figure 12: Modal and vortex shedding frequencies versus the flow velocity.

tween the natural modes of the structure and the vortex shedding, to occur at lower stream velocities than expected, when initially considering constant modal frequencies.

The shift of the modal frequencies towards the vortex shedding frequency of the structure enlightened in this paper is of primary importance when designing marine lifting surfaces. This study paves the way for further investigations in understanding fluid structure interactions for naval applications. These results would benefit from additional measurements at higher Reynolds numbers, which were not feasible without inducing cavitation in the hydrodynamic tunnel.

References

- R.D. Blevins, 1984 Review of sound induced by vortex shedding from cylinders, *Journal of Sound and Vibration*, Volume 92, Issue 4, Pages 455-470,
- Ducoin A., Astolfi J. A., Sigrist J.F., 2012. An experimental analysis of fluid structure interaction on a flexible hydrofoil in various flow regimes including cavitating flow, *European Journal of Mechanics - B/Fluids*, Volume 36, Pages 63-74,
- Lelong, A., Guiffant, P., and Astolfi, J.A., 2018. "An Experimental Analysis of the Structural Response of Flexible Lightweight Hydrofoils in Cavitating Flow." *ASME. J. Fluids Eng.* February; 140(2)
- Nicholls-Lee, R.F., Boyd, S.W. and Turnock, S.R., 2009. Development of high performance composite bend-twist coupled blades for a horizontal axis tidal turbine. ICCM17: 17th International Conference on Composite Materials, United Kingdom. 27 - 31 Jul 2009. 10 pp
- S.R. Turnock, A.M. Wright, 2000. Directly coupled fluid structural model of a ship rudder behind a propeller, *Marine Structures*, Volume 13, Issue 1, Pages 53-72,

.H.K. Williamson, and, and R. Govardhan, 2004. Vortex-Induced Vibrations. Annual Review of Fluid Mechanics 2004 36:1, 413-455

Y.L. Young,2008. Fluid-structure interaction analysis of flexible composite marine propellers, Journal of Fluids and Structures, Volume 24, Issue 6, Pages 799-818.

Vortex induced vibration of two tandem cylinders in subcritical regime

François Rigo^{1,2}, Vincent Denoël³ and Thomas Andrianne¹

¹ *Wind Tunnel Lab, University of Liège, Liège, Belgium, francois.rigo@uliege.be*

² *FRS-FNRS, National Fund for Scientific Research, Liège, Belgium*

³ *Structural & Stochastic Dynamics, University of Liège, Liège, Belgium*

Keyword: Fluid structure interaction, wind tunnel experimental testing, Van der Pol oscillator, spring mounted cylinders.

Vortex induced vibrations (VIV) have been widely studied for a singular cylinder. Many engineering applications also involve multiple body configurations and particularly cylinders in tandem, with a strong interaction between cylinders through wake interference, depending on the spacing between them.

The specific features of this interaction has been widely studied in terms of topology¹. Some studies² also propose to extend the well-known wake oscillator model from one to two tandem cylinders. These models based on a Van der Pol oscillator require empirical coefficients, particularly for the coupling terms between cylinder wakes, which have to be experimentally identified. Different configurations are thus required compared to the simple cases already studied³.

We propose to carry out an extensive experimental campaign in the low-subsonic wind tunnel of University of Liège to feed a VIV model. The quality of measures extends the knowledge in several aspects: (i) measurement in air instead of water, (ii) extensive pressure measurement on both cylinders, in case of (iii) free vibration test (both cylinders in free response) and extended to (iv) forced vibration test.

The parametric study consists in studying the geometric effects (spacing and angle of attack between cylinders) and, on a side basis, the influence of turbulence properties (intensity, integral length scales) is studied regarding their effect on the synchronization of both cylinders and their wakes.

The proposed work consists in a novel and complete (i) flow characterization in static, free and forced motion of both cylinders, (ii) identification of experimental parameters used to supply an improved VIV model.

¹ Sumner, D. (2010), Two circular cylinders in cross-flow: A review, *Journal of Fluid and Structures*, 26, 849-899.

² Facchinetti, M., de Langre, E., Fontaine, E., Bonnet, P., Etienne, S., Biolley, F. (2002), VIV of Two Cylinders in Tandem Arrangement: Analytical and Numerical Modeling, *Proceedings of the International Offshore and Polar Engineering Conference*, 12, Kitakyushu, Japan.

³ Arie, M., Kiya, M., Moriya, M., and Mori, H. (1983), Pressure Fluctuations on the Surface of Two Circular Cylinders in Tandem Arrangement, *ASME. J. Fluids Eng.* 105(2), 161-166.

Energy harvesting

Energy harvesting from FIV of different diameter cylinders

Md. Mahbub Alam, Chen Zhenlin, Qin Bin and Yu Zhou

*Institute for Turbulence-Noise-Vibration Interaction and Control, Harbin Institute of Technology (Shenzhen), Shenzhen 518055, China
Email: alam@hit.edu.cn; alamm28@yahoo.com*

Abstract

The energy harvesting from flow-induced vibration (FIV) of an elastically-supported cylinder (diameter D) immersed in the wake of another cylinder with diameter d is investigated systematically. The diameter ratio d/D is 0.4. The incoming flow velocity considered is $U_\infty = 1.54 \text{ m/s} - 9.0 \text{ m/s}$, corresponding to $Re = 3.3 \times 10^3 - 1.95 \times 10^4$. A controllable magnetic damping system that can add harnessing damping ratio ζ is used for converting wind energy to electrical energy. The ζ is varied up to 0.00340. Seven spacing ratios $L/d = 1.0, 1.5, 2.0, 2.5, 3.0, 3.5$ and 4.0 are considered, where L is the distance from the upstream cylinder center to the forward stagnation point of the downstream cylinder. The results indicate that the vibration responses and corresponding harnessed power and efficiency are influenced by reduced velocity U_r , L/d and ζ .

Keyword: energy harvesting, flow-induced vibration, efficiency.

1 Introduction

Among the different kinds of Flow-induced vibration (FIV), the vortex-induced vibration (VIV) of a circular cylinder has received considerable attention as an external source for energy harvesting (Akaydin et al., 2012; Soti et al., 2017). VIV is a self-limited amplitude vibration, occurring in the lock-in range only. When the damping ratio is increased, the lock-in range narrows and the vibration amplitude contracts, both adversely influencing the energy harvesting (Sarpkaya, 2004; Williamson and Govardhan, 2004). The galloping vibration, on the other hand, is not self-limiting; the vibration amplitude increases with increasing the reduced velocity of the flow. Typically, VIV occurs at a range of low reduced velocities while galloping initiating at a velocity in or beyond the lock-in range persists at high reduced velocities. As such, compared to energy harvesting from VIV, energy harvesting from galloping vibrations can be a better alternative. In the literature, the circular cylinder is the most investigated model because of its simplicity and extensive applications in engineering and nature. A circular cylinder, however, does not experience galloping, being an infinite-order rotational symmetry of its cross-section with respect to the flow. Two or more cylinders in proximity may undergo galloping as the combined cylinders or the downstream cylinders are not axis-symmetric with respect to the local flow (Barrero-Gil et al., 2010; Bokaian and Geoola, 1984).

Several investigations have been conducted on the energy extraction from the FIV of multiple cylinders. Zhang *et al.* (2017) investigated the impact of a downstream cylinder on the energy harvesting from VIV of the upstream one, with $L/d = 1.3 \sim 4.0$. They found that L/d strongly affects the harvested power and the bandwidth of the lock-in region. The harvested power was dramatically enhanced, compared with that of a single cylinder. Jung

and Lee (2011) examined the energy harvesting from the galloping response of an elastically-mounted downstream cylinder with $L/d = 3 \sim 13$. The average power of $50 \sim 370$ mW was harvested at $U_\infty = 2.5 \sim 4.5$ m/s, where U_∞ is the free-stream velocity. For the FIV experiment, Sun *et al.* (2015) designed a Virtual Spring–Damping System V_{ck} that could emulate springs and dampers efficiently and precisely. Thereafter, Sun *et al.* (2017) investigated the FIV of two tandem cylinders in the V_{ck} system for $L/d = 1.57 \sim 2.57$, claiming that a small L/d and/or a high f_n provide a high harnessed power P .

The above investigations were concerned with the two cylinders of the same diameter ($d/D = 1.0$). Recently, it has been found that a change in d/D has a remarkable effect on the flow structures, no matter the cylinders are fixed (e.g. Alam and Zhou 2008, Wang *et al.* 2018) or elastically mounted (e.g. Qin *et al.* 2017). Qin *et al.* (2017) investigated the vibration of the downstream cylinder placed in the wake of a fixed cylinder with $d/D = 0.2 \sim 1.0$, $L/d = 1.0 \sim 5.5$. Violent vibration of the downstream cylinder was not observed for $d/D = 1$ but was for $d/D < 1$, depending on L/d . That is, when the upstream cylinder size was small, the downstream cylinder was more prone to generating galloping vibrations. Since the cylinder is more prone to generating larger amplitude galloping vibration for $d/D < 1$ than for $d/D = 1$, one may expect more energy for the former d/D range than the latter. To the authors' knowledge, energy harvesting from FIV of different diameter cylinders has not been investigated in the literature. This work aims to experimentally investigate the energy harvesting from FIV of a cylinder submerged in the wake of another with $d/D = 0.4$. This d/D corresponded to initiation of vibration at a smaller reduced velocity (Qin *et al.* (2017)) and was also considered as a representative of $0.2 \leq d/D < 1.0$.

2 Experimental setup

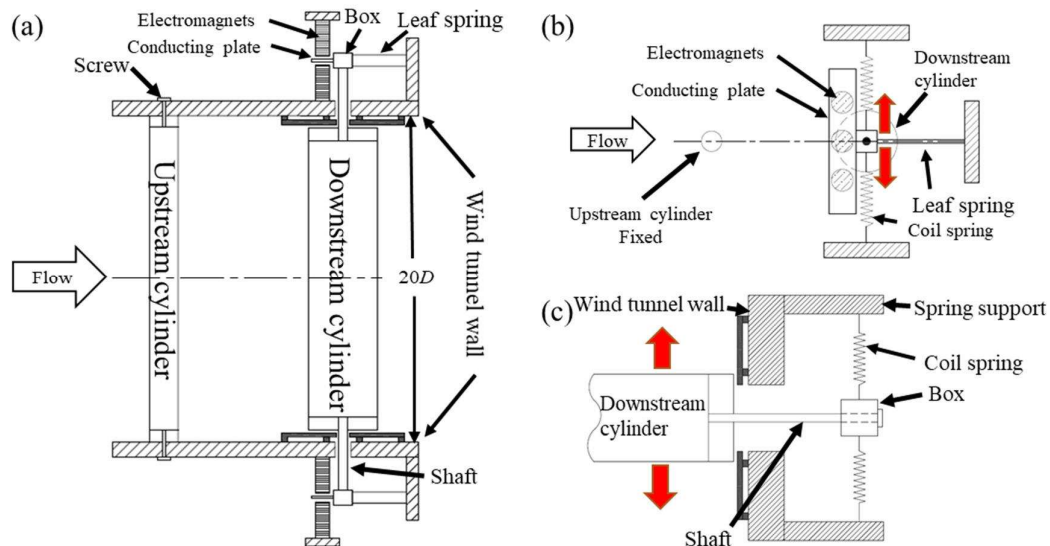


Figure 1: Experimental setup: (a) top view, (b) side view, and (c) front view.

Experiments were performed in a closed-circuit wind tunnel with the test section of $0.6 \text{ m} \times 0.6 \text{ m} \times 2.4 \text{ m}$. As shown in Fig. 1, the upstream cylinder with diameter $d = 12$ mm is fixed at its ends on the sidewalls of the wind tunnel. The downstream cylinder with diameter $D = 30$ mm and length $l = 545$ mm is connected to the supporting system via two shafts and cube boxes supported by spiral springs. A leaf spring is connected to the box so that the

cylinder can vibrate in the transverse direction only. Two end plates are mounted on the sidewalls of the wind tunnel to eliminate the side wall effects. In addition, the mass ratio $m^* = 4m/(\pi\rho D^2l) = 802$, where m is the total mass of the cylinder vibration system, and ρ is the density of the air. The spacing ratio L/d is varied by changing the position of the upstream cylinder. $L/d = 1.0, 1.5, 2.0, 2.5, 3.0, 3.5$ and 4.0 are considered. The aspect ratio L/d is 18.2 and the blockage ratio is 4.5%. The freestream velocity U_∞ is changed from 1.54 m/s and 9.0 m/s, corresponding to reduced velocity $U_r = U_\infty/f_n D = 4 \sim 23.4$ and $Re (= U_\infty D/\nu) = 3.3 \times 10^3 \sim 1.95 \times 10^4$, where ν is the kinematic viscosity of fluid.

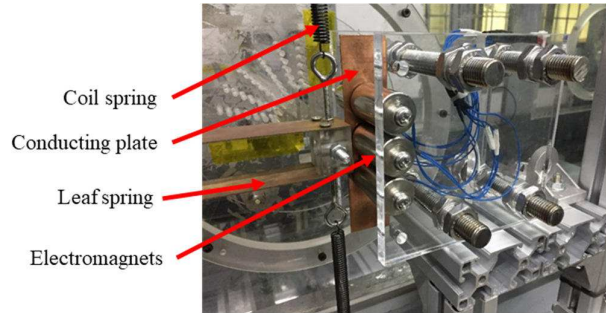


Figure 2: The photograph of the controllable magnetic damping system.

Each cylinder end was equipped with a controllable magnetic damping system used to change the damping of the vibrating system (Fig. 1a). A magnetic damping system consists of a copper conducting plate and six identical electromagnets (Fig. 2). The copper conducting plate with a thickness of 2 mm is attached to the vibrating system through the box, which can oscillate concordantly with the vibrating system. At each side of the copper conducting plate, three electromagnets are arranged uniformly, with the outer sides fastened to an acrylic sheet. A power supply (MS603D, MAISHENG), having a voltage range 0 ~ 28 V, is used to provide desired current to the magnet wires. In accordance with the electromagnetic induction effect, the mechanical energy of the plate transforms into electric energy, opposing the motion of the vibrating system. The induced force on the plate is opposite to the motion and proportional to the velocity of the plate, hence acts as a damping force which can be changed by changing the power supply voltage.

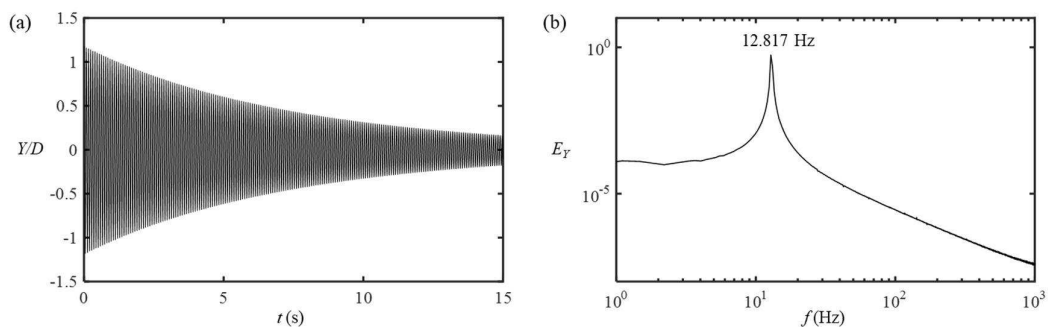


Figure 3: (a) Signal from a laser vibrometer after a plucking excitation, and (b) power spectrum of the displacement signal.

The cylinder displacement Y is measured by using a laser vibrometer (OFV-505/5000, Polytec), captured the displacement signal at a sampling frequency of 3 kHz in 60 seconds. The vibration amplitude A is calculated as $\sqrt{2}$ times root-mean-square of Y . The cylinder

vibration frequency is extracted from the fast-Fourier-transform based power spectral density function E_Y of Y . To estimate the structural damping ratio ζ_s and natural frequency f_n of the cylinder system, the downstream cylinder is given an initial displacement and then released to vibrate in the still air (Fig. 3a). The f_n is read from the power spectrum of the displacement signal, $f_n = 12.817$ Hz (Fig. 3b). The value of the structural damping ratio is obtained from the logarithmic decrement δ of the cylinder displacement through $\zeta_s = (\delta/2\pi)/\sqrt{1+(\delta/2\pi)^2}$. The ζ_s is obtained as 0.00091.

The total damping ratio ζ is composed of ζ_s and magnetic damping ratio ζ_m , i.e. $\zeta = \zeta_s + \zeta_m$. The ζ_m can be changed by controlling the voltage output V of the power supply. The estimation of ζ was done in the same way as those of ζ_s . At $V = 0$, $\zeta = \zeta_s$ since $\zeta_m = 0$. The ζ changes from 0.00091 to 0.00340 when V is increased from 0 to 28 V.

3 Mathematical model of energy harvesting from FIV

The mathematical model of energy harvesting is described in this section. The transverse vibration of the cylinder in the y -direction can be described by a second-order linear differential equation as (Bearman, 1984; Govardhan and Williamson, 2000; Williamson and Govardhan, 2004)

$$m\ddot{Y} + c\dot{Y} + kY = F_L(t) \quad (1)$$

where m is the total mass of the cylinder system; c is the total damping coefficient; k is the spring stiffness, and F_L is the lift force acting on the cylinder. The overdot represents a derivative with respect to time t .

The cylinder dynamics are periodic and nearly sinusoidal, and the predominant frequencies in Y is the same (Bearman, 1984). We can thus write

$$Y = A \sin(2\pi ft) \quad (2)$$

where $f = 1/T$ is the cylinder vibration frequency, A is the amplitude of the displacement.

The mechanical work done by the cylinder in a vibration cycle is

$$W_{Mech} = \int_0^T (m\ddot{Y} + c\dot{Y} + kY) \dot{Y} dt. \quad (3)$$

Only the term in phase with the velocity generates a nonzero energy term. The mechanical power of the cylinder is

$$P_{Mech} = \frac{1}{T} \int_0^T 4\pi m \zeta \dot{Y}^2 f_n dt = 8\pi^3 m \zeta (Af)^2 f_n. \quad (4)$$

The above equations hold when the oscillation is purely sinusoidal with constant amplitude, whereas the oscillation may not be of constant amplitude in experiments. To estimate P_{Mech} from experimental results, Eq. 10 can be rewritten as follows.

$$P = P_{Mech} = \frac{1}{t} \int_0^t 4\pi m \zeta \dot{Y}^2 f_n dt = \frac{1}{t} \sum_{i=1}^{f_s t} 4\pi m \zeta f_n \left(\frac{Y_{i+1} - Y_i}{1/f_s} \right)^2 \frac{1}{f_s}. \quad (5)$$

Where f_s is the sampling frequency, and t is sufficiently long, about 130 oscillation periods in the present experiment.

4 Vibration responses

In the case of the cylinder placed in the wake, Fig. 4 presents the dependence of vibration amplitude A/D on U_r and ζ for different values of L/d . Let us pay attention to the responses for $L/d = 1.0$ first (Fig. 4a). For $\zeta = 0.00091$ and 0.00093 , A/D escalating with increasing U_r reaches a peak at $U_r = 6.0$. It declines at $U_r = 6.0 \sim 8.9$ and grows for a further increase in U_r . Obviously, the growth of A/D in the latter range of U_r is due to galloping while the occurrence of a peak at $U_r = 6.0$ is associated with VIV. That is, the responses include combined VIV and galloping. For $\zeta \geq 0.00117$, the responses of the wake cylinder at small U_r (< 8) are similar to the single-cylinder case, showing VIV. Galloping vibration occurs at $U_r > 14 \sim 18$ (depending on ζ), with A/D enhancing with increasing U_r . A couple of observations can be made here. Firstly, VIV and galloping vibrations are separated. Secondly, in both VIV and galloping vibration regimes, A/D diminishes with increasing ζ . Thirdly, the bandwidth of the VIV regime shrinks when ζ is increased. Fourthly, the onset of galloping vibration (critical reduced velocity U_{rc}) delays when ζ is increased; i.e. $U_{rc} = 13.6, 14.7, 15.3, 15.8, 16.9$ and 17.5 for $\zeta = 0.0017, 0.0015, 0.00205, 0.00246, 0.00298$ and 0.00340 , respectively.

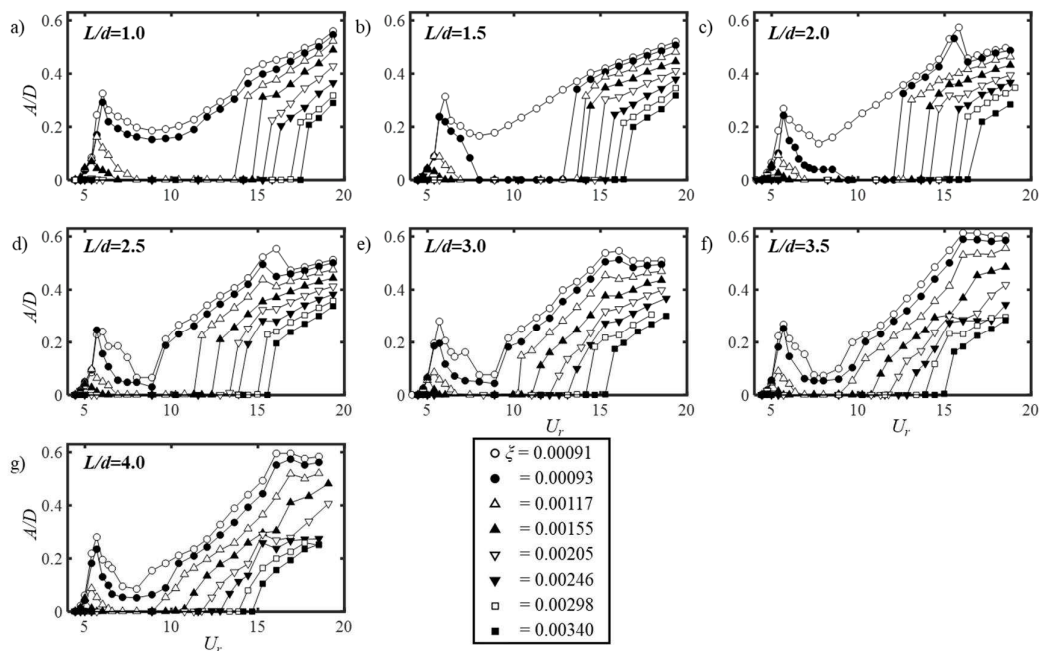


Figure 4: Dependence of A/D on U_r and ζ at (a) $L/d = 1.0$, (b) $L/d = 1.5$, (c) $L/d = 2.0$, (d) $L/d = 2.5$, (e) $L/d = 3.0$, (f) $L/d = 3.5$, and (g) $L/d = 4.0$.

At $L/d = 1.5$ and 2.0 , similar observations are made, except that $\zeta = 0.00093$ now has a separated VIV and galloping (Fig. 4b, c). Interestingly, at $L/d \geq 2.5$, again combined VIV and galloping materializes for $\zeta = 0.00091$ and 0.00093 and separated VIV and galloping for $\zeta \geq 0.00117$. For the separated VIV and galloping cases at $L/d \geq 2.5$, the inception of galloping shifts at a smaller U_r when L/d is higher. The A/D in the VIV regime for a given ζ does not change much with increasing L/d . At $L/d = 2.0 \sim 3.0$, there is a sudden small drop of A/D around $U_r = 15.6 \sim 16.3$ for $\zeta = 0.00091$ and 0.00093 while the drop flattens at $L/d \geq 3.5$.

The global view of the dependence of A/D on U_r and ζ can be illuminated from the contours

of A/D on the $\zeta \sim U_r$ plane (Fig. 5). A VIV peak is discernible at $U_r = 6.0$ for low ζ . When ζ is high, the A/D associated with VIV is small for all L/d . In the galloping region, the dependence of A/D on ζ and U_r is quite regular at different L/d . The boundary where the color suddenly changes represents the onset of galloping. In general, A/D increases with increasing U_r and decreasing ζ . Peaks appear at $U_r = 15.0 \sim 16.0$ for low ζ at $L/d = 2.0 \sim 4.0$.

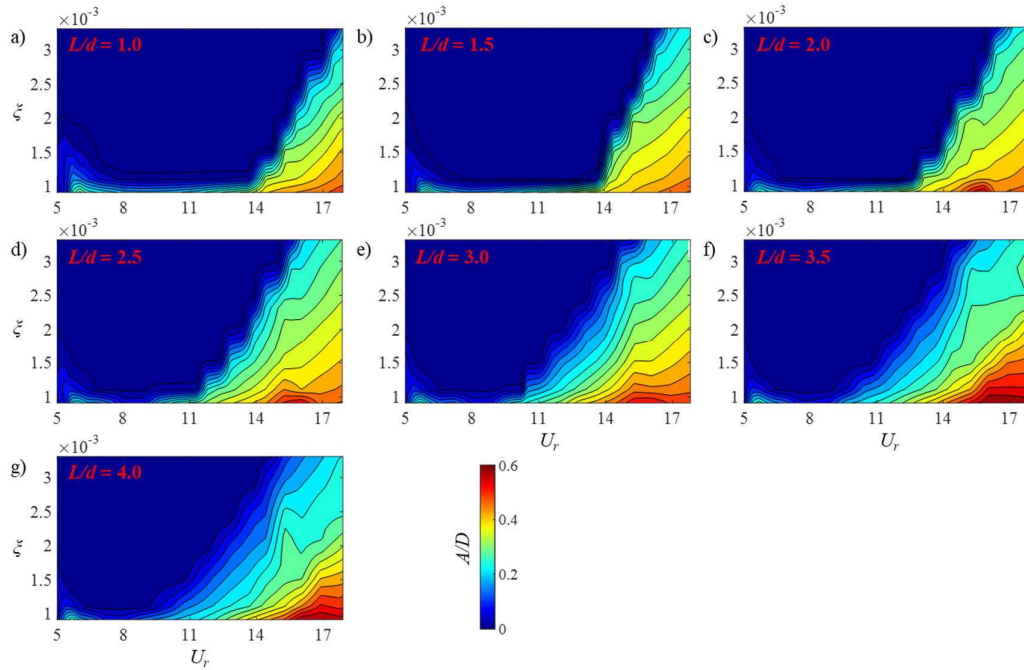


Figure 5: Contours of A/D on $U_r \sim \zeta$ plane at (a) $L/d = 1.0$, (b) $L/d = 1.5$, (c) $L/d = 2.0$, (d) $L/d = 2.5$, (e) $L/d = 3.0$, (f) $L/d = 3.5$, and (g) $L/d = 4.0$.

5 Harnessed power

The dependence of harnessed power P on U_r for various ζ at different L/d is shown in Fig. 6. The cylinder oscillated at its natural frequency in both VIV and galloping regimes (Qin *et al.* 2017). Thus, the power equation $P_{Mech} = 8\pi^3 m \zeta A^2 f_n^3$ (Eq. 4) states that power is directly proportional to ζ and A^2 , i.e. $P \propto \zeta A^2$. That is, P enhances at a greater rate with an increase in A than with an increase in ζ . For all the cases investigated, in the VIV regime, the P is small, with $P \leq 0.0186$ W. On the other hand, P is large in the galloping regime, three times more than that in the VIV regime or for single cylinder case. The wake cylinder with galloping vibration is thus better in view of energy harnessing. As seen in Fig. 4, A/D is larger for $\zeta = 0.00091$ than for other ζ in the entire range of U_r , regardless of L/d . The P at $\zeta = 0.00091$ thus dominates that at other ζ in the VIV regime. In the galloping regime, P data at different ζ come closer to one another (Fig. 6), compared to A/D data (Fig. 4). This is because while A/D is small at large ζ , the P is large at large ζ for a given A/D . On the whole, P rises as U_r increases. As mentioned before, A/D drops with U_r at around $U_r = 15.6 \sim 16.3$ or remains nearly unchanged when $U_r > 16.1$ for some cases (e.g. Fig. 4c, d). So does P for the same cases. Finally, P for the single-cylinder is also estimated (Fig. 6h), showing that only a small amount of energy is harnessed in the VIV range, given that the vertical scale for the single-cylinder case (Fig. 6h) is 8 times smaller than that of others.

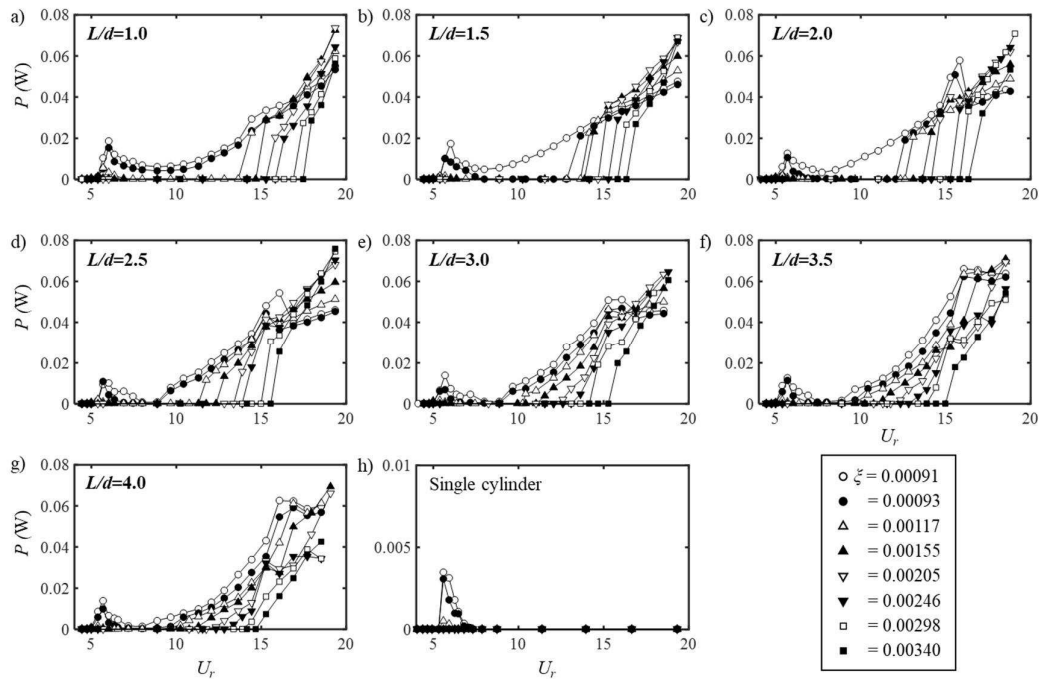


Figure 6: Dependence of P on U_r and ζ at (a) $L/d = 1.0$, (b) $L/d = 1.5$, (c) $L/d = 2.0$, (d) $L/d = 2.5$, (e) $L/d = 3.0$, (f) $L/d = 3.5$, and (g) $L/d = 4.0$, and (h) for the single cylinder.

7 Conclusions

An experimental investigation is performed on the energy harnessing from FIV of an elastically-mounted cylinder immersed in the wake of another of smaller diameter ($d/D = 0.4$). The L/d is varied from 1.0 to 4.0 while U_r is from 4.0 to 23.4. An electromagnetic damping system is used to extract energy from the oscillation cylinder. The vibration responses, harnessed power and harvesting efficiency are examined in L/d , U_r and ζ domains. While a single-cylinder experiences VIV only, the wake cylinder undergoes both VIV and galloping.

The VIV peak amplitude of the wake cylinder is significantly higher than that of a single-cylinder, with maximum amplitude $(A/D)_{max} = 0.31 \sim 0.33$ (depending on L/d) for the wake cylinder and $(A/D)_{max} = 0.14$ for the single-cylinder at $\zeta = 0.00091$. The vibration responses feature combined VIV and galloping for small ζ and separated VIV and galloping for high ζ . Separated galloping vibration occurs at $U_r > 14 \sim 18$ (depending on ζ), with A/D enhancing with increasing U_r . With ζ increasing, the vibration amplitude and bandwidth of VIV shrinks.

In the VIV regime, the P is small, less than 0.0186 W. On the other hand, P is three times larger in the galloping regime than in the VIV regime. In view of energy harnessing, the galloping is better than the VIV. The P in the VIV regime becomes maximum at the U_r where A/D is maximum while that in the galloping regime rises as U_r increases. A smaller ζ leads to a larger maximum P .

Acknowledgements

The authors wish to acknowledge the support given by the National Natural Science Foundation of China through Grants 11672096 and 91752112 and by Research Grant Council of Shenzhen Government through grant JCYJ20180306171921088.

References

- Akaydin, H.D., Elvin, N., Andreopoulos, Y., 2012. The performance of a self-excited fluidic energy harvester. *Smart Materials and Structures* 21 (2).
- Barrero-Gil, A., Alonso, G., Sanz-Andres, A., 2010. Energy harvesting from transverse galloping. *Journal of Sound and Vibration* 329 (14), 2873-2883.
- Bearman, P.W., 1984. Vortex shedding from oscillating bluff bodies. *Annual Review of Fluid Mechanics* 16, 195-222.
- Bokaian, A., Geoola, F., 1984. Wake-induced galloping of two interfering circular cylinders. *Journal of Fluid Mechanics* 146 (1).
- Govardhan, R., Williamson, C.H.K., 2000. Modes of vortex formation and frequency response of a freely vibrating cylinder. *Journal of Fluid Mechanics* 420, 85-130.
- Jung, H.-J., Lee, S.-W., 2011. The experimental validation of a new energy harvesting system based on the wake galloping phenomenon. *Smart Materials and Structures* 20 (5).
- Mahbub Alam, M., Zhou, Y., 2008. Strouhal numbers, forces and flow structures around two tandem cylinders of different diameters. *Journal of Fluids and Structures* 24 (4), 505-526.
- Qin, B., Alam, M.M., Zhou, Y., 2017. Two tandem cylinders of different diameters in cross-flow: flow-induced vibration. *Journal of Fluid Mechanics* 829, 621-658.
- Sarpkaya, T., 2004. A critical review of the intrinsic nature of vortex-induced vibrations. *Journal of Fluids and Structures* 19 (4), 389-447.
- Soti, A.K., Thompson, M.C., Sheridan, J., Bhardwaj, R., 2017. Harnessing electrical power from vortex-induced vibration of a circular cylinder. *Journal of Fluids and Structures* 70, 360-373.
- Sun, H., Ma, C., Kim, E.S., Nowakowski, G., Mauer, E., Bernitsas, M.M., 2017. Hydrokinetic energy conversion by two rough tandem-cylinders in flow induced motions: Effect of spacing and stiffness. *Renewable Energy* 107, 61-80.
- Sun, H., Soo Kim, E., Bernitsas, M.P., Bernitsas, M.M., 2015. Virtual Spring–Damping System for Flow-Induced Motion Experiments. *Journal of Offshore Mechanics and Arctic Engineering* 137 (6).
- Wang, L., Alam, M.M., Zhou, Y., 2018. Two tandem cylinders of different diameters in cross-flow: effect of an upstream cylinder on wake dynamics. *Journal of Fluid Mechanics* 836, 5-42.
- Williamson, C.H.K., Govardhan, R., 2004. Vortex-Induced Vibrations. *Annual Review of Fluid Mechanics* 36 (1), 413-455.
- Zhang, L.B., Dai, H.L., Abdelkefi, A., Wang, L., 2017. Improving the performance of aeroelastic energy harvesters by an interference cylinder. *Applied Physics Letters* 111 (7).

Influence of the sweep angle on power extraction performance of a fully-passive oscillating-plate hydrokinetic turbine prototype

1st Walfred Lee¹, 2nd Guy Dumas², 3rd Peter Oshkai¹

¹University of Victoria, Victoria, Canada, walfredlee@uvic.ca

²Laval University, Quebec City, Canada

Keywords: oscillating-foils, tomographic PIV, sweep angle, flat plate, leading-edge vortex

A self-sustained fully-passive flapping-foil hydrokinetic turbine prototype¹ that is able to achieve efficiency of power extraction up to 31% with a NACA 0015 foil is investigated experimentally using tomographic particle image velocimetry (tomo-PIV). The optimal power extraction performance regime for the oscillating foil occurs when the leading-edge vortex (LEV) is absent². The introduction of the sweep angle Λ , shown in Fig. 1, promotes spanwise flow along the plate, which leads to an instability of the core of the LEV. As the sweep angle is varied, interaction between the tip vortex and the LEV is observed⁴. The present study investigates the influence of the instability of the LEV and the interaction between the vortices on the power extraction performance of a fully-passive hydrokinetic turbine prototype that utilizes an oscillating flat plate.

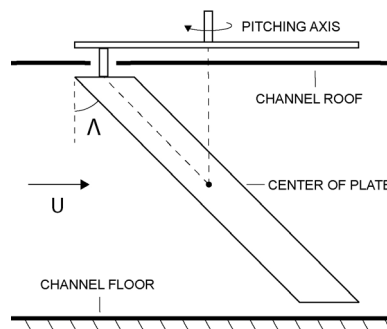


Figure 1: Schematic of the experimental setup.

The experiments were conducted in a flow channel using water as a working fluid. The uniform inflow velocity, U corresponded to the Reynolds number of 21000 based on the chord of the plate. The plate was undergoing elastically constrained oscillations in pitch and heave. Potential for power extraction from the heaving motion was measured by implementing an eddy-current brake. The three-dimensional velocity field in the wake of the oscillating swept plate was measured using tomo-PIV. The quantitative flow patterns were related to the cycle-averaged power coefficient and the efficiency of the turbine to provide insight into the physics of the fluid-structure interactions and their role in the turbine performance.

1. M. Boudreau, G. Dumas, M. Rahimpour, and P. Oshkai (2018). Experimental investigation of the energy extraction by a fully-passive flapping-foil hydrokinetic turbine prototype. *Journal of Fluids and Structures*, 82, 446-472.
2. T. Kinsey and G. Dumas (2014). Optimal Operating Parameters for an Oscillating Foil Turbine at Reynolds Number 500,000. *AIAA Journal*, 52, 9.
3. H. R. Beam, D. E. Rival, M. S. Triantafyllou (2012). On the stabilization of leading-edge vortices with spanwise flow. *Exp Fluids*, 52, 511-517.

Reliability Study of a Fully-Passive Oscillating Foil Turbine Concept

Dylan Iverson¹, Waltfred Lee¹, Guy Dumas², Peter Oshkai¹

¹*University of Victoria, Victoria, Canada, waltfredlee@uvic.ca*

²*Laval University, Quebec City, Canada*

Abstract

A self-sustained fully-passive flapping foil hydrokinetic turbine prototype is investigated experimentally. The foil was undergoing elastically constrained oscillations in pitch and heave in water at $Re = 21000$. The prototype was subjected to three distinct types of flow disturbances: symmetric vortices from a wake of an oscillating foil placed upstream of the test foil, boundary layer tripping in the form of distributed roughness on the surface of the foil, and freestream turbulence introduced via the fractal grid turbulence generator. Stable operation of the turbine could only be obtained under a limited range of kinematics of the upstream oscillating-foil. An overall increase in power extraction was observed when the turbine was subjected to the high freestream turbulence and when the surface roughness was applied.

Keyword: oscillating foil, tandem foils, fully-passive turbine, PIV

1 Introduction

The use of oscillating foils for hydrokinetic energy harvesting has been receiving interest in recent years, promising to overcome some of the limitations of established renewable energy technologies related to cost effectiveness and intermittency energy supply. These systems consist of a foil that undergo periodic translating and rotating motions in an incoming flow. These lift-based devices have been shown to reach energy extraction efficiencies matching or exceeding their traditional rotary counterparts. Oscillating foil turbines are particularly well-suited for shallow and wide flow channels, where their rectangular cross-sections can capture large portions of the flow. Moreover, they can operate efficiently in slower flows than conventional rotary designs. Thorough examinations of the oscillating foil turbine concept have been presented in reviews by (Young et al., 2014) and (Xiao and Zhu, 2014).

Several recent studies focused on oscillating foil systems that do not rely on complex mechanisms to kinematically constrain or prescribe the motion of the foil, creating so-called fully-passive systems. Here, the motion of the foil is self-induced and self-sustained through the interactions between the structure and the fluid, and the two degrees-of-freedom are not mechanically coupled.

Parametric studies by (Kinsey et al., 2011), along with many others, emphasized the importance of a properly coupled pitching (rotating) and heaving (translating) motions in the two degree-of-freedom system. Indeed, well prescribed kinematics can yield efficiencies as high as 43%.

Semi-passive systems, in which the pitching motion is prescribed while the heave motion is unconstrained, have been proposed by several research groups and exhibit reasonable efficiencies (Abiru and Yoshitake, 2011; Chen et al., 2018; Deng et al., 2015; Griffith et al., 2016; Kim et al., 2017; Shimizu et al., 2008; Sitorus et al., 2016; Teng et al., 2016; Wu et al., 2015; Wu et al., 2014; Zhan et al., 2017).

More recently, a fully-passive turbine prototype was developed by (Boudreau et al., 2018). The concept involves a foil that is elastically mounted in pitch and in heave. The design relies on non-linearities in the flow to limit the motion, resulting in self-sustained, limit-cycle oscillations. This prototype was used as the basis of the current study, and is described in further detail in Section 2.1.

Despite significant progress towards development of fully-passive oscillating foil turbines, several issues remain unresolved. The current study tests a fully-passive concept experimentally under distinct sets of prescribed flow conditions. These include periodic perturbations from an upstream oscillating foil, high freestream turbulence intensities, and the application of surface roughness elements to the foil's surface. The work intends to provide a baseline to assess the robustness and reliability of the novel technology in simulated real-world environments.

2 Experimental system and techniques

2.1. Fully-passive oscillating foil turbine

The fully-passive turbine in the current study is the same physical prototype used in the study by (Boudreau et al., 2018). A schematic of the two-degree-of-freedom turbine system is shown in Fig. 1. The NACA 0015 foil of chord length c was constrained to move only in a linear heave motion ($h(t)$), and a rotational pitch motion ($\theta(t)$) about its pitching axis, located a distance x_p from the leading edge. Both degrees of freedom were elastically mounted, with spring stiffnesses for heave and pitch of k_h and k_θ , respectively. Further, a linear damping was applied independently to the heave and the pitch degrees-of-freedom with values D_h and D_θ , respectively.

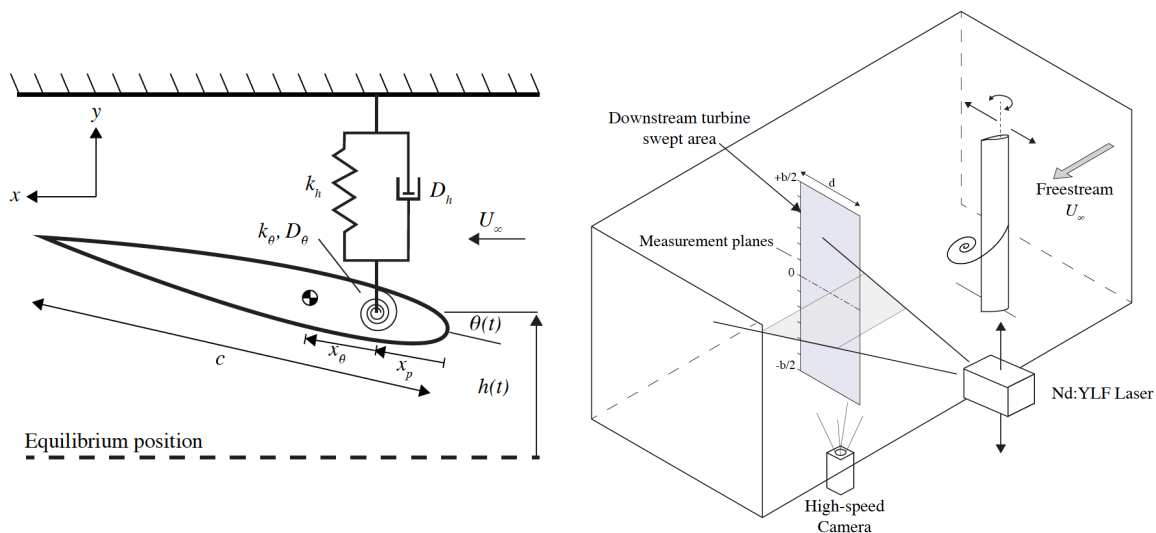


Figure 1: Schematic of the fully-passive turbine. Figure 2: Schematic of the experimental system.

No mechanical coupling was present between the degrees-of-freedom. That is, the foil moved in heave freely and independently of the pitch motion, and vice versa. However, it should be noted that an inertial coupling between degrees-of-freedom existed. A coupling between the hydrodynamic lift force and the hydrodynamic moment also indirectly related the degrees-of-freedom and was largely responsible for the self-sustained and periodic motions of the turbine.

The experiments were performed in a recirculating water channel with a cross-section of the test area of 45 cm x 45 cm and a length of the test area of 250 cm. The inflow velocity was controlled to a resolution of 0.004 m/s, and the ambient turbulence intensity of the flow was ~1% of the inflow for the considered range of velocities.

The baseline parameters of the fully-passive turbine are defined in Table 1.

Table 1: Baseline parameters of the fully-passive oscillating foil.

Parameter	Symbol	Units	Value
Reynolds number	Re		21000
Dimensionless heave stiffness coefficient	k^*_h		1.91 ± 0.03
Dimensionless pitch stiffness coefficient	k^*_θ		0
Heave damping coefficient of the eddy-current brake (prescribed energy sink)	$D^*_{h,e}$		1.23 ± 0.03
Damping coefficient of heave bearings	$D^*_{h,v}$		0.124
Damping coefficient of pitch bearings	D^*_θ		0.004

2.2 Symmetric perturbations of the inflow

The perturbations were achieved by placing an oscillating-foil with a prescribed motion profile 6.5 chord lengths upstream of the fully-passive turbine, as illustrated in the schematic of Fig. 2.

The parameters of the constrained foil, which hereafter are referred to as the upstream foil, are listed in Table 2. The pitch and heave motions of the upstream turbine were controlled by two independent servo motors. The upstream foil was prescribed sinusoidal pitch and heave motions throughout all tests, and the phase offset between the pitch and the heave motion profiles was set to 90° .

Table 2: Parameters of the upstream foil.

Parameter	Symbol	Value
Foil shape		NACA 0015
Chord length	c'	50 mm
Span	b'	380 mm
Pitching axis location	x'_p	$1/3 c'$

2.3 Quantitative flow imaging

Fluid velocity was measured using particle image velocimetry (PIV). A schematic of the PIV setup with the upstream foil is shown in Fig. 2. The flow was seeded with tracer particles with a mean diameter of 10 μm that were illuminated by a pulsed Nd:YLF dual diode-pumped laser. The images captured by a high-speed camera were processed with LaVision Davis 8.3 software using a multipass cross correlation technique. The field of view of images corresponded to the physical area of 325 mm x 325 mm, and the resolution of the measured velocity field was 0.26 vectors/mm.

2.4 Boundary layer tripping

A strip of distributed roughness elements (adhesive 40-grit sandpaper), 0.08c wide, was applied along the full span of the fully-passive oscillating turbine at the position of the maximum thickness, on both sides of the foil. The roughness elements corresponded to a roughness Reynolds number $u_k k/\nu = 600$, where k is the height of the roughness elements above the surface of the foil, and u_k is the flow velocity in the boundary layers at the height k . It was determined in previous tests that these distributed roughness elements were effective at tripping, i.e. promoting transition to turbulence, at the considered chord-based Reynolds number of 21000.

2.5 Variation of freestream turbulence

The turbulence intensity was increased relative to the ambient level of the flow channel by installing fractal grids upstream of the fully-passive turbine, perpendicular to the flow direction. The grids consisted of repeating patterns of squares of decreasing scales. Two grids were considered in the current study. Hereafter, they are referred to as grids N3 and N4, referring to their respective numbers of fractal iterations.

Four distinct inflow conditions were achieved by the application of different grids and by varying the location of the grids relative to the turbine.

The flow velocity was measured using PIV in the x-y plane in a 6c x 6c field of view centered at the equilibrium position of the fully-passive foil. The streamwise and the in-plane normal turbulent intensity components (I_x and I_y , respectively) were then calculated by averaging 300 PIV images recorded during 20 oscillation cycles of the turbine.

3 Results and discussion

3.1 Effect of symmetric perturbations of the inflow

Several parametric spaces, abbreviated hereafter as 'PSpace', were tested, where the motion of the upstream foil was varied. For all cases, the structural parameters of the downstream fully-passive turbine were held constant at baseline values, with the exception of changes in pitch stiffness. Table 2 lists the parameters associated with each case. There, the value of $k_\theta^* = \infty$ corresponds to the pitch axis being locked, creating a single-degree-of-freedom heave system.

In all considered cases, periodic vortices developed in the wake, on the scale of the chord length of the foil, either as a result of dynamic stall and the formation of a leading edge vortex, or a result of shear layer roll-up, depending on the dynamics of the upstream turbine. It is noted that the frequency of the upstream foil's motion directly corresponded to the frequency of the perturbation imposed on the downstream turbine, i.e., it could be directly interpreted as the frequency of the imposed vortices.

Table 2: Parameters of the tandem foil experiments

Parameter space	Upstream variables		Downstream variable
	H^*	θ'_0	k^*_θ
PSpace 1	0.90	75°	0
PSpace 2	0.90	80°	0
PSpace 3	1.50	80°	0
PSpace 4	0.90	80°	0.051
PSpace 5	0.90	80°	∞

The performance of the fully-passive turbine operating in the wake of the upstream turbine at conditions PSpace1 is shown in Fig. 4(a). Here, the heave amplitude of the upstream foil was set at $H^* = 0.90$, similar to that of the fully-passive baseline case in a uniform freestream. The pitch amplitude was set at 75° . The reduced frequency was varied in small increments in a range at and below the frequency corresponding to the fully-passive turbine operation in baseline, uniform freestream conditions. Outside of this range of frequencies, the fully-passive turbine was observed to have poor performance with unstable and non-periodic motions.

In each parametric space, the power extraction was significantly lower than that of the baseline case, which had a value of the power coefficient $C_p = 0.62$. This result is expected, considering the momentum deficit in which the turbine operated.

Under the operating parameters of PSpace1, the fully-passive turbine operated in two distinct regimes, depending on the dynamics and the time scale of the upstream perturbation. At high frequencies, there was a large variation in cycle-to-cycle performance, as indicated by the large standard deviations. It should be noted that a fully-passive turbine with baseline parameters in an undisturbed freestream oscillated at $f^* = 0.133$.

As the frequency of the upstream foil oscillations decreased below $f^* = 0.122$, the oscillations of the downstream turbine stabilized and became periodic at the frequency of the incoming vortices. The power coefficient significantly increased in the vicinity of this frequency threshold.

The results corresponding to PSpace2 and PSpace3 were qualitatively similar to those of PSpace 1 and are not shown herein. A notable difference is that in the case of PSpace2, there existed a second high-performance regime at lower frequency, where the fully-passive turbine exhibited high heave amplitudes. The parameters of PSpace3, where the amplitude of the oscillations of the upstream turbine was increased to $H^* = 1.5$, increased the width of the wake, in which the downstream turbine operated. Despite this difference, the highest magnitude of the power coefficient and the corresponding heave amplitude were similar to the corresponding values of PSpace1 and PSpace2.

The performance of the fully-passive turbine under the parameters of PSpace4 is shown in Fig. 3(b). In this case, light pitch springs were added, increasing the stiffness value to $k^*_\theta = 0.051$. For all tested frequencies of the upstream foil oscillations, the resulting pitch amplitudes of the fully-passive turbine were small, leading to essentially heave-only motion. However, the oscillations were stable, and they occurred at the frequency of the imposed

vortices. It should be noted that due to the momentum deficit in the wake of the upstream foil, the incoming velocity was below the critical flutter velocity for the system of this pitch stiffness. In other words, from a theoretical perspective, the divergence phenomenon that drives the motion of the fully-passive turbine is not expected to occur at this reduced velocity.

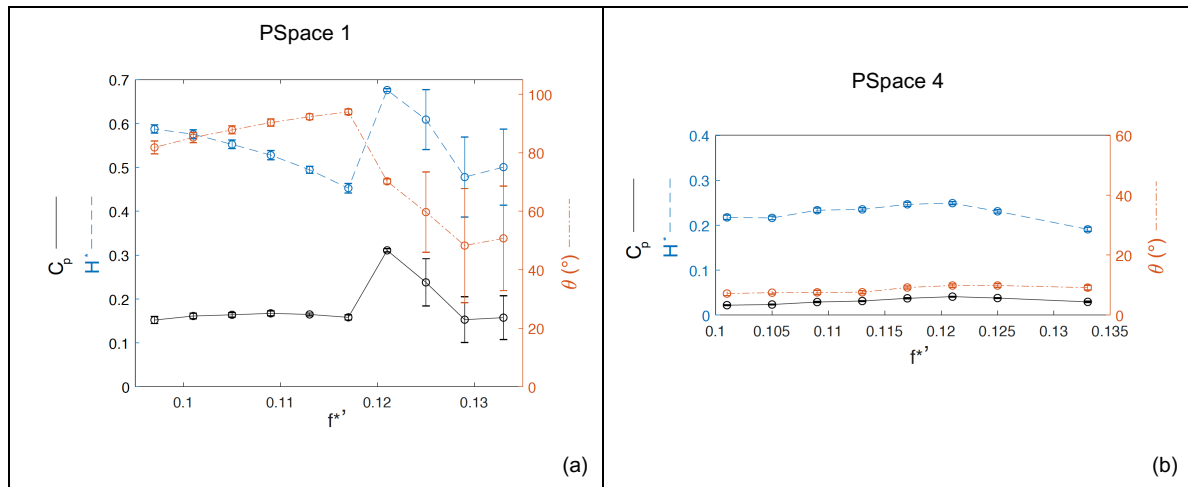


Figure 3: Averaged power coefficient, heave amplitude, and pitch amplitude of the fully-passive turbine for PSpace 1 (a) and PSpace 4 (b). $f^{*'}$ is the frequency of the upstream foil oscillations.

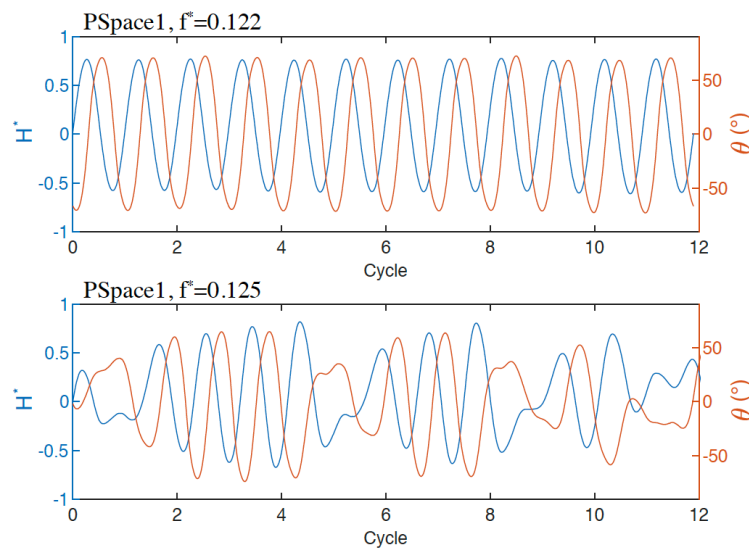


Figure 4: Heaving and pitching positions of the fully-passive turbine as functions of time over twelve oscillation cycles.

Likewise, under the parameters of PSpace 5, where the turbine motion was reduced to heave-only oscillations, its response (not shown herein) was similar to that under PSpace 4. This observation indicates that the motion occurred as a result of the low pressure regions associated with the large-scale vortices in the oncoming flow, rather than stall flutter.

The results shown in Fig. 3(a) suggest that the dynamics of the fully-passive turbine can be classified into two regimes: stable periodic oscillations and erratic motions. For parameter sets PSpace1, PSpace 2 and Pspace3, stable oscillations occurred at the frequencies of the upstream foil in the range $f^{*'}$ \leq 0.125. At higher frequencies, the fully-passive turbine intermittently resonated with the incoming flow perturbations. This effect is illustrated in Fig.

4, which shows the time traces of the pitching and the heaving motions of the turbine at the frequencies of the upstream foil immediately below and above the threshold value in PSpace1.

In the following, we investigated a hypothesis that the frequency of the flow perturbation that yielded the highest power extraction in each parametric space was associated with the natural oscillation frequency of the fully-passive turbine in a uniform flow with the velocity magnitude corresponding to the time-averaged wake of the upstream oscillating foil.

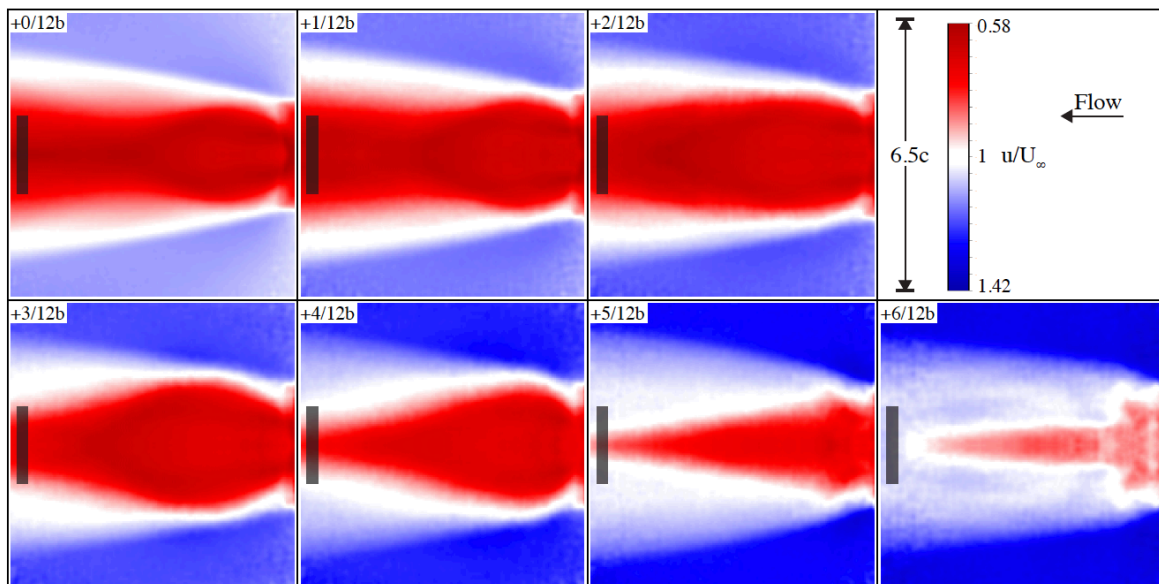


Figure 5: Patterns of time-averaged normalized streamwise velocity in the wake of the upstream oscillating foil under PSpace 1 at $f^* = 0.122$. The grey bars represent approximate location of the downstream turbine. The measurement planes correspond to the schematic of Fig. 3.

Fig. 5 shows the patterns of the normalized time-averaged streamwise velocity component in the wake of the upstream foil operating under the conditions of PSpace1 and the frequency of the upstream foil oscillations $f^* = 0.122$ at several horizontal planes along the span of the foils, which are indicated in the schematic of Fig. 2. The downstream turbine was removed during these measurements. Each image of Fig. 5 was obtained by ensemble-averaging 200 instantaneous velocity fields acquired at a frequency of 50 Hz. The white colour of the contours corresponds to the velocity value equivalent to the incoming freestream, U_∞ .

An estimate of the equivalent average velocity in the swept area of the downstream turbine was obtained by considering 13 planar velocity fields that were evenly spaced along the span of the foil as shown in Fig. 2. In each plane the streamwise velocity was averaged over the line segment traversed by the pitching axis of the turbine. The temporally and spatially averaged velocity in the entire swept area V_{reduced} was then calculated by averaging the velocity values from each horizontal plane.

The comparison of the turbine performance in the wake of the upstream oscillating foil with that in the equivalent uniform inflow with the reduced velocity magnitude is presented in Table 3. Here, an equivalent uniform inflow means that in a time-averaged sense, the fully-passive turbine was exposed to the same momentum flux as in the wake of the upstream oscillating foil, although the instantaneous incoming flow fields were different. The conditions

shown in Table 3 represent the reduced frequencies of the upstream foil oscillation that yielded the maximum power extraction in each parametric space. When operating in the equivalent uniform inflow, the fully passive turbine oscillated at significantly lower reduced frequencies. In contrast to the equivalent uniform inflow conditions, the turbine operating in a periodic wake demonstrated significant increases in power extraction. In particular, under the conditions of PSpace 3, the power coefficient in the case of the periodic wake inflow increased 3.84 times compared to the case of the equivalent uniform inflow.

Table 3: Turbine performance in unsteady wake and equivalent uniform flow

Parameter space	Unsteady wake		Uniform flow			
	f^{*}	$\overline{C_{P_{wake}}}$	V_{reduced}	f^{*}	$\overline{C_{P_{uf}}}$	$\overline{C_{P_{wake}}}/\overline{C_{P_{uf}}}$
PSpace 1	0.122	0.310	0.78	0.088	0.107	2.90
PSpace 2	0.117	0.090	0.75	0.081	0.065	1.39
PSpace 3	0.113	0.113	0.76	0.081	0.065	3.84

3.2 Effect of boundary layer tripping

To investigate the effects of boundary layers tripping, the baseline configuration of the fully-passive turbine (defined in Table 1) and the baseline configuration with added pitch stiffness of $k^*_\theta = 0.051$ were tested with and without the applied distributed roughness that is described in Section 2.4.

In the baseline case, the surface roughness did not have a significant influence on the turbine performance. In the presence of the surface trip, the peak pitching amplitude increased by 3° and the phase shift between the pitching and the heaving motions increased by 2° , compared to the baseline case with no trip. When the pitch stiffness was applied, the boundary layer trip yielded a decrease of the pitching amplitude by 3° and a 5% increase of the oscillation frequency, compared to the untripped case.

Similarly, in the baseline-with-pitch-stiffness case, the heaving amplitude was not affected by the presence of the boundary layer trip. The pitching position exhibited a different profile over an oscillation cycle (not shown herein) between the baseline and the baseline-with-pitch-stiffness cases, but the pitching amplitude was changed by approximately the same amount in the presence of the surface trip.

Overall, the influence of the boundary layer trip on the passive turbine performance was insignificant, because the turbine oscillations were governed by robust stall dynamics, which did not strongly depend on the boundary layer transition.

3.3 Effect of freestream turbulence

Turbine performance parameters in the baseline configuration for the four levels of the freestream turbulence intensity at $Re = 21000$ are presented in Table 4. The parameters were normalized with respect to their values corresponding to the ambient turbulence level. Other tested configurations, which are not presented herein, included a baseline configuration with added pitch stiffness of $k^*_\theta = 0.051$ and the baseline configuration at $Re = 25000$. These additional cases yielded qualitatively similar results to those of Table 4.

For all tested configurations, moderate turbulence levels ($\sim 10\%$) resulted in an increase of power extraction by the fully-passive turbine in the range of 5% to 13% with respect to the

ambient turbulence condition.

Table 4: Turbine performance under various inflow turbulence intensities.

Grid	Distance from turbine location	I_x	C_P	H^*	θ_0	f^*	ϕ
None	N/A	1.9%	1.00	1.00	1.00	1.00	1.00
N3	1.5 m	10.1%	1.11	1.03	1.01	1.0.1	1.01
N4	1 m	10.1%	1.09	1.01	1.01	1.03	0.98
N3	0.5 m	21.8%	0.92	0.97	1.01	0.97	1.07

4 Conclusions

The fully-passive turbine concept under investigation presents an opportunity to reduce the complexity of oscillating foil technologies aimed at energy harvesting. The reliability of the turbine operation was assessed by subjecting the foil to three distinct types of disturbances: periodic vortices from an oscillating foil placed upstream, boundary layer tripping by distributed roughness on the surface of the foil and moderate to high turbulence levels in the inflow.

When operating in the wake of an oscillating foil, the fully-passive turbine was sensitive to the frequency of the incoming vortices. The range of beneficial upstream frequencies was not consistent with the frequencies of the fully-passive turbine oscillations in a uniform inflow with an equivalent momentum flux.

Applying distributed roughness to the surface of the fully-passive foil and increasing the turbulence level of the inflow resulted in an increased power extraction by the turbine. It is suggested that both of these types of disturbances influenced the boundary layer dynamics, resulting in a moderate delay in the development of stall and increasing the instantaneous lift force.

Acknowledgements

The authors gratefully acknowledge assistance of Dr. M. Boudreau at all stages of this investigation and financial support by the Natural Sciences and Engineering Research Council of Canada (NSERC).

References

- Abiru, H., Yoshitake, A., 2011. Study on a flapping wing hydroelectric power generation system. *Journal of Environment and Engineering* 6, 178-186.
- Boudreau, M., Dumas, G., Rahimpour, M., Oshkai, P., 2018. Experimental investigation of the energy extraction by a fully-passive flapping-foil hydrokinetic turbine prototype. *Journal of Fluids and Structures* 82, 446-472.
- Chen, Y., Nan, J., Wu, J., 2018. Wake effect on a semi-active flapping foil based energy harvester by a rotating foil. *Computers & Fluids* 160, 51-63.
- Deng, J., Teng, L., Pan, D., Shao, X., 2015. Inertial effects of the semi-passive flapping foil on its energy extraction efficiency. *Physics of Fluids* 27, 053103.
- Griffith, M.D., Jacono, D.L., Sheridan, J., Leontini, J.S., 2016. Passive heaving of elliptical cylinders with active pitching - from cylinders towards flapping foils. *Journal of Fluids and Structures* 67, 124-141.
- Kim, D., Strom, B., Mandre, S., Breuer, K., 2017. Energy harvesting performance and flow structure of an oscillating hydrofoil with finite span. *Journal of Fluids and Structures* 70, 314-326.
- Kinsey, T., Dumas, G., Lalande, G., Ruel, J., Mehut, A., Viarouge, P., Lemay, J., Jean, Y., 2011. Prototype testing of a hydrokinetic turbine based on oscillating hydrofoils. *Renewable Energy* 36, 1710-1718.
- Shimizu, E., Isogai, K., Obayashi, S., 2008. Multiobjective design study of a flapping wing power generator. *Journal of Fluids Engineering* 130, 021104.
- Sitorus, P.E., Le, T.Q., KO, J.H., Truong, T.Q., Park, H.C., 2016. Design, implementation, and power estimation of a lab-scale flapping-type turbine. *Journal of Marine Science and Technology* 21, 115-128.
- Teng, L., Deng, J., Pan, D., Shao, X., 2016. Effects of non-sinusoidal pitching motion on energy extraction performance of a semi-active flapping foil. *Renewable Energy* 85, 810-818.
- Wu, J., Chen, Y., Zhao, N., 2015. Role of induced vortex interaction in a semi-active flapping foil based energy harvester. *Physics of Fluids* 27, 093601.
- Wu, J., Qiu, Y., Shu, C., Zhao, N., 2014. Pitching-motion-activated flapping foil near solid walls for power extraction: A numerical investigation. *Physics of Fluids* 26, 083601.
- Xiao, Q., Zhu, Q., 2014. A review of energy harvesters based on flapping foils. *Journal of Fluids and Structures* 46, 174-191.
- Young, J., Lai, J.C., Platzer, M.F., 2014. A review of progress and challenges in flapping foil power generation. *Progress in Aerospace Sciences* 67, 2-28.
- Zhan, J., Xu, B., Wu, J., Wu, J., 2017. Power extraction performance of of a semi-activated flapping foil in gusty flow. *Journal of Bionic Engineering* 14, 99-110.

A parametric study of vertical axis hydrokinetic turbines with chordwise-flexible blades

Pierre-Olivier Descoteaux¹ and Mathieu Olivier

Laboratoire de Mécanique des Fluides Numérique, Université Laval, Quebec City, Canada

¹ pierre-olivier.descoteaux.1@ulaval.ca

Keyword: fluid-structure interaction, vertical-axis turbine, flapping wing, aeroelasticity

This talk will present a parametric study of Vertical-Axis Turbines (VAT) equipped with chordwise-flexible blades. The study is carried out with numerical simulations based on a partitioned Fluid-Structure Interaction (FSI) code implemented within OpenFOAM in which an in-house structural finite-element solver is linked to a finite-volume flow solver. The 2D simulations are carried out at a Reynolds number of 10^7 , which is representative of hydrokinetic applications. The objective in using chordwise-flexible blades is to take advantage of the periodically changing hydrodynamic conditions. Indeed, as depicted in Fig. 1, the blade is subject to variations of apparent speed and angle of attack α throughout a single cycle. Therefore, pressure-based blade deformations can be used to improve passively the shape of the wing, provided that the structural parameters are chosen properly. On the other hand, inertia-based deformation, being solely governed by a steady centrifugal effect in VATs, are not relevant since they would produce a steady deformation.

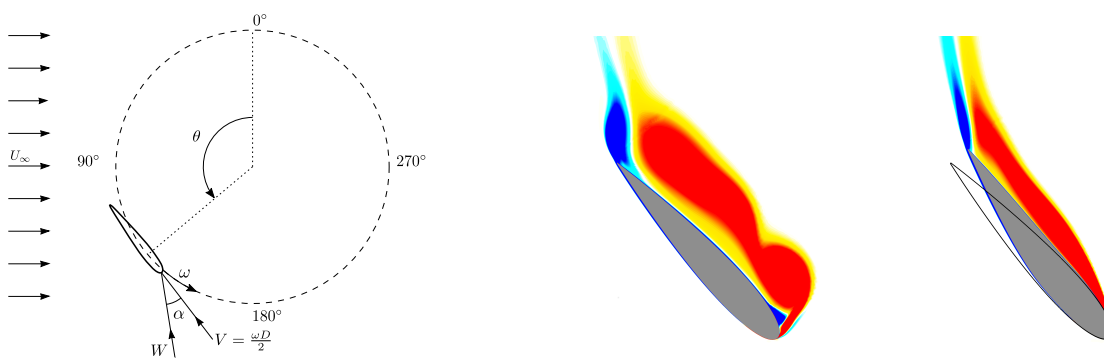


Figure 1: Kinematics of a VAT (left) and vorticity fields illustrating stall mitigation induced by blade flexibility (right).

The main focus of this analysis is to assess the conditions under which it is possible to increase the efficiency of VATs by allowing passive pressure-based foil deformations. The FSI effects related to the flexibility and inertia of the blade are being investigated and the mechanisms that allow efficiency improvements will be presented. Preliminary results show that a stall mitigation mechanisms helps in improving the efficiency of low tip speed ratio configurations (see Fig. 1). Results also shows that blade flexibility tends to extend the energy extraction angular range (θ) of the turbine which may provide interesting advantages when the turbine undergoes variation in incoming flow velocity.

Investigating the energy harvesting potential of intermittent oscillations in a pitch-plunge aeroelastic system

Ashwad Raaj Paramasivam¹, Anindya Roy² and Venkatramani Jagdish^{1*}

¹ *Shiv Nadar University, Greater Noida, India. Email:j.venkatramani@snu.edu.in*

² *Royal HaskoningDHV, George Hintzenweg 85, 3068 AX Rotterdam, The Netherlands.*

Abstract

Flexible structures, in the presence of on-coming flows, are susceptible to dynamic instabilities like aeroelastic flutter. Due to the presence of large-amplitude limit cycle oscillations (LCOs) in the post flutter regime, the hitherto aeroelastic community has focused on harvesting energy from the same. However, prolonged exposure to LCOs can lead to the accumulation of fatigue damage and in turn can be detrimental to the structural safety. To that end, the present study investigates a pre-flutter regime of oscillations called intermittency, for its energy harvesting potential. It is systematically shown that the fatigue damage incurred during intermittent oscillations is relatively smaller than that during the LCOs.

Keyword: Aeroelastic flutter, Energy harvesting, Intermittency, Structural safety, Fatigue damage.

1 Introduction

Aeroelastic structures are prone to flow induced instabilities such as flutter. Above a critical flow speed, the structure extracts continuous energy from the flow, and undergoes large amplitude LCOs. Due to the sustained nature of these oscillations, the prospect of generating power from these flutter oscillations (i.e. LCOs) has received considerable attention in the hitherto literature (Abdelkefi,2016). The salient features of these studies involved harvesting energy from LCOs by either inducing aereolastic flutter or augmenting an existing instability or improvising the harvester features to maximize the power output from LCOs. A common feature in all these studies is their dependence on the onset of flutter instability.

However, transgressions into regimes of flutter instabilities can induce substantial threats to the structural safety, either due to excursions above the first passage of time or due to the gradual accumulation of fatigue damage (Venkatesh et al., 2014). This leads to a precarious compromise between the structural safety versus the extracted energy.

Further, available studies have restricted its attention to a mean flow condition, where, by and large the transition to flutter occurs via a Hopf-bifurcation (Lee at al.,1999). This restriction leads to two-fold disadvantage, namely, (i) since the pre-flutter regimes in the mean flow situation correspond to a damped response, and one resorts to investigate the post flutter regime for extracting useful energy, (ii) in field, the flow is often superimposed by random temporal fluctuations. These flow fluctuations not only change the stability behavior of aeroelastic

systems (Poirel et al.,2016), but also give rise to distinct dynamical states that are not observed in its deterministic counterpart (Venkatramani et al.,2016). Consequently, assessing the energy harvesting potential of the harvester under uniform flow conditions may be inadequate to carry out power generation in realistic scenarios. Indeed, wind tunnel experiments conducted in (Venkatramani et al.,2016) showed that in the presence of randomly fluctuating flows, the onset of LCOs is presaged by a regime of oscillations called intermittency. These intermittent oscillations were characterized by the alternation of the response dynamics between large amplitude periodic oscillations and lower amplitude aperiodic oscillations in an unpredictable fashion.

Numerical investigations in aeroelastic systems (Venkatramani et al., 2017) demonstrated that the qualitative type of intermittency observed in pre-flutter regimes can be classified into two types based on the relative time scales of the input flow fluctuations with respect to the system time scales. Input flow fluctuations that have dominant long time scales gave rise to "on-off" intermittency, marked by the alternation between a periodic "on" state and a near rest "off" state. On the other hand, input flows containing rapidly fluctuating short time scales gave rise to "burst" intermittency, characterized by alternation between large amplitude bursts interspersed amidst low amplitude aperiodic oscillations. To the best of the authors' knowledge, the capability to harvest energy from either of these two intermittent oscillations, remains unexplored.

This study is devoted towards harvesting energy from noise induced intermittent oscillations in an aeroelastic system using numerical investigations. A pitch-plunge airfoil with cubic hardening nonlinearity in the pitch and plunge degrees of freedom is considered. The input flow is assumed to be fluctuating in nature. These fluctuations are modelled using canonical representations that can either give rise to (i) long time scale flow fluctuations or (ii) very small time scale fluctuations. The rationale behind choosing fluctuations with two different time scales is to investigate the energy harvesting potential of both "on-off" and "burst" type intermittency. An electromagnetic coupling is considered in the plunge degree of freedom so as to convert the aeroelastic oscillations into a current output as found in Yang et al., (2011). Finally, the fatigue damage incurred during the different regimes of oscillations are investigated. Since the loads are irregularly fluctuating, a rain flow counting algorithm is employed to extract the cycles from the stress time histories. A combination of S-N curves and Palmgren Miner's rule of linear fatigue damage accumulation is then used to compute the fatigue damage incurred (Venkatesh et al., 2014).

The organisation of the rest of the paper is as follows. The mathematical model of the airfoil and the canonical model that is used for modelling the flow fluctuation is presented in the subsequent section. In Section 3 the results obtained in non-fluctuating flows, fluctuating flows with long time scales and fluctuating flows possessing short time scales are discussed. Structural integrity of the aeroelastic system under different response dynamics is briefly presented in Section 4. The salient features that arises from this study are summarized in Section 5.

2 Mathematical Model

2.1 Structural Model

A three dimensional wing is modelled as a two degree of freedom pitch-plunge aeroelastic system. Experiments conducted on a cantilever wing have revealed that the manifestation of flutter oscillations are largely dictated by the bending (plunge) and torsional (pitch) modes (Dowell, 1989). Accordingly, the airfoil is modelled as a rigid - flat plate mounted on plunge and pitch springs. Such a representative model of the airfoil is called a "typical-section". However, to exhibit sustained LCOs, the presence of nonlinearity in the model is necessary. A simple way to incorporate the same is by assuming a cubic hardening nonlinearity in either of the degrees of freedom.

The conversion of oscillatory responses to an electrical output requires an electromechanical coupling and the design of the harvester must incorporate the same. An electromagnetic transduction mechanism consisting of a pair of fixed permanent magnets and a coil of wire that is attached to the airfoil through a massless bar, at the elastic axis, is used to convert the oscillatory response to an electrical output. This arrangement prevents the development of an additional degree of freedom via the transduction mechanism. Since the airfoil rotates about the elastic axis, only the plunge displacement is utilized for the transduction mechanism. A similar mechanism has been adopted in Yang et al., (2011). Following Faraday's law of electromagnetic induction, the relative movement of the coil with respect to the magnetic field produced by the magnets, induces an EMF in the coil. This, consequently introduces a current i in the circuit. By applying Kirchoff's voltage law, the following equation is derived.

$$i' + \frac{iRb}{LV} - \frac{Bib\epsilon'}{L} = 0. \quad (1)$$

where R is the resistance, L is the inductance, b is the semi-chord of the airfoil, V is the free stream velocity and ϵ is the non-dimensional displacement in the heave motion. The values of B and L are same as those provided in Yang et al., (2011).

The resulting electromagnetic force F_m , acting on the coil is given by

$$F_m = Bil. \quad (2)$$

The governing equations of motion of this nonlinear aeroelastic model are expressed as follows (Y.C Fung, 1955).

$$\epsilon'' + x_\alpha \alpha'' + 2\zeta_\epsilon \frac{\bar{\omega}}{U} \epsilon' + \left(\frac{\bar{\omega}}{U}\right)^2 (\epsilon + \beta_\epsilon \epsilon^3) = -\frac{1}{\pi\mu} C_L(\tau) + \frac{F_m}{mU^2 b\omega_\alpha^2}, \quad (3)$$

$$\frac{x_\alpha}{r_\alpha^2} \epsilon'' + \alpha'' + 2\frac{\zeta_\alpha}{U} \alpha' + \frac{1}{U^2} (\alpha + \beta_\alpha \alpha^3) = \frac{2}{\pi\mu r_\alpha^2} C_M(\tau). \quad (4)$$

Eqs. 3 and 4 represent the non dimensional equations of motion of a nonlinear aeroelastic section in the presence of an undisturbed flow U . The differentiation is carried out with respect to τ , non-dimensional time. The parameters associated with these equations and their corresponding values are as found in Lee et al., (1999).

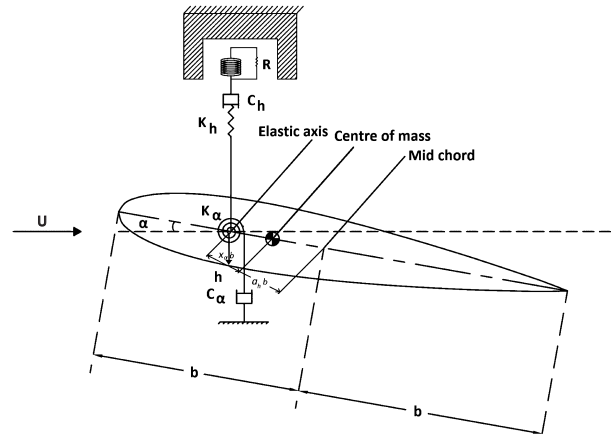


Figure 1: Schematic of airfoil section.

2.2 Aerodynamic Model

The flow over an airfoil executing small oscillations is assumed to be an inviscid and incompressible flow. The time dependent lift and moment on the airfoil is mathematically modelled using an unsteady aerodynamical formulation, as found in Y.C Fung, (1955). The model captures both the added mass effect due to surrounding air and the wake effect of the shed vortices and is not represented here for the sake of brevity.

2.3 Flow fluctuations

The flow U in Eqs. 3 and 4 are assumed to be fluctuating about a mean component U_m such that,

$$U(\tau) = U_m + f(\tau). \quad (5)$$

Here, $f(\tau)$ represents the fluctuating or time varying component of the flow speed and is modelled as a second order random process as found in Venkatramani et al., (2017). Mathematically, $f(\tau)$ is represented as

$$f(\tau) = \sigma U_m \sin(\tau \omega_r(\tau)), \quad (6)$$

where, σ is the intensity of the fluctuations, $\omega_r(\tau)$ is a time varying frequency of the sinusoid, such that, $\omega_r(\tau) = \omega_1 + \kappa R(\tau)$. Here, ω_1 is the mean frequency of the oscillations, $R(\tau)$ are uniformly distributed numbers in $[0, 1]$ and varies at each time step and κ is a constant scalar value and is of $\mathcal{O}(\omega_1)$. The fluctuations $\kappa R(\tau)$ have been added at each time step to introduce short time scales which contributes to the broad range of frequencies in the flow. This canonical model qualitatively captures the broadband of scales present in input flow fluctuations. For more details one can refer to the study by Venkatramani et al., (2017).

3 Results and discussions

This section focuses on investigating the energy harvesting potential of intermittent oscillations. The governing equations of motions (Eqs. 1-4) are solved using an adaptive time step based Runge Kutta algorithm in MATLAB. A stringent tolerance measure for the time step is imposed. With the mean flow speed (U_m) as a bifurcation parameter, the aeroelastic responses (pitch and plunge motions) are systematically obtained. First, the route to flutter via intermittency is shown by presenting the time histories of the responses. Then, the current output obtained at different dynamical regimes is computed. Finally, the fatigue damage incurred by the system is estimated at different dynamical regimes, and the trade off between structural integrity and energy output is discussed.

3.1 Intermittency route to aeroelastic flutter

Under the absence of flow fluctuations ($U_m = U$), any initial disturbance dies down at flow speeds $U < U_{cr}$ (refer Fig. 2(a)), where U_{cr} is the critical flow speed. The critical flow speed for this model is estimated to be $U_{cr} = 6.2$. At flow speeds $U > U_{cr}$, the response transforms itself to exhibit limit cycle oscillations through a Hopf bifurcation (refer Fig. 2(a)). However, in the presence of flow fluctuations, the onset of flutter is presaged by a regime of intermittent oscillations. The qualitative nature of the intermittency was found to be dictated by the nature of the flow fluctuation. A long timescale fluctuation gives rise to an "on-off" intermittency (refer Fig. 2(b)), where the response alternates between "on" states with periodic oscillations and an "off" state with the absence of oscillations. On the other hand, a short time scale fluctuation would give rise to a "burst" intermittency (refer Fig. 2(c)), characterised by the "burst" of periodic oscillations interspersed with aperiodic oscillations. As the flow speed is increased, the "on" and "burst" states become more frequent, and eventually gives rise to LCOs.

3.2 Energy output

The current responses obtained under the different flow conditions are presented here. To reiterate, ideal electrical parameters are assumed to compare the energy harvesting potential of the harvester at different dynamical regimes. Optimising the parameters to ensure maximum power output deserves a separate investigation and is beyond the scope of this study.

At uniform flow conditions, flow speeds $U < U_{cr}$, a fixed point response is observed (refer Fig. 3(a)). The initial disturbance eventually subsides, offering very little scope for harvesting energy. At flow speeds $U > U_{cr}$, large amplitude oscillations are observed refer (Fig. 3(b)), offering a good potential to harvest energy. However, it is worth reiterating that despite the relatively high current extracted from flutter oscillations, the onset of these detrimental instabilities can pose adverse threats to the structural integrity. Additionally, as seen in Section 1, encountering only damped or LCOs are possible when the flows are uniform and devoid of fluctuations. In the presence of input flow fluctuations, an intermittency route to flutter exists and its energy harvesting potential is systematically investigated next.

In the presence of longtime scale flow fluctuations, the route to flutter was observed to be presaged by a regime of intermittent oscillations exhibiting "on-off" intermittency (refer Fig.

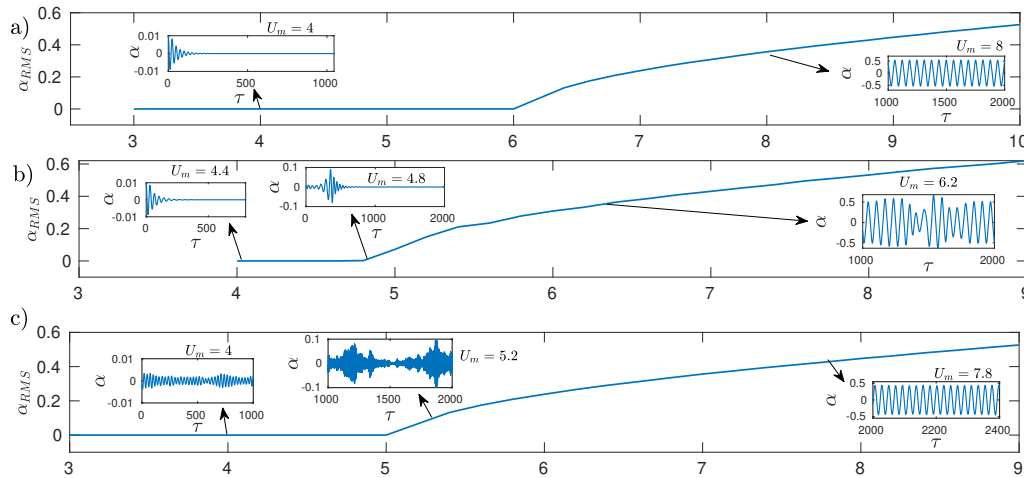


Figure 2: A plot between the root mean square (RMS) of the pitch responses vs mean flow speed (U_m) in (a) uniform flow conditions (in the absence of fluctuations $U_m = U$), (b) long time scale flow fluctuations, and (c) short time scale flow fluctuations. The responses display a Hopf bifurcation in (a). Any initial disturbance dies down at speeds $U < U_{cr}$, and, at speeds higher than U_{cr} , LCOs are exhibited. The flutter regime is presaged by a regime of intermittent oscillations characterized as "on-off intermittency" in (b), and, "burst" in (c). It can also be observed that the onset of flutter occurs at speeds $U_m > 4.8$ in (b) and $U_m > 6.2$ in (c), owing to the difference in the noise intensities of the flow fluctuations. Similar dynamics are observed in the plunge responses and are not shown here for the sake of brevity.

2(b)). The current response was found to exhibit qualitatively similar response, as shown in Fig. 4. The fixed point response exhibited at a mean flow speed $U_m = 4$ in Fig. 4(a) has a RMS of 0.0064 A, which as stated earlier, is too low for harvesting energy. On increasing the flow speed to $U_m = 5$, an "on-off" intermittent response with a RMS of 1.1 A is observed. On increasing the flow speed $U_m = 8$, LCOs are obtained with a RMS value of 27 A. Similarly, in the presence of short timescale fluctuations, the low amplitude noisy response obtained at $U_m = 4$ provides very little scope to harvest power (refer Fig. 4(a)). The intermittent response obtained at $U_m = 5.2$ has a RMS of 2.5 A (refer Fig. 4(b)). The large amplitude LCOs obtained at $U_m = 8$ provide a very good RMS output of 29.5 A. Given that the current output at different dynamical regimes has been discussed, we next compute the fatigue damage sustained at each regime in the next section.

3.3 Structural integrity

Earlier, it was observed that the presence of fluctuating flows disrupts the traditional route to flutter that occur via a Hopf bifurcation. Rather, a distinct regime of pre-flutter oscillations called intermittency is observed. Exploiting the dependence between the relative time scales of the input flow fluctuations and the system time scales, different types of intermittencies

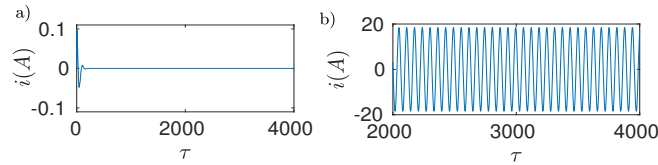


Figure 3: The current responses obtained under uniform flow conditions is presented here. (a) At a flow speed $U = 4$, a fixed point response can be observed. Given the eventual substitution of oscillations, no reasonable amount of power can be harvested. (b) LCOs being exhibited at a flow speed $U = 8$. The steady, large amplitude oscillations offers very good potential to harvest energy, but may pose a threat to the integrity of the structure through accumulation of fatigue.

were obtained. The energy extraction capacity of these regimes of pre-flutter oscillations were explored. In this section, it is argued that despite a relatively lower current output, the manifestation of intermittent oscillations poses much lesser threat to the structural integrity in comparison to the onset of flutter oscillations. To demonstrate the same, the fatigue damage incurred during these qualitatively different oscillatory states (namely, "burst" intermittency, "on-off" intermittency and LCOs) are computed.

Computing the fatigue damage is not a trivial task, since the shape of the airfoil cross section is complex. Since loading is present in both bending and torsional directions, one can compute fatigue damage under three conditions. Namely, (i) when pure shear stresses due to torsion is considered, (ii) normal stresses developed due to bending, and (iii) a combined von Mises stress (of equivalent sign). However, it has been demonstrated that the torsional stresses are much larger than the bending stress and numerically close to the von Mises stress (Venkatesh, 2014). Therefore, in this study, using the pitch time responses, only shear stresses are computed for estimating the fatigue damage accumulation. The non-circular nature of the cross section demands the estimation of a warping function based on the Prandtl theory (Gere, J. M Timoshenko, S. P., 1984). A Prandtl stress function ϕ is introduced such that

$$\tau_{xz} = \frac{\partial \phi}{\partial y}, \tau_{yz} = -\frac{\partial \phi}{\partial x}. \quad (7)$$

such that $\frac{\partial^2 \phi}{\partial x^2} + \frac{\partial^2 \phi}{\partial y^2} = -2G\theta$ (Venkatesh et al., 2014). The Aluminium alloy Al-6082 T-6 is chosen as the representative material for this study. One can refer to (Venkatesh et al., 2014) for details on the computation of the Prandtl stress function. Next, the maximum shear stress developed is computed using the following equation $\tau_{max} = \sqrt{\tau_{xz}^2 + \tau_{yz}^2}$. To compute the damage incurred, the critically stressed element, and the associated stresses must be identified. From Eqs. 7, the shear stresses τ_{xz} and τ_{yz} are found to be dependent on y and x , where x and y are the distance from the considered section to the leading edge and the neutral axis respectively. A sample stress history obtained at three different sections, is shown in Fig. 6.

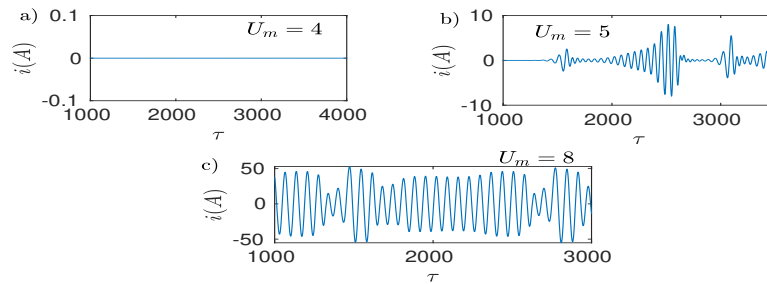


Figure 4: The current responses obtained under flow speeds with long timescale flow fluctuations is presented here. (a) At a mean flow speed $U_m = 4$, a fixed point response can be observed. Given the eventual damping of oscillations, no reasonable amount of power can be harvested. (b) At a mean flow speed $U_m = 5$, the response was observed to exhibit an "of-off" intermittency. The corresponding RMS value was computed as 1.1 A. (c) LCOs being exhibited at a flow speed $U_m = 8$. The steady, large amplitude oscillations offers very good potential to harvest energy, with a RMS of 27 A.

It can be observed that the maximum value of τ_{xz} can be obtained where the section of the airfoil has the maximum thickness, at $y = 0.12$ and $x = 0.6$ (refer Fig. 6). The RMS of the τ_{xz} response is computed as 164.24 MPa.

Similarly, the maximum value of τ_{yz} as seen Fig. 6(b), can be obtained at $y = 0.06$ and $x = 1.527$. The corresponding RMS value is 2.017 MPa, which is almost 81 times lower than the maximum τ_{xz} value, obtained at $y = 0.12$. The RMS value of the τ_{yz} responses at $y = 0.12$ is 0.102 MPa, which is negligible in comparison to the τ_{xz} value. So, for this study, the τ_{xz} response at the section with coordinates $y = 0.12$ and $x = 0.6$ is used to compute the fatigue damage incurred. To evaluate the damage at these values of x and y , a combination of the S-N curve and a cycle counting procedure is used to evaluate the fatigue damage of the random stress history using the Palmgren-Miner linear damage accumulation theory (Venkatesh et al., 2014).

The S-N relation of the corresponding material in case of a reversible torsional stress has been taken from (Carpinteri et al., 2003) and is as follows.

$$S_T = 446.3N^{-0.1207} \quad (8)$$

A rainflow counting cycle method is then used to extract the cycles (Rychlik, 1987). Then, the Palmgren-Miner linear damage accumulation theory is used to evaluate the damage sustained during the period of oscillations. The damage study is done during three different types of oscillations, namely "burst" intermittency, "on-off" intermittency and LCOs. The current study employs the WAFO toolbox (Brodtkorb et al., 2000), which has specified sub-routines to evaluate the same. The total damage accumulated were tabulated and shown; see Table 1. It can be observed that the damage values for both the cases of intermittency are comparable, and, the damage accumulated in the case of LCOs is significantly higher than the case where the structure undergoes intermittent oscillations, regardless of their classification. This can be attributed the period of continuous large amplitude oscillations associated with LCOs, which as a result, has a significant impact on the accumulated damage (Schijve, 2009).

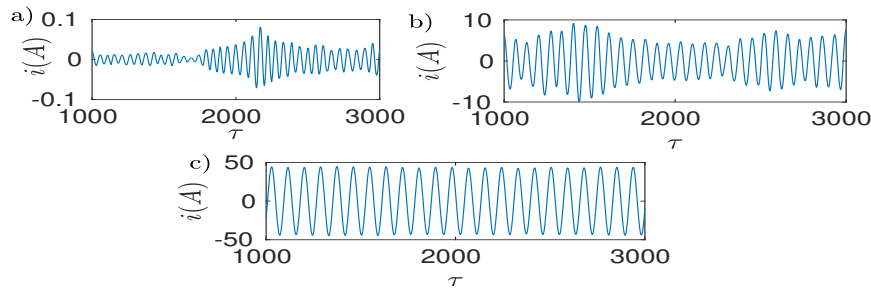


Figure 5: The current responses obtained under flow speeds with short timescale flow fluctuations is presented here. (a) At a mean flow speed $U_m = 4$, a fixed point response can be observed. Given the eventual substitution of oscillations, no reasonable amount of power can be harvested. (b) At a mean flow speed $U_m = 5.2$, the response was observed to exhibit an "burst" intermittency. The corresponding RMS value was computed as 2.5 A. (c) LCOs being exhibited at a flow speed $U_m = 8$, has a RMS of 29.5 A.

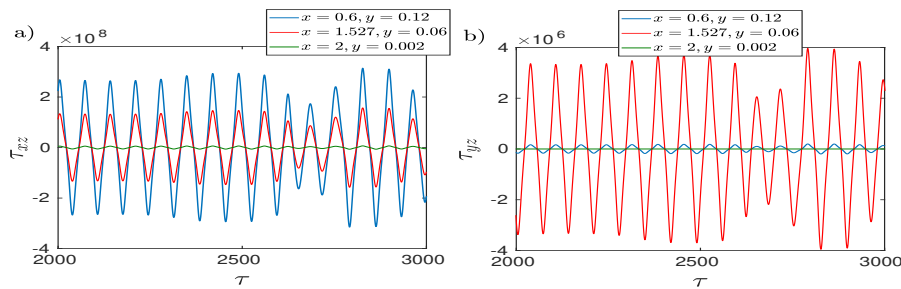


Figure 6: Variation of (a) τ_{xz} , and (b) τ_{yz} at coordinates $(x,y) \Rightarrow (0.6,0.12), (1.527,0.06)$ and $(2,0.0025)$.

While the range of the amplitude of the oscillations corresponding to LCOs and intermittent responses are comparable, the intermittent oscillations are more complex (defined in terms of broader content of frequencies) in nature and as a result the accumulated damage is much lower.

4 Conclusions

This study investigated the prospect of extracting useful energy from noise induced intermittent oscillations in a pitch-plunge aeroelastic system. A pitch-plunge airfoil with cubic hardening nonlinearity in the pitch degrees of freedom was considered. The flow was assumed to be temporally fluctuating. Based on isolated cases of either short or long time scale flow fluctuations, a "burst" or "on-off" intermittency was respectively encountered in the pre-flutter regime. Using an electromechanical coupling, the oscillatory responses were converted to a current output. It was observed that the power harvested during either of the intermittency regimes was lower than that of LCOs. However, the threat to structural safety was significantly lower in the case

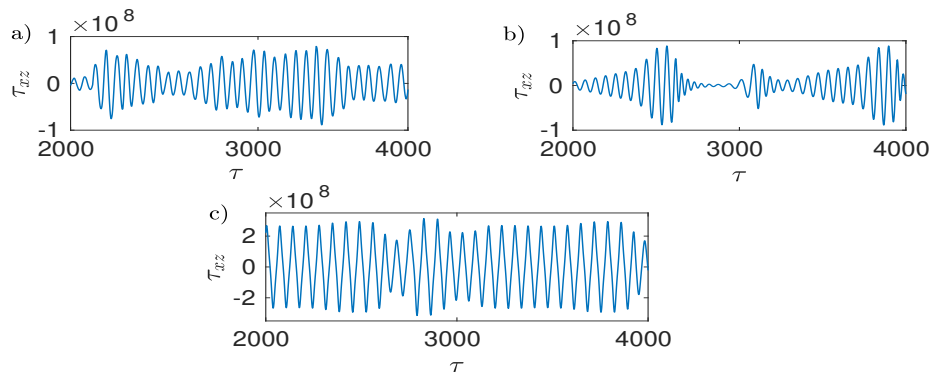


Figure 7: Variation of τ_{xz} for responses exhibiting, (a) "burst" intermittency, (b) "On-off" intermittency and (c) LCOs.

Table 1: Accumulated damage values.

"Burst" intermittency	"On-off" intermittency	Limit cycle oscillations
1.571×10^{-6}	4.9×10^{-6}	1.04

of intermittent oscillations in comparison to LCOs. To quantify the same, fatigue damages accumulated in the oscillatory regimes were computed.

To the best of authors' knowledge, the present study is the first to systematically investigate the interplay between intermittency, energy harvesting and the structural integrity in a noisy aeroelastic system. However, an in-depth investigation on maximizing the harvester performance under these noisy dynamical phenomenon is necessary. In particular, the present study has chosen a set of ideal harvester parameters to extract energy from "fully developed" intermittencies. It is well known that noise intensity and laminarity length can affect the manifestation of intermittency (Platt et al., 1993). The role of these dynamical parameters along with efficient optimizing of harvester designs can possibly give rise to improved power output - without compromising on the structural integrity. These are interesting avenues of future research to be undertaken by the authors.

5 References

- Abdelkefi, A. (2016). Aeroelastic energy harvesting: A review. *International Journal of Engineering Science*, 100, 112-135.
- Brottkorb, P. A., Johannesson, P., Lindgren, G., Rychlik, I., Ryden, J., & Sjö, E. (2000, January). WAFO-a Matlab toolbox for analysis of random waves and loads. In *The Tenth International Offshore and Polar Engineering Conference*. International Society of Offshore and Polar Engineers.
- Carpinteri, A., De Freitas, M., & Spagnoli, A. (Eds.). (2003). *Biaxial/multi-axial fatigue and fracture* (Vol. 31). Elsevier.

- Dowell, E. H. (1989). A modern course in aeroelasticity (Vol. 3). H. C. Curtiss, R. H. Scanlan, & F. Sisto (Eds.). Dordrecht, The Netherlands: Kluwer academic publishers.
- Fung, Y. C. (2008). An introduction to the theory of aeroelasticity. Courier Dover Publications.
- Gere, J. M., & Timoshenko, S. P. (1984). Mechanics of Materials . Brooks/Cole Engineering, 198(4).
- Lee, B. H. K., Jiang, L. Y., & Wong, Y. S. (1999). Flutter of an airfoil with a cubic restoring force. *Journal of fluids and structures*, 13(1), 75-101.
- Platt, N. S. E. A., Spiegel, E. A., & Tresser, C. (1993). On-off intermittency: A mechanism for bursting. *Physical Review Letters*, 70(3), 279.
- Poirel, D. C., & Price, S. J. (2001). Structurally nonlinear fluttering airfoil in turbulent flow. *AIAA journal*, 39(10), 1960-1968.
- Rychlik, I. (1987). A new definition of the rainflow cycle counting method. *International journal of fatigue*, 9(2), 119-121.
- Schijve, J. (2009). Fatigue damage in aircraft structures, not wanted, but tolerated?. *International Journal of Fatigue*, 31(6), 998-1011.
- Sreenivasan, K. (1991). Fractals and multifractals in fluid turbulence. *Annual Review of Fluid Mechanics*, 23(1), 539-604.
- Venkatesh, S., Sarkar, S., & Rychlik, I. (2014). Uncertainties in blade flutter damage prediction under random gust. *Probabilistic Engineering Mechanics*, 36, 45-55.
- Venkatramani, J., Nair, V., Sujith, R. I., Gupta, S., & Sarkar, S. (2016). Precursors to flutter instability by an intermittency route: a model free approach. *Journal of Fluids and Structures*, 61, 376-391.
- Venkatramani, J., Kumar, S. K., Sarkar, S., & Gupta, S. (2017). Physical mechanism of intermittency route to aeroelastic flutter. *Journal of Fluids and Structures*, 75, 9-26.
- Yang, J., Xiong, Y. P., & Xing, J. T. (2011, January). Investigations on a nonlinear energy harvesting system consisting of a flapping foil and an electro-magnetic generator using power flow analysis. In *ASME 2011 International Design Engineering Technical Conferences and Computers and Information in Engineering Conference* (pp. 317-324). American Society of Mechanical Engineers Digital Collection.

Flow-induced vibration of a cylinder between two walls for energy harvesting

Junyoung Kim¹ and Daegyoun Kim²

¹*Department of Mechanical Engineering, KAIST, Daejeon, Republic of Korea, jykim12@kaist.ac.kr*

²*Department of Mechanical Engineering, KAIST, Daejeon, Republic of Korea*

Keyword: Flow-induced vibration, Energy harvesting, Cylinder

We experimentally investigate the flow-induced vibration of a cylindrical structure arranged between two plane walls in order to explore its potential application to energy harvesting using periodic contact. In our model, if the walls are placed close enough, the cylinder collides with the walls periodically. We study the energy harvesting performance of the model by attaching energy harvesting devices to the walls. To change energy harvesting performance and the dynamics of the cylinder, we consider two main parameters, distance between two side walls and streamwise length of the walls.

Although the free-stream velocity at which the cylinder starts to collide with the walls is almost same regardless of these parameters, the velocity at which the cylinder stop to oscillate is obviously affected by these parameters. The cylinder collides at high free-stream velocity even beyond the lock-in region of an isolated cylinder with narrow gap and long walls. Moreover, depending on the free-stream velocity, the dynamics of the cylinder can be divided into several regions. At low free-stream velocity, the motion of the cylinder is stable and it collides with the walls continuously. However, in the high free-stream velocity region, the cylinder shows strong hysteresis and unstable motion. For the same experimental conditions, whether the cylinder collides with the walls is determined by its previous state: vibrating or not. Besides, even the oscillating cylinder sometimes stops suddenly. In this case, if we stimulate the cylinder, the cylinder starts to oscillate again. Finally, to change the free-stream velocity region at which the cylinder collides with the walls, we conducted additional experiments using a square cylinder and compared the energy harvesting performance.

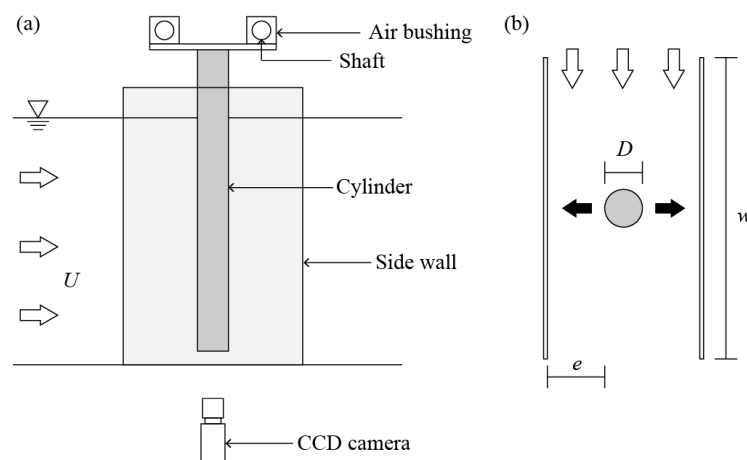


Figure 1: (a) Schematic diagram of experimental setup. (b) Geometric parameters for the experiments.

Blockage effects on the fully-passive flapping-foil turbine

Kevin Gunther and Guy Dumas¹

CFD Laboratory LMFN, Département de génie mécanique, Université Laval, Québec, Canada

¹ Guy.Dumas@gmc.ulaval.ca

Keywords: Flapping-foil turbine, Fluid-structure interaction, Confinement, Blockage effects

This work focusses on the effects of confinement on the behavior and performance of the fully-passive flapping-foil turbine. The device, illustrated in Figure 1, allows to extract a significant portion of the kinetic energy of an upstream flow as our group has shown recently in unconfined conditions [1]. A passive control composed of springs, viscous dampers and masses governs the uncoupled and free motions (pitch and heave) of the foil. This fluid-structure interaction strategy greatly simplifies the mechanical complexity related to previous fully-constrained designs [2]. The goals of the present study may be expressed as:

- Investigate the effects of an increase in confinement on the power extraction performances for a given set of structural parameters (m_h , D_h , k_h , $m_\theta x_\theta$, l_θ , D_θ and k_θ)
- Propose a simple and practical method of adaptation to maintain the optimal performances in a realistic range of confinement

The numerical investigation is conducted at $Re = 3.9 \cdot 10^6$ with a FSI algorithm implemented in the commercial finite-volume solver Star-CCM+ from Siemens. The flow is modeled with 2D URANS simulations using the Spalart-Allmaras one-equation turbulence model. The foil has a NACA 0015 profile. Confinement is controlled by varying the distance H of the symmetry plane boundaries applied above and below the turbine. Extension of the present important results to actual 3D confinement [3] will also be discussed.

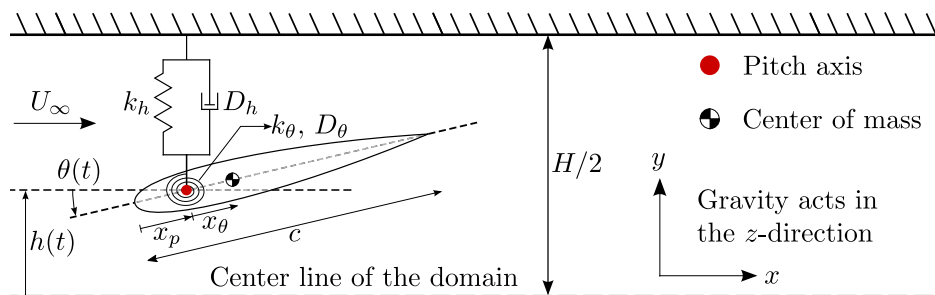


Figure 1: Schematic of the fully-passive flapping foil [1]

[1] Boudreau, M., Picard-Deland, M., & Dumas, G. (2020), A parametric study and optimization of the fully-passive flapping-foil turbine at high Reynolds number, *Renewable Energy*, vol.146, p.1958-1975.

[2] Kinsey, T., Dumas, G., Lalande, G., Ruel, J., Méhut, A., Viarouge, P., Lemay, J., & Jean, Y. (2011), Prototype testing of a hydrokinetic turbine based on oscillating hydrofoils, *Renewable Energy*, vol.36, p.1710-1718.

[3] Gauthier, E., Kinsey, T., Dumas, G. (2016), Impact of blockage on the hydrodynamic performance of oscillating-foils hydrokinetic turbines, *ASME Journal of Fluids Engineering*, vol.138, 091103 p.1-13.

Leaf Flutter Mechanism and its Application in the Wind Energy Harvesting

Kun Wang¹, Wei Xia^{1,2}, Haocheng Feng¹ and Shengping Shen¹

¹State Key Laboratory for Strength and Vibration of Mechanical Structures, Xi'an Jiaotong University, Xi'an 710049, China, kunwang@stu.xjtu.edu.cn

²Shaanxi Engineering Laboratory for Vibration Control of Aerospace Structures, School of Aerospace, Xi'an Jiaotong University, Xi'an 710049, China

Keyword: leaf flutter, wind energy harvesting (WEH), structural design, aeroelastic model, wind tunnel tests

Clean energy is one of the main concerns of today's world. From traditional wind turbine to piezoelectric energy harvesters, the wind energy harvesting (WEH) has been the focus of discussion. In order to develop self-sustainable MEMS devices, very flexible structures are applied in the energy harvesters to utilize the structural oscillations in the wind. A novel design of the flexible structures is proposed to mimic the flutter of Palm tree leaves. With the understanding of leaf flutter mechanism, the artificial "leaves" can start to flutter at relatively low-speed wind and oscillate with stable frequency, just like the Palm tree leaves.

In order to design the WEH structures, the natural observations of Palm leaves are firstly carried out. The material characteristics are observed and measured by either macroscopic observations or mechanical tests. Secondly, the aeroelastic models are established for the Palm leaves. The finite element leaf structural model is coupled with the lift surface aerodynamics in the aeroelastic model. Numerical simulations show that the mode coalescence between the bending and twisting vibration (Fig. 1A & Fig. 1B) excites the flutter. An artificial leaf is then designed for the energy harvester. In order to increase the coupling effects, the distributed balance weights with total mass of 2.8 grams are introduced into the artificial structure (Fig. 1C). The flutter characteristics and energy harvesting efficiency are tested in the low-speed wind tunnel at Xi'an Jiaotong University. The results show that the artificial structure starts to flutter at wind speed of 2.2m/s. With PZT patches bonded on the root of the flexible structure, the exported power density of the electricity reaches $1.44 \mu\text{W}/\text{cm}^3$.

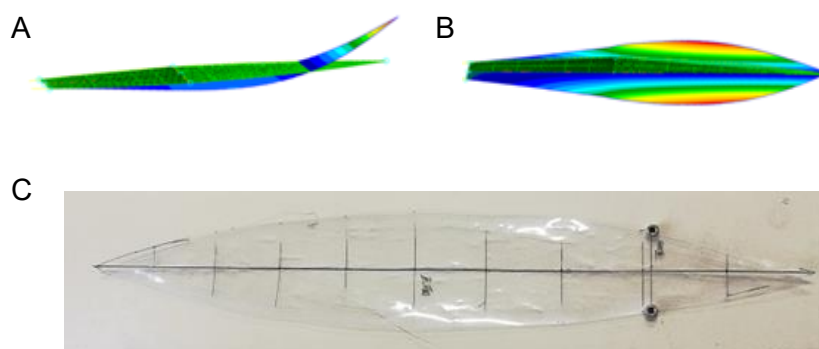


Figure 1: Leaf vibration mode and bio-inspired artificial leaf.
(A) Bending mode. (B) Twisting mode. (C) Artificial leaf.

1. McCarthy, J.M., Watkins, S., Deivasigamani, A. et al. (2016). Fluttering energy harvesters in the wind: A review. *Journal of Sound and Vibration*, 361, 355-377.

Axial transducer for energy harvesting from galloping

Maya Hage Hassan¹, Valentin Bernard², Xavier Amandolese^{3,2} and Pascal Hémon²

¹ *Université Paris-Saclay, CentraleSupélec, CNRS, Laboratoire de Génie Electrique et Electronique de Paris, 91192, Gif-sur-Yvette, France*

Sorbonne Université, CNRS, Laboratoire de Génie Electrique et Electronique de Paris, 75252, Paris, France

² *LadHyX, Ecole Polytechnique - CNRS, 91128 Palaiseau Cédex, France*

³ *LMSSC, Conservatoire National des Arts et Métiers, Paris, France*

Abstract

In this paper an electromagnetic transducer is optimized to harvest energy from a galloping harvesting system. An electromagnetic modeling of the harvester is firstly proposed by means of Finite Element Analysis (FEA). A comparison with experimental values is done for the model validation. A new transducer is developed to increase the harvesting energy and improve the efficiency. An electromechanical model is developed and validated by means of experimental measurements.

Keyword: energy harvesting, transducer, galloping

1 Introduction

The transverse galloping phenomenon consists in a self-excited linear oscillation of slender, non-circular structures in a cross flow. One of the earliest analytical description goes back to Den Hartog, who explained this phenomenon in 1943 (Den Hartog, 1985). Recently the idea emerged that the galloping phenomenon could be used for designing an energy harvester from wind or water current. Energy harvesting from transverse galloping has been previously studied analytically by Barrero-Gil et al., (2010) and Vicente-Ludlam et al., (2014). In previous work an energy harvester was presented and described experimentally in Hémon. P et al., (2017).

In this paper, the electromagnetic modelling of this harvester is proposed by means of Finite Element Analysis (FEA). A comparison with experimental values is then realized for the modelling validation. A new transducer is proposed to increase the harvesting energy and improve the efficiency. A Multiphysics model taking into consideration the electromagnetic, electrical and mechanical model is developed. A prototype is tested on the galloping setup to validate both mechanical and electromagnetic model.

The paper is organized as follows: after a short review of galloping, the experimental methodology regarding the measurements, galloping section model set-up are presented in section 2. The modelling and experimental validation of earlier transducer is given in section 3. The design of the new transducer is presented in section 4. Finally, the experimental results are discussed in section 5.

2 The galloping phenomenon

Galloping phenomenon is generally referred to be a one degree of freedom instability, in transverse or torsional motion, it can be modeled in the framework of a quasi-static aeroelasticity approximation and using a single-mode oscillator equation for the dynamics of the structure. Considering a square prism with mass m in a 2-dimensional cross flow supported by a spring with stiffness k and a damper with damping coefficient c , the single-mode equation of motion without forcing terms reads as follows:

$$m\ddot{y} + c\dot{y} + ky = 0 \quad (1)$$

If the system is subject to a cross flow, aerodynamic lift and drag forces act on the body. The aerodynamic forces are proportional to the square of the relative flow velocity, that is obtained as the vector sum of the solid and fluid velocity in an inertial reference frame.

$$\vec{u}_{rel} = \vec{u} - \dot{\vec{y}} \quad (2)$$

The drag force acts in the direction of \vec{u}_{rel} while the lift force acts perpendicular to it. In the reference frame of the section the effect of $\dot{\vec{y}}$ is a rotation of the incoming flow velocity by an angle $\alpha = \text{atan}(\dot{y}/u)$, as seen in Fig. 1. Projecting the aerodynamic forces on the y -direction of the 2-dimensional plane one obtains the vertical force F_y that affects the oscillator directly.

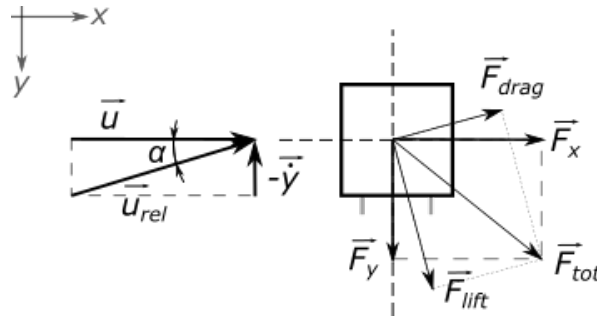


Figure 1: Forces on a section in a cross flow

The magnitude of the force depends on the non-dimensional lift and drag coefficients C_l and C_d that are functions of the angle of attack α .

$$F_l = \frac{1}{2}\rho u_{rel}^2 D C_l \quad F_d = \frac{1}{2}\rho u_{rel}^2 D C_d \quad (3)$$

where ρ is the density of the fluid and D and l are the dimension of the prism. Curves for C_l and C_d versus angle of attack α are determined by static wind tunnel experiments and can be found in literature for many cross sections. By projecting the forces onto the y axis, a combined lift and drag coefficient C_y can be defined as follows:

$$F_y = F_l \cos(\alpha) + F_d \sin(\alpha) = \frac{1}{2}\rho u_{rel}^2 D (C_l \cos(\alpha) + C_d \sin(\alpha)) \quad (4)$$

$$\Rightarrow C_y = (C_l \cos(\alpha) + C_d \sin(\alpha)) \quad (5)$$

Adding the transverse aerodynamic force to the oscillator equation, the galloping instability is described by the following equation of motion:

$$m\ddot{y} + c\dot{y} + ky = \frac{1}{2}\rho u^2 DIC_y(\alpha) \quad (6)$$

An electromagnetic transducer is studied to harvest the kinetic energy of this galloping structure. In the next section, a brief review of electromagnetic transducers is presented.

3 Electromagnetic transducers

Electromagnetic transducers are based on Faraday's law, that states that a variation of the magnetic flux inside a coil, e.g. due to a moving magnet, induces an electromotive force in the coil. The electromotive force (e_m) is equal to the time derivative of the flux ϕ :

$$e_m = -\frac{\partial\Phi}{\partial t} \quad (7)$$

If the change of flux is only caused by the change of the position y of a magnet, as is the case in galloping energy harvesting, the electromotive force can be also expressed as:

$$e_m = -\frac{\partial\Phi}{\partial y} \frac{\partial y}{\partial t} \quad (8)$$

$-\frac{\partial\Phi}{\partial y}$ often is denoted with the name k_E and represents a coupling coefficient between the magnet and the coil. In most of literature k_E is considered to be a constant value (El-Hami et al. (2001)). If the coil is integrated into a closed circuit with a load resistance R_L , the system is described by the following electrical equation :

$$e_m = k_E \dot{y} = L \frac{\partial i}{\partial t} + (R_L + R_i) i \quad (9)$$

Where, L is the inductance and R_i the resistance of the harvester coil. The force exerted between the stationary and moving part of the transducer, is given by :

$$F_{em} = k_E i \quad (10)$$

Where k_E can be calculated using NBI (El-Hami et al. (2001)). This formulation comes from the simplified case of a square coil of length l moving from a location without magnetic field into a location with constant magnetic flux density B . When considering the non-linear behavior of the ferromagnetic material, this coupling coefficient cannot be considered as constant. Since the mechanical system evolves at a much slower time scale than the electronic system, the inductance part of the equation is neglected. Thus the electromechanical coupling system that is considered for the galloping harvester is given by :

$$\begin{cases} m\ddot{y} + c\dot{y} + ky = \frac{1}{2}\rho u^2 DIC_y(\alpha) + k_E(y) i \\ (R_L + R_i) i = k_E \dot{y} \end{cases} \quad (11)$$

While in literature on electromagnetic energy harvesters the Laplace force is the only force appearing in the model, experiments and numerical tests show a strong influence of the static magnetic force in the y direction between the moving magnets and the stationary core. The influence of this static force can surpass the stiffness force for the used spring at low wind speeds. A static force is determined by *FEA* and added to the model.

4 Energy harvesting device

The electromagnetic transducer used in previous work (Hémon. P et al., (2017)) consists of a coil with 1800 turns, wound around a cylindrical ferromagnetic core of 4 mm diameter and a length of 17 mm. A stack of three neodymium N45 magnets ($B_r = 1,320$ T, $H_{cJ} = 923$ kA/m) with dimensions $5 \times 10 \times 3$ mm where mounted on the galloping set-up, and the coil was placed in front of the magnets Fig. 2. The magnets are located on the suspension beams that ensure the vertical stiffness of the aeroelastic system.

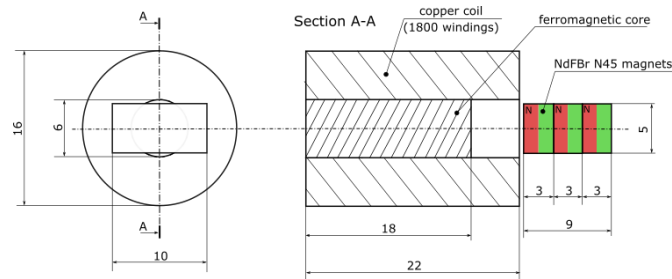


Figure 2: Drawing of the first transducer model

The magnet-coil-combination was modelled by means in 2D FEA using *FEMM*, as presented in Fig. 3 the flux lines due to NdFeB magnetic field are not optimally used, the flux is not totally enclosed in the ferromagnetic circuit to improve the electromotive force (emf).

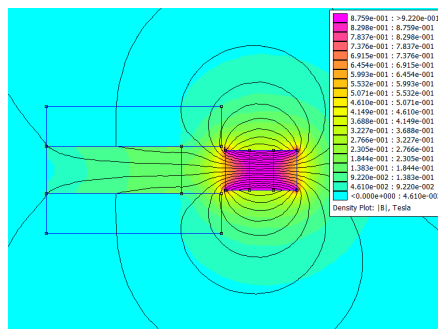


Figure 3: Flux direction and flux density of the magnetic field in the transducer (*FEMM* result)

For the given transducer, k_E is determined through a magnetostatic analysis using *FEMM* tool. The variation of k_E as function of magnets' position is given in Fig. 4. The calculation has been performed in a motion range of 50 mm from the equilibrium position in both directions, obtaining a curve for k_E as a function of the magnet position y .

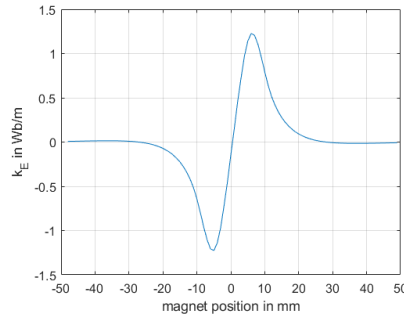


Figure 4: Result for k_E at every position of the magnet

To validate the proposed model, the $k_E(y)$ curve has been inserted into a *Simulink* model for the differential equation governing the circuit of the transducer and it is proposed to reconstruct the graph given in Fig. 5 the measured output voltage is at a load resistance of 80 . The same motion was imposed in the *Simulink* model, and the resulting voltage was observed. As can be seen in Fig. 5, the model can predict with high accuracy the shape of the output voltage.

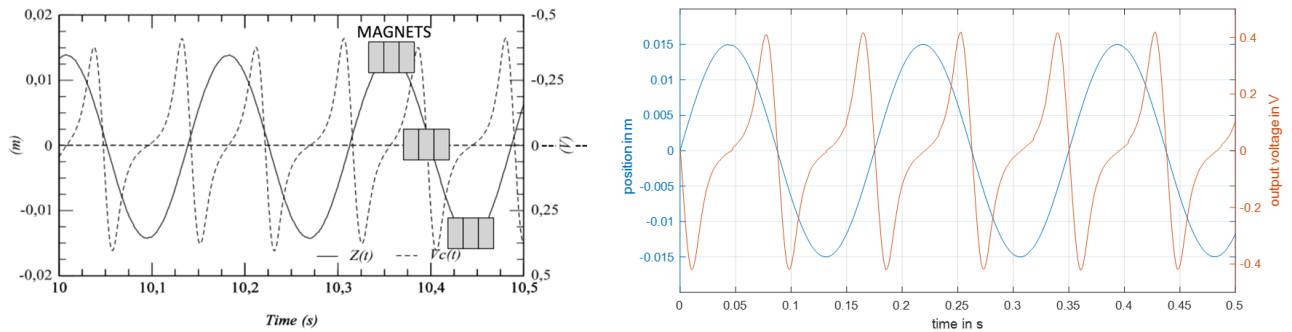


Figure 5: Left: experimental results obtained previously, right: results of the *Simulink* model

4.1 New proposals

New transducer designs are proposed and tested in simulation. The design are based on standardized E-shaped laminates in ferromagnetic FeCo material. A drawing of the proposal is shown in Fig. 6. It consist a coil wound around the central leg of an E-shaped core pieces, assembled from laminates. Three magnets are mounted on a ferromagnetic support with an air gap of 1 mm to the core. NdFeBr magnets with coercivity $H_c = 1042$ kA/m are chosen. These magnets are commonly sold under the name N45SH in the Chinese standard nomenclature. The design is meant to create a closed magnetic circuit in order to have maximum flux variation inside the coil, and therefore increase the output voltage.

The second proposal is similar to the first one, but aims to double the number of winding affected by the flux variation. A second E-shaped core with a coil on the central leg is placed in face of the first one. The magnets are now longer mounted on a ferromagnetic core, and are moving inside the air gap between the two cores. Dimensions and magnets are the same as in the single E proposal. Fig. 7 shows the *FEMM* model of this second proposal.

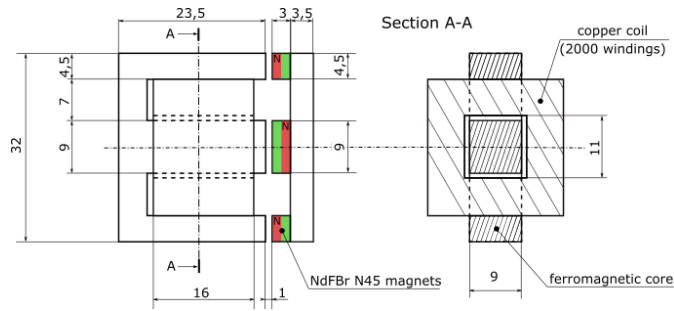


Figure 6: Single E transducer

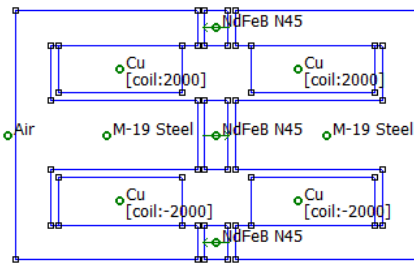


Figure 7: Double E transducer *FEMM*

When compared the single E proposal increases the k_E value by a factor of 25 and that of double-core proposal by a factor of 45 (Fig. 8).

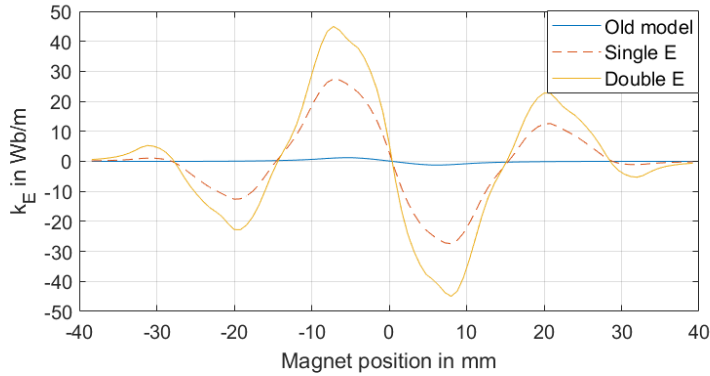


Figure 8: Comparison of k_E curves for the three transducers

In order to select the optimal transducer for this application, the global efficiency of the system is determined as function of the load resistance. Where it was defined as the ratio between the mechanical energy flowing across the swept area of the galloping beam and the electrical energy dissipated in the load resistance.

$$\mu = \frac{i_{rms}^2 R_L}{\frac{1}{2} \rho u^3 l (D + 2\hat{y})} \tag{12}$$

Where, $I(D + 2\hat{y})$ represents the area swept by the beam during its motion. Fig. 9 shows how the load resistance affects the efficiency of the harvester using the described transducers. The result show a strong effect of the load resistance. Fig. 10 gives the efficiency that can be obtained when optimizing the load resistance at every reduced velocity, as well as the resistance value that is found to be optimal according to the model.

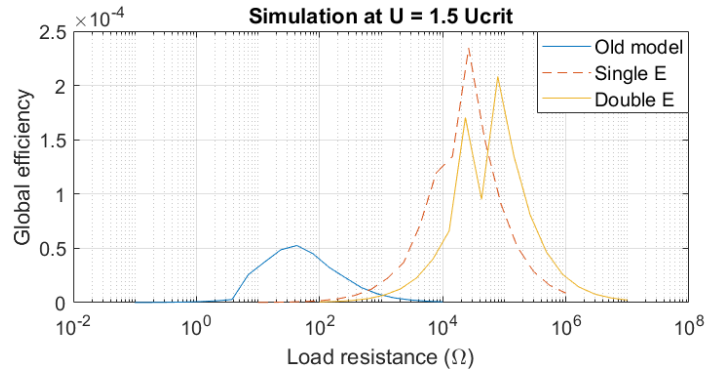


Figure 9: Effect of the load resistance on the efficiency of the harvester using three different transducers

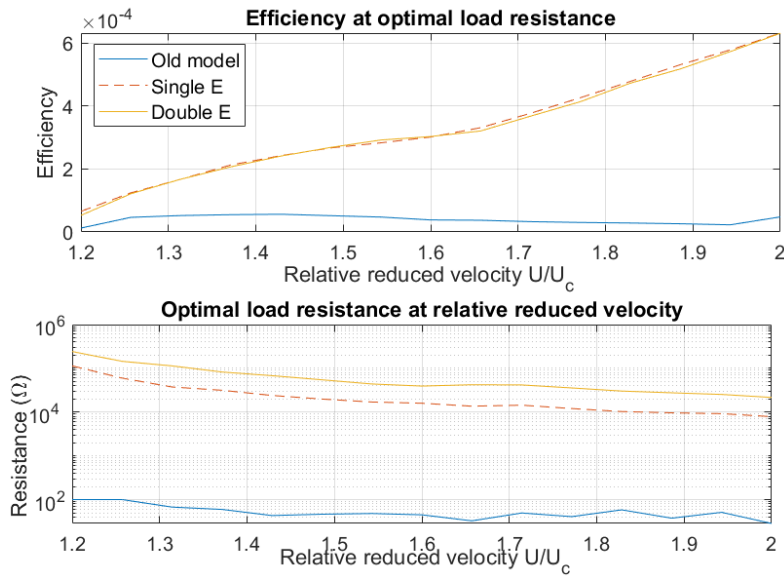


Figure 10: Efficiency achieved when using the optimal load resistance at each reduced velocity

Using this energy conversion chain, the efficiency of the single subsystems can be defined, it is found that the bulk of the inefficiency is due to the aerodynamics of the galloping phenomenon. In the range of parameters tested with the model, no more than 0.1% of the energy available in the wind are converted into mechanical energy in the oscillator. This is coherent with previous experimental results (Hémon. P et al., (2017)). From efficiency results, the single side E is selected to be experimentally validated.

5 Experimental validation

The magnet support is fixed onto the galloping beam, while the core with the coils is mounted on a linear guide that allows the transducer to be placed at any air gap between 1 mm and 20 mm. The air-gap of 5mm was chosen in order to minimize the static forces.

A new galloping set-up has been built, based on the set-up tested in (Hémon. P et al., (2017)). The set-up, shown in Fig. 11 consists in a square beam of length $l = 250$ mm and width $D = 17$ mm. Square plates made from Plexiglas are attached flat on both ends of the beam. This is meant to keep the flow 2-dimensional. This assembly is placed inside a closed loop wind tunnel. The assembly is suspended by one laminar and two linear springs both sides. No other constraining elements are used, in order to minimize the structural damping of the set-up.

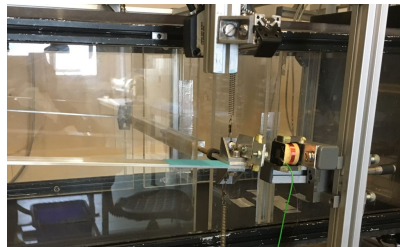


Figure 11: Experimental Set-Up

As for the transducer (Fig. 12), the coil was wound from 0.1 mm copper wire and contains 2000 windings. The resulting internal resistance of the coil R_i is 266Ω . As for the core it's made of laminated iron.

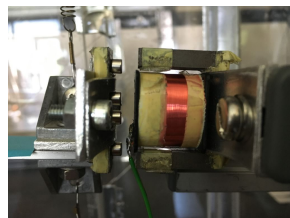


Figure 12: Photograph of the experimental transducer

The magnet support is fixed onto the galloping beam, while the core with the coils is mounted on a linear guide that allows the transducer to be placed at any air gap between 1 mm and 20 mm. The air-gap of 5mm was chosen in order to minimize the static forces.

In order to validate the correctness of the electromagnetic model of the transducer, the galloping set up with engaged transducer was tested at several wind speeds, recording the limit cycle oscillatory motion as well as the exact shape of the voltage on the load resistance. This data could then be compared to the voltage shape predicted by the model at that particular motion of the magnets to validate the transducer model. The validation was performed using a model that does not compute the aerodynamics and considers the motion of the oscillator as given. The experiment has been performed at wind speeds close to the critical velocity,

where the galloping model was expected to give good results for the motion. Wind speeds of 4.49 m/s and 5.66 m/s were chosen. To validate the model of the electromagnetic transducer, and in particular k_E , oscillations have been recorded and imposed on the model, comparing the resulting voltage to the measured voltage. When the approximation for small impedance is applied to equation 9, one obtains the following equation for the output voltage V_{out} :

$$V_{out} = \frac{R_L}{R_i + R_L} k_E \dot{y} \quad (13)$$

Voltage shape for a given motion is therefore a direct validation for the k_E curve that was computed using *FEMM*. Various motion aptitudes have been tested by applying setting wind speeds. A load resistance of 500 Ω was chosen for all wind speeds. The recorded motion has been converted into a time signal and imposed on a *Simulink* model that contains only the transducer, and disregards all the mechanics, must taking a forced motion as input. The results for various wind speeds can be seen in Fig. 13.

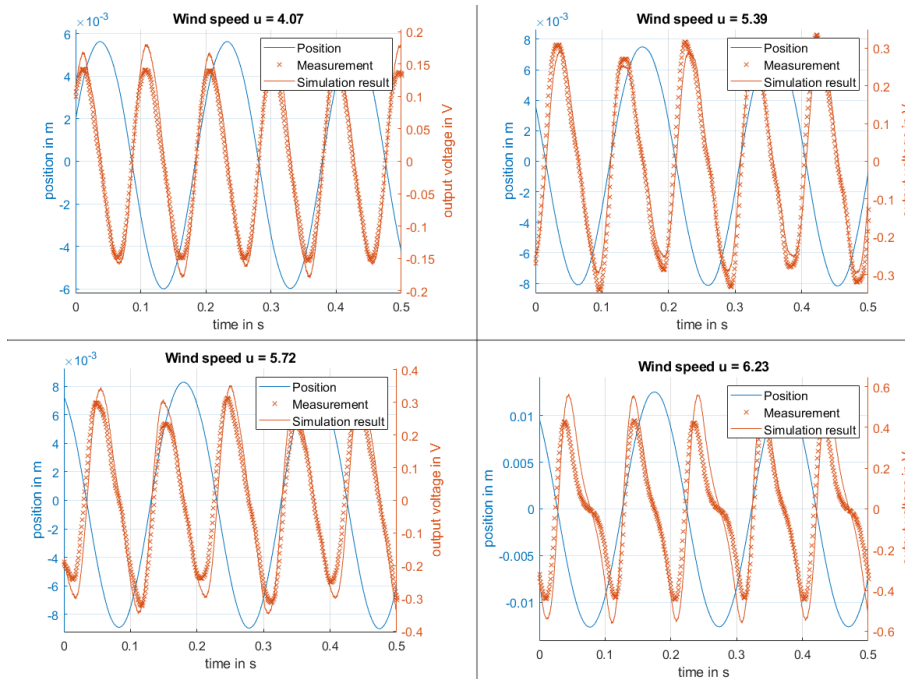


Figure 13: Measured and simulated voltage at different wind speeds.

In all cases, the model correctly predicts the output voltage. In terms of accuracy of the predicted amplitude, the results seem to vary between different measurements. This can be due to the used *BH curve* of the ferromagnetic part, and the equivalent depth of the circular magnets used in *FEMM*.

Experiments to determine the optimal load resistance have been carried out at two wind speeds, with the transducer set at an air gap of 5 mm. Wind speeds were chosen low to remain in the area where the predictions of the galloping model are more accurate. The results for measured efficiency at $u = 5.66$ m/s are given in Fig. 14. The model largely overestimates the motion amplitude as well as the efficiency. The amplitude is predicted to be about 3 times larger than the experiment for high load resistances, with a decreasing difference for lower R_L .

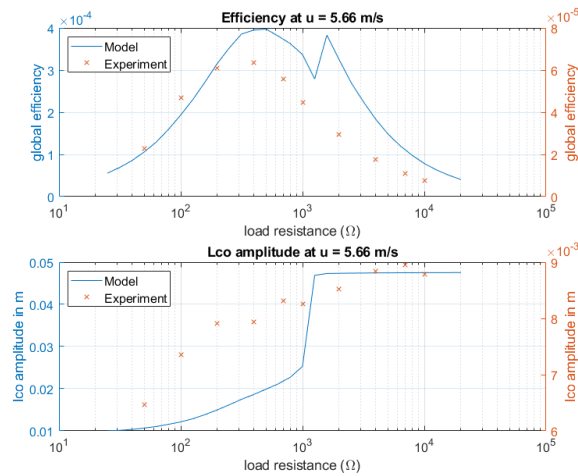


Figure 14: Measured and simulated efficiency and lco amplitude at wind speed of 5,66 m/s

6 Conclusion

In this paper an axial transducer is proposed to harvest energy from galloping. A multiphysics model of the transducer was able to predict the shape and amplitude of the output voltage given an input signal with reasonable precision. As for future work, an optimization of the geometry of the harvester could be performed. It might be interesting to inverse the design approach for the harvester and starting from a desired k_E vs y curve, an optimized transducer is proposed.

References

- M. P. Paidoussis, S. J. Price, and E. De Langre, Fluid-structure interactions: cross-flow-induced instabilities. Cambridge University Press, 2010
- Den Hartog, J.P., 1985. Mechanical Vibrations. Reprint of the 1934 edition. Dover, New York
- Barrero-Gil, A., Alonso, G., Sanz-Andres, A., 2010. Energy harvesting from transverse galloping. J. Sound and Vibration 329, 2873-2883.
- Vicente-Ludlam, D., Barrero-Gil, A., Velazquez, A., 2014. Optimal electromagnetic energy extraction from transverse galloping. J. Fluids and Structures 51, 281-291.
- Padoussis, M. P., 2016. Dynamics of tubular cylindrical structures in axial flow. In: Proceedings of the first International Symposium on Flutter and its Application, Paper ISFA-1K01, Tokyo, Japan.
- Sears, W.R., 1941. Some aspects of non-stationary airfoil theory and its practical application. Journal of the Aeronautical Sciences 8, 104-108.
- Hémon. P., Amandolese. X. and Andrianne. T., "Energy harvesting from galloping of prisms: A wind tunnel experiment," Journal of Fluids and Structures, vol. 70, pp. 390-402, 2017.
- El-Hami, M., Glynne-Jones, P., White, N., Hill, M., Beeby, S., James, E., Brown, A. and Ross, J., "Design and fabrication of a new vibration-based electromechanical power generator," Sensors and Actuators A: Physical, vol. 92, no. 1-3, pp. 335-342, 2001.

Numerical study on energy harvesting from VIV and galloping by a square cylinder

Peng Han¹², Guang Pan² and Baoshou Zhang¹³

¹ *Northwestern Polytechnical University, Xi'an, P.R. China, panguang@nwpu.edu.cn (second author)*

² *Ecole polytechnique, Palaiseau, France, peng@ladhyx.polytechnique.fr (first author)*

³ *University of Houston, Houston, USA bzhang28@central.uh.edu (third author)*

Keywords: vortex induced vibration, galloping, energy harvesting

Vortex-induced vibration (Flow-induced vibration) (VIV/FIV), may occur in many marine structures. In comparison with circular cylinders, square-shape cylinders vibrate more intensely and have advantages in energy harvesting from ocean, in particular in high Re region.

In this paper, a numerical study is carried out for the FIV energy harvesting of a square cylinder. The Reynolds-averaged Navier-Stokes equations are used in conjunction with the SST $k-\omega$ turbulence model to simulate the turbulent flow, and vibration equations are solved by using the Newmark-beta algorithm, which is verified by comparing the results with published data [1]. We investigate the effect of incidence angles and Reynolds number on FIV responses and energy conversion characteristics. Specifically, three typical incidence angles are selected and the Reynolds number is in the range of 24000-160000. Simulation results indicate that incidence angles and Reynolds number significantly affect the lock-in area, oscillation frequency, vibration responses, vortex shedding modes and the performance of energy conversion. Similar to the phenomena found by reference [2], galloping occurs at $\alpha=0^\circ$ when the Reynolds number is increased, therefore, not only the vibration frequency will no longer be controlled by vortex shedding frequency but also the square cylinder vibrates violently. The energy conversion efficiency reaches its maximum at the upper branch regardless of incidence angles. The angle $\alpha=45^\circ$ is considered as the most suitable arrangement for energy harvesting, which provides the highest efficiency and power in all cases. In this situation, amplitude of lower branch is magnified whereas the frequency is controlled by vortex shedding frequency.

1.Han, P., Pan, G., Tian, W., 2018. Numerical simulation of flow-induced motion of three rigidly coupled cylinders in equilateral-triangle arrangement. *Physics of Fluids* 30, 125107.

2.Nemes, A., Zhao, J., Lo Jacono, D., Sheridan, J., 2012. The interaction between flow-induced vibration mechanisms of a square cylinder with varying angles of attack. *Journal of Fluid Mechanics* 710, 102-130.

PIEZOELECTRIC ENERGY HARVESTING FROM PANEL FLUTTER OSCILLATION OF LAMINATED PLATES

Masaki KAMEYAMA¹, Keisuke IKEGAMI² and Naoya KASAHARA²

¹*Shinshu University, Nagano, JAPAN, kameyama@shinshu-u.ac.jp*

²*Graduate School at Shinshu University, Nagano, JAPAN*

Abstract

The present paper deals with the piezoelectric energy harvesting from supersonic panel flutter oscillation of simply-supported laminated plates. The aeroelastic flutter energy harvester is composed of a piezoelectric element attached to the structures and a conventional harvesting circuit. A diode bridge of four diodes is connected to the piezoelectric element and it provides a mechanism of current rectification. Aeroelastic analysis of simply-supported laminated plates with a piezoelectric element is based on a geometrically nonlinear finite element method and a quasi-steady aerodynamics. The effect of location of piezoelectric element on converged voltage in the harvesting system is examined through the numerical examples.

Keyword: Energy Harvesting, Supersonic Panel Flutter, Piezoelectric Element, Composite Materials, Optimal Placement

1 Introduction

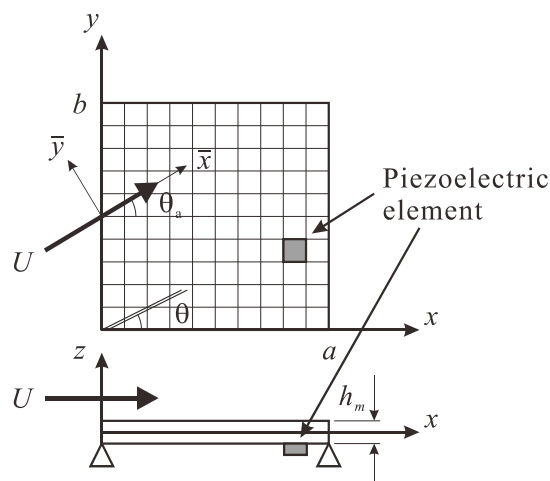
Aeroelastic characteristics have played the significant role in structural design. Flutter is one of the representative dynamic phenomena of aeroelastic instability, which results in catastrophic destruction of structures. Although flutter is recognized as a harmful phenomenon from the viewpoint of structural integrity, it can be conversely utilized as profitable energy source for vibration-based energy harvesting. So far, a lot of research on energy harvesting from aeroelastic vibration has been carried out (McKinney and De Laurier, 1981; Isogai et al., 2003; Abdelkefi, 2016; Kameyama and Makihara, 2016).

The present paper deals with the piezoelectric energy harvesting from supersonic panel flutter oscillation of simply-supported laminated plates. The aeroelastic flutter energy harvester is composed of a piezoelectric element attached to the structures and a conventional harvesting circuit. A diode bridge of four diodes is connected to the piezoelectric element and it provides a mechanism of current rectification. Aeroelastic analysis of simply-supported laminated plates with a piezoelectric element is based on a geometrically nonlinear finite element method and a quasi-steady aerodynamics. The effect of location of piezoelectric element on converged voltage in the harvesting system is examined through the numerical examples.

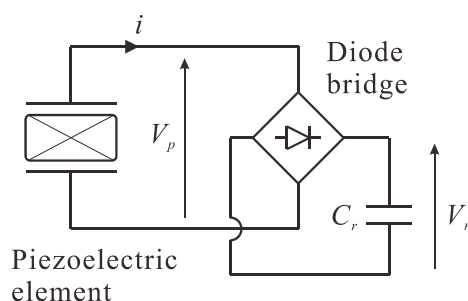
2 Fundamental Equations

2.1 *Supersonic panel flutter characteristics of laminated plates*

The finite element equation for linear supersonic panel flutter characteristics of simply-



(a) Simply-supported laminated plates ($a = b = 300$ mm, $h_m = 3$ mm).



(b) Conventional harvesting circuit.

Figure 1: Schematic of aeroelastic flutter energy harvester.

supported symmetrically laminated plates, which possesses a uniform thickness and material density, without piezoelectric elements can be described as follows:

$$[M_m]\{\ddot{W}(t)\} + g[D_a]\{\dot{W}(t)\} + ([K_{mL}] + \lambda[K_a])\{W(t)\} = \{0\}, \quad (1)$$

$$[D_a] = \frac{1}{\rho_m h_m} [M_m], \quad (2)$$

where the mass and linear stiffness matrices of laminated plates without piezoelectric elements are denoted by M_m and K_{mL} , the aerodynamic and aerodynamic damping matrices are denoted by K_a and D_a , the nodal displacement vector is denoted by $W(t)$, respectively. Here it is assumed that the aerodynamic forces acting on the vibratory panel surface in supersonic flow (velocity U , angle θ_a) are given by the linear piston theory (Ashley and Zartarian, 1956) and the upper surface of the panel is exposed to a high supersonic airflow at zero angle of attack. The dynamic pressure and aerodynamic damping parameters denoted by λ and g are defined as (Liao and Sun, 1993; Zhou et al., 1994)

$$\lambda = \frac{2q}{\sqrt{M^2 - 1}}, \quad (3)$$

$$g = \lambda \frac{1}{U} \frac{M^2 - 2}{M^2 - 1} = \sqrt{c_a} \sqrt{\lambda \frac{\rho_m h_m}{a}}, \quad (4)$$

Table 1: Material properties of CFRP.

E_L [GPa]	E_T [GPa]	G_{LT} [GPa]	ν_{LT}	ρ [kg/m ³]
142.0	10.8	5.49	0.30	1500

Table 2: Material properties of PZT.

d_{31} [pm/V]	C_p [nF]	E [GPa]	ν	ρ [kg/m ³]	Thickness [mm]
-240	74.3	63.0	0.30	7800	0.25

which can be expressed by using the dynamic pressure q and the Mach number M ($\sqrt{2} < M < 5$). The material density, thickness and length of plate are denoted by ρ_m , h_m and a , respectively. The aerodynamic damping coefficient is denoted by c_a . In case of $\lambda=0$, Eqs. 1 and 2 give the solution of the problem of finding the free vibration frequencies of the panel.

When a modal approach is introduced, the following equation can be obtained by the modal transformation ($W=\Phi W_m$) for Eqs. 1 and 2:

$$\left([\Omega]^2 + \lambda [\Phi]^T [K_a] [\Phi] \right) \{W_{m0}\} = \kappa [I] \{W_{m0}\}, \quad (5)$$

where the matrix with free-vibration eigenvalues on the diagonal and the corresponding modal matrix are denoted by Ω and Φ , respectively. The identity matrix is denoted by I and the amplitude of W_m is denoted by W_{m0} . Then the complex eigenvalues κ for a given dynamic pressure can be evaluated by solving the complex eigenvalue problem given by Eq. 5 as follows:

$$\kappa = \kappa_R + j\kappa_I = -\left(\omega^2 + \frac{g}{\rho_m h_m} \omega \right) = \left(\omega_I^2 - \omega_R^2 - \frac{g}{\rho_m h_m} \omega_R \right) + j \left(-\frac{g}{\rho_m h_m} \omega_I - 2\omega_R \omega_I \right), \quad (6)$$

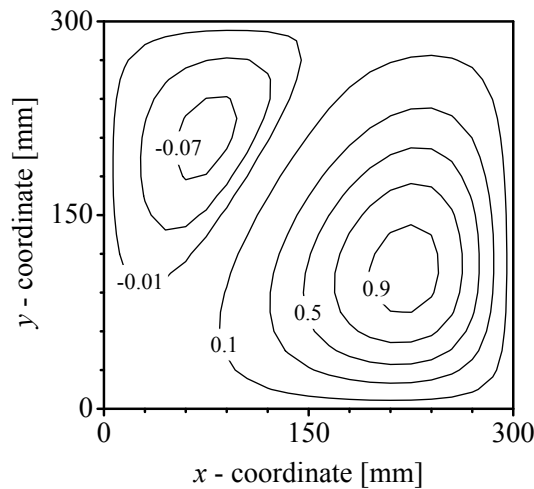
where $\omega = \omega_R + j\omega_I$. Then the stability of the aeroelastic system can be tested by using the obtained κ . The stability criterion can be described as the following inequality equation (Sander et al., 1973):

$$\frac{\kappa_I^2}{\kappa_R} > \left(\frac{g}{\rho_m h_m} \right)^2. \quad (7)$$

In the absence of aerodynamic damping ($g=0$), the flutter occurs when λ approaches a critical value λ_{cr} at which two of the real eigenvalues κ coalesce and become complex conjugate pairs. Here λ_{cr} is the critical flutter dynamic pressure parameter.

2.2 Piezoelectric energy harvesting from supersonic panel flutter oscillation of laminated plates

The aeroelastic flutter energy harvester is composed of a piezoelectric element attached to the structures and a harvesting circuit as shown in Fig. 1(a) and 1(b), respectively. A diode bridge of four diodes is connected to the piezoelectric element and it provides a mechanism of current rectification. The finite element equations for supersonic panel flutter characteristics of simply-supported symmetrically laminated plates with a piezoelectric element can be described as follows:


 Figure 2: Panel flutter mode shape ($\theta_a=0^\circ$).

$$[M_s]\{\ddot{W}(t)\} + g[D_a]\{\dot{W}(t)\} + ([K_{sL}] + [K_{sNL}] + \lambda[K_a])\{W(t)\} - \{\Theta_p\}V_p(t) = \{0\}, \quad (8)$$

$$-\{\Theta_p\}^T\{\dot{W}(t)\} + C_p\dot{V}_p(t) = -i(t), \quad (9)$$

where the mass, linear stiffness and nonlinear stiffness matrices of laminated plates with a piezoelectric element are denoted by M_s , K_{sL} and K_{sNL} , respectively, the effective piezoelectric coefficient vector and capacitance are denoted by Θ_p and C_p , the voltage across the piezoelectric element is denoted by $V_p(t)$ and the current flowing into a harvesting circuit is denoted by $i(t)$, which is related to the rectified voltage $V_r(t)$ by (Shu and Lien, 2006)

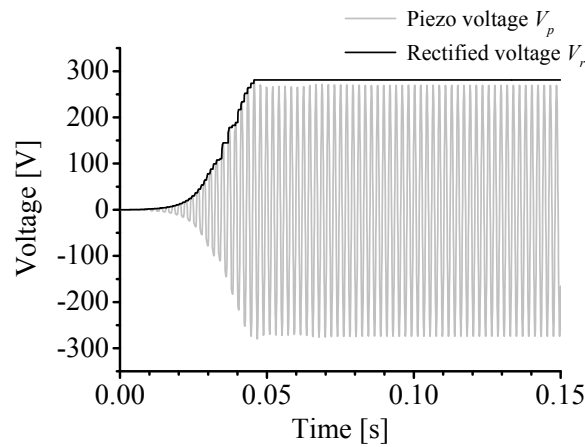
$$i(t) = \begin{cases} C_r\dot{V}_r & \text{if } V_p = V_r \\ -C_r\dot{V}_r & \text{if } V_p = -V_r \\ 0 & \text{if } |V_p| < V_r \end{cases}, \quad (10)$$

where the storage capacitance is denoted by C_r .

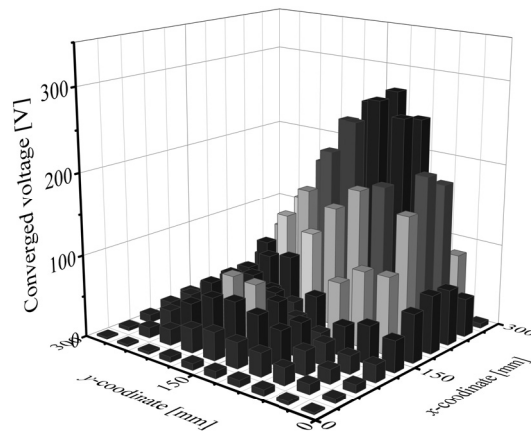
3 Numerical Results and Discussion

3.1 Numerical model

In this research, aeroelastic flutter energy harvesting with a $[0/\pm 45/90]_s$ simply-supported laminated plate is examined. Simply-supported laminated plates with a piezoelectric element shown in Fig. 1(a) are employed, where a ply fiber orientation angle is denoted by θ . Lead zirconate titanate (PZT) element is placed on the lower surface of the plate. The material properties of lamina of carbon/epoxy composite and PZT element are shown in Tabs. 1 and 2. Here the in-plane stiffness and piezoelectric characteristics of piezoelectric material are assumed to be isotropic in this research. The nine-noded isoparametric Mindlin plate element is employed in the present structural analysis based on the Mindlin plate



(a) Time histories of piezoelectric voltage and rectified voltage.



(b) Effect of location of piezoelectric element on converged voltage in harvesting system.

Figure 3: Results of energy harvesting ($\lambda^* = 1.1 \times \lambda_{cr}^*$, $\theta_a = 0^\circ$).

theory for linear analysis or the von Karman plate theory for nonlinear analysis, and 10×10 elements are used for the structural analysis. The sizes of PZT element are the same as that of a finite element in the structural analysis. The aerodynamic damping coefficient c_a in Eq. 4 is set to be 0.01 in this research. A modal reduction is performed using the lowest 30 modes to solve Eq. 5 after the vibration analysis. Newton-Raphson method and Newmark- β method are adopted to solve and numerically integrate the nonlinear equations described as Eqs. 8 and 9. Here the storage capacitor has a capacitance of 1.0 μF in this research.

3.2 Effect of location of piezoelectric element on harvesting performance

Fig. 2 shows the panel flutter mode shape of a $[0/\pm 45/90]_s$ simply-supported laminated plate without piezoelectric elements for $\theta_a = 0^\circ$ obtained by solving Eq. 5. This figure indicates that the supersonic panel flutter due to coupling between the natural vibration mode of $m=1$ and $n=1$ and that of $m=2$ and $n=1$ occurs at $\lambda^* = \lambda_{cr}^* = 287.7$. Here the number of half sine waves in the x and y directions are denoted by m and n , respectively. The dynamic pressure λ is non-

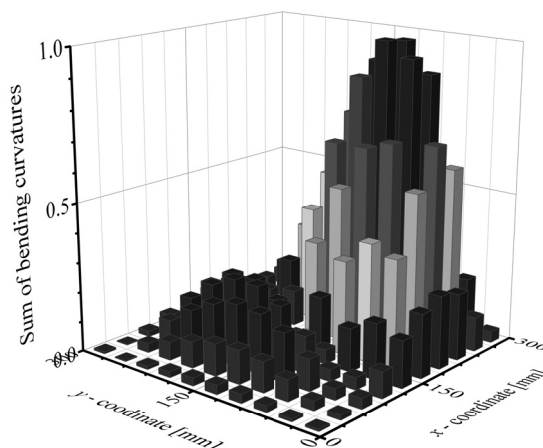


Figure 4: Absolute values of sum of plate bending curvatures ($\theta_a=0^\circ$).

dimensionalized by

$$\lambda^* = \frac{a^3}{D_0} \lambda, \tag{11}$$

where the out-of-plane stiffness D_{11} of a $[0]_s$ unidirectional laminate is denoted by D_0 . Fig. 3 shows the results of energy harvesting at non-dimensional dynamic pressure $\lambda^*=1.1 \times \lambda_{cr}^*$. Here the vibration of the plate is induced by sudden release of $1\mu\text{m}$ initial deflection at the center of the plate. In the case of the location of piezoelectric element shown in Fig. 1(a), the time histories of piezoelectric voltage and rectified voltage are shown in Fig. 3(a). As the aeroelastic vibration continued, the piezoelectric voltage and rectified voltage increased. Then the energy harvesting system reached a steady state and rectified voltage converged. Fig. 3(b) shows the effect of location of piezoelectric element on converged voltage in the harvesting system, which corresponds to the panel flutter curvature mode shape at non-dimensional linear critical dynamic pressure λ_{cr}^* . Here a piezoelectric element is placed on a finite element in the structural analysis. Fig. 4 shows the absolute values of a sum of plate bending curvature at the center of each finite element κ described as the following equation, which is obtained from Fig. 2,

$$F_c(\bar{x}, \bar{y}) = \frac{\partial^2 W_0(\bar{x}, \bar{y})}{\partial \bar{x}^2} + \frac{\partial^2 W_0(\bar{x}, \bar{y})}{\partial \bar{y}^2}, \tag{12}$$

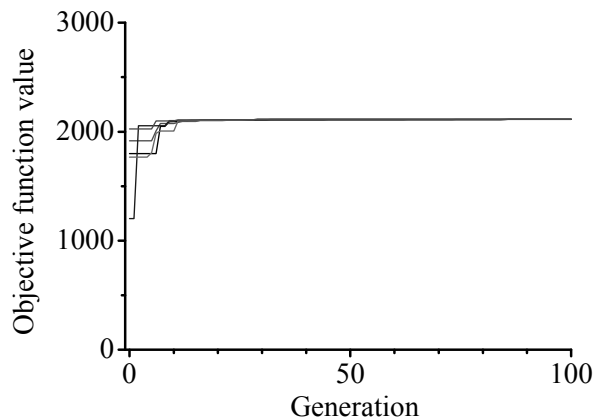
where the directions parallel and normal to the airflow are denoted by \bar{x} and \bar{y} , respectively, as shown in Fig. 1(a). It is indicated that the optimal location of piezoelectric element for energy harvesting can be determined based on the panel flutter curvature mode shape, by comparing with Fig. 3(b).

3.3 Optimal placement of a piezoelectric element

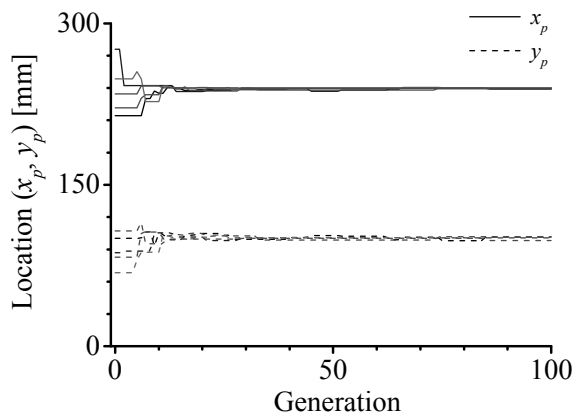
Next, we obtain the location of a piezoelectric element to maximize the harvesting performance in the present system by using numerical optimization techniques. In this research, location of the center of piezoelectric element (x_p, y_p) expresses the location of piezoelectric element. The objective function for optimal placement of a piezoelectric element maximizing harvesting performance can be stated as follows:

Table 3: Optimization results.

Angle of airflow θ_a [deg]	0		45	
Design variables	Continuous	Discrete	Continuous	Discrete
Location (x_p, y_p) [mm]	(239, 98)	(255, 105)	(203,250)	(195,255)
Converged voltage [V]	293.1	281.1	230.3	229.4



(a) Objective function values.



(b) Design variable values.

Figure 5: Convergence histories ($\theta_a=0^\circ$).

$$\max \iint_{S_p} |F_c(\bar{x}, \bar{y})| dS_p = \iint_{S_p} \left| \frac{\partial^2 W_0(\bar{x}, \bar{y})}{\partial \bar{x}^2} + \frac{\partial^2 W_0(\bar{x}, \bar{y})}{\partial \bar{y}^2} \right| dS_p, \tag{13}$$

where the area of piezoelectric element is denoted by S_p . In this research, differential evolution (Storn and Price, 1997) is adopted as an optimization method. DE is one of the stochastic population-based optimization algorithms for solving optimization problems over continuous design space. DE/rand/1/bin is adopted as the strategy for creation of the trial vector, which is the most common DE version. Crossover rate, CR , and scaling factor, F , are set to 0.9 and 0.9, respectively. Here 100 generations were allowed with population sizes of 10. Five trials were run for each DE changing seeds

for random numbers to give different initial populations.

The optimal location of a piezoelectric element obtained from Eq. 13 and the converged voltage in the case of the optimal location are shown for the case of $\theta_a=0^\circ$ and 45° in Tab.3. Being different to the optimal location of a piezoelectric element, it is noted that the optimal location of a piezoelectric element, which is determined by a round-robin calculation for all possible locations of a piezoelectric element placed on a finite element in the structural analysis, is also shown in this table. Fig. 5 shows the convergence histories of the maximum of the objective function values and the parameter values (correspond to the design variable values) of parameter vector with the maximal objective function value for each generation for the case of $\theta_a=0^\circ$. From this figure, it is found that the maximum of the objective function values and parameter values almost converge within 100 generations. These results indicate that the present optimization approach gives out sufficient results.

4 Conclusions

The present paper deals with the piezoelectric energy harvesting from supersonic panel flutter oscillation of simply-supported laminated plates. It is indicated through the numerical examples that the optimal location of piezoelectric element for energy harvesting can be determined based on the panel flutter curvature mode shape of the plate. An optimal placement of a piezoelectric element to maximize the harvesting performance in the present system has also been conducted by using differential evolution in this paper. It is also indicated through the numerical examples that the optimal location of a piezoelectric element can be determined by the proposed optimization method based on the panel flutter curvature mode shape of the plate.

References

- Abdelkefi, A., 2016. Aeroelastic energy harvesting: a review. *International Journal of Engineering Science* 100, 112-135.
- Ashley, H., Zartarian, G., 1956. Piston theory – a new aerodynamic tool for the aeroelastician. *Journal of Aeronautical Science* 23, 1109-1118.
- Isogai, K., Yamasaki, M., Asaoka, T., 2003. Application of CFD to design study of flutter-power-generation. NAL SP-57, 106-111 (in Japanese).
- Kameyama, M., Makihara, K., 2016. Piezoelectric energy harvesting from aeroelastic vibration with composite plate wings. In: *Proceedings of the First International Symposium on Flutter and its Application*, Paper ISFA-5R04, Tokyo, Japan.
- Liao, C. L., Sun, Y. W., 1993. Flutter analysis of stiffened laminated composite plates and shells in supersonic flow. *AIAA Journal* 31, 1897-1905.
- McKinney, W., De Laurier, J., 1981. The wingmill: an oscillating-wing windmill. *Journal of Energy* 5, 109-115.
- Sander, G., Bon, C., Geradin, M., 1973. Finite element analysis of supersonic panel flutter. *International Journal for Numerical Methods in Engineering* 7, 379-394.
- Shu, Y. C., Lien, I. C., 2006. Analysis of power output for piezoelectric energy harvesting systems. *Smart Material and Structures* 15, 1499-1512.
- Storn, R., Price, K., 1997. Differential evolution – a simple and efficient heuristic for global optimization over continuous spaces. *Journal of Global Optimization* 11, 341-359.
- Zhou, R. C., Xue, D. Y., Mei, C., 1994. Finite element time domain – modal formulation for nonlinear flutter of composite panels. *AIAA Journal* 32, 2044-2052.

Numerical analysis of a flapping flat plate for power generation

Chigozie Usuh¹, John Young¹ and Joseph C.S. Lai¹

¹*School of Engineering and IT, The University of New South Wales, Canberra, Australia, j.lai@adfa.edu.au*

Abstract

The power generation performance of a 2D flapping flat plate with prescribed sinusoidal pitching and plunging kinematics in a steady laminar flow at a Reynolds number of 1100 has been investigated using a Navier-Stokes solver. Results indicate a power efficiency as high as 34% for a flat plate with pitch amplitude of 75° , plunge amplitude of 1 chord (c), phase of 90° , a reduced frequency of 0.8, and a tip speed ratio of 0.57 at a pivot location $0.333c$ from the leading edge. This increase in performance of 5.4% over NACA0012 foil has been found to be largely due to the timing of formation and development of the leading edge vortex and its interactions with the trailing edge primarily enhanced by the uniform thickness of the plate. In contrast to NACA foils, doubling the plate's thickness could increase the power generated by close to 3% with negligible effect on the efficiency. Analyses of the effects of the geometry of the leading and trailing edges of the oscillating plate show that a streamlined/semi-circular leading edge and a blunt/rectangular trailing edge only improve the plate's ability to extract energy from the fluid by about 1.1% over the flat plate. Further investigation into selected pivot locations ($0.0c$, $0.1c$, $0.25c$, $0.333c$, $0.5c$, $0.75c$ & $1.0c$ from the leading edge) for the flat plate shows that the plate with a pivot location at $0.25c$ gives about 5.5% and 1.1% increase in the power coefficient (i.e. 0.873 to 0.920) and efficiency (i.e. 34.2% to 34.6%) respectively over the flat plate pivoted at $0.333c$.

Keyword: flapping foil power generator, CFD, leading edge vortex

1 Introduction

Water and wind are major sources of renewable energy. While conventional horizontal axis rotary wind turbines are popular in terms of power and efficiency at tip speed ratios greater than 5, both the turbine size and tip speeds (and hence aerodynamic noise) increase with power and their performance deteriorates significantly at low tip speeds. Flapping foils offer an alternative strategy for power generation from wind or water at low speeds and critical reviews of their performance and future challenges have been provided by Young et al (2014) and Xiao and Zhu (2014). Single flapping foil turbines can achieve an efficiency of 30%-40%, depending on the kinematics, the foil profile, the pivot location and flow conditions (such as uniform/shear flows, steady/unsteady flows, laminar/turbulent flows). The kinematic conditions for best performance fall within the range of the pitch amplitude θ_0 between 60° and 90° , the pivot location X_p between $0.20c$ and $0.75c$, the reduced frequency k between 0.60 and 1.2, when the plunge amplitude h_0 is fixed at $1c$ and the phase difference φ fixed at 90° . These kinematic conditions promote favourable formation and shedding of the leading edge vortices (LEVs), coupling of the motion of the LEVs and the flapping foil, energy recovery from the LEVs, in addition to a good synchronisation between the lift force and plunge velocity, and between the moment and

pitch velocity of the foil (Kinsey and Dumas, 2008; Peng and Zhu, 2009; Ashraf et al., 2011; Zhu, 2011). Most of the studies on the flapping-foil turbine concept used streamlined symmetrical foils (e.g. NACA profile) for power generation. Platzer and Sarigul-Klijin (2009), Platzer and Sarigul-Klijin (2010) and Platzer et al. (2011) investigated the performance of a flapping flat plate passively driven by the fluid flow for power generation. Flat plates were used because it was suspected that the generation of strong vortices from sharp leading edges may enhance the power output with the added advantage of reducing manufacturing complexity, acquisition and operating costs of flapping foil turbines. Preliminary numerical results of Usoh et al. (2012) indicate some improvement in the performance of a flat plate over that of NACA0012 foil.

The objective of this study was to examine the performance and associated physics of a flapping flat plate power generator at a Reynolds number of 1100. The effect of the leading edge (LE) and the trailing edge (TE) on power generation is explored by comparing the performance of a flat plate (blunt/rectangular LE and blunt/rectangular TE with sharp corners as fixed flow separation points) with that of a NACA foil (rounded LE and sharp TE) and a lens foil (sharp LE and sharp TE). As shown in Fig.1, the flat plate and the lens foil have the same chord length (c) and cross-sectional area as the NACA0012 foil.

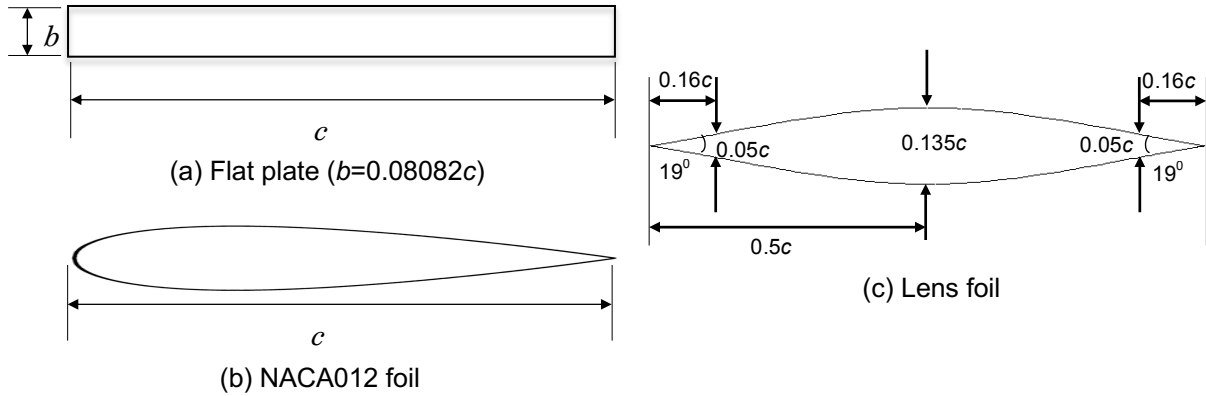


Figure 1: Three tested foils.

2 Numerical Details

2.1 Motion Kinematics & Performance Measures

Each foil in Fig. 1, pivoted at X_p from the leading edge, undergoes prescribed sinusoidal plunging in the lateral (y) direction with a plunge amplitude h_0 and sinusoidal pitching about the spanwise (z) axis with a pitch amplitude θ_0 ; and the plunge motion $y(t)$ leads the pitch motion $\theta(t)$ by a phase difference φ of 90° :

$$y(t) = h_0 \sin(\omega t + \varphi) \quad (1a)$$

$$\theta(t) = \theta_0 \sin(\omega t) \quad (1b)$$

where ω is the circular frequency. The plunge and pitch velocities are given respectively by

$$V_y(t) = \omega h_0 \cos(\omega t + \varphi) \quad (2a)$$

$$\Omega(t) = \omega \theta_0 \cos(\omega t) \quad (2b)$$

The non-dimensional reduced frequency k of the flapping foil is given by

$$k = \frac{\omega c}{U_\infty} = \frac{2\pi f c}{U_\infty} \quad (3)$$

where f is the flapping frequency.

For a flapping-foil turbine undergoing sinusoidal motion, the tip speed ratio (TSR) is related to the root-mean-square of the plunge velocity $V_{y(rms)}$ by

$$TSR = \frac{V_{y(rms)}}{U_\infty} = \frac{V_{y(max)}}{U_\infty\sqrt{2}} \quad (4)$$

where U_∞ is the free-stream velocity.

The total power P generated by a flapping foil turbine consists of two components: P_h due to the plunge motion and P_θ due to the pitch motion as given by

$$P(t) = P_h(t) + P_\theta(t) = [L \cdot V_y](t) + [M \cdot \Omega](t) \quad (5)$$

where L is the lift and M is the moment. The total power coefficient C_p may be expressed as:

$$C_p = \frac{P}{\frac{1}{2}\rho U_\infty^3 s c} = [C_{p(h)} + C_{p(\theta)}](t) = \left[C_L \cdot \frac{V_y}{U_\infty} + C_M \cdot \frac{\Omega \cdot c}{U_\infty} \right](t) \quad (6)$$

where C_L is the lift coefficient, C_M is the moment coefficient, ρ is the density of the fluid and s ($=1$ for 2D calculations) is the span. The efficiency η is the ratio of the mean power P_{mean} extracted to the available power within the swept area

$$\eta = \frac{P_{mean}}{\frac{1}{2}\rho U_\infty^3 d s} = C_p \text{ mean } \frac{c}{d} \quad (7)$$

where d is the overall displacement of the foil, taken as the maximum displacement either from the LE, TE or pivot location of the flapping foil over a flapping cycle:

$$d = \max\{2h_0, 2(h_0 + X_p \sin \theta_0) \text{ or } 2(h_0 - (c - X_p) \sin \theta_0)\} \quad (8)$$

2.2 Unsteady Flow Solver

All the numerical simulations here were undertaken using ANSYS 14 FLUENT CFD commercial software to solve the unsteady incompressible 2D Navier-Stokes equations. The pressure-based solver is used, with the SIMPLE pressure-velocity coupling and Green-Gauss node based gradient. Second-order spatial discretisation is used for the pressure and the momentum. The computational domain consists of an inner circular fluid domain and a square domain both centred at the foil's pivot location X_p . The circular domain is bounded by a sliding interface with a radius of $10c$, while the dimension of each side of the square domain is $70c$. As employed in Kinsey and Dumas (2008) and Ashraf et al. (2011), a source term method is adopted to enable the use of second order time-stepping rather than the default first order implicit method used by the dynamic mesh strategy. Normalised residuals were reduced to a maximum of 10^{-5} for every time step. Grid independence tests were conducted using a coarse grid of 65,000 cells with 450 nodes around the plate, a medium grid of 121,000 cells with 550 nodes around the plate and a fine grid of 190,400 cells with 700 nodes around the plate. Time steps of 500, 2000 and 4000 per cycle were used for the time-step independence study. Results indicate that the medium grid and 2000 time steps per cycle are sufficient for simulations of the flow around the flat plate. Similar tests confirm that it is sufficient to use 2000 time steps per cycle as well as a medium grid of 52,000 cells and 400 nodes around the NACA0012 foil; and 129,000 cells with 600 nodes around the lens foil. The grid and the method used were validated by the results ($C_{p \text{ mean}}=0.860$ and $\eta=33.9\%$) obtained which agree with Kinsey and Dumas (2008) to within 1% for a NACA0015 foil at $X_p=0.333c$, $h_0=1.0c$, $\theta_0=76.33^\circ$, $k=0.88$ and $Re=1100$.

3 Results and Discussions

All the calculations here were made for the kinematics which have been found by Kinsey and Dumas (2008) to be of high power extraction performance for a number of NACA profiles: $X_p = 0.333c$, $h_0 = 1.0c$, $\theta_0 = 75^\circ$, $\varphi = 90^\circ$, $k = 0.80$ and $Re = 1100$. At least 12 flapping cycles were calculated until the ratio of $C_{p\text{ mean}}$ for the current cycle to that of the previous cycle is less than 0.14%.

3.1 Performance of Flat Plate Vs NACA0012 foil and Lens foil

Results of the flat plate show a 5% and 14% improvement in the $C_{p\text{ mean}}$ (0.873) and η (34.2%) over the NACA0012 foil and the lens foil respectively. The physics for this improvement is examined as follows. The instantaneous C_p predicted for the flat plate in Fig. 2(a) is lower than that for NACA0012 foil from $t/T = 0.15$ to $t/T = 0.28$ and from $t/T = 0.65$ to $t/T = 0.78$; but higher from $t/T = 0.30$ to $t/T = 0.45$ and from $t/T = 0.80$ to $t/T = 0.95$. The pitch power in Fig. 2(b) generated for all three foils around $t/T = 0.30$ to $t/T = 0.48$ and from $t/T = 0.80$ to $t/T = 0.98$ is positive because C_M and Ω are synchronised (Fig. 2c). The plunge power (Fig. 2d) for all three foils is positive throughout the cycle because a nearly perfect synchronisation is achieved between C_L and V_y (Fig. 2e). The differences in the power generated by the three foils are due to the differences in the magnitude of the moment and lift produced. For example, around $t/T = 0.42$ and $t/T = 0.92$ in Fig. 2 (c) and (e), C_M and C_L produced by the flat plate are larger in magnitude than that of the NACA0012 foil and the lens foil, resulting in higher positive pitch and plunge power at these instants (Fig. 2b and Fig. 2d). A similar level of performance is also observed for the NACA0012 foil around $t/T = 0.20$ and $t/T = 0.70$ in Fig. 2(e). To determine the cause of the high and low moment and lift magnitudes produced by the three foils at certain instants in the flapping cycle, the vorticity fields (z-vorticity normalised by U_∞ / c) and pressure distributions are shown in Figures 3 and 4 respectively at $t/T = 0.20$ and $t/T = 0.42$.

At $t/T = 0.20$ in Fig. 3(a), where the foils are pitching in the counter-clockwise direction and plunging downwards, the sharp leading edges of the flat plate and the lens foil respectively cause the flow to separate earlier than the NACA0012 foil resulting in earlier development of and stronger leading edge vortices (LEVs). Vortex formation creates a suction effect due to low pressure on the occurring surface (i.e. either on the upper or lower surface) during the upward/clockwise or downward/counter-clockwise motion of the foil. Hence, timing the evolution of the LEVs is considered vital in achieving a better synchronisation between the velocities and their respective forces (Kinsey and Dumas, 2008; Ashraf et al., 2011; and Xiao et al., 2011). The attachment of the flow to the lower surface of the NACA0012 foil reduces the pressure at the LE compared with that of the flat plate and lens foil (Fig. 3b), thus producing higher pressure gradient and force in the y -direction (Fig. 2e). It is a similar case at $t/T = 0.70$, however the LEVs are formed on the upper surface of the three foils while the force in the y -direction is positive (that is lift force).

Around $t/T = 0.35$ to $t/T = 0.45$ during the clockwise (pitch) and downward (plunge) motion of the three foils (just before the mid-cycle, when the LEV has fully developed and is about to be shed), the C_p of the flat plate (Fig. 2a) is highest followed by that of the NACA0012 foil and then the lens foil. This is the result of the gap between the LEV (around the TE) and the surface of the NACA0012 foil, lens foil and flat plate; while Fig. 4(a) shows that the larger the gap between the LEV and the foil at the TE, the smaller the power generated in this period. For the three foils, there is a higher pressure gradient in the y -direction near the TE than near the LE (Fig. 4b) as a result of the larger LEV around the

TE (Fig. 4a). This enhances the moment and the pitch motion in the clockwise direction (from $t/T = 0.35$ to $t/T = 0.45$ in Fig. 2c), causing a rapid rise in the amount of positive pitch power generated by the foils ($t/T = 0.35$ to $t/T = 0.45$ in Fig. 2b).

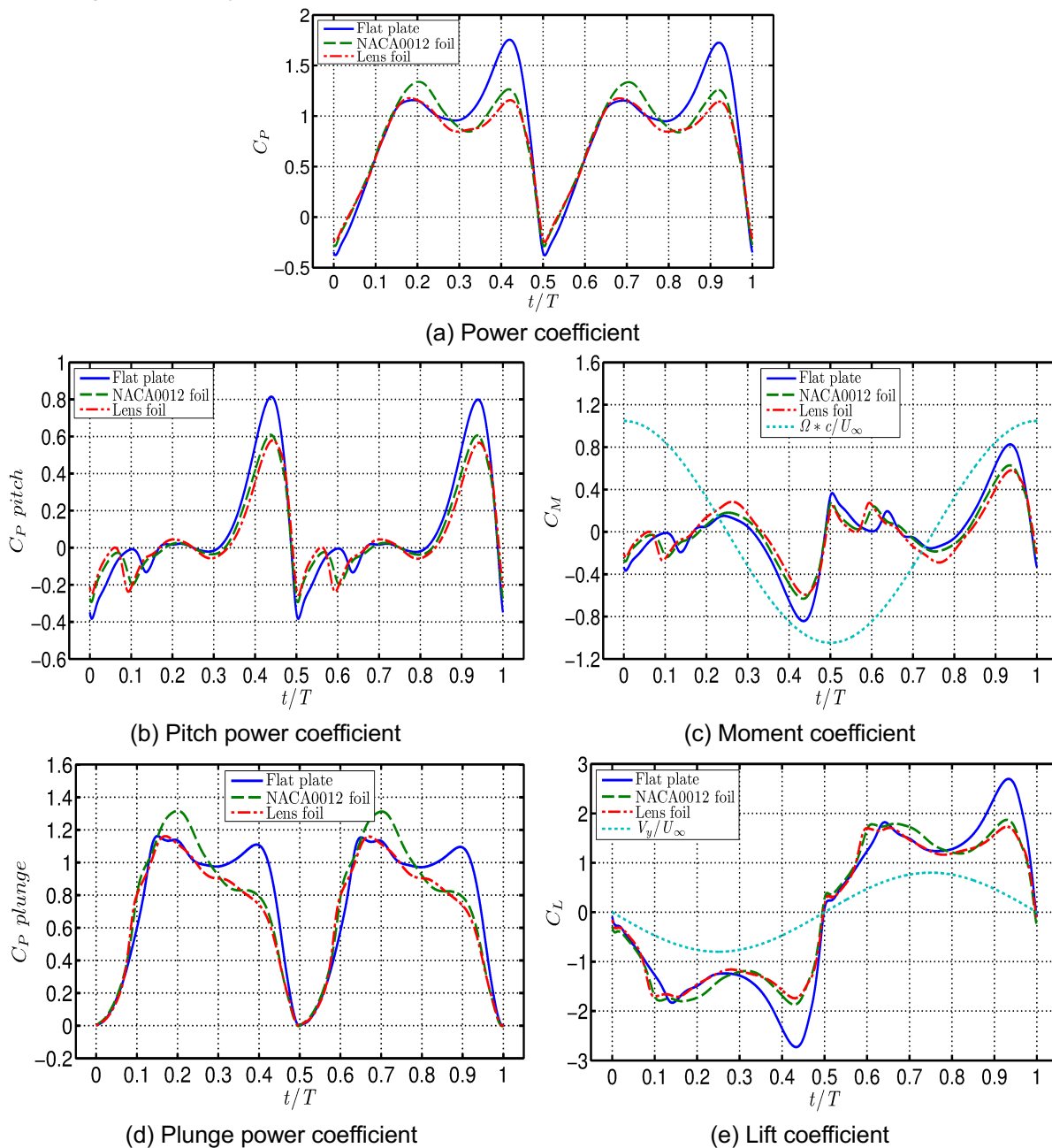


Figure 2: Comparisons of the power, moment and lift coefficients for the three foils.

Fig. 2(b) shows that for the NACA0012 foil and lens foil, positive pitch power occurs only from $t/T = 0.35$ to $t/T = 0.48$ and from $t/T = 0.85$ to $t/T = 0.95$; and this contributes significantly to the overall power output of the turbine during these times (Fig. 2a). On the other hand, the plunge power (Fig. 2d) of the flat plate is high and remains fairly constant from $t/T = 0.25$ to $t/T = 0.40$ and from $t/T = 0.75$ to $t/T = 0.90$; while that for the NACA0012 foil and lens foil decreases quite rapidly with time. This is because for the flat plate from $t/T = 0.25$ to $t/T = 0.40$, the negative plunge velocity decreases (Fig. 2e) while the negative lift force increases with time resulting in a nearly constant plunge power extracted during this period. In contrast, for the NACA0012 foil and lens foil, the increase in the negative lift force with time is much smaller than that for the flat plate, thus resulting in the reduction of the

plunge power during this period. As shown in Fig. 4(a), the nucleus of the larger LEV is closer to the TE for the flat plate than for the NACA0012 foil and the lens foil because of the uniform thickness of the flat plate. Hence, the lift force has a larger magnitude for the flat plate than the NACA0012 foil and the lens foil (Fig. 2e) and Fig. 4b).

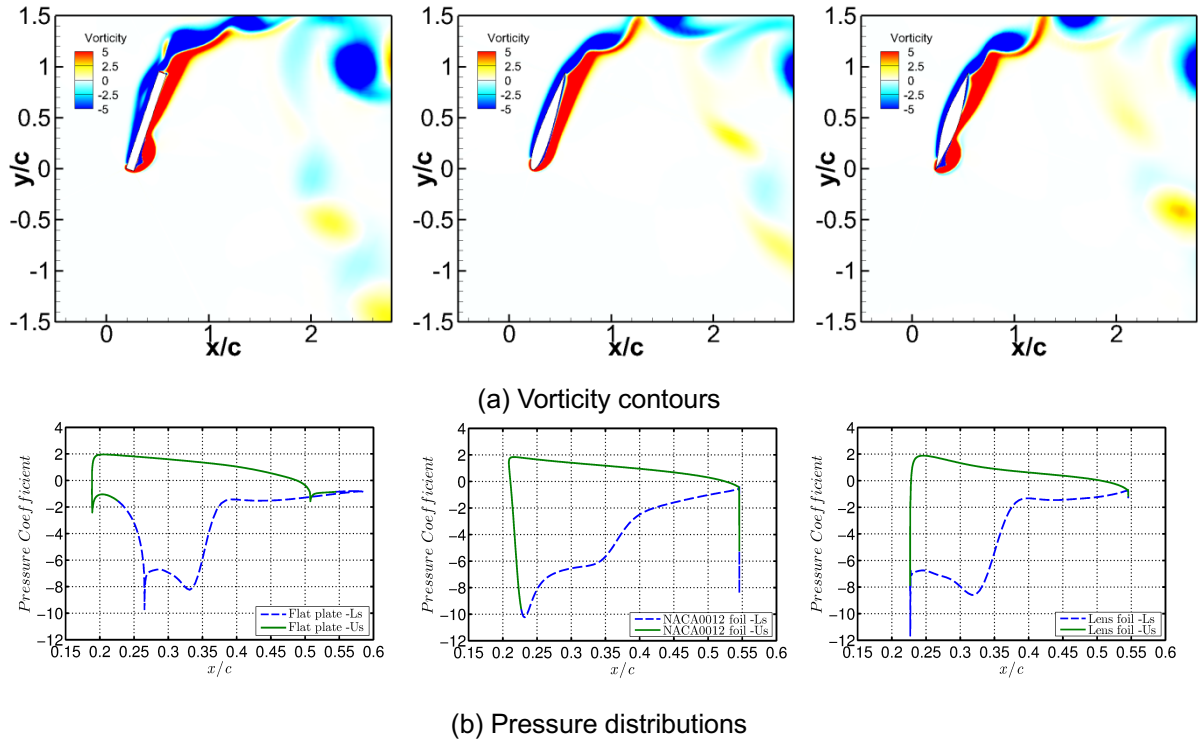


Figure 3: Vorticity contours and pressure distributions for the flat plate (left), NACA foil (middle) and lens foil (right) at $t/T=0.20$.

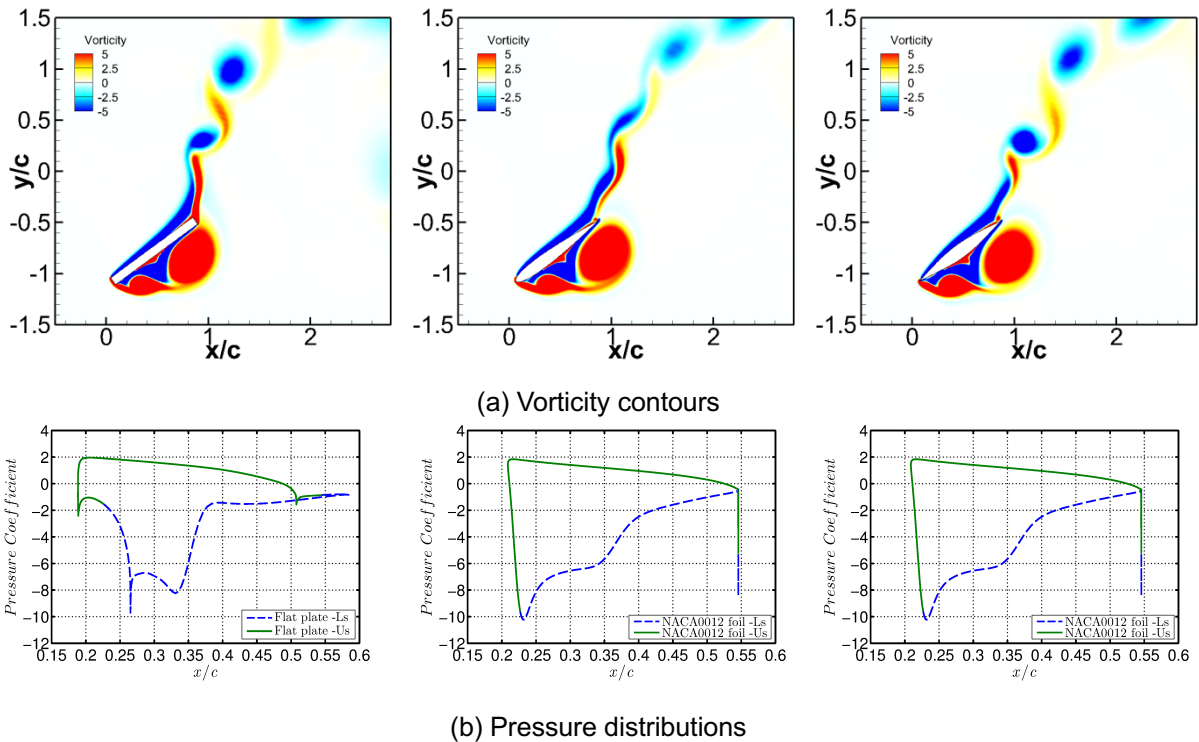
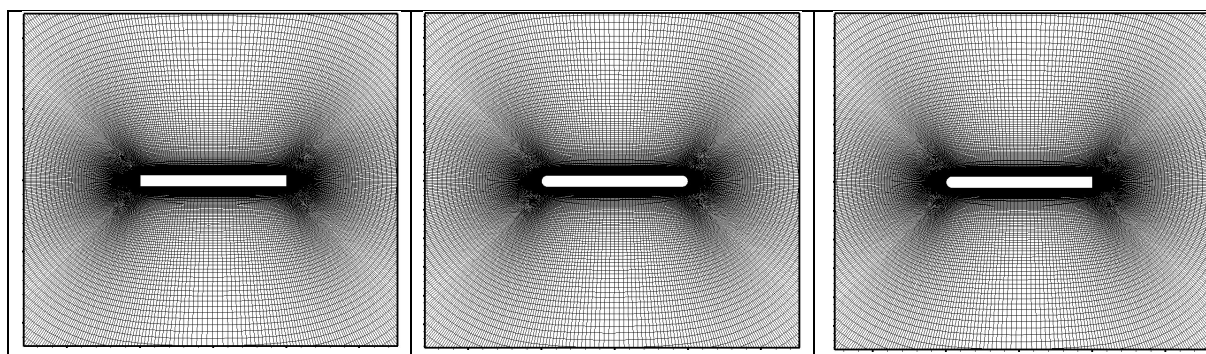


Figure 4: Vorticity contours and pressure distributions for the flat plate (left), NACA foil (middle) and lens foil (right) at $t/T=0.42$.

With regard to the effect of the LE geometry on the performance, the NACA0012 foil with rounded LE has the best performance (Fig. 2a) from $t/T = 0$ to $t/T = 0.28$ and from $t/T = 0.50$ to $t/T = 0.78$ during the formation of the LEV. Figure 3(a) at $t/T = 0.2$ shows that the flow over the surface of NACA0012 foil remains attached over a larger portion of its surface compared to the flat plate and the lens foil; reflecting the effects of a better timed flow separation and formation of LEVs. Consequently, this causes a smooth pressure drop at $x/c = 0.21$ (Fig. 3b) followed by a smooth increase along the chord length ($x/c = 0.22$ to $x/c = 0.53$) resulting in higher plunge power (Fig. 2d) compared to the flat plate and the lens foil. On the other hand, the sharp corners at the LE of the flat plate and the sharp LE of the lens foil (Fig. 3a) force a sharp and an early flow separation on the surfaces. Although the NACA0012 foil with a rounded LE produces a better performance than the lens foil and the flat plate (from $t/T = 0$ to $t/T = 0.28$ and from $t/T = 0.50$ to $t/T = 0.78$), the nature of interaction of the LEVs with the surface of the foil from the pivot location X_p to the TE also plays a significant role in the overall performance of the flapping-foil turbine. Further analysis of the vorticity contours at $t/T = 0.42$ in Fig. 4a reveal that the larger LEV of the lens foil is shed earlier, followed by the NACA0012 foil and then the flat plate. The low performance and similarity of the NACA0012 foil and the lens foil (Fig. 2a) from $t/T = 0.30$ to $t/T = 0.50$ and from $t/T = 0.80$ to $t/T = 1.0$ are due to the reduction of the thickness from the mid-chord and/or the pivot area to the TE. This causes the LEV shed in the previous cycle to convect further away from the wing surface near the TE, resulting in higher pressure on their lower surfaces. Thus the uniform thickness aft of the mid-chord and/or pivot area is beneficial for power generation.

These results of the flat plate, NACA0012 foil and the lens foil suggest that the geometry of the foil affects not only the formation, development and shedding of the LEV but also the duration for the attachment of the LEVs to the wing. Thus rounding the LE of the flat plate may enhance the turbine's performance at the early stages of the LEV development; while a uniform foil thickness along the chord length enhances its performance in the later stage of the evolution and shedding of the LEV.



(a) Rectangular LE and TE (b) Semicircular LE and TE (c) Semicircular LE and rect. TE
Figure 6 Grid details of three different plates.

3.2 Effect of the Leading and Trailing Edge Geometry

As a profiled LE and a uniform thickness have been identified as beneficial in flapping foil power generation, simulations were conducted for three plates with the same thickness over at least 90% of the chord length with rectangular LE and TE (Fig. 6a), semi-circular LE and TE (Fig. 6b) and semi-circular LE and rectangular TE (Fig. 6c). Note here that the semi-circular LE and/or TE have radius $0.5b$. Results in Fig. 7 show that a plate with a

semi-circular LE and a rectangular TE has the best overall performance for power generation. A semi-circular or rounded LE enhances the performance but profiling the TE (semi-circular or rounded TE) has a detrimental effect on the overall performance. Although there is an overall improvement of about 1% in the performance for the plate with semi-circular LE and rectangular TE over the flat plate, such increase is insignificant and may not justify the increase in manufacturing costs.

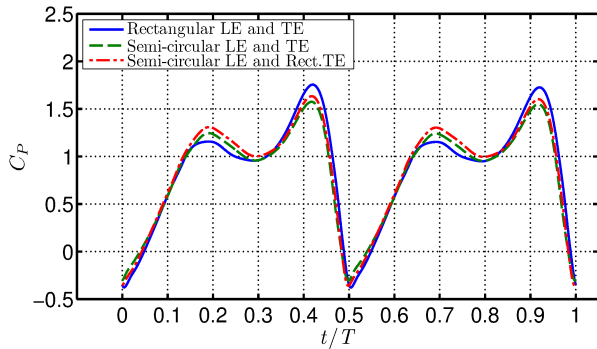


Figure 7: Effects of LE and TE on C_p .

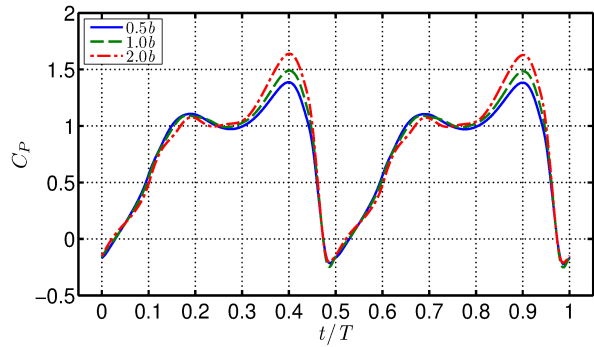


Figure 8: Effect of thickness on C_p .

Table 1: Effect of thickness on flat plate's performance.

Kinematic conditions	Thickness	C_p mean	η (%)
$k = 0.85$ and $\theta_o = 78^\circ$	$0.5b$	0.866	33.6
	$1b$	0.870	33.8
	$2b$	0.880	34.1
$k = 0.90$ and $\theta_o = 75^\circ$	$0.5b$	0.850	33.4
	$1b$	0.862	33.8
	$2b$	0.862	33.8
$k = 0.70$ and $\theta_o = 70^\circ$	$0.5b$	0.790	31.6
	$1b$	0.811	32.4
	$2b$	0.833	33.3

3.3 Effect of thickness

The flat plate's thickness b is increased by 100% (that is $2b$) and reduced by 50% (that is $0.5b$) while keeping the chord length constant. The grid density is maintained with the three different thicknesses. While the results for three different kinematic conditions in Table 1 and Fig. 8 show that the efficiency increases insignificantly with thickness, the power could increase by close to 3% per doubling of the thickness, depending on the kinematics. This is in contrast to the study of Kinsey and Dumas (2008) who found that the effect of thickness on the performance of a flapping foil turbine is weak by comparing NACA0002, NACA0020 and NACA0015 foils. The benefit of increase in power due to increase in thickness has to be considered together with the increase in material cost.

3.4 Effect of Pivot Location

The pivot location is another geometric parameter with a significant influence on the performance of flapping-foil turbines. A number of studies in the flapping-foil turbine concept have reported different pivot locations as best for the turbine's performance. This variation may be due to the differences in the kinematics (sinusoidal/non-sinusoidal motion and prescribed/passive motion) used. In order to establish the best pivot location for the flat plate, numerical simulations were conducted for pivot locations of $0.0c$, $0.1c$, $0.25c$, $0.333c$, $0.5c$, $0.75c$ and $1.0c$ from the LE. Figure 9 reveals that the optimal pivot location for $C_{p\text{ mean}}$ and η is at $X_p = 0.25c$ which provides more than 5% improvement in $C_{p\text{ mean}}$ and just over 1% in η than at $X_p = 0.333c$. It must be pointed out that this pivot location is also dependent on the kinematics and an optimal performance cannot be obtained without optimising all the relevant kinematic parameters.

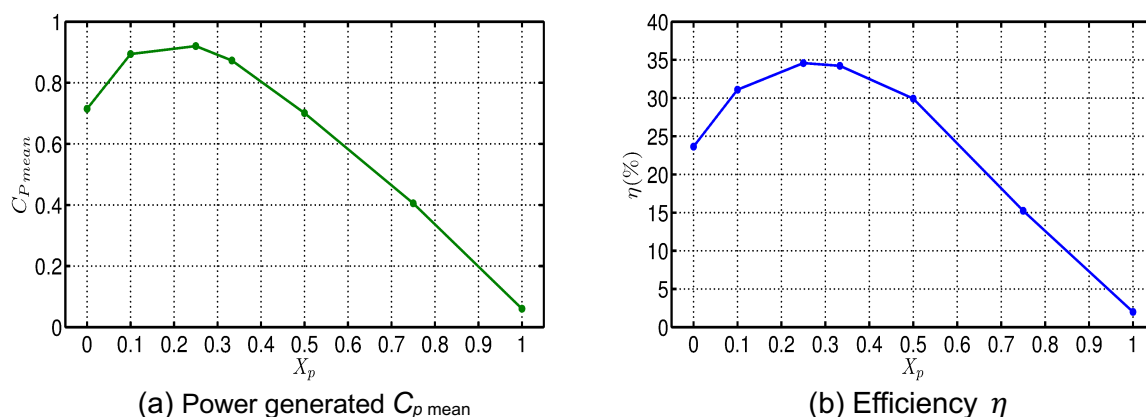


Figure 9: Variation of $C_{p\text{ mean}}$ and η with pivot location.

4 Conclusions

A 2D numerical study has been conducted using a commercial Navier-Stokes solver on a flapping flat plate in a laminar incompressible flow at a Reynolds number of 1100. The flat plate initially pivoted at $0.333c$ from the leading edge undergoes sinusoidal motion in both the pitch and the plunge directions. For $h_0 = 1c$, $\varphi = 90^\circ$, θ_0 of about 75° , and k of 0.80 and $Re = 1100$ (that is a tip speed ratio TSR of about 0.57), it achieves a maximum power generation $C_{p\text{ mean}}$ and power efficiency η of more than 0.87 and 34% respectively, about 5% and 14% higher than that of a NACA0012 foil and a lens foil respectively. This improved performance of the flat plate is primarily due to its uniform thickness enabling the LEVs to remain close to the surface especially aft of the mid-chord. Accordingly, this makes the flat plate an attractive option as a flapping foil turbine compared to profiled plates because it is simpler to manufacture (hence lower costs) with higher energy harvesting capability.

Results of the geometry of the LE and the trailing edge TE of a flapping flat plate in a laminar flow regime indicate that a combination of a semi-circular LE and a rectangular TE gives the best performance compared with rectangular/sharp LE and a semi-circular/sharp TE. This is because a rectangular/sharp LE causes early and/or ill-timed flow separation and detachment of the LEVs from the surface of the flapping flat plate. On the other hand, a rectangular TE with sharp corners (hence uniform thickness) enables the vortices to stay close to the surface enabling better power generation. The lens foil's performance is poor due to the combination of the negative effects of the sharp LE and TE on the evolution of the LEV.

The effect of the thickness of the flat plate on the power generated in the laminar flow

condition has been found to be sensitive to the kinematics and $C_{p\text{ mean}}$ could increase by close to 3% when the thickness was doubled.

The pivot location has been found to significantly affect the timing of the formation and evolution of the LEVs and subsequently the power generated by the flapping-foil turbine. A flapping flat plate pivoted at $0.25c$ from the LE achieves the best performance with $C_{p\text{ mean}} = 0.92$ and $\eta = 34.60\%$, resulting in an improvement of about 5% in the power generated $C_{p\text{ mean}}$ over that pivoted at $0.333c$ from the LE with a marginally better power efficiency. The location of the larger LEV which is closer to the TE when the flat plate is pivoted at $0.25c$ has enhanced the pitching moment at these times (from $t/T = 0.30$ to $t/T = 0.40$ and from $t/T = 0.80$ to $t/T = 0.90$).

Acknowledgements

This research was undertaken with the assistance of resources provided at the NCI National Facility systems at the Australian National University through the National Computational Merit Allocation Scheme supported by the Australian Government. The first author (Usoh, C.O.) acknowledges receipt of a University College Postgraduate Research Scholarship during the course of this study.

References

- Ashraf, M. A., Young, J., Lai, J. C. S. and Platzer, M. F. 2011. Numerical Analysis of an Oscillating-Wing Wind and Hydropower Generator. *AIAA Journal* 49 (7): 1374-1386.
- Kinsey, T. and Dumas, G. 2008. Parametric Study of an Oscillating Airfoil in a Power-Extraction Regime. *AIAA Journal* 46 (6): 1318-1330.
- Peng, Z. and Zhu, Q. 2009. Energy harvesting through flow-induced oscillations of a foil. *Physics of Fluids* 21 (12): 123602-123601 to 123609.
- Platzer, M. F. and Sarigul-Klijn, N. 2009. A Novel Approach to Extract Power from Free-Flowing Water and High-Altitude Jet Streams. ASME Energy Sustainability Conference San Francisco, California. USA.
- Platzer, M. F. and Sarigul-Klijn, N. 2010. A New Oscillating-Foil Power Generation for Sailingship-Based Renewable Energy Generation ASME Energy Sustainability Conference. Phoenix, Arizona. USA. .
- Platzer, M. F., Sarigul-Klijn, N., Young, J., Ashraf, M. A. and Lai, J. C. S. 2011. Renewable Hydrogen Production Using Sailing Ships. ASME IMECE2011 Conference., 11th to 17th November Denver, Colorado. USA.
- Usoh, C. O., Young, J., Lai, J. C. S. and Ashraf, M. A. 2012. Numerical Analysis of a Non-profiled Plate for Flapping Wing Turbines. Proceedings of the 18th Australasian Fluid Mechanics Conference AFMC., 3 - 7 December. Launceston, Australia.
- Xiao, Q., Liao, W., Yang, S. and Peng, Y. 2011. How motion trajectory affects energy extraction performance of a biomimic energy generator with an oscillating foil? *Renewable Energy* 37 (1): 61-75.
- Xiao, Q. and Zhu, Q., 2014 A review on flow energy harvesters based on flapping foils. *Journal of Fluids and Structures*, 46, 174-191.
- Young, J., Lai, J.C.S. and Platzer, M.F., 2014 A review of progress and challenges in flapping foil power generation.
- Zhu, Q. 2011. Optimal Frequency for Flow Energy Harvesting of a Flapping Foil. *Journal of Fluid Mechanics*. 675: 464 - 517.

Aero-elastic oscillations of circle cylinder with power takeoff

Peter R. Andronov, Sergey V. Guvernyuk, Galina Ya. Dynnikova

¹ M. V. Lomonosov Moscow State University, Research Institute of Mechanics, Michurinskii pr. 1, Moscow, 119192, Russia, e-mail: dyngy@mail.ru

Keyword: oscillations of circle cylinder, power takeoff, flow-structure interaction

Possibility of power takeoff from bodies performing resonant aero-elastic vibrations¹ is of great interest. The problem of transverse self-oscillations of circular cylinders with viscoelastic bonds in an unlimited flow of a viscous incompressible fluid is investigated. The task is solved in a complete conjugate formulation. The meshless non-iterative method was used for solving the problem². A fluid and a moving solid are described as a single dynamic system without splitting into successive dynamic and hydrodynamic stages. The motion of a fluid is modeled using two-dimensional Navier-Stokes equations with no-slip boundary conditions on the bodies surface. In fig.1(a) the time-dependence of cylinder center $y_c(t)$ is shown. The function $y_c(t)$ satisfies an equation of the form $m\ddot{y}_c(t) + c\dot{y}_c(t) + ky_c(t) = F_y(t)$, where the transverse hydrodynamic force F_y is determined via integral expressions depending on $y_c(t)$, non-zero component of vorticity and flow of vorticity from the bodies surface³. As a result the undamped self-oscillations of a cylinder in a flow have been reproduced. The mechanism of self-supporting of the auto-oscillations is identified and described in details. The comparison with the available data from other works¹ was made, that confirms suitability of the developed technology. It was found that when the natural frequency of the cylinder oscillations approaches the hydrodynamic frequency of the Karman street, a resonant increase in the amplitude of self-oscillations occurs (see the Fig.1(a); where $Sh=0.199$). Power takeoff dependence on the friction coefficient c and on the stiffness coefficient k is investigated.

This work has been supported by the Russian Foundation for Basic Research (project 18-31-20057).

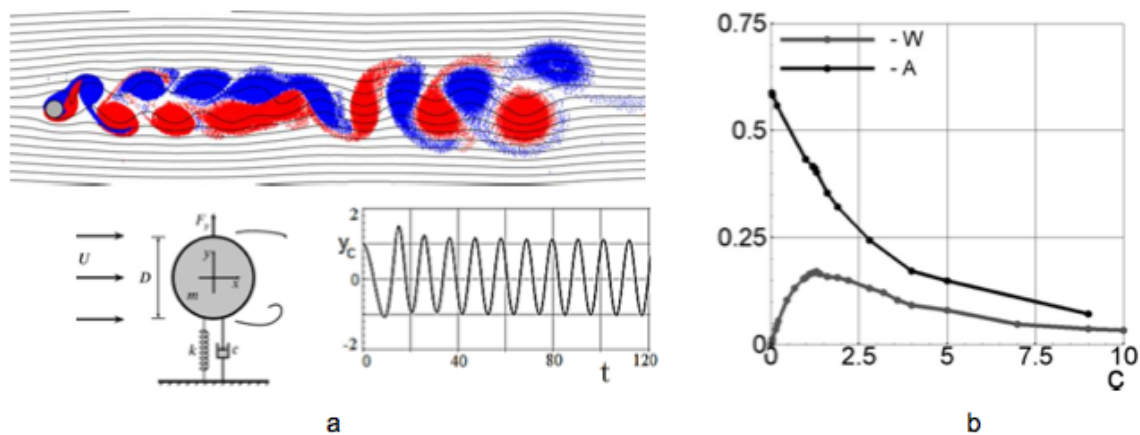


Figure.1. Vortex pattern around oscillating circular cylinder at $k = 13.6$, $c = 1.3$, $Re = 200$ (a). Averaged power takeoff and averaged amplitude dependences on the coefficient c at $\rho = 10$, $k = 13.6$ and $Re = 200$ (b).

¹ Atul Kumar Soti et al. (2018). Damping effects on vortex-induced vibration of a circular cylinder and implications for power extraction. J. Fluid Struct, 81, 289-308.

² P.R. Andronov, Y.A. Dynnikov, G.Ya. Dynnikova, S.V. Guvernyuk. (2019). Flow-induced oscillations of circular cylinder in a narrow channel. Aerospace Science and Technology, 93, No 105348.

³ G.Ya. Dynnikova, P.R. Andronov. (2018). Expressions of force and moment exerted on a body in a viscous flow via the flux of vorticity generated on its surface. European Journal of Mechanics, B/Fluids, 72, 293-300.

Performance of Wind Vibrational Power Generator by Flow-Induced Vibration of a Prism and Magnetostrictive Material

Ryohei NAGASE¹, Takahiro KIWATA², Takaaki KONO² and Toshiyuki UENO³

¹Graduate School of Natural Science and Technology, Kanazawa University,
nagase@ryuko.ms.t.kanazawa-u.ac.jp

²School of Mechanical Engineering, Kanazawa University

³School of Electrical and Computer Engineering, Kanazawa University

Keyword: Flow-induced Vibration, Wind, Energy Harvesting, Vibration-power Generator, Low-speed Galloping

Energy harvesting technology from ambient vibrations has been in the spotlight because of the development of low power consumption sensors and the wireless communication system like IoT (Internet of Things) devices [1]. The vibration-power generator combined flow-induced vibration by wind power with the magnetostrictive material, i.e. iron-gallium alloy, is developed by authors as shown in Fig. 1. It can generate electrical energy from low wind velocity of 1 m/s. The vibration-power generator is composed of “wind-receiving unit” and “power-generating unit”. The wind-receiving unit vibrates transversely against wind direction [2]. The purpose of the present study is to investigate the most suitable cross section of a cantilevered prism for transverse galloping and the performance of a wind power generator using the iron-gallium alloy as a magnetostrictive material.

The experiments were performed in a wind tunnel with a rectangular working section having a height of 1200 mm, a width of 300 mm, and a length of 2000 mm. The wind velocity U of this experiment was varied from 2.1 to 7.3m/s. Figure 2 shows the variation of the power of vibration-power generator with the reduced velocity $V_r (=U/f_c \cdot H; f_c, \text{Characteristic frequency of a prism}(=15.8\text{Hz}); H, \text{Height of a prism}(=30\text{ mm}))$ for a V-section prism. The peak power was 1.06 mW at $V_r = 8.65$. This peak power generation is enough to run a wireless sensor.

1. Ueno, T., Yamada, S., (2011), Performance of Energy Harvester Using Iron-Gallium Alloy in Free Vibration, IEEE Transactions on Magnetics, 47, 2407-2409
2. Kiwata, T., Yamaguchi, M., Kono, T., and Ueno, T., (2014), Water Tunnel Experiments on Transverse-galloping of Cantilevered Rectangular and D-section prisms, Journal of Fluid Science and Technology, 9, ,1-11.

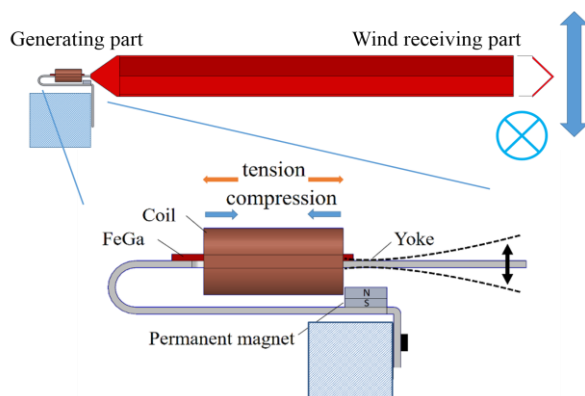


Fig.1 Vibration-power generator combined flow-induced vibration by wind power with the magnetostrictive material

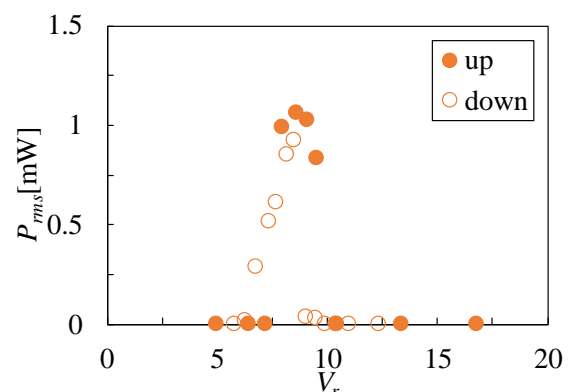


Fig.2 Variation of power with reduced velocity

Parameterised reduced order modelling of flutter-induced piezoelectric energy harvesters

C. Hoareau, L. Shang and A. Zilian

*Institute of Computational Engineering, FSTC, University of Luxembourg , Luxembourg,
christophe.hoareau@uni.lu*

Keyword: Energy harvesting, Reduced order model, Fluid-structure interaction, Limit cycle oscillations

The contribution discusses the reduced order modelling of flutter-induced piezoelectric energy harvesters. The prediction of ambient fluid flow energy conversion into electrical energy is still an area of research for the design of efficient autonomous piezo-ceramic power generators¹. In this specific context, one has to take into account the interaction between an immersed geometrically nonlinear elastic electro-mechanical structure and a subsonic incompressible fluid flow. A first challenge is to model and predict the nonlinear dynamic behavior in space and time of the multiphysics system². A second challenge is to quantify the sensitivity of the overall system under changing conditions (e.g. varying mean flow input velocity). A third challenge is to allow just-in-time feedback control to maximize the power output while minimizing exposure to fatigue. Generating a multi-parametric reduced basis, in order to reconstruct on-line approximations, becomes a relevant response to those three challenges.

We will expose several options for parameterised hypothesis-driven models of the multiphysics system at various complexity levels³ (bottom-up): from linear to geometrically nonlinear electro-mechanical models for the structure and from linear potential flows to nonlinear Navier-Stokes equations for the fluid. Those models will be discussed and in particular, the need to take into account large deformations to accurately capture Limit-Cycle Oscillations. Then, generic Model Order Reduction⁴ (top-down) based on in-silico generated data from fully nonlinear monolithic finite element - ALE (Arbitrary Euler Lagrange) simulations will be presented, compared and analyzed in terms of time/memory consumption and accuracy.

¹ De Marqui Jr, C., Tan, D., & Erturk, A. (2018). On the electrode segmentation for piezoelectric energy harvesting from nonlinear limit cycle oscillations in axial flow. *Journal of Fluids and Structures*, 82, 492–504.

² Ravi, S., & Zilian, A. (2017). Time and frequency domain analysis of piezoelectric energy harvesters by monolithic finite element modeling. *International Journal for Numerical Methods in Engineering*, 112(12), 1828–1847.

³ Hoareau, C., Deü, J.-F. & Ohayon, R. (2019). Prestressed Vibrations of Partially Filled Tanks Containing a Free-Surface Fluid: Finite Element and Reduced Order Models. *Proceedings of the VIII International Conference on Coupled Problems in Science and Engineering, COUPLED 2019, Barcelona, Spain, June*

⁴ Berkooz, G., Holmes, P., & Lumley, J. L. (1993). The proper orthogonal decomposition in the analysis of turbulent flows. *Annual review of fluid mechanics*, 25(1), 539-575.

Control and mitigation

Control of vortex-induced vibration of a single bridge girder by using active wake slit jets

Guan-Bin Chen^{1,2}, Wen-Li Chen^{1,2} and Dong-Lai Gao^{1,2}

¹ *Key Lab of Smart Prevention and Mitigation of Civil Engineering Disasters of the Ministry of Industry and Information Technology, Harbin Institute of Technology, Harbin, 150090 China. first-author-email:cgb2020@163.com*

² *Key Lab of Structures Dynamic Behavior and Control of the Ministry of Education, Harbin Institute of Technology, Harbin, 150090 China*

Keyword: a single bridge girder, periodic vortex shedding, vortex induced vibrations, topological structure

Flow past a single bridge girder is omnipresent in engineering applications. When incoming flow reaches a certain value, a single bridge girder is characterized by flow separation and periodic vortex shedding into the wake nearing to girder. When the frequency of vortex shedding behind girder closes to or equals to the girder's natural frequency, vortex induced vibrations might take place and will result in fatigue failure to the bridge girder. Nowadays, the span of girder is longer than that before that make its damping and stiffness is weaker. Therefore, effective control methods are desired to alleviate the periodic vortex shedding and suppress vortex-induced vibration (VIV) of a single bridge girder. In the study, an active control measure, whose feature is that the jet flow blows out from the slit setting on the leeward side of a single bridge girder was experimentally investigated to suppress the amplitude of VIV. Apart from measuring response of test girder, a particle image velocimetry (PIV) system was also applied to quantify the wake flow characteristics in order to obtain the control mechanism of the proposed active control method. It was found that the active wake slit jets implementation was very effective in alleviating the amplitude of VIV that illustrates it can suppress fluctuating amplitude of the dynamic wind loads acting on the test model. The wake flow field measured by PIV system revealed that the topological structure of wake vortex was changed with and without active wake slit jets. Due to the dynamic interactions between the jet flow and the periodic wake vortex, the size, distance of vortex, strength of vortex shedding and the vortex shedding mode was changed, which acted as the underlying mechanism of the active flow control. As a result, the periodic vortex shedding behind a single bridge girder was alleviated and the amplitude of VIV was enough attenuated.

Investigating Amplitude Death as a Possible Flutter Suppression Mechanism in a Pitch-Plunge Aeroelastic System

Ashwad Raaj Paramasivam^{1*}, Sirshendu Mondal² and J.Venkatramani¹

¹ Shiv Nadar University, Greater Noida, India. ^{1*} corresponding author ar747@snu.edu.in

² National Institute of Technology, Durgapur, India.

Keywords: Amplitude death, Flutter suppression, Nonlinear aeroelasticity.

Flutter is a dynamical phenomenon, wherein at a critical flow speed, there is a continuous extraction of energy from the flow to the structure¹, and in turn posing a threat to the integrity of the structure. Hence, deploying suppression mechanisms to combat flutter has been an important topic of research in the aeroelastic community. One such mechanism involving active controllers is called targeted energy transfer, where energy sinks are used to absorb the energy from the oscillating airfoil. The scope of the study was restricted to a unidirectional energy flow (from the airfoil to the energy sink). However, suppressing flutter using a bidirectional energy transfer has so far not been explored in literature. Studies in the nonlinear dynamics literature have shown that a coupled system can exhibit stationary dynamics, whose dynamics are otherwise non-stationary in the uncoupled state, and this phenomenon was termed as amplitude death (AD). Using AD as a measure to mitigate oscillatory or dynamic instabilities in engineering systems has been investigated recently. Deriving impetus from the same, we explore the potential of AD as a flutter suppression mechanism in aeroelastic systems. To that end, we consider two identical pitch-plunge airfoils, which are subjected to uniform flow conditions. The airfoils are coupled using a spring-viscous damper system only at the flutter regime. The coupled interactions of the airfoils are then analysed by obtaining the pitch and plunge responses. Further, the strength and the nature of the coupling between the airfoils are systematically varied to investigate its effect on the regime of AD.

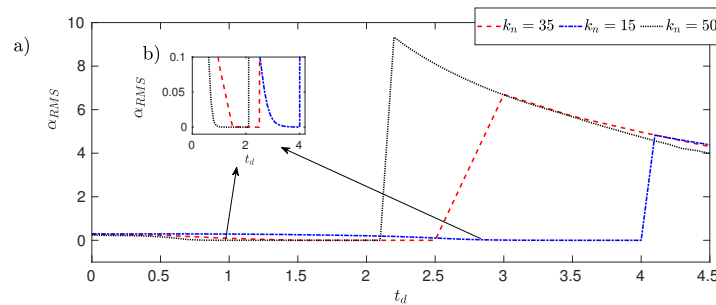


Figure 1: (a) Plot of the root mean square (RMS) of the pitch response vs the time delay (t_d) for coupling stiffness $k_n = 15, 35$ and 50 . An enlarged section displaying AD is shown in the inset (b).

¹ Ashwad Raaj et. al (2019). Synchronization of pitch and plunge motions during intermittency route to aeroelastic flutter. Chaos: An Interdisciplinary Journal of Nonlinear Science, 29(4), 043129.

Some computational aspects of active flutter suppression for co-design

Emmeline Faisse^{1,3}, Robin Vernay¹, Fabio Vetrano¹, Daniel Alazard² and Joseph Morlier³

¹ Airbus Operations SAS, 316 Route de Bayonne, Toulouse, France, emmeline.faisse@airbus.com

² ISAE-SUPAERO, Université de Toulouse, 10 Avenue Edouard Belin, BP-54032, Cedex 4, Toulouse 31055, France

³ Institut Clément Ader, Université de Toulouse, CNRS, ISAE-SUPAERO - INSA - Mines Albi, UPS, 3 rue Caroline Aigle, Toulouse, France

Keyword: computational flutter, aeroservoelasticity, co-design, active flutter suppression,

Active flutter suppression is an ongoing research topic in aeronautics and could lead to weight savings and more efficient aircraft if it is considered at an early design stage. Optimization for preliminary design needs to be multidisciplinary in order to reach an optimum. In the case of active flutter suppression, both structural and control parameters have to be included therefore a co-design strategy should be used.

The goal here is to assess co-design for designing a wing with active flutter suppression and compare two co-design strategies. The first strategy is a conventional nested optimization strategy or multi-discipline feasible. The second one used is the direct transcription method, which is a simultaneous optimization architecture. Flutter computation for optimization is examined in the frequency domain as well as in the time domain.

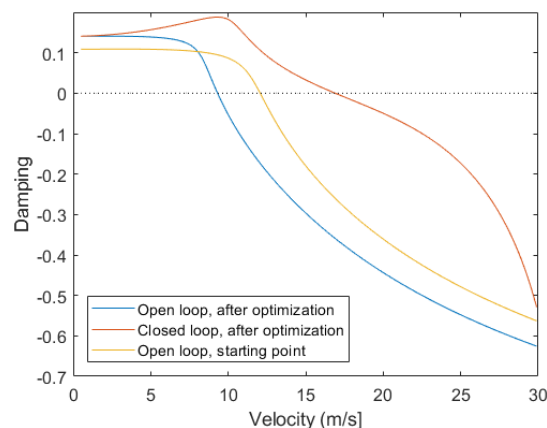


Figure 1: Evolution of damping with velocity of the flutter mode of a 2D airfoil, computed with a frequency method, before and after a nested optimization.

Two test-cases are considered. A simplified 2D airfoil is used to compare the optimization methods. They are then applied to a 3D wing mesh. Preliminary results are presented.

Mitigating the galloping of a square prism with a purely non-linear energy sink

Michael M. Selwanis¹, Sima W. Rishmawi^{1,2}, Guilherme Rosa Franzini³, Cédric Béguin¹ and Frédérick P. Gosselin^{1*}

¹ *Department of Mechanical Engineering, Polytechnique Montréal, Québec, Canada*

² *Birzeit university, Birzeit, Palestine*

³ *Offshore Mechanics Laboratory, Escola Politécnica, University of São Paulo, Brazil*

* frederick.gosselin@polymtl.ca

Keyword: square prism, galloping, non-linear energy sink, vibration absorption.

Galloping is a critical type of flow-induced vibrations (FIV) characterized by high amplitudes. In this research, we propose a non-linear energy sink (NES) for square prism galloping reduction. The proposed NES is a simple passive device that consists of a ball moving freely in a circular track. The square prism with the NES is modeled as a two-degree of freedom system. The governing equations are expressed as state equations then integrated numerically. The aerodynamic force coefficients affecting the prism are measured in the wind tunnel with a force balance. We use the Kolmogorov–Smirnov test to eliminate any systematic error. The fitting of these experimental aerodynamic coefficients feed the mathematical model. To study the NES effect, the calculated maximum amplitudes of the prism with and without the NES are compared. The proposed NES is 3D-printed and attached to the prism. We measure the vibrating amplitudes of the prism in the wind tunnel at different flow speeds with and without the NES. The experiments validate the numerical simulations and illustrate the usefulness of the NES in reducing square prism galloping. Thank to the numerical model, we study the influence of some parameters (radius ratio, mass ratio, and ball damping) on the NES behavior. The NES design we present is directly amenable to mitigate other types of FIV.

Flutter Suppression Test of Two-dimensional Supercritical Wing in Transonic Region

Kenichi SAITOH¹, Norio YOSHIMOTO²

¹Japan Aerospace Exploration Agency, Tokyo, Japan, ksaitoh@chofu.jaxa.jp

²Japan Aerospace Exploration Agency, Tokyo, Japan, yosimoto@chofu.jaxa.jp

Abstract

Active control was applied for an aeroelastic system of a two-dimensional supercritical wing with a trailing edge control surface. Stack piezo actuators with stroke magnification systems were used to activate the control surface. Phase effect of the controller was surveyed to obtain a proper controller. It achieved to modify a Limit Cycle Oscillation condition by 16% in equivalent air speed at a transonic flow region. An amplitude of the control surface deflection while effectively suppressing the LCO was about 0.2 deg RMS which is sufficiently smaller than the piezo actuator capability.

Keyword: Flutter suppression, Transonic flow, Wind tunnel test, Piezo actuator.

1 Introduction

Active Flutter Suppression (AFS) or Flutter Margin Augmentation (FMA) has been studied since 1960's as it is reviewed by Livne 2018. In this meaning, it is matured technology. However, application for commercial aircraft is rare. The Outboard Aileron Modal Suppression (OAMS) system of B-747-8/8F is one of recent application, which suppresses Limit Cycle Oscillation (LCO) observed in a certain flight condition at the flight test. LCO is often observed in transonic flow condition where a shock wave is generated on the surface and affects the aeroelastic response. LCO appears at lower dynamic pressure than a subsonic flutter. This phenomenon is called transonic dip. Regulations of aircraft design require 15% speed margins to the maximum design speed for flutter including LCO.

2 Test set up

2.1 Wind tunnel and support system

The test was performed at 0.6m × 0.6m transonic Flutter Wind Tunnel (FWT) in JAXA (Fig. 1). Specifications of FWT are listed in Tab. 1. A two-dimensional wing model is supported by an elastic support system which has two degrees of freedom in heaving and pitching motion (Fig. 2). The heaving stiffness is given by four plates located outside the flow area. Pitching stiffness is given by parts which have a cruciform cross section. Eq. (1) shows the motion of equation for the two-dimensional aeroelastic system.

$$\begin{bmatrix} 1 & x_\alpha \\ x_\alpha & r_\alpha^2 \end{bmatrix} \begin{bmatrix} \ddot{h} \\ \ddot{\alpha} \end{bmatrix} + \begin{bmatrix} 2\zeta_h \omega_h^* & 0 \\ 0 & r_\alpha^2 2\zeta_\alpha \omega_\alpha^* \end{bmatrix} \begin{bmatrix} \dot{h} \\ \dot{\alpha} \end{bmatrix} + \begin{bmatrix} \omega_h^{*2} & 0 \\ 0 & r_\alpha^2 \omega_\alpha^{*2} \end{bmatrix} \begin{bmatrix} h \\ \alpha \end{bmatrix} = \frac{1}{\mu\pi} \begin{bmatrix} -C_l \\ 2C_m \end{bmatrix} \quad (1)$$

where \bar{h} is a heaving displacement, α is a pitch angle, x_α is a static mass unbalance, r_α is a radius of gyration, ζ_h , ζ_α are damping ratios, ω_h^* , ω_α^* are non-dimensional angular

velocities, μ is a mass ratio, C_l is a lift coefficient and C_m is a pitching moment coefficient. The suffixes h and α indicate heaving and pitching value respectively. The equation is non-dimensionalized by the half chord length b , the total mass m and the specific time b/U_∞ , where U_∞ is the speed of uniform flow. Non-dimensional values in Tab. 2 are obtained by the stiffness and vibration test except mass parameters x_α and r_α . Mass parameters are estimated by an analysis and it is modified by the test. ω_h^* and ω_α^* are the values at Mach 0.80.

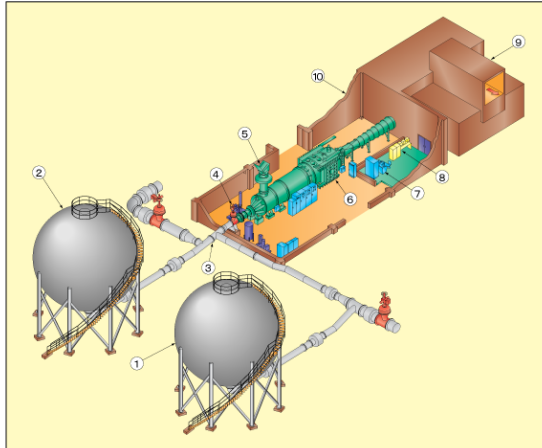


Figure 1: Bird view of Flutter Wind Tunnel (FWT) in JAXA

Table 1: Specifications of FWT

Mach range	0.54 – 1.15
Total pressure (P0) range	150 – 400 kPa
Duration	- 120 sec
Test section	0.6m × 0.6m
Operation sequence	Mach sweep P0 sweep Dynamic pressure sweep

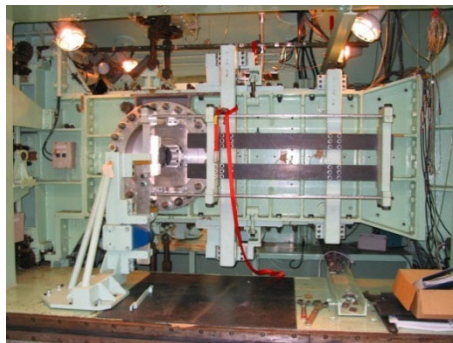


Figure 2: Two degrees of freedom elastic support system

Table 2: Non-dimensional parameters at Mach 0.80

x_α	r_α	ζ_h	ζ_α	ω_h^*	ω_α^*
0.0434	0.475	0.011	0.008	0.0574	0.0739

2.2 Wing model

Fig. 3. shows the wing model and its profile. The maximum thickness t/c is 0.115 at $x/c=0.375$. The airfoil is derived from a cross section of YXX aircraft designed by Japan Aircraft Development Company (JADC). JADC allowed us to use it for this study. Pressure

distributions were measured in a previous experiment and described in Saitoh et al. 2011. The test was performed with free transition condition. The wing has 20% chord length trailing edge control surface. It is activated by piezo actuators described following section. Its deflection angle is detected by two incremental encoders, MTL EAS-12. Four laser triangulators, KEYENCE LK-500, detect heaving displacement and pitch angle at the support system. Two laser triangulators, KEYENCE LK-G500, detect them at the center in span of the wing model and these signals are used in a feed back system. End plates are placed at both tips of the wing. Piezo actuator systems are equipped in the plates. The chord length of the wing is 0.25 m and the span is 0.53 m.

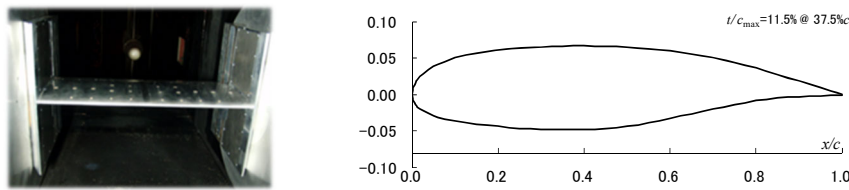


Figure 3: Wing model in the wind tunnel test section (left) and its profile (right)

3 Piezo actuators

Stack piezo actuators with stroke magnification systems are applied to activate the trailing edge control surface. The specifications of the stack piezo actuator are shown in Tab. 3. A stroke of the piezo actuator is magnified by about 10 times. Two piezo actuators with magnification systems form one pair as shown in Fig. 4. Two pairs of the systems are placed at both side ends of the wing model. Four actuator forces act on the control surface at the point 25.75 mm distant from the hinge line. An electric power of the piezo actuators is given through the amplifier which amplifies the input voltage by 30 times. Fig. 5 shows block diagram from input voltage to the control surface deflection. A piezo actuator has a hysteresis nature in its stroke against input voltage, resulting in the hysteresis of the control surface deflection as shown in Fig. 6. Voltage described as "Com" in Fig. 6 is shifted by 2.5 V to feed the amplifier. Although a stroke of the magnification system and distance between the hinge and the force acting point result in only 3.0 deg deflection, Fig. 6 shows more than 5 deg. Frequency response was obtained by giving sinusoidal command with a frequency sweep from 0.1 to 50 Hz. Fig. 7 shows open loop response from e_c to δ_R . The magnitude is the ratio from input voltage to the control surface deflection in deg. Larger input brings larger gain response whereas the phase keeps the same response. Two bumps at around 18 Hz and 24 Hz come from the elastic support system. The control surface deflection is regulated by PID controller expressed as follows.

$$PID = K_p + \frac{K_i}{s} + \frac{K_d}{T_f s + 1} \quad (2)$$

Coefficients taken as follows, gives almost flat frequency response.

$$(K_p, K_i, K_d, T_f) = (0.5, 0.5, 0.5, 1) \quad (3)$$

PID controller is realized by a digital system with 1000 Hz sampling frequency. Lag time caused by sampling at frequency f_s can be expressed by the first order Padé approximation as

$$e^{s/f_s} = \frac{-s+2f_s}{s+2f_s} \quad (4)$$

Measured data showed phase delay was the half of Eq. (4), therefore the following delay model was adopted.

$$\frac{-s+4f_s}{s+4f_s} \quad (5)$$

An aeroservoelastic model is constructed of the control surface, heave and pitch models as shown in Fig. 8. Closed loop frequency response was measured in wind on/off condition. The flow condition is Mach 0.80 and stagnation pressure $P_0=150\text{kPa}$. Target command δ_c is 2 deg-pp sinusoidal signal swept in frequency. Fig. 9 shows the response from e_c to δ_R in the PID closed loop. Fig. 10 shows the response from δ_c to δ_R . As the frequency increases, the inertial force of the control surface reduces the amplitude of the deflection. A wind gives aerodynamic stiffness and mass, resulting also in the reduction of the amplitude. Final aeroservoelastic models from δ_c to h and α are estimated in the third order transfer function as shown in Fig. 11. The low order model exhibits a model error especially at heave response around 20 Hz. The advantage of the model is described in the control law synthesis section.

Table 3 : Specification of stack piezo actuator

Manufacturer	Piezomechanik
Type	PSt 150/14/140
max. tensile force	approx. 1kN
max. load	7kN
max. force	7kN
max. stroke	140 μm
length	149mm
length of PZT	126mm
capacitance	55 μF
stiffness	30 N/ μm
resonance	7 kHz
poisson's ratio	0.33

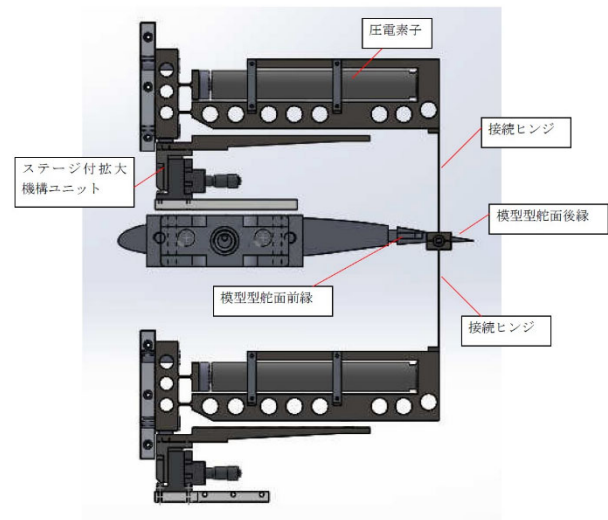


Figure 4: Control surface activated by piezo actuators

Table 4: Specification of stroke magnification system (average)

Manufacturer	Mechano Transformer
max. force	246 N
max. stroke	1338 μm
resonance	152 Hz
weight	1244 g

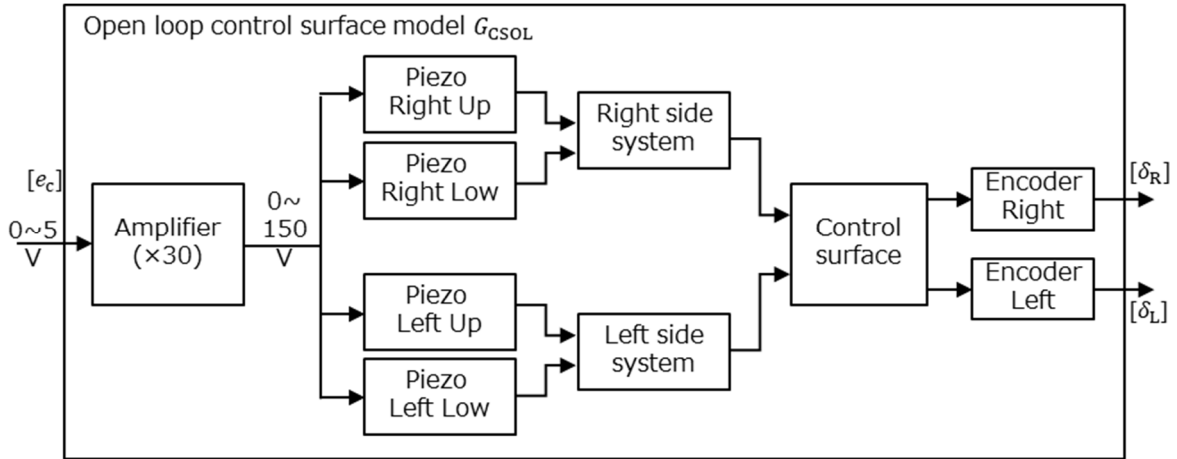


Figure 5: Block diagram from input e_c of piezo actuators to the control surface

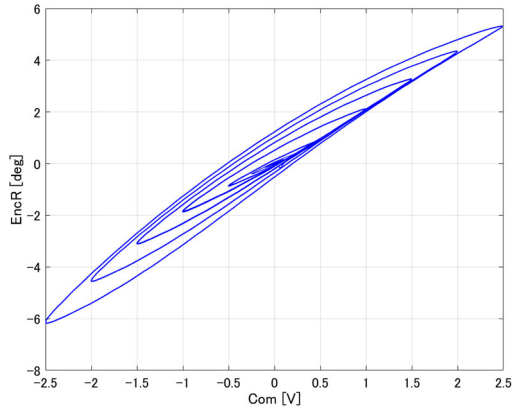


Figure 6: Quasi-steady (0.1Hz) Open loop response of the control surface from e_c -2.5V (as “Com”) to δ_R (as “EncR”)

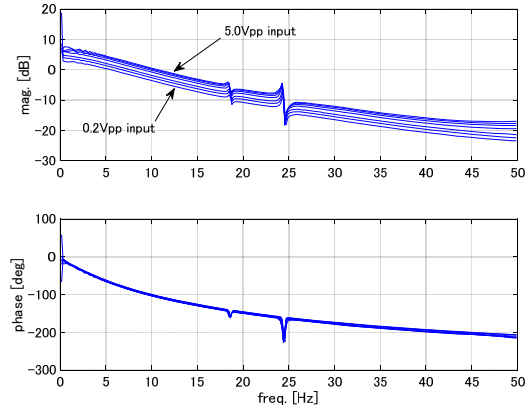


Figure 7: Open loop frequency response δ_R/e_c

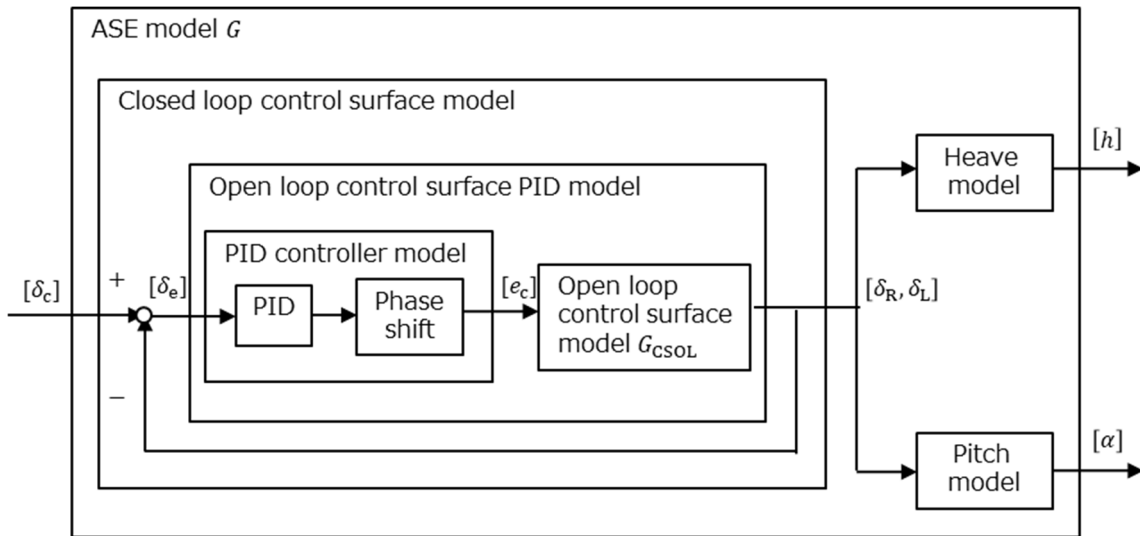


Figure 8: Aeroservoelastic model

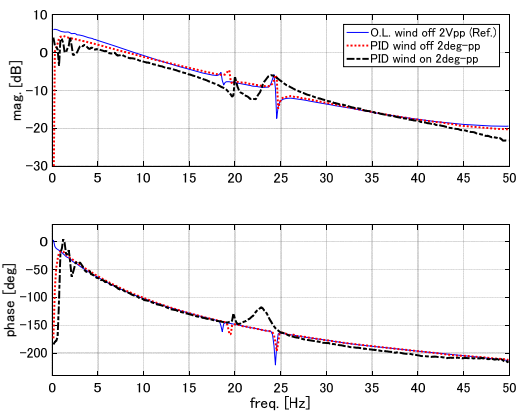


Figure 9: Piezo actuator system response δ_R/e_c in PID closed loop

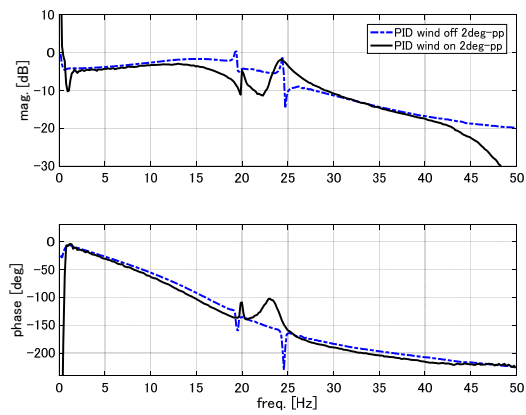


Figure 10: Closed loop frequency response δ_R/δ_c at wind ON/OFF

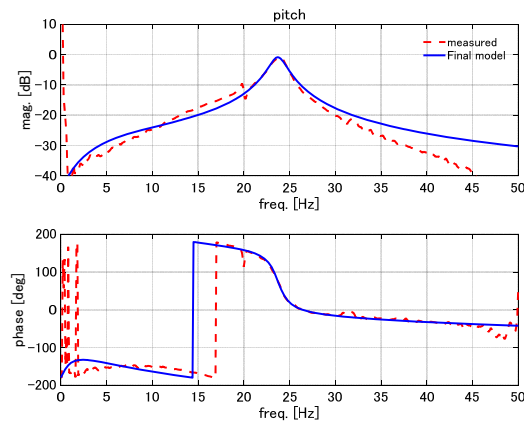
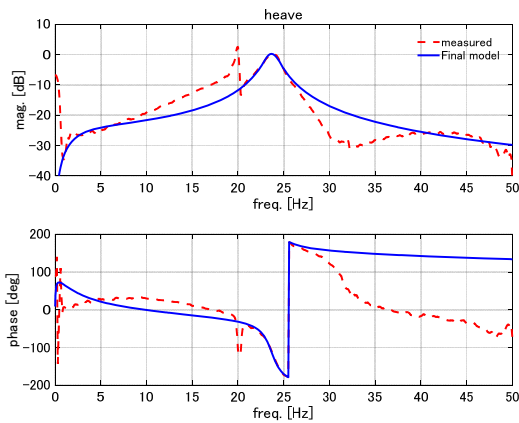


Figure 11: Final ASE mode h/δ_c (left) and α/δ_c (right)

4 Control law

Controller is synthesized by Normalized Left Coprime Factors (NLCF) approach which is one of H_∞ method (Baldelli et al. 1995). In this method, the plant G which is equal to Fig. 8 is augmented with loop shaping functions W_i and W_o as shown in Fig. 12. Controller K_i is synthesized for the augmented plant $G_s = W_oGW_i$ to obtain final controller as $K_f = W_iK_iW_o$. A lower order plant makes it easy to find robust controller. Tab. 5 gives the parameters for the NLCF controller synthesis. Shaping function has no dynamics but constant value. In the output shaping function W_o , a weight for heaving output is small. It is reasonable, because of the model error at heaving response. ε_{\max} is H_∞ norm of a permissible disturbance stabilized by a central controller of NLCF approach. ε is a kind of relaxed value to obtain the controller K_i . The sixth order controller K_f obtained by NLCF is reduced by the third order using Balanced Truncation Approximation (BTA). In the experiment, the controller did not work well, therefore a phase adjustment factor is introduced as shown in Fig. 13. For the phase shift function, Eq. (4) is applied with modifying as

$$P = \frac{-s+2f}{s+2f} \quad (6)$$

where f is obtained by

$$f = \frac{180f_t}{\varphi} \quad (7)$$

In this equation, φ is desired phase shift in deg at target frequency f_t . Fig. 14 shows frequency responses of the controller K_f and PK_f .

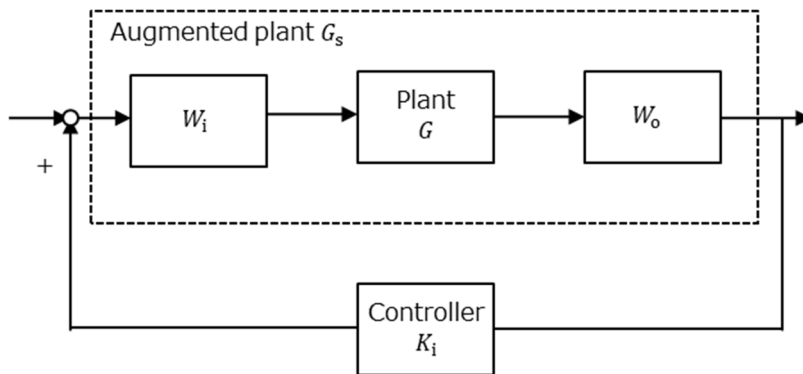


Figure 12: Augmented plant

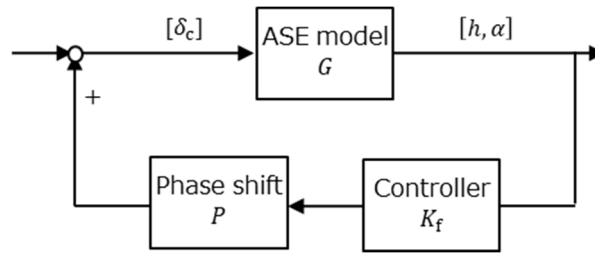


Figure 13: Final control system

Table 5: Parameters for the controller synthesis

W_i	W_o	ϵ_{\max}	ϵ
5	$\begin{bmatrix} 0.1 & 0 \\ 0 & 1 \end{bmatrix}$	0.696	$0.9\epsilon_{\max}$

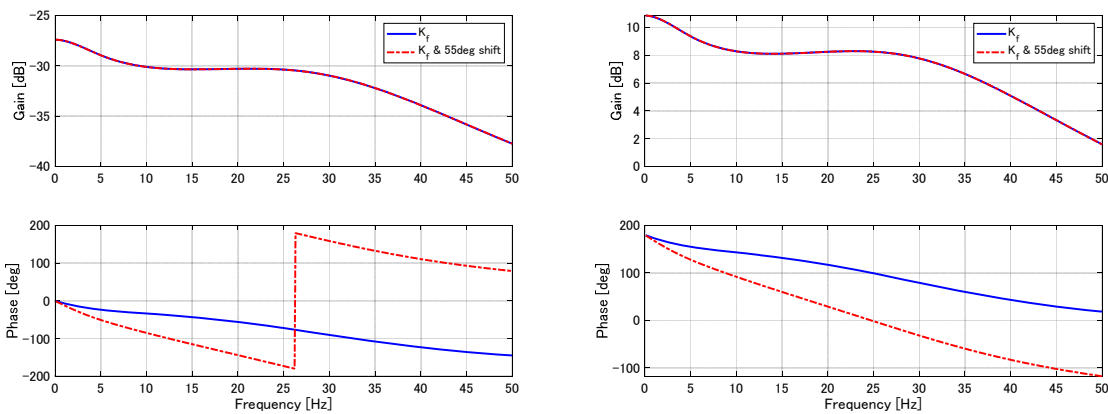


Figure 14: Bode diagram of the controller (δ_c/h ;left, δ_c/α ; right)

5 Experimental result

LCO boundary was detected by P0 sweep sequence in the wind tunnel test (Fig. 15). In the sequence, total pressure P0 was increased at 2 kPa/s with constant Mach number. A bottom of the transonic dip is at around Mach 0.80. Control effect with phase shift was investigated as shown in Fig. 16. The controller needs about 50 deg phase delay. The reason is not cleared yet. The controller effectively works within 10 deg around the center. Fig. 17 shows the heave and pitch response with and without the controller. The controller is shifted 55 deg in this case. An amplitude of the control surface deflection is sufficiently small comparing to the actuator capability while it suppresses the LCO as shown in Tab. 6.

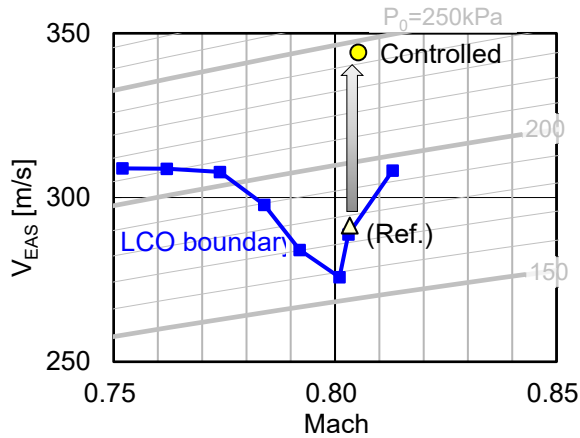


Figure 15: LCO boundary

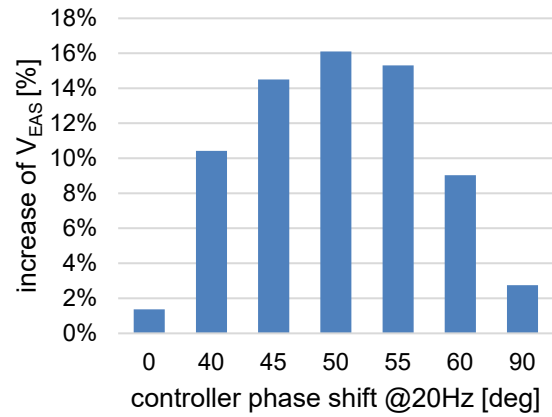


Figure 16: Phase shift and control effect

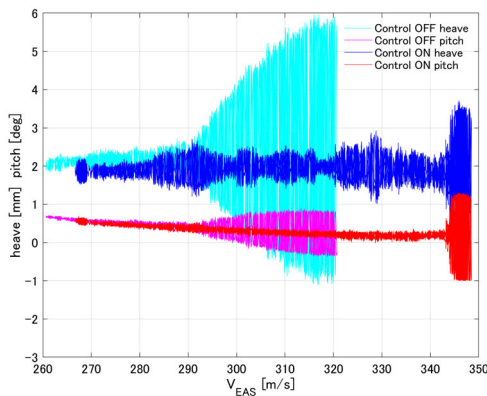


Figure 17: Heave and pitch response with control ON/OFF

Table 6: Control surface amplitude in case of Fig. 17 Control ON

V_{EAS} [m/s]	δ_{RMS} [deg]
338	0.17
346	0.78

6 Conclusions

Active control was applied to the two-dimensional aeroelastic wing system and successfully increased the LCO speed (EAS) by 16% in a transonic regime. The experiment is summarized as follows.

- The stroke magnification system of the stack piezo actuator effectively rotates the control surface.
- Inner loop with PID controller works well for the piezo actuator system which has hysteresis from input voltage to a stroke.
- Lower order mathematical model of an aeroservoelastic system is desirable for a controller design.
- The phase range for the effective controller is about only 10 deg.
- An amplitude of the control surface deflection was about 0.2 deg while the controller effectively suppressed the LCO. It is sufficiently small comparing to the actuator capability.

References

1. Baldelli, D. H., Ohta, H., Matsushita, H., Hashidate, M., and Saitoh, K., 1995. Flutter Margin Augmentation Synthesis Using Normalized Coprime Factors Approach, *Journal of Guidance, Control, and Dynamics*, Vol. 18, No. 4, pp. 802–811.
2. Livne, E., 2018. Aircraft Active Flutter Suppression: State of the Art and Technology Maturation Needs, *J. Aircraft*, Vol. 55, No. 1
3. Saitoh, K., Tamayama, M., Yoshimoto, N., 2011. Experimental Results of the Unsteady Pressure Distribution at Flutter in Transonic Flow. *International Forum on Aeroelasticity and Structural Dynamics*, Paris, IFASD-2011-015

Optimal wall deformation for mitigating the boundary layer instability

Tristan Leclercq¹, Olivier Marquet¹

¹ DAAA, ONERA, 8 rue des Vertugadins, 92190 Meudon, France, olivier.marquet@onera.fr

Keyword: fluid-structure interactions, boundary layer instability, resolvent analysis, optimal deformation

Recent works have shown that compliant walls bear the potential to mitigate the amplification of Tollmien-Schlichting waves in the Blasius boundary layer, thus opening a possibility to delay transition to turbulence. However, the coupling of an elastic coating with the boundary layer flow may trigger so-called travelling wave flutter modes, which may actually defeat the purpose of stabilizing the boundary layer. Besides, the very choice of an elastic patch with given material properties imposes constraints on the interface deformation that necessarily limit the efficiency of the stabilization of the TS waves.

In this work, we relax all constraints on the wall deformation, and we derive a new formulation to look for the deformation that would minimize the maximum amplification gain. We investigate this matter numerically using an exact linearization of the Arbitrary-Lagrangian-Eulerian equations¹. We show that the minimum value found for the maximum gain after optimization of the deformation is much lower than the gain computed with a passive elastic coating. We further show that the optimal wall deformation differs substantially from that obtained with a passive elastic coating.

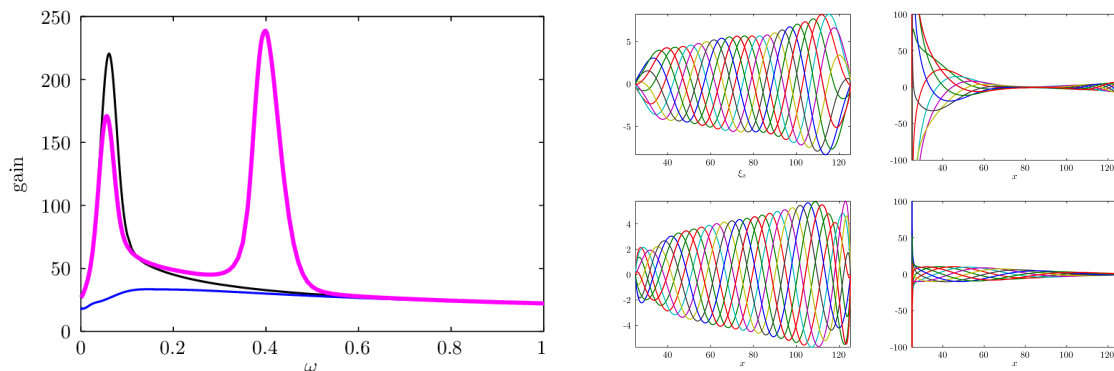


Figure 1 – Left: gain of the resolvent operator (black: no control, magenta: compliant coating, blue: optimal wall deformation). Right: comparison between the compliant coating interface deformation (left column) with the optimal deformation (right column).

¹ Pfister, J.L., Marquet, O., & Carini, M. (2019). Linear stability analysis of strongly coupled fluid-structure problems with the Arbitrary-Lagrangian-Eulerian method. *Computer Methods in Applied Mechanics and Engineering*, 355, 663-689.

Passive flutter control of aeroelastic wing with a flap-NES

Claudia Fernandez-Escudero^{1,2}, Sebastien Prothin¹, Guilhem Michon^{1,3}, Eric Laurendeau² and Annie Ross²

¹ISAE-Supaero, Toulouse, France, claudia.fernandez-escudero@isae-supaero.fr

²Polytechnique Montréal, Montréal, Canada

³ICA, Toulouse, France

Keyword: Aeroelasticity, Flutter, LCO, Nonlinear Dynamics, NES, Vibration Mitigation, Passive control

Aeroelasticity has always been a determining factor in aircraft design as it can threaten the structural integrity of the aircraft and, therefore, must be considered when defining the flight envelope. Recently, there have been developments, such as the use of more flexible materials and higher aspect ratio wings, which improve the aerodynamic efficiency of wings but they enhance the fluid structure interaction.

In order to avoid resonance in certain structures such as suspension bridges, nonlinear oscillators such as nonlinear energy sinks (NES) are used. The objective of such secondary systems is to absorb energy from the main system and dissipate its vibrations. A NES consist of an added mass, a linear damping and a cubic stiffness. The case of wing flutter is more complex than structural resonance since the wings mode's frequencies change with wind speed. The advantage of NESs over other linear tuned mass dampers is that they are efficient at a broadband frequency if they are correctly dimensioned.

With the objective of controlling passively a wing with a NES for minimum added mass and broadband frequency efficiency, the objective of this study is to equip a wing flap as a NES (figure 1). The use of a flap is advantageous as the structure is modified to the minimum and also that there is zero added mass in the system. The placement of the NES at the wing tip ensures its use inflow meaning that its natural frequencies will change with changing wind speed similarly to the rest of the wing structure.

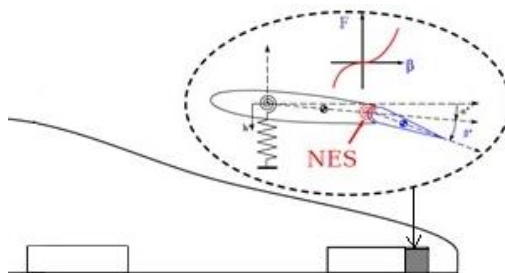


Figure 1: Configuration of wing with NES with zero added mass

The experimental campaign carried out on a 2D rigid wing with 3 DOFs has shown an amplitude reduction in the LCO's heave and pitch DOFs of up to 50% by using the flap-NES with respect to using a linear aileron configuration.

Mitigation of aeroelastic instability for a rectangular tapered shape structure

Olivier FLAMAND¹

¹*CSTB, Nantes, France, olivier.flamand@cstb.fr*

Abstract

A cable transportation system is being planned for an urban environment, requiring the use of slender tapered rectangular pylons.

The initial design process using Eurocode 1991-1-4:2005 identified a risk of vortex shedding excitation, excluding galloping risk with respect to the first natural frequencies of bending modes. We carried out wind tunnel tests on a rigid model reproducing the last 15m of the pylon, at a scale 1/10.

We mounted this rigid model horizontally in the wind tunnel in a grid turbulent flow, suspended on springs to reproduce bending modes and rotated the model about its axis to study various incidences of oncoming wind. Vortex shedding was observed for low wind speed close to 13m/s. Various shape improvements have been tested.

Keyword: rectangular cylinder, vortex shedding, stall flutter, damping.

1 Introduction

Cable cars have been particularly popular in the last decade for public transportation in dense urban areas. Among their various advantages, installation in an existing environment does not require huge civil engineering work and reduces expropriations, whilst maintenance and operation costs seem to be very competitive compared to other mass transport systems. Medellín, Constantine, La Paz, Singapore, Cali, Hong Kong, London, Ankara and Nizhny Novgorod are some cities that introduced gondola traffic.



Figure 1: cable transportation system in Medellín, with circular section pylon

Because gondolas are suspended on cables high above existing buildings, trees and ground transport systems, high rise supporting poles are required. If cable cars are subject to aerodynamic loads, their operation can be stopped in case of strong winds. Conversely, the framework composed of pylons and cables must resist the strongest winds events.

Pylons are usually made of circular section tubes, tapered from the ground. In such cases there is no reported problem with aerodynamic stability of the pylons. However in a recent project the architect specified tapered rectangular section pylons which could be prone to vortex shedding, based upon the Eurocode's rules. The same code indicates that galloping might not be a problem in the range of wind speed encountered on site, but it is well known that vortex shedding and galloping can have strong interdependence on such rectangular shape profiles (Parkinson 1981).

A first question to answer was the strength of excitation with a rectangular shape which is evolutive with height. A second input was the possibility to mitigate this excitation by changing the outside shape of the pylon, and finally check if such change was acceptable for the architect. Increasing structural damping was also a possible option.

2 Wind tunnel test conditions

The project includes five pylons, the heights of which range from 30m to 70m. Only the two highest poles present a strong risk of excitation, due to their lower natural bending frequencies. Resulting from the rectangular shape there are two orthogonal directions for the first two bending modes.



Figure 2: Planned pylons (left) and model in wind tunnel (right)

The pylons are hollow, made from steel and assembled by welding, which minimizes their mass and their damping ratio, leading to Scruton number values as low as $Sc=7.7$ for the first mode at 0.73Hz and $Sc=10$ for second mode at 0.85Hz in the case of the 70m high

structure. The total mass of this highest pylon is 340t.

The choice was made to reproduce only the top part of the pylon, which is subject to the strongest and the most uniform wind and also the main origin of aeroelastic force, by its large amplitude of oscillation. The scale of the model was fixed at 1/10, allowing to represent the top 15m of the core of the pylon with a 1.5m long model, the very top part of the pylon composed of four diverging and curved mast being not represented in the model.

The generalized mass of the two first bending modes of the highest pylon was not precisely known: the linear mass of the top part of the pylon, 2.45t/m, was reproduced on the wind tunnel model at the scale 1/10 with a value of 24.5 kg/m. The model was built using 15mm thick plywood and additional metallic weights were fixed inside to reach the right mass. Wind tunnel tests were performed with two mass conditions : a model lighter than the real pylon with a mass of 17.1kg and a model with the same mass as the real pylon weighing 37kg. The flow is slightly turbulent ($I_u=4\%$) with a grid mounted upstream.

All pylons of this project are tapered with similar shape on their top part. Our model was an evolving rectangular shape, from 331mm x 250mm at one end corresponding to the lower part in reality to 246mm x 156mm at the other end corresponding the top of the core in reality. It was mounted horizontally in the wind tunnel between two end walls with a 3mm gap and suspended from springs letting it freely vibrate at frequency of 4.83Hz for the light model and 3.06Hz for the heavy model. It has sharp edges. It was rotated around its horizontal axis to reproduce the various directions of oncoming wind in real installation.

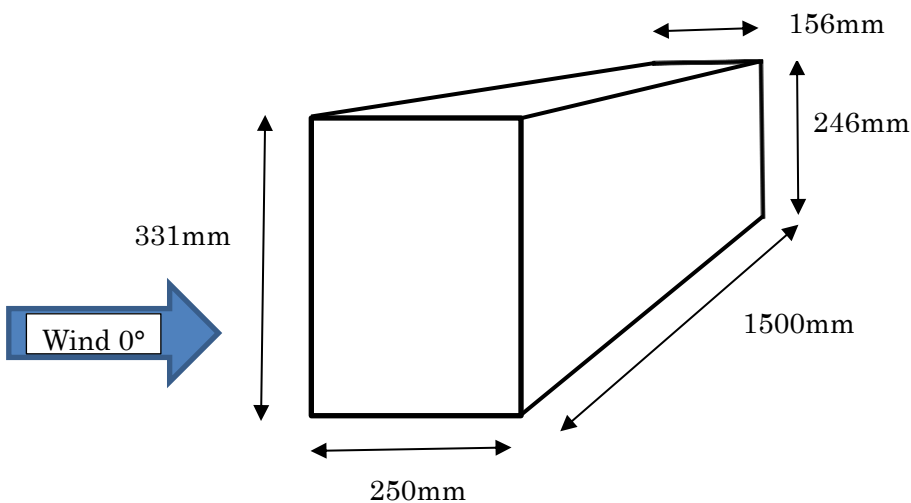


Figure 3 : Dimensions of the model

The model was suspended from springs allowing a structural damping as low as 0.05% of critical. Tests have been performed with this low damping value and with other damping ratios, 0.18%, 0.32%, 0.48%, 0.6%, 0.8%, 1.3%, 1.8%, 2%, 2.4%, 4.5% and 8% of critical.

3 Vibrations in initial shape and attempts to reduce it by shape improvement

In its initial shape the model was tested for wind directions ranging from 0° (direction perpendicular to the ropeway) to 90° (wind in the direction of the ropeway). For wind direction 0° the application of Eurocode's rules gives a Strouhal number of 0.12, leading to a prediction of critical velocity ranging from 20m/s at the largest dimension to 15m/s at the smallest one. For wind incidence 90° the ratio of height to depth of the rectangular shape leads to Strouhal number values from 0.10 at one end to 0.085 at other end, meaning the critical velocity could be assumed to lie between 18m/s and 13m/s. Accordingly the prediction of the critical velocity regarding vortex shedding of this tapered structure is not straightforward. Figure 4 presents results obtained from the wind tunnel tests, showing critical wind speeds smaller than predicted ones and vanishing of the vortex shedding excitation for wind incidence far from 0°, 90° and 45°. Wind incidences close to 0° show the same behavior as for the null incidence, which means in this direction the problem is much more pronounced that for incidence 90° or 45° where the critical incidence area is narrow.

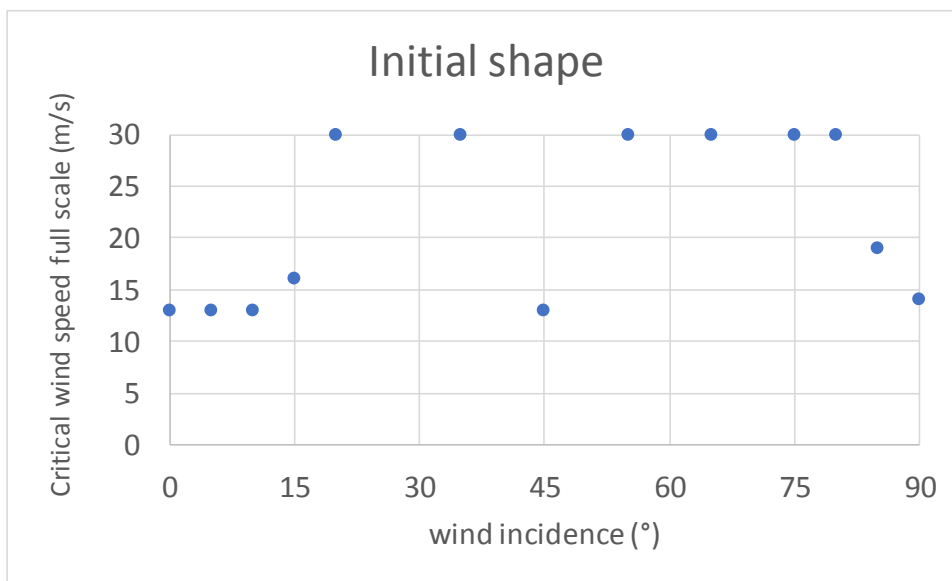


Figure 4 : Critical wind speed versus wind incidence for the model in its initial shape

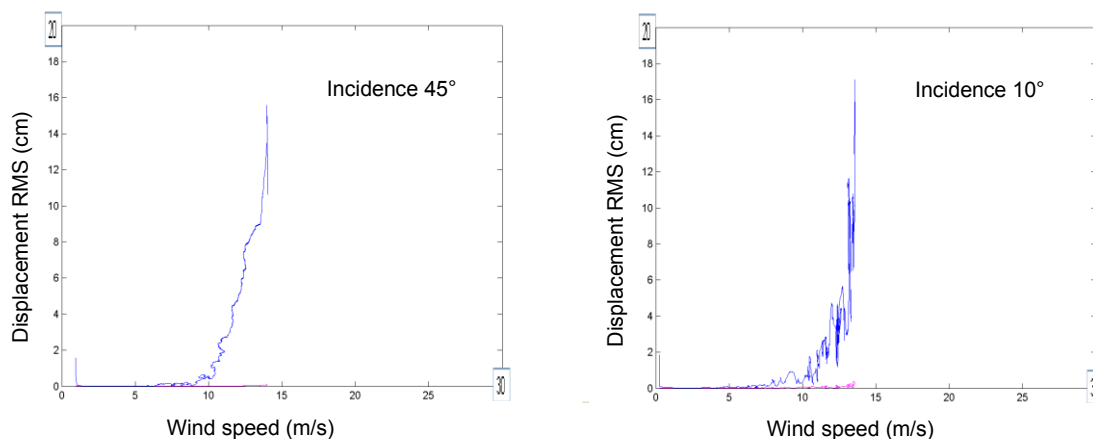


Figure 5 : Amplitude of vibration at full scale versus wind speed at full scale for initial shape

It can be seen from figure 5 that the sudden increase in vibration amplitude when the vortex shedding appears is similar for incidences close to 0° and incidence 45°. On the contrary,

tests performed with higher damping ratios showed the instability observed at incidence 90° with low damping vanished when damping was increased. At intermediate incidences vortex shedding excitation exists but does not lead to large amplitude vibrations.

The initial shape of the pylon was modified by addition of several devices to reduce the amplitude of the vortex shedding. None of them proved to be efficient enough to suppress vibrations at any wind incidence, when associated with a “nominal” damping ratio of 32% of critical.

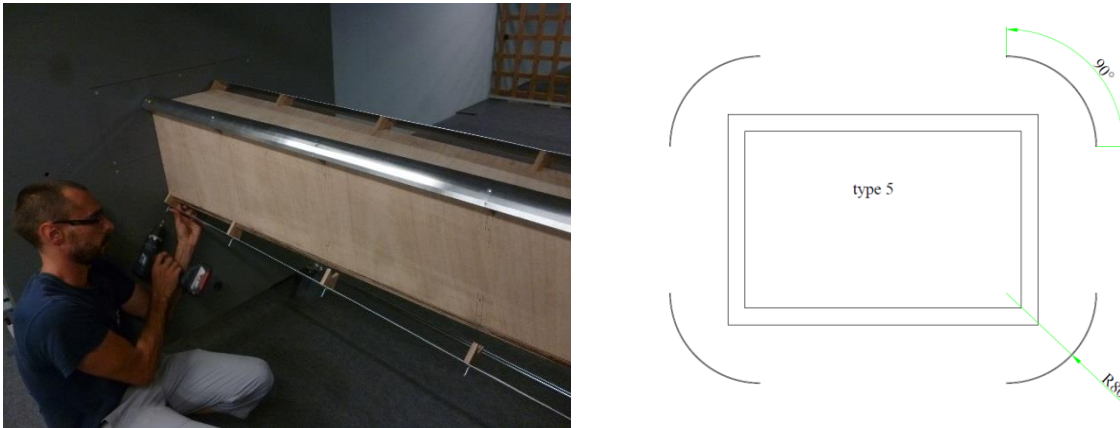


Figure 6 : First shape modification by addition of vanes in the corners

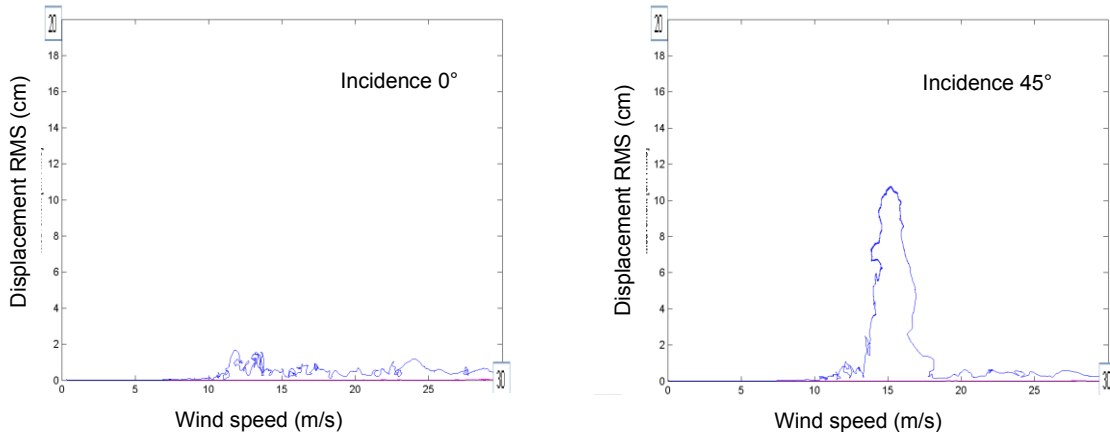


Figure 7 : Result of first shape modification by addition of vanes in the corners

The first shape improvement to be tested was the addition of round vanes at the corners of the rectangular shape (figure 6). This kind of device is used, for bridge decks for instance, to reduce distortion of stream lines and consequently reduce vortex shedding. It is efficient when the wind is not changing in mean incidence (horizontal flow aligned with the deck), but here, with a vertically standing pylon, the wind can be coming from any direction. This device is efficient for wind directions close to 0° and 90° , but it does not completely remove vortex shedding excitation for incidence 45° . In this case a vibration amplitude larger than 10cm is observed.

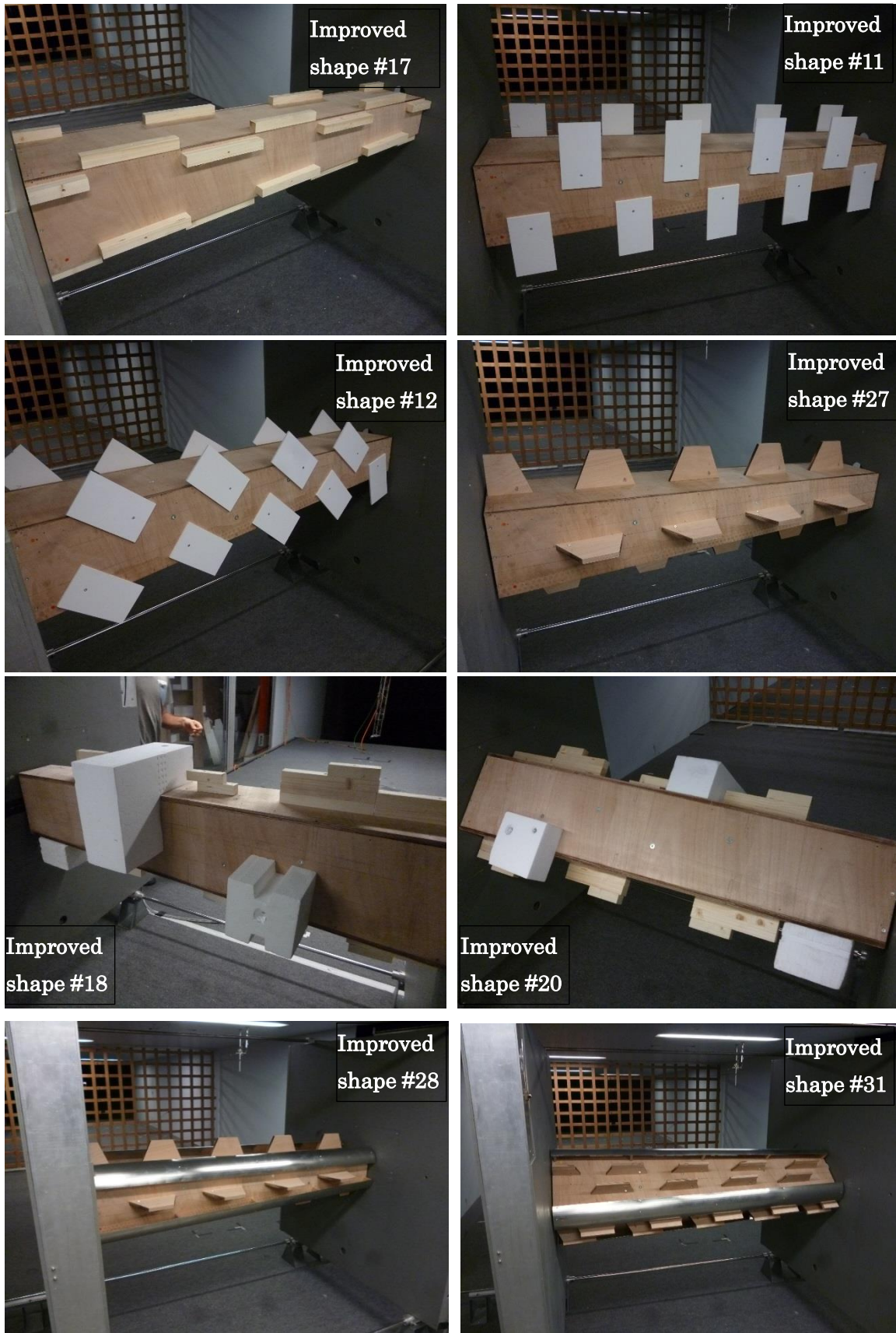


Figure 8 : Various shape improvement tested

Many other kinds of shape change are tested with the aim of introducing parasitic vortices, which could be efficient in disorganizing the wake. When such added devices have a dimension $1/10^{\text{th}}$ of the side of the pylon, they do not provide any change in the vortex shedding excitation. When their size is increased to $1/4$ of the side of the pylon they act on the critical wind speed, increasing it by 20%. With plates with a dimension one half of pylon's side located on two faces in a staggered arrangement there is no complete extinction of the vortex shedding excitation. Plates located in the middle of the four sides proved to be more effective but for some wind directions the model was still prone to excitation. The only shape improvement (Improved shape #18) that was really efficient in suppressing vortex shedding was a random arrangement of blocs of various dimensions.

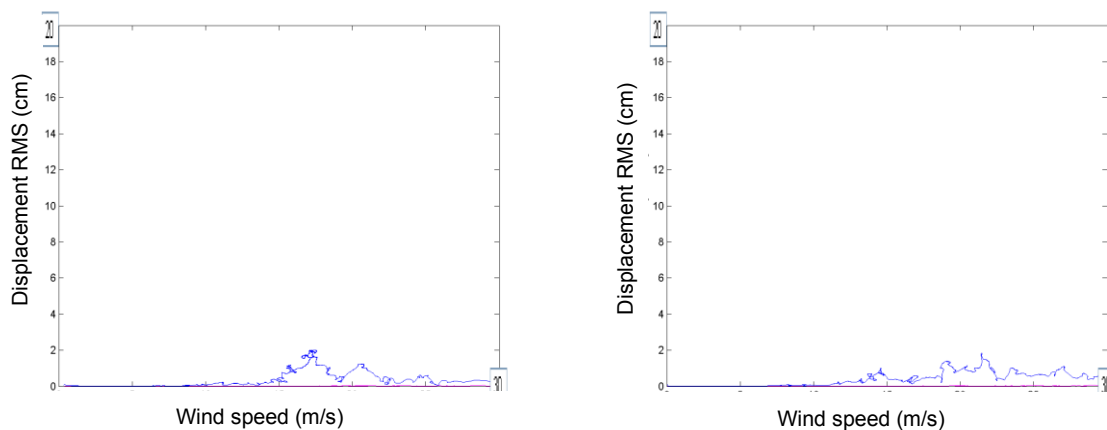


Figure 9 : Model vibrations observed with improved shape #18

A regular arrangement of vortex generators sometimes proved to be unstable, dramatically reducing the critical wind speed of galloping. The combination of corner vanes with turbulence generators located in the middle of faces of the rectangle also gives satisfactory results, whatever the wind direction. In this case the drag coefficient increase did not cause additional issues because the resistance of pylons to lateral loads is very high. But no one of these shape changes was accepted by the architect, due to their strong visual impact.

4 Vibration control by increasing structural damping

The only solution considered efficient to suppress vortex shedding excitation and increase the critical wind speed for galloping without changing the shape of the pylon is to increase the structural damping of the first bending modes.

To this end a series of tests was performed with the model at incidences 0° , 45° and 90° . Stability was easily attained at incidence 45° with a structural damping of 0.48% of critical. At incidence 90° a damping ratio of 1.3% of critical was necessary to reduce the amplitude of vortex shedding excitation. At incidence 0° the amplitude of excitation was so strong that the maximum could not be measured for damping ratios smaller than 1.3% of critical. With a damping ratio larger than 1.8% of critical it was possible to measure the maximum amplitude and follow its decrease when the structural damping was increased at incidence 0° . Even with a very large value of damping ratio the excitation did not completely vanish, indicating that the instability in this case is very strong.

Table 1 : Amplitude at full scale for high damping ratios

incidence (°)	Maxi RMS amplitude full scale (cm) for various damping ratios (% of critical)							
	0.48%	0.80%	1.30%	1.80%	2.00%	2.40%	4.50%	8%
0	20+	20+	20+	13	12.3	11	6.3	3.8
5								3.8
10								2.7
15								1.2
25								0.1
35								0.1
45	0.7	0.7						0.05
80								0.4
85								0.75
90	18	16	5.5					1.3

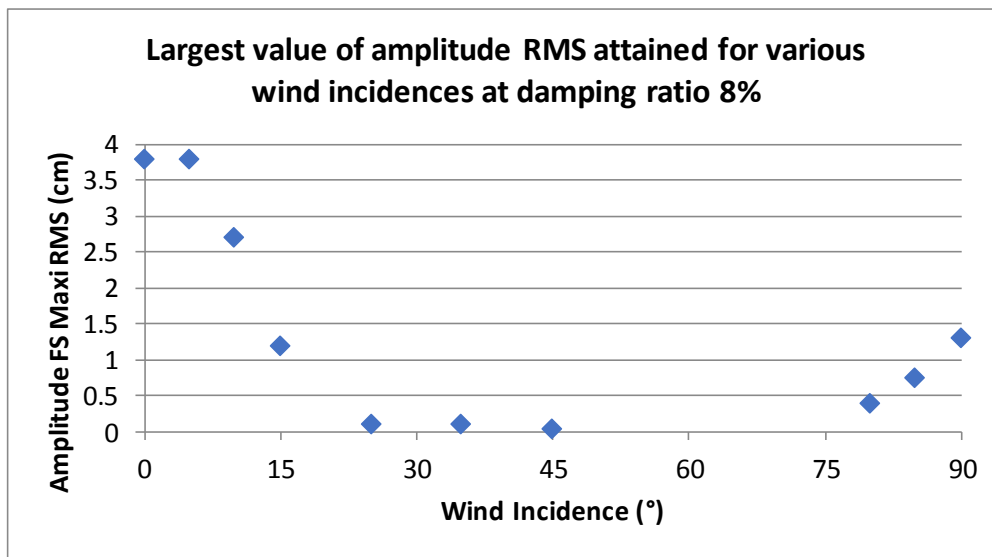


Figure 10 : Vibration amplitude RMS for damping ratio 8% for a range of incidences

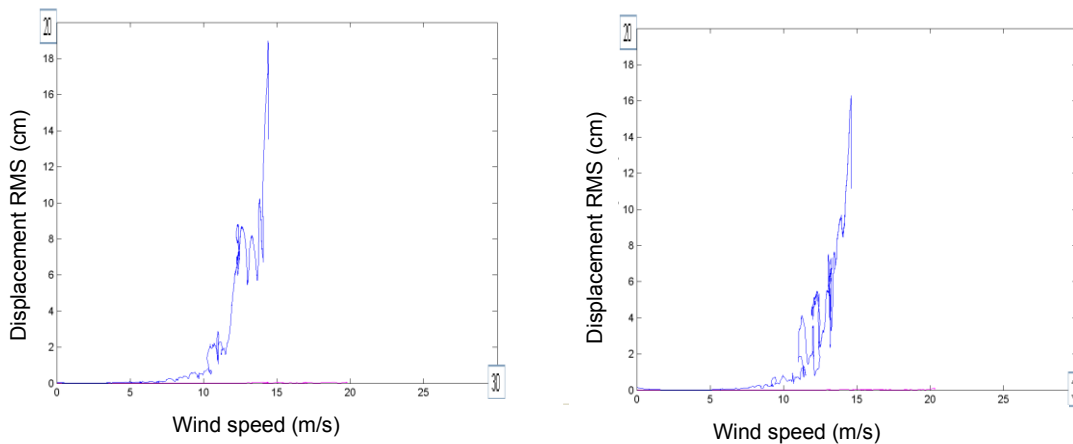


Figure 11 : Evolution of RMS of vibration amplitude at incidence 0°, with damping ratio 0.48% of critical on the left and damping ratio 1.30% of critical on the right.

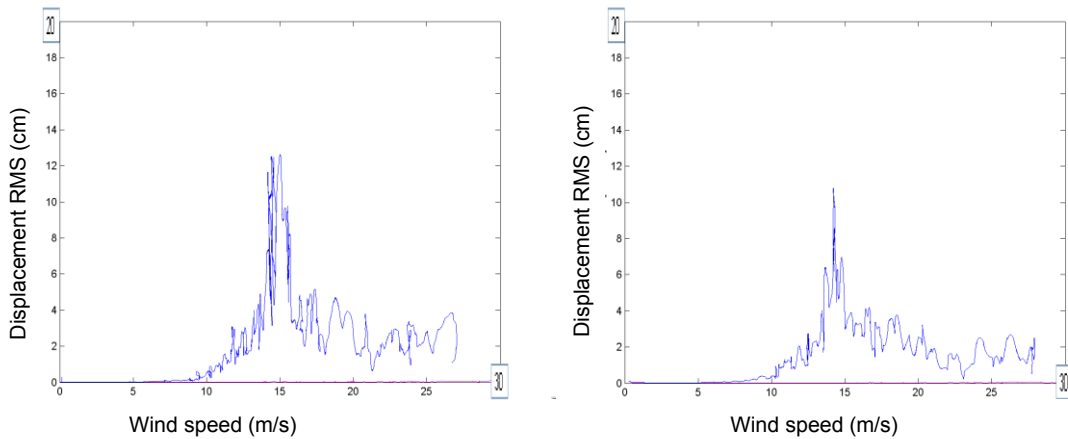


Figure 12 : Evolution of RMS of vibration amplitude at incidence 0° , with damping ratio 1.80% of critical on the left and damping ratio 2.0% of critical on the right.

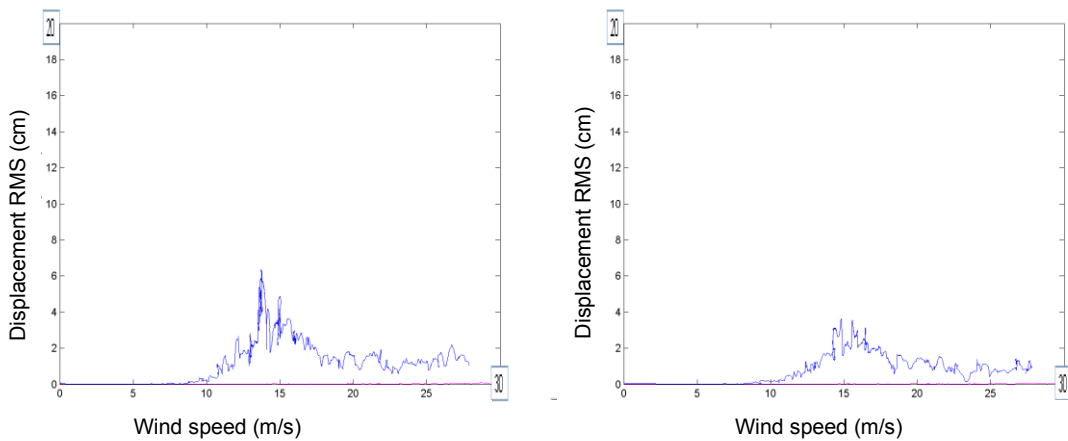


Figure 13 : Evolution of RMS of vibration amplitude at incidence 0° , with damping ratio 4.5% of critical on the left and damping ratio 8% of critical on the right.

The comparison of vibration amplitude at various damping ratios with an objective criteria used in cable transport world, which is a limit of top deflection to $1/300^{\text{th}}$ of the height, fixed the choice of a minimum structural damping ratio of 2.4% of critical. In this approach the effect of vertical mean wind speed gradient and the effect of real wind turbulence were not taken into account, assuming the influence of both parameters would have been favorable for stability.

This high level of structural damping was obtained in the real project with additional Tuned Mass Dampers (TMDs).

5 Conclusions

In the case of high rectangular pylons it is difficult to suppress aeroelastic excitations by common countermeasures such as corner vanes, because their efficiency is demonstrated only for some specific wind directions, whereas for a vertical standing structure strong wind could potentially come from any direction. Changing the pylon's shape by addition of vortex generators with the aim of disorganizing the vortex shedding phenomenon yields to strong

visual impact, which was not accepted by stakeholders. Increasing the damping is finally an effective solution that can be achieved by mean of tuned mass dampers, at reasonable cost and with very small visual impact. But in the case presented here of a rectangular tapered shape, the excitation by vortex shedding is very strong and even with a large increase in the structural damping the aeroelastic excitation is not completely suppressed. The design of the TMD system must be precise and it's commissioning done with care, taking into account the real mode shape, real mode frequency and real modal structural damping.

References

- Carassale, L., Freda, A., Marrè-Brunenghi, M., Experimental investigation on the aerodynamic behavior of square cylinders with rounded corners, *Journal of Fluids and Structures*, Volume 44, January 2014, Pages 195-204
- Eurocode 1991-1-4: 2005, "Wind loading on structures", CEN
- Hu, G., Tse, K. T., Kwok, K. C. S., Galloping of forward and backward inclined slender square cylinders, *Journal of Wind Engineering and Industrial Aerodynamics*, Volume 142, July 2015, Pages 232-245
- Mannini, C., Belloli, M., Marra, A. M. , Bayati, I., Giappino, S., Robustelli, F., Bartoli, G., Aeroelastic stability of two long-span arch structures: A collaborative experience in two wind tunnel facilities, *Engineering Structures* 119 (2016) 252–263
- Nakamura, Y., Tomonari, Y., Galloping of rectangular prisms in a smooth and in a turbulent flow, *Journal of Sound and Vibration*, Volume 52, Issue 2, 22 May 1977, Pages 233-241
- Parkinson, G. , Wawzonek, M., Some considerations of combined effects of galloping and vortex resonance, *Journal of Wind Engineering and Industrial Aerodynamics*, 8 (1981), pp. 135-143
- Scanlan RH, Simiu E. *Wind effects on structures*. 2nd edition. New York: John Wiley & Sons; 1978.
- Vickery, J., 1966. Fluctuating lift and drag on a long cylinder of square cross-section in a smooth and in a turbulent stream. *Journal of Fluid Mechanics* 25,481–494.

Vortex-induced vibration control research on Long-span Bridge by passive jets

Yang Wenhan¹, Chen Wenli¹ and Li Hui¹

¹*School of Civil Engineering, Harbin Institute of Technology, Harbin, China, yangwenhan@stu.hit.edu.cn*

Keyword: Vortex-induced vibration, passive control, self-issuing jet.

The long-span suspension bridge is sensitive to the external loading, for instance, the earthquake, vehicular loads, wind and wind-rain jointing loadings, which should be considered at the design phase. In the past engineering, the wind-induced vibration occurs frequently on the girder and the bridge attachments. In the 1990s, the vortex-induced vibrations (VIVs) have been found at the incoming velocity of approximately 5-10m/s on the Great Belt suspension Bridge during its deck-erection phase [1]. Therefore more and more researchers pay more attention on VIV mechanisms and controls of long-span Bridge.

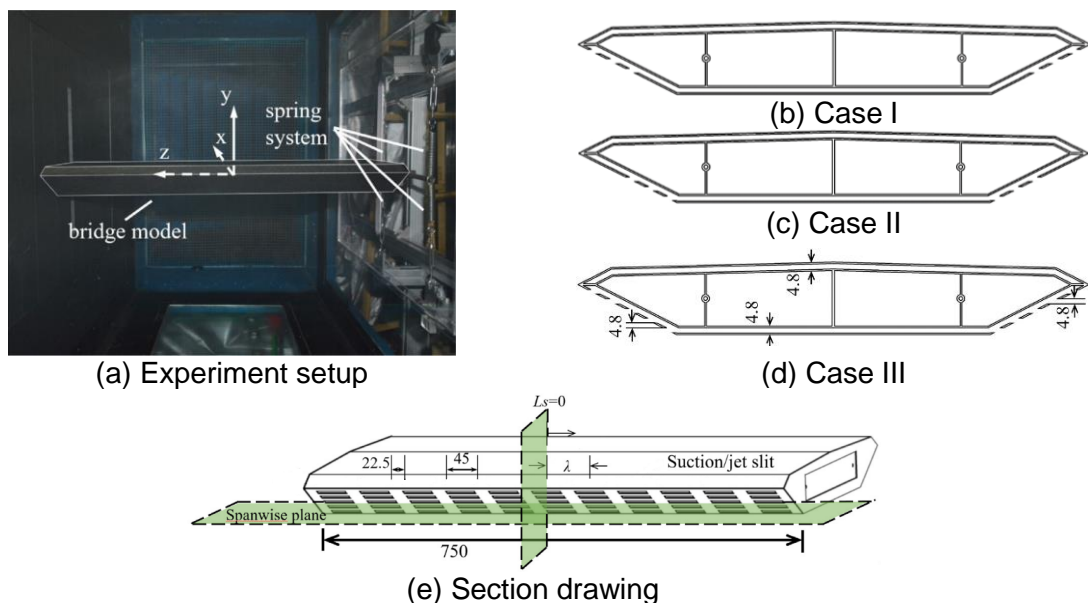


Figure 1: Experiment setup and layout chart of slits, unit: mm.

In this paper, we design a new control method, i.e., self-issuing jets, on the girder to change the flow field around the structure. The control effect on the VIVs is investigated through Particle Image Velocimetry instruments (PIV). The result shows that this method could suppress the response and decrease the length of the lock-in region, the shedding vortices is weakened by passive jets. At aspect of wake flow-field, the secondary instability was triggered by the interval arranged jets. The Mode-B stream-wise vortices were found at the span-wise laser plane along the tailing edge of bridge model. The flutter stability of the bridge with self-issuing jets was also be investigated and the critical velocity was less badly affected.

1. Larsen, A., Eisdahl, S., Andersen, J.E., Vejrum, T. (2000). Storebbælt suspension bridge vortex shedding excitation and mitigation by guide vanes. *Journal of Winds Engineering and Industrial Aerodynamics*, 88(2), 283-296.

FLUTTER SUPPRESSION USING MAGNETORHEOLOGICAL DAMPERS AND A LMI-BASED CONTROLLER

Pedro H. Foster Stangarlin¹, Frederico A. Ribeiro², Ruxandra M. Botez³ and Douglas D. Bueno⁴

^{1,2,4}*São Paulo State University (UNESP), School of Engineering of Ilha Solteira. Av. Brasil, 56, Ilha Solteira, SP, Brazil.*

³*École de Technologie Supérieure (ÉTS), LARCASE Laboratory of Research in Active Controls Avionics and Aeroservoelasticity. Montreal, QC, Canada.*

³Corresponding author: ruxandra.botez@etsmtl.ca

Abstract

Flutter is a dynamic phenomenon that may cause catastrophic failure in aircraft structural integrity. It is typically investigated when designing an aerial vehicle to ensure that is free of this instability within the flight envelope. However, active controllers have been investigated by the scientific community mainly due to the use of new materials employed to develop lighter and higher performance systems. In this context, this article investigates the combination of a magnetorheological damper with a Linear Matrix Inequality-based controller to design a semi-active control system. It is used to model the flow around the three degrees of freedom airfoil Unsteady aerodynamics formulation of Theodorsen. The Clipped Optimal approach is used to turn on/off the controller and a control gain is used to compute the electrical voltage to be applied on the magnetorheological device. The results show that this approach is a convenient strategy for designing semi-active controllers for flutter suppression.

Keyword: Flutter Suppression, Magnetorheological Damper, Clipped Optimal, Linear Matrix Inequality.

1 Introduction

“Flutter” is an unstable self-excited oscillatory phenomenon in which aerodynamic forces and structural characteristics of a flexible system generate increasing amplitude over time in a particular flight condition (Bisplinghoff et al. 1996, Wright & Cooper 2007). It is carefully investigated during new aerial vehicle development for designing safe flight aircraft, as required by aeronautical certification agencies.

Different strategies can be employed for designing an aircraft flutter free. Typically, a classical design considers mass addition and incremental stiffness to ensure a safe flight envelope. However, the use of new type of materials, and the interest of designing more efficient, lighter and higher performance systems, generates more flexible aircraft. In this context, the use of active and semi-active controllers for flutter suppression has been widely investigated in the literature, as described by Livne (2017).

Instead of using conventional actuators, a particular class of devices with rheological fluids has been shown as a convenient option for different engineering applications due to its high

capacity of energy dissipation and hysteresis behavior. Magnetorheological dampers (MRD) are semi-active devices that provide energy dissipation through changing the resistance of the fluid by turning it into a semi-solid as a function of the electrical current or electrical voltage, inputs (Jansen & Dyke 2000). MRDs have been employed in different applications involving vibration control, such as vehicle suspensions, bridges and buildings for seismic protection, among others (Spencer Jr. et al. 1996, Dyke et al. 1998). However, there is a limited number of works in literature investigating its use for flutter suppression.

In context, this work proposes the use of a magnetorheological damper combined with a feedback-based algorithm to design a semi-active controller for flutter suppression. A controller gain is computed by solving a Linear Matrix Inequality (LMI), which allows one to obtain a control input proportional to the system's state vector. Convex optimization is employed to achieve the LMI feasibility. The Clipped Optimal approach proposed by Dyke et al. (1996), is used to turn on and off the LMI controller. The control force is applied to the three degrees of freedom airfoil by the MRD. The feedback control input is used to compute the electrical voltage applied to the MRD to generate the dissipative force. The results show that this combined approach provides an efficient strategy for designing a semi-active system for flutter suppression.

2 Methodology

The aeroelastic equation of motion for the 3DOF airfoil illustrated in Fig. 1 is given by Eq. (1), where, \mathbf{M} is the mass matrix, \mathbf{B} is the damping matrix, \mathbf{K} is the stiffness matrix, $\mathbf{u}(t) = \{h(t) \ \theta(t) \ \beta(t)\}^T$ is the displacement vector, $q = \frac{1}{2}\rho V^2$ is the dynamic pressure, \mathbf{Q} the unsteady aerodynamic matrix defined by Theodorsen (1935) for each reduced frequency $k = \frac{\omega b}{V}$. V is the airspeed, ρ is the air density and b is the semi chord, $h(t)$ is the plunge, $\theta(t)$ is the pitch and $\beta(t)$ is the control surface rotation. $\mathbf{F}_{mrd}(t)$ is the MRD force vector.

$$\mathbf{M}\ddot{\mathbf{u}}(t) + \mathbf{B}\dot{\mathbf{u}}(t) + \mathbf{K}\mathbf{u}(t) + \mathbf{F}_{mrd}(t) = q\mathbf{Q}(k)\mathbf{u}(t) \quad (1)$$

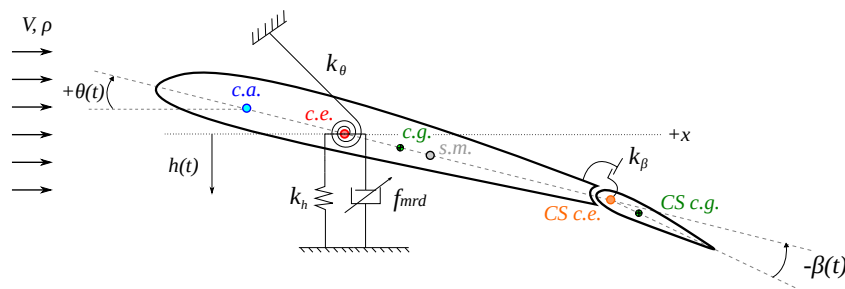


Figure 1: 3DOF system illustration

Theodorsen's matrix $\mathbf{Q}(k)$ can not directly be written in the time domain to obtain the system's state space representation. Therefore, an approximation method can be used to obtain it. In this work, the Least Square-based method proposed by Roger (1977) is used. The

unsteady aerodynamic matrix is then rewritten by:

$$\mathbf{Q}_{app}(s) = \mathbf{Q}_0 + \mathbf{Q}_1 s \left(\frac{b}{V} \right) + \mathbf{Q}_2 s^2 \left(\frac{b}{V} \right)^2 + \sum_{j=1}^{n_{lag}} \mathbf{Q}_{(j+2)} \left(\frac{s}{s + \frac{V}{b} \gamma_j} \right) \quad (2)$$

where the matrices \mathbf{Q}_0 , \mathbf{Q}_1 , \mathbf{Q}_2 and \mathbf{Q}_{j+2} , $j = 1, \dots, n_{lag}$ are calculated using a Least Square algorithm. Each j -th γ_j lag parameter is computed by an empirical equation (Eq. 3) proposed by Chen (2000), which considers the maximum reduced frequency k_{max} and the desired number n_{lag} of lag terms defined by the analyst.

$$\gamma_j = 1,7 k_{max} \left(\frac{j}{n_{lag} + 1} \right)^2 \quad (3)$$

The state matrix space system representation of Eq. (1) is given by:

$$\dot{\mathbf{x}}(t) = \mathbf{A}\mathbf{x}(t) + \mathbf{B}_c \mathbf{F}_{mrd}(t) \quad (4)$$

where \mathbf{A} is the aeroelastic dynamic matrix, $\mathbf{B}_c = [\mathbf{M}_a \mathbf{B}_0 \mathbf{0}]^T$ is the input matrix, and $\mathbf{x} = \{\dot{\mathbf{u}} \ \mathbf{u} \ \mathbf{u}_{a1} \ \dots \ \mathbf{u}_{an_{lag}}\}^T$ is the state vector, in which $\mathbf{u}_{a(j)}$ is the j -th vector of lag states (see Appendix A for details). $\mathbf{B}_0 = \{1 \ 0 \ 0\}^T$, $\mathbf{0}$ is a matrix of zeros $n(1 + n_{lag}) \times 1$, and n is the number of degrees of freedom.

The MRD force is described by Eq. (5), as discussed by Spencer Jr. et al. (1996). It is a modification of the Bouc-Wen model (Spencer Jr. et al. 1996), which exhibits high adherence to the experimental data, especially for hysteresis behavior observed in the force $f_{mrd}^h(t)$. This force is written in terms of the relative speed between the dampers end connectors. In this case, it is assumed that the MRD force is connected to the airfoil in the plunge degree of freedom, such that $\mathbf{F}_{mrd} = \{f_{mrd}^h \ 0 \ 0\}^T$, and because of this connection, f_{mrd}^h depends on the plunge velocity $\dot{h}(t)$, i.e.,

$$f_{mrd}^h(t) = c_1^{mrd} \dot{y}(t) + k_1^{mrd} [h(t) - h_0] \quad (5)$$

where

$$\dot{y}(t) = \frac{1}{(c_0^{mrd} + c_1^{mrd})} \left[\alpha^{mrd} z(t) + c_0^{mrd} \dot{h}(t) + c_0^{mrd} (h(t) - y(t)) \right]$$

$$\dot{z} = -\gamma^{mrd} |\dot{h}(t) - \dot{y}(t)| z |z|^{N-1} - \beta^{mrd} [\dot{h}(t) - \dot{y}(t)] |z|^N + A^{mrd} [\dot{h}(t) - \dot{y}(t)]$$

where $z(t)$ is defined as an evolutionary variable, $y(t)$ is an internal displacement, α is the stiffness of the damping force associated with the variable z , k_0 and k_1 are the stiffness springs, c_0 and c_1 are the viscous damping coefficients, h_0 is the initial plunge displacement. β , γ , A and N are hysteresis control parameters.

The MRD force is changed by applying electrical voltage E ; the influence of E on the MRD force is introduced by changing the parameters α^{mrd} , c_1^{mrd} and c_0^{mrd} using the following polynomial equations (Spencer Jr. et al. 1996):

$$\begin{aligned} \alpha^{mrd} &= \alpha_a + \alpha_b u_{BW} \\ c_1^{mrd} &= c_{1a} + c_{1b} u_{BW} \\ c_0^{mrd} &= c_{0a} + c_{0b} u_{BW} \\ \dot{u}_{BW} &= -\eta(u_{BW} - E) \end{aligned} \quad (6)$$

where u_{BW} , c_{1b} , c_{0b} and η are adjustable parameters (Spencer Jr. et al. 1996).

To design the controller, the MRD force f_{mrd} is initially replaced by a classical feedback control force f_c given by

$$f_c(t) = -\mathbf{G}\mathbf{x}(t) \quad (7)$$

where the matrix of gain $\mathbf{G}^{1 \times n(2+n_{lag})}$ is computed by solving the Lyapunov inequality

$$\mathbf{X}\mathbf{A}^T - \mathbf{G}_x^T \mathbf{B}_m^T + \mathbf{A}\mathbf{X} - \mathbf{B}_m \mathbf{G}_x < \mathbf{0} \quad (8)$$

for which $\mathbf{G} = \mathbf{G}_x \mathbf{X}^{-1}$. This inequality is obtained by considering a negative derivative of the Lyapunov closed-loop energy function $V_L = \mathbf{x}^T \mathbf{P} \mathbf{x}$, where $\mathbf{P} = \mathbf{X}^{-1}$, and details are found in Bueno et al. (2014). After computing the gain \mathbf{G} , the force f_c is computed for each time instant, and the MRD force is obtained according to the Clipped-Optimal control method proposed by Dyke et al. (1996).

The Clipped-Optimal (CO) control method is used to compute the electrical voltage E for its application to the MRD force as follows

$$E(t) = E_{max} \mathcal{H}\{[f_c(t) - f_{mrd}(t)] f_{mrd}(t)\} \quad (9)$$

where $\mathcal{H}(\cdot)$ is the Heaviside step function, and E_{max} is a predefined maximum electrical voltage. The idea behind the CO control is: if the MRD provides the desired optimal force, i.e., $f_{mrd}(t) = f_c(t)$, the electrical voltage E should remain at the present level. If the magnitude of the force produced by the damper is smaller than the magnitude of the desired optimal force, and the multiplication $f_{mrd}(t)f_c(t)$ is positive, the electrical voltage applied to the magnetorheological device is increased to the maximum level. Otherwise, the commanded voltage is set to zero (Dyke et al. 1996).

3 Results and Discussions

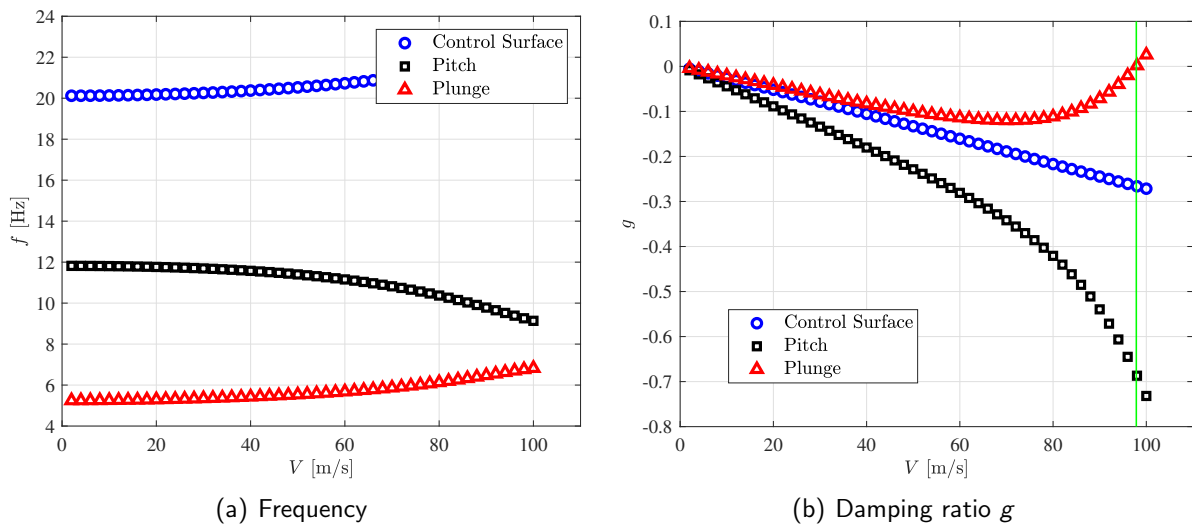
The proposed approach is evaluated by considering the three DOF airfoil shown in Figure 1. Its physical and geometrical properties are shown in table 1, Appendix A. The flutter speed is calculated by solving the associated eigenvalue problem for the open loop system. The V - g - f diagram is used to show the results. Figures 2 (a) and (b) show respectively the aeroelastic frequencies f and damping ratios g variations with airspeeds, and a vertical line is used to indicate the flutter speed (see Fig. 2 b). Flutter is defined by an unstable plunge mode for $V_f = 97,8563$ m/s.

The LMI-based controller gain is computed for two different cases. The first one corresponds to the flutter condition, which considers a marginally stable dynamic system. The second case comprises unstable condition defined at $V = 100$ m/s (i.e., beyond the flutter speed) to evaluate the MRD force needed to expand the flight envelope.

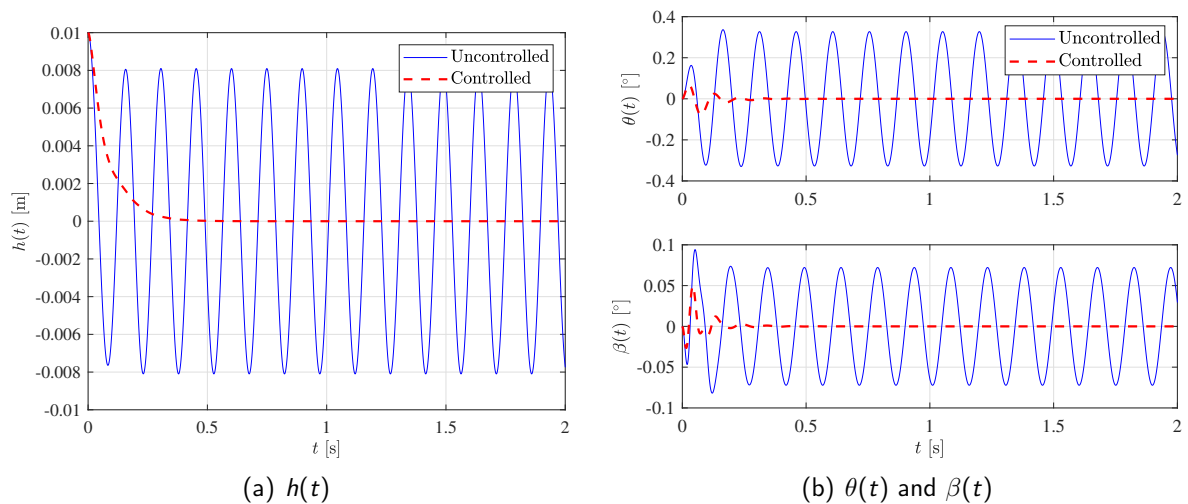
3.1 Marginally Stable System

Figures 3(a) and 3(b) show the airfoil time responses for the uncontrolled and controlled configurations when $V = V_f$. It is possible to note that the MRD suppresses the system's oscillation. As seen on Fig. 4, the system achieves its equilibrium condition quickly, in less than one second. Figures 4(a) shows a comparison between the classical control force (computed by Eq. 7) and

Figure 2: V-g-f Diagram for the Open Loop System.



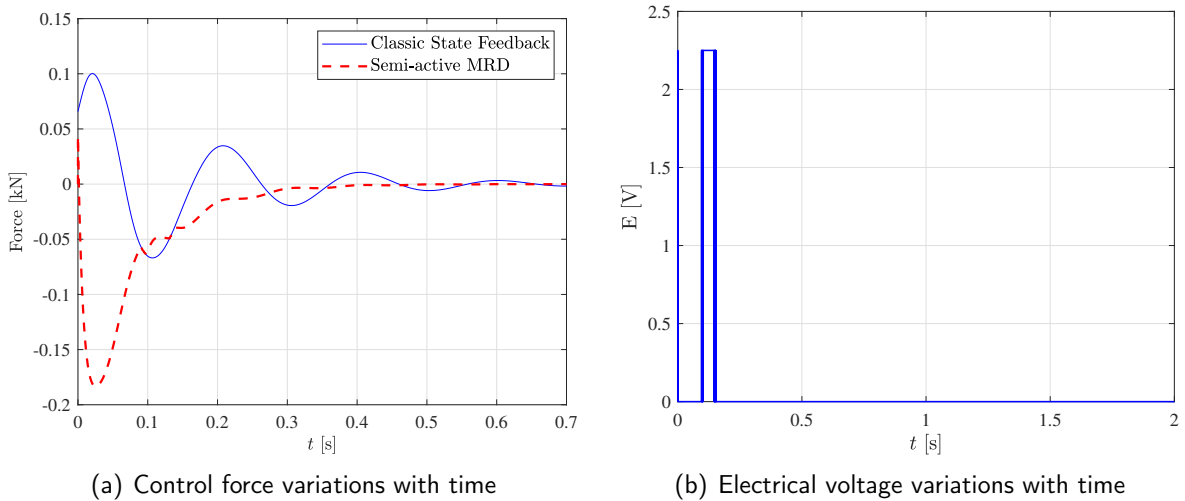
the controller force applied by the MRD (i.e., $f_{mrd}(t)$) over time. They are of equivalent order but different shapes during controller action. In addition, Figure 4(b) presents the electrical voltage applied to the magnetorheological device (MRD) (see the parameters in Table 2, Appendix A). Note that the controller is switched “on” at the first time instant, then “off” for few seconds, until it is switched “on” again (see the rectangular signal around 0.1 seconds).

 Figure 3: Time responses for the uncontrolled and controlled system for $V = V_f$.


3.2 Unstable System

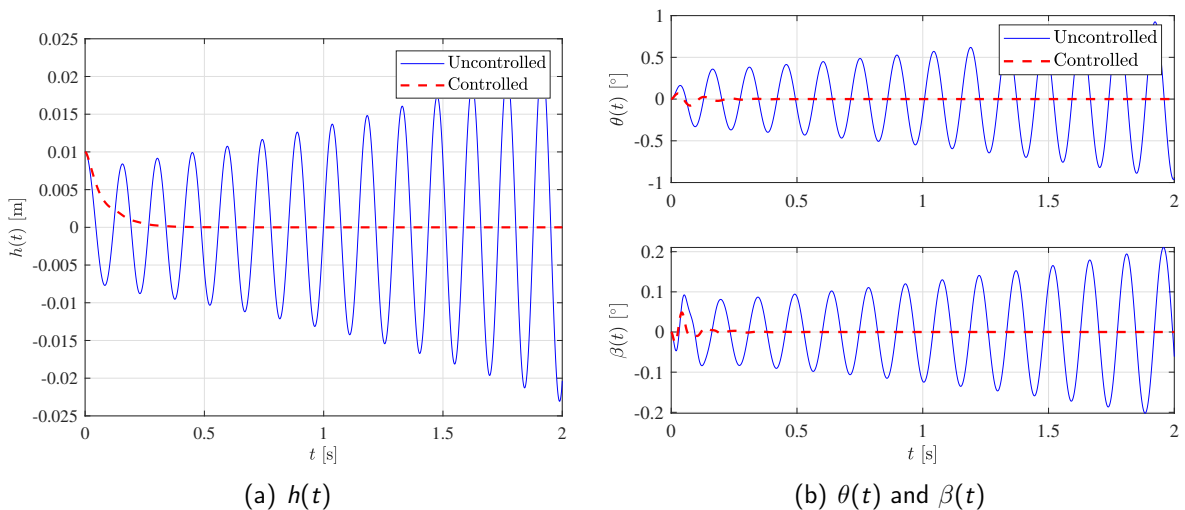
The controller is designed for $V_f < V = 100$ m/s, which means that an incremental airspeed is considered in comparison with respect to the flutter condition. Figure 5 shows the uncontrolled

Figure 4: Classical and semi-active control forces and electrical voltage applied to the magnetorheological device.



(and unstable) plunge response which is suppressed by using the MRD. Note that for this case, a second controller gain was computed also by solving the LMI-based problem. Figure 5 additionally shows the pitch θ and control surface β rotation over time, and it is thus observed that the controller stabilizes the system. These results show that the hysteretic damping provided by the MRD can properly dissipate the energy of motion during flight. Thus, it suggests that this type of device is a good option for expanding the flight envelope.

Figure 5: Time responses for the uncontrolled and controlled systems for $V > V_f$.



4 FINAL REMARKS

This article discussed an application of semi-active flutter suppression combining the use of a magnetorheological damper (MRD) with a feedback controller. A convex optimization problem was solved for computing a LMI-based gain, which allowed the design of a classical controller using state feedback. However, instead of applying that classical force, it the Clipped-Optimal approach was used to switch on/off the magnetorheological device by applying electrical voltage. The controlled system's responses were computed by considering the dissipative damper force acting on its motion. Additionally, the CO approach was used to apply electrical voltage for properly changing the MR dissipation characteristics.

The results showed that electrical voltage was applied on the MRD just for few seconds due to its high capacity of dissipation. However, the controller's performance was found to be higher if this semi-active approach was considered (in comparison with the classical feedback controller) once the system achieved the equilibrium condition with fewer oscillations. This work demonstrated that semi-active controller designed by combining MR with LMI properties can stabilize aeroelastic systems, thus, this controller was a good choice for flutter suppression.

Acknowledgements

The first and last authors thanks the São Paulo Research Foundation (FAPESP), Grant numbers 2016/20617-0 and 18/25194-6 for funding this research.

References

- Bisplinghoff, H. A., Raymond, L. & Halfman, R. L. (1996), *Aeroelasticity*, Dover Publications, INC.
- Bueno, D. D., Góes, L. C. S. & Gonçalves, P. J. P. (2014), 'Control of limit cycle oscillation in a three degrees of freedom airfoil section using fuzzy takagi-sugeno modeling', *Shock and Vibration* pp. 1–12.
- Chen, P. C. (2000), 'Damping perturbation method for flutter solution: The g-method', *AIAA Journal* **38**, 1519–1524.
- Dyke, S. J., Spencer, B. F., Sain, M. K. & Carlson, J. D. (1996), 'Modeling and control of magnetorheological dampers for seismic response reduction', *Smart Materials and Structures* **5**, 565–575.
- Dyke, S. J., Spencer Jr., B. F., Sain, M. . K. & Carlson, J. D. (1998), 'An experimental study of mr dampers for seismic protection', *Smart Materials and Structures: Special Issue on Large Civil Structures* **7**(5), 693–703.
- Jansen, L. M. & Dyke, S. J. (2000), 'Semi-active control strategies for mr dampers: A comparative study', *ASCE Journal of Engineering Mechanics* **126**(8), 795–803.

- Livne, E. (2017), 'Aircraft active flutter suppression: State of the art and technology maturation needs', *Journal of Aircraft* **55**(1), 410–452.
 URL: <https://doi.org/10.2514/1.C034442>
- Roger, K. (1977), 'Airplane math modelling methods for active control design', *AGARD Conference Proceeding* **9**, 4.1–4.11.
- Spencer Jr., B. F., Dyke, S. J., Sain, M. . K. & Carlson, J. D. (1996), 'Phenomenological model of a magnetorheological damper', *ASCE Journal of Engineering Mechanics* **123**(1-23), 230–238.
- Theodorsen, T. (1935), 'General theory of aerodynamic instability and the mechanism of flutter', *NACA Rept. 496* **13**, 374–387.
- Wright, J. & Cooper, J. (2007), *Introduction to Aircraft Aeroelasticity and Loads*, AIAA education series, John Wiley & Sons.

Appendix A) System Properties and Parameters

This appendix presents the physical and geometrical properties used to carry out the numerical simulations. The airfoil matrices are also shown herein, and complementary information can be found in [Theodorsen \(1935\)](#) and [Bueno et al. \(2014\)](#).

The airfoil properties are shown in Table 1, and Table 2 shows the parameters for the magnetorheological damper.

Table 1: Three DOF typical section airfoil physical and geometric properties. See [Theodorsen \(1935\)](#) for details.

Parameter	Value
airfoil semi-chord	$b = 0.7 [m]$
airfoil mass	$m = 20 [kg]$
plunge uncoupled frequency	$f_h = 5.5 [Hz]$
pitch uncoupled frequency	$f_\theta = 11 [Hz]$
surface control (CS) uncoupled frequency	$f_\beta = 20 [Hz]$
elastic center (e.c.) measured from semi-chord (s.m.)	$a = -0.4$
location of CS e.c. measured from s.m	$c = 0.6$
center of gravity (c.g.) from e.c.	$x_\theta = 0.2$
CS c.g coordinate from c.e	$x_\beta = 0.0125$
airfoil radius of gyration referred a	$r = (0.25)^{1/2}$
CS radius of gyration referred to the hinge a	$r = (0.00625)^{1/2}$
air density	$\rho = 1.225 [kg/m^3]$

Table 2: MRD parameter.

Parameter	Value
k_1	5000 [N/m]
c_{0a}	2100 [Ns/m]
c_{0b}	350 [Ns/m]
α_a	1.4×10^4
α_b	6.95×10^4
η	190 [s ⁻¹]
N	2
x_0	0.0

The dynamic matrix \mathbf{A} and the matrices of aeroelastic mass \mathbf{M}_a , damping \mathbf{B}_a and stiffness \mathbf{K}_a are respectively given by

$$\mathbf{A} = \begin{bmatrix} -\mathbf{M}_a \mathbf{B}_a & -\mathbf{M}_a \mathbf{K}_a & q \mathbf{Q}_3 & \cdots & q \mathbf{Q}_{2+n_{lag}} \\ \mathbf{I} & \mathbf{0} & \mathbf{0} & \cdots & \mathbf{0} \\ \mathbf{I} & \mathbf{0} & -\frac{V}{b} \gamma_1 \mathbf{I} & \cdots & \mathbf{0} \\ \vdots & \vdots & \mathbf{0} & \ddots & \cdots \\ \mathbf{I} & \mathbf{0} & \vdots & \cdots & -\frac{V}{b} \gamma_{n_{lag}} \mathbf{I} \end{bmatrix} \quad (10)$$

$$\mathbf{M}_a = \mathbf{M} - q \frac{b^2}{V^2} \mathbf{Q}_2 \quad (11)$$

$$\mathbf{B}_a = \mathbf{B} - q \frac{b}{V} \mathbf{Q}_1 \quad (12)$$

$$\mathbf{K}_a = \mathbf{K} - q \mathbf{Q}_0 \quad (13)$$

where \mathbf{I} is the identity matrix $n \times n$ and $\mathbf{0}$ is a $n \times n$ square matrix of zeros. Each γ_j was computed by Eq. (3) for $n_{lag} = 7$.

Passive alleviation of static and dynamic loads via aeroelastic tailoring of a composite wing

Nicolò Fabbiane¹, François-Xavier Irisarri² and Arnaud Lepage¹

¹ DAAA, ONERA – Université Paris-Saclay, 92322 Châtillon, France

² DMAS, ONERA – Université Paris-Saclay, 92322 Châtillon, France

Abstract

Composite materials allow to tailor the material elastic properties in the structures. In aeroelasticity, this opens up the possibility to passively enhance the coupled aerostructural characteristics. In this work, the design of a composite wing is addressed with the aim to alleviate static and dynamic aeroelastic loads; these two objectives are quantified by the root-bending-moment in a high load-factor condition and the deformation amplitude of the wing under gust. A two-step approach of the optimal design of the structure is adopted. A Pareto front is computed via an aeroelastic model of the wing; the aerodynamic loads are modelled, depending on the load-case, either via the DLM or the RANS equations. The best-compromise design is chosen via a criterion based on the jig-shape and, finally, the stacking-sequences are computed via a specialised evolutionary algorithm.

Keywords: aeroelastic tailoring, passive load-alleviation, gust response, composite materials, bi-objective optimisation.

1 Introduction

Aeroelastic-tailoring can be defined as “the embodiment of directional stiffness into an aircraft structural design to control aeroelastic deformation, static or dynamic, in such a fashion as to affect the aerodynamic and structural performance of that aircraft in a beneficial way” (Shirk et al., 1986). The consolidation of composite material technologies spread even further the design capabilities in this direction. Several studies have been dedicated to this topic in the last decades (see Jutte and Stanford, 2014, for an extended and exhaustive review), each one focusing on different aspects of the problem: optimisation to static loads (Dillinger, 2014), blending constraints (Macquart et al., 2016; Bordogna et al., 2020), and gust response (Rajpal et al., 2019), to cite some of the most recent developments.

This work aims to evaluate the potential of aeroelastic-tailoring by conceiving a composite wing to be tested by means of wind-tunnel experiments, as a part of a larger project that sees the collaboration of ONERA and DLR. The construction of two wind-tunnel demonstrators – one for each institution – is previewed with the general objective to passively alleviate gust-loads.

The design of the ONERA model is here presented. After a brief introduction to the wing-geometry, optimisation variables, and parameters (Section 2), the optimisation procedure and the sizing load-cases are discussed (Section 3). The optimal design-points are presented in the form of a Pareto-front and, between them, the final design is chosen (Section 4). Finally, the stacking-sequence is computed (Section 5), leading to manufacturing.

Table 1 – Materials' properties.

	$E_{(1)}$ (GPa)	$E_{(2)}$ (GPa)	$\nu_{(12)}$	G (GPa)	ρ kg/m ³	h_{ply} mm	ϵ_t mε	ϵ_c mε	ϵ_s mε
ply	31.3	5.34	0.29	1.90	1727	0.17	30	20	20
foam	0.095	–	0.30	0.014	80				

2 Geometry and structural parameters

The geometry is based on the Common Research Model (NASA CRM); the flight-shape used in the model-design is obtained by scaling the CRM geometry to a root-to-tip span equal to 550 mm, resulting in a root chord and reference surface of approximately 248 mm and 729 cm².

The structural configuration of the wing is given by two composite skins – upper and lower –, filled by a polymeric foam; the simplicity of this configuration has been chosen to ease the manufacturing process, due to the small size of the model. The material of choice for the wing-skin is a glass-fiber/epoxy composite with a fiber volume-fraction equal to 0.39; a standard low-density polymeric foam is instead adopted for the filling, see Table 1. The uni-directional composite ply is considered as an orthotropic material with its first principal direction oriented as the fibers; the thickness of a single ply is 0.17 mm and it can withstand deformations in tension (ϵ_t), compression (ϵ_c), and shear (ϵ_s) up to 30 mε, 20 mε, and 20 mε respectively.

A finite-element (FE) model of the wing structure is created in NASTRAN (MSC Software, 2017) by discretising the composite-skins by quadrangular plate-elements and the internal foam by hexahedral volume-elements. A clamp boundary-condition is considered at the root section.

2.1 Design variables and parameters

Laminated composite plates are obtained by stacking different composite plies that, in the general framework, could have their own properties and thickness, as well as their own orientation. For this study, a single prototype ply is considered and the different stacks will only differ by the number and the orientation of the plies. The order in which the different plies are stacked is called *stacking-sequence*, that drives the mechanical behaviour of the laminate-plate. The latter can be locally expressed in the form of the constitutive law,

$$\begin{bmatrix} \mathbf{F} \\ \mathbf{M} \end{bmatrix} = \begin{bmatrix} \mathbf{A} & \mathbf{B} \\ \mathbf{B} & \mathbf{D} \end{bmatrix} \begin{bmatrix} \boldsymbol{\epsilon} \\ \boldsymbol{\kappa} \end{bmatrix} \quad (1)$$

where \mathbf{F} and \mathbf{M} are the local in-plane and bending loads applied to the composite stack and $\boldsymbol{\epsilon}$ and $\boldsymbol{\kappa}$ the local strains and curvatures of the plate (Tsai and Hahn, 1980). The relation between load and deformation is given by the stiffness matrix. This can be divided in: (i) \mathbf{A} that describes the *membrane* behavior, i.e. the direct link between \mathbf{F} and $\boldsymbol{\epsilon}$; (ii) \mathbf{D} that describes the *bending* behaviour, i.e. the direct link between \mathbf{M} and $\boldsymbol{\kappa}$; (iii) \mathbf{B} that couples the two behaviours. All these matrices are a function of the stacking sequence; in particular, $\mathbf{B} = \mathbf{0}$ when a symmetric stack is considered, as it is the case in this study.

The natural choice for the design variables would be the stacking-sequence itself. However, this poses some technical challenges, namely an optimisation with an undetermined number

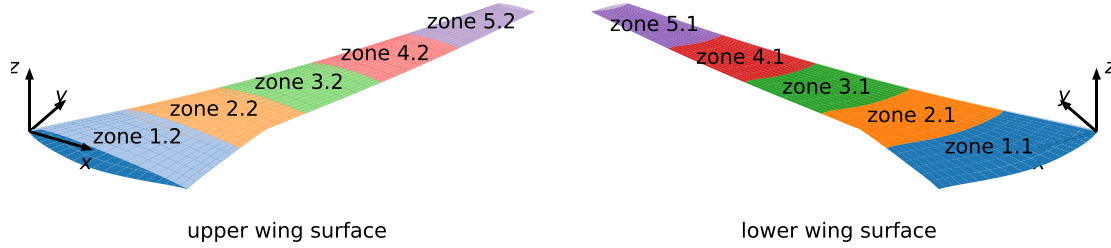


Figure 1 – Wing-geometry and regions for the composite-optimisation.

of variables and a non-smooth description of the functions of interest. A solution to this is given by the *lamination parameters* (Miki and Sugiyama, 1993), i.e. a parameterisation of the stiffness matrix in Equation (1) that is based on the homogenisation of the composite stack. The local properties of the material are hence described by the relations,

$$\begin{aligned} \mathbf{A} &= h \left(\Gamma_0 + \Gamma_1 \xi_1^A + \Gamma_2 \xi_2^A + \Gamma_3 \xi_3^A + \Gamma_4 \xi_4^A \right) \\ \mathbf{D} &= \frac{h^3}{12} \left(\Gamma_0 + \Gamma_1 \xi_1^D + \Gamma_2 \xi_2^D + \Gamma_3 \xi_3^D + \Gamma_4 \xi_4^D \right) \end{aligned} \quad (2)$$

where $\xi_{1,2,3,4}^A$ and $\xi_{1,2,3,4}^D$ are the lamination parameters for the membrane stiffness-matrix \mathbf{A} and bending stiffness-matrix \mathbf{D} , h is the total thickness of the laminate plate, and Γ_i are the Tsai-Pagano material parameters of the composite ply (Tsai and Pagano, 1968).

The design variables are hence defined as the total thickness h and the 8 lamination parameters $\xi_{1,2,3,4}^A, \xi_{1,2,3,4}^D$; the homogenised properties of the laminated plate are considered uniform in each of the 10 design-zones in Figure 1, resulting in a total of $(1 + 8) \times 10 = 90$ design variables. To ensure that the solutions are representative of actual laminates, compatibility conditions have to be enforced between the membrane and the bending lamination parameters as additional constraints to the optimisation (Diaconu and Sekine, 2004). Lower and upper limits are enforced on the laminate thickness for manufacturing and geometrical reasons: the total thickness h is hence bounded between 1.70 mm (10 plies) and 3.74 mm (22 plies).

3 Design procedure

The goal of the design is to alleviate the static and dynamic loads on the wing, while respecting a prescribed flight-shape; this leads to specific choices on load-cases and optimisation strategy.

3.1 Load-cases and constraints

The considered load-cases span the typical sizing conditions for the aeronautic design (Table 2): a nominal cruise, a high load-factor condition and the response to gusts of variable time-scale. The asymptotic flow conditions are based on the ones expected in the wind-tunnel during the experiments; the Mach number M is chosen to match the design condition for the CRM model and the other quantities are computed based on the hypothesis of an isentropic flow. Similarly, harmonic gusts are considered due to limitations of the experimental gust-generation apparatus.

The loads representing the cruise condition are based on high-fidelity simulations via the in-house ONERA solver elsA (Cambier et al., 2013). The aerodynamic mean-flow is computed

Table 2 – Load-cases and constraints for the design procedure.

	cruise	max-load	gusts
type	static	static	equiv. static
method	RANS solver (rigid flight-shape)	DLM + FE model (aeroelastic trim)	DLM + FE model (aeroelastic response)
flight conditions	$M = 0.85$, $q = 31.95$ kPa, and $U = 276$ m/s $c_L = 0.5$ $c_L = 1.0$ 5 <i>worst</i> cases $Re \approx 4 \times 10^4$ $\Delta\alpha_g = 0.25^\circ$ $\{f_i\}_g = \{40, \dots, 120\}$ Hz		
constraints	$-\epsilon_c/3 < \epsilon_{l,II} < \epsilon_t/3$ and $\epsilon_s^{max} < \epsilon_s/3$		

for the scaled CRM geometry of the wing, here taken as reference flight-shape and the angle-of-attack of the wing have been tuned to match the typical cruise condition of a lift coefficient C_L equal to 0.5. The retrieved pressure field is interpolated on the structural model – more precisely at the center of the plate-elements describing the composite skin – and, then, introduced as a pressure-load (\mathbf{f}_{cruise}). The jig-shape of the wing is updated at each outer iteration of the design loop in order to ensure that the flight-shape is met under the precomputed cruise loads, see Algorithm 1.

The *max-load* case, instead, takes into account the aeroelastic behaviour of the wing in the loads computation. The doublets-lattice-method (DLM) is used as a model for the wing aerodynamic; a flat aerodynamic mesh is generated based on the form in plan of the wing and coupled to the structural FE model via the native tools available in MSC NASTRAN. Thanks to this aeroelastic model, the wing is trimmed, by acting on the angle of attack, to a lift coefficient equal to 1.0; this C_L value is chosen to represent a 2g-maneuver.

The same aeroelastic model is also used in the evaluation of the gust loads. These will be taken into account in the optimisation procedure as equivalent-static-loads (Park, 2011); this method allows to take into account dynamic load-cases as static loads, based on the a dynamic simulation of the dynamic phenomenon of interest. In this work, harmonic gusts are considered: Figures 2a and 2b report the fluctuations of the tip-displacement and the root-bending-moment forced by an harmonic gust of frequency $f = 75$ Hz and amplitude $\Delta\alpha = 0.25^\circ$. From this response, the time \bar{t} that maximises the tip displacement is chosen as sizing state; the full displacement field $\mathbf{x}'(\bar{t})$ is retrieved and the resulting equivalent-static-loads \mathbf{f} are computed via the stiffness matrix of the complete structural model \mathbf{K} as,

$$\mathbf{f} = \mathbf{f}_{cruise} + \mathbf{K} \mathbf{x}'(\bar{t}) \quad (3)$$

where the precomputed cruise-loads \mathbf{f}_{cruise} are added to the fluctuation field. The forces thus calculated return, in a static simulation, a displacement field that will reproduce the dynamically computed gust response around the cruise condition. Only the gusts with the 5 largest tip-displacements are retained for the optimisation procedure, as reported in Figure 2c, where it can be also noticed the change in phase-shift between tip-displacement and root-bending-moment when sliding in frequency.

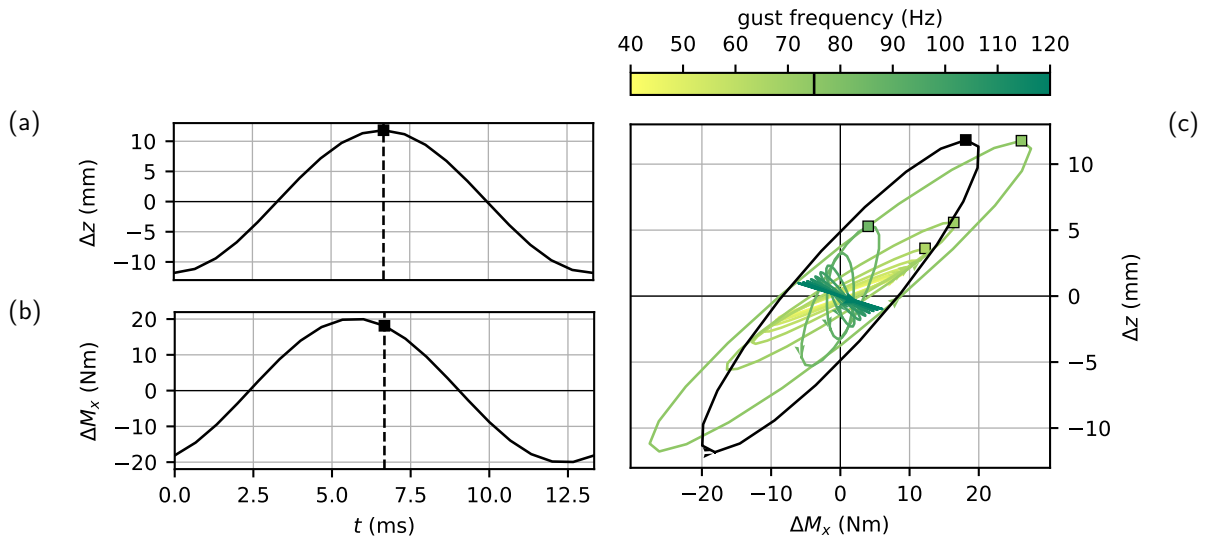


Figure 2 – Harmonic gust response and sizing conditions. (a-b) report the fluctuation of tip-displacement and root-bending-moment for a gust at 75 Hz and amplitude $\Delta\alpha = 0.25^\circ$. The time of maximum tip-displacement is chosen as sizing-condition (black-square). The black line in (c) report the phase-diagram representation of the response in (a-b); the colored lines report the same response for different gust frequencies. The squares indicate the retained sizing-cases.

Strain constraints are enforced; principal and maximal-shear strains are extracted at top and bottom of each plate-element and limited by the values in Table 1, with a safety-factor 3.

3.2 Optimisation strategy

The optimisation loop is reported in Algorithm 1 for the general objective function $J(\mathbf{p}; \boldsymbol{\pi})$, where \mathbf{p} is the vector containing the design variables and $\boldsymbol{\pi}$ the one for the optimisation parameters. At each step of the outer loop, the equivalent static loads are recomputed for the retained gust-cases and fed to the MSC NASTRAN built-in optimiser; once the solution that optimises the general cost function J has been found, the jig-shape is updated via the new stiffness matrix. This loop is repeated N times; in the last M outer steps the thickness of the laminate-plates is fixed to an integer multiple of $2 h_{ply}$ and only the lamination parameters are optimised. This improves, at least from a thickness point-of-view, the feasibility of the identified optimal-solution and it will facilitate the identification of the corresponding stacking-sequence.

The number of external steps N is set to 10, with $M = 3$ rounded-thickness iterations.

4 Pareto front

The choice of the cost function J drives the optimisation; since the aim is the alleviation of both static and dynamic aeroelastic loads on the wing, a bi-objective strategy is pursued. On the static side, the objective is to minimise the root-bending-moment for the max-load case and, by this, to alleviate the structural loads when an off-cruise condition is encountered. On the

Algorithm 1: Design loop when minimising the generic cost function J

```

for  $n \leftarrow 0$  to  $N - 1$  do
    Collect the equivalent-static-loads  $\{\mathbf{f}_i\}_g$  for the harmonic gust cases  $\{f_i\}_g$ 
    forall  $f_i \in \{f_i\}_g$  do
        Solve the forced, aeroelastic problem
        solve:  $\mathbf{M} \ddot{\mathbf{x}}' + (\mathbf{K}^{(n)} + \mathbf{K}_a(f_g; M)) \mathbf{x}' = \Delta \alpha_g \mathbf{B}_g \cos(f_g t / 2\pi)$  [sol 146]
        Compute the equivalent static loads for the time of maximal tip-displacement
        return  $\mathbf{f}_i \leftarrow \mathbf{f}_{cruise} + \mathbf{K}^{(n)} \mathbf{x}'(\bar{t})$  [sol 101]

    if  $n \leq N - M$  then  $\mathbf{p} := \{\{h, \xi_{1,2,3,4}^A, \xi_{1,2,3,4}^D\}_i\}$   $\boldsymbol{\pi} := \{\Gamma_0, \Gamma_1, \Gamma_2, \Gamma_3, \Gamma_4\}$ 
    else
        Round the thickness to the closest integer multiple of  $2h_{ply}$ 
        forall  $h \in \{h_i\}$  do  $h \leftarrow \text{round}(h / (2h_{ply}) 2h_{ply})$ 
        Re-define the design variables to lamination parameters only
         $\mathbf{p} := \{\{\xi_{1,2,3,4}^A, \xi_{1,2,3,4}^D\}_i\}$   $\boldsymbol{\pi} := \{\{h\}_i, \Gamma_0, \Gamma_1, \Gamma_2, \Gamma_3, \Gamma_4\}$ 

        Composite material optimisation
        minimise  $J(\mathbf{p}; \boldsymbol{\pi})$  [sol 200]
         $\mathbf{p}$ 
        loads and constraints: See Table 2 + compatibility conditions for  $\xi_i^{(\cdot)}$ 

        Update jig-shape
         $\mathbf{x}_{jig}^{(n+1)} \leftarrow \mathbf{x}_{cruise} - \mathbf{K}^{(n+1)^{-1}} \mathbf{f}_{cruise}$  [sol 101]
    
```

When NASTRAN is used in a step, the solution type is reported in squared brackets.

dynamic side, an ensemble measurement of the response to the harmonic gusts is considered: this is quantified by the root-mean-squared of the tip-displacement on the retained gust-loads.

Figure 3 reports the Pareto front obtained for these two objective functions. As a first step, the optimal-mass design is computed and used as a reference point (white square). Starting from this solution, the boundaries for the two cost-functions of interest are calculated (vertical and horizontal dashed lines) and, finally, the points that trace the Pareto front. The color-scale indicates the distance in mass from the reference solution.

An ϵ -constrained method is used to identify these points (Haimes et al., 1971); this method consists in a series of consecutive optimisations for one of the cost functions – in this case, the gust response – while the other one – the root-bending-moment – is constrained to be lower than a certain value. In this manner, the Pareto front can be covered by computing the consecutive optimal points for the first (and free) objective, for increasing values of the second (and constrained) one. So that this strategy works, the two cost-functions are required to be antagonist to each other, condition that is verified for this choice of objective functions.

The jig-shape is computed as part of the optimisation procedure; Figure 4a shows how the twist-angle along the span coordinate y changes for the different points of the Pareto front. The distance between flight-shape and jig-shape is an indication of the overall flexibility of the wing, the larger the distance the more flexible the structure. Stiffer solutions are also heavier, and

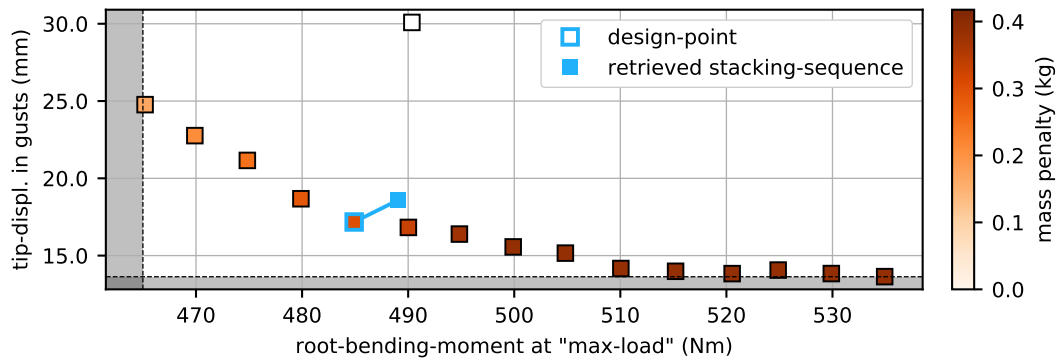


Figure 3 – Pareto front. The color-scale report the mass penalty with respect to the optimal-mass solution, here in white. The light-blue contoured point is the selected design-point, while the light-blue square reports the performance of the retrieved stacking-sequence (see Section 5 and Figure 7). The optimal limits for the two cost functions are reported by the shaded areas.

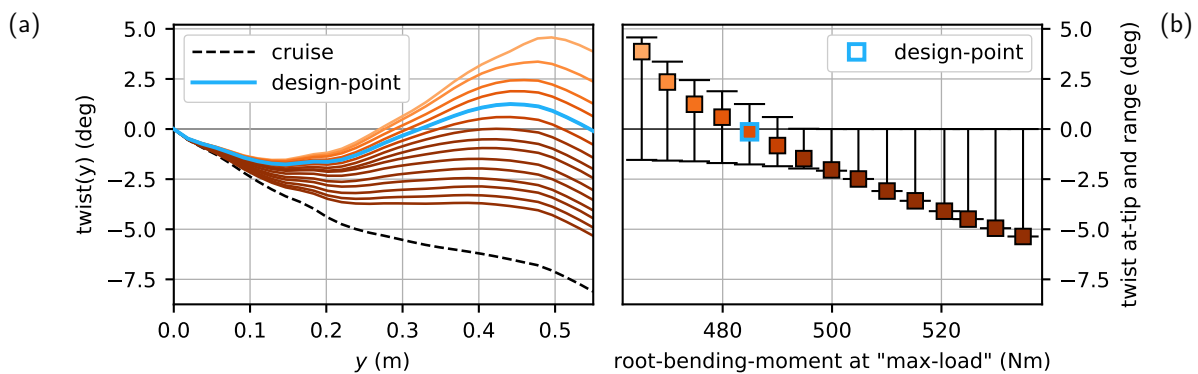


Figure 4 – Design-point criterion. The jig-shape twist is reported in (a) for each point of the Pareto-front in Figure 3. Squares and error-bars in (b) report the twist at the wing-tip and twist-range, as a function of the root-bending-moment.

they are characterised by a larger root-bending-moment; as the flexibility increases, the wing becomes lighter, the root-bending-moment decreases at the cost of an increased gust-response.

4.1 Design-point

In a bi-objective optimisation, the definition of an unique design-point requires to arbitrarily pick a *best compromise* between the two objectives of the Pareto front; in this work, the jig-shape is considered as a criterion for this choice. Figure 4b resumes the information in Figure 4a and shows the twist at the wing-tip and the span-wise twist-range as a function of the root-bending-moment. The *flattest* jig-shape – i.e. the one with the most limited variation of twist angle – can be identified and chosen as the final design-point, light-blue square in Figures 3 and 4b.

The value of the design variables at chosen design-point are visualised in Figure 5; the color-

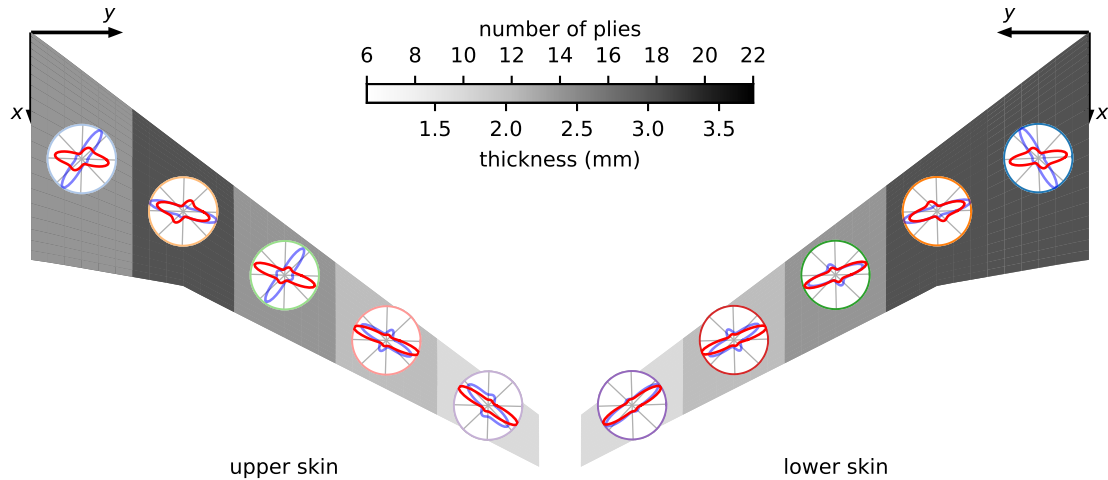


Figure 5 – Design point. The design variables – thickness and composite properties – are reported; the material properties are represented via the polar-plot of the engineering modulus, in red for the membrane-stiffness (\mathbf{A} tensor) and in blue for the flexion one (\mathbf{D} tensor).

scale reports the local thickness of the laminate plate, while the polar-plots are a representation of the in-plane anisotropy of the constitutive law, i.e. how the stiffness of the base-ply is redistributed by the lamination parameters. This visualisation reports the engineering modulus,

$$E(\theta) = \frac{1}{\mathbf{T}(\theta)^{-1} \mathbf{A}^{-1} \mathbf{T}(\theta)} \quad (4)$$

where θ is the polar angle, \mathbf{A} is the membrane tensor, and $\mathbf{T}(\theta)$ is the rotation operator for the deformation vector ϵ (Dillinger, 2014); the red lines report the engineering modulus, while the blue ones a corresponding quantity computed for the flexion tensor \mathbf{D} . The overall membrane-stiffness is oriented as the wing sweep; the misalignment occurs either for the flexion tensor or for marginal redistributions of the membrane-stiffness in the root region.

A further insight in the design process can be given by the constraints, since different wing regions are sized by different load-cases; Figure 6 shows, for each element, which load-case pushes the evaluated strains the closest to the constraint boundary. Two load cases rise from this analysis; the max-load that sizes the root-to-kink region and the 75 Hz gust that interests the rest of the wing. The first one only activates the constraints in a few elements in the kink region. The second one, instead, affects the tip region, but with a constraint far from being activated; this is due to the imposed technological limit of a minimum of 10 plies that clearly oversized the structure for strain constraint. It has to be noticed that this analysis returns only a view on the sizing by strain-constraint and it does not allow an insight of the role played by the load-cases in the objective-functions, of a more *global* nature.

5 Towards manufacturing

Up to this point, the constitutive law describing the laminate plates have been described via the lamination parameters, as introduced in Section 2.1. This description allows for an easier

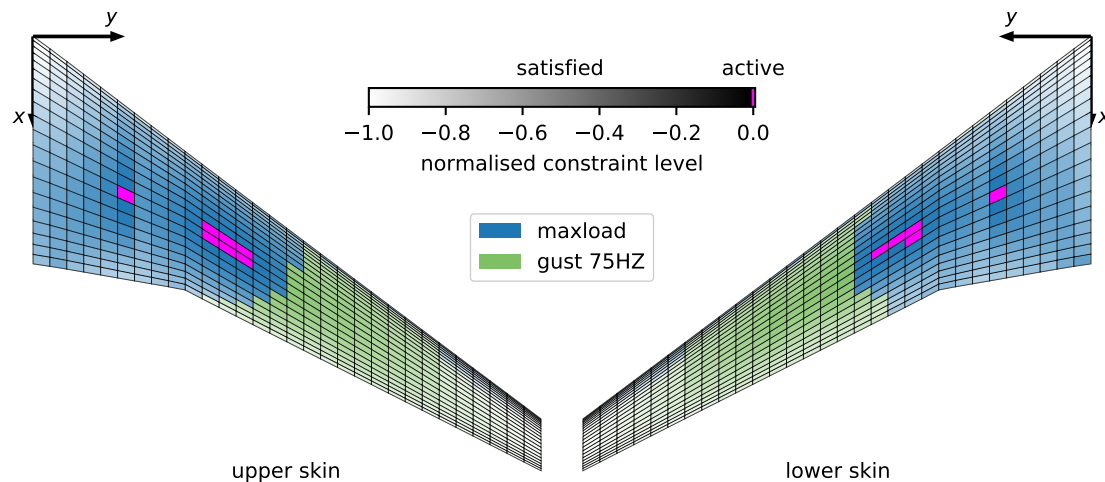


Figure 6 – Sizing load-cases. The color shows, for each element of the model, the load case that pushes the strains the closest to the failure envelope. The saturation indicates the proximity to the boundary; if the constraint is *active* – i.e. it is on the boundary within a normalised constraint value of 5×10^{-3} – the element is colored in magenta.

implementation of the optimisation algorithm but, on the other hand, it does not give the information needed to manufacture the laminate-plate; the stacking-sequence has thus to be recovered from the homogenised description by the lamination parameters. This task – called *inverse problem* – is a crucial point of the design procedure and, most importantly, its solution could be not unique (see for instance Vannucci and Verchery (2001)).

The inverse problem is here solved by a second optimisation via a specialised evolutionary algorithm based on the work by Irisarri et al. (2014); Figure 7 shows the identified stacking-sequence for the upper and lower skin; the gap between the design-point (dashed lines) and the retrieved stacking-sequence (solid lines) is minimised but it is still present. This is mainly due to the manufacturing constraints taken into account in the optimization: (i) ply angles are allowed to take value in the set $\{-60, -45, \dots, 90\}$ and the ply thickness is fixed, which defines a discrete sampling of the design space; (ii) ply-continuity, or *blending*, is imposed between the regions in order to avoid strength-related issues. This significantly reduces the design space of the discrete optimization with respect to the design space of the continuous optimization. Indeed, all laminates are coupled due to the ply-continuity constraints, whereas they are assumed to be independent in the continuous optimization. Recent studies investigated the possibility of taking into account the *blending* problem by introducing additional constraints already at the stage of the lamination-parameter optimisation (e.g. Bordogna et al., 2020).

Lastly, the performance registered by the identified stacking-sequence are reported on the Pareto front in Figure 3 by the red square; the root-bending-moment at max-load is higher as the gust response but it places in the vicinity of the design-point. All the strain constraints are satisfied and the wing results flutter-stable up to Mach 0.95 by a FEM-DLM analysis.

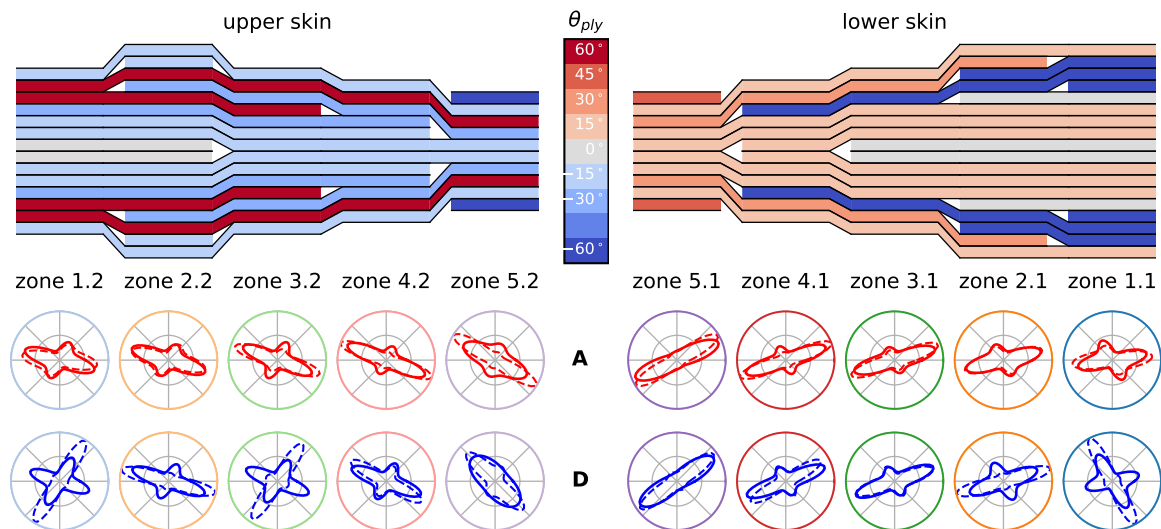


Figure 7 – Stacking-sequence for the upper (left) and the lower (right) skin. The bottom part of the figure shows, for the membrane and flexion tensors **A** and **D**, the deviation between the material properties prescribed by the continuous optimisation (dashed lines) and the properties for the retrieved stacking-sequence (solid lines).

6 Conclusions

A composite wing is successfully designed to alleviate static and dynamic aeroelastic loads. The structure is built from two composite-skins each divided in 5 design-regions, where thickness and laminate properties – parameterised via the lamination-parameters formalism – are optimised.

A bi-objective optimisation is performed; based on the performance in a high-load condition and in gust. The optimisation process takes into account 7 load-cases; the nominal cruise, the high-load condition, and 5 load-cases representing the response to harmonic gusts with different frequencies. Among the multiple optimal-designs identified in the form of a Pareto front, the final design-point is chosen via a criterion on the jig-shape.

As the final step of a bi-step design-strategy, the stacking-sequences are retrieved for the identified design-point via a specialised evolutionary algorithm. The performance and constraints of the discrete, manufacturable solution are verified and compared with the continuous optimum. The here-presented design is currently being manufactured at DLR. Wind-tunnel experiments will take place at ONERA in summer 2020 to validate its performance against the numerical simulations.

Acknowledgements

The authors would like to acknowledge Fabien Huvelin for the RANS simulations in cruise condition and Christophe Blondeau and Marco Tito Bordogna for the fruitful discussions and collaboration. The present work is part of the Common Research Project FIGURE – a collaboration between ONERA and DLR – and ONERA’s joint research project CARACAL.

References

- Bordogna, M.T., Lancelot, P., Bettebghor, D., De Breuker, R., 2020. Static and dynamic aeroelastic tailoring with composite blending and manoeuvre load alleviation. *Struct. Multidisc. Optim.* .
- Cambier, L., Heib, S., Plot, S., 2013. The onera elsa cfd software: input from research and feedback from industry. *Mechanics & Industry* 4(3), 159–174.
- Diaconu, C.G., Sekine, H., 2004. Layup Optimization for Buckling of Laminated Composite Shells with Restricted Layer Angles. *AIAA Journal* 42(10), 2153–2163.
- Dillinger, J.K.S., 2014. Static aeroelastic optimization of composite wings with variable stiffness laminates. Phd thesis, TU Delft, The Netherlands.
- Haimes, Y.V., Lasdon, L.S., Wismer, D.A., 1971. On a bicriterion formation of the problems of integrated system identification and system optimization. *IEEE Trans. Syst., Man, Cybern. Syst.* SMC-1(3), 296–297.
- Irisarri, F.X., Lasseigne, A., Leroy, F.H., Le Riche, R., 2014. Optimal design of laminated composite structures with ply drops using stacking sequence tables. *Composite Structures* 107, 559–569.
- Jutte, C.V., Stanford, B.K., 2014. Aeroelastic Tailoring of Transport Aircraft Wings: State-of-the-Art and Potential Enabling Technologies. Tech. Rep. NASA/TM-2014-218252, NASA.
- Macquart, T., Werter, N., Breuker, R.D., 2016. Aeroelastic design of blended composite structures using lamination parameters. *J. Aircraft* 54(2).
- Miki, M., Sugiyama, Y., 1993. Optimum design of laminated composite plates using lamination parameters. *AIAA J.* 31(5), 921.
- MSC Software, 2017. MSC Nastran 2018 Design Sensitivity and Optimization User's Guide.
- NASA CRM. Common Research Model. Website: page last modified on September 10, 2019. URL <https://commonresearchmodel.larc.nasa.gov/>.
- Park, G.J., 2011. Technical overview of the equivalent static loads method for non-linear static response structural optimization. *Struct. Multidisc. Optim.* 43, 319–337.
- Rajpal, D., Gillebaart, E., Breuker, R.D., 2019. Preliminary aeroelastic design of composite wings subjected to critical gust loads. *Aerosp. Sci. and Tech.* 85, 96–112.
- Shirk, M.H., Hertz, T.J., Weisshaar, T.A., 1986. Aeroelastic tailoring - theory, practice, and promise 23(1).
- Tsai, S.W., Hahn, T.H., 1980. Introduction to composite materials. Technomic Publishing Company, Lancaster, Pennsylvania.
- Tsai, S.W., Pagano, N.J., 1968. Invariant properties of composite materials. In: Tsai, S.W., Halpin, J.C., Pagano, N.J. (editors), *Composite materials workshop*, St. Louis, Missouri, 1967, 233–253. Technomic Publishing Company, Lancaster, Pennsylvania.
- Vannucci, P., Verchery, G., 2001. Stiffness design of laminates using the polar method. *Intl. J. Solids and Struct.* 38(50-51), 9281–9294.

Mitigation of trailing edge flow-induced vibrations of hydrofoil with piezoelectric resonant shunt

L. Pernod^{1,2}, B. Lossouarn¹, J.-A. Astolfi², J.-F. Deü¹ and X. Amandolese¹

¹Laboratoire de Mécanique des Structures et des Systèmes Couplés (LMSSC), Conservatoire national des arts et des métiers (Cnam), 292 Rue Saint-Martin, 75003, Paris, France, laetitia.pernod@lecnam.net

²Institut de Recherche de l'Ecole Navale (IRENav), EA 3634, Ecole Navale, 29240, Brest, France, jacques-andre.astolfi@ecole-navale.fr

Keyword: vortex-induced vibration, resonant piezoelectric shunt, passive vibration damping, water tunnel, analytical model

Marine lifting surfaces may undergo flow-induced vibrations due to fluid sources of excitation that may be random (the turbulent incoming flow) or tonal (the trailing edge vortex shedding). Both type of flow-induced vibrations lead to shorter life cycles due to structural fatigue. Vortex-induced vibrations are also critical to the acoustic performances, since it may result in the phenomenon of hydrofoil singing. As such, this work investigates the potential of the electromechanical coupling inherent to piezoelectric materials for passive vibration damping of a simple hydrofoil subjected to von Kármán vortex shedding from its trailing edge. The hydrofoil is equipped with piezoelectric ceramics connected to a passive inductor in order to act as a piezoelectric resonant shunt.

Hydrodynamic tests have been performed in the IRENav water tunnel for various Reynolds numbers. It shows a significant lock-in phenomenon between the von Kármán vortex shedding and the first torsional mode (Fig. 1). Passive control strategies, using the piezoelectric resonant shunt device, have been tested. An analytical electro-hydroelastic model is also used to better understand and optimize the control strategy.

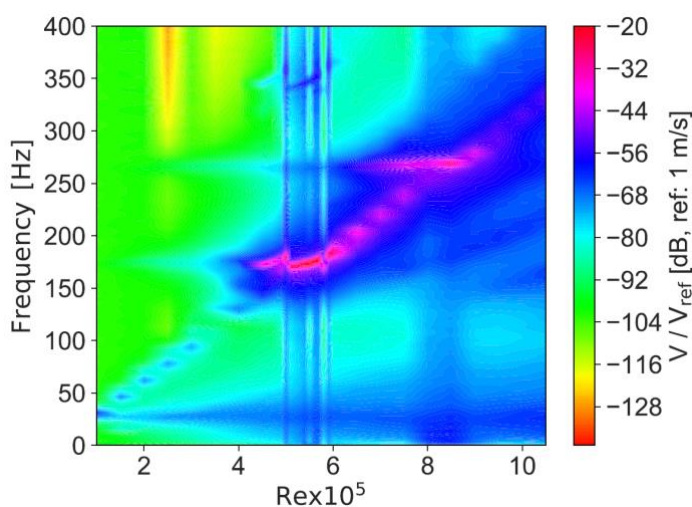


Figure 1: Spectrogram of the hydrofoil tip-velocity as a function of the Reynolds number

Topology Optimization of Control Surface with Aeroelastic Effect

Lyu Jinan, Guo Li, Wang Xinjiang

China Academy of Aerospace Aerodynamics, Beijing 100074, China, madas1@126.com

Structure weight reduction is becoming more and more important in modern aircraft design. At present aircraft design is mainly based on experience to arrange the beam and rib position of the control surface, the shape and size of the structure is subject to the traditional manufacturing technology¹. Recently, with the development of additive manufacturing (AM) technology, 3D printing technology has been able to achieve the rapid manufacturing of complex 3D structures. It is possible to achieve the control surface structure optimization and complete the manufacturing based on the topology optimization method².

A method based on topology optimization to reduce the weight of high-speed control surface is introduced in this paper. The loads of air vehicle is the fundamental element considered to design structure of air vehicle. Aerodynamic loads were obtained using CFD/CSD numerical simulation method. For the calculation strategy, loose-coupling strategy was adopted to solve the aerodynamic load under the static aeroelastic deformation of a wing with a large chord ratio³ and Fluid dynamics and structural equation are solved respectively. The solution of the control equation of flow field is based on the conserved three-dimensional compressible integral N-S equation described by ALE (arbitrary Lagrangian-Eulerian). Commercial finite element solvers were used to solve the structure response. The RBF (Radial basis function) method was adopted to interpolate between fluid and structure mesh⁴. For the numerical simulation, the mesh used in CFD simulation is shown in Fig.1 and the pressure distribution of control surface calculated using CFD simulation are shown in Fig.2.

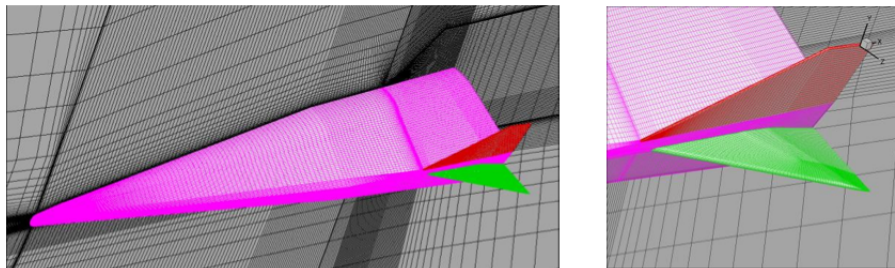


Figure 1: Mesh used in CFD simulation.

In the topological optimization part, flight aerodynamic load boundary conditions are applied on the control surface and structural weight reduction as the optimize the constraint and the minimum compliance as the optimization goal. The control surface of high-speed air vehicle is shown in Fig.3. Compared with the solid control surface, the optimal constraint is to reduce the weight by 30%, and the optimization target is to minimize the overall flexibility (maximum stiffness). The optimization results are shown in figure 4. The results showed that the optimization greatly reduced the weight of the structure. After that, the optimized structure is verified meeting the stiffness requirements under aerodynamic loading using finite element method. Finally, the optimized structure was printed with photosensitive resin material as shown in Fig.5.

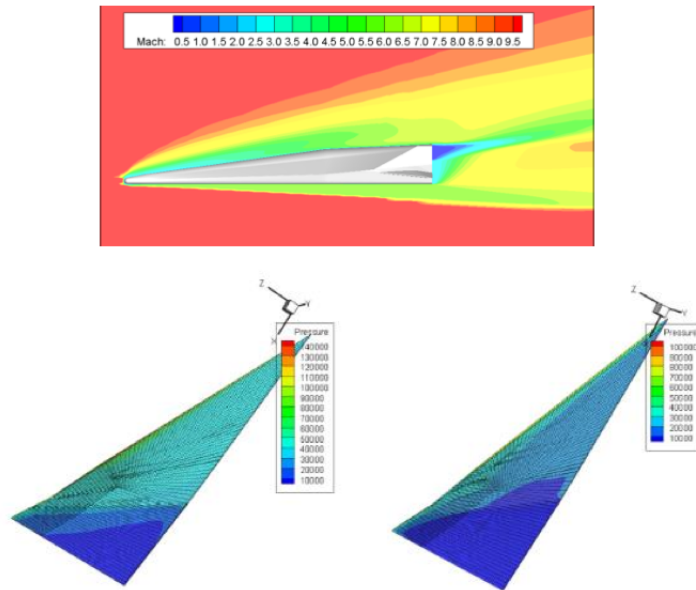


Figure 2: Pressure distribution of the high-speed control surface.

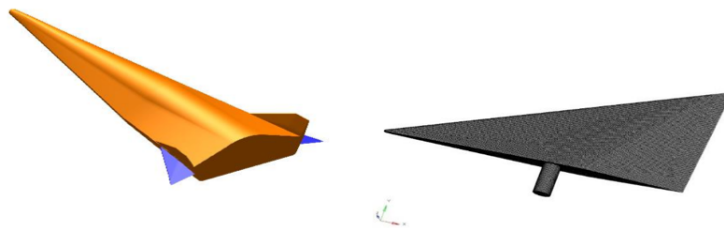


Figure 3: Shape of high-speed air vehicle control surface.

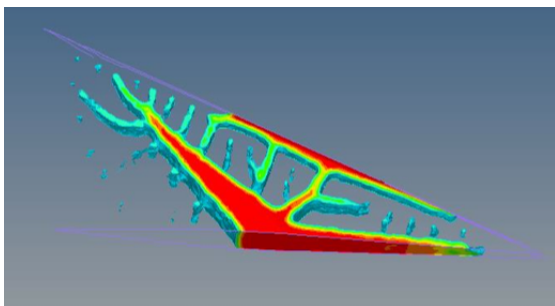


Figure 4: Result of topology optimization.



Figure 5: 3D print of topology optimization structure.

¹ Krog, L., Tucker, A., Rollema, G., and Boyd, R. Topology Optimization of Aircraft Wing Box Ribs[C], Proceedings of the Altair Technology Conference, Airbus UK Ltd Advance Numerical Simulations Department, Troy, MI, 2004.

² Haris HameedMian,GangWang, Zheng-YinYe. Numerical investigation of structural geometric nonlinearity effect in high-aspect-ratio wing using CFD/CSD coupled approach[J]. Journal of Fluids and Structures, 2014, 49,186-201.

³Guo li,Lv jinan, Ji chen,Liuzqiang,Identification of flutter boundary for a hypersonic vehicle wing as X-15 by experiment and numerical simulation[C]. AIAA paper 2017-2237.

⁴ Tsai H, F. Wong A, Cai J, et al. Unsteady flow calculations with a parallel multi-block moving mesh algorithm[J]. AIAA journal, 2001, 39 (6): 1021-1029.

Flutter (fundamentals)

A new divergence mechanism

Vasily Vedeneev

Lomonosov Moscow State University, Moscow, Russia, vasily@vedeneev.ru

Abstract

There are two types of aeroelastic instabilities, divergence and flutter. A general divergence mechanism described in textbooks consists of decrease of one of natural frequencies down to zero due to negative aerodynamic stiffness, coalescence with its paired frequency, and transformation to one damped and one growing frequency. Most examples of this mechanism use quasi-steady aerodynamics, which, at first sight, is suitable for divergence analysis due to its static nature.

In this study we show that when using unsteady aerodynamics, the analytical structure of eigenfrequencies essentially changes; namely, no frequency coalescence occurs, but eigenfrequencies become damped. The divergence mode is not a continuation of a natural mode, but separates from a continuous spectrum that exists in the aeroelastic system due to the wake behind the wing when unsteady aerodynamics is used, but is absent in quasi-steady case.

Keyword: divergence, unsteady aerodynamics

1 Introduction

In most of aeroelasticity textbooks [1–3], divergence and flutter are considered separately: divergence as static instability, where steady aerodynamics is employed, and flutter as dynamic instability, where the use of unsteady aerodynamics is crucial for correct flutter prediction.

In this paper we re-analyze the classical stability problem of two-degree-of-freedom (bending and torsional) system, focusing on divergence, but using, unlike most of other studies, fully unsteady Theodorsen aerodynamics. In Section 2 we introduce aeroelastic model used with variations in all textbooks. Section 3 is devoted to the eigenfrequency analysis in the framework of different simplified aerodynamic formulations that yield classical divergence mechanism. However, slight improvement of the aerodynamics immediately yields inability of the divergence to originate from a structural natural mode. In Section 4 we re-analyse the problem using fully unsteady aerodynamics and confirm this result. We give an analytical proof of non-existence of the divergence mode at subcritical flow speed, which is, therefore, cannot be a transformed structural mode. To go deeper into this problem, we give a closed-form solution of the initial-value problem that establishes the connection between the origin of the divergence mode, continuous spectrum, and branch cut of Theodorsen function. In Section 5 we compare present results with previous studies. Finally, in Section 6 we summarize the results.

2 Rectangular wing as a toy model

We consider a classical two-degree-of-freedom aeroelastic model of a thin unswept rectangular wing (Fig. 1). We will follow the book [3], where the equations of motion are derived in chapter

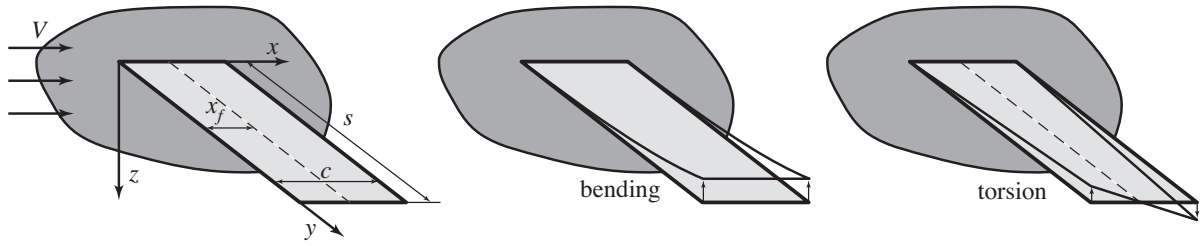


Figure 1: Rectangular wing and its bending and torsional degrees of freedom.

10.2 by using simplified aerodynamic model. We will briefly re-derive equations of motion for the case of fully unsteady aerodynamics.

The wing span is s and the chord is c . We will assume that the wing cross-section is a thin plate so that the aerodynamic centre and elastic axis are located at $c/4$ and x_f downstream from the leading edge, respectively. The two degrees of freedom correspond to bending and torsional modes, with EI and GJ being bending and torsional stiffnesses (Fig. 1). Assuming simple bending and torsional shapes, the general wing motion has the form

$$z(x, y, t) = \left(\frac{y}{s}\right)^2 q_b(t) + \left(\frac{y}{s}\right) (x - x_f) q_t(t),$$

where q_b and q_t are generalized coordinates corresponding to bending and torsion. Applying Lagrange's equation as done in [3, §10.2.1], we find the equations of motion:

$$m \begin{pmatrix} \frac{sc}{5} & \frac{s}{4} \left(\frac{c^2}{2} - cx_f \right) \\ \frac{s}{4} \left(\frac{c^2}{2} - cx_f \right) & \frac{s}{3} \left(\frac{c^3}{3} - c^2 x_f + x_f^2 c \right) \end{pmatrix} \begin{pmatrix} \ddot{q}_b \\ \ddot{q}_t \end{pmatrix} + \begin{pmatrix} \frac{4EI}{s^3} & 0 \\ 0 & \frac{GJ}{s} \end{pmatrix} \begin{pmatrix} q_b \\ q_t \end{pmatrix} = \begin{pmatrix} Q_b \\ Q_t \end{pmatrix}, \quad (1)$$

where Q_b and Q_t are generalized aerodynamic forces corresponding to bending and torsional motions. To calculate Q_b and Q_t , we will use strip theory, assuming that aerodynamic forces produced by each cross-section can be taken from corresponding two-dimensional problem for a thin plate. Let the wing undergo harmonic motion with elastic axis deflection $z = z_0 e^{i\omega t}$ and pitch $\theta = \theta_0 e^{i\omega t}$. The two-dimensional aerodynamic forces are readily given by Theodorsen theory. Derivation of generalized aerodynamic forces Q_b and Q_t yields the following expression:

$$\begin{pmatrix} Q_b \\ Q_t \end{pmatrix} = \begin{pmatrix} -\rho V^2 \begin{pmatrix} \frac{s}{5} L_z & \frac{bs}{4} L_\theta \\ -\frac{bs}{4} M_z & -\frac{b^2 s}{3} M_\theta \end{pmatrix} - i\omega \rho V \begin{pmatrix} \frac{sb}{5} L_z & \frac{b^2 s}{4} L_\dot{\theta} \\ -\frac{sb}{4} M_z & -\frac{b^3 s}{3} M_\dot{\theta} \end{pmatrix} \end{pmatrix} \begin{pmatrix} q_b \\ q_t \end{pmatrix}, \quad (2)$$

where the oscillatory aerodynamic derivatives are expressed through the Theodorsen function

$$C(k) = \frac{K_1(ik)}{K_0(ik) + K_1(ik)}, \quad (3)$$

$b = c/2$, and $k = \omega b/V$ is the reduced frequency [3, §9.4] (note that the expression for $M_\dot{\theta}$ in [3] has a misprint)

Table 1: Parameters used in calculations.

Wing span (s)	7.5 m	Bending Stiffness (EI)	$2 \times 10^7 \text{ N} \times \text{m}^2$
Chord (c)	2 m	Torsional Stiffness (GJ)	$2 \times 10^5 \text{ N} \times \text{m}^2$
Elastic axis (x_f)	$0.48c$	Mass axis	$0.5c$
Mass per unit area (m)	200 kg/m^2	Air density (ρ)	1.225 kg/m^3

Substituting these expressions into Eq. (1), we finally obtain aeroelastic equations of motion that yield the following eigenvalue problem:

$$\mathcal{F}(\omega) = \det(-\omega^2 \mathbf{M} + i\omega \mathbf{D}_a(k) + (\mathbf{K}_a(k) + \mathbf{K})) = 0, \quad (4)$$

$$\mathbf{M} = m \begin{pmatrix} \frac{sc}{5} & \frac{s}{4} \left(\frac{c^2}{2} - cx_f \right) \\ \frac{s}{4} \left(\frac{c^2}{2} - cx_f \right) & \frac{s}{3} \left(\frac{c^3}{3} - c^2 x_f + x_f^2 c \right) \end{pmatrix}, \quad \mathbf{D}_a(k) = \rho V \begin{pmatrix} \frac{sc}{10} L_z & \frac{c^2 s}{16} L_\theta \\ -\frac{c^2 s}{16} M_z & -\frac{c^3 s}{24} M_\theta \end{pmatrix},$$

$$\mathbf{K}_a(k) = \rho V^2 \begin{pmatrix} \frac{s}{5} L_z & \frac{cs}{8} L_\theta \\ -\frac{cs}{8} M_z & -\frac{c^2 s}{12} M_\theta \end{pmatrix}, \quad \mathbf{K} = \begin{pmatrix} \frac{4EI}{s^3} & 0 \\ 0 & \frac{GJ}{s} \end{pmatrix}. \quad (5)$$

The eigenvalue problem is solved numerically by iterative method. At the first iteration we assume $k = 0$, calculate corresponding aerodynamic matrices (M_θ and L_θ are forced to be zero at the first iteration as discussed in [3, §9.4]), and solve the Eq. (4) with respect to ω , obtaining four roots ω_n^0 , $n = 1 - 4$. One of the roots is chosen and calculated by subsequent iterations. Assume that the j -th iteration of the root, ω^j is calculated. We recalculate $k^j = \omega^j b/V$, recalculate aerodynamic matrices, and again solve Eq. (4) with respect to ω . Iterations are repeated until the convergence is achieved with a given accuracy. For the case of slow convergence, which occurs near the divergence boundary, weighting of the $(j + 1)$ -th root is used with the relaxation coefficient $\varkappa = 0.1$: $\omega_{\text{final}}^{j+1} = (1 - \varkappa)\omega^{j+1} + \varkappa\omega^j$.

Calculations are started at sufficiently small V , where each solution is associated with a wing eigenmode in still air. Next, the velocity is gradually increased, with the initial guess of k taken from the converged solution from the previous step in velocity. In this way we obtain continuous branch of eigenfrequencies with the velocity V as a parameter.

In this study, we will focus on transition to divergence that, by definition, occurs through zero eigenfrequency. Putting $\omega = k = 0$, we immediately derive the divergence speed:

$$V_{\text{div}} = \sqrt{\frac{3GJ}{\rho c^2 s^2 e \pi}}$$

3 Divergence mechanism through simplified aerodynamics

In the calculations below we will use parameters used in [3, §10.8], given in Table 1, that correspond to natural circular frequencies of the wing $\omega_t = 8.92 \text{ rad/s}$, $\omega_b = 17.83 \text{ rad/s}$ (torsional and bending, respectively) and the divergence speed $V_{\text{div}} = 54.9 \text{ m/s}$.

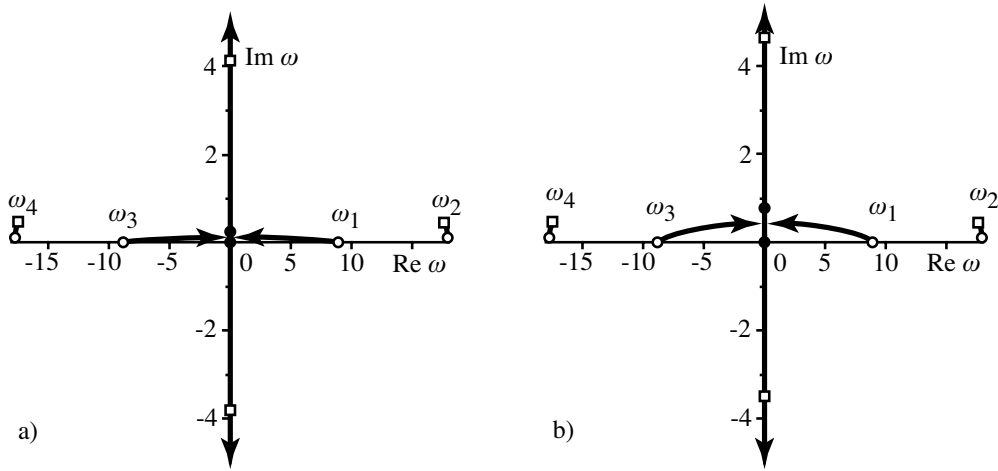


Figure 2: Eigenfrequency loci when changing the flow speed V from $V = 10$ m/s (\circ) to $V = V_{div} = 54.9$ m/s (\bullet) and further to $V = V_{div} + 5 = 59.9$ m/s (\square): a) quasi-steady aerodynamics, b) simplified unsteady aerodynamics with real $M_{\dot{\theta}}$.

3.1 Quasi-steady aerodynamics

We start with the simplest aerodynamic formulation, quasi-steady aerodynamics. Taking the limit $k \rightarrow 0$, $C(k) \rightarrow 1$, we have the following aerodynamic derivatives and the eigenvalue problem with the following aerodynamic matrices:

$$L_z = 0, \quad L_{\dot{z}} = 2\pi, \quad L_{\theta} = 2\pi, \quad M_z = 0, \quad M_{\dot{z}} = 4\pi e, \quad vM_{\theta} = 4\pi e, \quad e = \frac{1}{2} \left(\frac{1}{2} + a \right), \quad (6)$$

$$\mathbf{D}_a = \rho V \begin{pmatrix} \frac{sc}{10} 2\pi & 0 \\ -\frac{c^2 s}{8} e 2\pi & 0 \end{pmatrix}, \quad \mathbf{K}_a = \rho V^2 \begin{pmatrix} 0 & \frac{sc}{8} 2\pi \\ 0 & -\frac{c^2 s}{6} e 2\pi \end{pmatrix}.$$

The result of calculations is shown in Fig. 2a. At small V the wing has four slightly damped eigenfrequencies close to natural frequencies: $\omega_{1,3} \approx \pm\omega_t$ and $\omega_{2,4} \approx \pm\omega_b$. When the velocity increases, torsional frequencies $\omega_{1,3}$ move toward each other, coalesce at the imaginary axis, and become pure imaginary. After the coalescence, one of the frequencies moves down, crosses at $V = V_{div}$ zero frequency and becomes growing. This mechanism is a classical transition to divergence: the divergence mode is generated by the interaction of the first (torsion) mode with its paired frequency due to negative aerodynamic stiffness.

3.2 Simplified unsteady aerodynamics with real $M_{\dot{\theta}}$

Following [3], let us include unsteady term $M_{\dot{\theta}}$, which has the most important effect:

$$\mathbf{D}_a = \rho V \begin{pmatrix} \frac{sc}{10} 2\pi & 0 \\ -\frac{c^2 s}{8} e 2\pi & -\frac{c^3 s}{24} M_{\dot{\theta}} \end{pmatrix}, \quad \mathbf{K}_a = \rho V^2 \begin{pmatrix} 0 & \frac{sc}{8} 2\pi \\ 0 & -\frac{c^2 s}{6} e 2\pi \end{pmatrix}. \quad (7)$$

As suggested in [3, §9.6], the value $M_{\dot{\theta}} = -1.2$ is chosen as a good approximation for practically important range of real k (the actual value is not important for the divergence mechanism).

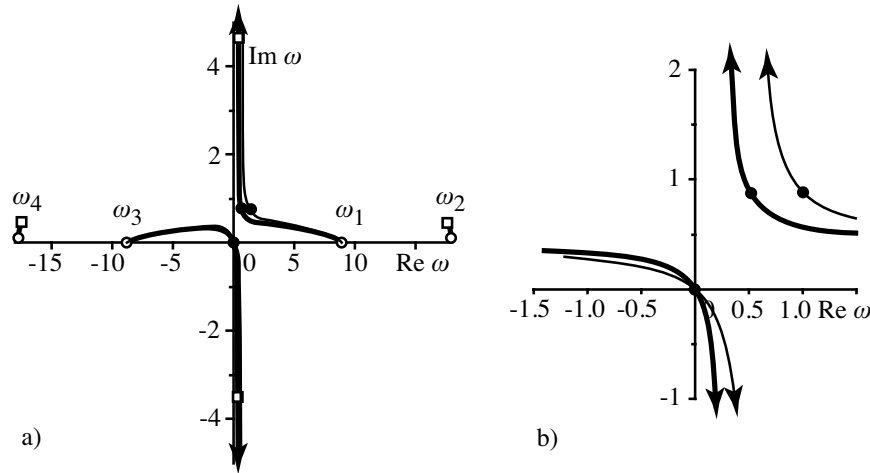


Figure 3: Eigenfrequency loci calculated with simplified unsteady aerodynamics with complex $M_{\dot{\theta}}$ when changing the flow speed V from $V = 10$ m/s (\circ) to $V = V_{div} = 54.9$ m/s (\bullet) and further to $V = V_{div} + 5 = 59.9$ m/s (\square): a) general view, b) enlarged view around zero frequency. $M_{\dot{\theta}} = -1.2 + i$ (bold lines) and $M_{\dot{\theta}} = -1.2 + 2i$ (thin lines).

Results of calculations shown in Fig. 2b are similar to quasi-steady aerodynamics. The only change is that the coalescence occurs at different velocity, which does not affect the divergence velocity.

However, the real value of $M_{\dot{\theta}}$ is not satisfactory, because the modes are damped, reduced frequencies k are complex, and the actual values of $M_{\dot{\theta}}$ should also be complex.

3.3 Simplified unsteady aerodynamics with complex $M_{\dot{\theta}}$

The easiest way to take imaginary part of reduced frequency into account is to consider complex constant value of $M_{\dot{\theta}}$. The eigenvalue problem stays polynomial, but its coefficients become complex. Hence, the frequency coalescence, in general, does not occur at any V , but changes to hyperbola-type interaction. Fig. 3 shows results of calculation for $M_{\dot{\theta}} = -1.2 + i$ and $M_{\dot{\theta}} = -1.2 + 2i$ (the value of the imaginary part does not qualitatively change the eigenfrequency loci), where approaching of eigenfrequencies and passing each other occurs instead of coalescence. The transition to divergence, of course, occurs at the same value V_{div} through zero frequency.

This type of mode interaction is common for binary (coupled-mode) flutter in many aeroelastic systems. However, the same interaction does not look satisfactory for the case of divergence. It was mentioned above that the eigenfrequencies with $\text{Re } \omega > 0$ and $\text{Re } \omega < 0$ must be exactly symmetrical with respect to imaginary axis, because they correspond to exactly the same wing motion. Indeed, for each frequency $\omega = \omega_r + i\omega_i$ and eigenvector $(X_b, X_t)^T = (X_{br} + iX_{bi}, X_{tr} + iX_{ti})^T$ it is easy to see that the eigenfrequency $\omega = -\omega_r + i\omega_i$ and eigenvector $(X_b, X_t)^T = (X_{br} - iX_{bi}, X_{tr} - iX_{ti})^T$ correspond to the same $\text{Re}(X_b, X_t)^T e^{i\omega t}$, i.e., the same physical motion. However, this fundamental symmetry is absent in Fig. 3, and obviously will be absent for any constant complex value of $M_{\dot{\theta}}$.

To resolve this problem, we now switch to full unsteady aerodynamics defined by Eq. (5), and re-analyze the divergence mechanism, which is a matter of the next section of the paper.

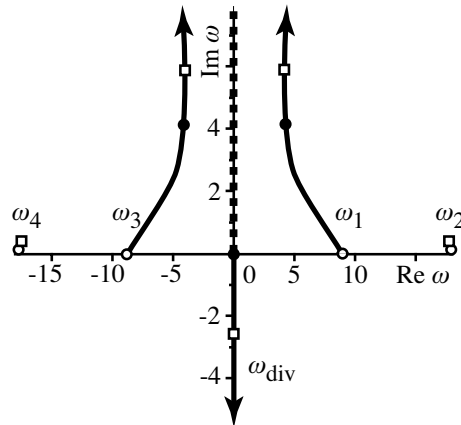


Figure 4: Eigenfrequency loci calculated through full unsteady aerodynamics when changing the flow speed V from $V = 10$ m/s (\circ) to $V = V_{div} = 54.9$ m/s (\bullet) and further to $V = V_{div} + 5 = 59.9$ m/s (\square). Dashed curve shows the continuous spectrum.

4 Divergence mechanism through the full unsteady aerodynamics

4.1 Divergence modelling using the full Theodorsen theory

When using full Theodorsen aerodynamics, Eq. (5), the behaviour of ω_1 and ω_3 curves becomes symmetrical, but both they become highly damped (Fig. 4). However, if take the divergence mode, i.e. $V = V_{div}$ and $\omega = 0$, as initial guess, the numerical processes for $V > V_{div}$ converges and gives the fifth eigenfrequency branch (Fig. 4).

To analyze where the divergence mode transforms to at low flow speeds, we started decreasing back the speed. However, surprisingly, the numerical procedure diverges for any $V < V_{div}$, so that this mode has no continuation from supercritical to subcritical speeds. To demonstrate that the absence of the divergence mode for $V < V_{div}$ is not a numerical issue but a real phenomenon, we give in the next section a rigorous proof.

4.2 Proof of the non-existence of the divergence mode at subcritical flow velocity

Let us have the solution $\omega = k = 0$ at $V = V_{div}$. We take a small velocity deviation $V = V_{div} + V'$ and find a solution of Eq. (4) that tends to zero as $V' \rightarrow 0$, i.e. find the divergence mode frequency in the vicinity of the divergence boundary.

To obtain aerodynamic derivatives for small k , we consider the asymptotic expansion of K -Bessel functions [4, 9.6.9, 9.6.54] and find the expansion of the Theodorsen function (3):

$$C(k) \sim \frac{1/(ik)}{1/(ik) - \ln(ik/2) - \gamma} \sim 1 + ik \left(\gamma + \ln \left| \frac{k}{2} \right| \right) - k \operatorname{Arg}(ik),$$

where γ is the Euler-Mascheroni constant. Then we expand aerodynamic derivatives at small reduced frequency, neglecting terms of the order of k^2 and smaller in z and θ derivatives, and by neglecting terms of the order of k and smaller in \dot{z} and $\dot{\theta}$ derivatives. Neglecting ω^2 term in (4) as infinitesimal, substituting aerodynamic derivatives, and retaining terms of the order of

V' , k , and $k \ln k$, we have the eigenvalue problem in the following form:

$$k \left(a \frac{1-2a}{1+2a} + \gamma + \ln \left| \frac{k}{2} \right| + i \operatorname{Arg}(ik) - \rho V_{div}^2 \frac{3}{2} \frac{s^4}{4EI} \right) = 2i \frac{V'}{V_{div}}. \quad (8)$$

Taking separately real and imaginary part of this equation, it is easy to show that a root can exist only for $\operatorname{Re} k = 0$. In this case from the real part of (8) we obtain $\operatorname{Arg}(ik) = 0$, i.e. $k = -i\kappa$, $\kappa \in \mathbb{R}$, $\kappa > 0$. The leading term of the imaginary part of (8) is

$$-\kappa \ln \left| \frac{\kappa}{2} \right| = 2 \frac{V'}{V_{div}}.$$

This equation has a positive real root $\kappa(V')$ for $V' > 0$. This root corresponds to the divergence eigenmode, and it exists only for $V' \geq 0$. Indeed, for $V' < 0$ we have $\kappa(V') < 0$, $\operatorname{Arg}(ik) = \pi$, which does not satisfy (8).

We have proved that at flow speed slightly exceeding V_{div} a growing divergence mode exists, whose frequency tends to zero as $V \rightarrow V_{div} + 0$, but no mode exists for $V < V_{div}$. In other words, the divergence mode is not a continuation of a natural mode of the wing but is an additional eigenmode that exists only for $V \geq V_{div}$. This phenomenon is due to singularity of Theodorsen function at $k = 0$, and it does not manifest itself if simplified aerodynamics is used.

The fact that for the same aeroelastic system there are four eigenmodes at $V < V_{div}$, and five eigenmodes at $V \geq V_{div}$, looks unusual. To resolve this phenomenon, we now consider the solution of the initial-value problem.

4.3 Divergence in the framework of initial-value problem

To formulate the initial-value problem, consider equations of motion (1) yielding the eigenvalue problem (4). For the case of general time-domain motion, generalized aerodynamic forces Q_b and Q_t are functions of t that can be written in the form of convolution integrals, whose kernels are expressed through the Wagner function [1, §5-7], [2, §6.7].

With the equations of motion, we specify the following initial conditions:

$$q_b(0) = q_b^0, \quad \dot{q}_b(0) = \dot{q}_b^1, \quad q_t(0) = q_t^0, \quad \dot{q}_t(0) = \dot{q}_t^1, \quad q_{b,t}(t) = \dot{q}_{b,t}(t) = 0, \quad t < 0,$$

where q_b^n , \dot{q}_t^n are given constants. Note that as aerodynamic loads are calculated as convolution integrals of the wing displacement and velocity, not only initial conditions at $t = 0$, but total preceding motion history for $t < 0$ must be specified. Physically, this feature reflects the effect of the wake that is convected downstream but “remembers” the wing motion in the past.

To solve the integro-differential system of equations (1) with given initial conditions, we perform Laplace transformation defined as

$$\xi_{b,t}(\omega) = \xi(\omega) \{q_{b,t}\} = \int_0^{+\infty} q_{b,t}(t) e^{-i\omega t} dt.$$

In contrast to classical definition with the parameter s we use the parameter $\omega = -is$ to more evidently connect the solution of the initial-value problem with eigenvalue problem. Then the transformed system of equations (1) is as follows:

$$(-\omega^2 \mathbf{M} + i\omega \mathbf{D}_a(k) + (\mathbf{K}_a(k) + \mathbf{K})) \begin{pmatrix} \xi_b \\ \xi_t \end{pmatrix} = \begin{pmatrix} P_b \\ P_t \end{pmatrix}, \quad (9)$$

where $P_{b,t}$ are functions of the initial conditions $q_{b,t}^n$ and ω . We used here the fact that Laplace transformation of time-domain generalized aerodynamic forces yields frequency-domain Theodorsen aerodynamics. We solve this linear algebraic system by using Cramer's rule:

$$\xi_b = \frac{C_b(q_{b,t}^n, \omega)}{\mathcal{F}(\omega)}, \quad \xi_t = \frac{C_t(q_{b,t}^n, \omega)}{\mathcal{F}(\omega)}. \quad (10)$$

Here $\mathcal{F}(\omega)$ is the determinant (4) of the system (9), and $C_{b,t}$ are determinants of the same matrix where either first or second column is substituted by the right-hand side of the system.

Now, apply the inverse Laplace transformation to (10) by using Mellin's inverse formula [5]:

$$q_{b,t}(t) = \frac{1}{2\pi} \int_{-\infty-i\zeta}^{+\infty-i\zeta} \xi_{b,t}(\omega) e^{i\omega t} d\omega, \quad (11)$$

where the integration path is a horizontal line located below all singularities of $\xi_{b,t}(\omega)$.

Next, we move up the integration path. The integral (11) is not changed due to Cauchy theorem while the integrand does not have singularities. There are two types of singularities. First, zeroes ω_n of the denominator (10), where the integrand has poles. Each crossing of a pole yields the separation of the corresponding eigenmode term from the integral. The second type of singularity is the branch point of the Theodorsen function at $\omega = k = 0$. As the branch cut of the Theodorsen function occupies imaginary positive ray, we deform the integration path to embrace both sides of the branch cut. Then the final solution of the initial-value problem is

$$q_{b,t}(t) = \frac{1}{2\pi} \int_0^{+i\infty} [\xi]_{b,t}(\omega) e^{i\omega t} d\omega + \sum_{n=1}^p i \frac{C_{b,t}(q_{b,t}^n, \omega_n)}{\partial \mathcal{F}(\omega_n) / \partial \omega} e^{i\omega_n t}, \quad (12)$$

where $[\xi]$ is the jump of ξ on the branch cut, and p is the number of eigenfrequencies.

We conclude that the general solution of the initial-value problem is the linear combination of two terms: eigenmodes that form discrete spectrum of the problem, and the integral over pure imaginary damped frequencies that form continuous spectrum.

The physical nature of the continuous spectrum originates from the wake behind the wing. As discussed above, the wake "memory" of the wing motion in the past results in aerodynamic loads depending not only on the instant wing position and velocity, but on all the preceding motion history. The continuous spectrum expresses the wake "memory" effect.

Recall that, mathematically, continuous spectrum exists due to the branch cut of the Theodorsen function. It is now clear that the divergence eigenmode that exists only at $V \geq V_{div}$ (Fig. 4) does not come from "nowhere" but separates from the continuous spectrum at $V = V_{div}$. If simplified aerodynamics is used, aerodynamic derivatives are constants, and no continuous spectrum is present. This reflects the fact that, physically, quasi-steady aerodynamics ignores the wake behind the wing. In this formulation the divergence mode is the continuation of natural mode branch, according to the classical divergence mechanism described in textbooks [1–3].

5 Comparison with other studies

5.1 Aeroelastic analyses through the full Theodorsen theory

The existence of the continuous spectrum in the aeroelastic system modeled through the exact Theodorsen theory was previously shown in [6, 7]. However, no connection between the continuous spectrum and the divergence mechanism was established in those studies.

While there are a lot of papers using various approximations and numerical techniques, aeroelastic analysis through the exact Theodorsen theory was conducted in a limited number of studies, and the work [11] is a one where transition to divergence was observed. Their figures 3, 4, 11 clearly indicate that loci of structural eigenfrequencies do not coalesce and do not yield the divergence eigenmode. The latter, exactly as in the present study, does not exist for $V < V_{div}$ and appears only at $V \geq V_{div}$. But the relation between the existence of the divergence mode only at $V \geq V_{div}$ and the continuous spectrum was not established in that study.

5.2 Numerical studies

Consider numerical representations of the continuous spectrum. First, Jones approximation of Wagner function yields the approximation of Theodorsen function as a rational function [6]. In addition to structural roots, the appearance of two “aerodynamic lag” roots was observed [8–10], such that divergence was originated from those “aerodynamic lag”, but not structural, modes.

A different approach was used in [12]. Time-domain vortex-lattice method was used, and the results were transformed to the frequency domain. First, it was observed, that besides the structural frequencies, there exist hundreds (equal to the number of vortex elements along the wake) of frequencies that represent the unsteady wake behind the wing. Although not all those frequencies correspond to monotonically damped motion, the oscillating part of the motion was diminished when the numerical resolution was increased (e.g., see Fig. 5 of [12]). At that, the number of additional frequencies increased when the numerical resolution, i.e., the number of vortex elements along the wing surface and the wake, was increased. The principal conclusion of the numerical part of that study was the divergence originating from “aerodynamic” but not structural mode (see Fig. 24a of [12]), which is in accordance with the present results.

5.3 Experimental study

The most impressive evidence of the divergence not originating from a structural mode is given by the experimental part of [12]. During the wind tunnel experiment on a quasi-2D wing, frequency and damping of structural modes were continuously measured in air-on conditions. It was shown that when increasing the flow speed, the frequencies and damping did not approach zero when the flow speed approached the divergence speed (see discussion on pp. 79-80, 109-118 of [12]). On the contrary, the divergence appeared suddenly, without any precursor in structural modes, which is in agreement with the general theory of the presented paper.

6 Summary and concluding remarks

We have shown that when modeling unsteady aerodynamics using full Theodorsen theory, transition to divergence occurs not because of the mode coalescence, but through the appearance of an additional divergence mode that exists at post-divergence speeds, but is absent at subcritical speeds. This mode separates at $V = V_{div}$ from the continuous spectrum (Fig. 4) that reflects the influence of the wake behind the wing on the aerodynamic loads of the aeroelastic system.

When using simplified aerodynamics, such as quasi-steady theory, aerodynamic derivatives are constants and do not have any branch cuts. Physically, this corresponds to neglecting the wake effect. In such problem formulation, the divergence mode occurs after the interaction of an eigenmode with its paired mode, according to the classical divergence mechanism [1–3].

Note that the divergence velocity is not changed comparing to the value obtained in steady-flow approximation, because the transition occurs through $\omega = 0$, where (and only where!) the steady theory is the exact solution. The practical conclusion of this study is as follows. In flight tests the approach of the instability boundary should be detected in advance. Often, the tracking of structural damping and frequencies of the wing at in-flight conditions is used, and the approach of divergence is detected by rapid decrease of the structural frequency. This study shows that divergence can occur without falling of the structural frequencies to zero, i.e. without any precursor in the structural mode. The experimental study [12] fully confirms this point. Hence, such dynamic indicators of the divergence approach should be used with care.

Acknowledgements

The work is supported by the Russian Foundation for Basic Research (project 18-31-20057).

References

- [1] Bisplinghoff, R.L., Ashley, H., Halfman, R.L., *Aeroelasticity*. Addison-Wesley, Cambridge, 1955.
- [2] Fung, Y.C., *An introduction to the Theory of Aeroelasticity*. Dover, New York, 1969.
- [3] Wright, J.R., Cooper, J.E., *Introduction to Aircraft Aeroelasticity and Loads*. John Wiley & Sons, Chichester, 2015, doi:10.1002/9781118700440.
- [4] *Handbook of Mathematical Functions*, edited by M. Abramowitz and I. A. Stegun, Applied Mathematics Series 55. National Bureau of Standards, Washington, 1964.
- [5] Kolmogorov, A.N., Fomin, S.V., *Elements of the Theory of Functions and Functional Analysis*. Dover, New York, 1999.
- [6] Edwards, J.W., "Unsteady Aerodynamic Modeling for Arbitrary Motions," *AIAA Journal*, Vol. 17, No. 4, 1979, pp. 365–374.
- [7] Stark, V.J.E., "General Equations of Motion for an Elastic Wing and Method of Solution," *AIAA Journal*, Vol. 22, No. 8, 1984, pp. 1146–1153.
- [8] Chen, P.C., "Damping Perturbation Method for Flutter Solution: The g-Method," *AIAA Journal*, Vol. 38, No. 9, 2000, pp. 1519–1524.
- [9] Rodden, W.P., Bellinger, E.D., "Aerodynamic Lag Functions, Divergence, and the British Flutter Method," *Journal of Aircraft*, Vol. 19, No. 7, 1982, pp. 596–598.
- [10] Rodden, W.P., Stahl, B., "A Strip Method for Prediction of Damping in Subsonic Wind Tunnel and Flight Flutter Tests," *Journal of Aircraft*, Vol. 6, No. 1, 1969, pp. 9–17.
- [11] Edwards, J. W., Wieseman, C. D., "Flutter and divergence analysis using the generalized aeroelastic analysis method," *Journal of Aircraft*, Vol. 45, No. 3, 2008, pp. 906-915.
- [12] Heeg, J., "Dynamic Investigation of Static Divergence: Analysis and Testing," NASA/TP-2000-210310, 2000.

A Note on Mechanism of Two-Degree-of-Freedom Flutter

Masato Tamayama¹ and Jiro Nakamichi¹

¹*Japan Aerospace Exploration Agency (JAXA), Tokyo, Japan*
tamayama.masato@jaxa.jp, jirohnm@aol.com

Abstract

In order to clarify the mechanism of two degree-of-freedom (2DOF) flutter, a new analytical formulation is proposed. In the present method, freedoms are mutually transformed to each other by use of the phase difference and the amplitude ratio between the two modes. And the linear unsteady aerodynamic loads are properly applied to damping oscillation. In a result, the 2DOF problem is reduced apparently to simple free vibration problems with single degree-of-freedom so that stability analyses are simplified. Calculated results will be demonstrated. It is shown that the behavior of each mode can be easily tracked and can be rationally interpreted in accordance with variations of not only the flow velocity but other system parameters. Also, in the course of developing the scheme, 2DOF flutter will be clarified.

Keyword: Flutter, Unsteady Aerodynamics, Two Degree-of-Freedom, Flutter Mechanism

1 Introduction

Flutter is defined as a self-excited oscillation of elastic structures in flow field. A large portion of flutter characteristics of aircraft wings or long span suspension bridges can be studied by a classical binary model which is the representative of a cross section of those structures.

The dynamics of the model are described by a set of vibration equations to which self-excited aerodynamic forces are applied. The stability analyses are done usually by complex eigenvalue analyses which are, so called, *U-g* method or *p-k* method. In the process of those analyses, bifurcation frequently occurs where two modes are mutually switched by each other. If it occurs, the behaviors of the modes are no longer exactly traced. In order to ameliorate this kind of difficulties, Matsumoto et al. (2010) proposed a method called Step-by-Step (SBS) method, in which the behaviors of the two modes can be traced step by step independently of each other.

In this paper the SBS method has been modified. One of the degrees of freedom is transformed to the other by use of the phase difference between the two modes and the amplitude ratio. In a result the flutter equations are reduced apparently to a set of single-degree-of-freedom equations. The resultant flutter equations reveal the physical roles of individual unsteady aerodynamic elements not only in the stiffness term but also in the damping term.

In the flutter analyses, the unsteady aerodynamic forces are led either theoretically or experimentally. In the former case, Theodorsen's linear theory (1935) or Scanlan's flutter derivatives (1971) is used. In the latter case, wind tunnel test data are analyzed and formed into the aerodynamic coefficients similar to the theoretical ones. CFD numerical simulations

are also available to implement these coefficients. In any cases they consist of the gains and the phase differences of the unsteady aerodynamic forces to the harmonic motion of the model. So, they must be carefully applied to damped oscillations. The present paper proposes a way of introducing those linearized forces into the flutter analyses more rationally than the conventional methods, which enables us clearly to understand the mechanism of 2 DOF flutter.

The overview of the formulations will be described, and the computed results will be presented. Furthermore, by looking into the physical meanings of the present formulation, the mechanism of 2DOF flutter will be detailed and clarified.

2 Preliminaries for analyses

2.1 Flutter equations

Figure 1 shows the binary system used in the present study, which has mass unbalance around an elastic axis with two degrees of freedom; heaving h (down ward positive) and pitching α (nose-up positive). If these natural modes $\phi_i(x)$ ($i=1,2$) and the corresponding circular frequencies ω_i ($i=1,2$) (hereafter, simply referred to frequency) are obtained, arbitrary possible flutter mode shape of the system can be approximated by a linear combination of $\phi_i(x)$ as

$$\bar{z}^{(n)}(t, x) = \sum_{i=1}^2 \bar{q}_i^{(n)}(t) \cdot \phi_i(x) \quad (2-1)$$

where

$$\begin{cases} \phi_1(x) = -b\xi_1 - (x-ba) \\ \phi_2(x) = -b\xi_2 - (x-ba) \end{cases} \quad (2-2)$$

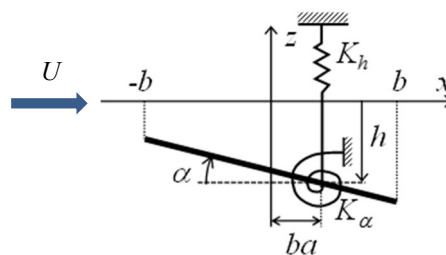


Figure 1: Binary system

And where ξ_i ($= h_i/b\alpha_i$) ($i=1,2$) are the natural mode amplitude ratios of h_i/b to α_i introduced by Nakamichi, Tamayama and Kodama (2019).

The natural modes are orthogonal to each other. Then the mass matrix and stiffness matrix of the system are diagonalised. The equations of motion of the system are written in a linear form as

$$\begin{cases} \ddot{\bar{q}}_1 + 2\zeta_{01}\omega_1\dot{\bar{q}}_1 + \omega_1^2\bar{q}_1 = \omega^2\bar{F}_{11}\bar{q}_1 + \omega^2\bar{F}_{12}\bar{q}_2 \\ \ddot{\bar{q}}_2 + 2\zeta_{02}\omega_2\dot{\bar{q}}_2 + \omega_2^2\bar{q}_2 = \omega^2\bar{F}_{21}\bar{q}_1 + \omega^2\bar{F}_{22}\bar{q}_2 \end{cases} \quad (2-3a,b)$$

where \bar{q}_i ($i=1,2$) are generalized coordinates associated with the 1st and 2nd natural modes, respectively. \bar{F}_{ij} are generalized unsteady aerodynamic coefficients. Those are complex function of reduced frequency k ($=b\omega/U$), and indicate the gains of the generalized unsteady aerodynamic forces and their phase lags to the motions of the relevant system natural modes.

\bar{q}_i ($i=1,2$) are also complex functions of t , and assumed by following forms with the damping ratios ζ_i and the phase lag angles ψ_i ;

$$\bar{q}_1 = q_{01}e^{\bar{p}t}e^{-i\psi_1}, \quad \bar{q}_2 = q_{02}e^{\bar{p}t}e^{-i\psi_2}, \quad \bar{p} = (-\zeta + i)\omega \quad (2-4)$$

It is noted here that the system has two modes which shall be identified by Branch 1 ($n=1$) and Branch 2 ($n=2$). Unless otherwise confusing, the upper suffix n will be omitted hereafter.

2.2 Transformation of degree of freedom and aerodynamic coefficient

The possible flutter mode $Z^{(n)}$ will form Branch n on the $U-\omega$ or $U-\zeta$ diagrams. $Z^{(n)}$ have been assumed by superposing the natural modes of the system. We consider the n -th natural mode as the reference mode on Branch n . Namely, the amplitude and the phase angle of the other will be measured based upon the n -th mode. By introducing the amplitude ratios $g_{i/n}$ and the phase difference angles $\Delta_{ni}\psi$ between the i -th and the n -th modes (Fig.2), \bar{q}_i can be expressed by \bar{q}_n like

$$\bar{q}_i^{(n)} = g_{i/n} e^{-i\Delta_{ni}\psi} \bar{q}_n^{(n)} \quad (i=1,2, n=1,2) \quad (2-5)$$

where

$$g_{i/n} = q_{0i} / q_{0n} \quad (i=1,2, n=1,2) \quad (2-6)$$

and

$$\Delta_{ni}\psi = \psi_i - \psi_n, \quad (2-7)$$

$$(g_{1/1} = g_{2/2} = 1 \quad \Delta_{11}\psi = \Delta_{22}\psi = 0)$$

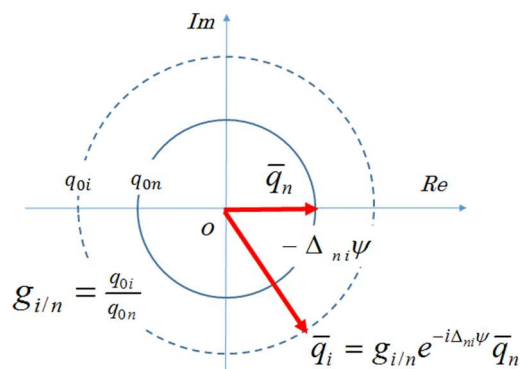


Figure 2: Normalization of \bar{q}_i ($i=1,2$)

If Eqs.(2-5) are expanded for the sake of concreteness, they become to be

$$\bar{q}_1^{(1)} = g_{1/1} e^{-i\Delta_{11}\psi} \bar{q}_1^{(1)} = \bar{q}_1^{(1)}, \quad \bar{q}_2^{(1)} = g_{2/1} e^{-i\Delta_{12}\psi} \bar{q}_1^{(1)} \quad \text{on Branch 1 } (n=1) \quad (2-8)$$

$$\bar{q}_1^{(2)} = g_{1/2} e^{-i\Delta_{21}\psi} \bar{q}_2^{(2)}, \quad \bar{q}_2^{(2)} = g_{2/2} e^{-i\Delta_{22}\psi} \bar{q}_2^{(2)} = \bar{q}_2^{(2)} \quad \text{on Branch 2 } (n=2) \quad (2-9)$$

By applying those relations to the right of Eqs.(2-3), the unsteady aerodynamic force terms will be;

$$\left. \begin{aligned} \bar{F}_{11} \bar{q}_1^{(1)} &= \bar{F}_{11} g_{1/1} e^{-i\Delta_{11}\psi} \bar{q}_1^{(1)} = \bar{\Phi}_{11} \bar{q}_1^{(1)} \\ \bar{F}_{12} \bar{q}_2^{(1)} &= \bar{F}_{12} g_{2/1} e^{-i\Delta_{12}\psi} \bar{q}_1^{(1)} = \bar{\Phi}_{12} \bar{q}_1^{(1)} \end{aligned} \right\} \quad \text{on Branch 1 } (n=1) \quad (2-10)$$

$$\left. \begin{aligned} \bar{F}_{21} \bar{q}_1^{(2)} &= \bar{F}_{21} g_{1/2} e^{-i\Delta_{21}\psi} \bar{q}_2^{(2)} = \bar{\Phi}_{21} \bar{q}_2^{(2)} \\ \bar{F}_{22} \bar{q}_2^{(2)} &= \bar{F}_{22} g_{2/2} e^{-i\Delta_{22}\psi} \bar{q}_2^{(2)} = \bar{\Phi}_{22} \bar{q}_2^{(2)} \end{aligned} \right\} \quad \text{on Branch 2 } (n=2) \quad (2-11)$$

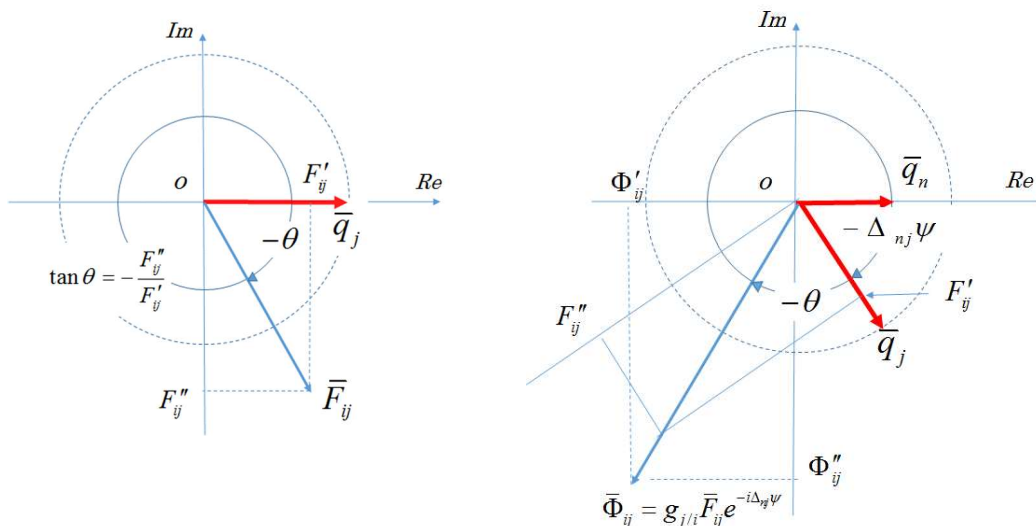
where, if complex number \bar{F}_{ij} and $\bar{\Phi}_{ij}$ are expressed by $\bar{F}_{ij} = F'_{ij} + iF''_{ij}$ and $\bar{\Phi}_{ij} = \Phi'_{ij} + i\Phi''_{ij}$, respectively, then,

$$\begin{aligned} \bar{\Phi}_{ij} &= \Phi'_{ij} + i\Phi''_{ij} \\ &= g_{j/i} \left\{ \left(F'_{ij} \cos \Delta_{ij}\psi + F''_{ij} \sin \Delta_{ij}\psi \right) + i \left(-F'_{ij} \sin \Delta_{ij}\psi + F''_{ij} \cos \Delta_{ij}\psi \right) \right\} \quad (i=n, j=1,2) \quad (2-12) \end{aligned}$$

These expressions mean that the unsteady aerodynamic force caused by the motion of the

1st natural mode can be transformed into that caused by the motion of the 2nd natural mode and vice versa. Note that in the case of $i = j$, $\bar{\Phi}_{11} = \bar{F}_{11}$ and $\bar{\Phi}_{22} = \bar{F}_{22}$. New augmented unsteady aerodynamic coefficients $\bar{\Phi}_{ij}$ have been introduced. They consist of the original unsteady aerodynamic coefficients \bar{F}_{ij} , their phase lag angles and the amplitude ratios between the i -th mode and the j -th mode. They will take an important role later to enable us to eliminate either degree of freedoms in the flutter equations.

In Figs.3, the relationships among $\bar{\Phi}_{ij}$, \bar{F}_{ij} and \bar{q}_i ($i=1,2$) is illustrated to show the physical meanings of the augmented aerodynamic coefficients $\bar{\Phi}_{ij}$.



(a) relation between \bar{F}_{ij} and \bar{q}_j ($i=1,2$) (b) relation among $\bar{\Phi}_{ij}$, \bar{F}_{ij} , \bar{q}_j and \bar{q}_n
 Figures 3: Conversion of unsteady aerodynamic coefficient ($\zeta_i = 0$)

Unsteady aerodynamic force \bar{F}_{ij} is usually lagged in phase by θ to the wing motion \bar{q}_j , as is shown in Fig.3(a). Further there is a phase difference between \bar{q}_j and \bar{q}_n . It is found in Figs.3(b) that the real and the imaginary parts of $\bar{\Phi}_{ij}$ are identical to the in-phase and the out-of-phase components of \bar{F}_{ij} with respect to \bar{q}_n , multiplied by the amplitude ratio $g_{j/n}$. The aerodynamic forces imposed on the i -th mode by the j -th mode, i.e., $\bar{F}_{ij}\bar{q}_j$ has been transformed into $\bar{\Phi}_{ij}\bar{q}_n$ which is looked on the force apparently due to the n -th mode (the reference mode) on Branch n ($n=1,2$).

2.3 Relation between \bar{q}_i and $\dot{\bar{q}}_i$

Generally, if the displacements \bar{q}_i ($i=1,2$) are assumed by Eqs.(2-4), the relation between displacement \bar{q}_i and its velocity $\dot{\bar{q}}_i$ is

$$\dot{\bar{q}}_i = \bar{p}\bar{q}_i = -\zeta\omega\bar{q}_i + i\omega\bar{q}_i \quad (2-13)$$

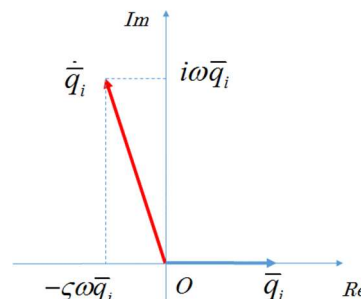


Figure 4: Relation between \bar{q}_i and $\dot{\bar{q}}_i$

As is shown in Fig.4, the first term, $-\zeta\omega\bar{q}_i$ on the right of Eq.(2-13) is in the same phase to \bar{q}_i . Therefore it has an effect apparently to reduce the stiffness of the system. It coincides with the fact that the frequency of the system will decreases in its value with damping

increasing. The second term will contribute to the damping. The out-of-phase component $i\omega\bar{q}$ in the aerodynamic forces in Eq.(2-3) will be replaced later by $\dot{\bar{q}}$ and $\zeta\omega\bar{q}_i$ so as $i\omega\bar{q}_i = \dot{\bar{q}}_i + \zeta\omega\bar{q}_i$ in Eqs.(2-3).

2.4 Amplitude ratio

To make the process complete, the amplitude ratios, $g_{1/2}$ and, $g_{2/1}$, which appear in the previous sections, need to be derived. For this purpose, Eqs. (2-3) are rewritten as

$$\begin{cases} \ddot{\bar{q}}_1 + 2\zeta_{01}\omega_1\dot{\bar{q}}_1 + (\omega_1^2 - \omega^2\bar{F}_{11})\bar{q}_1 = \omega^2\bar{F}_{12}\bar{q}_2 \\ \ddot{\bar{q}}_2 + 2\zeta_{02}\omega_2\dot{\bar{q}}_2 + (\omega_2^2 - \omega^2\bar{F}_{22})\bar{q}_2 = \omega^2\bar{F}_{21}\bar{q}_1 \end{cases} \quad (2-14a,b)$$

If we enhance on the first equation, it can be looked on a forced vibration of \bar{q}_1 with $\omega^2\bar{F}_{12}\bar{q}_2$ imposed as an external force, which is governed by the second equation. The amplitude ratio and the phase difference of \bar{q}_2 to \bar{q}_1 , those are, $g_{2/1}$ and $\Delta_{12}\psi$, will be led from the second equation. Substituting \bar{q}_2 and \bar{q}_1 assumed by Eqs.(2-4) into Eq.(2-14b), after some manipulations, it will be found $g_{2/1}$ and $\Delta_{12}\psi$ are to be in a relation as

$$\frac{q_{02}}{q_{01}} e^{-i\Delta_{12}\psi} = \frac{\omega^2\bar{F}_{21}}{p^2 + 2\zeta_{02}\bar{p}\omega_2 + \omega_2^2 - \omega^2\bar{F}_{22}} = \frac{\sqrt{(F'_{21})^2 + (F''_{21})^2}}{\sqrt{(G'_2)^2 + (G''_2)^2}} e^{-i(\theta_1 - \theta_2)} \quad (2-15)$$

where

$$G'_2 = -F'_{22} + \left(\frac{\omega_2}{\omega}\right)^2 - 2\zeta \cdot \zeta_{20} \left(\frac{\omega_2}{\omega}\right) - (1 - \zeta^2), \quad G''_2 = -F''_{22} + 2\zeta_{20} \left(\frac{\omega_2}{\omega}\right) - 2\zeta \quad (2-16)$$

$$\theta_1 = \tan^{-1} \left(\frac{-F''_{21}}{F'_{21}} \right), \quad \theta_2 = \tan^{-1} \left(\frac{-G''_2}{G'_2} \right) \quad (2-17)$$

By comparing the first and the last expressions of Eq.(2-15), $g_{2/1}$ and $\Delta_{12}\psi$ must be

$$g_{2/1}(\omega, \zeta) = \frac{q_{02}}{q_{01}} = \frac{\sqrt{(F'_{21})^2 + (F''_{21})^2}}{\sqrt{(G'_2)^2 + (G''_2)^2}} \quad (2-18)$$

and

$$\Delta_{12}\psi = \theta_1 - \theta_2 \quad (2-19)$$

As for Branch 2, the same procedure is applied to the first equation of Eq.(2-14a), the amplitude ratio $g_{1/2}$ and the phase difference $\Delta_{21}\psi$ are obtained as

$$g_{1/2}(\omega, \zeta) = \frac{q_{01}}{q_{02}} = \frac{\sqrt{(F'_{12})^2 + (F''_{12})^2}}{\sqrt{(G'_1)^2 + (G''_1)^2}} \quad (2-20)$$

$$\Delta_{21}\psi = \theta_2 - \theta_1, \quad (2-21)$$

where

$$G'_1 = -F'_{11} + \left(\frac{\omega_1}{\omega}\right)^2 - 2\zeta \cdot \zeta_{10} \left(\frac{\omega_1}{\omega}\right) - (1 - \zeta^2), \quad G''_1 = -F''_{11} + 2\zeta_{10} \left(\frac{\omega_1}{\omega}\right) - 2\zeta \quad (2-22)$$

$$\theta_1 = \tan^{-1} \left(\frac{-F''_{12}}{F'_{12}} \right), \quad \theta_2 = \tan^{-1} \left(\frac{-G''_1}{G'_1} \right) \quad (2-23)$$

The amplitude ratio g_{ij} and the phase difference $\Delta_j\psi$ vary with respect to the system frequency ω and damping ratio ζ . Although further discussions will be left out for the sake of limited space in this paper, the similar discussions to those made in the case of general forced vibration might be done about the behaviors of g_{ij} and $\Delta_j\psi$.

3 Transformed flutter equations

Branch 1 expresses the behaviors of $\bar{z}^{(1)}(t)$ defined by Eq.(2-1), on which \bar{q}_1 is varying accompanied by \bar{q}_2 with the amplitude ratio $g_{2/1}$ and the phase lag $\Delta_{12}\psi$ behind \bar{q}_1 . By substituting Eq.(2-10) with Eq.(2-12), (2-18) and Eq.(2-19) into Eq.(2-14a), \bar{q}_2 can be eliminated from Eq.(2-14a), and the following equation is obtained.

$$\ddot{\bar{q}}_1 + [2\zeta_{10}\omega_1 - \omega F''_{11} - \omega\Phi''_{12}] \dot{\bar{q}}_1 + [\omega_1^2 - \omega^2 F'_{11} - \omega^2\Phi'_{12} - \zeta\omega^2 F''_{11} - \zeta\omega^2\Phi''_{12}] \bar{q}_1 = 0 \quad (3-1)$$

where $i\omega\bar{q}_i$ is replaced by $i\omega\bar{q}_i = \dot{\bar{q}}_i + \zeta\omega\bar{q}_i$ and where $\bar{\Phi}_{ij}$ are defined by Eq.(2-12).

Equation (3-1) governs Branch1. It looks like a free vibration equation with single-degree-of-freedom with respect to \bar{q}_1 .

For Branch 2, it becomes as

$$\ddot{\bar{q}}_2 + [2\zeta_{20}\omega_2 - \omega F''_{22} - \omega\Phi''_{21}] \dot{\bar{q}}_2 + [\omega_2^2 - \omega^2 F'_{22} - \omega^2\Phi'_{21} - \zeta\omega^2 F''_{22} - \zeta\omega^2\Phi''_{21}] \bar{q}_2 = 0 \quad (3-2)$$

Though $\bar{\Phi}_{ij}$ look like usual aerodynamic coefficients, they include much information on the relations among the unsteady aerodynamic coefficients, the amplitude ratios and the phase differences between the relevant modes.

4 Stability analyses for flutter boundary

Incidentally, dynamics of a given free vibration is described with its fundamental frequency ω_n for an undamped vibration system and the damping ratio ζ_n as follows;

$$\ddot{x} + 2\zeta_n\omega_n\dot{x} + \omega_n^2x = 0 \quad (4-1)$$

As is well known, the system frequency ω and the system damping ratio ζ are expressed by

$$\omega = \sqrt{1 - \zeta_n^2} \omega_n, \quad 2\zeta\omega = 2\zeta_n\omega_n \quad (4-2)$$

Comparing Eq.(4-1) with Eq.(3-1), after some manipulations, the following relations are obtained for branch 1.

$$\begin{cases} (1 + \zeta^2)\omega^2 = \omega_1^2 - \omega^2 [F'_{11} + \Phi'_{12}] - \zeta\omega^2 [F''_{11} + \Phi''_{12}] \\ 2\zeta\omega = 2\zeta_{10}\omega_1 - \omega [F''_{11} + \Phi''_{12}] \end{cases} \quad (4-3a,b)$$

where

$$\begin{aligned} \bar{\Phi}_{ij} &= \Phi'_{ij} + i\Phi''_{ij} \\ &= g_{ji} \left\{ (F'_{ij} \cos \Delta_j\psi + F''_{ij} \sin \Delta_j\psi) + i(-F'_{ij} \sin \Delta_j\psi + F''_{ij} \cos \Delta_j\psi) \right\} \quad (i = 1, 2, j = 1, 2) \end{aligned} \quad (2-12)$$

$$g_{2/1}(\omega, \zeta) = \frac{\sqrt{(F'_{21})^2 + (F''_{21})^2}}{\sqrt{(G'_2)^2 + (G''_2)^2}} \quad (2-18)$$

$$\Delta\psi_{12} = \theta_2 - \theta_1, \quad (2-19)$$

$$G'_2 = -F'_{22} + \left(\frac{\omega_2}{\omega}\right)^2 - 2\zeta \cdot \zeta_{20} \left(\frac{\omega_2}{\omega}\right) - (1 - \zeta^2), \quad G''_2 = -F''_{22} + 2\zeta_{20} \left(\frac{\omega_2}{\omega}\right) - 2\zeta \quad (2-16)$$

$$\theta_1 = \tan^{-1} \left(\frac{-F''_{21}}{F'_{21}} \right), \quad \theta_2 = \tan^{-1} \left(\frac{-G''_2}{G'_2} \right) \quad (2-17)$$

It is found that Eqs. (4-3) form a set of simultaneous nonlinear algebraic equations with with subsidiary conditions Eqs.(2-12) and (2-16)~(2-19). The unknowns are ω and ζ . Once they are specified, the amplitude ratio $g_{2/1}$ and the phase difference $\Delta\psi_{12}$ are determined.

In order to obtain the solutions of Eqs.(4-3), the Newton-Raphson Method is employed. Residuals of the Eqs. (4-3) are defined by

$$\begin{cases} R_1(\omega, \zeta) = (1 + \zeta^2)\omega^2 - \{\omega_1^2 - \omega^2 [F'_{11} + \Phi'_1] - \zeta\omega^2 [F''_{11} + \Phi''_1]\} \\ R_2(\omega, \zeta) = \zeta\omega - \{2\zeta_{10}\omega_1 - \omega [F''_{11} + \Phi''_1]\} \end{cases} \quad (4-4a,b)$$

Then the increments of ω and ζ at an iteration step are computed in a familiar manner as

$$\omega^{m+1} = \omega^m + \Delta\omega^m, \quad \zeta^{m+1} = \zeta^m + \Delta\zeta^m \quad (4-5)$$

$$\begin{bmatrix} \Delta\omega^m \\ \Delta\zeta^m \end{bmatrix} = - \begin{bmatrix} d(R_1, R_2) \\ d(\omega, \zeta) \end{bmatrix}_{\omega=\omega^m, \zeta=\zeta^m} \begin{bmatrix} R_1(\omega^m, \zeta^m) \\ R_2(\omega^m, \zeta^m) \end{bmatrix} \quad (4-6)$$

Repetitive calculations for the branch 1 are summarized as below;

- Step 1 specify flow velocity, U^N
- Step 2 assume ω^m and ζ^m
- Step 3 calculate the reduced frequency by $k = b\omega^m/U^N$
- Step 4 evaluate unsteady aerodynamic coefficients \bar{F}_{ij} which are functions of k
compute $g_{2/1}$ and $\Delta\psi_{12}$
- Step 5 calculate the residuals, $R_1(\omega^m, \zeta^m)$ and $R_2(\omega^m, \zeta^m)$
- Step 6 calculate $\Delta\omega^m$, $\Delta\zeta^m$ and ω^{m+1} , ζ^{m+1} .
- Step 7 continue with steps 2~6 until both of $|\Delta\omega^m|$ and $|\Delta\zeta^m|$ become smaller than a predefined value as converging criteria
a set of converged solutions $(\omega^m, \zeta^m, g_{2/1}, \Delta\psi_{12})$ associated with a flow velocity U^N is obtained
- Step 8 back to Step 1 with $U^{N+1} = U^N + \Delta U$

Finally the converged solution $(\omega, \zeta, g_{2/1}, \Delta\psi_{12})$ at each iteration step will be plotted with respect to U . That shows branch 1.

The obtained ζ vs. U curve shows variations of the damping ratios on Branch 1. As is done in the flutter analyses, for example, in U - g method and p - k method, the flutter velocity is defined as the velocity at the point where the damping ratio ζ vanishes.

The present formulation is completely symmetry in scheme between branch1 and branch 2. Therefore, the plot of branch 2 can be drawn in the similar procedure to that described above for branch 1.

5 Computed results and discussions

In the present studies, the unsteady aerodynamic forces are modeled by Theodorsen's linear theory. Even if the unsteady aerodynamic forces can not be obtained theoretically, those are acquired from wind tunnel tests or CFD numerical simulations as is mentioned in the section 1. Matsumoto et al. (2010) used Scanlan's flutter derivatives for their development of SBS method. In any cases, it should be noted that they are derived with the assumption that system is in a simple harmonic oscillation, that is, with no damping. They should be applied to the cases limited to those with no decay. If damping is small, however, like near flutter boundary, they might be applicable.

In the SBS method, each component of unsteady aerodynamics is introduced as $\omega^2 A \bar{q} + \omega A^* \dot{\bar{q}}$, where A and A^* are the flutter derivatives. In the present method, on the other hand, they are expressed as $\omega^2 (F' + iF'') \bar{q}$ using complex unsteady aerodynamic coefficients. If the system has no damping, there are no differences between both methods. Otherwise, there are differences.

Theodorsen's unsteady aerodynamic force can be rewritten like

$$\omega^2 (F' + iF'') \bar{q} = \omega^2 F' \bar{q} + \omega F'' (i\omega \bar{q}) = \omega^2 F' + \omega F'' (\dot{\bar{q}} + \zeta \omega \bar{q}) = \omega^2 (F' + \zeta F'') \bar{q} + \omega F'' \dot{\bar{q}} \quad (5-1)$$

Comparing it with Scanlan's force, an additional term $\zeta F''$ is found in the first term of the last expression. As it will be incorporated into the stiffness terms in Eqs.(3-1) and (3-2), it has an effect apparently to reduce the stiffness of the system if it is in a positive damping oscillation. It coincides with the fact that the system frequency will decrease in its value in the case of a damping vibration. From this viewpoint, the model of unsteady aerodynamic force has been improved in the present studies so as is more rational than that in the SBS method.

Another advantage of the present approach is that the flutter mechanism has been clearly interpreted. Attention being paid to the damping terms of Eqs.(3-1) and (3-2). they consist of not only the original structural damping but also the damping due to the unsteady aerodynamic forces expressed by $\bar{\Phi}_{ij} \bar{q}_i$. $\bar{F}_{ij} \bar{q}_j$ has been transformed into $\bar{\Phi}_{ij} \bar{q}_i$ using the amplitude ratio and phase difference between \bar{q}_i and \bar{q}_j as well as \bar{F}_{ij} . $\bar{\Phi}_{ij} \bar{q}_i$ mean the gains and the phase lags of the generalized self-excited forces induced by and imposed to \bar{q}_i , itself. Then not only the gains and the phase lags of the unsteady aerodynamic forces but also the amplitude ratios and phase differences between \bar{q}_i and \bar{q}_j have significant influences on the behaviors of the damping terms.

Eq.(3-1) and Eq.(3-2) together with Figs.3 interpret well the flutter onset process. They will be easily extended to multi-degree-of-freedom flutter analyses by more general form like

$$\ddot{\bar{q}}_i + \left[2\zeta_{i0} \omega_i - \omega \sum_{j=1}^r \bar{\Phi}_{ij}'' \right] \dot{\bar{q}}_i + \left[\omega_i^2 - \omega^2 \sum_{j=1}^r \bar{\Phi}_{ij}' - \zeta \omega^2 \sum_{j=1}^r \bar{\Phi}_{ij}'' \right] \bar{q}_i = 0 \quad (5-2)$$

$$\begin{cases} \bar{\Phi}_{ij}'(\omega, \zeta) = g_{j/i} \left(F_{ij}' \cos \Delta_{ij} \psi - F_{ij}'' \sin \Delta_{ij} \psi \right) \\ \bar{\Phi}_{ij}''(\omega, \zeta) = g_{j/i} \left(F_{ij}' \sin \Delta_{ij} \psi + F_{ij}'' \cos \Delta_{ij} \psi \right) \end{cases} \quad \Delta_{ij} \psi = \psi_j - \psi_i, \quad g_{j/i} = \frac{q_{0j}}{q_{0i}} \quad (i = 1, r, j = 1, r)$$

Much more information will be included in $\bar{\Phi}_{ij}\bar{q}_i$, which will take very important roles.

5.1 Numerical Examples

A case presented by Bisplinghoff et al.(1957) in their text book as ‘Case (u)’ is simulated. It can be realized by setting the system parameters as shown in Tab.1. The corresponding non-dimensional parameters are also shown in Tab.2. The obtained results are shown in Figs.5.

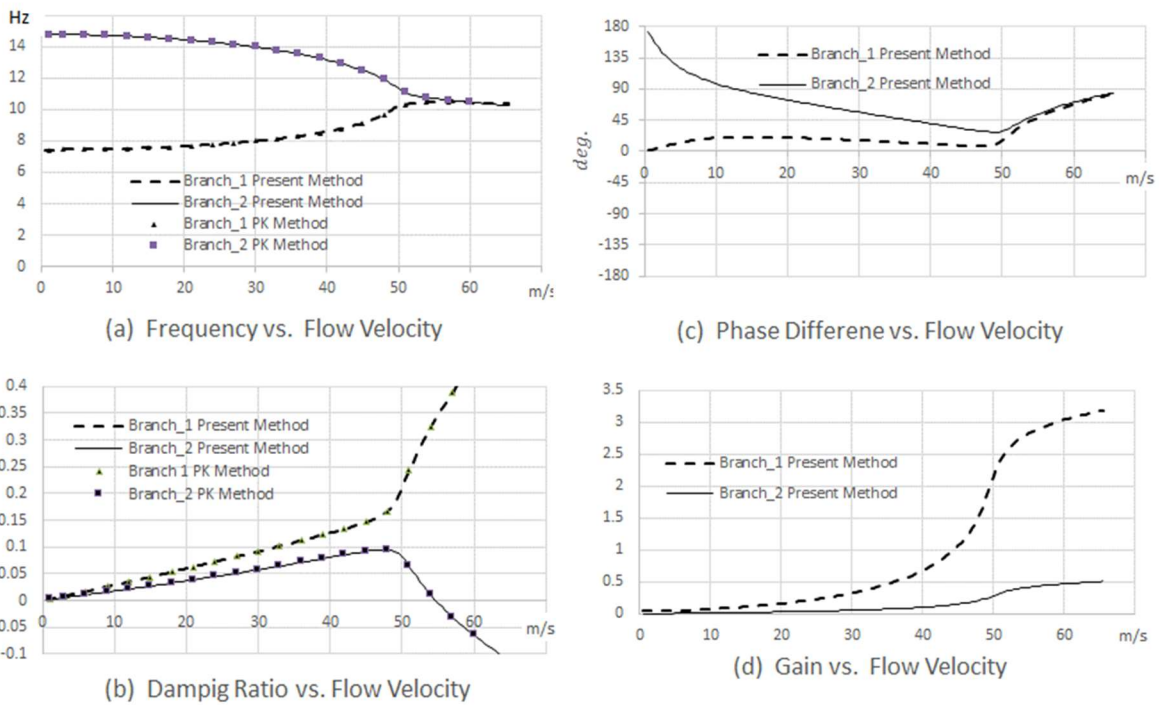
Table 1: Dimensional parameters

ρ (kg / m ³)	M (kg / m)	b (m)	ω_α (rad / s)	ω_h (rad / s)	I (kgm ² / m)	S_α (kgm / m)
1,23	6.93	0.3	83.3	50.0	0.1556	4.158

Table 2: Non-dimensional parameters

a	x_α	r_α^2	μ	ω_h/ω_α	ζ_{10}	ζ_{20}
-0.45	0.2	0.25	20	0.6	0	0

$$S_a = mbx_\alpha, \quad I_a = mb^2r_\alpha^2, \quad \mu = m/\pi\rho b^2$$



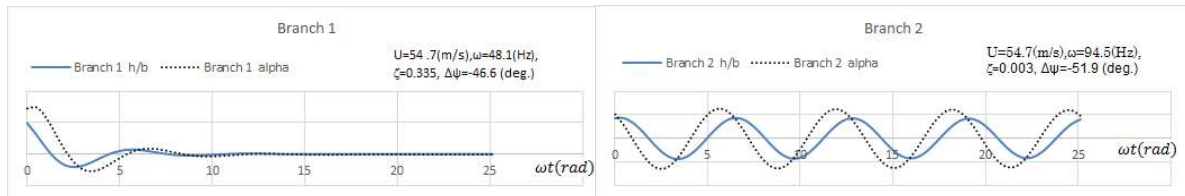
Figures 5: Numerical example of MSBS Case(u) in Bisplinghoff et al. (1957)

$$(\omega_h/\omega_\alpha = 0.2, \quad a = -0.45, \quad x_\alpha = 0.2, \quad r_\alpha^2 = 0.25, \quad \mu = 20, \quad \zeta_{01} = \zeta_{02} = 0)$$

In the present studies, the flutter mode shape were assumed by Eq.(2-1), superposing the two natural modes of the system with generalized coordinates q_i ($i=1,2$). In the course to flutter, there exist two modes, branch 1 and branch 2. Using the quantities derived in this paper, they are expressed in real forms;

$$\text{Re}[\bar{z}^{(n)}(t, x)] = \sum_{i=1}^2 g_{i/n} e^{-\zeta^{(n)}\omega^{(n)}t} \cos(\omega^{(n)}t - \Delta_{ni}\psi)\phi_i(x) \quad (n=1,2) \quad (5-3)$$

The time histories of the heaving and pitching displacements on the two Branches near flutter point are shown in Figs.6. It is found that the branch 2 (wash-out, higher frequency mode) is going into flutter at the flow velocity, 54.7 m/s with frequency, $\omega = 67.3 \text{ (rad/s)}$ (10.7Hz , $k = 0.37$). The Branch 1 (wash-in, lower frequency mode) is strongly damping.



Figures 6: Time histories of heaving and pitching motions of Branch 1 and Branch 2 near flutter point: heaving(downward positive), pitching (noseup positive)

6 Conclusions

A new flutter analysis method has been proposed by modifying the SBS, Step-by-Step, method. The method is characterized;

1. unsteady aerodynamic forces are introduced more rationally than the original SBS,
2. the 2DOF system is reduced apparently to single-degree-of-freedom systems, in which the damping terms and the stiffness terms are constituted so as they interpret well the physical meanings of the system parameters,
3. the resultant damping terms show that the phase lags of the unsteady aerodynamic forces as well as the phase differences between the superposed natural modes have important roles to keep the system stability,
4. individual branches can be tracked with respect to the flow velocity more clearly than the conventional stability analyses,
5. in our numerical experiments, there are no discrepancies in the flutter velocities between the present method and the conventional p - k method.

As future tasks, the followings are encouraged;

1. extension to multi degrees of freedom problems based upon the present approach,
2. further investigation of the behaviors of 2DOF flutter, for instance, bifurcations, roles of each force \bar{F}_{ij} , influence of the structural parameters and so on.

References

- Bisplinghoff, R.L., Ashley, H and Halfman, R.L., 1957. Aeroelasticity. John Wiley and Sons, Inc., New York, NY.
- Matsumoto, M., Matsumiya, H., Fujiwara, S. and Ito, Y., 2010. New Consideration on Flutter Properties Based on Step-by-Step Analysis, Journal of Wind Engineering and Industrial Aerodynamics, Vol.98, pp.429-437.
- Nakamich, J., Tamayama, M. and Kodama, M., 2019. Aeroelasticity, (written in Japanese), Maruzen Publishing.
- Scanlan, R.H., Tomko, J.J., 1971. Airfoil and Bridge Deck Flutter Derivatives, Journal of Engineering Mechanics, Vol.97, No.EM6, pp1717-1737.
- Theodorsen, T., 1935. General Theory of Aerodynamic Instability and the Mechanism of Flutter, NACA-R496

Flutter analysis (methods and models)

A Deep Learning Approach to Model Nonlinear Aerodynamic Forces

1st Hanyu Mei¹, 2nd Haili Liao² and 3rd J.H.G. Macdonald³

¹*Southwest Jiaotong University, Chengdu, China, mhanyu8866@gmail.com*

²*Southwest Jiaotong University, Chengdu, China, hlliao@swjtu.edu.cn*

³*Department of Civil Engineering, University of Bristol, Bristol, UK, john.macdonald@bristol.ac.uk*

Keyword: nonlinear aerodynamic force, Deep Learning, Recurrent Neural Network

In many scientific fields, empirical models are employed to enable designers and researchers to conduct numerical analysis as well as to facilitate computational simulations of engineering systems. For example, in the field of wind resistance of long-span bridges, empirical motion-induced force model proposed by Scanlan has been used for several decades for carrying out linear analysis on calculating the responses of bridge girders. Traditional methods for developing and tuning empirical models usually combine physical intuition with simple regression techniques on limited data sets. While the rise of high-performance computing is opening up new possibilities for applying Machine Learning or Deep Learning to physical systems to develop advanced data-driven empirical models based on high fidelity experimental or simulating results, a key question when using data-driven algorithms to develop these empirical models is how domain knowledge should be incorporated into the Deep Learning process. This paper presents a new approach to model nonlinear aerodynamic forces in the time domain by utilizing Deep Learning techniques. To incorporate the prior empirical model into the Deep Learning framework, a basis of invariant input features is chosen empirically based on the prior Taylor Expansion form of motion-induced nonlinear aerodynamic forces and Quasi-steady theory-based buffeting force model. Then, the Recurrent Neural Network (RNN) is introduced and evolved to meet this specific question. This Neural Network (NN) is constructed by choosing the time series of forces as the output, and is trained upon the basis by inputting the discrete measured data of nonlinear aerodynamic forces of 5:1 rectangular cylinder obtained from the forced vibration system under turbulent flow in wind tunnel. Furthermore, the l_1 -norm regularization term is added in the loss function of the neural network to penalize the weights of each neuron so as to realize the feature selection. In addition, white noise is intentionally added in the input data to render the RNN scheme more robust. Lastly, results are discussed by evaluating the fitting accuracy as well as validating the prediction performance with regard to the model's robustness. It is shown that the proposed approach based on RNN could embed the invariance properties into the input features corresponding to the empirical classical framework by regarding NN as characteristics of the nonlinear aerodynamic forces and this implicit model yields high performance with satisfying accuracy and robustness. This data-driven approach can also be extended to full-bridge (3-D) model by taking the correlation of aerodynamic forces into account and has shown a remarkable potential for applications to other unsolved problems in wind engineering, e.g. reconstruction of wind pressure on tall buildings, vortex-induced forces or responses of structures in turbulence.

1. Wu T, Kareem A. Modeling hysteretic nonlinear behavior of bridge aerodynamics via cellular automata nested neural network[J]. *Journal of Wind Engineering and Industrial Aerodynamics*, 2011, 99(4): 378-388.
2. Hu G, Liu L, Tao D, et al. Investigation of wind pressures on tall building under interference effects using machine learning techniques[J]. *arXiv preprint arXiv:1908.07307*, 2019.
3. Li S, Laima S, Li H. Data-driven modeling of vortex-induced vibration of a long-span suspension bridge using decision tree learning and support vector regression[J]. *Journal of Wind Engineering and Industrial Aerodynamics*, 2018, 172: 196-211.

Aeroelastic optimisation of aeronautical composite structures considering uncertainties

Mahshid Sharifi¹, Angela Vincenti¹ and Jean-Camille Chassaing¹

¹ Sorbonne Université, CNRS, Institut Jean Le Rond d'Alembert, UMR 7190, F-75005 Paris, France
Email of the first author: mahshid.sharifi@etu.sorbonne-universite.fr

Keywords: Aeroelastic flutter - Composite structures - Robust optimisation

Composite structures have gained a predominant place in aeronautics, thanks to their high strength-to-weight and stiffness-to-weight ratio which can be exploited for tailoring their optimal aeroelastic behaviour [1,3]. This work focuses on optimising the aeroelastic response of composite plates by allowing a systematic investigation of the complete domain of anisotropic composite laminates and by selecting multiple domains of anisotropy [2]. As shown in Fig. 1a, the mode switch observed in the response surface may be responsible for dramatic reduction of the flutter margin when parametric uncertainties due to the manufacturing process are taken into account (Fig. 1b).

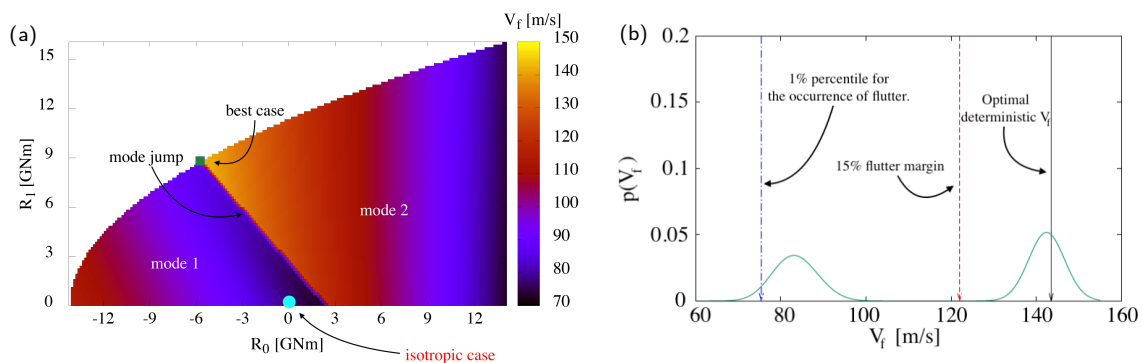


Figure 1: (a) Response surface of the flutter velocity V_f for a 16-layer orthotropic laminated rectangular plate wing. (b) Distribution of V_f due to uncertainty in thicknesses and orientation angles of the aeroelastic optimal laminate.

The purpose of this work is to develop uncertainty quantification and robust optimization methods in order to alleviate the limits of purely deterministic optimisation. Uncertainty in all the constitutive parameters of the laminate, both angles and thicknesses will be considered for the aeroelastic optimization of straight and swept laminated plates for low-speed flows.

¹ C.T. Nitschke, A. Vincenti, J-C Chassaing, Influence of stochastic perturbations of composite laminate layups on the aeroelastic flutter of a cantilevered plate wing, Composite Structures, Volume 220, Pages 809-826, 15 July 2019

² Scarth, Carl, et al. "Uncertainty quantification of aeroelastic stability of composite plate wings using lamination parameters." Composite Structures 116 (2014): 84-93.

³ Kameyama, Masaki, and Hisao Fukunaga. "Optimum design of composite plate wings for aeroelastic characteristics using lamination parameters." Computers & structures 85.3-4 (2007): 213-224.

Flutter Analysis of Large Flexible Aircraft based on Structural ROM Method and Nonlinear Substructure Method

1st An Chao¹, 2nd Xie Changchuan² and 3rd Yang Chao³

¹*Beihang University, Beijing, China, ac_buaa@163.com*

²*Beihang University, Beijing, China*

³*Beihang University, Beijing, China*

Abstract

This paper presents a framework for analyzing the stability characteristics of a very flexible aircraft. Considering geometrical nonlinearity, aircraft is divided into nonlinear wing components and linear fuselage component. Structural ROM method is used for wing structure modeling and nonlinear substructure method is used for comprehensive assembling wing ROM and fuselage linear modes together to obtain integrated aircraft dynamic equations. Non-planar double lattice method (DLM) is used as aerodynamic model. Stability analysis is based on the linearization around the trim configuration. The numerical results for a flexible flying wing aircraft model indicate coupling effects between rigid-body motions and elastic modes are important for this type of aircraft.

Keyword: Flutter, Reduced Order Model (ROM), Substructure, Geometrical Nonlinearity

1 Introduction

As the representative of the very flexible airplane, high-altitude long-endurance (HALE) aircrafts usually attract extensive attention. Because of its weight and large flexibility, the wing of HALE will produce large deformation during the flight. Geometric nonlinearity becomes a very important factor that affects aeroelastic stability and response. For the design requirement of HALE, Hodges, Cesnik and Patil proposed the concept of fixed wing aircraft geometric nonlinear aeroelastic problem in 1999^{1,2}. Lots of research with diverse content of related research has been carried out³⁻⁶. For large flexible aircraft, especially flying wing aircraft, the frequency differences between elastic modes and rigid-body motions tend to be sufficiently small such that the coupled effect cannot be ignored⁷. Furthermore, the structure becomes nonlinear due to the large deformation. Nonlinear aeroelasticity and flight dynamics should be considered simultaneously⁸. In addition, tailless airplanes with relatively low rigid-body pitch inertias can have relatively high short-period frequencies that interact with elastic deformations, resulting in a dynamic instability, which is known as body-freedom flutter⁹.

Structural reduced order model (ROM) is an efficient method to analysis nonlinear response problem of large flexible structure. It shows us computational inexpensive mathematical representation of structure analysis in nonlinear aeroelastic problem and offers the potential for real-time domain analysis. Muravyov et al. used the surrogate model to satisfy the structural nonlinear dynamics equation¹⁰. In addition, Mignolet et al. reported that the nonlinear stiffness can be described using an equation with the quadratic and cubic terms of the basis function¹¹. Based on that formulation, McEwan et al. implemented the Modal/FE (MFE) method to conduct analysis with a number of serial static load cases¹². Harmin and Cooper implemented the MFE method to model the geometric nonlinearities of large flexible wing in aeroelastic analysis¹³. An et al. modified MFE method to evaluate the accuracy of analysis and applied the method into static trim and nonlinear gust response problem¹⁴⁻¹⁵.

For more complex aircraft structures, such as the entire aircraft system, decomposing it into several simple substructure and using the boundary conditions between the substructures to assemble dynamic equations could be an efficient method for structure modeling. Compared with the overall modal structure reduction method, the substructure method can still guarantee low model order and high calculation accuracy. In practical applications, the component mode synthesis (CMS) method including the fixed interface CMS and the free interface CMS is widely used.

Applications of CMS in local nonlinear dynamic problem have attracted attention of many scholars. Clough et al. investigated substructure method to local nonlinear problem first¹⁶. Tan et al. divided the structure into linear substructure components and nonlinear substructure components¹⁷. The interactions between substructures were replaced by boundary forces to solve the transient response problem of local nonlinear structures. Fey et al. reduced the cantilever structure with nonlinear support and studied the nonlinear frequency domain response problem¹⁸.

Most nonlinear substructures method focuses on the connection nonlinearities. As long as the nonlinear interface connection relationship is given, substructure itself is still a linear structure. The major source of geometric nonlinearities for large flexible aircraft is the wing component. The fuselage and other components of aircraft maintain linearity in analysis of geometric nonlinear problems. Processing all aircraft structures as nonlinear structures will greatly increase the computational cost. The substructure method considering geometric nonlinearities factors in structure domain should become important methodology for large flexible aircraft modeling. Karpel et al. added virtual mass elements to the substructures to simulate the effects of other substructures components¹⁹. They analyzed the static and dynamic response characteristics of large flexible structures. This method divides the wing component into segments processing rather than as a whole structure in order to interface with the fuselage, so it is more like a combination of nonlinear CMS and finite segment method. Kantor et al. extended this method and applied it into a simple large flexible aircraft²⁰. With strip theory, geometrically nonlinear aeroelastic analysis was implemented. At present, substructure method considering geometric nonlinearities is still immature, and applications in aeroelastic analysis are still in the exploratory stage.

This paper is committed for aeroelastic problem associated with stability including geometric nonlinearities based on structural ROM and nonlinear substructure method. Aircraft is divided into nonlinear wing components and linear fuselage components, structural ROM is used for wing structure modeling. Non-planar double lattice method (DLM) is used as aerodynamic model. To validate the method introduced, a very flexible flying wing model is taken as numerical model. Results of aeroelastic flutter analysis as well as stability analysis with linearization of dynamic equations are provided.

2 Theory

2.1 Structural Reduced Order Model

The development of the Structural ROM is based on equations derived from a Galerkin approach to solve geometric nonlinear dynamics in a weak form¹⁰. The equation of motion of the structure may often be given in dynamic equation as:

$$\frac{\partial (F_{ij} S_{jk})}{\partial X_k} + \rho_0 b_i^0 = \rho_0 \ddot{u}_i \quad (1)$$

Where the tensor S is the second P-K stress tensor, the tensor F is the deformation gradient tensor, ρ_0 is the mass density of the structure, and b^0 is the vector of the body force. X denotes the position vector of the structure in the reference configuration, and x denotes the deformed position vector. With Galerkin approach, a truncated basis of linear modes is chosen as the basis functions with no consideration of foreshortening effects first. A third-degree polynomial form describes the nonlinear relationship and the dynamic equation

in terms of the generalized coordinates can be expressed as:

$$M_{ij}q_j + E_{ij}^{(1)}q_j + E_{ijl}^{(2)}q_jq_l + E_{ijlp}^{(3)}q_jq_lq_p = F_i \quad (2)$$

Where M_{ij} are the terms of the reduced mass matrix, F_i is the modal component of the external force, and $E_{ij}^{(1)}$, $E_{ijl}^{(2)}$ and $E_{ijlp}^{(3)}$ are the components of the tensors of the reduced stiffness. Einstein summation convention is applied to the formulation. It should be noted that the analytical expressions of the mass matrix and stiffness matrix can be achieved directly relative to the basis functions and the relations of the materials. However, this is impractical, especially when the FEM model is complex.

When a truncated basis of the linear modes is chosen as the basis function, M_{ij} and $E_{ij}^{(1)}$ can be expressed in the formulation as:

$$\begin{cases} M_{ij} = M_i, i = j \\ M_{ij} = 0, i \neq j \end{cases} \quad (3)$$

$$\begin{cases} E_{ij}^{(1)} = E_i, i = j \\ E_{ij}^{(1)} = 0, i \neq j \end{cases} \quad (4)$$

Where M_i represents the modal mass term of the i -th basis function, and E_i is the modal stiffness term of the i -th basis function. The formulation of the nonlinear dynamic equations corresponding to the i -th basis function can be written as:

$$M_iq_i + E_iq_i + E_{ijl}^{(2)}q_jq_l + E_{ijlp}^{(3)}q_jq_lq_p = F_i \quad (5)$$

The structure dynamic equations in modal space have been obtained and generalized coordinates q_i namely.

Foreshortening effects under large deformations have a substantial influence on geometric nonlinear problems, especially aeroelastic problems. The shortening effect on the spanwise projection of a wing will change the aerodynamic distribution considerably. A truncated basis of the linear modes is chosen as the basis function herein. However, a few linear modes truncated will not show the shortening effect of the wing in ROM analysis. Therefore, two orthogonal spanwise modes are taken into the established ROM to describe the foreshortening effects of the wing. A combination of truncated linear modes and orthogonal spanwise modes is generated as a basis function in the nonlinear structural ROM.

As described before, an explicit calculation of the nonlinear stiffness is not practical. Consequently, regression analysis is used to identify the nonlinear stiffness coefficients $E_{ijl}^{(2)}$ and $E_{ijlp}^{(3)}$, the static formulation of Eq.(5) is:

$$E_{ijl}^{(2)}q_jq_l + E_{ijlp}^{(3)}q_jq_lq_p = F_i - E_iq_i \quad (6)$$

Evidently, if there are a set of specified static loads and corresponding structural deformations, the unknown nonlinear stiffness terms related to the applied loads and the structural displacement resultant can be solved by using regression analysis. The set of specified loads and corresponding structural deformations can be denoted as the static test load case and calculated by a commercial FEM software package.

Through the abovementioned analysis, regression analysis is performed using the commercial software package on the actual deformation and load testing after FEM analysis, and thus the accuracy of the nonlinear stiffness coefficients directly depends on the rationality of the selected test load case, which is related to the success of recovery of the nonlinear structure equation. The selection of test load cases must emphasize that the aerodynamic force on the wing should be a follower force, which more closely resembles the actual characteristics of the aerodynamic force. That is, taking an oriented load as the load test case cannot satisfy the requirements. In this paper, the aerodynamic force under the deformation combined bending and torsion modes is chosen as the test load case. The formulation of the wing deformation, which generates aerodynamic forces, should be:

$$f_{AIR}\{w\} = f_{AIR}\left(\sum a_i\{\phi_i\}_{bend} + \sum a_j\{\phi_j\}_{torsion}\right) \quad (7)$$

Here, $\{\phi_i\}_{bend}$ and $\{\phi_j\}_{torsion}$ represent the investigated bending and torsion modes, respectively, and $a_{i,j}$ represents the scalar mode weight factors, through which the selected test cases contain the nonlinear characteristics of the structure investigated in our research.

2.2 Nonlinear Substructure Method

For large flexible aircraft, take wing components as nonlinear components and fuselage component as linear component. Considering substructure $(\alpha=1, \dots, l_1, l_2, \dots, n)$ system, each substructure dynamic equation in physics coordinates can be expressed as:

$$\begin{pmatrix} \mathbf{m}_{ii} & \mathbf{m}_{ib} \\ \mathbf{m}_{bi} & \mathbf{m}_{bb} \end{pmatrix}^{(\alpha)} \begin{Bmatrix} \ddot{\mathbf{u}}_i \\ \ddot{\mathbf{u}}_b \end{Bmatrix}^{(\alpha)} + \begin{pmatrix} \mathbf{k}_{ii} & \mathbf{k}_{ib} \\ \mathbf{k}_{bi} & \mathbf{k}_{bb} \end{pmatrix}^{(\alpha)} \begin{Bmatrix} \mathbf{u}_i \\ \mathbf{u}_b \end{Bmatrix}^{(\alpha)} + \begin{Bmatrix} \mathbf{g}_i(\mathbf{u}) \\ \mathbf{g}_b(\mathbf{u}) \end{Bmatrix}^{(\alpha)} = \begin{Bmatrix} \mathbf{O} \\ \mathbf{G}_b \end{Bmatrix}^{(\alpha)} + \begin{Bmatrix} \mathbf{f}_i \\ \mathbf{f}_b \end{Bmatrix}^{(\alpha)} \quad (8)$$

Subscript i, b representative interior and boundary coordinates, $\mathbf{g}(\mathbf{u})$ is nonlinear section, \mathbf{G}_b is the boundary load vector, and \mathbf{f} is external force vector. Displacement and Force coordination conditions on interface can be expressed as:

$$\mathbf{u}_b^{(l_1)} = \mathbf{u}_b^{(l_2)} \quad (9)$$

$$\mathbf{G}_b^{(l_1)} + \mathbf{f}_b^{(l_1)} + \mathbf{G}_b^{(l_2)} + \mathbf{f}_b^{(l_2)} = \mathbf{0} \quad (10)$$

Applied fixed interface CMS method to nonlinear wing components analysis, when give $\mathbf{u}_b^{(nl)} = \mathbf{0}$, structure dynamic equation is:

$$\mathbf{m}_{ii}^{(nl)} \ddot{\mathbf{u}}_i^{(nl)} + \mathbf{k}_{ii}^{(nl)} \mathbf{u}_i^{(nl)} + \mathbf{g}_i(\mathbf{u}_i, \mathbf{u}_b = \mathbf{0})^{(nl)} = \mathbf{0} \quad (11)$$

Use linear modes to reduce order with $\mathbf{u}_i^{(nl)} = \Phi_i^{(nl)} \mathbf{q}_i^{(nl)}$, low-order equation is:

$$\ddot{\mathbf{q}}_i^{(nl)} + \Omega_i^{(nl)} \mathbf{q}_i^{(nl)} + \tilde{\mathbf{g}}_i^{(nl)}(\mathbf{q}_i)^{(nl)} = \mathbf{0} \quad (12)$$

Eq.(12) has the similar formulation with reduced order model in section 2.1. Introduce restrained modes Ψ_b to translate displacement:

$$\begin{Bmatrix} \mathbf{u}_i \\ \mathbf{u}_b \end{Bmatrix}^{(nl)} = [\Phi_i \quad \Psi_b]^{(nl)} \begin{Bmatrix} \mathbf{q}_i \\ \mathbf{u}_b \end{Bmatrix}^{(nl)} = \begin{pmatrix} \Phi_{ii} & \Psi_{ib} \\ \mathbf{O}_{bi} & \mathbf{I}_{bb} \end{pmatrix}^{(nl)} \begin{Bmatrix} \mathbf{q}_i \\ \mathbf{u}_b \end{Bmatrix}^{(nl)} \quad (13)$$

The structure dynamic equation can be reformulated as:

$$\begin{pmatrix} \mathbf{I} & \mathbf{M}_{ib} \\ \mathbf{M}_{bb} & \mathbf{M}_{bb} \end{pmatrix}^{(nl)} \begin{Bmatrix} \ddot{\mathbf{q}}_i \\ \ddot{\mathbf{u}}_b \end{Bmatrix}^{(nl)} + \begin{pmatrix} \Omega_i & \mathbf{O} \\ \mathbf{O} & \mathbf{K}_{bb} \end{pmatrix}^{(nl)} \begin{Bmatrix} \mathbf{q}_i \\ \mathbf{u}_b \end{Bmatrix}^{(nl)} + \begin{Bmatrix} \tilde{\mathbf{g}}_i(\mathbf{q}_i, \mathbf{u}_b) \\ \tilde{\mathbf{g}}_b(\mathbf{q}_i, \mathbf{u}_b) \end{Bmatrix}^{(nl)} = \begin{Bmatrix} \mathbf{O} \\ \mathbf{G}_b \end{Bmatrix}^{(nl)} + \begin{Bmatrix} \tilde{\mathbf{f}}_i \\ \tilde{\mathbf{f}}_b \end{Bmatrix}^{(nl)} \quad (14)$$

Where $\mathbf{M}_{ib} = \Phi_{ii}^T (\mathbf{m}_{ii} \Psi_{ib} + \mathbf{m}_{ij})$, $\mathbf{M}_{bi} = \mathbf{M}_{ib}^T$, $\mathbf{M}_{bb} = \Psi_{ib}^T (\mathbf{m}_{ii} \Psi_{ib} + \mathbf{m}_{ij}) + \mathbf{m}_{ji} \Psi_{ib} + \mathbf{m}_{jj}$, $\tilde{\mathbf{f}}_i = \Phi_{ii} \mathbf{f}_i$, $\tilde{\mathbf{f}}_b = \Psi_{ib} \mathbf{f}_i + \mathbf{f}_b$. Only the geometrical nonlinearity problem is considered here, and the nonlinearity problem of aircraft substructure interface connection is not considered.

Apply linear mode reduction method to fuselage component analysis with main linear modes Φ_k and residual modes Ψ_d . The structure dynamic equation can be reformulated as:

$$\begin{pmatrix} \mathbf{I} & \mathbf{O} \\ \mathbf{O} & \mathbf{M}_{dd} \end{pmatrix}^{(l)} \begin{Bmatrix} \ddot{\mathbf{q}} \\ \ddot{\mathbf{G}}_b \end{Bmatrix}^{(l)} + \begin{pmatrix} \Omega & \mathbf{O} \\ \mathbf{O} & \mathbf{K}_{dd} \end{pmatrix}^{(l)} \begin{Bmatrix} \mathbf{q} \\ \mathbf{G}_b \end{Bmatrix}^{(l)} = \begin{Bmatrix} \tilde{\mathbf{f}}_k \\ \tilde{\mathbf{f}}_d \end{Bmatrix}^{(l)} \quad (15)$$

Where $\mathbf{M}_{dd} = \Psi_d^T \mathbf{m} \Psi_d$, $\mathbf{K}_{dd} = \Psi_d^T \mathbf{k} \Psi_d$, $\tilde{\mathbf{f}}_k = \Phi_k^T \begin{Bmatrix} \mathbf{f}_i \\ \mathbf{G}_b + \mathbf{f}_b \end{Bmatrix}$, $\tilde{\mathbf{f}}_d = \Psi_d^T \begin{Bmatrix} \mathbf{f}_i \\ \mathbf{G}_b + \mathbf{f}_b \end{Bmatrix}$. Considering the

specified aircraft formulation, structure can be divided into left wing component, right wing component and fuselage component. Structure dynamic equations can be expressed as:

$$\begin{pmatrix} \mathbf{I}_{lw} & \mathbf{M}_{iblw} \\ \mathbf{M}_{bilw} & \mathbf{M}_{bblw} \end{pmatrix} \begin{Bmatrix} \ddot{\mathbf{q}}_{ilw} \\ \ddot{\mathbf{u}}_{blw} \end{Bmatrix} + \begin{pmatrix} \boldsymbol{\Omega}_{ilw} & \mathbf{O} \\ \mathbf{O} & \mathbf{K}_{bblw} \end{pmatrix} \begin{Bmatrix} \mathbf{q}_{ilw} \\ \mathbf{u}_{blw} \end{Bmatrix} + \begin{Bmatrix} \tilde{\mathbf{g}}_{ilw}(\mathbf{q}_{ilw}) \\ -\mathbf{G}_{bblw} \end{Bmatrix} = \begin{Bmatrix} \tilde{\mathbf{f}}_{ilw} \\ \tilde{\mathbf{f}}_{blw} \end{Bmatrix} \quad (16)$$

$$\begin{pmatrix} \mathbf{I}_{rw} & \mathbf{M}_{ibrw} \\ \mathbf{M}_{birw} & \mathbf{M}_{bbrw} \end{pmatrix} \begin{Bmatrix} \ddot{\mathbf{q}}_{irw} \\ \ddot{\mathbf{u}}_{brw} \end{Bmatrix} + \begin{pmatrix} \boldsymbol{\Omega}_{irw} & \mathbf{O} \\ \mathbf{O} & \mathbf{K}_{bbrw} \end{pmatrix} \begin{Bmatrix} \mathbf{q}_{irw} \\ \mathbf{u}_{brw} \end{Bmatrix} + \begin{Bmatrix} \tilde{\mathbf{g}}_{irw}(\mathbf{q}_{irw}) \\ -\mathbf{G}_{bbrw} \end{Bmatrix} = \begin{Bmatrix} \tilde{\mathbf{f}}_{irw} \\ \tilde{\mathbf{f}}_{brw} \end{Bmatrix} \quad (17)$$

$$\begin{pmatrix} \mathbf{I}_{fu} & \mathbf{O} \\ \mathbf{O} & \mathbf{M}_{dfu} \end{pmatrix} \begin{Bmatrix} \ddot{\mathbf{q}}_{ifu} \\ \ddot{\mathbf{G}}_{bfu} \end{Bmatrix} + \begin{pmatrix} \boldsymbol{\Omega}_{ifu} & \mathbf{O} \\ \mathbf{O} & \mathbf{K}_{dfu} \end{pmatrix} \begin{Bmatrix} \mathbf{q}_{ifu} \\ \mathbf{G}_{bfu} \end{Bmatrix} = \begin{Bmatrix} \tilde{\mathbf{f}}_{kfu} \\ \tilde{\mathbf{f}}_{dfu} \end{Bmatrix} \quad (18)$$

Subscript lw, rw, fu represent left wing, right wing and fuselage. Displacement and force coordination conditions are:

$$\mathbf{u}_{blw} = \mathbf{u}_{bfulw} \quad (19)$$

$$\mathbf{u}_{brw} = \mathbf{u}_{bfurw}$$

Where the $\mathbf{u}_{bfulw}, \mathbf{u}_{bfurw}$ is connection freedom between fuselage with left wing and right wing.

2.3 Aerodynamics Model

Non-planar DLM can be used to complete stable analysis. Unsteady aerodynamic force is given as:

$$\boldsymbol{\Phi}_S \mathbf{f}_A = q_\infty [\mathbf{A}_{SS0} \mathbf{q}_S + \frac{c_{ref}}{2V_\infty} \mathbf{A}_{SS1} \dot{\mathbf{q}}_S + \frac{c_{ref}^2}{4V_\infty^2} \mathbf{A}_{SS2} \ddot{\mathbf{q}}_S] + \mathbf{D} \mathbf{x}_a \quad (20)$$

Structure model and aerodynamic model can be linearized around trim configuration⁹ and comprehensive assembled to a state-space model:

$$\dot{\mathbf{x}}_{ae} = \mathbf{A}_{ae} \mathbf{x}_{ae} \quad (21)$$

Where \mathbf{x}_{ae} is the state variable vector and \mathbf{A}_{ae} is the state matrix. The eigenvalues of state matrix represent the stability of system.

3 Numerical Results

3.1 Flying wing model

A numerical example of flying wing model is given here to illustrate the theoretical modeling process and stable characteristics of rigid-elastic coupled problem. Fig.1 shows the flying wing model used to implement the stability analysis established in this paper. Main design parameters have been given in Table.1. This flying wing is constructed of a central wing-fuselage fusion, two side wings, and a vertical tail at each wing tip. Two control surfaces are arranged at the trailing edge of the wing, acting as elevators, ailerons, and wing flaps via differential and linkage motion control. The FEM model of the flying wing is constructed with beam elements and concentrated mass elements. The non-planar DLM are used to establish the unsteady aerodynamic model for the flying wing. For longitudinal flight analysis, three degrees of freedom of longitudinal rigid-body motions and elastic modes are considered. Small perturbation linearized is based on the nonlinear trim analysis under large-amplitude deflection and the structural modes are different in different load conditions.

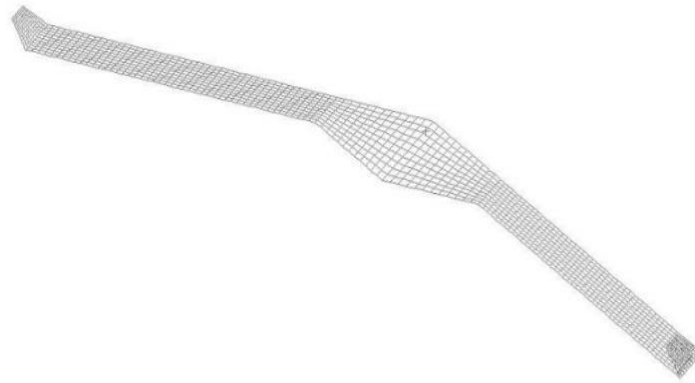


Figure 1: Flying Wing

Table 1: Design parameters of flying wing

Wing span	Wing area	Aspect ratio	Airfoil of wing	Mass
4.80m	1.345m ²	17.1	EMX-07	20.0kg
I_{xx}	I_{yy}	I_{zz}	I_{xz}	Fuselage Length
3.572kgm ²	0.834kgm ²	4.005kgm ²	0.003kgm ²	1.033m

3.2 Numerical results

Consider the case of straight level flight and conduct the longitude stability analysis. In elastic analysis, only elastic modes are involved in dynamic equations and rigid-body motions are not consideration. In the integrated analysis, both elastic modes and rigid-body motions are considered. Additionally, to reveal effects caused by geometric nonlinearity, both linear and nonlinear results are illustrated. In linear analysis, there are no nonlinear stiffness terms in structural ROM of wing components. Fig.2 shows the linear flutter analysis results with only elastic modes. The critical flutter speed is 49.0m/s, and mode 5 participates in flutter. Fig.3 shows the nonlinear flutter analysis results with only elastic modes. The critical flutter speed is 36.5m/s, which is different form linear analysis results. Nonlinearities affect stability obviously. Now, take motions of the rigid body into consideration, Fig.4 shows the linear analysis results with rigid-body motion and elastic modes. Two branches of root locus cross the imaginary axis within the calculation range. When the flight speed reaches 30.0m/s, the short period mode locus crosses the imaginary

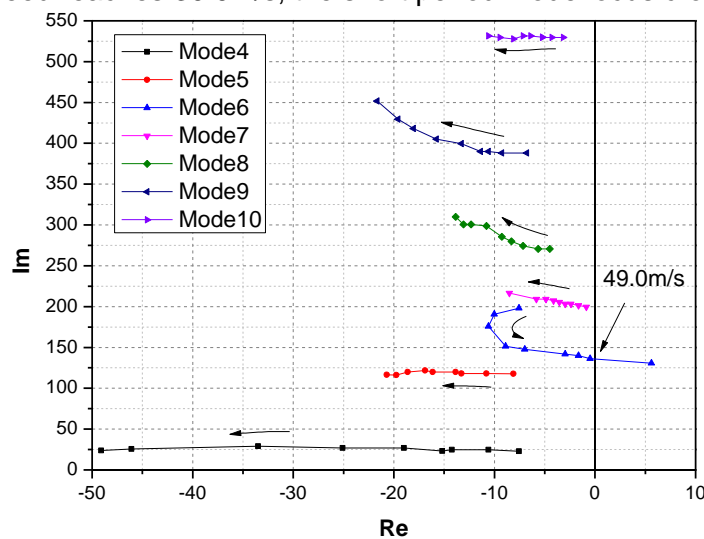


Figure 2: Linear elastic analysis results

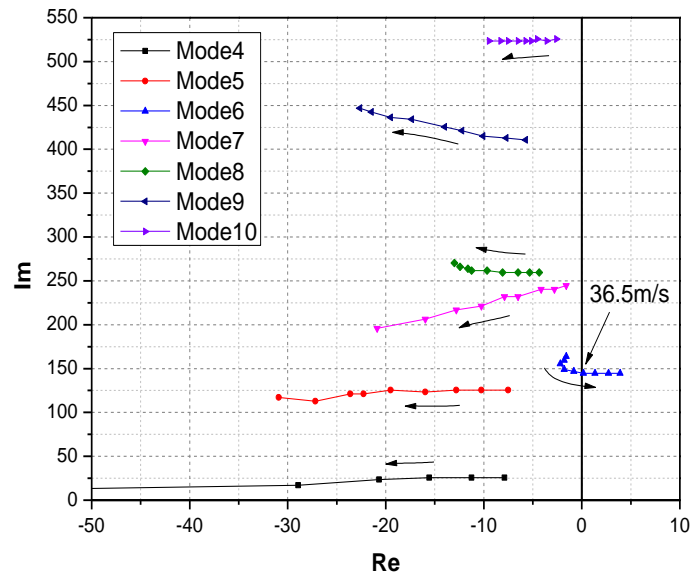


Figure 3: Nonlinear elastic analysis results

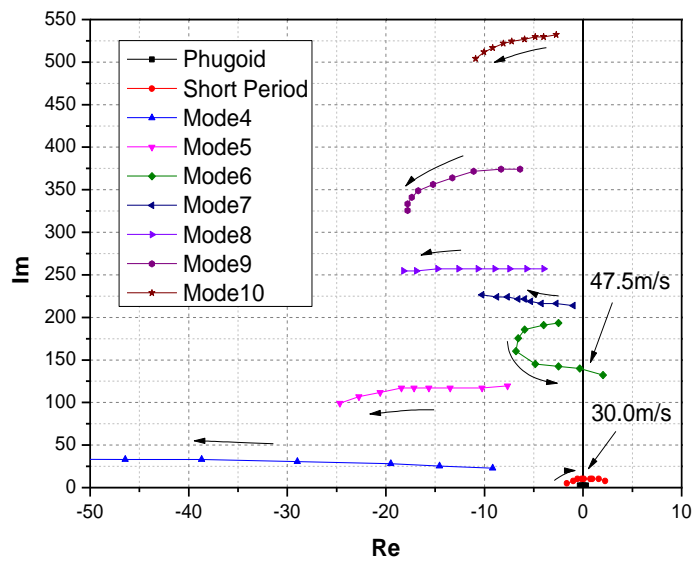


Figure 4: Linear integrated analysis results

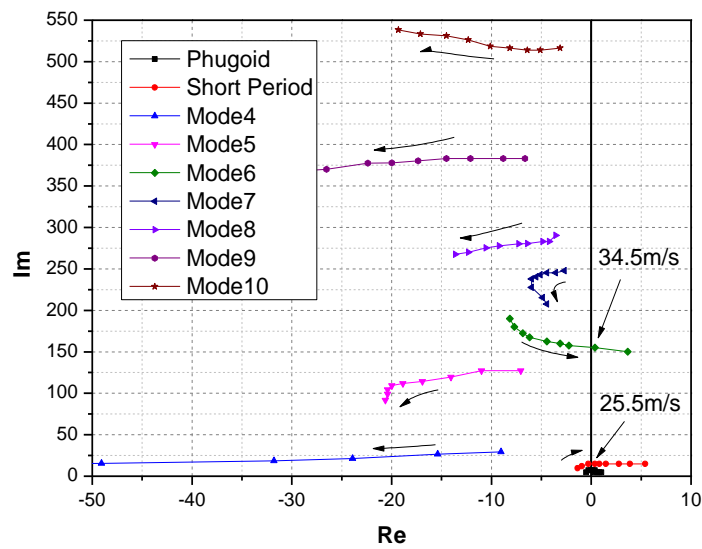


Figure 5: Nonlinear integrated analysis results

axis, and the rigid-elastic coupling becomes unstable. Fig.5 shows the linear analysis results with rigid-body motion and elastic modes. Two branches of root locus cross the imaginary axis within the calculation range. When the flight speed reaches 25.5m/s, the short period mode locus crosses the imaginary. Nonlinearities affect stability obviously as well. Compared with elastic flutter analysis results, the critical stability flight speed of the coupled aeroelasticity and flight dynamics system is lower.

3 Conclusions

A theoretical framework for the stability analysis of the very flexible aircraft is established in this paper. The structural ROM is used for wing components modeling and nonlinear substructure method is used for aircraft system modeling. Non-planar DLM is used for aerodynamics modeling. The state-space equations are obtained, which can deal with rigid-elastic coupling problem.

A very flexible flying wing model is selected as an example to illustrate the stability problem. Because of large flexibility and small pitching inertial of such aircraft, the critical stability flight speed is affected obviously by nonlinearities and rigid-motions. The flight dynamics and aeroelastic analysis should be performed simultaneously.

References

1. Patil, M.J., Hodges, D.H., On the importance of aerodynamics and structural geometrical nonlinearities in aeroelastic behavior of high-aspect-ratio wings, 41st AIAA/ASME/ASCE/AHS/ASC structures, structural dynamics, and materials conference and exhibit. Reston: AIAA; 2000.
2. Patil, M.J., Nonlinear aeroelastic analysis, flight dynamics, and control of a complete aircraft, Atlanta: Georgia Institute of Technology; 1999.
3. Tang, D.M., Dowell, E.H., Experimental and theoretical study on aeroelastic response of high-aspect-ratio wings, *AIAA Journal*, 2001; 39(8): 1430-41
4. Frulla, G., Cestino, E., Marzocca, P., Critical behavior of slender wing configurations, *Proc I MechE Part G: J Aerosp Eng*, 2009: 224(1): 587-600
5. Abbas, L. Chen, Q., Marzocca P., Milanese, A., Nonlinear aeroelastic investigations of stores-induced limit cycle oscillations. *Proc I MechE PartG: J Aerosp Eng* 2008,222(1): 63-80
6. Kim, K., Strganac, T., Aeroelastic Studies of a cantilever wing with structural and aerodynamic nonlinearities. 43rd AIAA/ASME/ASCE/AHS/ASC structures, structural dynamics, and materials conference and exhibit. Reston: AIAA; 2002.
7. Yang, C., Huang, C., and Wu, Z.G., Progress and challenges for aeroservoelasticity research, *ATCA Aeronautica and Astronautica Sinica*, 2015, 36(4): 1011-1033
8. Patil, M.J., Hodges, D.H., Flight Dynamics of Highly Flexible Flying Wings, *Journal of Aircraft*, 2006, 43(6): 1790-1799
9. Xie, C.C., Yang, L., Liu, Y., and Yang, C., Stability of very flexible aircraft with coupled nonlinear aeroelasticity and flight dynamics, *Journal of Aircraft*, 2018
10. Muravyov, A.A., Rizzi, S.A., Determination of nonlinear stiffness with application to random vibration of geometrically nonlinear structures. *Comput Struct*, 2003, 81:1513–23.
11. Mignolet, M.P., Soize, C., Stochastic reduced order models for uncertain geometrically nonlinear dynamical systems. *Comput Methods Appl Mech Eng*, 2008, 197:3951–63.
12. McEwan, M.I., Wright, J.R., Cooper, J.E., Leung, A.Y.T., A combined modal/finite element analysis technique for the dynamic response of a nonlinear beam to harmonic excitation. *J Sound Vib* 2001;243 (4):601–24.
13. Harmin, M.Y., Cooper, J.E., Aeroelastic behavior of a wing including geometric nonlinearities. *Aeronaut J* 2011;115(1174):767–77.
14. Xie, C.C., An, C., Liu, Y., Yang, C., Static aeroelastic analysis including geometric nonlinearities based on reduced order model. *Chin J Aeronaut* 2017, 30(2):638–50.
15. An,C., Yang, C., Xie, C.C., Yang, L., Flutter and gust response analysis of a wing model including geometric nonlinearities based on a modified structural ROM, *Chin J Aeronaut* 2020, 33(1): 48-63
16. Clough, R.W., Wilson, E.L., Dynamic Analysis of Large Structural Systems with Local Nonlinearity *Computer Method in Applied Mechanics and Engineering*, 1979, 17(18): 107-129
17. Tan, M.A., Cai, C.W., Substructure method in local nonlinear system response analysis(in

Chinese), *Vibration & Shock*, 1987, 23, 25-34

18. Fey, R.H.B., Van Campen, D.H., Kraker, D., Long Term Structural Dynamics of Mechanical Systems with Local Nonlinearities, *Journal of Vibration and Acoustics*, 1996, 118: 147-153

19. Bernhammer, L.O., Breuker, R.D., Karpel, M., Geometrically Nonlinear Structural Modal Analysis using Fictitious Masses[J]. *AIAA Journal*, 2017, 55(10): 3584-3593

20. Kantor, E., Raveh, D.E., Cavallaro, R., Nonlinear Structural, Nonlinear Aerodynamic Model for Static Aeroelastic Problem[J]. *AIAA Journal*, 2018

Parameter identification of fluid–rigid body interactions using data assimilation

Jean-Camille Chassaing¹, Vincent Mons²

¹ Sorbonne Université, CNRS, Institut Jean Le Rond d'Alembert, UMR 7190, F-75005 Paris, France, jean-camille.chassaing@sorbonne-universite.fr

² ONERA, The French Aerospace Lab, F-92190 Meudon, France

Keywords: Fluid-structure interaction, aeroelastic flutter - vortex induced oscillations

Data assimilation (DA) techniques provide a powerful framework to solve inverse problems in order to determine unknowns in the set-up of a CFD code from synthetic or experimental observations. Recently, a variational data assimilation approach was successfully applied to the identification of initial conditions of unsteady flows past a rotationally oscillating cylinder [1]. In the present work, we investigate the ability of using data assimilation schemes for the identification of aeromechanical parameters and initial conditions for fluid-structure interactions (FSI) due to elastically mounted rigid bodies subject to a laminar flow (Fig. 1). To this end, an ALE-based Navier-Solver is employed to compute the unsteady wake flow due to the free motion of 1DOF and 2DOF spring-mass systems. Then, the inverse problem is solved using a four-dimensional ensemble-based variational (4DEnVar) scheme [2], which does not require the computation of first-order adjoint model associated to the CFD code. The robustness and efficiency of the 4DEnVar algorithm are investigated for various FSI problems and wake dynamics [3], including vortex induced oscillations of a cylinder, galloping of a rigid body with a square cross section and aeroelastic flutter of a bridge deck in pitch and plunge motion.

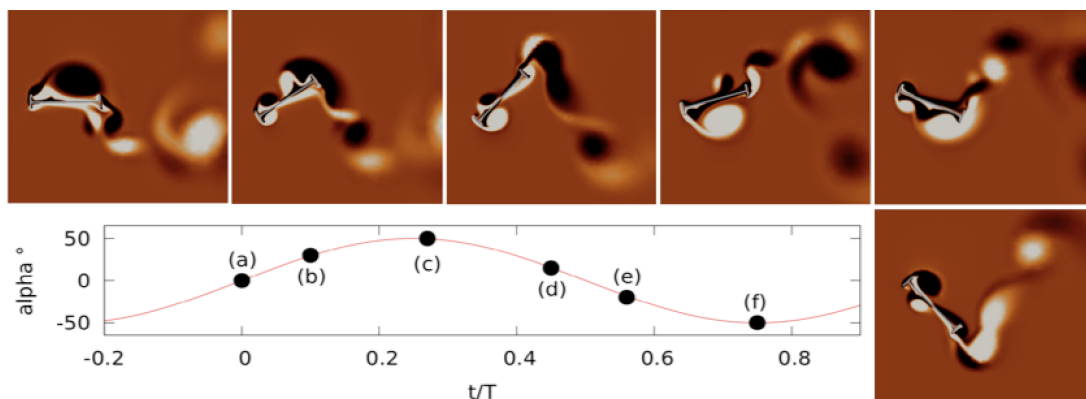


Figure 1: Example of reference FSI solution of the aeroelastic flutter of a typical bridge section [2] whose synthetic measurements in the wake flow are used to identify the structural properties using DA.

¹ V. Mons, J.-C. Chassaing, P. Sagaut. Optimal sensor placement for variational data assimilation of unsteady flows past a rotationally oscillating cylinder, *Journal of Fluid Mechanics*, 823: 230-277, 2017

² C. Liu, Q. Xiao, B. Wang An ensemble-based four-dimensional variational data assimilation scheme. Part I: technical formulation and preliminary test, *Mon. Weather Rev.*, 136, pp. 3363-3373, 2008

³ W. Dettmer and D. Peric. A computational framework for fluid-rigid body interaction : Finite element formulation and applications. *Computer Methods in Applied Mechanics and Engineering*, 195 :1633-1666, 2006

Flutter analysis based on state-space model of unsteady vortex-lattice method

Lan Yang¹, Changchuan Xie² and Chao Yang³

¹ *Beihang University, Beijing, China, yanglanby@buaa.edu.cn*

² *Beihang University, Beijing, China*

³ *Beihang University, Beijing, China*

Abstract

This paper is aimed at introducing a time-domain flutter solution based on state-space model of unsteady vortex-lattice method(UVLM). Unsteady aerodynamic analysis for arbitrary kinematics of the wing including the elastic vibration of the structure can be conducted by UVLM. Then it is coupled with structural dynamics based on finite element method(FEM) and provides aeroelastic response under different flight speeds. The flutter boundary can be determined by the displacement response results. The implementation of a cantilever wing is verified against classical solutions by $p-k$ method.

Keyword: flutter, vortex-lattice method, state-space model.

1 Introduction

Flutter is one of the most important aeroelastic instabilities in aircraft design. When the flight speed increases over the flutter boundary, the aircraft structure will oscillate severely under the interaction of aerodynamic loads, structural internal force and inertial force until the structure damage happens.

Classical flutter analysis is commonly based on Theodorsen theory(1) for 2D cases and doublet-lattice method(DLM)(2) for 3D cases, which are frequency domain unsteady aerodynamic formulations. The aircraft is assumed to have harmonic motions under a series of reduced frequency. And flutter problem is solved by solving the eigenvalue problem of a frequency domain linear equation using some dedicated numerical methods like $v-g$, $p-k$, and g method. Although such methods are widely used and integrated in commercial software like MSC. Nastran, there are some limitations. Because of the form of frequency-dependended aerodynamic matrices, an artificial damping is introduced when solving the flutter equation. Therefore only at the flutter point this artificial term is eliminated and the solution reflects on actual physical situation(3). Moreover, it is more intuitive to judge the system stability by response in time domain. Especially for nonlinear systems, flutter is not simply an exponential vibration but limit-cycle oscillation(LCO), which can only be modelled in time domain.

Unsteady vortex-lattice method (UVLM) provides a medium-fidelity tool of aerodynamic load computation in time domain and is applied generally in aeroelastic researches(4). It is based on potential flow equations and allows various aerodynamic configuration with arbitrary motions in time domain. It is able to describe the wake roll-up situation when using a free-wake model, which is more accurate than a flat wake in situations of large-amplitude motions and large deformations, while DLM is restricted to small out-of-plane harmonic motions with a flat wake, which is not suitable for such cases. As a time-domain method, UVLM is

easy to use in response problems and multidisciplinary problems such as coupled aeroelasticity and flight dynamics and aeroservoelasticity. The transient aerodynamic response can be obtained without a rational function approximation which may lead to a phase difference if used inappropriately.

The implementation of UVLM is introduced in detail by Katz and Plotkin(5). Many researches on aerodynamic and aeroelastic problems have been conducted using different forms of UVLM. Hall proposed a discrete-time state-space model of UVLM in order to construct reduced order models of unsteady aerodynamic flows(6). Werter et al developed a continuous-time state-space formulation of UVLM and applied it to arbitrary nonuniform flows(7). Palacios et al introduced a non-dimensional state-space model of UVLM and then linearized it to couple with beam dynamics to generate a framework of aeroelasticity(8).

This paper is aimed to solve flutter problems based on a continuous-time state-space UVLM model. Referring to the time-stepping solution of UVLM, the continuous-time state-space form is developed using a fixed wake model. Unsteady boundary conditions and unsteady Kutta condition for the trailing edge are applied to build the fluid dynamic equation. The unsteady aerodynamic force is obtained by unsteady Bernoulli equation. The method can be applied to compressible flow by Prandtl-Glauert transformation. Integrated with structural dynamic equations based on FEM by surface spline interpolation, the aeroelastic response can be simulated and therefore the flutter boundary is confirmed. Although this paper only provides a linear solution, it can be extended to nonlinear cases readily by using nonlinear structure models. In the numerical part, a cantilever wing is researched to testify this time-domain flutter solver. The flutter result is consistent with the conventional $p-k$ method.

2 Continuous-time state-space model of UVLM

For inviscid irrotational flow, potential flow theory is a powerful tool for aerodynamic analysis. The governing equation under small-disturbance hypothesis can be written as

$$\left(1 - M_\infty^2\right)\phi_{xx} + \phi_{yy} + \phi_{zz} - 2\frac{M_\infty}{a_\infty}\phi_{xt} - \frac{1}{a_\infty^2}\phi_{tt} = 0 \quad (1)$$

After the Prandtl-Glauert transformation and ignoring the terms of time derivative, it is reduced to Laplace equation:

$$\nabla^2\Phi = 0 \quad (2)$$

Then we can use vortex rings to model the disturbance caused by the wing. As Figure 1 shows, the lifting surface is divided into quadrilateral elements in chordwise and spanwise directions. The wake is also discretized into several elements, each of which is of equal size Δx in the streamwise direction. And the length of the wake is set as 10 chord lengths. For flutter analysis we use flat fixed wake model, but it is also allowed to use a nonplanar free wake model for more precise calculation. The velocity induced by a vortex ring at an arbitrary position is calculated by the Biot-Savart law:

$$\mathbf{w} = \frac{\Gamma}{4\pi} \int_C \frac{d\mathbf{l} \times \mathbf{r}}{r^3} \quad (3)$$

Then the Neumann boundary condition can be described as

$$\mathbf{K}_b \boldsymbol{\Gamma}_b(t) + \mathbf{K}_{w0} \boldsymbol{\Gamma}_{w0}(t) + \mathbf{K}_{wl} \boldsymbol{\Gamma}_{wl}(t) = \mathbf{w}(t) \quad (4)$$

where $\boldsymbol{\Gamma}_b, \boldsymbol{\Gamma}_{w0}, \boldsymbol{\Gamma}_{wl}$ are vortex strength of wing boundary elements, the first row of wake

elements and other wake elements, respectively. $\mathbf{K}_b, \mathbf{K}_{w0}, \mathbf{K}_{wl}$ are the corresponding aerodynamic influence coefficient matrices calculated using Eq.(3). $\mathbf{w}(t)$ on the right side of the equation is the kinematic velocity of the lifting surface due to the motion of the wing projected on the normal direction of each element, including the rigid body motion and the structural oscillation.

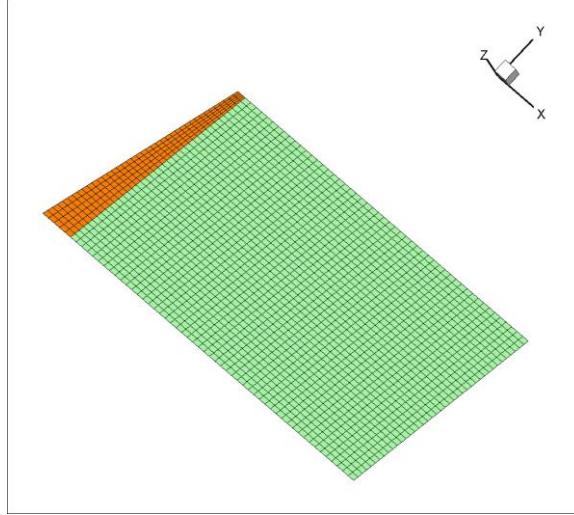


Figure 1 Vortex lattice model for a wing

The unsteady Kutta condition of the trailing edge can be written as

$$\dot{\Gamma}_{w0}(t) = \frac{1}{\Delta t} [\Gamma_{w0}(t + \Delta t) - \Gamma_{w0}(t)] = \frac{1}{\Delta t} [\mathbf{C}_1 \Gamma_b(t) - \Gamma_{w0}(t)] \quad (5)$$

It is actually the first order approximation from the discrete time stepping formulation, which means the strength of the most recently shed wake vortex ring is set equal to that in the previous time step. According to the Helmholtz theorems, once the wake vortex is shed, its strength stays unchanged, which means

$$\dot{\Gamma}_{wl}(t) = \frac{1}{\Delta t} [\Gamma_{w_{i,j}}(t + \Delta t) - \Gamma_{w_{i,j}}(t)] = \frac{1}{\Delta t} [\Gamma_{w_{i,j-1}}(t) - \Gamma_{w_{i,j}}(t)] \quad (6)$$

Summarizing Eq. (4) to (6) and integrating Γ_{w0} and Γ_{wl} into one vector Γ_w , the continuous-time state-space model of UVLM is deduced:

$$\dot{\Gamma}_w(t) = \mathbf{A}_c \Gamma_w(t) + \mathbf{B}_c \mathbf{w}(t) \quad (7)$$

After solving this ordinary differential equation, the aerodynamic loads can be obtained by unsteady Bernoulli equation:

$$\Delta p_{ij} = \rho_\infty \left\{ \mathbf{V}_{l,ij} \cdot \boldsymbol{\tau}_1 \frac{\partial \tilde{\Gamma}_{b,ij}}{\partial \tau_1} + \mathbf{V}_{l,ij} \cdot \boldsymbol{\tau}_2 \frac{\partial \tilde{\Gamma}_{b,ij}}{\partial \tau_2} + \frac{\partial \Gamma_{b,ij}}{\partial t} \right\} \quad (8)$$

where $\boldsymbol{\tau}_1, \boldsymbol{\tau}_2$ are two tangent vectors and \mathbf{V}_l is the local velocity of the panel. It can also be written in state-space form:

$$\mathbf{F}_A(t) = \mathbf{A}_1 \Gamma_w(t) + \mathbf{A}_2 \mathbf{w}(t) + \mathbf{A}_3 \dot{\mathbf{w}}(t) \quad (9)$$

This UVLM model is suitable for arbitrary unsteady motions when setting different kinematic motions $\mathbf{w}(t)$. When applied to aeroelastic analysis, the unsteady downwash should include the structural vibration velocity interpolated from the results of structural dynamics.

3 Aeroelastic model

In this paper, structural dynamics is based on finite element method, which is widely used in aeroelastic domain:

$$\mathbf{M}\ddot{\mathbf{u}} + \mathbf{K}\mathbf{u} = \mathbf{F}_S \quad (10)$$

After obtaining the displacements and the vibration velocity of structure grids, the normal vectors of aerodynamic elements are updated. And the vibrations also contribute to the local downwash:

$$w_k = (\mathbf{V}_\infty + \mathbf{V}_{motion}) \cdot (\mathbf{n}_0 + \Delta\mathbf{n}) \quad (11)$$

which is another cause to the elastic incremental aerodynamic loads.

The interpolation between the aerodynamic and structural model is based on generalized surface spline method(9). It describes the mapping relation from an N-dimension space to an M-dimension space, which is expressed as

$$w^k(\mathbf{X}) = c_1^k + \sum_{p=1}^N c_{p+1}^k x_p + \sum_{i=1}^n c_{N+1+i}^k r_i^2 \ln(r_i^2 + \varepsilon) \quad (12)$$

where $\mathbf{X}_i = \{x_i^1, \dots, x_i^N\}$ ($i=1, 2, \dots, n$) is the given vector in N-dimension space and $\mathbf{W}_i = \{w_i^1, \dots, w_i^M\}$ ($i=1, 2, \dots, n$) is the corresponding image vector. When we apply it into the displacement interpolation, the relation between the given displacements of structural grids \mathbf{U}_S and the displacements vector of aerodynamic grids \mathbf{U}_A can be written in matrix form using

$$\mathbf{U}_A = \mathbf{G}\mathbf{U}_S \quad (13)$$

where \mathbf{G} is the spline matrix based on Eq. (12). The equivalence between the aerodynamic force \mathbf{F}_A and the structural force \mathbf{F}_S is then established through the virtual work principle

$$\delta\mathbf{U}_A^T \mathbf{F}_A = \delta\mathbf{U}_S^T \mathbf{F}_S \quad (14)$$

Thus the force interpolation relation yields

$$\mathbf{F}_S = \mathbf{G}^T \mathbf{F}_A \quad (15)$$

Through the interpolation, the tangent mapping can be obtained as well by calculating the first-order partial derivatives of Eq.(12). According to the definition of tangent vector and tangent mapping, it's easy to obtain the tangent or normal vectors of the configuration. In linear cases, the interpolation matrices only need to be calculated once because of the small deformation

hypothesis.

4 Numerical investigations

In this paper, a high aspect ratio wing is taken as an example for aeroelastic response analysis. The detailed design parameters of the wing is presented in Table 1. The structural stiffness is all provided by a cross-section single aluminous beam, which is located at 40% of the local chord. The ribs are only used for maintaining the wing shape. Figure 2 shows the finite element model of the wing. And Table 2 shows the first six natural modes of the structure model.

Table 1 Design parameters

Item	Value
Semi span (mm)	1542.1
Chord of the wing root (mm)	263
Chord of the wing tip (mm)	71
Aspect ratio	18.6
Reference area (mm ²)	2.6e+5
Beam location	40% of the local chord
Weight (kg)	3.1

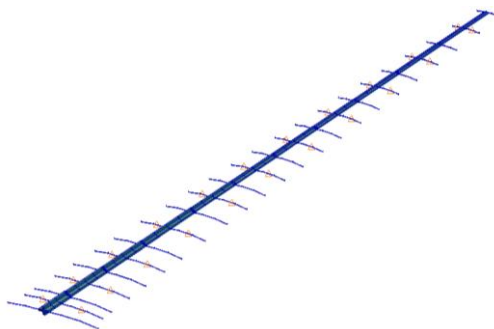


Figure 2 Finite element model of a cantilever wing

Table 2 Natural mode information

Mode	Frequency (Hz)
1st vertical bend (V1)	3.28
1st horizontal bend (H1)	5.07
2nd vertical bend (V2)	9.89
2nd horizontal bend (H2)	16.87
3rd vertical bend (V3)	25.15
1st twist (T1)	29.75

In order to judge the stability of the aeroelastic system, a disturbance of velocity is set as the initial condition of the structural dynamics. And the flutter boundary is obtained by the aeroelastic response along with increasing flight speed.

Figure 3 shows the aeroelastic response of the wing tip in time-domain under different flight speeds. When the flight speed is under the flutter boundary, the displacement disturbance vanishes, illustrated in (a) and (b) of Figure 3. The response of displacement becomes almost equal amplitude when the flight speed nearly reached the flutter speed, shown in (c). If the flight speed is over the flutter boundary, the aeroelastic response diverges as shown in (d). Figure 4 shows the fast Fourier transform result of the response, which tells the flutter frequency is 14.5Hz.

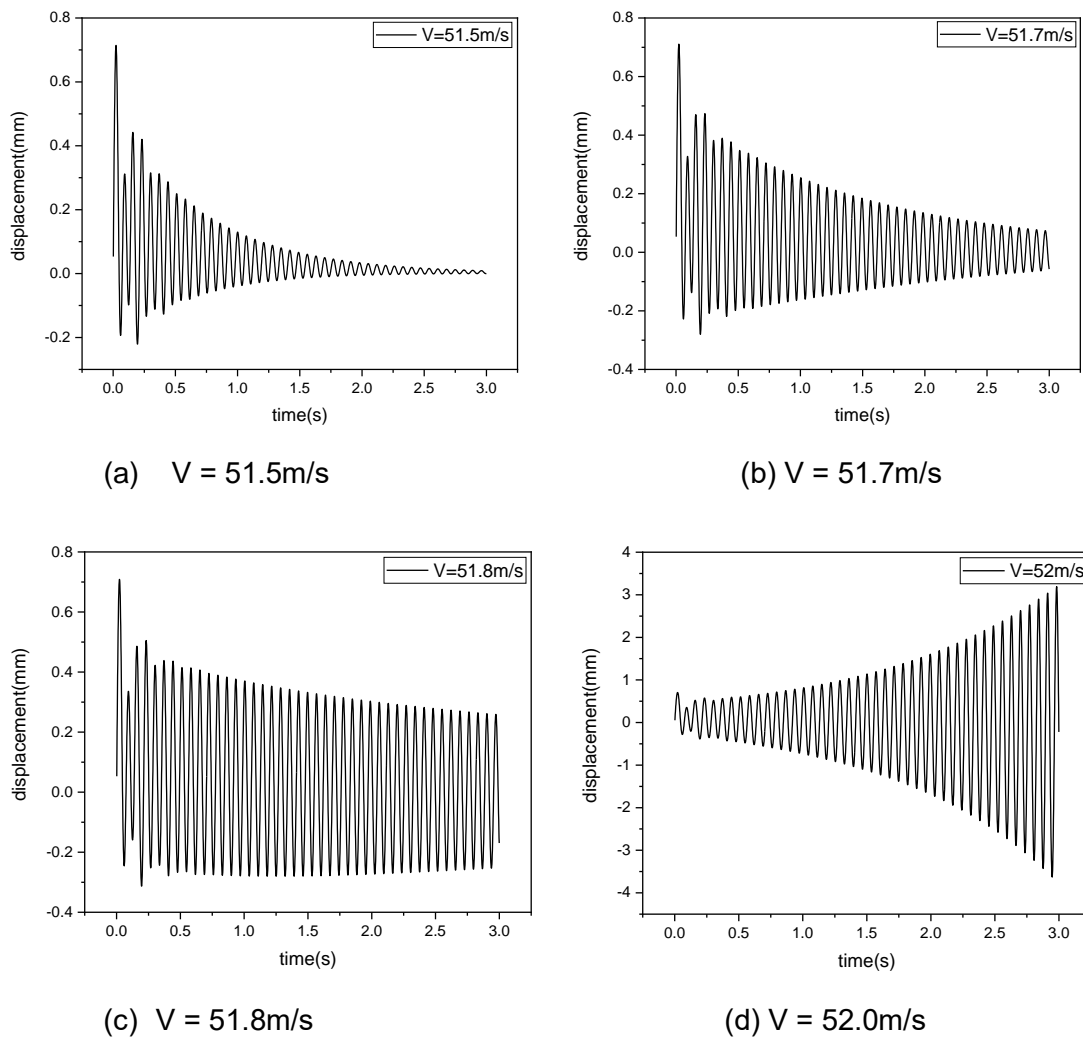


Figure 3 Aeroelastic response of the cantilever wing under different flight speeds

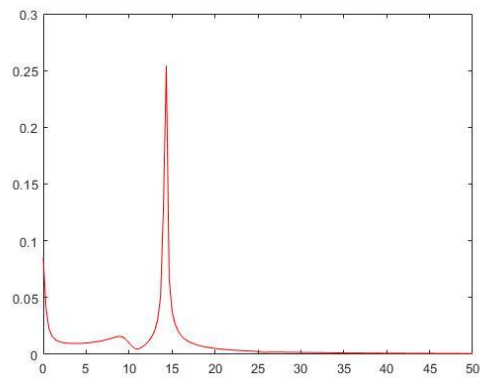


Figure 4 Fast Fourier transform of the time-domain response

The flutter result based on time-domain aeroelastic response is compared with conventional analysis based on p-k method. As *Figure 5* shows, when the flight speed reaches 50.2m/s, the 1st vertical bending mode couples with the 1st twist mode and causes flutter. The corresponding flutter frequency is 14.6Hz. The consistence of the flutter results based on two methods proves the effectiveness of the formulation we introduced in this paper.

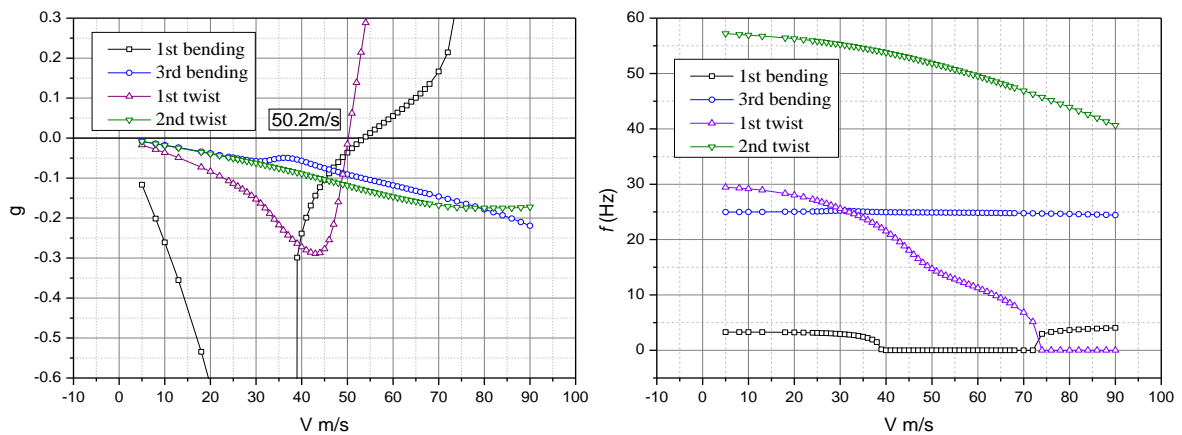


Figure 5 Flutter analysis based on p-k method

5 Conclusions

In this paper, a time-domain flutter solution based on continuous-time state-space model of UVLM is proposed. Finite element method is used in structural dynamic analysis. Dynamic aeroelastic response analysis is conducted by coupling aerodynamics and structural dynamics with interpolation. Through comparison of the time-domain aeroelastic response results under different flight speeds, the flutter boundary can be obtained. This flutter formulation is testified by the frequency-domain solver based on p-k method. Although this paper provides a linear flutter case, it is easily applied to nonlinear aeroelastic systems by using nonlinear structural models. The time-domain aeroelastic solution also has advantages in flutter suppression and gust problems.

References

1. Theodorsen T. General Theory of Aerodynamic Instability and the Mechanism of Flutter. 1934.
2. Albano E, Hodden WP. A Doublet-Lattice Method for Calculating Lift Distributions on Oscillating Surfaces in Subsonic Flows. *AIAA J.* 1969;7(2):279–85.
3. Roizner F, Karpel M. Aeroservoelastic stability analysis using response based parameteric flutter margins. In: International Forum on Aeroelasticity and Structural Dynamics (IFASD). Como, Italy; 2017. p. 1–13.
4. Murua J, Palacios R, Graham JMR. Applications of the unsteady vortex-lattice method in aircraft aeroelasticity and flight dynamics. *Prog Aerosp Sci [Internet]*. 2012;55:46–72. Available from: <http://dx.doi.org/10.1016/j.paerosci.2012.06.001>
5. Katz J, Plotkin A. *Low-Speed Aerodynamics*. McGraw-Hill Inc; 1991.
6. Hall KC. Eigenanalysis of unsteady flows about airfoils, cascades, and wings. *AIAA J.* 2008;32(12):2426–32.
7. Werter NPM, De Breuker R, Abdalla MM. Continuous-Time State-Space Unsteady Aerodynamic Modeling for Efficient Loads Analysis. *AIAA J [Internet]*. 2017;56(3):905–16. Available from: <https://arc.aiaa.org/doi/pdf/10.2514/1.J056068>
8. Palacios R, Simpson RJ, Maraniello S. State-space realizations of potential-flow unsteady aerodynamics with arbitrary kinematics. In: 58th AIAA/ASCE/AHS/ASC Structures, Structural Dynamics, and Materials Conference. 2017. p. 1–17.
9. Xie C, Yang C. Surface Splines Generalization and Large Deflection Interpolation. *J Aircr.* 2007;44(3):1024–6.

Investigating Stochastic Resonance in a Classical Flutter System using Recurrence Networks

Varun H S¹, M.S. Aswathy¹ and Sunetra Sarkar¹

¹*Department of Aerospace Engineering, Indian Institute of Technology Madras, Chennai, India, varun2693@gmail.com*

Keyword: Pitch-plunge aeroelastic system, Stochastic Resonance, Recurrence Networks.

In this work, we investigate the effect of external additive noise on a thin airfoil undergoing motion in pitch and plunge degrees of freedom in the presence of a uniform, incompressible flow using concepts from recurrence networks. Aeroelastic flutter and its onset is one of the prominent criteria for design of airfoils and noise has been known to change the dynamics of such structures substantially¹. In this study, we consider the effect of additive noise and observe that the noise brings in major dynamical changes in the airfoil response. The deterministic system undergoes a sub-critical Hopf bifurcation beyond which the system enters a state of limit cycle oscillation (LCO), and the reduced velocity at which this occurs is called flutter point. A saddle node bifurcation occurs at a reduced velocity lower than the flutter point, which births two LCOs — one stable and another unstable, and this reduced velocity is called the turning point. Thus, when the reduced velocity is in the region between the turning and the flutter point, the system displays a bi-stable behaviour. We observe that this bi-stable behaviour leads to interesting dynamics when external noise acts on the system directly. In the presence of noise, the system jumps between the two attractors ($\vec{0}$ fixed-point and the stable LCO) displaying intermittent dynamics. As we fix the reduced velocity in the bi-stable regime and vary the noise intensity (σ), we observe an interesting phenomenon in the flutter system called stochastic resonance². At very low values of σ the system does not display intermittent dynamics producing a low value of signal-to-noise ratio (SNR). As σ is increased the system hops between the two attractors and the SNR value increases. When σ is further increased, the system dynamics is completely dictated by the external noise and the SNR value decreases. This phenomenon where SNR value reaches a peak at an optimum noise intensity is termed as stochastic resonance². We characterize this phenomenon by also using the power spectrum estimates and mean residence time of the responses. As a next step, to characterize and visualize the dynamics of the responses effectively, we represent the time series as a complex network. This is done by interpreting the recurrence matrix derived from the phase space as its associated adjacency matrix³. These networks are studied to provide insights into various measures like clustering coefficient and closeness centrality³, revealing more details on the dynamics of the system.

¹ Venkatramani, J., Nair, V., Sujith, R.I., Gupta, S., Sarkar, S. (2016). Precursors to flutter instability by an intermittency route: A model free approach. *Journal of Fluids and Structures*, 61, 376-391.

² Dykman, M., McClintock, P. (1999). Stochastic Resonance. *Science Progress*, 82, 113-134.

³ Donner, R.V., Zou, Y., Donges, J.F., Marwan, N., Kurths, J. (2010). Recurrence networks- a novel paradigm for nonlinear time series analysis. *New Journal of Physics*, 12, 033025.

A Long Short-Term Memory neural network-based self-excited force model of nonlinear post-critical flutter

Wenjie Li¹, Shujin Laima² and Hui Li³

^{1, 2, 3} School of Civil Engineering, Harbin Institute of Technology, Harbin, China, lwj_hit@126.com (W. Li).

Keyword: Nonlinear aerodynamics, post-critical flutter, self-excited force model, LSTM.

Due to strong nonlinear properties of post-critical flutter, the generalization of self-excited force model for entire flutter process (including growth stages, decay stages and steady limit cycle oscillations (LCOs)) of bluff bodies is a very critical issue. In this paper, a self-excited force model based on LSTM neural networks incorporated with the numerical simulation of governing equation of the dynamic system is proposed to describe the nonlinearity of post-critical flutter behaviors, which is shown in Fig. 1.

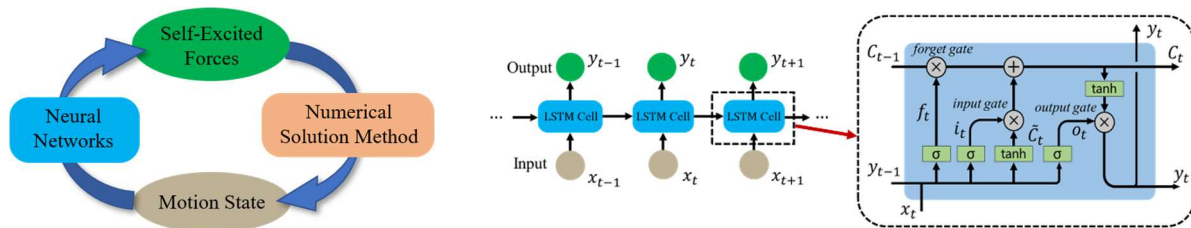


Fig. 1 Schematic diagram of the self-excited force model based on proposed LSTM networks.

A series of flutter tests of spring-suspended sectional models with different leading edges are conducted to investigate the effects of aerodynamic configurations on the flutter behaviors. The shape of leading edges is an isosceles triangle and the vertex angles varied from 90° to 180°, including 105°, 120°, 130°, 135°, 140°, 150°, 165° and 180° (a 180° vertex angle means a rectangular leading edge) and the flutter responses and self-excited forces are measured to collect data.

In tests, as the leading edge becomes bluffer and the vertex angle is larger than 105°, the type of flutter transforms from divergent flutter to post-critical flutter. The experimental data from specimens with 135°, 140° and 165° are employed to train the proposed networks. And the experimental data from specimens with 120°, 130°, 150° and 180° are employed as predictions to verify the effectiveness and generalization of the trained networks.

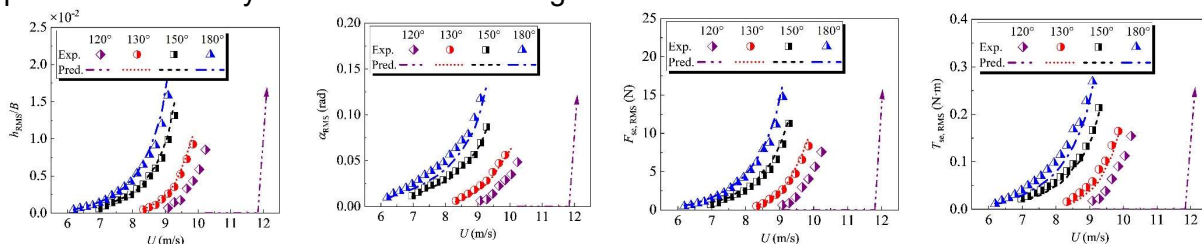


Fig. 2 RMS of the predicted response and self-excited force amplitude of the LCOs

It can be seen from Fig. 2 that the varying tendency of the predicted response and self-excited force amplitude versus an increasing wind speed agrees well with the experimental results except the specimen of 120°. The aerodynamic configuration of the specimen of 120° as a special specimen is close to the transition configuration where the category of flutter transforms from divergent flutter to post-critical flutter. As a result, a small change of the configuration will make a drastic effect to the aerodynamic characteristic of the flutter. That means the trained self-excited force model is very sensitive to the shape parameter for the specimen of 120°.

Model-Free Nonlinear Flutter Forecasting in Fluid-Structural Systems with Multiple Varying Parameters

Cristina Riso¹, Carlos E.S. Cesnik², and Bogdan I. Epureanu³

¹ *Research Fellow, University of Michigan, Ann Arbor, MI, criso@umich.edu*

² *Clarence "Kelly" Johnson Professor, University of Michigan, Ann Arbor, MI, cesnik@umich.edu*

³ *Authur F. Thurnau Professor, University of Michigan, Ann Arbor, MI, epureanu@umich.edu*

Abstract

High-performance nonlinear flutter and post-flutter predictions are critical for designing a variety of fluid-structural systems. However, these predictions are frequently prohibitive due to their high computational cost. Moreover, existing flutter and post-flutter prediction methods require knowledge of the system equations and allow for variations in only one control parameter at a time. To address these shortcomings, this paper presents a novel model-free method for nonlinear flutter forecasting in fluid-structural systems with multiple varying parameters. The method uses only output data from a handful of transient responses in the pre-bifurcation regime. Flutter and post-flutter dynamics of a geometrically nonlinear wing are forecasted for varying speed and torsion stiffness, showing good agreement with time-marching results.

Keyword: Nonlinear flutter, post-flutter dynamics, model-free bifurcation forecasting

1 Introduction

High-performance nonlinear flutter predictions are critical for designing a variety of fluid-structural systems such as very flexible aircraft, wind turbines, suspension bridges, and energy harvesters. Furthermore, predicting post-flutter dynamics of these systems is also critical as subcritical limit-cycle oscillations can arise before reaching the flutter boundary [1].

Several model-based techniques exist for predicting nonlinear flutter bifurcations including direct time marching, harmonic balance, nonlinear perturbation methods, and numerical continuation (see Ref. [2] for a review). These techniques have given valuable insights into bifurcations of simple nonlinear fluid-structural systems, but they are frequently impractical for large-scale systems due to the heavy computational effort they require. Furthermore, model-based nonlinear flutter and post-flutter analysis techniques typically consider only one varying control parameter at a time (e.g., speed). Thus, these techniques are unsuited to design applications that require computations for several operating conditions and parameter choices. Finally, most of model-based techniques require knowledge of the system equations, and thus, they are highly intrusive and inapplicable whenever an accurate model of the system is not available.

Model-free techniques have been proposed that forecast nearby flutter bifurcations by fitting and extrapolating stability metrics evaluated using output data from transient responses of the system in the pre-bifurcation regime [3–5]. Alternate model-free approaches also exist that identify a reduced-order model of the system from transient outputs and use it for predicting

flutter [6–8]. These model-free techniques are applicable to linear and nonlinear fluid-structural systems using output data from numerical simulations or experimental tests. However, they do not provide information on the post-flutter dynamics.

Recently, a model-free method, called the bifurcation forecasting method [9–16], was proposed for predicting nonlinear flutter bifurcations and post-flutter dynamics of fluid-structural systems by leveraging the critical slowing down (CSD) phenomenon [17]. As a system control parameter approaches its critical value at a point on the flutter boundary, the CSD leads to longer transients before the system recovers its initial equilibrium state after being perturbed in the pre-flutter regime. The CSD can be quantified based on output data from pre-bifurcation transient responses and used for predicting a range of the bifurcation diagram without entering the post-flutter regime or requiring knowledge of the system equations.

The bifurcation forecasting method is a promising approach for predicting nonlinear flutter and post-flutter dynamics of large-scale fluid-structural systems. The method is non intrusive and can be applied using data from black-box numerical simulations or experiments. However, the method assumes one varying control parameter at time. To address this shortcoming, this paper proposes a novel generalized bifurcation forecasting method for systems with multiple varying parameters. The proposed method enables efficient, model-free flutter bifurcation forecasting in multi-dimensional control-parameter spaces, which is of interest for design space exploration, sensitivity analysis, and uncertainty quantification of large-scale nonlinear fluid-structural systems.

The paper is organized as follows. The proposed method is presented in Sec. 2. The method is demonstrated in Sec. 4 on a geometrically nonlinear wing test case described in Sec. 3 and verified with alternate approaches. Concluding remarks are given in Sec. 5.

2 Theoretical Formulation

A multi-parameter bifurcation forecasting method is derived in Sec. 2.1 for a one-dimensional system. Application to large-dimensional fluid-structural systems is discussed in Sec. 2.2.

2.1 One-Dimensional Non-Oscillatory System

Consider a one-dimensional non-oscillatory nonlinear system governed by N control parameters listed in the vector $\boldsymbol{\mu} = [\mu_1, \dots, \mu_N]$. The system governing equation can be written as

$$\dot{r} = f(r, \boldsymbol{\mu}), \quad (1)$$

where r is amplitude and the overdot denotes the derivative with respect to time t . The recovery rate of the system is introduced as:

$$\lambda := \frac{d}{dt} \ln r = \frac{\dot{r}}{r}, \quad (2)$$

and is generally a nonlinear function of r and $\boldsymbol{\mu}$. System equilibrium solutions r_0 such that $f(r_0, \boldsymbol{\mu}_0) = 0$ bifurcate for certain values of the control parameters defining the critical stability boundary. The post-critical bifurcation diagram in the $\boldsymbol{\mu} - r$ space satisfies:

$$\lambda(r, \boldsymbol{\mu}) = 0. \quad (3)$$

For a fixed amplitude $r = \tilde{r}$, Eq. (3) defines a section of the bifurcation diagram in the control-parameter space that is a boundary of dimension $N - 1$. For $r = r_0$, this reduces to the system critical stability boundary and the recovery rate reduces to the damping of the linearized system.

Close to a point $\tilde{\boldsymbol{\mu}}_c = [\tilde{\mu}_{1c}, \dots, \tilde{\mu}_{Nc}]$ on the stability boundary, that is, a point in the control-parameter space such that $\lambda(r_0, \tilde{\boldsymbol{\mu}}_c) = 0$, Eq. (1) can be expanded in a Taylor series:

$$\dot{r} = r \left[\alpha_0(r) + \sum_{i=1}^N \alpha_1^{(i)}(r)(\mu_i - \tilde{\mu}_{ic}) + \sum_{i,j=1}^N \alpha_2^{(ij)}(r)(\mu_i - \tilde{\mu}_{ic})(\mu_j - \tilde{\mu}_{jc}) + HOT \right]. \quad (4)$$

The coefficients α_0 , $\alpha_1^{(i)}$, and $\alpha_2^{(ij)}$ ($i, j = 1, \dots, N$) are polynomial functions of r independent of $\boldsymbol{\mu}$ and they characterize the bifurcation type (subcritical or supercritical). Since the Taylor series expansion in Eq. (3) is with respect to the control-parameter vector $\boldsymbol{\mu}$ and not amplitude r , it holds for large amplitudes. This is a key feature of the method that allows predicting large ranges of the bifurcation diagram in a neighborhood of $\tilde{\boldsymbol{\mu}}_c$.

Using Eq. (4) and truncating higher-order terms, Eq. (2) is rewritten as:

$$\lambda(r, \boldsymbol{\mu}) \approx \alpha_0(r) + \sum_{i=1}^N \alpha_1^{(i)}(r)(\mu_i - \tilde{\mu}_{ic}) + \sum_{i,j=1}^N \alpha_2^{(ij)}(r)(\mu_i - \tilde{\mu}_{ic})(\mu_j - \tilde{\mu}_{jc}). \quad (5)$$

At a fixed amplitude, the recovery rate λ decreases quadratically with the distance $\boldsymbol{\mu} - \tilde{\boldsymbol{\mu}}_c$ due to the CSD. At a fixed point in the control-parameter space, the recovery rate varies nonlinearly with amplitude as described by the coefficients α_0 , $\alpha_1^{(i)}$, and $\alpha_2^{(ij)}$ ($i, j = 1, \dots, N$).

The above formulation provides a framework for forecasting the bifurcation diagram of the system (1) in a neighborhood of $\tilde{\boldsymbol{\mu}}_c$ using only output data from a handful of transient responses in the pre-bifurcation regime. Specifically, the method requires $N_\mu \geq 1 + N$ transient responses when only the first-order terms are retained in Eq. (4). This increases to $N_\mu \geq 1 + N + N(N + 1)/2$ when the second-order terms are also retained¹. The transient responses must be obtained for control-parameter vector samples $\boldsymbol{\mu}_l$ ($l = 1, \dots, N_\mu$) defining $N_\mu - 1$ linearly independent directions in the control-parameter space. However, perturbations used for generating the transient responses can be of any amplitude and type.

For each control-parameter vector sample $\boldsymbol{\mu}_l$ ($l = 1, \dots, N_\mu$), the system in Eq. (1) is perturbed from its equilibrium configuration to collect output data $r(t_k, \boldsymbol{\mu}_l) = r_{kl}$ ($k = 1, \dots, N_r$). These output data can be obtained from black-box numerical simulations (when a model of the system is available) or even from experimental tests. Once output data are collected, recovery rates $\lambda(r_k, \boldsymbol{\mu}_l) = \lambda_{kl}$ ($k = 1, \dots, N_r$, $l = 1, \dots, N_\mu$) can be computed for each amplitude and control-parameter vector sample using finite differences:

$$\lambda \approx \frac{\ln r_+ - \ln r_-}{2\Delta t}, \quad (6)$$

where r_+ and r_- are the response amplitudes at the times $t + \Delta t$ and $t - \Delta t$, respectively, and Δt is the time step.

¹Assuming that the bifurcation mechanism does not change for small variations in the control parameters, the symmetry condition $\alpha_{ij} = \alpha_{ji}$ reduces the number of necessary transient responses from N^2 to $1 + N + N(N + 1)/2$.

Next, recovery rates at a selected amplitude \tilde{r}_k are fitted in the control-parameter space using a polynomial function consistent with Eq. (4):

$$\lambda(\tilde{r}_k, \boldsymbol{\mu}) = a_0(\tilde{r}_k) + \sum_{i=1}^N a_1^{(i)}(\tilde{r}_k) \mu_i + \sum_{i,j=1}^N a_2^{(ij)}(\tilde{r}_k) \mu_i \mu_j . \quad (7)$$

where $a_0(\tilde{r}_k)$, $a_1^{(i)}(\tilde{r}_k)$, and $a_2^{(ij)}(\tilde{r}_k)$ are the coefficients of the fitting function at the amplitude \tilde{r}_k . Once these coefficients are known, Eq. (7) can be used for computing points on the bifurcation diagram at the amplitude $r = \tilde{r}_k$ along any direction in the $\boldsymbol{\mu}$ space.

The control parameter vector at a point on the bifurcation diagram can be written as $\tilde{\boldsymbol{\mu}} = \boldsymbol{\mu}_0 + \tilde{\delta} \bar{\boldsymbol{\mu}}$, where $\boldsymbol{\mu}_0$ is a reference point in the control-parameter space, $\bar{\boldsymbol{\mu}}$ is a unit vector with origin at $\boldsymbol{\mu}_0$, and $\tilde{\delta}$ is a scalar unknown determined by enforcing:

$$\lambda(\tilde{r}_l, \tilde{\boldsymbol{\mu}}) = a_0(\tilde{r}_l) + \sum_{i=1}^N a_1^{(i)}(\tilde{r}_l) (\mu_{0_i} + \tilde{\delta} \bar{\mu}_i) + \sum_{i,j=1}^N a_2^{(ij)}(\tilde{r}_l) (\mu_{0_i} + \tilde{\delta} \bar{\mu}_i) (\mu_{0_j} + \tilde{\delta} \bar{\mu}_j) = 0 . \quad (8)$$

Solving Eq. (8) for different directions $\bar{\boldsymbol{\mu}}$ (or for different reference points $\boldsymbol{\mu}_0$) allows one to build a section of the bifurcation diagram in the $\boldsymbol{\mu}$ space at the amplitude $r = \tilde{r}_k$ without requiring additional output data. Next, repeating for different amplitudes allows one to build a range of the bifurcation diagram in the $\boldsymbol{\mu} - r$ space.

The proposed method has unique features compared to existing methods for bifurcation analyses. The method accounts for variations in an arbitrary number of control parameters, it does not use the system equations, and it has low output data requirements. These features make the method an efficient and non-intrusive approach for numerical or experimental bifurcation analyses of large-scale fluid-structural systems. Once recovery rates are known along certain directions in the $\boldsymbol{\mu}$ space, ranges of the bifurcation diagram can be forecasted in different directions without requiring additional output data, which favors parametric analyses. Finally, the method can characterize large-amplitude ranges of the bifurcation diagram because it does not linearize the system dynamics. The only assumption is that the system dynamics be smooth with respect to the control parameters in a neighborhood of the point $\tilde{\boldsymbol{\mu}}_c$, so that the Taylor expansion in Eq. (4) remains valid.

2.2 Large-Dimensional Oscillatory Systems

Section 2.1 detailed the proposed method formulation for a 1D non-oscillatory system where all the outputs can be used for computing recovery rates using Eq. (6). However, nonlinear fluid-structural systems typically exhibit oscillatory transient responses where output data at subsequent times correspond to different phases and cannot be used in Eq. (6). Furthermore, while oscillatory responses may involve many modes, only one mode is typically involved in the flutter bifurcation and exhibits CSD.

These problems can be addressed by means of signal decomposition and phase fixing as proposed in previous work on the one-parameter bifurcation forecasting method [11–16]. Signal decomposition allows for isolating the response contribution due to the bifurcating mode in the transient responses. Next, a phase is fixed for the decomposed transient signal for the degree of freedom (DOF) of interest for forecasting the bifurcation diagram for the selected phase.

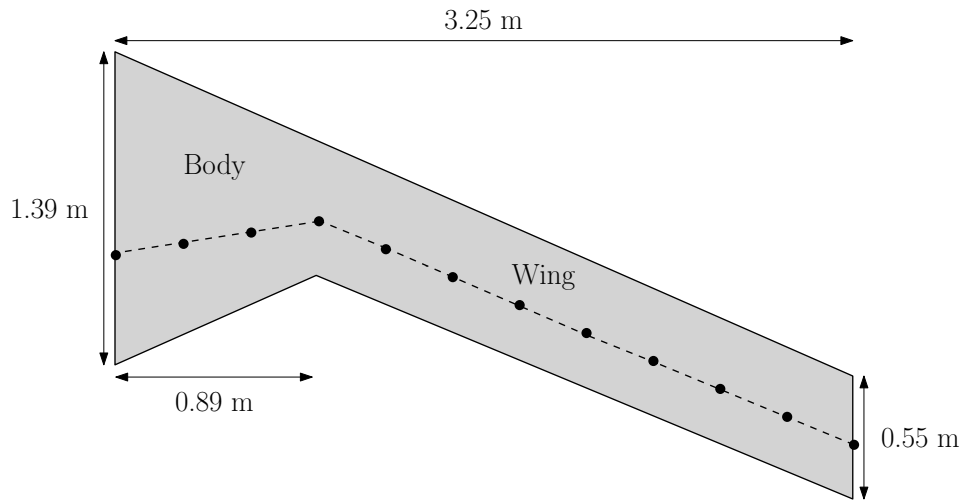


Figure 1: BWB half-vehicle planform and reference beam axis (dashed line).

3 Test Case

The fluid-structural test case used in this work is based on the blended-wing-body (BWB) aircraft model introduced in Ref. [18]. This test case is chosen for its geometrically nonlinear behavior and the availability of bifurcation analysis results previously obtained by the authors using the one-parameter bifurcation forecasting method [19, 20].

This work considers the half-vehicle BWB as clamped at the centerline. The configuration is assumed to be at zero angle of attack and self weight is neglected. Output data for applying the method are obtained by simulating transient responses of the half-vehicle BWB to “1-cosine” gust inputs having maximum amplitude of 4 m/s and duration of 0.1 s. Gust responses are simulated using the University of Michigan’s Nonlinear Aeroelastic Simulation Toolbox (UM/NAST) [18]. This is a low-order multidisciplinary framework for simulating very flexible aircraft using a geometrically exact strain-based beam formulation [21] coupled to various aerodynamic formulations and to the rigid-body equations of motion (for free flight).

The half-vehicle BWB planform along with the location and discretization of the UM/NAST reference beam axis are shown in Fig. 1. The model aerodynamic and structural properties are reported in Table 1. The structure is subdivided into a stiffer 3-element center body and a flexible 8-element wing. Nine concentrated masses of 2 kg are equally spaced along the wing reference beam axis, with an additional mass of 80 kg placed at the body nose. The first 10 in-vacuum natural frequencies are reported in Table 2. Unsteady aerodynamics is modeled using the Peters’ finite-state unsteady airfoil theory [22] combined with a NACA0012 lookup table at Reynolds number 1.5×10^5 and Mach number 0.041 for determining the aerodynamic coefficients along the span. A tip loss factor is used for including three-dimensional effects.

Note that the BWB model in UM/NAST is described for completeness, but it is not used when applying the proposed method. The method uses only output data from BWB gust responses where UM/NAST is treated as a black box.

Table 1: BWB aerodynamic and structural properties.

Property	Body	Wing
Chord at member root (m)	1.39	0.55
Chord at member tip (m)	0.55	0.55
Reference axis location at member root (% chord)	64.38	45.60
Reference axis location at member tip (% chord)	45.60	45.60
Axial stiffness (N)	1.69×10^8	1.55×10^8
Torsion stiffness (N·m ²)	2.25×10^6	1.10×10^4
Out-of-plane bending stiffness (N·m ²)	7.50×10^5	1.17×10^4
In-plane bending stiffness (N·m ²)	3.50×10^7	1.30×10^5
Mass per unit span (kg/m)	50	6.20
Out-of-plane moment of inertia per unit span (kg·m)	0.70	5.00×10^{-4}
In-plane moment of inertia per unit span (kg·m)	22.00	4.62×10^{-3}

Table 2: BWB natural vibration frequencies in undeformed shape.

Mode #	Mode type	Frequency (Hz)
1	Out-of-plane bending	2.19
2	In-plane bending	7.36
3	Out-of-plane bending	13.74
4	Out-of-plane bending	38.32
5	In-plane bending	46.75
6	Out-of-plane bending	66.25
7	Out-of-plane bending	88.19
8	Out-of-plane bending	95.45
9	In-plane bending	134.19
10	Torsion	134.77

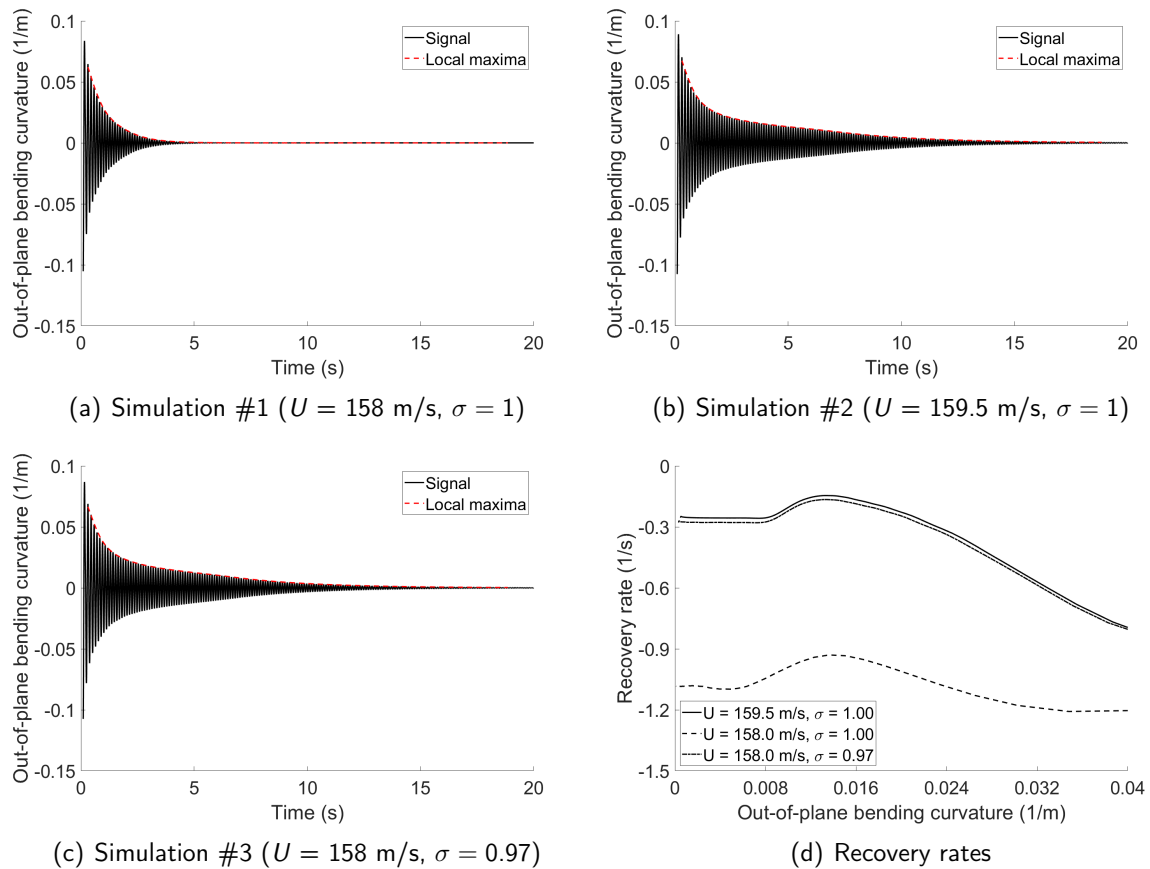


Figure 2: BWB transient responses and recovery rates for varying flow speed U and wing torsion stiffness scaling factor σ .

4 Results

The multi-parameter bifurcation forecasting method proposed in Sec. 2 is applied to the clamped BWB considering the flow speed U and the scaling factor for the wing torsion stiffness σ as the varying control parameters ($\mu = [U, \sigma]$). With this choice, and assuming a first-order Taylor expansion in Eq. (5) corresponding to a linear recovery rate fitting, the method requires a minimum of three transient responses. Two transient responses are obtained at $U = 158 \text{ m/s}$ and $U = 159.5 \text{ m/s}$ while considering the baseline wing torsion stiffness, that is, $\sigma = 1$. One additional transient response is obtained at $U = 158 \text{ m/s}$ and $\sigma = 0.97$, which corresponds to a 3% lower wing torsion stiffness.

Output data from the transient responses are used for forecasting the bifurcation diagram as a function of U and σ using the procedure detailed in Sec. 2. With no loss in generality, the method is applied considering the local maxima of the transient signals for the out-of-plane bending curvature at the 8th BWB element (see Fig. 2). However, one could have used transient signals for any other element or strain measure. Signal decomposition is not applied because contributions from modes that do not bifurcate are negligible in the transient responses for this application and flight conditions.

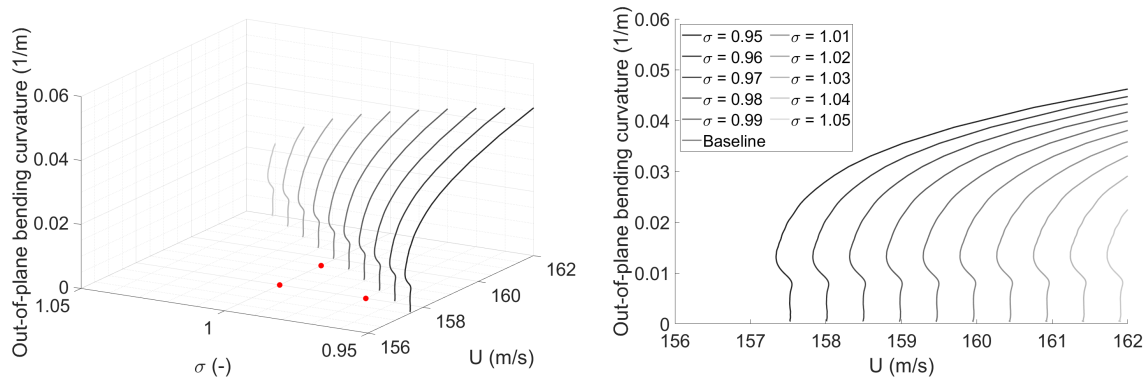


Figure 3: BWB multi-parameter bifurcation forecasting results for varying speed U and wing torsion stiffness scaling factor σ (red markers denote control-parameter values where output data are collected).

The obtained transient responses and recovery rates are shown in Fig. 2. Recovery rates from different transient responses are fitted using a bi-linear polynomial in U and σ for forecasting the bifurcation diagram at each amplitude. Specifically, the proposed method is used for investigating the sensitivity of the bifurcation diagram to variations in the wing torsion stiffness. This is done by solving Eq. (8) for varying μ_0 after fitting the recovery rates in Fig. 2(d) at each amplitude.

Results in Fig. 3 show the bifurcation diagrams forecasted by keeping $\mu_{0_1} = U = 158$ m/s while varying $\mu_{0_2} = \sigma$ between 0.95 and 1.05, which corresponds to a $\pm 5\%$ variation in the wing torsion stiffness with respect to the baseline design. The BWB shows a subcritical behavior characterized by a narrow bi-stability region, as observed in previous work [19, 20]. While variations in the wing torsion stiffness influence the amplitude of post-flutter responses, they do not modify the type of bifurcation behavior. Note that the bifurcation diagrams for varying wing torsion stiffness in Fig. 3 are obtained efficiently using only output data from the three transient responses shown in Fig. 2. This is a unique feature of the proposed multi-parameter bifurcation forecasting method that makes it a valuable tool for repeated computations required in design space exploration, sensitivity analysis, and uncertainty quantification.

Bifurcation diagrams for selected values of the wing torsion stiffness scaling factor $\sigma = 0.98, 1, 1.02$ are compared with results from the one-parameter bifurcation forecasting method and with UM/NAST time marching solutions in Fig. 4. Results from the one-parameter bifurcation forecasting method are obtained by considering two transient responses at two pre-bifurcation speeds for each new wing design. Comparisons are shown in Fig. 4. The bifurcation diagrams obtained with the one-parameter and the multi-parameter bifurcation forecasting methods match for $\sigma = 1$. This is expected because the same transient responses for $\sigma = 1$ are used in both methods. The results for $\sigma = 0.98$ and $\sigma = 1.02$ show slight discrepancies because the multi-parameter bifurcation forecasting method is applied without using any data for those values of the wing torsion stiffness scaling factor. This is the main advantage of the proposed formulation that considerably decrease the computational cost of bifurcation sensitivity analyses while providing accurate results. The good agreement between the one-parameter and the two-parameter forecasting results shows that the BWB bifurcation diagram can be reason-

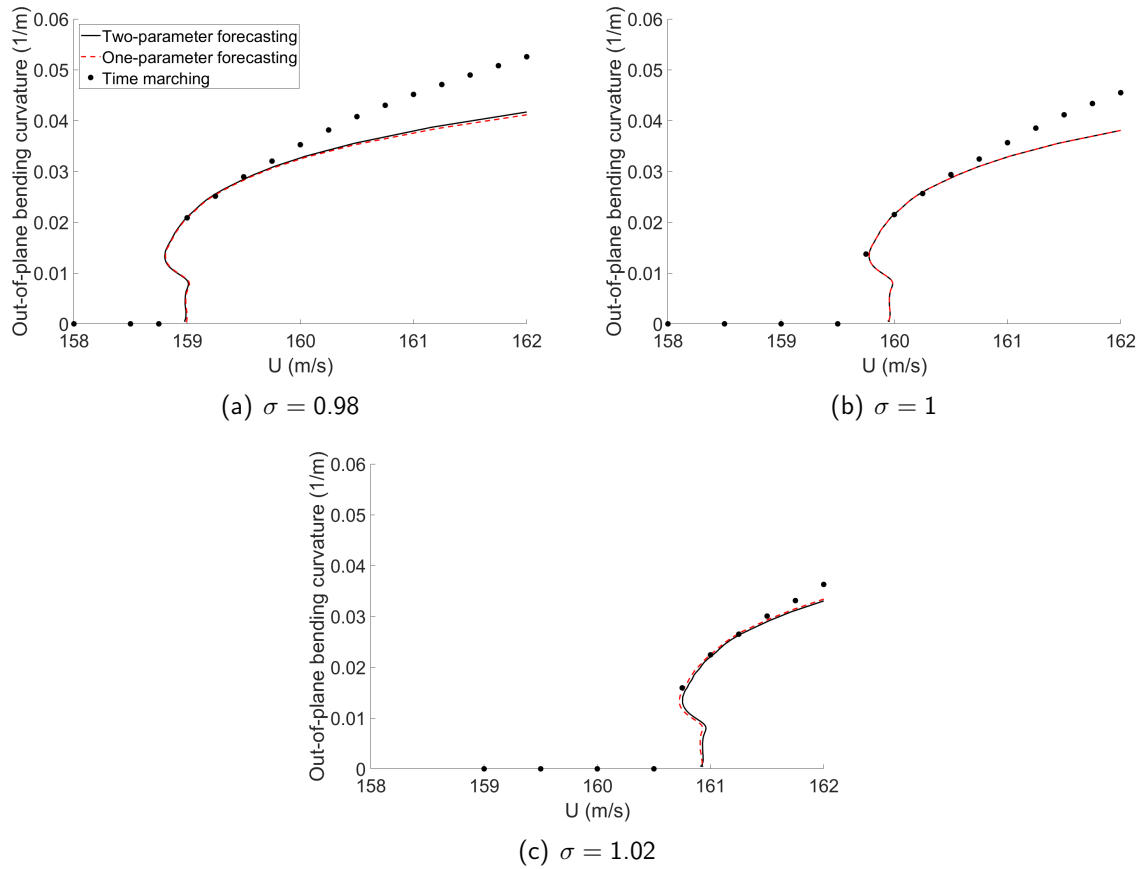


Figure 4: Verification of the BWB multi-parameter bifurcation forecasting results in Fig. 3 for wing torsion stiffness scaling factor $\sigma = 0.98, 1, 1.02$.

ably assumed to vary linearly with U and σ for small variations in the wing torsion stiffness. Furthermore, both the one-parameter and two-parameter forecasting results match well with the reference solution from time-marching simulations. Errors increase as moving away from the flutter point, as expected because of the extrapolation used in the forecasting procedure. This issue can be improved by increasing the number of transient responses in order to use a second-order Taylor expansion in Eq. (5), and thus, a quadratic fitting and extrapolation of the recovery rates. However, higher-order expansions also increase the sensitivity of forecasting results to the presence of numerical errors or noise in the output data.

For completeness, the flutter speeds obtained from the bifurcation diagrams in Fig. 3 are compared in Table 3 with reference results from the UM/NAST flutter solver. The flutter speeds from the proposed multi-parameter bifurcation forecasting method match the reference values with errors below 0.2% in the range of wing designs considered although they are obtained using only three transient responses in the pre-flutter regime.

Table 3: BWB flutter speed for varying wing torsion stiffness scaling factor σ .

σ (-)	Flutter speed (m/s)		
	UM/NAST	Proposed method	Error
0.95	157.34	157.52	0.12%
0.96	157.84	158.01	0.11%
0.97	158.34	158.49	0.10%
0.98	158.83	158.98	0.09%
0.99	159.31	159.46	0.09%
1.00	159.80	159.95	0.10%
1.01	160.27	160.43	0.10%
1.02	160.74	160.92	0.11%
1.03	161.21	161.40	0.12%
1.04	161.66	161.89	0.14%
1.05	162.12	162.37	0.16%

5 Concluding Remarks

This paper presented a novel method for forecasting nonlinear flutter bifurcations and post-flutter responses of fluid-structural systems with multiple varying parameters. The method uses only output data from a handful of transient responses in the system pre-flutter regime without requiring knowledge of the system equations. Flutter and post-flutter dynamics of a geometrically nonlinear wing were forecasted for varying speed and wing torsion stiffness using output data from a limited number of transient simulations. Results were verified with solutions obtained using the one-parameter bifurcation forecasting method and direct time marching, showing good agreement in the predicted bifurcation diagrams. The results showed in this work demonstrate that the proposed multi-parameter bifurcation forecasting method is a promising approach for efficient model-free nonlinear flutter forecasting in applications involving multiple varying parameters. The proposed method is thus of interest for design space exploration, sensitivity analysis, and uncertainty quantification of large-scale nonlinear fluid-structural systems.

References

- [1] Dowell, E. H., Edwards, J., and Strganac, T., "Nonlinear Aeroelasticity," *Journal of Aircraft*, Vol. 40, No. 5, 2003, pp. 857–874. doi:10.2514/2.6876.
- [2] Jonsson, E., Riso, C., Lupp, C. A., Cesnik, C. E. S., Martins, J. R. R. A., and Epureanu, B. I., "Flutter and Post-Flutter Constraints in Multidisciplinary Design Optimization," *Progress in Aerospace Sciences*, Vol. in press, 2019. doi:10.1016/j.paerosci.2019.04.001.
- [3] Torii, H., and Matsuzaki, Y., "Flutter Margin Evaluation for Discrete-Time Systems," *Journal of Aircraft*, Vol. 38, No. 1, 2001, pp. 42–47. doi:10.2514/2.2732.
- [4] Dimitriadis, G., and Cooper, J. E., "Flutter Prediction from Flight Flutter Test Data," *Journal of Aircraft*, Vol. 38, No. 2, 2001, pp. 355–367. doi:10.2514/2.2770.
- [5] Jacobson, K. E., Kiviaho, J. F., Kennedy, G. J., and Smith, M. J., "Evaluation of Time-Domain Damping

- Identification Methods for Flutter-Constrained Optimization," *Journal of Fluids and Structures*, Vol. 87, 2019, pp. 174–188. doi:10.1016/j.jfluidstructs.2019.03.011.
- [6] Zhang, W., Lv, Z., Diwu, Q., and Zhong, H., "A Flutter Prediction Method with Low Cost and Low Risk from Test Data," *Aerospace Science and Technology*, Vol. 86, 2019, pp. 542–557. doi: 10.1016/j.ast.2019.01.043.
- [7] Kim, T., "System Identification for Coupled Fluid-Structures: Aerodynamics is Aeroelasticity Minus Structure," *AIAA Journal*, Vol. 49, No. 3, 2011, pp. 503–512. doi:10.2514/1.J050245.
- [8] Kim, T., "Flutter Prediction Methodology Based on Dynamic Eigen Decomposition and Frequency-Domain Stability," *Journal of Fluids and Structures*, Vol. 86, 2019, pp. 354 – 367. doi: 10.1016/j.jfluidstructs.2019.01.022.
- [9] Lim, J., and Epureanu, B. I., "Forecasting a Class of Bifurcations: Theory and Experiment," *Physical Review E*, Vol. 83, 2011, pp. 016203–016203–9. doi:10.1103/PhysRevE.83.016203.
- [10] Lim, J., and Epureanu, B. I., "Forecasting Bifurcation Morphing: Application to Cantilever-Based Sensing," *Nonlinear Dynamics*, Vol. 67, No. 3, 2012, pp. 2291–2298. doi:10.1007/s11071-011-0146-8.
- [11] Ghadami, A., and Epureanu, B. I., "Forecasting Subcritical and Supercritical Flutter Using Gust Responses," *ASME International Mechanical Engineering Congress and Exposition*, Vol. Volume 4A: Dynamics, Vibration, and Control, 2015. doi:10.1115/IMECE2015-53105.
- [12] Ghadami, A., and Epureanu, B. I., "Bifurcation Forecasting for Large Dimensional Oscillatory Systems: Forecasting Flutter Using Gust Responses," *Journal of Computational and Nonlinear Dynamics*, Vol. 11, 2016, pp. 061009–061009–8. doi:10.1115/1.4033920.
- [13] Yamasaki, H., and Epureanu, B. I., "Forecasting Supercritical and Subcritical Hopf Bifurcations in Aeroelastic Systems," *International Journal of Non-Linear Mechanics*, Vol. 94, 2017, pp. 400–405. doi: 10.1016/j.ijnonlinmec.2016.12.009.
- [14] Ghadami, A., and Epureanu, B. I., "Forecasting the Post-Bifurcation Dynamics of Large-Dimensional Slow-Oscillatory Systems using Critical Slowing Down and Center Space Reduction," *Nonlinear Dynamics*, Vol. 88, 2017, pp. 415–431. doi:10.1007/s11071-016-3250-y.
- [15] Ghadami, A., Cesnik, C. E. S., and Epureanu, B. I., "Model-Less Forecasting of Hopf Bifurcations in Fluid-Structural Systems," *Journal of Fluids and Structures*, Vol. 76, 2018, pp. 1–13. doi: 10.1016/j.jfluidstructs.2017.09.005.
- [16] Ghadami, A., and Epureanu, B. I., "Forecasting Critical Points and Post-Critical Limit Cycles in Non-linear Oscillatory Systems using Pre-Critical Transient Responses," *International Journal of Non-Linear Mechanics*, Vol. 101, 2018, pp. 146–156. doi:10.1016/j.ijnonlinmec.2018.02.008.
- [17] Strogatz, H., *Nonlinear Dynamics and Chaos with Applications to Physics, Biology, Chemistry, and Engineering*, Westview Press, Boulder, 2001.
- [18] Su, W., and Cesnik, C. E. S., "Nonlinear Aeroelasticity of a Very Flexible Blended-Wing-Body Aircraft," *Journal of Aircraft*, Vol. 47, No. 5, 2010, pp. 1539–1553. doi:10.2514/1.47317.
- [19] Riso, C., Ghadami, A., Cesnik, C. E. S., and Epureanu, B. I., "Model-Free Forecasting of Limit Cycle Oscillations in Geometrically Nonlinear Wings," *18th International Forum on Aeroelasticity and Structural Dynamics*, Savannah, GA, 2019.
- [20] Riso, C., Ghadami, A., Cesnik, C. E. S., and Epureanu, B. I., "Data-Driven Forecasting of Post-Flutter Responses of Geometrically Nonlinear Wings," *AIAA Journal*, in review.
- [21] Su, W., and Cesnik, C. E. S., "Strain-Based Geometrically Nonlinear Beam Formulation for Modeling Very Flexible Aircraft," *International Journal of Solids and Structures*, Vol. 48, No. 16-17, 2011, pp. 2349–2360. doi:10.1016/j.ijsolstr.2011.04.012.
- [22] Peters, D. A., Hsieh, M. C. A., and Torrero, A., "A State-Space Airloads Theory for Flexible Airfoils," *Journal of the American Helicopter Society*, Vol. 52, No. 4, 2007, pp. 329–342. doi:10.4050/JAHS.52.329.

Response-Based Stability Analysis and Test Applications Using Parametric Flutter Margins

Moti Karpel

Technion – Israel Institute of Technology, Haifa, Israel, motiwork@gmail.com

Keyword: Flutter analysis, flutter tests

While most aeroservoelastic (ASE) design and certification calculations are performed using linear frequency-domain models, increasing portions require adequate evaluation of nonlinear aerodynamic, structural or control-system effects. An Increased-Order Modeling (IOM) methodology was developed for this purpose and presented a few years ago [1]. It has been applied to dynamic loads analysis at Airbus D&S [2] using the Dynresp code.

A new Parametric Flutter Margin (PFM) method [3] for response-based flutter analysis was recently added to the IOM concept. Being based on a single stabilizing parameter, such as a certain modal damping value or discrete mass that enhances the ASE stability, the PFM method facilitates very efficient massive sensitivity studies with respect to selected stabilizing parameters. Furthermore, it facilitated safer flutter tests where flutter or nonlinear limit-cycle oscillation (LCO) boundaries of a certain configuration are positively identified while actually testing a more stable configuration. Two proof-of-concept wind-tunnel tests have already been performed with very encouraging results.

A generalized frequency-domain ASE equation of motion for response analysis is cast in the form

$$\begin{cases} [A(i\omega)]\{x(i\omega)\} = [B(i\omega)]\{u(i\omega)\} \\ \{y(i\omega)\} = [C(i\omega)]\{x(i\omega)\} \end{cases}$$

The resulting time-domain $\{x(t)\}$ may be modified by a convolution process, using the IOM method, to include the nonlinear effects of terms in $\{y(t)\}$ on terms in $\{x(t)\}$. A PFM stability analysis is performed by adding a stabilizing parameter, p_f , such that $[A(i\omega)]$ is replaced by $[A(i\omega) + p_f B(i\omega)C(i\omega)]$ where the input and output vectors are of the same size. It can be shown that the velocity-frequency point for which there is an excitation vector $\{u_f(i\omega)\}$ that yields $\{y_f(i\omega)\}$ that satisfies $\{y_f(i\omega)\} = \{u_f(i\omega)\} / p_f$, must be a flutter onset point. The resulting eigenvalues and eigenvectors indicate the flutter conditions and modes. The resulting response to external excitation of the unstable modes, whether linear or nonlinear, may be used for extracting the associated load distributions using the mode-displacement or summation-of-force methods. The PFM results may be used for a direct evaluation of the incremental flutter parameter, Δp_f , that causes flutter at selected velocities. Associated perturbation analyses may yield efficient ASE design with flutter and control-margin constraints.

The unified IOM-PFM model construction and solution processes for obtaining flutter/LCO characteristics, without and with nonlinear elements, will be presented and discussed in the full paper. The usage of the IOM-PFM framework in designing, conducting and post processing wind-tunnel and flight flutter tests will also be discussed and demonstrated using numerical simulations.

- [1] Karpel, M., "Increased-Order Modeling Framework for Nonlinear Aeroservoelastic Analysis," *Proceedings of the International Forum on Aeroelasticity and Structural Dynamics*, Paper No. 2011-71, Paris, France, June 2011.
- [2] Reyes, M., Climent, H., Karpel, M., Arevalo, F. and Maderuelo, C., "Increased-Order Aeroservoelastic Modeling in Practice," *Proceedings of the International Forum on Aeroelasticity and Structural Dynamics*, Paper No. 2011-71, Como, Italy, June 2017.
- [3] Roizner, F., and Karpel, M., "Parametric Flutter Margin Method for Aeroservoelastic Stability Analysis", *AIAA Journal*, Vol. 56, No. 3, 2018, pp. 1011-1022.

Improvement of the Unsteady Two-color PSP Applicable to Wind-Tunnel Experiments Using Dynamically-vibrated Airfoil Models

Ayana Wakayama¹ and Daiju Numata²

¹Tokai University, Kanagawa-ken, Japan, 9bemm090@mail.u-tokai.ac.jp

²Tokai University, Kanagawa-ken, Japan, numata.daiju@tsc.u-tokai.ac.jp

Abstract

In this study, to clarify aeroelastic problems in transonic flight region, some types of sprayable two-color pressure-sensitive paints (PSP) were developed for measuring unsteady pressure field fluctuated by aeroelastic phenomena. For this purpose, effects of the dispersant added to the PSP and the content of titanium dioxide in PSPs to some characteristics of PSP was evaluated by results of static and dynamic calibration tests to developed PSPs. From results of static and dynamic calibration tests, it was found that higher pressure and temperature sensitivity was shown in case of PSP with dispersant. In addition, by increasing the content of titanium oxide in the PSP, it was found that it is possible to improve the time response characteristics of the PSP.

Keyword: Aeroelastic phenomenon, Unsteady flow, Pressure-sensitive Paint (PSP)

1 Introduction

Recently, development of the supersonic aircraft is actively promoted in various countries. As flight speed of aircrafts increases, it is becoming increasingly important to consider aeroelastic problem in aircraft development. As one of such aeroelastic problems, there is "aileron buzz" problem in transonic flight region. This phenomenon is aileron's vibration in transonic flight caused by changing aerodynamic force around the airfoil which is occurred by shock-wave/flow-field interaction. The type of aileron buzz is classified three patterns as difference of its vibration mechanism or position of shock waves by Lambourne as shown in Fig. 1 (Lambourne, 1964).

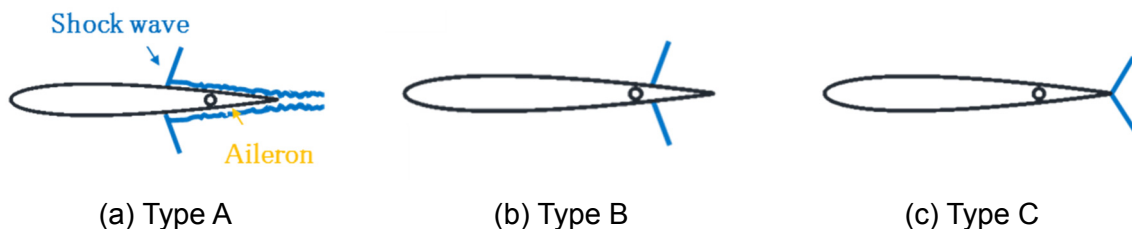


Figure 1: Classification of aileron buzz pattern

In "type A", flow separation occurs behind shock wave which appears on airfoil region upstream of the aileron. By this flow separation, vibration of the aileron is generated. In "type B", shock wave appears on the surface of the aileron. Position of shock wave moves depending on movement of the aileron. In "type C", position of shock wave moves onto the trailing edge of the aileron, and flow speed on all the surface of the aileron become supersonic. These mechanisms are not completely clarified yet, and further detailed

research of flow phenomena on the airfoil under aileron buzz is needed to clarify aileron buzz. To clarify vibration phenomena like aileron buzz, it is necessary to clarify unsteady aerodynamic phenomena caused by shock-wave/flow-field interaction on the surface of the airfoil. Therefore, it is important to measure unsteady pressure field on the surface of the airfoil and clarify its phenomenological background. To measure unsteady pressure fluctuation on the test model like the airfoil in wind-tunnel testing, for example, various mechanical or electrical unsteady pressure sensors are generally used. However, pressure measurement by using this kind of sensors has limitation in spatial resolution and also difficult to install those on the thin wing model for wind-tunnel testing, for example, which simulate wings for hypersonic flyers. Therefore, other pressure measurement methods with high spatial resolution is needed.

In this study, we focused on Pressure-Sensitive Paint (PSP) technique (Liu, T. and Sullivan, J.P., 2004) in order to solve these problems. PSP is a kind of the pressure sensor and uses quenching phenomenon of the pressure-sensitive dye by oxygen called "oxygen quenching" in measurement. The luminescence dye in PSP is excited by the excitation light source, and luminescence intensity from the excited dye varies depending on oxygen concentration around the excited dye, in other words, pressure around the excited dye. This technique realizes pressure distribution measurement of all over the surface of the test model which was painted PSP. Therefore, PSP measurement technique is much better than conventional discrete pressure measurement techniques in this point.

In PSP measurement which is conducted in wind-tunnel testing, "intensity-based method" is generally used to measure pressure field using PSP. In principle, to calculate pressure distribution on the test model, wind-on and wind-off images during experiment, in which shape and/or position of the test model captured in those images are same in each picture, is needed for intensity-based method. However, for example, in dynamic wind-tunnel testing, the test model vibrates and/or deforms during experiment time-sequentially. Therefore, in DWT, it is difficult to apply this kind of PSP measurement technique because model shape and model position captured in wind-on and wind-off images in DWT are generally different in each image. Therefore, just taking the ratio like general PSP measurements cause errors due to these factors, and emission intensity ratio for calculating pressure is not be able to be calculated accurately in DWT. For example, Nakakita et al. (2009) conducted unsteady PSP measurement in transonic wind-tunnel testing to clarify transonic flutter phenomena on the thin wing, and it succeeded to reveal pressure changes and shock waves behavior on the wing in transonic flutter condition from PSP measurement results. However, although qualitative pressure field data on the wing in transonic flutter condition was able to visualize by applying PSP technique, the quantitative one was not able to get from this experiment because shape of the wing in transonic flutter condition drastically deformed time-sequentially.

As a method solving such the problem, there is the two-color PSP technique. The two-color PSP is made by the mixing reference dye called a second-dye, which doesn't have pressure sensitivity, into the normal PSP. The second-dye is a dye that can be excited by the same excitation light source as the pressure-sensitive dye called a first-dye, and has different emission wavelength. Luminescence from these two dyes are simultaneously acquired by imaging devices, and luminescence from the first-dye is used as a signal emission and luminescence from the second-dye is used as a reference emission, respectively. Therefore, by using the two-color PSP, PSP measurement for the test model in dynamic situation become possible. For example, for past research conducted by Mitsuo, K. and Asai, K. (2001), it is succeeded to measure the pressure field around a cylinder model by applying a two-color PSP. This result indicated that to avoid each problem caused by changing

luminescent pattern of the excitation light due to a model deformation between wind-on and wind-off images in wind tunnel testing is possible.

In past research, based on those background, we tried to develop some two-color PSPs (Wakayama and Numata, 2019). However, their PSP characteristics are not yet sufficient for use in dynamic measurement held in dynamic wind-tunnel testing, and it is necessary to further improve pressure sensitivity, temperature sensitivity, time response, and so on. In this study, to improve characteristics of these unsteady two-color PSPs, configuration of two-color PSP was changed, and some characteristic tests, for example, pressure sensitive test, temperature sensitive test and time response test, was conducted. We focused on the effect of dispersant and titanium dioxide content in PSP in this study, and investigate it.

2 Experimental principle

2.1 Pressure-Sensitive Paint (PSP)

PSP is a type of the pressure sensor that uses the pressure-sensitive dye receiving oxygen quenching. The luminescence dye is fixed on the test model using an oxygen-permeable binder and then excited by the excitation light source and emits luminescence. Luminescence intensity from the excited dye varies depending on oxygen concentration around the excited dye. Therefore, by detecting this emission change from PSP, we can calculate pressure on PSP.

In PSP measurement, pressure distribution on the test model in wind-on condition is calculated using luminescence intensity ratio obtained by taking the ratio of the wind-on image and the wind-off image in experiment. Luminescence intensity ratio is converted to pressure by applying Stern-Volmer relationship shown in Eq. 1.

$$\frac{I_{\text{ref}}}{I} = A(T) + B(T) \frac{P}{P_{\text{ref}}} \quad (1)$$

In Eq. 1, I , P and T is luminescence intensity, pressure and temperature, respectively. $A(T)$ and $B(T)$ are Stern-Volmer coefficients obtained from calibration test. Suffix "ref" means reference condition.

Main component of general measurement system for PSP measurement is composed of the excitation light source which excites the PSP, a photodetector which measures light emission of the PSP and a PC which is used for data processing as shown in Fig. 2. The excitation light source emits light with wavelength suitable for exciting dye molecules of the PSP, and is irradiated to the test model continuously. In experiment, it causes measurement error when light with same wavelength band of emission wavelength of the PSP from the excitation light source is incident on the photodetector. Therefore, optical filters that transmit only the excitation wavelength band of the PSP dye are attached on the head of the excitation light source. In addition, time variation of irradiation intensity of the excitation light source also gives error to the measurement result. Since LED light source have relatively high time stability, they are often used as an excitation light source for PSP measurement. A digital camera which uses CCD or CMOS as an image sensor is mainly used as a photodetector. In addition, incident of excitation light and disturbance light in the image sensor of the photodetector causes noise and/or measurement error. Therefore, by attaching the optical filter corresponding to emission wavelength band of the PSP in front of the photodetector, these lights are eliminated.

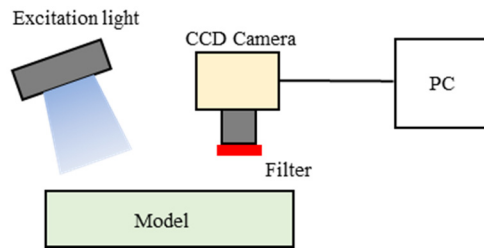


Figure 2: Conceptual diagram of PSP measurement system

2.2 Unsteady PSP

In unsteady PSP measurement, it is necessary for emission intensity change of the PSP to follow pressure change due to aerodynamic phenomena. Therefore, the PSP which can be applied to unsteady phenomena is required to have faster time response than that of the steady PSP. For this purpose, unsteady PSPs using various porous binders were developed. Porous binders have a large surface area and an open structure to oxygen as compared with conventional polymer-type binders. Therefore, oxygen permeability of porous binders is much higher than that of conventional polymer binders, and the response time of PSPs which use porous binders are on the order of $10\mu\text{s}$. Thin-layer chromatography (TLC) plate (Baron, A.E. et al., 1993), hydrothermal coating (Bacsa, R.R. and Gratzel, M., 1996), anodized aluminum (Asai, K., 1997) (Sakaue, H. et al., 1999), polymer/ceramic composite (Scroggin, A.M., 1999), porous filter (Erausquin, R.G., 1998) and so on have been evaluated as porous materials for the unsteady PSP.

In this study, the polymer/ceramic composite is used as a binder for the unsteady PSP. The polymer/ceramic binder is a sprayable porous binder and consists of a large amount of ceramic particles and a very small amount of polymers. In this study, the titanium oxide was used as a ceramic particle. Fig. 3 shows a conceptual diagram of structure of the PC-PSP.

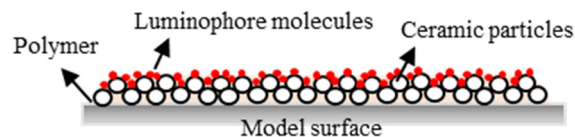


Figure 3: Structure of PC-PSP

There are a lot of adsorption methods of the pressure-sensitive dye on polymer/ceramic binders. In this study, we used a last coat method. In this method, surface of the test model which is painted binder is overcoated with a dye using a spray-gun.

2.3 Two-color PSP

In general PSP measurement, pressure at wind-on situation on the surface of the test model is calculated from the luminescence intensity ratio image obtained by taking the ratio of the wind-on image and the wind-off image captured in experiment. However, if the test model moves, vibrates and/or deforms during experiment, for example during dynamic measurement in dynamic wind-tunnel testing (DWT), calculation of luminescence intensity ratio is difficult because difference occurs between shape and/or position of the test model captured in each of images. Therefore, in general, to apply conventional PSP measurement techniques to dynamic measurement is difficult. In such cases, it is effective to use two-color PSP measurement method in which a second-dye (reference dye) that does not have

pressure sensitivity is mixed with the normal PSP. In this method, two emission signals from two dyes in the two-color PSP are simultaneously detected by the photodetector and use those signals as a wind-on image and a wind-off image. Fig. 4 shows conceptual diagram of two-color PSP method.

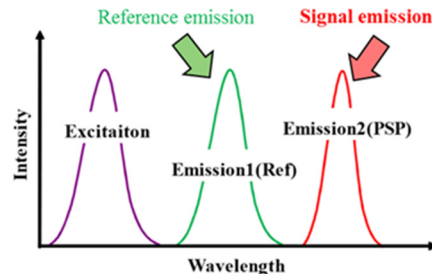


Figure 4: Conceptual diagram of two-color PSP method

In order to detect two emission wavelength bands simultaneously, an imaging device such as a high-speed color camera or a two-wavelength splitter optical system is generally used. In this study, the two-wavelength splitter optical system is used as a detector which can install any optical filters. Fig. 5 shows the conceptual diagram of measurement system for two-color PSP method.

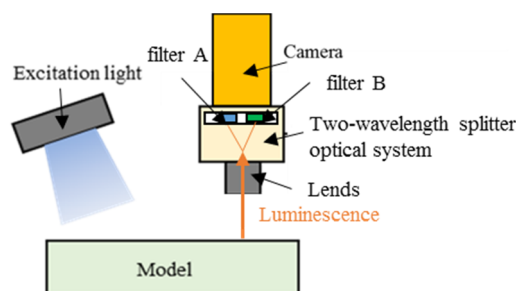


Figure 5: Conceptual diagram of measurement system for two-color PSP method

3 Development of two-color PSPs

3.1 Configuration of PSP

Tab. 1 shows configuration of PSP in this study. The sample “No.1” is a baseline PSP which is developed in past our research. Pressure sensitivity, temperature sensitivity and time-response characteristic of PSPs were investigated at each samples by conducting some calibration tests, and compared with those by sample “No.1”.

In this study, Platinum(II)-5,10,15,20-tetrakis-(2,3,4,5,6-pentafluorophenyl)-porphyrin (PtTFPP) (Frontier Science, CAS No. 109781-47-7) is used as a pressure-sensitive dye, and BAM-G (TOKYO KAGAKU KENKYUSHO CO., LTD., BG-51) is used as a reference dye. The binder solution is made from toluene (Wako Pure Chemical Industries, Ltd., CAS No. 108-88-3) as a solvent, poly(isobutyl methacrylate) (poly(IBM)) (Polysciences, Inc., CAS No. 54116) as a polymer, titanium dioxide (TiO₂, rutile form) (Wako Pure Chemical Industries, Ltd., CAS No. 209-07075) as a ceramic particle, BAM-G as a reference dye and dispersant (SANNOPCO LIMITED, SN sparse 2190). After adding an appropriate amount of glass beads into the solution, the binder solution was stirred for about 12 hours by using a table-top ball mill.

The dye solution is made from toluene and methanol (Wako Pure Chemical Industries, Ltd., CAS No, 131-01826) as a solvent and PtTFPP as a pressure-sensitive dye.

In this study, the binder solution and the dye solution were prepared separately. At the time of coating on the test model, the binder solution was painted firstly. After that, the dye solution was also painted on the binder-painted test model.

Table 1: Configuration of binder and dye solution

	Binder solution					Dye solution	
	Solvent	Ceramic particle	Polymer	Dispersant	Reference dye	Solvent	Pressure Sensitive dye
1 Baseline	Toluene	TiO ₂ 95 %	Poly (IBM)	-	BAM-G	Toluene Methanol	PtTFPP
2		TiO ₂ 95 %		SN sparse 2190			
3		TiO ₂ 97 %					
4		TiO ₂ 98 %					

3.2 Experimental system

Fig. 6 shows a schematic diagram of the static calibration system. This calibration chamber is composed of a pressure chamber for setting test samples, a pressure controller for controlling pressure inside the pressure chamber and a temperature controller for controlling temperature of the test sample. A dry vacuum pump and a high-pressure source are connected to the pressure controller. By using this pressure controller, pressure in the calibration chamber can be adjusted in the range of 0.2 kPa to 1,000 kPa. The temperature controller controls temperature of the test sample using a Peltier element, and adjustable temperature range is approximately 0 deg.C to 50 deg.C. However, this range varies depending on the size and material of the test sample. By using these devices, the calibration system can arbitrarily change pressure and temperature on and around the test sample set in the chamber.

The high-performance LED light (IL-104 UV LED, Hardsoft) is used as the excitation light source. These becomes the excitation light source with specific wavelength band by attaching arbitrary optical filters. In addition, a neutral-density (ND) filter (Zeta ND-8 (W) 77 mm, Kenko) was also attached to the head of the light source to adjust intensity of excitation light emitted from the light source to the measurement target. Fluorescence detection from test samples is performed with a CCD camera, a CMOS camera. In this case, luminescence from test samples is recorded as an image data by a CCD camera (HAMAMATSU PHOTONICS, C4742-80-12AG). Also, to measure pressure using the two-color PSP, it is necessary to capture two emissions of different wavelength from the measurement target. Therefore, to this purpose, we developed a special two-wavelength splitter optical system (nac Image Technology, special order) to be installed between the lens and the CCD camera and used two optical filter ($525 \pm 25\text{nm}$ and $650 \pm 25\text{nm}$, bandpass).

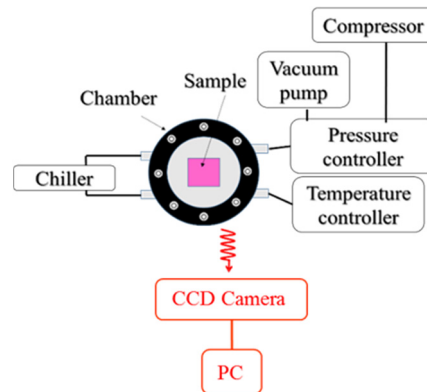


Figure 6: Static calibration system for the molecular imaging sensor at Tokai University

In addition, an acoustic resonance tube is used to evaluate frequency response characteristics of developed PSPs (Fig. 7). In this device, firstly a speaker attached to the end of a tube is driven to generate an air columnar resonance phenomenon generated in a closed tube, thereby generating periodic pressure fluctuations on the PSP sample. At the time of a test, after detecting a periodic luminescence intensity fluctuation caused by pressure fluctuations with a photodetector, the luminescence intensity fluctuation is converted into pressure. By comparing the converted pressure value with the output value of the unsteady pressure sensor installed in the sample, gain and phase characteristics of the PSP can be clarified with respect to input pressure fluctuations.

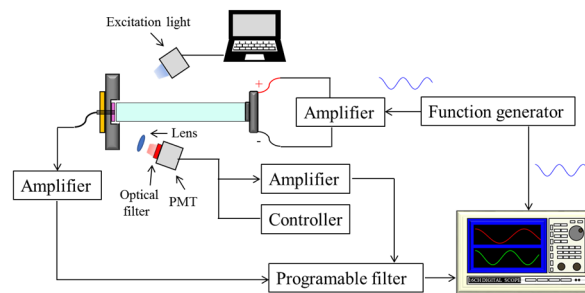


Figure 7: Dynamic characteristic test system

3.3 Experimental condition

Tab. 2 shows the test condition for static and dynamic characteristic test. In static test, pressure sensitivity was investigated at pressure in the range of 1 kPa to 1,000 kPa and sample temperature of 20 deg.C. Also, in order to measure temperature sensitivity, pressure was fixed at 100 kPa, and sample temperature was changed from 10 deg.C to 30 deg.C for 5 conditions. In addition, in dynamic test, 18 resonance frequencies are chosen for this test and frequency range is from 508 to 10,000 Hz. The temperature of this test sample is kept at 20 deg.C and pressure is 100 kPa. In this study, these tests were conducted to five difference samples receptivity.

Table 2: Static and dynamic characteristic experimental condition

	Pressure [kPa]	Temperature [deg.C]	Frequency [Hz]
Pressure sensitivity	1 ~ 1000	20	
Temperature sensitivity	100	10 ~ 30	
Time responsivity		20	508 ~ 10,000

4 Result and discussion

4.1 Pressure sensitivity

Fig. 8 shows the measurement results of the pressure sensitivity of each developed two-color PSPs at 20 deg.C. In Fig.8, the vertical axis indicates I_{ref}/I and horizontal axis indicates pressure, respectively. In this case, I and I_{ref} is luminescence intensity at tested pressure condition and luminescence intensity at reference pressure, respectively. As shown in Fig.8, relationship between I_{ref}/I is almost same however slightly different. Tab. 3 shows pressure sensitivity of each developed PSPs calculated by the relationship between I_{ref}/I shown in Fig. 8. Although pressure range of this calibration test is from 1 to 1,000 kPa, the calculation of pressure sensitivity was conducted around atmospheric pressure because wind tunnel experiment is conducted in an atmospheric pressure. Tab.3 indicated that PSP with dispersant shows lower pressure sensitivity compared with the PSP without dispersant. In addition, Tab. 3 is also indicated that, by increasing the content of titanium dioxide, pressure sensitivity of PSP is increasing.

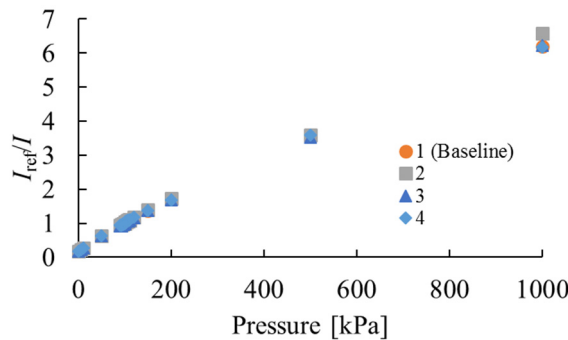


Figure 8: Luminescence intensity ratio I_{ref}/I vs. pressure at 20 deg.C

Table 3: Pressure sensitivity of developed two-color PSP

Sample No.	1 (Baseline)	2	3	4
Pressure sensitivity [%/kPa]	0.83	0.88	0.92	0.93

4.2 Temperature sensitivity

Fig. 9 shows the measurement results of temperature sensitivity of each developed two-color PSPs at 100 kPa pressure condition. In Fig.9, the vertical axis indicates I/I_{ref} and horizontal axis indicates temperature, respectively. In this case, I and I_{ref} is luminescence intensity at tested temperature and luminescence intensity at reference temperature, respectively. Tab. 4 shows temperature sensitivity calculated from relationship between I/I_{ref} and temperature shown in Fig.9. Tab.4 indicated that PSP with dispersant shows higher temperature sensitivity compared with the PSP without dispersant. In addition, Tab. 4 is also indicated that, by increasing the content of titanium dioxide, temperature sensitivity of PSP is increasing.

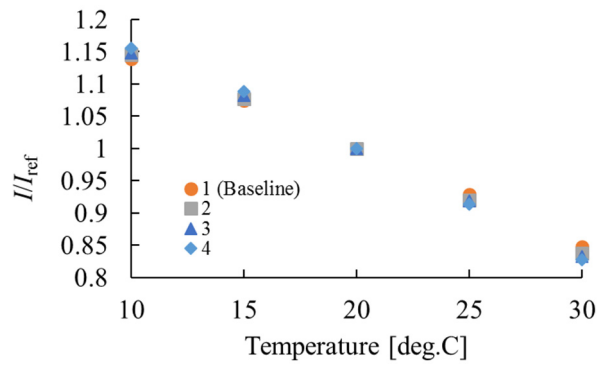


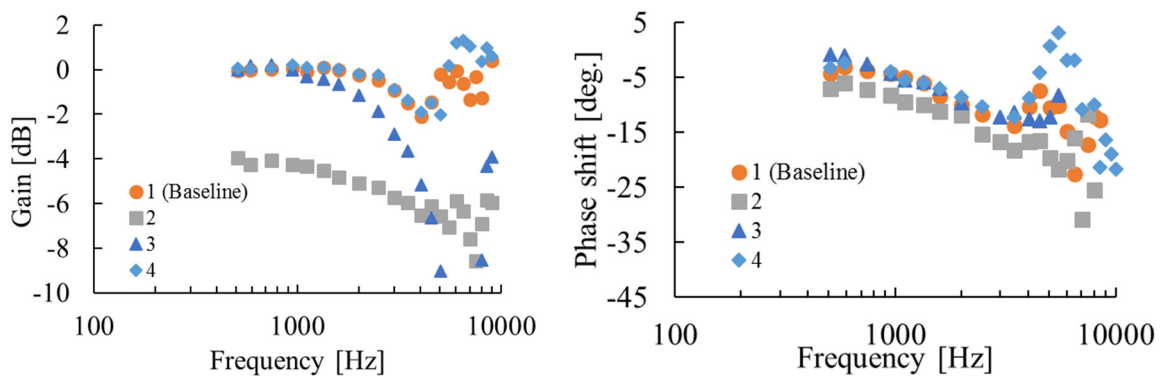
Figure 9: Luminescence intensity ratio I/I_{ref} vs. temperature at 100 kPa

Table 4: Temperature sensitivity of these two-color PSPs

Sample No.	1 (Baseline)	2	3	4
Temperature sensitivity [%/deg.C]	-1.45	-1.55	-1.59	-1.66

4.3 Time responsivity

Fig. 10 shows the time response characteristics of each samples. In Fig.10 (a), the vertical axis indicates gain and horizontal axis indicates frequency. In Fig.10 (b), the vertical axis indicates phase and horizontal axis indicates frequency. As shown in Fig.10, even if the content of titanium oxide is completely same in each PSPs, by containing dispersant in PSP, response time of PSP becomes drastically worse compared with the PSP without dispersant. However, Fig.10 is also indicated that, by increasing the content of titanium dioxide, response time of PSP is increasing. Fig.10 is also indicated that, by increasing the content of titanium oxide in the PSP, it is possible to improve the time response characteristics of the PSP to a level equivalent to the baseline PSP.



(a) Gain diagram

(b) Phase diagram

Figure 10: Time responsivity of two-color PSPs

5 Conclusions

In this study, we tried to improve some characteristics of unsteady two-color PSPs which can be applied in transonic wind-tunnel testing which is conducted for clarifying aerodynamic phenomena around the airfoil caused by aileron buzz. From results, although addition of dispersant in PSP improved the pressure sensitivity of the PSP, it deteriorated the

temperature sensitivity and the time responsiveness of the PSP. However, by increasing the content of titanium oxide, the time response of the PSP was significantly improved. By these results, it is considered that the PSP with dispersant and much titanium oxide has higher performance as a PSP than the PSP of the baseline.

In the future, we plan to conduct a dynamic wind-tunnel testing which applied the developed unsteady two-color PSP to airfoil model.

References

- Asai, K., "Luminescent Coating with an Extremely High Oxygen Sensitivity at Low Temperatures," Patent Pending, No. H9-207351, 1997.
- Bacsa, R.R. and Gratzel, M., "Rutile formation in hydrothermally crystallized nanosized titania," 200 J. Am. Ceram. Soc. 79, pp.2185–88, 1996
- Baron, A.E., Danielson, J.D.S., Gouterman, M., Wan, J.R., Callis, J.B. and McLachlan, B., "Submillisecond response times of oxygen-quenched luminescent coatings," Rev. Sci. Instrum. 64, pp. 3394–402, 1993.
- Erausquin, R.G., "Cryogenic temperature- and pressure-sensitive fluorescent paints," MS thesis. Sch. Aeronaut. Astronaut, Purdue Univ., West Lafayette, IN, 1998.
- Lambourne, "Control-Surface Buzz", Reports and Memoranda, No.3364, 1964.
- Mitsuo, K., Asai, K., "Pressure-Distribution Measurement using Binary Pressure-Sensitive Paint with a Reference Phosphor", 2001.
- Nakakita K, Arizono H and Ito M, "Unsteady Pressure-sensitive Paint Visualization of Transonic Flutter on Thin Wing", JAXA special publication: Proceedings of the Wind Technology Association, 81st, JAXA-SP-09-005, 2009.
- Sakaue, H., Sullivan, J.P., Asai, K., Iijima, Y. and Kunimasu, T., "Anodized aluminium pressure-sensitive paint in a cryogenic wind tunnel," Proc. 45th Int. Instrumentation Symposium (Research Triangle Park, NC: Instrument Society of America), pp.345–54, 1999.
- Scroggin, A.M., Slamovich, E.B., Crafton, J.W., Lachendo, N., Sullivan, J.P., "Porous polymer/ceramic composites for luminescent-based temperature and pressure measurement," Mater. Res. Soc. Proc. 560, pp. 347–52, 1999.
- T. Liu and J. P. Sullivan, "Pressure and Temperature Sensitive Paints", Springer-Verlag, 2004.
- Wakayama, A. and Numata, D., "Development of Two-color Pressure-sensitive Paint for Investigating Aerodynamic Vibration Phenomena in Transonic Flow", 32nd International Symposium on Shock Waves, P-05-0361, 2019.

Structural and Flutter Characteristics of Wing Model with Metal Additive Manufacturing for Wind Tunnel Test

Natsuki Tsushima¹, Kenichi Saitoh², Hitoshi Arizono² and Kazuyuki Nakakita²

¹*Aeronautical Directorate, Japan Aerospace Exploration Agency, Tokyo, Japan, tsushima.natsuki@jaxa.jp*

²*Aeronautical Directorate, Japan Aerospace Exploration Agency, Tokyo, Japan*

Abstract

This additive manufacturing technology has a potential to improve manufacturing costs and may help to achieve high-performance aerospace structures. One of application candidates would be a wind tunnel wing model. A wing tunnel model requires sophisticated designs and precise fabrications for accurate experiments, which frequently increase manufacturing cost. The additive manufacturing technique may help to reduce the expensive testing cost and allow us to investigate aeroelastic characteristics of new designs of aerospace structures as many as we need. In this paper, a metal wing model with the additive manufacturing technique for a flutter test will be studied. Structural/aeroelastic characteristics of an additively manufactured wing model will be evaluated numerically and experimentally.

Keyword: Flutter, aeroelasticity, aircraft, structural analysis, Additive Manufacturing.

1 Introduction

Flutter is a phenomenon involving fluid-structure interaction, which sometimes leads to critical aircraft incidents. Therefore, aeroelastic stability (flutter) analysis plays an important role in the design of aircraft to ensure its safety. Flutter characteristics can be evaluated by numerical analysis, and those analytical results are often verified by wind tunnel experiments with wing models. Those wing models must satisfy strict requirements in terms of structural and aeroelastic characteristics avoiding structural failure and producing flutter within the wind tunnel test environment. Due to the strict requirements, flutter wing models tend to cost significantly and limit numbers of observations.

At the same time, additive manufacturing (AM) technology has recently gained a good deal of attention in aerospace research institutes and industries as a potential technique to facilitate structural developments (Goh et al., 2017). Recent advances in AM technology and automated assembly have enabled sophisticated 3D-printed structures to be fabricated at low cost. Therefore, this technology has a potential to create wing models for flutter wind tunnel test declining the manufacturing cost. With the potential improvement of manufacturing costs and performance of aerospace structures (Bauer et al., 2017; Berger et al., 2017), AM technology has already been applied to actual aerospace vehicles. For example, Banfield et al. developed a 3D printed unmanned air vehicle (UAV) using AM technique to construct a small UAV. Their flight test demonstrated the capability of stable flight. More recently, A full-scale model of Langley Aerodrome No. 8 (LA-8) have been studied taking advantage of AM technology. It is reported that about 80% of the LA-8 model is fabricated by 3D printers. The AM technique helps engineers to easily modify the model

designs and collect data. Although the AM technique is useful to construct complicated structures, it is known that mechanical properties of structures created by the AM technique vary depending on printing process variables (Adelnia et al., 2006; Cuan-Urquizo et al., 2019; Rodriguez et al., 1999). Therefore, a precise understanding of correlations between the process variables and structural properties of AM-based structure is important.

In this paper, a metal wing model with the additive manufacturing technique for a flutter test is studied. Structural/aeroelastic characteristics of an additively manufactured wing model are evaluated numerically and experimentally. To obtain structural properties of AM-based metal structure with Ti6Al4V, a series of tensile experiments are performed. A manufacturing accuracy of AM-based wing model is then investigated. Finally, based on the evaluation results, a wing model for flutter wind tunnel test is designed. The aeroelastic stability of the designed wing model is analyzed by numerical simulation.

2 Structural Evaluation of Metal AM Structure

Tensile test specimens to evaluate structural characteristics of AM-based structures are firstly fabricated based on Electron Beam Melting (EBM) using ArcamQ20. Tensile tests with the specimens are performed for the evaluations of their tensile properties in accordance with Japanese Industrial Standards (JIS) Z2201. The geometry of specimens is a dumbbell shape (No. 5) with the gage length of 50 mm and the thickness of 4 mm. The main process variables are summarized in Tab. 1. The specimens are additively manufactured with Ti6Al4V. The tensile tests are performed with five specimens. A picture of experimental setup is shown in Fig. 1. The strain is measured using a 50-mm gage length extensometer (Instron Corp.). The crosshead speed is 1.0 mm/min.

Stress-strain curves of the tensile tests are shown in Fig. 2. Good reproducibility is observed according to the results, demonstrating the capability of the metal additive manufacturing to provide enough accuracy in terms of structural properties with fixed process variables. Note that the result of Specimen 1 is the second trial because the first test was aborted due to loose grip of the crosshead. Tensile properties obtained by the experiments are summarized in Tab. 2. The most values are averages of the five specimens, while the yield strength is an average of four specimens without the result of Specimen 1.

Table 1: Process variables.

Powder	Layer height, mm	Speed function (SF)
Ti6Al4V	0.08	20

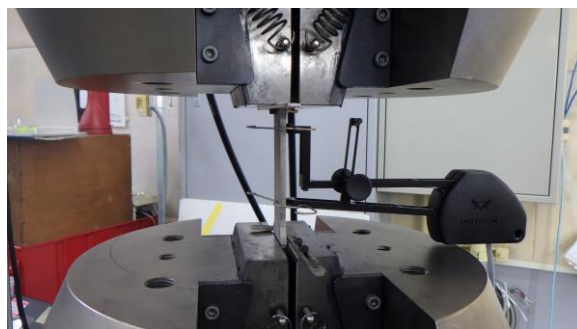


Figure 1: Tensile test setup with the additively manufactured structure using Ti6Al4V.

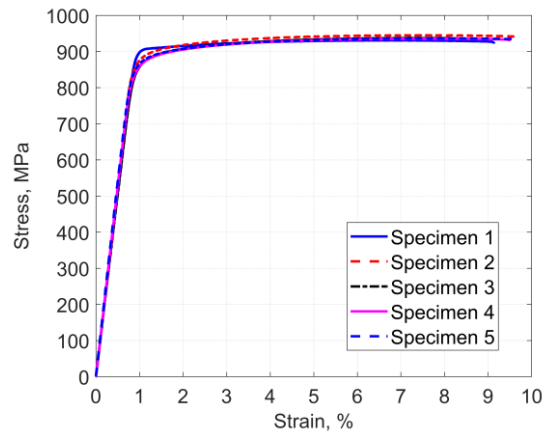


Figure 2: Stress-strain curves the additively manufactured structures using Ti6Al4V.

Table 2: Tensile properties of AM-based structures with Ti6Al4V.

Powder	Young's modulus, GPa	Yield strength, MPa	Ultimate tensile strength, MPa	Elongation, %	Density, g/cm ³
Ti6Al4V	104.87	866.22	937.56	9.2627	4.3730

3 Structural Evaluation of Metal AM Wing Model

To evaluate a quality of wing model fabricated with EBM prior to design and build an actual flutter wind tunnel model, a thin tapered wing model is constructed as a shell structure with the thickness of 0.9 mm. The wing model used for the evaluation is shown in Fig. 3. Since it is aimed to evaluate only the structural properties, not aerodynamic characteristics, a post-process for surface treatment is not performed for the wing model. The geometry of the wing is given in Tab. 3. The span is 189.565 mm, while the root and tip chords are 64.176 and 20.839 mm, respectively. The wing tip is closed with a 0.9-mm wall. The process variables and material used are the same as the ones for the tensile specimens. Poisson's ratio is assumed to be 0.33.

A static load test with the wing model is performed to evaluate structural characteristics of the wing model. The test result is compared with a solution of static structural simulation obtained by MSC.Nastran. In the finite element analysis, a wing model is discretized into 2096 elements using triangular shell elements as shown in Fig. 4. Fig. 5 describes the test environment of the static load test. Since the wing model is constructed with a basement, which can be attached to a measurement section of a wind tunnel, the basement is tightly clamped in order to set the cantilevered boundary condition. A 0.9-N weight is installed on the tip of the wing at mid-chord. The mid-chord vertical displacement at 10-mm from the tip is measured using a laser displacement sensor (OMRON Corp.). Tab. 4 shows the measured and simulated vertical displacements. The results showed excellent agreements.

In addition, a vibration test is carried out to obtain the natural frequency of the first bending mode for the wing model. With the same boundary condition, a uniaxial accelerometer (PCB Piezotronics of North Caroline, Inc.) is installed on a 3-mm location from the wing tip to measure the uniaxial acceleration. An impulsive load is applied on the tip, and the acceleration data is transferred to a Fast Fourier Transform analyzer (Ono Sokki Co., Ltd.) through a signal conditioner (PCB Piezotronics of North Caroline, Inc.). Tab. 5 compares the measured natural frequency and a solution of modal analysis from MSC.Nastran. The

measured and simulated natural frequencies of the first bending mode are also in a good agreement with an error less than 1%. The result ensured that a hollow wing model could be accurately built by additive manufacturing with Ti6Al4V in terms of stiffness and vibration characteristics.

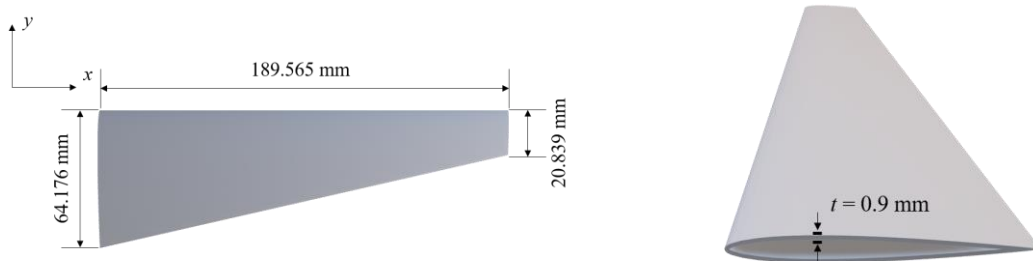


Figure 3: Planform (left) and cross section at root (right) of the wing model.

Table 3: Geometry of the wing.

Property	Value
Span, mm	189.565
Root chord, mm	64.176
Tip chord, mm	20.839
Airfoil profile	NACA0010
Shell thickness, mm	0.9

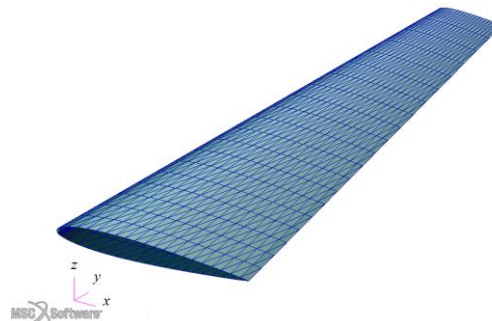


Figure 4: Finite element model of the wing.

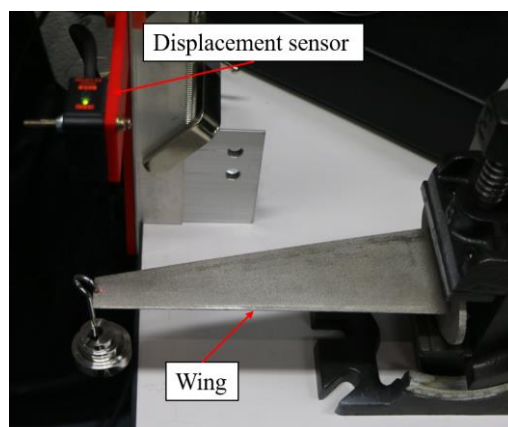


Figure 5: Static load test setup.

Table 4: Vertical displacement at 10 mm from the tip obtained from the test and simulation.

Result	Vertical displacement, mm
Simulation	0.102
Experiment	0.100

Table 5: Natural frequencies of the wing model obtained from the test and simulation.

Result	Natural frequency, Hz
Simulation	164.698
Experiment	163.512

Moreover, surface roughness of metal wing model fabricated with the additive manufacturing without post surface treatments is measured to decide if the post-processing is necessary. The values of surface roughness in the area of 2.0 mm x 2.0 mm are measured using a one-shot 3D measuring microscope (Keyence Corp.) as shown in Fig. 6. Tab. 6 lists the measured results at different surface locations of the wing model. It was confirmed that post surface treatments were necessary for an actual wind tunnel wing model since the surface is not smooth enough for a wind tunnel testing.

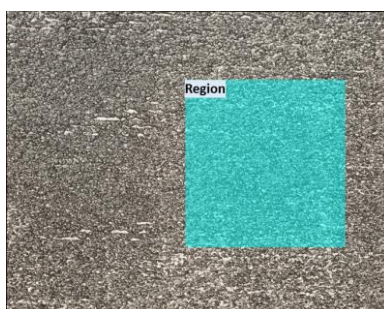


Figure 6: A picture of the upper wing surface in the vicinity of the root.

Table 6: Surface roughness of the wing model at different locations.

Inner upper surface Sa, μm	Outer upper surface Sa, μm	Inner lower surface Sa, μm	Outer lower surface Sa, μm
22.584	47.243	54.025	61.783

4 Wing Model with Metal AM for Flutter Testing

A wind tunnel wing model for a flutter test is designed to investigate the flutter characteristics of a wing model fabricated by the metal AM technology. Numerical simulations are then performed to evaluate the structural and aeroelastic characteristics of the designed wing model. The designed thin rectangular wing model is shown in Fig. 7. The aft portion of the wing is designed as a shell structure with the thickness of 0.6 mm. The front section (about 3 mm from the leading-edge) is modeled as a solid structure. The geometry of the wing is given in Tab. 7. The span and chord lengths are 300 mm and 30 mm, respectively. The process variables and material properties are again the same as the

ones for the tensile specimens. The aft portion is modeled with 3240 triangular shell elements, while the front section is modeled with 690 tetrahedral elements. The finite element model of the wing is shown in Fig. 8. The wing tip is closed with a 0.6-mm wall in the actual flutter model, but the tip wall is omitted in the finite element model.

A modal analysis is firstly performed to obtain the natural frequencies of the wing model with a cantilevered boundary condition. Tab. 8 shows the simulated natural frequencies obtained by the modal analysis from MSC.Nastran. A flutter analysis is then carried out to evaluate the aeroelastic stability of the designed wing. In the simulation, the PK-method is used to predict aeroelastic instabilities. Mach number is swept from 0.08 to 0.8 with the air density of 1.225 kg/m³. Fig. 9 shows the V-g plot obtained from the analysis. According to the result, it is predicted that the wing model encounters aeroelastic instability around 163.38 m/s ($M = 0.48$) with the second flatwise bending mode.

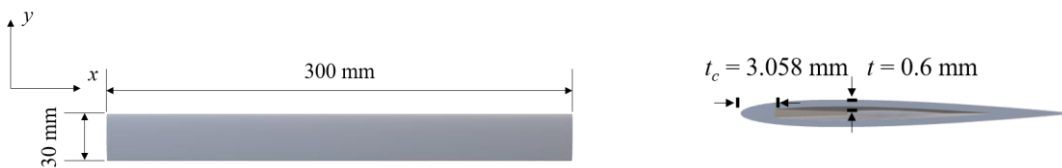


Figure 7: Planform (left) and cross section at root (right) of the flutter wing model.

Table 7: Geometry of the flutter wing.

Property	Value
Span, mm	300
Root chord, mm	30
Airfoil profile	NACA0008
Leading-edge section width, mm	3.058
Shell thickness (aft portion), mm	0.6



Figure 8: Finite element model of the wing for a flutter test.

Table 8: Natural frequencies of the wing model for lower modes.

Mode	Natural frequency, Hz
1st flatwise bending	20.265
2nd flatwise bending	121.86
1st edgewise bending	276.91
1st torsion	298.00

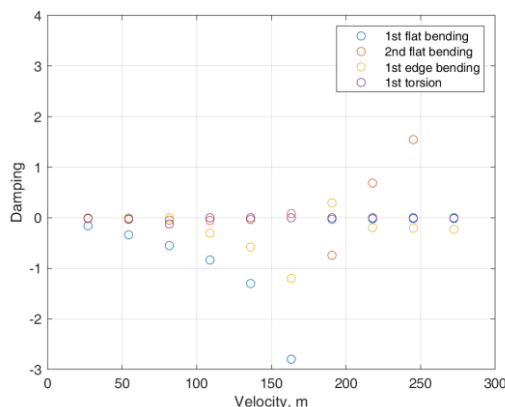


Figure 9: V-g plot of the wing model.

5 Conclusions

This paper studied a metal wing model with the additive manufacturing technique for a flutter test. Structural/aeroelastic characteristics of an additively manufactured wing model were evaluated numerically and experimentally. A series of experiments with the tensile specimens as well as evaluations of the additively manufactured wing model showed reliable manufacturing accuracies of the AM-based structures and wing. Finally, the metal wing model with the additive manufacturing technique for flutter testing was designed based on the evaluation results. The aeroelastic stability analysis of the designed wing model predicted that the flutter wing model would encounter an aeroelastic instability with second flatwise bending mode around the flow speed of 163 m/s. In our future works, wind tunnel tests with the designed wing model will be conducted.

Acknowledgements

The authors wish to acknowledge Japan Additive Manufacturing and Processing Technology (JAMPT) Corp. for the help of constructing the metal structures and wings.

References

- Adelnia, R., Daneshmand, S., Aghanajafi, S., 2006. Production of Wind Tunnel Testing Models with Use of Rapid Prototyping Methods. In: Proceedings of the 6th WSEAS international conference on Robotics, control and manufacturing technology, Hangzhou, China.
- Bauer, J., Meza, L.R., Schaedler, T.A., Schwaiger, R., Zheng, X., Valdevit, L., 2017. Nanolattices: An Emerging Class of Mechanical Metamaterials, *Advanced Materials*, 29(40), 1701850 (1701851-1701826).
- Berger, J.B., Wadley, H.N.G., McMeeking, R.M., 2017. Mechanical Metamaterials at the Theoretical Limit of Isotropic Elastic Stiffness, *Nature*, 543, 533–537.
- Cuan-Urquizo, E., Barocio, E., Tejada-Ortigoza, V., Pipes, R.B., Rodriguez, C.A., Roman-Flores, A., 2019. Characterization of the Mechanical Properties of Fff Structures and Materials: A Review on the Experimental, Computational and Theoretical Approaches, *Materials*, 12(6), 895.
- Goh, G.D., Agarwala, S., Goh, G.L., Dikshit, V., Sing, S.L., Yeong, W.Y., 2017. Additive Manufacturing in Unmanned Aerial Vehicles (Uavs): Challenges and Potential, *Aerospace Science and Technology*, 63, 140-151.

Rodriguez, J., Thomas, J., Renaud, J., 1999. Maximizing the Strength of Fused-Deposition Abs Plastic Parts. In: Proceedings of the 10th Solid Freeform Fabrication Symposium (SFF), Austin, TX.

A Novel Feature-Based Recombined Deep Learning

Method for Aeroelasticity

Yixing Wang¹, Renkun Han¹ and Gang Chen^{1*}

*¹State Key Laboratory for Strength and Vibration of Mechanical Structures, School of Aerospace Engineering, Xi'an Jiaotong University, Xi'an, China
aachengang@xjtu.edu.cn*

Abstract

Although NN (Neural Network) is an efficient model for reducing order of fluid system, they are seldom used in aeroelasticity system. A feature-based recombined Deep Learning technique to capture characteristics of fluid system and aeroelastic response prediction method was proposed. A novel DNN (Deep Neural Network) method to improve the accuracy and generalization capability through adopting convolutional neural network to extract the specially processed disturbance information of boundary in flow field. The predicted results show good consistence with the full-order computations. The proposed method has a great potential to the aeroelasticity design and control.

Keyword: Deep Learning, Convolutional Neural Network, Machine Learning, Reduced Order Model, Aeroelasticity

1. Introduction

Some reduced order models have also been used, such as POD (Proper Orthogonal Decomposition) [1], Volterra model [2], DMD (Dynamic Mode Decomposition) [3, 4], and so on. However, their insufficient capabilities in nonlinear and multi-scale simulations [5] seriously limit application. Nowadays, the booming AI (Artificial Intelligence) has become an area with many practical applications and active research topics. Deep learning, as an important method of AI, allows computers to learn independently from experience and to understand the world by establishing a hierarchical conceptual system [6]. In fact, universal approximation theorem shows that a neural network that satisfies certain specific requirements can approximate any Borel measurable function with arbitrary precision from a finite-dimensional space to another finite-dimensional space, as long as it is based on a sufficient number of hidden units [7-9]. For real fluid problem, by dispersion of flow field and the bounded continuity nature of the actual physical parameters, we could conclude that it is a continuous function defined on the bounded closed set in \mathbf{R}^n , that is to say it is Borel measurable. So, the character of fluid system could be learned and mastered well by deep learning, a technique that uses neural network.

Even though there must be a neural network that can represent the objective function we want, we cannot guarantee that the training algorithms of deep learning could get this function. As stated in [6],

this is mainly because there is no universally superior learning algorithm. No Free Lunch Theorem [10] further tells us that the most advanced algorithms we can designed and the simplest algorithms that simply group all points directly to one class have same average performance on all possible tasks. Fortunately, however, the conclusions only hold true when we consider the generation distributions on all possible data. For real problems, if we make pre-assumptions on probability distributions, we could design learning algorithms that work well on these distributions [6]. This means that the focus of machine learning is not to find an absolute best learning algorithm, but to find a distribution that is related to the real world in which artificial intelligence acquires experience, and to design learning algorithms for this distribution. In view of this, in order to achieve deep learning about fluid system, we should pay more attention to the method of feature extraction, i.e. the content and form of input data. Since Ling [11] first applied deep neural network to fluid mechanics, there are some attempts in this area [12-15]. These studies mainly focused on the validation of effectiveness of deep learning in fluid prediction. Most of them only use parameters such as angle of attack and Mach number as input, and did not take the content and form of data that includes more extensive input such as geometric shape into account. Beyond these, Zhang [15] has compared the prediction results of two different input data form on 2D airfoil profile. In this study, the use of pixel density as an input has greatly improved the prediction performance compared with the simple use of geometric coordinates. This also confirms there would be significant effect of the content and form of input data on deep learning as described above. For simple 2D geometric objects such as circle, while Miyanawala [12] uses the distance from each grid point to the boundary in a rectangular grid as input to predict the drag coefficient some good results are obtained. Nevertheless, the existing researches only limit on several special simple geometric objects such as circle. In order to achieve the wide application of deep learning in fluid mechanics, it is imperative to develop a feature extraction method that can be applied to general geometric shapes and is suitable for deep learning. In addition, in the existing studies that take the geometric shape into account, there is a great deal of redundancy in input, for example, the region except the boundary in Zhang's research [15], and inside the objects in Miyanawala's [12]. This kind of information is not only meaningless but also occupies a large amount of input space. Therefore, the expression with high efficiency of input data is also indispensable.

In this paper, we proposed a novel feature extraction method, i.e. the content and form of input data, and assessed its effectiveness. This method is unique in that it not only expresses the geometric shape but also maximally imitates the boundary's influence on flow field in real world using the disturbance information of an object to the surrounding as the input. As stated above, one of the aims of machine learning study is to find a distribution that is related to the real world. Besides, the proposed method is suitable for nearly all geometric shape and there is no redundancy in input. Thus, the technique could be applied in more general scope with higher execution efficiency. In order to synthesize different kinds of input variables such as geometric shape, angle of attack, etc. a synthesized serial deep learning network structure is introduced in this paper. Moreover, we have

adopted this method to generate whole flow field. Within the error threshold, the proposed DNN (Deep Neural Network) model has good performance. At last, we try to apply this new method to aeroelasticity.

2. Methodology

2.1 Framework

AI (Artificial Intelligence) has already become a field with many practical applications and active research contents. As the most important method in AI, 'Deep Learning' surpasses the current neuroscience view of machine learning models, and it appeals to the more general principle of learning multi-level combinations. Deep Learning allows the computer to learn from experience and understand the real world based on a hierarchical conceptual system in which every concept is defined by the relationship with some relatively simple concepts. If we draw a map for the connections between these concepts, we will get a map with many levels, i.e. 'Deep' [6]. In fact, the network framework and training algorithm that are same as today's Deep Learning have been popular since 1980s [17, 18]. However, it was generally deemed that deep networks with multi-levels were difficult to train in the 20 years since then. In 2006, due to a breakthrough in training algorithm [19] and the follow-up studies [20, 21], Deep Learning has been spring up. Luckily there was the appearance of the effective training algorithm, the important value of deep networks [20, 22-24] being realized, i.e., reflecting more real world. Today, deep neural networks have outperformed AI systems based on other machine learning techniques and hand-designed functions [6]. Therefore, for efficient machine learning about fluid system, this paper focus on deep learning technique. Since the structure of flow field representation is network-like, we use Deep Convolutional Neural Network to model it. The main features of CNN (Convolutional Neural Network) are sparse interactions, parameter sharing, and equivariant representations[6].

In order to handle different inputs and obtain extensiveness, the first layer of the network is input layer. Although the input of CNN is a matrix, different input representation methods, i.e., different feature extraction methods have great impacts on the performance as we discussed in the first Section. We have proposed a novel feature extraction method in this paper and will give a description of it in the second part of this section. In Section 3.2, the great impact on the performance of networks caused by different feature extraction methods will be demonstrated.

Besides the geometric shape, other parameters indicating the condition of fluid system are also important, for example, the angle of attack, the velocity of incoming flow, the viscosity of fluid, and so on. However, the characteristic of these parameters is different with geometric information, which implies that we can't import them in the same layer. For settling this problem, we introduce recombined deep learning network structure to synthesize these different kinds of input variables. According to the principle of the feature extraction of CNN, the underlying neurons deal with local geometric information. With the increase of the layers level, neurons establish relationships between the larger areas of the flow field. Therefore, the parameters that represent the entire fluid system

should be imported in higher-level layer. It's the most suitable location when Deep Network could represent the influence of the boundary on the entire flow field. Importing these parameters too early or too late actually gives them artificially inappropriate importance and this will lead to bad generality or even failure of modeling because it does not conform to the real world. If we let the network deem these parameters that should affect the whole field only act on local areas or have greater importance, It's obvious that the model can't be able to represent the real world. In this paper, we import these parameters that represent the entire fluid system in the first full-connection layer, and do a simple comparison about the location's effect in Section 3.3.

The output of the Deep Network is the fluid force. In addition to these, the CNN also includes rectification and down-sampling layers following convolution or full-connection layer. The number of layers is determined empirically, which will be explored in Section 3.3.

The process that CNN uses to produce output is called feed-forward process. In this process, features in a certain area are firstly extracted by convolution operation, and then nonlinear mapping is imported into the network by rectification function which is also called activation function in most cases. Krizhevsky [25] has pointed out that the rectified linear unit (ReLU) has better performance than tanh units in image recognition tasks. Zhang's research [15] also shows that the learning capability is significantly higher with the ReLU unit. Since the emphasis of this paper is not on activation functions, the rectification function we used is ReLU:

$$f(x) = \max(0, x) \quad (1)$$

More information on rectification function can refer to [6, 25]. After the rectification function, a down-sampling/pooling layer is usually used to delete redundant information and reduce the matrix size, but it's optional. The usual pooling techniques are to perform the maximum, minimum and average operations area-by-area like convolution operation. At last, after the flow condition parameters are imported through the fully connected layer and perform rectification and regression process, the predicted values are obtained. For training the network, we adopt Back-propagation process in which we use the SGDM (Stochastic Gradient Descent Method with momentum) [17] to adjust the weight or other parameters. The detailed introduction about Back-propagation process can also refer to [6, 12].

2.2 Feature extraction

As discussed in Section 1, No Free Lunch Theorem [10] tells us that there is no universal good algorithm for machine learning. But for real problems, if we make pre-assumptions on probability distributions, we could design learning algorithms that work well on these distributions [6]. This means that the focus of machine learning is actually to find a distribution that is related to the real world in which artificial intelligence acquires experience, and to design learning algorithms for this distribution. In view of this, the method of feature extraction, i.e. the content and form of input data, is of great significance to the success of deep learning. Zhang [15] has compared the prediction results of two different input data form on 2D airfoil profile and gets the conclusion that the use of

pixel density as an input has greatly improved the prediction performance compared with the simple use of geometric coordinates. This confirms that feature extraction method has significant effect on deep learning, especially about fluid system. These are further affirmed in Section 3.2. Miyanawala [12] uses the distance from each grid point to the boundary in a rectangular grid as input to predict the drag coefficient and gets some good results. However, the existing researches only limit on several special simple geometric objects such as circle and can't be used in complex geometry. In order to achieve the wide application of deep learning about fluid mechanics, it is imperative to develop a feature extraction method that can be applied to general geometric shapes and is suitable for deep learning. In addition, there is a great deal CNN input redundancy in existing research, for example, the region except the boundary in Zhang's research [15], and inside the objects in Miyanawala's [12]. This kind of information is not only meaningless but also occupies a large amount of input space. Therefore, the expression with high efficiency of input data is also indispensable.

1) Ascertain the scope

Set a certain area around the object. The principles of determining the size of this area are to completely include object and to ensure that near the boundary of the area the curvature of mesh lines generated by the step 2 is close to 0, i.e. less than 10^{-6} . Since this area is for extraction of geometric and generated surrounding disturbance information, it is not the same as CFD (Computational Fluid Dynamics) in which the discretization of equations and calculated fluid variables are the central factor of consideration. Therefore, the scope does not need to be set as large as the grid area in CFD. It only needs to include the object and its surrounding area where the object has intense influence on.

2) Generate grid

For the scope set in Step 1, use the Laplace equation with no source term method to generate structured grid. This method we adopted is different with the current commonly used methods and belongs to the method using elliptic partial differential equations. Detailed introduction about this method can refer to [26-29], and the related mathematical theory can be found in [30, 31]. There are two aspects to be noted in this step. Firstly, O-grid can't be used and we should use blocks with the same topological shape as the selected area. After defining the mapping of the boundary, use the Laplace method mentioned above to generate mesh. Secondly, we should make the grid nodes as dense as possible to ensure that the boundaries and the generated internal grid lines are discretized undistorted, which is the same as the requirements in CFD.

3) Extract curvature

For every grid node, calculate the curvature of the grid line that is in the same direction with the incoming flow. Another effective method is to calculate the Gaussian Curvature at each grid node.

For the reason that the Gaussian Curvature is a surface's intrinsic measurement, as the Gauss theorem egregium [32] expresses, when we want to express the disturbance of flow field caused by boundary the second method will complete the goal perfectly with uniqueness and higher accuracy. In the condition that the incoming flow direction is random and for 3D problem, this method is also applicable. In view of the above reasons, we recommend the second method. The comparison of these methods will be shown in Section 3.3. In Section 4.1, the rationality of these methods will be elaborated. Next, before Section 3.3, we will only use the first method.

4) Construct matrix as input

Establish a single-channel multi-dimensional matrix corresponding to the grid area, wherein each element corresponds to a unique grid node, and the index value of the element in the matrix is equal to the index value of the corresponding grid node in the entire structured grid. The data of each element in the matrix is the curvature value calculated in Step 3. At last, in order to conform to the requirements of deep networks, the operations of Normalization, Mean Subtraction, etc. for the matrix data may be necessary. After these steps, we will obtain the input data for neural network.

2.3 Training data & hyper-parameters

In order to verify the effectiveness of the proposed method, the predicted value in this paper is mainly focused on the lift and drag coefficients of airfoils and several simple shapes such as ellipse. For preparing data as real as possible, we have adopted the Navier-Stokes equations based full-order CFD simulations in which the viscous fluid variables were calculated by finite volume method with Spalart-Allmaras turbulence model [33].

3. Numerical simulation and discussion

3.1 Validation for steady flow prediction

3.1.1 Model description

In this section we will illustrate the effectiveness of this method briefly. We use the subset data from Miyanawala's research [12], which is about the time mean drag coefficients of bluff body shapes immersed in a uniform flow. The variable in our research is the aspect ration of ellipses and these ratios include 1, 2, 3, 4, 5, 7, and 10. We have grouped them as the training set with ratio 1, 2, 3, 5, and 7 and as test set with ratio 4, 10. The geometric shape is simple, so the constructed network is easy to train and doesn't need large dataset. In addition, if a network could be well trained with small amount of samples, this just shows the generalization of this method. Therefore, when classify data sets, we deliberately divide the data that is not in the range of the training set such as the ellipse with aspect ration 10 into the test set to test the generalization ability of our method.

3.1.2 Feature extraction

The information that characterizes the influence of the boundary on the flow field. This information not only represents the boundary, but also extracts the impact of the boundary, instead of just providing the boundary information directly to deep network for learning. For the semi-ellipses whose long-short axis ratios are respectively 3, 5, and 10, the results produced after carrying out the above steps, i.e. the contour of curvature of grid lines are shown in Figure 1.

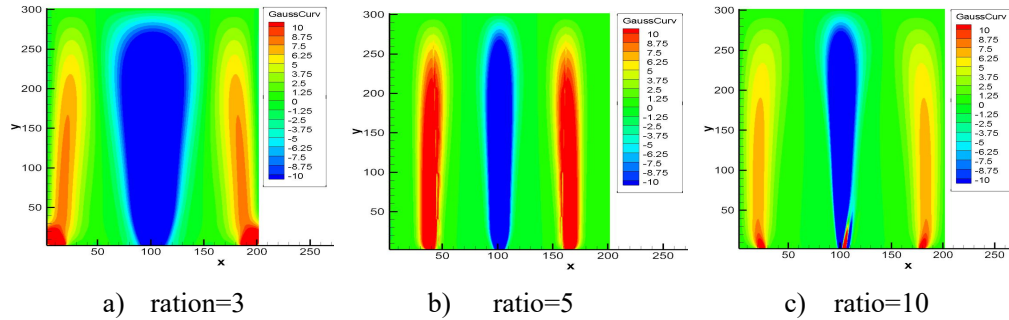


Figure 1: the contour of curvature of grid lines with different long-short ratio

3.1.3 Numerical results

After training, the predicted results using our method are shown in a), Figure 2. From Figure 2, we can see our method whose max error is 3.57% is more accurate and more generalized compared with the results produced by Miyanawala’s method [12] whose max error is 14.65% on the specified dataset.

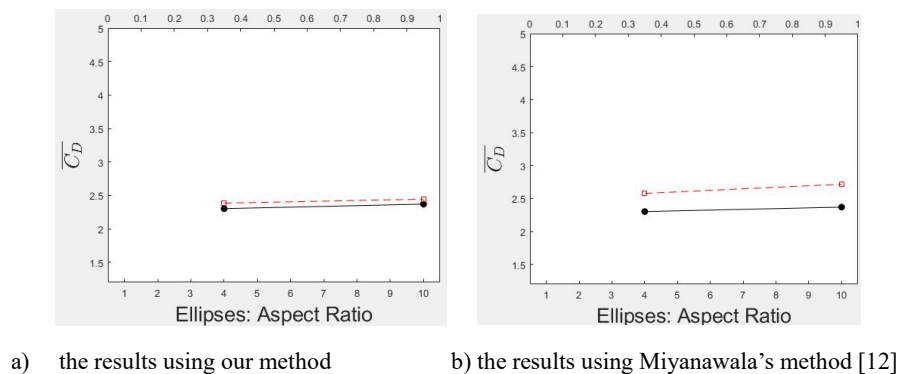
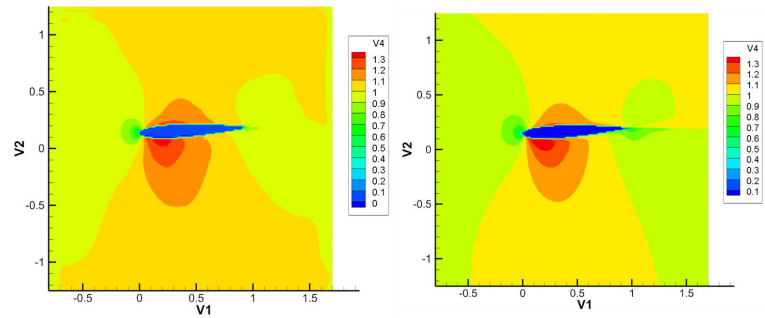


Figure 2: the predicted results

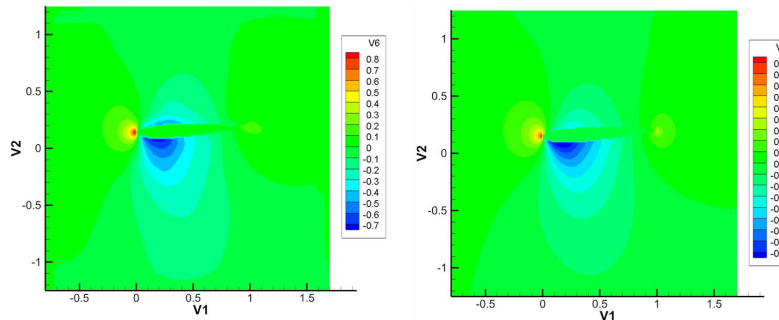
3.2 Further Exploration for Airfoil flow

We use the Deep Learning technique to predict the whole flow field of NACA0012 airfoil. The results are shown in Figure 3. From the figure, we can see that for the main flow field variables, the predicted values are in good agreement with the CFD calculation results. There is a high degree of agreement for pressure and velocity. But for density, there are some bifurcates near the boundary. We infer this is caused by the reason that neural network has same processing weight for whole field. This is what we are committed to further study.



a) the contour of U generated by Deep Learning Network

b) the contour of U generated by CFD Computing



c) the contour of P generated by Deep Learning Network

d) the contour of P generated by CFD Computing

Figure 3: the comparison of flow field generated by Deep Learning Network and CFD Computing

3.3 Aeroelastic response prediction

This section focuses on the application of the new method to aeroelasticity. Firstly, we use another neural network to predict the force coefficient. Secondly, we combine these networks and solid mechanism solver to do prediction of aeroelasticity response. Figure 4 shows the comparison of lift coefficient generated by aeroelasticity system simulated by Deep Learning-based and CFD-CSD computing. It can be seen that the predicted responses by the deep neural network agree well with that of the CFD-CSD simulation.

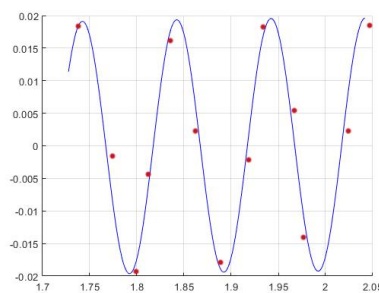


Figure 4: the comparison of lift coefficient generated by aeroelasticity system simulated by Deep Learning-based (red dot) and CFD-CSD computing (blue line)

4. Conclusions & further work

A feature-based Deep Learning technique to capture characteristics of fluid system and predict forces is carried out in this paper. Different from the existing approaches, we use a novel DNN (Deep

Neural Network) method to improve the accuracy and generalization capability through adopting convolutional neural network to extract the specially processed disturbance information of boundary in flow field. Using 2D model, the DNN is fed by the specially processed curvature of flow field grid as the input and the aerodynamic forces computed by the full order CFD simulation as the target data.

References

- [1] P. Holmes, J.L. Lumley, G. Berkooz, C.W. Rowley, *Turbulence, coherent structures, dynamical systems and symmetry*, Cambridge university press, 2012.
- [2] W. Silva, Identification of Nonlinear Aeroelastic Systems Based on the Volterra Theory: Progress and Opportunities, *Nonlinear Dynamics*, 39 (2005) 25-62.
- [3] P.J. Schmid, L. Li, M.P. Juniper, O. Pust, Applications of the dynamic mode decomposition, *Theoretical and Computational Fluid Dynamics*, 25 (2011) 249-259.
- [4] P.J. Schmid, Dynamic mode decomposition of numerical and experimental data, *Journal of fluid mechanics*, 656 (2010) 5-28.
- [5] J.N. Kutz, Deep learning in fluid dynamics, *Journal of Fluid Mechanics*, 814 (2017) 1-4.
- [6] I. Goodfellow, Y. Bengio, A. Courville, Y. Bengio, *Deep learning*, MIT press Cambridge, 2016.
- [7] G. Cybenko, Approximation by superpositions of a sigmoidal function, *Mathematics of control, signals and systems*, 2 (1989) 303-314.
- [8] K. Hornik, M. Stinchcombe, H. White, Multilayer feedforward networks are universal approximators, *Neural networks*, 2 (1989) 359-366.
- [9] M. Leshno, V.Y. Lin, A. Pinkus, S. Schocken, Multilayer feedforward networks with a nonpolynomial activation function can approximate any function, *Neural networks*, 6 (1993) 861-867.
- [10] D.H. Wolpert, The lack of a priori distinctions between learning algorithms, *Neural computation*, 8 (1996) 1341-1390.
- [11] J. Ling, A. Kurzawski, J. Templeton, Reynolds averaged turbulence modelling using deep neural networks with embedded invariance, *Journal of Fluid Mechanics*, 807 (2016) 155-166.
- [12] T.P. Miyanawala, R.K. Jaiman, An Efficient Deep Learning Technique for the Navier-Stokes Equations: Application to Unsteady Wake Flow Dynamics, (2017).
- [13] S. Lee, D. You, Prediction of laminar vortex shedding over a cylinder using deep learning, arXiv preprint arXiv:1712.07854, (2017).
- [14] Z. Wang, D. Xiao, F. Fang, R. Govindan, C. Pain, Y. Guo, Model identification of reduced order fluid dynamics systems using deep learning, *International Journal for Numerical Methods in Fluids*, 86 (2018) 255-268.
- [15] Y. Zhang, W.J. Sung, D.N. Mavris, Application of Convolutional Neural Network to Predict Airfoil Lift Coefficient, in: 2018 AIAA/ASCE/AHS/ASC Structures, Structural Dynamics, and Materials Conference, 2018, pp. 1903.

- [16] A.S. Morcos, D.G. Barrett, N.C. Rabinowitz, M. Botvinick, On the importance of single directions for generalization, arXiv preprint arXiv:1803.06959, (2018).
- [17] D.E. Rumelhart, G.E. Hinton, R.J. Williams, Learning representations by back-propagating errors, *nature*, 323 (1986) 533.
- [18] L. Yann, Modèles connexionnistes de l'apprentissage, in, PhD thesis, These de Doctorat, Universite Paris 6, 1987.
- [19] G.E. Hinton, R.R. Salakhutdinov, Reducing the dimensionality of data with neural networks, *science*, 313 (2006) 504-507.
- [20] Y. Bengio, Y. LeCun, Scaling learning algorithms towards AI, *Large-scale kernel machines*, 34 (2007) 1-41.
- [21] C. Poultney, S. Chopra, Y.L. Cun, Efficient learning of sparse representations with an energy-based model, in: *Advances in neural information processing systems*, 2007, pp. 1137-1144.
- [22] O. Delalleau, Y. Bengio, Shallow vs. deep sum-product networks, in: *Advances in Neural Information Processing Systems*, 2011, pp. 666-674.
- [23] R. Pascanu, C. Gulcehre, K. Cho, Y. Bengio, How to construct deep recurrent neural networks, arXiv preprint arXiv:1312.6026, (2013).
- [24] G.F. Montufar, R. Pascanu, K. Cho, Y. Bengio, On the number of linear regions of deep neural networks, in: *Advances in neural information processing systems*, 2014, pp. 2924-2932.
- [25] A. Krizhevsky, I. Sutskever, G.E. Hinton, Imagenet classification with deep convolutional neural networks, in: *Advances in neural information processing systems*, 2012, pp. 1097-1105.
- [26] J.F. Thompson, Z.U. Warsi, C.W. Mastin, Boundary-fitted coordinate systems for numerical solution of partial differential equations—a review, *Journal of computational Physics*, 47 (1982) 1-108.
- [27] J.F. Thompson, Z.U. Warsi, C.W. Mastin, *Numerical grid generation: foundations and applications*, North-holland Amsterdam, 1985.
- [28] J.F. Thompson, F.C. Thames, C.W. Mastin, Automatic numerical generation of body-fitted curvilinear coordinate system for field containing any number of arbitrary two-dimensional bodies, *Journal of computational physics*, 15 (1974) 299-319.
- [29] A.M. Winslow, Numerical solution of the quasilinear Poisson equation in a nonuniform triangle mesh, *Journal of computational physics*, 1 (1966) 149-172.
- [30] C.W. Mastin, J.F. Thompson, Transformation of three-dimensional regions onto rectangular regions by elliptic systems, *Numerische Mathematik*, 29 (1978) 397-407.
- [31] C.W. Mastin, J.F. Thompson, Elliptic systems and numerical transformations, *Journal of Mathematical Analysis and Applications*, 62 (1978) 52-62.
- [32] J. Oprea, *Differential geometry and its applications*, MAA, 2007.
- [33] P. Spalart, S. Allmaras, A one-equation turbulence model for aerodynamic flows, in: *30th aerospace sciences meeting and exhibit*, 1992, pp. 439.

Structural and Aerodynamic Models for Aeroelastic Analysis of Corrugated Morphing Wings

Natsuki Tsushima¹, Hitoshi Arizono¹, Kensuke Soneda², Tomohiro Yokozeki²,
Taro Imamura², and Weihua Su³

¹Japan Aerospace Exploration Agency, Tokyo, Japan, tsushima.natsuki@jaxa.jp

²The University of Tokyo, Tokyo, Japan

³The University of Alabama, Tuscaloosa, AL, USA

Keyword: Flutter, aeroelasticity, aircraft, structural analysis.

A correlation study of two different aeroelastic analysis frameworks with different fidelities for morphing wings with corrugated structures, which have been verified/validated in previous works, will be presented in the paper. One uses a corotational shell finite element method and unsteady vortex-lattice aerodynamic loads to simulate aeroelastic behaviors of morphing wings involving large deformation¹. The other couples a nonlinear beam theory and the same aerodynamic model or a CFD code for aeroelastic analysis². Numerical studies explore aeroelastic characteristics of corrugated morphing wings and compare numerical solutions of the two different frameworks. This work allows to understand the nonlinear aeroelastic characteristics of composite and corrugated wings and assess feasible domains of the methodologies to simulate such morphing wings numerically.

In previous works, a morphing wing strategy using a simple wiring actuation mechanism with corrugated structures has been studied³. Due to the anisotropy, corrugated structures are stiffer in one direction and softer in another direction. The dual functions of a morphing wing, including spanwise load bearing and chordwise morphing, are therefore possible by taking advantage of the extremely anisotropic property of corrugated structures. One advantage of the corrugated morphing scheme is that it is easy to fabricate corrugated structures. Additionally, corrugated structures can be conveniently actuated with commercially available actuators and wires although other driving methods may also be adopted. A promising morphing capability of such corrugated morphing wing has been demonstrated in the previous works with wind tunnel experiments³. However, improvement of aerodynamic characteristics and adaptivity to flight condition with the corrugated-based camber morphing should be further evaluated. Energy to drive such wings also remains to be investigated. In this paper, a series of static aeroelastic simulations for a morphing wing with corrugated structures will be performed using the aeroelastic frameworks.

1. Tsushima, N., Yokozeki, T., Su, W., and Arizono, H. (2019). Geometrically nonlinear static aeroelastic analysis of composite morphing wing with corrugated structures. *Aerospace Science and Technology*, 88, 244-257.

2. Sato, K., and Yokozeki, T. (2017). Aero-structural evaluation of morphing control surface using corrugated panels. *Transactions of the Japan Society for Aeronautical and Space Sciences*, 15(APISAT-2016), a7-a15.

3. Takahashi, H., Yokozeki, T., and Hirano, Y. (2016). Development of variable camber wing with morphing leading and trailing sections using corrugated structures. *Journal of Intelligent Material Systems and Structures*, 27(20), 2827-2836.

Time domain and time spectral reduced order models for aeroelasticity

F. Di Donfrancesco^{1,2}, A. Placzek¹ and J.-C. Chassaing²

¹ DAAA/ONERA, Université Paris Saclay, F-92322 Châtillon, France, antoine.placzek@onera.fr

² Sorbonne Université, CNRS, Institut Jean Le Rond d'Alembert, F-75005 Paris, France, jean-camille.chassaing@sorbonne-universite.fr

Abstract

In this paper we address the construction of time and frequency domain Reduced Order Models for the Navier-Stokes equations. A classical basis obtained by the Proper Orthogonal Decomposition is used for the Galerkin projection of the governing equations and additional interpolation techniques based on the Discrete Empirical Interpolation Method are considered to evaluate efficiently the nonlinear terms. The applicability of this kind of ROMs for aeroelastic applications is first investigated in the time domain to reproduce the flow field around an oscillating cylinder at low Reynolds number. Then a second type of reduced order model dedicated to periodic flows is developed on the basis of the Time Spectral Method. Numerical tests demonstrate the potentiality of the proposed technique on the test case of an oscillating airfoil in subsonic and transonic regimes.

Keyword: Reduced Order Model, Proper Orthogonal Decomposition, Time Spectral Method, Discrete Empirical Interpolation Method

1 Introduction

Reduced-Order Models (ROMs) have been developed for decades in fluid dynamics as a way to decrease the cost of evaluating high fidelity solutions from a Full Order Model (FOM). Indeed, applications like parametric studies, optimization or control involving many queries to the FOM need fast evaluations which should be as accurate as possible. Projection based ROMs can be classically constructed using a basis built from a set of solutions snapshots whose meaningful content is extracted via a Proper Orthogonal Decomposition. Such projections lead to an explicit reduced operator in the linear or polynomial case (Hall et al. 1999; Placzek et al. 2011) but no explicit form can be obtained in general for nonlinear operators.

Flow non-linearities however arise commonly in aeronautical applications because of shock interaction, flow separation,... but also because of aeroelastic phenomena involving for example limit-cycle oscillations. High fidelity FOMs are therefore required to determine accurately the flow field but the large number of degrees of freedom involved in such models leads to unaffordable computational costs whose reduction represents one of the main motivation of this work. The projection based ROMs lacks efficiency when non-linearities are involved since in the general case the non-linear term has to be evaluated at the FOM level for each iteration.

To tackle this problem, the solution considered in the present paper is first to approximate the non-linear residual term using masked projection approaches like the Discrete Empirical Interpolation Method and its variants (Chaturantabut et al. 2010; Drmač et al. 2016). The non-linear term is thus interpolated (or fitted) on a small set of judiciously selected mesh points using an additional Proper Orthogonal Decomposition (POD) basis for the residual term. Interpolation techniques that preserve the basis structure are then implemented to update the basis content for new parameter values. An alternative solution proposed by Thomas et al. 2010 is to derive a Taylor series expansion of the reduced non-linear residual FOM solver which solves Euler or Navier-Stokes equations with the Time Spectral Method (TSM) (Hall et al. 2002; Gopinath et al. 2005). The resulting reduced operators are evaluated with automatic differentiation tools.

In the context of aeroelasticity, the FOM considered in the present paper is based on the Arbitrary Lagrangian Eulerian (ALE) formulation (Donea et al. 2004) and the problem of mesh deformation has to be taken into consideration, also at the ROM level. Following Anttonen et al. 2003 the POD basis for the snapshots of the solution and residual term can still be computed without explicitly taking care of the mesh deformation: the resulting POD modes are thus associated to the mesh connectivities in an “index” based framework and their usual spatial correlation meaning is no longer obvious. The mesh deformation is then taken into account in the approximated non-linear residual term of the ROM where the metric is updated with respect to the structural motion. This type of POD modes have been successfully used by Freno et al. 2014 in the time domain to address subsonic and transonic flows around airfoils subject to forced oscillations but the nonlinear term was treated at the FOM level. Other formulations considering a change of reference frame or small perturbations (Placzek et al. 2011; Bourguet et al. 2011) or the use of fictitious domains (Liberge et al. 2010) to keep the spatial correlations of the POD modes have also been derived for fluid-structure interaction problems.

The present methodology developed by Di Donfrancesco 2019 is first applied to build a ROM in the time domain on an apparently simple test case to highlight the difficulties of such time-domain ROMs to provide stable solutions on long term when masked projection approaches are used to approximate the non-linear term. The TSM formulation of the ROM is investigated on the same test case and show better robustness even with respect to parameter changes. The long term stability of the solution is no longer a problem since a periodic solution is sought.

2 Governing equations for the full and reduced order models

2.1 Full Order Model in the time domain

The high fidelity FOM considered in the present paper is defined by the compressible Navier-Stokes equations. The ALE formulation is required to deal with aeroelastic problems involving possibly a non inertial and deformable spatial domain. Once discretized with hexahedral Finite Volumes, the semi-discrete form of the equations for a control cell $\Omega_i(t)$ reads:

$$\frac{d}{dt}(\mathcal{V}(\Omega_i)\mathbf{w}_i) = - \sum_{j=1}^6 \mathbf{F}_i(\mathbf{w}_i, \mathbf{w}_j, \mathbf{s}_i) \mathbf{n}_j + \mathcal{V}(\Omega_i)\mathbf{T}_i = -\mathbf{R}_i(\mathbf{w}_i, \mathbf{w}_j, \mathbf{s}_i) \quad (1)$$

where $\mathbf{w}_i = [\rho_i, (\rho\mathbf{u})_i, (\rho e)_i]$ is the vector of the numerical approximation of the conservative variables in the control cell $\Omega_i(t)$ and \mathbf{w}_j with $j \neq i$ is the approximation in neighbor control

cells involved in the spatial discretization scheme used to define the numerical fluxes \mathbf{F}_i through the cell faces with normals \mathbf{n}_j . The ALE formulation introduces the mesh grid velocity \mathbf{s}_i to take into account the grid deformation and the source term \mathbf{T}_i may include additional terms due to a change of reference frame or some particular boundary conditions.

The spatial domain discretization $\Omega = \bigcup_{i=1}^N \Omega_i$ usually involves a large number of control cells N . The collection of the vectors of conservative variables \mathbf{w}_i in each control cell may be assembled in a single vector $\mathbf{W} \in \mathbb{R}^{N_v}$ with $N_v = N \cdot n_v$ and n_v the number of conservative variables. The semi-discrete Navier-Stokes equations may then be formally written as an initial value problem defined by the nonlinear system of equations $d/dt(\mathcal{V}\mathbf{W}) = \tilde{\mathbf{R}}(\mathbf{W}, \mathbf{S})$ or similarly:

$$\frac{d\mathbf{W}}{dt} = \frac{\tilde{\mathbf{R}}(\mathbf{W}, \mathbf{S})}{\mathcal{V}} - \frac{d\mathcal{V}}{dt} \frac{\mathbf{W}}{\mathcal{V}} = \mathbf{R}(\mathbf{W}, \mathbf{S}) \quad (2)$$

with \mathcal{V} a diagonal matrix with all the control cell volumes $\mathcal{V}(\Omega_i)$ and \mathbf{S} a vector containing all the mesh grid velocities \mathbf{s}_i . The previous equations are solved in the time domain with a high-order finite volume code (Chassaing et al. 2013) and will serve in the following as a basis to build the ROM and as a numerical reference to compare results from the ROM.

2.2 Projection based Reduced Order Model in the time domain

The first step of construction of the ROM consists in looking for an approximation of the conservative field \mathbf{W} as the sum of a base solution \mathbf{W}_b and a linear combination of appropriate spatial modes gathered in a basis Φ :

$$\mathbf{W}(t) \approx \mathbf{W}_b + \Phi \mathbf{a}(t) \quad (3)$$

In this work, the spatial modes are computed with the Proper Orthogonal Decomposition (POD) of a set of representative solutions, or ‘‘snapshots’’, of the FOM. The POD is indeed the most widely used approximation basis for fluid dynamics reduced-order modeling because of its optimal properties in a certain sense and its straightforward computation with the Singular Value Decomposition (SVD).

Assuming that the snapshots are centered with respect to a base solution \mathbf{W}_b (steady, time-averaged or initial solution for example) and collected in a matrix $\mathcal{W}_b = [\mathbf{W}(t_1) - \mathbf{W}_b, \dots, \mathbf{W}(t_{N_t}) - \mathbf{W}_b] \in \mathbb{R}^{N_v \times N_t}$ with N_t the number of collected snapshots, the set of snapshot may be decomposed with the SVD as:

$$\mathcal{W}_b = \Phi \Sigma \mathbf{V}^T = \Phi \mathbf{A} \quad (4)$$

where the matrix $\Phi \in \mathbb{R}^{N_v \times N_r}$ is an orthonormal matrix containing the left singular vectors corresponding to the POD mode vectors, with $N_r = \text{rank}(\mathcal{W}_b) \leq \min(N_v, N_t)$. The diagonal matrix $\Sigma \in \mathbb{R}^{N_r \times N_r}$ contains the singular values of \mathcal{W}_b listed in order of decreasing magnitude. Finally the matrix $\mathbf{V} \in \mathbb{R}^{N_t \times N_r}$ contains right singular vectors and the product $\mathbf{A} = \Sigma \mathbf{V}^T$ may be viewed as coordinates associated to the POD modes so that a snapshot from the set \mathcal{W}_b can be recomputed exactly as $\mathbf{W}(t_i) = \mathbf{W}_b + \Phi \mathbf{a}(t_i)$ with $\mathbf{a}(t_i) \in \mathbb{R}^{N_r}$ the i -th column of \mathbf{A} . The previous expression has finally the expected form of Eq. (3).

In the first step of reduction, only the first POD modes are kept in the basis Φ since they contain most of the data to approximate the snapshots. A common measure of the basis

truncation is given by the relative information content defined by $E_{N_q} = \sum_{i=1}^{N_q} \sigma_i^2 / \sum_{i=1}^{N_r} \sigma_i^2$ with $N_q \leq N_r$. In the second step of reduction, the snapshots approximation Eq. (3) with the truncated basis $\Phi = [\phi_1, \dots, \phi_{N_q}]$ with $N_q \ll N_v$ is substituted in the FOM Eq. (2) and the Galerkin projection leads to the reduced set of N_q equations for the modal coordinate vector \mathbf{a} :

$$\frac{d\mathbf{a}(t)}{dt} = \Phi^T \mathbf{R}(\mathbf{W}_b + \Phi \mathbf{a}(t), \mathbf{S}) \quad (5)$$

The previous system of equations is a small dynamical system whose solution is the modal coordinate vector \mathbf{a} which, combined to the POD basis Φ , provides the full flow field vector \mathbf{W} any time instant t , possibly not included in the snapshots database \mathbf{W}_b . The reduced order model should also be able to provide a solution for other parameter values typical of the studied system provided that the spatial basis is updated.

The residual term \mathbf{R} for the compressible Navier-Stokes equations is non-linear and cannot be expressed explicitly in terms of the coordinates $\mathbf{a}(t)$ unless specific approximations are introduced. Without any additional work, the evaluation of this term at each time step has to be performed at the FOM level but the gain in computational time, if any, is very limited since numerical operations are performed on large vectors of dimension N_v . To tackle this issue, the non-linear term may be approximated in the same way as the snapshots:

$$\mathbf{R}(\mathbf{W}(t)) \approx \mathbf{R}(\mathbf{W}_b) + \Psi \mathbf{c}(t) \quad (6)$$

where the matrix $\Psi \in \mathbb{R}^{N_v \times N_p}$ is obtained from a POD of the set of residual snapshots $\mathcal{R}_b = [\mathbf{R}(\mathbf{W}(t_1)) - \mathbf{R}(\mathbf{W}_b), \dots, \mathbf{R}(\mathbf{W}(N_t)) - \mathbf{R}(\mathbf{W}_b)]$ and the vector $\mathbf{c}(t) \in \mathbb{R}^{N_p}$ gathers the coordinates associated to the POD modes of the residual term. The evaluation of this vector from the FOM residual with $\mathbf{c}(t) \approx \Psi^T [\mathbf{R}(\mathbf{W}(t)) - \mathbf{R}(\mathbf{W}_b)]$ would still involve costly operations sizing with N_v . We thus resort to masked projection techniques like the Discrete Empirical Interpolation Method (DEIM) (Chaturantabut et al. 2010) or its QDEIM variant (Drmač et al. 2016) to evaluate the unsteady term of the residual only on a small subset $N_f \ll N_v$ of control cells. The masked projection matrix $\mathbf{P} = [\mathbf{e}_{\varphi_1}, \dots, \mathbf{e}_{\varphi_{N_f}}] \in \mathbb{R}^{N_v \times N_f}$ with \mathbf{e}_{φ_i} the i -th column of the identity matrix of size N_v corresponds to the cell selection operation and has to be expanded to neighbor cells so that the residual term can be evaluated locally as $\mathbf{P}^T \mathbf{R}(\mathbf{W}) = \mathbf{R}_p(\tilde{\mathbf{P}}^T \mathbf{W})$ where \mathbf{R}_p is the residual operator evaluated only in the N_f cells and $\tilde{\mathbf{P}} \in \mathbb{R}^{N_v \times (N_f + N_s)}$ is the expanded masked matrix with N_s the number of required neighbor cells depending on the spatial discretization scheme. The application of the masked matrix to Eq. (6) then provides the approximation $\mathbf{c}(t) \approx \Theta [\mathbf{R}_p(\tilde{\mathbf{P}}^T \mathbf{W}(t)) - \mathbf{R}_p(\tilde{\mathbf{P}}^T \mathbf{W}_b)]$ for the modal coordinates with the matrix Θ depending on the invertibility of the matrix $\mathbf{P}^T \Psi$:

$$\Theta = \begin{cases} (\mathbf{P}^T \Psi)^{-1} & \text{if } N_f = N_p \\ (\Psi^T \mathbf{P} \mathbf{P}^T \Psi)^{-1} \Psi^T \mathbf{P} & \text{if } N_f > N_p \end{cases} \quad (7)$$

These usual (Q)DEIM approximations provide as many interpolation points as the number of residual POD modes ($N_f = N_p$), but oversampling ($N_f > N_p$) is sometimes beneficial to improve the accuracy as successfully shown by Di Donfrancesco 2019 using a Block QDEIM approach. Finally the ROM with the approximation of the non-linear term is obtained after the substitution of the residual term approximation Eq. (6) in Eq. (5) and the replacement of the modal coordinate \mathbf{c} by its approximation with the masked projection and reads:

$$\frac{d\mathbf{a}(t)}{dt} = \Phi^T (\mathbf{I} - \Psi \Theta \mathbf{P}^T) \mathbf{R}(\mathbf{W}_b) + \Phi^T \Psi \Theta \mathbf{R}_p(\tilde{\mathbf{P}}^T (\mathbf{W}_b + \Phi \mathbf{a}(t))) \quad (8)$$

2.3 Full Order Model formulated with the Time Spectral Method

Provided that the FOM solution is periodic with period $T = 2\pi/\omega$, the conservative field vector and the residual term may be approximated by their truncated Fourier series $\mathbf{W} \approx \sum_{k=-N_h}^{N_h} \widehat{\mathbf{W}}_k e^{jk\omega t}$ and $\mathbf{R} \approx \sum_{k=-N_h}^{N_h} \widehat{\mathbf{R}}_k e^{jk\omega t}$ with $\tilde{N}_h = 2N_h + 1$ coefficients. The Fourier coefficients $\widehat{\mathbf{W}}_k$ are associated to their temporal counterpart $\mathbf{W}(t_n)$ at different time instants via the Discrete Fourier Transform (DFT). The matrix of Fourier coefficients $\widehat{\mathbf{W}} = [\widehat{\mathbf{W}}_{-N_h}, \dots, \widehat{\mathbf{W}}_{+N_h}]^T$ is then derived from the temporal snapshots matrix $\mathbf{W} = [\mathbf{W}(t_0), \dots, \mathbf{W}(t_{2N_h})]^T$ with $t_n = nT/\tilde{N}_h$ via the weight matrix \mathcal{E} with general term $\mathcal{E}_{k,n} = \tilde{N}_h^{-1} e^{-2j\pi kn/\tilde{N}_h}$ such that $\widehat{\mathbf{W}} = \mathcal{E}\mathbf{W}$.

Since the Fourier basis with the exponential functions $\{e^{jk\omega t}\}_{k=-N_h}^{N_h}$ is orthonormal, the truncated Fourier series of eq.(2) with N_h harmonics reduces to a set of \tilde{N}_h equations which can be recast in the condensed matrix form: $\mathcal{D}\widehat{\mathbf{W}} = \widehat{\mathcal{R}}(\mathbf{W})$ with $\widehat{\mathcal{R}}$ the matrix of Fourier coefficients for the residual term and $\mathcal{D} = \text{diag}(-j\omega N_h, \dots, j\omega N_h)$. The explicit derivation of the residual term with respect to the Fourier coefficients of the conservative variables $\widehat{\mathcal{R}}(\mathcal{E}^{-1}\widehat{\mathbf{W}})$ may be cumbersome and the Time Spectral Method (Hall et al. 2002; Gopinath et al. 2005) recasts the problem in the time domain while keeping the truncated Fourier approximation for the conservative variables and the residual term. The equations then read $\mathcal{E}^{-1}\mathcal{D}\mathcal{E}\mathbf{W} = \mathcal{R}(\mathbf{W})$ where the left hand side is the spectral approximation of the time derivative operator with N_h harmonics. For each time instant, the spectral derivative operator which couples all the time instants may be expressed analytically (Gopinath et al. 2005) and the problem is solved with a pseudo-time stepping technique. In practice the TSM problem uses the residual vector and Jacobian matrix provided by ONERA's code *elsA* (Cambier et al. 2013; Blondeau et al. 2019):

$$\frac{d\mathbf{W}(t_n)}{d\tau} = D_t(\mathbf{W}(t_n)) - \mathbf{R}(\mathbf{W}(t_n)) = \mathbf{R}_{\text{TSM}}(\mathbf{W}(t_n)) \quad \forall 0 \leq n < 2N_h + 1 \quad (9)$$

2.4 Projection based Reduced Order Model with the Time Spectral Method

In this section we introduce a Reduced Order Time Spectral Method (ROTSM) which reduces the computational cost and exhibits better convergence properties than the Full Order TSM (FOTSM). The snapshot database \mathbf{W} contains the different time instants and is approximated by a POD such that $\mathbf{W}(t_n) = \Phi \mathbf{a}(t_n)$. Note that unlike the POD for the time domain Eq. (3), the snapshots are not centered around a base field and the basis is not truncated since the rank $N_r = \tilde{N}_h$ is already very small.

The residual \mathbf{R}_{TSM} in Eq. (9) can be rewritten with the POD for each time instant as $D_t(\Phi)\mathbf{a}(t_n) - \mathbf{R}(\Phi\mathbf{a}(t_n))$ and depends on the vector $\mathbf{a} = [\mathbf{a}(t_0), \dots, \mathbf{a}(t_{2N_h})]$ since the evaluation of the derivative operator couples all the time instants. The \tilde{N}_h equations for all time instants can be gathered in a single residual term $\mathcal{R}_{\text{TSM}}(\mathbf{a})$ and the system of equations is solved iteratively with Newton's method so that the increment $\Delta \mathbf{a}^{(m)}$ for the iteration m is given by:

$$\mathcal{J}^{(m)} \Delta \mathbf{a}^{(m)} = -\mathcal{R}_{\text{TSM}}(\mathbf{a}^{(m)}) \quad (10)$$

with $\mathcal{J}^{(m)} = \mathbf{J}^{(m)} \Phi_D$, where the residual Jacobian is $\mathbf{J}_{i,j}^{(m)} = \partial \mathcal{R}_{\text{TSM}}(\Phi \mathbf{a}(t_i)) / \partial (\Phi \mathbf{a}(t_j))$ and Φ_D is a block diagonal matrix with the POD basis, see (Di Donfrancesco 2019) for further details. The system Eq. (11) can finally be projected on the basis Φ_D to obtain a very small

system of \tilde{N}_h equations such that:

$$\left[\Phi_D^T \mathcal{J}^{(m)} \right] \Delta \mathbf{a}^{(m)} = -\Phi_D^T \mathcal{R}_{\text{TSM}}(\mathbf{a}^{(m)}) \quad (11)$$

This last formulation is apparently attractive since the projected Jacobian and residual terms in Eq. (11) scale with \tilde{N}_h . However since the residual is nonlinear, it has to be first evaluated with the FOTSM and then projected, unless an additional approximation is introduced. The masked projection approaches used in the time domain could as well be considered to approximate the residual and the Jacobian of the ROTSM and further work has to be conducted to evaluate this approach. Note that although Eq. (10) is not projected, the computational cost for the resolution is still reduced since the Jacobian \mathcal{J} has only \tilde{N}_h^2 columns instead of $\tilde{N}_h \cdot N_v$ with the FOTSM. The convergence is also accelerated with respect to the FOM since the initial guess for \mathbf{a} comes from the projection of an initial field \mathbf{W}_0 on the POD basis which is presumably a good representation of the solution.

2.5 POD basis adaptation for parametrized ROMs

The ROMs detailed in previous sections have to provide accurate solutions in a certain range of a parameter λ . A global POD basis can be computed from a set of snapshots including different time instants and different parameter values: $\mathcal{W} = [\mathbf{W}(t_1, \lambda_1), \dots, \mathbf{W}(t_M, \lambda_P)]$. However the resulting POD modes are no longer optimal for any parameter value and many modes have to be considered since the first modes represent average fields common to all parameter values (Amsallem 2010; Di Donfrancesco 2019). Another solution is to compute several POD bases Φ_{λ_p} from the snapshots sets $\mathcal{W}_{\lambda_p} = [\mathbf{W}(t_1, \lambda_p), \dots, \mathbf{W}(t_M, \lambda_p)]$ for $p = 1, \dots, P$. In this case the POD bases are optimal for each parameter λ_p . Then the POD basis for a new parameter value $\lambda^* \notin \Lambda = \{\lambda_p\}_{p=1}^P$ is interpolated on the tangent space of the Grassmann manifold associated to the set of POD bases (Amsallem 2010). Such a procedure has been successfully used by Freno et al. 2014 for example on similar aeroelastic problems. Once in the tangent space, the interpolation can be performed with any classical interpolation method and the interpolated point is then sent back to the Grassmann manifold to obtain a representative subspace for the new parameter value.

3 Numerical applications

3.1 Time domain ROM for the flow around an oscillating cylinder at low Reynolds number

The accuracy of the time domain ROM is investigated on the example of an oscillating cylinder in a laminar cross-flow at $\text{Re} = 185$. The vertical motion of the cylinder is prescribed with the function $y(t) = A \sin(2\pi ft)$ and different values of the normalized amplitude $A_r = A/d$ and frequency $f_r = f/f_\zeta$ with d the cylinder diameter and f_ζ the vortex shedding frequency are investigated by Di Donfrancesco 2019. Numerical simulations have been conducted for $(A_r, f_r) = (0.2, 0.8)$ and $(0.5, 1.2)$ where secondary frequencies are observed in the flow field.

The Navier-Stokes equations are solved first with the FOM on a deforming grid to generate a set a snapshots selected after the transient phase. The relative information content of the POD modes is plotted in Fig. 1a and the first POD modes for $(A_r, f_r) = (0.2, 0.8)$ are shown in Fig. 1b. The time integration of the ROM is performed with a 4 steps Runge-Kutta method

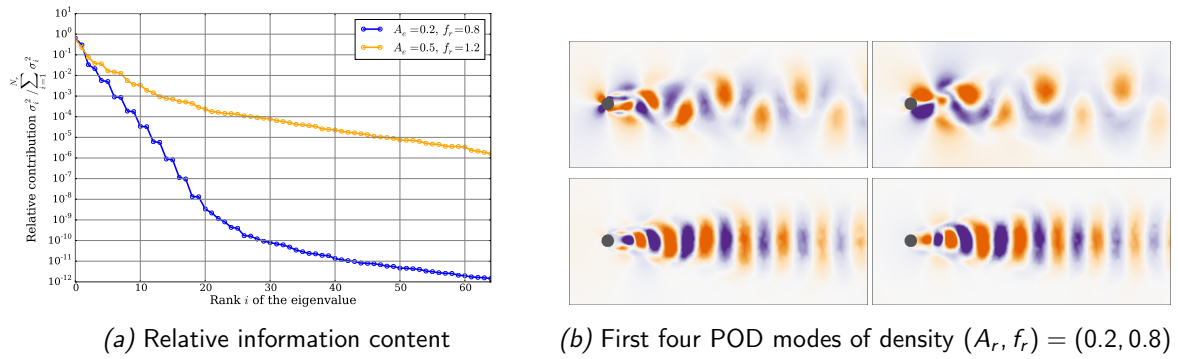


Figure 1 – POD analysis of the oscillating cylinder at $Re = 185$.

for a single period of vortex shedding corresponding to the sampling time interval to compute the POD. Only $N_q = 12$ modes are sufficient to reproduce accurately the vortex shedding. Several tests have been conducted to check the robustness of the masked projection methods to approximate the nonlinear residual term.

The solution time histories of the first 3 modal coordinates $a_i(t)$ are plotted in Fig. 2a and 2b. Then the nonlinear term is approximated with the BQDEIM using N_p nonlinear residual POD modes and $N_f = b \cdot N_p$ interpolation points with $b = n_v = 4$ and $N_p = 14$ for $(A_r, f_r) = (0.2, 0.8)$ and $b = 20$ and $N_p = 40$ for $(A_r, f_r) = (0.5, 1.2)$. The results plotted in Fig. 2a and 2b are also satisfactory in both cases (see the difference plotted on the right axis) and the relative error for the density field at the last time instant plotted in Fig.2c is lower than 3% (less than 1.2% for $(A_r, f_r) = (0.2, 0.8)$).

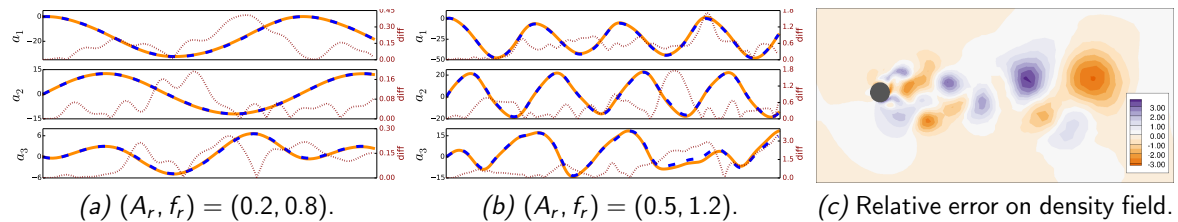


Figure 2 – Comparison of the first three modal coordinates time histories (— FOM, — ROM) and density field error at $Re = 185$.

Additional test cases have been investigated in (Di Donfrancesco 2019) and a parametric investigation of the ROM with respect to the amplitude and frequency variation has also been conducted. Satisfactory results are obtained but the long term stability of the ROM is not always ensured for a new parameter value, even for this low Reynolds number test case. Note that the number of interpolation cells has to be increased up to 6% of the total number of cells in the second case $(A_r, f_r) = (0.5, 1.2)$ presented here. Special care has therefore to be taken for parametric investigations in order to ensure that a sufficient number of cells is used for the interpolation, whatever the value of the considered parameter.

3.2 ROTSM for the transonic flow around an oscillating airfoil

The second test case considered here is a transonic pitching NACA64A010 airfoil. Di Donfrancesco (2019) has shown that simulations with the time domain ROM fail to converge on

long term even in subsonic regime at $Ma = 0.50$ without masked projection and the robustness of the ROTSM is therefore demonstrated here. A reference simulation is first run for $Ma = 0.796$ with the Euler FOTSM implemented in (Blondeau et al. 2019) with $N_h = 1$ harmonic only. The prescribed harmonic pitch motion is defined by $\alpha(t) = \alpha_0 + \hat{\alpha} \sin(2\pi ft)$ with $\alpha_0 = -0.22^\circ$, $\hat{\alpha} = 1.01^\circ$ and the frequency is set to $f = 34.4$ Hz.

The 3 TSM snapshots and the corresponding POD modes are plotted in Fig. 3. The POD basis is not truncated since the size is already very small. The convergence of the ROTSM is much faster than the one of the FOTSM since the initial uniform freestream solution is projected on the POD basis and provides a good guess for the modal coordinates. As shown in Fig. 4a the residual is close to the one of the FOM solution in about 20 iterations; it does not decrease further since the ROTSM solution (which is necessarily in the subspace spanned by the POD basis) can not be better than the FOTSM solution. The skin pressure is perfectly reproduced, as well as the lift and drag forces whose time history can be evaluated over a complete cycle of oscillation from its Fourier series as shown in Fig. 4b.

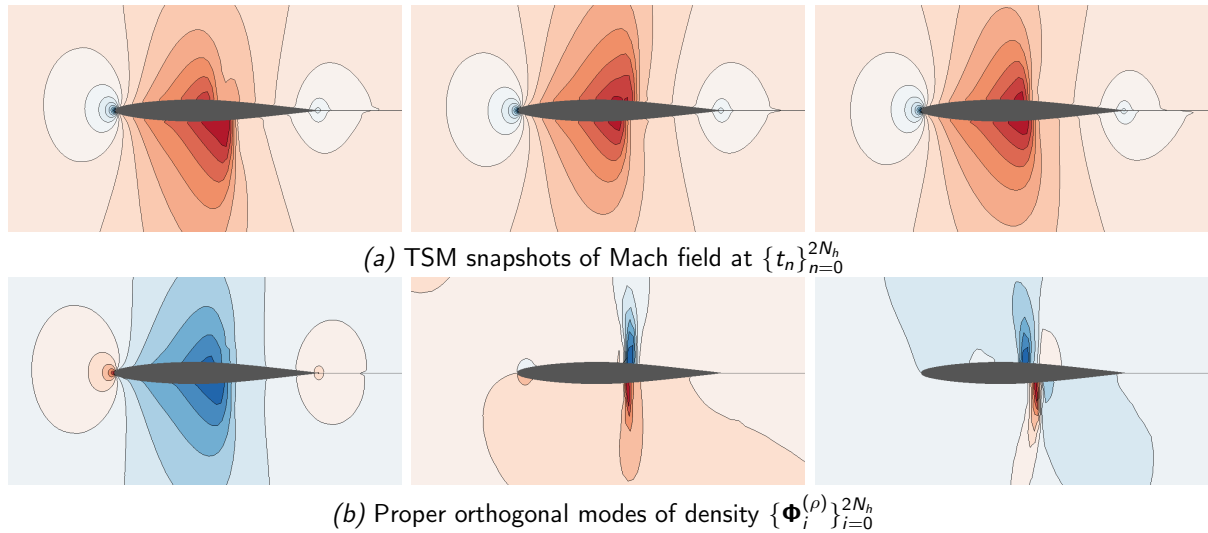


Figure 3 – TSM snapshots and POD modes for the pitching airfoil at $Ma = 0.796$ with $N_h = 1$.

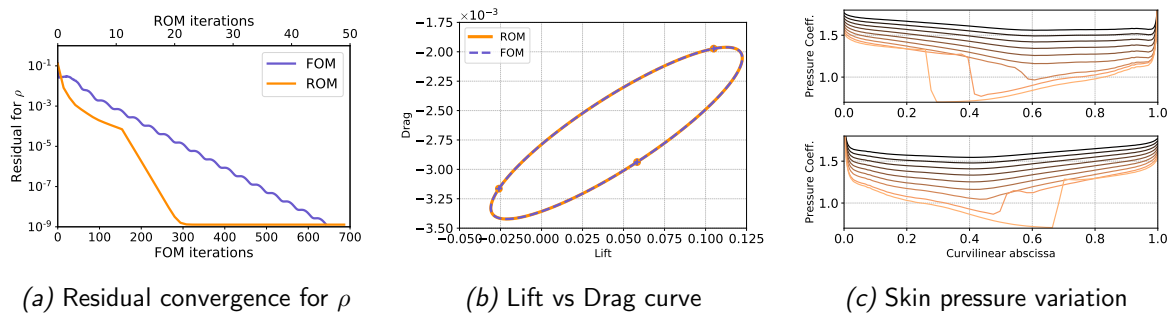


Figure 4 – ROTSM vs FOTSM results (a), (b) and database of skin pressure at t_0 .

A database of reference simulations is then run at different Mach numbers $Ma \in [0.50; 0.84]$ from subsonic to transonic regime. The range of variation for the skin pressure is illustrated in Fig. 4c. A strong pressure gradient develops for $Ma \geq 0.76$. A set of POD bases is first constructed with a regular sampling for $Ma \in \{0.52, 0.56, 0.60, 0.64, 0.68, 0.72, 0.76, 0.80, 0.84\}$

and the ROTSM is evaluated for new values of the Mach number $Ma^* \in \{0.58, 0.74, 0.79, 0.81\}$. Different interpolation methods on the tangent plane of the Grassmann manifold are compared in Tab. 1 for the average and maximal value of the relative error between the skin pressure computed by the ROTSM with respect to the FOTSM for the $2N_h + 1$ time instants.

Table 1 – Relative error in percentage for the skin pressure at all time instants between the FOM and the ROM for several interpolated Mach numbers with the first database.

	Mean error			Max. error		
	Linear	Spline	Lagrange	Linear	Spline	Lagrange
Ma = 0.58	$8,15 \cdot 10^{-2}$	$4,06 \cdot 10^{-2}$	$1,07 \cdot 10^{-1}$	$8,38 \cdot 10^{+1}$	$4,58 \cdot 10^{+1}$	$2,18 \cdot 10^{+1}$
Ma = 0.74	$2,95 \cdot 10^{-1}$	$4,30 \cdot 10^{-1}$	$2,39 \cdot 10^{-1}$	$5,50 \cdot 10^{+1}$	$1,09 \cdot 10^{+2}$	$5,00 \cdot 10^{+1}$
Ma = 0.79	$7,29 \cdot 10^{-1}$	$6,70 \cdot 10^{-1}$	$7,59 \cdot 10^{-1}$	$1,78 \cdot 10^{+2}$	$1,59 \cdot 10^{+2}$	$2,10 \cdot 10^{+2}$
Ma = 0.81	$7,55 \cdot 10^{-1}$	$8,21 \cdot 10^{-1}$	$1,71 \cdot 10^{+0}$	$1,79 \cdot 10^{+2}$	$2,94 \cdot 10^{+2}$	$8,97 \cdot 10^{+2}$

The relative mean error for the airfoil skin pressure is overall under 1% and increases with the Mach number. The maximal relative error is however much higher and increases significantly when the flow becomes transonic. The spline or Lagrange interpolation methods provide accurate results in subsonic regime but should be avoided when the flow becomes transonic because spurious oscillations in the interpolation lead to inaccurate results.

A second database for $Ma \in \{0.50, .6, .70, .74, .76, 0.77, .78, .8, .82, .84\}$ is considered with a finer sampling in the transonic regime and less points in the subsonic one. Results in Table 2 indicate that the error can be substantially decreased in the transonic regime for $Ma = 0.79$ and 0.81 but the integration sometimes fails with Lagrange interpolation. The error in the subsonic regime is larger than with the first database since the sampling is now coarser. Accurate results in subsonic and transonic regimes thus require a fine sampling in both regimes.

Table 2 – Relative error in percentage for the skin pressure at all time instants between the FOM and the ROM for several interpolated Mach numbers with the second database.

	Mean error			Max. error		
	Linear	Spline	Lagrange	Linear	Spline	Lagrange
Ma = 0.58	$1,75 \cdot 10^{-1}$	$1,34 \cdot 10^{-1}$	—	$1,06 \cdot 10^{+2}$	$1,29 \cdot 10^{+2}$	—
Ma = 0.74	$3,03 \cdot 10^{+0}$	$3,03 \cdot 10^{+0}$	$3,03 \cdot 10^{+0}$	$2,98 \cdot 10^{+2}$	$2,98 \cdot 10^{+2}$	$2,99 \cdot 10^{+2}$
Ma = 0.79	$3,41 \cdot 10^{-1}$	$3,56 \cdot 10^{-1}$	$5,91 \cdot 10^{-1}$	$3,69 \cdot 10^{+1}$	$2,73 \cdot 10^{+1}$	$8,71 \cdot 10^{+1}$
Ma = 0.81	$3,92 \cdot 10^{-1}$	$3,75 \cdot 10^{-1}$	—	$3,39 \cdot 10^{+1}$	$2,24 \cdot 10^{+1}$	—

4 Conclusions

ROMs in the time and frequency domains have been developed and used for aeroelastic applications in subsonic and transonic regime. For low Mach numbers, time domain ROMs with masked projection techniques provide accurate results, at least for short term time integration. An original BQDEIM approach was implemented to enable oversampling for the nonlinear term approximation and to improve the accuracy of the time domain ROM. When the Mach number increases, time domain ROMs lack robustness and the ROTSM formulation proved to be more robust. The parametric response has been investigated with several interpolations methods and database of POD bases. The database has to be refined to capture accurately the shock in the transonic regime and linear or spline interpolations are more stable than Lagrange interpolation.

References

- Amsallem, D. (2010). "Interpolation on Manifolds of CFD-based Fluid and Structural Reduced-Order Models for On-Line Aeroelastic Predictions". PhD Thesis. Stanford University.
- Anttonen, J., P. King, and P. Beran (2003). "POD-Based reduced-order models with deforming grids". *Mathematical and Computer Modelling* 38.1, pp. 41–62.
- Blondeau, C. and C. Liauzun (2019). "A Modular Implementation of the Time Spectral Method for Aeroelastic Analysis and Optimization on Structured Meshes". *18th International Forum on Aeroelasticity and Structural Dynamics*. IFASD-2019-032. Savannah, Georgia, USA.
- Bourguet, R., M. Braza, and A. Dervieux (2011). "Reduced-order modeling of transonic flows around an airfoil submitted to small deformations". *Journal of Computational Physics* 230.1.
- Cambier, L., S. Heib, and S. Plot (2013). "The Onera elsA CFD software: Input from research and feedback from industry". *Mechanics & Industry* 14, pp. 159–174.
- Chassaing, J.-C., X. Nogueira, and S. Khelladi (2013). "Moving Kriging reconstruction for high-order finite volume computation of compressible flows". *Computer Methods in Applied Mechanics and Engineering* 253, pp. 463–478.
- Chaturantabut, S. and D. C. Sorensen (2010). "Nonlinear model Reduction via Discrete Empirical Interpolation". *SIAM Journal on Scientific Computing* 32.5, pp. 2737–64.
- Di Donfrancesco, F. (2019). "Reduced Order Models for the Navier-Stokes equations for Aeroelasticity". PhD Thesis. Sorbonne University.
- Donea, J. et al. (2004). "Encyclopedia of Computational Mechanics". Vol. 1: Fundamentals. John Wiley & Sons. Chap. 14: Arbitrary Lagrangian-Eulerian Methods, pp. 1–25.
- Drmač, Z. and S. Gugercin (2016). "A New Selection Operator for the Discrete Empirical Interpolation Method - Improved a priori error bound and extensions". *SIAM Journal on Scientific Computing* 38.2.
- Freno, B. A. and P. G. Cizmas (2014). "A proper orthogonal decomposition method for nonlinear flows with deforming meshes". *International Journal of Heat and Fluid Flow* 50.
- Gopinath, A. and A. Jameson (2005). "Time Spectral Method for Periodic Unsteady Computations over Two- and Three- Dimensional Bodies". *43rd AIAA Aerospace Sciences Meeting and Exhibit*. Reno (NV).
- Hall, K. C., J. P. Thomas, and E. H. Dowell (1999). "Reduced-Order Modelling of Unsteady Small-Disturbance Flows using a Frequency-Domain Proper Orthogonal Decomposition Technique". *37th Aerospace Sciences Meeting and Exhibit*. Reno (NV).
- Hall, K. C., J. P. Thomas, and W. S. Clark (2002). "Computation of Unsteady Nonlinear Flows in Cascades Using a Harmonic Balance Technique". *AIAA Journal* 40.5, pp. 879–886.
- Liberge, E. and A. Hamdouni (2010). "Reduced order modelling method via proper orthogonal decomposition (POD) for flow around an oscillating cylinder". *Journal of Fluids and Structures* 26.2, pp. 292–311.
- Placzek, A., D.-M. Tran, and R. Ohayon (2011). "A nonlinear POD-Galerkin reduced-order model for compressible flows taking into account rigid body motions". *Computer Methods in Applied Mechanics and Engineering* 200.49-52, pp. 3497–14.
- Thomas, J. P., E. H. Dowell, and K. C. Hall (2010). "Using Automatic Differentiation to Create a Nonlinear Reduced-Order-Model Aerodynamic Solver". *AIAA Journal* 48.1, pp. 19–24.

Assessment of flutter methods by numerical correlations with wind tunnel test data on U-tail configuration

Sylvie Dequand¹, Arnaud Geeraert¹ and Guy-Daniel Mortchelewicz¹

¹ONERA, The French Aerospace Lab, Aerodynamics, Aeroelasticity & Acoustics Department (DAAA/MSAE), Châtillon, France, Sylvie.Dequand@onera.fr

Keyword: Aeroelasticity, High-Fidelity simulations, Flutter, Empennage

Aircrafts can be designed with different aft body configurations and all kinds of empennages exist. This study focuses on the aeroelastic behavior of intersecting surfaces typically arising on aircraft tail, such as U-tail. It presents aerodynamic and flutter correlations between experimental and numerical results, in subsonic and transonic domain for a wind tunnel model representative of such aircraft tail.

Wind tunnel tests¹ (WTT) were carried out in ONERA S2MA pressurized wind tunnel on innovative tail concepts in the framework of the Cleansky research program. This test campaign provided a thorough experimental database for flutter mechanism evaluation of intersecting airfoil surfaces.

High-fidelity fluid-structure coupling simulations are performed using the elsA CFD solver² (ONERA-Airbus-Safran property). The aim is to evaluate the ability of our high-fidelity numerical tools to reproduce complex aerodynamic phenomena due to flow interactions between the different airfoil surfaces and to predict the sensitivity of the aeroelastic stability to the geometric parameters (dihedral, yaw angle).

Steady and unsteady pressure coefficients along different slices of the airfoil surfaces have been measured at different aerodynamic conditions and are compared to numerically predicted pressure coefficients. The aeroelastic stability of the studied configuration is also investigated. Different numerical methods can be applied such as the Forced Harmonic Excitation, the Pulse and the Direct Coupling methods. Data obtained with these numerical methods are compared to Wind Tunnel Test data and to results obtained with the low-fidelity DLM method.



Figure 1: Flutter model wall-mounted in the test section of the transonic pressurized wind tunnel S2MA (Onera) (2016) – Pressure distribution at the empennage intersecting surfaces.

1. Geeraert, A., Lepage, A., Stephani, P., Feldmann, D., Häberli, W. (2017). Wind tunnel flutter tests of a U-tail configuration. Part 1: Model design and testing. IFASD, Como, Italy.
2. Cambier, L., Heib, S., Plot, S. (2013). The Onera elsA CFD software: input from research and feedback from industry, *Mechanics & Industry*, 14, 159-174.
3. Mortchelewicz, G.D., Le Bihan, D. (2018). Pulse method for flutter prediction, 58th IACAS, Tel-Aviv, Israël.

This work has been funded within the frame of the JTI Clean Sky 2, AIRFRAME Integrated Technology Demonstrator platform "AIRFRAME ITD" (contract N CSJU-CS2-GAM-AIR-2014-15-01 Annex 1, Issue B04, October 2nd, 2015) being part of the Horizon 2020 research and Innovation framework programme of the European Commission.

Development of Bi-Luminophore Anodized-Aluminum Pressure-Sensitive Paint for Flutter Wind-Tunnel Experiment

Daiju Numata¹ and Ayana Wakayama²

¹*Tokai University, Kanagawa-ken, Japan, numata.daiju@tsc.u-tokai.ac.jp*

²*Tokai University, Kanagawa-ken, Japan, 9bemm090@mail.u-tokai.ac.jp*

Abstract

In this study, in order to develop unsteady pressure-sensitive paint (PSP) applicable to flutter wind-tunnel testing, we improved conventional anodized-aluminum PSP (AA-PSP) to a two-color PSP. We focused on sulfuric acid-based AA-PSP, and tried to improve this types of AA-PSP. As a result, the effect of dye adsorption time to the surface of the AA-PSP and concentration of the dye solution on the properties of AA-PSP-based two-color PSP was clarified.

Keyword: Pressure-Sensitive Paint, Wind Tunnel, Flutter, Flow Visualization

1 Introduction

The investigation of the flutter phenomenon is an important issue directly related to the safety of aircraft, and the investigation is experimentally being promoted by aerodynamic tests using a flutter wind tunnel. In such a situation, in recent years, the use of pressure-sensitive paints (PSP) ((Liu et al., 2004)) for the purpose of understanding the flutter phenomenon has attracted attention. PSP is a pressure sensor using a photochemical reaction of luminescent dye, and, it is composed of dye molecules and a binder which fix dyes on the surface of the measurement target. PSP is applied to the test model and excited by excitation light source like LED, laser etc. with appropriate wavelength, and the dye is excited and emits light. The emission intensity from fluorescent dye decreases as the oxygen concentration increases due to oxygen quenching. By using this characteristics, the surface pressure distribution on the test model can be measured by detecting emission light intensity from excited PSP.

However, it is generally difficult to measure the pressure distribution using PSP technique on a surface of the airfoil model with severe deformation and vibration such as fluttering. To calculate pressure value from captured images, model shape in captured images need to keep completely same. However, test models for aeroelastic experiment in wind-tunnel vibrates, moves and/or deforms during experiment. Therefore, it is difficult to apply PSP technique to these kind of experiments. For example, the PSP measurement in the flutter test conducted by Nakakita et al. (Nakakita et al. 2009 & 2012) succeeded in capturing the qualitative pressure change on the aluminum wing model that greatly deformed with the flutter, but could not determine the quantitative pressure value. As a method solving such a problem, there is the two-color PSP technique (Numata et al. 2018 & 2019). This PSP technique uses two luminescent dye, and by getting emissions from these simultaneously in measurement and using these as a wind-on and wind-off images, PSP measurement in flutter wind-tunnel experiment becomes possible. In particular, anodized-aluminum PSP (AA-PSP) has a time response on the order of kHz or higher (Asai, 1997, Sakaue, 1999).

Therefore, when AA-PSP is improved to a two-color PSP and used in a flutter test, a high-speed unsteady phenomenon can enable to be captured with high time resolution.

In this study, in order to develop unsteady PSP applicable to flutter wind-tunnel testing, we improved conventional AA-PSP to a two-color PSP. We focused on sulfuric acid-based AA-PSP, and tried to improve this types of AA-PSP.

2 Measurement principle

2.1 Pressure-Sensitive Paint (PSP)

Pressure-Sensitive Paint (PSP) is an optical pressure measurement technique widely used in aerodynamic tests, especially wind-tunnel testing (Liu et al. 2004). The PSP consists of a luminescent molecule, known as a luminophore, and a binder adhere the luminophore to the model surface. When luminophore molecules inside the binder are excited by the excitation light with UV or visible wavelength, they emit light with longer wavelength. Luminescent intensity of the PSP is reduced in presence of oxygen in test gas by photo-physical process known as oxygen quenching. This intensity change of luminescence is correlated with oxygen concentration that is proportional to pressure in gas. Therefore, local surface pressure can be determined from detected luminescence intensity.

One of the advantage of PSP measurement comparing with conventional pressure measurement techniques is that pressure distribution can be measured as two-dimensional images with high spatial resolution. In conventional aerodynamic testing, a pressure-tap or an unsteady pressure sensor was mainly used for pressure-measurement on surface of the test model. However, this conventional pressure measurement technique is only able to measure spatially-discrete pressure distribution on the surface of the test model due to the limitation of installing and manufacturing these sensors on it. Therefore, PSP measurement technique has advantage compared with conventional point-measurement pressure sensors. To calculate pressure distributions on the test model which is applied to the PSP, the wind-on image (I , image including luminescent intensity change caused by aerodynamic phenomena) is acquired during the experiment and the wind-off reference image (I_{ref} , image including luminescent intensity of the test model before experiment) is also acquired. The dark current image (I_{dark} , shutter-closing image of photodetector like the high-speed video camera) is subtracted from both images, and luminescence intensity ratio by taking the ratio of the wind-on image and wind-off image ($(I_{ref} - I_{dark}) / (I - I_{dark})$) is obtained. Luminescence intensity ratio is converted to pressure by applying Stern-Volmer relationship shown in Eq. (1),

$$\frac{I_{ref} - I_{dark}}{I - I_{dark}} = A(T) + B(T) \frac{P}{P_{ref}} \quad (1)$$

where P , I and $A(T)$ and $B(T)$ represents pressure, luminescence intensity and calibration coefficients, respectively.

2.2 Anodized-Aluminum PSP (AA-PSP)

As one of application field of PSP technique, there are unsteady high-speed aerodynamic phenomena represented by shock-wave phenomena (Asai et al. 2000) (Gongora-Orozco et al. 2010). To apply PSP technique to these high-speed phenomena, improvement of time responsiveness of the PSP is important. To capture high-speed flow phenomena accurately, especially shock-wave phenomena, the PSP with O(kHz) or higher response time is needed. Time response of the PSP depends on two factors, photochemical reaction time and

diffusion time of oxygen molecules diffusing into the binder. The response time of the traditional PSP was mainly limited by the oxygen diffusivity of the binder since polymer binders have low oxygen diffusivity.

To improve response time of the PSP from the viewpoint of oxygen diffusivity, fast-responding PSPs using porous binders were developed for unsteady pressure measurement. There are various types of porous pressure-sensitive paints in use, depending on the type of binder (mostly inorganic material). For example, Baron et al. (Baron, et al. 1993) used a commercial porous silica-gel thin-layer chromatography (TLC) plate. Asai et al. (Asai et al. 2000) developed another type of porous binder by using a porous alumina as a binder, which was later modified by Sakaue et al. (Sakaue et al. 1999) and called Anodized-Aluminum PSP (AA-PSP). Fig. 1 shows schematic of AA-PSP.

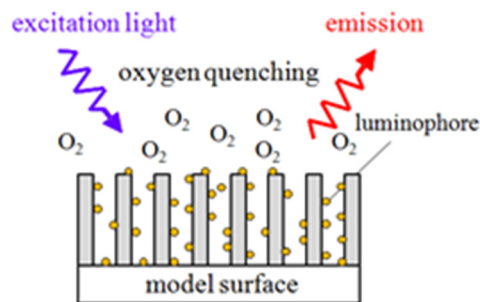


Figure 1: Schematic of the anodized-aluminum PSP (AA-PSP)

Various luminophores are adsorbed on the surface of the porous alumina via chemical and physical force. These porous PSPs have much faster time response characteristic than conventional polymer-based PSPs because of its high oxygen diffusivity.

2.3 Two-color PSP

In general PSP measurement, pressure at wind-on situation on the surface of the test model is calculated from the luminescence intensity ratio image obtained by taking the ratio of the wind-on image and the wind-off image captured in experiment. However, if the test model moves, vibrates and/or deforms during experiment, for example during flutter experiment, calculation of luminescence intensity ratio is difficult because difference occurs between shape and/or position of the test model captured in each of images. Therefore, in general, to apply conventional PSP measurement techniques to dynamic measurement is difficult. In such cases, it is effective to use two-color PSP measurement method in which a second-dye (reference dye) that does not have pressure sensitivity is mixed with the normal PSP. In this method, two emission signals from two dyes in the two-color PSP are simultaneously detected by the photodetector and use those signals as a wind-on image and a wind-off image. Fig. 2 shows conceptual diagram of two-color PSP method.

In order to detect two emission wavelength bands simultaneously, an imaging device such as a high-speed color camera or a two-wavelength splitter optical system is generally used. In this study, the two-wavelength splitter optical system is used as a detector which can install any optical filters.

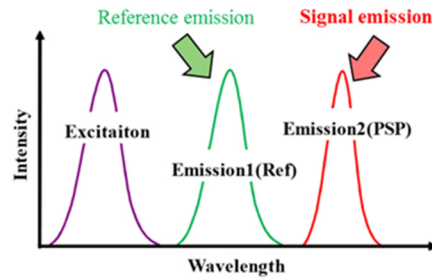


Figure 2: Conceptual diagram of two-color PSP method

3 Experimental setup and condition

3.1 Sample fabrication

In this study, we focused on sulfuric acid-based AA-PSP. Sulfuric acid was used as an electrolyte for anodization. The energizing time, electrolyte temperature, and post-treatment time for making anodized test samples were similar to those decided from in the past research (Numata et al. 2019). AA-PSP using anodized aluminum by using this anodization condition has a response time of 9,000 Hz to the pressure change (Numata et al. 2019). In this study, a chiller was used to keep the electrolyte temperature constant. Tris (4,7-diphenyl-1,10-phenanthroline) ruthenium (II) dichloride (Bath-Ru) was used as a pressure-sensitive dye and Fluorescein was used as a reference dye, respectively. Pressure sensitive dye and reference dye was dissolved in chloroform to make a dye solution. Amount of the pressure sensitive dye in solvent is 1 mM. In the experiment, three types of dye solutions were prepared: a dye solution containing no reference dye, a dye solution containing a fixed amount of the reference dye, and a dye solution in which the amount of the reference dye was reduced to 40 %. The anodized aluminum samples were dipped using each of these dye solutions, and the effects of dipping time and concentration of the reference dye on PSP characteristics were investigated.

In this study, in order to investigate the effect of dipping time and concentration of reference dye in dye solution on the characteristics of AA-PSP, several anodized samples were made with dipping time as a parameter. In this study, samples were prepared by changing the dipping time by 6 patterns (10 min., 20 min., 30 min., 40 min., 50 min. and 60 min.). After samples are prepared, it is subjected to a calibration test to clarify pressure sensitivity. In this study, the sample temperature during the calibration test was 20 deg.C.

3.2 Calibration system for PSP

Fig. 3 shows a schematic diagram of the static calibration system (Numata, 2017). This calibration chamber is composed of a pressure chamber for setting test samples, a pressure controller for controlling pressure inside the pressure chamber and a temperature controller for controlling temperature of the test sample. A dry vacuum pump and a high-pressure source are connected to the pressure controller. By using this pressure controller, pressure in the calibration chamber can be adjusted in the range of 0.2 kPa to 1,000 kPa. The temperature controller controls temperature of the test sample using a Peltier element, and adjustable temperature range is approximately 0 deg.C to 50 deg.C. However, this range varies depending on the size and material of the test sample. By using these devices, the calibration system can arbitrarily change pressure and temperature on and around the test sample set in the chamber.

A xenon continuous light source or LED light is used as the excitation light source. These becomes the excitation light source with specific wavelength band by attaching arbitrary optical filters. Fluorescence detection from test samples is performed with a CCD camera, a CMOS camera or the spectrofluorophotometer, etc. If emission wavelength from test samples is known, detection of luminescence from test samples is performed by using any cameras. In this case, luminescence from test samples is recorded as an image data. Optical filters is attached to the front of the camera because it is necessary to transmit only luminescence from the PSP to the image sensor of the camera.

The spectrofluorophotometer is also used to clarify excitation and emission wavelength of PSP samples. This makes it possible to measure excitation and emission spectrum under arbitrary pressure and temperature environment.

In this study, a bandpass filter of 650 ± 50 nm was used to detect luminescence from pressure-sensitive dyes. Similarly, a 525 ± 20 nm bandpass filter was used to detect emission from the reference dye. The excitation light source is a xenon light source equipped with a 500 nm short-pass filter.

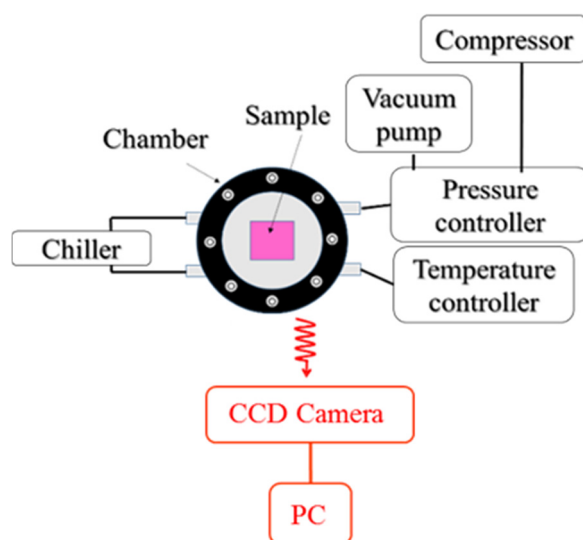


Figure 3: Static calibration system for the molecular imaging sensor at Tokai University

4 Result and discussion

4.1 Pressure sensitivity of PSPs without reference dye

Firstly, the effect of dipping time on pressure sensitivity of AA-PSP without reference dye was investigated. Figure 4 shows a Stern-Volmer plot of developed PSPs without reference dye in the pressure range of 0.2 kPa to 200 kPa at a sample temperature of 20 deg.C. The vertical axis is the emission intensity ratio I_{ref} / I , and the horizontal axis is the test pressure, respectively. The reference pressure in this case is 100 kPa.

As shown in Figure 4, it can be seen that the Stern-Volmer plot is not significantly depending on the dipping time. The pressure sensitivity of each PSPs near atmospheric pressure was approximately 0.8 %/kPa. The peak of the emission intensity was obtained under the condition of a dipping time of 20 minutes. However, the emission intensity of these PSPs near the atmospheric pressure is lower than that of PSPs using dichloromethane as a dye solvent.

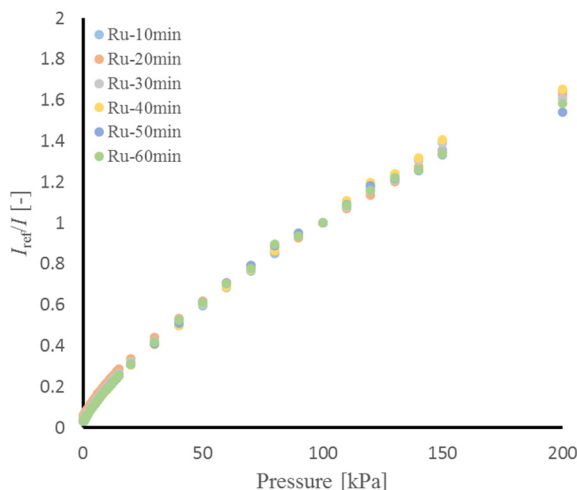


Figure 4: Effect of dipping time to Stern-Volmer plot of PSPs without reference dye (Pressure range: 0.2 kPa to 200 kPa)

4.2 Pressure sensitivity of PSPs with reference dye

Secondly, the effect of reference dye on pressure sensitivity of AA-PSP was investigated. Figure 5 shows a Stern-Volmer plot of developed two types of two-color PSPs in the pressure range of 0.2 kPa to 200 kPa at a sample temperature of 20 deg.C. The vertical axis is the emission intensity ratio I_{ref}/I , and the horizontal axis is the test pressure, respectively. The reference pressure in this case is 100 kPa.

As shown in Fig.5, it can be seen that the nonlinearity of the Stern-Volmer curve is increased for all dye concentrations. In addition, it can be seen that the rate of change in emission intensity near the atmospheric pressure is small, and that the pressure sensitivity is reduced by mixing the reference dye. In addition, pressure sensitivity of PSPs near atmospheric pressure decreases as the concentration of the reference dye decreases. Therefore, in order to obtain high pressure sensitivity with a two-color PSP using fluorescein, it is necessary to increase the concentration of the fluorescein in the dye solution.

Focusing on the relationship between the dipping time and the pressure sensitivity, a similar tendency is observed under any of the conditions. In both types of two-color PSPs, it can be seen that the nonlinearity of the Stern-Volmer curve becomes weaker as the dipping time increases, and the pressure sensitivity near the atmospheric pressure increases.

From these results, it can be seen that when improving sulfuric acid-based AA-PSP to a two-color AA-PSP, it is necessary to further increase the concentration of the reference dye in dye solution in order to increase pressure sensitivity. However, at this time, it is necessary to consider the balance between the emission intensity of the PSP dye and the emission intensity of the reference dye.

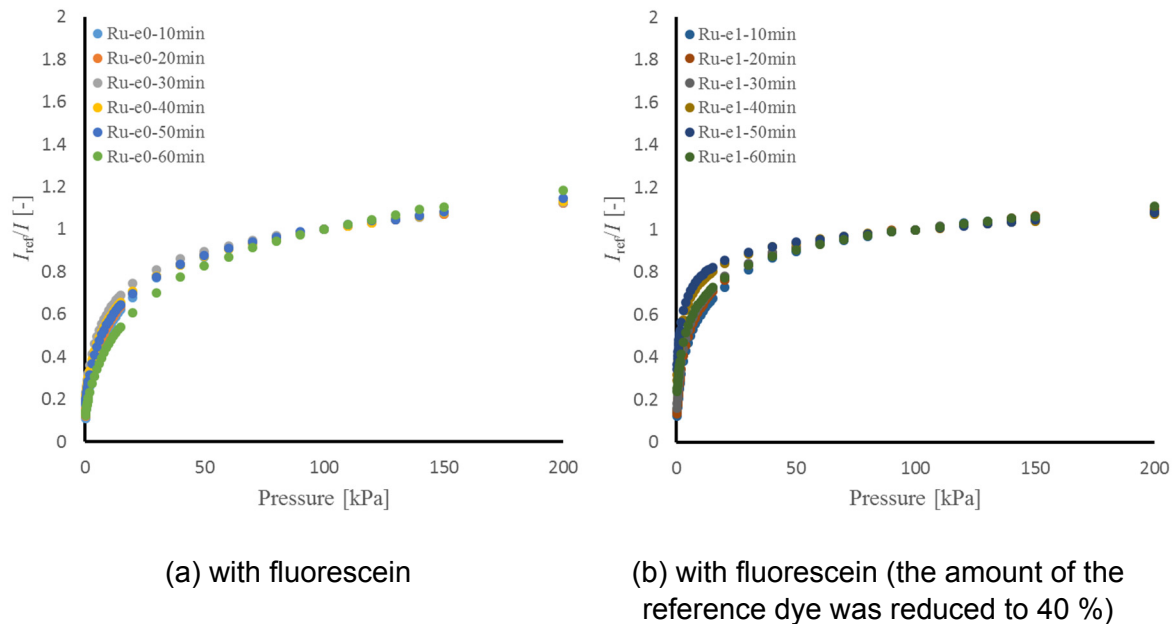


Figure 5: Effect of dipping time to Stern-Volmer plot of PSPs without reference dye (Pressure range: 0.2 kPa to 200 kPa)

5 Conclusions

In this study, in order to develop unsteady pressure-sensitive paint (PSP) applicable to flutter wind-tunnel testing, we improved conventional anodized-aluminum PSP (AA-PSP) to a two-color PSP. We focused on sulfuric acid-based AA-PSP, and tried to improve this types of AA-PSP. As a result, the effect of dye adsorption time to the surface of the AA-PSP and concentration of the dye solution on the properties of AA-PSP-based two-color PSP was clarified. From results of calibration tests, it can be seen that when improving sulfuric acid-based AA-PSP to a two-color AA-PSP, it has been found that to increase the pressure sensitivity, it is necessary to increase the concentration of the reference dye.

References

- Asai, K., "Luminescent Coating with an Extremely High Oxygen Sensitivity at Low Temperatures," Patent Pending, No. H9-207351, 1997.
- Asai, K., Nakakita, K., Kameda, M. and Teduka, K., "Recent topics in fast-responding pressure-sensitive paint technology at National Aerospace Laboratory", In Proceedings of the 19th International Congress on Instrumentation in Aerospace Simulation Facilities, Institute of Electrical and Electronics Engineers Inc., Piscataway, NJ, 25-36, 2000.
- Baron, A.E., Danielson, J.D.S., Gouterman, M., Wan, J.R., Callis, J.B. and McLachlan, B., "Submillisecond response times of oxygen-quenched luminescent coatings," Rev. Sci. Instrum. 64, pp. 3394–402, 1993.
- Gongora-Orozco, N., Zare-Behtash, H. and Kontis, K., "Global unsteady pressure-sensitive paint measurements of a moving shock wave using thin-layer chromatography", Measurement, 43 Issue 1, 152-155, 2010.
- Nakakita K, Arizono H and Ito M, "Unsteady Pressure-sensitive Paint Visualization of Transonic Flutter on Thin Wing", JAXA special publication: Proceedings of the Wind Technology Association, 81st, JAXA-SP-09-005, 2009.

Kazuyuki Nakakita & Hitoshi Arizono "Visualization of Unsteady Pressure Behavior of Transonic Flutter Using Pressure-Sensitive Paint Measurement", 27th AIAA Applied Aerodynamics Conference, AIAA 2009-3847, 2012.

Numata, D., "Development of Calibration System for Evaluating PSP Characteristics under High-pressure Environment", 6th German-Japanese Joint Seminar - High-speed Molecular Imaging Technology for Interdisciplinary Research, 2017.

Numata, D. and Ohtani, K., "Surface Pressure Measurement on Supersonic Free-Flight Projectiles Using Unsteady PSP Techniques", 2018 AIAA Aviation Forum, AIAA-2018-3315, 2018.

Daiju Numata and Kiyonobu Ohtani, "Development of Ultrafast-Response Bi-Luminophore PSP for Surface Pressure Measurement on Supersonic Projectiles", 32nd International Symposium on Shock Waves, OR-05-0347, 2019.

Daiju Numata and Ayana Wakayama, "Improvement of Anodized-Aluminum Pressure-Sensitive Paint for High Reynolds Number Wind-Tunnel Testing", in Proceedings of the ASIA PACIFIC INTERNATIONAL SYMPOSIUM ON AEROSPACE TECHNOLOGY (APISAT 2019), 2019.

D. Numata, S. Kawazoe, and A. Wakayama, "Development of Acoustic Resonance Tube for Evaluating Time Response Characteristics of Unsteady Pressure-Sensitive Paints", Proceeding of the Sixteenth International Conference on Flow Dynamics, OS13-1, 2019.

Sakaue, H., Sullivan, J.P., Asai, K., Iijima, Y. and Kunimasu, T., "Anodized aluminium pressure-sensitive paint in a cryogenic wind tunnel," Proc. 45th Int. Instrumentation Symposium (Research Triangle Park, NC: Instrument Society of America), pp.345–54, 1999.

T. Liu and J. P. Sullivan, "Pressure and Temperature Sensitive Paints", Springer-Verlag, 2004.

Self-excited force models of nonlinear coupled flutter and model parameter identification via free vibration sectional model test

Le-Dong Zhu¹, Guang-Zhong Gao²

¹*State Key Laboratory of Disaster Reduction in Civil Engineering / Department of Bridge Engineering, Tongji University, Shanghai, China, Ledong@Tongji.edu.cn*

²*Highway College, Chang'an University, Xi'an, Shaanxi, China*

Abstract

Time histories of dynamic vertical and torsional displacements of and self-excited lift force and pitching moment acting on a spring-suspended sectional model of a typical flat closed-box bridge deck were measured simultaneously during the occurrence of nonlinear self-limiting coupled flutters. A pair of nonlinear mathematical models of self-excited forces was then presented via trial-and-error. A 2D analysis approach for nonlinear coupled flutter was proposed for carrying out the trial-and-error as well as for identifying the model parameters based on an approximate linear complex mode decomposition. A feasible approach for identifying the model parameters was finally put forward correspondingly and verified via comparing the calculated displacement responses of the nonlinear coupled flutter with the measured ones.

Keyword: nonlinear coupled flutter, nonlinear self-excited force, mathematical model, parameter identification, 2D analysis of nonlinear coupled flutter

1 Introduction

Although flutter of long-span bridges is conventionally treated as a linear problem of wind-induced instability based on various types of linear self-excited force models (Scanlan, 1978; Xie and Xiang, 1985; Agar, 1989; Scanlan and Jones, 1990; Namini et al., 1992; Zasso, 1996; Ge and Tanaka, 2000; Chen et al., 2001; Ding, et al., 2002), its nonlinear behaviors, characterized by phenomena of self-limiting of vibration response, limit cycles oscillation(LCO), distortion of vibrating form of aeroelastic self-excited forces from sinusoidal wave, higher-order multiple frequency components in aeroelastic self-excited forces, amplitude-dependence of linear flutter derivatives, nonlinear hysteresis effects of measured aeroelastic self-excited forces, etc., have been found on bluff bridge decks with various type of cross sections, such as flat rectangular section, π -shape section, twin edge-girder section, fully-closed and semi-closed box sections, etc., by various researchers (Noda, 2003; Diana et al., 2004, 2008 and 2010; Náprstek et al., 2007, 2008, 2011; Xu and Chen, 2009; Liao et al., 2011; Amandolese, 2013; Zhu and Gao, 2015, 2016; Zhu et al., 2016; Zhang, 2017; Zhang et al., 2017; Gao et al., 2018). To explore the nonlinear mechanism of flutter and self-excited forces and predict the nonlinear flutter responses of long-span bridges, mathematically modeling nonlinear aeroelastic forces on bridge decks is very necessary, but still not sufficient.

Náprstek et al. (2007, 2011) proposed a nonlinear self-excited forced model as an extension of classical linear formula by combining Rayleigh or Van der Pol with Duffing types of nonlinear heave-torsion coupled differential equations, and then extensively

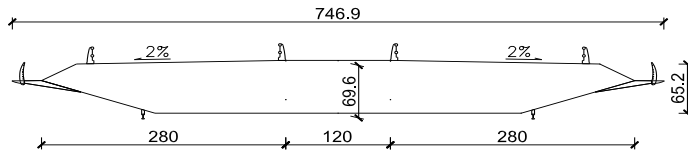
explored various nonlinear behaviors in post-critical state (Náprstek et al., 2007). Diana et al. (2008) proposed a numerical approach to model the various aerodynamic nonlinearities using a rheological mechanical model, and an improved version of a band superposition method to model the aerodynamic nonlinear effect induced by large-amplitude fluctuations of instantaneous angle of attack arising from torsional and vertical motion as well as turbulent wind components (Diana et al., 2013). Liu and Ge (2013) proposed a set of nonlinear differential equations with internal states to model nonlinear and unsteady characteristics of bridge aerodynamics. Wu and Kareem (2013) established a nonlinear convolution scheme using Volterra series to model nonlinear self-excited force. However, the above modelling of nonlinear self-excited forces are rather complicated and inconvenient for practical applications. Based on the equivalent linearization approach, Zhu and Gao presented a nonlinear model of self-excited torsional moment for the single degree of freedom (SDOF) nonlinear torsional flutter of a twin edge-girder deck by considering the amplitude-dependent effect of linear flutter derivatives (Zhu and Gao, 2016), but it is not effective enough for exploring the mechanism of nonlinear flutter in details. In this connection, Gao and Zhu (2018) proposed and verified a relative simplified nonlinear mathematical model of self-excited torsional moment similar to the Scanlan's linear model by introducing a cubic angle velocity term and a cubic angle displacement term to consider the nonlinear effects of aerodynamic damping and stiffness. In conjunction with a correspondingly proposed two-step least square approach based on the measured series of periodical work and reactive work for the identification of model parameters, this simplified nonlinear mathematical model is very convenient to application and is feasible and reliable to predict the stable amplitude of nonlinear SDOF torsional flutter. However, flutter of flat fully-closed box deck, which has been used frequently in long-span bridges, commonly show a coupled pattern in vertical and torsional degrees of freedom with some phase difference which may change during vibration. In this connection, a pair of nonlinear mathematical model of aeroelastic self-excited lift force and torsional moment of the nonlinear coupled flutter as well as the corresponding model parameter identification approach were then presented and are going to be introduced infra.

2 Wind tunnel test of sectional model on nonlinear coupled flutter

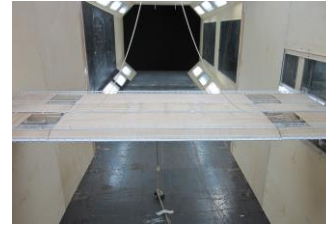
A typical flat fully-closed box deck as shown in Fig.1 was taken as the background for the investigation of nonlinear coupled flutter in this study. A series of spring suspended sectional model test were carried out in TJ-2 wind tunnel in Tongji University, and the time histories of the vertical and torsional displacements as well as the self-excited lift force and torsional moment were simultaneously measured when self-limiting nonlinear coupled flutter happened at different testing wind speeds. The detailed information about the fully-closed box deck as well as the sectional model tests of nonlinear coupled flutter, including the measurement of dynamic displacement responses, the measurement and verification of self-excited lift force and torsional moment can be referred to Zhu et al. (2016).

It was found from the test results that the flutter of the concerned flat fully-closed box deck always exhibited notable coupled pattern in torsional and vertical DOFs, and both the vertical and torsional displacement responses of the coupled flutter were dominated by the first-order component of the 2nd fundamental frequency of the sectional model system, which corresponding to the torsional frequency of model system without wind. Furthermore, the wave shapes of both the time histories of the self-excited lift and torsional moment deviates notably from normal sinusoidal curves, and the spectra also contain significant peaks at higher-order multiple frequencies. This means that the self-excited lift and

torsional moment of this kind of flat fully-closed box deck has notable nonlinearity.



(a) cross section



(b) Sectional model in TJ-2 wind tunnel

Figure 1: Wind tunnel test of spring-suspended sectional model of fully-closed box deck

3 Nonlinear mathematical models of self-excited forces of coupled flutter

The nonlinearity of aeroelasticity is due to the complex nonlinear behaviors of the interaction between the structural vibration and the surrounding flows. From a quasi-steady perspective, it can be interpreted as the result of the continuous change of the structural aerodynamic shape along the transient resultant wind including the effect of relative wind caused by structural vibration, i.e., the continuous change of effective attack angle of the transient resultant wind. Therefore, the nonlinear self-excited forces can be expressed nonlinear functions of the displacement and velocity of torsional angle response, even those of the vertical displacement response, which can cause the change of effective attack angle of and thus the aerodynamic shape along the transient resultant wind. However, by noticing that the flutter mode of the nonlinear coupled flutter of flat closed box decks evolves from the initial torsional mode of the structure without wind action, it can be inferred that the nonlinearity of the self-excited forces of coupled flutter should be mainly resulted by the displacement and velocity of torsional angle. Further based on the observed spectral characteristics of the measured excited forces, the following nonlinear mathematical model of the self-excited lift force (L_{se}) and torsional moment (M_{se}) were presented via trial-and-error.

$$L_{se} = \rho U^2 B \left[KH_1^* \frac{\dot{h}}{U} + KH_2^* \frac{B\dot{\alpha}}{U} + K^2 (H_3^* + H_{3,30}^* \alpha^2 + H_{3,50}^* \alpha^4) \alpha + K^2 H_4^* \frac{h}{B} \right] \quad (1a)$$

$$M_{se} = \rho U^2 B^2 \left\{ KA_1^* \frac{\dot{h}}{U} + K \left[A_2^* + A_{2,03}^* \left(\frac{B\dot{\alpha}}{U} \right)^2 + A_{2,05}^* \left(\frac{B\dot{\alpha}}{U} \right)^4 \right] \frac{B\dot{\alpha}}{U} + K^2 A_3^* \alpha + K^2 A_4^* \frac{h}{B} \right\} \quad (1b)$$

where, U is the wind speed; ρ is the air density; B is the deck width; h , α and \dot{h} , $\dot{\alpha}$ are the vertical and torsional displacements and velocity of nonlinear flutter, respectively; H_i^* and A_i^* are the linear aeroelastice parameters while $H_{3,jk}^*$ and $A_{2,jk}^*$ are the nonlinear aeroelastic parameters of the self-excited forces to be identified via wind tunnel test, the subscripts j and k represent the order numbers of the torsional angle (α) and angle velocity ($\dot{\alpha}$) in the corresponding nonlinear terms.

4 2D Approximate linear complex modal decomposition approach for nonlinear coupled flutter analysis of 2DOF oscillation system

Comparing the calculated responses of nonlinear flutter with the measured results is necessary for developing the nonlinear mathematical models of self-excited forces via trial-and-error and also for verifying the final proposed nonlinear mathematical model.

Therefore, a 2D analysis approach for calculating the displacement responses of nonlinear coupled flutter of the sectional model system was firstly developed based on an approximate linear complex modal decomposition.

The motion equations of nonlinear coupled flutter of the 2-DOF sectional model system can be written as follows:

$$(J + J_0)\ddot{\alpha} + \tilde{c}_\alpha(\rho_\alpha)\dot{\alpha} + \tilde{k}_\alpha(\rho_\alpha)\alpha = M_{se}(\alpha, \dot{\alpha}, h, \dot{h}) \quad (2a)$$

$$(m + m_0)\ddot{h} + \tilde{c}_h(\rho_h)\dot{h} + \tilde{k}_h(\rho_h)h = L_{se}(\alpha, \dot{\alpha}, h, \dot{h}) \quad (2b)$$

where, J and J_0 is the structural and non-wind-induced added inertial moments of mass while m and m_0 is the structural and non-wind-induced added mass of sectional model per unit length; $\tilde{c}_\alpha(\rho_\alpha), \tilde{k}_\alpha(\rho_\alpha)$ and $\tilde{c}_h(\rho_h), \tilde{k}_h(\rho_h)$ are, respectively, the equivalent linearized transient amplitude-dependent structural damping coefficients and stiffness coefficients of torsional and vertical vibrations of the sectional model system; ρ_α and ρ_h are the transient vibration amplitudes of nonlinear flutter of the sectional model system, respectively.

Under an arbitrary initial excitation, the transient responses of the 2-DOF sectional model oscillation system during the initial phase will contain two frequency components, respectively corresponding to two natural modes. Before the occurrence of nonlinear flutter, both of the two vibration components will decay because the system damping ratios of two the vibration modes are positive. When the wind speed exceeds the onset wind speed of nonlinear flutter, the system damping ratio of the flutter mode corresponding to the torsional mode at zero wind speed will become negative during the early stage of nonlinear flutter while that of the non-flutter mode corresponding to the vertical mode at zero wind speed will commonly keep positive and get larger and larger with the increase of wind speed. Thus, the transient response of the non-flutter mode will decay soon with time, and the response of the flutter mode will grow firstly, and the increasing rate of the vibration amplitude will get down gradually to zero due to the nonlinear effect of aeroelasticity, and final the flutter vibration become a stable LCO at a single frequency. This has been demonstrated in many sectional model tests of nonlinear flutter.

However, if one calculates the system responses by solving the Eq.1 directly in time domain by using a hybrid time-frequency domain model of self-excited forces, where all the linear or nonlinear aeroelastic parameters of the force models are expressed as functions of reduced frequency, the calculated responses of the non-flutter mode may not decay, which does not comply with the test results. This is because only one reduced frequency can be input for determining the self-excited forces, but the transient responses contain two frequency components. Therefore, the self-excited forces generated by the transient responses of the non-flutter mode will be wrongly calculated, leading to the fake modal responses disturbing the normal flutter responses.

To solve this problem, a 2D approximate linear complex decomposition (ALCMD) approach is thus proposed for the nonlinear coupled flutter analysis of 2DOF oscillation system. The foundation of this approach is that the nonlinear aerodynamic stiffness is quite small compared with structural stiffness and its effect on system stiffness can be ignored. The procedure of this 2D ALCMD approach is as follows:

(1) Complex modal analysis based on the following linear equations simplified from Eq.1

$$\ddot{\mathbf{y}}(t) + \mathbf{C}^e \dot{\mathbf{y}}(t) + \mathbf{K}^e \mathbf{y}(t) = 0 \quad (3)$$

$$\mathbf{y}(t) = (h, \alpha)^T, \mathbf{C}^e = \begin{bmatrix} 2\omega_h \xi_h - H_1 & -H_2 \\ -A_1 & 2\omega_\alpha \xi_\alpha - A_2 \end{bmatrix}, \mathbf{K}^e = \begin{bmatrix} \omega_h^2 - H_4 & -H_3 \\ -A_4 & \omega_\alpha^2 - A_3 \end{bmatrix} \quad (4)$$

Eq.3 can then be transformed to the following state equation:

$$\dot{\mathbf{x}}(t) = \mathbf{A}\mathbf{x}(t), \quad \mathbf{x}(t) = [\mathbf{y}(t) \dot{\mathbf{y}}(t)]^T, \mathbf{A} = \begin{bmatrix} \mathbf{0} & \mathbf{I} \\ -\mathbf{K}^e & -\mathbf{C}^e \end{bmatrix} \quad (5)$$

The linear system expressed by Eq.5 has two pairs of conjugated complex eigen values and eigen vectors as follows:

$$\lambda_1, \lambda_1^*, \lambda_2, \lambda_2^*; \quad \Psi_1, \Psi_1^*, \Psi_2, \Psi_2^*; \quad \Psi_r = [\phi_{hr} \quad \phi_{ar} \quad \lambda_r \phi_{hr} \quad \lambda_r \phi_{ar}]^T \quad (6)$$

(2) Approximate decomposition of the nonlinear equation of Eq.2

Eq.2 of the nonlinear system can be written as the following state equation:

$$\dot{\mathbf{x}}(t) = \mathbf{A}\mathbf{x}(t) + \mathbf{F}_{se,non} \quad (7)$$

$$\begin{aligned} \mathbf{F}_{se,non} &= \begin{bmatrix} 0 & 0 & L_{se,non}(\alpha, \dot{\alpha}, h, \dot{h}) & M_{se,non}(\alpha, \dot{\alpha}, h, \dot{h}) \end{bmatrix}^T \\ &= \begin{bmatrix} 0 & 0 & L_{se,non}(\mathbf{x}) & M_{se,non}(\mathbf{x}) \end{bmatrix}^T \end{aligned} \quad (8)$$

where, $L_{se,non}(\alpha, \dot{\alpha}, h, \dot{h})$ and $M_{se,non}(\alpha, \dot{\alpha}, h, \dot{h})$ are the nonlinear parts of the self-excited lift force (L_{se}) and torsional moment (M_{se})

By operating the following regular transformation on the state variable \mathbf{x} ,

$$\mathbf{x} = \mathbf{P}\mathbf{z}, \mathbf{P} = [\Psi_1 \quad \Psi_1^* \quad \Psi_2 \quad \Psi_2^*] \quad (9)$$

where, \mathbf{z} is the generalized coordinates of complex modes, and it nonlinear state equation can be expressed as follows:

$$\dot{\mathbf{z}}(t) = \mathbf{P}^{-1}\mathbf{A}\mathbf{P}\mathbf{z} + \mathbf{P}^{-1}\mathbf{F}_{se,non} = \mathbf{\Lambda}\mathbf{z} + \mathbf{P}^{-1}\mathbf{F}_{se,non} \quad (10)$$

$$\mathbf{\Lambda} = [\lambda_1 \quad \lambda_1^* \quad \lambda_2 \quad \lambda_2^*] \quad (11)$$

Strictly speaking, the vertical and torsional DOFs in Eq.10 are not decomposed completely because there are coupled terms existing in the nonlinear part of the self-excited forces ($\mathbf{F}_{se,non}$). However, as mentioned above, the responses of the non-flutter mode will decay rapidly with time, therefore, the coupling effect of non-flutter mode responses in $\mathbf{F}_{se,non}$ should be very weak and can be ignored. Thus, the coupled nonlinear equation shown as Eq.2 can be approximately decomposed, and the responses of flutter mode can be express with the following two equation conjugated with each other:

$$\dot{z}_3(t) = \lambda_2 z_3(t) + \mathbf{P}^{-1}(3,:) \mathbf{F}_{se,non} \quad (12a)$$

$$\dot{z}_4(t) = \lambda_2^* z_3^*(t) + \mathbf{P}^{-1}(4,:) \mathbf{F}_{se,non} \quad (12b)$$

Solving anyone of the above two conjugated equations in time domain with Runge-Kutta method or Newmark- β method step by step yields the vertical and torsional responses of nonlinear coupled flutter.

$$\mathbf{x} = \Psi_2 z_3(t) + \Psi_2^* z_4^*(t) = 2 \text{Re}[\Psi_2 z_3(t)] \quad (13)$$

5 Parameter identification of nonlinear self-excited force models of coupled flutter

The identification of the parameters of the proposed nonlinear self-excited lift force and torsional moment for analyzing the couple flutter as shown in Eq.1 can be carried out by following steps.

(1) Identifying the equivalent Scanlan linear flutter derivatives by using the modified least square (MLS) method proposed by Ding et al. (2012)

By using the recorded free vibration response signals of sectional model system, the complex modal parameters of the sectional model system under different wind speeds are to be identified at first, where, the interval of wind speed should be sufficient small. Then, for every specified reduced frequencies or reduced wind speeds, the corresponding complex modal parameters of the sectional model system can be obtained by interpolation according to the tested values at two adjacent testing wind speeds. Afterwards, the Scanlan linear flutter derivatives H_i^* and A_i^* can be identified for all specified reduced frequencies or reduced wind speeds.

For the reduced wind speeds within occurrence region of nonlinear flutter, the complex modal parameters as well as the equivalent linear flutter derivatives in small amplitude case during the early stage and in the large amplitude case during the stable stage of nonlinear flutter vibration need to be identified. The equivalent linear flutter derivatives at small amplitude and large stable amplitude are denoted as $H_{i,s}^*$, $A_{i,s}^*$ and $H_{i,L}^*$, $A_{i,L}^*$, respectively.

(2) Establishing the following relationships among the nonlinear aeroelastic parameters in the proposed nonlinear mathematical models of self-excited forces ($H_{3,jk}^*$ and $A_{2,jk}^*$), the equivalent linear flutter derivatives ($H_{i,s}^*$, $A_{i,s}^*$ and $H_{i,L}^*$, $A_{i,L}^*$) and the transient amplitude of torsional displacement response (a_α) based on the equivalent linearization approach:

$$H_{3,L}^* = H_{3,s}^* + \frac{3}{4} a_\alpha^2 H_{3,30}^* + \frac{5}{8} a_\alpha^4 H_{3,50}^* \quad (14a)$$

$$A_{2,L}^* = A_{2,s}^* + \frac{3}{4} K^2 a_\alpha^2 A_{2,03}^* + \frac{5}{8} K^4 a_\alpha^4 A_{2,05}^* \quad (14b)$$

(3) Establishing the relationships among the nonlinear aeroelastic parameters and the nonlinear damping parameters by using the vibration signals during the growing stage of nonlinear flutter.

As derived in Section 4, the generalized coordinate of the torsional flutter mode can be written as:

$$\dot{z}_t = \lambda_t z_t + \mathbf{P}^{-1} \mathbf{F}_{se,non} \Big|_t \quad (15)$$

By separating the real part and imaginary part of the above generalized coordinate, one can obtain the following equation about the generalized coordinate:

$$\ln a(t) - \ln a(t_0) = \delta_0 (t - t_0) + C_1 \int_{t_0}^t a^2 d\tau + C_2 \int_{t_0}^t a^4 d\tau \quad (16)$$

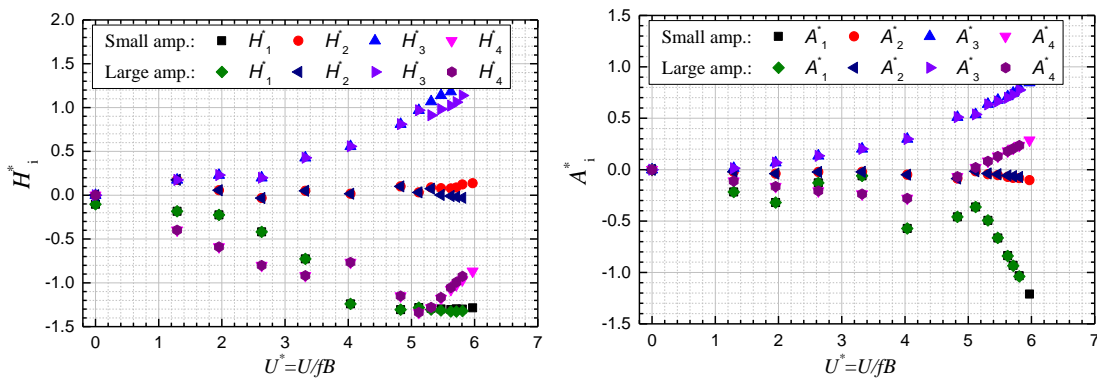
where, δ_0 is the logarithmic decrement of linear damping of the torsional flutter mode; C_1 and C_2 are two coefficients of nonlinear damping and can be identified according to Eq.16 by using the measured signals of torsional flutter responses. Then, the relationships among the nonlinear aeroelastic parameters and the nonlinear damping parameters can be founded as follows:

$$\frac{C_1}{3\rho U^2 BK^2} = \frac{q_{1,r}}{m} H_{3,30}^* - \frac{q_{2,i} BK^2}{J_m} A_{2,03}^* \quad (17a)$$

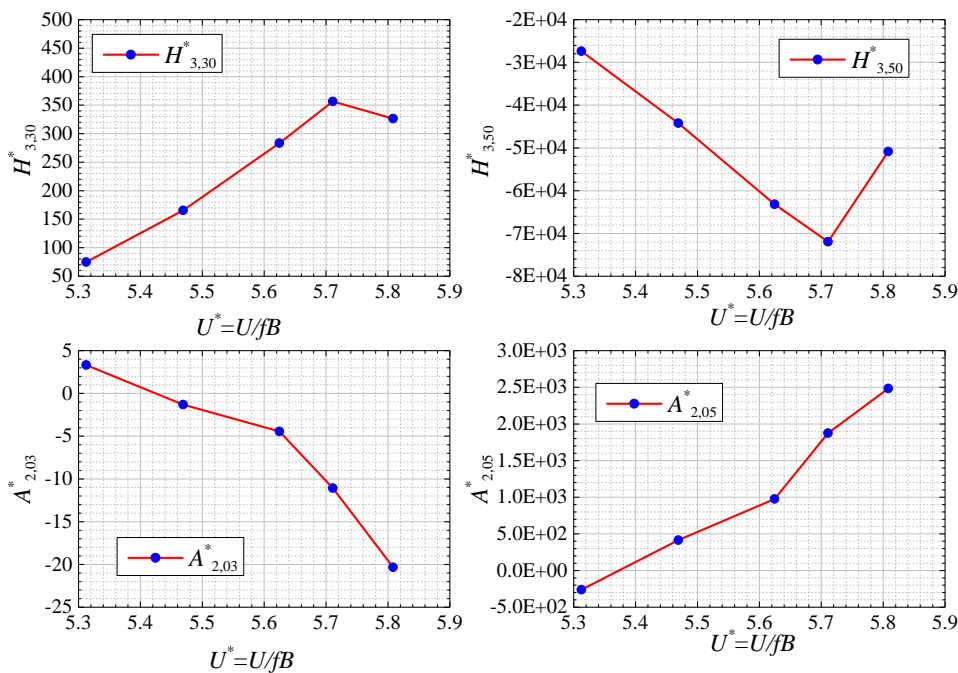
$$\frac{C_2}{10\rho U^2 BK^5} = \frac{q_{1,r}}{m} H_{3,50}^* - \frac{q_{2,i} BK}{J_m} A_{2,05}^* \quad (17b)$$

where, $q_{1,r}$ and $q_{2,i}$ are two constants with respect to the parameters of linear complex mode and mass. The nonlinear aeroelastic parameters ($H_{3,jk}^*$ and $A_{2,jk}^*$) can then be determined by solving the equation of Eq.14 and Eq.17.

Fig.2 exhibits the identified linear and nonlinear aeroelastic parameters of the nonlinear mathematical model of coupled self-excited lift force and torsional moment (see Eq.1) of the fully-closed box deck as shown in Fig.1b. The corresponding wind attack angle is 5° .



(a) Linear aeroelastic parameters (flutter derivative)



(b) Nonlinear aeroelastic parameters

Figure 2: Identified results of aeroelastic parameters of nonlinear self-excited force models of the fully-closed box deck (5° wind attack angle)

6 Verification of the nonlinear self-excited force model and parameter identification approach

In this section, the proposed nonlinear mathematical model of the coupled self-excited forces as well as the proposed identification approach of aeroelastic parameters of nonlinear self-excited force model are verified via comparing the responses of nonlinear flutter of the sectional model system of the flat closed-box deck calculated by using the proposed 2D ALCMD approach with the test results. Fig.3 shows the comparisons between the calculated time histories of both the vertical and torsional responses with the corresponding tested results for the wind attack angle of 5° and the reduced wind speed of $U^*=5.808\text{m/s}$. Fig.4 exhibits the comparisons between the calculated stable amplitudes of both the vertical and torsional responses at different reduced wind speeds with the corresponding tested results.

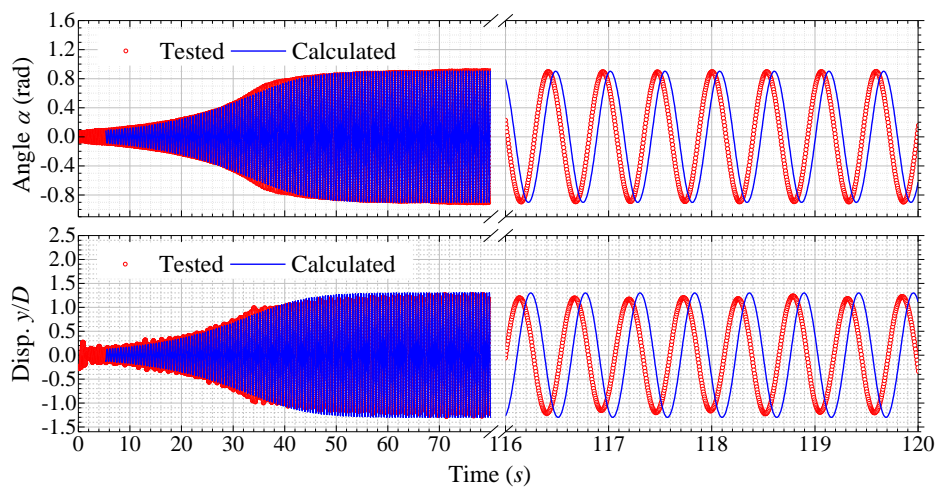


Figure 3: Comparisons between the calculated time histories of nonlinear flutter responses of the sectional model system (5° wind attack angle, $U^*=5.808\text{m/s}$)

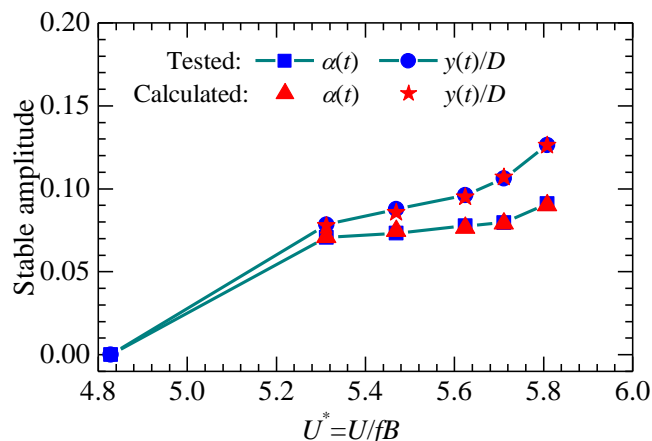


Figure 4: Comparisons between the calculated stable amplitudes of nonlinear flutter responses of the sectional model system (5° wind attack angle)

It can be found from these figures that the two sets of responses agree well to each other, except that there are some phase differences of long term responses because the nonlinear aerodynamic stiffness related to α for self-excited torsional moment and related to h for self-excited lift are excluded from the proposed nonlinear mathematical models. This proves that the proposed mathematical model of the coupled nonlinear self-excited force

model are suitable to flat fully-closed box deck, and the proposed parameter identification approach for the nonlinear mathematic model as well as the 2D ALCMD approach for analyzing the nonlinear flutter responses of 2 DOF system are feasible and reliable.

7 Conclusions

Nonlinear mathematical models of self-excited lift force and torsional moment forces and corresponding model parameter identification method were presented for predicting responses of nonlinear coupled flutter analysis. A 2D approximate linear complex mode decomposition approach was also proposed for calculating nonlinear coupled flutter responses of 2D sectional model system. The proposed mathematical models of couple self-excited forces and the parameter identification method as well as the ALCMD analysis method were finally verified to be feasible and reliable.

Acknowledgements

The work described in this paper was jointly supported by the National Natural Science Foundation of China (Grants 51938012, 51808052, 51478360), and the Fundamental Research Fund for State Key Laboratories of China (Grant No. SLDRCE15-A-03) which the authors are very grateful to.

References

- Agar, T.J.A., 1989. Aerodynamic flutter analysis of suspension bridges by a modal technique. *Engineering Structures* 11, 75-82.
- Amandolese, X., Michelin, S. and Choquel, M., 2013. Low speed flutter and limit cycle oscillations of a two-degree-of-freedom flat plate in a wind tunnel. *Journal of Fluids and Structures* 31, 244-255.
- Chen, X.Z., Kareem, A., and Matsumoto, M., 2001. Multimode coupled flutter and buffeting analysis of long span bridges. *Journal of Wind Engineering and Industrial Aerodynamics* 89, 649-664.
- Diana, G., Resta, F. and Rocchi, D., 2008. A new numerical approach to reproduce bridge aerodynamic non-linearities in time domain. *Journal of Wind Engineering and Industrial Aerodynamics* 96, 1871-1884.
- Diana, G., Resta, F., Zasso, A., Belloli, M., and Rocchi, D., 2004. Forced motion and free motion aeroelastic tests on a new concept dynamometric section model of the Messina suspension bridge. *Journal of Wind Engineering and Industrial Aerodynamics* 92, 441-462.
- Diana, G., Rocchi, D., and Argentini, T., 2013. An experimental validation of a band superposition model of the aerodynamic forces acting on multi-box deck sections. *Journal of Wind Engineering and Industrial Aerodynamics* 113, 40-58.
- Diana, G., Rocchi, D., Argentini, T., Muggiasca, S., 2010. Aerodynamic instability of a bridge deck section model: linear and nonlinear approach to force modeling. *Journal of Wind Engineering and Industrial Aerodynamics* 98, 363-374.
- Ding Q.S., Chen A.R. and Xiang H.F., 2002. Coupled flutter analysis of long-span bridges by multimode and full-order approaches. *Journal of Wind Engineering and Industrial Aerodynamics* 90, 1981-1993.
- Ding, Q.S., Wang J., and Zhu L.D., 2012. Coupled free vibration technique for identifying flutter derivatives of bridge decks. *Journal of Vibration and Shock* 31(24), 5-8, 25. (in Chinese)
- Gao, G., Zhu, L., Han, W., and Li, J. 2018. Nonlinear post-flutter behavior and self-excited force model of a twin-side-girder bridge deck. *Journal of Wind Engineering and Industrial Aerodynamics* 177, 227-241.

- Ge, Y.J., and Tanaka, H., 2000. Aerodynamic flutter analysis of cable-supported bridges by multi-mode and full-mode approaches. *Journal of Wind Engineering and Industrial Aerodynamics* 86, 123-153.
- Liao, H.L., Wang, Q., Li, M.S. and Ma, C.M. 2011. Aerodynamic hysteresis effects of thin airfoil and streamline box girder under large amplitude oscillation. In: *Proceedings of the 13th International Conference on Wind Engineering, Amsterdam, The Netherlands.*
- Liu, S.Y. and Ge, Y. J., 2013. Fitting method of nonlinear differential equations for aerodynamic forces of bridge decks. In: *Proceedings of the 12th Americas Conference on Wind Engineering, Seattle, USA.*
- Namini, A., Albrecht, P., and Bosch, H., 1992. Finite element-based flutter analysis of cable-suspended bridges. *Journal of Structural Engineering ASCE* 118(6), 1509-1526.
- Náprstek, J., and Pospíšil, S., 2011. Post-critical behavior of a simple non-linear system in a cross-wind. *Engineering Mechanics* 18, 193–201.
- Náprstek, J., Pospíšil, S. and Hračov, S., 2007. Analytical and experimental modeling of non-linear aeroelastic effects on prismatic bodies. *Journal of Wind Engineering and Industrial Aerodynamics* 95, 1315-1328.
- Náprstek, J., Pospíšil, S., Hö ffer, R., Sahlmen, J., 2008. Self-excited nonlinear response of a bridge-type cross section in post-critical state. In: *Proceedings of the 6th International Colloquium on Bluff Body Aerodynamics and Applications (BBAA6). Milano, Italy.*
- Noda, M., Utsunomiya, H., Nagao, F., Kanda, M. and Shiraishi, N., 2003. Effects of oscillation amplitude on aerodynamic derivatives. *Journal of Wind Engineering and Industrial Aerodynamics* 91, 101-111.
- Pigolotti, L., Mannini, C., Bartoli, G., and Thiele, K., 2015. Wind tunnel tests on elongated rectangular plates under flutter motion: limit-cycle oscillations and preliminary energy harvesting considerations. In: *14th International Conference on Wind Engineering (ICWE14). Porto Alegre, Brazil.*
- Scanlan, R.H., 1978. The action of flexible bridge under wind, I: flutter theory. *Journal of Sound and Vibration* 60(2), 187-199.
- Scanlan, R.H., and Jones, N.P., 1990. Aeroelastic analysis of cable-stayed bridges. *Journal of Structural Engineering ASCE* 116(2), 1279-297.
- Wu, T., and Kareem, A., 2013. A nonlinear convolution scheme to simulate bridge aerodynamics. *Computers and Structures* 128, 259-271.
- Xie, J.M., and Xiang, H.F., 1985. State-space method for 3D flutter analysis of bridge structures. In: *Proceedings of Asia Pacific Symposium on Wind Engineering, India, 269-276.*
- Xu, F.Y., Chen, A.R., 2009. Flutter test and analysis for the suramadu bridge in Indonesia. *China Civil Engineering Journal* 42 (1), 35–40. (in Chinese).
- Zasso, A., 1996. Flutter derivatives: Advantages of a new representation convention. *J. Wind Engineering and Industrial Aerodynamics* 60, 35-47.
- Zhang Z., 2017. Soft flutter and parameters identification of nonlinear self-excited aerodynamic force of bridge girders. PhD Dissertation, Tongji University, Shanghai.
- Zhang, M.J., Xu, F.Y., Ying, X.Y., 2017. Experimental investigations on the nonlinear torsional flutter of a bridge deck. *Journal of Bridge Engineering* 22 (8), 04017048.
- Zhu L., and Gao G., 2015. Influential factors of soft flutter phenomenon for typical bridge deck sections. *Journal of Tongji University* 43(9), 1289-1294 and 1382. (in Chinese)
- Zhu, L., Gao, G., and Hao, W., 2016. Nonlinear phenomena of coupled flutter responses and self-excited forces of a flat closed-box bridge deck. In: *Proceedings of the first International Symposium on Flutter and its Application, Tokyo, Japan.*
- Zhu, L.D., Gao, G.Z., 2016. A nonlinear self-excited force model for soft flutter phenomenon of a twin-side-girder bridge section. *Journal of Vibration and Shock* 35 (21), 29–35 (in Chinese)

Index

- Abdelbaki, A.R., 242
Abdukhakimov, F., 187
Aksenov, A.A., 244
Alazard, D., 438
Allandrieu, R., 272
Amandolese, X., 145, 333, 402, 483
Andrianne, T., 79, 277, 354, 365
Andronov, P.R., 431
Arévalo, F., 146
Arizono, H., 129, 248, 554, 572
Arnold, J., 82
Astolfi, J.A., 191, 355, 483
Aswathy, M.S., 530
- Béguin, C., 439
Bai, H., 344
Barrera, J., 146
Benetti Ramos, L., 261
Benner, B., 188
Bergmann, M., 261
Bernard, V., 402
Bernay, B., 79
Bethi, R.V., 118
Bin, Q., 368
Boersma, P., 188
Bose, C., 92, 260, 270, 271
Bot, P., 355
Botez, R.M., 217, 463
Braune, M., 134
Bueno, D.D., 463
- Cao, F., 311
Cao, N., 322
Cesnik, C.E.S., 532
Changchuan, X., 80, 512
Chao, A., 512
Chao, Y., 80, 512
Chassaing, J-C., 511, 521, 573
Chatterjee, R., 270
Chen, G-B., 436
Chen, G., 562
Chen, W-L., 436
- Chen, W., 280
Chen, Y., 243
Climent, H., 146
Couliou, M., 272
Currier, T.M., 145, 188
- Danilkin, S., 190
de la Cruz, V.R., 146
de Langre, E., 241
Deü, J-F., 483
Denoël, V., 343, 365
Dequand, S., 583
Descoteaux, P-O., 387
Di Donfrancesco, F., 573
Dimitriadis, G., 48, 79, 92, 354
Dowell, E.H., 196
Dubois, R., 79
Dubois, R., 354
Ducoin, A., 191
Dumas, G., 376, 377, 400
Dynnikova, G.Y., 431
- Ellingsen, Ø. M., 333
Emilian, J., 271
Epureanu, B.I., 532
- Faïsse, E., 438
Fabbiane, N., 472
Faure, T.M., 167
Feng, H., 401
Fernandez-Escudero, C., 451
Flamand, O., 452
Foster Stangarlin, P.H., 463
Freydin, M., 196
Fujita, K., 248
- Gali, S.V., 118
Gao, D-L., 436
Gao, D., 280
Gao, G-Z., 592
Ge, Y., 311
Geeraert, A., 583

- George, S., 191
Gosselin, F.P., 274, 439
Gunther, K., 400
Gupta, S., 270
Guvernyuk, S.V., 431
- Hémon, P., 333, 402
Hage Hassan, M., 402
Han, P., 412
Han, R., 562
Hanai, T., 291
Hebler, A., 134
Hehaibo, 68
Hirata, K., 276
Hiroaki, K., 206
Hoareau, C., 433
Horacek, J., 271
Huera-Huarte, F., 342
Hui, L., 462
- Ikegami, K., 413
Imamura, T., 135, 572
Intesaaf, A., 277
Iollo, A., 261
Irisarri, F-X., 472
Irpanni, H., 301
Ishimoto, J., 276
Isogai, K., 78
Iverson, D., 377
Iwase, T., 178
- Jinan, L., 484
- Kameyama, M., 413
Kanduri, V.S., 271
Karpel, M., 146, 543
Kasahara, N., 413
Kato, G., 276
Kato, K., 322
Katsuchi, H., 301
Kheirandish, H.R., 129
Kheiri, M., 156, 217
Kim, D., 216, 399
Kim, H., 216
Kim, J., 216, 399
Kim, Y.C., 193
Kirsch, B., 167
Kishitani, T., 178
Kiwata, T., 432
Koch, C., 82
- Kolotnikov, M., 187
Kono, T., 432
- Lübker, J., 245
Lai, J.C.S., 421
Laima, S., 531
Lan, Y., 80
Larsen, A., 281
Laurendeau, E., 451
Leclercq, T., 241, 450
Lee, W., 376, 377
Legrand, M., 217
Lepage, A., 472
Leroy, L., 355
Li, G., 484
Li, H., 280
Li, H., 531
Li, W., 531
Liao, H., 510
Liu, Y., 243
Lossouarn, B., 483
- Macdonald, J.H.G., 510
Mahbub Alam, Md., 259, 344, 368
Mai, H., 134
Majumdar, D., 258, 260
Makarov, P., 187
Mallik, W., 93
Mannini, C., 332
Marquet, O., 166, 261, 272, 273, 450
Martínez, Á., 146
Martínez, P., 146
Massai, T., 332
Matsuda, K., 322
Matsumiya, H., 353
Mazikina, T., 190
Mei, H., 510
Michon, G., 451
Misra, A.K., 242
Mitchel, T., 262
Mizota, T., 2
Modarres-Sadeghi, Y., 145, 188
Mondal, S., 437
Mons, V., 521
Montagnier, O., 167
Morlier, J., 438
Mortchelewicz, G-D., 583
Moulin, J., 166
Muhammad, Z., 259

- Murozono, M., 248
Mysa, R.C., 227
- Nagai, H., 248
Nagasaki, S., 248
Nagase, R., 432
Naito, Y., 276
Nakakita, K., 554
Nakamichi, J., 498
Nakamura, K., 248
Nakano, M., 276
Naresh, S., 277
Nishihara, T., 353
Noguchi, T., 276
Numata, D., 544, 584
- Olivier, M., 387
Oshkai, P., 376, 377
- Paidoussis, M.P., 217, 242
Pan, G., 412
Paramasivam, A.R., 388, 437
Peake, N., 241
Pernod, L., 483
Pfister, J-L., 272, 273
Placzek, A., 573
Poplingher, L., 106
Prothin, S., 451
- Rønne, M., 281
Ramanarivo, S., 262
Raveh, D.E., 93, 106
Raynaud, G., 261
Redkin, D., 190
Rendu, Q., 189
Riazat, M., 156
Ribeiro, F.A., 463
Rigo, F., 365
Rishmawi, S.W., 439
Riso, C., 532
Ristroph, L., 262
Rosa Franzini, G., 439
Ross, A., 451
Roy, A., 388
- Saitoh, K., 440, 554
Salinas, M.F., 217
Santos, E., 146
Sarkar, S., 258, 260, 270, 530
Selwanis, M.M., 439
- Shang, L., 433
Sharifi, M., 511
Shen, S., 401
Shi, X., 344
Shigetomi, K., 322
Shimizu, M., 353
Shishaeva, A.S., 244
Shkurov, V., 190
Soneda, K., 135, 572
Su, W., 572
Sundar, R., 258
Sushko, G.B., 244
- Tadrist, L., 277
Takeguchi, M., 291
Tamayama, M., 498
Tamura, Y., 193
Tanigawa, H., 276
Taruishi, S., 353
Tavallaeinejad, M., 217
Teleshev, V., 190
Toyama, N., 291
Tsushima, N., 135, 554, 572
- Ueno, T., 432
Usuh, C., 421
- Vahdati, M., 189
Varun, H.S., 530
Vedeneev, V., 187, 487
Vedeneev, V.V., 244
Venkatraman, K., 227
Venkatramani, J., 118, 271, 388, 437
Vernay, R., 438
Vetrano, F., 438
Vicenti, A., 511
- Wakayama, A., 544, 584
Wang, K., 401
Wang, Y., 562
Watanabe, M., 206
Wenhan, Y., 462
Wenli, C., 462
- Xia, W., 401
Xiaolong, C., 68
Xie, C., 522
Xinjiang, W., 484
- Yamada, H., 301

Yamamoto, I., 264
Yang, C., 522
Yang, L., 522
Yang, Y., 311
Yashiro, S., 248
Yi, L., 68
Yokozeki, T., 135, 572
Yoshimoto, N., 440
Young, J., 421
Yukino, T., 353

Zastrow, J.C.I., 81
Zhang, B., 412
Zhao, L., 311
Zhenlin, C., 368
Zhitao, Z., 80
Zhou, Y., 368
Zhu, L-D., 592
Zilian, A., 433

Sponsored by

MÜLLER-BBM
VibroAkustik Systeme

Organized by



LadHyX

le **cnam**



X. Amandolese & P. Hémon (ed.)
Proceedings of the Second International Symposium on Flutter and its Applications
Paris, 12-14 May, 2020